Mohamed Haddar
Fakher Chaari
Abdelmajid Benamara
Mnaouar Chouchane
Chafik Karra
Nizar Aifaoui *Editors*

Design and Modeling of Mechanical Systems—III

Proceedings of the 7th Conference on Design and Modeling of Mechanical Systems, CMSM'2017, March 27–29, Hammamet, Tunisia

🐎 Springer

Lecture Notes in Mechanical Engineering

Lecture Notes in Mechanical Engineering (LNME) publishes the latest developments in Mechanical Engineering—quickly, informally and with high quality. Original research reported in proceedings and post-proceedings represents the core of LNME. Also considered for publication are monographs, contributed volumes and lecture notes of exceptionally high quality and interest. Volumes published in LNME embrace all aspects, subfields and new challenges of mechanical engineering. Topics in the series include:

- Engineering Design
- Machinery and Machine Elements
- Mechanical Structures and Stress Analysis
- Automotive Engineering
- Engine Technology
- Aerospace Technology and Astronautics
- Nanotechnology and Microengineering
- Control, Robotics, Mechatronics
- MEMS
- Theoretical and Applied Mechanics
- Dynamical Systems, Control
- Fluid Mechanics
- Engineering Thermodynamics, Heat and Mass Transfer
- Manufacturing
- Precision Engineering, Instrumentation, Measurement
- Materials Engineering
- Tribology and Surface Technology

More information about this series at http://www.springer.com/series/11236

Mohamed Haddar · Fakher Chaari
Abdelmajid Benamara · Mnaouar Chouchane
Chafik Karra · Nizar Aifaoui
Editors

Design and Modeling of Mechanical Systems—III

Proceedings of the 7th Conference on Design and Modeling of Mechanical Systems, CMSM'2017, March 27–29, Hammamet, Tunisia

الانارة للاستشارات

Editors
Mohamed Haddar
National School of Engineers of Sfax
Sfax
Tunisia

Mnaouar Chouchane
National School of Engineers of Monastir
Monastir
Tunisia

Fakher Chaari
National School of Engineers of Sfax
Sfax
Tunisia

Chafik Karra
Sfax Preparatory Engineering Institute
Sfax
Tunisia

Abdelmajid Benamara
National School of Engineers of Monastir
Monastir
Tunisia

Nizar Aifaoui
National School of Engineers of Monastir
Monastir
Tunisia

Preface

The seventh edition of the "International Congress Design and Modelling of Mechanical Systems" CMSM'2017 was held in Hammamet, Tunisia, from 27 to 29 March 2017. This congress was organized jointly between two Tunisian research laboratories: the Laboratory of Mechanics, Modelling and Production of the National school of Engineers of Sfax and the Laboratory of Mechanical Engineering of the National School of Engineers of Monastir.

This book is the third volume of the LNME book series "Design and Modelling of Mechanical Systems". It contains 123 papers presented during the CMSM'2017 congress. More than 300 participants discussed during the 3 days of the congress, latest advances in the field of design and modeling of mechanical systems. Similar to the past editions, the topics presented and discussed during the congress were very broad covering of research topics of mechanical modeling and design.

The organizers of the conference were honored by the presence of 10 keynote speakers, who are experts in the field of modeling of mechanical systems, namely:

- Prof. Jean Yves Choley, Laboratory QUARTZ, SUPMECA, Paris, France
- Prof. José Antunes, Applied Dynamics Laboratory, IST, Lisbon, Portugal
- Prof. Mohamed Najib Ichchou, Laboratory of Tribology and System Dynamics, Ecole centrale de Lyon, France
- Prof. Mabrouk Ben Tahar, Laboratory Roberval, Université de Technologie de Compiégne, France
- Prof. Jean-François Deu, Structural Mechanics and Coupled Systems Laboratory, CNAM, Paris, France
- Prof. Abdelkhalek El Hami, Laboratory Optimization and Reliability in Structural Mechanics, INSA Rouen, France
- Prof. Ming J. Zuo, University of Alberta, Edmonton, Alberta, Canada
- Prof. Yvon Chevalier, Supmeca, Paris, France

- Prof. Hachmi Ben Dhia, MSSMat Laboratory, CentraleSupélec, Paris-Saclay University, France
- Prof. Taoufik Boukharouba, Laboratory of Advanced Mechanics "LMA", USTHB, Alger—Algeria.

Each chapter included in this book was rigorously reviewed by two referees. Our gratitude goes to all members of the scientific committee for their valuable efforts to reach a high quality of contributions.

We would like also to thank all authors, presenters, and participants of seventh edition of CMSM'2017. Finally, special thanks go to Springer for their continuous support of this conference.

Hammamet, Tunisia   Mohamed Haddar
March 2017   Fakher Chaari
                                                               Abdelmajid Benamara
                                                               Mnaouar Chouchane
                                                                     Chafik Karra
                                                                     Nizar Aifaoui

Contents

Enhancing Efficiency of InGaN Nanowire Solar Cells by Applying Stress

Rabeb Belghouthi, Tarek Selmi and Hafedh Belmabrouk

Abstract In photovoltaic solar cells, p-n junctions have been considered a very promising structure to improve the carrier collection efficiency and accordingly the conversion efficiency. The basic processes for a solar cell to work are the generation of electron–hole pairs, separation, and recombination of those carriers in external circuits. The step of critical importance here is the electron–hole pair separation. The inner piezopotential, formed in the crystal by applying a stress which is called piezophototronic effect, interferes directly in the separation and recombination process, and consequently affects the solar cell performance. Recently, elaborated models including the piezophototronic effect were proposed to simulate metal/semiconductor and a p-n junction based in ZnO, but discussion of results has been limited to the output and the open-circuit voltage. In the present work, we will attempt to extend systematically the modeling of photovoltaic conversion on solar cell. The piezophototronic effect is included both in transport equation and photocurrent. Finally, the experimental results of organic solar cells support our theoretical model. Using the piezoelectric effect created by external stress, our study not only provides the first basic theoretical understanding about the piezophototronic effect on the characteristics of an inorganic solar cell, but also assists the design for higher performance solar cells.

R. Belghouthi (✉)
Laboratory of Electronics and Microelectronics, University of Monastir,
Monastir 5019, Tunisie
e-mail: rabebbelghouthi@gmail.com

T. Selmi
Department of Mechanical and Mechatronics, Faculty of Engineering,
Sohar University, Sohar, Oman
e-mail: tarakissat@gmail.com

H. Belmabrouk
Department of Physics, College of Science AlZulfi, Majmaah University,
Al Majmaah 11952, Saudi Arabia
e-mail: hafedh.belmabrouk@gmail.com

1 Introduction

Currently, the technology of semiconductor with piezoelectric properties such as ZnO, Cds InN, and GaN seems to be most promising for the realization of electronic and optoelectronic devices. By using coupled semi-conducting and piezoelectric properties, some piezoelectric devices including nano-generators (Wang and Song 2006), piezoelectric field effect transistors (Kwon et al. 2008), piezoelectric diode (Yang et al. 2011a), and solar cell (Yang et al. 2011b) have been successfully demonstrated. In recent years, various articles have reported the effect of piezophototronic on performance solar cells. This effect describes the phenomenon that the efficiency of charge generation, separation, or recombination is tuned by the polarization charge at the interface created by external stress. The performance of devices can be enhanced or degraded depending on the sign of the charges. As it is found, the piezoelectric charges localized at the interface are positive, they will contribute to the increase of electric field and consequently improve the quantum efficiency of dissociation. Even though the charges are negative, they will be a decrease in the electric field which adversely affects their performance of the cell (Yang et al. 2011a, b); Piezopolarization charges at p-n junction interface directly with the separation and recombination process and it has been theoretically predicted (Maugin et al. 1988) as well as experimentally proved (Zhang et al. 2012) that this effect does affect solar cell efficiencies. The working principal of the piezoelectric solar cell is based on using the high electric field in the depletion region to separate the electron-trou pairs that incident photons produce. The solar cell performance can be tuned by piezoelectric charges created at the junction area under strain. However, all the previous studies were concentrated on demonstrating the effect itself without providing guidance on how the selection and the tuning of materials properties can strengthen the piezophototronic effect. The main objectif of the present paper is to examine the piezophototronic effect on the inorganic solar cell performance. The best example to describe that is InGaN. Our attention is focused especially on InGaN mainly due to their tunable band gaps and superior photovoltaic characteristics (Wen et al. 2013); For InGaN, the band gap can vary continuously from ultraviolet at 0.77 eV to the infrared at 3.42 eV, which matches well with the whole solar spectrum. Additionally, InGaN-related systems show many other favorable properties including high absorption coefficients, high carrier mobility, saturation velocities, and a superior radiation resistance (Belghouthi et al. 2016). Inevitably, the strain introduced in the device by applying a stress may strongly affect the open-circuit voltage, maximum output power, and fill factor. These elements are the main key parameters that can help us to evaluate the performance of the solar cell. So, we can be effective by playing on the sign and the value of stress modulated and optimized the effectiveness of the solar cell. Tensile

strain is defined as positive, and compressive strain is defined as negative. Our analytical results are obtained for InGaN piezoelectric p-n junction solar cell under simplified conditions, which provides a basic physical picture for understanding the mechanism of the piezoelectric solar cell. Results provided by the piezophotronic enhancing efficiency are applicable to all solar cell systems involving piezoelectric semiconductor material. The objective of our study is also to assist a new design of higher performance solar cells. Finally, experimental results of organic solar cells support our theoretical model.

2 Basic Equations

The schematic of InGaN p-n solar cell is shown in Fig. 1; A z-axis is divined along the c-axis of InGaN nanowire with z = 0 representing the end of the p-type. The length of the p-region and n-region respectively are taken as 20 nm and 80 nm. For the design purpose, the diameter of the nanowire is assumed to be 20 nm, and we assume that the p-type region is non-piezoelectric and n-type is piezoelectric. The piezoelectric charges are considered as surface charges at the bulk piezoelectric material because the region within which the piezoelectric polarization charges distribute is much smaller than the volume of the bulk crystal, making it reasonable to assume that the piezoelectric charge are distributed at a surface of zero thickness and it is taken as $W_p = 0.25$ nm, which is about one atomic layer in thickness.
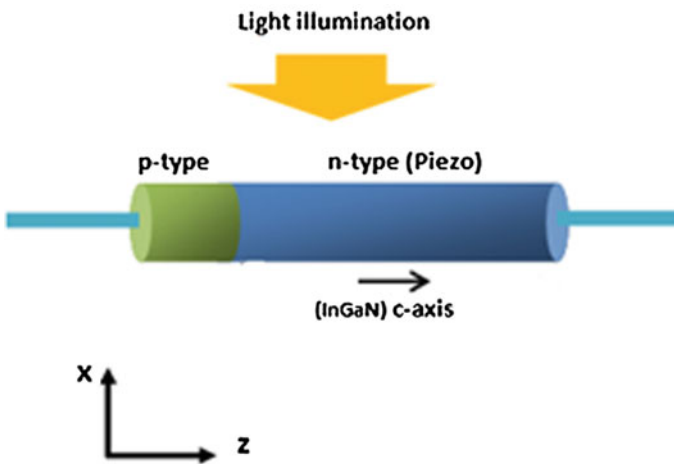
Fig. 1 Schematic of a InGaN nanowire piezoelectric solar cell based on a p-n junction with the n side being piezoelectric and the c-axis pointing away from the junction

2.1 Space Charge Model

In a semiconductor material, the effect of polarization is expressed as

$$D = \varepsilon_0 \varepsilon_r E + P, \tag{1}$$

where D is the displacement vector, E represents the built-in electric field, $\varepsilon_0 \varepsilon_r$ denotes the total dielectric constant of the host lattice, and P is the net polarization given by:

$$(P)_i = e_{ijk} S_{jk}, \tag{2}$$

where e_{ijk} is the piezoelectric tensor and S is the uniform strain.

Taking into account the spreading of polarization charges, the sheet concentration ∇_s can be simulated by a bulk density with a rectangular profile according to

$$\rho_{pz}(z) = \begin{cases} 0 & for \quad z < 0 \\ \frac{P}{W_p} & for \quad 0 < z < W_p \\ 0 & for \quad W_p < z < W_D \end{cases} \tag{3}$$

Using this model of spreading, the total space charge density in the photovoltaic cell can be written as

$$\rho(z) = \begin{cases} -qN_A & for \quad -W_A < z < 0 \\ qN_D + \frac{P}{W_p} & for \quad 0 < z < W_p \\ qN_D & for \quad W_p < z < W_D \end{cases}, \tag{4}$$

where N_A and N_D are the doping concentrations of acceptors and donors, W_A and W_D represent the depletion widths in the p-InGaN and n-InGaN sides and q is the elementary unit electron charge (Fig. 2).

The electrostatic electric field as well as the space charge potential can be calculated from Poisson equation.

$$E(z) = \begin{cases} \frac{-qN_A(z + W_A)}{\varepsilon_S}; & -W_A < z < 0 \\ \frac{-qN_D(W_D - z) + \rho_{pz}(W_p - z)}{\varepsilon_S}; & 0 < z < W_p \\ \frac{-qN_D(W_D - z)}{\varepsilon_S}; & W_p < x < W_D \end{cases} \tag{5}$$

ε_s is the permittivity given as follows (Belghouthi et al. 2015):

$$\varepsilon_s(In_x Ga_{1-x} N) = 15.3x + 8.9(1 - x) \tag{6}$$
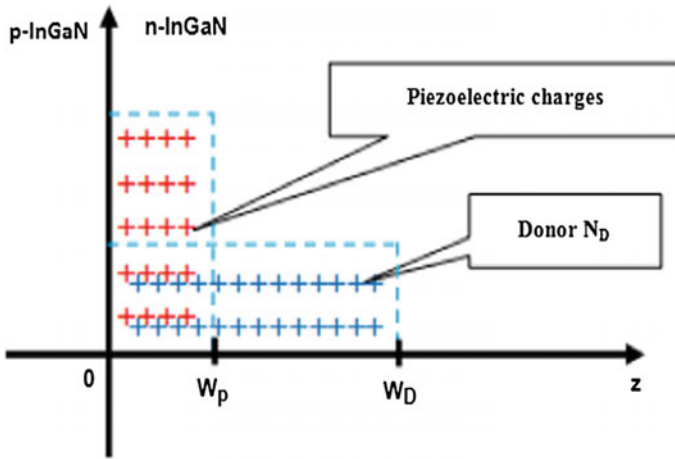
Fig. 2 Profile of piezoelectric charges and donor charge distribution

2.2 Current–Voltage Characteristics and Photovoltaic Parameters

For a solar cell, the working principle is based on using high electric fields in the depletion region in order to assist the separation of electron–hole pairs generated by incident photons. Moreover, the piezoelectric potential can significantly modify the band gap edges and control carrier generation at the p-n hetero-junction. The dynamics of the charge transport is governed by the well-known local electron and hole current densities and the continuity equations. In this study, we aim to develop a new model to evaluate the total current J_{pn} taking account the presence of polarization charges. We will first recall the conventional model and then we will explain how piezoelectric charges modify the saturation current.

2.2.1 Conventional Model

For an ideal p-n junction solar cell, the total current density reads

$$J_0 = J_{pn0}\left[\exp\left(\frac{qV}{k_B T}\right) - 1\right] - J_{ph} \tag{7}$$

V is the applied voltage. The saturation current is given by

$$J_{pn0} = \frac{qD_p}{L_p}p_{no} + \frac{qD_n}{L_n}n_{po}, \tag{8}$$

where p_{n0} and n_{p0} are the thermal equilibrium carrier concentration in n-type and in p-type semiconductors. The thermal equilibrium hole concentration pn0 in the n-type semiconductor dominates the saturation current. Thus, we obtain

$$J_{pn0} = \frac{qD_p}{L_p} p_{no} \tag{9}$$

The thermal equilibrium hole concentration is given by

$$p_{no} = n_i \exp\left(\frac{E_i - E_{F0}}{k_B T}\right) \tag{10}$$

Here ni is the intrinsic carrier density, Ei is the intrinsic Fermi level and EF0 is the Fermi level without polarization effect. Zhang et al. (2012) proposed a revised version of the conventional model as an attempt to explain the piezophototronic effects on the photovoltaic conversion in nano-/microwire solar cells. In this study, we adopt the same approach and we propose to modify some expression in order to take account the effect of polarization charges. Equation (7) becomes

$$J = J_{pn}\left[\exp\left(\frac{qV}{k_B T}\right) - 1\right] - J_{ph} \tag{11}$$

The modified expression of the saturation current density Jpn will be detailed hereafter.

The saturation current density is given by

$$J_{pn} = \frac{qD_p}{L_p} p_n = \frac{qD_p}{L_p} n_i \exp\left(\frac{E_i - E_F}{k_B T}\right) \tag{12}$$

The expression of Fermi level is revised as

$$E_F = E_{F0} - \frac{q^2 \rho_{pz} W_p^2}{2\varepsilon_s}, \tag{13}$$

where E_{F0} is the Fermi level without polarization and E_F is the Fermi level with polarization effect. Using the new expression of Fermi level, the saturation current density is rewritten as

$$J_{pn} = J_{pn0} \exp\left(\frac{-q^2 \rho_{pz} W_p^2}{2\varepsilon_s k_B T}\right) \tag{14}$$

2.3 Results and Discussion

The performance of the solar cell is deliberated in terms of short-circuit current density Jph, open-circuit voltage (Voc), and efficiency (η). In our simulation work, we first aimed to study the piezophototronic effect on saturation current. For that aim, we suppose that the photocurrent does not depend on strains. Figure 3 shows the current–voltage curves for p-n solar cell at different strains.

For the positive strain case in the proposed model, the positive piezoelectric charges at p-n interface attract the electron. Their accumulation near the p-n junction produces a significant reduce in the built-in potential. As a result, the corresponding current density is enhanced. On the other side, for a negative strain (compressive strain) case, negative piezoelectric charges are created adjoining the p-n interface Their attraction of the holes to the local region, produces an increase in the built-in potentials and a drop in currents. Thus, the value of Voc is given by the difference between quasi-Fermi levels of the p-type and n-type semiconductor. This value is reduced when strain is slowly applied by decreasing as a consequence the Voc as shown in Fig. 4.

The same behavior is observed when efficiency is studied on function of strain as shown in Fig. 5. To check the validity of our theoretical model in the absence of experimental results on piezoelectric InGaN solar cell, we intend to compare our simulation results with previous experimental results on piezoelectric organic solar cells. A p-n solar cell is produced by using a p-type material which is the (P3HT) and an n-type material which is the ZnO microwire. Experimental measures shows that the open-circuit voltage Voc decreases linearly with a linear increase in strain
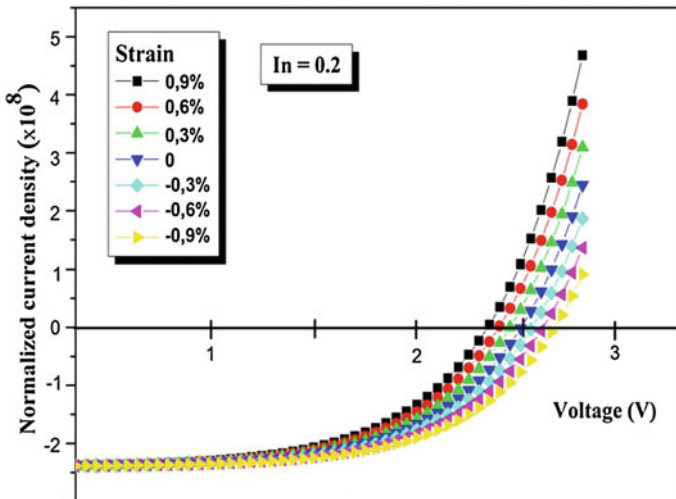
Fig. 3 Normalized current density of a $In_{0.2}Ga_{0.8}N$ nanowire p-n junction piezoelectric solar cell as function of applied voltage under several strains (−0.9 to 0.9%)
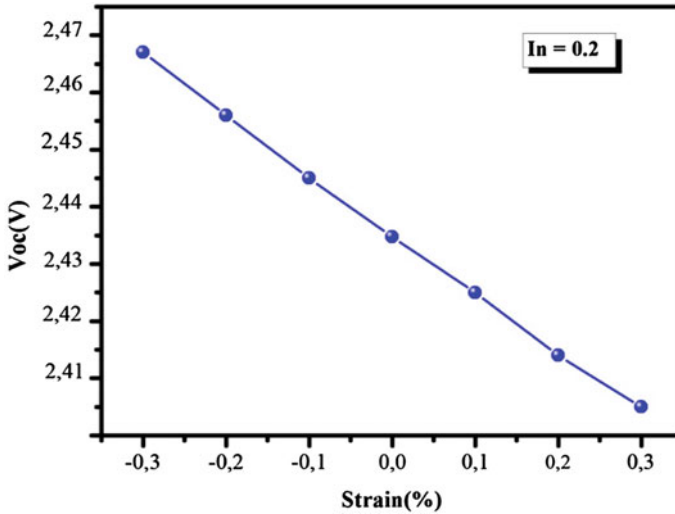
Fig. 4 Open-circuit voltage of a $In_{0.2}Ga_{0.8}N$ nanowire p-n junction piezoelectric solar cell as a function of strain
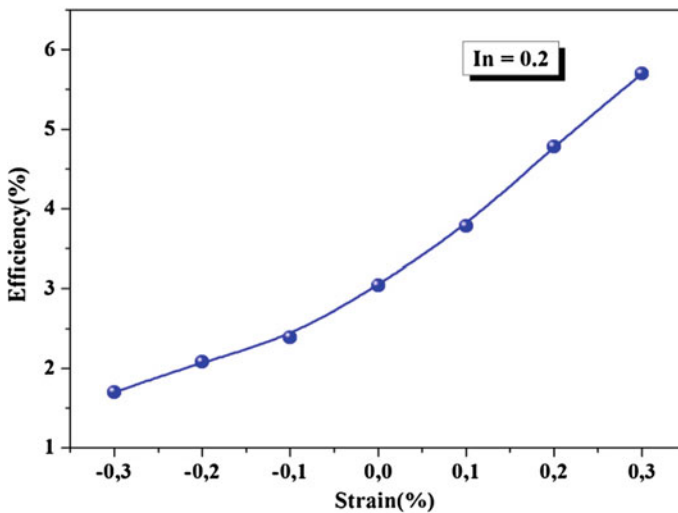
Fig. 5 Efficiency of a $In_{0.2}Ga_{0.8}N$ nanowire p-n junction piezoelectric solar cell as a function of strain

(Wang 2012) also studies experimentally the performance of solar cell based on ZnO/P3HT under strains. The efficiency is increased under 0.32% tensile strain and it is decreased under 0.32% compressive strain. The analytical result is verified by experiments. The above model explains that the performance of the solar cell is dominated by the piezophototronic effect.

3 Conclusion

In the present paper, the piezophototronic effect is demonstrated in the InGaN solar cell. We have studied theoretically the effect generated by the strain on the open-circuit voltage and on the current density. These elements are the main key parameters that can help us to evaluate strongly the performance of the solar cell. This study has the advantage of calculating photovoltaic parameters as a function of stress that can be varied at will. On a fundamental level, the study of the electrical characteristics has the advantage of showing the positive effects of stress, which can improve the performance of solar cells. Applied physics, this work gives an idea about the design of the most optimized architectures.

References

Belghouthi R, Taamalli S, Echouchene F, Mejri H, Belmabrouk H (2015) Mater Sci Semicond Process 40:424–428
Belghouthi R, Salvestrini JP, Gazzah MH, Chevelier C (2016) Superlattices Microstruct 100:168–178
Kwon S-S, Hong W-K, Jo G, Maeng J, Kim T-W, Song S, Lee T (2008) Adv Mater 20:4557–4562
Maugin GA (1988) Appl Math Mech 96
Sze SM (1981) Physics of semiconductor devices. Wiley, New York
Wang ZL, Song JH (2006) Science 312:242–246
Wang ZL (2012) Adv Mater 24:4630
Wen X, Wu W, Wang ZL (2013) Nano Energy 1093:2
Yang Q, Wang WH, Xu S, Wang ZL (2011a) Nano Lett 11:4012–4017
Yang Y, Guo W, Zhang Y, Ding Y, Wang X, Wang ZL (2011b) Nano Lett 11:4812–4817
Zhang Y, Yang Y, Wang ZL (2012) Dyn Art 5:6850

Injection Fault Detection of a Diesel Engine by Vibration Analysis

Ezzeddine Ftoutou and Mnaouar Chouchane

Abstract In this paper, the potential of vibration analysis for early detection of fuel injection faults in an internal combustion diesel engine, having six cylinders in line, has been investigated. The main sources of vibration of a diesel engine, as well as the mechanism of propagation of these sources to the engine structure have been presented. Using the tarring screw of the injector, the injection pressure in one of the cylinders has been gradually reduced from its nominal value, respectively, by 10 and 50%. Two signals are acquired using an analog-to-digital dynamic acquisition card. The first is the TDC signal in cylinder 1 measured using an inductive sensor. The second is the vibration signal which has been measured, on the cylinder head of the engine using a piezoelectric accelerometer. The vibration signal has been analyzed in the crank-angle domain, the frequency domain using the Fast Fourier Transformation, and in the angle-frequency domain using the Short Fourier Transform. The analysis of the injection fault signals in the three domains showed that in the crank-angle domain, a visual analysis gives limited information; in the frequency domain, the identification of the cylinder with the faulty injector is not possible; and in the angle-frequency domain, the detection of the injection fault and the identification of the faulty cylinder are possible and not complicated.

Keywords Injection fault · Diesel engine · Vibration analysis
Fault detection

E. Ftoutou (✉) · M. Chouchane
Laboratory of Mechanical Engineering (LGM), National Engineering
School of Monastir (ENIM), University of Monastir, Avenue Ibn Eljazzar,
5019 Monastir, Tunisia
e-mail: ezzeddine.ftoutou@issatkas.rnu.tn

M. Chouchane
e-mail: mnaouar.chouchane@enim.rnu.tn

11

1 Introduction

Early detection of diesel engine faults is essential in order to take early correction actions and avoid costly repair. Injection faults due to defects in a fuel pump, fuel lines, and injectors affect the power of the engine, increase the polluting particles in the exhausted gas, increase the radiated noise, and reduce the life cycle of the engine. Higher injection pressure increases the pollutants in the emission and increases fuel consumption. A lower pressure, however, reduces the engine power and efficiency (Çelikten 2003).

Vibration measurement on the engine block or cylinder head is a non-intrusive method and has been used successfully for fault detection of diesel engines (Chandroth 1999; Antoni et al. 2002; Geng et al. 2003; Antoni et al. 2004; Carlucci et al. 2006; Ftoutou et al. 2012; Ftoutou and Chouchane 2016). Signal processing techniques of the vibration signals are used to extract features sensitive to faults and less sensitive to noise. In the present work, the potential for early detection of injection defaults using vibration signals is investigated. In the experimental work, a six-cylinder in-line diesel engine has been used. The injector pressure of one of the cylinders has been reduced gradually from its nominal value by 10 and 50%. Vibration signal has been analyzed in the angular domain, the frequency domain and angle-frequency domain.

2 Vibration Analysis of an IC Engine

The measured vibration on the engine depends on the excitations and the propagation path. The main sources of excitation likely to affect the engine vibration response include impacts due to piston clearances (piston slaps), fuel injection pressure, high rise of gas pressure during combustion, and the impacts of admission and exhaust valves. Some of these faults affect the vibration signal simultaneously and during a limited portion of the engine cycle. A fault is usually detected by comparing the vibration signal of the faulty engine to the reference signal or signature. In angular domain, the presence of several simultaneous faults makes the separation of the sources a difficult task in time or angular domain. Classical Fourier spectrum is more useful for the analysis of stationary signals associated to rotating machines. For nonstationary engine vibration signals, the spectrum tends to smear frequency components. Joint time–frequency analysis methods or angle-frequency analysis have more potential for source separation since the frequency content of the signal is analyzed during time or angle variation.

3 Internal Sources of Vibration in an IC Diesel Engine

Measured at any point on the internal combustion engine structure, the vibratory signal is composed of a very complex superposition of the contributions of different vibratory sources modified by their respective transmission paths. These sources originate from several internal phenomenon's in the engine and excite the natural modes of the engine. The vibration is amplified at the natural frequencies of the engine. Therefore, the produced vibration and the noise radiated from the engine result from the combination of the excitations and the dynamic response of the structure. Diesel engine vibration is caused by several mechanical and thermal sources applied sometimes simultaneously at different phases of the engine cycle. In the following, the main sources of vibration of a diesel engine, as well as the mechanism of propagation of these sources to the engine structure are described.

3.1 Combustion Forces

During the phase of combustion, a significant and brief increase of the pressure in the engine cylinders occurs. The combustion causes a descending motion of the pistons and the rotation of the crankshaft. The combustion force is sometimes described as comparable to a hammer stroke and depends on the power demand of the engine. Excitations due to combustion forces are periodic and spread to frequencies up to several kHz (Lecelère 2003). The shock of the combustion pressure applies a direct excitation on the engine head (1), Fig. 1. This path constitutes the first way of propagation. On the other hand, the shock due the sudden pressure rise excites the mobile components (piston-rod-crankshaft) in two ways
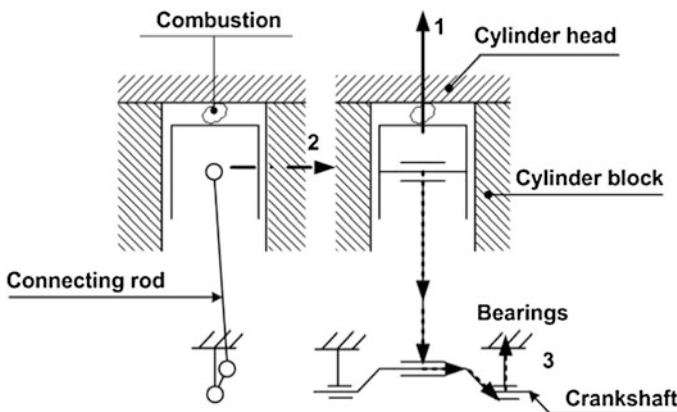
Fig. 1 Combustion force

- the transverse excitation (2), Fig. 1, is transmitted through the piston to the cylinders while conjugating with the piston slap,
- the vertical excitation (3), Fig. 1, propagates through the mobile parts to the crankcase bearings.

3.2 Piston Slaps

Piston slap is another important source of vibration in diesel engines. It is caused by the inversion of the inertia forces of the piston in the neighborhood of the top dead center (TDC). Piston slap results from the succession of two strong shocks. One shock is applied by the upper part of the piston while the other shock is applied by the lower part of the piston. The piston slap vibration covers a large range of frequencies that spread up to several kHz.

3.3 Inertia Forces

The alternating motion in the engine excites the moving parts (piston, rod, and crankshaft) by the action of the highly variable inertia forces. The inertia forces are quasi-harmonic and results into mechanical vibrations in the low frequencies, up to the first few lower harmonics of the rotating speed of the crankshaft (Lecelère 2003). The inertia forces vibration depends on the engine regime, its geometry, and the mass and inertia of the moving parts. The inertia forces are transmitted to the cylinders by the pistons at positions in the neighborhood of the TDC, at the time when friction forces are inverted and vary significantly in time. The inertia forces are also transmitted to the crankshaft bearings through the crankshaft.

3.4 The Injection Forces

The injection of diesel fuel under a high pressure (about 270 bars for the engine used in this study) during a very short time (some micro-seconds) creates a mechanical shock. Furthermore, the spring of the needle of each fuel injector is also a source of secondary importance contributing to cylinder head vibration.

3.5 The Distribution System Forces

Distribution system vibrations are generated by the impacts of the intake and exhaust valves on their seats as well as the excitation of the valve tails by the rocker arms. The camshaft generates vibrations which are transmitted to the upper part of the engine through the rockers and the rocker arms. Gas flow in the manifolds and through the intake and exhaust valves and the gearing of the distribution belt or gears are also additional sources of vibration.

4   Measurement Set Up

In this study, an internal combustion diesel engine having six cylinders in line, a power of 260 CV at 2200 rpm and a maximum torque of 1020 Nm at 1200 rpm are used. The fuel is injected directly into the combustion chambers at a pressure of 270 bars in the following order 1-5-3-6-2-4. A piezoelectric accelerometer has been used for the acquisition of the vibration signal. The signal provided by the accelerometer is first amplified by a charge amplifier and then connected to an analog input channel of a PC plug-in acquisition card. A second input channel of the acquisition card has been used for the reference signal used to identify the TDC of cylinder 1. Figure 2 shows, from top to bottom: TDC signal and vibration signal. The time interval between two pulses is equal to the period of one engine cycle (two crankshaft revolutions, i.e., 720° of crankshaft rotation).
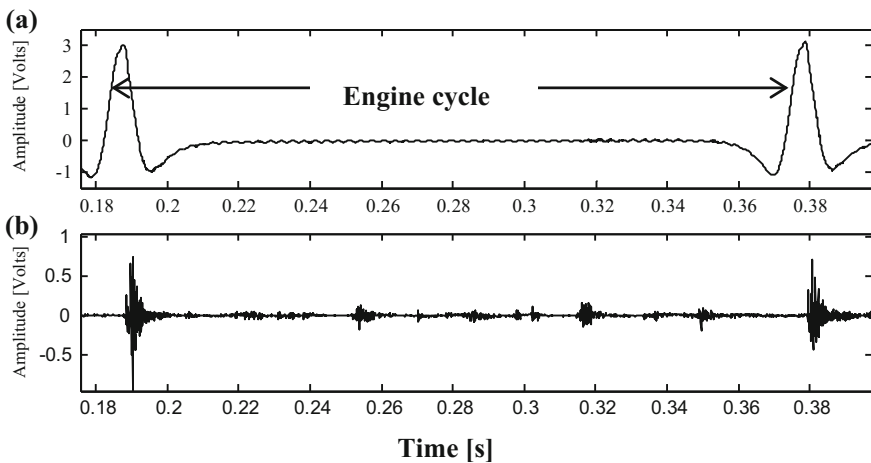
Fig. 2 Measured signals. **a** the TDC signal and **b** the vibration signal

5 Analysis in the Time Domain

In the time domain, a visual analysis gives usually limited information. Figure 3 represents three signals corresponding to the three sstudied cases (nominal injection pressure and pressures reduced respectively by 10% and 50% for cylinder 6). Each signal covers one cycle (two crankshaft rotations). Every signal contains 4096 samples.

Statistical analysis of one cycle signal can be used to compute scalar parameters such as maximal value, the mean, the root mean square, Skewness, the Kurtosis, and other parameters (Ftoutou et al. 2012). These parameters can further be computed for segments of the divided signals. For example, the signals shown in Fig. 3 contain six events and may therefore be divided into six segments. The vibration due to the combustion in the cylinder 6 is more sensitive to the injection faults induced into this cylinder. The scalar parameters for the interval highlighted in Fig. 3 are expected to have larger variation caused by the simulated faults. The statistical analysis of the vibrations signals is not presented in this paper.

The reference vibration signal corresponding to the no-fault state measured on the cylinder head is shown in Fig. 3a. The reference signal corresponds to an idle speed of 500 rpm and no applied charge. The vibration level when any one of the pistons reaches its TDC is significantly higher for a crank-angle rotation of about 10°. These vibrations, occurring six times per cycle, are essentially due to fuel injection and combustion pressure and can be visually detected. The accelerometer used for vibration measurement has been fixed in the vertical direction between cylinder 3 and 4. Thus, the vibrations due to combustion in these chambers are the highest respectively at an angle 240° and 600°. The vibration due to cylinders distant from the accelerometer has a lower energy. Figure 3b, c show the vibration

Fig. 3 Vibration signals in the time domain. **a** For a nominal injection pressure, i.e. 270 bars, **b** for an injection pressure reduction of 10% and **c** for an injection pressures reduction of 50%
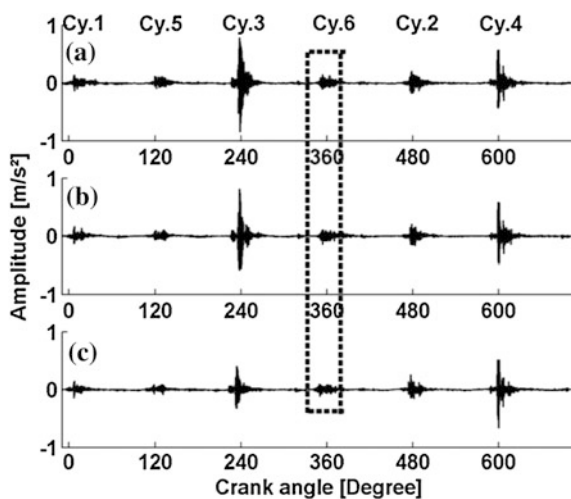
Fig. 4 Frequency spectrum
of the vibration signals of
Fig. 3. **a** For a nominal
injection pressure, i.e.
270 bars, **b** for an injection
pressure reduction of 10% and
c for an injection pressures
reduction of 50%
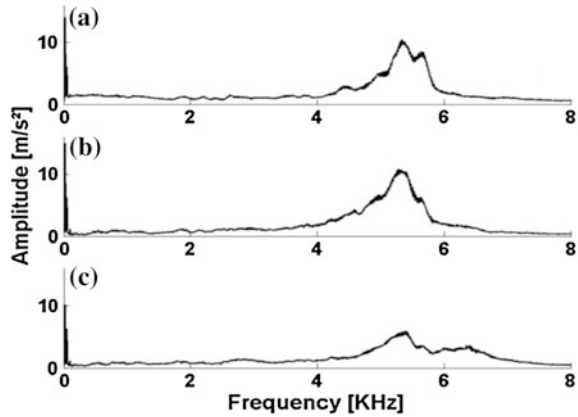
signals when the injection pressure at cylinder 6 is reduced respectively by 10% and
50%. The effect of these induced faults in the angular domain is hardly noticeable.

6   Frequency Analysis

The vibration signals in the frequency domain are obtained using the Fast Fourier
Transformation (FFT). Figure 4 shows the spectrum of the reference case (no fault)
and the spectrum of each of the two faulty cases. Each spectrum has been average
over 100 spectrums of 100 successive cycles. Each cycle contains 4096 samples.
The FFT bloc size is 4096, which is equal to the number of samples in one cycle.

Figure 4a–c shows the vibration spectrum of the signals of Fig. 3. High vibra-
tion energy can be observed between 4 and 6 kHz. Even though a reduction of the
pressure by 50% has reduced the vibration energy in this frequency domain, it is not
possible from this spectrum to determine which cylinder has a faulty injector.

7   Time–Frequency Analysis

For stationary signals, frequency analysis is a useful and the most frequently used
signal processing tool. The frequency content of nonstationary signals, however,
varies with time and therefore time–frequency analysis tools should be used for a
more in depth analysis. Parametric and nonparametric approach can be used for
frequency analysis and time–frequency analysis. The parametric approach fits a
model to the data and has the advantage of not being prone to spectral leakage due
to signal truncation. The Short Fourier Transformation (STFT), used in this work, is
a basic time–frequency method. It permits the processing of a signal by decom-
posing the signal into short blocs and computing the spectrum of each bloc.
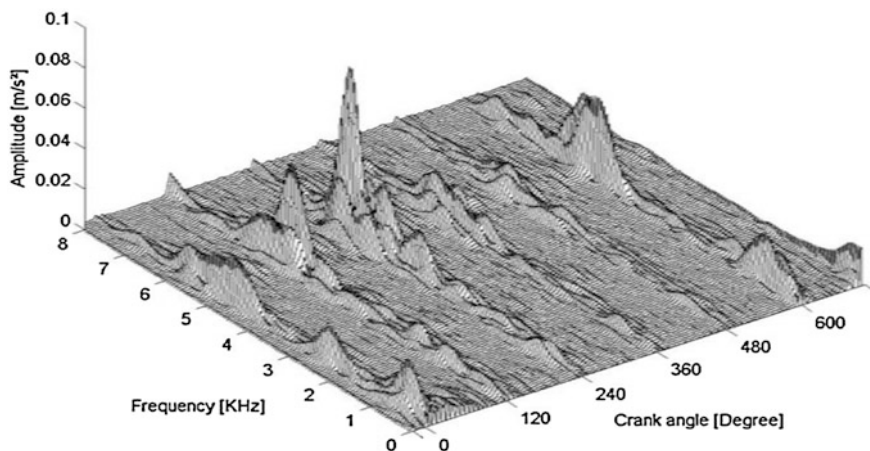
Fig. 5 Angle-frequency representation of the reference signal

Different type of windows can be used to reduce spectral leakage. A Gaussian window is usually used. Certain overlaps of bloc samples are frequently applied in order to reduce information loss since the window function time–frequency analysis methods are used to determine the frequency content at each time (Chandroth 1999; Stankovic and Böhme 1999; Antoni et al. 2002; Antoni et al. 2004; Carlucci et al. 2006; Wang et al. 2008; Ftoutou and Chouchane 2016). For the engine vibration, angle-frequency analysis in which time is replaced by the crank angle is more useful and has been used in this research work. Angle-frequency spectrum, Fig. 5, is given for the reference no-fault state. Large vibration levels occur at crank angles integer-multiple of 120°, when the piston of each cylinder reaches the top dead position and immediately afterward during combustion. The vibrations at these angles are significantly larger in the 4–6 kHz frequency domain and last about 10° especially for cylinders 3 and 4. Low frequency vibrations, due probably to the motion of the pistons and other moving parts, appear particularly away from the TDC positions and reach a maximum frequency around 50 Hz. It is expected that an increase of crankshaft and piston bearing gaps affect particularly these lower vibrations. An injection fault, however, is expected to affect higher frequency vibration. Figures 5, 6, and 7 show the angle-frequency spectrum of the reference signal and those with 10 and 50% pressure reduction of the injector of cylinder 6. By examining these figures, around the 360° angle, multiple peaks in the 4–6 kHz region, which are affected by the injection pressure alteration, are observed.
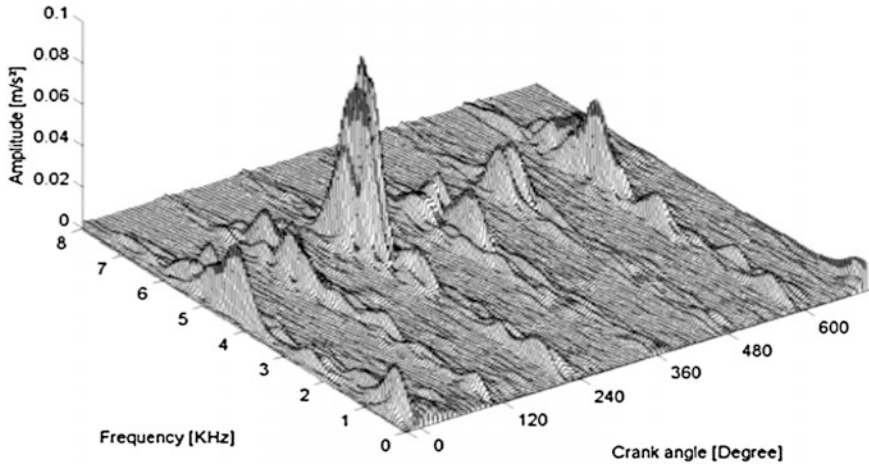
Fig. 6 Angle-frequency representation for pressure reduction of 10%
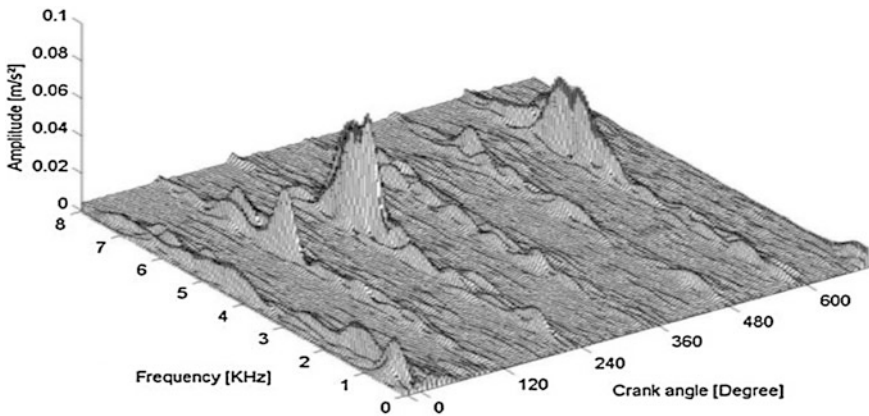
Fig. 7 Angle-frequency representation for a pressure reduction of 50%

8   Conclusion

Angle-frequency representation of the vibration signal measured on the cylinder head are shown to be useful for the detection of injection faults. This type of representation has the potential of separating several sources of excitation occurring at the same time but having different frequency content. Further research work can be oriented toward the extraction of features from the angle-frequency spectrum. The engine faults may then be identified using these features.

References

Antoni J, Danière J, Guillet F (2002) Effective vibration analysis of IC engines using cyclostationarity. Part I: A methodology for condition monitoring. J Sound Vib 257(5):815–837

Antoni J, Danière J, Guillet F (2004) Cyclostationarity modelling of rotating machine vibration signals. Mech Syst Signal Process 18:1285–1314

Carlucci AP, Chiara FF, Laforgia D (2006) Analysis of the relation between injection parameter vibration and block vibration of an internal combustion diesel engine. J Sound Vib 295:141–164

Çelikten I (2003) An experimental investigation of the effect of the injection pressure on engine performance and exhaust emission in direct injection diesel engines. Appl Therm Eng 23:2051–2060

Chandroth G (1999) Acoustic emission, cylinder, pressure and vibration: a multisensor approach to robust fault diagnosis. Dissertation, UK

Ftoutou E, Chouchane M, Besbès N (2012) Internal combustion engine valve clearance fault classification using multivariate analysis of variance and discriminant analysis. Trans Inst Measure Control 34(5):566–577

Ftoutou E, Chouchane M (2016) Feature extraction using S-Transform and 2DNMF for diesel engine faults classification. In Fakhfakh T et al (eds) Advances in acoustics and vibration. Springer, Berlin, Heidelberg

Geng Z, Chen J, Hull JB (2003) Analysis of engine vibration and design of applicable diagnosing approach. Int J Mech Sci 45:1391–1410

Lecelère Q (2003) Etude et développement de la mesure indirecte d'efforts: application à l'identification des sources internes d'un moteur Diesel. Dissertation, INSA, Lyon, France

Stankovic L, Böhme JF (1999) Time-frequency analysis of multiple resonance in combustion engine signals. Sig Process 79:15–28

Wang C, Zhong Z, Zhang Y (2008) Fault diagnosis for diesel valve trains based on time-frequency images. Mech Syst Signal Process 22:1981–1993

A Nonlinear Analysis of a Flexible Unbalanced Cracked Rotor-Bearing System

N. Ferjaoui and M. Chouchane

Abstract Establishment of a new approach for investigating the dynamic behavior of a cracked rotor system is the goal of the present research. This paper provides a breathing crack model of a rotating shaft supported by hydrodynamic bearings. The modeling is based on the hypothesis that a short hydrodynamic bearing, unbalance, and crack defect causes instability and change the dynamic behavior of the rotor. A nonlinear dynamic analysis of the system highlights the interactions, especially, unbalance defect, and crack defect. The global model can be characterized by nonlinear state equations which are solved iteratively by numerical integration. The major interest of presenting this model is that it allows to analyses the effect of a transverse cracks on the dynamic response of a hydrodynamic journal bearing system. Analysis of transverse cracks defects, on the stability and the dynamic behavior of the rotor-bearing system and further certain operating conditions were performed by applying bifurcation diagrams, Poincare section, the trajectory center of the journal, and power spectrum.

Keywords Nonlinear analysis · Cracked rotor · Hydrodynamic bearing Stability limit

1 Introduction

The appearance of the crack in the rotor is the sever faults of the rotating machinery. The presence of the crack affects the dynamic behavior of the system by reduction of the stiffness of the rotor. Many researches in the last four decades studies the effects of the crack in the dynamic behavior of the rotor-bearing system. Many

N. Ferjaoui (✉) · M. Chouchane
Laboratory of Mechanical Engineering, National Engineering School of Monastir,
University of Monastir, Avenue Ibn Eljazzar, 5019 Monastir, Tunisia
e-mail: nizar.ferjaoui@yahoo.fr

M. Chouchane
e-mail: mnouar.chouchane@enim.rnu.tn

approaches are proposed to analyze the dynamic behaviors of cracked rotor based on tow known models, the first is the model of opening and closing crack or switching model: the stiffness of the rotor, corresponding to the closed crack switches with the stiffness corresponding to the open crack model. The second model is the breathing crack model. Many studies are presented to identify the effects of the crack in stability of the rotor and many methods are used to prove the presence of the crack, such as, FEM, Wavelet transforms, harmonic method, and numerical method.

Sinou and Lees (2007) showed that the presence of a transversal crack in a rotating shaft amended the dynamic response of the trajectory of the journal center. Later, they detected the existence of the crack in the shaft by the change of the trajectory of the journal center near half of the first critical speed (Sinou and Lees 2007). Patela and Darpe (2008) studied the crack shaft using breathing model. The bifurcation diagram, poincaré maps, and trajectory of the journal center are employed to analyse the dynamic response of the system. Xue and Cao (2011) used rotor trajectory diagrams, bifurcation diagrams and Poincaré maps to study the effect of crack depth, rotating speed, and orientation angle of unbalance on the dynamic behavior of the rotor. The evolution of the orbit at half rotational frequency is considered as an indicator to predict the presence of a crack in the shaft. Chaofeng and Hexing (2013) studied the effect of a crack on the stability threshold speed by using bifurcation diagrams, Poincare sections, and trajectories of the shaft center. The crack fault decreases the stability threshold speed of the rotor when the crack becomes deeper. The results of the simulation have been validated experimentally. Luo et al. (2014) introduced a nonlinear model of the cracked rotor-bearing system. The Finite Element Method is used to find steady-state response of the cracked rotor. The analysis shows that the increase of the depth of the crack reduces the stability threshold speed of the system.

In this paper, a nonlinear model of an unbalanced crack rotor supported by two hydrodynamic bearings is investigated and the impact of the crack depth on the dynamic response of the rotor is established.

2   Model of an Unbalanced Flexible Cracked Rotor

The model studied on a flexible crack rotor, constituted of a centrally located unbalanced disk, mounted symmetrically on hydrodynamic bearings (see Fig. 1a). The shaft has a transverse crack located close to the disk. O_b is the bearing center, O_j is the dynamic position of the journal center, and f_ε, f_ϕ are the radial and tangential components of the hydrodynamic forces, corresponding to the Half Summerfield condition, applied on the journal.
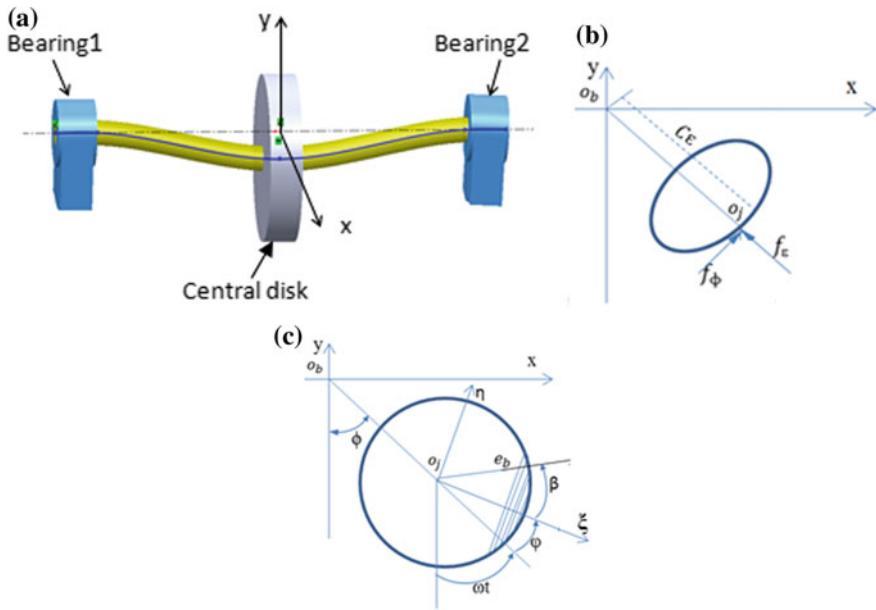
Fig. 1 a A general view of the rotor, **b** forces/applied on the journal, **c** coordinate system associated to the crack

The coupled equations of motion of the system are given as follows:

$$[M]\begin{Bmatrix} \ddot{x} \\ \ddot{y} \end{Bmatrix} + [K_I]\begin{Bmatrix} x - c\varepsilon\,\cos(\phi) \\ y + c\varepsilon\,\sin(\phi) \end{Bmatrix} = m\,e_b\,\omega^2 \begin{Bmatrix} \cos(\omega t + \varphi) \\ \sin(\omega t + \varphi) \end{Bmatrix} - mg\begin{Bmatrix} 0 \\ 1 \end{Bmatrix} \qquad (1)$$

The rotor mass matrix [M] is defined as $[M] = \begin{bmatrix} m & 0 \\ 0 & m \end{bmatrix}$,

Where ϕ attitude angle, β unbalance angle, and φ angular position of the crack
The stiffness matrix of the cracked shaft in inertial coordinate system is given by

$$[K_I] = \begin{bmatrix} k_{xx} & k_{xy} \\ k_{yx} & k_{yy} \end{bmatrix} = \begin{bmatrix} k & 0 \\ 0 & k \end{bmatrix} - f(\psi)\frac{k}{2}\begin{bmatrix} \Delta k_1 + \Delta k_2\cos(2\omega t) & \Delta k_2\sin(2\omega t) \\ \Delta k_2\sin(2\omega t) & \Delta k_1 - \Delta k_2\cos(2\omega t) \end{bmatrix},$$
$$(2)$$

where

$$\Delta k_1 = \Delta k_\xi + \Delta k_\eta; \ \Delta k_2 = \Delta k_\xi - \Delta k_\eta.$$

The function $f(\psi)$ depends on the angular position of the crack and is defined as follows (Gómez-Mancilla 2005)

$$f(\psi) = \frac{1 + \cos(\psi)}{2}, \tag{3}$$

where

$$\psi = \omega t + \varphi.$$

The equations of motion for the journal center are derived using Newton's second law as follows (Fig. 1b) (Wang 2005):

$$\begin{bmatrix} \sin\phi & \cos\phi \\ -\cos\phi & \sin\phi \end{bmatrix} \begin{Bmatrix} f_\varepsilon \\ f_\phi \end{Bmatrix} + \begin{bmatrix} k_{xx} & k_{xy} \\ k_{yx} & k_{yy} \end{bmatrix} \begin{Bmatrix} x - c\varepsilon \sin\phi \\ y + c\varepsilon \cos\phi \end{Bmatrix} = \begin{Bmatrix} 0 \\ 0 \end{Bmatrix} \tag{4}$$

The dimensionless tangential and radial components of the fluid film forces, for the short bearing theory and the half Sommerfeld condition are (Frêne 1997)

$$\begin{aligned}
\bar{f}_\varepsilon &= \frac{f_\varepsilon}{mc\omega^2} = -\frac{\Gamma}{\varpi}\left[\frac{2\varepsilon^2(1-2\phi)}{(1-\varepsilon^2)^2} + \pi\frac{(1+2\varepsilon^2)\dot{\varepsilon}}{(1-\varepsilon^2)^{2.5}}\right] \\
\bar{f}_\phi &= \frac{f_\phi}{mc\omega^2} = \frac{\Gamma}{\varpi}\left[\pi\frac{(1-2\phi)\varepsilon}{2(1-\varepsilon^2)^{1.5}} + \frac{4\varepsilon\dot{\varepsilon}}{(1-\varepsilon^2)^2}\right]
\end{aligned} \tag{5}$$

Using Eqs. (1) and (5), the motion for the journal center and disk center are governed by six first-order differential equations

$$\begin{aligned}
\dot{x}_1 &= -\left[\pi\left(1-x_1^2\right)^{2.5}\bar{f}_\varepsilon + 4x_1\left(1-x_1^2\right)^2\bar{f}_\phi\right]\frac{1}{\varpi\Gamma(\pi^2 + 2(\pi^2-8)x_1^2)} \\
\dot{x}_2 &= 0.5 - \left[4\left(1-x_1^2\right)^2\bar{f}_\varepsilon + \frac{2\pi\left(1-x_1^2\right)^{1.5}(1+2x_1^2)}{x_1}\bar{f}_\phi\right]\frac{1}{\varpi\Gamma(\pi^2 + 2(\pi^2-8)x_1^2)} \\
\dot{x}_3 &= x_4 \\
\dot{x}_4 &= -\frac{\bar{k}}{\varpi^2}\left(1 - \frac{f(\psi)}{2}(\Delta k_1 + \Delta k_2\cos(2\tau))(x_3 - x_1\sin(x_2))\right) \\
&\quad + \frac{\bar{k}}{\varpi^2}\frac{f(\psi)}{2}\Delta k_2 \sin(2\tau)(x_5 + x_1\cos(x2)) + \bar{e}_b\cos(\tau+\varphi) \\
\dot{x}_5 &= x_6 \\
\dot{x}_6 &= -\frac{\bar{k}}{\varpi^2}\left(1 - \frac{f(\psi)}{2}(\Delta k_1 - \Delta k_2\cos(2\tau))(x_5 + x_1\cos(x_2))\right) \\
&\quad + \frac{\bar{k}}{\varpi^2}\frac{f(\psi)}{2}\Delta k_2 \sin(2\tau)(x_3 - x_1\sin(x_2)) + \bar{e}_b\sin(\tau+\varphi) - \frac{1}{\bar{\omega}^2}
\end{aligned} \tag{6}$$

3   Numerical Results and Discussion

A nonlinear analysis of the flexible cracked rotor supported by hydrodynamic bearings is examined. The equations of motion (Eq. 6) are solved using numerical integration method. In this study, the numerical integration is carried out using the Runge–Kutta method. The dimensionless speed ratio is taken as a control parameter in the bifurcation analysis.

   The nonlinear dynamic analysis of the crack rotor is based on the trajectories of the journal center, the bifurcation diagrams, the Poincaré maps, and the amplitude spectra. These methods are used together to evaluate the effect of the crack on the dynamic response of the system. The dimensionless stiffness Δk_ξ and Δk_η of the shaft due to the crack is increased progressively. Three values of the dimensionless stiffness crack depth are considered relative to the crack couple (Δk_ξ, Δk_η) equal to (0.07, 0.02), (0.2, 0.03), and (0.4, 0.16) (Gómez-Mancilla 2005).

   Figure 2 shows the bifurcation diagram of a unbalanced cracked rotor for a small depth of the crack depicted by $\Delta k_\xi = 0.07$, $\Delta k_\eta = 0.02$, $\Gamma = 0.1$, $\bar{e}_b = 0.05$ and $\bar{k} = 10$. For $\varpi \leq 2.85$ the rotor is stable and the journal motion is an orbit in contrast to the uncracked rotor which has a stable equilibrium point. For $\varpi = 0.5$, the motion of the journal center is periodic (Fig. 3a–c). For low rotor speed, the small crack does not affect the stability limit but it has an influence on the dynamic behavior of the system. For $\varpi = 2$, the motion is double periodic (Fig. 3e) and fractional harmonic components 1/2X, 3/2X, etc., appears (Fig. 3f). When the rotor speed increases, the amplitude of the first fractional harmonic component increases and exceeds the amplitude of the first harmonic components (Fig. 3i) and the motion become quasi-periodic for $\varpi \geq 2.6$ (Fig. 3h)
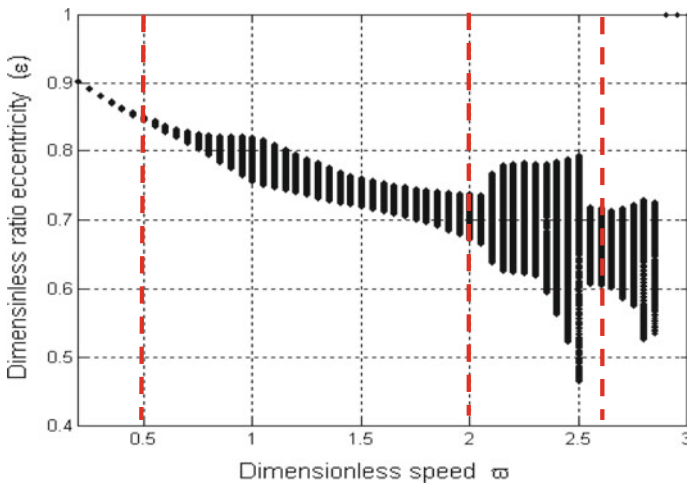
Fig. 2 Bifurcation diagram of an unbalanced flexible cracked rotor for $\Gamma = 0.1$, $\bar{e}_b = 0.05$, $\bar{k} = 10$, $\Delta k_\varepsilon = 0.07$ and $\Delta k_\eta = 0.02$
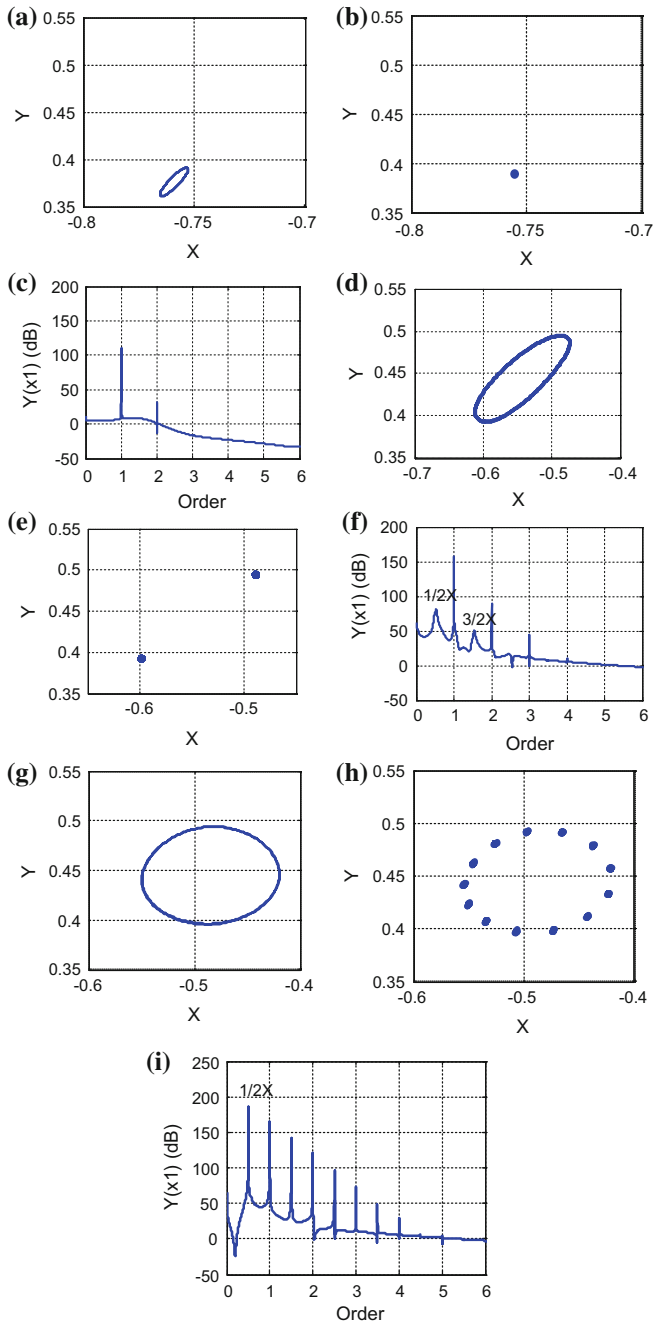
Fig. 3 Trajectory of the journal center, Poincaré section and power spectrum for $\Gamma = 0.1$, $\bar{e}_b = 0.05$, $\bar{k} = 10$, $\Delta k_\varepsilon = 0.07$ and $\Delta k_\eta = 0.02$ for $\varpi = 0.5$; $\varpi = 2$ and $\varpi = 2.6$
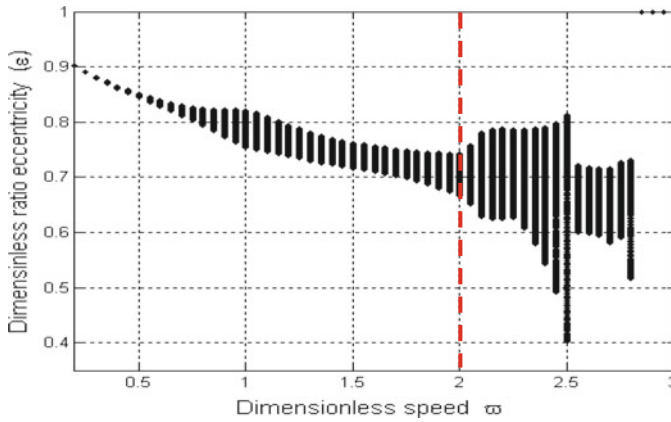
Fig. 4 A bifurcation diagram of unbalanced flexible cracked rotor for $\Gamma = 0.1$, $\bar{e}_b = 0.05$, $\bar{k} = 10$, $\Delta k_\varepsilon = 0.2$ and $\Delta k_\eta = 0.03$

When the depth of the crack increases, a slight decrease in the limit of stability is observed (Fig. 4). The motion of the journal center has not significantly changed (Fig. 5a, b) but the amplitude of the fractional harmonic components increases (Fig. 5c).
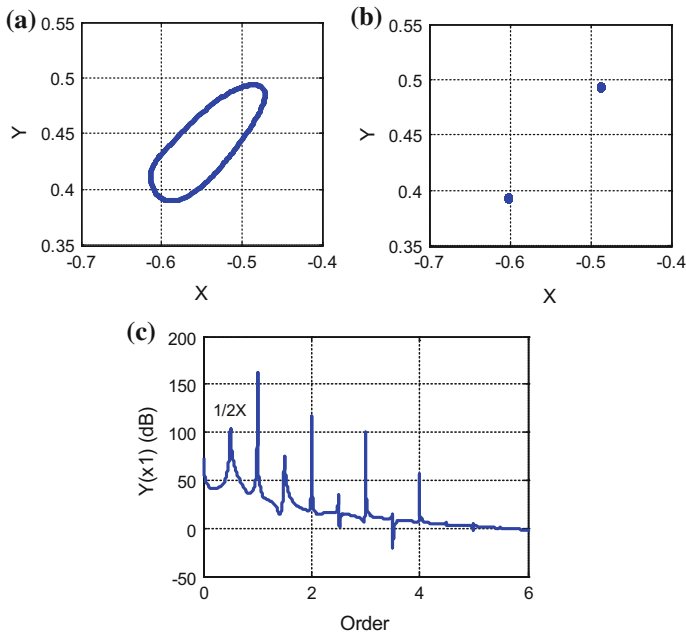
Fig. 5 Trajectory of the journal center, Poincare section and power spectrum: $\Gamma = 0.1$, $\bar{e}_b = 0.05$, $\bar{k} = 10$, $\Delta k_\varepsilon = 0.2$ and $\Delta k_\eta = 0.03$ for $\varpi = 2$
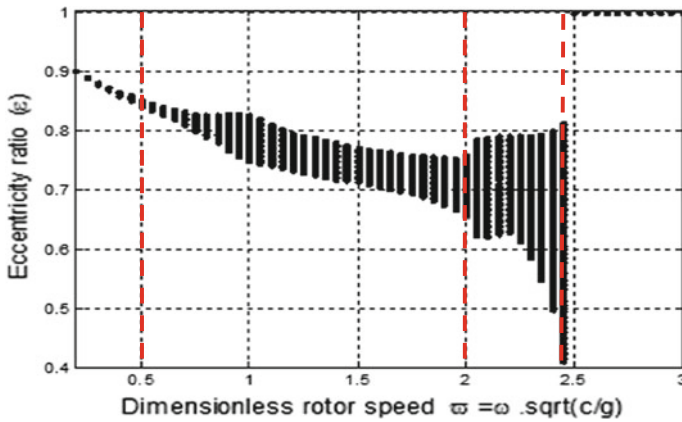
Fig. 6 Bifurcation diagram of unbalanced flexible cracked rotor for $\Gamma = 0.1$, $\bar{e}_b = 0.05$, $\bar{k} = 10$, $\Delta k_\varepsilon = 0.4$ and $\Delta k_\eta = 0.16$

In Fig. 6, the analysis of unbalanced cracked conditions was carried out for a large rotor crack parameter $\Delta k_\xi = 0.4$ and $\Delta k_\eta = 0.16$. The diagram shows the influence of the depth of the crack on the limit of the stability of the rotor. The limit of stability decreases significantly when the crack depth increases, it passed from 2.8 to 2.4 (Chaofeng and Hexing 2013). For $\varpi = 0.5$, the motion of the journal is periodic (Fig. 7a–c). A periodic doubling motion is observed for $\varpi = 2$ (Fig. 7d, e) and a half rotational frequency 1/2X is shown in the power spectrum (Fig. 7f). The amplitude of the half rotational frequency is lower than the amplitude of the first rotational frequency component. Near the stability limit, the motion has become quasi-periodic for $\varpi = 2.45$ (Fig. 7g, h) and the amplitude of the half rotational frequency component becomes higher than the amplitude of the first rotational frequency component (Fig. 7i).

4 Conclusion

A nonlinear dynamic analysis of the unbalanced flexible cracked rotor-bearing system is investigated. Bifurcation diagram, Poincaré section, and trajectory of the journal center are used to study the effect of the unbalance and the crack on the dynamic behavior and on the stability of the system. The presence of the crack in the shaft changes the dynamic behaviors of the system and decreases the limit of stability when the crack is deeper. The appearance of a component at half rotational frequency of the system and the increase of its amplitude is considered as an indicator of the presence of a crack in the shaft.
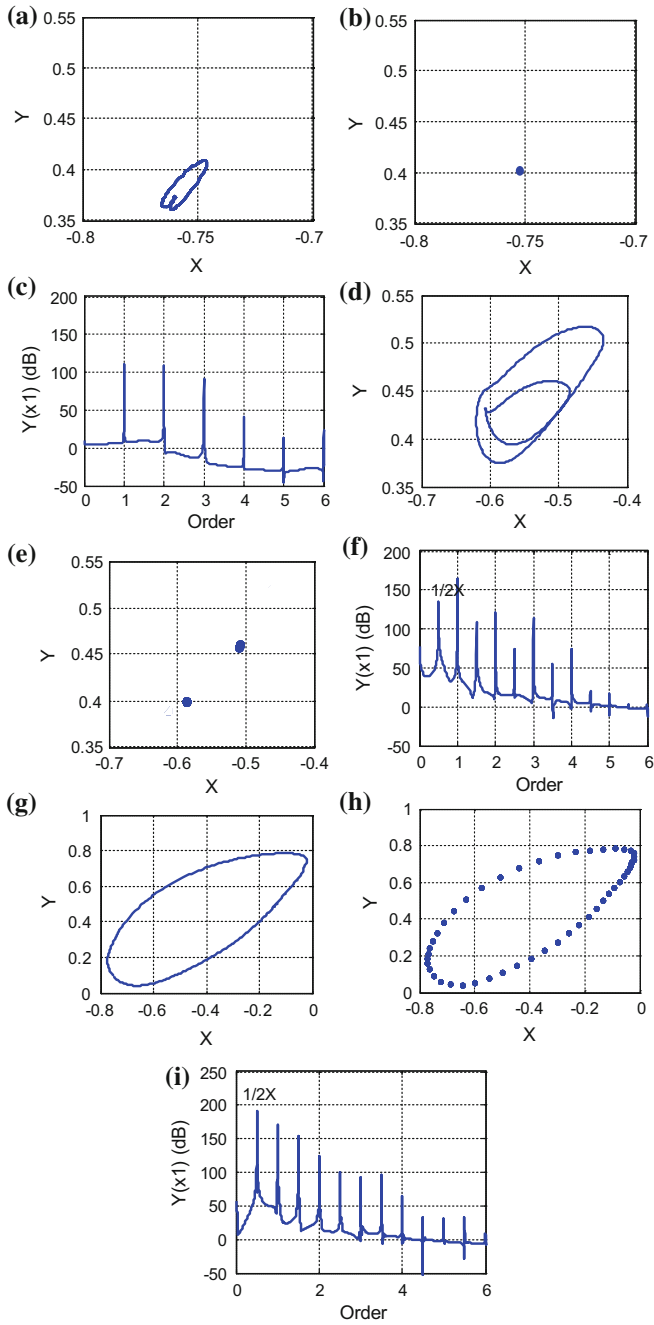
Fig. 7 Trajectory of the journal center, Poincaré section and power spectrum: $\Gamma = 0.1$, $\bar{e}_b = 0.05$, $\bar{k} = 10$, $\Delta k_\varepsilon = 0.4$ and $\Delta k_\eta = 0.16$ for $\varpi = 0.5$, 2 and 2.45

References

Chaofeng LI, Hexing YU (2013) Simulations and experimental investigation on motion stability of a flexible rotor-bearing system with a transverse crack. Chin J Mech Eng 26(6)

Frêne J, Nicolas D, Degueurce B (1997) Hydrodynamic lubrication bearings and thrust bearings. Elsevier, Tribology Series, Amsterdam

Gómez-Mancilla J (2005) A simple crack breathing mechanism for rotor systems with crack depth nonlinear evolution ISCORMA-3. Cleveland, Ohio, pp 19–23

Gomez-Mancilla JC, Machorro-Lopez JM (2005) Local resonance of crack-imbalance orientations and orbital evolution to detect mid-span rotor cracks: part 2, experimental validation IMAC-XXIII In: Conference & exposition on structural dynamics

Luo Y, et al (2014) Study on nonlinear vibration and crack fault of rotor-bearing-seal coupling system. Sens Transducers 165(2):1–7

Patela TH, Darpe AK (2008) Influence of crack breathing model on nonlinear dynamics of a cracked rotor. J Sound Vib 311:953–972

Sinou JJ, Lees AW (2007) A non-linear study of a cracked rotor. Eur J Mech A Solids 26:152–170

Wang J (2005) On the stability of rotor bearing systems based on hopf bifurcation theory. PhD thesis, Jiao Tong University

Xue S, Cao J (2011) Nonlinear dynamic analysis of a cracked rotor-bearing system with fractional order damping. IDETC/CIE 2011 August 28–31. Washington, DC, USA

Optimized Nonlinear MDOF Vibration Energy Harvester Based on Electromagnetic Coupling

I. Abed, N. Kacem, N. Bouhaddi and M. L. Bouazizi

Abstract Vibration energy harvesters (VEHs) provide an efficient solution for implementing self-sustained low power microelectromechanical systems. When operating linearly, unimodal VEHs have a narrow operating bandwidth. Consequently, their performances can be significantly reduced if the VEH resonance frequency and the excitation frequency do not coincide. In order to overcome this issue, we propose an optimized nonlinear multi-degree of freedom (MDOF) vibration energy harvesting system based on electromagnetically coupled beams. The dynamic equations of the equivalent discrete nonlinear MDOF model, which include the magnetic nonlinearity, the mechanical nonlinearity due to the mid-plane stretching of the beams and the electromagnetic damping, are derived and numerically solved using the harmonic balance method coupled with the asymptotic numerical method. A multiobjective optimization procedure is defined and performed using a non-dominated sorting algorithm (NSGA) in order to find the optimal solution in terms of performances by taking advantage of the nonlinear coupling and the modal interactions. The proposed strategy enables scavenging the

I. Abed · N. Kacem (✉) · N. Bouhaddi
Department of Applied Mechanics, FEMTO-ST Institute, CNRS/UFC/ENSMM/UTBM,
University of Bourgogne Franche-Comté, 24 rue de l'Epitaphe, 25000 Besançon, France
e-mail: najib.kacem@femto-st.fr

I. Abed
e-mail: issam.abed@femto-st.fr

N. Bouhaddi
e-mail: noureddine.bouhaddi@femto-st.fr

I. Abed
National School of Engineering of Tunis (ENIT), University of Tunis El Manar (UTM),
Tunis, Tunisia

I. Abed · M. L. Bouazizi
Preparatory Engineering Institute of Nabeul, M'Rezgua, 8000 Nabeul, Tunisia
e-mail: mohamedlamjed@gmail.com

M. L. Bouazizi
Mechanical Department, College of Engineering, Prince Sattam Bin Abdulaziz University,
KSA, Al-Kharj, Saudi Arabia

vibration energy with a frequency bandwidth ranging from 22 to 32 Hz and a normalized harvested power of 312 μW cm^{-3} g^{-2}.

Keywords Energy harvesting · Multiobjective optimization · Nonlinear dynamics · Electromagnetic coupling

1   Introduction

The mechanical structures are exposed to ambient and internal vibrations, aiming at producing energy through the use of appropriate transducers, which convert the mechanical force to electric power (Williams and Yates 1996). The accumulated energy in these cases can be stored and used. With the innovated trend of smart technologies, Vibration Energy Harvesters (VEHs) can be used in a variety of fields, such as environmental monitors, wireless sensors and medical implants. Linear unimodal VEHs have a narrow operating bandwidth, thus, limiting their application in real-world environments. Several approaches, such as resonant frequency tuning techniques (Leland and Wright 2006), multimodal energy harvesting (Arafa et al. 2011) and the exploitation of nonlinearities (Mann and Sims 2009; Mahmoudi et al. 2014) have been suggested in order to overcome this limitation. For instance, Roundy et al. (2005) suggested multiple proof masses attached on a clamped-clamped beam. Yang et al.'s electromagnetic generator (Yang et al. 2009), based on three fixed magnets along a beam vibrating at the top of three coils and operating in three modes of vibration is a direct implementation of this idea. Arafa et al. (2011) used a dynamic magnifier for the 2-DOFs cantilever piezoelectric VEH. This magnifier is made up of a spring-mass system, which is placed between the fixed ends of the piezoelectric beam and the vibrating base structure. Kim et al. (2011) came up with a VEH consisting of two piezoelectric cantilevers coupled with a common proof mass and utilizing both translational and rotational degrees of freedom. Masana and Daqaq (2011) suggested a nonlinear analysis of an electromechanical generator composed of a piezoelectric clamped–clamped beam. Mann and Sims (2009) proved analytically and experimentally how magnetic levitation could be used to extend device bandwidth through a hardening response. Yet, this extension is limited by a dry friction dissipation phenomenon. To overcome this issue, Mahmoudi et al. (2014) suggested an alternative consisting in guiding the moving magnet vertically in an elastic way by means of sandwich beams, combined with hybrid piezoelectric and electromagnetic transductions.

Multiple magnetic levitation was proposed, for the first time, combining nonlinearity and multimodal interactions (Bitar et al. 2015, 2016), enabling a significant improvement of the bandwidth and normalized power (Abed et al. 2015, 2016). As an extension of the latter study, one can suggest the multimodal optimization of an equivalent 2-DOF discrete model of two continuums beam models. The coupled

nonlinear equations of motion are derived and solved using the asymptotic numerical method (ANM) and the harmonic balance method (HBM) (Cochelin and Vergez 2009; Jallouli et al. 2016). Then, a multiobjective optimization procedure is performed through NSGA-II algorithm in order to enhance the performances of the nonlinear MDOF energy harvesting system, by taking advantage of modal interactions and geometric nonlinearity.

2 System Modeling

2.1 Equivalent Nonlinear Discrete Model

Based on a multimodal nonlinear vibration energy harvesting approach (Abed et al. 2015, 2016), we propose an extension of nonlinear vibration energy harvester based on electromagnetic transduction (Mahmoudi et al. 2014) for MDOF VEH systems. Thus, one can take advantages of modal interactions, geometric, and magnetic nonlinearities in order to obtain high performances in terms of bandwidth and harvested power. We propose an equivalent discrete model of a continuous beam system depicted in Fig. 1. The coupled magnets (M_{eq}) are placed between two fixed magnets (M) at the top and the bottom. All opposed surfaces of the magnetic poles have the same pole and between the separating distance of each two adjacent magnets, a wire-wound copper coils are wrapped horizontally around the separation distance between the magnets. M is the mass of magnet, M_{eq} is the equivalent mass, k_{10}, k_{12}, k_{23}, $k^L eq$ are the linear stiffness, α_{10}, α_{12}, α_{23}, λ_{10}, λ_{12}, λ_{23}, $k^{NL} eq$ represent the nonlinear stiffness, c_{e1}, c_{e2}, c_{e3} denote the electromagnetic damping and c is the mechanical damping.

Fig. 1 Equivalent electromechanical system
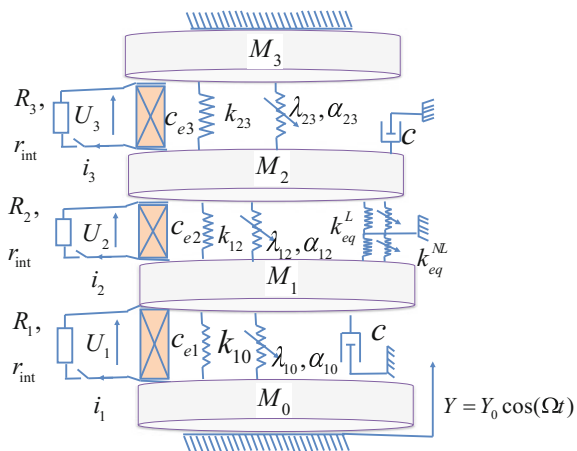
The moving magnets motion is described with the reference frames (v_1 and v_2):

$$\begin{cases} F_1^m = \begin{pmatrix} k_{10}v_1 + k_{12}(v_1 - v_2) + \alpha_{10}v_1^2 - \alpha_{12}(v_1 - v_2)^2 \\ + \lambda_{10}v_1^3 + \lambda_{12}(v_1 - v_2)^3 + k_{eq}^L v_1 + k_{eq}^{NL} v_1^3 \end{pmatrix} \\ F_2^m = \begin{pmatrix} k_{21}(v_2 - v_1) + k_{23}v_2 + \alpha_{21}(v_2 - v_1)^2 - \alpha_{23}v_2^2 \\ + \lambda_{21}(v_2 - v_1)^3 + \lambda_{23}v_2^3 + k_{eq}^L v_2 + k_{eq}^{NL} v_2^3 \end{pmatrix} \end{cases} \tag{1}$$

The linear and nonlinear stiffness can be written as follows:

$$\begin{array}{ccc} k_{10} = \dfrac{\mu_0 Q_0 Q}{2\pi d_0^3} & \alpha_{10} = \dfrac{3\mu_0 Q_0 Q}{4\pi d_0^4} & \lambda_{10} = \dfrac{\mu_0 Q_0 Q}{\pi d_0^5} \\[3mm] k_{12} = k_{21} = \dfrac{\mu_0 Q^2}{2\pi d_1^3} & \alpha_{12} = \alpha_{21} = \dfrac{3\mu_0 Q^2}{4\pi d_1^4} & \lambda_{12} = \lambda_{21} = \dfrac{\mu_0 Q^2}{\pi d_1^5}, \\[3mm] k_{23} = \dfrac{\mu_0 Q_3 Q}{2\pi d_2^3} & \alpha_{23} = \dfrac{3\mu_0 Q_3 Q}{4\pi d_2^4} & \lambda_{23} = \dfrac{\mu_0 Q_3 Q}{\pi d_2^5} \end{array} \tag{2}$$

where Q_i (i = 0, 1, 2, 3) represents the magnetic intensity of each moving magnet, μ_0 refers to the magnetic permeability and d_i (i = 0, 1, 2) designates the gap between two adjacent magnets. The magnetic intensity of fixed magnets is written as Q = S × H_c, with S and H_c are respectively the cross section and coercive force.

2.2 Equations of Motion of the System Under Harmonic Ground Excitation

The equations of dynamic motion of the 2-DOF nonlinear system are:

$$M \begin{pmatrix} \ddot{v}_1 \\ \ddot{v}_2 \end{pmatrix} + C \begin{pmatrix} \dot{v}_1 \\ \dot{v}_2 \end{pmatrix} + (K - K_\alpha + K_\lambda) \begin{pmatrix} v_1 \\ v_2 \end{pmatrix} = -F_{eq} \ddot{Y} \begin{pmatrix} 1 \\ 1 \end{pmatrix}, \tag{3}$$

where

$$M = \begin{pmatrix} M_{eq} & 0 \\ 0 & M_{eq} \end{pmatrix} \qquad C = \begin{pmatrix} c_{eq} + c_{e1} + c_{e2} & -c_{e2} \\ -c_{e2} & c_{eq} + c_{e1} + c_{e2} \end{pmatrix}$$

$$K = \begin{pmatrix} k_{eq}^L + k_{12} + k_{10} & -k_{12} \\ -k_{21} & k_{eq}^L + k_{23} + k_{21} \end{pmatrix} \quad K_\alpha = \begin{pmatrix} (\alpha_{12} - \alpha_{10})v_1 & \alpha_{12}(v_2 - 2v_1) \\ \alpha_{21}(2v_2 - v_1) & (\alpha_{23} - \alpha_{21})v_2 \end{pmatrix}$$

$$K_\lambda = \begin{pmatrix} (\lambda_{10} + \lambda_{12})v_1^2 + 3\lambda_{12}v_1^2 & -\lambda_{12}(v_2^2 + 3v_1^2) \\ -\lambda_{21}(v_1^2 + 3v_2^2) & (\lambda_{21} + \lambda_{23})v_2^2 + 3\lambda_{23}v_2^2 \end{pmatrix}$$

$$\tag{4}$$

and

$$M_{eq} = \frac{13L}{35}\rho_s S_s + M \quad c = 2\xi\sqrt{\frac{k_{eq}}{M_{eq}}} \quad F_{eq} = \frac{L}{2}\rho_s S_s + M$$
$$k_{eq} = \frac{12E_s I_s}{L^3} \quad k_{eq}^{NL} = \frac{18E_s S_s}{25L^3}$$
(5)

2.3 Power Transferred to the Electrical Circuit

The average power delivered to the electrical load is

$$P = \frac{\Omega}{2\pi}\int_0^{\frac{2\pi}{\Omega}} p(t)\,dt = \frac{\Omega^2}{2}\left(c_{e1}V_1^2 + c_{e2}\left(V_1^2 - V_2^2\right) + c_{e3}V_2^2\right),$$
(6)

where $v_1(t) = V_1\cos(\Omega t)$, $v_2(t) = V_2\cos(\Omega t)$ are the displacements of the moving magnets, under harmonic ground excitation.

3 Multiobjective Optimization

Our main goal consists in the exploitation of the geometric nonlinearity and the nonlinear magnetic coupling in order to increase the harvested power and the bandwidth. To do so, two objective functions g_1 and g_2 have been defined: the first one "g_1" is related to the distance between eigenfrequencies while the second one concerns the intermodal distance between the harvested powers taken at the natural frequencies (Abed et al. 2016).

$$\begin{cases} g_1 = \frac{f_1}{f_2 - f_1} \\ g_2 = \frac{|P_1 - P_2|}{P_{n1}} \end{cases},$$
(7)

where P_{n1} and P_1 are the normalized power and the harvested power at the first eigenfrequency f_1 and P_2 is the harvested power at the second eigenfrequency f_2.

In order to increase the performance of the nonlinear MDOF energy harvesting system, the resonance peaks must be close to each other in terms of natural frequencies and modal harvested power amplitudes. The objective functions g_1 and g_2 are used in an optimization method (NSGA-II) (Dep et al. 2002). Two cost functions are simultaneously minimized with respect to the eight design parameters (L_c, r_0, r_3, h_s, d_2, 2L, b and M) retained after a sensitivity analysis.

$$\text{Minimize} \qquad [g_1(x), g_2(x)],$$
$$x = [L_c, r_0, r_3, h_s, d_2, 2L, b, M]^T, \qquad (8)$$

The Pareto-optimal solutions achieved by NSGA-II after 200 generations are shown in Fig. 2. The Pareto-optimal front is convex, where three solutions have been selected. The frequency responses in terms of amplitude, phase, and harvested power are shown in Fig. 3 for design parameters of solution 1 and an excitation amplitude $Y_0 = 0.06$ mm.

It shows that the two moving magnets vibrate in phase below the critical amplitude (Kacem et al. 2009, 2010, 2011; Juillard et al. 2008) for the frequencies $f_1 = 22$ Hz and $f_2 = 32$ Hz.

Figure 4 and Table 1 display the comparison between the selected solutions in term of normalized harvested power. The first retained solution has the highest normalized power close to 312 µW cm^{-3} g^{-2} while the third one has the largest bandwidth (BW = 75%).

Fig. 2 Pareto-optimal solutions obtained by multiobjective optimization
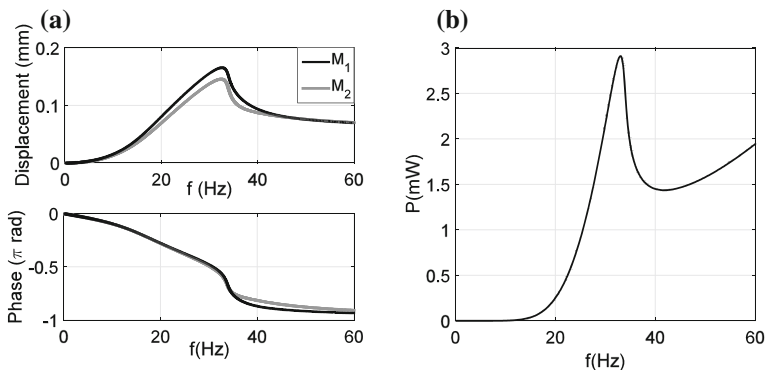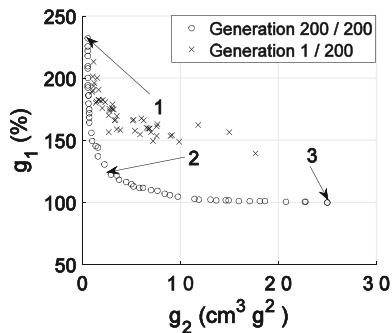
Fig. 3 Frequency responses in terms of **a** amplitude and phase **b** harvested power

Fig. 4 Frequency responses in term of normalized harvested power of the optimal solutions
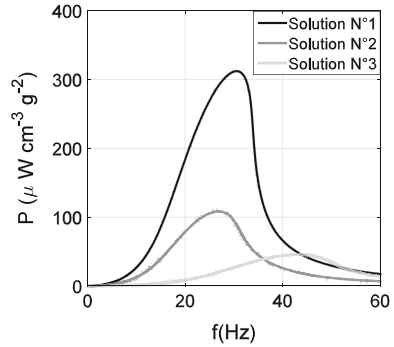
Table 1 Performances of the VEH for the three selected optimal solutions

Parameters	Solution 1	Solution 2	Solution 3
f_1 (Hz)	22	21	35
f_2 (Hz)	32	39	71
P_n (μW cm^{-3} g^{-2})	312	109	46
BW (%)	15	35	75

4 Conclusion

In this paper, an optimized nonlinear MDOF energy harvesting system based on electromagnetic coupling is proposed. While taking into account the mechanical nonlinearity, the magnetic nonlinearity and the electromagnetic damping and considering frequency-dependent excitation amplitude, the equations of motion have been derived and solved using the asymptotic numerical method and the harmonic balance method. A multiobjective optimization procedure is introduced and performed using NSGA-II algorithm in order to select the optimal designs in terms of performances. The optimized nonlinear MDOF VEH system enables harvesting the vibration energy in the frequency range 22–32 Hz with a normalized harvested power of 312 μW cm^{-3} g^{-2}.

References

Abed I, Kacem N, Bouazizi ML, Bouhaddi N (2015) Nonlinear 2-dofs vibration energy harvester based on magnetic levitation. In Shock and Vibration, Aircraft/Aerospace, and Energy Harvesting, vol 9. Springer International Publishing pp 39–45

Abed I, Kacem N, Bouhaddi N, Bouazizi ML (2016) Multi-modal vibration energy harvesting approach based on nonlinear oscillator arrays under magnetic levitation. Smart Mater Struct 25(2):025018

Arafa M, Akl W, Aladwani A, Aldraihem O, Baz A, (2011) Experimental implementation of a cantilevered piezoelectric energy harvester with a dynamic magnifier. Proc SPIE 7977 79770Q

Bitar D, Kacem N, Bouhaddi N, Collet M (2015) Collective dynamics of periodic nonlinear oscillators under simultaneous parametric and external excitations. Nonlinear Dyn 82(1):749–766

Bitar D, Kacem N, Bouhaddi N, (2016) Investigation of modal interactions and their effects on the nonlinear dynamics of a periodic coupled pendulums chain. Int J Mech Sci. https://doi.org/10.1016/j.ijmecsci.2016.11.030

Cochelin B, Vergez C (2009) A high order purely frequency-based harmonic balance formulation for continuation of periodic solutions. J Sound Vib 324(12):243–262

Deb K, Pratap A, Agarwal S, Meyarivan T (2002) A fast and elitist multiobjective genetic algorithm: NSGA-II. IEEE Trans Evolut Comput 6(2):182–197

Jallouli A, Kacem N, Bourbon G, Le Moal P, Walter V, Lardies J (2016) Pull-in instability tuning in imperfect nonlinear circular microplates under electrostatic actuation. Phys Lett A 380(46):3886–3890

Juillard J, Bonnoit A, Avignon E, Hentz S, Kacem N, Colinet E (2008) From MEMS to NEMS: closed-loop actuation of resonant beams beyond the critical duffing amplitude. IEEE Sensors Lecce 2008:510–513

Kacem N, Hentz S, Pinto D, Reig B, Nguyen V (2009) Nonlinear dynamics of nanomechanical beam resonators: improving the performance of NEMS-based sensors. Nanotechnology 20(27):275501

Kacem N, Baguet S, Hentz S, Dufour R (2010) Nonlinear phenomena in nanomechanical resonators: mechanical behaviors and physical limitations. Mécanique Ind 11(6):521–529

Kacem N, Hentz S, Baguet S, Dufour R (2011) Forced large amplitude periodic vibrations of non-linear Mathieu resonators for microgyroscope applications. Int J Non-Linear Mech 46(10):1347–1355

Kim I-H, Jung H-J, Lee BM, Jang S-J (2011) Broadband energy-harvesting using a two degree-of-freedom vibrating body. Appl Phys Lett 98(21):214102

Leland ES, Wright PK (2006) Resonance tuning of piezoelectric vibration energy scavenging generators using compressive axial preload. Smart Mater Struct 15(5):1413

Mahmoudi S, Kacem N, Bouhaddi N (2014) Enhancement of the performance of a hybrid nonlinear vibration energy harvester based on piezoelectric and electromagnetic transductions. Smart Mater Struct 23(7):075024

Mann B, Sims N (2009) Energy harvesting from the nonlinear oscillations of magnetic levitation. J Sound Vib 319(12):515–530

Masana R, Daqaq MF (2011) Electromechanical modeling and nonlinear analysis of an axially-loaded energy harvesters. J Vib Acoust 133(1):011007

Roundy S, Leland E, Baker J, Carleton E, Reilly E, Lai E, Otis B, Rabaey J, Wright P, Sundararajan V (2005) Improving power output for vibration-based energy scavengers. Pervasive Comput IEEE 4(1):28–36

Williams C, Yates R (1996) Analysis of a micro-electric generator for microsystems. Sens Actuators A 52(13):8–11

Yang B, Lee C, Xiang W, Xie J, He JH, Kotlanka RK, Low SP, Feng H (2009) Electromagnetic energy harvesting from vibrations of multiple frequencies. J Micromech Microeng 19(3):035001

Sub-hourly Validation of the Direct Normal Solar Irradiance Clear Sky Models

I. Loghmari and Y. Timoumi

Abstract The Direct Normal Irradiance (DNI) is the fuel for all concentrating solar energy systems. It could either be measured by means of highly sophisticated instruments or computed using DNI models. These models utilize meteorological and atmospheric parameters as inputs to predict instantaneously the DNI in regions where no measurements are available. This paper presents a performance analysis of the Ineichen, Iqbal and Solis models to predict the direct normal irradiance when we present low-quality input parameters. The models have been used to predict DNI in a southern Tunisian region. The prediction results have been compared to measurements. The sub-hourly statistical evaluation of these models shows the following errors: when the DNI is higher than 700 W/m^2 (at noon), the Iqbal model is the most accurate prediction model with a relative root mean square error (rmse %) equal to 9.82%. The same model has recorded the best accuracy when DNI is lower than 700 (the sun is close to the horizon), the rmse% reaches 27.88%. Such results clearly show that presenting a limited quality inputs to the models, at the limit, can be accepted to perform DNI prediction at noon but they are not suitable to predict effectively the DNI when the sun is close to the horizon.

Keywords Direct normal irradiance · Atmospheric and meteorological parameters · Clear sky models · Desert region

1 Introduction

The knowledge of the availability of direct normal irradiance (DNI) in a specific region plays a crucial role to perform a reliable estimation of the performance of concentrating solar energy systems. Due to the high spatial and temporal variability

I. Loghmari (✉) · Y. Timoumi
Mechanical Engineering Laboratory, University of Monastir, Monastir, Tunisia
e-mail: yesine@live.fr

Y. Timoumi
e-mail: Youssef.Timoumi@enim.rnu.tn

39

of the DNI and the high cost measuring equipment, it is not obvious to determine, with high precision, the available DNI in a particular area. A wide variety of clear sky models is developed in the literature and used to compute instantaneously the DNI in a region devoid of measuring equipment (Bakirci 2009).

Ineichen (2016) compared seven clear sky models (Kasten, MC-clear, CPCR2, REST2, ESRA, simplified Solis and Bird) to 22 solar radiation ground station measurements located in Europe and in the Mediterranean regions. The REST2 (Gueymard 2003), the MC-clear (Lefevre 2013) and the simplified Solis (Ineichen 2008) models are revealed as the best predicting models. The standard deviation varies from ±4 to ±5%.

Energer and Mills (2015) tested nine clear sky models (Ineichen, Ineichen-Perez, Bird, Mac, Molineau, simplified Solis, ESRA, Iqbal and REST2) to estimate the DNI over Australia. The results of predictions were compared against 20 ground measuring stations. The model of ESRA (Rigollier et al. 2000), Iqbal (1983) and REST2 (Gueymard 2003) were the most accurate models. The relative root mean square error varies from 3.48 to 9.67%.

Gueymard (2012) compared 18 clear sky models with high-quality measurements over five different sites. Based on statistical indicators: the model of REST2, simplified Solis, Hoyt, Bird and Iqbal were the best predicting models to estimate the DNI.

Younes and Muneer (2007) tested four models: REST2, ESRA, MRM and Yang model to predict solar radiation over six Spanish stations. Based on a developed error score, the Yang (2001), MRM (Muneer 1998) and REST2 model were judged to be of "satisfactory performance".

Alam (2006) compared three DNI prediction models: CPCR2, Yang and REST2 to estimate the DNI over four Indian sites. The REST2 (Gueymard 2003) model was the most accurate model to predict the DNI with a maximum relative root mean square error equal to 6.5%.

Ineichen (2006) evaluated eight clear sky models: Bird, Solis, Molineau, Ineichen-Perez, ESRA, CPCR2, Kasten and REST2, using 16 measuring stations located between the latitude 28° and 45°. The models predicted the DNI with a bias error varying between 2 and –25 W/ and a relative mean square error ranging from 27 to 34 W/m^2. The Solis model was the most performing model to predict the solar radiation.

These clear sky models use meteorological and atmospheric data as input parameters to perform instantaneous DNI prediction over the day. Therefore, a high-quality DNI estimation is directly related to the precision of the input parameters. In clear sky condition, the aeorol optical depth (aod) is one of the most atmospheric input parameters affecting the DNI (Gueymard and George 2005). So, in order to conduct a reasonable sub-hourly validation of the clear sky models, the aod and other input parameters should also be presented with a sub-hourly resolution. Unfortunately, high-quality aod databases or other atmospheric data are not generally available. Indeed, except few aod measurement datasets such as

AERONET and SKYNET and high-quality modelled databases such as MATCH (Schroedter-Homscheidt and Oumbe 2013), most of the available aod datasets are presented with limited quality average values (Sengupta 2015). Ineichen (2006) has used a short-term (1 year) monthly aod database as an input parameter to clear sky models. In a subsequent work, the same author (Ineichen 2016) has used two sources of daily aod database, the first is retrieved from measurements and the second source is extracted from MAC II project. Both of the used aod databases represent only daily values that do not reflect the real aod sub-hourly variability.

Most of clear sky models have been validated using low-quality inputs parameter over all the day (Engerer and Mills 2015), but no study found in the literature details the impact of a low-quality input parameter on the sub-hourly uncertainty of the clear sky models. This paper addresses to cover this lack in the literature by investigating the impact of a daily-100 km spatial resolution aod database on the accuracy of three clear sky models.

2 Direct Normal Irradiance Modelling

2.1 Clear Sky Models

The clear sky models use atmospheric, meteorological and geographic parameters as inputs in order to perform an instantaneous computation of the direct normal solar radiation (DNI) throughout the day (Fig. 1).

Three of the best and largely used clear sky models have been selected to compute and evaluate the DNI. The choice of the simplified Solis (Ineichen 2008), Ineichen (Ineichen and Perez 2002) and Iqbal (Wong and Chow 2001) models was based on the availability of input parameters in the desired region and their simplicity of implementation.

The aerosol optical depth (aod), the air mass (am), the Link Turbidity (TL), the Ozone column (loz) and the Water vapour column (W) are required to implement these models.
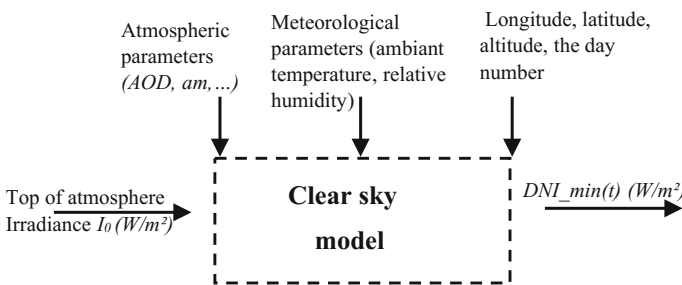
Fig. 1 Clear sky model representation

2.2 Capturing Input Parameters

As shown in Fig. 1, there are mainly four types of input parameters that must be introduced to a clear sky model in order to perform the calculation of the DNI in a specific region. This section presents the sources from where these input parameters have been retrieved:

Top of atmosphere

The value of I0 = 1367 W/m^2 has been used in our study.

Atmospheric parameters

Aerosol optical depth (aod): daily average values extracted from the NASA 100 km spatial resolution database (NASA 2016) are used in this study.

Water vapour column (W): Awter equation has been used in this study to calculate W (Atwater and Ball 1976):

$$W = \exp\left(0.0704074\left(Ta - Rh\right)/5\right) + 0.02023 \tag{1}$$

Ta stands for the ambient temperature and Rh is the relative humidity. Daily average values of Ta and Rh have been adopted in this study.

Ozone column (loz): For the ozone column, a general average value of 340 DU (Ineichen 2006) was used in this study.

Link Turbidity (TL): Monthly average values, extracted from the Soda database (Soda 2016), was used to represent the link Turbidity in a specific region.

Airmass (am): An expression, presented by Eq. 2, was adopted to calculate the am (Kasten 1965):

$$am = \left[\sinh + 0.506(h + 6.08)^{-1.636}\right]^{-1} \tag{2}$$

h is the sun elevation.

3 Calculation of the Direct Normal Irradiance Using Clear Sky Models

3.1 Models Implementation

The three clear sky models were implemented on *MATLAB 2012* software to calculate the direct normal irradiance instantaneously throughout the day. In Fig. 2 we show the result of the calculation of the Ineichen, Solis and Iqbal models in a south Tunisian region called Tataoine during the day of 10 June 2013.

In Fig. 2, the results of the DNI calculations were presented in 10-min resolution. Such resolution corresponds exactly to measurement resolution extracted from a meteorological station located in the region.
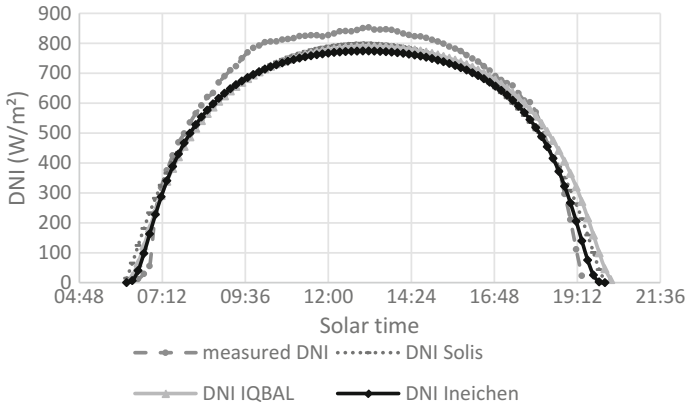
Fig. 2 Clear sky model calculation of the direct normal irradiance (DNI) in Tataoine region, date: June 10, 2013

Fig. 3 Comparison of direct normal irradiance (DNI) measured and calculated by Solis model for the summer season
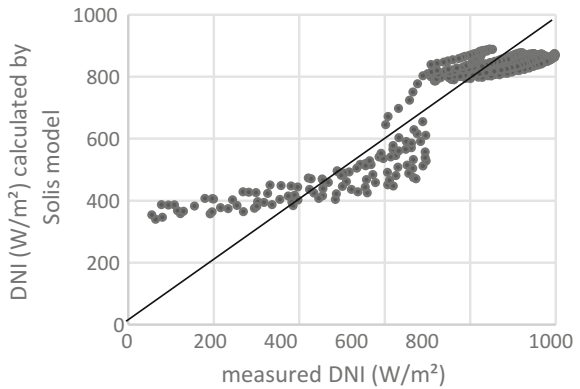
4   Models Evaluation

To evaluate the developed clear sky models, we compared their results with the measurements of a high-quality first class Kipp&Zonen CHP1 Pyrheliometer. 20 days, covering all the seasons of the year, i.e. from every season we took 5 days, have been selected to evaluate the models. An example of the modelled and measured DNI for the summer season, represented by the following 5 days: 10 June 2013; 12 June 2012; 9 June 2011; 21 June 2015 and 9 June 2011 is presented in Figs. 3, 4 and 5.

For each season, we compared every clear sky model with 10-min resolution measurement, i.e. more than 1400 points that represent 20 days have been compared.

Fig. 4 Comparison of direct normal irradiance (DNI) measured and calculated by Iqbal model for the summer season
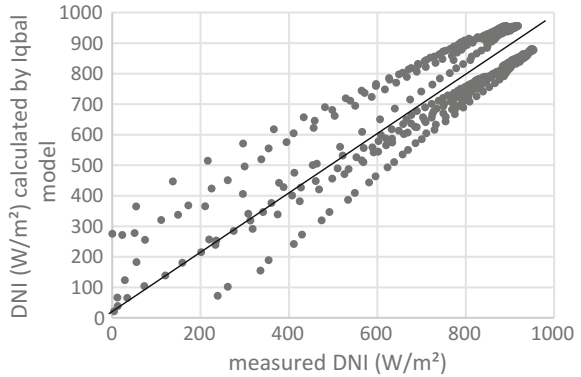
Fig. 5 Comparison of direct normal irradiance (DNI) measured and calculated by Ineichen model for the summer season
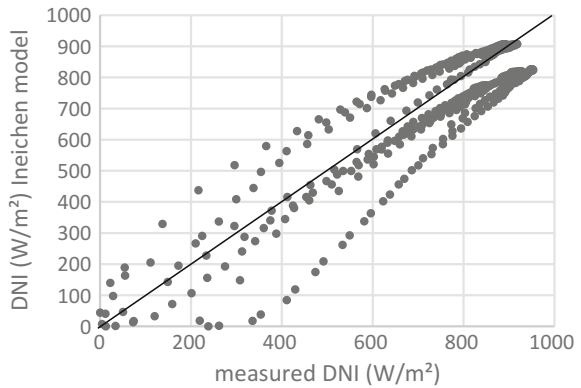
We used the root mean square error (rmse), the mean bias (mbe) error to evaluate our clear sky models. The obtained results are presented in Fig. 6.

The results presented in Figs. 3, 4 and 5 show that the models are likely suitable to predict DNI at high intensity. Indeed, when DNI is lower than 700 W/m², the points marked by all clear sky models are more dispersed with respect to the first bisector (y = x). However, these dots marked by calculated DNI are more convergent to the first bisector when DNI is higher than 700 W/m².

The inter-seasonal evaluation of the three clear sky models (Fig. 6) shows the superiority of the Iqbal model to predict DNI in Tataouine region with 14.21% rmse % and –4.8% mbe.

It is important to mention that, for all the clear sky models, the mbe% is negative, which shows that, on average, the models are underestimating the DNI.

For low-intensity DNI (DNI $\leq$ 700 W/m²) when the sun is close to the horizon, i.e. early morning or at the evening, the accuracy of clear sky models is relatively low.

In order to perform a reasonable study of the accuracy of clear sky models to compute DNI over the journey, we conducted a discrete evaluation of the models based on the DNI intensity:

- $50 \leq DNI \leq 700$ W/m^2;
- $701 \leq DNI \leq 800$ W/m^2;
- $801 \leq DNI \leq 1100$ W/m^2.

In Fig. 7, we presented the evaluation results of our three clear sky models for each interval.

The results of the evaluation presented in Fig. 7 are consistent with those presented in Figs. 3, 4 and 5. Indeed, the accuracy of the three clear sky models increases with the DNI intensity. The Ineichen model has the lowest accuracy for all the DNI intervals. The Iqbal model is the most accurate model to estimate DNI for its highest and lowest interval, i.e. when $50 \leq DNI \leq 700$ W/m^2 and
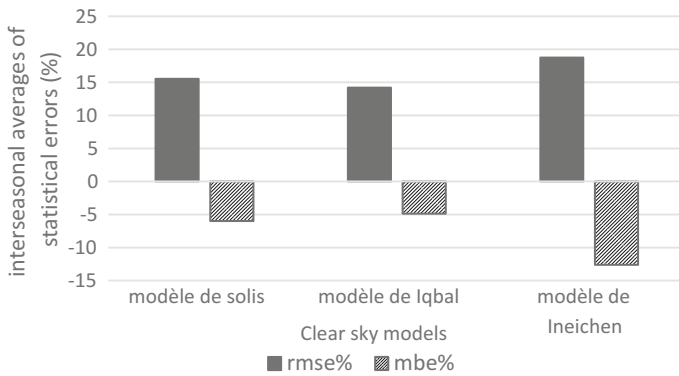
Fig. 6 Interseasonal root mean square error (rmse%) and mean bias error (mbe%) recorded by the three clear sky models

Fig. 7 The root mean square error rmse% recorded by clear sky models at every DNI interval
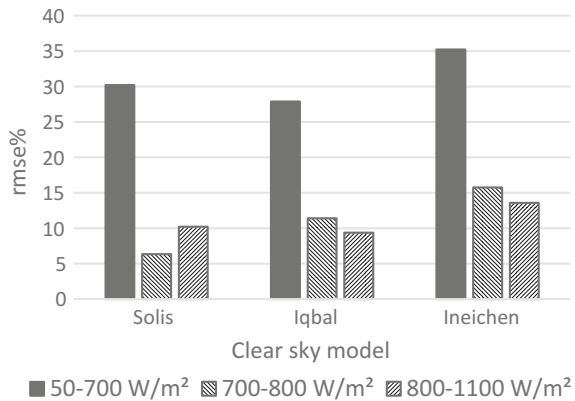
$801 \leq DNI \leq 1100$ W/m^2. However, Solis model is the most favourable model to predict DNI for $701 \leq DNI \leq 800$ interval.

The results of evaluation presented in Figs. 6 and 7 show that the precisions of the models were generally low. This could be explained by the fact that the introduced input parameters are with low quality, e.g. daily average values of *aod, Ta, Rh...*etc. For this reason, it is not reasonable to introduce low-quality input parameters and expect high-quality DNI estimation. Especially when the DNI is low, the achieved accuracy is not acceptable. This result is in agreement with the one presented by, Ineichen (2006) when he showed that when the sun is close to the horizon (high zenith angle) the precision of the DNI models was considerably reduced. Hence it is absolutely important to look on high-quality input parameter in order to achieve high-quality DNI estimation.

5 Conclusion

In order to estimate the performance of the concentrating solar energy technologies, the DNI should be predicted with a high accuracy in the desired potential implementation site. This solar energy component can be measured with high-cost prices, or computed using models. In this paper, we have conducted a sub-hourly evaluation study of three DNI clear sky models. The purpose is to criticize the DNI clear sky models sub-hourly accuracy when we present a limited quality input parameter.

The results of the model evaluation show that the DNI clear sky models perform very well when the DNI is at high intensity (DNI ≥ 700 W/m^2). It is recommended to use the Iqbal model to predict the sub-hourly DNI. However, when the sun is close to the horizon (low DNI intensity), due the low accuracy achieved, it is not suitable to compute the DNI using a clear sky model with low-quality input parameter.

References

Journal Article

Alam S (2006) Prediction of direct and global solar irradiance using broadband models: validation of REST model. Renewable Energy 31(8):1253–1263

Atwater MA, Ball JT (1976) Comparison of radiation computations using observed and estimated precipitable water. J Appl Meteorol 15:1319–1320

Bakirci K (2009) Estimation of solar radiation by using ASHRAE clear-sky model in erzurum Turkey. Energy Sour Part A 31(3):208–216

Engerer NA, Mills FP (2015) Validating nine clear sky radiation models in Australia. Sol Energy 120:9–24

Gueymard CA (2003) Direct solar transmittance and irradiance predictions with broadband models. Part I: detailed theoretical performance assessment. Sol Energy 74(5):355–379

Gueymard CA, George R (2005) Gridded aerosol optical depth climatological datasetsover continents for solar radiation modeling. International solar energy society solar world congress proceedings. Orlando, Florida

Gueymard CA (2012) Clear-sky irradiance predictions for solar resource mapping and large-scale applications: improved validation methodology and detailed performance analysis of 18 broadband radiative models. Sol Energy 86(8):2145–2169

Ineichen P (2008) A broadband simplified version of the Solis clear sky model. Sol Energy 82:758–762

Ineichen P (2006) Comparison of eight clear sky broadband models against 16 independent data banks. Sol Energy 80:468–478

Ineichen P (2016) Validation of models that estimate the clear sky global and beam solar irradiance. Sol Energy 132:332–344

Ineichen P, Perez R (2002) A new airmass independent formulation for the linke turbidity coefficient. Sol Energy 73(3):151–157

Iqbal M (1983) An introduction to solar radiation. Academic Press Inc, New York

Kasten F (1965) A new table and approximation formula for the relative optial air mass. Archiv für Meteorologie, Geophysik und Bioklimatologie, Serie B, 14(2): 206–223

Lefevre MO (2013) McClear: a new model estimating downwelling solar radiation at ground level in clear-sky conditions. Atmos Measur Tech 6:2403–2418

Muneer TG (1998) Evaluation of an all-sky meteorological radiation model against long-term measured hourly data. Energy Convers Manage 39(3):303–317

Rigollier C, Bauer O, Wald L (2000) On the clear sky model of the ESRA—European solar radiation atlas—with respect to the heliosat method. Sol Energy 68(1):33–48

Schroedter-Homscheidt M, Oumbe A (2013) Validation of an hourly resolved global aerosol model in answer to solar electricity generation information needs. Atmos Chem Phys 13 (7):3777–3791

Wong LT, Chow WK (2001) Solar radiation model. Appl Energy 69(3):191–224

Yang KH (2001) A hybrid model for estimating global solar radiation. Sol Energy 70(1):13–22

Younes S, Muneer T (2007) Clear-sky classification procedures and models using a world-wide data-base. Appl Energy 84(6):623–645

Online Document (no DOI available)

NASA (2016) http://giovanni.sci.gsfc.nasa.gov/giovanni Accessed 01 Jan 2017

Sengupta M, Habte A, kurtz S, Dobos A, Wilbert S, Lorenz E, Stoffel T, Renné D, Myers D, Wilcox S, Blanc P, Perez R (2015) Best practices handbook for the collection and use of solar resource data for solar energy applications. Technical report NREL/TP-5DT. Accessed 01 Jan 2017

Soda (2016) http://www.soda-is.com/eng/index.html Accessed 01 Jan 2017

Microstructure and Mechanical Properties of Friction Stir Welded AA2024-T3 Joints

Khaled Boulahem, Sahbi Ben Salem and Jamel Bessrour

Abstract This paper focuses on the examination of macrostructure and microstructure of friction–stir-welded AA2024-T3 joints. The tool rotation speed and the traverse speed, the most important process parameters of FSW, are evaluated through tensile strength test and microhardness test. The analysis of microstructure showed a zonal transition from the base material to a heat-affected zone; a thermo-mechanical affected zone and a nugget zone in the center of the weld with a grain sizes were different. From this investigation, it is found that the tensile strength and percentage elongation increase with the traverse speed decreasing, whereas it increases as tool rotation speed increases up to the 750 rpm and then decreases with further increase of tool rotation speed. As a result, increasing the tool rotational speed leads to the increase in hardness nugget zone than that in the thermo-mechanically affected zone and affected zone. The microhardness was strongly dependant on tool rotation speed and it increases with the increasing of this parameter from 600 to 750 rpm.

Keywords Friction stir welding · Joints defects · Microstructure
Ultimate tensile strength · Percentage elongation · Microhardness

K. Boulahem (✉)
ISET Jendouba, Jendouba University Campus, 8100 Jendouba, Tunisia
e-mail: khaboulahem@yahoo.fr

S. Ben Salem
IPEI Nabeul, Mrazka University Campus, 8000 Nabeul, Tunisia
e-mail: sahbi_bensalem@yahoo.fr

K. Boulahem · S. Ben Salem · J. Bessrour
Labo MAI, National Engineering School of Tunis, University of Tunis El Manar, Tunis, Tunisia
e-mail: jamel.bessrour@enit.rnu.tn

49

1 Introduction

Friction stir welding is solid-state joining process without filler metal developed by The Welding Institute in 1991. Significant advantages can be obtained when compared with fusion joining processes for aluminum. This technique is useful to join aluminum alloys especially 2xxx and 7xxx series that are difficult to weld by traditional fusion processes. Among the 2xxx series aluminum alloy, AA2024-T3 is most used in various industrial sectors, including the construction, aerospace aircraft, and automotive due to its high strength, excellent fatigue, and corrosion resistance. Thus, it has been chosen as the workpiece material in this study. With FSW, the interaction of a tool rotating and traversing along the joint line creates heat from friction between its shoulder and the base material, giving rise to plastic deformation with its pin.

From the open literatures, there are numerous contributions regarding the mechanical and microstructure properties in friction stir welding of aluminum alloys. Tehyo et al. (2012) investigated the influence of process parameters on metallurgical and mechanical properties of dissimilar FS welded joint between semi-solid metal 356-T6 and aluminum alloy 6061-T651 and reported that an increase in the tool traverse speed increases the tensile strength of the specimen. Furthermore, Silva et al. (2011) studied the effect of joining parameters on tensile strength, hardness, material flow, and microstructure of dissimilar FS-welded joints between AA2024-T3 and AA7075-T6 and reported that the lowest hardness value is shown in the heat-affected zone (HAZ) at the retreating side. In another study, Trimble et al. (2015) established the influence of tool pin profile on the microstructure and hardness of FSW joints of AA2024-T3 aluminum alloy and observed that the pin profiles with flat surface features and/or flutes produced consolidated joints with no defects and the heat-affected zone (HAZ) had the lowest hardness across the weld profile for each pin type tested. On another topic, (Bahemmat et al. 2012) noticed the effect of FSW parameters on the weldability, mechanical properties, and grain size of FS-welded dissimilar aluminum alloys AA2024-T4 and AA7075-O. Thus, (Liu et al. 2013) studied the quality of AA 6061-T6 welded by using self-reacting friction stir welding. They announced that the percentage elongation and ultimate tensile strength of joints increased with increasing tool traverse speed and the tensile fracture was located at the heat-affected zone on the advancing side.

Most of these previous works on AA2024-T3 aluminum alloy were carried out at the macrostructure analysis to eventual defects, the microscopic observation of the grain size in the welding zones and the influence parameters process on mechanical properties of joints to improve joint reliability. The microstructure and mechanical properties of friction stir welded of AA2024-T3 existing in the open literature will be discussed in this paper. The work included macrostructure, microstructure examination of joints, and evaluation of the influence of tool rotation and traverse speeds on the tensile test and microhardness test.

2　Experimental Work and Conditions

This study carried out using milling machine. The workpieces materials used were AA2024-T3 aluminum alloy plates in the form of $100 \times 110 \times 4$ clamped on the machine milling table as shown in Fig. 1a. The chemical composition and mechanical properties of the base material are presented in Tables 1 and 2. The longitudinal direction of the FSW was perpendicular to the rolling direction of AA 2024-T3 aluminum alloy. The weld tool, shown in Fig. 1b, had the following geometry type Wiper™ scrolls: flat shoulder of 13 mm in diameter with three equally spaced spiraled arcs, M4 threaded pin length of 3.7 mm with three equally spaced flats tapered with an included angle of 10º. The FSW tool employed in this study was made using AISI H13 tempered steel. In addition, the title angle tool is 3° to facilitate the mixing of the material.

Tensile tests were carried out on ETI-E0015 mechanical tester at strain stress of $1{,}67 \times 10^{-2}$ mm/s at room temperature. The tensile tests were performed according to ASTM E8-M in order to determine the mechanical properties (ultimate tensile strength, and percentage elongation). For the analysis of microstructural changes due to the FSW process, the joints were cross-sectioned perpendicularly to the welding direction and were etched with a standard Keller's reagent (5 ml HF, 20 ml HCl, 2 ml HNO_3, 20 ml H_2O). Microstructures of the joints were examined using the optical microscope. The linear intercept method based on ASTM: E112-13 was used to find the average grain size. Vickers microhardness of the
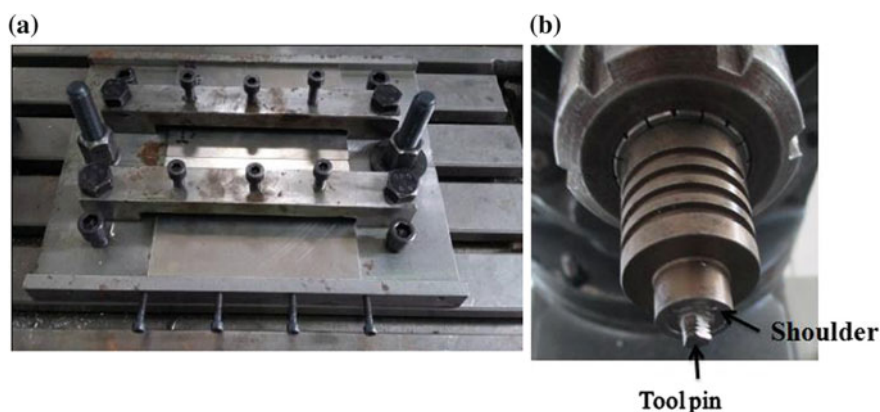
Fig. 1 Friction stir welding process **a** the clamping devices, **b** welding tool shape

Table 1 Chemical compositions and mechanical proprieties of AA2024-T3	Si	Fe	Cu	Mn	Mg	Cr	Zn	Al
	0.5	0.5	3.8	0.3	1.8	0.1	0.25	Balance

Table 2 Mechanical properties of the base plate AA2024-T3

Yield strength (MPa)	Tensile strength (MPa)	Elongation (%)	Vickers hardness (*HV*)
320	460	18	125

Table 3 Friction stir welding parameters and their levels

No.	Parameters	Notation	Unit	Levels		
				Min	Middle	Max
1	Rotation speed	N	rpm	600	750	900
2	Traverse speed	T	mm/min	100	150	200

specimens was measured above the mid-section from the base metal, employing a 100 gf load, loading time of 15 s and interval of 0.5 mm, using Vicker's microhardness tester MICROVICKERS-DM2A. The parameters selected for experimentation are tool rotational speed (N) and traverse speed (T) (Table 3).

3   Results and Discussion
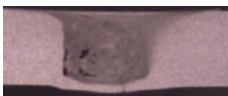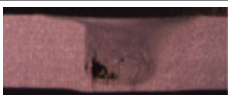
3.1   *Range of Process Parameters*

Usually, the FSW joints defects are undesirable irregularities that fail to generate the required heat for bonding, inadequate material mixing, and stirring to take place. Thus, FSW joints are prone to defects such as pin hole, lack of penetration, void, tunnel defect, kissing bond, zigzag line and cracks, due to the excess or insufficient heat input, abnormal stirring in the welded joints, default tool geometry (Kim et al. 2006; Zhang et al. 2015). The working range of each process parameter, such as tool rotational and traverse speeds, was decided upon by inspecting the macrostructure analysis and preliminary tests, in order to determine the existing defects and to define the permissible range of variation for each of the driving parameters. Minimum and maximum values are obtained for each of the two parameters which define the limits of the studied domain without exceeding the capacity of the milling machine (vibration). The macrostructure of the joints and visual inspection made at working range of process parameters, such as tool rotational and traverse speeds are presented in Table 4.

From the macrostructure, it can be inferred that the tool rotation speed was lower than 600 rpm; it produces less heat which causes insufficient material flow and less plasticization in stir zone and hence tunnel defect was observed. Whereas, the tool rotational speed was higher than 900 rpm tunnel defect was observed and a large mass of flash was ejected outside due to the softening of the metal by the excess heat input.

In addition, the tunnel at the advance side of the weld and surface lack of fill were observed for a welding speed higher than 200 mm/min due to insufficient heat

Table 4 Effect of tool rotation and traverse speeds on macrostructure

Parameters range		Macrograph and visual inspection		Defects
Rotation speed (rpm)	<600			• Tunnel defect at the advancing side
	>900			• Tunnel defect at the advance side • Excessive flash
Traverse speed (mm/min)	<100			• Tunnel defect at the advance side • Lack of shoulder contact
	>200			• Tunnel defect at the advance side • Surface lack of fill

input, an increase of the plastic strain rate of the material and abnormal stirring material generates a lack of consolidation due to insufficient material flow. For a lower traverse speed than 100 mm/min, tunnel defects were observed due to the contribution of excessive heat per unit length of the weld, low plastic deformation of the metal, any vertical movement of the metal, and a lack of shoulder contact with the base material are identified.

3.2 Macroscopic and Microscopic Analysis

According to the optical macroscopic and microscopic investigation, four distinct zones have been identified: Stirred zone (nugget), thermo-mechanically affected zone (TMAZ), heat-affected zone (HAZ), and Base Metal (BM) (Elangovan et al. 2008). Macroscopic appearance of the cross-section of the joint produced at rotation speed of 750 rpm and transverse speed of 150 mm/min is shown in Fig. 2.
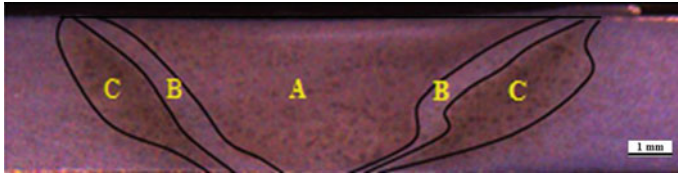
Fig. 2 Formation of different areas of FSW AA2024-T3: **A** base metal, **B** heat-affected zone, **C** thermo-mechanical affected zone and **D** nugget zone
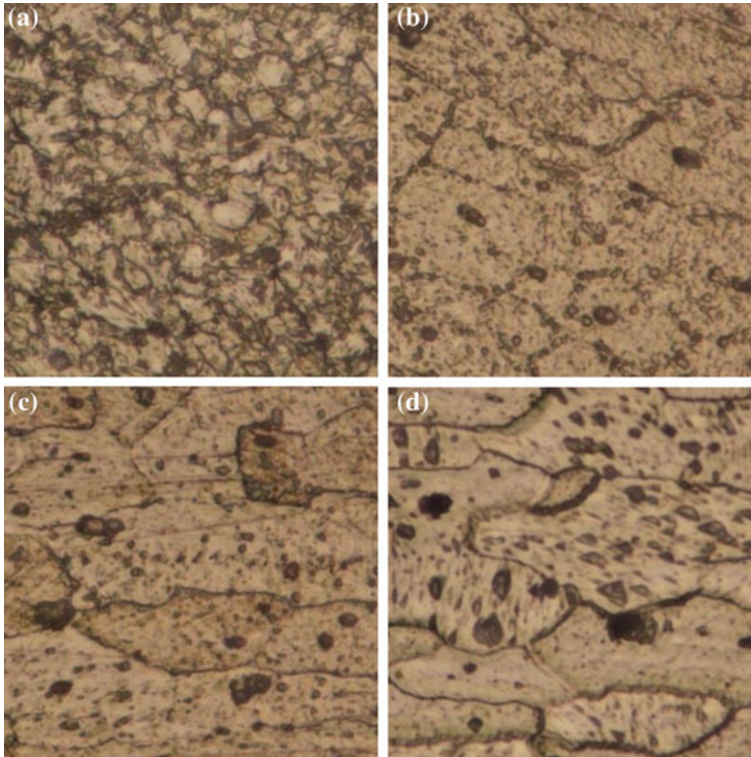
Fig. 3 Grain morphology at x1000 magnification of **a** NZ, **b** TMAZ, **c** HAZ and **d** base metal

Figure 3 shows typical grain structures of different regions in FSW AA2024- T3. First, the nugget zone (NZ) consists of fine equiaxed grains due to high temperature and extensive plastic deformation with a total dynamic recrystallization (Cam 2011). Then, adjacent to the nugget is thermo-mechanical affected zone (TMAZ), which undergoes an insufficient plastic deformation resulting in partial recrystallization. In the HAZ which is adjacent to the TMAZ, microscopic examination always revealed a same granular texture as the Base Metal. This region subjected to a thermal cycle but is not deformed during welding (Cam 2011; Cam et Mistikoglu 2014).

To evaluate the grain structure of the different zone, the average grain size is considerate. For example, the average grain size in the middle thickness of welding joint at tool rotation speed of 750 rpm and traverse speed 150 mm/min is as follows: The grain size in the (NZ) is of the order of 2.56 μm, whereas that in the (TMAZ) is of the order of 48 μm, the (HAZ) is of the order of 60 μm and the grain size in the parent metal is of the order of 65 μm. The difference of zone is a consequence of the influence of plastic deformation and heat input on recrystallized grain zone.

3.3 Tensile Tests

The tensile properties of welds obtained with rotational speeds are presented in Table 5. Subsequently, traverse speed was kept constant at 150 mm/min and rotation speed was varied to establish the process window. The levels for rotation speed were fixed as 600, 750, and 900 rpm to represent low, medium, and high levels, respectively. We have observed that the ultimate tensile strength and percentage elongation of the AA2024-T3 joints fabricated increase as tool rotation speed increases up to the 750 rpm and then decrease with further increases of tool rotation speed. The joint fabricated with a rotational speed of 750 rpm produced higher strength properties of the joints. The maximum ultimate tensile strength of the joints is 392 MPa equivalent to 85% of that of the base metal. The maximum percentage elongation is 9.72% about 54% when compared with that of the base metal. According to the results, an increase of the rotation speed at 750 mm/min results in an increase in the temperature, the plastic strain rate of the material, and a lack of stirring, in agreement with other observations (Franchim et al. 2011; Khodir et al. 2006). But, an increase over 750 rpm metallurgical transformation produced a coarsening recrystallized grains and a lowering dislocation density discourage the ultimate tensile strength (Kumar et al. 2015).

According to Table 5, the tool rotation speed was kept constant at 600 rpm and the traverse speed was fixed as 100,150, and 200 mm/min. The tensile strength and percentage elongation progressively decreased with increasing the traverse speed.

Table 5 Friction stir welding parameters and their levels

Tool rotation speed (rpm)	Traverse speed (mm/min)	Tensile properties			
		Rm (MPa)	Error	A%	Error
600	100	364	3.54	10.49	0.52
	150	279	5.12	4.94	0.07
	200	205.67	8.92	3.05	0.06
750	150	392	3.01	9.72	0.16
900	150	275.7	7.47	4.7	0.24

The lowest traverse speed generated high heat input and encourages plastic flow of materials loads. Then, the highest welding speed results a decrease of peak temperature and generates a poor plastic flow of the materials being welded leading to a lower ultimate tensile strength and percentage elongation.

The joint fabricated with a traverse speed of 100 mm/min produced higher strength properties of the joints. The maximum ultimate tensile strength of the joints is 364 MPa equivalent to 74.78% of that of the base metal. The maximum elongation is found to be 10.49%, about 58.27% when compared with that of the base metal.

3.4 Microhardness Test

Figure 4 represents the influence of tool rotation speed, fixed to 600 and 750 rpm, on microhardness distribution. The traverse speed were kept constant at 150 mm/min. The important observations can be made from their study: First, the hardness distribution profiles exhibited a "W"-like distribution across the weld. Second, the hardness of the two welds in the SZ and TMAZ regions was lower in comparison to that of the base materials. Second, the hardness of base metal from 138 ± 4 and 139 ± 3 HV at 600 rpm and 750 rpm, respectively, at a constant traverse speed 150 mm/min. Third, the hardness of the SZ produced using lower tool rotation speed 600 rpm was found be slightly less than that produced using higher tool rotation speed 750 rpm, it values were respectively 117 ± 2, 123 ± 3 HV. In spite of small grain size and the lowest hardness, values were observed in
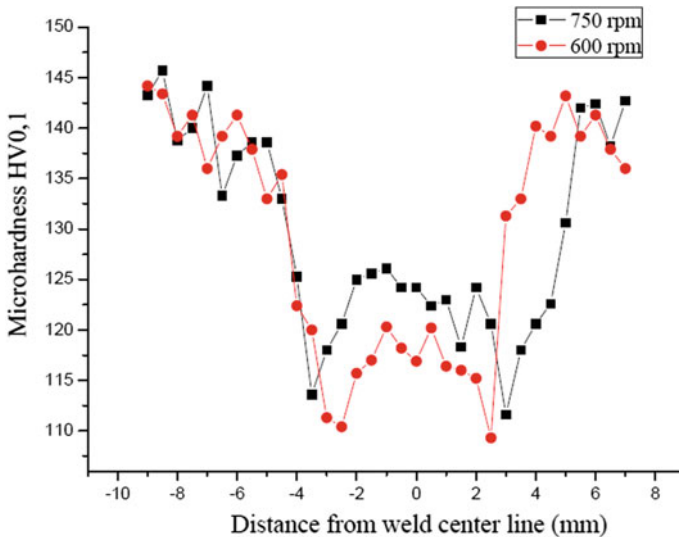
Fig. 4 Microhardness results of welded joint prepared at different a rotational speeds

the TAMZ both sides of the NZ, the values were 110 ± 1, 114 ± 4 HV at 600, 750 rpm. Then, the decrease in hardness at the TMAZ is attributed to the coarsening and dissolution of strengthening precipitates induced during the weld thermal cycle of welding (Mishra and Ma 2005).

4 Conclusions

In this investigation, an attempt has been made to study defects, microstructural, microhardness tests, and tensile tests of the friction Stir welding (FSW) of AA 2024-T3 aluminum alloy. In summary, the main conclusions drawn from this work are:

1. The analyses of macrostructure provided the working range of welding parameters.
2. The analyses of microstructure showed four regions: Base metal (BM), a heat-affected zone, a thermo-mechanically affected zone (TAMZ), and a nugget zone (NZ).
3. The average grain size in the four zones showed in the following order of BM > HAZ > TMAZ > NZ.
4. The ultimate tensile strength and percentage elongation increase as tool rotation speed increases up to the 750 rpm and then decrease with further increases of tool rotation speed.
5. Increasing the traverse speed, at a constant rotation speed, resulted a decrease of ultimate tensile strength and percentage elongation.
6. Increasing the rotation speed, at a constant transverse speed, resulted an increase of hardness nugget zone.

References

Bahemmat P, Haghpanahi MB, Givi M, Seighalani R (2012) Study on dissimilar friction stir butt welding of AA7075-O and AA2024-T4 considering the manufacturing limitation. Int J Advanc Manuf Technol 939–953

Cam G (2011) Friction stir welded structural materials beyond Al-alloys. Int Mater Rev 56:1–48

Cam G, Mistikoglu S (2014) Recent developments in friction stir welding of Al-alloys. J Mater Eng Perform 1936–1953

Elangovan K, Balasubramanian V, Valliappan M (2008) Influences of tool pin profile and axial force on the formation of friction stir processing zone in AA6061 aluminum alloy. Int J Advanc Manuf Technol 285–295

Franchim AS, Fernandez FF, Travessa DN (2011) Microstructural aspects and mechanical properties of friction stir welded AA2024-T3 aluminum alloy sheet. Mater Des 4684–4688

Khodir SA, Shibayanagi T, Naka M (2006) Control of hardness distribution in friction stir welded aa2024-t3 aluminum alloy. Mater Transac 1560–1567

Kim YG, Fujii H, Tsumura T, Komazaki T, Nakata K (2006) Three defect types in friction stir welding of aluminum die casting alloy. Mater Sci Eng A 250–254

Kumar PV, Reddy GM et al (2015) Microstructure, mechanical and corrosion behavior of high strength AA7075 aluminium alloy friction stir welds—effect of post weld heat treatment. Def Technol 11(4):362–369

Liu H, Hou JC, Guo H (2013) Effect of welding speed on microstructure and mechanical properties of self-reacting friction stir welded 6061-T6 aluminum alloy. Mater Des 872–878

Mishra RS, Ma ZY (2005) Friction stir welding and processing. Mater Sci Eng: R: Rep 50(1–2):1–78

Silva A, Arruti E, Janeiro G, Aldanondo E, Alvarez P, Echeverria A (2011) Material flow and mechanical behaviour of dissimilar AA2024-T3 and AA7075-T6 aluminum alloys friction stir welds. Mater Des 2021–2027

Tehyo M, Muangjunburee P, Binraheem A, Chuchom S, Utamarat N (2012) Influence of friction stir welding parameters on metallurgical and mechanical properties of dissimilar joint between semi-solid metal 356-T6 and aluminum alloys 6061-T651. Songklanakarin J Sci Technol 415–421

Trimble D, Mitrogiannopoulos H, O'Donnell GE, McFadden S (2015) Friction stir welding of AA2024-T3 plate—the influence of different pin types. Mech. Sci: pp 51–55

Zhang XX, Ni DR, Xiao BL, Andrä H, Gan W, Hofmann M, Ma ZY (2015) Determination of macroscopic and microscopic residual stresses in friction stir welded metal matrix composites via neutron diffraction. Acta Materialia: pp 161–173

On the Elementary Wear Mechanisms of UD-GFRP Composites Using Single Indenter Scratch Test

S. Mzali, F. Elwasli, A. Mkaddem and S. Mezlini

Abstract This paper deals with the investigation of friction and wear mechanisms involved when scratching parallel to fiber orientation of unidirectional glass fiber reinforced polymers (UD-GFRP) composite. A single indenter scratch test (SST) was performed at room temperature and constant sliding speed, using high speed steel conical indenter. The dominant damage modes owing to SST were inspected at different attack angle and load using scanning electron microscope (SEM). The apparent friction and the damage modes were investigated as function of the test parameters, particularly, the attack angle and the normal load. The experimental findings reveal that the attack angle has a most important role in controlling apparent friction if compared with applied normal load. However the wear mechanisms were more sensitive to both attack angle and normal load. The correlation between wear modes and tribological parameters was emphasized and the scratch map was parallel to fiber orientation built. Six domains were identified and the different wear mechanism transitions were detailed.

Keywords UD-GFRP · SST · Friction · Wear · Scratch map

S. Mzali (✉) · F. Elwasli · S. Mezlini
Laboratoire Génie Mécanique, École Nationale d'Ingénieurs de Monastir,
Université de Monastir, Monastir, Tunisia
e-mail: mzalislah@hotmail.com

F. Elwasli
e-mail: elwaslifatma@gmail.com

S. Mezlini
e-mail: salah.mezlini@gmail.com

A. Mkaddem
Faculty of Engineering, Mechanical Engineering College, University of Jeddah, PO Box 80327, Jeddah 21589, Saudi Arabia
e-mail: amkaddem@uj.edu.sa

A. Mkaddem
MSMP-EA7350, Arts et Métiers ParisTech, Rue Saint Dominique, BP. 508, 51006 Châlons-en-Champagne, France

1   Introduction

In recent years, by virtue of their conspicuous mechanical properties and low weight, the composite materials have received significant attention. In addition, they are likewise being broadly used in several applications, namely aeronautics, transport, and astronautics industries (Schmid et al. 2015; Farooq and Myler 2015; Choi et al. 2007; Nithin et al. 2015). For numerous applications, the highlighting of their tribological behavior, particularly, the friction and the elementary damage modes still remain, nevertheless, a big challenge. The experimentation as well as the finite element modeling of such material are still hard due to their heterogeneous nature which makes it complicated to control the interface behavior and the interaction between the elementary wear mechanisms of its different constituents. The investigations of the wear mechanisms evolution of these latter request a local analysis. This approach allows studying the tribological behavior of each constituent of the composite separately. In many researches, several abrasive techniques have been used to characterize the composite materials tribological behavior and the most known one is the scratch test (Carrión-Vilches et al. 2015; Wee et al. 2015; Briscoe et Evans 1989).

Using block-on-ring abrasion test, Kim et al. (2012) investigated the effect of both rate of fiber and sliding direction on short glass fibers reinforced polyamide 12 (S-GFRPA12) tribological behaviors, particularly, friction, and wear. They showed that the wear rate and the friction coefficient of the S-GFRPA12 are significantly sensitive to the amount of glass fiber and indeed both decrease with increasing fiber content. They demonstrated that the best wear resistance was obtained for 30 wt% of glass fiber. They have also studied the fiber orientation and found that sliding in normal fiber orientation show a slightly lower friction coefficient than those in parallel fiber orientation.

Quintelier et al. (2006) studied the tribological behavior of glass fiber reinforced polyester (GFRP) composites using pin-on-disk test at dry sliding. They showed that initial fibers fracture is always produced in a cross section whatever the fibers orientation. When sliding perpendicularly to the fiber orientation, the fiber bending induces longitudinal strains which initiate the fiber fracture. However, when sliding parallel to the fiber orientation, shearing forces are provoked by the high stresses. The SEM observations showed that the typical GFRP wear mechanisms are matrix breaking, fiber fracture, and pullout and interface debonding.

Kohl et al. (2016) investigated the influence of the frictional behavior and the micro-indentation test on GFRP viscoelastic properties. They proved that, when sliding a diamond stylus against the GFRP composite, the friction coefficient increases with the decrease of the sliding speed. This was assigned to the stylus possessing more time to penetrate in the material at the lower speed. They, also, showed that the Von Mises stress distribution is sensitive to the scratch speed.

The material relaxation has a time to occur at low sliding velocity and thus the contact area is larger causing a lower stress distribution after a while. However, at low sliding velocity higher stress distribution has been observed.

The present paper suggests an experimental investigation of SST of UD-GFRP composite using a conical steel indenter. The friction and wear mechanisms sensitivity to the tribological parameters, particularly, the attack angle and the normal load, when scratching parallel to fibers orientation, will be highlighted. An analysis of the elementary wear mechanisms using SEM observations will be done. Mapping was used to emphasize the prevailing wear mechanisms and to highlight the correlation between tribological parameters and wear mechanisms.

2 Materials and Methods

2.1 Specimen Preparation

Commercially available GFRP composite (supplier: Qinhuangdao Shengze New Material Technology Co., Ltd.) was supplied as pultruded rectangular section (50 × 6 mm^2) bar of 1000 mm length. A cutting machine was used to cut the test specimens (at size of 50 × 50 × 6 mm^3) under lubrication, at room temperature and using resinoïd cut-off wheel of ⌀230 × 1.6 mm^2 in dimensions (Type: PRESI A0, Abrasive grain: Al2O3). The reinforcement used for the composite material is unidirectional E-glass fiber with a weight percentage of 21 wt% and an average diameter of 23 μm. The considered material is, in addition, filled with ASP400 clay filler with a weight percentage of 14 wt%. The 50 × 50 mm^2 sample face was subjected to the sliding of the conical indenter parallel to fiber orientation.

2.2 Scratch Test

Scratching tests were carried out on a new test device (Fig. 1) whose specifications were already detailed in (Mzali et al. 2013, 2017). The scratch setup was designed with several features and functionalities. It allows the variation of the test parameters, particularly, the normal load, the attack angle, the scratch length, and speed. The device ensures, via a specific system, the sample face to be parallel to the motion of the uncoated HSS conical indenter (W18Cr4 V) with a diameter of 3 mm. The hardness of the adopted indenter is 64 HRC (Wang et al. 2008). During all the tests, realized at room temperature and without lubrication, the scratch length and speed are fixed at 30 mm, and 210 mm min^{-1}, respectively. Nevertheless, the attack angle and the normal load range in 10°–60°, and 20–50 N, respectively.
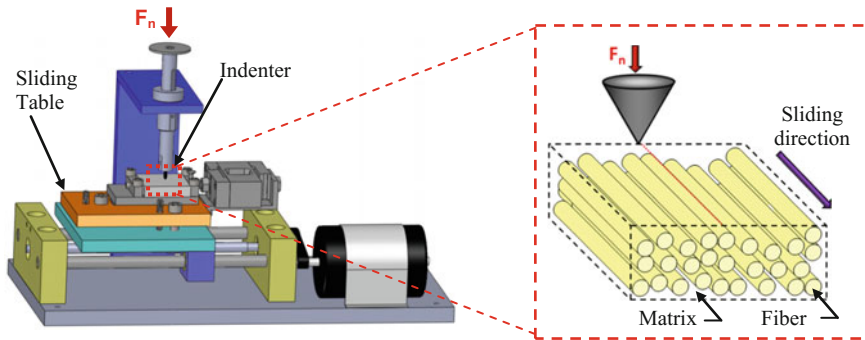
Fig. 1 Scratch device

Then, the Coulomb's law was used to calculate the apparent friction coefficient (μ_{app}). SEM observation was also carried out to investigate the micro-scale GFRP composite surface wear mechanisms.

3 Results and Discussion

3.1 Elementary Wear Mechanisms

To emphasize the different elementary damage mode, SEM observations were carried out. Microscopic analysis has been performed, in order to have a better comprehension of the tribological behavior of the GFRP composite. Figure 2 shows several wear mechanisms of the scratched GFRP composite. Different damage modes were perceived, namely, the matrix ploughing, the fibers fracture, the fiber erosion, the fiber rupture in series, the fiber/matrix interface debonding, the fibers pullout, etc. In the same groove, several elementary damage modes can coexist, but one wear mechanism dominates depending on the tribological parameters.

According to the micrographs, for the low attack angles, the wear accentuates with the increase of the normal load. This may perhaps be perceived, when 10° attack angle was used, through the comparison between Fig. 2a–c. Whereas fiber rupture in series dominates at 50 N, discontinuous matrix tearing acts under 30 and 20 N. Similar behavior was observed at 30° attack angle. Increasing the normal load provokes the transition of dominant wear mechanisms from matrix ploughing (Fig. 2d and e) to premature fiber fracture (Fig. 2f).

However, for higher attack angle, i.e., 45°, both fiber and matrix were affected. When increasing the normal load, the interface debonding (Fig. 2g and h) promotes the apparition of the fiber pullout (Fig. 2i). Furthermore, when the highest attack angle was used, previous wear mechanisms switch to fiber explosion and crushing
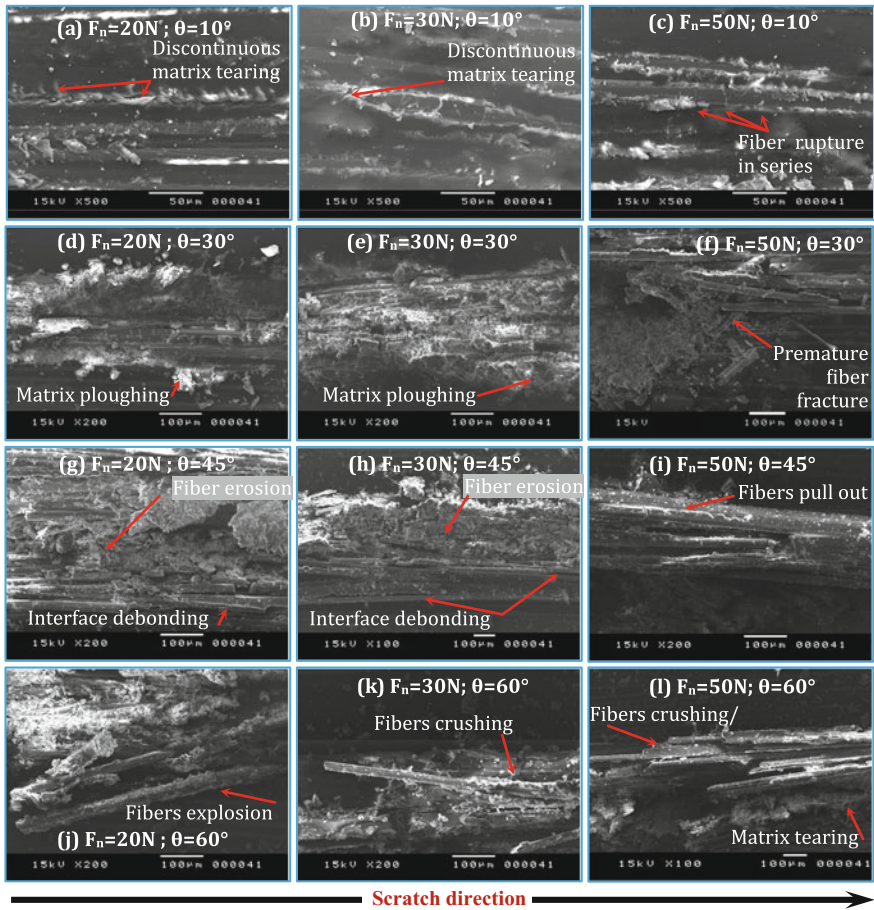
Fig. 2 SST dominant wear mechanisms

(Fig. 2j and k) and for the largest load, i.e., 50 N matrix tearing mechanism (Fig. 2l) dominates.

3.2   Friction Analysis

In order to investigate the apparent friction coefficient to normal load and attack angle sensitiveness, SST using a range of attack angles from 10° to 60° and different normal load varying from 20 to 50 N are carried out. Figure 3 shows the apparent friction coefficient evolution versus both attack angle and normal load.
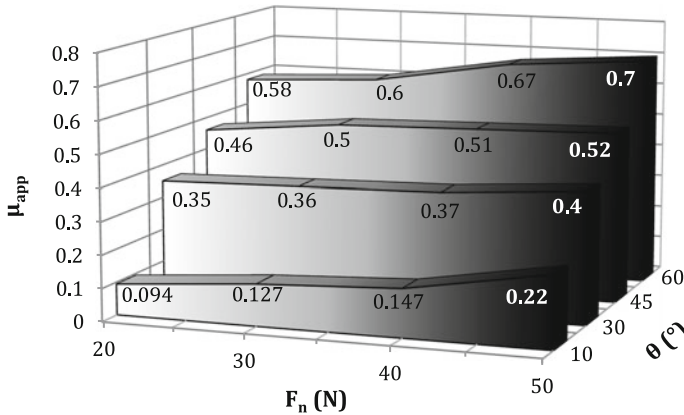
Fig. 3 Apparent friction coefficient versus normal load and attack angle

3.2.1   Influence of the Normal Load

For the lowest attack angle of 10° and low normal load ($F_n \leq 40$ N) a slight increase of 35% is shown. At these test conditions, only matrix is affected. However, increasing the normal load to 50 N affects considerably the apparent friction coefficient which is multiplied by 2.34. This friction behavior is due to the transition of the prevailing wear mechanisms from ploughing and discontinuous matrix tearing to fiber rupture in series.

In case of larger attack angle, the apparent friction coefficient can be considered insensitive to the normal load. Indeed the friction gaps which are recorded from 30°, 45°, and 60° attack angle are about 14%, 13%, and 20%, respectively. At these test conditions, both matrix and fibers are damaged and more severe wear mechanisms are observed.

3.2.2   Influence of the Indenter Geometry

Another reading of the chart makes it possible to study the effect of the attack angle on the apparent friction coefficient. The latter seems to exhibit higher sensitivity to this tribological parameter. Indeed, independently of normal load the apparent friction coefficient evolution shows sharp monotic increase with the increase of the attack angle. When the attack angle passes from 60° to 10° the minimum friction reduction gap, recorded for Fn = 20 N, is about 68%. This result is already experimentally proven, when sliding perpendicularly to the unidirectional glass fiber orientation (Mzali et al. 2013). For the lowest attack angle, larger contact surface is observed, the indenter action seems to be similar to a spherical pin action and no severe material damage occurs. When sliding against the sample surface, the

indenter induces lower resistance force. Thus, lower apparent friction coefficients are found.

However, when larger attack angles are used, the contact surface is much lower. Besides, larger penetration is observed and when the indenter slides against the damaged material induces a greater resistance force resulting in a higher apparent friction coefficient.

3.3 Scratch Map

The scratching of GFRP composite is followed by several surface wear modes or mechanisms under different test conditions. The correlation between these wear mechanisms and tribological parameters allows the identification of the action domain of each wear modes. Therefore, according to SEM observations, the wear maps were built in order to highlight the wear mechanisms limits. Particular attention was, first, given to the sensitivity of the mechanisms of material deformation and removal to normal load and attack angle.

Figure 4 illustrates a SST map for GFRP composite. The map shows the prevailing damage modes when scratching, at constant velocity (210 mm/min) under dry condition, GFRP composite using attack angle ranging from 10° to 60° and a range of normal loads (20–50 N). The map presents the strong sensitivity of the dominant wear mechanisms to the attack angle and normal load. These two parameters seem to have a strong influence upon the transition of the wear mechanism from ploughing towards brittle fracture. Thereby, six elementary prevailing wear mechanisms were distinguished. The following remarks can be hence drawn

Fig. 4 Scratch map (θ vs. F_n)
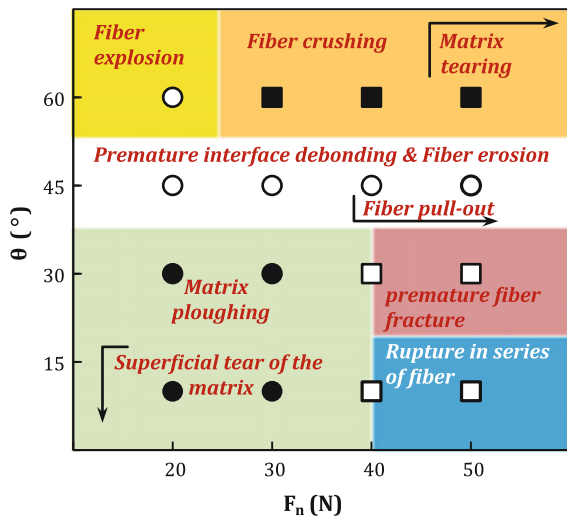
- **$10° \leqslant \theta \leqslant 40° - F_n < 40\,N$**

This domain seems to be the largest one of the wear map. At the relatively low normal loads and the low attack angles, the dominant wear modes were assessed as mainly being ploughing associated sometimes with discontinuous matrix superficial tearing. At these conditions, when the indenter slides against the GFRP composite surface provokes neither fiber fracture nor severe matrix material removal. The material flows plastically around the indenter tip due to the wide-ranging plastic deformation. However, when the indenter slides upon close-to-surface glass fiber the thin surface of polyester is affected and several matrix micro-cracks appear.

- **$10° \leqslant \theta < 20° - F_n \geqslant 40\,N$**

In this case, discontinuous polyester superficial tearing which fully operates in the domain discussed just above ($10° \leq \theta \leq 40° - F_n < 35\,N$) turns into fiber rupture in series associated sometimes with matrix secondary partial ploughing. The scratches are deeper enough to share and remove the superficial layer of the polyester, which causes first the eroding of fibers and motivating the fiber rupture in series.

- **$20° \leqslant \theta < 40° - F_n \geqslant 40\,N$**

In this domain, the GFRP composite behavior is dominating by premature fracture of fiber. Therefore, the fiber failure takes place away from the indenter tip and relatively large fiber debris resulting.

- **$40° \leqslant \theta < 50°$**

Within this domain, premature fiber/matrix interface debonding dominates in combination with fiber erosion and favors generally fiber pullout. For relatively low loads, fiber/matrix interface debonding provokes a plastic flow of the matrix around the fibers which was exposed and eroded. For larger normal load, the indenter penetration increases. Therefore, the contact area between the indenter and the superficial fiber layer becomes larger, which coerce the fiber pullout.

- **$50° \leqslant \theta \leqslant 60° - F_n < 25\,N$**

This is pointed out as the smallest domain of the wear map. The dominant wear mechanism was considered as mainly being fiber explosion. This wear mechanism was mainly provoked by the fiber excessive buckling.

- **$50° \leqslant \theta \leqslant 60° - F_n \geqslant 25\,N$**

In this domain, increasing the normal load increases the indenter penetration and forces the shared fibers by compression to crash. Consequently, the dominant wear mechanism is fiber failure in series and fiber crushing. However, for larger normal load ($F_n \geq 45\,N$) the previous mechanisms are combined with tearing of the matrix.

4 Conclusions

In this investigation, the study of elementary damage modes in SST when sliding parallel to fiber orientation has been performed. An experimental approach was used to identify the evolution of the wear mechanisms of the UD-GFRP composite. Special focus is given to the correlation between the tribological parameters, namely, attack angle and normal load and the damage mechanisms. According to the experimental results the following conclusions can be hence drawn:

- Based on SEM observations, several UD-GFRP composite wear mechanisms, particularly, the tearing of the matrix, the matrix ploughing, the fiber erosion, premature fracture of fibers, the fibers fracture, the fiber rupture in series, the fibers explosion, the fibers pullout, the fiber/matrix interface debonding and the fiber crushing was observed and was found to be sensitive to the test parameters.
- The normal load was found to be of insignificant effect on apparent friction coefficient. However, wear mechanisms and μ_{app} show high sensitivity to the attack angle. Increasing the attack increases μ_{app} and provokes the switch of the dominant wear mechanisms from matrix ploughing and fiber rupture in series to matrix tearing, fibers crushing and pullout.
- The scratch map of the UD-GFRP composite has been generated. This map presents six domains, which dominate wear mechanisms depending on the tribological parameters. The scratch map gives information about wear mechanisms which could happen due to abrasion or use. Thus, it could support the material design and selection as well as elaboration of damage and wear materials models.

References

Briscoe BJ, Evans PD (1989) Scratch hardness as an evaluation of cure temperature for glass fibre reinforced polyester. Compos Sci Technol 34:73–90. http://dx.doi.org/10.1016/0266-3538(89)90078-X

Choi J, Kelly D, Raju J (2007) A knowledge-based engineering tool to estimate cost and weight of composite aerospace structures at the conceptual stage of the design process. Aircr Eng Aerosp Technol 79(5):459–468. http://dx.doi.org/10.1108/00022660710780588

Carrión-Vilches FJ, González-Vivas A, Martínez-Mateo IJ, Bermúdez MD (2015) Study of the abrasion resistance under scratching of polybutylenetereftalate–glass fiber composites. Tribol Int 92:365–378. http://dx.doi.org/10.1016/j.triboint.2015.07.004

Farooq U, Myler P (2015) Finite element simulation of buckling-induced failure of carbon fibre-reinforced laminated composite panels embedded with damage zones. Acta Astronaut 115:314–329. http://dx.doi.org/10.1016/j.actaastro.2015.05.039

Kohl GJ, Bierwisch N, Ngo Truc T, Favaro G, Renget E, Schwarzer N (2016) Determining the viscoelastic behavior of polyester fiberglass composite by continuous micro-indentation and friction properties. Wear 350–351:63–67. http://dx.doi.org/10.1016/j.wear.2016.01.005

Kim SS, Shin MW, Jang H (2012) Tribological properties of short glass fiber reinforced polyamide 12 sliding on medium carbon steel. Wear 274–275:34–42. http://dx.doi.org/10.1016/j.wear.2011.08.009

Mzali S, Mezlini S, Zidi M (2013) Effect of tribological parameters on scratch behavior of a unidirectional E-glass fiber reinforced polyester composite. Tribol Surf Mater Interfaces 4:175–182. http://dx.doi.org/10.1179/1751584X13Y.0000000048

Mzali S, Mkaddem A, Elwasli F, Mezlini S (2017) Towards an advanced modeling of failure mechanisms' interaction in fiber-reinforced polyester: a mixed-mode loading concept. Compos Struct 160:70–80. http://dx.doi.org/10.1016/j.compstruct.2016.10.074

Nithin KKC, Gupta G, Lakhera S, Shaikh A (2015) Structural optimization of composite stiffened panel of a transport aircraft wing using CAE tools. Mater Today Proc 2:2588–2594. http://dx.doi.org/10.1016/j.matpr.2015.07.213

Quintelier J, De Baets P, Samyn P, Van Hemelrijck D (2006) On the SEM features of glass–polyester composite system subjected to dry sliding wear. Wear 261:703–714. http://dx.doi.org/10.1016/j.wear.2006.01.006

Schmid ED, Salem DR (2015) Fabrication technique and thermal insulation properties of micro- and nano-channeled polymer composites. Acta Astronaut 116:68–73. http://dx.doi.org/10.1016/j.actaastro.2015.06.015

Wang J, Liu YB, An J, Wang LM (2008) Wear mechanism map of uncoated HSS tools during drilling die-cast magnesium alloy. Wear 265:685–691. http://dx.doi.org/10.1016/j.wear.2007.12.009

Wee JW, Park SY, Choi BH (2015) Observation and understanding of scratch behaviors of glass fiber reinforced polycarbonate plates with various packing pressures during the injection molding process. Tribol Int 90:491–501. http://dx.doi.org/10.1016/j.triboint.2015.05.009

Multiobjective Assembly Line Resource Assignment and Balancing Problem of Type 2

Hager Triki, Wafa Ben Yahia, Ahmed Mellouli and Faouzi Masmoudi

Abstract The lively field of assembly line problem often has a significant impact on the performance of manufacturing systems. In this context, Assembly Line Balancing Problems (ALBPs) are widely cited in the literature. The ALBP is one of the most important problems among the other problems of assembly lines like designing and managing. The fundamental ALB Problem (ALBP) is the way of getting an optimal assignment of tasks to the stations respecting well-determined constraints and reaching certain objectives. In the previous research, there are many studies on developing methods for solving Simple Assembly Line Balancing Problems (SALBP) and their various extensions. Each extension is motivated by several real-life applications. This paper presents a new extension of SALBP-2, so-called Multiobjective Assembly Line Resource Assignment and Balancing Problem of type 2 (MOALRABP-2). The problem is a tri-criteria one, which aims to minimize simultaneously the following objectives: the cycle time, the mean absolute deviation and the cost per time unit (hour) of a line for a fixed number of stations to satisfy the constraints of precedence between tasks and compatibility between resources. A new version of Multiobjective Evolutionary Algorithm (MOEA) named Hybrid MOEA (HMOEA) is elaborated to seek a set of diverse

H. Triki (✉)
Laboratory of Mechanic, Modeling and Production (LA2MP),
Engineering School of Sfax, University of Sfax, Sfax, Tunisia
e-mail: Hager_Triki@yahoo.fr

H. Triki
Higher Institute of Industrial Management of Sfax, Sfax, Tunisia

W. B. Yahia · F. Masmoudi
Laboratory of Mechanics, Modelling and Production Research Laboratory (LA2MP),
National School of Engineering of Sfax (ENIS), University of Sfax, Sfax, Tunisia
e-mail: wafa.benyahia@hotmail.fr

F. Masmoudi
e-mail: faouzi.masmoudi@enis.rnu.tn

A. Mellouli
National School of Engineering of Sousse (ENISo), University of Sousse, Sousse, Tunisia
e-mail: ahmed.mellouli.eniso@gmail.com

optimal solutions. In addition, the MOEA parameters are optimized using the Taguchi method. The effectiveness of the HMOEA was assessed through a set of problems. The results comparisons show a quite promising higher performance for the HMOEA.

Keywords Precedence and compatibility constraints · Cycle time
Mean absolute deviation · Cost per hour · Multiobjective evolutionary algorithm

1 Introduction

The mutation of market pushes manufacturers to look for the best possible methods for managing their production system to satisfy quickly and efficiently the customer's requests. Among production systems, the assembly lines are used extensively in mass production systems to increase systems' efficiency and speed, to decrease per-unit cost, and to make the manufacture and control easier (Mozdgir et al. 2013). In order to respond to these diverse market needs, the Assembly Line Balance (ALB) must be taken into consideration because ALB has often had a significant impact on the performance of manufacturing systems over the past few years. The most prominent problem of the ALBP family is the SALBP (Simple Assembly Line Balancing Problem) (Baybars 1986; Scholl 1999; Becker and Scholl 2006). For instance, SALBP-2 minimizes Cycle time C, in other words it maximizes the production rate for a given Number of stations "m" (Baybars 1986). By varying the constraints and adding others objectives, different extensions of SALBP have been figured in the literature dealing with some particular features of real world problems such as incompatibilities among tasks (Kyungchul et al. 1997) and the resource assignment (Triki et al. 2017). All these versions are NP-hard (Gutjahr et al. 1964).

In this context, this paper provides a new extension of SALBP-2 called Multiobjective Assembly Line Resource Assignment and Balancing Problem-2 (MOALRABP-2). This problem is tri-objective one. It aims to minimize first, the Cycle time, second (C), the Mean Absolute Deviation (MAD) and third, the Cost per time unit Hour (C/H) of a line for a fixed number of stations.

In most of the assembly lines, minimizing cycle time which is the first objective is an important issue for the production managers, since it is the main reason for increasing the production rate (Hamta et al. 2011). The second objective which is minimizing the mean absolute deviation (MAD) of the workloads given by Rachamadugu and Talbot (1991) aims at smoothing the workload among stations of the assembly line. The third objective which is minimizing the Cost per unit (Hour) (C/H) (Triki et al. 2017) is the sum of all cost types of resource (purchase cost Bukchin and Tzurm 2000, production cost Hamta et al. 2011 and so on) divided by the period of amortization.

The proposed ALBP takes into account the precedence and compatibility constraints between tasks and between resources respectively.

Due to the NP-hardness, a new meta-heuristic "Hybrid Multiobjective EA (HMOEA)" is elaborated. Four well-known performance measures from the literature are used to evaluate the proposed algorithm compared to other algorithms, which are non-dominated solution, maximum spread, spacing, and compilation time.

The outline of the rest of this paper is as follows: Sect. 2 describes the problem MOALRABP-2. Section 3 presents the steps of the HMOEA. Section 4 illustrates the experimental results to select MOEA parameters and shows computational results. Finally, concluding remarks are presented in Sect. 5.

2 Problem Assumptions

The basic assumptions of the considered problem "MOALRABP-2" are listed as follows:

(1) The line is semi-automatic.
(2) Each resource must be selected from a given set of resource types.
(3) Each resource has a specific cost per hour.
(4) The number of resources is available without limitations within each type, but there are only R types of resource available ($R \geq 1$).
(5) Every resource is assigned to only one task.
(6) Each resource type is not necessarily able to perform all assembly tasks. In case that task is not executed by a specified resource, the processing time of this task is set infinity.
(7) The precedence relationship among assembly tasks is known and invariable.
(8) The operation cannot be subdivided.
(9) The processing time of an assembly task is deterministic and depends on the allocated resource type.
(10) A simple product type is assembled on the line.
(11) No buffer is considered between the workstations
(12) A paced line with given m stations.
(13) Every task is assigned to only one workstation.
(14) The compatibility constraints between resources are included in the assignment of tasks to stations.
(15) Machines are considered as reliable during the considered horizon.
(16) No maintenance action is considered.
(17) Machines are always available.

3 The Main Steps of the Hybrid Multiobjective Genetic Algorithm

Because of the NP-hardness, it is necessary to use meta-heuristic algorithms such as the EA method for large-scale problems. In this work, a new version of MOEA is suggested to solve an important variant of the assembly line problem MOALRABP-2.

In this setting, a newly proposed algorithm called Hybrid Multiobjective Evolutionary Algorithm (HMOEA) executes SPEA2 (Strength Pareto Evolutionary Algorithm 2) (Zitzler 2001) in combination with MWPMOGA (Modified Weighted Pareto-based Multiobjective Genetic Algorithm) (Wang et al. 2012).

3.1 Phase 1: Generation of Initial Population and Empty Archive

- The initial population P0 (t = 0, t: number of generations) with N chromosomes is randomly generated by assuring the feasibility of the precedence relations between tasks. The length of the chromosome is equal to the number of tasks and each gene of the chromosome defines a task. The second line of the chromosome represents the resources assigned to tasks.
- An empty archive set A0, with size Na $\leq$ N, is created at the beginning of the algorithm. An archive contains non-dominated solutions previously found (the so-called external non-dominated set). At each generation, non-dominated individuals are copied to the external non-dominated set (Coello 2007). Consequently, the archive notion is used for maintaining the non-dominated solutions over many generations.

3.2 Phase 2: Evaluation 1: Calculation of the Objective Function Value

The cost per hour C/H(k) of chromosome (k) is the sum of cost per hour of all existing resources on the line. Whereas, the cycle time C(k) and MAD (k) of chromosome (k) are determined by the following steps:

- Step 1: Determining the initial cycle time value, which is a Lower Bound (LB) calculated as follows:

Table 1 The steps of task assignment to stations

Proposed chromosome		1	4	3	2	5	6	7	9	8	10	11
Resource selected		1	4	2	1	4	2	2	5	1	3	4
Pi		3	5	4	3	5	4	10	6	9	6	14
Step 1	LB	C = LB = 14										
Step 2	Station	S1				S2		S3	S4	S5	S6	S7
Step 3		m = 7 > 6 = > C = C + 1 = > C = 15 go to step2										
Step 2	Pi	3	5	4	3	5	4	10	6	9	6	14
	Station	S1				S2		S3	S4	S5		S6
	Station time	15				9		10	6	15		14
Step 3	m = 6 the desired number of S go to step 4											
Step 4	Station time	15				9		10	6	15		14
	$\lvert \overline{T} - t_s \rvert$	1				5		4	8	1		0
	MAD	3										
Step 5	End procedure: the cycle time of this chromosome is C = 15 and MAD = 3											

$$LB = \max \left(\max_{1 \leq i \leq n} \{P_i\}, \frac{\sum_{i=1}^{n} P_i}{m} \right) \qquad (1)$$

- Step 2: Identifying the stations by the procedure of Akpınar and MiracBayhan (2011). In this paper, this procedure is applied by taking into account the constraints of compatibility between resources instead of the zoning constraints: Tasks are assigned to stations according to the task sequence in the chromosome as long as the predetermined cycle time is not overtaken. Once this cycle time is exceeded at least for one model, or the compatibility constraints of the set of Incompatible Resource (IR) are not satisfied, a new station is opened for assignment and the procedure is repeated until the last task is assigned.
- Step 3: If the obtained number of stations is equal to a given "m" go to Step 4, otherwise, the cycle time C is incremented by 1 and go to Step 2.
- Step 4: Calculating the MAD of this chromosome.
- Step 5: Finishing the procedure and presenting the cycle time and the MAD of chromosome. Table 1 illustrates the steps of assignment of tasks to stations for an example of precedence graph G shown in Fig. 1 (m = 6 stations (S) and n = 11, resources (1, 5) ∈ IR).

3.3 Phase 3: Evaluation2: Calculation of Fitness Value

The fitness value is based on the fitness value of SPEA2. The fitness of SPEA2 is a strength indicator, which measures the solution quality of the individuals with high

Fig. 1 The mixed crossover
operator
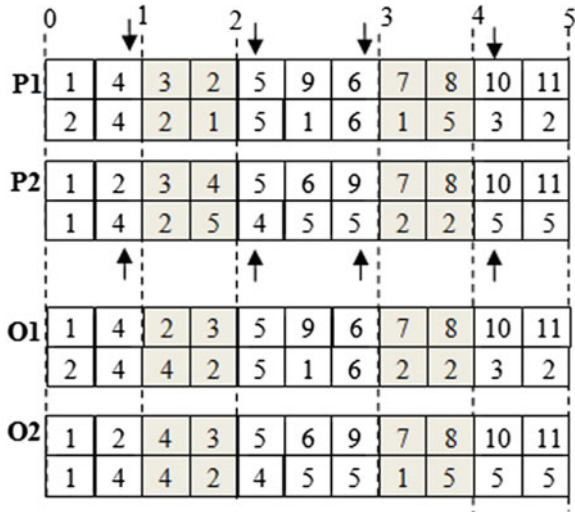
"precision" and "diversity". The fitness value $Fs(i)$ of SPEA2 (Zitzler 2001) is calculated simply by adding density value $D(i)$ to the raw fitness value $R(i)$ as follows:

$$Fs(i) = R(i) + D(i) \tag{2}$$

- $R(i) = \sum_{j \in P_t \cup A_t,\, i > j} S(j)$, The symbol $>$ indicates domination ($i > j$ indicates that i dominates j), when $R(i) = 0$ corresponds to a non-dominated individual.

  The strength value $S(i) = |\{j | j \in P_t,\ i \prec j\}|$ corresponds to the number that dominates i.

- $D(i)$: The individual's density to differentiate the individuals having identical raw fitness values is estimated by the kth nearest neighbor method as

$$D(i) = \frac{1}{\sigma_i^k + 2}, \tag{3}$$

while σ_i^k symbolizes the objective-space distance between individual i and the kth nearest neighbor and

$$k = \sqrt{N + N_a} \tag{4}$$

3.4 Phase 4: Reproduction: Selection and Crossover Operator

- The "Roulette Wheel strategy" (Holland 1975) is chosen as the selection strategy. A selection probability is assigned to each chromosome based on its fitness value calculated by the previous phase
- In this work, mixed crossover operator developed in Triki et al. (2017) is used. This crossover operator works as follows:

  - The four points cut each parent into five parts (0–1, 1–2, 2–3, 3–4, 4–5), as shown in Fig. 1. All elements from parts (0–1, 2–3, 4–5) of the first parent (P1) are copied to identical positions in the offspring 1(O1).
  - All the elements within the parts (1–2, 3–4) of the (P1) undergo the following procedure.
  - The tasks are reordered according to the order of their appearance in the second parent vector (P2) to generate the remaining parts of (O1).
  - The tasks are performed by resources which belong to (P2).

  The second offspring (O2) is generated by the same steps, with the roles of its parents reversed.

3.5 Phase 5: Elitist Preservation Strategy

The elitist preservation strategy of HMOEA, based on two notions, is proposed to generate the new population. The notions are presented as follows:

- The archive consists on the best individuals of the previous population.
- The weighted value of objective function $O(k)$ of MWPMOGA (Wang et al. 2012). It lets to compare among non-dominated solutions of the same level by using weighted value of objective function according to preferences of decision makers.

In order to preserve the best solutions appeared during the optimization process, the archive and offspring population after evolution are combined into one population.

Then, the elitist preservation strategy of HMOEA is executed through two steps:

- **Step 1: Updating A$_t$**
  The non-dominated solutions of the populations of parents P$_t$ is duplicated in an archive A$_t$ with t $\geq$ 1 (A$_0$ = $\varnothing$). If these solutions' size is less than *Na*, then A$_t$ is completed by the best dominated solutions. The creation of A$_t$ is realized by a proposed procedure. This procedure is executed by the following stages:

- Stage 1: the current population P_t undergoes a sorting based on non-dominated sorting procedure (Deb et al. 2002) to rank and divide the individuals into different non-dominated fronts.
- Stage 2: if the last individual of the first *Na* individuals of P_t is reached inside individuals belonging to the same range, stage 3 is executed; otherwise, go to stage 4.
- Stage 3: these individuals are sorted again according to $O(k)$ (Eq. (5)).
- Stage 4: the first *Na* individuals of P_t are preserved in A_t and the remaining are rejected based on the levels.

- **Step 2: Creation of a new population P_{t+1}**

  Let Q_t is the current population obtained by the reproduction of P_t. Q_t is combined to the individuals of archive A_t to form one population $R_t = Q_t \cup A_t(N + Na)$. The new population is generated by a procedure based on the elitist preservation strategy of MWPMOGA. This procedure is executed by the following stages:

  - Stage 1: the current population R_t undergoes a sorting based on non-dominated sorting procedure (Deb et al. 2002) to rank and divide the individuals into different non-dominated fronts. If there are more than two individuals belonging to the same range, stage 2 is executed; otherwise, go to stage 3.
  - Stage 2: these individuals are sorted again according to weighted value of objective function $O(k)$ as shown in Eq. (5).

$$O(k) = W_C\left(\frac{C(k) - C_{\min}}{C_{\max} - C_{\min}}\right) + W_{MAD}\left(\frac{MAD(k) - MAD_{\min}}{MAD_{\max} - MAD_{\min}}\right) + W_{C/H}\left(\frac{C/H(k) - C/H_{\min}}{C/H_{\max} - C/H_{\min}}\right)$$

$$(5)$$

  $C_{\min}$, $C_{\max}$, $MAD_{\min}$, $MAD_{\max}$, $C/H_{\min}$, $C/H_{\max}$: represent the minimum and maximum values of each objective value.
  W_C and W_{MAD}: represent the weights of each objective function
  With,

$$W_C + W_{MAD} + W_{C/H} = 1 \qquad (6)$$

  - Stage 3: the first N individuals of R_t are preserved (P_{t+1}) and the remaining are rejected based on the levels.

3.6 *Phase 6: New Generation*

The population created from the previous phase becomes a new population (N).

3.7 Stopping Criteria

The HMOEA stops when a predefined number of generations is reached or returned to Evaluation1.

3.8 Presentation of Better Solutions (Output)

At the output of the HMOEA is the Pareto, which consists on the set of better solutions.

4 Computational Results

The proposed algorithm is tested using a set of instances randomly generated to obtain the better combination of HMOEA parameters. In the following instances tests, the weights of the objective functions are respectively $W_{c/H} = 0.5$, $W_c = 0.3$ and $W_{MAD} = 0.2$. The parameters of algorithm include population size, number of generation, crossover rate, and mutation rate. Each parameter has three levels: population size at 120, 150, and 180; number of generation at 20n, 50n, and 100n; crossover rate at 0.6, 0.7, and 0.8; and mutation rate at 0.15, 0.17, and 0.2. Taguchi method is used for experimental design for optimal parameters combination.

There are four factors and three levels in the design of this experiment, and the target is to obtain as large the number of optimal solutions as possible. Therefore,
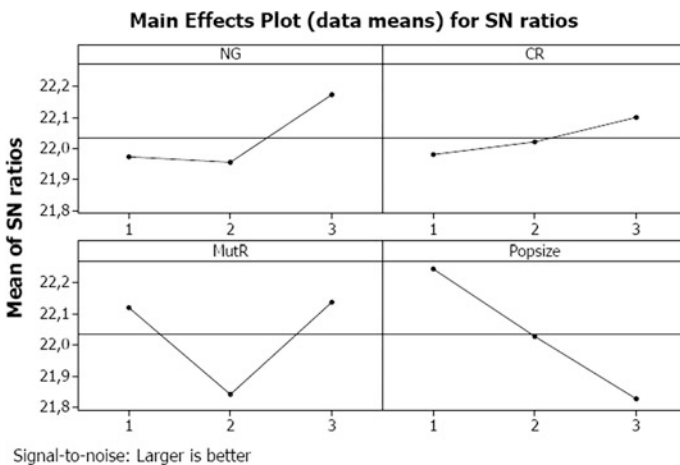
Fig. 2 The evaluation of SN ratio

Table 2 Comparison of algorithms on all problem types

Algorithms			MWPMOGA	HMOEA
	n	m	NS	NS
Small	30	7–14	11	15
Medium	70	3–25	9	12
Large	148	3–15	6	8

the "larger is better" principle is used to evaluate signal to noise ratio (SN ratio). The calculation result by using Minitab14 is as shown in Fig. 2. From this figure, we know that the optimal combination of parameters is as: population size (popsize) at 180, number of generation (NG) at 100n, crossover rate (CR) at 0.8 and mutation rate (MutR) at 0.2.

According to Table 2, HMOEA has a superior performance in comparison with MWPMOGA, concerning the number of non-dominated solutions (NS).

5   Conclusion

This work presented a new variant of assembly line balancing problem called: MOALRABP-2 (Multiobjective Assembly Line Resource Assignment and Balancing Problem-2). The purpose of this work was to obtain a better assignment of tasks to the stations and to find the best set of resources taking into account their cost per hour. MOALRABP-2 is a tri-objective optimization problem where the decision maker provides the main objective and the secondary objectives. In fact, the resolution method has to be able of biasing the search according to the user's preferences. For this purpose, a new proposed MOEA called HMOEA, which executes SPEA2 in combination with MWPMOGA by adding some modifications, was elaborated.

References

Akpına S, MiracBayhan G (2011) A hybrid genetic algorithm for mixed model assembly line balancing problem with parallel workstations and zoning constraints. Eng Appl Artif Intel 24:449–457

Baybars I (1986) A survey of exact algorithms for the simple assembly line balancing problem. Manage Sci 21:909–932

Becker C, Scholl A (2006) A survey on problems and methods in generalised assembly line balancing. Euro J Oper Res 168:694–715

Bukchin J, Tzurm M (2000) Design of flexible assembly line to minimize equipment cost. IIE Trans 32:585–598

Coello CAC, Aguirre AH, Zitzler E (2007) Evolutionary multi-objective optimization. Euro J Oper Res 181:1617–1619

Deb K, Agrawal S, Pratap A, Meyarivan T (2002) A fast and elitist multiobjective genetic algorithm: NSGA-II. IEEE Trans Evolut Comput 6(2):182–197

Gutjahr AL, Nemhauser GL (1964) An algorithm for the line balancing problem. Manage Sci 11:308–315

Hamta N, Fatemi Ghomi SMT, Jolai F, Bahalke U (2011) Bi-criteria assembly line balancing by considering flexible operation times. Appl Math Model 35:5592–5608

Holland HJ (1975) Adaptation in natural and artificial systems. The University of Michigan Press, Ann Arbor

Kyungchul P, Sungsoo P, Wanhee K (1997) A heuristic for an assembly line balancing problem with incompatibility, range, and partial precedence constraints. Comput Ind Eng 32(2):321–332

Mozdgir A, Mahdavi I, Seyedi Badeleh SI, Solimanpur M (2013) Using the Taguchi method to optimize the differential evolution algorithm parameters for minimizing the workload smoothness index in simple assembly line balancing. Math Comput Model 15:57–137

Rachamadugu R, Talbot B (1991) Improving the quality of workload assignments in assembly lines. Int J Prod Res 29:619–633

Scholl A (1999) Balancing and sequencing assembly lines, 2nd edn. Physica, Heidelberg

Triki H, Mellouli A, Masmoudi F (2017) A multi-objective genetic algorithm for assembly line resource assignment and balancing problem of type 2 (ALRABP-2). J Intell Manuf 28:371–385

Wang HS, Che ZH, Chiang CJ (2012) A hybrid genetic algorithm for multi-objective product plan selection problem with ASP and ALB. Exp Syst Appl 39:5440–5450

Zitzler E, Laumanns M, Thiele L (2001) SPEA2: improving the strength pareto evolutionary algorithm. Computer Engineering and Networks Laboratory (TIK), Swiss Federal Institute of Technology (ETH), Zurich, Switzerland, pp 1–21

Dynamic Vibration of Vertical Axis Wind Turbine Geared Transmission System

Imen Bel Mabrouk, Abdelkhalek El Hami, Lassaad Walha,
Bacem Zgal and Mohamed Haddar

Abstract Dynamic study of Darrieus turbine bevel spur gear subjected to transient aerodynamic loads is carried out in this study. The aerodynamic torque is obtained by solving the two-dimensional unsteady incompressible Navier–Stocks equation with the k-ω Shear Stress Transport turbulence model. The two-dimensional computational model is validated with experimental results. A three-dimensional dynamic model of one-stage bevel gear system is developed. The periodic fluctuations of the gear meshes' stiffness and the unsteady aerodynamic torque fluctuations are the main sources of excitation for the gear system. The originality of our work is the correlation between complex aerodynamic phenomena and the mechanical gearing system vibration. The effect of the rotational speed on the overall dynamic behavior of the Darrieus turbine is also discussed. The present study shows that the rotational speed significantly affects the aerodynamic efficiency. Whereas, there is a small influence on the dynamic response of the bevel gear system.

Keywords Darrieus turbine · Aerodynamic torque
Computational fluid dynamic · Bevel gear · Dynamic vibration

I. B. Mabrouk (✉) · A. E. Hami
National Institute of Applied Sciences of Rouen, Saint Etienne du Rouvray, France
e-mail: belmabrouk.imen@gmail.com

A. E. Hami
e-mail: Abdelkhalak.elhami@insa-rouen.fr

L. Walha · B. Zgal · M. Haddar
National School of Engineers of Sfax, Sfax, Tunisia
e-mail: walhago@gmail.com

B. Zgal
e-mail: bacem.zghal@isgis.rnu.tn

M. Haddar
e-mail: mohamed.haddar@enis.rnu.tn

1 Introduction

Currently, wind power is becoming a vital source of energy and wind turbine is the most important of the wind energy. There are generally two types of wind turbines; Horizontal Axis Wind Turbines (HAWTs) and Vertical Axis Wind Turbines (VAWTs). VAWT has received more attention due to its efficiency in urban regions compared to HAWT. It can operate in all wind directions without any yawing mechanism. The inherent characteristics of omni-directionality of VAWTs make them more suitable to harnessing the turbulent flow. Other advantages include the simplicity in construction and low noise. The Darrieus turbine is the most common VAWT, it is based on the lift force to generate torque. According to the literature review, the main research methods for Darrieus rotor involve computational fluid dynamics (CFD), momentum theory, and experimental wind tunnel test. Despite the simplicity of the momentum theory (Paraschivoiu and Delclaux 1983; Coy and Loth 1983), all the classical aerodynamic tools are unable to predict the complexity of the flow around the turbine. They need experimental data to be validated using wind tunnel test, which are expensive in term of time and cost. To overcome the limitations of the empirical methods and experimental wind tunnel tests, we seek to investigate the wind performance of a VAWT using a numerical method based on a CFD approach. This method achieves considerable improvements in the understanding of the VAWT thanks to its inherent flexibility for analyzing complex unsteady flow around wind turbines. The most important advantage of the CFD approach is its ability to simulate the configurations at the wind tunnel test conditions and to generate results that are compared favorably with experimental data. The (CFD) method has been widely used in the literature to fully characterize the aerodynamic performance of the VAWT (Castelli et al. 2011; Castelli et al. 2012; Mohamed 2012; Howell et al. 2010). As far as the dynamic behavior of wind turbine gearboxes is concerned, several studies have been conducted on dynamic modeling of the bevel-gears transmission. Most of the research works use simple lumped parameter models involving a spring–mass–damper system (El Hami et al. 2015; Driss et al. 2014). Some studies are devoted to the dynamic behavior of bevel gear systems only subjected to internal excitations (Driss et al. 2014). Another research studies the dynamic response of gearing system excited by fixed wind speed (Aboudi et al. 2011). This kind of analysis is limited to empirical torque excitation. There still exists a large knowledge gaps in the simulation of the VAWT completed mechanism. Analyzing an unsteady flow around the blade airfoil in a turbulent regime aims to fulfilling this gap. The originality of our work is the correlation between complex aerodynamic phenomena and mechanical gearing system vibration. The rotational speed of wind turbine rotor is the core problem of wind turbine engineering. The main purpose of this study is to characterize the global dynamic behavior of the Darrieus turbine by investigating the effect of the rotational speed on both power production and dynamic vibration of bevel gear system in nonstationary regime.

2 Dynamic Model

The global dynamic model of the one-stage bevel spur gear system in 3D is presented in Fig. 1. This model is composed of two-blocks. Each block (i) is supported by a flexible bearing with traction–compression stiffness (k_{xi}, k_{yi}, k_{zi}) and bending stiffness ($k_{\psi i}$, $k_{\Phi i}$) (i = 1:2).

The first one includes the rotor modeled by the drive wheel (11) which is connected to the bevel spur gear (12) via a shaft with a torsional rigidity $k_{\theta 1}$. The second block (i = 2) contains the bevel spur gear (21), the receiving wheel (22) and a shaft with torsion stiffness $k_{\theta 2}$.

For each block (i), there are seven degrees of freedom: linear displacements (x_i, y_i, z_i) and angular displacement (Φ_i, ψ_i) of the bearing (i), in addition to the displacement of every wheel (θ_{11}, θ_{12}) in the first block and (θ_{21}, θ_{22}) in the second block, respectively.

The pair of bevel gear is linked through flexible teeth. The gear-mesh contacts are modeled by a linear time varying stiffness k (t) along the lines of action on the
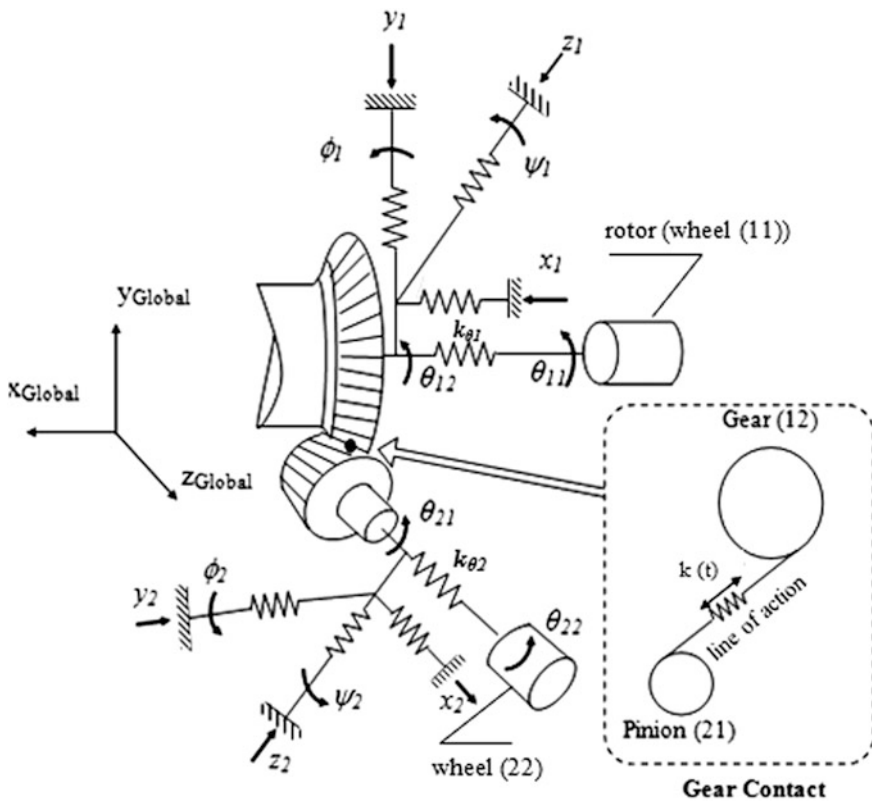
Fig. 1 Dynamic model of the one-stage bevel spur gear system
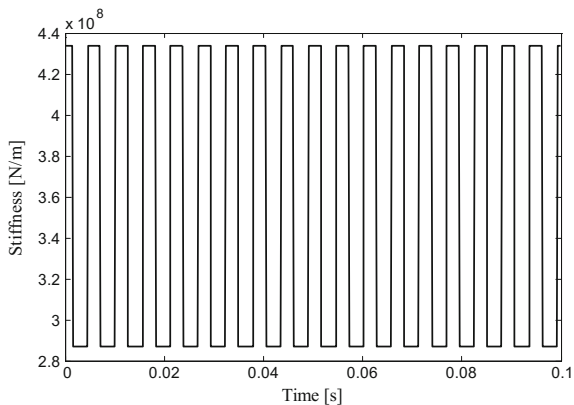
bevel gear stage. Figure 2 presents the mesh stiffness fluctuation, corresponding to internal source of excitation of the bevel spur gear system. In this study, we modeled the gear mesh stiffness variation k (t) by a square wave form (Fig. 2).

According to Lagrange's formalism, the motion equations describing the dynamic behavior of the system are given following the usual matrix form:

$$[M]\{\ddot{q}\} + [C]\{\dot{q}\} + ([K_S] + [K(t)])\{q\} = \{F(t)\} \tag{1}$$

[M]   is the total mass matrix,
[K$_s$]   is the average stiffness matrix of the structure,
[K (t)]   is the mesh stiffness matrix,
[C]   is the viscous damping matrix,
{F (t)}   is the load vector,
{q(t)}   is the vector of the model generalized coordinates, it is in the form:

$$\{q(t)\} = \{x_1, y_1, z_1, x_2, y_2, z_2, \phi_1, \psi_1, \phi_2, \psi_2, \theta_{11}, \theta_{12}, \theta_{21}, \theta_{22}\} \tag{2}$$

The Newmark method is used to resolve the equations of motion (Eq. 1) obtained by the Lagrange formalism.

3   Torque Modeling

The aim of this section is to numerically predict the unsteady torque of a three-bladed Darrieus VAWT, operating at different angular velocities for a constant wind speed (9 m/s) (Castelli et al. 2011; Howell et al. 2010; Castelli et al. 2012). The main geometrical features of the rotor are summarized in Table 1 (Castelli et al. 2011).

The tip speed ratio (TSR) is defined as the ratio between the tangential speed of the blade (ωR) and the free wind speed.

3.1 Model Geometry and Spatial Discretization

The 2D computational model is divided into two main zones as shown in Fig. 3; a fixed rectangular outer zone, and a circular inner zone, characterized by a moving mesh. The inner rotor zone includes three symmetric airfoil blades rotating at the same angular velocity.

The left side and the right side of the rectangular stationary domain are defined as a velocity-inlet and pressure outlet respectively. Wall function is set to the blade

Parameters	Value
D_{rotor} (mm)	1030
H_{rotor} (mm)	1456.4
N [-]	3
A (m^2)	1.236
$H_{wind\ tunnel}$ (mm)	4000
$W_{wind\ tunnel}$ (mm)	3800
c (mm)	85.8
σ (-)	0.5
Spoke-blade connection	0.5 c

Table 1 Validation model main features
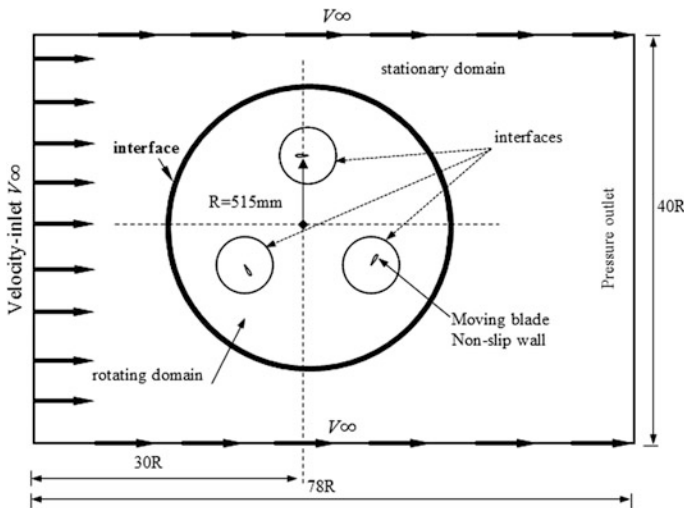
Fig. 3 2D Computational domain and boundary conditions

airfoil with non-slip boundary. The velocity of both side edges of the fixed domain is set to be equal to the wind speed.

Unstructured grids with different mesh size are generated, using ANSYS meshing advanced sizing functions. Mesh interfaces are used between the stationary domain and the rotating turbine, and between the rotating domain and the smaller blade areas, (three circles). The conservative interface boundary condition leads to ensuring the continuity in the flow field. We also adopt a gradual transfer of the grid size from the higher to the lower zone of gradient in order to account for the slight variation of flow. The three-airfoil blades are enclosed in a control circle to refine the mesh around the blades. These technical meshes reduce the number of grid elements and get a more accurate simulation with a faster convergence. The unsteady flow is solved by using a Sliding Mesh technique (SM). Mesh-independent test shows that more than 119128 cells have approximately no change of the output result. We adopt the optimum mesh configuration. The total number of grids is 119128 cells in which more than 85517 cells are distributed around the rotor blades. The meshing details of the rotor and of the small area around a blade are illustrated in Fig. 4.
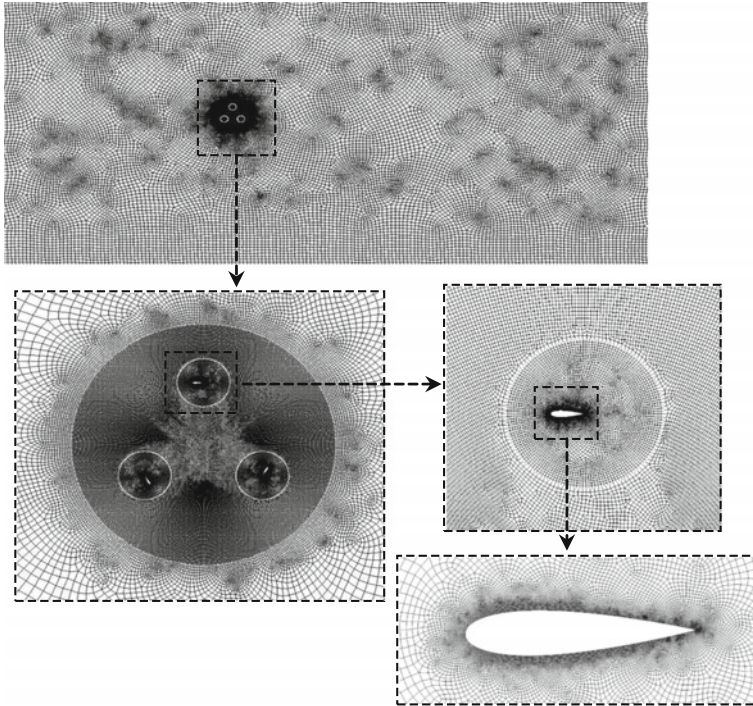
Fig. 4 Mesh discretization for VAWT flow field simulation

3.2 Turbulence Model Validation

The 2D rotor is analyzed at seven different rotational speeds. TSR values range between 1.435 and 3.293 (Castelli et al. 2011) (Fig. 5). The scope is to verify the accuracy of CFD data with experimental data. Numerical turbulence model has been validated in comparison with the published experimental results and CFD for a straight-bladed Darrieus turbine (Castelli et al. 2011). Figure 5 shows the effect of the turbulence model. These results give an excellent agreement between experimental and proposed CFD model for the target function, power coefficient (Cp), when using the k-ω Shear Stress Transport (SST) model. This model is adopted for the turbulence closure to present the transient simulations. It is suggested that the k-ω SST model is the best accurate and robust model for the prediction of the dynamic behavior of a vertical axis wind turbine compared to popular turbulence models (Wafula et al. 2015; Gasser et al. 2014).

3.3 Problem Setup in Fluent

Semi-Implicit Method for Pressure Linked Equations (Denk 2007) scheme is applied for the coupling of pressure and velocity, which have a second-order implicit transient formulation. For all the equations, a second-order upwind spatial discretization algorithm is used. For the solution, the convergence criteria are set as 10^{-5}. Time step is calculated using rotational speed of the rotor. Maximum iteration per time step is set to 400 iterations.

Fig. 5 Validation of proposed computational model, compared to publish experimental and CFD results for Darrieus rotor (Raciti Castelli et al. 2011)
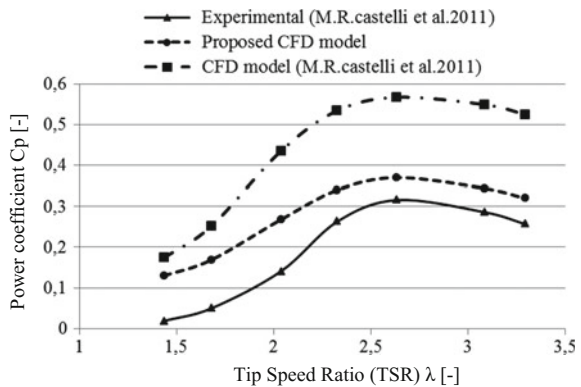
4 Numerical Results

The effect of the tip speed ratio (TSR) on the VAWT instantaneous aerodynamic torque is presented in Fig. 6. The total torque of the entire cycle is mostly positive in different tip speed ratios, which suggests a positive overall performance. The torque maximum values significantly increase with the increase of the rotational speed. However, it drops after $\lambda = 2.634$, indicating that it is headed to its optimum operating point.

The wind turbine bevel spur gear parameters are tabulated in Table 2.

The dynamic responses of the bevel spur gear system, in both time and frequency domain (FFT), are investigated for different rotational speeds excitations. For example, the linear displacements of the second bearing in the X-direction for $\lambda = 3.293$ and $\lambda = 2.634$ are respectively presented in Figs. 7 and 8. The angular displacements of the first bearing ($\Phi1$) is presented in Fig. 9.

Fig. 6 Effect of the TSR on the unsteady torque
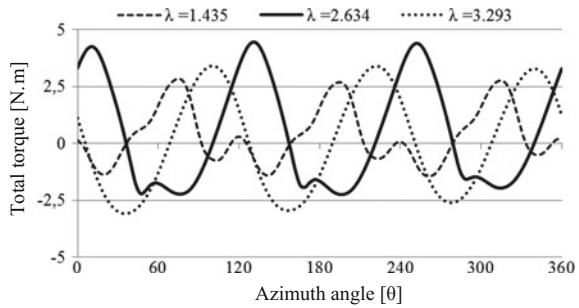
Table 2 Characteristics of the studied bevel spur gear system

Parameters	Value
Teeth number	45/18
Teeth module	0.004
Bearing stiffness	$k_{xi} = k_{yi} = 210^8$, $k_{zi} = 410^8$
Torsional shaft stiffness	$K_{\theta i} = 310^8$ (i = 1:2)
Pressure angle	$\alpha = 20°$
Average mesh stiffness	$K_{moy} = 410^8$

Fig. 7 Linear displacement of the second bearing in the X-direction for $\lambda = 3.293$
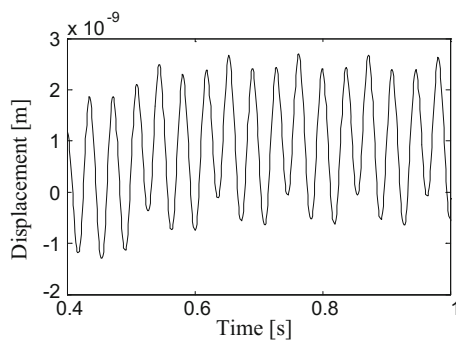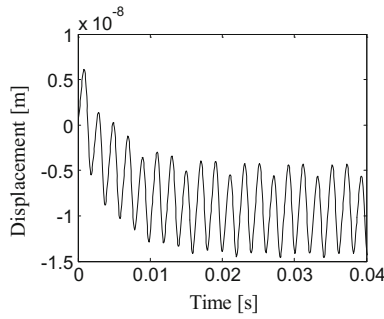
Fig. 8 Linear displacement of the second bearing in the X-direction for $\lambda = 2.634$
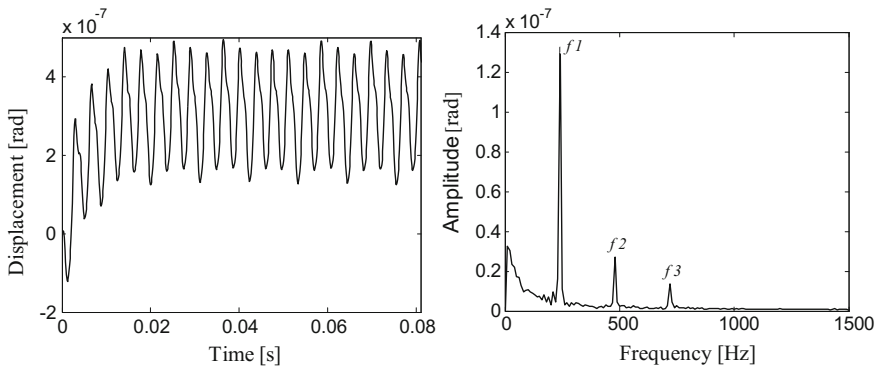
Fig. 9 Angular displacement and the corresponding frequency responses in the $\Phi1$-direction for $\lambda = 1.435$

The frequency domain representation, indicates peaks, correspond only to the aerodynamic torque frequencies ($f1$, $f2$, $f3$).

These results indicate that the dynamic behavior of the bevel spur gear system is slightly sensitive to the variation of the rotor angular velocity. Considering the correlation between aerodynamic efficiency and bevel spur gear dynamic responses, it seems better to select the optimum rotational speed ($\omega = 46$ rad $\cdot$ s^{-1} corresponding to $\lambda = 2.634$) to achieve better performance of the studied turbine.

5   Conclusion

In this paper, the effect of the rotational speed on the global dynamic behavior of the Darrieus wind turbine gearing system, in nonstationary regime, is investigated. A three-dimensional model of a one-stage bevel spur gear is developed. The results show that unsteady simulation under the k-ω SST turbulence model with sliding

mesh is suitable for this kind of simulation. It is found that $\lambda = 2.634$ generates the best performance according to the power production. Also, it is demonstrated that the rotational speed significantly affects the aerodynamic performance, whereas, there is a small change on the dynamic vibration of the Darrieus turbine geared transmission system.

References

Abboudi K, Walha L, Driss Y, Maatar M, Fakhfakh T, Haddar M (2011) Dynamic behavior of a two-stage gear train used in a fixed-speed wind turbine. Mech Mach Theory 46:1888–1900

Castelli MR, De Betta S, Benini E (2012) Effect of blade number on a straight-bladed vertical-axis Darrieus wind turbine. Int J Mech Aerosp Eng

Castelli MR, Englaro A, Benini E (2011) The Darrieus wind turbine: Proposal for a new performance prediction model based on CFD. Energy. 36:4919–4934

Coy HM, Loth JL (1983) Optimization of Darrieus turbines with an upwind and downwind momentum model. Energy. 4:31–38

Danao LA, Eboibi O, Howell R (2013) An experimental investigation into the influence of unsteady wind on the performance of a vertical axis wind turbine. Appl Energy 107:403–411

Denk K (2007) Development of a pressure-based solver for both incompressible and compressible flows. PhD Thesis

Driss Y, Hammami A, Walha L, Haddar M (2014) Effects of gear mesh fluctuation and defaults on the dynamic behavior of two-stage straight bevel system. Mech Mach Theory 71:86

El Hami A, Guerine A, Fakhfakh T, Haddar M (2015) A polynomial chaos method to the analysis of the dynamic behavior of spur gear system. Structural Eng and Mech. 819:831–853

Gasser EH, Amany H, Youssef ME (2014) Numerical investigation of medium range Re number aerodynamics characteristics for NACA0018 airfoil. Inet J of CFD Letters. 6:175–187

Howell R, Ning Q, Jonathan E, Naveed D (2010) Wind tunnel and numerical study of a small vertical axis wind turbine. Rew Energy. 35:412–422

Mohamed MH (2012) Performance investigation of H-rotor Darrieus turbine with new airfoil shapes. Energy. 47:522–530

Paraschivoiu I, Delclaux F (1983) Double multiple streamtube model with recent improvements. Energy. 3

Wafula D, Cong W, Yingjie W, Joseph NK, Angelo L, Danao M (2015) A numerical analysis of unsteady inflow wind for site specific vertical axis wind turbine. Rew Energy. 76:648–661

Free Vibration of a Multi-span Road Bridge Supported by Point Elastic Supports

Moussa Guebailia and Nouredine Ouelaa

Abstract The modelling of mechanical systems plays a primordial role in the study of structural dynamics and the vibrations that result. One presents in this work the modelling of a road bridge by a continuous multi-span orthotropic plate supported by point elastic supports along the longitudinal direction and with three-point elastic supports on the transversal direction. One has found that when the parameter of the elastic support is greater than zero, which means that the elastic supports have a high rigidity; the behaviour of the elastic supports tends towards the behaviour of the rigid supports. Note that the values of the bridge natural frequencies switch between those of a free-free bridge for the case of a lower support' parameter and those of a simply support bridge for the upper case. Finally, one carried out the generalized modelling of the behaviour of a road bridge supported by point elastic supports for *N* spans by using the computer tool for carrying out different calculations and makes it possible to have a view of many cases of Road Bridge properties.

Keywords Point elastic support · Natural frequency · Bridge
Free vibration · Rigid support

1 Introduction

The study and analysis of the dynamic behaviour of Road Bridge excited by the passage of a vehicle requires the study and evaluation of the free vibration behaviour of the bridge structure. The model adopted to study the bridge is an orthotropic continuous plate supported by point elastic supports along the bridge and on

M. Guebailia (✉)
Mechanical Department FST, Kasdi Merbah University, Ouargla, Algeria
e-mail: guebailiamoussa2@hotmail.com

M. Guebailia · N. Ouelaa
Mechanics & Structures Laboratory, 08 May University, Guelma, Algeria
e-mail: n_ouelaa@yahoo.fr

91

the transverse direction in three positions. In the majority of works in this area model, the bridge by simply supported continuous plates or beam and in order to approximate to the real behaviour of the bridge we propose the elastic support. Farghaly et al. (2017) investigate the changes in the magnitude of natural frequencies and their associated modal shapes of Timoshenko beam with respect to different system design parameters. The studied beam includes an intermediate extended eccentric rigid mass mounted on two elastic segments. They consider several end and intermediate conditions.

2 Bridge Model

The bridge is modelled by an orthotropic thin plate with three spans (Fig. 1) supported by elastic stiffness supports K.

The motion equation of the presented model is shown (1).

$$\bar{m}\frac{\partial^2 w}{\partial t^2} + D_x\frac{\partial^4 w}{\partial x^4} + 2H\frac{\partial^4 w}{\partial x^2 \partial y^2} + D_y\frac{\partial^4 w}{\partial y^4} = 0 \tag{1}$$

We solve the equation of the motion of the bridge by the local estimation method (Guebailia et al. 2013) of the value of x.
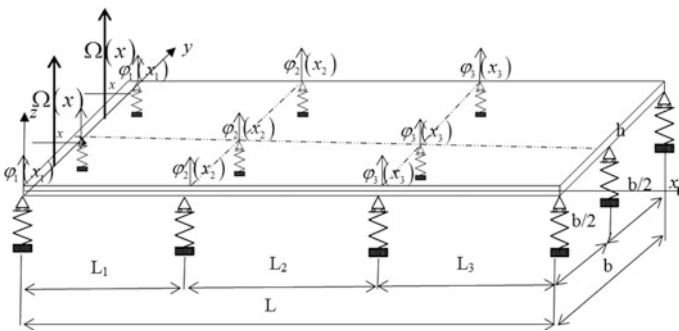
Fig. 1 Bridge model

3   Mode Shape Functions

We present the different mode shapes functions

$$
\phi_{ij}(x,y) = \begin{cases} \varphi_i(x_i).\begin{cases} h_j(y_j) \\ H_j(y_j) \end{cases} \\ \Omega_i(x_i).\begin{cases} h_j(y_j) \\ H_j(y_j) \end{cases} \end{cases}
\tag{2}
$$

These mode shape functions are defined on the domains for x and y following:

Let $R = \frac{K}{E.I}$, R is the support parameter. In order to determinate the admissible function $\varphi_i(x_i)$, on apply the boundary conditions as follows:

$$
\begin{aligned}
\left.\frac{d^3\varphi_1(x_1)}{dx_1^3}\right|_{x_1=0} &= -R.\varphi_1(x_1=0) \\
\left.\frac{d^3\varphi_3(x_3)}{dx_3^3}\right|_{x_3=L_3} &= R.\varphi_3(x_3=L_3)
\end{aligned}
\quad \text{and} \quad
\begin{cases}
\left.\frac{d^2\varphi_1(x_1)}{dx_1^2}\right|_{x_1=0} = 0 \\
\left.\frac{d^2\varphi_3(x_3)}{dx_3^2}\right|_{x_3=L_3} = 0
\end{cases}
$$

And also by respecting the continuity on the middle supports:

For continuity conditions on all intermediate elastic supports; four types of conditions must be imposed. These are the continuity of the shear force, bending moment, admissible function of the mode shape and finally the slope.

$$
\begin{cases}
\left.\frac{d^3\varphi_i(x_i)}{dx_i^3}\right|_{x_i=L_i} = (-1)^{i+1}.R.\varphi_i(x_i=L_i) + \frac{d^3\varphi_{i+1}(x_{i+1}=0)}{dx_{i+1}^3} \\
\left.\frac{d^2\varphi_i(x_i)}{dx_i^2}\right|_{x_i=L_i} = \frac{d^2\varphi_{i+1}(x_{i+1}=0)}{dx_{i+1}^2} = 0
\end{cases}
\quad (i=1,\ \ldots,\ 2)
$$

$$
\begin{cases}
\varphi_i(x_i)|_{x_i=L_i} = \varphi_{i+1}(x_{i+1})|_{x_{i+1}=0}, \\
\left.\frac{d\varphi_i(x_i)}{dx_i}\right|_{x_i=L_i} = \left.\frac{d\varphi_{i+1}(x_{i+1})}{dx_{i+1}}\right|_{x_{i+1}=0}
\end{cases}
\quad (i=1,\ \ldots,\ 2)
$$

$\Omega_i(x_i)$: The admissible function applied for the entire width of the plate and for the entire length of the bridge. This function is that of a free-free beam. To determinate it on apply these boundary conditions

$$
\begin{cases}
\left.\frac{d^2\Omega_i(x_i)}{dx_i^2}\right|_{x_i=0} = 0, & \left.\frac{d^2\Omega_i(x_i)}{dx_i^2}\right|_{x_i=L} = 0 \\
\left.\frac{d^3\Omega_i(x_i)}{dx_i^3}\right|_{x_i=0} = 0, & \left.\frac{d^3\Omega_i(x_i)}{dx_i^3}\right|_{x_i=L} = 0
\end{cases}
$$

Then the function of mode shapes along the bridge is defined as follows:

$$
\left\{
\begin{aligned}
\varphi_i(x_i) & \left\{
\begin{aligned}
& = A_1.\sin(k_i.x) + B_1.\cos(k_i.x) + C_1.sh(k_i.x) + D_1.ch(k_i.x) \\
& \text{For} \quad (0 \le x \le l_1) \\
& = A_2.\sin(k_i.(x-l_1)) + B_2.\cos(k_i.(x-l_1)) + C_2.sh(k_i.(x-l_1)) \\
& \quad + D_2.ch(k_i.(x-l_1)) \\
& \text{For} \quad (l_1 \le x \le l_1 + l) \\
& = A_3.\sin(k_i.(x-l_1-l_2)) + B_3.\cos(k_i.(x-l_1-l_2)) \\
& \quad + C_3.sh(k_i.(x-l_1-l_2)) + D_3.ch(k_i.(x-l_1-l_2)) \\
& \text{For} \quad (l_1 + l_2 \le x \le L)
\end{aligned}
\right. \\
\Omega_i(x_i) & \left\{
\begin{aligned}
& = \sin(k_i.x_i) + sh(k_i.x_i) + \theta.(\cos(k_i.x_i) + ch(k_i.x_i)) \\
& \text{For} \quad x_i \in [0,\ L],\, y \in \left]0, \tfrac{b}{2}\right[\cup \left]\tfrac{b}{2}, b\right[
\end{aligned}
\right.
\end{aligned}
\right.
$$

$H_j(y_j)$: The admissible function of mode shapes applied to the entire width of the plate ($y \in [0, b] \wedge x = \{0, l_1, l_1 + l_2, L\}$).

This function is that of a continuous beam with two equal spans ($b/2$) Supported by point elastic supports

For the boundary conditions, we have the shear force balancing on the boundaries ($y_1 = 0$ et $y_2 = $ b/2):

$$
\left. \frac{d^3 H_1(y_1)}{dy_1^3} \right|_{y_1 = 0} = -R.H_1(y_1 = 0)
$$

$$
\left. \frac{d^3 H_2(y_2)}{dy_2^3} \right|_{y_2 = b/2} = R.H_2(y_2 = b/2)
$$

The bending moment at the outer edges of the beam is zero

$$
\left\{
\begin{aligned}
\left. \frac{d^2 H_1(y_1)}{dy_1^2} \right|_{y_1 = 0} &= 0 \\
\left. \frac{d^2 H_2(y_2)}{dy_2^2} \right|_{y_2 = b/2} &= 0
\end{aligned}
\right.
$$

For continuity conditions on all intermediate elastic supports, we have the continuity of shear force, bending moment, mode shapes and slope.

$$
\left\{
\begin{aligned}
\left. \frac{d^3 H_1(y_1)}{dy_1^3} \right|_{y_1 = b/2} &= R.H_1(y_1 = b/2) + \frac{d^3 H_2(y_2 = 0)}{dy_2^3} \\
\left. \frac{d^2 H_1(y_1)}{dy_1^2} \right|_{y_1 = b/2} &= \frac{d^2 H_2(y_2 = 0)}{dx_2^2} \\
\left. H_1(y_1) \right|_{y_1 = b/2} &= \left. H_2(y_2) \right|_{y_2 = 0}, \\
\left. \frac{dH_1(y_1)}{dy_1} \right|_{y_1 = b/2} &= \left. \frac{dH_2(y_2)}{dy_2} \right|_{y_2 = 0}
\end{aligned}
\right.
$$

Fig. 2 First two mode shapes
($R = 0$)
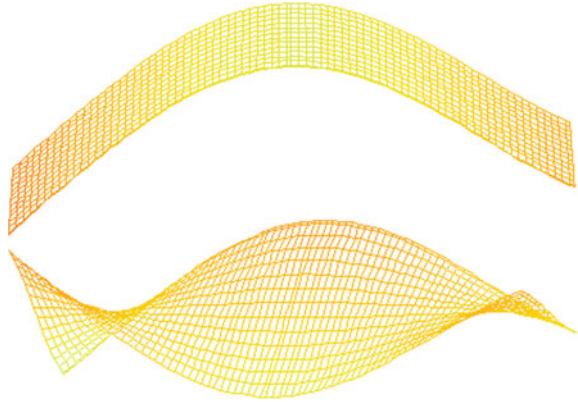
Validate example

The bridge data are taken from the reference (Zhu 2002)

On Fig. 2 we present the first two mode shapes of the case of a three-span bridge supported by elastic supports without stiffness ($R = 0$). The natural frequencies are 1.09, 2.45 Hz.

On Fig. 3, the first two mode shapes of the case of a three-span bridge supported by elastic supports with stiffness R>>. The natural frequencies are 4.13, 5.38 Hz.

Figure 4 shows, the superposition of the natural frequencies of different stiffness values of the elastic supports with support parameter R varying from 0 to 242 compared with the natural frequencies obtained for the case of a simply supported and symmetrical three-span bridge of reference (Zhu 2002). We find that when the support parameter $R > 0$, which means that the elastic supports have a high rigidity; Tend towards a behaviour of rigid supports.

Fig. 3 First two mode shapes
(R>>)
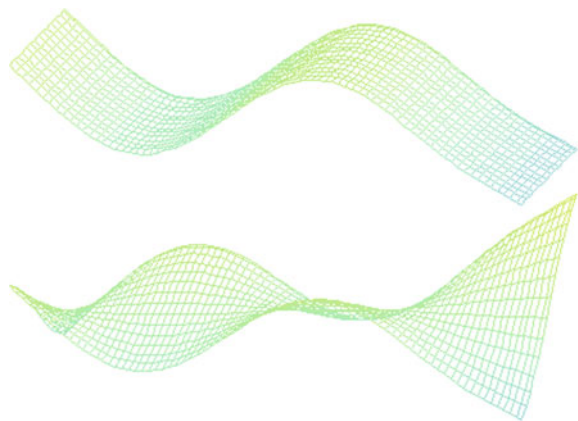
Fig. 4 Elastic point support
behaviour
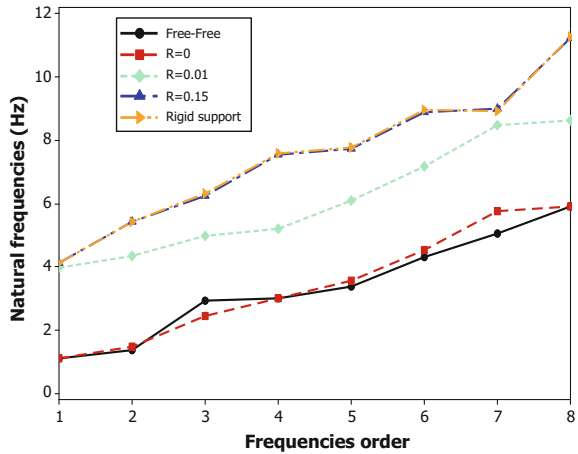
4   Conclusion

We have presented in this paper the modelling of a road bridge by a continuous
multi-span orthotropic plate supported by point elastic supports along the longi-
tudinal direction and even its width at positions $y = 0$, $y = b/2$ and $y = b$.

We have found that when the support parameter $R > 0$, which means that the
elastic supports have a high rigidity; the behaviour of the point elastic supports
tends towards a behaviour of the rigid supports.

It may be noted that the Eigen Frequency values of the bridge are switched
between the behaviour of a free-bridge for the case of a lower support parameter
and the behaviour of a bridge simply supported for the case of a ratio of rigidity.

Bibliography

Farghaly SH, El-Sayed TA (2017) Exact free vibration analysis for mechanical system composed
    of Timoshenko beams with intermediate eccentric rigid body on elastic supports: an
    experimental and analytical investigation. Mech Syst Signal Process 82:376–393
Guebailia M, Ouelaa N, Guyader JL (2013) Solution of the free vibration equation of a multi span
    bridge deck by local estimation method. Eng Struct 48:695–703
Zhu XQ, Law SS (2002) Dynamic load on continuous multi-lane bridge deck from moving
    vehicles. J Sound Vib 251(4):697–716

Modelization and Multimodel Control of Ship Electric Propulsion System

Habib Dallagi, Chiheb Zaoui and Samir Nejim

Abstract The ship propulsion system is a nonlinear and uncertain system. To overcome these constraints, in order to synthesize a powerful command, the multimodel control is promising. This paper deals with the modeling and multimodel control of complex uncertain systems. The approach is based on the principle of generating model bases, which can be local or generic, determined according to procedures using Kharitonov's algebraic approach. The evaluation of the relevance of the models is ensured by means of validations calculated on line by referring to the responses of the process. Such validities are used to generate the multimodel control according to a strategy by fusion. Two fusion methods are then proposed: A merge at the level of the elementary commands and another at the level of the control parameters. This work deals with the development of a model base, as well as the synthesis of a multimodel control law. In this sense it is proposed to study the electric propulsion of ships as well as its composition. Next, we propose a technique for modeling the electric propulsion system of a ship and synthesized a multimodel control law. Finally, we will model the propulsion system based on a synchronous motor with permanent magnet and synthesize a law of control according to the multimodel approach.

Keywords Ship · Electric propulsion · Modeling · Multimodel control

H. Dallagi (✉) · C. Zaoui · S. Nejim
U.R Automation & Robotics Marine (ARM), Naval Academy, Menzel Bourguiba
Tunisia
e-mail: habib.dallagi@ept.rnu.tn

C. Zaoui
e-mail: chiheb.zaoui@gmail.com

S. Nejim
e-mail: nejim.samir@planet.tn

1 Introduction

In order to satisfy the constant need for automation while satisfying the requirements of reliability and robustness, the automaton is confronted with increasingly complex control problems. Indeed, taking into account the different physical aspects of a process, while making the minimum approximation, nonlinear, nonstationary and/or uncertain systems can become inoperative. Since the complexity of the control is intimately linked to the complexity of the model considered, it has proved necessary to think of simpler modeling. Several approaches differ but all aim to replace the single model by a library of simpler models, such as Linear Variable Parameter Control, polytopic, fuzzy and multimodel approaches. The principle of multimodel representation offers the possibility to design control laws from the linear partial commands associated with each model. The global command can be deduced by a mode of fusion well suited to the approach adopted. This paper deals with the modeling and control of a ship's electric propulsion system. This system is highly nonlinear, complex and uncertain parameter. For this purpose the multimodel control ensures a desired behavior and performance. In this sense main parts are dealt with in this work, namely

- The modelization of the electric propulsion system by applying the multimodel approach, then linearize this model around a nominal operating point, and finally synthesize a library of models and a multimodel control law by return of states.
- The study of the multimodel modeling technique such as local modeling and generic modeling as well as the validity calculation method and the various multimodel control strategies such as the merging strategy and the commutation strategy of the partial commands.
- Validation by numerical simulation of the proposed control approach (Fig. 1).

Fig. 1 Ship movement
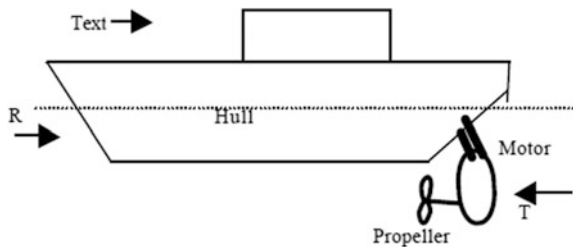
2 Modeling of the Ship Electric Propulsion System

The propulsion of the ship is ensured by a permanent magnet synchronous motor coupled to a propeller with fixed blades whose main components can be decomposed into subsystems. Figure 2 gives an overview of the structure of the ship's electric propulsion system as well as the inputs and outputs of the various subsystems (Guo et al. 2005).

In the following subsections, we will study each subset constituting the whole of the electric propulsion system.

Where: R: hull resistance applied by the sea which is opposed to the ship movement, T: propeller thrust, Text: external force.

2.1 Model of the Permanent Magnet Synchronous Motor

The ship is propelled by a permanent magnet synchronous motor. The mathematical model of the permanent magnet synchronous machine in the Park reference is given by the following system (Babu 2011):

$$\begin{cases} \frac{di_d}{dt} = -\frac{R_s}{L_d}i_d + \frac{p\Omega L_q i_q}{L_d} + \frac{1}{L_d}u_d \\ \frac{di_q}{dt} = -\frac{R_s}{L_q}i_q - p\Omega\frac{L_d}{L_q}i_d - \frac{p\Omega\Phi_f}{L_q} + \frac{1}{L_d}u_q \end{cases} \tag{1}$$

where: Rs: Stator resistance, L_d: Longitudinal inductance L_q: Transverse inductance, p: Number of pole pairs, Φ_f: Excitation flux, u_d, u_q: Longitudinal and transverse components of stator voltage, Ω propeller rotation speed in rd/s, i_d, i_q: longitudinal and transverse components of stator current.

Electromagnetic torque of the motor

$$C_e = p(L_d - L_q)i_d i_q + p\Phi_f i_q \tag{2}$$
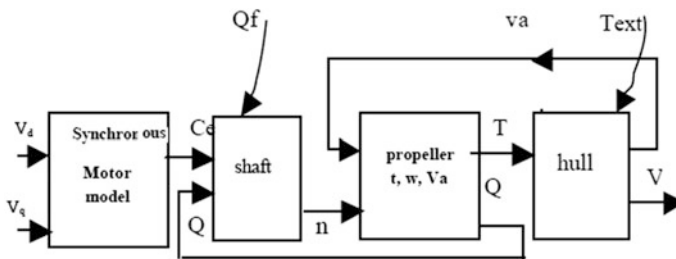
Fig. 2 Functional scheme of the propulsion system

The mechanical equation is:

$$I_m \frac{d\Omega}{dt} = C_e - Q \tag{3}$$

With: C_e: electromagnetic torque and Q: propulsion torque, I_m: inertia moment.

2.2 Total Hull Resistance Model

It is known in fluid mechanics that the displacement of bodies in a fluid undergoes on the part of the fluid a certain resistance which is generally a function of the speed of movement of the body and of the characteristics of the body dimensions and fluid (specific weight and viscosity).

The usual ship is a floating body which evolves in the interstice of two fluids namely water and air. Consequently, during its movement, it undergoes the resistance of these two fluids, one called hydrodynamic resistance due to the presence of water and the other called aerodynamic resistance due to the presence of air. Thus, in its movement, the vessel's live craft undergoes a resistance on the part of the water, while its dead works (superstructures and emerged parts) undergo resistance from the air. The combination of these two resistances, without taking into account any resistance due to the simultaneous existence of the two fluids, constitutes the ship advancement resistance. The advancement resistance of the bare and smooth hull, in its simplest form, consists of three main components:

- The Friction resistance R_F or viscous resistance: It is a function of the Reynolds number Re and the relative roughness of the shell due to the movement of the shell in a viscous fluid;
- The Residual Resistance R_r, it is composed of

    - The Wave resistance R_w due to the energy the ship must provide to the wave system it generates on the surface of the water during its movement.
    - The vortical resistance R_{tr} due to the formation of vortices due to changes in hull shape.

    The sum of the resistances (frictional resistance or viscous resistance) and (residual resistance), in calm water and in the absence of the appendages constitutes the "hydrodynamic resistance" of the hull.

- Aerodynamic resistance R_{air}: It is due to the movement of the ship, more precisely, of its dead works and superstructures, in the air.

    In the case of the ship's hull it is necessary to add to these three main components, two other components, namely:

– The resistance of the appendages R_{app} due to the presence of the hull appendages (rudder, stabilizing fins, anti-roll keel, etc.),
– The additional resistance R_{add} due to sea conditions (wave effects)

The ship advancement total resistance to advancement is thus given by the expression

$$R_T = R_F + R_w + R_{tb} + R_{air} + R_{app} + R_{add}$$

Or, by replacing it $R_r = R_w + R_{tb}$, it is written: $R_T = R_F + R_r + R_{air} + R_{app} + R_{add}$

The resistance to calm water advance of a bare hull (without appendages) at a given speed is defined as the force required to tow the hull at that given speed in the absence of any interference from the towing system used. By neglecting the resistance of air, it is given by the expression: $R_T = R_F + R_r$.

2.3 Estimation of the Resistance to Advancement

Figure 3 shows the variations of various components of the ship "Quantum 9000" resistance to advance and its total resistance as a function of the displacement velocity. The analysis of the behavior of the various components of the resistance to walking shows that at low speed it is the viscous (friction) resistance which is preponderant and that from 20 knots the resistance of the waves begins to take This is all the more remarkable as the speed increases and approaches the cruising speed of the ship. Wave resistance becomes dominant for speeds above 28 knots. Figure 3 shows that the resistance of appendages and the aerodynamic resistance, compared with the wave and friction resistances, can be negligible (Dallagi and Nejim 2015).

Total advancement resistance

$$R_T = R_w + R_f + R_{app} + R_{air} \tag{4}$$

This total resistance to advancement R can be represented by a function of the square of the speed of the ship

$$R_T = aV^2 \tag{5}$$

Models of the propeller Thrust T and the propeller torque Q

$$T = \rho\, K_T\, D^4\, n^2 \tag{6}$$

$$Q = \rho\, K_Q\, D^5\, n^2, \tag{7}$$

where: T, Q: thrust and propeller torque. K_T, K_Q: coefficient of propeller thrust and torque, ρ: sea water density, D: propeller diameter, n: propeller speed.

The coefficients K_T and K_Q depend on the advance speed of the propeller Va and the propeller advance coefficient J:

$$V_a = (1 - \omega)V \tag{8}$$

$$J = \frac{V_a}{nD} \tag{9}$$

where: V: vessel speed, w: wake ratio.

Figures 4 and 5 respectively show the diagrams of the coefficients K_T and K_Q as a function of J.

The coefficients K_T and K_Q can be written as a function of J in the following forms.

$$K_T = r_1 + r_2 J \tag{10}$$

Fig. 3 Decomposition of resistance
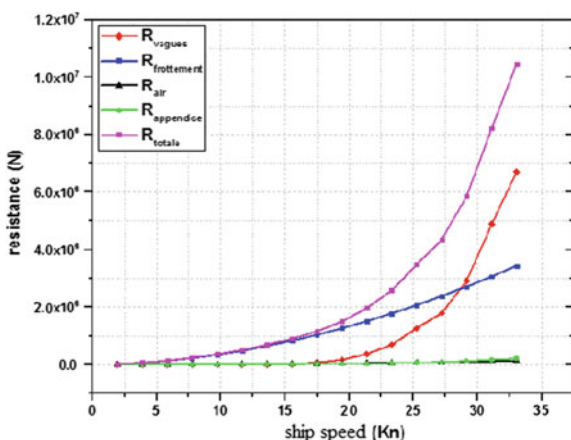
Fig. 4 Coefficients K_T function of J
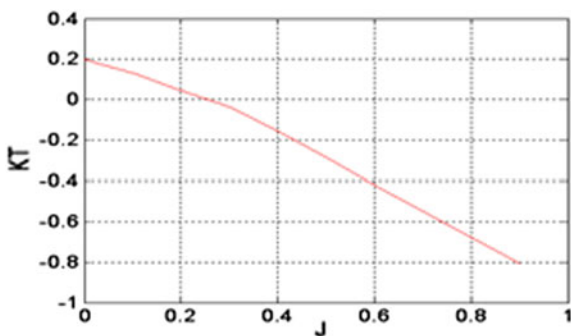
Fig. 5 Coefficients K_Q function of J
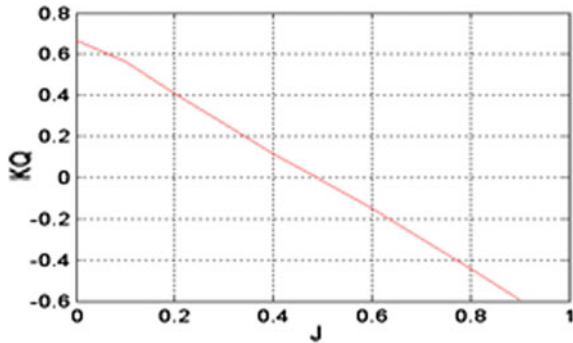
$$K_Q = s_1 + s_2 J \tag{11}$$

By replacing Eqs. (8)–(11) in expressions (5) and (6), the new expressions of propeller thrust and torque given by (12) and (13):

$$T = r_1 \rho n^2 D^4 + r_2 \rho nD^3 (1 - \omega)V \tag{12}$$

$$Q = s_1 \rho n^2 D^5 + s_2 \rho nD^4 (1 - \omega)V \tag{13}$$

Equation of motion of the ship: The ship floating on the sea surface is subjected to external and hydrodynamic forces.

$$m \dot{V} = - R_T + (1 - t) T - T_{ext} \tag{14}$$

where: *t:* suction coefficient, *m*: ship's weight.

By replacing Eqs. (5) and (12) in expressions (14), we obtain the new expression of the motion of the ship given by (15).

$$\dot{V} = - \frac{\alpha}{m}V^2 + \frac{(1 - t)r_1 \rho D^4}{4\pi^2 m}\Omega^2 + \frac{(1 - t)(1 - \omega)r_2 \rho D^3}{2\pi m}\Omega V - T_{ext}, \tag{15}$$

where: $n = 60/2\pi$

Mechanical equation of the shaft line: By replacing Eqs. (2) and (13) in expressions (3), the new mechanical equation of the shaft line given by (16) is obtained.

$$\Omega = \frac{1}{I_m}p(L_d - L_q)i_d i_q + \frac{p_f}{I_m}i_q - \frac{s_1 \rho D^5}{4\pi^2 I_m}\Omega^2 - \frac{s_2 \rho D^4 (1 - \omega)}{2\pi I_m}\Omega V \tag{16}$$

Global propulsion system model

$$
\begin{cases}
\dfrac{di_d}{dt} = \dfrac{-R_s}{L_d} i_d + \dfrac{L_q}{L_d} p\Omega i_q + \dfrac{u_d}{L_d} \\
\dfrac{di_q}{dt} = \dfrac{-R_s}{L_q} i_q - \dfrac{L_d}{L_q} p\Omega i_d - \dfrac{\Phi_f}{L_q} p\Omega + \dfrac{u_q}{L_d} \\
\dfrac{d\Omega}{dt} = \dfrac{1}{I_m} p(L_d - L_q) i_d i_q + \dfrac{p\Phi_f}{I_m} i_q - \dfrac{s_1 \rho D^5}{4\pi^2 I_m} \Omega^2 - \dfrac{s_2 \rho D^4 (1-\omega)}{2\pi I_m} \Omega V \\
\dfrac{dV}{dt} = \dfrac{-\alpha V^2}{m} + \dfrac{(1-t) r_1 \rho D^4 \Omega^2}{4\pi^2 m} + \dfrac{(1-t)(1-\omega) r_2 \rho D^3}{2\pi m} \Omega V - T_{ext}
\end{cases}
\tag{17}
$$

The system (17) is nonlinear and can be given the following form:

$$
\begin{cases}
\dot{x} = f(x) + g_1(x)u + g_2 T_{ext} \\
y = h(x)
\end{cases}
\tag{18}
$$

with: $x = [\,i_d \quad i_q \quad \Omega \quad V\,]^T u = [\,u_d \quad u_q\,]^T, y = [\,y_1 \quad y_2\,]^T = [\,h_1(x) \quad h_2(x)\,]^T = [\,i_d \quad V\,]^T$.

3   Local Models

A local model is a model that describes the characteristics of the process in the vicinity of an operating point. It represents a partial view of the complete system since it can only reproduce the behavior of the process in the vicinity of this particular operating point. If the process is described by an unusable complex model, it is possible to define a set of local models by linearization of the complex model in the vicinity of certain operating points. If no model is available then it will be necessary to use identification algorithms considering each time a subset of data corresponding to a particular operating point (Gao and O'Dwyer 2002).

For a system which has different operating modes, it is advantageous to construct different local models, each specific to a particular operating point of the system. This strategy makes it possible, on the one hand, to simplify the modeling task, since in order to determine each model, only the data relating to the corresponding operating regime are considered. On the other hand, it makes it possible to simplify the control task, since the models thus obtained are sufficiently manageable to deduce simple and efficient commands. Let a process be represented in the continuous domain by the following nonlinear form:

$$
\begin{cases}
\dot{x}(t) = f(x(t), u(t)) \\
y(t) = g(x(t), u(t))
\end{cases}
\tag{19}
$$

The linearization of the system (19) around an operating point makes $(x_i, u_i) \in \mathfrak{R}^p \times \mathfrak{R}^m$ it possible to elaborate the model (Mi), whose structure is written: (Mi)

$$
\begin{cases}
\dot{x}_i(t) = A_i(x(t) - x_i(t)) + B_i(u(t) - u_i(t)) + f(x_i(t), u_i(t)) \\
y_i(t) = C_i(x(t) - x_i(t)) + g(x_i(t), u_i(t))
\end{cases}
\tag{20}
$$

Then this local model is written in the form

$$
(\mathrm{M}_i) \begin{cases}
\dot{x}_i(t) = A_i x(t) B_i u(t) + d_i \\
y_i(t) = C_i x(t) + e_i
\end{cases}
\tag{21}
$$

Thus, the global model relative to the considered process, having n operating points (x_i, u_i), is written according to the multimodel structure below

$$
\begin{cases}
\dot{x}(t) = \sum_{i=1}^{n} v_i(t) \, (A_i x(t) + B_i u(t) + d_i) \\
y(t) = \sum_{i=1}^{n} v_i \, (C_i x(t) + e_i)
\end{cases},
\tag{22}
$$

where: $x_i(t) \in \mathfrak{R}^m, u_i(t) \in \mathfrak{R}^p$ and $y_i(t) \in \mathfrak{R}^q$ are respectively the state, the control and the output of the process for the model (M_i), $v_i(t)$ is the relevance coefficient relative to the model (M_i), called validity.

d_i and e_i Are the linearization constants, which are calculated as follows:
$$
\begin{cases}
d_i = f(x_i, u_i) - A_i x_i - B_i u_i \\
e_i = g(x_i, u_i) - C_i x_i
\end{cases}.
$$

4   Linearization of the Nonlinear Model

By linearizing this system around its nominal operating point, it comes

$$
\begin{cases}
\dot{x} = Ax + Bu \\
y = Cx
\end{cases}
\tag{23}
$$

The matrices A, B, and C of constant matrices of suitable dimensions. These matrices are respectively the Jacobean ones presented as follows:

$$
A = \frac{\partial f}{\partial X}\big|_{X=X0}; \ B = \frac{\partial f}{\partial u}\big|_{u=u_0} \text{ and } C = \frac{\partial h}{\partial X}\big|_{X=X0}
$$

The model matrices of the global model are represented below

$$
A = \begin{bmatrix} a_{11} & a_{12} & a_{13} & a_{14} \\ a_{21} & a_{22} & a_{23} & a_{24} \\ a_{31} & a_{32} & a_{33} & a_{34} \\ a_{41} & a_{42} & a_{43} & a_{44} \end{bmatrix}, B = \begin{bmatrix} \frac{1}{L_d} & 0 \\ 0 & \frac{1}{L_q} \\ 0 & 0 \\ 0 & 0 \end{bmatrix}, C = \begin{bmatrix} 1 & 0 & 0 & 0 \\ 0 & 0 & 0 & 1 \end{bmatrix}; a_{11} = \frac{-R}{L_d}; a_{12} = \frac{L_q}{L_d} p\Omega_0,
$$

$$
a_{13} = \frac{L_q}{L_d} p i_{q0}, \quad a_{14} = 0, \quad a_{21} = \frac{-L_d}{L_q} p\Omega_0, \quad a_{22} = \frac{-R}{L_q},
$$

$$
a_{23} = \frac{-L_d}{L_q} p i_{d0} - \Phi_f \frac{p}{L_q}, \quad a_{24} = 0, \quad a_{31} = \frac{3p}{2J_m}(L_d - L_q)i_{q0},
$$

$$
a_{32} = \frac{3p}{2I_m}\left(\Phi_f + (L_d - L_q)i_{d0}\right), \quad a_{33} = \frac{-2s_1\rho\Omega_0 D^5}{4\pi^2 I_m} - \frac{-s_2\rho D^4(1-w)V_0}{2\pi I_m},
$$

$$
a_{43} = \frac{(1-t)(1-w)r_2\rho D^3 V_0}{2\pi m} + \frac{2(1-t)r_1\rho\Omega_0 D^4}{4\pi^2 m}, \quad a_{34} = \frac{-s_1\rho\Omega_0 D^4(1-w)}{2\pi I_m}
$$

$$
a_{44} = \frac{(1-t)(1-w)r_2\rho D^3\Omega_0}{2\pi m} - \frac{2aV_0}{m}, \quad a_{42} = 0, \quad a_{41} = 0
$$

The nominal operating point is: $x_0 = (i_{d0}, \quad i_{q0}, \quad \Omega_0, \quad V_0) = (200\,\text{A}, \quad 530\,\text{A}, \quad 9.2\,\text{m/s}, \quad 5\,\text{m/s})$

5   Synthesis of the Model Basis

The matrices of the model show that it admits uncertain parameters such as the resistance of the stator phases R, which varies according to the temperature of the sea water and the speed of rotation in the rotor. To simplify the modeling of this system, we propose to approximate it by the generic modeling approach (Karmani et al. 2013).

To determine the basis of the models of this system, it is proposed to determine the two extreme models M_1 and M_2 respectively corresponding to the extreme values of the resistance of the stator phases. The characteristic matrices of these two models are shown below (Dhaoui et al. 2015).

Model M_1:Model $M2$:

$$
A_1 = \begin{bmatrix} a'_{11} & a_{12} & a_{13} & a_{14} \\ a_{21} & a'_{22} & a_{23} & a_{24} \\ a_{31} & a_{32} & a_{33} & a_{34} \\ a_{41} & a_{42} & a_{43} & a_{44} \end{bmatrix}, B_1 = B, C_1 = C, A_2 = \begin{bmatrix} a''_{11} & a_{12} & a_{13} & a_{14} \\ a_{21} & a''_{22} & a_{23} & a_{24} \\ a_{31} & a_{32} & a_{33} & a_{34} \\ a_{41} & a_{42} & a_{43} & a_{44} \end{bmatrix}, B_2 = B, C_2 = C
$$

with : $a'_{11} = \frac{-R\text{max}}{L_d}, a'_{22} = \frac{-R\text{max}}{L_q}$, with: $a'_{11} = \frac{-R\text{min}}{L_d}, a'_{22} = \frac{-R\text{min}}{L_q}$.

In addition, we propose to use an average model M_3 which corresponds to the mean value of the resistance of the stator phases

$$A_3 = \frac{A_1 + A_2}{2}, \quad B_3 = \frac{B_1 + B_2}{2} = B, \quad C_3 = \frac{C_1 + C_2}{2} = C$$

Modèle M_3 :

$$A_3 = \begin{bmatrix} a_{11}''' & a_{12} & a_{13} & a_{14} \\ a_{21} & a_{22}''' & a_{23} & a_{24} \\ a_{31} & a_{32} & a_{33} & a_{34} \\ a_{41} & a_{42} & a_{43} & a_{44} \end{bmatrix} \quad \text{with:} a_{11}''' = \frac{-(R\min + R\max)}{2L_d}, \quad a_{11}''' = \frac{-(R\min + R\max)}{2L_q}$$

Finally, the library or the base of the models of our system is constituted by the three models M_1, M_2 and M_3 defined above.

6 Application of the Multimodel Control to the Ship Electric Propulsion System

6.1 Calculation of Validities

The multimodel design of a complex system is deduced from all the models constituting the basis. Each of these models represents the process with a certain degree of relevance that varies over time (Karmani et al. 2013). It is therefore essential to quantify this degree of relevance, called validity, of each model to construct the global model (Dallagi 2013). Thus, the validity coefficients of the models of the database are estimated online, during the evolution of the process according to the residuals (Khaldi 2004).

$$r_i(t) = \frac{\|x(t) - x_i(t)\|}{\sum_{j=1}^{n} \|x(t) - x_j(t)\|}; \forall i = 1, \ldots, n \tag{24}$$

$$r_i(t) = \frac{\|y(t) - y_i(t)\|}{\sum_{j=1}^{n} \|y(t) - y_j(t)\|}; \forall i = 1, \ldots, n \tag{25}$$

Then the validity, which must be inversely proportional to the residue, can be calculated according to the relation

$$v_i = \frac{1 - r_i}{\sum_{j=1}^{3} (1 - r_j)}; \forall i = 1, 2, 3 \tag{26}$$

And consequently, the normalization of reinforced validities $v_i^{renf}(t)$ leads to such that the validity expression:

$$v_i^{norm}(t) = \frac{v_i^{renf}(t)}{\sum_{j=1}^n v_j^{renf}(t)}; \forall i = 1, 2, 3 \tag{27}$$

$v_i(t)$ and the residue $r_i(t)$ of the model *(Mi)* verify the property of the convex $\sum_{i=1}^n v_i(t) = 1$ and. $\sum_{i=1}^n r_i(t) = 1$.

In some cases, the 'bad' models, whose validity is weak, undermine the multimodel representation of the process. It is therefore necessary to use enhanced validity to favor the 'good' models, whose validity is strong, to the detriment of the 'bad'. Enhanced validity is defined at each moment by

$$v_i^{renf}(t) = v_i(t) \prod_{j=1, j \neq i}^n (1 - v_i(t)) \; \forall i = 1, 2, 3 \tag{28}$$

And consequently, the normalization of reinforced validities $v_i^{renf}(t)$ leads to the expression:

$$v_i^{norm}(t) = \frac{v_i^{renf}(t)}{\sum_{j=1}^n v_j^{renf}(t)}; \forall i = 1, \ldots, n \text{ Such as } \sum_{i=1}^n v_i^{norm}(t) = 1 \tag{29}$$

6.2 Feedback Control

This control strategy consists in imposing a desired dynamic behavior by means of appropriate state returns and without the use of regulators. The advantage of this type of control is therefore to avoid the risk of introducing new modes in the looped system. The law of feedback control is defined by (Dallagi and Sabri 2015).

$$u_i(t) = -K_i x(t) + F_i u_{ref}(t) \; \forall i = 1, \ldots, n, \tag{30}$$

where: K_i and $u_{ref}(t)$ are respectively the state feedback gain vector and the con-sign. The state feedback control condition is to calculate the gain K_i of the matrix by a pole placement such that the Eigen values of the matrix $(A_i\text{-}B_i\,K_i)$ are placed in prefixed positions. For multimodel systems the control law is given by:

$$u(t) = - \sum_{j=1}^n v_j^{norm}(t) K_j x(t) \quad \forall j = 1, \ldots, n \tag{31}$$

Therefore, in free mode, the global command can be written as follows:
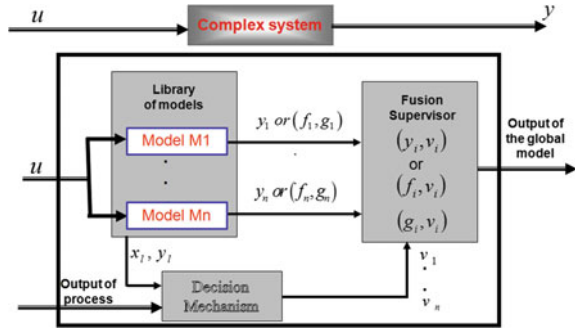
$$u(t) = - \sum_{j=1}^{n} v_j(t) \, K_j x(t) \; \forall j = 1, \ldots, n \tag{32}$$

The ordering gains of the generic models are given by k_1, k_2 and k_3
These gains are subsequently merged to determine the overall gain

$$k = \sum_{i=1}^{3} v_i^{norm} k_i \tag{33}$$

Consequently, the multimodel system equipped with this multimodel control becomes

$$\begin{cases} \dot{x}(t) = \sum_{i=1}^{n} \sum_{j=1}^{n} v_i(t) \, v_j(t) \left(A_i - B_i K_j \right) x(t) \; \forall i, j = 1, \ldots, n \\ y_i(t) = \sum_{i=1}^{n} v_i(t) \, C_i x(t) \end{cases} \tag{34}$$

The application of this type of control requires that each of the models be controllable. By definition, a model (M_i) defined by the pair (A_i, B_i) is said to be controllable if it is possible, by acting only on the input, and in a finite time x_{fi}, to reach a given final state from an initial state x_{0i}.

Verification of controllability requires testing if the matrix $\zeta(A_i, B_i)$ is of full rank.

$$\zeta_{(A_i, B_i)} = \begin{pmatrix} B_i & A_i B_i & \ldots & A_i^{n-1} B_i \end{pmatrix} \forall i = 1, \ldots, n \tag{34}$$

6.3 Calculation of the Matrix F

The state equations and output under static conditions are written
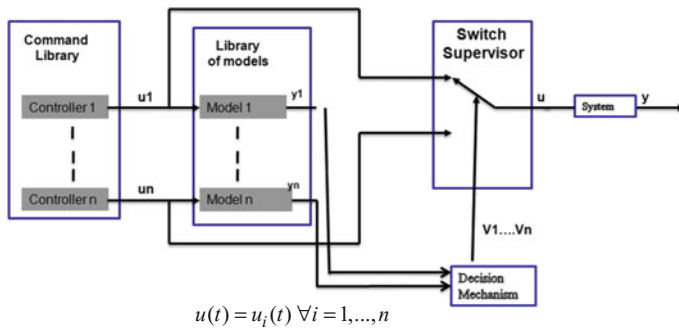
Fig. 7 Switching control strategies

$$\begin{cases} 0 = (A_i - B_i K_i)\, x_i(t) + B_i\, F_i\, u_{ref}(t) \\ y_i(t) = C_i\, x_i(t) \end{cases} \tag{35}$$

$$\begin{cases} x_i(t) = (A_i - B_i K_i)^{-1} B_i\, F_i\, u_{ref}(t) \\ y_i(t) = C_i\, (A_i - B_i K_i)^{-1} B_i\, F_i\, u_{ref}(t) \end{cases} \tag{36}$$

Consequently one obtains

$$F_i = -\left[C_i (A_i - B_i K_i)^{-1}\, B_i\, \right]^{-1} \tag{35}$$

6.4 Control by the Multimodel Approach

Figure 6 gives a multimodel representation of the complex systems and Fig. 7 shows the switching control strategies.

7 Results and Interpretations

The study of the availability of the proposed control law is considered in this section and applied to the electric propulsion system characterized by the parameters: $r_1 = 0.5$, $r_2 = -1.1$, $s_1 = 0.075$, $s_2 = -0.1375$, $t = 0.178$, $w = 0.2304$, $\rho = 1025$ kg/m^3, $D = 4$ m, $m = 20690000$ kg, $a = 4.70010^3$, $Rs = 0.0148$, $Ld = 0.0060$, $Lq = 0.0059$, $p = 4$, $S = 5MVA$, $U = 4.160$ kV. $\Delta Rs = 10\%$.

The performances of the proposed strategy control law are depicted in the Figs. 8–11. The ship speed is needed to reach the reference speed value $V_{ref} = 5$

Fig. 8 Ship speed evolution

Ship speed
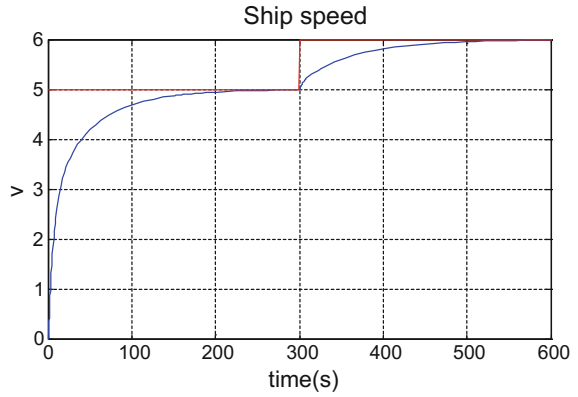
Fig. 9 Current i_d evolution
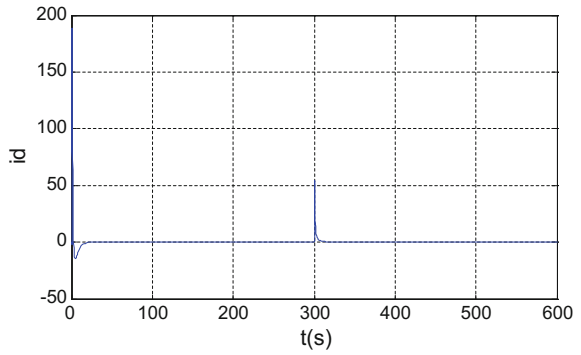
Fig. 10 Motor speed evolution

Motor speed
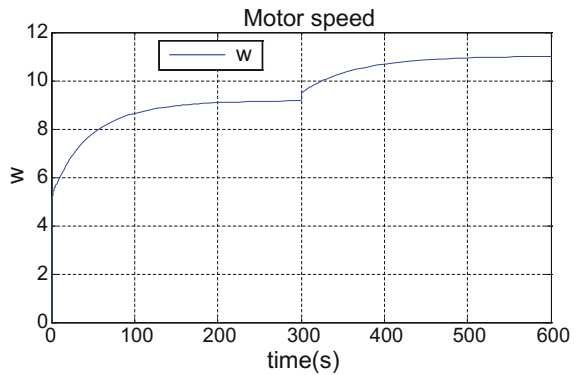
Fig. 11 Current i_q evolution
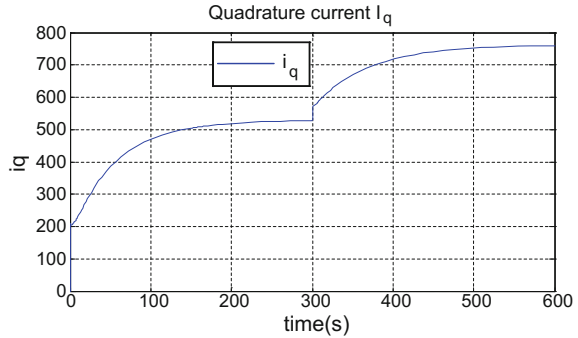
m/s in the interval [0 300 s] and $V_{ref} = 6$ m/s in the interval [300 600 s]. It appears from Fig. 8, that the proposed control law allows a convergence towards the desired value of the ship speed v. Furthermore, if we impose $i_{dref} = 0$, then the electromagnetic torque becomes proportional to component of statoric current iq. In order to control the motor speed, on acts the statoric current component iq, i.e., on the developed torque by controlling the voltage component v_q. It appears from the curves Fig. 8 that the proposed control law allows a rapid convergence towards the component of the ship speed.

8   Conclusion

The work presented in this paper has focused on modeling and multimodel control of ship electric propulsion system. More specifically, it is a question of modeling the propulsion system consisting of a ship and its propulsion system based on a permanent magnet synchronous motor. The system obtained is multivariable, strongly nonlinear and with uncertain parameters. In order to overcome this problem, the multimodel approach has been applied to the studied process, taking into account the parametric variations arising on the stator resistors. In this sense, three generic models have been developed (two generic models and an average model) forming the basis of the models. A multimodel control law by state feedback has been developed in order to ensure a good continuation of the ship speed and the motor speed. By means of a numerical simulation study of the studied system equipped with the elaborate multimodel control, it is clear that the controlled variables converge rapidly and from the beginning of the transient regime towards their references. Moreover, this control approach has proved to be robust with respect to parametric variations and has shown good performances in controlling the ship speed and the motor on the one hand and the stator current on the other.

References

Babu SA (2011) Direct torque control of permanent magnet synchronous motor. Int J Sci Eng Res 2(10)

Dallagi H (2013) Systems fault detection of nonlinear systems multi model structure: application to a Ship Propulsion System. In: 5th International congress conception design and modeling of mechanical, Djerba – Tunisia, pp 25– 27

Dallagi H, Nejim S (2015) Sliding mode control of ship electric propulsion system. In: 12th International multi-conference on systems, signals & devices, Mahdia, Tunisia, pp 16–19

Dallagi H, Sabri B (2015) State feedback control of ship electric populsion system In: 6th International congress on design and modeling of mechanical systems CMSM 2015, Hammamet, Tunisia, pp 23–25

Dhaoui M, kam M, Sbita L (2015) Multimodel control and fuzzy optimization of an induction motor, Int J Artif Intell Appl (IJAIA), 4(1)

Gao R, O'Dwyer (2002) A multiple model networks for non-linear modelling and control. In: proceedings of the 3rd Wismar symposium on automatic control, Wismar, Germany

Guo Y, Zheng H-Y, Wang B-L, Shen A-D (2005) Design of ship electric propulsion simulation system. In: Proceedings of the 4th international conference on machine learning and cybernetics, Guangzhou, pp 18–21

Karmani N-T, Soudani D, Naceur M, Benrejeb M (2013) On an internal multimodel control for nonlinear multivariable systems-a comparative study. Int J Adv Comp Sci Appl (IJACSA) 4 (7):66–71

Khaldi Z-K (2004) Sur la modélisation et la commande multimodèle des processus complexes et/ ou incertain. These

Strategy of Image Capture and Its Impact on Correspondence Error in Reconstructed 3D-Images-Based Point

Jezia Yousfi, Samir Lahouar and Abdelmajid Ben Amara

Abstract The metric distance error between the calculated point and the real point in 3D measurement coordinate system is due to optimization methods carried out in 2D image plane. Euclidian image-based 3D reconstruction is carried out in three major steps, geometric primitive extraction, correspondence, and triangulation. Extraction and triangulation are purely geometric tasks but the correspondence step is a challenge in precision. In this paper, we study 3D object reconstruction based on a set of 2D images. We used a robot arm to move accurately the camera and we study the influence of the motion. It has been demonstrated that the impact of a correspondence error on the reconstruction accuracy of a 3D images-based reconstructed point may vary depending on the image capture strategy. Two modes of motion have been adopted. The first is an axial mode making the camera close or far from the object acting like a zoom. The second mode is lateral where the camera moves parallel to the object. It has been shown that axial mode leads to greater errors compared to the lateral mode. The impact of the geometric parameters of photographing on images-based 3D reconstruction error is also discussed.

Keywords Images-based 3D reconstruction · Camera calibration
Images correspondence · Primitive extraction

J. Yousfi (✉)
LGM, ISET Kairouan, University Campus Raccada, 3191 Kairouan, Tunisia
e-mail: yousfi.jezia@yahoo.fr

S. Lahouar · A. Ben Amara
LGM, ENIM, University of Monastir, Avenue Ibn EL Jazzar, 5019 Monastir, Tunisia
e-mail: samirlahouar@gmail.com

A. Ben Amara
e-mail: benamara.enim@gmail.com

1   Introduction

Cameras have become ubiquitous and cheaper, which made the process of 3D reconstruction based on images more and more interesting. Image-based 3D reconstruction is widely used in several domains such as; computer vision, virtual reality, robotics (Nefti-Meziani and Manzoorb 2015) quality control in mechanical manufacturing, civil infrastructure (Fathi et al. 2015), biomedicine, architecture/ archaeology, and security systems.

To understand the process of 3D reconstruction from images it is important to first understand the process of image formation. When a 3D scene is photographed by a camera, the projection is made on a 2D image, so the third coordinate or the depth of the primitives of this scene is lost. The fact of going back to this parameter from images is a challenging problem in terms of precision because the image formation process is not invertible (Robertson and Cipolla 2009). The process of image-based 3D reconstruction starts with capturing images from the scene to be reconstructed. Then the primitives of two or more images will be extracted and matched. In this study we showed that the positions of the camera when taking images has an influence on the impact of the unavoidable correspondence errors on the precision of the 3D reconstructed images-based point. By adopting a pinhole projection model, it has been shown that in the phase of correspondence between two points of two images, a correspondence error does not have the same impact on the position of the 3D point to be reconstructed. To study the relationship between the image pickup position and the impact of the correspondence error on a reconstructed 3D point, a camera mounted to a controlled robot arm was used. Images taken are used to calibrate the camera. From the result of the camera calibration program we extract the extrinsic parameters of the camera during the images photographing task.

From these results we compute the translation vector of a capture position from an image to the next one; this parameter is compared to the practical one, computed from the robot coordinate system. The results are then discussed. Figure 1 shows the procedure described below.
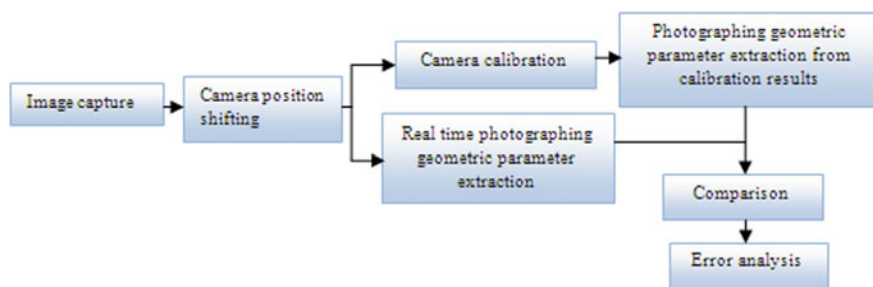
Fig. 1 Procedure steps chronology

2   Adopted Projection Camera Model

The projection model adopted is the perspective or pinhole one. Figure 2 illustrates the projection geometry of the pinhole model of a 3D world coordinate point M(X, Y, Z). An image point m can be located in a metric (x, y) or pixellic (u, v) coordinates. Point C is the projection center, and physically, is the lens center. The image point is the intersection of the projection ray (MC) and the image plane. The center of the metric coordinate system (x, y) is the intersection of the image plan and the optical axis, and the center of the pixellic coordinate system corresponds to the left up or dawn corner image point.

For a perspective camera model, the relationship between the coordinate of the lens center C(X, Y, Z) and an image point m(x, y) rises from the properties of the perspective projection.

$$\frac{Xc}{x} = \frac{Yc}{y} = \frac{Zc}{f} \tag{1}$$

$$\begin{pmatrix} x \\ y \\ 1 \end{pmatrix} = \begin{pmatrix} f & 0 & 0 \\ 0 & f & 0 \\ 0 & 0 & 1 \end{pmatrix} \cdot \begin{pmatrix} \frac{Xc}{Zc} \\ \frac{Yc}{Zc} \\ 1 \end{pmatrix} \tag{2}$$

This can be expressed in homogenous coordinate system as

$$\begin{pmatrix} x \\ y \\ 1 \end{pmatrix} = \begin{pmatrix} f & 0 & 0 & 0 \\ 0 & f & 0 & 0 \\ 0 & 0 & 1 & 0 \end{pmatrix} \cdot \begin{pmatrix} Xc \\ Yc \\ Zc \\ 1 \end{pmatrix} \tag{3}$$

Fig. 2 Geometric pinhole projection model
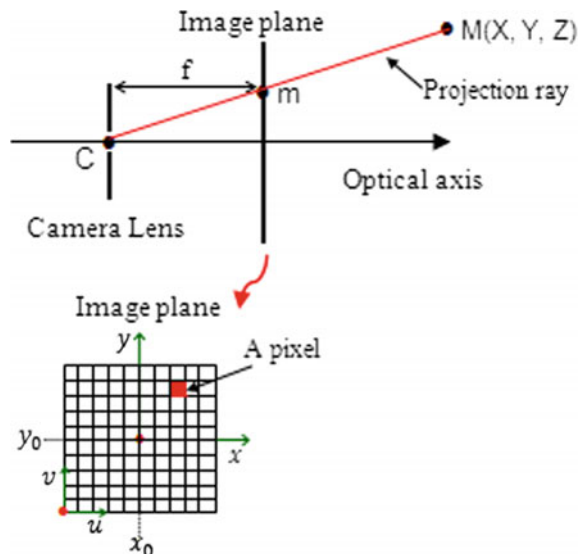
The relationship between metric and pixellic coordinates of a point m of the image is expressed as following:

$$
\begin{pmatrix} u \\ v \\ 1 \end{pmatrix} = \begin{pmatrix} k_u & 0 & 0 \\ 0 & k_v & 0 \\ 0 & 0 & 1 \end{pmatrix} \cdot \begin{pmatrix} 1 & 0 & x_0 \\ 0 & 1 & y_0 \\ 0 & 0 & 1 \end{pmatrix} \begin{pmatrix} x \\ y \\ 1 \end{pmatrix},
\tag{4}
$$

where k_u and k_v are x and y pixels density respectively. Parameters x_0 and y_0 are the metric coordinates of the image center.

Then

$$
\begin{pmatrix} u \\ v \\ 1 \end{pmatrix} = \begin{pmatrix} f.k_u & 0 & k_u.x_0 & 0 \\ 0 & f.k_v & k_v.y_0 & 0 \\ 0 & 0 & 1 & 0 \end{pmatrix} \cdot \begin{pmatrix} X_C \\ Y_C \\ Z_C \\ 1 \end{pmatrix},
\tag{5}
$$

where f the focal distance of the camera. A rigid transformation can convert a word point M(X, Y, Z) to the center of projection $C(X_C, Y_C, Z_C)$ by a couple of translation vector t and a rotation (three by three) matrix R. So the expression of the relation between M and C coordinates is as follows:

$$
\begin{pmatrix} X_C \\ Y_C \\ Z_C \\ 1 \end{pmatrix} = \begin{pmatrix} R & -R.t \\ 0 & 1 \end{pmatrix} \cdot \begin{pmatrix} X \\ Y \\ Z \\ 1 \end{pmatrix}
\tag{6}
$$

$$
\begin{pmatrix} u \\ v \\ 1 \end{pmatrix} = \underbrace{\begin{pmatrix} f.k_u & 0 & k_u.x_0 & 0 \\ 0 & f.k_v & k_v.y_0 & 0 \\ 0 & 0 & 1 & 0 \end{pmatrix}}_{MI} \cdot \underbrace{\begin{pmatrix} R & -R.t \\ 0 & 1 \end{pmatrix}}_{ME} \cdot \begin{pmatrix} X \\ Y \\ Z \\ 1 \end{pmatrix}
\tag{7}
$$

MI is the intrinsic projection matrix and ME in the extrinsic one.

$$
\begin{pmatrix} u \\ v \\ 1 \end{pmatrix} = \underbrace{\begin{pmatrix} P11 & P12 & P13 & P14 \\ P21 & P22 & P23 & P24 \\ P31 & P32 & P33 & P34 \end{pmatrix}}_{P} \times \underbrace{\begin{pmatrix} X \\ Y \\ Z \\ 1 \end{pmatrix}}_{M}
\tag{8}
$$

P is the projection matrix of the point M.

3 Camera Calibration

The goal of the camera calibration is to estimate the internal parameters of the camera and the geometric relations between the camera and the scene (Weng et al. 1992; Chen et al. 2014; Xue et al. 2007). In camera calibration, the intrinsic and extrinsic parameters are obtained by using a number of points having known coordinates in the coordinate system of the world and the image. Zhang (2000) proposed a flexible technique for camera calibration when a calibration target with a precisely manufactured pattern is involved. Zhang's calibration algorithm uses the extracted corner points of the checkerboard pattern to compute a projective transformation between the image points of the n different images, up to a scale factor. Zhang's method has been implemented by Jean-Yves Bouguet in MATLAB and C++ in Intel OpcnCV library. In this work we used Zhang's camera calibration technique. The calibration target is a flat plate with fixed size black and white grids (Fig. 3).

4 Robot System Used and Experimental Results

Experimental tests are performed in the laboratory LGM ENIM. The camera is attached to a robot arm (Fig. 4) of the type "RV-1A", a compact robot developed by Mitsubishi. The robot system have a vertical multi-joint structure and it comprises five different lengths articulated arms, a wrist (72 mm), a fore arm (160 mm), an elbow block (90 mm), an upper arm (250 mm), and shoulder. It guarantees six degrees of freedom with different operating range, J1 (from –150 degrees to +150 degrees), J2 (from –60 degrees to +120 degrees), J3 (from +60 degrees to +155 degrees), J4 (from –160 degrees to +160 degrees), J5 (from –90 degrees to +90 degrees) and J6 (from –200 degrees to +200 degrees).

Multiple views of the calibration pattern were captured by the camera mounted on a robot hand; that could provide controlled motions and captured images at various positions. For each position of image taking x, y, and z; coordinates provided by the robot coordinate system are saved. To take images m1, m2, m3, m4, m5, m6, m7, m8 the camera moves along axis x; the images m9, m10, m11, m12,

Fig. 3 The calibration planar check board pattern used during the process of calibration

Fig. 4 Different parts of the used robot system
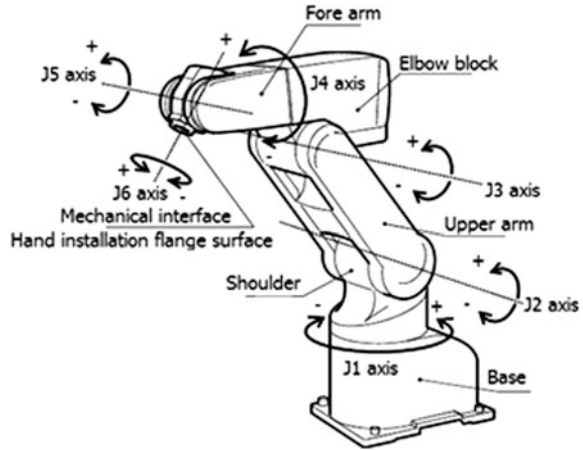
Fig. 5 Extrinsic parameters visualization
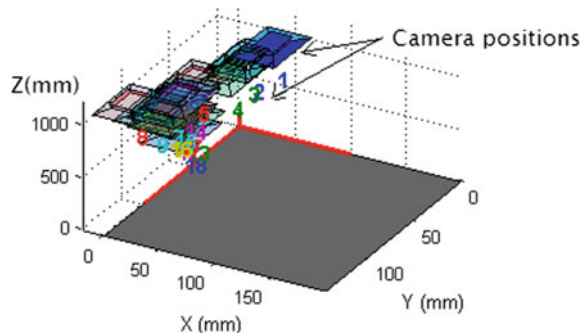
m13 are photographed according to axis y and the images m14, m15, m16, m17, m18 are photographed according to axis z (Fig. 5).

Experimental results are given in Table 1. X (robot) Y (robot) and Z (robot) are the coordinates of the capture positions given by the robot arm system. X (prg) Y (robot) and Z (robot) are the relative positions given by the calibration program. Disp (robot) and disp (prog) are respectively the translation module from an image mi to an image mi + 1 from the robot data and the calibration program. Error is the difference between disp (robot) and disp (prg).

5 Results Analysis

5.1 Experimental Analysis

The difference between the experimental and the theoretical values for images 1–13 did not exceed 1.24 mm. For images from 14 to 18 the difference becomes

Table 1 Experimental results

Images	X (robot)	Y (robot)	Z (robot)	Tx (robot)	Ty (robot)	Tz (robot)	Disp (robot)	Tx (prog)	Ty (prog)	Tz (prog)	Tx (prog)	Ty (prog)	Tz (prog)	Disp (prog)	Error
m1	-60.88	-314.95	502.43			0		-17.63	-16.85	952.17					
m2	-53.67	-314.95	502.43	7.21	0	0	7.21	-24.34	-19.31	951.76	-6.71	-2.46	-0.41	7.16	-0.05
m3	-47.69	-314.95	502.43	5.98	0	0	5.98	-29.61	-20.17	951.74	-5.27	-0.86	-0.02	5.34	-0.64
m4	-37.24	-314.95	502.43	10.45	0	0	10.45	-38.87	-21.05	952.35	-9.26	-0.87	0.60	9.32	-1.13
m5	-28.53	-314.95	502.43	8.71	0	0	8.71	-46.65	-21.61	950.41	-7.78	-0.56	-1.94	8.04	-0.67
m6	-20.07	-314.95	502.43	8.46	0	0	8.46	-54.15	-22.86	950.98	-7.50	-1.24	0.57	7.62	-0.84
m7	-9.86	-314.95	502.43	10.21	0	0	10.21	-63.25	-23.44	951.16	-9.10	-0.58	0.18	9.12	-1.09
m8	-0.9	-314.95	502.43	8.96	0	0	8.96	-71.27	-26.15	947.75	-8.02	-2.71	-3.41	9.13	0.17
m9	-0.9	-304	502.43	0	10.95	0	10.95	-71.48	-36.56	948.12	-0.22	-10.41	0.38	10.42	-0.53
m10	-0.9	-289.56	502.43	0	14.44	0	14.44	-72.11	-51.98	945.34	-0.63	-15.42	-2.79	15.68	1.24
m11	-0.9	-277.62	502.43	0	11.94	0	11.94	-72.41	-63.05	944.31	-0.30	-11.07	-1.02	11.12	-0.82
m12	-0.9	-270.9	502.43	0	6.72	0	6.72	-72.49	-69.37	943.52	-0.08	-6.32	-0.80	6.38	-0.34
m13	-0.9	-261.19	502.43	0	9.71	0	9.71	-72.63	-78.37	942.58	-0.14	-9.00	-0.94	9.05	-0.66
m14	-0.9	-261.19	560.67	0	0	58.24	58.24	-72.20	-78.75	1074.89	0.42	-0.38	132.31	132.31	74.07
m15	-0.9	-261.19	542.25	0	0	-18.42	18.42	-72.84	-79.46	1032.17	-0.64	-0.71	-42.72	42.73	24.31
m16	-0.9	-261.19	527.07	0	0	-15.18	15.18	-73.19	-79.75	997.28	-0.35	-0.29	-34.89	34.89	19.71
m17	-0.9	-261.19	519.11	0	0	-7.96	7.96	-73.39	-79.94	978.77	-0.19	-0.19	-18.51	18.51	10.55
m18	-0.9	-261.19	460.86	0	0	-58.25	58.25	-74.10	-80.20	845.43	-0.72	-0.26	-133.34	133.34	75.09

important, and attends 75 mm. When images were taken in positions corresponding
to a varying z coordinate the error becomes more important. In fact for images 14,
15, 16, 17, and 18 the photographing procedure is called axial model, we speak
about this model for a camera zooming or a camera moving in parallel to its optic
axis, i.e., for a camera attached to a robot arm or for a camera moving on a railway.
The curve of Fig. 6 represents the module of the translation vector extracted from
the calibration program and from the robot system.

Figure 7 shows that when the camera moves axially with respect to the scene,
the difference between the measurements given by the calibration program and the
robot system (Error) is proportional to the difference ΔZ.
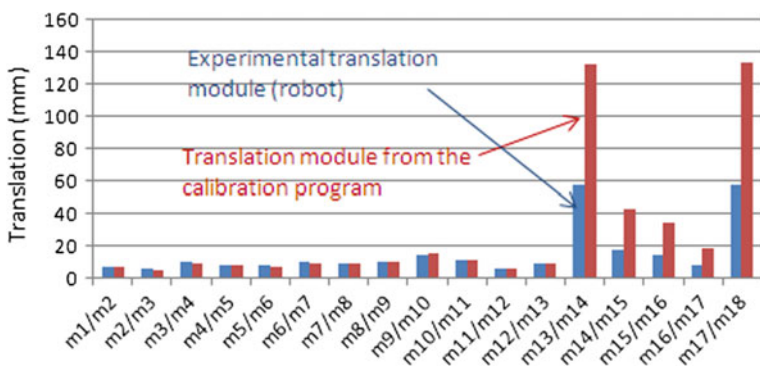
Fig. 6 Robot experimental translation module and translation module from calibration program

Fig. 7 Variation of ΔT with the variation of the displacement ΔZ of the camera
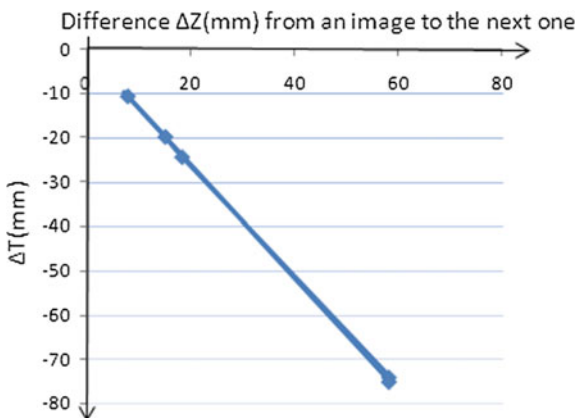
5.2   Analytical Analysis

An analytical study is carried out to deal with the relationship between the strategy of motion of the camera from one image to another and the influence of the error of correspondence on the point reconstructed from two images. The axial and lateral movements are studied. The analytic expressions of the position of a reconstructed point are given as a function of the geometric parameters of the problem. The variation of the position of the reconstructed point is shown for each type of motion. Figure 8 gives a geometrical representation of a point reconstructed from two image points taken by an axial movement (a) and a lateral movement (b). The figure also shows the point Mr. reconstructed in the presence of an error of correspondence.

When the correspondence between the two image points m_1 and m_2 is made with an error on the y coordinate of the point m_1 the coordinates Y and Z of the reconstructed 3D points are written as follows:

$$\text{For axial moving camera:} \begin{cases} \frac{z+f}{f} = \frac{y}{y_1} \\ \frac{z+f-d}{f} = \frac{y}{y_2} \end{cases} \rightarrow \begin{cases} y = \frac{d}{f}\left(\frac{(y_1+\delta y)y_2}{y_2-(y_1+\delta y)}\right) \\ z = \frac{d.y_2}{y_2-(y_1+\delta y)} - f \end{cases} \quad (9)$$

$$\text{For lateral moving camera:} \begin{cases} \frac{z+f}{f} = \frac{y}{y_2} \\ \frac{z+f}{f} = \frac{y-d}{y_1} \end{cases} \rightarrow \begin{cases} y = \frac{d.y_2}{y_2-(y_1+\delta y)} \\ z = \frac{df}{y_2-(y_1+\delta y)} - f \end{cases} \quad (10)$$

To study the influence of the error of correspondence on the precision of the position of the reconstructed 3D point based on images; the error is varied up to 1 mm.
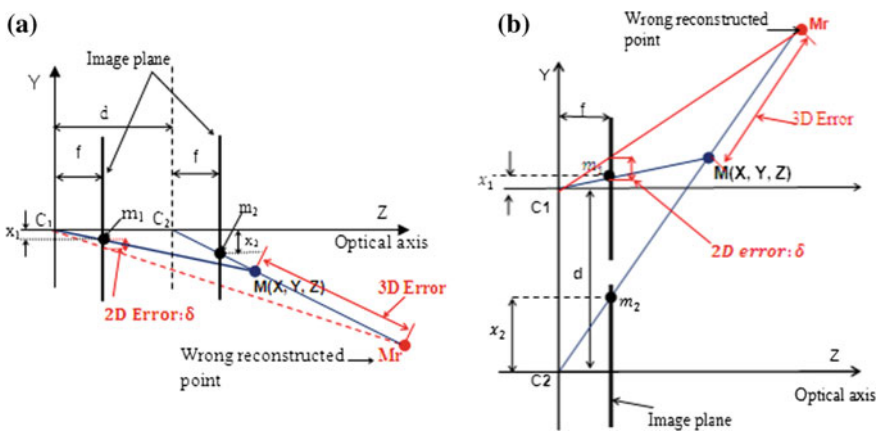
Fig. 8 Geometric explanation of the impact of the correspondence error on the translation vector of the camera in axial (**a**) and lateral (**b**) image capture

Figure 9a shows the variation in the position of the reconstructed point from the images of the points M (500, 500) for an error of correspondence between the two image points going to 1 mm. Figure 9b shows the distance between some points and the reconstructed ones for an error of 0.3 mm.

The curves of Fig. 10 show that for a camera in axial movement and for a reconstruction error of 0.3 mm; the reconstruction error for points at different positions on a straight line Y = Z is larger than those for points on a straight line Y = Z (Figs. 11, 12, 13).

A comparison between the results of a camera in lateral and axial motion was carried out. And it has been observed that the difference is remarkable for the reconstruction of a point lying on a straight line Y = cte, i.e., for points that are farther and farther from the camera along its optical axis, which matches the experimental results.

The curve in the figure shows that the distance between the two image pick-ups also has an influence on the reconstruction error of a point.
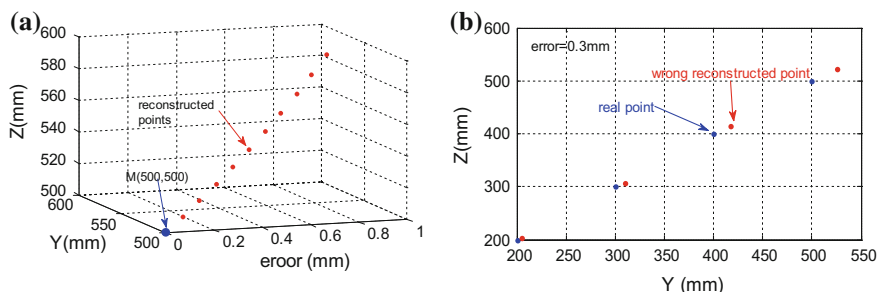
Fig. 9 Reconstructed points as a function of the correspondence error for an axial camera moving
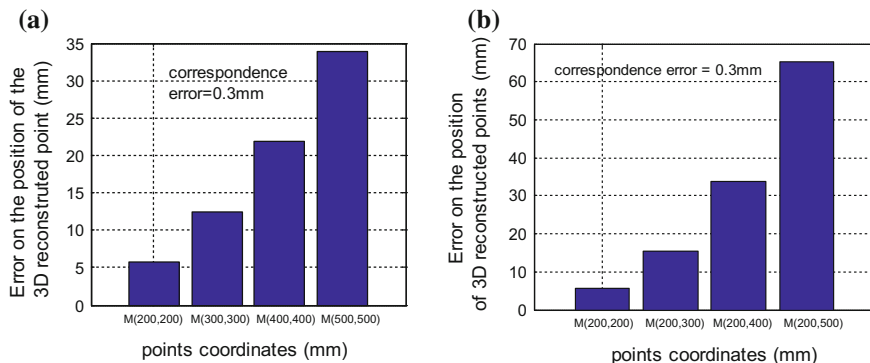
Fig. 10 Error on the position of the 3D reconstructed point for points at positions Y = Z (**a**) and points on a line Y = constant (200) (**b**) for a camera in axial motion
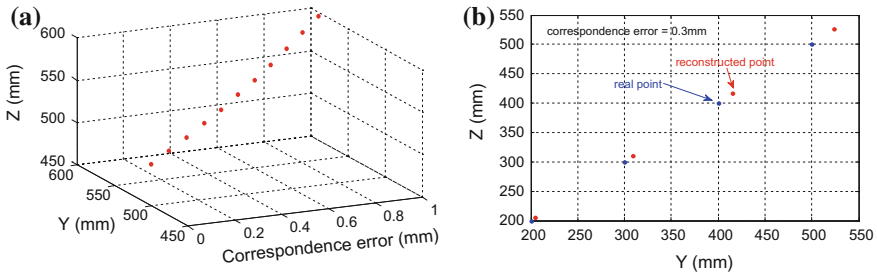
Fig. 11 Reconstructed points as a function of the correspondence error for an lateral moving camera
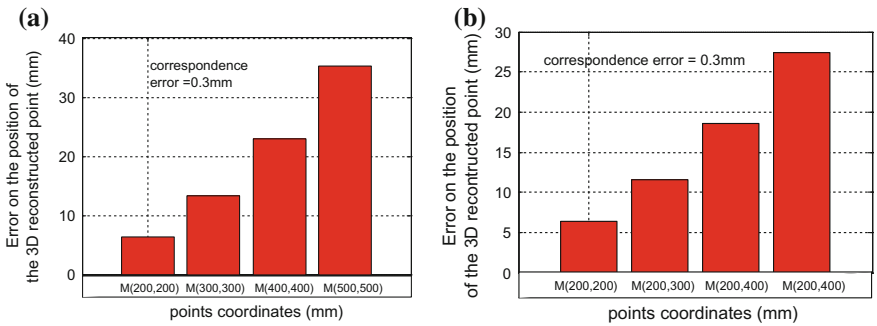
Fig. 12 Error on the position of the 3D reconstructed point for points at positions Y = Z (**a**) and points on a line Y = constant (200) (**b**) for a camera in lateral motion
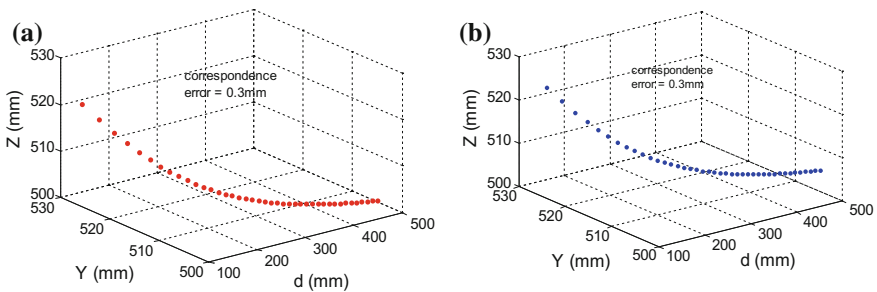
Fig. 13 Influence of the distance d between the two optical centers on the reconstruction error of a point for a camera in axial movement (**a**) and a camera in lateral movement (**b**)

6   Conclusion

Correspondence error has a great influence on the position of the reconstructed 3D point. The experimental results showed that the capture of images in axial mode leads to an inflation of the impact of the error of correspondence on the error of the position of the reconstructed 3D point. Knowing that the translation vector is used for the calculation of the projection matrix of a camera, this can induce a serious error on the position of the reconstructed 3D point. As experimental results, the analytical studies have also shown that in axial or lateral mode of motion the impact of the error of correspondence on the position of the reconstructed point is important. It has been shown that in axial or lateral mode as the distance between the two imaging poses increases; the error on the 3D images-based reconstructed point decreases.

References

Chen Z, Liao H, Zhang X (2014) Telecentric stereo micro-vision system: Calibration method and experiments. Opt Lasers Eng 57:82–92

Fathi H, Dai F, Lourakis M (2015) Automated as-built 3D reconstruction of civil infrastructure using computer vision: achievements, opportunities, and challenge. Adv Eng Inform 29:149–161

Nefti-Meziani S, Manzoorb U (2015) 3D perception from binocular vision for a low cost huma noid robot NAO. Robot Auton Syst 68:129–139

Robertson D, Cipolla R (2009) Structure from motion, in: practical image processing and computer vision, Wiley

Xue T, Wu B, Zhu JG, Ye SH (2007) Complete calibration of a struct uniform stereovision sens free-pos planar pattern Sens Actuators A 135:185–191

Zhang Z (2000) A Flexible New Technique for Camera Calibration. IEEE Trans Pattern Anal Mach Intell 22(11):1330–1334

Analytical and Numerical Approach for the Dynamic Behavior of a Beam Under a Moving Load

Mouldi Sbaiti, Khemais Hamrouni, Abdessattar Aloui and Mohammed Haddar

Abstract The dynamic behavior of structures subjected to moving loads has aroused particular interest in the field of mechanics. In this field, theoretical studies were presented by several researchers to estimate the dynamic responses of these structures. The moving loads on the beams cause deformations. These deformations must remain in the elastic domain in order to allow the beam to fulfill its role. For this purpose, the determination of the beam deformations of the beam under a moving load is imperative. The main objective of this work is to study the deflection of simply supported beams under moving loads. Analytical and numerical models have been developed to describe the behavior of an elastic IPE200 beam. In the analytical and numerical methods, the principle consists in formulating the dynamic equations of motion. This method allowed us to determine the deflection of the beam subjected to a moving load. The results obtained by the two methods are compared.

Keywords Beam · Deflection · Moving load · Analytical model Numerical method · Dynamic behavior

M. Sbaiti (✉) · K. Hamrouni · A. Aloui · M. Haddar
Laboratory of Mechanic, Modelisation and Production (LA2MP), ENIS, Sfax, Tunisia
e-mail: mouldi.lammp@gmail.com

K. Hamrouni
e-mail: khemais.hamrouni@gmail.com

A. Aloui
e-mail: abdessattar.aloui@issatgb.rnu.tn

M. Haddar
e-mail: mohamed.haddar@enis.rnu.tn

M. Sbaiti · K. Hamrouni · A. Aloui
High Institute of Applied Sciences and Technology Gabes, Gabes, Tunisia

M. Haddar
National School of Engineering of Sfax, University of Sfax, Sfax, Tunisia

127

1   Introduction

The problem of the dynamic behavior of structures subjected to moving loads has always encouraged special interest in the field of civil and mechanical engineering as well as in the field of naval engineering and aeronautics. In all these areas, theoretical studies were presented by various researchers to develop computational methods in order to estimate the dynamic responses of these structures.

The dynamic behavior of beams under moving loads has been investigated by many authors (e.g., Abu Hilal and Zibdeh 2000; Fryba 1999; Oguamanam et al. 1998). Considering the moving load as a force, most studies have given some analytical solutions. Some of them (Cifuentes 1989; Wu et al. 2000; Mohebpour et al. 2016) have studied the subject for constant mass motion using finite element techniques. During the last century, the investigation of the dynamic behavior of beam structures under moving loads has been a topic of interest. The dynamic response under multiple moving loads may be obtained by a direct integration technique coupled with finite element discretization. However, for beam structures, finite element models based on exact dynamic expressions lead to higher precision with only one element per span (Hayashikawa and Watanabe 1981; Wu et al. 2000, Wu 2003). Michaltsos (1996) studied the effects of the dynamic deflection of a simply supported beam including moving mass of constant magnitude and velocity using first approximation series solution. Mehri et al. (2009) presented the linear dynamic response of uniform Euler Bernoulli beams with different boundary conditions excited by a moving load using a dynamic green function and studied the effects of velocity of load and other parameters.

In this paper, computation of dynamic response of beam with numerical and analytical method was carried out by using MATLAB software to see the influence of velocity variations and the position of moving load on dynamic response of beam after which deflection decreases as the velocity increases further.

2   Analytical Method

The beam submitted to a moving load F along the beam at a constant speed v, was simply supported at both ends (Fig. 1).

Fig. 1 A moving load traversing a beam
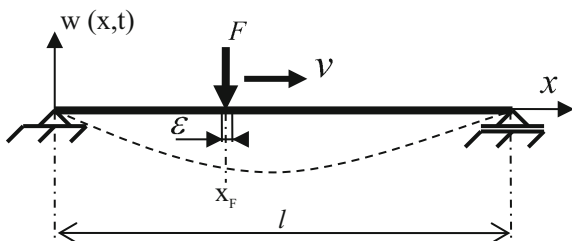
The beam motion equation takes the following form:

$$\frac{\partial^2}{\partial x^2}\left[EI(x)\frac{\partial^4 w\,(x,t)}{\partial x^4}\right]+\rho\,S(x)\frac{\partial^2 w\,(x,t)}{\partial t^2}=p(x,t) \tag{1}$$

The point force with a load distributed over a very small length ε may be modeled through the following system of equations:

$$p\,(x,t)=\begin{cases}\frac{F}{\varepsilon},\,vt\le x\le vt+\varepsilon\\0,\,x\notin[vt,\,vt+\varepsilon]\end{cases},\text{ with }\varepsilon\to 0 \tag{2}$$

The general solution of the dynamic equation of the beam is in the following form:

$$w(x,t)=\sum_{i=1}^{\infty}X_i(x)T_i(t) \tag{3}$$

With $X_i(x)=\sin\frac{i\pi x}{l}$ a function this satisfies the boundary conditions of the beam.

For a constant section $S(x)=S$ and after the separation of variables and based on the orthogonality of the functions $X_i(x)$ we have

$$\frac{\partial^2 T_i(t)}{\partial t^2}+\omega_i^2 T_i(t)=\frac{\int_0^l p(x,t)X_i(x)dx}{\rho S\int_0^l X_i^2(x)dx} \tag{4}$$

The equation becomes

$$\frac{\partial^2 T_i(t)}{\partial t^2}+w_i^2 T_i(t)=\frac{2F}{\rho Sl}\sin\,vt \tag{5}$$

A particular solution of this equation is

$$T_{i0}^*(t)=\frac{2Fl}{\rho S(\omega_i^2 l^2-i^2\pi^2 v^2)}\sin\frac{i\pi}{l}vt \tag{6}$$

Hence, we obtain

$$T_i(t)=a_i\cos\omega_i t+b_i\sin\omega_i t+\frac{2Fl}{\rho S(\omega_i^2 l^2-i^2\pi^2 v^2)}\sin\frac{i\pi}{l}vt \tag{7}$$

To determine the constants a_i and b_i, we assume that at the moment $t=0$, the force is at the point $x=0$, that means

Then, we get

$$\begin{cases}T_i(0)=0\\\frac{\partial T_i}{\partial t}(0)=0\end{cases}\Rightarrow\begin{cases}a_i=0\\b_i=-\frac{2Fl}{\rho S(\omega_i^2 l^2-i^2\pi^2 v^2)}\frac{i\pi}{l\omega_i}\end{cases} \tag{8}$$

A series solution of Eq. (1) in terms of linear normal modes can be found out in
the form

$$w(x,t) = \sum_{i=1}^{\infty} \frac{2Fl}{\rho S(\omega_i^2 l^2 - i^2\pi^2 v^2)} \left(\sin\frac{i\pi}{l}vt - \frac{i\pi v}{l\omega_i}\sin\omega_i t \right) \sin\frac{i\pi x}{l} \qquad (9)$$

To avoid the resonance phenomenon, the speed v must be different to $\frac{l\omega_i}{i\pi}$.

The deflection response for moving load conditions of the beam, obtained by the
theoretical method, is illustrated using the MATLAB code.

2.1 Results and Discussions

To apply the previously developed theoretical results, a beam with a cross-section
of I shape is chosen. This kind of beam is designed to resist maximum bending
moment. The characteristics of the I section beam IPE200 are presented in the
Table 1.

Table 1 Dimensions and properties

	C (mm)	D (mm)	B (mm)	A (mm)	S (mm^2)	Iz (mm^4)
IPE 200	200	100	5.6	8.5	2850	1943
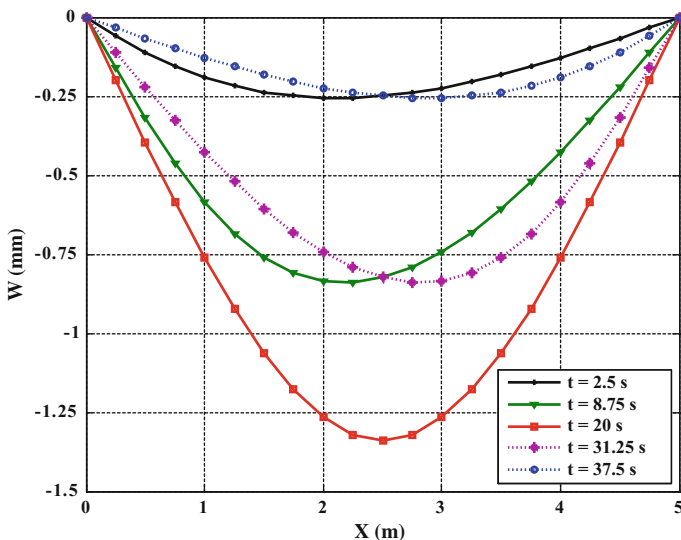
Fig. 2 Dynamic response of beam with different value of times with transverse position of the
beam (F = 2000 N, v = 0.125 m/s)
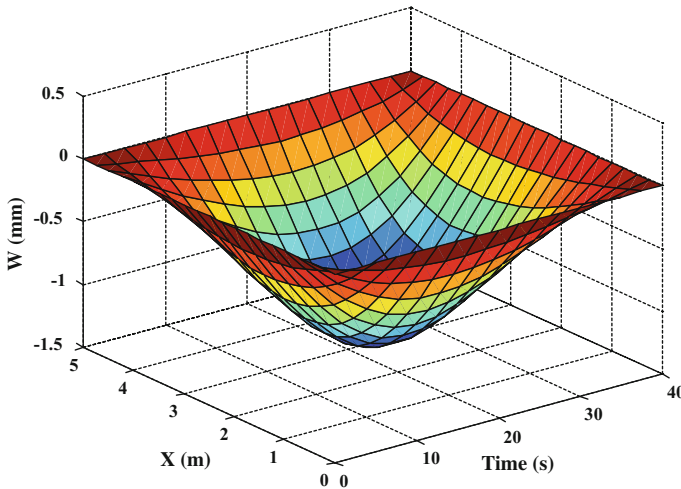
Fig. 3 Mid-span deflection of beam traversed by a moving load (F = 2000 N, v = 0.125 m/s)

An analytical work is applied on the dynamic response of a simply supported beam subjected to moving load. As shown in the Fig. 2, the maximum points of the curves slightly move towards the right end and left with an increasing of the length.

The effect of the time parameters and transverse position on the deflection of the beam was also studied. We find that the farther away from the center of the beam x = 2.5 m, the lower the deflection value is. The middle of the beam corresponds to the position of the maximum deflection (Fig. 3).

3 Numerical Method

To validate the results of the present model, a beam subjected to a moving load is investigated and compared with the analytical result. The force F can be modeled with the Dirac function as follows:

$$F(t) = \int_0^l p(x,t)\delta(x - x_F)dx \tag{10}$$

The solution of the dynamic equation of the beam can be written as

$$w(x,t) = \sum_{i=1}^{\infty} Y_i(x)q_i(t) \tag{11}$$

Using the Lagrange equations

$$\frac{d}{dt}\left(\frac{\partial T}{\partial \dot{q}_i}\right) - \frac{\partial T}{\partial q_i} + \frac{\partial U}{\partial q_i} = \frac{\partial W}{\partial q_i} \tag{12}$$

This can be represented in matrix form

$$[M]\dot{\underline{q}}(t) + [K]\underline{q}(t) = \underline{f}(t) \tag{13}$$

This is an equation of the form

$$[\bar{K}]\underline{q}_t = \bar{F}_t \tag{14}$$

$[\bar{K}] = [b_1 M + K]$: Fictitious stiffness matrix $\bar{F}_t = \underline{f}(t) + [M]\left(b_1\underline{q}_{t-\Delta t} - b_2\dot{\underline{q}}_{t-\Delta t} - b_3\ddot{\underline{q}}_{t-\Delta t}\right)$: Fictional effort.

Newmark iterative schema is used with the increments of time ($t = \Delta t, 2\Delta t, N\Delta t$) for determining the vector $\underline{q}_t = (q_1(t), \ldots, q_i(t), \ldots, q_n(t))$.

3.1 Numerical Results and Discussions

We notice that the shape of the deflection is the same and the maximum of the deflection is located in the middle of the apron for the two positions of the load.
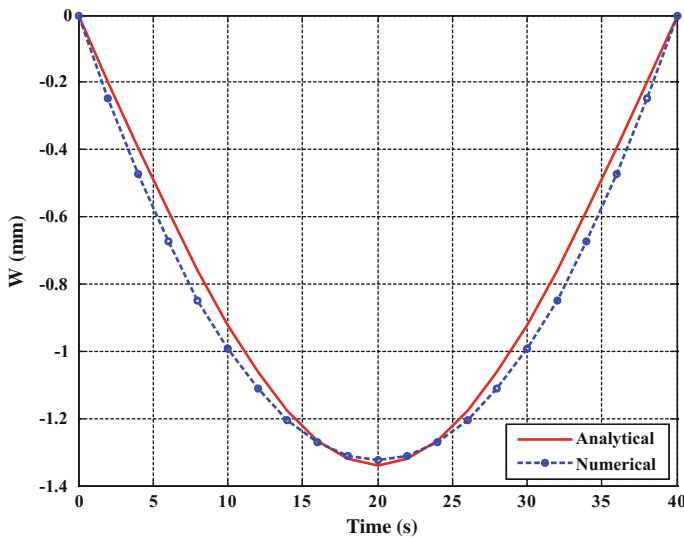
Fig. 4 Comparison between numerical method and analytical model deflection with times and value of moving load (F = 2000 N, v = 0.125 m/s)

Fig. 5 Comparison between numerical method and analytical model deflection with velocity and position of moving load (F = 2000 N, t = 5 s)
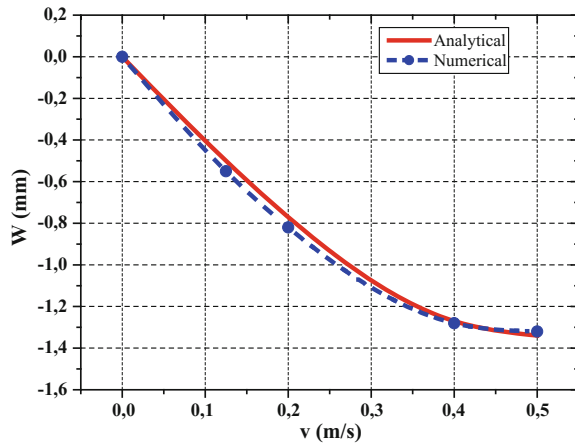
For the mobile load, we notice that the two methods give almost the same value of the maximum deflection of the beam. The maximum deviation is about 2%. A good versatility is seen between the analytical and numerical methods (Fig. 4).

Figure 5 shows the deflection for different values of the velocity. We note that the maximum response is given by the higher velocity, which explains the taking into account of the velocity effect of on the response dynamics of the beam.

4   Conclusion

The contribution of this study relates to the use of an analytical model coupled with a numerical method to study the dynamic response of beam structures under a constant moving load. The beam deflections were obtained with different positions of moving load, time, and velocity. The influence of these parameters was also investigated.

- The influence of variation of parameters, i.e., the position of the moving load and time on the dynamic response was studied. It may be concluded that the position of the maximum deflection of a beam occurs at mid-span.
- The increase of velocity of the moving load increases the dynamic deflection, the maximum deflection starts decreasing with its maximum deflection load position shifting towards the right till it reaches the end of the beam.
- The analytical solutions approximately have the same precision as those provided by the numerical solutions; the maximum deviation is about 2%.

References

Abu Hilal M, Zibdeh HS (2000) Vibration analysis of beams with general boundary conditions traversed by a moving force. J Sound Vib 229(2):377–388

Cifuentes AO (1989) Dynamic response of a beam excited by a moving mass. Finite Elem Anal Des 5:237–246

Fryba L (1999) Vibration solids and structures under moving loads. Thomas Telford House, London

Hayashikawa T, Watanabe N (1981) Dynamic behavior of continuous beams with moving loads. J Eng Mech Div 107(1):229–246

Mehri B, Davar A, Rahmani O (2009) Dynamic greenFunction solution of beams under a moving load with different boundary conditions. ScientiaIranica 16:273–279

Michaltsos G, Sopianopoulos D, Kounadis AN (1996) The effect of moving mass and other parameters on the dynamic responce of a simply supported beam. J Sound Vib 191:357–362

Mohebpour SR, Vaghefi M, Ezzati M (2016) Numerical analysis of an inclined cross-ply laminated composite beam subjected to moving mass with consideration the Coriolis and centrifugal forces. Eur J Mech A/Sol, 59:67–75

Nguyen TP, Pham DT, Hoang PH (2016) A new foundation model for dynamic analysis of beams on nonlinear foundation subjected to a moving mass. Procedia Eng 142:166–173

Oguamanam DCD, Hansen JS, Heppler GR (1998) Dynamic response of an overhead crane system. J Sound Vib 213(5):889–906

Savin E (2001) Dynamic amplification factor and response spectrum for the evaluation of vibrations of beams under successive moving loads. J Sound Vib 248(2):267–288

Wu JJ (2003) Use of equivalent beam models for the dynamic analyses of beam plates under moving force. Comp Str 81:2749–2766

Wu JJ (2008) Transverse and longitudinal vibrations of a frame structure due to a moving trolley and the hoisted object using moving finite element. Int J Mech Sci 50:613–625

Wu JJ, Whittaker AR, Cartmell MP (2000) The use of finite element techniques for calculating the dynamic response of structures to moving loads. Comp Str 78:789–799

CFD Modeling of Wastewater Discharges in a Sewer System

Sonia Ben Hamza, Nejla Mahjoub Saïd, Hervé Bournot and Georges Le Palec

Abstract The malfunctioning of combined sewer systems can lead to an uncontrolled discharge of wastewater into receiving environments causing very serious pollution. The protection of these environments requires a control of the flows and the pollutants concentration. This approach takes into account the hydraulic operation of the sewer systems and the mechanism of the pollutant transfer. In this work, we are interested in a portion of a sewer system of Monastir city in order to reproduce the hydraulic phenomena that occur there. The numerical study was treated using "ANSYS Fluent" software. The standard k-ε turbulence model and the multiphase VOF model are used in this work. The exploitation of the results is mainly carried out on the flow rates, the water velocities, and the free surface. Then, we described the evolution of the pollutant concentration, the free surface, and the sediment deposition by examining the various mechanisms of the turbulent flow.

Keywords Free surface · Pollutant · Sediment · Turbulent flow
Sewer system

S. Ben Hamza (✉)
LGM, National Engineering School of Monastir, University of Monastir,
Monastir, Tunisia
e-mail: soniabenhamza@yahoo.fr

N. Mahjoub Saïd
LGM, Preparatory Institute for Engineering Studies, University of Monastir,
Monastir, Tunisia
e-mail: nejla.mahjoub@fsm.rnu.tn

H. Bournot · G. Le Palec
IUSTI, UMR CNRS 7543, University of Aix-Marseille, Marseille, France
e-mail: georges.lepalec@univ-amu.fr

1 Introduction

The transfer of wastewaters into sewer systems has been studied since a long of time by many researchers (Benyahia 2006; Buyer 2002; Gromaire-Mertz 1998; Jaumouillié 2003; Kanso 2004; Kuss 2010; Zgheib 2009). Thus, several numerical and experimental tools are used in order to treat the dispersion of pollution in networks. For example, Gromaire-Mertz (1998) used an experimental system to control the quality of wastewater in an urban network at different levels of the water cycle. The results show that combined sewer systems are not only pollutant transport systems, but they constitute physicochemical reactors that control the quality of wastewater in rainy and dry conditions.

Jaumouillié (2003) used the CFX software to determine the distribution of velocities and pollutant concentrations, and then to reproduce the hydraulic mechanisms that occur in sewer systems. The three-dimensional code was parameterized from the results obtained in a well-determined environment. Kanso (2004) analyzed the calculation models of pollutants from urban discharges in rainy weather. Thus, a methodology based on Bayesian theory yielded reliable results allowing the analysis of the pollutants concentration between two rainy events and within the same rainfall event on the site studied.

Kuss (2010) used a UV/Visible spectrophotometer to detect peaks in bacteriological pollution by measuring the concentration of pollutants entering the sewage treatment plant. These techniques have been applied to develop a rain-flow model in a rural–urban watershed. The results showed that the presence of pollutants in wastewater is responsible for the diffusion of electromagnetic radiation.

In this work, we propose a numerical study of free surface turbulent flows in a portion of a sewer system, using data provided by the National Sanitation Office (ONAS) of Monastir city, in order to highlight the hydraulic behavior of the dissolved and particulate pollutants dispersion.

2 Mathematical Modeling

2.1 Geometry Description

The sewer system in the region of Monastir is a combined sewer, i.e., it collects both wastewater and stormwater. The tunnel has a rectangular shape (Fig. 1), and it presents the terminal portion of the sewerage network of Monastir. The geometry was constructed in 3D using "ANSYS Workbench" software.

The characteristic dimensions of this geometry are given in Fig. 1. As illustrated in this figure, the lengths $L_1 = 34.3$ m, $L_2 = 20.1$ m and $L_3 = 108.6$ m are respectively, the lengths of the sewer portions studied in this work. The origin of the Cartesian coordinates system (O, X, Y, Z) is located at the bottom of L_3. Noted
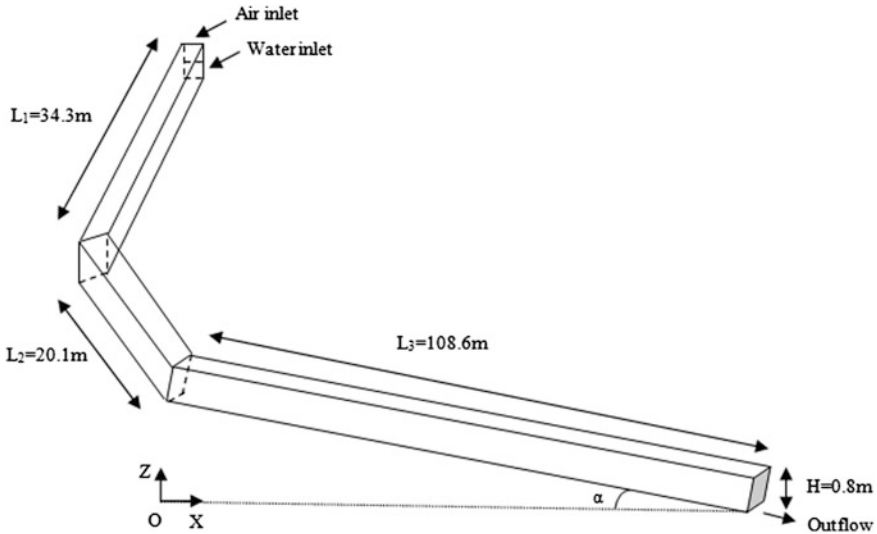
Fig. 1 Computational domain geometry

that H = 0.8 m is the height of the sewer. The corresponding section is S = 1.2 m^2 and the inclination angle of the sewer system is α = 2.16%.

2.2 Assumptions and Boundary Conditions

A three-dimensional free surface flow in turbulent regime was considered in this study. The fluids are air and water, which were assumed Newtonian and immiscible. The temperature is constant along the calculation domain.

The operating principle of the flow is as follows: water is injected at the inlet of the sewer with a well-determined height "h" and a velocity "U" also given. Between the level of the free surface and the top of the sewer, air was introduced at atmospheric pressure. Under the influence of its initial velocity and the inclination of the sewer, the water flows from the inlet to the outlet of the network.

Pollutants are injected from time-dependent sources in a turbulent free surface flow. These pollutants are rejected from industrial discharge such as calcium sulfate $CaSO_4$ with a solubility of 2.1 g/l, and suspended sediments with a density of 1600 kg/m^3. The initial water height is h = 0.35 m, the initial flow velocity is U = 3 m/s (the flow rate Q = 1.57 m^3/s). These measurements are the real values given by ONAS of Monastir. The calculation of the turbulent intensity and the hydraulic diameter allows us to obtain the initial values of the turbulence at the inlet (Table 1).

Table 1 Relevant input parameters of the simulation

Air	Air inlet	$U = 0$ m/s
	Air outlet	$\frac{\partial \widetilde{u}}{\partial x} = \frac{\partial \widetilde{v}}{\partial x} = \frac{\partial \widetilde{w}}{\partial x} = 0, \frac{\partial k}{\partial x} = 0, \frac{\partial \varepsilon}{\partial x} = 0$
	Sewer wall	$u = v = w = 0, k = 0, \frac{\partial \varepsilon}{\partial y} = 0$
Water	Water inlet	$U = 3$ m/s, $h = 0.35$ m
	Water outlet	$\frac{\partial \widetilde{u}}{\partial x} = \frac{\partial \widetilde{v}}{\partial x} = \frac{\partial \widetilde{w}}{\partial x} = 0, \frac{\partial k}{\partial x} = 0, \frac{\partial \varepsilon}{\partial x} = 0$
	Free surface	$\frac{\partial k}{\partial y} = 0, \frac{\partial \varepsilon}{\partial y} = 0$
	Sewer wall	$u = v = w = 0, k = 0, \frac{\partial \varepsilon}{\partial y} = 0$

2.3 Governing Equations

To model the turbulent flow, the Reynolds-Averaged Navier–Stokes (RANS) equations, based on the Reynolds decomposition, are solved for unsteady and incompressible fluids. The governing equations are written in the Cartesian coordinates system as follows:

The equation of continuity

$$\frac{\partial \rho}{\partial t} + \frac{\partial(\rho\, U_i)}{x_i} = 0 \tag{1}$$

The equation of momentum

$$\frac{\partial(\rho\, U_i)}{\partial t} + U_j \frac{\partial(\rho\, U_i)}{\partial x_j} = -\frac{\partial P}{\partial x_i} + \frac{\partial}{\partial x_j}\left[\mu\left(\frac{\partial U_i}{\partial x_j} + \frac{\partial U_j}{\partial x_i}\right) - \rho\overline{u_i' u_j'}\right] + \rho\, g_i + S_{i,s} \tag{2}$$

The equation of concentration for the dissolved pollutant

$$\frac{\partial C}{\partial t} + \frac{\partial(U_i C)}{\partial x_i} = -\frac{\partial(\overline{u_i' C'})}{\partial x_i} \tag{3}$$

The equation of suspended particle motion

$$\frac{du_i^p}{dt} = \frac{3\nu\, C_D Re_p}{4d^2 S}\left(u_i - u_i^p\right) + g_i \tag{4}$$

and

$$\frac{dx_i}{dt} = u_i^p, \tag{5}$$

where $\overline{u_i' u_j'}$ is the Reynolds stresses and $\overline{u_i' C'}$ is the turbulent fluctuation term. Prediction of turbulence requires the use of a turbulence closure model to obtain a closed equations' system. The k-ε model was chosen for its ability to model the turbulent features. It has also a minimum computational requirement compared with

other turbulence models (Choi and Garcia 2002; Huang et al. 2010). This model is based on the Boussinesq hypothesis.

The multiphase model used in this work is the Volume of Fluid model (VOF). The idea with the VOF method is that the interface between two phases is tracked. This is done by a phase indicator function that indicates the fractional amount of fluid at a certain position. This method can simulate flows including the shape and evolution of the free surface. This means that the free surface boundary can be efficiently simulated. The dispersion of particles due to turbulence in the fluid phase is predicted using the discrete random walk (DRW) model that includes the effect of instantaneous turbulent velocity fluctuations on the particle trajectories through the use of stochastic methods. In this approach, "ANSYS Fluent" predicts the turbulent particles' dispersion by integrating the trajectory equations for individual particles, using instantaneous fluid velocity along the particle path during the integration. By computing the trajectory in this manner for a sufficient number of representative particles, the random effects of turbulence on the particle dispersion is accounted for.

3 Numerical Method

The numerical simulations were carried out using "ANSYS Fluent" software. RANS equations are solved using an implicit scheme of first order in time and space by the finite volume method. "ANSYS Fluent" provides flexibility in choosing discretization schemes for each governing equation. The discretized equations, along with the initial and boundary conditions, were solved using a segregated solution method. Using the segregated solver, the governing equations were solved sequentially (i.e., segregated from one another). The second-order implicit SIMPLE scheme is used in this study. It was selected in order to improve accuracy and to calculate the pressure–velocity coupling. It uses a relationship between velocity and pressure corrections to enforce mass conservation and obtain the pressure field. The two-phase coupling system is numerically solved with an under-relaxation iterative scheme. The Lagrangian approach is used for the prediction of the particle's dispersion in turbulent flows. This approach assumes that a number of particle trajectories are simulated in a given turbulence field, i.e., the particles are considered individually. The tracking of the interface between the two phases is done by a phase indicator function that indicates the fractional amount of fluid at a certain position. This interface is reconstructed using the geometric reconstruction "Geo-reconstruct" method. This scheme represents the interface between fluids using a piecewise-linear approach. It is assumed to have a linear slope within each cell and uses this linear shape for calculation of the advection of fluid through the cell faces. The mesh was generated using "ANSYS Fluent Meshing", which is ANSYS pre-processing tool of Fluent. This preprocessor is a single interface for geometry meshing. In this study, a tetrahedral mesh was used. The total number of cells is equal to 680 000. Figure 2 shows in detail the mesh used for the computational domain.
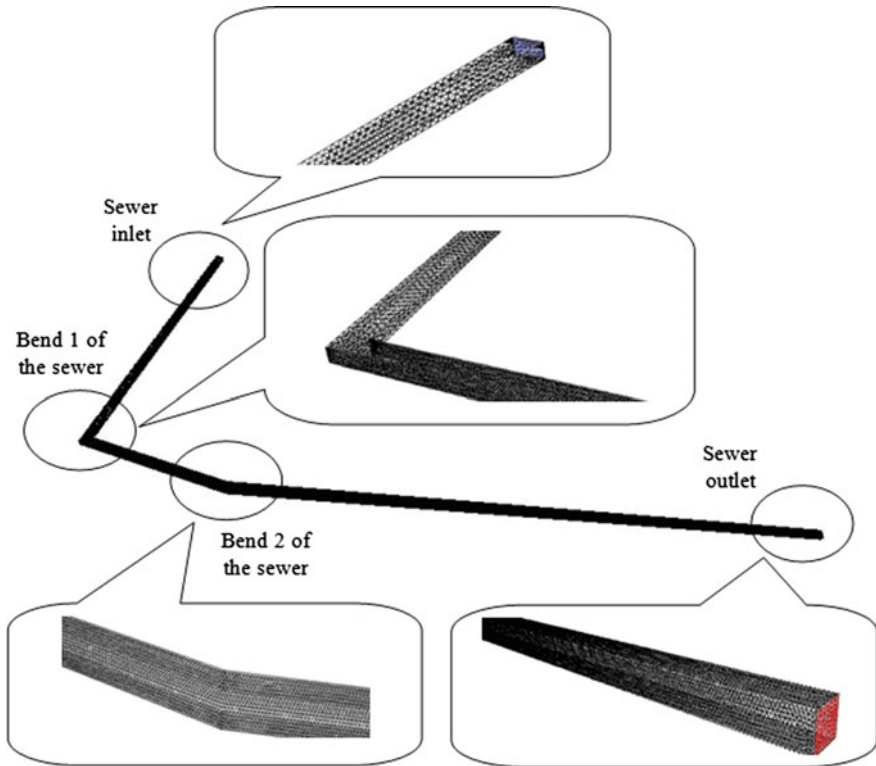
Fig. 2 Meshing of the computational domain

A mesh independence study is done to ensure that the solution is appropriate. We have run the simulation in a sewer system using the k-ε model, for progressively finer grids by changing the global grid size starting from a coarse mesh and refining it until numerical results were no more dependent on the mesh size. The convergence takes too long and requires more computer memory for the finer grid, but there is no significant change in the results. Hence, for the best compromise between accuracy of results and computation time, a mesh size of 680 000 cells was retained for all given simulations.

4 Results and Discussion

4.1 Free Surface Evolution

Figure 3 shows the evolution of the free surface at a velocity of 3 m/s and a height of 0.35 m (the flow rate $Q = 1.57$ m^3/s) for a cross section in the median plane of
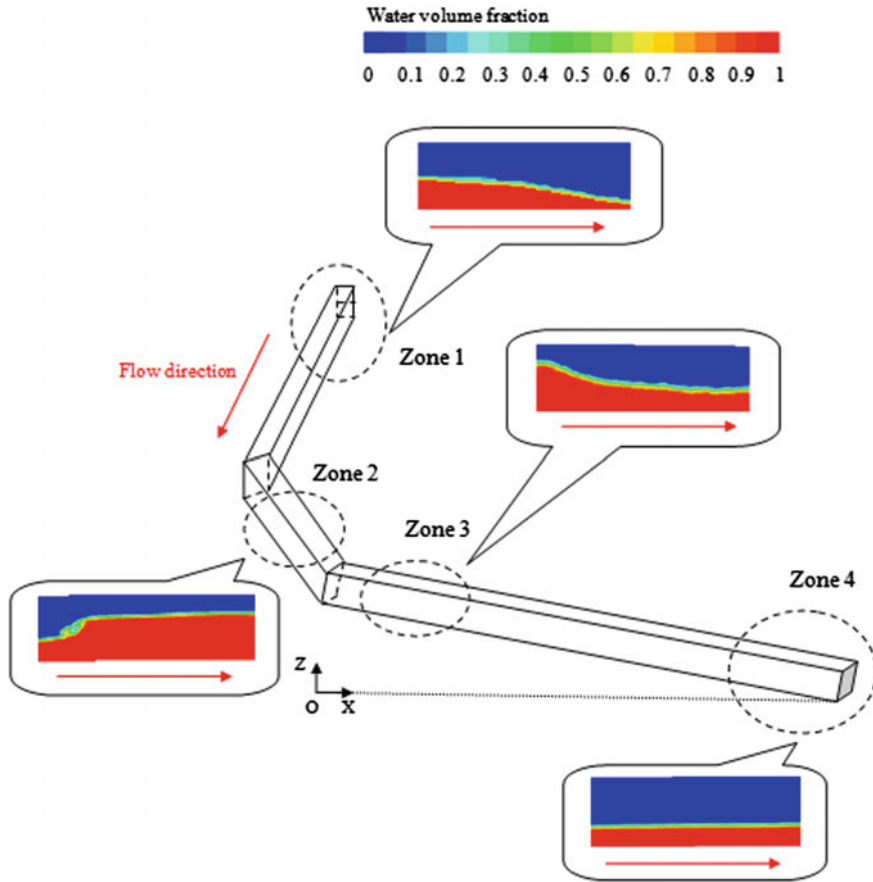
Fig. 3 Evolution of the free surface for a cross-section in the median plane of the sewer

the sewer system. It is noted that, in zone 1, there is a decrease in the free surface. Indeed, the flow is characterized by a gradually accelerated non-uniform motion, this being due to the fact that the parameters characterizing the flow (water height, velocity, flow rate) change along this section. Then, in zone 2 the free surface increases after its passage through the first bend of the sewer. Indeed, in this second zone, the flow is characterized by a rapidly decelerated non-uniform motion: the parameters which characterize the flow change abruptly with discontinuities, thus causing a large dissipation of the energy. This usually occurs in the vicinity of the bend following a sudden change in direction. Subsequently, the flow undergoes a second decrease in the free surface, following its passage through the second bend. In this zone, the flow is characterized by a rapidly accelerated non-uniform motion: the velocity increases rapidly in the direction of the flow.

Finally, it can be seen that the level of the free surface remains constant along the last part of the sewer. Thus, the flow is characterized by a uniform motion: the

parameters which characterize the flow remain invariable along this part, without any sudden change of direction.

4.2 Pollutant Dispersion

Figure 4 shows the concentration contours of the dissolved pollutant ($CaSO_4$) at a velocity of 3 m/s and a height of 0.35 m (the flow rate Q = 1.57 m^3/s) for a cross section in the median plane of the sewer system. It is noted that the pollutant, in zone 1, is going down toward the bottom under the effect of diffusion and convection phenomenon. This dispersion mechanism is due to the drop in the level of the free surface in this zone. So, we observe that the cloud of pollutant follows the flow. Then, in zone 2 there is an abrupt rise in the cloud of pollutant after passing
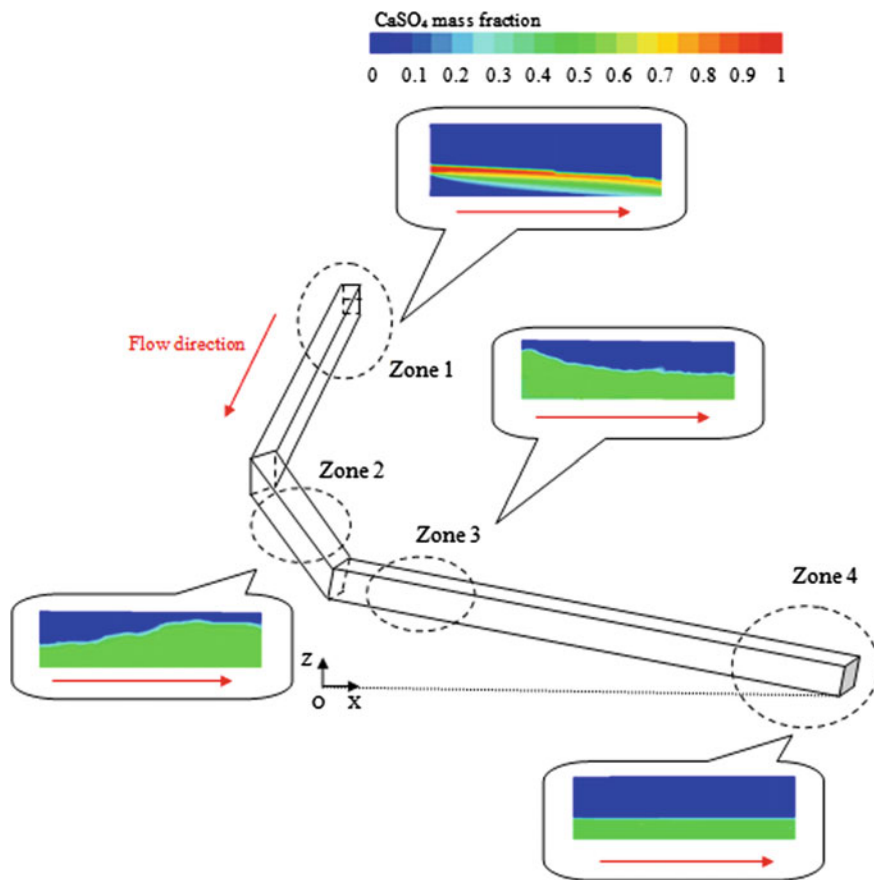
Fig. 4 Pollutant concentration for a cross-section in the median plane of the sewer

through the first bend, which is explained by the increase in the level of the free surface in this portion of the sewer system. In this region, the pollutant is totally dispersed throughout the flow, this mechanism being favored by the turbulences generated by the change of direction.

Finally, in zones 3 and 4, the wastewater and the dissolved pollutant are mixed together and the concentration field is quasi-uniform after passing through the second bend of the sewer system.

4.3 Sediment Deposition

According to Fig. 5, which represents the percentages of deposited particles in the sewer system for a cross section in the median plane, it is noted that there are two peaks. A first peak is observed at the first bend with a deposition rate of 12.09% at a flow rate of 3.75 m³/s; then of 14.53% at a flow rate of 2.92 m³/s and then, of 17.26 m³/s at a flow rate of 1.57 m³/s.
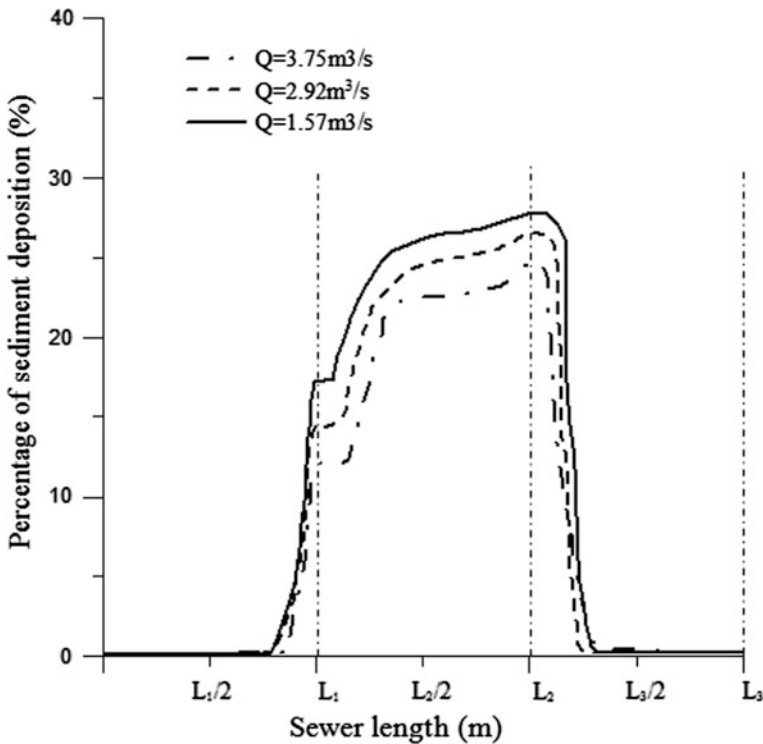
Fig. 5 Percentage of sediment deposition for different flow rates in the sewer system

The second peak is observed at the second bend with a deposition rate of 24.82% at a flow rate of 3.75 m³/s, then of 26.52% at a flow rate of 2.92 m³/s and then, of 27.81 m³/s at a flow rate of 1.57 m³/s.

Thus, it can be deduced that the suspended particle has a very high deposition rate between the two bends; whereas in the rest of the sewer there is practically no
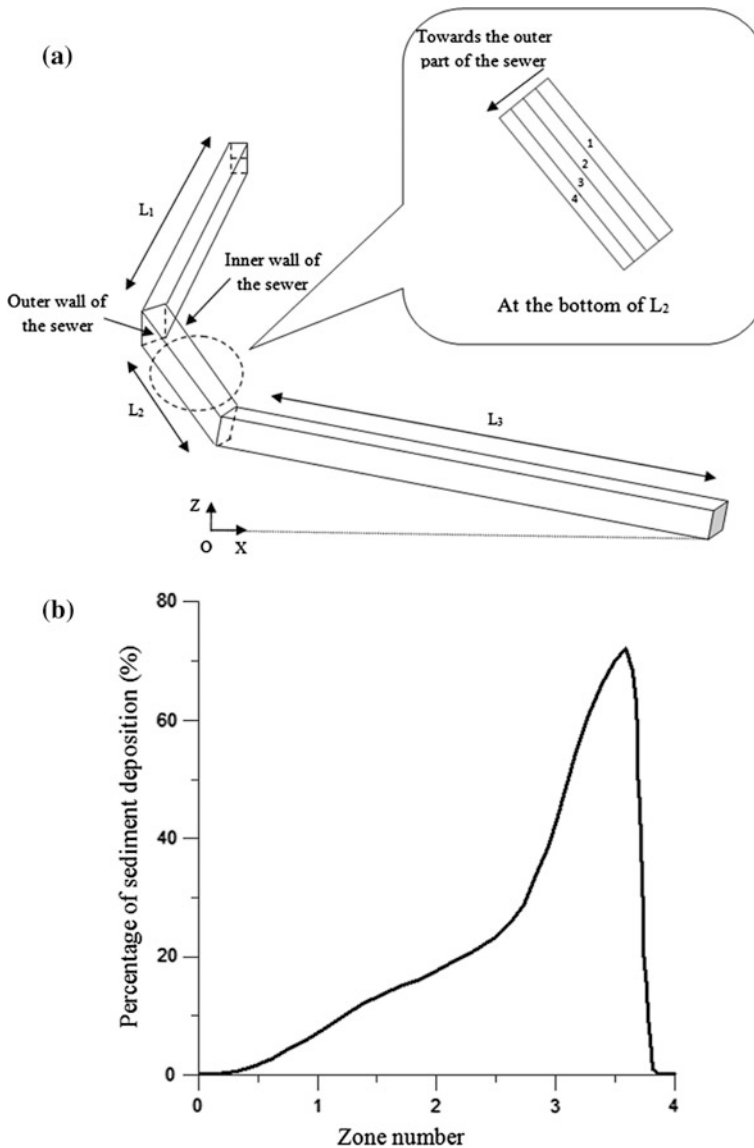
Fig. 6 **a** Overview at the bottom of L_2, **b** Sediment deposition rates at the bottom of L_2

deposition rate. On the other hand, it is noted that the higher the flow rate (high velocity) the lower the deposition rate. From these results, it is concluded that the deposition rate increases with the decrease in the flow rate.

Figure 6 shows the percentages of deposited particles at the bottom of the sewer system in the portion L_2, where a high deposition rate has been observed.

It can be seen from this figure that the rate of deposition of suspended particle is very high in the vicinity of zone 4 (between zone 3 and zone 4), i.e., at the outer part of the bend, and reaches a maximum value of 72.2% for a flow rate of 2.92 m^3/s. In the inner part of the bend, the deposition rates are very low. Thus, it can be deduced that the solid particles are deposited more easily at the bends of the sewer system, which corresponding to the recirculation zones at the bottom.

5 Conclusion

In this paper, a numerical simulation of dissolved and particulate pollutants in a sewer system was developed, in order to simulate the sediment transport in turbulent two-phase flows. This simulation was achieved by modeling the computational domain using the finite volume method together with the VOF model.

The distribution of dissolved pollutant in the turbulent air-water flows was set at the free surface. We found that the presence of bends in a sewer system creates strong disturbances in the flow, which generally changed the flow structure. The pollutant is affected by this disturbance, as well as the turbulence created in these regions. This phenomenon produces an increase in the level of the water surface.

After that, we explore the sediment transport by considering a stochastic tracking (DRW) model. Particles dispersion and deposition in various regions of the sewer are examined. We found that suspended particles have a very high deposition rate in the outer parts of the sewer system, i.e., in the bends of the networks (corresponding to the recirculation zones at the bottom).

These findings may be of great help in cost-effective scientific countermeasures to be taken into consideration for accident or planned pollutants discharged into sewer systems.

References

Benyahia KM (2006) Variabilité spatiale des caractéristiques et des origines des polluants de temps de pluie dans le réseau d'assainissement unitaire parisien. PhD thesis, Ecole Nationale des Ponts et Chaussées, France

Buyer M (2002) Transport de flux en réseau d'assainissement: modèle 1d pour l'hydraulique des collecteurs et déversoirs avec prise en compte des discontinuités. PhD thesis, Université Louis Pasteur—Strasbourg I, France

Choi SU, Garcia MH (2002) k-ε turbulence modeling of density currents developing two dimensionally on a slope. J Hydraul Eng 128:55–63

Gromaire-Mertz MC (1998) La pollution des eaux pluviales urbaines en réseau d'assainissement unitaire: Caractéristiques et origines. PhD thesis, Ecole Nationale des Ponts et Chaussées, France

Huang H, Chen G, Zhang QF (2010) The distribution characteristics of pollutants released at different cross-sectional positions of a river. Environ Pollut 158:1327–1333

Jaumouillié P (2003) Hétérogénités des vitesses et des concentrations dans les collecteurs d'assainissement: application à la mesure des flux polluants. PhD thesis, Université de Bordeaux I, France

Kanso A (2004) Evaluation des Modèles de Calcul des Flux polluants des Rejets Urbains par Temps de Pluie—Apport de l'Approche Bayésienne. PhD thesis, Ecole Nationale des Ponts et Chaussées, France

Kuss D (2010) Gestion intégrée de rejets d'assainissement: applicabilité de la mesure de pollution par spectrophotométrie UV/Visible. PhD thesis, Université de Strasbourg

Zgheib S (2009) Flux et sources des polluants prioritaires dans les eaux urbaines en lien avec l'usage du territoire. PhD thesis, Ecole Nationale des Ponts et Chaussées, France

Surrogate-Based Multidisciplinary Design Optimization for Stiffened Panels Application

Hamda Chagraoui and Mohamed Soula

Abstract This paper is devoted to propose and apply a surrogate-based multidisciplinary design optimization (MDO) method on stiffened panels with several substructures and objectives. This method combines Kriging Surrogate Model (KSM), which is used to predict the exact responses of objectives and constraint functions, and an Improved Multi-Objective Collaborative Optimization (IMOCO) to solve the MDO problems. In the KSM-IMOCO scheme, each exact optimization problem at structure and substructure level is replaced by a metamodel to limit the computational burden. To demonstrate the applicability of the proposed KSM-IMOCO method, we treat an engineering example of kind stiffened panel. Results obtained from the application of the KSM-IMOCO approach on optimization problem of a stiffened panel kind L are compared with the traditional optimization (TO), without passing by the approximation tools, and it has been shown the sovereignty of the proposed KSM-IMOCO method. These results indicate that the proposed KSM-IMOCO method significantly reduces computational burden, and improves the convergence rate for solving the exact multidisciplinary optimization problem.

Keywords Multidisciplinary design optimization · Kriging surrogate model
Improved multi-objective collaborative optimization · Traditional optimization
KSM-IMOCO · Stiffened panels

H. Chagraoui (✉) · M. Soula
Laboratory of Applied Mechanics and Engineering, ENIT, Department of Mechanical
Engineering ENSIT-Tunis University of Tunisia, Tunis, Tunisia
e-mail: hmdchagraoui@gmail.com

M. Soula
e-mail: Soulamed2003@Yahoo.fr

1 Introduction

Stiffened panels consist of plates/shells reinforced by stiffening elements (stringers, frames). These panels are widely used in marine structures such as ship hulls and in catamarans, and in aircraft structures such as fuselages and wings to achieve weight saving. Weight savings in stiffened panels is an important design objective. It can have significant impact on the aircraft in terms of stiffness, speed, and fuel consumption.

The stiffened panel design problems are complex and multidisciplinary in nature, which involve multiple substructures. Therefore, we can decompose its global optimization problem into several sub-problems, which can be treat by multiple teams in parallel. Consequently, problems solving become more efficient with a reduced computational burden. A better way able to tackle complex optimization problems in an efficient way taking into account several substructures simultaneously using the collaborative optimization (CO) approach (Yi et al. 2007).

CO is a multidisciplinary design optimization (MDO) method (Yi et al. 2007), it proposes to decompose the global problem into an optimization problem, at the structure level, to search the optimal global variables, coupled with several optimization sub-problems, at the substructure level, to find the optimal local variables. Many researchers have shown interest to use the MDO approach in order to address the computational challenges that arise when tackling various complex engineering optimization problems. For example, Chagraoui et al. (2016) proposed an Improved Multi-Objective Collaborative Optimization (IMOCO) to solve the multi-objective and multi-Physics optimization problem of multi-physics behavior of microstructures. Aute and Azarm (2006) presented a new Genetic Algorithm based approach for MOCO to handle the multi-objective CO problems.

The typical CO scheme habitually face problems with high computational burden, which prevents proper searching on the design space. An alternative to deal with the challenge of reducing computational cost during extensive design space exploration is the use of surrogate model, thereby speeding up the overall CO process. Some authors have used surrogate model methods in CO framework to limit computational burden during the optimization process. In this direction, Hu et al. (2013) developed a new Approximation Assisted Multi-objective collaborative Robust Optimization New AA-McRO under interval uncertainty for MDO. Sobieski et al. (1998) developed a local response surface method to estimate a subsystem optimization output in CO. Simpson et al. (2001) used a Kriging surrogate model to build global prediction in an MDO framework.

The organization of the remainder of this paper is as follows: In Sect. 2, the integrated KSM-IMOCO method, which combines the Kriging Surrogate Model (KSM) and Improved Multi-Objective Collaborative Optimization (IMOCO) is formulated. In Sect. 3, an engineering example of kind stiffened panel optimization problem is used to show the effectiveness of the KSM-IMOCO method. The paper concludes with a summary in Sect. 4.

2   Integrated KSM-IMOCO Method

The integrated KSM-IMOCO method is obtained by the combination between a Kriging Surrogate Model (KSM) (Tamijani et al. 2013) used as a metamodel and an Improved Multi-Objective Collaborative Optimization (IMOCO) method (Chagraoui et al. 2016) to handle the multidisciplinary design optimization (MDO) problem. The hierarchically IMOCO method solve the global optimization problem into three levels of optimization, structure level, substructure level, and coordinator level, as shown in Eqs. (1)–(3). The optimization problem at structure level aims to optimize the structure objectives functions respecting structure constraints, while a series of n at substructure level optimization problems in Eq. (2) each optimizes the substructure objectives functions respecting substructure constraints. In addition, the coordination optimization problems in Eq. (3) aims to reduce the difference between the shared and the coupling variables transferred from different substructures in order to avoid conflict during the optimization.

Structure optimization problem (upper level)

$$
\begin{aligned}
&\min_{X_s} \quad f_s(X_s, x_i^*) \\
&s.t \quad g_s(X_s) \le 0 \\
&\qquad X_s \equiv \left[x_{sh}^s, a_{ij}^s, a_{ji}^s \right]
\end{aligned}
\tag{1}
$$

Substructure optimization problems (middle level)

$$
\begin{aligned}
&\min_{X_i} \quad (f_i(X_i) + ICC_i) \\
&s.t \quad g_i(X_i) \le 0 \\
&\qquad y_{ij} = Y_i(X_i) \\
&\qquad ICC_i = \left\| 1 - \frac{x_{sh}^i}{x_{sh}^s} \right\|_2 + \sum_{j \ne i}^{I} \left\| 1 - \frac{y_{ij}}{a_{ij}^s} \right\|_2 + \sum_{j \ne i}^{I} \left\| 1 - \frac{a_{ji}^i}{a_{ji}^s} \right\|_2 \\
&\qquad X_i \equiv \left[x_i, x_{sh}^i, a_{ji}^i \right]
\end{aligned}
\tag{2}
$$

Coordination optimization problems (lower level)

$$
\min_{X} C(X) = \sum_{i=1}^{I} \left\| 1 - \frac{x_{sh}}{x_{sh}^i} \right\|_2 + \sum_{i=1}^{I} \sum_{j \ne i}^{I} \left\| 1 - \frac{a_{ij}}{y_{ij}} \right\|_2 + \sum_{i=1}^{I} \sum_{j \ne i}^{I} \left\| 1 - \frac{a_{ij}}{a_{ij}^i} \right\|_2
\tag{3}
$$
$$
X \equiv \left[x_{sh}, a_{ij} \right]
$$

The optimization problem at structure level aims to find structure's optimal design variables X_s that contains the shared variables x_{sh}^s between the substructures and the auxiliary variables (a_{ij}^s, a_{ji}^s) by optimizing the structure level objectives functions f_s subject to structure constraints g_s. The superscript $(^*)$ indicates that the design variables are optimized at substructure level (middle level) optimizer. Likewise, in the ith substructure's optimizer $(i = 1, \ldots, I)$ in Eq. (2), each optimizer

aims to improves the substructure's objectives functions f_i limited by local constraints g_i while respecting the design variable X_i, which includes substructure's design variables x_i, shared variables x_{sh}^i and auxiliary (target) variables a_{ji}^i. The coupling variables y_{ij} represent the output from substructure i and are used as input parameters in substructure j, which defined as Y_i function. The interdisciplinary consistency constraint of ith substructure's ICC_i in Eq. (2) aims to reduce the difference between the substructure's shared variables x_{sh}^i and the structure's shared variables x_{sh}^s. In addition, this constraint decreases the difference between the coupling variable y_{ij} and the auxiliary variable a_{ji}^i obtained and sent from the structure level, likewise the minimizing of the difference is performed between the local auxiliary variable a_{ji}^i and the structure's auxiliary variable a_{ji}^s. After the assessment of the substructure's optimization problems, all optimal design variables passed to the coordination problem, Eq. (3), in order to select the substructure's optimal design variables (x_i^*) with the minimum value of the single objective function (see Eq. (3)) these variables are then passed to structure's optimizer in
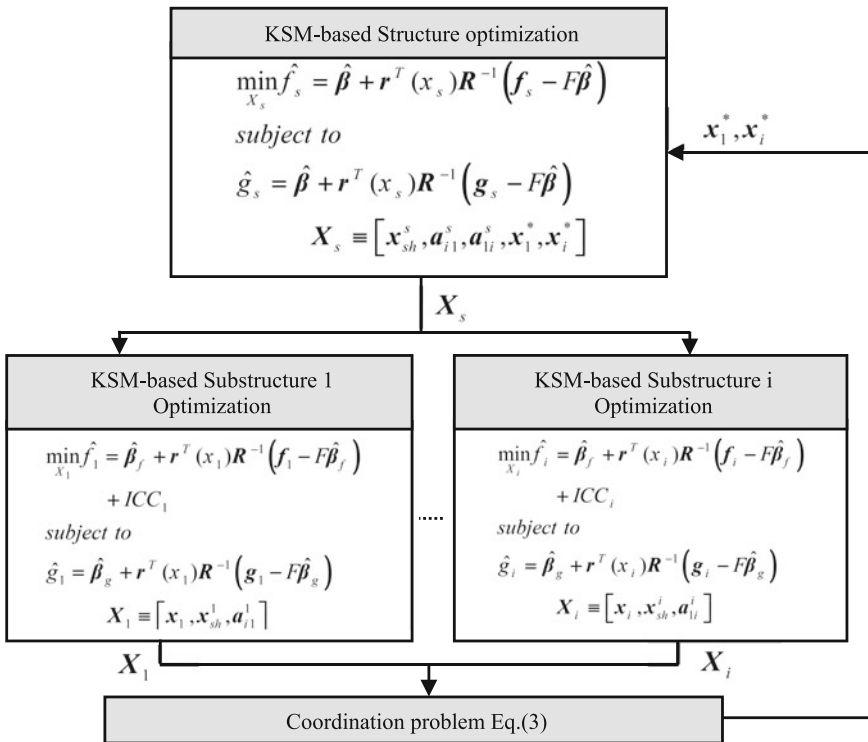
Fig. 1 Flowchart of integrated KSM-IMOCO model

Eq. (1). The main objective of optimization problem in Eq. (1) is to obtain a whole of Pareto optimal solutions for the structure optimization problem.

The use of the KSM aims to substitute the exact objectives and constraints functions at structure and substructure levels a metamodel (surrogate model). The surrogate model of each objective and constraint function is computed according to Huang et al. (2011), Tamijani et al. (2013)

$$\hat{y}(x) = \boldsymbol{\beta} + r^T(x)R^{-1}(y - F\boldsymbol{\beta}), \tag{4}$$

where F and $\boldsymbol{\beta}$ represent the regression functions with second-order polynomial and regression coefficients vectors, respectively. R^{-1} is the correlation matrix between the sample points, and r^T is the correlation vector between any new point and the original sample points. $\hat{y}(x)$ is an estimated of exact response $y(x)$.

Figure 1 shows the proposed flowchart of the proposed KSM-IMOCO approach for the optimal design of coupled MDO problem. In this proposed approach, KSM predictor replaces each exact optimization problem at structure and substructure level by a metamodel as shown in Fig. 1.

3 MDO of Stiffened Panel L-Type Based on Integrated KSM-IMOCO Model

This section presents the application of the proposed KSM-IMOCO for solving the MDO problem of stiffened panel L-type. The design of stiffened panel is intended for minimum mass and a maximum first eigenfrequency. Figure 2 shows the dimensional variables of the stiffened panel of length (L_1 = 3245 mm). Five longitudinal stiffeners reinforce it. The FE model of the stiffened panel L-type, as shown in Fig. 3, is discretized in 2460 elements and 2573 nodes (Table 1; Fig. 3). The panel and stiffeners material has Young's modulus of E = 210 GPa, the poison's ratio is ν = 0.3 and the density is equal to 7850 kg/m^3 (Cho et al. 2015).
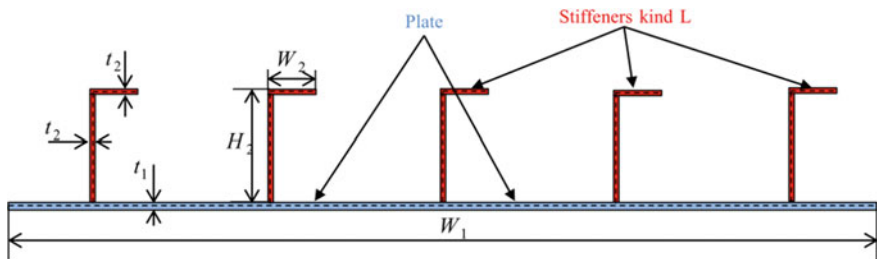
Fig. 2 Cross-section of stiffened panel L-type

Observation node (42)
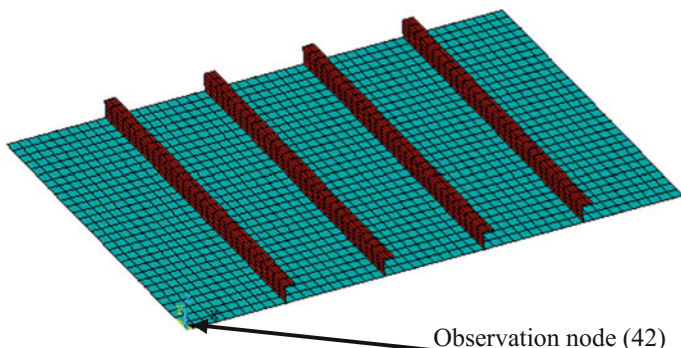
Fig. 3 Finite element model of the stiffened panel L-type

Table 1 Geometry and discretization FE model of the stiffened panel L-type (Cho et al. 2015)

Mesh element	Variables	Dimension (mm)	Number of elements	Total
Plate	L1	3425	30	Number of elements: 2573, Number of nodes: 2460
	W1	4225	50	
	t1	10		
Stiffener L	H2	90	4	
	W2	150	4	
	t2	9		

3.1 Traditional Optimization: TO

The exact optimization problem of stiffened panel to solve, see Eq. (5), has for purpose to maximize the eigenfrequency (f_{panel}), to minimize the displacement at node 42 (D_{42}) and to minimize the total mass ($Mass_{panel}$) of the studied panel.

$$\min \begin{cases} -f_{panel}(X) \\ D_{42}(X) \\ Mass_{panel}(X) \end{cases}$$
$$X \in [L, t_1, H_2, W_2, t_2, E, \rho] \tag{5}$$

3.2 KSM-IMOCO Method

This section presents the formulation of the stiffened panel's optimization problem within KSM-IMOCO. In other words, metamodel-based-IMOCO, as shown in Fig. 4. In this KSM-IMOCO framework, the exact optimization problem, Eq. (5), is

decomposed into an optimization problem at the structure level, which seeks the global optimum variables of the panel, and two optimization problems at the substructure level, which finds the local optimum design variables. Indeed, the substructure level contains two substructures (plate and stiffener) as shown in Fig. 4.

The details of the structure and substructure optimization specifics, containing the objectives functions, constraints and the design variables are shown in Table 2.

As indicated in Fig. 4, The decomposed optimization problem of stiffened panel contains three levels: (a) structure optimization problem at **upper level**, (b) substructure optimization problem at **middle level,** and (c) coordination problem at **lower level**.

At upper level, the multi-objective optimization of stiffened panel aims to maximize the predicted first eigenfrequency ($\hat{f}_{panel}$), to minimize the predicted displacement at node 42 ($\hat{D}_{42}$) and to minimize the total mass ($Mass_{panel}$) with
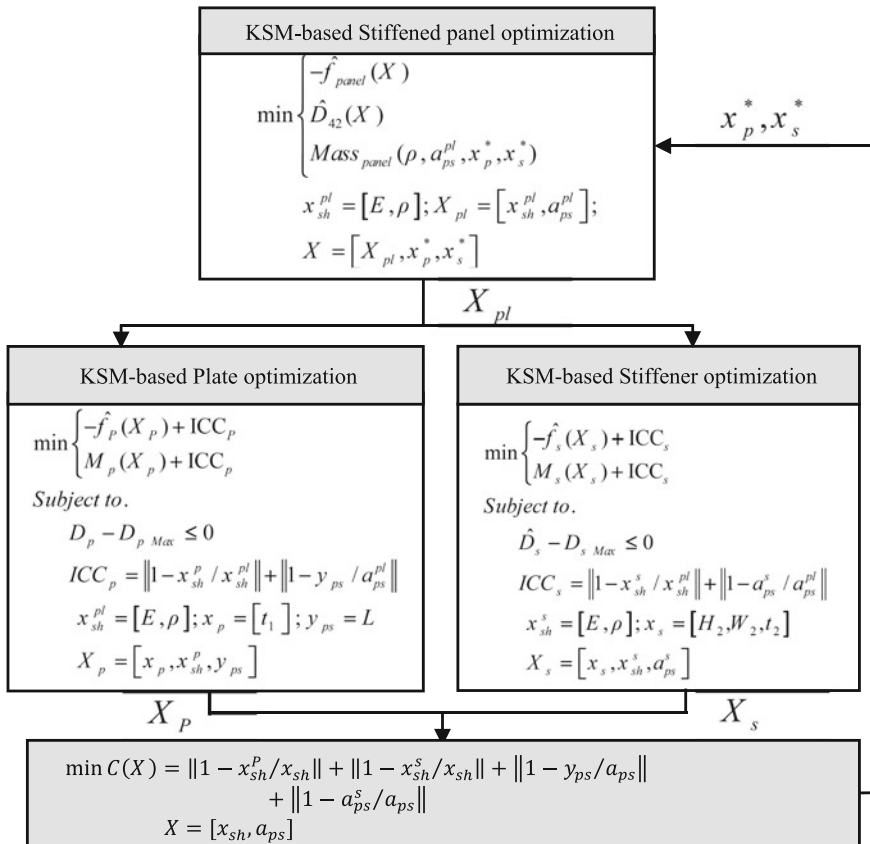
Fig. 4 Stiffened panel L-type optimization problem decomposed in the KSM-IMOCO framework

Table 2 Structure and substructure optimization specifics

IMOCO method			
	Structure (stiffened panel)	Substructure 1 (plate)	Substructure 2 (stiffener)
Objectives functions	f_{Panel}, D_{42}, $Mass_{Panel}$	f_P, M_P	f_s, M_s
Constraints		$g_p = D_p - D_{PMax} \leq 0$	$g_s = D_s - D_{sMax} \leq 0$
Design variables	$X = \left[X_{pl}, x_p^*, x_s^* \right]$	$X_p = \left[x_P, x_{sh}^p, y_{ps} \right]$	$X_s = \left[x_s, x_{sh}^s, a_{ps}^s \right]$
KSM-IMOCO method			
Objectives functions	$\hat{f}_{Panel}$, $\hat{D}_{42}$, $Mass_{Panel}$	$\hat{f}_P$, M_P	$\hat{f}_s$, M_s
Constraints		$\hat{g}_p = \hat{D}_p - D_{PMax} \leq 0$	$\hat{g}_s = \hat{D}_s - D_{sMax} \leq 0$
Design variables	$X = \left[X_{pl}, x_p^*, x_s^* \right]$	$X_p = \left[x_P, x_{sh}^p, y_{ps} \right]$	$X_s = \left[x_s, x_{sh}^s, a_{ps}^s \right]$

respect to the shared variables $[E, \rho]$ and the auxiliary variable a_{ps}^{pl} corresponds to the coupling variable y_{Ps}. The optimal local variables (x_P^*, x_s^*) are found at the substructure level.

At middle level, the multi-objective optimization problem of **the shell** (**plate**) aims to maximize the predicted local eigenfrequency ($\hat{f}_p$) and the mass (M_p) with respect the local variables x_p subject to the local constraint ($D_{p\,Max}$). Equally, the optimization problem of **the stiffener** as shown in Fig. 4 aims to increase the estimated objective function ($\hat{f}_s$) and to reduce a minimum of the stiffener's mass (M_s) which is associated with a local constraint ($D_{s\,Max}$). The optimal design variables obtained by the optimization problem of the stiffener is indicated by X_s, which includes the stiffener optimizer's variables x_s, shared variables x_{sh}^s and auxiliary variables a_{ps}^s.

At lower level, the best optimal local variables (x_P^*, x_s^*) are obtained after solving the coordination problem, see Fig. 4, according the smallest value of the penalty function, which are then transferred towards the structure level.

For this example, the obtained structure level Pareto-optimal solutions of the stiffened panel optimization problem from TO and KSM-IMOCO methods are shown in Fig. 5. This figure shows the Pareto-optimal frontier in 3D space as well as projections of this front in 2D space. Figure 5b, c, d represents the projection pairs (Displacement-Frequency, Frequency-Total Mass and Displacement-Total mass) in 3D space, respectively. According to Fig. 5, it was observed a significant overlap between Pareto-optimal frontiers obtained by the two approaches (TO and KSM-IMOCO). The TO method converges using **12862**s, while KSM-IMOCO requires **30**s, and therefore TO need longer computational time because of the method does not uses the surrogate model, and does not share the computational burden between the different substructures.
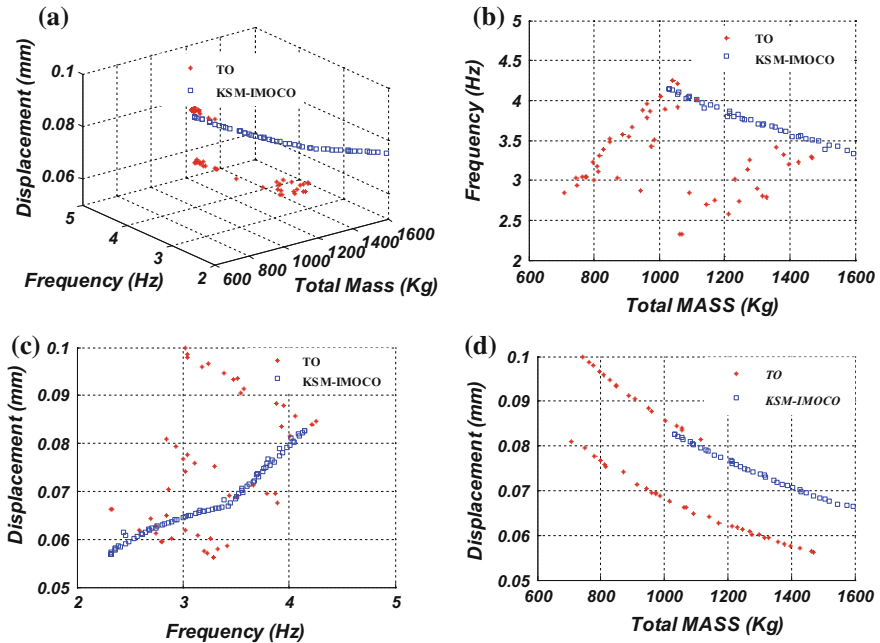
Fig. 5 Pareto optimality frontiers of the stiffened panel optimization problem at structure level obtained by TO and KSM-IMOCO methods

4   Conclusion

In the present work, we proposed an effective KSM-IMOCO method for optimal design of stiffened panels. It combines the KSM that aims to predict the exact responses and the IMOCO to solve the multidisciplinary optimization problem. The KSM-IMOCO method is used to treat the optimization problem of stiffened panel L-type. The efficiency and effectiveness of the proposed KSM-IMOCO method in dealing with engineering problem are showed with obtained results.

References

Aute V, Azarm S (2006) Genetic algorithms based approach for multidisciplinary multiobjective collaborative optimization. In: 11th AIAA/ISSMO multidisciplinary analysis and optimization conference, Portsmouth, Virginia. AIAA Press. https://doi.org/10.2514/6.2006-6953

Chagraoui H, Soula M, Guedri M (2016) A robust multi-objective and multi-physics optimization of multi-physics behavior of microstructures. J Cent South Univ 23(12):3225–3238. https://doi.org/10.1007/s11771-016-3388-2

Cho DS, Kim BH, Kim JH, Vladimir N, Choi TM (2015) Forced vibration analysis of arbitrarily constrained rectangular plates and stiffened panels using the assumed mode method. Thin Walled Struct 90:182–190

Huang Z, Wang C, Chen J, Tian H (2011) Optimal design of aeroengine turbine disc based on Kriging surrogate models. Comput Struct 89:27–37. https://doi.org/10.1016/j.compstruc.2010.07.010

Hu W, Azarm S, Almansoori A (2013) New approximation assisted multi-objective collaborative robust optimization (new AA-McRO) under interval uncertainty. Struct Multidisc Optim 47 (1):19–35. https://doi.org/10.1007/s00158-012-0816-2

Simpson TW, Korte JJ, Mauery TM, Mistree F (2001) Kriging models for global approximation in simulation-based multidisciplinary design optimization. AIAA J 39(14):2233–2241. https://doi.org/10.2514/2.1234

Sobieski IP, Manning VM, Kroo IM (1998) Response surface estimation and refinement in collaborative optimization. In: 7th AIAA/USAF/NASA/ISSMO symposium multidisciplinary analysis and optimization. St. Louis, U.S.A. https://doi.org/10.2514/6.1998-4753

Tamijani AY, Mulani SB, Kapania RK (2013) A framework combining meshfree analysis and adaptive kriging for optimization of stiffened panels. Struct Multidisc Optim 49:577–594. https://doi.org/10.1007/s00158-013-0993-7

Yi SI, Shin JK, Park GJ (2007) Comparison of MDO methods with mathematical examples. Struct Multidisc Optim 35(5):391–402. https://doi.org/10.1007/s00158-007-0150-2

Friction Compensation in a 2DOF Robot Manipulator

Said Grami and Raouf Fareh

Abstract Through this work, a compensation of the GMS friction in two degree of freedom planar robot manipulator is presented. The compensation is done using an online least square estimator to identify the friction force and then to be injected in the control law. The least square estimator has a linear formulation over the unknown parameters. However, the dynamic equation of the GMS friction needs a switching function to guarantee the transition between its two phases. This switching function is based on the unknown parameters. Therefore, the problem of the switching function was solved using an approximated switching function based on a prior values of the stiffness and the Stribeck coefficients. The compensation of the friction force is validated using an experimental apparatus that generate an experimental position, velocity and acceleration which are used as desired trajectories. The experimental friction force was injected in the joints of the robot manipulator modeled in MAT-LAB. The performance of the system without compensation of the friction is compared to the performance with compensation of friction force. The performance of the approach proposed showed a good tracking of the desired trajectories using a simple proportional derivative controller.

Keywords GMS friction · Estimation · Robot · Compensation · Control

1 Introduction

During the past years, the robot manipulators are widly used in a lot of applications such as medical application (Junpeng et al. 2016; Do et al. 2015), Stir Welding process (Qui et al. 2016), vehicle production, etc. However, the accuracy and preci-

S. Grami (✉)
Dhofar University, Salalah, Oman
e-mail: sgrami@du.edu.om

R. Fareh
University of Sharjah, Sharjah, UAE
e-mail: rfareh@sharjah.ac.ae

sion are needed in these applications: The robot should, in general, track a desired path with desired speed then the control of the robot is the key of its performance and effectiveness.

Since, the robot is a mechanical system that has a certain number of joints in motion so the friction is usually present in such system. The effect of the friction is very important in robot manipulator (Chernous and Shunderyuk 2010) because it can generate a shuttering, limit cycle (Garofalo and Ott 2016) and even instability in the performance of the system. The friction occurs when there are two rough surface in contact with relative motion. It is considered as undesired phenomenon in control of mechanical systems. For that reason a lot of works in literature are done to find a suitable mathematical model in order to be integrated in the compensation procedure of the friction. The friction modeling began by a static representation (Armstrong et al. 1994) then dynamic representation which represent more phenomena related to the behavior of the friction. However, all the models of friction present a drawback by missing certain friction behavior that have an important effect specially at low speed motion.

A new model of friction is introduced by Al-Bender et al. (2005) has the ability to model the majority of friction phenomena. This model is called Generalized Maxwell Slip (GMS) model, which will be used in this work.

The compensation of friction in robot manipulator has been widely investigated. In fact, a lot of research works were introduced to propose a compensation of friction force such as (Vorochaeva et al. 2015) and (Chernous and Shunderyuk 2010) in which they tried to compensate the Coulomb component of friction only (Miyasaka et al. 2015) propose a compensation of the only coulomb and viscous component of friction in surgical robot system. in the same manner, (Junpeng et al. 2016) propose a compensation of the Coulomb and viscous friction in 3 DOF lower limb rehabilitation robot. Coulomb, viscous and stribeck components of friction are compensated in two wheeled robot by Fuquan et al. (2015). More complete friction (Lugre model) is compensated in space robot by Liu et al. (2015).

The compensation of friction in the robot manipulators presented are using a non complete model of friction, so they are obliged to use a complicated control procedure to guarantee the robustness of the controller and to get a good performance. In this work, a compensation of the most realistic model of friction (GMS) in a robot manipulator is proposed. To do that, an online GMS friction estimation is used to estimate both dynamic and static effect of friction. The estimation is based on an online least square algorithm. The estimated friction force will be used to compensate the effect of the real friction in the position control of a two degree of freedom robot. Compared to the previous work, the advantage of this approach is the use of the most realistic model of friction in the compensation procedure and the use of simple scheme of control such as proportional-derivative and proportional-integral controller.

Fig. 1 2DOF robot
manipulator
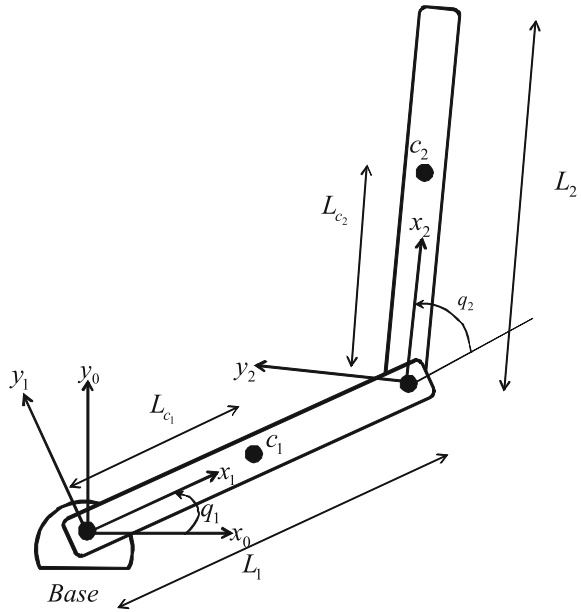
2 Robot Manipulator Dynamic

The dynamic of two degree of freedom planar robot manipulator (Fig. 1) can be described by the following equation.

$$M(q)\ddot{q} + V(\dot{q}, q) + F(\dot{q}) = \tau \tag{1}$$

The matrix $M(q)$ represents the inertia matrix of the robot, the matrix $V(\dot{q}, q)$ represents the Centrifugal, Coriolis and gravity matrix, and finally the matrix $F(\dot{q})$ is the friction matrix. q, $\dot{q}$ and $\ddot{q}$ are the joint position angle, the joint angular velocity and the joint angular acceleration vectors, respectively. The vector τ represents the torque vector in the joints.

The inertia matrix of two degree of freedom robot manipulator can be written as follows:

$$M(q) = \begin{bmatrix} M_{11} & M_{12} \\ M_{21} & M_{22} \end{bmatrix} \tag{2}$$

where the different terms of the inertia matrix are given by

$$M_{11} = m_1 L_{c_1}^2 + I_{z_1} + m_2(L_1^2 + L_{c_2}^2 + 2L_1 L_{c_2} c_2) + I_{z_2}$$
$$M_{12} = m_2(L_{c_2}^2 + L_1 L_{c_2} c_2) + I_{z_2}$$
$$M_{21} = m_2(L_{c_2}^2 + L_1 L_{c_2} c_2) + I_{z_2} \quad (3)$$
$$M_{22} = m_2 L_{c_2}^2 + I_{z_2}$$

where (m_1, L_1, L_{c_1}) and (m_2, L_2, L_{c_2}) are the mass, the length and the location of the center of mass of the first and the second link of the robot, respectively. The terms I_{z_1} and I_{z_2} represent the mass moment of inertia for the first and the second joint. The Centrifugal and Coriolis matrix $V(\dot{q}, q)$ can be written as follows

$$V(\dot{q}, q) = \begin{bmatrix} V_1 \\ V_2 \end{bmatrix} \quad (4)$$

where the terms of the matrix $V(\dot{q}, q)$ are presented below

$$V_1 = -m_2 L_1 L_{c_2} s_2 \dot{q}_2(2\dot{q}_1 + \dot{q}_2) + g(m_1 c_1 L_{c_1}$$
$$+ m_2(c_1 L_1 + c_{12} L_{c_2})) \quad (5)$$
$$V_2 = m_2 L_1 L_{c_2} s_2 \dot{q}_1^2 + g(m_2 c_{12} L_{c_2})$$

c_i and s_i, $i = 1, 2$ represent the notations of the function cosine and sine of the angle q_i, respectively.
c_{ij} and s_{ij}, $i, j = 1, 2$ are the notations of the function cosine and sine of the angle $q_i + q_j$, respectively.

The matrix $F(\dot{q})$ is the friction matrix and it is given as follows

$$F(\dot{q}) = \begin{bmatrix} F_1 \\ F_2 \end{bmatrix} \quad (6)$$

where F_1 and F_2 are the friction force in the first joint and in the second joint, respectively.

In this paper, F_1 and F_2 represent the friction forces in the joints which are modeled by GMS friction model presented in detail in the next section.

3 GMS Friction Model

The generalized maxwell slip model of friction (Al-Bender et al. 2005) is the most recent friction model presented in literature. It models the majority of friction phenomena that can be found in friction behavior.

The GMS friction model is described by two phases: the pre-sliding phase and the sliding phase. Each phase is modeled by a dynamic equation. A switching function is integrated to the dynamic model to guarantee the transition from one phase to another.

   The GMS friction model can be described microscopically by N masses attached to N springs which are excited by one variable which is the velocity.

- If the stage i is in pre-sliding phase, the friction force has a dynamic described by the following equation

$$\frac{dF_i}{dt} = k_i v \tag{7}$$

and the stage i continues to be in the pre-sliding phase till the friction force satisfy the condition $F_i = \alpha_i s_i(v)$. This condition is the first switching function.

- If the stage i is in sliding phase, the dynamic equation of the friction changes to the following equation

$$\frac{dF_i}{dt} = sign(v)\alpha_i C\left(1 - \frac{F_i}{\alpha_i s_i(v)}\right) \tag{8}$$

and the stage i continues to slide till the value of the velocity crosses zero. This condition is the second switching function.

Where k_i is the coefficient of elasticity of the stage i, F_i is the friction force of the stage i and C is a constant that characterize the hysteresis phenomenon in the friction force.

   The function $s_i(v)$ is the Stribeck function in the stage i and α_i is a weighting coefficient of the stage i. In order to simplify the friction model and to avoid handling a lot of parameters, only one stage of the friction is considered so the Stribeck function can be written as follows

$$s_i(v) = S(v) = sign(v)\sigma_c + sign(v)(\sigma_s - \sigma_c)e^{-\theta_s v^2} \tag{9}$$

where σ_c and σ_s are the Coulomb and Static coefficient, respectively. The parameter θ_s is the Stribeck coefficients.

The GMS friction model will be used in the robot manipulator and the objective of this work is to compensate the friction using a simple proportional derivative controller.

4   Least Square Estimation

For the compensation of the friction force, the online least square estimation (Lozano and Taoutaou 2001) is used. The estimator is based on a model given by

$$y = \theta^T \phi \tag{10}$$

where θ is the vector of unknown parameters and ϕ is the regressor vector which is known.

A matrix P is defined by:

$$P(t) = \left[\int_0^t \phi(\tau)\phi^T(\tau)d\tau \right]^{-1} \tag{11}$$

The dynamic of the estimator can be given by the following equation

$$\dot{\hat{\theta}}(t) = P(t)\phi(t)\left(y(t) - \phi^T(t)\hat{\theta} \right) \tag{12}$$

where the dynamic of the matrix P can be written as follows:

$$\dot{P}(t) = -P(t)\phi(t)\phi^T(t)P(t) \quad P(0) > 0 \tag{13}$$

The online least square estimator is based on linear and continuous formulation (Eq. 10). However, the friction model is nonlinear over its parameters and it is composed of two phases with a switching function. The solution of theses different problems is given in previous works (Grami and Bigras 2008; Grami and Aissaoui 2011). In fact, to solve the problem of nonlinearity of the friction model, a linearization about a nominal value was done. A filtering approach with a suitable commutation function were proposed to solve the problem of the switching function. Due to the proposed solution, the model of friction is transformed to a suitable formulation for which, the online square estimator can be used.

5 Switching Function

As described in Sect. 3, the switching function in the friction model is used to guarantee the transition from pre-sliding phase to the sliding phase and vice versa. The transition from sliding phase to pre-sliding phase occurs when the velocity crosses the value zero. This condition is detectable because the velocity signal is accessible. However, the trasition from the pre-sliding phase to sliding phase is guaranteed by the equality between the friction force and the Stribeck function which are both completely unknown.

To overcome this problem, the switching function from the pre-sliding phase to sliding phase is approximated. The approximation could be done in 2 steps:

Step 1 A prior value $\bar{k}$ and $\bar{\sigma}_c$ of the stiffness coefficient k and the coulomb coefficient σ_c should be found using offline identification. For the value of $\bar{k}$ is found using a test in pre-sliding phase and the value of σ_c can be found using any estimation procedure.

Step 2 The approximation of the switching function is built based on the a prior values of $\bar{k}$ and $\bar{\sigma}_c$ as shown in the following equation

$$\left| \int_{t_i}^{t} \bar{k}v\,dt + \bar{\sigma}_c sign(v(t_i^-)) \right| > \bar{\sigma}_c{}^+ \tag{14}$$

where t_i is the instant that precede the instant of switching from the sliding phase to pre-sliding phase i.e. when the velocity crosses the value zero and t_i^- is an infinitesimal instant before t_i. The parameter $\bar{\sigma}_c{}^+$ is defined by:

$$\bar{\sigma}_c{}^+ = \bar{\sigma}_c + \epsilon \tag{15}$$

where ϵ is an infinitesimal positive constant.

The terms $\bar{\sigma}_c sign(v(t_i-))$ and $\bar{\sigma}_c^+$ represent the approximation of the initial condition $F(t_i)$ and the Stribeck function $S(v)$, respectively. The quantity ϵ is introduced to ovoid switching at the beginning of the integration.

6 Control Law

The objective of this section is to introduce the control law of the robot manipulator, which is subject to an experimental friction generated by a linear motor having a surface in contact with a fixed mass. The control law of the robot will be based on a simple proportional derivative controller. To do that, the first stage of the control law is a linearized control law in which the estimated friction force is integrated in order to compensate the real friction force in each joint. The second stage of the control law is a simple proportional derivative controller (PD) which, will ensure the tracking of the desired trajectories. More details concerning the control law are shown in the Fig. 2 and the following equations. The first stage of the controller is a linearized control law which, can be defined by:

$$\tau = M(q)u + V(\dot{q}, q) + \hat{F}(\dot{q}) \tag{16}$$

where u is the control signal given by a PD controller as follows:

$$u = \ddot{q}_d + K_d\dot{\tilde{q}} + K_p\tilde{q} \tag{17}$$

where $\tilde{q} = q_d - q$ is the tracking error including the Eq. (16) in the model of the robot (Eq. (1)), we get the following equation:

$$M(q)\ddot{q} + V(\dot{q}, q) + F(\dot{q}) = \tau = M(q)u + V(\dot{q}, q) + \hat{F}(\dot{q}) \tag{18}$$

then, combining the Eqs. (17) and (18), we can write

$$M(q)(u - \ddot{q}) + (\hat{F}(\dot{q}) - F(\dot{q})) = 0 \qquad (19)$$

If the persistence of excitation is guaranteed, the estimated friction force will converge to the real friction force, so we can have

$$lim \ \hat{F}(\dot{q}) = F(\dot{q}) \qquad (20)$$

Hence, the Eq. (19) can be written by

$$M(q)(u - \ddot{q}) = 0 \ \text{then} \ u = \ddot{q} \qquad (21)$$

Now, combining the Eq. (21) with the Eq. (17), we get the dynamic equation of the error as follows:

$$\ddot{\tilde{q}} + K_d \dot{\tilde{q}} + K_p \tilde{q} = 0 \qquad (22)$$

The controller gains K_p and K_d are calculated using pole placement to get a zero overshoot and settling time T_s. Hence $K_p = \lambda^2$, $K_d = 2\lambda$ where $\lambda = \dfrac{4.73}{T_s}$. So, Since the dynamic of the error is a second order differential equation with constant coefficient, the pole placement guarantee the stability of error and if there is persistence of excitation, the error in the closed loop will converge to zero.

7 Experimental Setup

Because of the nonavailability of a real robot manipulator, a combined approach is used to validate the control of the robot. The friction force is generated from a linear motor having a surface in contact with a fixed mass. From the apparatus, the friction force is collected using a load sensor. The position, the velocity and the acceleration are collected from a position sensor installed in the apparatus. The velocity and the acceleration are calculated from the position and filtered in a program installed in the real time computer. A second computer is used to collect data from the real-time computer through the software MATLAB. The dynamic of the robot manipulator is programmed in MATLAB. However, the data of the desired position, velocity, and acceleration are collected from the experimental apparatus. The experimental friction is injected in the robot manipulator model (Fig. 2). Since the robot manipulator has two joints, so the experiment was done two times with two different conditions.
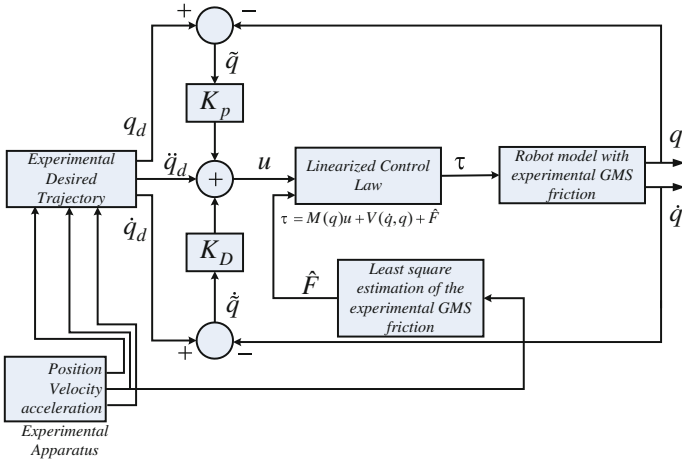
Fig. 2 The control schema of the robot manipulator

7.1 Performance Without Friction Compensation

In order to show the friction effect on the control performance of the robot manipulator, the experimental was done without injecting the estimated friction force in the control law. The Figs. 3 and 4 represent the desired position and the actual position for the first joint and the second joint respectively. It is shown that the friction affects considerably the performance of the tracking. The errors of tracking are presented

Fig. 3 Desired position angle q_{d1} and actual position angle q_1 (no friction compensation)

Desired and actual angle position for joint 1

- - Actual position
— Desired position

$q_1\ and\ q_{d1}\ (rad)$

Time (s)
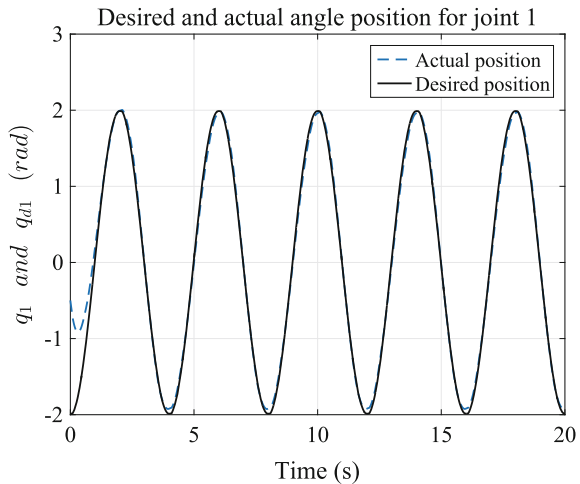
Fig. 4 Desired position
angle q_{d2} and real position
angle q_2 (no friction
compensation)

Desired and actual angle position for joint 2
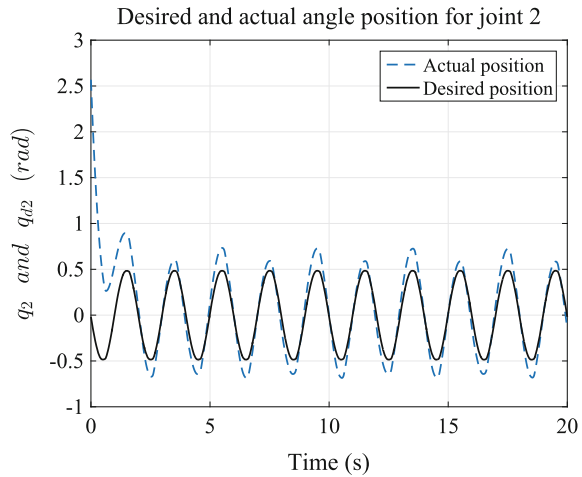
Fig. 5 Position angle error
for joint 1 (no friction
compensation)

Position angle error for joint 1
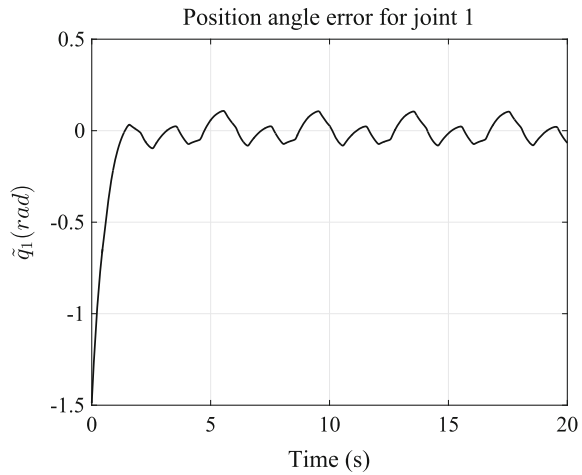
in Fig. 5 for the first joint and in the Fig. 6 for the second joint. It is clear from the
figures of error that the system cannot track the desired position with accuracy. It is
worthy to note that if there is error of 0.2 rad in the joint for a 0.5 m length means
that there will be at least 10 cm of error for the position tracking, which cannot be
tolerated in the robot manipulator position control.

Fig. 6 Position angle error for joint 2 (no friction compensation)
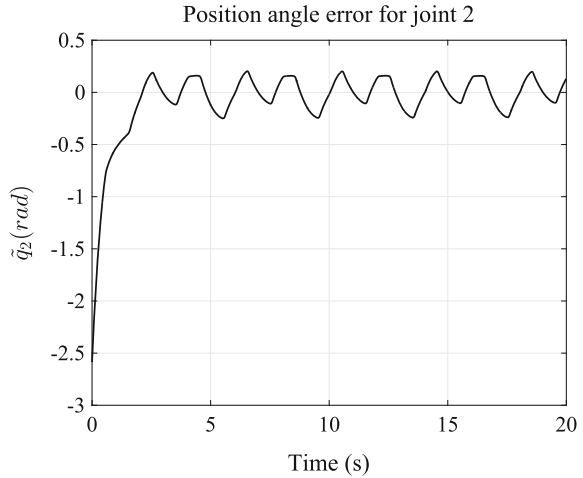
7.2 Performance With Friction Compensation

In this section, the friction compensation is investigated in the robot control as explained in the Sect. 6. In fact, using the least square estimator with the proposed approximated switch, the experimental friction is estimated and identified. The estimated friction is used in the control law to compensate for the real friction in the robot manipulator joints.

As presented in the Figs. 7 and 8, the tracking of the position angle in the first and the second joint are better than the tracking without friction compensation. The errors of tracking are converging to zero (Fig. 9) for both first and second joint (Fig. 10).

Fig. 7 Desired position angle q_{d1} and actual position angle q_1 (with friction compensation)
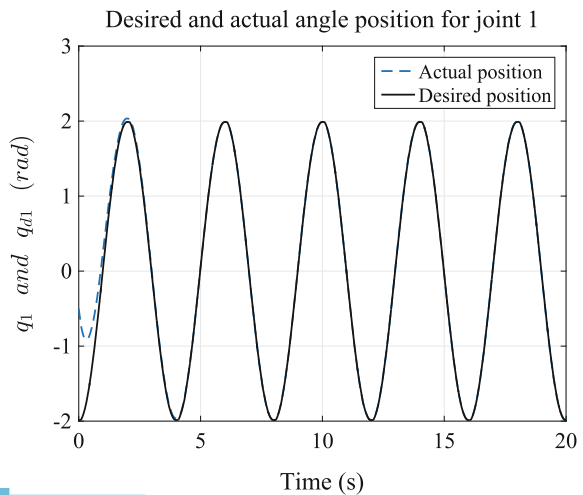
Fig. 8 Desired position angle q_{d2} and real position angle q_2 (with friction compensation)

Desired and actual angle position for joint 2
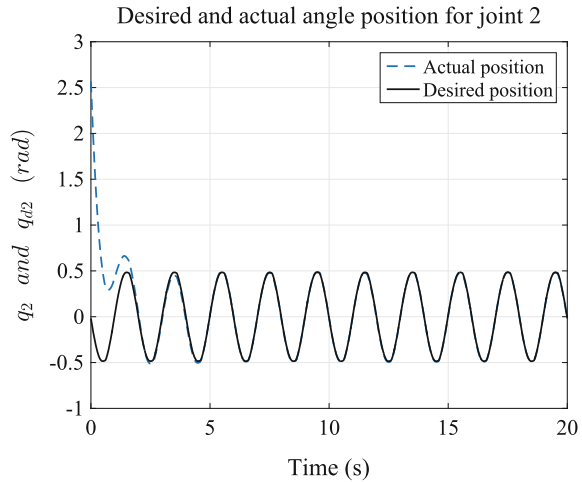
Fig. 9 Position angle error for joint 1 (with friction compensation)

Position angle error for joint 1
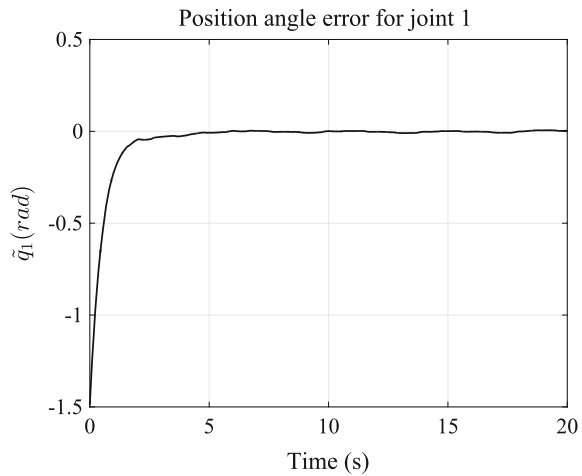
The Figs. 11 and 12 present the actual friction force and the estimated friction force using the approximated switching function. As shown, the estimated friction forces are close to the experimental friction forces. As a conclusion for this section, it is shown that the control of the robot manipulator is presenting a low performance when the friction forces in the joints are not compensated. In fact, an important difference is shown in the performance of the control without friction compensation and with friction compensation.

Fig. 10 Position angle error for joint 2 (with friction compensation)

Position angle error for joint 2
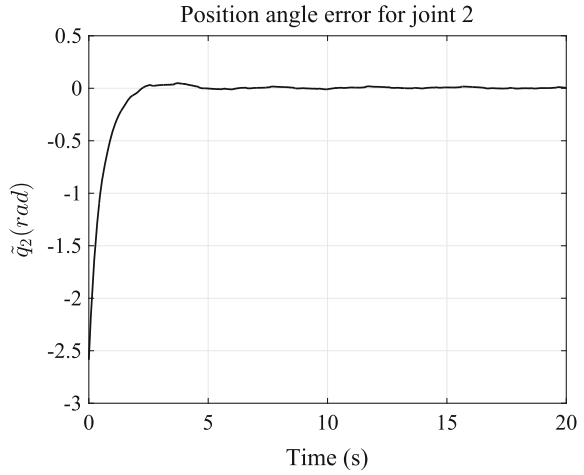
Fig. 11 Actual and estimated friction for the joint 1

Estimated and actual friction in joint 1
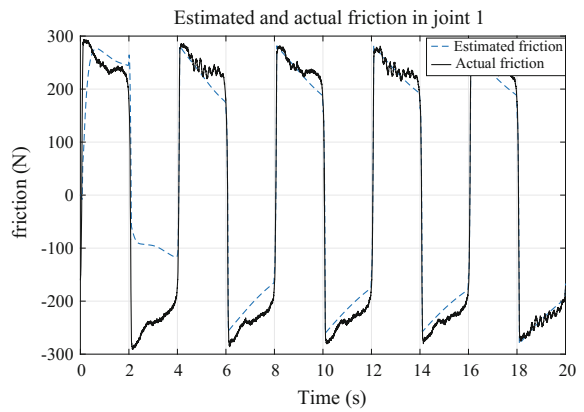
Fig. 12 Actual and estimated friction for the joint 2

Estimated and actual friction in joint 2
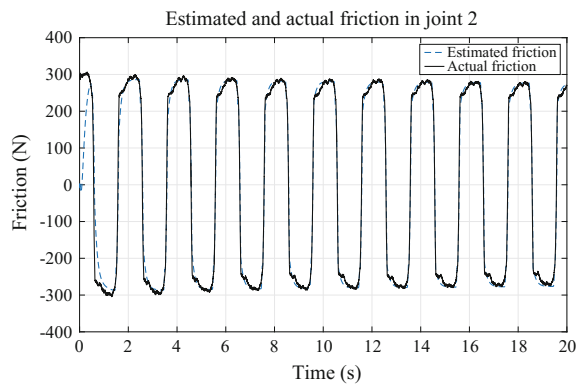
8 Conclusion

The compensation of GMS friction in two degree of freedom robot was presented. In order to identify the friction force, an online least square estimator was used and an approximated switching function was proposed to be used instead of the ideal switching function which is based on unknown parameters of the friction model.

A experimental test was done to show the efficiency of the approach proposed for the control of the robot manipulator using a simple proportional derivative controller.

The results of the experiment showed that without the compensation of friction, the performance of the system was not acceptable but with friction compensation the system was tracking the desired position and the desired velocity with a good accuracy.

References

Al-Bender F, Swevers J, Lampaert V (2005) The generalized Maxwell-slip model : a novel model for friction simulation and compensation. IEEE Trans Autom Control 50(1):1883–1887

Armstrong-Hélouvry B, Dupont P, de Wit CC (1994) A survey of models, analysis tools and compensation methods for the control of machines with friction. Automatica 30(7):1083–1138

Chernous'ko FL, Shunderyuk MM (2010) The influence of friction forces on the dynamics of two-link mobile robot. J Appl Math Mech 74:13–23

Dai F, Gao X, Jiang S, Gua W, Liu Y (2015) A two-wheeled inverted pendulum robot with friction compensation. Mechatronics. https://doi.org/10.1016/J.Mechatronics.2015.06.011

Do TN, Tjahjowidodo T, Lau MWS, Phee SJ (2015) Nonlinear friction modelling and compensation control of hysterisis phenomena for a pair of tendon-sheath actuated surgical robots. Mech Syst Signal Process 60:770–784

Garofalo G, Ott C (2016) Limit cycle control using energy function regulation with friction compensation. IEEE Robot Autom Lett 1(1):90–96

Grami S, Bigras P (2008) Identification of a new friction model based on robust adaptive observer. Int J Modell Identif Control 5(4):297–304

Grami S, Aissaoui H (2011) Filtering approaches for online identification of GMS friction model. In: EUROCON 2011—International conference on computer as a tool

Liu XF, Li HQ, chen YJ, Cai GP (2015) Dynamics and control of space robot considering joint friction. Mechatronics 111:1–18

Lozano R, Taoutaou D (2001). Identification et commande adaptative. Hermes Sciences Publication

Miyasaka M, Matheson J, Lewis A, Hannaford B (2015) Measurement of the cable-polly coulomb and viscous friction for a cable-driven surgical robotics system. In: 2015-IEEE/RSJ International conference on intelligent robots and systems. pp 804–810

Qin J, Lèonard F, Abda G (2016) Real time trajectory compensation in robot friction stir welding using state estimation. IEEE Trans Control Syst Technol. https://doi.org/10.1109/TSCT.20162536482

Vorochaeva LY, Naumov GS, Yatsun SF (2015) Simulation and motion of a three-link robot with controlled friction forces on a horizontal rough surface. J Comput Syst Sci Int 54(1):151–164

Wu J, Gao J, Song R, Li R, Jiang L (2016) The design and control of a 3DOF lower limb rehabilitation robot. Mechatronics 33:13–22

Anisotropic Elastic–Viscoplastic Modelling of a Quasi-unidirectional Flax Fibre-Reinforced Epoxy Subjected to Low-Velocity Impact

M. Abida, J. Mars, F. Gehring, A. Vivet and F. Dammak

Abstract In the past decades, research was directed towards the use of plant fibres instead of synthetic fibres as reinforcement of composites. Due to their high specific mechanical properties coupled with low cost and their wide availability at the European scale, flax fibres could be considered as the most interesting plant fibres. Experimental tests carried out on flax fibre-reinforced composites have shown that these latter are characterized by a nonlinear viscoelastic–viscoplastic behaviour. In this paper, our work was focused on modelling the elastic–viscoplastic behaviour of a quasi-unidirectional flax fibre-reinforced composites. First of all, we developed a three-dimensional elastic–viscoplastic model taking into account the orthotropic elasticity and the anisotropic viscoplastic behaviour of quasi-unidirectional flax/epoxy composites. Then, based on tensile tests at different strain rates, we identified the isotropic hardening using an optimized exponential Johnson–Cook law. The model was validated against experimental data. Finally, we implemented the behaviour model in a UMAT procedure of the finite element code ABAQUS/Implicit and simulated low-velocity impact behaviour of a flax/epoxy

M. Abida (✉) · J. Mars · F. Dammak
Mechanical Modeling and Manufacturing Laboratory (LA2MP),
National School of Engineers of Sfax, University of Sfax,
BP 1173-3038 Sfax, Tunisia
e-mail: marwa.abida@unicaen.fr

J. Mars
e-mail: jamelmars@yahoo.fr

F. Dammak
e-mail: fakhreddine.dammak@enis.rnu.tn

M. Abida · F. Gehring · A. Vivet
Normandie University, ENSICAEN, UNICAEN, CEA, CNRS, CIMAP,
14000 Caen, France
e-mail: florian.gehring@unicaen.fr

A. Vivet
e-mail: alexandre.vivet@unicaen.fr

circular plate. Simulation has shown that the impact velocity has a great influence on the behaviour of flax fibre-reinforced epoxy composite plate.

Keywords Viscoplastic model · Flax fibre · Composite · 3D simulation Anisotropic behaviour · Hill criterion

1 Introduction

In the past decades, researchers have become more interested in plant fibres which originate from renewable resources as reinforcement of composites instead of synthetic fibres. In fact, natural fibres are eco-friendly that is why their use in the industrial application is ever increasing (Bos 2004). As they offer many advantages namely high specific mechanical properties coupled with low cost and a wide availability at the European scale, flax fibres could be considered as the most interesting plant fibres (Gourier et al. 2014). Actually, experimental tests have shown that flax fibre-reinforced composites are characterized by a nonlinear viscoelastic–viscoplastic behaviour (Poilane et al. 2014). In order to use flax fibre as reinforcement in composites for structural applications, a rough comprehension and a correct prediction of their behaviour is needed. However, few researches were carried out in this domain.

This work was divided into three sections; the first section was devoted to establishing a 3D viscoplastic model which takes into account the anisotropic behaviour. In this model, the plasticity was described using Hill criterion. The second section consisted of identifying an optimized exponential Johnson–Cook law. Stress–strain curves for different values of strain rates were used in order to identify the viscoplastic behaviour of flax fibre-reinforced composites. Finally, the third section consists of testing the performance of the model. Actually, a low-velocity impact test on a flax/epoxy circular plate composite was simulated to validate the identified model. This viscoplastic isotropic hardening model was implemented into a user-defined material (UMAT) subroutine for the finite element code ABAQUS/Implicit.

2 Flax/Epoxy Composite Behaviour

2.1 *Experimental Anisotropic Behaviour*

The material tested was a quasi-unidirectional flax-reinforced epoxy composite, based on so-called FUD 180 flax reinforcement supplied by LINEO NV Company. In the studied flax/epoxy composite, all plies had the same orientation.

Table 1 Elastic properties of FUD180-based composite materials (Cherif et al. 2016)

E_{11} (GPa)	$E_{22} = E_{33}$ (GPa)	$G_{12} = G_{13}$ (GPa)	G_{23} (GPa)	$\nu_{12} = \nu_{13}$	ν_{23}
29.2 ± 1.0	4.7 ± 0.3	1.86 ± 0.17	1.66 ± 0.15	0.37 ± 0.01	0.40 ± 0.06

The quasi-unidirectional flax/epoxy composite is marked by an anisotropic behaviour. Using tensile tests on samples with different fibre orientations (0°, 45° and 90°), the elastic properties of this composite were identified and given in Table 1 (Cherif et al. 2016).

2.2 3D Model Formulation: Orthotropic Elasticity and Anisotropic Viscoplasticity

A 3D viscoplastic model with isotropic hardening, taking into account the orthotropic elasticity and anisotropic plasticity was established.

The total strain tensor $\boldsymbol{\varepsilon}$ is composed of an elastic strain tensor $\boldsymbol{\varepsilon}^e$ and a viscoplastic (irreversible) strain tensor $\boldsymbol{\varepsilon}^p$.

$$\boldsymbol{\varepsilon} = \boldsymbol{\varepsilon}^e + \boldsymbol{\varepsilon}^p \tag{1}$$

The elastic strain is related to stress tensor $\boldsymbol{\sigma}$ by the elastic stiffness by the rigidity matrix as

$$\boldsymbol{\sigma} = \mathbf{D} : \boldsymbol{\varepsilon}^e \tag{2}$$

The compliance matrix $\mathbf{S}$ which is the inverse of the elasticity matrix $\mathbf{D}$ was expressed as follows:

$$\mathbf{D} = \mathbf{S}^{-1}; \quad \mathbf{S} = \begin{bmatrix} \frac{1}{E_1} & -\frac{\nu_{12}}{E_1} & -\frac{\nu_{13}}{E_1} & 0 & 0 & 0 \\ & \frac{1}{E_2} & \frac{-\nu_{23}}{E_2} & 0 & 0 & 0 \\ & & \frac{1}{E_3} & 0 & 0 & 0 \\ & Sym & & \frac{1}{G_{12}} & 0 & 0 \\ & & & & \frac{1}{G_{13}} & 0 \\ & & & & & \frac{1}{G_{23}} \end{bmatrix} \tag{3}$$

The yield criterion can be written as

$$f = \varphi(\boldsymbol{\sigma}) - (\sigma_Y + R); \quad \sigma_p = \sigma_Y + R \tag{4}$$

where σ_Y is the initial yield stress, $\varphi(\boldsymbol{\sigma})$ is the equivalent stress and R is the drag stress in isotropic hardening. In our case, the yield stress is equal to $\sigma_Y = 33\,\text{MPa}$

and we chose to express the drag stress R by an optimized Johnson–Cook law defined as

$$\sigma_p = \left(\sigma_y + Q(1 - \exp(-\beta\varepsilon^p)) + k\varepsilon^p\right)\left(1 + C\text{Log}(\dot{\varepsilon}_0/\dot{\varepsilon}_0)\right) \tag{5}$$

With k is the asymptotic hardening modulus, Q and β describe the nonlinear part of the tensile curve when plasticity appears, and C represents the strain rate sensitivity coefficient. $\dot{\varepsilon}_0$ is the reference strain rate and $\dot{\varepsilon}$ represents the strain rate.

The identification of the modified Johnson–Cook law consists in determining the material parameters Q, β, k, and C.

In order to express the anisotropic plasticity, the equivalent stress $\varphi(\boldsymbol{\sigma})$ can be described by the Hill criterion (Hill (1948)).

$$\varphi(\boldsymbol{\sigma}) = \sqrt{\boldsymbol{\sigma}^T \mathbf{H} \boldsymbol{\sigma}} \tag{6}$$

$$\mathbf{H} = \begin{bmatrix} H+G & -H & -G & 0 & 0 & 0 \\ & H+F & -F & 0 & 0 & 0 \\ & & F+G & 0 & 0 & 0 \\ & & & 2N & 0 & 0 \\ & Sym & & & 2M & 0 \\ & & & & & 2L \end{bmatrix} \tag{7}$$

H, G, F, N, M and L are Hill material constants (Hill (1948)) to be identified. The details of the formulation and numerical implementation of the present model can be found in (Wali et al. 2015, 2016; Mars et al. 2015; Ben Said et al. 2016; Belhassen et al. 2016; Koubaa et al. 2017).

The previous tensile stress–strain curves obtained with composite samples with different fibre orientations (0°, 45° and 90°) were also used to determine the Hill's material parameters (Table 2).

In order to identify the material parameters of the optimized Johnson–Cook law and thus determine the behaviour of flax fibre-reinforced epoxy, tensile tests at different strain rates carried out by Poilane et al. (2014) were explored. The strain rates were $\dot{\varepsilon}_0 = 10^{-6}\,\text{s}^{-1}$, $\dot{\varepsilon} = 10^{-5}\,\text{s}^{-1}$, $\dot{\varepsilon} = 10^{-4}\,\text{s}^{-1}$ and $\dot{\varepsilon} = 10^{-3}\,\text{s}^{-1}$. According to these tests, flax fibre-reinforced epoxy composites are characterized by a viscoplastic behaviour. The identification of the Johnson-–Cook material parameters was accomplished in two steps. In the first step, we identified the hardening

Table 2 Hill's material parameters

F	G	H	N	M	L
4.38	0.50	0.50	3.20	3.20	3.20

Table 3 Material parameters of the optimized Johnson–Cook law

Q (MPa)	β	K (MPa)	C
6.015	1210	20684	0.152

Fig. 1 Model validation by comparison with the experimental curves from Poilane et al. (2014)

Fig. 1 Model validation by comparison with the experimental curves from Poilane et al. (2014)
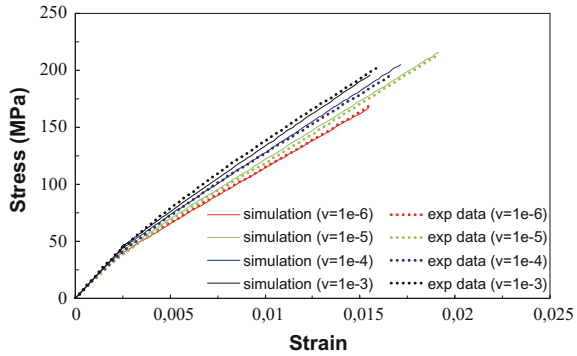
parameters (Q, β and k) using the least square method for the stress–strain curve at the reference strain rate ($\dot{\varepsilon}_0 = 10^{-6}$ s^{-1}). Then, as a second step, we proceeded to determine the coefficient C by inserting the values of the hardening parameters and of the strain rates in Eq. (8). The identified material parameters of the optimized Johnson–Cook law were given in Table 3.

$$\frac{\sigma}{\sigma_0} - 1 = CLog\left(\frac{\dot{\varepsilon}}{\dot{\varepsilon}_0}\right); \quad \sigma_0 = \left(\sigma_y + Q(1 - \exp(-\beta\varepsilon^p)) + k\varepsilon^p\right) \tag{8}$$

Our model was validated with the experimental data as shown in Fig. 1.

Experimental and the simulation stress–strain curves were represented Fig. 1. The model (simulation curves) was validated against experimental curves.

3 Three-Dimensional Low-Velocity Impact Simulation

3.1 3D Model

In this section, low-velocity impact tests on a flax/epoxy circular plate composite were simulated in order to validate the model and to deal with the impact phenomenon encountered in the aeronautics and automotive fields. The impactor chosen was a steel hemispherical nosed cylinder of 10 mm radius and 28.6 g mass. The projectile hits flax/epoxy circular plate of 60 mm radius and 1 mm thickness with an initial velocity V_0 (Koubaa et al. 2017; Mars et al. 2015). The circular plate was clamped at its borders and the projectile was subjected only to a movement in the Y direction (Fig. 2). The contact between the impactor and the plate was referred to as ''hard'' contact. Both of the geometries meshed with 8-node hexahedral elements (C3D8). In order to obtain more accurate results, the meshing was refined in the contact zone in the circular plate and in the impactor.

The identified behaviour model was implemented into a UMAT subroutine of the finite element code ABAQUS/Implicit. This UMAT procedure was used to simulate 3D low-velocity impact behaviour of a quasi-unidirectional flax-reinforced epoxy composite.

3.2 Numerical Results

The response of the flax/epoxy composite plate was dependent on the impact velocity. As shown in Fig. 3, the impact force curves contained several undulations. In fact, this can be explained by the rigidity of the plate. As the impactor sinks into the plate and the impactor velocity still has not reached zero, this latter tries to
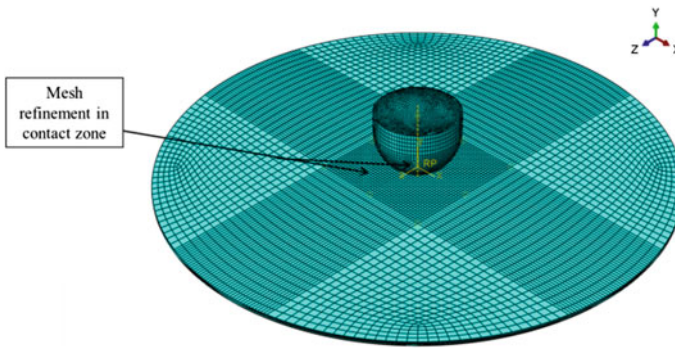
Fig. 2 Model and meshing representation

Fig. 3 Evolution of the impact force in time for different impact velocities (v = 5 m/s and v = 10 m/s)
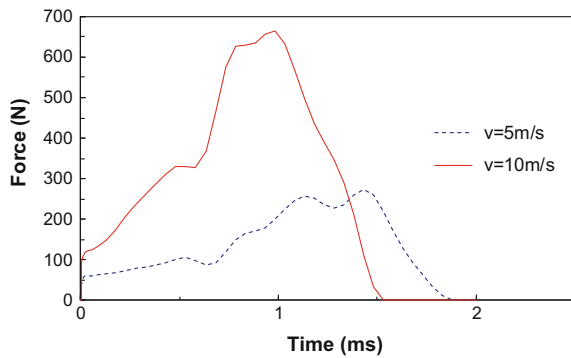
amortize the choc and reject the projectile. Thus, this induces the undulations seen the impact force response. The evolution of the impact force in time for different impact velocities, given in Fig. 3, showed that when the impact velocity increased, the impact force increased but the impact time decreased which is expected. Qualitatively, this is a proof of a valid model implementation. However, it requires experimental validation tests that are being currently developed.

4   Conclusion

In this paper, the viscoplastic behaviour of quasi-unidirectional flax fibre-reinforced epoxy composite was investigated. Using tensile tests at different strain rates, we established a 3D formulation in order to model the anisotropic viscoplastic beha-viour of flax fibre-reinforced composite. Actually, we developed a 3D viscoplastic model with isotropic hardening using Hill criterion. Then, an identification of the optimized Johnson–Cook law was carried out. The model identified was imple-mented in a UMAT/ABAQUS to simulate 3D low-velocity impact behaviour. A circular plate was subjected to an impact at different initial velocities. The numerical results showed that the impact velocity has a great influence on the response of the composite plate. Experimental impact tests remain planned as a future work in order to validate the model in the same ranges of strain rate.

References

Belhassen L, Koubaa S, Wali M, Dammak F (2016) Numerical prediction of springback and ductile damage in rubber-pad forming process of aluminum sheet metal. Int J Mech Sci 117:218–226

Ben Said L, Mars J, Wali M, Dammak F (2016) Effects of the tool path strategies on incremental sheet metal forming process. Mech Ind 17(4):411

Bos HL (2004) The potential of flax fibers as reinforcement for composite materials. Eindhoven Technische Universiteit Eindhoven, p 192. http://www.greengran.com/download/thesisBos.pdf

Cherif ZE, Poilâne C, Vivet A, Ben Doudou B, Chen J (2016) About optimal architecture of plant fiber textile composite for mechanical and sorption properties. Compos Struct 140:240–251

Gourier C, Le Duigou A, Bourmaud A, Baley C (2014) Mechanical analysis of elementary flax fiber tensile properties after different thermal cycles. Compos A 64:159–166

Hill R (1948) A Theory of the yielding and plastic flow of anisotropic metals. Proc R Soc: Math, Phys Eng Sci 193(1033):281–297

Koubaa S, Mars J, Wali M, Dammak F (2017) Numerical study of anisotropic behavior of Aluminum alloy subjected to dynamic perforation. Int J Impact Eng 101:105–114

Mars J, Wali M, Jarraya A, Dammak F, Dhiab A (2015) Finite element implementation of an orthotropic plasticity model for sheet metal in low velocity impact simulations. Thin-Walled Struct 89:93–100

Poilane C, Cherif ZE, Richard F, Vivet A, Ben Doudou B, Chen J (2014) Polymer reinforced by flax fibers as a viscoelastoplastic material. Compos Struct 112:100–112

Wali M, Chouchene H, Ben Said L, Dammak F (2015) One-equation integration algorithm of a
    generalized quadratic yield function with Chaboche non-linear isotropic/kinematic hardening.
    Int J Mech Sci 92:223–232

Wali M, Autay R, Mars J, Dammak F (2016) A simple integration algorithm for a non-associated
    anisotropic plasticity model for sheet metal forming. Int J Numer Methods Eng 107(3):
    183–204

Dynamic Simulation of a Partial Unloaded Walking Within the Cable Driven Legs Trainer Using MATLAB SimMechanics

Houssein Lamine, Sami Bennour and Lotfi Romdhane

Abstract This paper focuses on a dynamic simulation of a partial unloaded walking motion within a gait training machine using the simulation tool: MATLAB SimMechanics. This training machine emulates the walking through: a body weight support device and a cable driven leg manipulator. The human body is modeled as a multi-segment articulated mechanism. Length and inertia specifications of body segments are determined based on anthropometric data. The main external forces acting on the human body are the unloading force applied to the upper body, the ground reaction force and the actuation wrench produced by the leg manipulator. The Matlab SimMechanics software is used to simulate dynamically the walking motion in order to calculate the required wrench to drive the lower limb during a cycle of a normal gait. In fact, the human body is created according to kinematic and dynamic modeling, and besides, the external forces are applied to the body segments. Considering a body having a mass of 100 kg and a height of 1.7 m, curves of actuation wrench are retrieved.

Keywords Gait training · SimMechanics · Dynamic simulation

H. Lamine (✉) · S. Bennour · L. Romdhane
Mechanical Laboratory of Sousse (LMS), National Engineering School of Sousse,
University of Sousse, 4000 Sousse, Tunisia
e-mail: houssein.lamine@gmail.com

S. Bennour
e-mail: sami.bennour@gmail.com

L. Romdhane
e-mail: lotfi.romdhane@gmail.com

L. Romdhane
Mechanical Engineering Department, American University of Sharjah, Sharjah,
United Arab Emirates

179

1 Introduction

Gait training machine is employed to relearn walking for subjects attained with neurological deficits. Intense and task-oriented training leads to the regeneration and the repair of the nervous systems, which is the motion control system of the human body. In contrast to therapist-assisted rehabilitation, the robotized machines promote recovery of ambulation by increasing the total duration of therapy and decreasing the labor and intensive workload (Maria et al. 2013; Hornby et al. 2005). Such machines comprise essentially a body weight support system to suspend the upper body and an actuated orthosis to move the lower limb.

So far, market available machines can be classified into 2 forms: a serial robot attached to the thigh and the leg (e.g., Lokomat (Colombo et al. 2000) and ReoAmbulator (West 2004)), and second ones are devices that use movable footplates to drive the feet (e.g., the gait trainer (Hesse and Uhlenbrock 2000) and the G-EO (Hesse et al. 2010)). In our case, we are interested in a gait trainer that moves the lower limb through an orthosis placed at the leg and controlled by a cable robot. This machine is called Cable Driven Legs Trainer (CDLT). This design has some interesting advantages mainly high dynamic performance, less intrusion, and low cost.

The paper is organized as follows: In Sect. 2, an overview of the CDLT is presented. Then the required data of a normal human gait are given in Sect. 3. A dynamic modeling is formulated in Sect. 3 and an inverse dynamic simulation using MATLAB SimMechanics is investigated in Sect. 5. Finally, the results of a case study using the developed model are shown.

2 Overview of the Cable Driven Legs Trainer and Kinematic Modeling

The CDLT is a cable robot-based rehabilitation machine shown in Fig. 1a. It comprises: (i) a Body Weight Support Device (BWSD) to suspend the patient in vertical posture while applying a certain amount of unloading, (ii) a Cable Driven Leg Manipulator (CDLM) to move the lower limb in the sagittal plane through a leg's orthosis controlled by a set of cables and (iii) a Treadmill to emulates the forward movement of walking.

In this work, we are interested in the actuation wrench to be produced by the CDLM in order to drive the lower limb during a gait cycle.

The body is represented by a planar four-link mechanism (Fig. 1b): the upper body (known also as head, arms, and trunk (HAT) segment (Zajac et al. 2002), the thigh, the leg, and the foot. The linkage between the trunk and the fixed frame is modeled as a prismatic joint. For the hip, knee, and ankle, they are modeled as revolute joints. Thus, the body is characterized by 4 DOF.
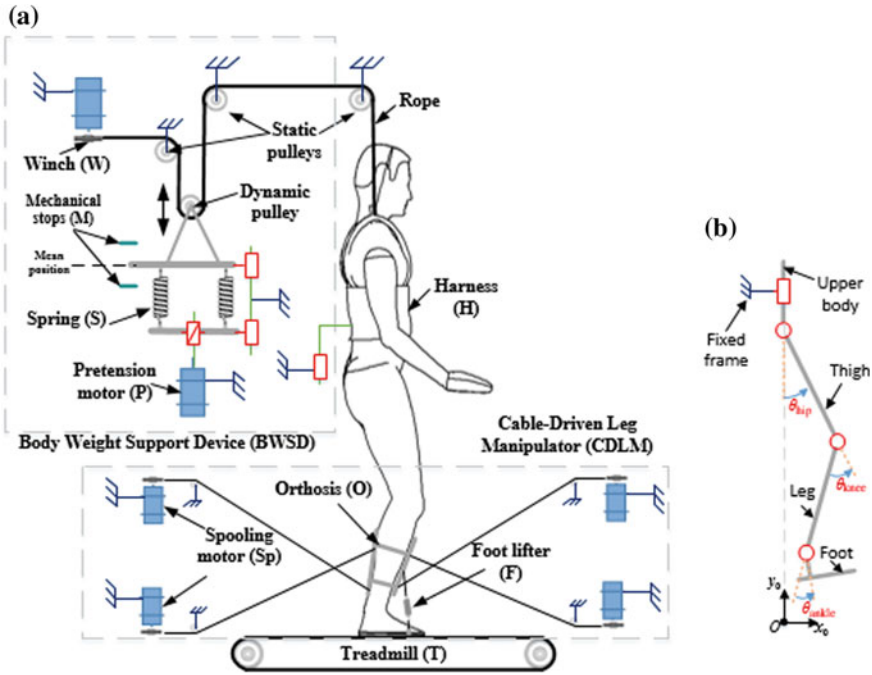
Fig. 1 **a** Diagram of the Cable-Driven Legs Trainer (CDLT), and **b** Kinematic model

3 Normal Human Gait Data

The human gait data are the joint trajectories and the ground reaction force. These two information are obtained from an experiment performed in the biomechanics laboratory of PPRIME institute (Poitiers University, France), using an optical motion capture system and a force platform.

A gait cycle is defined as a sequence of repetitive events, starting and ending with the same event. The two legs have the same series of events, with a phase shift of one-half cycle (Whittle 2014). A normal walk cycle has two main phases: Stance phase and Swing phase. During stance time the foot is on the ground, over the swing time the foot is no longer in contact with the ground (Vaughan et al. 1999).

The movement of the lower extremity is the vertical displacement of the pelvis and the flexion-extension of the hip, the knee, and the ankle. During a gait cycle, the kinematics are given in Fig. 2.

Considering the dynamics of a human gait, the ground reaction force acting on the foot is shown in Fig. 3, it includes normalized vertical (*NRv*) and antero-posterior (*NRap*) reaction curves. The term normalized refers to a normalization relative to the body mass.

Further information on the gait data can be found in Whittle (2014), Vaughan et al. (1999), Winter (2009).
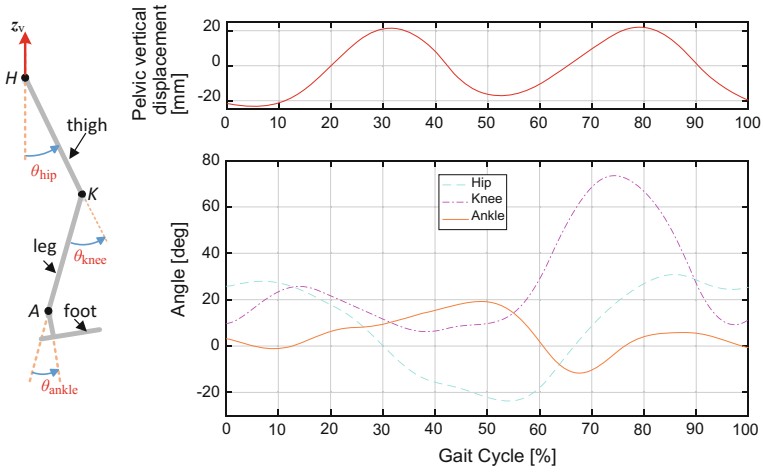
Fig. 2 Kinematics of the lower limb during a gait cycle

Fig. 3 Normalized ground
reaction
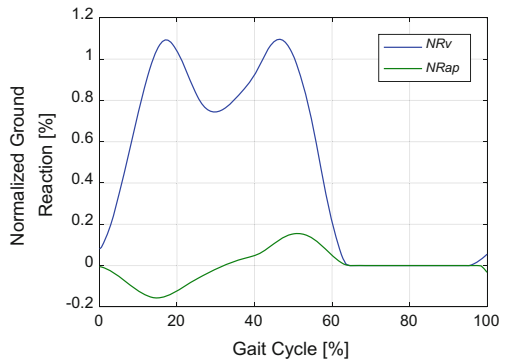
4 Dynamic Modeling

In this section, we give the necessary data and formulations, required for the
SimMechanics model. It is worth mentioning that the proposed dynamic modeling
is based on the following assumptions:

- All the joints are considered passive, thus muscles contribution is ignored which
  can be viewed as the most disadvantageous case,
- The orthosis is solitary to the leg,
- The lower limb kinematics are the same as during a normal walking.
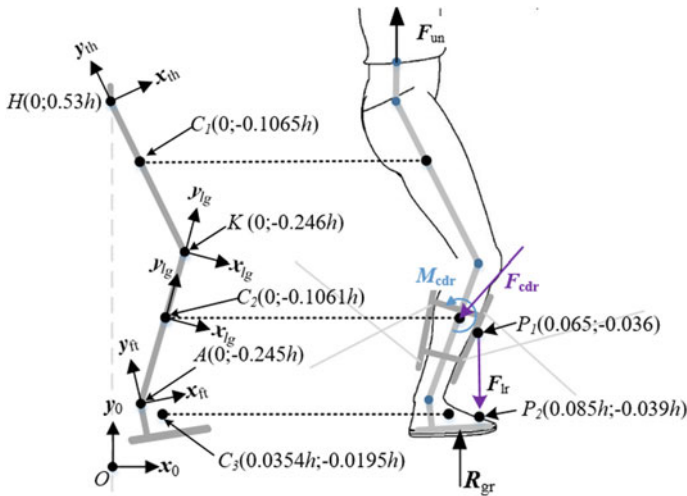
Fig. 4 Kinematic model and external loads acting on the human body

4.1 Length and Inertia Specifications

Based on anthropometric measurements, the geometric and inertia proprieties of body segments can be written as a fraction of the mass and/or the height of the body. Hereby, reference (Winter 2009) is used to get the body anthropometric specifications, geometric data are shown in Fig. 4.

Coordinates of C_1, K, C_2, A, C_3, P1, and P_2 are defined in relation to their local frames as a fraction of the body height h.

4.2 Formulation of External Loads

The main external loads acting on the human body are as follows:

- F_{un}, the unloading force produced by the springs included in the BWSD and applied at the upper body through the harness system:

$$F_{uny} = (k/2) \cdot (y_0 + \Delta y/2) \text{ such that } y_0 = (BWS \cdot g \cdot m)/(k/2) \tag{1}$$

$k = 4$ Nm is the total springs constant, g $= 9.81$ m/s^2 is the gravity acceleration, m is the body mass, and the instantaneous position Δy follows the pelvic displacement curve (see Fig. 2). The springs offset y_0 is calculated based on the desired amount of unloading BWS.

Fig. 5 Curve of α coefficient
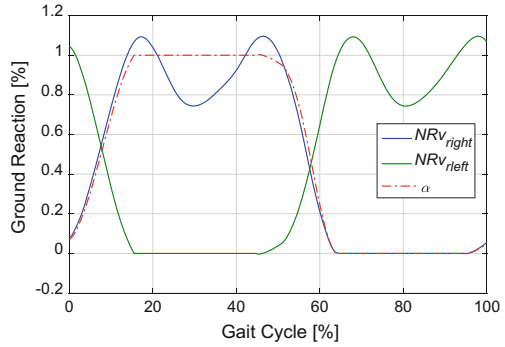
- R_{gr}, the ground reaction force applied at the sole of the foot:

$$R_{gr} = W_n \cdot NR_{gr} \text{ such that } W_n = m \cdot g - F_{uny} \text{ and } NR_{gr} = \begin{pmatrix} NRv & NRap \end{pmatrix}^T \quad (2)$$

- The resultant force and moment (F_{cdr} and M_{cdr}), which are the actuation unknowns to be generated by the cable robot in order to achieve walking.
- F_{lr}, the foot lifter force acting between the leg's orthosis and the foot in order to stabilize the ankle joint during the swing phase of the gait cycle.

Here, an important issue is how to model the participation of one limb in supporting the weight of the upper body. For that, a coefficient named α is defined such that is equal to 1 during single limb stance and zero during swing time. Throughout double support phases, it varies from 0 to 1, and is calculated based on the vertical normalized ground reaction NRv of the two foot: $\alpha = (NRv_{right} + NRv_{left}) / NRv_{right}$. Figure 5 shows the change of this factor along with the variation of NRv of the feet over one gait cycle.

5   SimMechanics-Based Dynamic Simulation

In this section, we describe the way in which the inverse dynamic problem is solved employing MATLAB SimMechanics Software.

The first step in model development is the creation of body parts and the definition of joints. The developed SimMechanics model is shown in Fig. 6. According to the kinematic human model (Fig. 1b): the "Upper body" has a prismatic joint with the fixed frame "Base" and the body segments ("Upper Body," "Thigh," "Leg + Orthosis," and "Foot") are articulated with a set of 3 revolute joint blocks: "Hip joint," "Knee joint," and "Ankle joint". Furthermore, geometric and inertia specifications are written into body blocks.

In a second step, the external loads are applied according to the formulation investigated in Sect. 3. The unloading force "Fun" is computed inside the block
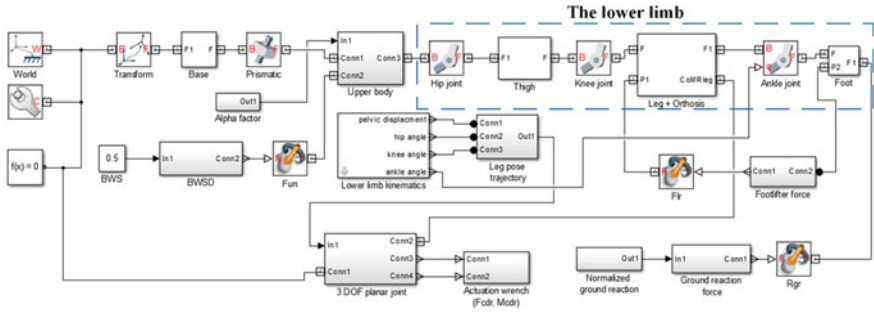
Fig. 6 MATLAB SimMechanics Model

"BWSD" with respect to the desired unloading amount "BWS" using Eq. (1). Knowing the position of placement points P_1 and P_2, the foot lifter force F_{lr} is computed based on moment equilibrium of the foot weight about the ankle joint. Based on the normalized ground reaction, the "Rgr" force is computed using Eq. (2) and it is applied on the foot segment. Lastly, by inputting the curve of α coefficient (see Fig. 5), the action of the upper body force on the thigh is computed inside the block "Upper body."

In order to obtain the actuation wrench produced by the robot during a gait cycle, the used technique is to actuate the lower limb through an active joint "3 DOF planar joint" placed at the leg center of mass, for the other joints, they are kept passive. This custom joint has two linear and one rotational DOFs. The data of the block "Lower limb kinematics" are fed to the block "leg pose trajectory", in which the leg trajectory is computed using the Eq. (3) and then sent to the leg segment for actuation.

$$\begin{pmatrix} {}^0C_{2x} \\ {}^0C_{2y} \\ \phi_{lg} \end{pmatrix} = \begin{pmatrix} C_{2y} \cdot \sin(\theta_{knee} - \theta_{hip}) - K_y \cdot \sin(\theta_{hip}) \\ H_y + K_y \cdot \cos(\theta_{hip}) + C_{2y} \cdot \cos(\theta_{knee} - \theta_{hip}) \\ \theta_{hip} - \theta_{knee} \end{pmatrix} \qquad (3)$$

The output information from this simulation is collected from the block "Actuation wrench (F_{cdr}, M_{cdr})" which is computed by the software solver inside the "3 DOF joint" block.

It is worth mentioning that the developed model is parametrized, i.e., the parameter values of blocks can be set in command line. Thereby all geometric and inertial properties of the human body can be easily changed through the execution's script.

Validation of the developed model is carried out taking the example of a body having a mass $m = 100$ kg, a tall $h = 1.7$ m, an amount of unloading $BWS = 50\%$ and a gait cycle time $t_{gc} = 1.4$ s. Table 1 summarizes all the dynamic simulation data.

Once all dynamic simulation data are set, the model is executed and the obtained curves of the leg trajectory and the actuation wrench are visualized, respectively, in Figs. 7 and 8.

Table 1 Dynamic simulation data

Parameters	Value	Parameters	Value	Parameters	Value
h (m)	1.7	I_{th} (kg m^2)	0.181	C_1 (m; m)	(0; −0.1803)
m_{ub} (kg)	67.8	I_{lg} (kg m^2)	0.0742	C_2 (m; m)	(0; −0.1811)
m_{th} (kg)	10	I_{ft} (kg m^2)	0.0068	C_3 (m; m)	(0.0613; −0.0331)
m_{lg} (kg)	4.65	I_{or} (kg m^2)	0.0153	P_1 (m; m)	(0.065; −0.036)
m_{ft} (kg)	1.45	k (kN/m)	4	P_2 (m; m)	(0.1445; −0.0663)
m_{or} (kg)	1.2	g (m/s^2)	9.81		
BWS (%)	50	t_{gc} (s)	1.4		
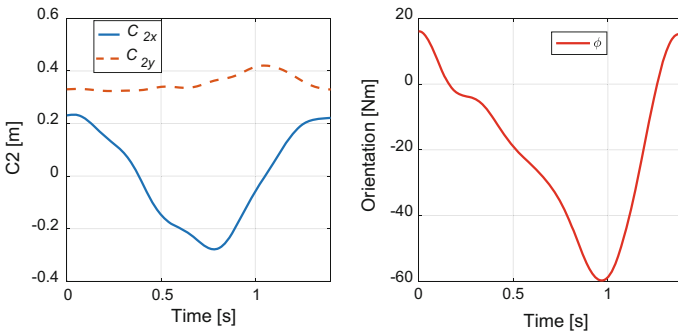
Fig. 7 Leg pose trajectory of the leg during a gait cycle
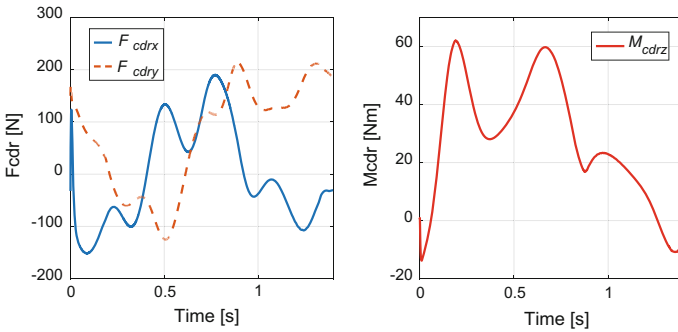
Fig. 8 Variation of the actuation wrench (Fcdr, Mcdr)

For both F_{cdrx} and M_{cdrz}, curves vary inversely proportional to the position abscissa C_{2x} and the orientation ϕ, respectively, which confirms that the external wrench is used to resist forces going in the same direction of motion. Now, considering F_{crdy} during the swing phase from 0.88 to 1.32 s approximately, this component is positive since we need an upward force in order to maintain the leg in the air, otherwise it is the sum of forces propagating from the ground and the upper

body. Note that for the carried simulation, the joints are assumed to be passive, therefore, only forces can be transmitted. Besides, taking into account muscle participation in producing motion will affect the curves of actuation wrench.

6 Conclusion

A dynamic simulation of an unloaded walking was carried out using MATLAB SimMechanics. Details including kinematic and dynamic modeling were presented. Then, a SimMechanics model was developed and simulated using the kinematics of a normal human gait. The actuation wrench was determined for a body having a mass of 100 kg and a height of 1.7 m. This result can be used to assess the progress of a gait recovery. Ongoing works are underway to present more realistic models regarding the simulation of a gait.

References

Colombo G et al (2000) Treadmill training of paraplegic patients using a robotic orthosis. J Rehabil Res Dev 37(December):693–700

Hesse S, Uhlenbrock D (2000) A mechanized gait trainer for restoration of gait. J Rehabil Res Dev 37(6):701–708

Hesse S, Waldner A, Tomelleri C (2010) Innovative gait robot for the repetitive practice of floor walking and stair climbing up and down in stroke patients. J Neuroeng Rehab 7:30

Hornby TG, Zemon DH, Campbell D (2005) Robotic-assisted, body-weight-supported treadmill training in individuals following motor incomplete spinal cord injury. Phys Ther

Maria C et al (2013) Locomotor training with partial body weight support in spinal cord injury rehabilitation: literature review 26(4):907–920

Vaughan CL et al (1999) Dynamics of human gait. Kiboho Publishers

West RG (2004) Powered gait orthosis and method of utilizing same

Whittle MW (2014) Gait analysis: an introduction. Butterworth-Heinemann

Winter DA (2009) Biomechanics and motor control of human movement. Wiley

Zajac FE, Neptune RR, Kautz SA (2002) Biomechanics and muscle coordination of human walking: part I: introduction to concepts, power transfer, dynamics and simulations. Gait Posture 16(3):215–232

Hysteresis Identification Models: A Review

Khaoula Hergli, Haykel Marouani and Mondher Zidi

Abstract Magnetic properties of soft ferromagnetic materials are very sensitive to high mechanical and thermal stresses. In order to characterize its changing magnetic behavior, this chapter deals with the study of the choice of the performant magnetic hysteresis model, which can be able to model perfectly the thermo–magnet–mechanical coupling of a fully processed non-oriented Fe-3 wt%Si steel sheet. Therefore, our study focuses on identifying the model parameters for different static models by application of an appropriate optimization technique. For simple models, a direct identification is used, and the GA technique will be applied for complex ones. The performance of the model depends on the error that it presents with the measurements as well as its ability to reproduce properly the experimental hysteresis studied. Our study is based on the static models of Rayleigh, Potter, Frolich, and Preisach. Identification results show that the Preisach and Frolich static models can model the hysteresis curve of the Fe-3 wt%Si steel sheet more accurately than the other models studied.

Keywords Magnetic hysteresis modeling · Parameter identification
Soft ferromagnetic materials

K. Hergli (✉) · M. Zidi
University of Monastir, LGM, ENIM, Avenue Ibn-Eljazzar, 5019 Monastir, Tunisia
e-mail: hergli.khaoula@gmail.com

M. Zidi
e-mail: mondherzidi@gmail.com

H. Marouani
College of Engineering, Muzahimiyah Branch, King Saud University,
2454, Riyadh 11451, Saudi Arabia
e-mail: h.marouani@gmail.com

1   Introduction

Magnetic materials are widely used in various engineering applications and electromechanical systems such as shape memory alloy for seismic dampers and arterial stents, piezoelectric, piezoceramic, electric transformers, and electromechanical actuators which makes the hysteresis modeling one of the most interesting fields of study. The main magnetic properties are defined by the magnetic field H (A/m), the magnetization M (A/m), the magnetic induction B (T), the susceptibility χ (dimensionless), and the permeability μ (H/m). The magnetic behavior and the properties of a material can be learned by studying its hysteresis loop which shows a nonlinear relationship between magnetic induction (B) and magnetic field (H) as shown in Fig. 1.

Several mathematical models have been developed to describe the hysteresis cycle, such as (Rayleigh 1887; Fröhlich 1881; Preisach 1935) models. In fact, in order to produce the magnetization process for a given magnetic material, particularly when studying a complex magnetic system under thermal and mechanical stresses, it is necessary to identify the model parameters and evaluate its performances with regard to experimental data. For some models, the identification of their parameters is achieved by simply reading the measured cycle. Others require the development of an efficient identification technique. Algorithms applied to identify model variable are mainly classified into two groups: Deterministic methods and Stochastic ones. The Deterministic methods are rarely used as they are based on the resolution of the gradient of the objective function. While the stochastic methods can be adapted to different forms of problems, they are based on
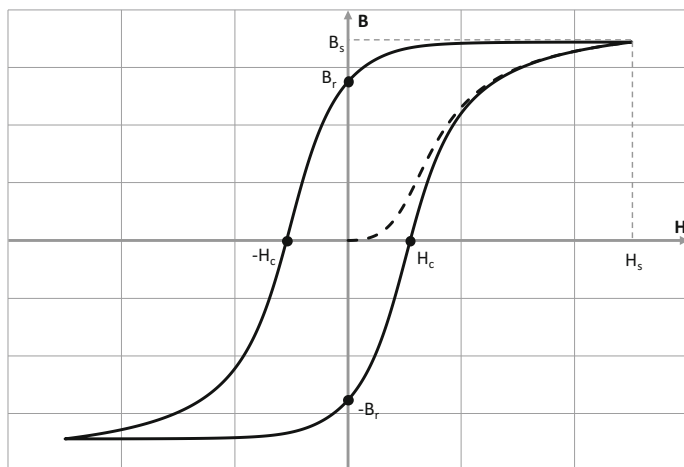
Fig. 1 Hysteresis loop (Bs: saturation flux density; Br: remanence flux; Hs: maximal magnetizing force; Hc: coercivity)

the random evolution and require a lot of evaluation of the objective function to end up guessing the optimum. Among these stochastic methods, the most widely used for magnetic domain are neural network (Zakerzadeh et al. 2011), genetic algorithm (Anh and Kha 2008; Belkebir et al. 2009), PSO (Marion 2008), and nonlinear least squares method (Levenberg 1944; Marquardt 1963; Belkebir et al. 2009).

2 Experimental Hysteresis

Various magnetic measurement systems have been developed for different applications such as magnetic behavior under applied mechanical stress (Sipeky and Ivanyi 2005) and thermal modeling of magnetic components (Quondam et al. 2016).

The experimental setup (Fig. 2) was validated by several experimental studies (Matsubara et al. 1989; Iordache et al. 2003). It consists of two U ferrite cores maintained in contact with the sample. Primary windings are wound on the central limbs of the yokes and the secondary winding surround the specimen. This double-yoke arrangement leads to a better homogeneous distribution of the magnetic field in the measurement zone. Moreover, it minimizes the negative effects of the overhang and of the eddy currents on the measurements accuracy.

The used sample is a fully processed non-oriented Fe-3 wt%Si steel sheet of 0.35 mm thick. The specimen are strips which are 20 mm wide and 250 mm long, cut in the rolling direction, and vacuum annealed at 720 °C for 2 h in order to eliminate the residual stresses which originate from the manufacturing process (Hubert 1998). Figure 3 shows the experimentally obtained hysteresis loop.

From this curve, we extract the reference data in Table 1.
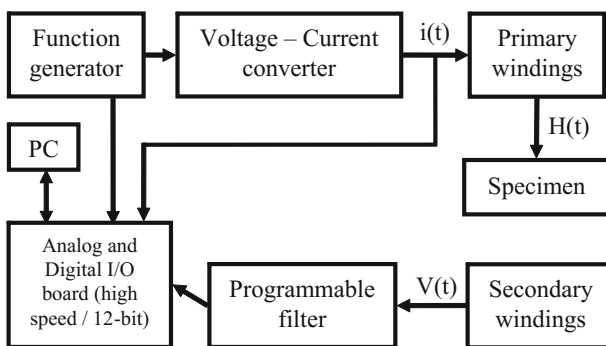
Fig. 2 Block diagram of the magnetic measurement test apparatus
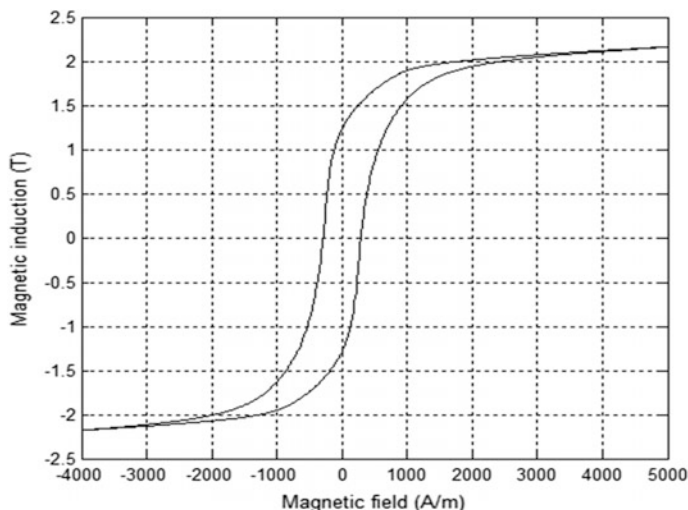
Fig. 3 Experimental hysteresis of a Fe-3 wt%Si steel

Table 1 Experimental reference data

Parameters	Value
H_s (A/m)	5400
H_c (A/m)	300
B_s (T)	2.179
B_r (T)	1.25
f (Hz)	1

3 Static Models

3.1 Rayleigh Model

The classical Rayleigh model of scalar ferromagnetism describes the H-B relation by a Prandtl–Ishlinskii model of play-type. According to the literature (Rayleigh 1887), this model is designed for modeling high-coercivity materials and it is fully determined by four experimental parameters (H_s, B_s, B_r, and frequency f). So, for a field varying between $-H_s$ and $+H_s$, the magnetic density B is expressed by the following expression:

$$B(H) = (\mu_{in} + \eta H_s) H + \frac{1}{2} sign(\alpha) \eta (H^2 - H_s^2) \tag{1}$$

where, μ_{in} et η are defined, respectively, by the following expressions (2 and 3).
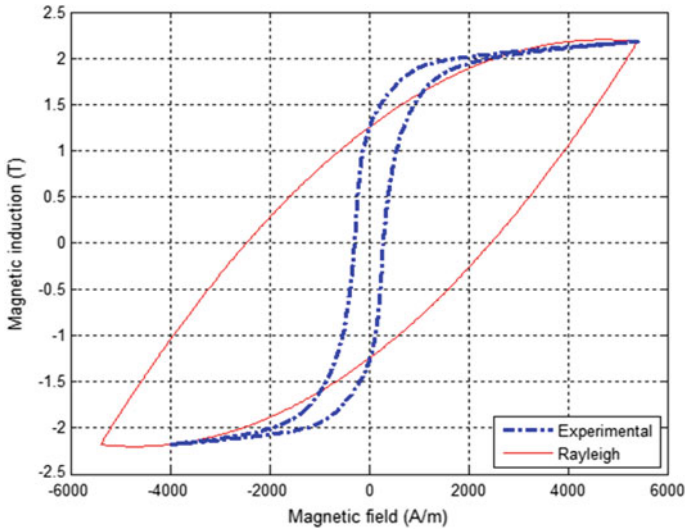
Fig. 4 Comparison of Rayleigh hysteresis and experimental major cycle

$$\mu_{in} = \frac{B_s}{H_s} - \eta H_s \tag{2}$$

$$\eta = \frac{2B_r}{H_s^2} \tag{3}$$

Figure 4 presents a comparison of the resulting curve and the experimental one. The shape of the hysteresis loop provided by Rayleigh model proves that it is adaptable only to magnetic materials with high coercivity (contrary to our used material).

3.2 Frölich Model

The Fröhlich model (Fröhlich 1881) is more adapted for the low hysteresis loss materials. The model is fully determined by four experimental parameters (H_s, H_c, B_s, and B_r) which are picked up directly from the experimental cycle.

The relation B (H), defined by the expression (4), allows to create the hysteresis curve as shown in Fig. 5.

$$B = \frac{H - sign(\alpha) \times H_c}{\alpha + \beta|H - sign(\alpha) \times H_c|} \tag{4}$$
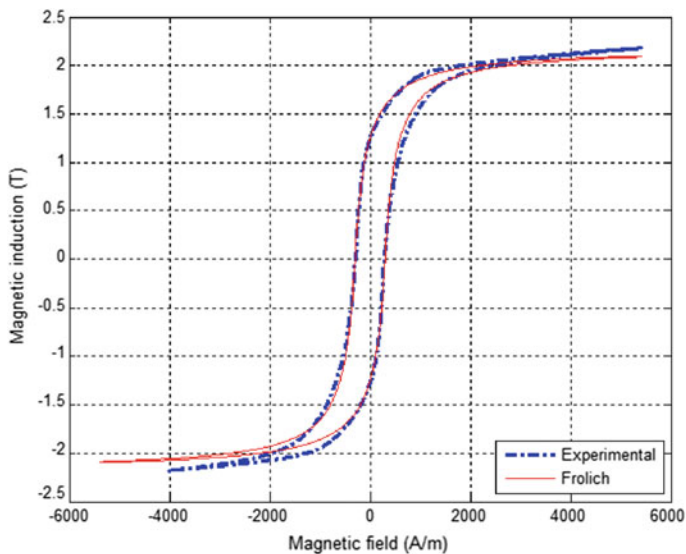
Fig. 5 Comparison of Frölich hysteresis and experimental major cycle

where sign(α) takes the value $+1$ for the ascending branch of the cycle and the value -1 for the descending branch. Then, α and β are defined, respectively, by Eqs. (5 and 6).

$$\alpha = H_c \left(\frac{1}{B_r} - \frac{1}{B_s} \right) \tag{5}$$

$$\beta = \frac{1}{B_s} \tag{6}$$

The resulting curve and the experimental cycle (Fig. 5) appear superimposable with a minor error which denotes that it is an adequate model for the modeling of the chosen material in this study.

3.3 Potter Model

It is a simple mathematical model that describes the evolution curve of the magnetization M by an analytical equation parametrized in α as follows:

$$B(H, \alpha) = B_s \left[sign\,(\alpha) - \alpha \left(- \tanh \left(\frac{H_c - H\,sign\,(\alpha)}{H_c} \tanh^{-1} \left(\frac{B_s}{B_r} \right) \right) \right) \right] \tag{7}$$
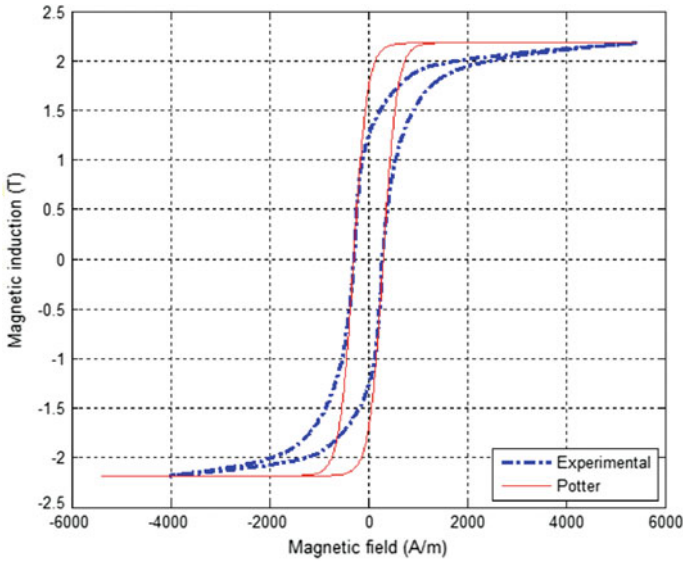
Fig. 6 Comparison of Potter hysteresis and experimental major cycle

where sign(α) takes the value $+1$ for the ascending branch of the cycle and the value -1 for the descending branch.

Using the parameters on Table 1, the resulting curve compared to the experimental cycle (Fig. 6) shows a moderately significant error. This error is not small enough to consider the Potter model as performant to perfectly model the magnetic behavior of our soft ferromagnetic steel.

3.4 Preisach Model

The Preisach analysis (Preisach 1935; Mayergoyz 1991), is mainly designed to describe hysteretic systems with complex behaviors. It is based on decomposing of the system into several elementary hysteretic entities called hysterons. The distribution of the elementary cycles defines the Preisach distribution function which is expressed as follows.

$$M(t) = \iint p(\alpha, \beta)\, \phi_{\alpha\beta}[H(t)]\, d\alpha\, d\beta \tag{8}$$

The distribution function can be identified using analytical approaches like Gaussian function, Lorentz function, and the Lorentz modified function LMF (Preisach 1935).

The LMF is defined by the coercivity H_c, a regulator coefficient k and two parameters a and b. The distribution function by LMF is then given as

$$p(\alpha, \beta) = \frac{ka^2}{(a + (\frac{\alpha}{H_c} - b)^2)(a + (\frac{\beta}{H_c} + b)^2)} \tag{9}$$

Then, the total magnetization M(t) is expressed by (10)

$$M_t = M_{(t-1)} \pm 2 \iint_s \frac{k\,a^2}{(a + (\frac{\alpha}{H_c} - b)^2)(a + (\frac{\beta}{H_c} + b)^2)}\, d\alpha\, d\beta \tag{10}$$

The classical Preisach model is completely determined by five parameters: two of them are experimentally deduced (H_s, H_c) and the remaining ones are numerically identified. The identification is accomplished using the genetic algorithm approach via Matlab.

The comparison of the resulting hysteresis and the experimental cycle (Fig. 7) shows a partial correspondence between the two cycles. According to the literature, this model is adaptable for a variety of hysteresis patterns and it is essentially used for describing static magnetic behavior for ferroelectric and ferromagnetic materials under thermal effects (Quondam et al. 2016).
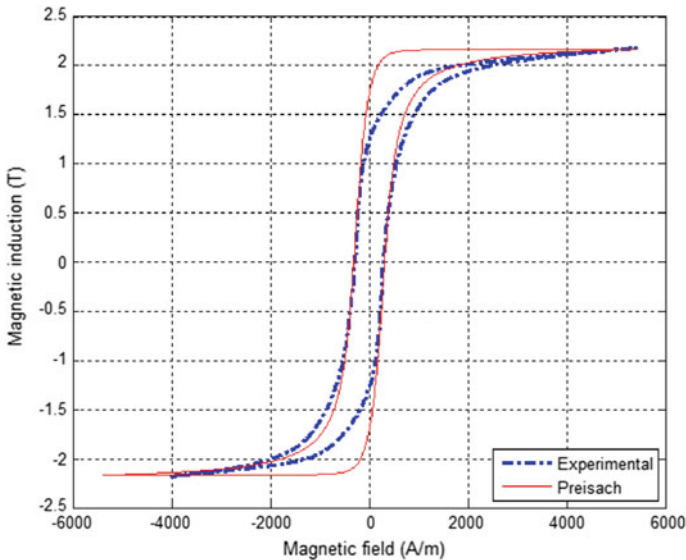
Fig. 7 Comparison of Preisach hysteresis and experimental major cycle

Table 2 Error values

Model	ε (%)
Rayleigh	75.70
Frölich	4.53
Potter	12.37
Preisach	8.41

4 Synthesis

In this section, we resume the results of the error calculation between estimated results and measured data which are listed in Table 2. Taking into account that the hysteresis cycle is symmetrical, the comparison between analytical and experimental models is carried out on a single branch of the major curve (ascending branch). The comparison criteria is the percentage error ε given by the following expression (11)

$$\varepsilon = \frac{\sum \left| \frac{B_{sim}(i) - B_{\exp}(i)}{B_{\exp}(i)} \right|}{N} \times 100 \tag{11}$$

where B_{sim} is the simulated magnetic induction, $B_{\exp}$ is the experimental magnetic induction, and N is the number of points.

The error results show that the Frölich model is the best fitting model for the Fe-3 wt%Si steel hysteresis loop. The Preisach model can be also used to reproduce the magnetic behavior.

5 Conclusion

The main objective of this study was to examine the capability of different static hysteresis models for valuing the magnetic behavior of ferromagnetic material Fe3%Si. The results obtained using Frölich model are close to the measured values. Furthermore, both Frölich and Preisach models can be used in magnetic modeling for soft ferromagnetic materials as revealed by the uses statistical criteria. Once the best hysteresis model is identified, further investigations on the modelization of the heat and mechanical stress effects on the magnetic behavior can be conducted.

References

Anh KK, Kha NB (2008) Modeling and control of shape memory alloy actuators using Preisach model, genetic algorithm and fuzzy logic. J Mech Sci Technol 20(5):636–642

Belkebir A, Abdelhadi B et Benoudjit A (2009) Identification et optimisation par algorithmes génétiques des paramètres du modèle de l'hystérésis magnétique de Chua, Revue des sciences et de la technologie, 1

Fröhlich O (1881) Investigations of dynamoelectric machines and electric power transmission and theoretical conclusions therefrom. Electrotech Z 2:134–141

Hubert O (1998) Doctorat thesis, Universite de Technologie de Compiegne, France

Iordache VE, Hug E, Buiron N (2003) Magnetic behavior versus tensile deformation mechanisms in a non-oriented Fe–(3 wt.%)Si steel. Mater Sci Eng A 359(25):62–74

Levenberg K (1944) A method for the solution of certain nonlinear problems in least squares. Q Appl Math 2:164–168

Marion R (2008) Identification of Jiles-Atherton model parameters using Particle Swarm Optimization. IEEE Trans Magn 44:894–897

Marquardt DW (1963) An algorithm for least–squares estimation of nonlinear parameters, journal of the society for Industrial and Applied Mathematics 11(2):431–441

Matsubara K, Nakata T, Takahash N, Fujiwara K, Nakano M (1989) Effects of the overhang of a specimen on the accuracy of a single sheet tester. Phys Scr 40:529–531

Mayergoyz I (1991) Mathematical Models of Hysteresis. Springer, New York, Berlin

Preisach F (1935) Über die magnetischeNachwirkung. Z. für Phys 94:277–302

Quondam AS, Faba A, Carlotti G, Cardelli E (2016) Vector hysteresis model identification for iron-silicon thin films from micromagnetic simulations. Phys B 486:97–100

Lord Rayleigh (1887) On the behaviour of iron and steel under the operation of feeble magnetic forces. Phil Mag 142(23):225–245

Sipeky A, Ivanyi A (2005) Stress dependent Preisach-type magnetic hysteresis model. In: First international Phd Symposium in PECS, Hungary: 52

Zakerzadeh MR, Finouzi M, Sayyaadi H, Shouraki SB (2011) Hysteresis nonlinearity identification using new Preisach model-based artificial neural network approach. J Appl Math 1:28–38

Static Behavior of Carbon Nanotubes Reinforced Functionally Graded Nanocomposite Cylindrical Panels

S. Zghal and A. Frikha

Abstract This chapter deals with the static behavior of carbon nanotubes reinforced functionally graded cylindrical nanocomposite panels. In fact, with the rapid progress of nanotechnology, the use of as kinds of reinforcements in composite structures has attracted the attention of many researchers in the last years. The modeling is based on the Kirchhoff–Love finite element model which constitutes a convenient model to describe the kinematics of shells especially when thin structures are investigated. For the constitutive material law, the modified rule of mixture is adopted which introduces some efficiency parameters to take into account the dependence scale of carbon nanotubes. Four types of distributions of carbon nanotubes are considered which are uniformly and three functionally graded profiles. Static analyses in terms of deflections are presented in order to show the effects of volume fraction of carbon nanotubes as well as the length-to-radius ratio on bending behavior of functionally graded shell structures reinforced by carbon nanotubes. The obtained results are compared to those available in the literature leading hence to outline the performance and the accuracy of the presented model.

Keywords Carbon nanotubes · FG-CNTRCs · Finite element method Static analysis

1 Introduction

Since the discovery of carbon nanotubes (CNTs) by Ijiima (1991) and due to their exceptional mechanical, electrical, and thermal properties, the CNTs are considered as excellent reinforcement materials for high performance structural and

S. Zghal (✉) · A. Frikha
Mechanical Modeling and Manufacturing Laboratory (LA2MP),
National School of Engineers of Sfax, University of Sfax, B.P 1173-3038, Sfax, Tunisia
e-mail: souhirzghal@yahoo.fr

A. Frikha
e-mail: frikhaahmed@yahoo.fr

199

multifunctional composites. Furthermore, the manufacturing process of nanocomposite demonstrates that the CNTs are distributed either uniformly or randomly which results in spatially uniform mechanical properties of nanocomposites. On the other hand, the new discovery of functionally graded materials (FGMs) constitutes an alternative to overcome the drawbacks of the traditional composite materials like cracks and delamination phenomenon (Hajlaoui et al. 2012). Hence, the combination between FGM concept and carbon nanotubes leads to the so-called functionally graded carbon nanotube reinforced composites (FG-CNTRCs) which constitute a new advanced class of materials. As well as, the investigations of the mechanical behavior of FG-CNTRC beams (Lin and Xiang 2014), plates (Shen 2009), and panels (Zhang et al. 2014) have attracted the attention of many researchers. A comprehensive literature review on mechanical characteristics of these structures is presented in Liew et al. (2015) which covers static, free vibration, buckling, postbuckling, and nonlinear analysis.

According to the open literature regarding theories for modeling (FG-CNTRC structures), the most used one is the first shear deformation theory (FSDT). Nevertheless, this theory assumes a constant variation of transverse shear deformations with the use of shear correction coefficients which can be prohibitive in the finite element procedure, see Hajlaoui et al. (2015, 2016, 2017). For high order theories, there are many researches regarding FGM structures. One can be referred to Wali et al. (2014, 2015) and Frikha et al. (2016) among others. However, for FG-CNTRCs, only few papers use high order model to describe the mechanical behavior of such structures, see Natarajan et al. (2012). So, it appears attractive to investigate these FG-CNTRCs with a convenient model.

Since the finite element method requires a computational effort which can be expensive with the above-mentioned models and to ensure the compromise accuracy/efficiency, we propose in this chapter, a kinematic model based on Kirchhoff–Love hypothesis. Even this model neglect the effect of transverse shear deformations, it presents a suitable choice for the modeling of FG-CNTRC cylindrical panels favored by its simple implementation in most finite elements' codes and low computational effort. The CNTs are assumed uniaxially aligned in axial direction and functionally graded in thickness direction of the panels. The effective material properties of FG-CNTRC cylindrical panels are estimated using the modified rule of mixture. The static analysis is presented in terms of deflections varying in the volume fraction of carbon nanotube and the length-to-radius ratio hence leads to perform the applicability of the proposed model.

2 Carbon Nanotubes Reinforced Composite Panels

The geometry of the studied cylindrical panel is shown in Fig. 1. This panel is assumed to be thin of length L, radius R, span angle θ_0, and thickness h.

In addition, this panel is made of a mixture of single-walled carbon nanotubes (SWCNTs) and the matrix in which the CNTs are assumed to be uniaxially aligned

in axial direction and functionally graded in thickness direction of the cylindrical panels, that is, UD is uniformly distributed, FG-V, FG-O, and FG-X denote the other three types of functionally graded distributions of CNTs (Fig. 2).

According to the (CNTs) distributions, the volume fraction of CNTs $V_{CNT}(z)$ for each case can be expressed as follows:

$$V_{CNT}(z) = \begin{cases} V_{CNT}^* & (UD) \\ \left(1 + \frac{2z}{h}\right)V_{CNT}^* & (FG-V) \\ 2\left(1 - \frac{2|z|}{h}\right)V_{CNT}^* & (FG-O) \\ 2\left(\frac{2|z|}{h}\right)V_{CNT}^* & (FG-X) \end{cases} \tag{1}$$

where V_{CNT}^* is given by

$$V_{CNT}^* = \frac{w_{CNT}}{w_{CNT} + (\rho^{CNT}/\rho^m) - (\rho^{CNT}/\rho^m)w_{CNT}} \tag{2}$$

Fig. 1 Geometry properties of CNTRC panel
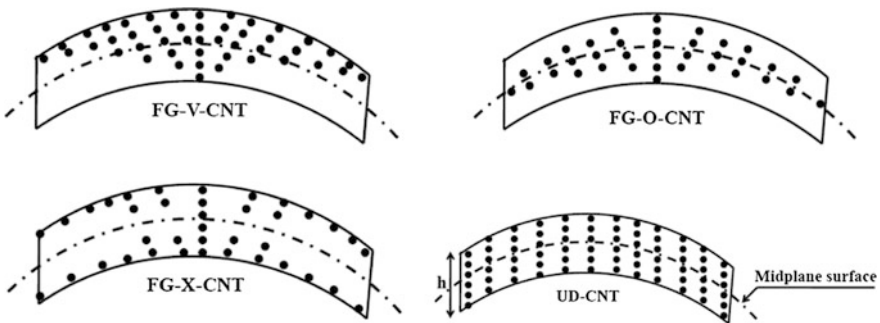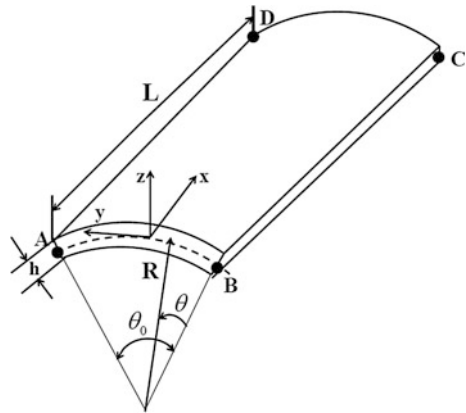
Fig. 2 Various distributions of CNTs of FG-CNTRC panel

w_{CNT} represents the fraction of mass of the (CNTs); ρ^m and ρ^{CNT} denote the densities of the matrix and CNTs, respectively. Since the effective material properties of FG-CNTRC panels are highly dependent on the structure of CNTs)(Seidel and Lagoudas 2006), several micromechanical models have been proposed to predict the effective material properties of CNTRCs such as the modified rule of mixture which constitutes one of the most effective homogenization approaches. Thereby, the effective Young's and shear moduli of the CNTRC materials are determined according to the modified rule of mixture as follows (Shen and Xiang 2012):

$$\begin{cases} E_{11} = \eta_1 V_{CNT} E_{11}^{CNT} + V_m E_m \\ \dfrac{\eta_2}{E_{22}} = \dfrac{V_{CNT}}{E_{22}^{CNT}} + \dfrac{V_m}{E_m} \\ \dfrac{\eta_3}{G_{12}} = \dfrac{V_{CNT}}{G_{12}^{CNT}} + \dfrac{V_m}{G_m} \end{cases} \tag{3}$$

where E_{11}^{CNT} E_{22}^{CNT}, and E_m are the Young's modulus of CNTs and isotropic matrix, respectively. G_{12}^{CNT} and G_m are the shear modulus of CNTs and matrix, respectively. The efficiency coefficients $\eta_j (j = 1, 2, 3)$ are obtained from the molecular dynamic (MD) simulations (Shen and Xiang 2012). As well as, V_m and V_{CNT} are the matrix and CNTs volume fractions, respectively, which are related by:

$$V_m + V_{CNT} = 1 \tag{4}$$

The effective density and Poisson's ratio of CNTRC panel are given as:

$$\begin{cases} \rho = \rho^m V_m + \rho^{CNT} V_{CNT} \\ \nu_{12} = \nu_{12}^{CNT} V_{CNT}^* + \nu^m V_m \end{cases} \tag{5}$$

ν_{12}^{CNT} and ν^m are the Poisson's ratios of CNTs and matrix phase, respectively.

3   Theoretical Formulations

In this section, the kinematics of the discrete Kirchhoff quadrilateral shell element is briefly described. In fact, the reference C_0 and current C_t configurations of the CNTRC shell are assumed to be smooth, continuous, and differentiable.

3.1   Displacement Field and Strains of CNTRCs Panels

According to Kirchhoff–Love Theory, the displacement field is expressed, using convective coordinates $(\xi^1, \xi^2, \xi^3 = z)$. The position vectors of any material point

(q), whose normal projection on mid-surface is the material point (p), in initial and current configurations, are given, respectively, by

$$\mathbf{X}_q(\xi^1, \xi^2, z) = \mathbf{X}_p(\xi^1, \xi^2) + z\mathbf{D}(\xi^1, \xi^2), \quad \mathbf{x}_q = \mathbf{x}_p + z\mathbf{d} \tag{6}$$

where $z \in [-h/2, h/2]$ is the thickness of the shell structure and $\mathbf{d}$ is the shell director vector. The Lagrange strain field can be decoupled in the membrane $\mathbf{e}$, bending $\boldsymbol{\chi}$, and shear $\boldsymbol{\gamma}$ parts as follows

$$\mathbf{e} = \left\{ \begin{array}{c} e_{11} \\ e_{22} \\ 2e_{12} \end{array} \right\}, \quad \chi = \left\{ \begin{array}{c} \chi_{11} \\ \chi_{22} \\ 2\chi_{12} \end{array} \right\}, \quad \gamma = \left\{ \begin{array}{c} \gamma_1 \\ \gamma_2 \end{array} \right\} \tag{7}$$

Based on the zero transverse shear strain assumption, $\boldsymbol{\gamma} = \mathbf{0}$, the generalized membrane and bending stresses resultants $\mathbf{N}$ and $\mathbf{M}$ can be expressed as follows:

$$\mathbf{N} = \left[\begin{array}{c} N^{11} \\ N^{22} \\ N^{12} \end{array} \right], \quad \mathbf{M} = \left[\begin{array}{c} M^{11} \\ M^{22} \\ M^{12} \end{array} \right] \tag{8}$$

$$\left[\begin{array}{c} \mathbf{N} \\ \mathbf{M} \end{array} \right] = \left[\begin{array}{cc} \mathbf{H}_{11} & \mathbf{H}_{12} \\ \mathbf{H}_{12} & \mathbf{H}_{22} \end{array} \right] \left[\begin{array}{c} \mathbf{e} \\ \chi \end{array} \right], \quad (\mathbf{H}_{11}, \mathbf{H}_{12}, \mathbf{H}_{22}) = \int_{-h/2}^{h/2} \left(1, z, z^2\right) \mathbf{H} dz \tag{9}$$

where $\mathbf{H}$ represents the in-plane linear elastic submatrix which is expressed for an orthotropic CNTRC panel as follows:

$$\mathbf{H} = \mathbf{T}_1^{\mathrm{T}} \mathbf{H}_L \mathbf{T}_1, \quad \mathbf{H}_L = \left[\begin{array}{ccc} H_{LL} & H_{LT} & 0 \\ H_{LT} & H_{TT} & 0 \\ 0 & 0 & G_{LT} \end{array} \right] \tag{10}$$

The subscript L and T indicate the longitudinal and transverse directions for an orthotropic CNTRC panel in the principal material coordinates axes (L-T-N). The components H_{LL}, H_{LT}, H_{TT}, and G_{LT} are functions of engineering constants (Reddy 1997) which their forms stick with the effective properties of the CNTRC panel mentioned in Eq. (2). $\mathbf{T}_1$ is the transformation matrix from the local orthotropic system to local Cartesian system given by

$$\mathbf{T}_1 = \left[\begin{array}{ccc} c^2 & s^2 & cs \\ s^2 & c^2 & -cs \\ -2cs & 2cs & c^2 - s^2 \end{array} \right], \quad c = \cos(\theta), \quad s = \sin(\theta) \tag{11}$$

3.2   Variational Principle and Finite Element Approximation

For flexural strength analysis, the governing equations of CNTRC panels are derived from the variational principle which is based on the weak form of equilibrium:

$$G = \int_A (\mathbf{N} \cdot \delta\mathbf{e} + \mathbf{M} \cdot \delta\boldsymbol{\chi}) dA - G_{ext} = 0 \tag{12}$$

where $\delta\mathbf{e}$ and $\delta\boldsymbol{\chi}$ are the variations of shell strains. In the finite element approximation, the displacement vector, its variation, and increment are approximated using the isoparametric concept. However, a quadratic interpolation is used for the director vector $\mathbf{d}$ as in Wali et al. (2014), and Frikha and Dammak (2017). By introducing the kinematic constraint, $\gamma = \mathbf{0}$, over the element boundaries under integral form, one can deduce the strain-displacement relations. Then, the discrete form of Eq. (12) leads to a nonlinear equation which can be solved by the Newton iterative procedure. For more details, see Wali et al. (2014), and Frikha and Dammak (2017).

4   Numerical Results

In this section, the static behavior of FG-CNTRC cylindrical panel is presented in order to outline the applicability and the efficiency of the proposed model. The geometry of the panel is h = 0.002 m; h/R = 0.002 and L/R = 0.1. Poly(methyl methacrylate), referred as PMMA, is used for isotropic matrix and armchair single walled (10, 10) for carbon nanotubes. The material properties of both matrix and (CNTs) at room temperature (300 K) are given in Table 1.

Three values of volume fraction of CNTs are considered here: for $V^*_{CNT} = 0.11$, the efficiency parameters are: $\eta_1 = 0.149$; $\eta_2 = \eta_3 = 0.934$; for $V^*_{CNT} = 0.14$, these coefficients are equal to: $\eta_1 = 0.150$; $\eta_2 = \eta_3 = 0.941$ and for $V^*_{CNT} = 0.17$, $\eta_1 = 0.149$, and $\eta_2 = \eta_3 = 1.381$.

The nondimensional deflections $\bar{w} = w/h$ of simply supported FG-CNTRC cylindrical panel are depicted in Fig. 3 for different volume fractions of CNTs V^*_{CNT} under uniformly distributed load $q_0 = 0.1$ MPa. The obtained results using the

Table 1   Mechanical properties of isotropic matrix and SWCNTs of FG-CNTRC panel

Armchair (10, 10) (SWCNTs)	PMMA matrix
$E^{CNT}_{11} = 5646.6$ GPa	$E_m = 2.5$ GPa
$E^{CNT}_{22} = 7080$ GPa	$\rho^m = 1150$ kg/m^3
$G^{CNT}_{12} = 1944.5$ GPa	$\nu^m = 0.34$
$\rho^{CNT} = 1400$ kg/m^3	
$\nu^{CNT}_{12} = 0.175$	

Fig. 3 Nondimensional deflection versus the volume fraction of CNTs for various CNTs distributions of FG-CNTRC cylindrical panel
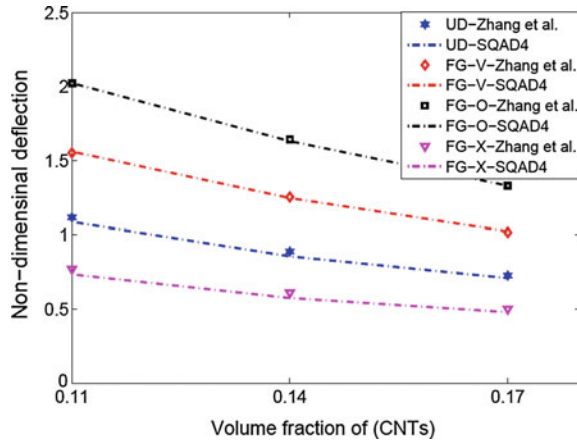
Fig. 4 Effect of variation of length-to-radius-ratios on nondimensional deflection of FG-CNTRC cylindrical panel
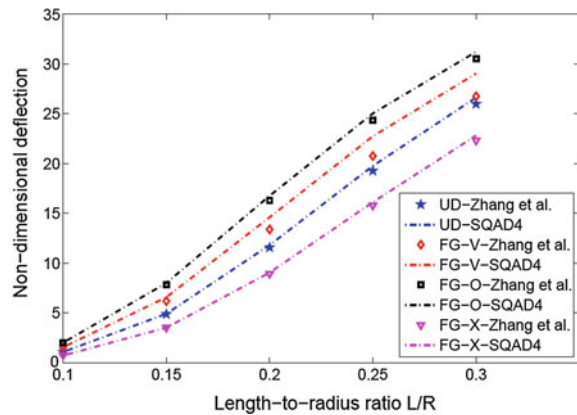
developed finite element SQAD4 are compared to those given by Zhang et al. (2014). A good agreement between the results leads to validate the proposed model. In addition, the effect of length-to-radius ratio on static behavior of FG-CNTRC panel is examined. Figure 4 shows that the FG-O-CNTRC panel has the highest value of nondimensional deflection, whereas the FG-X-CNTRC panel has the lowest one. This can be explained by the form of distribution of reinforcements which can affect the stiffness of the FG-CNTRC panels. In fact, more the distribution of CNTs is close to top and bottom surfaces, more the stiffness of the FG-CNTRC panels increases. Thereby, the desired stiffness can be achieved by adjusting the distribution of CNTs along the thickness direction of the panel. On the other hand, the variation of length-to-radius ratio (L/R) has a significant effect on the static behavior of FG-CNTRC panels which manifest by an increase in the nondimensional deflection. Moreover, the obtained results are in good agreement with those derived from the literature (Zhang et al. 2014). Therefore, the proposed method has the ability to draw the static behavior of FG-CNTRC panels with good accuracy.

5 Conclusion

In this chapter, the static behavior of FG-CNTRC cylindrical panels is investigated using the discrete Kirchhoff–Love finite element model. The CNTs are assumed to be graded in thickness direction and the effective material properties are estimated through a micromechanical model based on modified rule of mixture. The static behavior is performed in terms of nondimensional deflection varying the volume fraction of CNTs and the length-to-radius ratio. Results reveal that these parameters have a significant influence on the flexural strength of FG-CNTRC panels. On the other hand, the provided comparison study showed the accuracy and the efficiency of the present method.

References

Frikha A, Dammak F (2017) Geometrically nonlinear static analysis of functionally graded material shells with a discrete double directors shell element. Comput Method Appl Mech Eng 315:1–24

Frikha A, Wali M, Hajlaoui A, Dammak F (2016) Dynamic response of functionally graded material shells with a discrete double directors shell element. Compos Struct 154:385–395

Hajlaoui A, Jarraya A, Kallel-Kammoun I, Dammak F (2012) Buckling analysis of a laminated composite plate with delaminations using the enhanced assumed strain solid shell element. J Mech Sci Technol 26(10):3213–3221

Hajlaoui A, Jarraya A, El Bikri K, Dammak F (2015) Buckling analysis of functionally graded materials structures with enhanced solid-shell elements and transverse shear correction. Compos Struct 132:87–97

Hajlaoui A, Wali M, Ben Jdidia M, Dammak F (2016) An improved enhanced solid shell element for static and buckling analysis of shell structures. Mech Ind 17(5):510

Hajlaoui A, Triki E, Frikha A, Wali M, Dammak F (2017) Nonlinear dynamics analysis of FGM shell structures with a higher order shear strain enhanced solid-shell element. Lat Am J Solids Struct 14:72–91

Iijima S (1991) Helical microtubules of graphitic carbon. Nature 354:56–58

Liew KM, Lei ZX, Zhang LW (2015) Mechanical analysis of functionally graded carbon nanotube reinforced composites: a review. Compos Struct 120:90–97

Lin F, Xiang Y (2014) Vibration of carbon nanotube reinforced composite beams based on the first and third order beam theories. Appl Math Modell 38:3741–3754

Natarajan S, Haboussi M, Ganapathi M (2012) Application of higher-order structural theory to bending and free vibration analysis of sandwich plates with cnt reinforced composite face sheets. Compos Struct 113:197–207

Reddy JN (1997) Mechanics of laminated composite plates: theory and analysis, 2nd edn. Florida, New York

Seidel GD, Lagoudas DC (2006) Micromechanical analysis of the effective elastic properties of carbon nanotube reinforced composites. Mech Mater 38:884–907

Shen HS (2009) Nonlinear bending of functionally graded carbon nanotube-reinforced composite plates in thermal environments. Compos Struct 91:9–19

Shen HS, Xiang Y (2012) Nonlinear vibration of nanotube-reinforced composite cylindrical shells in thermal environments. Comput Method Appl Mech Eng 213–216:196–205

Wali M, Hajlaoui A, Dammak F (2014) Discrete double directors shell element for the functionally graded material shell structures analysis. Comput Method Appl Mech Eng 278:388–403

Wali M, Hentati T, Jaraya A, Dammak F (2015) Free vibration analysis of FGM shell structures with a discrete double directors shell element. Compos Struct 125:295–303

Zhang LW, Lei ZX, Liew KM, Yu JL (2014) Static and dynamic of carbon nanotube reinforced functionally graded cylindrical panels. Compos Struct 111:205–212

A Four-Node Shell Element for Geometrically Nonlinear Analysis of Thin FGM Plates and Shells

A. Frikha, S. Trabelsi and S. Zghal

Abstract This chapter presents a static behavior of geometrically nonlinear of Functionally Graded Material (FGM) thin shell structures. The proposed model, based on Kirchhoff shell element, consists in annulling the transverse shear deformation. The developed model is generalized to plates and shells such as cylindrical, conical, spherical, and hyperboloid shells. Material properties are assumed to be graded through the thickness by varying the volume fraction of the ceramic and the metallic constituents using power-law distribution. Numerical results are presented for pinched hemisphere. The load parameter is plotted versus the deflection in the two loading point A and B. Numerical results are compared with previous works. A good agreement between the present results and the literature confirms the high accuracy of the current nonlinear model for an isotropic material. The load parameter of FGM pinched hemisphere is plotted versus the deflection at the loading points by varying the power index from metal to ceramic. The deflection gap between the loading points A and B increases with the power index.

Keywords FGM shells · Finite element analysis · Geometrically nonlinear theory

1 Introduction

Shell structures are more and more replaced by composites because of their improved mechanical properties. However, the abrupt change of the properties across the interface between different constituents in conventional composites causes

A. Frikha (✉) · S. Trabelsi · S. Zghal
Mechanical Modeling and Manufacturing Laboratory (LA2MP),
National School of Engineers of Sfax, University of Sfax, BP 1173-3038, Sfax, Tunisia
e-mail: frikhaahmed@yahoo.fr

S. Trabelsi
e-mail: sorourtrabelsi@yahoo.fr

S. Zghal
e-mail: souhirzghal@yahoo.fr

209

a high interlaminar stresses leading to delamination. In addition, conventional composites are not resistant to high temperatures. To overcome the thermomechanical disadvantages of conventional composites, a special kind of composite, known as functionally graded materials with a gradual transition of material properties from ceramic to metal, are made. This kind of composite was introduced as ultrahigh temperature-resistant materials due to low thermal conductivity of ceramic.

The Kirchhoff Classical thin Plate Theory (CPT) consists in annulling the transverse shear deformation. This model, which only applies for the thin structures, has been used by several authors to develop linear and nonlinear elements. Alijani et al. (2011) studied the nonlinear vibrations of FGM doubly curved shallow shells. They considered the thermal effect, the CPT assumption, and Donnell nonlinearity. Using the CPT with an improved Donnell equations and plane stress assumption, Bich and Nguyen (2012) examined the nonlinear vibration of functionally graded circular cylindrical shells.

Linear and nonlinear FGM shells are studied in the literature with analytical and numerical methods. Using a discrete double directors shell element, static, free vibration, and forced vibration of composite and FGM shell structures were studied by Wali et al. (2014, 2015) and Frikha et al. (2016a). Another approach based on the solid-shell finite element was used for geometrically nonlinear analysis of FGM plates and shells (Hajlaoui et al. 2012, 2015, 2016, 2017).

The purpose of this chapter is to present a nonlinear general formulation based on discrete form of Kirchhoff–Love theory. The static response of FGM shells under geometrically nonlinear is investigated.

2 Fundamental Equations of Discrete Kirchhoff Shell Model

In this section, the geometry and kinematics of nonlinear discrete Kirchhoff quadrilateral shell model are briefly described. The reference surface of the shell is assumed to be smooth, continuous, and differentiable. Initial and current configurations of the shell are denoted by C_0 and C_t, respectively.

2.1 Kinematic Assumptions

Variables associated with C_0 (respectively C_t) are denoted by uppercase letters (respectively lowercase). Vectors will be denoted by bold letters. The reference surface in an arbitrary configuration, initial or deformed, is described by the same parametric coordinates ξ^1 and ξ^2. The position of any point (q) of the shell domain is given in C_0 and C_t by:

$$\mathbf{X}_q(\xi^1, \xi^2, z) = \mathbf{X}_p(\xi^1, \xi^2) + z\mathbf{D}(\xi^1, \xi^2), \mathbf{x}_q = x_p + z\mathbf{d} \qquad (1)$$

where $z \in [-h/2, h/2]$ is the thickness variable of the shell and $\mathbf{d}$ is the shell director vector. The covariant basis at the point q at C_0 and C_t can be deduced and yield the following membrane, bending, and shear strains:

$$\mathbf{e} = \left\{ \begin{array}{c} e_{11} \\ e_{22} \\ 2e_{12} \end{array} \right\}, \boldsymbol{\chi} = \left\{ \begin{array}{c} \chi_{11} \\ \chi_{22} \\ 2\chi_{12} \end{array} \right\}, \boldsymbol{\gamma} = \left\{ \begin{array}{c} \gamma_1 \\ \gamma_2 \end{array} \right\} \qquad (2)$$

$$e_{\beta\gamma} = \frac{1}{2} \left(a_{\beta\gamma} - A_{\beta\gamma} \right), \chi_{\beta\gamma} = \frac{1}{2} \left(b_{\beta\gamma} - B_{\beta\gamma} \right), \gamma_\beta = \mathbf{a}_\beta \cdot \mathbf{d} - \mathbf{A}_\beta \cdot \mathbf{D} \qquad (3)$$

The kinematic constraint, $\gamma = \mathbf{0}$, will be imposed in a discrete form in the finite element approximation (Frikha et al. 2016a, b). Then, only the membrane and bending stresses resultants are present and can be written as:

$$\mathbf{N} = \left[\begin{array}{c} N^{11} \\ N^{22} \\ N^{12} \end{array} \right], \mathbf{M} = \left[\begin{array}{c} M^{11} \\ M^{22} \\ M^{12} \end{array} \right] \qquad (4)$$

This stress resultants are related to the Lagrange strains by

$$\left[\begin{array}{c} \mathbf{N} \\ \mathbf{M} \end{array} \right] = \left[\begin{array}{cc} \mathbf{H}_{11} & \mathbf{H}_{12} \\ \mathbf{H}_{12} & \mathbf{H}_{22} \end{array} \right] \left[\begin{array}{c} \mathbf{e} \\ \boldsymbol{\chi} \end{array} \right], (\mathbf{H}_{11}, \mathbf{H}_{12}, \mathbf{H}_{22}) = \int_{-h/2}^{h/2} \left(1, z, z^2 \right) \mathbf{H} dz \qquad (5)$$

where $\mathbf{H}$ is the in-plane linear elastic matrix defined by

$$\mathbf{H} = \frac{E(z)}{1 - \nu^2(z)} \left[\begin{array}{ccc} 1 & \nu(z) & 0 \\ \nu(z) & 1 & 0 \\ 0 & 0 & (1 - \nu(z))/2 \end{array} \right] \qquad (6)$$

2.2 Weak Form and Linearization

Using the total Lagrangian formulation, the weak form of equilibrium equation is given by:

$$G = \int_A (\delta\mathbf{e}.\mathbf{N} + \delta\boldsymbol{\chi}.\mathbf{M})dA - G_{ext} = 0 \qquad (7)$$

where $\delta\mathbf{e}$ and $\delta\boldsymbol{\chi}$ are the variations of shell strains. The discrete form of Eq. (8) is a nonlinear equation which can be solved by the Newton iterative procedure. The consistent tangent operator for the Newton solution procedure can be constructed

by the directional derivative of Eq. (8) in the direction of the increment $\Delta\boldsymbol{\Phi} = (\Delta\mathbf{u}, \Delta\mathbf{d})$. It is a conventional practice to split the tangent operator into geometric and material parts. The geometric part results from the variation of the virtual strains, $\delta\mathbf{e}$ and $\delta\boldsymbol{\chi}$, while holding stress resultants, $\mathbf{N}$ and $\mathbf{M}$, constant. However, the material part results from the variation of stress resultants, $\mathbf{N}$ and $\mathbf{M}$, while holding the virtual strains, $\delta\mathbf{e}$ and $\delta\boldsymbol{\chi}$, constant.

$$DG.\Delta\boldsymbol{\Phi} = DG_G.\Delta\boldsymbol{\Phi} + DG_M.\Delta\boldsymbol{\Phi} \tag{8}$$

$$DG_G.\Delta\boldsymbol{\Phi} = \int_A (\Delta\delta\mathbf{e}.\mathbf{N} + \Delta\delta\boldsymbol{\chi}.\mathbf{M})dA, \; DG_M.\Delta\boldsymbol{\Phi} = \int_A (\delta\mathbf{e}.\Delta\mathbf{N} + \delta\boldsymbol{\chi}.\Delta\mathbf{M})dA \tag{9}$$

Using Eq. (6), the material part can be written as

$$DG_M.\Delta\boldsymbol{\Phi} = \int_A (\delta\mathbf{e}.(\mathbf{H}_{11}\Delta\mathbf{e} + \mathbf{H}_{12}\Delta\boldsymbol{\chi}) + \delta\boldsymbol{\chi}.(\mathbf{H}_{21}\Delta\mathbf{e} + \mathbf{H}_{22}\Delta\boldsymbol{\chi}))dA \tag{10}$$

For the numerical implementation, the presented formulation is based upon a four-nodes nonlinear shell element. The displacement vector is defined as $\mathbf{u} = \mathbf{x}_p - \mathbf{X}_p$. This vector, its variation, and increment are approximated using the isoparametric concept. However, a quadratic interpolation is used for the director vector $\mathbf{d}$ as in Wali et al. (2014). By introducing the kinematic constraint, $\gamma = 0$, over the element boundaries under integral form one can deduce the strain-displacement relations

$$\begin{bmatrix} \delta\mathbf{e} \\ \delta\boldsymbol{\chi} \end{bmatrix} = \begin{bmatrix} \mathbf{B}_m \\ \mathbf{B}_b \end{bmatrix} [\Delta\boldsymbol{\Phi}] \tag{11}$$

For more details of the development of the $\mathbf{B}_m$ and $\mathbf{B}_b$ matrices and the geometric part, see Frikha and Dammak (2017).

3 Functionally Graded Materials

In this chapter, the FGM structures are made of a mixture metal and ceramic with a continuous variation in the composition through the thickness. The FGM material properties P, corresponding to the Young's modulus and Poisson's ratio at thickness coordinate z, can be evaluated by the mixture rule:

$$P(z) = [P_c - P_m]V_c(z) + P_m, \; V_c(z) = \left(\frac{1}{2} + \frac{z}{h}\right)^p \tag{12}$$

where P(z), P_m, and P_c denote, respectively, the effective material property, the properties of the metal and ceramic. $V_c(z)$ is the volume fraction and p is the power-law index.

4 Numerical Results

The applicability of the proposed theory and the performance of the finite element implementation are assessed by a numerical simulation including large rotation. In this chapter, a pinched hemisphere shell, which is a popular benchmark problem for shell analysis, is considered with an 18 hole at the top subjected to two inward and two outward forces F. From the geometrical symmetry of the hemisphere, the analysis is reduced to one quadrant, Fig. 1a. The spherical geometry is defined by the radius $R = 10$ and the thickness $t = 0.04$. The material properties are the Young's modulus $E = 6.82510 \times 10^7$ and the Poisson's ratio $\nu = 0.3$. The loads F are increased to 450 to compare with the results by Saleeb et al. (1990), Simo et al. (1990), and Kim et al. (2008).

Figure 2 shows a good performance of Kirchhoff model (SQAD4) and Mindlin model (S4) in large displacement and finite rotation analysis. The initial and deformed configurations, subjected to $F = 450$, obtained using SQAD4 element mesh are shown in Fig. 1b–c.

The mechanical behavior of FGM under the applied forces is analyzed in this section. The effect of the power index p of FGM on the deflection at loading points A and B in FGM pinched hemisphere is investigated in Fig. 3. For metal pinched hemisphere $p = 0$, a considerable difference exists between deflections at point A and B. For ceramic pinched hemisphere, deflections at points A and B are close and less important than those of metallic structure. This relative deflection between A and B decreases between the metal to ceramic.
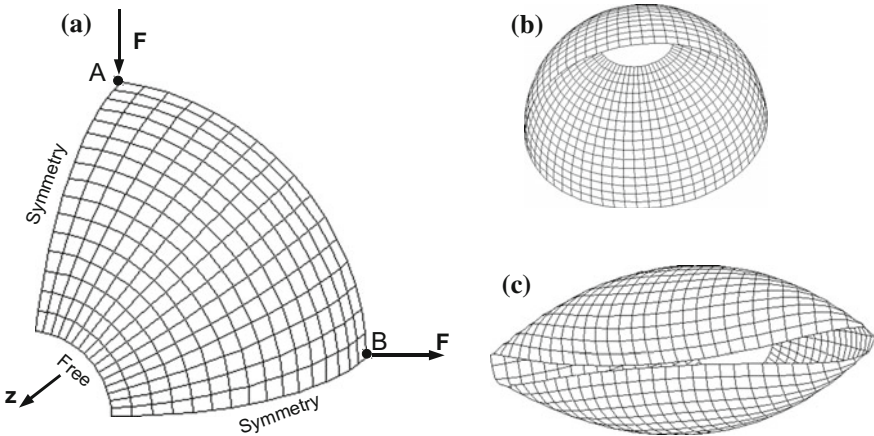
Fig. 1 Pinched hemisphere **a** applied loads **b** initial geometry **c** deformed geometry
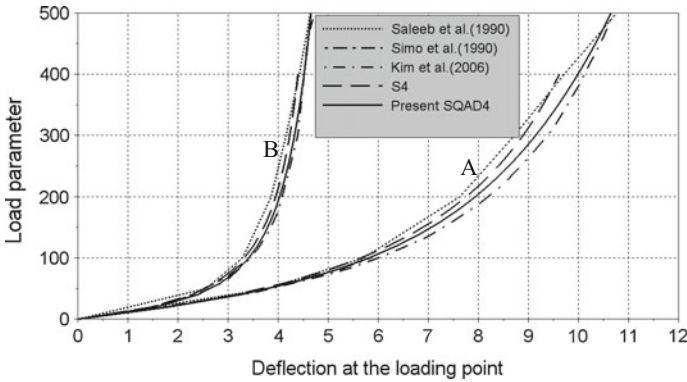
Fig. 2 Center deflection versus load parameter for isotropic pinched hemisphere
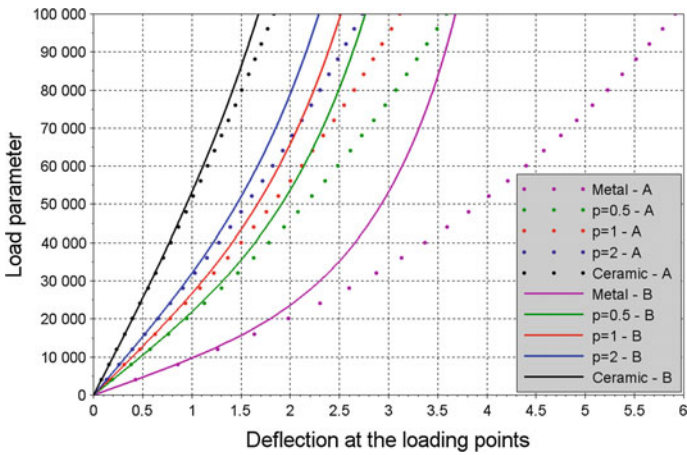
Fig. 3 Center deflection versus load parameter for FGM pinched hemisphere

5   Conclusion

Finite element model based on a discrete Kirchhoff shell element is presented to study the geometrically nonlinear static behavior of 3D-FGM shell structures. The grading function is assumed through the thickness direction. The validation of this model is based on comparing results to the literature for spherical cap made of isotropic material. A good agreement is obtained between the present results and the reference results. The effect of the power index on the deflection at the loading points of pinched hemisphere is analyzed.

References

Alijani F, Amabili M, Karagiozis K, Bakhtiari-Nejad F (2011) Nonlinear vibrations of functionally graded doubly curved shallow shells. J Sound Vib 330:1432–1454

Bich DH, Nguyen NX (2012) Nonlinear vibration of functionally graded circular cylindrical shells based on improved Donnell equations. J Sound Vib 331:5488–5501

Frikha A, Wali M, Hajlaoui A, Dammak F (2016a) Dynamic response of functionally graded material shells with a discrete double directors shell element. Compos Struct 154:385–395

Frikha A, Hajlaoui A, Wali M, Dammak F (2016b) A new higher order C0 mixed beam element for FGM beams analysis. Compos Part B 106:181–189

Frikha A, Dammak F (2017) Geometrically nonlinear static analysis of functionally graded material shells with a discrete double directors shell element. Comput Methods Appl Mech Eng 315:1–24

Hajlaoui A, Jarraya A, Kallel-Kammoun I, Dammak F (2012) Buckling analysis of a laminated composite plate with delaminations using the enhanced assumed strain solid shell element. J Mech Sci 26(10):3213–3221

Hajlaoui A, Jarraya A, El Bikri K, Dammak F (2015) Buckling analysis of functionally graded materials structures with enhanced solid-shell elements and transverse shear correction. Compos Struct 132:87–97

Hajlaoui A, Wali M, Ben Jdidia M, Dammak F (2016) An improved enhanced solid shell element for static and buckling analysis of shell structures. Mech Ind 17(5):510

Hajlaoui A, Triki E, Frikha A, Wali M, Dammak F (2017) Nonlinear dynamics analysis of FGM shell structures with a higher order shear strain enhanced solid-shell element. Lat Am J Solids Struct 14:72–91

Kim KD, Lomboy GR, Han SC (2008) Geometrically nonlinear analysis of functionally graded material (FGM) plates and shells using a four-node quasi-conforming shell element. J Compos Mater 42:485–511

Saleeb AF, Chang TY, Graf W, Yingyeunyong S (1990) A hybrid/mixed model for nonlinear shell analysis and its applications to large-rotation problem. Int J Numer Methods Eng 29:407–446

Simo JC, Fox DD, Rifai MS (1990) Resultant geometrically exact shell model. Part iii: computational aspects of the nonlinear theory. Comput Methods Appl Mech Eng 79:21–70

Wali M, Hajlaoui A, Dammak F (2014) Discrete double directors shell element for the functionally graded material shell structures analysis. Comput Methods Appl Mech Eng 278:388–403

Wali M, Hentati T, Jaraya A, Dammak F (2015) Free vibration analysis of FGM shell structures with a discrete double directors shell element. Compos Struct 125:295–303

Post-buckling of FSDT of Functionally Graded Material Shell Structures

S. Trabelsi, S. Zghal and A. Frikha

Abstract Based on the First-order Shear Deformation Theory (FSDT), this paper performs the geometric nonlinear analysis of Functionally Graded Material (FGM) shell structures. In this theory, a constant transverse shear deformation is considered and a shear correction factor is required. In order to avoid transverse shear locking, the assumed natural strain method (ANS) is incorporated in the finite element formulation. In addition, the variational principle is used to obtain the governing equation and the Newton–Raphson iterative method is adopted to solve the nonlinear equations. The constituent of FG shells consists of ceramic and metal. These constituents are graded through the thickness by varying the volume fraction using a power-law distribution. The post-buckling responses of simply supported cylindrical panel are examined. The effects of volume fraction are also investigated. Numerical results are compared with previous works. A good agreement among the present results and the literature confirms the high accuracy of the current nonlinear model.

Keywords FGM shells · FSDT · Finite element analysis · Geometrically nonlinear theory · Post-buckling

1 Introduction

Functionally Graded Materials occupy a leadership position in mechanical, civil, aerospace, and engineering in the modern industries. They are kinds of composite that have a continuous variation of material properties from one surface to another. These

S. Trabelsi (✉) · S. Zghal · A. Frikha
Mechanical Modeling and Manufacturing Laboratory (LA2MP), National School
of Engineers of Sfax, University of Sfax, BP 1173-3038 Sfax, Tunisia
e-mail: sorourtrabelsi@yahoo.fr

S. Zghal
e-mail: souhirzghal@yahoo.fr

A. Frikha
e-mail: frikhaahmed@yahoo.fr

217

materials consist of a mixture of ceramic and metal. The ceramic constituting the material provides high temperature resistance due to its low thermal conductivity.

FGM cylindrical shells are widely used in many modern technique fields such as pressure vessels, structures for aerospace, aircraft, etc. Therefore, the investigation on post-buckling characteristics of cylindrical panel is of great interest for engineering design and manufacture. Simitses (1996) reviewed the problem of buckling of moderately thick laminated cylindrical shells. He considered as loads the axial compression, lateral pressure, and torsion applied individually or in combination. Nonlinear buckling and post-buckling analysis for axially compressed functionally graded cylindrical shells were investigated in Huang and Han (2009). Li and Lin (2010) analyzed nonlinear buckling and post-buckling of anisotropic laminated cylindrical shell subjected to pressure loads. Dung and Hoa (2013) presented the research on nonlinear buckling and post-buckling behaviors of functionally graded cylindrical shells subjected to uniform external pressure. Kar and Panda (2016) examined the post-buckling behavior of shear deformable functionally graded curved shell panels subjected to edge compression.

Moreover, using FGM in thermal protection systems exposed to elevated temperatures, introduce an additional membrane stress state that may initiate buckling and post-buckling. Thermal buckling analysis of functionally graded cylindrical shell was investigated by Shahsiah and Eslami (2003). Shen (2002) studied post-buckling analysis of axially loaded functionally graded cylindrical panels in thermal environments. Yang et al. (2006) examined the thermo-mechanical post-buckling of FGM cylindrical panels with temperature-dependent properties.

The Mindlin hypothesis consists in considering the effects of the transverse shear deformation. Fu and Waas (1995) employed FSDT to study the initial post-buckling behavior of thick rings subjected to pressure loads. Simitses et al. (1993) presented linear buckling analysis of laminated shells subjected to external pressure.

Recently, some researches on linear and nonlinear FG shells are elaborated with analytical and numerical methods. Using a discrete double directors shell element, static, free vibration, and forced vibration of composite and FGM shell structures was studied by Wali et al. (2014, 2015), Hajlaoui et al. (2015, 2016, 2017), Frikha et al. (2016) and Frikha and Dammak (2017).

The purpose of this paper is to present a nonlinear general formulation based on Mindlin's first-order shear deformation theory. The behavior of simply supported cylindrical panel subjected to concentrated load is investigated.

2 Fundamental Equations

In this section, the geometry and kinematic of nonlinear FSDT shell model is briefly described. The reference surface of the shell is assumed to be smooth, continuous, and differentiable. Initial and current configurations of the shell, are denoted by C_0 and C_t, respectively. Variables associated to C_0 (resp. C_t) are denoted by upper case letters (resp. lower case). Vectors will be denoted by bold letters.

2.1 Kinematic Assumptions

For the development of nonlinear theory, we consider a material point (q) and (p) of the shell domain, in the configurations C_t and C_0. Here (p) is located on the reference surface of the shell and (q) is located at a distance z on the shell director **D**. The position vector of (q), in C_0 and C_t, are given respectively by

$$\mathbf{X}_q = \mathbf{X}_p + z\mathbf{D}, \quad \mathbf{x}_q = x_p + z\mathbf{d} \tag{1}$$

where $z \in [-h/2, h/2]$ is the thickness coordinate of the shell, **d** is the director vector resulting from the rigid rotation of the shell direction (Parisch 1991). We assume that $\mathbf{X}_q$ and $\mathbf{x}_q$ are functions of curvilinear surface coordinates (ξ^α). The state of deformation is defined by means of Green's strain tensor which can be written in the form

$$E_{ij} = \frac{1}{2}\left(g_{ij} - G_{ij}\right), \quad i, j = 1, 3 \tag{2}$$

This strain tensor can be decomposed in in-plane and transverse shear strains as

$$\begin{cases} E_{\alpha\beta} = e_{\alpha\beta} + z\chi_{\alpha\beta} \\ \gamma_{\alpha3} = 2E_{\alpha3} = g_{\alpha3} - G_{\alpha3} \end{cases}, \alpha, \beta = 1, 2 \tag{3}$$

where $g_{\alpha\beta}$ and $G_{\alpha\beta}$ are the covariant components of metric tensor in C_t and C_0 respectively. $e_{\alpha\beta}$, $\chi_{\alpha\beta}$ and $\gamma_{\alpha3}$ are membrane, bending and transverse shear strains given by

$$e_{\alpha\beta} = \frac{1}{2}\left(a_{\alpha\beta} - A_{\alpha\beta}\right), \chi_{\alpha\beta} = \frac{1}{2}\left(b_{\alpha\beta} - B_{\alpha\beta}\right), \gamma_{\alpha3} = \mathbf{a}_\alpha \cdot \mathbf{d} - \mathbf{A}_\alpha \cdot \mathbf{D} \tag{4}$$

In matrix notation, the membrane, bending, and shear strains vectors are given by

$$\mathbf{e} = \begin{bmatrix} e_{11} \\ e_{22} \\ 2e_{12} \end{bmatrix}, \chi = \begin{bmatrix} \chi_{11} \\ \chi_{22} \\ 2\chi_{12} \end{bmatrix}, \gamma = \begin{bmatrix} \gamma_{13} \\ \gamma_{23} \end{bmatrix} \tag{5}$$

2.2 Weak Form

Since we will formulate the equilibrium in its weak form, we must define the membrane, bending and shear stresses resultants, which can be written in the form

$$\mathbf{N} = \int_{-h/2}^{h/2} \begin{bmatrix} S^{11} \\ S^{22} \\ S^{12} \end{bmatrix} dz, \mathbf{M} = \int_{-h/2}^{h/2} \begin{bmatrix} S^{11} \\ S^{22} \\ S^{12} \end{bmatrix} z dz, \mathbf{T} = \int_{-h/2}^{h/2} \begin{bmatrix} S^{13} \\ S^{23} \end{bmatrix} dz \qquad (6)$$

These stress resultants and strain fields in Eqs. (6) and (5) can be grouped to form the generalized stress and strain as

$$\mathbf{R} = \begin{bmatrix} \mathbf{N} \\ \mathbf{M} \\ \mathbf{T} \end{bmatrix}, \Sigma = \begin{bmatrix} \mathbf{e} \\ \chi \\ \gamma \end{bmatrix} \qquad (7)$$

Using Eq. (6), $\mathbf{R}$ and Σ are related by the following equation:

$$\mathbf{R} = \mathbf{H_T} \Sigma, \mathbf{H_T} = \begin{bmatrix} \mathbf{H_m} & \mathbf{H_{mb}} & \mathbf{0} \\ \mathbf{H_{mb}} & \mathbf{H_b} & \mathbf{0} \\ \mathbf{0} & \mathbf{0} & \mathbf{H_s} \end{bmatrix} \qquad (8)$$

$$(\mathbf{H_m}, \mathbf{H_{mb}}, \mathbf{H_b}) = \int_{-h/2}^{h/2} (1, z, z^2) \mathbf{H} dz, \mathbf{H}_s = \int_{-h/2}^{h/2} \mathbf{H}_\tau dz \qquad (9)$$

where $\mathbf{H}$ and $\mathbf{H}_\tau$ are in-plane and out-of-plane linear elastic sub-matrices, which can be expressed in the Cartesian system as

$$\mathbf{H} = \frac{E(z)}{1 - \nu^2(z)} \begin{bmatrix} 1 & \nu(z) & 0 \\ \nu(z) & 1 & 0 \\ 0 & 0 & \frac{(1-\nu(z))}{2} \end{bmatrix}, \mathbf{H}_\tau = \frac{E(z)}{2(1+\nu(z))} \begin{bmatrix} 1 & 0 \\ 0 & 1 \end{bmatrix}, \qquad (10)$$

where $E(z)$ and $v(z)$ are the Young's modulus and the Poisson's ratio respectively. Using the total Lagrangian formulation, the weak form of equilibrium equation is given by

$$G = \int_A [\mathbf{N} \cdot \delta\mathbf{e} + \mathbf{M} \cdot \delta\chi + \mathbf{T} \cdot \delta\gamma] \, dA - G_{ext} = 0 \qquad (11)$$

where G_{ext} is the external virtual work. $\delta\mathbf{e}, \delta\chi$ and $\delta\gamma$ are the variations of shell strains.

3 Finite Element Implementation

In the following section, we elaborate the numerical implementation of the presented shell formulation with a four node shell element. We assume that the mid-surface has been decomposed into finite elements A_e. Using an isoparametric approach, the surface displacement field and the director vector are approximated by

$$\mathbf{u} \;=\; \sum_{i=1}^{4} N_i \mathbf{u}_i, \mathbf{d} \;=\; \sum_{i=1}^{4} N_i \mathbf{d}_i \tag{12}$$

Then, the variation of membrane and bending strains can be written as

$$\delta \mathbf{e} = \mathbf{B}_m \, \delta \boldsymbol{\Phi}_n, \delta \boldsymbol{\chi} = \mathbf{B}_b \, \delta \boldsymbol{\Phi}_n, \tag{13}$$

where $\delta \boldsymbol{\Phi}_n$ is the node variables vector and $\mathbf{B}_m$ and $\mathbf{B}_b$ are the membrane and bending strain-displacement matrices defined as

$$\mathbf{B}_m^I = \begin{bmatrix} \mathbf{B}_{mu}^I & \mathbf{0} \end{bmatrix}, \mathbf{B}_{mu}^I = \begin{bmatrix} \mathbf{a}_1^T N_{i,1} \\ \mathbf{a}_2^T N_{i,2} \\ \mathbf{a}_2^T N_{i,1} + \mathbf{a}_1^T N_{i,2} \end{bmatrix} \tag{14}$$

$$\mathbf{B}_b^I = \begin{bmatrix} \mathbf{B}_{bu}^I & \mathbf{B}_{bd}^I \end{bmatrix}, \mathbf{B}_{bu}^I = \begin{bmatrix} \mathbf{d}_{,1}^T N_{i,1} \\ \mathbf{d}_{,2}^T N_{i,2} \\ \mathbf{d}_{,2}^T N_{i,1} + \mathbf{d}_{,1}^T N_{i,2} \end{bmatrix}, \mathbf{B}_{bd}^I = \mathbf{B}_{mu}^I \tag{15}$$

For, the transverse shear strain, the assumed natural transverse method of Bathe and Dvorkin (1985) is used and give the following strain-displacement relation

$$\delta \boldsymbol{\gamma} = \mathbf{B}_s \, \delta \boldsymbol{\Phi}_n \tag{16}$$

$$\mathbf{B}_s = \begin{bmatrix} N_{1,1} \mathbf{d}_B^T & N_{2,1} \mathbf{a}_B^T & N_{2,1} \mathbf{d}_B^T & N_{2,1} \mathbf{a}_B^T & N_{3,1} \mathbf{d}_D^T & N_{3,1} \mathbf{a}_D^T & N_{4,1} \mathbf{d}_D^T & N_{3,1} \mathbf{a}_D^T \\ N_{1,2} \mathbf{d}_A^T & N_{4,2} \mathbf{a}_A^T & N_{2,2} \mathbf{d}_C^T & N_{3,2} \mathbf{a}_C^T & N_{3,2} \mathbf{d}_C^T & N_{3,2} \mathbf{a}_C^T & N_{4,2} \mathbf{d}_A^T & N_{4,2} \mathbf{a}_A^T \end{bmatrix} \tag{17}$$

where A, B, C, and D denote the mid-points of the elements boundaries. With Eqs. (14), (15) and (16), the weak form, Eq. (11), can be computed. This leads to a nonlinear equation witch can be solved with the Newton method. For more details of the linearization, see (Wali et al. 2014 and Frikha and Dammak 2017).

4   Functionally Graded Materials

In the present paper, the FGM structures are made of a mixture metal and ceramics with a continuous variation of the composition through the thickness. The FGM material properties P, corresponding to the Young's modulus and Poisson's ratio at thickness coordinate z, can be evaluated by the mixture rule

$$P(z) = [P_c - P_m] V_c(z) + P_m, V_c(z) = \left(\frac{1}{2} + \frac{z}{h} \right)^p \tag{18}$$

where P(z), P_m and P_c denote respectively the effective material property, the properties of the metal and ceramic. $V_c(z)$ is the volume fraction, varies according to the power-laws distribution and P is the power law index.

5 Cylindrical Panel Subjected to Concentrated Load

The nonlinear analysis behavior of simply supported cylindrical panel subjected to concentrated load is analyzed. The geometrical properties of the cylindrical panel, given in Fig. 1, are $L = 6$, $R = 2.5$, $h = 0.01$, $E = 10^7$, $\nu = 0.3$. Only one quarter of the cylindrical panel with 10×12 four node mesh is modeled. A displacement of 1.4 is applied in 100 steps.

The load-displacement curve at the applied point for isotropic cylindrical panel with discrete Kirchhoff element SQAD4 (Dammak et al. 2005) and the present FSDT S4 element are plotted in Fig. 2. The load-displacement curve is in good agreement with the reference result from Brendel and Ramm (1980). It is shown a similar behavior around the instability obtained by the Kirchhoff and the Mindlin models. Beyond the instability, the difference between Kirchhoff and Mindlin models increases.

Now consider an FGM simply supported cylindrical panel made of Alumina and Aluminum. Young's modulus for aluminum is $E_m = 70 \times 10^9$ and for Alumina is

Fig. 1 Geometrical parameters of cylindrical panel
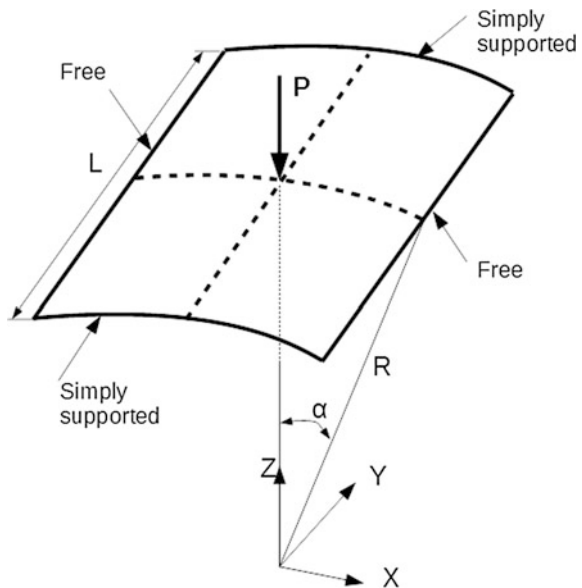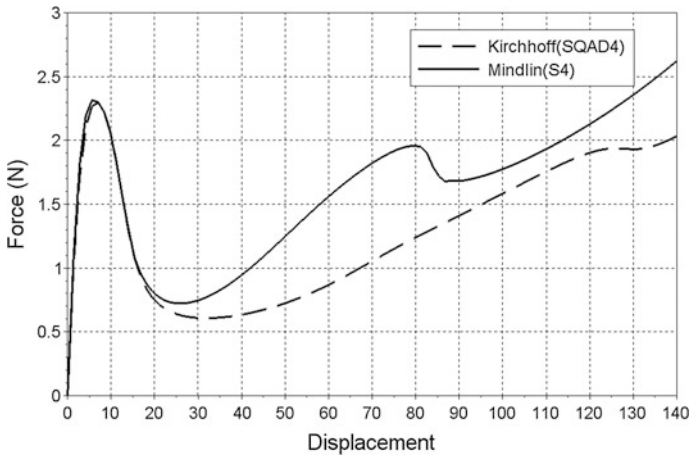
Fig. 2 Load-displacement curve of isotropic simply supported cylindrical panel
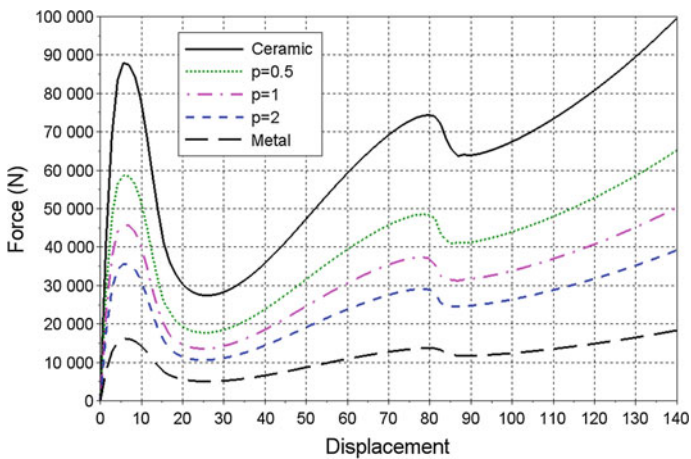
Fig. 3 Load-displacement curve of FGM simply supported cylindrical panel

$E_c = 380 \times 10^9$. Poisson's ratio is considered to be constant 0.3. To validate the proposed formulation, a displacement of 1.4 is imposed. The load-displacement curve of FGM simply supported cylindrical panel is presented in Fig. 3. It is observed that the generated force by cylindrical panel made of ceramic is higher than it is of metal. Moreover, it is shown that the generated force decreases by the increase of power law index.

6 Conclusion

Finite element model based on the Mindlin's first-order shear deformation theory is presented to study the geometrically nonlinear static behavior of 3D-FGM-shell structures. The grading function is assumed through the thickness direction. The validation of the present model is based on comparing results to the literature for a simply supported cylindrical panel subjected to concentrated load. A good agreement is obtained between the present results and the reference results.

References

Bathe KJ, Dvorkin E (1985) A four-node plate bending element based on Mindlin/Reissner plate theory and a mixed interpolation. Int J Numer Methods Eng 21:367–383

Brendel B, Ramm E (1980) Linear and nonlinear stability analysis of cylindrical shells. Compt Struct 12:549–558

Dammak F, Abid S, Gakwaya A, Dhatt G (2005) A formulation of the non linear discrete Kirchhoff quadrilateral shell element with finite rotations and enhanced strains. Revue Européenne des Eléments Finis 14(1):7–31

Dung DV, Hoa LK (2013) Nonlinear buckling and post-buckling analysis of eccentrically stiffened functionally graded circular cylindrical shells under external pressure. Thin Wall Struct 63:117–124

Frikha A, Dammak F (2017) Geometrically non-linear static analysis of functionally graded material shells with a discrete double directors shell element. Comput Methods Appl Mech Eng 315:1–24

Frikha A, Wali M, Hajlaoui A, Dammak F (2016) Dynamic response of functionally graded material shells with a discrete double directors shell element. Compos Struct 154:385–395

Fu L, Waas AM (1995) Initial post-buckling behavior of thick rings under uniform external hydrostatic pressure. Compos Struct 62:338–345

Hajlaoui A, Jarraya A, El Bikri K, Dammak F (2015) Buckling analysis of functionally graded materials structures with enhanced solid-shell elements and transverse shear correction. Compos Struct 132:87–97

Hajlaoui A, Wali M, Ben Jdidia M, Dammak F (2016) An improved enhanced solid shell element for static and buckling analysis of shell structures. Mech Ind 17(5):510

Hajlaoui A, Triki E, Frikha A, Wali M, Dammak F (2017) Nonlinear dynamics analysis of FGM shell structures with a higher order shear strain enhanced solid-shell element. Lat Am J Solids Struct 14:72–91

Huang H, Han Q (2009) Nonlinear elastic buckling and post-buckling of axially compressed functionally graded cylindrical shells. Int J Mech Sci 51:500–507

Kar VR, Panda SK (2016) Post-buckling behaviour of shear deformable functionally graded curved shell panel under edge compression. Int J Mech Sci 318–324

Li ZM, Lin ZQ (2010) Non-linear buckling and postbuckling of shear deformable anisotropic laminated cylindrical shell subjected to varying external pressure loads. Compos Struct 92:553–567

Parisch H (1991) An investigation of a finite rotation four node assumed strain shell element. Int J Num Methods Eng 31:127–150

Shahsiah R, Eslami MR (2003) Thermal buckling of functionally graded cylindrical shell. J Therm Stresses 26(3):277–294

Shen HS (2002) Postbuckling analysis of axially-loaded functionally graded cylindrical panels in thermal environment. Int J Solids Struct 39:5991–6010

Simitses GK (1996) Buckling of moderately thick laminated cylindrical shells: a review. Compos P B: Eng 581–587

Simitses GK, Tabiei A, Anastasiadis JS (1993) Buckling of moderately thick, laminated cylindrical shells under lateral pressure. Compos Eng 3:409–417

Wali M, Hajlaoui A, Dammak F (2014) Discrete double directors shell element for the functionally graded material shell structures analysis. Comput Methods Appl Mech Eng 278:388–403

Wali M, Hentati T, Jaraya A, Dammak F (2015) Free vibration analysis of FGM shell structures with a discrete double directors shell element. Compos Struct 125:295–303

Yang J, Liew KM, Wu YF, Kitipornchai S (2006) Thermo-mechanical post-buckling of FGM cylindrical panels with temperature-dependent properties. Int J Solids Struct 43:307–324

A New Cumulative Fatigue Damage Model for Short Glass Fiber-Reinforced Polyamide 66

E. Chebbi, J. Mars, H. Hentati, M. Wali and F. Dammak

Abstract Fatigue damage of short glass fiber-reinforced composite is a quite complex phenomenon, and a large research effort is being spent on it these days. Furthermore, fatigue damage in such materials, fatigue damage kinetic exhibits three stages, namely: (i) matrix microcracking and damage initiation, (ii) coalescence and propagation of microcracks and (iii) macroscopic cracks propagation up to material failure. The proposed model is based on the stiffness degradation rule of short glass fibers-reinforced polyamide 66. This new versatile phenomenological fatigue damage model attempts to predict fatigue damage growth in its three stages. The characteristics of damage growth and accumulation of short glass fiber-reinforced polyamide 66 under fatigue bending loading were studied in this paper. Experimental data from bending fatigue tests were used to identify the model parameters. Results showed that this model is capable of describing the three stages of damage evolution of theses composite materials. Furthermore, the predicted fatigue life is in good agreement with the experimental ones.

Keywords Fatigue model · Polyamide 66 · Glass fiber · Damage accumulation

E. Chebbi (✉) · J. Mars · H. Hentati · M. Wali · F. Dammak
Mechanical Modeling and Manufacturing Laboratory (LA2MP), National Engineering
School of Sfax, University of Sfax, B.P. 1173, 3038, Sfax, Tunisia
e-mail: chebbi.elouni@gmail.com

J. Mars
e-mail: jamelmars@yahoo.fr

H. Hentati
e-mail: hamdi.hentati@yahoo.fr

M. Wali
e-mail: mondherwali@yahoo.fr

F. Dammak
e-mail: fakhreddine.dammak@enis.rnu.tn

1   Introduction

The fatigue damage behavior investigation is one of the most important focuses of engineering design of composite materials and it is the basis to predict fatigue life of composite structures. However, fatigue damage of composite materials is more complex than that of metals. Moreover, short glass fiber-reinforced polyamide 66 (PA66GFs) are very inhomogeneous since their mechanical properties result from the combination of the matrix, the glass fibers and of the interface (matrix/glass fiber) properties (Benaceur et al. 2008; Atidel et al. 2011; Chebbi et al. 2016a). Consequently, the fatigue behavior of PA66GFs is quite a complex phenomenon since it is influenced by a large number of loading and structural parameters. Under cyclic loading, the material irreversible degradations will occur in micro-local field and lead to fatigue damage. As a result, of fatigue damage accumulation a change in the macroscopic mechanical properties of the composite is observed. This phenomenon can be monitored through the material strength or stiffness degradation. Based on experimental investigations, Reifsnider et al. (1983) concluded that fatigue damage evolution is nonlinear in composite materials.

The specimen behavior exhibits three distinct stages of stiffness degradation during displacement controlled bending fatigue tests (Fig. 1): (i) The first stage shows rapid stiffness reduction caused by the development of matrix microvoids; (ii) In the second stage, the dominant damage mechanisms are coalescence and propagation of the microcracks. A gradual stiffness reduction of the material occurs in an approximately linear manner. The majority of fatigue life is categorized under this region. (iii) The last stage is characterized by sudden stiffness reduction followed by total failure. The most dominant failure in this region is fiber fractures and macroscopic crack propagation (Nouri et al. 2009; Esmaeillou et al. 2012) .

Fig. 1 Fatigue damage evolution
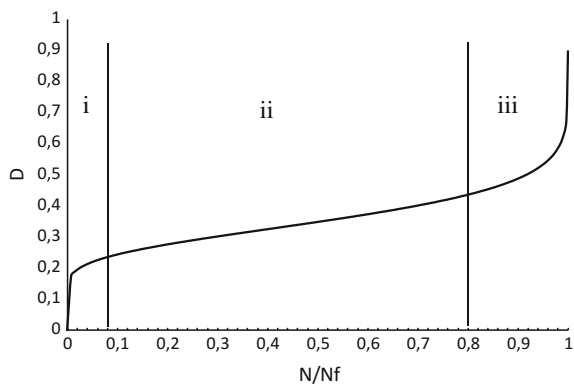
Fatigue damage development has been investigated and modeled based on strength degradation, stiffness degradation and energy dissipation of composites (Subramanian et al. 1995; Gu and Yao 1999; Mao and Mahadevan 2002; Zhai and Yao 2002; Epaarachchi and Clausen 2005).

In the open literature, fatigue damage of composite materials has been extensively investigated and modeled. Poursartip et al. (1986) presented a phenomenological model to investigate the of fatigue damage of a carbon fiber composite laminate. The unidirectional damage growth rate is a power function of the stress amplitude and of the mean stress, and it is independent of damage when cycling is at constant stress amplitude. Sidoroff and Subagio (1987) proposed a unidirectional fatigue damage evolution different in tensile and compressive regime and depend on the applied strain amplitude and the damage itself. Similar expressions were derived by Liu and Lessard (1994) and Kawai (2004). A new fatigue damage model was proposed by Van Paepegem and Degrieck (2001), similar to the one proposed by Sidoroff and Subagio (1987), but used the stress amplitude instead of the strain amplitude. The developed model is validated through experimental results for plain-woven glass/epoxy composite. In Taheri-Behrooz et al. (2008), the authors presented a list of four earlier developed models for unidirectional stiffness degradation and proposed their own models.

Continuum damage mechanics (CDM) approach coupled with a fatigue predictor to make a fatigue damage formalism are investigated in several contributions. The theory of continuum damage was first introduced by Kachanov (1958) to explain the process of degradation of materials. The success of this approach has encouraged its extension to fatigue damage.

Many of the developed fatigue damage models are based on the small strain assumption. This consideration can be coupled with a single damage variable or with several damage variables to results in an isotropic or anisotropic damage model respectively. Based on the theory of anisotropic damage and in the framework of continuum damage mechanics, Ladevèze and Le Dantec (1992) formulated a new phenomenological fatigue damage model for laminate composites. This model was formulated under the plane-stress assumptions. Furthermore, it has been reformulated by Sedrakian et al. (2002) in terms of strain energy to make the numerical implementation in finite elements code easier. The same model was extended by Nouri et al. (2009) to predict nonlinear cumulative diffuse fatigue damage in short glass fiber-reinforced polyamide 66. The developed model allowed predicting the three damage stages observed for this material. Therefore, damage rate was assumed to be the sum of a power function and an exponential law, to capture all the three stages.

In this paper, fatigue damage development of short glass fiber-reinforced polyamide 66 was investigated and a phenomenological fatigue damage model defined by material stiffness degradation is developed. Experimental data from bending fatigue tests were employed to identify the model parameters, and the results show that the model can describe the three stages of damage evolution.

2 Material and Testing Procedures

The material studied is a short fiber reinforced polyamide 66, containing 20% and 30% by weight of short glass fibers. Polyamide 66 and polyamide 66 containing 30% wt glass fibers were used to produce molded composites with 0, 10, 20, and 30% wt glass content. They were respectively designed as PA66GF00, PA66GF10, PA66GF20, and PA66GF30. Rectangular plates by dimensions of $125 \times 105 \times 4$ mm, and ISO 527-2 specimens are obtained by molding injection see Chebbi et al. (2016b). The mechanical behavior was investigated using ISO 527-2 specimens under tensile testing. The tensile tests were carried out at room temperature using a 10 kN Instron testing machine equipped with a RUDLPH laser extensometer under cross-head speed of 1 mm/min.

Fatigue tests were performed using an in house developed testing machine. The outcoming shaft of the motor has a rotational speed of 1500 rpm. A variable-frequency drive is used to provide different fatigue testing frequencies. The alternating displacement ($u(t)$) is imposed using an adjustable crank-linkage mechanism. This mechanism imposes an alternating movement to the slider through the connecting rod. At the end of the slider, a force gage is connected to the specimen fixture in order to measure the force acting in the composite specimen. The other end of the specimen is clamped using four clumping bolts at equal constant torque (Chebbi et al. 2016b).

3 Fatigue Damage Model

The concept of damage accumulation may be used as a more suitable approach to predict the fatigue life of structures of composite materials. However, fatigue damage cannot be measured directly. Therefore, for quantitative evaluation of fatigue damage, Young's modulus or the stiffness of composite materials are often used to evaluate the fatigue damage due to cyclic loading. Fatigue damage can be defined in the term of Young's modulus as follows (Lemaitre and Chaboche 1990):

$$D = 1 - \frac{E}{E_0}, \tag{1}$$

where D the accumulated fatigue damage, E_0 is initial Young's modulus, and E is Young's modulus of the material subjected to the Nth cycling loading.

The experimental results show that the measured Young's modulus or stiffness just before complete failure of the specimen is not zero. Therefore, a new damage parameter can be defined with the final Young's modulus E_f as (Mao and Mahadevan 2002):

$$D = \frac{E_0 - E}{E_0 - E_f} \tag{2}$$

In this paper, a new versatile damage accumulation model is presented to describe the degradation of composite materials. This model aims to predicts the three stages of damage growth. The proposed fatigue damage growth rate is of the form:

$$\frac{dD}{dN} = \left(1 - (1-D)^{\frac{1}{\beta}}\right)^{\frac{\alpha - 1}{\alpha}} \left(\frac{\Delta\sigma}{M(1-D)}\right)^{\frac{1-\beta}{\beta}} \tag{3}$$

D is the damage scalar variable and N is the number of cycles. $\Delta\sigma$ is the amplitude of the applied stress. β and M are a material constants. The function α links the damage to the cyclic loading, it may be expressed as

$$\alpha = c(\Delta\sigma)^{-d} \tag{4}$$

The number of cycles to failure N_f under a constant loading amplitude is obtained by integrating Eq. (3) from $D = 0$ (initial undamaged state) to $D = 1$ (Total failure):

$$N_f = \alpha \cdot \beta \cdot M^{\frac{1-\beta}{\beta}} (\Delta\sigma)^{-\frac{1-\beta}{\beta}} \tag{5}$$

The damage evolution is given by the following equation:

$$D = 1 - \left(1 - \left(\frac{N}{N_f}\right)^\alpha\right)^\beta \tag{6}$$

Based on the experimental results, least square fitting procedure using the modified algorithm of Levenberg Marquardt was applied to determine the model parameters. The function that defines the least-squares problem can be written as

$$F = \min \sum_{test=1}^{nt} \sum_{pt=1}^{np} \left(1 - \frac{D_{Exp}}{D_{Num}}\right)^2, \tag{7}$$

where nt is the number of tests for each material, np is the number of experimental points for each test, D_{Exp} is the damage experimental value and D_{Num} is the damage numerical value (Eq. 6). The obtained values of the model parameters are listed out in Table 1.

Table 1 Values of the parameters of the presented model

	c	d	M	β
PA66GF20	444.88×10^5	4.523	878.5	0.1286
PA66GF30	62.267	1.423	567.05	0.107

4   Results and Discussion

Curves presented in Figs. 2 and 3 give the fatigue damage growth obtained under loading amplitude of $u_{max} = 10$ mm for two different fiber contents.

Fatigue damage curves show three stages: In the first stage, multiple damage modes are acting within the material and the fatigue damage raises rapidly. The damage increases in a linear manner during the second stage due to crack growth and coalescence until it reaches saturation. In the final stage fiber failure, interfacial debonding leads to the sudden failure of the composite material. These results are in good agreement with experimental observation found by Reifsnider et al. (1983). It is worthwhile to note that there is a good agreement between experimental results and numerical ones. Equation (6) is capable of describing the nonlinear damage evolution macro-mechanically in all periods of the fatigue life of composite
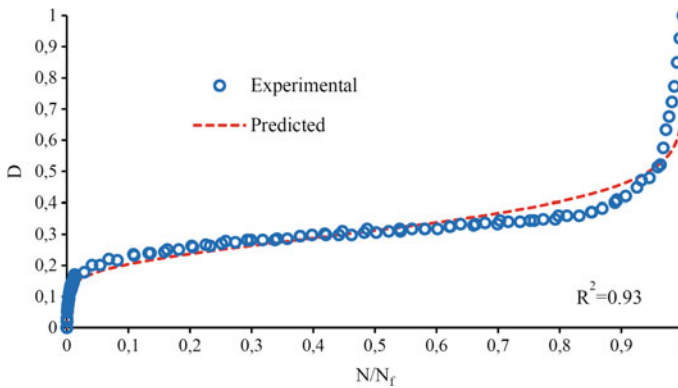
Fig. 2   Damage growth under imposed displacement $u_{max} = 10$ mm (PA66GF20)
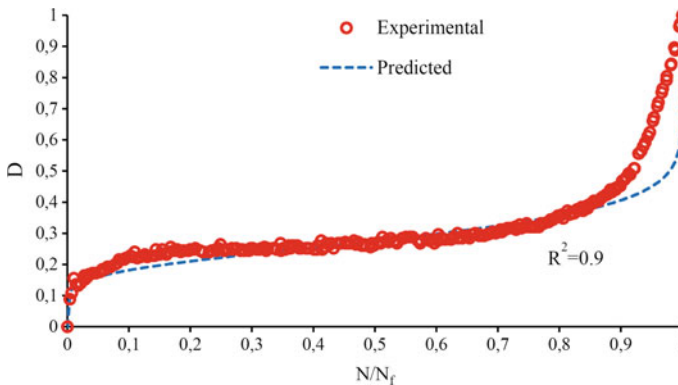
Fig. 3   Damage growth under imposed displacement $u_{max} = 10$ mm (PA66GF30)

materials. The damage consists mainly in the onset, the coalescence and the propagation of matrix microcracks. During the initial stage of the fatigue life, the main damage type is the matrix microcracks and microvoids. Damage starts after a few number of loading cycles inducing an initial high stiffness reduction of the composite material. The second stage corresponds to the coalescence and the propagation of the microcracks at the fiber–matrix interface. This stage is characterized by a gradual stiffness reduction of the material. The last stage is characterized by fiber fracture and macroscopic cracks propagation. This third stage may result in a rapid stiffness reduction leading to the total material ruin.

5   Conclusion

Fatigue damage accumulation in short glass fiber-reinforced polyamide 66 materials is investigated in this paper. Experimental results show that damage evolution in the composite under fatigue loading occurs according to three different stages. During the first stage, fatigue damage grows rapidly due to the occurrence of multiple damage modes within the material. The damage increases steadily and slowly during the second stage. During the third and final stage, the damage again grows rapidly due to the fracture of fibers.

A cumulative fatigue damage model is proposed to describe the three stages of damage evolution in composite materials. By comparison with experimental fatigue test data, a reasonably good predictive capability of the new model has been demonstrated.

References

Atidel G, Saintier N, Dhiab A, Dammak F (2011) Etude du comportement mécanique d'un polyamide 66 chargé de fibres de verre courtes. Mécanique & Industrie 12(5):333–342

Benaceur I, Othman R, Guegan P, Dhieb A, Damek F (2008) Sensitivity of the flow stress of nylon 6 and nylon 66 to strain-rate. Int J Mod Phys B 22(9–11):1249–1254

Chebbi E, Wali M, Dammak F (2016a) An anisotropic hyperelastic constitutive model for short glass fiber reinforced polyamide. Int J Eng Sci 106:262–272

Chebbi E, Mars J, Wali M, Dammak F (2016b) Fatigue behavior of short glass fiber reinforced polyamide 66: experimental study and fatigue damage modelling. Period Polytech Mech 60:247–255

Epaarachchi JA, Clausen PD (2005) A new cumulative fatigue damage model for glassfibre reinforced plastic composites under step/discrete loading. Compos A 36:1236–1245

Esmaeillou B, Ferreira P, Bellenger V, Tcharkhtchi A (2012) Fatigue behavior of polyamide 66/glass fiber under various kinds of applied load. Polym Compos 33:540–547

Gu Y, Yao W (1999) Residual strength of fiber-reinforced plastics under fatigue loading. Acta Mater Compos Sin 16:98–102

Kachanov ML (1958) Time of the rupture process under creep conditions. TVZ Akad Nauk SSR Otd Tech Nauk 8:26–31

Kawai M (2004) A phenomenological model for off-axis fatigue behavior of unidirectional polymer matrix composites under different stress ratios. Compos A 35:955–963

Ladevèze P, Le Dantec E (1992) Damage modelling of the elementary ply for laminated composites. Compos Sci Tech 43:257–267

Lemaitre L, Chaboche JL (1990) Mechanics of solid materials. Cambridge University Press, London

Liu B, Lessard LB (1994) Fatigue and damage tolerance analysis of composite laminates: stiffness loss damage modeling and life prediction. Compos Sci Technol 51:43–51

Mao H, Mahadevan S (2002) Fatigue damage modeling of composite materials. Compos Struct 58:405–410

Nouri H, Meraghni F, Lory P (2009) Fatigue damage model for injectionmolded short glass fiber reinforced thermoplastics. Int J Fatigue 31:934–942

Poursartip A, Ashby MF, Beaumont PWR (1986) The fatigue damage mechanics of a carbon fiber composite laminate: I-Development of the model. Compos Sci Tech 25:193–218

Reifsnider KL, Henneke EG, Stinchcomb WW, Duke JC (1983) Damage mechanics and NDE of composite laminates. In: Hashin Z, Herakovich CT (Recent advances) (eds) Mechanics of composite materials. Pergamon Press, New York, pp 399–420

Sedrakian A, Ben Zineb T, Billoet JL (2002) Contribution of industrial composite parts to fatigue behavior simulation. Int J Fatigue 24:307–318

Sidoroff F, Subagio B (1987) Fatigue damage modelling of composite materials from bending tests. In: Matthews FL, Buskell NCR, Hodgkinson JM, Morton J (eds). Sixth international conference on composite materials (ICCM-VI) and second European conference on composite materials (ECCM-II), vol 4. Proceedings, 20–24 July, London, UK, Elsevier, pp 4.32–4.39

Subramanian S, Reifsnider KL, Stinchcomb WW (1995) A cumulative damage model to predict the fatigue life of composite laminates including the effect of a fiber matrix interphase. Int J Fatigue 17:343–351

Taheri-Behrooz F, Shokrieh MM, Lessard LB (2008) Residual stiffness in cross-ply laminates subjected to cyclic loading. Compos Struct 85:205–212

Van Paepegem W, Degrieck J (2001) Experimental setup for and numerical modelling of bending fatigue experiments on plain woven glass/epoxy composites. Compos Struct 51:1–8

Zhai H, Yao W (2002) A survey on stiffness reduction models of fiber reinforced plastics under cyclic loading. Adv Mech 32:69–80

Independent Loops Selection in a Hydraulic Looped Network

Zahreddine Hafsi, Sami Elaoud, Manoranjan Mishra and Mohsen Akrout

Abstract As a preliminary important phase for a hydraulic network analysis procedure, loops identification process is studied in this paper by presenting an automated algorithm to select a set of independent loops for the network equilibrium. Through the presented study, the hydraulic network is modeled as an undirected graph edges-vertices. Also, to take into consideration the mechanical characteristics of the network, weights are assigned to pipes based on their hydraulic resistances. The assigned weights are taken as a selection criterion for loops identification. A numerical code under Matlab environment is generated and the established framework is tested on a set of real case networks. The obtained results are compared to those issued from previous researchers. Thus, the framework has proved its efficiency in identifying a set of independent loops even for complex network topologies. The mutual independence of the obtained loops is verified which allows to use the presented algorithm to build a general automated framework for water distribution network analysis.

Z. Hafsi (✉) · S. Elaoud · M. Akrout
Laboratory of Applied Fluids Mechanics, Process and Environment Engineering,
National Engineering School of Sfax, Sfax, Tunisia
e-mail: zahreddine.hafsi@enis.tn

M. Mishra
Department of Mathematics, Indian Institute of Technology Ropar,
Rupnagar 140001, Punjab, India
e-mail: manoranjan@iitrpr.ac.in

1 Introduction

The word "network" in its broad sense is used in the majority of science domains. Depending on the field of study (electricity, fluid mechanics, telecommunication, etc.), the "network" has its proper characteristics. Nevertheless, in general, any network may be defined as a set of edges-vertices i.e., a set of branches linked via nodes. In that way, the network can be treated as a graph and the graph theory has been always used to deal geometrically with any network independently of the field of study (Harary 1969; Georgios et al. 2011). In fluid mechanics, gas, and hydraulics networks obey to the latter definition. Among the hydraulic networks, water distribution networks are the most encountered worldwide, their topologies range from simple to more complex. Such networks may adopt a tree, a looped or a hybrid topology.

The principal aim of a hydraulic network analysis is to determine the flow rate distribution within the network pipes as well as the pressure in nodes. The latter analysis is based essentially on Kirchhoff's laws viz. Nodes and loops laws (Krope et al. 2006).

For a simple tree network topology, the hydraulic analysis is easy to accomplish since the flow direction is evident and the network involves no loops, hence only nodes equations are to solve. Nevertheless, complexity arises when it comes to analyzing looped networks, the situation often encountered in water distribution network feeding consumers in a city for instance. In fact, and to write loops law, a set of independent loops is required to be defined prior to any hydraulic analysis. Thus, a graph study is to be performed to fulfill this preliminary step. In literature, many algorithms were presented for loops identification process (Alvarruiz et al. 2015; Creaco and Franchini 2014, 2015; Alvisi et al. 2011). The latter algorithms were mainly utilized to look for optimum parameters to design a water distribution network (Bragalli et al. 2008).

In this paper, a loops identification algorithm is built in order to accomplish the first phase in the automation of water network analysis.

A graph study is performed to identify a set of independent loops in an undirected graph. The loops identification process is applied to real topologies and the accuracy of the algorithm is proved. Contrary to most previously established algorithms, the aim of this study, rather than a selection of a set of minimum loops (geometrically), is to build an efficient algorithm taking in consideration the mechanical and structural characteristics of the real hydraulic network in parallel with its geometric layout.

2 Fundamentals of Water Looped Network Analysis

The water looped network equilibrium is reposed on nodes law traducing mass continuity and loops law traducing energy conservation.

For each node i of the hydraulic network, mass conservation is written

$$\left(\sum q_{in} - \sum q_{out}\right)_i = 0 \tag{1}$$

where q denotes the volumetric flow rate.

Loops law stipulates that the sum of the pressure drops within a closed loop is null. In literature, different formulas exist to express the frictional pressure drop along a pipe, e.g., the Hazen Williams formula (Alvarruiz et al. 2015) and the Darcy Weisbach formula. The latter formula is written (Walski et al. 2001)

$$\Delta H = \frac{8\lambda L}{\pi^2 g D^5} q^2 \tag{2}$$

where λ is the friction factor coefficient between water and the pipe wall, g is the gravitational acceleration, D is the pipe diameter, and L is its length.

The friction factor coefficient may be calculated using the Moody diagram or also via correlations that express the latter coefficient as a function of the flow parameters and the pipe characteristics e.g., the Colebrook White expression

$$\lambda = -2 \log_{10}\left(\frac{e}{3.7D} + \frac{2.51}{\text{Re}\sqrt{\lambda}}\right) \tag{3}$$

where e is the pipe internal roughness and Re is the Reynolds number.

Considering a looped network of p pipes and n nodes (from which n_0 source nodes), the number of independent loops that features the network is (Creaco and Franchini 2015)

$$l = p - n + n_0 \tag{4}$$

The analysis of the network requires the determination of p unknowns (the flow rates through the p pipes) i.e., p independent equations are needed; l loops equations and $(n - n_0)$ nodes equations (equations of source nodes are disregarded as they are always dependent on the other consumption nodes equations). A nonlinear system of p independent equations is then written.

3 Independent Loops Identification Process

3.1 Looped Network Definition

A looped network is defined by an incidence matrix pipe-nodes A of size $[p \times n]$, the latter may be written $A = [A12; A10]$ where $A12$ is the incidence matrix pipes-consumption nodes and $A10$ is the incidence matrix pipes-source nodes (Creaco and Franchini 2014, 2015).

Fig. 1 Network example
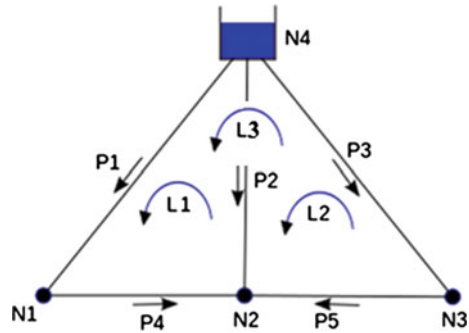
The selection of the independent loops in which energy conservation is applied is a step to be performed prior to any hydraulic analysis, for instance, considering the simple network of Fig. 1 (Alvarruiz et al. 2015). The network features $p = 5$ pipes and $n = 4$ nodes ($n_0 = 1$) thus $l = 2$ loops.

For this case, the loops choice is obvious since the latter network features in global three loops from which we choose two independent ones L1 and L2. In a general way, any combination C_3^2 of two loops from the three available is valid to write loops law. For a graph study based on a minimum topological length as a selection criterion, the big loop L3 will be disregarded. Nevertheless, this approach is not always the optimum one in a whole framework of network analysis as it will be discussed in coming sections.

To the set of the independent loops, an incidence matrix M_{31} of size $[l \times p]$ is associated (Creaco and Franchini 2014, 2015; Todini and Rossman 2013). $M_{31}(j, k) = \pm 1$ depending on the agreement between the assumed flow direction in the pipe k belonging to the loop j and the rotation direction of the loop j, otherwise $M_{31}(j, k) = 0$. For the simple network of Fig. 1 and considering loops L1 and L2, the matrices A and M_{31} are written as follows

$$A = \begin{pmatrix} \overbrace{\begin{matrix} 1 & 0 & 0 \end{matrix}}^{A_{12}} & \overbrace{-1}^{A_{10}} \\ 0 & 1 & 0 & -1 \\ 0 & 0 & 1 & -1 \\ -1 & 1 & 0 & 0 \\ 0 & 1 & -1 & 0 \end{pmatrix}; \quad M_{31} = \begin{pmatrix} 1 & -1 & 0 & 1 & 0 \\ 0 & 1 & -1 & 0 & -1 \end{pmatrix}$$

Since the loop identification result is not unique, the matrix M_{31} may have different definitions depending on the set of the selected loops. Generally, in the optimization algorithms encountered in literature, the target was to determine the shortest loops i.e., the matrix M_{31} the more sparse (formed up by the independent loops that feature the minimum number of pipes).

Whatever the set of the identified independent loops, the condition $M_{31} \cdot A_{12} = 0$ has to be fulfilled.

In the case of more than one source node, for each additional source node, an additional loop is formed. Then, a fictitious loop linking each additional source node to the principal one is considered (Creaco and Franchini 2014), another option is to transform the initial network layout to be a single source network by connecting all additional source nodes to the principal one (Alvarruiz et al. 2015; Creaco and Franchini 2015).

3.2 Loops Identification Algorithm

In this section, the outlines of the algorithm presented by Creaco and Franchini (2014) are followed up. The latter algorithm is reposed on the following steps:

(i) Starting from a layout of a single source looped network, a Minimum Spanning Tree (MST) is determined (Kruskal 1956; Prim 1957) and a vector $V = (v_1, \ldots, v_l)$ of the removed pipes to obtain the MST is constructed.

(ii) For the first element of the vector V, the corresponding pipe v_1 is removed from the original layout and the shortest path linking their two ends is searched for (Dijkstra 1959; Bellman 1958). Then, the concerned pipe is added to the path to form the first loop (the first row r_1 in the matrix M_{31} is built).

(iii) For a pipe v_i ($2 < i \leq l$), a test has to be done to check if it belongs to a previously built loop. If it belongs to a row r_k, both pipes v_1 and v_k are removed simultaneously from the layout and then two loops are formed relating the ends of each pipe. The selection criterion of the loop to retain is its independence from the previously identified loops, if both loops fulfill that condition, the loop of the minimum topological length is chosen and the row r_i of M_{31} is constructed.

(iv) The process is conducted till obtaining the l independent loops.

It is to note that, for the case of parallel loops (loops featuring only two nodes), these ones have to be determined first, removed from the layout and then the previous algorithm is applied to identify other loops (Creaco and Franchini 2015).

That was an overview of the loops identification algorithm. For this algorithm, as far as the minimum loops are concerned, the step (iii) is of crucial importance to select the optimum independent loops, depending on the complexity of the network topology, this step may be time-consuming. Thus, and as our aim is to determine a set of independent loops to balance the water distribution network disregarding an optimal choice, a first modification is made to the latter algorithm in a way that step (iii) will be omitted. The idea is; instead of considering the original layout and removing the concerned pipe for each iteration, we consider from the beginning the MST layout (we remove all pipes of vector V simultaneously) and for each step we

look for the shortest path linking the two end nodes of the concerned pipe of vector V. In that case, for each iteration, we are sure that the concerned pipe doesn't belong to any of the yet determined loops and only one loop is formed for each iteration.

The optimization of the loops selection was not a priority for the proposed modification. Nevertheless, and since the presented loops identification algorithm is, in fact, a first step for the analysis of the looped network, an optimization of the selected loops may be considered by assigning a weight to the pipes prior to the identification process. Thus, a second modification is made to the latter algorithm by considering assigned weights to the network pipes as a selection criterion for loops rather than the minimum topological length.

As actually the network is a set of pipes and nodes which are real components having mechanical characteristics, weights based on these characteristics may be assigned to pipes. Thus, Instead of allowing the algorithm considering a minimum topological length to build the MST, the geometrical length may be the base of weight assignment for each pipe so that the network pipes are sorted according to their lengths and the shortest pipes will be the less weighted (having the minimum lengths). Nevertheless, for hydraulic networks analysis, considering the hydraulic resistance Eq. (2) $R_h = 8\lambda L / \left(\pi^2 g D^5\right)$ as a criterion for weight assignment is likely to result in a set of more optimized independent loops that speed up the hydraulic analysis (Travers 1967). The adoption of this weight assignment basis is justified by the fact that in a node the flow is always looking for the less resistive path to follow and the shortest pipe is not always a less resistive one as stipulated by the expression of R_h.

4   Results and Discussion

The algorithm of the loops identification process is applied to three case studies, a simple network example and two real water distribution networks Modena (Creaco and Franchini 2015; Bragalli et al. 2008) and Fossolo (Bragalli et al. 2008; Raad 2011). Table 1 resumes the topological characteristics of each network. For the studied cases, the clockwise rotation of a loop is assumed to be a rotation in the positive direction.

The first network case plotted in Fig. 2 is treated as a geometrical graph and the MST as well as the independent loops are determined without assignment of weights i.e., the topological length will be the basis of the MST construction.

For this simple network, a matrix M_{31}^a representing the set of the minimum independent loops is easy to determine manually, such matrix may also be found

Table 1 The studied networks characteristics	Network	p	n	n_0	l	Parallel loops
	Simple case	12	9	1	4	0
	Fossolo	58	37	1	22	0
	Modena	317	272	4	49	0
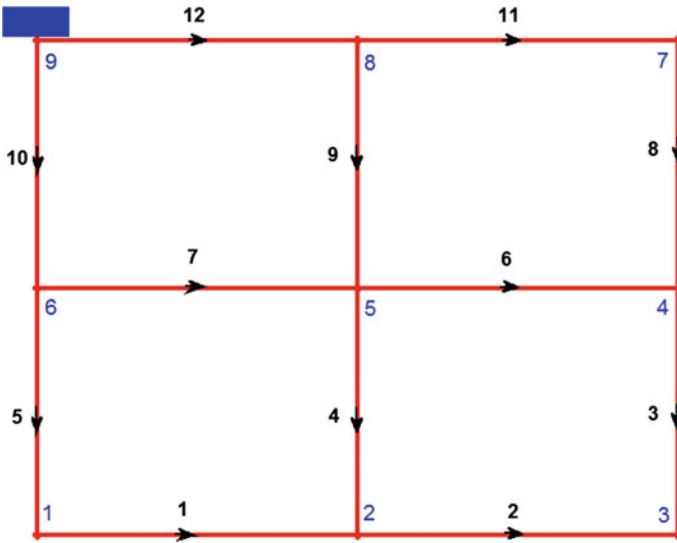
Fig. 2 Simple network layout

using an optimized algorithm (Creaco and Franchini 2014) taking in consideration step (iii) of the previous section.

The matrices M_{31}^a and M_{31}^b issued respectively from an optimized algorithm and from the modified one presented in this paper are:

$$M_{31}^a = \begin{pmatrix} 0 & 0 & 0 & 0 & 0 & 0 & -1 & 0 & 1 & -1 & 0 & 1 \\ 0 & 0 & 0 & 0 & 0 & -1 & 0 & 1 & -1 & 0 & 1 & 0 \\ 0 & -1 & 1 & -1 & 0 & 1 & 0 & 0 & 0 & 0 & 0 & 0 \\ -1 & 0 & 0 & 1 & -1 & 0 & 1 & 0 & 0 & 0 & 0 & 0 \end{pmatrix}$$

and

$$M_{31}^b = \begin{pmatrix} -1 & 0 & 0 & 1 & -1 & 0 & 0 & 0 & 1 & -1 & 0 & 1 \\ 0 & 1 & -1 & 1 & 0 & -1 & 0 & 0 & 0 & 0 & 0 & 0 \\ 0 & 0 & 0 & 0 & 0 & 0 & -1 & 0 & 1 & -1 & 0 & 1 \\ 0 & 1 & -1 & 1 & 0 & 0 & 0 & -1 & 1 & 0 & -1 & 0 \end{pmatrix}$$

It is obvious that an optimized algorithm gives a more sparse matrix, but it is to mention also that the less sparse matrix M_{31}^b was rapidly obtained by the presented algorithm (about 0.075547 s in a Matlab 2012a environment) and both matrices are of full rank i.e., representing a set of independent loops that may be used to write loops law for a hydraulic network analysis.

The geometrical (pipes diameters and lengths) and topological (upstream and downstream nodes) characteristics of Fossolo and Modena networks reported in an
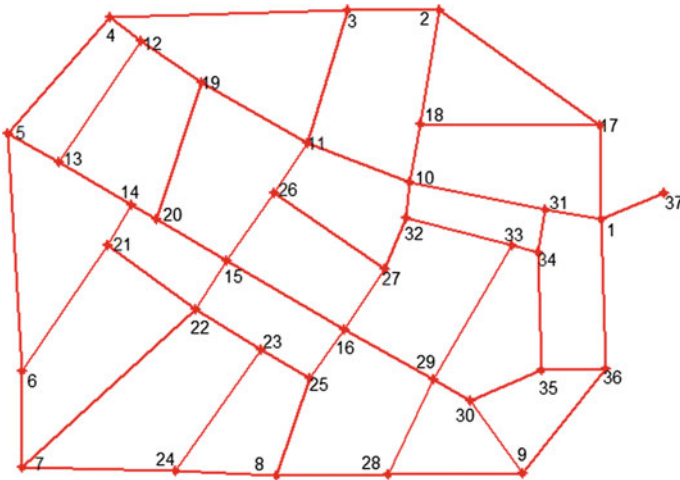
Fig. 3 Layout of Fossolo network

Excel or a text file (http://emps.exeter.ac.uk) are the inputs of the established Matlab code.

In Figs. 3 and 4, are plotted, respectively, the layouts of Fossolo and Modena networks based on their real geometrical characteristics.

As shown in Table 1, Modena network involves four source nodes; one is chosen as a principal node (ID 269) to which the other three nodes (IDs 270, 271,
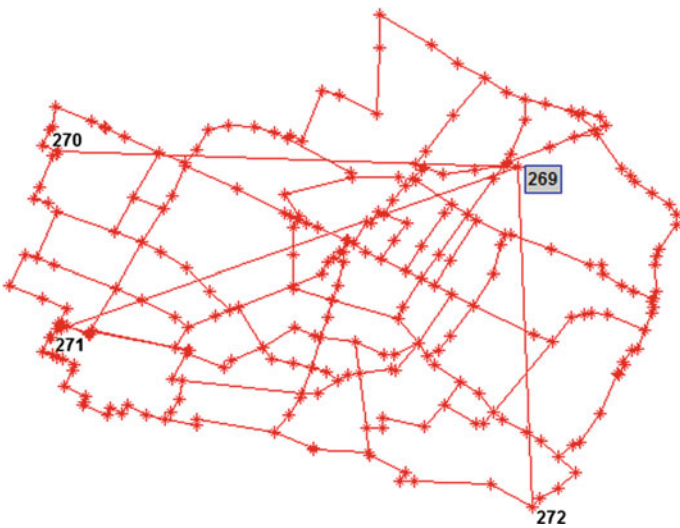
Fig. 4 Layout of Modena network

and 272) are linked and then the obtained layout, as presented in Fig. 4, is considered for the loops identification process.

For both networks, the material of the pipe is considered to be cast iron whose absolute roughness is 0.26 mm (Binder 1973).

For these two real case studies, prior to the loop identification process, weights are assigned to the pipes based on the minimum hydraulic resistance criterion. Thus, for each pipe, an evaluation of R_h is needed which require to calculate the friction factor λ for each pipe. Nevertheless, in the implicit expression of λ (Eq. (3)), the Reynolds number needs to be determined which is actually a function of the flow rate within the considered pipe and this flow rate itself is not yet known as it is, in fact, the aim of the whole equilibrium process.

At the moment of entering a junction between two pipes, the flow tends to follow the less resistive path i.e., the pipe having the smaller friction factor. The friction factor of Eq. (3) involves two main terms, one describing the friction between the fluid and the pipe internal wall, and another describing the friction between the fluid molecules which is related to the fluid viscosity and the instantaneous flow rate. For an element of fluid entering a junction, just prior to the flow splitting and as the flow in both downstream pipes to the junction is not yet developed, a less resistive pipe is simply the less rough. Thus, disregarding the fluid viscosity effect in Eq. (3), a friction factor (denoted λ^*) was calculated considering only the pipe's internal roughness effect.

$$\lambda^* = -2 \log_{10}\left(\frac{e}{3.7D}\right) \tag{5}$$

Actually, the latter relation called von Karman's relation (Dobrnjac 2012) was also widely used to approximate the friction factor coefficient in the case of fully turbulent flow (high Reynolds number) in rough pipes.

Using Eq. (3), the hydraulic resistance of all pipes of each network is evaluated and weights are assigned to pipes (the less resistant pipes are the less weighted) by sorting the hydraulic resistances in ascending (As non nulls, the R_h's themselves may be considered as weights). Table 2 shows, for Fossolo network, the calculated hydraulic resistance R_h and the assigned weight to each pipe. A similar weights assignment was attributed to Modena network pipes.

For Fossolo network, the established algorithm results in a full rank matrix M_{31} of size 22 × 58 determining the 22 independent loops of the network.

For Modena network, the same procedure leads also to a full rank matrix M_{31} of size 49 × 317 representing the 49 independent loops of the network from which there are three fictious loops due to the three sources nodes linked to the principal one. The condition $M_{31} \cdot A_{12} = 0$ is also verified for the studied cases.

As expected, the obtained matrices M_{31} for Fossolo and Modena networks feature a big number of non-zero elements nz, in fact, these matrices even if they determine accurately a set of independent loops for the networks, they are not the sparsest possible ones comparing to related researches (Creaco and Franchini 2015). Their sparsities are plotted in Fig. 5 and Fig. 6 respectively.

Table 2 Assigned weights for Fossolo network pipes

Pipe ID	Weight	Pipe ID	Weight	Pipe ID	Weight
1	22	21	11	41	26
2	58	22	5	42	55
3	43	23	7	43	27
4	56	24	12	44	32
5	35	25	15	45	23
6	57	26	30	46	41
7	46	27	25	47	33
8	53	28	6	48	17
9	45	29	8	49	51
10	49	30	14	50	50
11	38	31	36	51	34
12	29	32	40	52	48
13	21	33	42	53	16
14	2	34	19	54	10
15	3	35	18	55	31
16	4	36	52	56	37
17	9	37	47	57	28
18	13	38	39	58	1
19	20	39	44		
20	24	40	54		
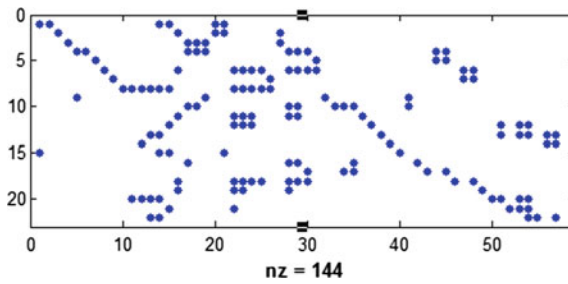
Fig. 5 Sparsity of loops matrix for Fossolo network
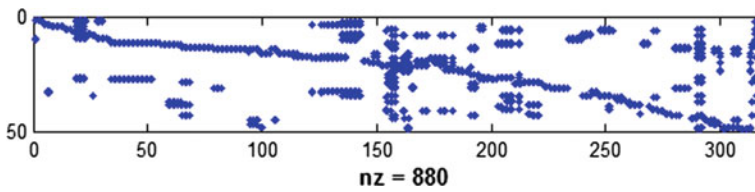
Fig. 6 Sparsity of loops matrix for Modena network

5 Conclusion

In this paper, an algorithm of loops identification in water distribution network was presented and its efficiency was proved through the study of real network topologies of different complexity levels.

The presented algorithm, even if it is not well optimized compared to related works, it is built considering a selection criterion (less resistive pipes) that may speed up a further step of network equilibrium based on the selected loops.

Once integrated into a framework of looped network analysis the presented algorithm may be modified to reach a compromise between the rapidity convergence and the accuracy of obtained results (pressure in nodes and flow rate in pipes).

References

Alvarruiz F, Martínez-Alzamora F, Vidal AM (2015) Improving the efficiency of the loop method for the simulation of water distribution systems. J Water Resources Plann Manage

Alvisi S, Creaco E, Franchini M (2011) Segment identification in water distribution systems. UrbanWater J 8(4):203–217. https://doi.org/10.1080/1573062X.2011.595803

Bellman R (1958) On a Routing Problem. Q Appl Math 16(1):87–90

Binder RC (1973) Fluid mechanics. Prentice-Hall Inc, Englewood Cliffs, NJ

Bragalli C, D'Ambrosio C, Lee J, Lodi A, Toth P (2008) Water network design by MINLP. Rep. No. RC24495, IBM Research, Yorktown Heights, NY

Centre for Water Systems, University of Exeter UK, http://emps.exeter.ac.uk/engineering/research/cws/resources/benchmarks/design-resilience-pareto-fronts/data-files. Accessed 07 Jan 2017

Creaco E, Franchini M (2014) Comparison of Newton-Raphson global and loop algorithms for water distribution network resolution. J Hydraul Eng 140(3)

Creaco E, Franchini M (2015) The identification of loops in water distribution networks. In: 13th computer control for water industry conference, CCWI 2015. https://doi.org/10.1016/j.proeng.2015.08.878

Dijkstra EW (1959) A note on two problems in connexion with graphs. Numer Math 1:269–271

Dobrnjac M (2012) Determination of friction coefficient in transition flow region for waterworks and pipelines calculation. Ann Fac Eng Hunedoara-Int J Eng

Georgios AP, Maria S, Charalampos NM, Theodoros GS, Sophia K, Jan A, Reinhard S, Pantelis GB (2011) Using graph theory to analyze biological networks. BioData Mining 2011 (4):10. https://doi.org/10.1186/1756-0381-4-10

Harary F (1969) Graph Theory. Addison-Wesley, Reading, MA

Krope J, Dobersek D, Goricanec D (2006) Flow pressure analysis of pipe networks with linear theory method. In: Proceedings of the 2006 WSEAS/IASME international conference on fluid mechanics, Miami, Florida, USA, pp 59–62

Kruskal JB (1956) On the shortest spanning subtree of a graph and the travelling salesman problem. Proc Am Math Soc 7:48–50

Prim R (1957) Shortest connection networks and some generalizations. Bell Syst Tech J 36:1389–1401

Raad DN (2011) Multi-objective optimization of water distribution systems design using metaheuristics. Dissertation, University of Stellenbosch

Todini E, Rossman AL (2013) Unified framework for deriving simultaneous equation algorithms for water distribution networks. J Hydraul Eng 139(5)

Travers K (1967) The mesh method in gas network analysis. Gas J 332:167–174

Walski TM, Chase DV, Savic DA (2001) Water distribution modeling. Haestad Press, Waterbury

Canonical Variable Analysis for Fault Detection, System Identification and Performance Estimation

Xiaochuan Li, Fang Duan, Tariq Sattar, Ian Bennett and David Mba

Abstract Condition monitoring of industrial processes can minimize downtime and maintenance costs while enhancing the safety of operation of plants and increasing the quality of products. Multivariate statistical methods are widely used for condition monitoring in industrial plants due to the rapid growth and advancement in data acquisition technology. However, the effectiveness of these methodologies in real industrial processes has not been fully investigated. This paper proposes a CVA-based approach for process fault identification, system modeling and performance estimation. The effectiveness of the proposed method was tested using data acquired from an operational industrial centrifugal compressor. The results indicate that CVA can be effectively used to identify abnormal operating conditions and predict performance degradation after the appearance of faults.

Keywords Condition monitoring · Canonical variable analysis · Fault detection
System identification · Performance estimation

X. Li (✉) · F. Duan · T. Sattar · D. Mba
School of Engineering, London South Bank University, London, UK
e-mail: lix29@lsbu.ac.uk

F. Duan
e-mail: duanf@lsbu.ac.uk

T. Sattar
e-mail: sattartp@lsbu.ac.uk

D. Mba
e-mail: mbad@lsbu.ac.uk

I. Bennett
Shell Global Solutions International B.V., Rijswijk, Netherlands
e-mail: Ian.bennett@shell.com

1 Introduction

Modern industrial facilities such as natural-gas processing plants are becoming increasingly complex and large-scale due to the use of machines of different nature. The complexity of large-scale industrial facilities makes it difficult to build first-principle dynamic models for condition monitoring (Russell et al. 2000). Thus, existing condition monitoring approaches for industrial processes are typically derived from routinely monitored system operating data. Due to the advancement in instrument and automation technology, long-term and high-frequency measurements can be taken with the different sensors mounted on the machinery systems. The monitored data are easily stored and explored to extract important process condition information. Many methodologies have been developed to combine the multivariate process data for analysis, such as state-space-based models (Negiz and Çinar 1997a), time series analysis (Negiz and Çinar 1997b), and dimensionality reduction techniques (Chiang et al. 2000; Yang et al. 2012; Komulainen et al. 2004; Ku et al. 1995).

The main advantage of dimensionality reduction techniques over traditional approaches is that they can take into consideration the possible correlation between the different measured variables, hence facilitating fault detection and system identification (Ruiz-Carcel et al. 2016). Two early examples of process monitoring techniques are principal component analysis (PCA) (Ku et al. 1995) and partial least-squares (PLS) analysis (Muradore and Fiorini 2012). Both PCA and PLS assume that the monitored variables are time-independent (i.e., the observations at one time instant are not correlated with those in the past time instants). This assumption might not hold true for real industrial processes (especially chemical and petrochemical processes) because measurements driven by noises and disturbances often show strong correlation between the past and future time instances (Odiowei and Cao 2010). Dynamic extensions of PCA and PLS, so-called dynamic PCA and dynamic PLS, have been proposed to solve this problem, making them more suitable for dynamic processes monitoring. Although DPCA and DPLS have been successfully applied to dynamic systems, they have been reported not to be able to fully capture some important dynamic behaviors of the system working under varying operating conditions (Jiang et al. 2015a; Ruiz-Carcel et al. 2016).

Aside from approaches derived from PCA and PLS, the canonical variable analysis (CVA) is also a multivariate monitoring tool. CVA is a state-space-based method which takes both serial correlations and relationship between correlated variables into account, hence is more suitable for dynamic process modeling (Odiowei and Cao 2010). The performance of CVA has been tested by several researchers using computer-simulated data (Jiang et al. 2015b; Huang et al. 2015) and data obtained from small-scale test rigs (Ruiz Cárcel and Mba 2014). However, the effectiveness of CVA in real complex industrial processes has not been fully studied. In this investigation, we propose a CVA-based method for abnormal behavior detection, system identification, and performance estimation of petrochemical process. To prove the validity of the method, it was tested using process

data acquired from an industrial centrifugal compressor operating in the real world. The results indicate that it is possible to perform fault detection and prognosis using real-life data.

2 Methodology

2.1 CVA for Fault Detection

CVA is a dimension reduction technique to monitor the process by converting the multidimensional observed data into a health indicator. Process data acquired from the system operating under normal operating conditions are used to determine the threshold for normal operating limits. The process faults can be identified when the value of the health indicator exceeds the threshold.

The objective of CVA is to maximize the correlation between two sets of variables (Russel et al. 2000). For this purpose, the measurement vector $y_k \in \mathfrak{R}^m$ (measurement at each time point containing m variables) is expanded at each time point k by considering p past measurements and f future measurements to give the past and future vectors $y_{p,k} \in \mathfrak{R}^{mp}$ and $y_{f,k} \in \mathfrak{R}^{mf}$.

$$y_{p,k} = [y_{k-1}^T y_{k-2}^T \ldots y_{k-p}^T]^T \in \mathfrak{R}^{mp} \tag{1}$$

$$y_{f,k} = [y_k^T y_{k+1}^T \ldots y_{k+f-1}^T]^T \in \mathfrak{R}^{mf} \tag{2}$$

To avoid the domination of variables with larger absolute values, the past and future vectors are normalized to zero means to get $\widehat{y_{p,k}}$ and $\widehat{y_{f,k}}$. The vectors calculated at different time points are arranged in columns to produce past and future truncated Hankel matrices Y_p and Y_f:

$$Y_p = [\widehat{y_{p,p+1}}, \widehat{y_{p,p+2}}, \ldots, \widehat{y_{p,p+M}}] \in \mathfrak{R}^{mp \times M} \tag{3}$$

$$Y_f = [\widehat{y_{f,p+1}}, \widehat{y_{f,p+2}}, \ldots, \widehat{y_{f,p+M}}] \in \mathfrak{R}^{mf \times M} \tag{4}$$

where $M = n - f - p + 1$, n represents the total number of observations for y_k.

To find the linear combinations that maximize the correlation between the two sets of variables, the Hankel matrix H can be decomposed using Singular Value Decomposition (SVD):

$$H = \sum_{ff}^{-1/2} \sum_{pf} \sum_{pp}^{-1/2} = \cup \sum V^T \tag{5}$$

where Σ_{pp}, Σ_{ff} and Σ_{pf} represent the sample-based covariance and cross-covariance matrix of matrices Y_p and Y_f. The mp-dimensional past vector Y_p can be converted into the r-dimensional canonical variates z by:

$$z = J \cdot Y_p \tag{6}$$

where J represents the transformation matrix, and $J = V_r^T \sum_{pp}^{-1/2}$. The truncated matrix $V_r \in \Re^{r \times M}$ can be obtained by selecting the first r columns of V having the highest pairwise correlation with those of $\cup$ (Samuel and Cao 2015). Then, the Hotelling health indicator can be calculated as:

$$T_k^2 = \sum_{i=1}^{r} z_{k,i}^2 \tag{7}$$

Since the Gaussian distribution does not hold true for nonlinear processes, the normal operating limits are derived from the actual probability density function of the indicator using Kernel Density Estimation (KDE) (Odiowei and Cao 2010). Faults will be considered every time the health indicator exceeds the threshold.

2.2 CVA for System Identification and Performance Estimation

CVA can be used to build a state-space model which describes the dynamic behavior of the system using process data. Given the past of the measured system inputs u_k and measured outputs y_k, the following state-space model can be built:

$$x_{k+1} = A x_k + B u_k + w_k \tag{8}$$

$$y_k = C x_k + D u_k + E w_k + v_k \tag{9}$$

where x_k is a r-order state vector, w_k and v_k are independent white noise, and A, B, C, D and E are coefficient matrices. According to (Larimore 1990), when the order of the system r is equal or greater than the actual order of the system, the state estimate $z = J \cdot Y_p$ can be used to replace x_k. The unknown coefficient matrices A, B, C and D can then be estimated via multivariate regression (Larimore 1990):

$$\begin{bmatrix} \widehat{A} & \widehat{B} \\ \widehat{C} & \widehat{D} \end{bmatrix} = \mathrm{Cov}\left[\begin{pmatrix} z_{k+1} \\ y_k \end{pmatrix}, \begin{pmatrix} z_k \\ u_k \end{pmatrix} \right] \cdot \mathrm{Cov}^{-1}\left[\begin{pmatrix} z_k \\ u_k \end{pmatrix}, \begin{pmatrix} z_k \\ u_k \end{pmatrix} \right] \tag{10}$$

The procedure of system identification and performance estimation using the model described above can be summarized as follows:

1. Determine the input (manipulated) and output (measured performance variables) variables;
2. Collect data for past system input $u_{p,k}$ and output $y_{p,k}$;
3. Estimate future system input $u_{f,k}$ by looking at production plan or estimating from the past input values;
4. Determine the number of states and number of past and future lags for the collected data;
5. Estimate the parameters in the state-space model using Eq. (10);
6. Predict future output $y_{f,k}$ as per Eqs. (8) and (9);
7. Validate the proposed model by looking at the average prediction error for each one of the measured variables.

This procedure will allow operators to access how the system will behave for the specified system inputs.

3 Application to Centrifugal Compressor Data

CVA has been successfully used to perform condition monitoring using computer-simulated data (Lee and Lee 2008; Juricek et al. 2001) and data acquired from small test rigs (Ruiz-carcel et al. 2016). In this investigation, the capabilities of CVA for fault detection and system identification were tested using data captured from an operational industrial centrifugal compressor.

Centrifugal compressors are widely used in oil and gas industry for gas transport, gas lift, and gas injection. They are typically operating under high pressure and high load conditions, and are therefore subject to performance degradation. The compressor used in this study is automated using a condition monitoring system, where the signals from different sensors can be visualized. A total of 50 variables including three process inputs (i.e., rotational speed, inlet temperature, and inlet pressure) and 47 performance variables were recorded, sampling at a 1-hour interval. The recorded data consist of 25,900 observations (i.e., the total monitoring time is more than 3 years in length).

In order to fully capture the dynamic characteristics of the compressor under various operating conditions, nine periods of data were used to train the CVA algorithm to obtain the normal operating limits of T_k^2, and the training data sets were intentionally chosen to cover various operating speeds and ambient temperatures. The number of time lags (p and f) is determined by computing the autocorrelation function of the summed squares of all measurements (Odiowei and Cao 2010). The autocorrelation function indicates how long the signal is correlated with itself, and thus can be used to determine the maximum number of significant lags. In this investigation, the number of p and f was set to 15. The optimal number of dimensions retained r is determined by considering the dominant singular values in the matrix D (Negiz and Çinar 1998). After several tests, r = 25 was finally adopted

to represent the order of the system for the purpose of fault detection. The 99% confidence interval was employed in this study to minimize the false alarm rate.

3.1 Results Obtained for Fault Detection

As mentioned previously, nine data sets were used to train the CVA algorithm for fault detection. In addition to the training data sets, a period of data (hereafter referred to as data set C1) was obtained from the machine operating under faulty conditions for testing the trained algorithm. The fault evolution of the testing data can be seen in Fig. 1. According to the event logs provided by the machine operator, the monitoring system gave in total five warnings (as shown in Fig. 1) during this period of time. The first warning happened in the 78th sample, and the machine continued to operate until the 215th sample and was then forced to completely shut down at the 217th sample. Figure 2 demonstrates the results in
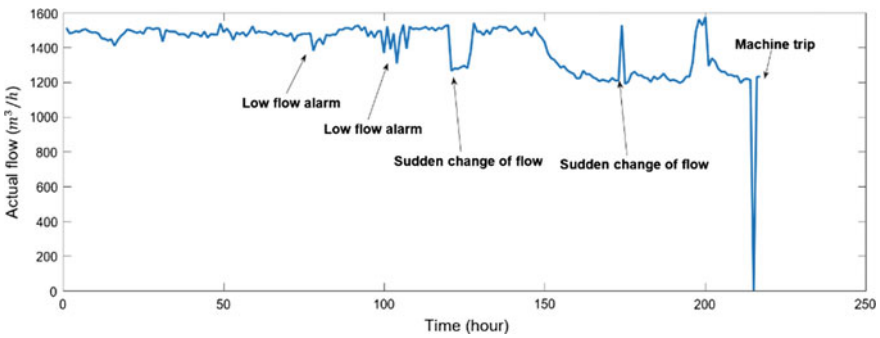
Fig. 1 Actual flow for data set C1
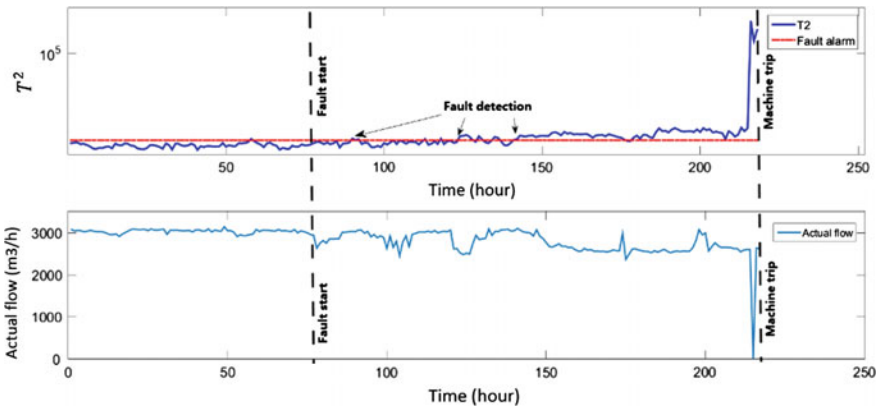
Fig. 2 T^2 for data set C1

terms of fault detection. The fault was detected by the T^2 indicator at sample 140 after several short alarms.

3.2 Results Obtained for System Identification and Performance Estimation

In addition to fault detection, plant operators may be more interested in how the system will behave given the future system input conditions and how the estimated behavior will affect the plant operation. The future system inputs can be obtained by looking at the production schedule or estimating from the past inputs. The processes described below are for prediction of future system behavior for the specified inputs.

In order to build a dynamic model as described in Eqs. (8) and (9), it is necessary to first determine the canonical variates z. Similar to the procedure described in Sect. 3, nine training data sets were used to train the CVA model to obtain z. Second, the past system inputs x_k and outputs y_k were obtained from the first 145 samples of the data set C2 (hereafter referred to as C2-1), as shown in Fig. 3. They were then used to construct a dynamic state-space model using the procedures described in Sect. 2.2.

In order to maximize the accuracy of the built model, the past inputs x_k obtained from C2-1 was first used to predict the response of the system and the results were compared with the past outputs y_k to determine the prediction error. After several analyses testing, different values for r, $r = 32$ was finally adopted to give the minimum prediction error. The validated model was then used to make estimations of the process variables y_k of C2-2. Figure 4 shows the prediction results of the most significant variables of C2-2. The results show that the model causes large
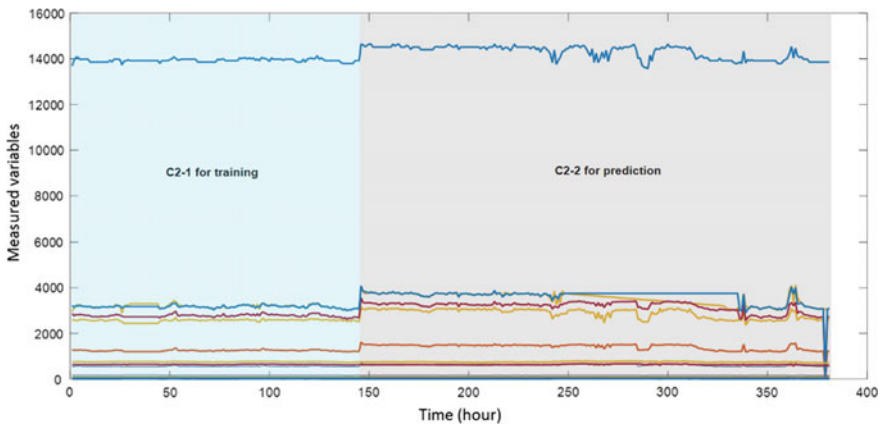
Fig. 3 All measured variables in data set C2
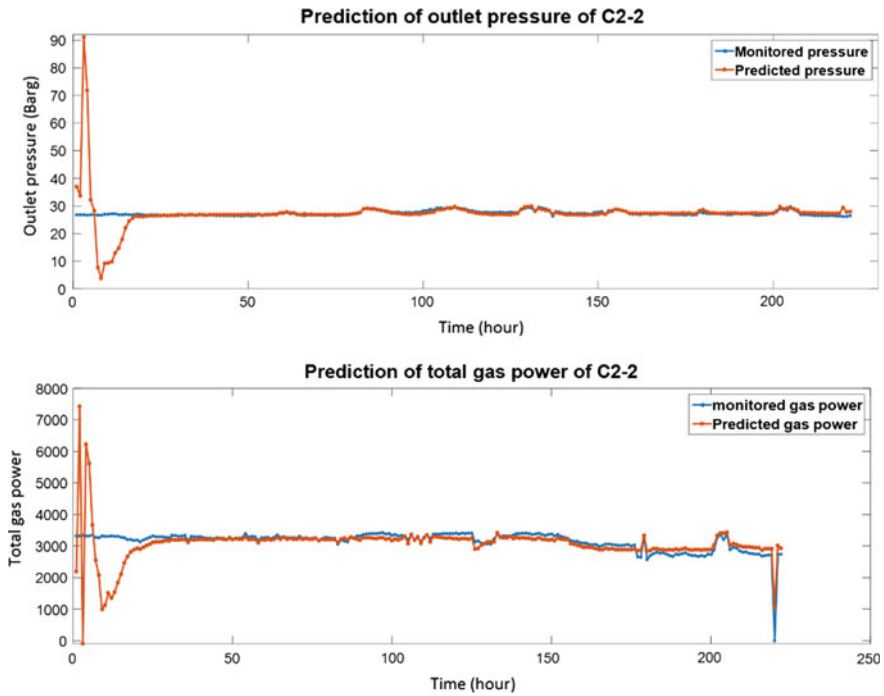
Fig. 4 Prediction results of the selected most significant variables of C2-2

oscillations at the very beginning, but the oscillations dissipated quickly and the steady-state estimations are close to the actual measurements. Figure 5 shows all the measured variables in dataset C3.

Similar to the procedure described above, the methodology was applied to predict the system outputs of another data set C3. Figure 6 shows the prediction results of the most significant variables of C3-2. The estimation is able to accurately represent the system behavior. Table 1 shows the average prediction error for the most significant variables of data set C2-2 and C3-2. The prediction error for each one of the significant variables was calculated by computing the mean of the difference between the predicted and measured signal:

$$e_i = \frac{1}{T} \sum_{t=1}^{T} \left| \frac{y_{t,i} - \widehat{y_{t,i}}}{y_{t,i}} \right|$$

where $y_{t,i}$ denotes the measured value of the ith variable at time t, and $\widehat{y_{t,i}}$ represents the estimated value of y_i and time t, and T denotes the total number of observations of the testing data set.
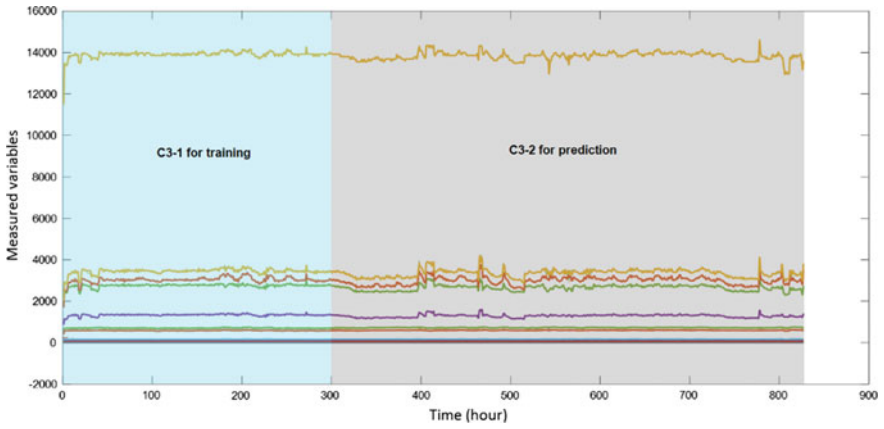
Fig. 5 All measured variables in data set C3
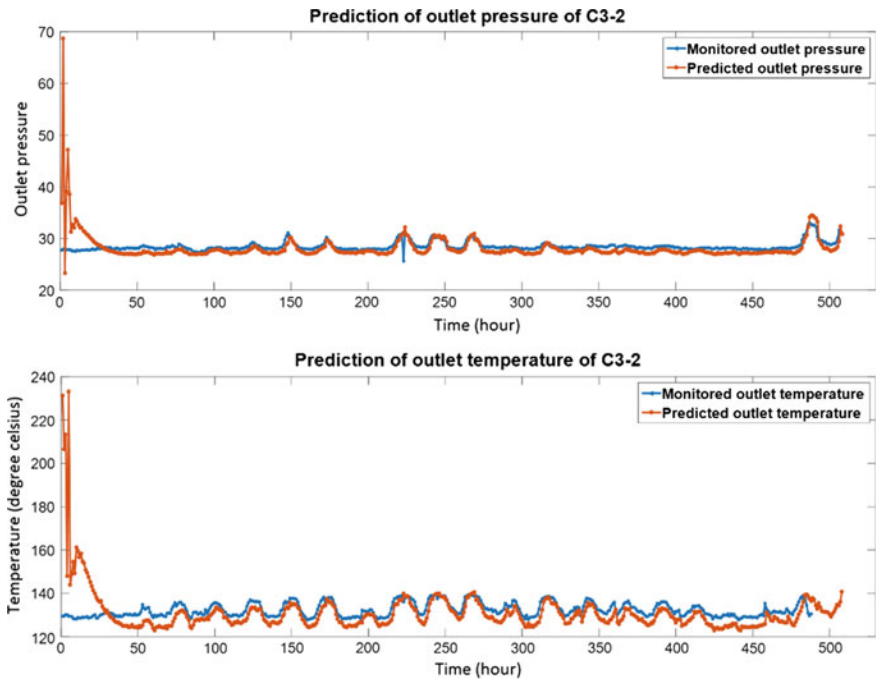
Fig. 6 Prediction results of the selected most significant variables of C3-2

Table 1 Average prediction error for significant variables

Data set	Outlet pressure (%)	Outlet temperature (%)	Ploy head (%)	Ploy head efficiency (%)	Bearing temperature V24 (%)	Total gas power (%)
C2-2	5.96	11.91	6.21	7.53	10.33	7.55
C3-2	3.63	3.67	6.14	2.75	15.33	8.37

4   Conclusion

Process data acquired from an operational industrial centrifugal compressor have been used to test the capabilities of CVA for fault detection, system identification, and performance estimation. The faults in data set C1 were successfully detected by T^2 health indicator within a short detection time. CVA was also employed to build a state-space model for system identification. In order to fully capture the dynamics of the compressor, nine training data sets were selected from different operating conditions to train the CVA algorithm. The trained CVA model was then used to predict the future system outputs for the specified system inputs. Although very fast and large oscillations were observed in the initial estimations, the average prediction error was low, proving that the model is able to represent the system dynamics under different operating conditions.

Although the results of this study clearly show the superior performance of the CVA algorithm for dynamic process monitoring, some things require further investigation. First, if CVA is employed to detect faults for a system operating under variable working conditions, it may produce high false alarm rates because the sudden changes in working conditions can be mistaken for performance degradations. Second, CVA-based performance estimation is based on the premise that the future system inputs are obtained from the production plan or from forecasts based on historic inputs, but the actual future inputs may be different from the forecasts due to process uncertainties, leading to inaccurate performance estimations. In addition, the proposed method is unable to predict the system behavior without knowing the future information. Therefore, more work should be conducted to apply the CVA for prognosis without future inputs.

References

Chiang LH, Russell EL, Braatz RD (2000) Fault detection and diagnosis in industrial systems. Springer, New York, London

Huang LZ, Cao YP, Tian XM, Deng XG (2015) A Nonlinear quality-relevant process monitoring method with kernel input-output Canonical Variate analysis. IFAC-PapersOnLine 48:611–616. https://doi.org/10.1016/j.ifacol.2015.09.035

Jiang B, Zhu X, Huang D, Braatz RD (2015a) Canonical variate analysis-based monitoring of process correlation structure using causal feature representation. J Process Control 32:109–116. https://doi.org/10.1016/j.jprocont.#

Jiang B, Huang D, Zhu X, Yang F, Braatz RD (2015b) Canonical variate analysis-based contributions for fault identification. J Process Control 26:17–25. https://doi.org/10.1016/j.jprocont.2014.12.001

Juricek BC, Seborg DE, Larimore WE (2001) Identification of the Tennessee Eastman challenge process with subspace methods. Control Eng Pract 9:1337–1351. https://doi.org/10.1016/s0967-0661(01)00124-1

Komulainen T, Sourander M, Jämsä-Jounela SL (2004) An online application of dynamic PLS to a dearomatization process. Comput Chem Eng 28:2611–2619. https://doi.org/10.1016/j.compchemeng

Ku W, Storer RH, Georgakis C (1995) Disturbance detection and isolation by dynamic principal component analysis. Chemometr Intell Lab Syst 30:179–196. https://doi.org/10.1016/0169-7439(95)00076-3

Larimore WE (1990) Canonical variate analysis in identification, filtering, and adaptive control. In: Proceedings of the 29th IEEE conference on decision and control, pp 596–604

Lee C, Lee IB (2008) Adaptive monitoring statistics with state space model updating based on canonical variate analysis. Korean J Chem Eng 25:203–208. https://doi.org/10.1007/s11814-008-0037-y

Muradore R, Fiorini P (2012) A PLS-Based statistical approach for fault detection and isolation of robotic manipulators. IEEE Trans Ind Electron 59:3167–3175. https://doi.org/10.1109/tie.2011.2167110

Negiz A, Çlinar A (1997a) Statistical monitoring of multivariable dynamic processes with state-space models. AIChE J 43:2002–2020. https://doi.org/10.1002/aic.690430810

Negiz A, Çinar A (1997b) PLS, balanced, and canonical variate realization techniques for identifying VARMA models in state space. Chemometr Intell Lab Syst 38:209–221. https://doi.org/10.1016/s0169-7439(97)00035-x

Negiz A, Çinar A (1998) Monitoring of multivariable dynamic processes and sensor aditing. J Process Control 8:375–380. https://doi.org/10.1016/s0959-1524(98)00006-7

Odiowei PP, Cao Y (2010) Nonlinear dynamic process monitoring using canonical variate analysis and kernel density estimations. IEEE Trans Ind Inf 6:36–45. https://doi.org/10.1109/tii.2009.2032654

Ruiz-Cárcel C, Lao L, Cao Y, Mba D (2016) Canonical variate analysis for performance degradation under faulty conditions. Control Eng Pract 54:70–80. https://doi.org/10.1016/j.conengprac

Ruiz Cárcel C, Mba D (2014) A benchmark of canonical variate analysis for fault detection and diagnosis—IEEE Xplore document. http://ieeexplore.ieee.org/document/6915178/?part=1

Russell EL, Chiang LH, Braatz RD (2000) Fault detection in industrial processes using canonical variate analysis and dynamic principal component analysis. Chemometr Intell Lab Syst 51:81–93

Samuel R, Cao Y (2015) Kernel canonical variate analysis for nonlinear dynamic process monitoring. In: Cao Y (ed) 9th international symposium on advanced control of chemical processes. http://ac.els-cdn.com/S2405896315011155/1-s2.0-S2405896315011155-main.pdf?_tid=8a1aa7e2-d649-11e6-a59a-00000aacb35d&acdnat=1483952382_e2740e26016619a37b573e7cc86ccc74

Yang Y, Chen Y, Chen X, Liu X (2012) Multivariate industrial process monitoring based on the integration method of canonical variate analysis and independent component analysis. Chemometr Intell Lab Syst 116:94–101. https://doi.org/10.1016/j.chemolab.2012.04.013

Effects of Using Flexible Die Instead of Flexible Punch in Rubber Pad Forming Process

L. Belhassen, L. Ben Said, S. Koubaa and M. Wali

Abstract Flexible forming with rubber pad is a forming technique that is commonly used in the aeronautic and automotive industries to produce parts with complex shapes from thin sheet metal. The purpose of this chapter is to compare between using flexible punch or flexible die in sheet metal forming with rubber pad. A finite element simulation is carried out to predict the behavior of the flexible stamping process of aluminum sheet metal with the two techniques of forming. For the sheet metal, an elastoplastic constitutive model is adopted and implemented in ABAQUS/Standard software via UMAT subroutine. However, a Mooney–Rivlin hyperelastic model is adopted for the rubber pad. Results predicted numerically consist of comparing the variation of some key parameters process using two deformation styles in order to produce safety parts without localized severe deformation. It was found that using rubber as flexible die may reduce the thinning rate and values of equivalent plastic strain in the formed part. Also, based on the Forming Limit Diagram (FLD) analysis, using flexible die instead of flexible punch may successfully form part without necking and micro crack and without localized severe deformation that can lead to fracture.

Keywords Flexible punch and die · Specimen thinning · Mooney–Rivlin theory · Forming Limit Diagram

L. Belhassen · L. Ben Said · S. Koubaa · M. Wali (✉)
Mechanical Modeling and Manufacturing Laboratory (LA2MP), National School
of Engineers of Sfax, University of Sfax, B.P 1173, 3038 Sfax, Tunisia
e-mail: mondherwali@yahoo.fr

L. Belhassen
e-mail: lachhel@yahoo.fr

L. Ben Said
e-mail: bensaid_rmq@yahoo.fr

S. Koubaa
e-mail: koubaasana@yahoo.fr

1 Introduction

Rubber forming process is widely used in the aeronautic and automotive industries. It's performed with the aid of only a rigid tool half to form the workpiece through the desired shape. Soft materials are used as medium pressure transmitted to produce complex shape. Compared with the conventional forming process, flexible forming presents some advantages. Indeed, using this process may avoid the alignment problems between the punch and the die. Also, rubber pad can be used for different parts with different shapes which conduct to lower tool costs.

Several researchers have been interested in studying this kind of the sheet metal forming process. Thiruvarudchelvan (1993), in his review, presented different processes that can be used in forming with soft tools. Browne and Battikha (1995), using flexible die, were interested to optimize the aluminum sheet forming in order to produce parts without defects. Sala (2001) conducted a numerical and experimental investigation to identify optimal parameters that governed the process of stamping aluminum alloys using rubber pad. Lee et al. (2003) studied the rubber pad bending process. Authors affirmed that hardness of rubber is considered the crucial parameter that affected the radius of bending. Watari et al. (2003) were interested in optimizing the flexible punching process with urethane as rubber pad. They determined a range of hardness from 80° to 90° Shore A. Later, Dirikolu and Akdemir (2004) performed a finite element investigation to study the effect of hardness of rubber in flexible forming process. They determined a hardness range of polyurethane rubber from 55° to 70° Shore A in order to ensure a safe product. Liu et al. (2010) studied two deformation styles of using convex or concave die in rubber pad forming process. They concluded that using convex die may lead to uniform distribution of the thickness along the formed part. Ramezani et al. (2010) confirmed that polyurethane rubber as flexible punch is more suitable for sheet metal forming compared to silicon and natural rubber. Other works funded in the literature are interested in analyzing friction in flexible forming process. Ramezani et al. (2009) developed a friction model to study friction force between sheet and flexible tools in rubber pad forming process. Authors affirmed that using this friction model, numerical and experimental results are in good agreement. Peng et al. (2009) confirmed that friction between sheet and flexible punch does not have important effect in the thinning of the formed part compared to the friction between the workpiece and the rigid die that involved the sheet thinning.

These mentioned works are interested in optimizing the flexible forming process with the aid of rubber pad as flexible punch or flexible die. Studying the difference between the use of rubber as punch or die is neglected. This is the main objective of this chapter. A stamping of aluminum sheet metal with polyurethane rubber is simulated numerically. An elastoplastic model with J_2 yield criteria and isotropic hardening behavior is introduced. Initially, the numerical simulation is validated with the experimental results of Ramezani et al. (2010) in terms of the variation of

the thickness along the formed part. Then, a comparison between the use of flexible die or flexible punch is carried out to study the influence of the two styles of forming the sheet metal in the thinning, the equivalent plastic strain, and forces due to contact pressure transmitted by the rubber to the surface of the aluminum sheet metal.

2 Numerical Process Simulation

A 3D finite element model was built according to two configurations using flexible die or flexible punch as shown in Fig. 1. Considering the punch as soft tool, the rubber contained in a rigid container will be acting as the blank against the rigid die. Whereas when the die becomes flexible, the final desired shape of the part is taken by a rigid punch that is going to stamp the blank against a soft material. Die and punch are considered as rigid bodies. A Mooney–Rivlin theory is used to model the hyperelastic behavior of polyurethane rubber which was modeled using C3D8R elements (An 8-node linear brick, reduced integration, hourglass control). The blank was discretized using S3R elements (A 3-node triangular thin or thick shell, finite membrane strain). The friction law used is the Coulomb law. An automatic
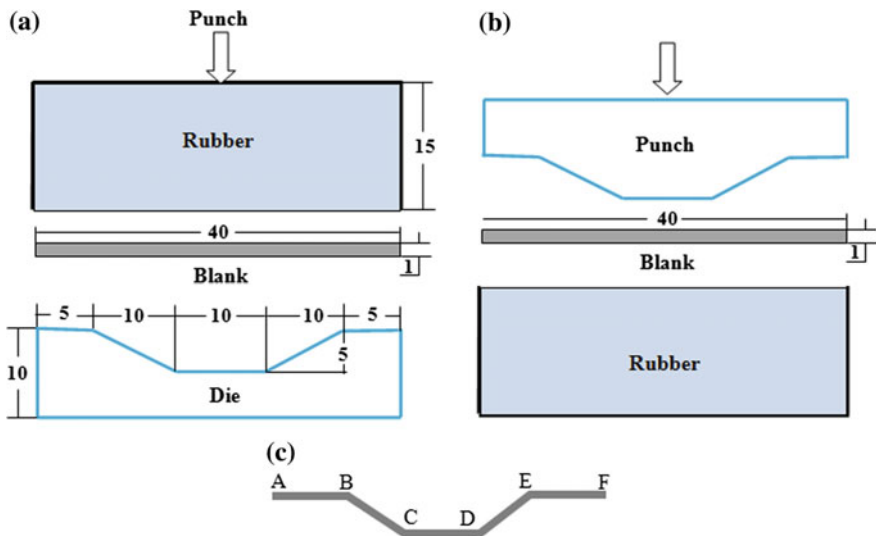
Fig. 1 Schematic representation of the numerical model: **a** Flexible punch. **b** Flexible die. **c** The shape of the formed part

Table 1 Mooney–Rivlin constants for polyurethane rubber (Belhassen et al. 2016)

	Hardness shore A	C_1 (MPa)	C_2 (MPa)
Polyurethane rubber	50	0.302	0.076
	90	2.824	0.706

surface to surface contact is adopted to model the interfaces between die/blank and rubber/blank. A friction coefficient of 0.25 is used between the blank/rubber and a 0.15 friction coefficient is introduced between blank/die. These friction coefficients are adopted in the numerical study of Ramezani et al. (2010).

The constitutive behavior of the blank is considered as isotropic J_2 elastoplasticity with isotropic hardening; kinematic hardening is absent. The material of the blank is an aluminum alloy AA5754-O ($\upsilon = 0.334$, $E = 70$ GPa).

The hardening behavior of the blank material is modeled by the exponential law as:

$$\sigma = \sigma_y + Q\left(1 - e^{-\beta\varepsilon_p}\right) = 95 - 159\left(1 - e^{-9\varepsilon_p}\right) \text{ MPa} \tag{1}$$

An hyperelastic behavior is considered for the polyurethane rubber with the Mooney–Rivlin model. For this model, the free energy function W takes the form:

$$W = C_1(\bar{I}_1 - 3) + C_2(\bar{I}_2 - 3) + \frac{1}{D_1}(J - 1)^2 \tag{2}$$

where $\bar{I}_1$ and $\bar{I}_2$ are deviatoric strain component invariants; J represents volume change, and C_1, C_2, D_1 are material constants. We assumed a fully incompressible behavior for rubber with Poisson's ratio $\nu = 0.4997$ and D_1 equal to zero. Mooney–Rivlin constants for polyurethane rubber are listed in Table 1.

3 Numerical Validation

An elastoplastic model with nonlinear isotropic hardening is used to describe the behavior of the blank sheet during the rubber pad forming process. This model is implemented in Abaqus/Standard via a user-defined subroutine (UMAT). The details of the formulation and numerical implementation of the present model can be found in (Wali et al. 2015, 2016; Mars et al. 2015; Ben Said et al. 2016 and Koubaa et al. 2017).

As a numerical validation, the rubber pad forming process using flexible punch is examined by comparing the predicted distribution of thickness along the half of the formed part with the experimental results of Ramezani et al. (2010).

Table 2 Aluminum sheet material properties AA6061-T4 (Ramezaniet al. 2010)

E (GPa)	67.3
v	0.334
Hardening curve (MPa)	$\sigma = \sigma_y + k\varepsilon_p^n = 150 + 340\varepsilon_p^{0.15}$
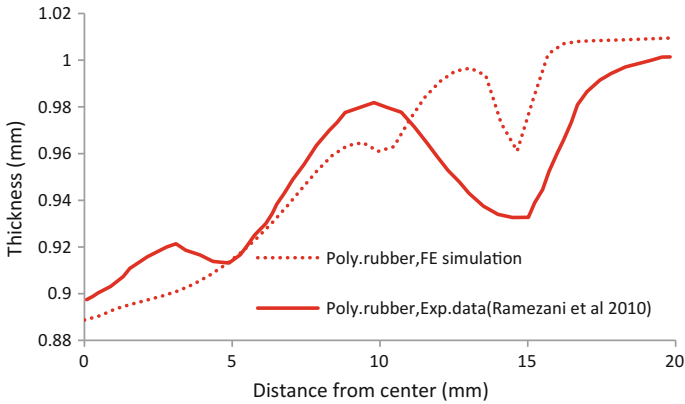
Fig. 2 Thickness distribution of the half of the formed part

The polyurethane rubber used has a hardness of 50 Shore A. The material of the blank used in this section is the AA6061-T4. The mechanical proprieties of the AA6061-T4 are listed in Table 2.

As seen in Fig. 2, the predicted thickness distribution of the thickness along the half of the formed part is in good agreement with the experimental measure of the thickness presented in the work of Ramezani et al. (2010).

4 Results and Analysis

The hardness of polyurethane rubber used in this finite element simulation is 90 Shore A. The difference between using flexible punch or flexible die in rubber-forming process will be investigated in terms of distribution of force due to contact pressure, the distribution of the thickness along the formed part and the equivalent plastic strain.
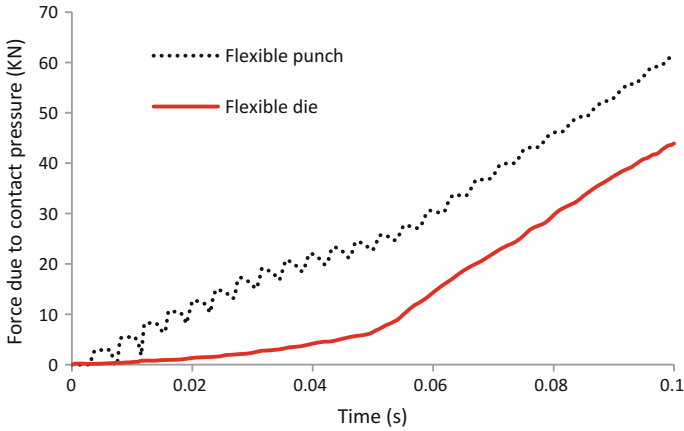
Fig. 3 Prediction of the force due to contact pressure between the rubber and the blank

4.1 Pressure Analysis Between the Rubber and the Blank

Figure 3 shows the variation of the force due to contact pressure between the rubber and the blank. It is clear to see that when using rubber as flexible die, force decreases significantly compared with the case when the soft material is used as flexible punch. At the end of the stamping step, the value of the force with flexible die is 44 KN, whereas the value is 62 KN when the die is considered rigid element.

4.2 Thinning Analysis

In this section, the thickness distribution predicted numerically will be investigated. As it is shown in Fig. 4, the use of rubber as flexible die may decrease thinning along the formed part remarkably. Indeed, thinning decreases by the rate of 5.9% in points "C" and "D" in the case of flexible die. The decreasing in the thickness in the region "C–D" is explained by the fact that this region is in continuous contact during the step of stamping. It is characterized by a concentrated load. Using flexible punch and rigid die may lead to the occurrence of damage mainly in the two points "C" and "D."

4.3 Strain Analysis

The development of the equivalent plastic strain is shown in Fig. 5. It is clear to notice from this figure the important role of using a flexible die instead a flexible
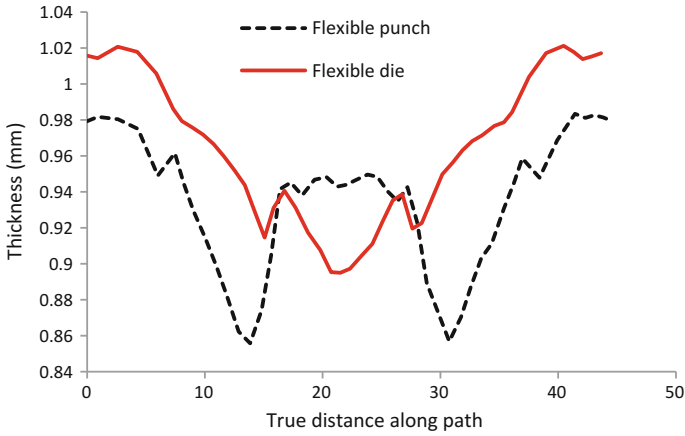
Fig. 4 Prediction of the distribution of the thickness along the formed part
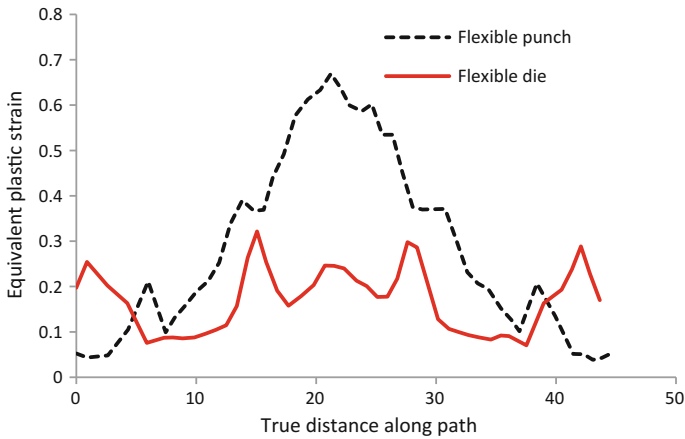
Fig. 5 Distribution of equivalent plastic strain along the formed part

punch in order to reduce the equivalent plastic strain along the stamped part mainly in the region "C–D." This region is characterized by a severe deformation. Highest values of the equivalent plastic strain in this area, using flexible punch, may be explained by the important rubber load applied to the sheet that increasing the thinning rate like it is presented in Fig. 4.
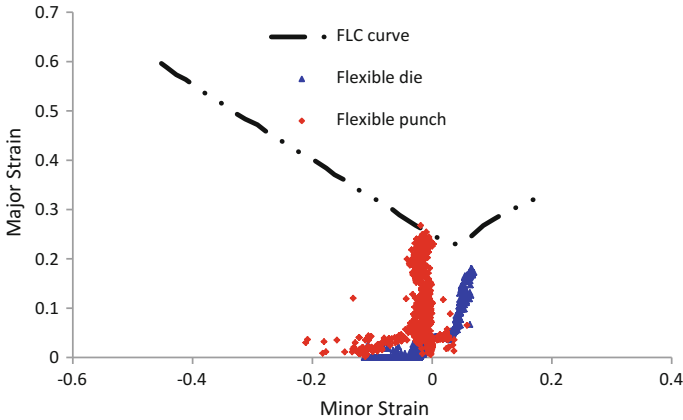
Fig. 6 Finite element prediction of strain distribution

4.4 FLD Analysis

Figure 6 shows the predicted distribution of major strain with the variation of the minor strain for the two cases of study of rubber-forming process.

In Fig. 6, it is plotted the forming limit curve of the AA5754-O in order to determinate the limit of strain and to choose the appropriate technique for a successfully formed part without necking and micro crack that lead to fracture. It is clearly seen that, using rubber as flexible punch, maximum values of major strains are located near the FLC curve. Also, as it shown in Fig. 7, "C–D" region presents the highest values of equivalent plastic strain that may lead to severe localized deformation and make fracture eventually. Whereas, using the soft material as flexible die may avoid the occurrence of micro defects and necking because all the maximum values of major strains are too far of the FLC curve.
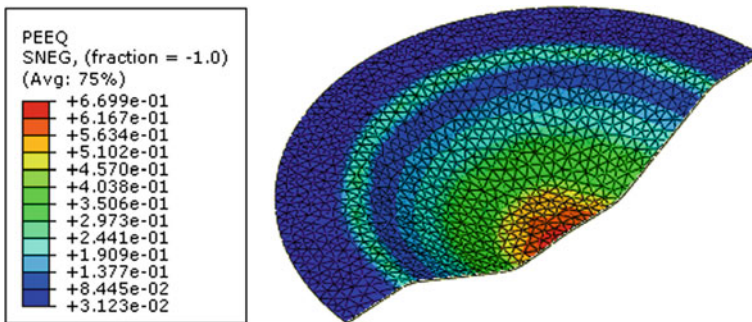
Fig. 7 Finite element simulation of the equivalent plastic strain along the formed part using flexible punch

5 Conclusion

A finite element simulation has been performed in this work in order to study the influence of using flexible punch or flexible die in rubber pad forming process. Predicted results show that the use soft material as flexible die may reduce the thinning rate and values of equivalent plastic strain. By an FLD analysis, it can be concluded that introducing rubber as flexible die may delay the occurrence of the micro crack and lead to produce safe parts without defects.

References

Belhassen L, Koubaa S, Wali M, Dammak F (2016) Numerical prediction of springback and ductile damage in rubber-pad forming process of aluminum sheet metal. Int J Mech Sci 117:218–226

Ben Said L, Mars J, Wali M, Dammak F (2016) Effects of the tool path strategies on incremental sheet metal forming process. Mech Ind 17(4):411

Browne DJ, Battikha E (1995) Optimisation of aluminium sheet forming using a flexible die. J Mater Process Technol 55:218–223

Dirikolu MH, Akdemir E (2004) Computer aided modelling of flexible forming process. J Mater Process Technol 148:376–381

Lee JW, Kwon HC, Rhee MH, Im YT (2003) Determination of forming limit of a structural aluminum tube in rubber pad bending. J Mater Process Technol 140:487–493

Liu Y, Hua L, Lan J, Wei X (2010) Studies of the deformation styles of the rubber-pad forming process used for manufacturing metallic bipolar plates. J Power Sources 195:8177–8184

Koubaa S, Mars J, Wali M, Dammak F (2017) Numerical study of anisotropic behavior of Aluminum alloy subjected to dynamic perforation. Int J Impact Eng 101:105–114

Mars J, Wali M, Jarraya A, Dammak F, Dhiab A (2015) Finite element implementation of an orthotropic plasticity model for sheet metal in low velocity impact simulations. Thin-Walled Struct 89:93–100

Peng L, Hu P, Lai X, Mei D, Ni J (2009) Investigation of micro/meso sheet soft punch stamping process-simulation and experiments. Mater Des 30:783–790

Ramezani M, Ripin ZM, Ahmad R (2009) Computer aided modelling of friction in rubber-pad forming process. J Mater Process Technol 209:4925–4934

Ramezani M, Ripin ZM, Ahmad R (2010) Sheet metal forming with the aid of flexible punch, numerical approach and experimental validation. CIRP J Manuf Sci Technol 3:196–203

Sala GA (2001) Numerical and experimental approach to optimize sheet stamping technologies: (Part II)—aluminium alloys rubber-forming. Mater Des 22(4):299–315

Thiruvarudchelvan S (1993) Elastomers in metal forming: a review. J Mater Process Technol 39:55–82

Wali M, Autay R, Mars J, Dammak F (2016) A simple integration algorithm for a non-associated anisotropic plasticity model for sheet metal forming. Int J Numer Meth Eng 107(3):183–204

Wali M, Chouchene H, Ben Said L, Dammak F (2015) One-equation integration algorithm of a generalized quadratic yield function with Chaboche non-linear isotropic/kinematic hardening. Int J Mech Sci 92:223–232

Watari H, Ona H, Yoshida Y (2003) Flexible punching method using an elastic tool instead of a metal punch. J Mater Process Technol 137:151–155

On the Use of NC Milling and Turning Machines in SPIF Process of Asymmetric Parts: Numerical Investigation

L. Ben Said, L. Belhassen, J. Mars and M. Wali

Abstract Incremental sheet forming is a flexible process that benefits from the evolution of CNC machine tools; it usually uses a three-axis NC milling machine even for asymmetric parts. This paper presents a numerical simulation of single point incremental forming (SPIF) process of asymmetric part, manufactured using two types of NC machines: NC milling machine and NC turning machine. A finite element model (FEM) is developed by using the commercial FE code ABAQUS/Explicit. An elastoplastic constitutive model with quadratic yield criterion of Hill'48 and isotropic hardening behavior has been considered for the sheet metal. A user material subroutine (VUMAT) is used to implement this material behavior. Results including thickness variation, deformed shape, and forming force along Z-axis are presented. A remarkable difference has been observed in the results obtained from the use of these two machines. In fact, NC lathe machine is a good alternative to manufacture asymmetric parts and many advantages can be mentioned, such as the remarkable decrease of thinning and vertical force which improves formability during the ISF operation.

Keywords SPIF · Isotropic hardening · Thinning · Milling machine
Lathe machine

L. Ben Said · L. Belhassen · J. Mars · M. Wali (✉)
Mechanical Modeling and Manufacturing Laboratory (LA2MP), National School
of Engineers of Sfax, University of Sfax, BP 1173, 3038 Sfax, Tunisia
e-mail: mondherwali@yahoo.fr

L. Ben Said
e-mail: bensaid_rmq@yahoo.fr

L. Belhassen
e-mail: lachhel@yahoo.fr

J. Mars
e-mail: jamelmars@yahoo.fr

269

1   Introduction

Incremental sheet forming (ISF) is a die-less forming process, having several advantages compared to conventional stamping process. This innovative process takes advantage of the development of NC machines. This makes ISF a highly versatile and flexible process reducing tooling costs and increasing material formability. This process is able to manufacture complicated shapes with high precision in the case of small-batch production and prototyping. A hemispherical tool locally deforms the sheet following a predetermined trajectory resulting from NC program implemented on NC machine. In view of the lack of programming software devoted to incremental forming, that makes it difficult to obtain conformal parts in incremental procedure. The majority of research groups in the scientific community studying incremental forming mention experiments carried out on two simple part shapes: A truncated cone or a truncated pyramid (Behera et al. 2013). These two simple parts allow the study of major problems related to ISF process like forming forces, springback effect, thinning, formability limit, dimensional accuracy, failure mechanism, etc (Salem et al. 2016; Jin et al. 2016; Wang et al. 2016; Li et al. 2015; Ben Said et al. 2016). Some cases of industrial applications have also been studied; in the medical field, for example, a portion of the ankle prosthesis has been made (Ambrogio et al. 2004). A low dimensional accuracy is found in this application for this purpose this type of parts is not yet industrialized. Still in the same medical field, a cranial implant (Duflou et al. 2007) was made from a 0.7 mm thick titanium sheet and then was cut by laser. In other areas citing the automotive field, for example, the company AMINO manufactured a front hood of Honda S800, this company also manufactured at the 1/25 scale the front of a Japanese TGV named SHINKANSEN. The majority of the examples studied show the interest of ISF process for prototype parts or small series manufactured by plastic deformation with more precision. The majority of experimental investigations performed in ISF process are for the case of single point incremental forming using three-axis NC milling machines (Jackson and Allwood 2009). This type of NC machines is the most widely used in incremental forming in view of the availability of these machines in the majority of research laboratories, the same NC program used in milling process, the same CAM method accessible with this type of machines. Moreover, these NC machines have shown a rigidity allowing them to be the most used in ISF. However, other machines have been applied; Belchior et al. (2014) used a serial industrial robot in order to evaluate the suitability of these machines for incremental forming operations. Also, Fang et al. (2014) used a six-axis robot for manufacturing parts with electric heating of the sheet metal used. Robotic machines are less rigid and have a difficulty in programming tool paths, which makes them more expensive in ISF. In our days, the Japanese company AMINO Corporation is specialized in the manufacture of machines dedicated to incremental forming process. The use of these machines in the industrial sector is still rather limited but represents an interesting alternative to study.

One can notice that the majority of these studies investigated ISF process of truncated cone or pyramid parts by means of three-axis NC milling machines. If we consider the high level of the progress of NC turning machines, in our days, turning centers with more than two axes are very much available in industry. This makes an NC lathe machine a good alternative to be used in incremental forming field especially for the case of asymmetric parts.

This paper presents a numerical comparison between the use of NC milling and turning machine in SPIF process of asymmetric part. A finite element model (FEM) is developed by using the commercial FE code ABAQUS. An elastoplastic constitutive model with quadratic yield criteria of Hill'48 and isotropic hardening behavior has been adopted. Results including thickness variation, deformed shape, and forming force along Z-axis are presented over this numerical investigation.

2 Elastoplastic Constitutive Equations

A summary of the resulting set of equations considered in this paper is presented in this section. These equations are used to model anisotropic yielding and nonlinear isotropic hardening. The assumption of strain rate decomposition is written as

$$\dot{\varepsilon} = \dot{\varepsilon}^e + \dot{\varepsilon}^p, \tag{1}$$

where $\dot{\varepsilon}$ is the strain rate tensor, $\dot{\varepsilon}^p$ is the plastic part of the strain rate tensor, and $\dot{\varepsilon}^e$ is the elastic part of the strain rate tensor. The stress–strain relation is given by

$$\boldsymbol{\sigma} = \mathbf{D} : \boldsymbol{\varepsilon}^e \tag{2}$$

where $\boldsymbol{\sigma}$ is the stress tensor, $\mathbf{D}$ is the general elastic operator. We consider one of the most common yield criteria that is used in the simulation of forming processes, Hill'48 quadratic yield function, which is given with isotopic hardening as follows:

$$f = \varphi(\boldsymbol{\sigma}) - \sigma_p(\kappa), \ \ \varphi(\boldsymbol{\sigma}) = \sqrt{\boldsymbol{\sigma}^T \mathbf{H} \boldsymbol{\sigma}} \tag{3}$$

Then the flow rule can be written as

$$\dot{\varepsilon}^p = \dot{\gamma} \frac{\partial f}{\partial \boldsymbol{\sigma}} = \dot{\gamma} \mathbf{n}, \ \ \mathbf{n} = \frac{1}{\varphi} \mathbf{H} \boldsymbol{\sigma}, \tag{4}$$

where $\sigma_p(\kappa)$ define the nonlinear isotropic hardening and $\mathbf{H}$ is a fourth-order tensor which defines the yield criterion. In isotropic elastic material and Hill'48 criteria with plane stress condition, $\mathbf{H}$ and $\mathbf{D}$ are simply

$$\mathbf{H} = \begin{bmatrix} G+H & -H & 0 \\ -H & F+H & 0 \\ 0 & 0 & 2N \end{bmatrix} \tag{5}$$

$$\mathbf{D} = \frac{E}{1-\nu^2} \begin{bmatrix} 1 & \nu & 0 \\ \nu & 1 & 0 \\ 0 & 0 & (1-\nu)/2 \end{bmatrix} \tag{6}$$

where *F*, *G*, *H,* and *N* are material constants obtained by tests of the material in different orientations. The details of the formulation and numerical implementation of the present model can be found in Wali et al. (2015, 2016), Mars et al. (2015), Ben Said et al. (2016), Belhassen et al. (2016) and Koubaa et al. (2017).

3   Results and Discussions

In this section, a truncated cone manufactured by SPIF process was investigated and the results are carried out from two numerical treatments. The first simulates the ISF operation by means of NC milling machine and the second using an NC lathe machine. The AA1050 aluminum alloy material is used. The elastic properties and Hill'48 coefficients of this material, given in Table 1, are from Ben Ayed et al. (2014).

The isotropic hardening behavior is modeled by the Swift law

$$\sigma(\kappa) = 119.5(0.000142 + \kappa)^{0.235} \tag{7}$$

The sheet blank used in these simulations is trimmed at the size of $300 \times 300 \times 1$ mm^3, clamped in his border along 50 mm. This aluminum sheet is discretized with shell elements S3R in ABAQUS/Explicit with five integration points through the thickness. The studied part is manufactured by a hemispherical punch tool having a diameter of 10 mm and considered as a rigid body. The final part is a truncated cone with a wall angle of 45°, having a large diameter of 140 mm and a depth of 50 mm. The friction coefficient between punch tool and sheet metal is assumed to be 0.1, to consider a lubricated contact.

Table 1 Mechanical properties of the aluminum AA1050 material

Elastic prop.		Hill'48 coefficients			
E (GPa)	ν	F	G	H	N
70	0.33	0.703	0.662	0.338	1.707

Fig. 1 Final shape of studied part
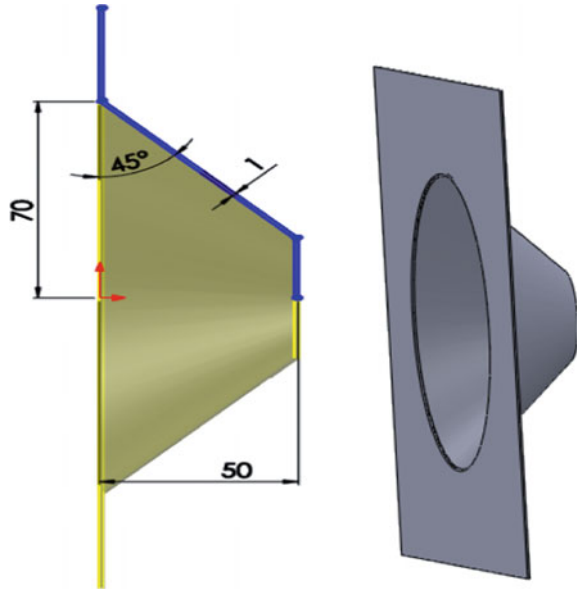
Fig. 2 Tool path using a milling machine
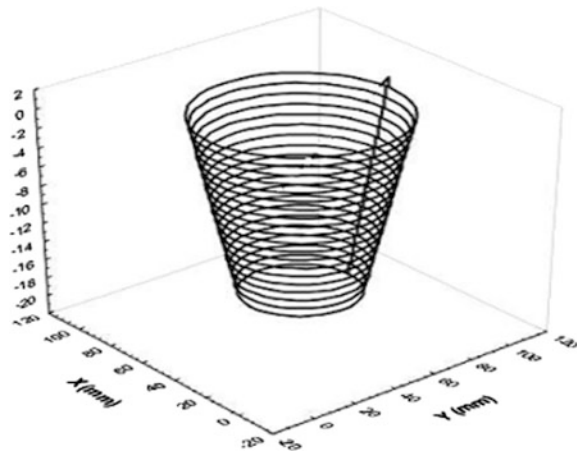
The tool path used and the final shape are presented in Figs. 1, 2 and 3. In NC milling machine case, the tool path consists of successive circular paths with a vertical step size value (Δz) of 1 mm per loop. In turning machine case, the tool path will be a sort of a spiral strategy over each penetration plane. This trajectory results from the rotation of the part (Mounted to the mandrel) around the Z axis and the facing displacement along the X-axis. These two paths are generated using the CAM software CATIA V5R17 through the two CAM milling and turning modules.
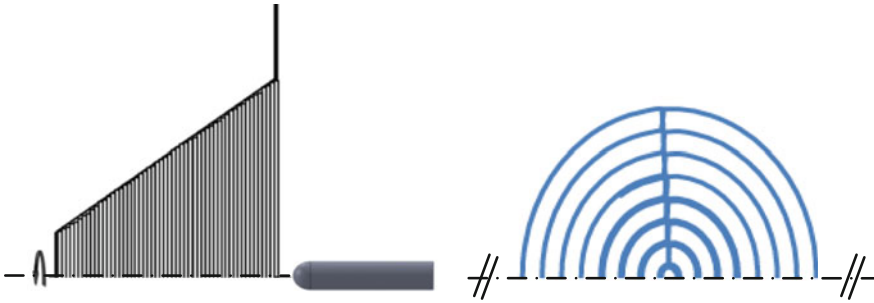
Fig. 3 Tool path using a turning machine

Fig. 4 Thickness variation in the cut plane Y = 0
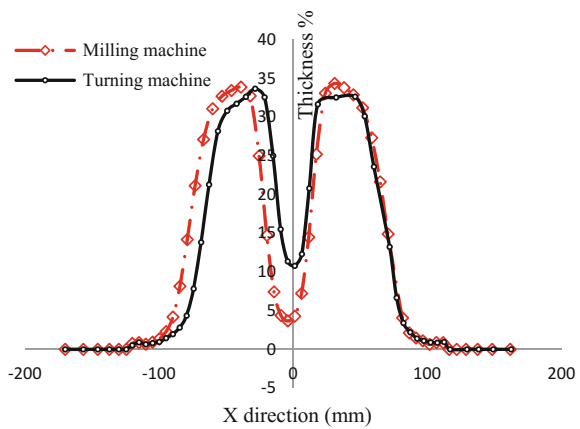
3.1 Thinning Evolution

The thickness variation along the lamination direction of the sheet and over the part depth is presented in Figs. 4 and 5.

These figures make a comparison between thinning evolution resulted from the use of the two types of NC machines. A little superiority of thinning value during the SPIF operation is looked for the case of part manufactured using NC milling machine. A nonsymmetrical evolution is looked in this result compared to the result of thinning for the case of NC lathe machine. Indeed, the use of NC turning machine to manufacture asymmetric part in ISF process reduces thinning of sheet metal which improves formability and delays failure during the ISF operation.

Fig. 5 Thinning evolution over the part depth
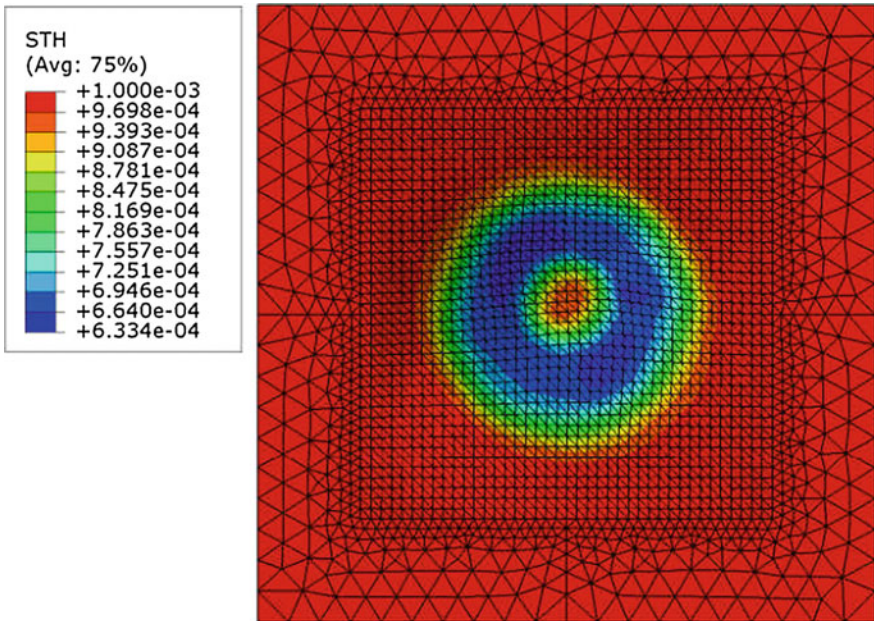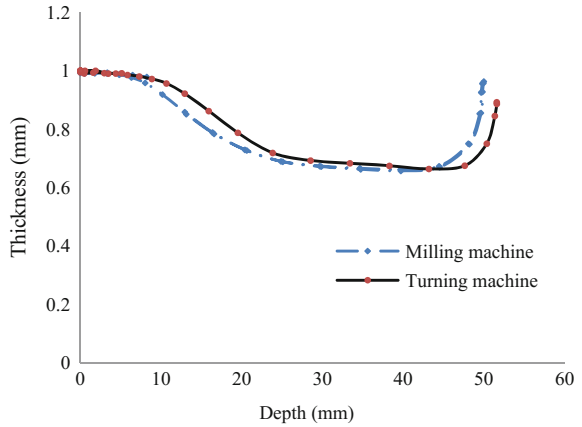
Fig. 6 Thickness distribution in the case of NC milling machine

Figures 6 and 7 denote that the maximum of thinning is concentrated principally in the vicinity of the tool path for the case of NC milling machine. The use of lathe machine distributes the thinning over the hole deformed zone.
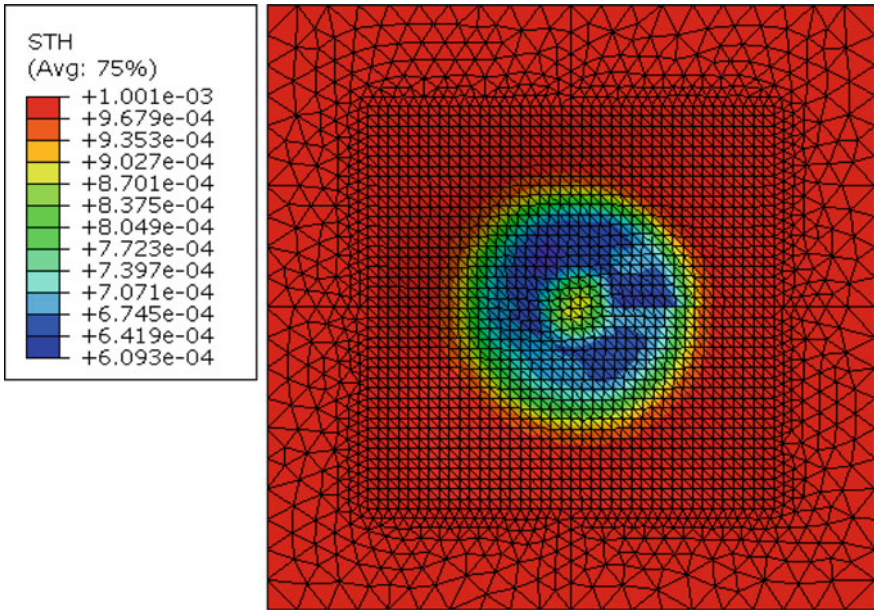
Fig. 7 Thickness distribution in the case of NC turning machine

Fig. 8 Evolution of the maximum forming force Fz-max
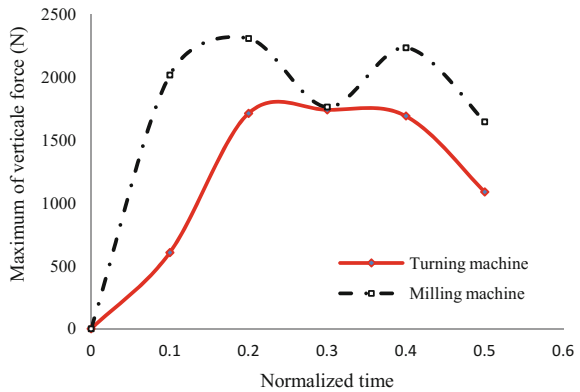
3.2 Forming Force

The evolution of the maximum of vertical force during the ISF operation of the conic part is illustrated in Fig. 8. According to this figure, using NC lathe machine during the SPIF process of the truncated cone can notably decrease the vertical force during the operation. This has a direct impact on the damage response and geometric accuracy of the manufactured part. Furthermore, reducing the forming forces is the same to reduce reactions on the sensitive slides of the NC machine for

Fig. 9 Deformed shape
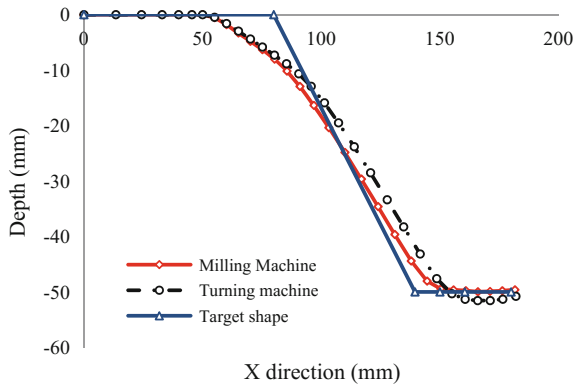
better protection of these parts. Recalling that these slides have a relatively high maintenance cost, so it is preferable in the possible cases to use an NC lathe machine instead of a milling machine.

3.3 Geometrical Profile

Figure 9 relates the comparison between the geometrical profiles of parts calculated through FE simulations for the case of use of the two types of NC machines. This figure depicts the deformed shape for the two machines and the CAD part named in this figure as target shape. One can note that a little difference is remarked between the two shapes. The geometrical profile resulting from SPIF process using an NC milling machine seems to be more correct because the result is closer to the target shape. In the case of use of an NC lathe machine, the springback effect is more remarkable. However, the advantage of using an NC lathe machine (relative to a milling machine) is that a finishing contour pass can be added to improve final shape and surface quality especially when using a penetration value fairly high during the first pass. This is impossible without the fourth axis in milling machine.

4 Conclusion

Investigations on the use of NC lathe machine in incremental sheet forming process remain few, especially since the use of this type of machine is possible in the case of asymmetric parts and this can lead to a reduced costs and better results. In this paper, a finite element model was developed to compare the use of NC milling machine and turning machine in SPIF operations of asymmetric parts. An elasto-plastic constitutive model with quadratic yield criterion of Hill'48 and isotropic hardening behavior has been adopted.

Many differences are looked in the results of SPIF process of a conic part using the two types of NC machines. Many advantages are given in the use of NC turning machine citing the decrease of thinning and forming force as well as the advantage of the possibility of adding a finishing pass without the need of fourth axis required when using the milling machine. NC lathe machine is a good alternative that can replace milling machine to manufacture asymmetric parts in ISF process especially since the cost of using this type of NC machine is reduced compared to the use of NC milling machine or machining center. An experimental comparison should be added in our next works at the aim to validate the numerical results and to verify the efficiency of NC lathe machine in ISF applications.

References

Ambrogio G, Costantino I, De Napoli L, Filice L (2004) Influence of some relevant process parameters on the dimensional accuracy in incremental forming: a numerical and experimental investigation. J Mater Process Technol 154:501–507

Belchior J, Leotoing L, Guines D, Courteille E, Maurine PA (2014) Process/Machine coupling approach: application to robotized incremental sheet forming. J Mater Process Tech 214:1605–1616

Behera AK, Verbert J, Lauwers B, Duflou JR (2013) Tool path compensation strategies for single point incremental sheet forming using multivariate adaptive regression splines. Comput Aided Des 45:575–590

Belhassen L, Koubaa S, Wali M, Dammak F (2016) Numerical prediction of springback and ductile damage in rubber-pad forming process of aluminum sheet metal. Int J Mech Sci 117:218–226

Ben Ayed L, Robert C, Delamézière A, Nouari M, Batoz JL (2014) Simplified numerical approach for incremental sheet metal forming process. EngStruct. 62–63:75–86

Ben Said L, Mars J, Wali M, Dammak F (2016) Effects of the tool path strategies on incremental sheet metal forming process. Mech Ind 17(4):411

Duflou J, Callebaut B, Verbert J, De Baerdemaeker H (2007) Laser assisted incremental forming. Formability and accuracy improvement. Ann CIRP

Fang Y, Lua B, Chena J, Xua DK, Oub H (2014) Analytical and experimental investigations on deformation mechanism and fracture behavior in single point incremental forming. J Mater Process Technol 214:1503–1515

Jackson K, Allwood J (2009) The mechanics of incremental sheet forming. J Mater Process Technol 209:1158–1174

Jin K, Guo X, Tao J, Wang H, Kim N, Gu YA (2016) Model of one-surface cyclic plasticity with Lemaitre damage criterion for plastic instability prediction in the incremental forming process. Int J Mech Sci 114:88–97

Koubaa S, Mars J, Wali M, Dammak F (2017) Numerical study of anisotropic behavior of aluminum alloy subjected to dynamic perforation. Int J Impact Eng 101:105–114

Li Y, Daniel William JT, Liu Z, Lu H, Meehan PA (2015) Deformation mechanics and efficient force prediction in single point incremental forming. J Mater Process Technol 221:100–111

Mars J, Wali M, Jarraya A, Dammak F, Dhiab A (2015) Finite element implementation of an orthotropic plasticity model for sheet metal in low velocity impact simulations. Thin-Walled Struct 89:93–100

Salem E, Shin J, Nath M, Banu M, Taub AI (2016) Investigation of thickness variation in single point incremental forming. Proc Manuf 5:828–837

Wali M, Autay R, Mars J, Dammak F (2016) A simple integration algorithm for a non-associated anisotropic plasticity model for sheet metal forming. Int J Numer Meth Eng 107(3):183–204

Wali M, Chouchene H, Ben Said L, Dammak F (2015) One-equation integration algorithm of a generalized quadratic yield function with Chaboche non-linear isotropic/kinematic hardening. Int J Mech Sci 92:223–232

Wang J, Nair M, Zhang Y (2016) An efficient force prediction strategy in single point incremental sheet forming. Proc Manuf 5:761–771

Application of the Independent Component Analysis in the Estimation of the Road Disturbance Applied on a Nonlinear Suspension System

Dorra Ben Hassen, Mariem Miladi, Mohamed Slim Abbes, S. Caglar Baslamisli, Fakher Chaari and Mohamed haddar

Abstract One of the major factors that can affect the vehicle performance and the passenger comfort is the road disturbance. The objective of this study is to identify this road excitation acting on the vehicle using blind source separation (BSS) technique which is the independent component analysis (ICA). This method is applied on a nonlinear suspension system since the vehicle has a nonlinear behavior. The studied system is a quarter-car model, it contains the most basic features of the vertical model of the vehicle. The estimation method is very efficient due to its simplicity and short computing time. It is based only on the knowledge of the dynamic responses of the system under study. The validation of the obtained results using the ICA method was done by computing three performance criteria. Finally, a good agreement is found between the original signals and the estimated ones.

Keywords Nonlinear behavior · Quarter-car model · Road disturbance
ICA

D. Ben Hassen (✉) · M. Miladi · M. S. Abbes · F. Chaari · M. haddar
Mechanics, Modeling and Production Laboratory, National Engineering
School of Sfax (ENIS), BP 1173, 3038 Sfax, Tunisia
e-mail: dorra.benhassen@yahoo.fr

M. Miladi
e-mail: mariam.mi@hotmail.fr

M. S. Abbes
e-mail: ms.abbes@gmail.com

F. Chaari
e-mail: fakher.chaari@gmail.com

M. haddar
e-mail: mohamed.haddar@enis.rnu.tn

S. Caglar Baslamisli
Department of Mechanical Engineering, Hacettepe University,
Beytepe, 06800 Ankara, Turkey
e-mail: caglar.baslamisli@gmail.com

1 Introduction

The suspension system is an important component of the vehicle. It permits to maintain the comfort of the passenger (Agharkakli et al. 2012). In most of the studies, the suspension is modeled using linear dampers and springs. But actual suspensions have nonlinear behavior. So, the nonlinear effect should be taken into account to study this system (Hasbullah et al. 2015; Aldaier and Wang 2011). In this context, many authors developed a nonlinear suspension system in order to study its influence on the vehicle dynamics. Li et al. (2004) used nonlinear suspension stiffness and a nonlinear tire stiffness in the case of heavy vehicle coupled with a nonlinear road excitation. He concluded that the coefficient of nonlinearity affects road handling and passenger comfort. Khekare (2009) developed another nonlinear model of tire stiffness in order to study the performance of the vehicle on absorbing road disturbance. Other factor that can affect the vehicle performance is the road excitation. So many studies were carried out in this domain in order to estimate this road disturbance (Harris et al. 2010; Doumiati et al. 2011). In this paper, the estimation of the road profile disturbance is done using a new technique which is the independent component analysis applied on a nonlinear vehicle suspension system. This technique was largely used in many domains (Sika 2008; Gelle et al. 2003) since it is simple and requires only the knowledge of the dynamic response of the system under study.

This paper is structured as follows: in the first section, we present a brief description of the ICA method then the studied system and its mathematical formulation are presented and finally a good agreement between the original excitation and the estimated one is obtained.

2 Brief Description of the ICA

The ICA is an important technique of blind source separation. It aims to decompose a random signal x in a linear combination of statistically independent components (Abbes et al. 2011; Dhief et al. 2016)

The vector of the observed signals X can be written as (Hassen et al. 2017)

$$X(t) = [A]\{S\}, \tag{1}$$

where A is the mixing matrix and S is the vector of the source signals.

The objective of the ICA is to estimate A and S based only on the knowledge of the vector X. This estimation necessitates some assumptions and pretreatments (the observed signals must be centered and whitened)

The interested author can refer to Taktak et al. (2012), Dhief et al. (2016).

3 Description of the Studied System

The studied system is defined as a nonlinear quarter-car vehicle model (Fig. 1).

This system is composed of two degrees of freedom. M_1 designs the sprung mass and M_2 is the unsprung mass. The road disturbance is noted $y(t)$.

The studied suspension system is modeled as a linear damper in parallel with a nonlinear spring. The tension of the spring is obtained using a Taylor series expansion of the elasticity equations as follows (Li et al. 2004):

$$F_k = k_1 \Delta l + \beta_1 k_1 \Delta l^2 + \beta_2 k_1 \Delta l^3, \tag{2}$$

where

Δl is the difference between the two displacements X_1 and X_2.

β_1, β_2 are two nonlinear constants. Their values are taken from (Shaohua Li et al. 2004)

$$\beta_1 = 10\% \text{ and } \beta_2 = 60\% \tag{3}$$

The tire is modeled as a spring with a nonlinear stiffness k_2 in parallel with a linear damper c_2. The expression of the nonlinear tire stiffness is taken from Li et al. (2004) as

$$F_t = k_2 \Delta l + \beta_3 k_2 \Delta l^2 \tag{4}$$

with

Fig. 1 Nonlinear quarter-car model
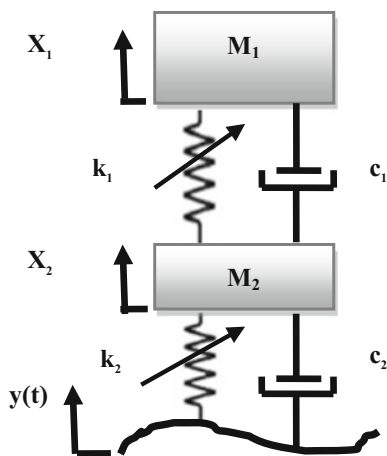
Δl is the difference between the displacement X_2 and the road excitation $y(t)$.

β_3 is the nonlinear tire coefficient. Its value is considered as 40% (Hasbullah et al. 2015)

Then the equations of motion can be written in a matrix form as

$$[M]\{\ddot{X}\} + [C]\{\dot{X}\} + [K]\{X\} + \{F_{NL}\} = \{F\},\tag{5}$$

where $\{X\}$, $\{\dot{X}\}$, and $\{\ddot{X}\}$ are displacement, velocity, and acceleration vectors, respectively. $[M]$, $[C]$, and $[K]$ are the mass, the damping, and the stiffness matrices of the studied system, respectively. $\{F\}$ is the excitation force vector due to road disturbance. $\{F_{NL}\}$ is the nonlinear spring force vector.

The matrices that appear in Eq. (5) are given by:

$$[M] = \begin{bmatrix} M_1 & 0 \\ 0 & M_2 \end{bmatrix} [C] = \begin{bmatrix} c_1 & -c_1 \\ -c_1 & c_1 + c_2 \end{bmatrix}$$

$$[K] = \begin{bmatrix} k_1 & -k_1 \\ -k_1 & k_1 + k_2 \end{bmatrix} \{F\} = \begin{bmatrix} 0 \\ k_2 y(t) + c_2 \dot{y}(t) \end{bmatrix}$$

$\{F_{NL}\}$ is defined by Eqs. (2) and (4).

To solve this system of equations, the implicit scheme of Newmark coupled with Newton–Raphson method was used. A residue is computed. At each iteration k, this residue has the following expression:

$$R_{i+1}^k = [\bar{K}]\{X\}_{i+1}^k + F_{NL}^k - \{\bar{F}\}_{i+1}\tag{6}$$

with

$$[\bar{K}] = [K] + a_0[M] + a_1[C]\tag{7}$$

and

$$\{\bar{F}\}_{i+1} = \{F\} + [M]\left(a_0\{X_i\} + a_2\{\dot{X}_i\} + a_3\{\ddot{X}_i\}\right)\\ + [C]\left(a_1\{X_i\} + a_4\{\dot{X}_i\} + a_5\{\ddot{X}_i\}\right)\tag{8}$$

If the residue is not acceptable, i.e., $R > \varepsilon$, a correction should be made for the displacement vector as follows:

$$\{\Delta X\} = \left(\frac{\partial R}{\partial X}\bigg|_{i+1}^k\right)^{-1}\left(-R_{i+1}^k\right)\tag{9}$$

So that the displacement will be

$$\{X\}_{i+1}^{k+1} = \{X\}_{i+1}^{k} + \{\Delta X\} \tag{10}$$

4 Results of the Road Disturbance Estimation

4.1 Case of a Sinusoidal Road Profile

The excitation in this case is a harmonic signal defined by the following equation:

$$y(t) = 0.2 \ 10^{-2} \ \sin (2\pi f t) \ \text{ where } f = 4.4 \, \text{Hz} \tag{11}$$

To apply the ICA on the studied systems, it is necessary to know the vector of the observed signals. This vector is composed by the suspension deflection and the chassis's acceleration as shown in Fig. 2.

From these observed signals, the ICA can reconstruct the original road excitation as shown in Fig. 3.

Referring to this figure, it can be said that the ICA allows reconstructing the road disturbance applied to the quarter-car model.

In order to study the efficiency of the ICA, some performance criteria are studied (Miladi et al. 2012): The modal assurance criterion (MAC), the normalized mean square error (NMSE), and the relative error (Er). Table 1 summarizes the obtained results.
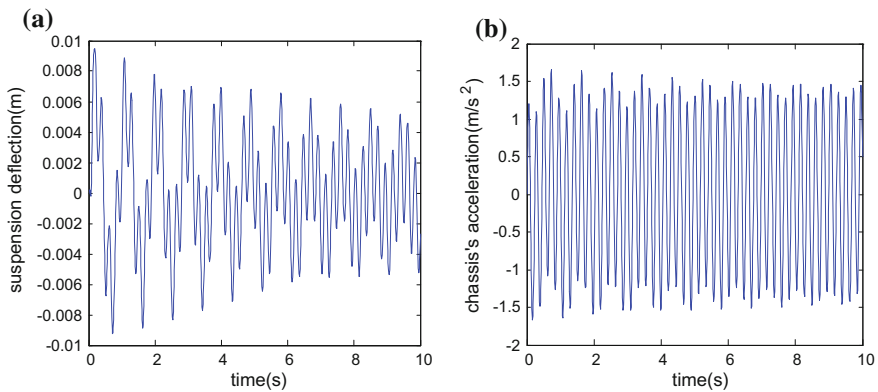
Fig. 2 Vibratory responses of the nonlinear quarter-car vehicle model **a** suspension deflection, **b** chassis's acceleration
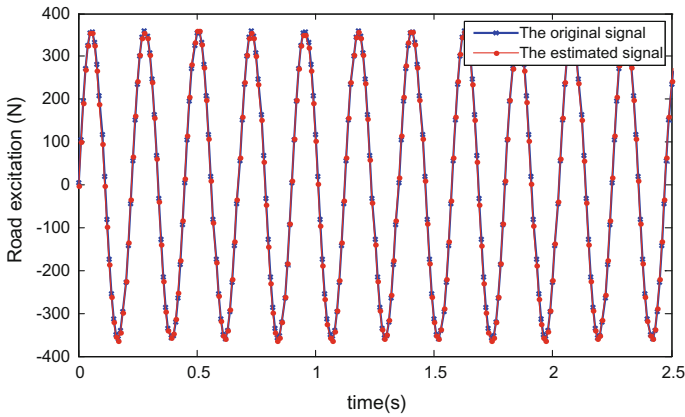
Fig. 3 Comparison between the original sinusoidal excitation and the estimated one

Table 1 Performance criteria of the first studied case

	MAC	NMSE	Er (%)
First case	0.999	0.001	2.04

It is noticed that the Mac value is very close to one. This proves that there is a good agreement between the original signal and the estimated one. Also the two other performance criteria (NMSE and the relative error) have small values and this is a good indicator. So, the ICA permits to recover the original signal with a slight lag due to the effect of the nonlinearity components of the studied system.

4.2 Case of a Bumpy Road

The excitation in this second case is a bump signal. It is defined by the following equation:

$$y(t) = \left\{ \begin{array}{l} 0.5 \times 10^{-2} \frac{1 - \cos (2\pi t)}{2} \ \text{if} \ 3 \leq t \leq 4 \\ \qquad 0 \quad \text{otherwise} \end{array} \right\} \qquad (12)$$

The observed signals are presented by Fig. 4.

From these signals, which constitute the only input for the ICA algorithm, we reconstruct the road excitation as shown in Fig. 5.

(a)

(b)
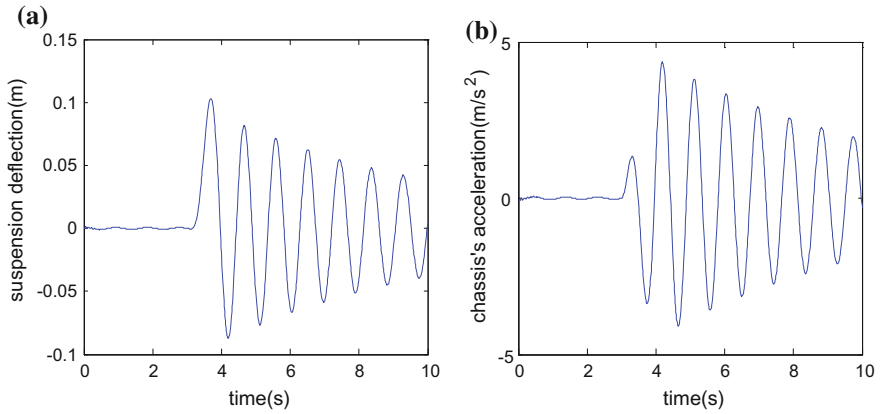
Fig. 4 Vibratory responses of the nonlinear quarter-car vehicle model **a** suspension deflection, **b** chassis's acceleration
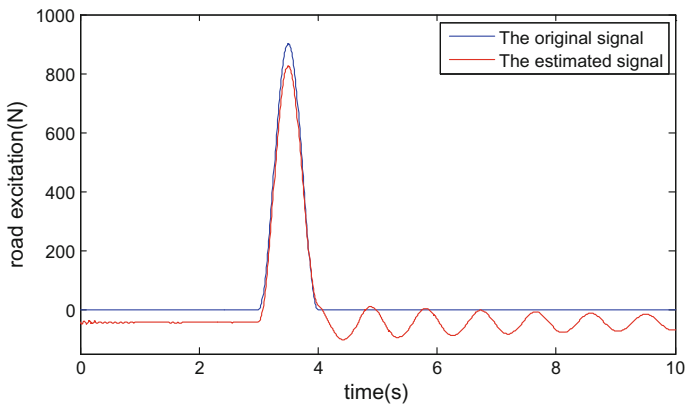
Fig. 5 Comparison between the original bump excitation and the estimated one

Table 2 Performance criteria of the second studied case		MAC	NMSE	Er (%)
	Second case	0.91	0.0869	8.6

As shown in Table 2 we note that there is small deflection of the reconstructed signals and this is due to the nonlinearity effects. But when observing the values of the three performance criteria, it can be said that the original excitation and the estimated one are very close.

5 Conclusion

In this study, the ICA is applied to a nonlinear quarter-car model in order to reconstruct the road disturbance. This technique is simple and does not require a long computing time. The validation of the obtained results is done by computing three performance criteria and it is noticed that there is a good agreement between the original signal and the estimated one even with the nonlinearity effects.

This will be of a great importance when designing passive suspension on the one hand and for the choice of the best controller law on the other.

References

Abbes MS, Chaabane MM, Akrout A, Fakhfakh T, Haddar M (2011) Vibratory behavior of a double panel system by the operational modal analysis. Int J Model Simul Sci Comput 2 (04):459–479

Agharkakli A, Sabet GS, Barouz A (2012) Simulation and analysis of passive and active suspension system using quarter car model for different road profile. Int J Eng Trends Technol 3(5):636–644

Aldair AA, Wang WJ (2011) Design an intelligent controller for full vehicle nonlinear active suspension systems. Int J Smart Sens Intell Syst 4(2):224–243

Dhief R, Taktak M, Tounsi D, Akrout A, Haddar M (2016) Application of the independent components analysis in the reconstruction of acoustic sources in duct systems. Arab J Sci Eng 1–10

Doumiati M, Victorino A, Charara A, Lechner D (2011) Estimation of road profile for vehicle dynamics motion: experimental validation. In: Proceedings of the 2011 American control conference. IEEE, pp 5237–5242

Gelle G, Colas M, Serviere C (2003) Blind source separation: a new pre-processing tool for rotating machines monitoring? IEEE Trans Instrum Meas 52(3):790–795

Harris NK, González A, OBrien EJ, McGetrick P (2010) Characterisation of pavement profile heights using accelerometer readings and a combinatorial optimisation technique. J Sound Vib 329(5):497–508

Hasbullah F, Faris WF, Darsivan FJ, Abdelrahman M (2015) Ride comfort performance of a vehicle using active suspension system with active disturbance rejection control. Int J Veh Noise Vib 11(1):78–101

Hassen DB, Miladi M, Abbes MS, Baslamisli SC, Chaari F, Haddar M (2017) Application of the operational modal analysis using the independent component analysis for a quarter car vehicle model. In: Adv Acoust Vib 125–133. Springer

Khekare A (2009) Straight line braking performance of a road vehicle with non linear tire stiffness formulation

Li S, Yang S, Guo W (2004) Investigation on chaotic motion in hysteretic non-linear suspension system with multi-frequency excitations. Mech Res Commun 31(2):229–236

Miladi M, Akrout A, Fakhfakh T, Ben Tahar M, Haddar M (2012) Dynamic modal analysis of a laminated double glazing system. In: 1st international conference on composite dynamics, Arcachon—France, pp 22–24

Sika G (2008) Dynamique des transmissions en régime transitoire. Doctoral dissertation, Lyon, INSA

Taktak M, Tounsi D, Akrout A, Abbès MS, Haddar M (2012) One stage spur gear transmission crankcase diagnosis using the independent components method. Int J Veh Noise Vib 8(4):387–400

Contribution to the Evaluation of Uncertainties of Measurement to the Data Processing Sequence of a CMM

Gheribi Hassina and Boukebbab Salim

Abstract This paper propose a procedure to estimate uncertainties in measurement process using the coordinate measuring machines (CMMs) in the aim to inspect manufacturing surface parameters. On these machines, surfaces must be measured by a number of points higher than the parameters necessary to their mathematical definitions. However, the representation of the same element can be very different according to the average materials and the protocol used during the measuring step. The real contact points between the stylus and the measured surface being unknown, one substitutes to it a measured point. This last is calculated starting from coordinates of the stylus center, the normal vector (n_i), and the stylus radius, which generates uncertainty on the real position of the measured point. This uncertainty is even propagated on the inspected surface parameters. The procedure proposed by this work permits to estimate the uncertainties on the surface parameters which characterize the geometrical surface, a data processing model in Visual Basic 6 was developed which makes it possible automatically to determine the whole of these parameters, and thus their uncertainties.

Keywords Coordinate measuring machines (CMM) · Associated surface Uncertainties · Acquisition and modeling

G. Hassina
Faculté de Technologie, Département de Génie Mécanique,
Université 20 Aout 1955, 21000 Skikda, Algeria
e-mail: gheribi_hassina@yahoo.fr

B. Salim (✉)
Faculté des Sciences de la Technologie, Département Génie des Transports,
Université des Frères Mentouri Constantine 1, 25000 Constantine, Algeria
e-mail: boukebbab@yahoo.fr

291

1 Introduction

The coordinates measuring machines (CMMs) are largely widespread to check dimensions of the parts manufactured in industry. However, it cannot measure geometrical dimensions directly corresponding to the geometrical characteristics of ISO standard of the part. In fact, the acquisition of surfaces results in a series of set of points. All points represents a sample of surface where it has been probed. However, it contains information on the localization of surface and its intrinsic geometrical characteristics (Linares et al. 2006). The whole of these characteristics makes it possible to the geometric standard to adapt to the set of points. The association of a theoretical surface to the set of the palpated points is based on the calculation of the distances 'di' between the palpated points and itself surface (Fig. 1). Obtaining the equation of 'di' can require various aspects according to the selected assumption. If the assumption of small displacements is then retained, a torsor represents the relative position and the orientation of associated surface compared to a local reference frame (Linares et al. 2002). If great displacements are used, a matrix based on conventions of the angles of Euler or vectorial rotation is used (Linares et al. 2002). The associated surface is obtained after minimization of the distance between the acquisition point Mi and theoritical surface according to a criterion optimization. At this time of measurement stage the results are certainly affected by uncertainties.

The evaluation of measurement uncertainties on a CMM is an important line of research in the field of coordinate metrology. However, several authors have used

Fig. 1 Association of a theoretical surface to set of points
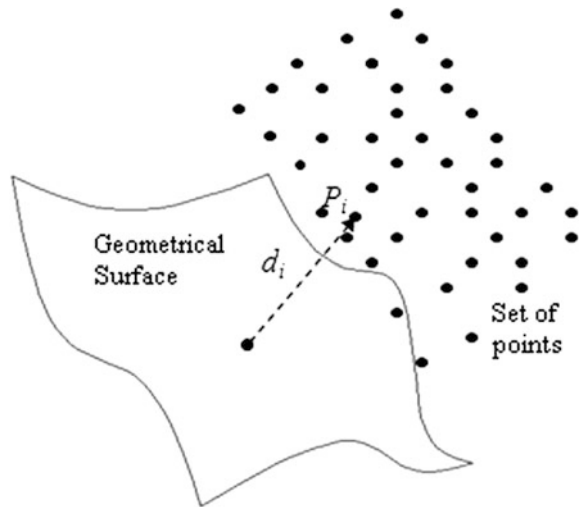
Monte Carlo methods to calculate CMM measurement uncertainties; these methods make use of Virtual CMMs that should simulate realistic CMM behavior (Van Gestel 2011; Du et al. 2016; Štrbac et al. 2016) and permit to simulate the random influential variables of the measurement process. Others use the analytical method, which consists in using the uncertainties resulting from the calibration (machine geometry, stylus calibration, etc.) and measurement, and then propagating them in the measurement range until the magnitude to be verified (Phillips et al. 2001; Antonio et al. 2003; Curran et al. 2004). There is also the method described in the ISO 5725 standards (Arencibia et al. 2015).

2 Principle of the Coordinate Measuring Machine

In any phase of verification of a specification on CMM, it is necessary to perform several elementary operations (Bourdet 1999). Figure 2 summarizes all these operations.

3 Nonlinear Method (in Great Displacement)

The method in great displacement gives us a possibility of knowing the results of optimization in the local reference frame (reference mark part), then in the total reference frame (reference mark machine). In this method, the trigonometrically functions of the matrix of rotation are not linearized with the first order. We can speak about a function of variation optimized Yi not linearized (Linares et al. 2002).
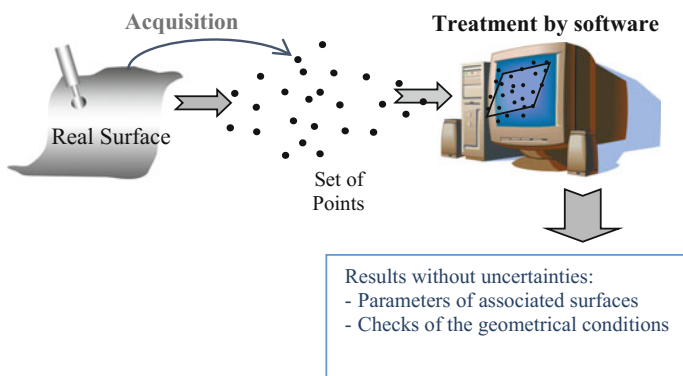
Fig. 2 Principle of the coordinate measuring machine

4 Plane Surface Model

Each measured point Mi of coordinates (X_j) j = 1 to 3 is known in the coordinate system of the CMM. The attributes of the associated surface are calculated after optimization of the distance y_i Fig. 3.

$$y_i = \vec{OM}_i \cdot \vec{n}_i - h \Rightarrow \frac{\partial \sum_{i=1}^{m} y_i^2}{\partial a_k} = 0 \qquad (1)$$

4.1 Modeling of Cylindrical and Circular Surfaces

The same treatment is carried out in the case of a cylindrical surface, thus circular. The parameters of associated surface are calculated after optimization of the distance Yi using the least-squares methode. As already mentione, the distance Yi is

Fig. 3 Plane surface model (Linares et al. 2002)
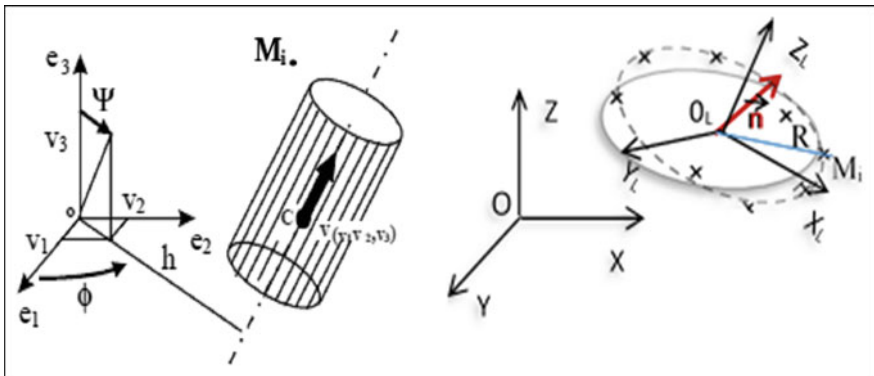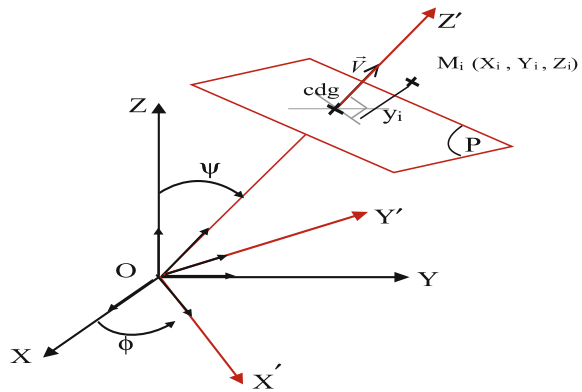
Fig. 4 Optimization case: cylinder and circle

the variation between the real surface characterized by the cloud of points and the theoritical surface it which is associated to him. That is to say R the ray of cylindrical surface associated and M_i a real point of coordinates (x_i, y_i, z_i) (Fig. 4) known in the reference mark CMM. We obtain algebraic measurement

$$y_i = \|M_i M_{th}\| = d_i - R \tag{2}$$

with: M_{th} is a point pertaining to the associated cylinder.

5 Component Count of the Random Vector

In three-dimensional metrology, and in the case of the vectorial representation of a theoretical surface, the random vectors met belong to the maximum to R^6. For example, in the case of the plan, the random vector had like components: $\vec{a}_i = [\psi, \phi, w]^t$. When $\vec{a}_i$ random vector of dimension "n" and components (n = 3) its expectation vector and its matrix of covariance are given by the following relation (Bachmann et al. 2004).

$$E(\vec{a}_i) = \begin{cases} E(\psi) \\ E(\phi) \\ E(w) \end{cases} \tag{3}$$

$$Cov(a_i) = \begin{bmatrix} V(\psi) & Cov(\psi, \phi) & Cov(\psi, w) \\ Cov(\phi, \psi) & V(\phi) & Cov(\phi, w) \\ Cov(w, \psi) & Cov(w, \phi) & V(w) \end{bmatrix} \tag{4}$$

The step taken by this work for the calculation of uncertainties of measurement is based on the matrix formulation developed by Yua (1997), Courtois (1998) and Nigam et al. (1993).

6 The General Program Structure

Figure 5 described the general structure of our program. The windows display the results of optimization of a plane, cylinder, circle, and verification of geometric conditions (perpendicularity, parallelism and coaxiality).

To validate our program, we took the case of a plan, cylinder, and circle

1. Plan1 defined by 24 palpated points.
2. Cylinder defined by 16 point palpated with a radius of 10 mm.
3. Circle defined by 16 palpated points, with a radius of 44 mm (Jalid et al. 2007).
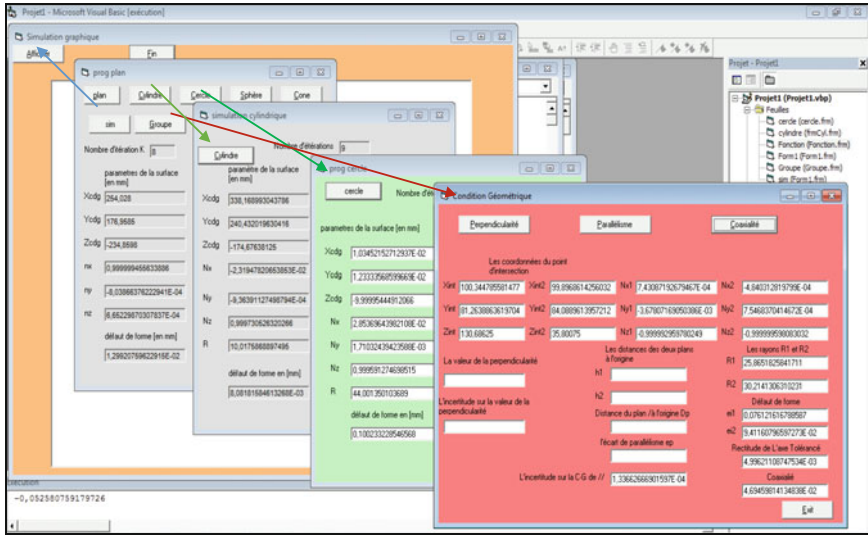
Fig. 5 Structure of the program

From this moment, we inject all the topographic surveys into the developed computer model, which will be used on the one hand for the determination of the parameters.

The indications X_{cdg}, Y_{cdg}, Z_{cdg} are the coordinates of the gravity center of the associated surface. The values of n_x, n_y, n_z are the coordinates of the direction vector of the associated surface, and the df is the form defect. The variable R corresponds to the radius of the cylindrical or circular surface. The values Uc are the uncertainties on each quantity Tables 1, 2 and 3.

The treatment of cloud points "case of the circle" carried out by the program developed by Jalid et al. (2007), are following in Table 4.

By comparing our results obtained after optimization (radius R=44.0013) with Jalid et al. 2007 results (radius R=43.99952), we find that the parameter which characterize the associated circle are correctly estimate.

Table 1 The parameters of plane	Vector V and center of gravity	Uncertainty Uc (mm)
	$n_x = -1.4878E\text{-}02$	$\pm 4.353E\text{-}06$
	$n_y = 8.38578\ E\text{-}04$	$\pm 7.584E\text{-}05$
	$n_z = 0.9998889$	$\pm 6.488E\text{-}08$
	$X_{cog} = 86.68249$	$\pm 3.166E\text{-}20$
	$Y_{cog} = 212.13013$	± 0.000
	$Z_{cog} = -167.7286$	$\pm 2.124E\text{-}18$
	$d_f = 2.0426E\text{-}02$	$\pm 1.153E\text{-}05$

Table 2 The parameters of cylinder

Vector V and center of gravity	Uncertainty Uc (mm)
$n_x = -2.31949\text{E-}02$	$\pm 2.885\text{E-}07$
$n_y = -9.36327\text{E-}04$	$\pm 3.037\text{E-}06$
$n_z = 0.9997305$	$\pm 6.700\text{E-}09$
$X_{cog} = 338.169$	$\pm 1.808\text{E-}05$
$Y_{cog} = 240.432$	$\pm 1.632\text{E-}05$
$Z_{cog} = -174.676$	$\pm 4.200\text{E-}07$
$d_f = -4.757\text{E-}03$	$\pm 6.338\text{E-}07$
$R = 10.017$	$\pm 1.513\text{E-}06$

Table 3 The parameters of circle

Vector V and center of gravity	Uncertainty Uc (mm)
$n_x = 2.85369\text{E-}02$	$\pm 3.843\text{E-}02$
$n_y = 1.71032\text{E-}03$	$\pm 2.359\text{E-}02$
$n_z = 0.999591$	$\pm 1.099\text{E-}03$
$X_{cog} = 1.0345\text{E-}02$	$\pm 1.827\text{E-}02$
$Y_{cog} = 1.2333\text{E-}02$	$\pm 2.114\text{E-}03$
$Z_{cog} = -9.999954$	$\pm 6.602\text{E-}02$
$d_f = -9.185\text{E-}02$	$\pm 2.022\text{E-}03$
$R = 44.0013$	$\pm 1.134\text{E-}02$

Table 4 Results of the circle (Jalid et al. 2007)

	circle radius R = 44 mm	
	Parameters in mm	($\pm$) Uncertainties in µm
x_c	0.01036	2.705
y_c	0.01236	2.701
z_c	−9.99931	2.702
n_x	0.00000068242	0.087
n_y	−0.0000003425	0.087
n_z	−1.0000000000	0.955
Radius	43.99952	1.911

7 Discussion of the Results

According to whole of the results obtained (case of the plan), we note that the doubts about the position of the barycenter are considerably lower than (null) comparatively to that of the directing vector (the normal). However, a very weak difference an almost negligible is observed between the values of uncertainty according to three respective directions' X, Y and Z (Fig. 6).

Uncertainty on the vector position and orientation
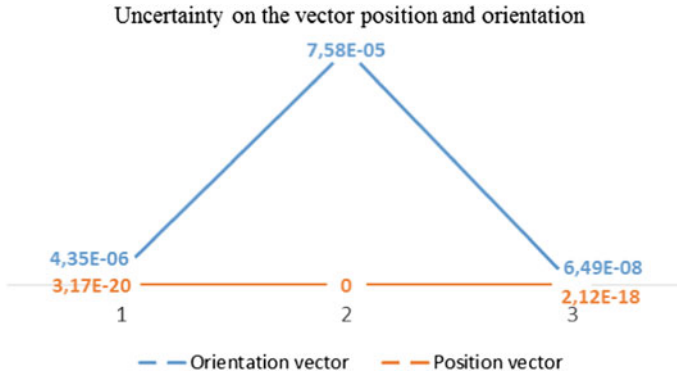
Fig. 6 Uncertainty of position and orientation vector for plane

Uncertainty on the vector position and orientation
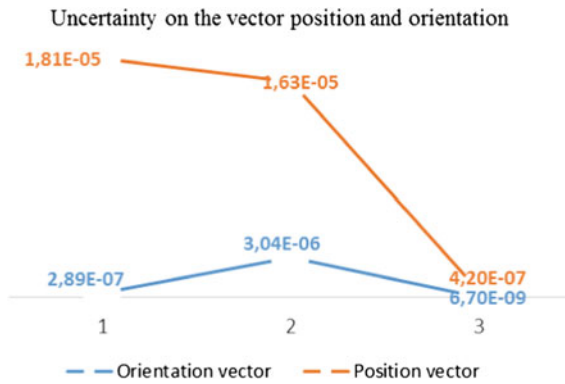
Fig. 7 Uncertainty of position and orientation vector for cylinder

In the case of the cylinder, we observe that uncertainties on the directing vector are not very small compared to those of the position of the barycenter, and also the doubt is weak on the component of the vector following X compared to Y, because the palpated points are extended along X-axis than the Y-axis (Fig. 7).

However in the circle case, we observe a very weak variation is announced between the values of uncertainty according to two respective directions' Y and Z (Fig. 8).

Moreover, to test our program, we took the case of the geometrical condition of coaxiality of a part presented in Anselmetti (2011). For this reason, the two readings of coordinates of acquired points are introduced which define the two cylindrical surfaces in the expanded program. By comparison with the results given by

Anselmetti (2011), we observe that all the parameters correspond to the two associated elements, are correctly estimated. The following figure graphically shows that the tolerance element is entirely included in the tolerance zone (Fig. 9), which is a cylinder with a diameter of 0.05 mm and centered on the axis of the reference cylinder. According to the results obtained, the coaxiality is t = 0.04694 with their uncertainty U(t) = 1.3366 10^{-04} < 0.05 (to calculate the uncertainty on the coaxiality fault, we use the formulation of the propagation of the uncertainties on a scalar Linares et al. 1999) which shows that the geometric condition is satisfied.
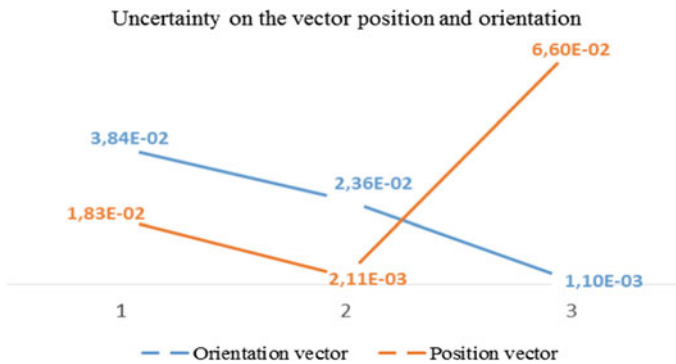
Fig. 8   Uncertainty of position and orientation vector for circle
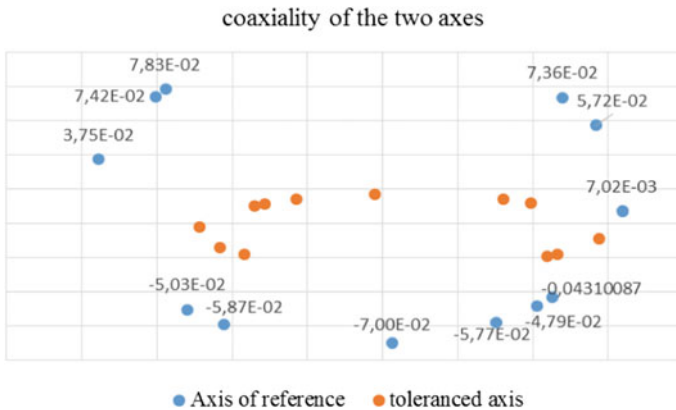
Fig. 9   Tolerance zone of the coaxiality geometrical condition

8 Conclusion

By this work a procedure to estimate uncertainties in measurement process is presented. The procedure proposed permits to estimate the uncertainties on the surface parameters which characterize the geometrical real surface, a data processing model in Visual Basic 6 was developed which makes it possible automatically to determine the whole of these parameters, and thus their uncertainties.

Indeed, several sources of errors affect the quality of measurement on a CMM, in this case to evaluate uncertainties of measurement, the experimental methods remain most adequate

References

Anselmetti B (2011) Manuel de tolérancement volume 5, Métrologie avec les normes ISO, Lavoisier, paris

Antonio P-F, Di Giacomo Benedito (2003) CMM uncertainty analysis with factorial design. Precis Eng 27:283–288

Arencibia R-V, Souza C, Henara L, Antonio F (2015) Simplified model to estimate uncertainty in CMM. J Braz Soc Mech Sci Eng 37:411–421. Eng. https://doi.org/10.1007/s40430-014-0157-8

Bachmann J, Linares J-M, Sprauel J-M, Bourdet P (2004) Aide in decision-making: contribution to uncertainties in three-dimensional measurement. Precis Eng 28:78–88. https://doi.org/10.1016/S0141-6359(03)00079-5

Bourdet P (1999) Logiciels des machines à mesurer tridimensionnelle. Techniques de l'Ingénieur, traité Mesures et Contrôle, R 316:1–22

Courtois S (1998) Réalisation d'un logiciel de choix de plans d'expériences piloté par réseau de neurones. In: Séminaire de CNRIUT'98, Fontaine bleau, France, pp 209–222

Curran E, Phelan P (2004) Quick check error verification of coordinate measuring machines. J Mater Process Technol 155–156:1207–1213. https://doi.org/10.1016/j.jmatprotec.2004.04.337

Du Z, Mengrui Z, Zhaoyong W, Jianguo Y (2016) Measurement uncertainty on the circular features in coordinate measurement system based on the error ellipse and Monte Carlo methods. Meas Sci Technol 27(12)

Jalid A, Hariri S, Senelaer J-P, Gharad A (2007) Un algorithme pour l'estimation des paramètres de courbes (ou surfaces) et leurs incertitudes en mesure tridimensionnelle. In: 5ème conférence internationale CPI (conception et production intégrées) Rabat, Morocco

Linares JM, Sprauel JM, Bourdet P (1999) propagation de l'incertitude d'acquisition dans la chaine de traitement d'une MMT, 9èmes congrès internationale de métrologie Bordeaux, France du, pp 18–21

Linares J-M, Bachmann J, Sprauel J-M (2002) Détermination des incertitudes des surfaces associées. Mécanique Industries 3(3):261–266

Linares J-M, Mailhé J, Spraue J-M (2006) uncertainties of multi sensors CMM measurements applied to high quality surfaces. XVIII Imeko world congress metrology for a sustainable development, Rio De Janeiro, Brazil

Nigam S-D, Guilford J-D, Turner J-U (1993) Derivation of generalized datum frames for geometric tolerance analysis. In: ASME design automation conference, Albuquerque

Phillips SD, Sawyer D, Borchardt B, Ward D, Beutel DE (2001) Novel artifact for testing large coordinate measuring machines. Precis Eng 25:29–34

Štrbac B, Radlovački V†, Ačko, B, Spasić-Jokić V, Župunski, L, Hadžistević, M (2016) The use of Monte Carlo simulation in evaluating the uncertainty of flatness measurement on a CMM. JPE (J Prod Eng) 19(2):69–71

Van Gestel N (2011) Determining measurement uncertainties of feature measurements on CMMs, these of Doctorate, Katholieke Universiteit Leuven – Faculteit Ingenieurs wetens chappen Kasteel park Arenberg 1-bus 2200, B-3001 Heverlee

Yua H-T (1997) evaluation and uncertainty analysis of vectorial tolerances. Precis Eng 20 (02):123–137

Integrated AHP-TOPSIS Approach for Pareto Optimal Solution Selection in Multi-site Supply Chain Planning

Houssem Felfel and Faouzi Masmoudi

Abstract In this paper, a multi-objective, multi-period, multi-product stochastic model for a multi-site supply chain planning problem under demand uncertainty is proposed. The decisions to be made include the amounts of product to be produced, the amounts of products to be transported between the different sites and customers as well as the amounts of inventory of finished or semi-finished products. The developed model aims simultaneously to minimize the expected total cost, to maximize the customer demand satisfaction level and to minimize the downside risk. The e-constraint method is applied to solve the considered model and to generate the set of Pareto optimal solutions. This set of Pareto represents the trade-off between the different objective functions. Then, an integrated approach of the Analytic Hierarchy Process (AHP) and the Technique for Order Preference by Similarity to Ideal Solution (TOPSIS) methods is applied in order to select the best compromise Pareto solution. A numerical example is presented to illustrate the proposed approach.

Keywords Multi-supply chain planning · Multi-objective · Stochastic programming · AHP · TOPSIS

1 Introduction

In the face of today's highly competitive markets, manufacturing companies are required to expand their production capacity by adding more sites or outsourcing. Therefore, an integrated planning approach that coordinates the different entities of the multi-site supply chain should be established.

H. Felfel (✉) · F. Masmoudi
Laboratory of Mechanics, Modeling and Production, National School of Engineers of Sfax,
University of Sfax, Road of Soukra km 3.5 BP1173, 3038 Sfax, Tunisia
e-mail: houssem.felfel@gmail.com

F. Masmoudi
e-mail: faouzi.masmoudi@enis.rnu.tn

303

A lot of attention has been made in the literature to treat multi-site supply chain planning problems. Many of these works are dealing with deterministic approaches (Felfel et al. 2014, 2015c, Ayadi et al. 2016). However, real multi-site supply chain planning problems are characterized by many sources of uncertainty such as customer demand. Thus, the assumption that these parameters are deterministic will lead to unrealistic results. So, it is crucial to develop an optimization planning model that takes into account existing uncertainties. Two-stage stochastic programming approach (Birge and Louveaux 1997) is widely used in the literature to deal with optimization problem under uncertainty. In this approach, the first-stage variables include the decisions to be made "here-and-now" before the revelation of the random events. The second-stage variables represent the variables that should be made in a "wait-and-see" mode after the revelation of uncertainty.

The minimization of the cost and the maximization of the profit are widely treated in multi-site supply chain planning problem. One can refer to Moon et al. (2002), Jackson et al. (2003), Lin and Chen (2006) and Felfel et al. (2015b). Nevertheless, other important criteria such as the customer demand satisfaction and the risk of having high total cost should be treated in multi-site supply chain planning problems. It is worthwhile mentioning that the objective functions usually conflict with each other in multi-objective optimization problem. Thus, the solution of this problem consists on a front of Pareto optimal solutions which represents the trade-off between the different objectives.

To solve the multi-objective optimization problem, the task of the decision maker consists on obtaining the front of Pareto optimal solutions and finding the most preferred compromise solution. The selection of a best solution from the front of Pareto can be considered as multiple criteria decision-making (MCDM) problem. A lot of methods have been developed in the literature for MCDM (Vincke 1992) such as AHP, ANP, ELCTRE, PROMETHEE, VIKOR and TOPSIS, etc. The technique for order performance by similarity to ideal solution (TOPSIS) and the analytic hierarchy process (AHP) were successfully applied in different areas such as supply chain management and logistics, manufacturing systems, design, engineering, and other many topics (Behzadian et al. 2012). To gain the benefits of these two methods, an integrated approach of the AHP and TOPSIS methods is applied to rank and to select the best compromise Pareto solution in a multi-objective supply chain planning problem.

The main objective of this paper is to develop a multi-objective, multi-product, multi-period, multi-site supply chain production and transportation model under demand uncertainty. The proposed model aims simultaneously to minimize the total cost, to maximize the customer demand satisfaction and to minimize the downside risk. In order to incorporate uncertainty in the considered model, a two-stage stochastic programming approach is adopted. An integrated approach of AHP and TOPSIS method is adopted to select the best Pareto optimal solution. Indeed, the AHP method is applied to determine the weights of the objectives and the TOPSIS method is used to rank the Pareto optimal solutions. A numerical example is presented to illustrate the proposed approach.

The remainder of the article is organized as follows. In Sect. 2, the problem statement is introduced. Section 3 describes the developed stochastic multi-objective planning model. In Sect. 4, the solution approach is presented. Section 5 details the numerical example and the computational results. Finally, Sect. 6 draws conclusions on this work and suggests future research.

2　Problem Statement

The supply network considered in this paper consists of a manufacturing system including many production sites that cooperate together in order to expand their capacities and competences. The end product is produced through different processes defined as multi-stage. Each production stage may involve more than one site, creating a multi-site supply chain structure. The considered supply chain is managed in a centralized way. The planning horizon contains several time period. Furthermore, finished products are characterized by unstable and uncertain demand. This uncertain demand could lead whether to excessive production and inventory costs or unsatisfied customer.

The objective of the considered multi-site supply chain planning problem is to minimize the total expected costs, to maximize the customer demand satisfaction level, and to minimize the downside risk (DRisk). The total costs include production costs, inventory costs, penalty costs of lost demand, and transportation costs. Model decision variables comprise the amount of product to be produced at each site in each period, the amount of inventory of each finished or semi-finished product that should be maintained on each site in each period, the amount of lost demand as well as the quantity of products to be transported between upstream and downstream sites and customers considering demand uncertainty.

3　Proposed Stochastic Mathematical Model

A multi-objective two-stage stochastic programming model is proposed in this section to deal the considered problem. The first-stage decisions include the quantity of products to be produced at each plant as well as the transportation quantity of products between the different plants. Decisions such as the quantity of products to be delivered to the customer, the inventory level and the lost demand quantity are considered as second-stage decisions. To formulate the mathematical model, we introduce the following indices parameters and decision variables:

Indices	
L_i	Set of direct successor plant of site i
ST_j	Set of stages ($j = 1, 2, …, N$)
i, i'	Production plant index ($i, i' = 1, 2, …, I$) where i belongs to stage n and i' belongs to stage $n + 1$
s	Scenario index ($s = 1, 2, …, S$)
k	Product index ($k = 1, 2, …, K$)
t	Period index ($t = 1, 2, …, T$)
Decision variables	
P_{ikt}	Production amounts of product k at plant i in period t
S_{ikt}^s	Quantity of end of period inventory of product k for scenario s at plant i in period t
JS_{ikt}^s	Quantity of end of period inventory of semi-finished product k for scenario s at plant i in period t
$TR_{i->i',kt}$	Quantity of product k transported from plant i to i' in period t
$TR_{i->CUS,kt}^s$	Quantity of product k transported from the last plant i to customer for scenario s in period t
$Dlost_{kt}^s$	Lost demand amounts of finished product k for scenario s in period t
$Q_{i,k}$	Amounts of product k received by plant i for scenario s in period t
Parameters	
cp_{ik}	Production unit cost for product k in at plant i
$ct_{i->i',k}$	Transportation unit cost of between plant i and i' for product k
$ct_{i->CUS,k}$	Transportation unit cost between the last plants i and the customer
cs_{ik}	Inventory unit cost of finished or semi-finished product k at plant i
D_{kt}^s	Demand of finished product k for scenario s in period t
DL	Distribution time of the finished products
pe_k	Penalty cost of product k
$capp_{it}$	Production capacity at plant i in period t
$caps_{it}$	Inventory capacity at plant i in period t
$capt_{i->i',t}$	Transportation capacity at plant i in period t
b_k	Time needed for the production of a product k [min]
π^s	The occurrence probability of scenario s where $\sum_{s=1}^{S} \pi^s = 1$

Problem formulation

$$
\begin{aligned}
\min E\left[Cost\right] = & \sum_{s=1}^{S} \pi^s \sum_{t=1}^{T} \sum_{k=1}^{K} \sum_{i=1}^{I} cs_{ik}\left(S_{ikt}^s + JS_{ikt}^s\right) + pe_k Dlost_{k,t}^s \\
& + ct_{i->CUS,k} TR_{i->CUS,kt}^s + \sum_{t=1}^{T} \sum_{k=1}^{K} \sum_{i=1}^{I} cp_{ik} P_{ikt} + ct_{i->i',k} TR_{i->i',kt}
\end{aligned}
\tag{1}
$$

$$\max E\left[DS\right] = \sum_{s=1}^{S} \pi^s DS^s = \sum_{s=1}^{S} \pi^s \frac{\sum_{t=1}^{T} \sum_{k=1}^{K} D_{kt}^s - Dlost_{kt}^s}{\sum_{t=1}^{T} \sum_{k=1}^{K} D_{kt}^s} \tag{2}$$

$$DS^s \geq MDS \tag{3}$$

$$\min DRisk_\Omega = \sum_{s} \pi^s \psi^s \tag{4}$$

$$\psi^s \geq Cost_s - \Omega, \qquad \psi^s \geq 0, \ \forall s \tag{5}$$

$$S_{ik,t}^s = S_{ik,t-1}^s + P_{ikt} - \sum_{i' \in L_i} TR_{i- > i',kt}, \quad \forall i \in ST_{j<N}, \ \forall k,t,s \tag{6}$$

$$\sum_{i=1}^{I} S_{ik,t}^s = \sum_{i=1}^{I} S_{ik,t-1}^s + P_{ikt} - TR_{i- > CUS,kt}^s, \quad \forall i \in ST_{j=N}, k,t,s \tag{7}$$

$$JS_{ik,t}^s = JS_{ik,t-1}^s + Q_{ikt} - P_{ikt}, \quad \forall i,k,t,s \tag{8}$$

$$Dlost_{kt}^s = D_{kt}^s - TR_{i- > CUS,kt}^s, \quad \forall k,t,s \tag{9}$$

$$Q_{i'k,t+DL} = \sum_{i' \in L_i} TR_{i- > i',kt}, \quad \forall i,k,t,s \tag{10}$$

$$\sum_{k=1}^{K} b_k P_{ikt} \leq capp_{it}, \qquad \forall i,t \tag{11}$$

$$\sum_{k=1}^{K} S_{ikt}^s + JS_{ikt}^s \leq caps_{it}, \qquad \forall i,t,s \tag{12}$$

$$\sum_{k=1}^{K} TR_{i- > i',kt} \leq captr_{it}, \qquad \forall i,t,s \tag{13}$$

$$P_{ikt}, S_{ikt}^s, JS_{ikt}^s, TR_{i- > i',kt}, TR_{i- > CUS,kt}^s, Q_{i,k}, Dlost_{kt}^s \geq 0, \quad \forall i,k,t,s \tag{14}$$

The first objective function (1) aims to minimize the expected total cost (E [Cost]). The occurrence probability π^s of each scenario is considered in order to calculate the expected total cost. Equations (2) and (3) attempt to maximize the customer demand satisfaction level (MDS). The third objective function (4) aims to minimize the downside risk (DRisk) where ψ^s is a positive variable that measures deviation between the scenario cost value and a target Ω as shown in Eq. (8).

Constraints (6) and (7) provide the balance for the inventory level of products. Constraint (8) represents the inventory balance for the semi-finished products. Constraint (9) provides the balance equation for lost products demand. Constraint (10) gives the balance equations for the transportation between the different production stages. The set of constraints (11)–(13) denote the capacity constraints. Constraint (14) is the nonnegativity restriction on the decision variables.

4   Solution Approaches

4.1   Generation of the Front of Pareto Optimal Solutions

The obtained mathematical formulation can be finally expressed as follows:

$$\min\{E\,[Cost],\ -MDS, DRisk\,\}$$
$$s.t.\ Eqs.\ (1)-(14) \tag{15}$$

The solution of the above problem consists of a set of Pareto optimal solutions. This set of Pareto represents the trade-offs that exist between the considered objective functions. In order generate this set of Pareto, we have applied the e-constraint method proposed by Haimes et al. (1971). This approach was widely used to solve multi-objective supply chain planning problems (Guillén et al. 2005; Franca et al. 2010; Felfel et al. 2015a). The main principle of this technique is to select one of the objective functions to be optimized whereas the other objectives are transformed into constraints with allowable bounds ε_i. In order to generate the entire set of Pareto optimal solutions, the level of ε_1 and ε_2 are changed as follows:

$$\min\,\{E\,[Cost]\}$$
$$s.t.\ Eqs.\ (1)-(14)$$
$$DRisk \le \varepsilon_1 \tag{16}$$
$$MDS \ge \varepsilon_2$$

4.2   Selection of the Best Pareto Optimal Solution

The selection of the most preferred Pareto optimal is based on a combination of the AHP method with the TOPSIS method. The analytic hierarchy process method (AHP) is a tool to evaluate and analyze multi-criteria decision-making problem first developed by Saaty (1980). In this paper, this method is used to determine the relative importance of each objective function. In order to obtain these weights, a pairwise comparison matrix is should be developed using Saaty preference scale detailed in Table 1.

Table 1 Preference scale (Saaty 1980)

Value (b_{ij})	Description (i over j)
1	Equal importance
3	Weak importance
5	Strong importance
7	Very strong importance
9	Absolute importance
2, 4, 6, 8	Intermediate values

Then, the Technique for Order Preference by Similarity to Ideal Solution (TOPSIS), developed by Hwang and Yoon (1981), is conducted to achieve the final ranking of the Pareto optimal solutions based on the weights obtained by the AHP method. In the TOPSIS approach, we calculate the best Pareto optimal solution that has simultaneously the farthest distance from the negative ideal solution and the shortest distance from the ideal solution. The positive ideal solution is a solution that attempts to minimize the expected total cost, to minimize the downside risk and to maximize the customer demand satisfaction level, whereas the negative ideal solution is the opposite of the previous one. For more details concerning each method, one can refer to Ayadi et al. (2016) and Felfel et al. (2017).

5 Illustrative Example

The considered example consists of a multi-site manufacturing network which contains five production stages with eight plants and two finished products. The planning horizon includes eight time periods where the length of each period is one week. It is assumed that the uncertain demand is considered as a set of discrete scenarios generated randomly and associated with known probability. The numerical example is solved using LINGO 14.0 and MS-Excel 2010 on a 32-bit with an INTEL(R) Core (TM) 2Duo CPU, T5670@1.8 GHZ, 1.8 GHZ, 2 GB RAM.

In this paragraph, the e-constraint method is used to solve the multi-objective stochastic supply chain planning problem and to generate the set of Pareto optimal solutions. The obtained set of Pareto drawn in Fig. 1 contains 30 points. It should be noted that every point of the set of Pareto shown in Fig. 1 represents a particular set of supply chain planning decisions.

In order to apply the AHP method, each pair of objective functions is compared pairwise to determine their relative importance using the ratio scale shown in

Fig. 1 Set of Pareto optimal solutions
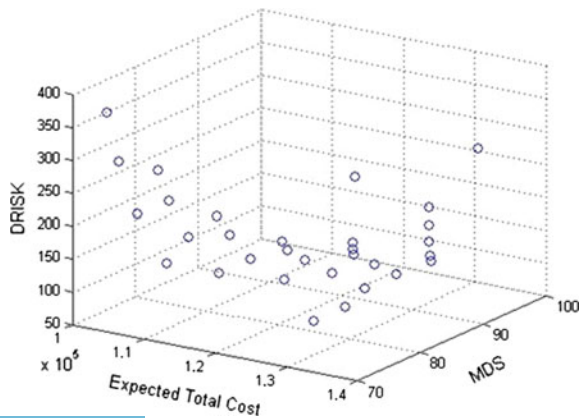
Table 1. It is worth mentioning that expected the total cost is considered more important for the decision maker than the other objective functions. The least important objective is considered to be the DRisk. The relative weights of the different objectives are detailed in the last column of Table 2.

Table 2 Pairwise comparison of the objective functions and obtained weights

	E [Cost]	MDS	DRisk	Weight
E [Cost]	1	3	6	0.655
MDS	0.33	1	3	0.250
DRisk	0.17	0.33	1	0.095

Table 3 Separation measure from the ideal solution and negative ideal solution and relative closeness coefficient

Solution	D_j^+	D_j^-	CC_j^*	Rank
S1	0.019	0.0318	0.3739	30
S2	0.0242	0.0244	0.4975	28
S3	0.0264	0.0237	0.5266	24
S4	0.0284	0.0234	0.5482	22
S5	0.0302	0.0233	0.5641	19
S6	0.0309	0.0234	0.5691	17
S7	0.0283	0.0178	0.614	11
S8	0.0291	0.0176	0.6231	8
S9	0.0298	0.0176	0.6291	7
S10	0.0296	0.0203	0.5935	15
S11	0.0297	0.0233	0.5605	20
S12	0.029	0.0142	0.6714	2
S13	0.0296	0.0144	0.6726	1
S14	0.0292	0.0163	0.6418	6
S15	0.0288	0.0197	0.5938	14
S16	0.0288	0.024	0.5462	23
S17	0.028	0.0152	0.6481	5
S18	0.0283	0.0148	0.6562	3
S19	0.0288	0.0155	0.6496	4
S20	0.0284	0.0189	0.6001	12
S21	0.0284	0.0264	0.5183	25
S22	0.0266	0.0218	0.5498	21
S23	0.0272	0.0189	0.59	16
S24	0.0278	0.0168	0.6231	9
S25	0.0284	0.0174	0.6205	10
S26	0.028	0.0275	0.5043	27
S27	0.0272	0.0316	0.4628	29
S28	0.0265	0.0259	0.5062	26
S29	0.027	0.0209	0.5643	18
S30	0.0278	0.0189	0.5954	13

Subsequently, the TOPSIS method is applied to evaluate and select the compromise solution based on the weights obtained by AHP method. The separation distances of each Pareto solution from the positive and negative ideal solution D_j^+ and D_j^- respectively, the relative closeness measure CC_j^* to the ideal solution, as well as the rank of each Pareto solution are reported in Table 3. According to Table 3, the most preferred Pareto optimal solution is S13 since it has highest CC_j^* value of 0.6726.

6 Conclusion

In this paper, a two-stage stochastic, multi-objective, multi-site, multi-period, supply chain production and transportation model is developed. Three objective functions are considered which are the minimization of the expected total cost, the minimization of the DRisk, and the maximization of the customer demand satisfaction level. A front of Pareto optimal solutions is generated for the proposed model by means of the e-constraint method. Subsequently, an integrated approach of AHP and TOPSIS methods is applied in order to select the best Pareto solution. In the first step, the weights of each objective are calculated using the AHP approach. Then, in the second step, the Pareto optimal solutions are ranked by using TOPSIS to find the most preferred solution. As future work, other multi-criteria decision-making approach could be evaluated in order to compare their performance with the proposed integrated approach.

References

Ayadi O, Felfel H, Masmoudi F (2016) Analytic hierarchy process-based approach for selecting a Pareto-optimal solution of a multi-objective, multi-site supply-chain planning problem. Eng Optim 1–17
Behzadian M, Otaghsara SK, Yazdani M, Ignatius J (2012) A state-of the-art survey of TOPSIS applications. Expert Syst Appl 39:13051–13069
Birge JR, Louveaux F (1997) Introduction to stochastic programming. Springer, New York
Felfel H, Ayadi O, Masmoudi F (2014) Multi-objective optimization of a multi-site manufacturing network. Lect Notes Mech Eng 69–76
Felfel H, Ayadi O, Masmoudi F (2015a) A multi-objective multi-site supply chain planning problem under risk and uncertainty. Des Model Mech Syst-II 1:151–160
Felfel H, Ayadi O, Masmoudi F (2015b) A stochastic programming approach for a multi-site supply chain planning in textile and apparel industry under demand uncertainty. Int J Supply Oper Manage 2(3):925–946

Felfel H, Ayadi O, Masmoudi F (2015c) A decision making approach for a multi-objective multi-site supply network planning problem. Int J Comput Integr Manuf. https://doi.org/10.1080/0951192X.2015.1107916

Felfel H, Ayadi O, Masmoudi F (2017) Pareto optimal solution selection for a multi-site supply chain planning problem using the VIKOR and TOPSIS methods. Int J Serv Sci Manage Eng Technol

Franca RB, Jones EC, Richards CN, Carlson JP (2010) Multi-objective stochastic supply chain modeling to evaluate tradeoffs between profit and quality. Int J Prod Econ 127(2):292–299

Guillén G, Mele FD, Bagajewicz MJ, Espuña A, Puigjaner L (2005) Multiobjective supply chain design under uncertainty. Chem Eng Sci 60(6):1535–1553

Haimes YY, Lasdon LS, Wismer DA (1971) On a bicriterion formulation of the problems of integrated system identification and system optimization. IEEE Trans Syst Man Cybern 1:296–297

Hwang CL, Yoon K (1981) Multiple attribute decision making: methods and applications. Springer, New York

Jackson J, Grossmann IE (2003) A temporal decomposition scheme for nonlinear multisite production planning and distribution models. Ind Eng Chem Res 42:3045–3055

Lin JT, Chen YY (2006) A multi-site supply network planning problem considering variable time buckets—a TFT-LCD industry case. Int J Adv Manuf Technol 33(9–10):1031–1044

Moon C, Kim J, Hur S (2002) Integrated process planning and scheduling with minimal total tardiness in multi-plants supply chain. Comput Ind Eng 43:331–349

Saaty TL (1980) The analytic hierarchy process. McGraw-Hill, New York

Vincke P (1992) Multicriteria decision aid. Wiley, New York

Reciprocating Compressor Prognostics

Panagiotis Loukopoulos, Suresh Sampath, Pericles Pilidis, George Zolkiewski, Ian Bennett, Fang Duan, Tariq Sattar and David Mba

Abstract Reciprocating compressors are vital components in oil and gas industry, though their maintenance cost can be high. The valves are considered the most frequent failing part accounting for almost half the maintenance cost. Condition-Based Maintenance and Prognostics and Health Management which is based on diagnostics and prognostics principles can assist towards reducing cost and downtime while increasing safety and availability by offering a proactive means for scheduling maintenance. Although diagnostics is an established field for reciprocating compressors, there is limited information regarding prognostics, particularly given the nature of failures can be instantaneous. This paper compares several prognostics methods (multiple liner regression, polynomial regression, K-Nearest Neighbours Regression (KNNR)) using valve failure data from an operating industrial compressor. Moreover, a variation about Remaining Useful

P. Loukopoulos (✉) · S. Sampath · P. Pilidis
School of Aerospace, Transport and Manufacturing,
Cranfield University, Cranfield, UK
e-mail: p.loukopoulos@cranfield.ac.uk

S. Sampath
e-mail: s.sampath@cranfield.ac.uk

P. Pilidis
e-mail: p.pilidis@cranfield.ac.uk

G. Zolkiewski · I. Bennett
Shell Global Solutions, Rijswijk, Netherlands
e-mail: george.zolkiewski@hotmail.com

I. Bennett
e-mail: Ian.Bennett@shell.com

F. Duan · T. Sattar · D. Mba
School of Engineering, London South Bank University, London, UK
e-mail: duanf@lsbu.ac.uk

T. Sattar
e-mail: sattartp@lsbu.ac.uk

D. Mba
e-mail: mbad@lsbu.ac.uk

313

Life (RUL) estimation process based on KNNR is proposed along with an ensemble method combining the output of all aforementioned algorithms. In conclusion, it is showed that even when RUL is relatively short given the instantaneous failure mode, good estimates are feasible using the proposed methods.

Keywords Reciprocating compressor · Prognostics · Instantaneous failure CMSM'2017

1 Introduction

Reciprocating compressors are essential components in oil and gas industry, being one of most commonly used type of equipment, requiring high reliability and availability (Bloch 2006). Despite their popularity, their maintenance cost can be several times higher than that of other compressor types (Tran et al. 2014). Bloch (2006) notes that valves are the most common failing part (36%), making them the weakest component, accounting for half the maintenance cost (Griffith and Flanagan 2001).

In order to decrease downtime and cost, while increasing availability and safety, efficient maintenance is essential (Bloch 2006) since reciprocating failures can cause from production loss to human casualties (Tran et al. 2014). Condition-Based Maintenance and Prognostics and Health Management (CBM/PHM) (Vachtsevanos et al. 2006) is a policy founded on the diagnostics (Vachtsevanos et al. 2006) and prognostics (Sikorska et al. 2011; Vachtsevanos et al. 2006) principles and has gaining traction during recent years due to its proactive nature making it an effective tool that moves towards this direction. The equipment of interest is mounted with sensors collecting Condition Monitoring (CM) measurements which are analysed for diagnostics purposes. In case of a fault, this information is used to estimate Remaining Useful Life (RUL) enabling the user to schedule maintenance in advance thus avoiding any unnecessary actions. Although diagnostics is an established area for valve failures (Annicchiarico et al. 2013; Tran et al. 2014), there is limited information about prognostics on reciprocating compressors. Ergo, the purpose of this paper is comparison of several prognostics methods regarding accuracy and variability.

The methods employed belong to data-driven class where historical information was utilised to model the degradation process and are suitable when there is limited physical understanding of system under study. Moreover, direct RUL estimation was used where relationship between information and RUL is modelled requiring knowledge of historical and current information and is useful during absence of failure threshold. The techniques implemented were: Multiple Linear Regression (MLR) and Polynomial Regression (PR) which belong to trend extrapolation, one of the simplest methods and most commonly used one in industry (Sikorska et al. 2011; Zio and Di Maio 2010), and K-Nearest Neighbours Regression (KNNR) which belongs to similarity-based prognostics, an emerging trend with great

potential (You and Meng 2011). Moreover, a RUL estimation variation based on KNNR was proposed.

Trend extrapolation is one of the most preferred prognostics method in industry, though there are limited published works (Sikorska et al. 2011). Zhao et al. (2016) used S-transform, Gaussian pyramid, local binary pattern, PCA and linear discriminant analysis for pre-processing along with MLR for RUL estimation for bearings. Li and Nilkitsaranont (2009) employed MLR for prognostics of gas turbine engine during early degradation stage while quadratic regression was used when degradation deteriorated. MLR has also been used extensively as a benchmarking tool, along with PR, used either to compare performance of proposed methodology, usually found inferior (Loutas et al. 2013), or to compare performance of several algorithms (Saxena et al. 2009). These works used either experimental (Loutas et al. 2013; Saxena et al. 2009; Zhao et al. 2016) or simulated (Li and Nilkitsaranont 2009) raw sensor data.

In similarity-based prognostics, a reference data base is created with historical failures which are compared with an ongoing case via distance analysis. Wang et al. (2008) used MLR for fusion, curve fitting for smoothing and segmented failure trajectories. RUL was estimated based on similar reference RULs by measuring distance of ongoing failure trajectory section with historical ones. Zio and Maio (2010) segmented and normalised failure signals. During normal operation, RUL was estimated as Mean Time to Failure (MTTF). After fault detection, RUL was calculated as weighted sum of historical RULs based on fuzzy similarity of current segment and reference ones. You and Meng (2011) segmented historical failures. RUL of current segment was estimated based on weighted RUL of similar historical ones. During similarity analysis, more recent measurements within segment had greater importance. These works used either experimental (You and Meng 2011) or simulated (Wang et al. 2008; Zio and Di Maio 2010) raw sensor data. Similarity-based prognostics has been implemented on turbofan engines (Wang et al. 2008), fission reactor (Zio and Di Maio 2010) and ball grid array solder joints of printed circuit boards (You and Meng 2011).

Despite its simplicity, KNNR has found limited applications regarding prognostics. Rezgui et al. (2014) combined support vector regression with KNNR for diagnostics and prognostics of reverse polarity fault. Hu et al. (2014) extracted features and used KNNR, optimised by particle swarm optimisation and k-fold cross validation, for RUL estimation of lithium-ion battery. These works used either experimental (Hu et al. 2014) or simulated (Rezgui et al. 2014) data. On the other hand, KNNR has found popularity in other fields like forestry (Chirici et al. 2008; Haara and Kangas 2012) or traffic forecasting (Li et al. 2012; Yuan and Wang 2012).

The methods were compared with non-uniformly sampled historical valve failure data from an industrial reciprocating compressor retrieved from a server rather than raw sensor measurements commonly used. Use of actual information addressed a major prognostics challenge: limited works utilising real-life data

(Sikorska et al. 2011), demonstrating PHM's applicability and benefits in industry, and its implementation to failure modes that are instantaneous in contrast to slowly time varying ones usually examined. Principal Components Analysis (PCA) and Statistical Process Control (SPC) were employed to create Hotelling T^2 and Q residuals metrics proposed to be used as HIs and direct RUL estimation predictors.

The rest of the paper is organised as follows. Section 2 analyses HI creation process and overviews prognostics methods and evaluation metrics used. Section 3 describes data acquisition procedure. Section 4 presents results followed by a discussion. Section 5 contains concluding remarks.

2 Prognostics Methods Overview

2.1 Health Indicator Creation

Due to availability of historical information, data-driven techniques were utilised for reciprocating compressor prognostics. For such methods it is essential information used reflect degradation process adequately and can be achieved via HIs. In this work, Hotelling T^2 and Q residuals metrics constructed by PCA and SPC were proposed as HIs describing compressor's valve degradation, along with RUL estimation predictors.

PCA is a dimensionality reduction technique that projects a number of correlated variables in a lower space via a linear transformation (components), while preserving maximum possible variance within original set, creating a new group of uncorrelated and orthogonal latent variables (scores) (Jolliffe 2002). Calculation of principal components was done with use of singular value decomposition (Jolliffe 2002). Selection of appropriate number of components was done employing Cumulative Percentage of Variance (CPV) (Jolliffe 2002).

SPC is used to monitor a univariate process for diagnostics purposes, which is considered to be healthy when its value lies within some statistical limits decided by control chart used. For multivariate process, PCA is used to facilitate multivariate process control by reducing number of monitored variables and decorrelating them. After PCA model has been created, its scores and residuals can be used for SPC. Control charts employed in this work are Hotelling T^2 and Q residuals, most widely used ones regarding PCA/SPC (Kruger and Xie 2012). Hotelling metric for score matrix T is (Kruger and Xie 2012):

$$T^2 = \sum_{i=1}^{k} \frac{t_i}{s_i^2} \tag{1}$$

with t_i ith principal component scores, s_i^2 its variance. Q metric for residual matrix R is (Kruger and Xie 2012):

$$Q = \sum_{i=1}^{n} (x_i - \widehat{x}_i)^2 \qquad (2)$$

with $\widehat{x}_i$ reconstructed values of x_i.

Procedure of creating HIs is divided in two phases. In phase I healthy data are used to create a PCA model, while in phase II new data are projected on healthy PCA model calculating their metrics and creating HIs.

2.2 Prognostics Methods

HIs describing the degradation process were employed by prognostics techniques to estimate compressor's RUL. The methods used in this work were multiple linear and polynomial regression, K-nearest neighbours along with a proposed RUL estimation variation, and an ensemble methodology, all of which are described below.

2.2.1 Multiple Linear Regression (MLR)

MLR is used to predict the $n \times 1$ dependent variable Y as linear combination of $n \times p$ independent ones X (Montgomery and Runger 2003): $y_i = \beta_0 + \beta_1 x_{i1} + \ldots + \beta_p x_{ip} + \varepsilon_\iota$, with $\beta_0, \beta_1, \ldots, \beta_p$ regression coefficients to be estimated, ε the residuals, and $i = 1, \ldots, n$. Parameters are calculated utilising least squares algorithm (Montgomery and Runger 2003):

$$\widehat{\beta} = \left(X'X\right)^{-1} X'Y \qquad (3)$$

Fit of model on data can be assessed using adjusted coefficient of determination (Montgomery and Runger 2003): $R^2_{adjusted} = 1 - \frac{SS_E/(n-p)}{SS_T/(n-1)}$, with $SS_E = \sum E^2$ and $SS_T = \sum \left(Y - \overline{Y}\right)^2$, (Montgomery and Runger 2003). It ranges from zero indicating bad fit to one indicating perfect fit.

MLR was trained using historical failures and applied for direct RUL estimation, with HIs being independent variables and RUL dependent one.

2.2.2 Polynomial Regression (PR)

PR can be seen as an extension to MLR where predictors are also included in power form. A second order polynomial for two regressors is (Montgomery and Runger 2003): $y_i = \beta_0 + \beta_1 x_{i1} + \beta_{11} x_{i1}^2 + \beta_2 x_{i2} + \beta_{22} x_{i2}^2 + \beta_{12} x_{i1} x_{i2} + \varepsilon$. Estimation of coefficients is done as in (3).

Depending on polynomial order, number of parameters can be significantly large leading to overfitting. Stepwise regression is most widely used selection process for including an optimum number of regressors (Montgomery and Runger 2003). It is an iterative procedure where terms are included or removed from the model based on a partial F-test, leading to Polynomial Stepwise Regression (PSR). Adequacy of model can be examined using $R^2_{adjusted}$. Prognostics application of SPR is the same as MLR.

2.2.3   K-Nearest Neighbours Regression

KNNR estimates the regression function without making any assumptions about underlying relationship of $n \times q$ dependent X and $n \times 1$ independent Y variables (Haara and Kangas 2012) by utilising similarity analysis (Yuan and Wang 2012). Let u be a new sample, resemblance if its predictors and historical ones is calculated using Euclidean distance (Chirici et al. 2008; Li et al. 2012; Rezgui et al. 2014; Yuan and Wang 2012) the most commonly used similarity metric (Haara and Kangas 2012; Hu et al. 2014): $d(u, x_i) = \|u - x_i\| = \sqrt{\sum_{j=1}^{q} (u_j - x_{ij})^2}$, with $i = 1, \ldots, n$. u's response value is (Haara and Kangas 2012; Hu et al. 2014): $y_u = \frac{\sum_{l=1}^{K} w_l y_l}{\sum_{l=1}^{K} w_l}$, with K number of most similar historical points to current sample, w_l and y_l weight and response value of lth neighbour. Weighting can be done in various ways. Formulation used here was proposed as:

$$w_l = 1 - d_l / \sum_{l=1}^{K} d_l \tag{4}$$

Optimum K can be found via k-fold cross validation (Chirici et al. 2008).

In this work, pointwise similarity was used instead of segmented where only latest information was compared with historical samples. Furthermore, RUL was estimated using K most similar samples from all historical data, meaning that one failure might have more than one common points with current sample while another might have none. This method shall be denoted as KNNR 1.

2.2.4   Proposed Variation of KNNR-Based RUL Estimation

A variation of RUL estimation process based on KNNR is also proposed. Rather than applying KNNR on all historical data, it is implemented on each historical case instead. RUL is weighted sum of RULs from each case based on similarity results. In this variation, instead of using K most similar points from each case only most similar one was used. This variation shall be denoted as KNNR 2.

2.2.5 Ensemble Prognostics Method

In this project, an ensemble methodology was also tested where output of each prognostics algorithm reviewed in this chapter was combined. Fusion was undertaken via averaging having the following form:

$$Ensemble = (MLR + SPR + KNNR\,1 + KNNR\,2)/4 \qquad (5)$$

2.3 Prognostics Metrics

In order to quantitatively benchmark performance of methods two criteria were used, as there is no universal criterion available yet (Saxena et al. 2008). Let $\Delta RUL(t) = RUL(t) - \widehat{RUL}(t)$ be difference of actual and estimated RUL at time t, $t = 1, \ldots, N$ number of available samples. Cumulative Relative Accuracy (CRA) measuring accuracy is (Saxena et al. 2008): $CRA = \frac{1}{N}\sum_{i=1}^{N} RA(i)$, with $RA(i)$ the Relative Accuracy at each time instance (Saxena et al. 2008): $RA(i) = 1 - \frac{|\Delta RUL(i)|}{RUL(i)}$. CRA ranges in $(-\infty, 1]$ with 1 indicating perfect score. Mean Absolute Deviation (MAD) regarding volatility is (Saxena et al. 2008): $MAD = \frac{1}{N}\sum_{i=1}^{N} |\Delta RUL(i) - median(\Delta RUL(i))|$. It ranges in $[0,\infty)$ with 0 indicating perfect score.

3 Data Acquisition

Prognostics was performed using information from an operational industrial two-stage, four-cylinder, double-acting reciprocating compressor that has been used in various applications. The measurements (process and mechanical) stream continuously to a central location for e-maintenance diagnostics. The large volume of data produced requires a huge amount of storage, thus a ruleset was created deciding which values should be stored, leading to non-uniformly sampled sets. To compensate, linear interpolation is used.

The fault mode under study was a valve failure, where a broken valve plate led to leakage. There were 13 cases available that all took place in the same cylinder where either Head End (HE) or Crank End (CE) discharge valve failed. The valves were of same type, model and manufacturer. Historical information of 16 temperature measurements, one for each valve was extracted with sampling period $T_s = 1\,\text{s}$ $(f_s = 1\,\text{Hz})$. In order to filter out external effects, temperature ratios of HE/CE suction and discharge valves were calculated leading to eight variables that were used for analysis.

4   Results

4.1   *Application of Prognostics Methods*

After collecting historical information, each method was trained using 12 failures for model building while the 13th was kept for testing. RUL was logarithmically transformed to improve model fit and was estimated directly by being considered as dependent variable with T^2 and Q being independent ones. For PR third order was maximum order examined. $R^2_{adjusted}$ values for MLR and PR were 0.67 and 0.77 respectively, indicating adequate fit. For KNNR data were centred and scaled to unity. In KNNR 1 optimum K was selected via 10-fold cross validation ranging from 1 to 200 as 14, while for KNNR 2 optimum K was decided a priori as K = 1. All methods were implemented in Matlab (*Bioinformatics Toolbox* ^{TM} *User βϵ^{TM} s Guide* 2015; *Statistics and Machine Learning Toolbox User's Guide* 2016). Training outcome of each method can be found below.

4.2   *Results*

Figure 1 contains prognostics results for failure case 11, giving a qualitative perspective of each method's performance. X-axis indicates time while y-axis RUL at each time stamp, with $t = 0$ the moment fault was detected (RUL = 246) and $t = 246$ the moment of failure (RUL = 0). Graph consists of a number of lines. Black indicates actual RUL as observed in situ, and rest correspond to each algorithm's estimations. All methods perform comparably well with best performing being the ensemble technique (magenta line) as it tracks closely RUL evolution, followed by polynomial regression (cyanide line), while worst performing seems to be KNNR 2 (green line) which continuously underestimates RUL. KNNR 1 (red line) and MLR (blue line) perform adequately. It can be noted that all methods converge to actual RUL as time passes.

Quantitative inspection of methods' performance can be done via metrics found in Table 1. The prognostics horizon for all metrics is from moment of fault detection until failure, meaning all available samples were considered in calculation. Results indicate that ensemble method outperforms the rest being superior in both accuracy and precision. The remaining techniques perform comparably well. Overall, quantitative results are in accordance with qualitative ones. Furthermore, results confirmed the claim of lack of universal metrics since the same method might be suitable or not depending on metric used. This calls for more effort to be put towards this direction.
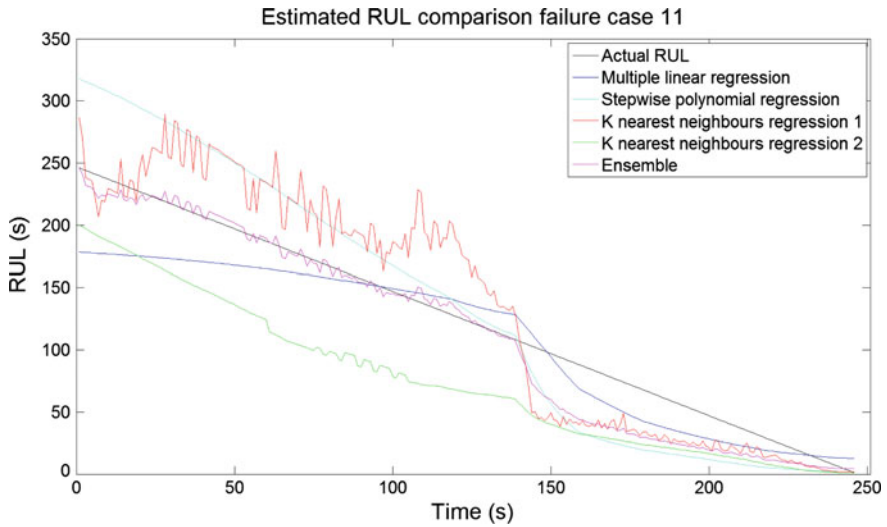
Fig. 1 RUL estimation for failure case 11

Table 1 Evaluation metrics failure case 11

Methods		MLR	PR	KNNR 1	KNNR 2	Ensemble
Performance metrics	CRA	0.71	0.60	0.65	0.51	**0.75**
	MAD	16.97	35.61	33.53	14.36	**13.75**

Based on prognostics results presented in this section, there are some comments that can be made. PSR and MLR performed similarly well with PSR being superior based on both qualitative and quantitative results, as it could better reflect the complex relationship between RUL and HIs by including interaction and higher order terms of HIs, overcoming MLR's rigidness. KNNR 1 tended to outperform KNNR 2 indicating that even when considering more than one similar case from the same failure during RUL estimation can increase accuracy. On the other hand, KNNR 2 displayed lower variation hinting that considering each case separately can reduce volatility. Ensemble method's performance is highly dependable on individual performance of compromising methods. Its components performed well thus it displayed the best overall performance based on both qualitative and quantitative results. Its output could be seen as refinement of prognostics estimations of its elements.

Importance of HI quality should be noted, as performance of algorithms is also heavily dependent on quality of HIs used since they reflect degradation process. The HIs that were used (T^2 and Q) encapsulated adequately failure evolution confirmed by good results, tracking closely fault propagation through time.

5 Conclusions

In this project, four prognostics techniques (MLR, PR, KNNR 1), along with a RUL estimation variations (KNNR 2), and an ensemble method combining aforementioned algorithms' output, were benchmarked using valve failure data from an operational industrial reciprocating compressor, addressing lack of works regarding reciprocating compressor prognostics. Also, use of actual data tackled lack of works regarding implementation of prognostics in industrial applications demonstrating PHM's potency. Ensemble was superior as it tracked closely actual RUL evolution through time while also having the highest metric values. PR outperformed MLR due to being more versatile. KNNR 1 was more accurate than KNNR 2 while the latter was less volatile, differences that can be attributed to their RUL calculation process. T^2 and Q metrics, proposed to be used as HIs and employed by each algorithm as predictors for direct RUL estimation, were able to adequately encapsulate the degradation process given the good RUL estimates, confirming their suitability as health indicators. In general, all methods performed comparably well yielding good RUL estimates as shown both in qualitative (graphs) and quantitative (metrics) results, regardless of the instantaneous nature of failure mode under study.

References

Annicchiarico C, Babbini A, Capitani R, Tozzi P (2013) Numerical and experimental testing of composite rings for reciprocating compressor valves. In: ASME 2013 pressure vessels and piping conference. ASME. https://doi.org/10.1115/PVP2013-97984

Bioinformatics Toolbox ™ User β€™ s Guide (2015) The MathWorks, Inc

Bloch HP (2006) A practical guide to compressor technology, 2nd edn. Wiley, Hoboken, NJ

Chirici G, Barbati A, Corona P, Marchetti M, Travaglini D, Maselli F, Bertini R (2008) Non-parametric and parametric methods using satellite images for estimating growing stock volume in alpine and Mediterranean forest ecosystems. Remote Sens Environ 112:2686–2700. https://doi.org/10.1016/j.rse.2008.01.002

Griffith WA, Flanagan EB (2001) Online continuous monitoring of mechanical condition and performance for critical reciprocating compressors. In: 30th turbomachinery symposium, Texas, Houston

Haara A, Kangas A (2012) Comparing k nearest neighbours methods and linear regression – is there reason to select one over the other? Math Comput For Nat Sci 4:50–65

Hu C, Jain G, Zhang P, Schmidt C, Gomadam P, Gorka T (2014) Data-driven method based on particle swarm optimization and k-nearest neighbor regression for estimating capacity of lithium-ion battery. Appl Energy 129:49–55. https://doi.org/10.1016/j.apenergy.2014.04.077

Jolliffe IT (2002) Principal component analysis, 2nd edn. Springer, New York, Springer Series in Statistics. https://doi.org/10.1007/b98835

Kruger U, Xie L (2012) Statistical monitoring of complex multivariate processes. Wiley, Chichester, UK. https://doi.org/10.1002/9780470517253

Li S, Shen Z, Xiong G (2012) A k-nearest neighbor locally weighted regression method for short-term traffic flow forecasting. In: 2012 15th international IEEE conference on intelligent transportation systems. IEEE, pp 1596–1601. https://doi.org/10.1109/ITSC.2012.6338648

Li YG, Nilkitsaranont P (2009) Gas turbine performance prognostic for condition-based maintenance. Appl Energy 86:2152–2161. https://doi.org/10.1016/j.apenergy.2009.02.011

Loutas TH, Roulias D, Georgoulas G (2013) Remaining useful life estimation in rolling bearings utilizing data-driven probabilistic E-support vectors regression. IEEE Trans Reliab 62:821–832. https://doi.org/10.1109/TR.2013.2285318

Montgomery DC, Runger GC (2003) Applied statistics and probability for engineers, 3rd edn. Wiley

Rezgui W, Mouss NK, Mouss L-H, Mouss MD, Benbouzid M (2014) A regression algorithm for the smart prognosis of a reversed polarity fault in a photovoltaic generator. In: 2014 1st international conference on green energy ICGE 2014. IEEE, pp 134–138. https://doi.org/10.1109/ICGE.2014.6835411

Saxena A, Celaya J, Balaban E, Goebel K, Saha B, Saha S, Schwabacher M (2008) Metrics for evaluating performance of prognostic techniques. In: 2008 international conference on prognostics and health management. IEEE, pp 1–17. https://doi.org/10.1109/PHM.2008.4711436

Saxena A, Celaya J, Saha B, Saha S, Goebel K (2009) Evaluating algorithm performance metrics tailored for prognostics. Conf Proc, IEEE Aerosp. https://doi.org/10.1109/AERO.2009.4839666

Sikorska JZ, Hodkiewicz M, Ma L (2011) Prognostic modelling options for remaining useful life estimation by industry. Mech Syst Signal Process 25:1803–1836. https://doi.org/10.1016/j.ymssp.2010.11.018

Statistics and Machine Learning Toolbox User's Guide (2016) The MathWorks, Inc

Tran VT, AlThobiani F, Ball A (2014) An approach to fault diagnosis of reciprocating compressor valves using Teager-Kaiser energy operator and deep belief networks. Expert Syst Appl 41:4113–4122. https://doi.org/10.1016/j.eswa.2013.12.026

Vachtsevanos G, Lewis F, Roemer M, Hess A, Wu B (2006) Intelligent fault diagnosis and prognosis for engineering systems. Wiley, Hoboken, NJ, USA. https://doi.org/10.1002/9780470117842

Wang T, Jianbo Y, Siegel D, Lee J (2008) A similarity-based prognostics approach for remaining useful life estimation of engineered systems. In: 2008 international conference on prognostics and health management. IEEE, pp 1–6. https://doi.org/10.1109/PHM.2008.4711421

You M-Y, Meng G (2011) A generalized similarity measure for similarity-based residual life prediction. Proceedings of the institution of mechanical engineers part E. J Process Mech Eng 225:151–160. https://doi.org/10.1177/0954408911399832

Yuan Z-W, Wang Y-H (2012) Research on K nearest neighbor non-parametric regression algorithm based on KD-tree and clustering analysis, In: 2012 4th international conference on computational and information sciences. IEEE, pp 298–301. https://doi.org/10.1109/ICCIS.2012.246

Zhao M, Tang B, Tan Q (2016) Bearing remaining useful life estimation based on time–frequency representation and supervised dimensionality reduction. Measurement 86:41–55. https://doi.org/10.1016/j.measurement.2015.11.047

Zio E, Di Maio F (2010) A data-driven fuzzy approach for predicting the remaining useful life in dynamic failure scenarios of a nuclear system. Reliab Eng Syst Saf 95:49–57. https://doi.org/10.1016/j.ress.2009.08.001

Dynamic Analysis of Bevel Gear
in Presence of Local Damage
in NonStationary Operating Conditions

M. Karray, F. Chaari, M. T. Khabou and M. Haddar

Abstract Most of the researches describe models of gearboxes under stationary operating conditions. However, considering the real situation, the assumption of stationarity cannot be kept longer because during service, gearboxes usually run under fluctuating load conditions. The purpose of this chapter is to study the influence of time-varying loading conditions on a spiral bevel gear dynamic behavior in presence of a local damage. The speed–torque characteristic of the driving motor is considered. The load variation induces speed variation, which causes variation in the gearmesh stiffness period. Using an implicit Newmark's time-step integration, the dynamic response shows impulses corresponding to the meshing of the cracked tooth; their amplitude level depends on the amplitude of the load. In order to put in evidence the time-varying load effects, spectral analysis is unsuited and time–frequency analysis is used instead. The horizontal lines over wide frequency band corresponding to each mesh period of the defected tooth are observed.

1 Introduction

Industrial gear systems situation forces to consider real operating conditions such as time-varying loads, so gearbox vibration is modulated by the fluctuation of torque load as shown by Bartelmus and Zimroz (2009). Randall (1982) states that the amplitude of a gearbox, caused by the meshing between gears, is modulated by the fluctuation of torque load. The influence of the loading conditions is identified using

M. Karray (✉) · F. Chaari · M. T. Khabou · M. Haddar
Laboratory of Mechanics Modeling and Production, National School of Engineers
of Sfax, BP1173, 3038 Sfax, Tunisia
e-mail: maha-karray@hotmail.fr

M. Haddar
e-mail: Mohamed.haddar@enis.rnu.tn

Smoothed Wigner–Ville Distribution by Chaari et al. (2011). Time–frequency analysis is considered more suitable by Baydar and Ball (2000) than spectral analysis to track the degradation of a gear under different load conditions. (Bartelmus et al. 2010) studied the influence of load conditions on dynamic behavior of spur gear. Karray et al. (2012) studied the dynamic behavior of bevel gear transmission in presence of teeth defects in stationary conditions. This chapter will investigate the effect of local damage on the dynamic behavior of bevel gear which is a major component in the gearbox of an excavator in nonstationary conditions by modeling single stage bevel gear transmission using a lumped parameter model. The simulation of the dynamic behavior is achieved in the time domain using an implicit Newmark's time-step integration scheme.

2 Mathematical Modeling of the Transmission

2.1 Modeling of the Bevel Gear Model

We consider a dynamic model of spiral bevel gear divided into two rigid blocks as shown in Fig. 1. Each block has five degrees of freedom: three translations x_i, y_i, z_i (i = 1, 2) and two rotations θ_m and θ_1 for the pinion and θ_2 and θ_r for the wheel.

The gear bodies are assumed to be rigid cone disks and the shafts are considered with torsional stiffness. The mesh stiffness is modeled by a linear stiffness $k_e(t)$ acting along the line of action.

Fig. 1 Spiral bevel gear model
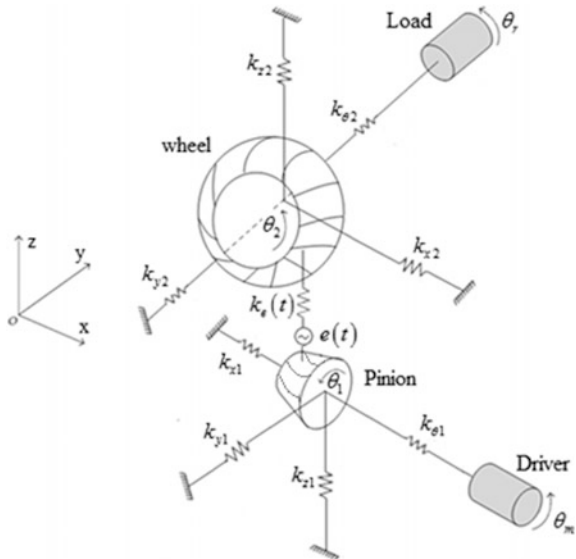
2.2 Modeling of the Torques

The driving torque is related to the motor speed as following (Wright 2005):

$$C_m = \frac{T_b}{\left(1 + (s_b - s)^2 \left(\frac{a}{s} - bs^2\right)\right)} \tag{1}$$

where a and b are constant properties of the motor, s_b and T_b are the slip and torque at breakdown, and s is the proportional drop in speed given by:

$$s = 1 - \frac{\Omega}{\Omega_s} \tag{2}$$

where Ω_s is the synchronous velocity of the motor.

2.3 Modeling of the Time-Varying Gearmesh Stiffness

When the rotational speed N_1 is constant, time-varying gearmesh stiffness $K_m(t)$ is modeled by a periodic function.

For variable speed conditions, $K_m(t)$ will be no longer periodic. Figure 2 shows the evolution of the gearmesh stiffness. A decrease in the gearmesh stiffness period due to an overloading of the motor is noticed (Chaari et al. 2011).
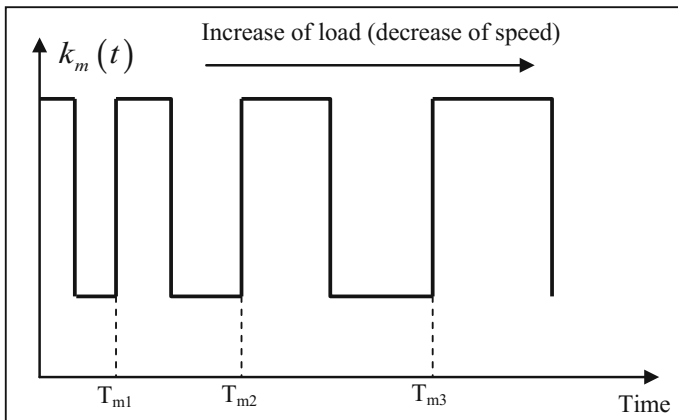
Fig. 2 Evolution of the gearmesh stiffness

2.4 Equation of Motion of the System

The equation of motion of the system is obtained by applying Lagrange formulation and is given by:

$$[M]\{\ddot{q}\} + [C]\{\dot{q}\} + [K(t)]\{q\} = \{F\} \tag{3}$$

where q, M, C, K, F are, respectively, the displacement vector, the mass, the damping, the stiffness matrix, and the force vector (Karray et al. 2012).

3 Numerical Simulation

The characteristics of the motor are given in Table 1 while the parameters of bevel gear are given in Table 2.

Considering a load fluctuating in a saw-tooth shape with a frequency $f_L = 5$ Hz, it is rising from 3000 to 7000 Nm.

Table 1 Motor characteristics (Molina 2009)

Motor type	MT 90L
Electrical characteristics	6 poles, 50 Hz, 3 phases, 415 V
Output power (kW)	320
Full load speed (rpm)	990
Full load torque (Nm)	3086
Torque starting	2.7
Ratio breakdown	3.2
Slip	0.315
Motor constant a	1.711
Motor constant b	1.316

Table 2 Parameters of bevel gear transmission (Molina 2009)

	Pinion	Gear
Number of teeth Z	27	62
Mass (kg)	275	600
Moment of inertia (kg m^2)	6.4	17.25
Axial stiffness k_{x1}, k_{y2} (N/m)	10^9	2.3×10^9
Lateral stiffness k_{y1}, k_{z1}, k_{x2}, k_{z2} (N/m)	8.8×10^9	1.3×10^{10}
Torsional stiffness $k_{\theta 1}$, $k_{\theta 2}$ (Nm/rd)	1.2×10^4	7.4×10^4
Pressure angle α	20	
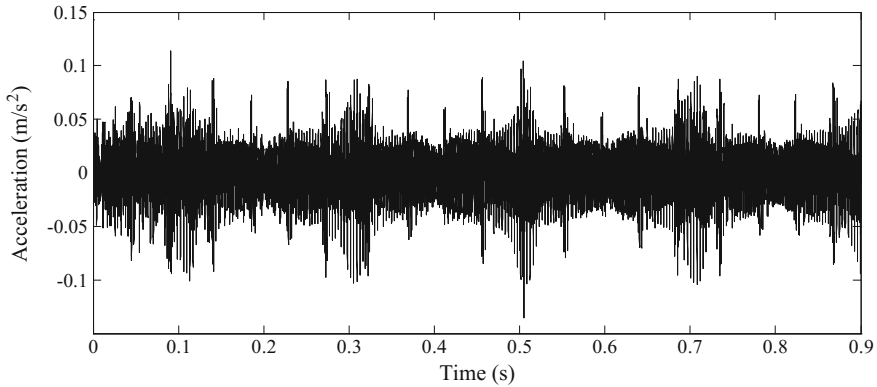
Fig. 3 Evolution of pinion bearing acceleration for a local damage defect

To overcome a periodic increase in load, rotational speed of the motor will decrease. It is rising from 965 to 835 rpm (Chaari et al. 2011).

The rotational speed of the motor is $N_1 = 990$ rpm which corresponds to a mean gearmesh frequency $f_m = 445.5$ Hz and a mean period $T_m = 0.0022$ s.

In order to model the mesh stiffness reduction induced by a crack on one pinion tooth, it is necessary to compute the instantaneous frequency of the pinion in nonstationary condition. After that, a reduction is operated each one rotation of the pinion, e.g. after each Z_1 mesh period.

Figure 3 shows the acceleration on pinion bearing. Impulses are observed corresponding to the meshing of the cracked tooth. The amplitude level of the impulses depends on the amplitude of the load. They are much more important if load level is high.
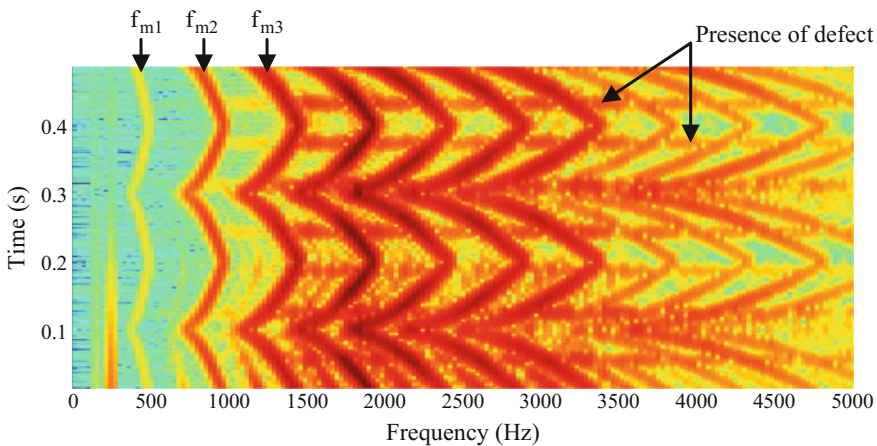
Fig. 4 Spectrogram of the pinion bearing acceleration for local damage defect

The spectrogram of the pinion bearing acceleration of damaged transmission presented in Fig. 4 shows clearly horizontal lines over wide frequency band corresponding to each mesh period of the defected tooth.

4 Conclusion

In this chappter, a gearbox diagnosis under nonstationary operating conditions is considered. The driving motor was modeled for the nonstationary case. Variable torques on the transmission output lead to variable speed which was modeled in the mesh stiffness fluctuation by variability in the mesh period according to the instantaneous speed of the transmission. Simulations of the dynamic behavior of the system showed high amplitude modulation in the time responses. Spectral analysis is unsuited to characterize the frequency content of the vibration signals and should be replaced by time–frequency analysis. The analysis becomes more complicated by the presence of defects.

References

Bartelmus W, Zimroz R (2009) Vibration condition monitoring of planetary gearbox under random varying. Mech Syst Signal Process 23:246–257

Bartelmus W, Chaari F, Zimroz R, Haddar M (2010) Modeling of gearbox dynamics under time-varying non stationary load for distributed fault detection and diagnostics. Eur J Mech A Solids 29:637–646

Baydar N, Ball A (2000) Detection of gear deterioration under varying load conditions by using the instantaneous power spectrum. Mech Syst Signal Process 14:907–921

Chaari F, Zimroz R, Bartelmus W, Fakhfakh T, Haddar M (2011) Gearbox vibration signal amplitude and frequency modulation. J Shock Vibr 18:1–18

Karray M, Chaari F, Viadero F, Fdez. del Rincon A, Haddar M (2012) Dynamic response of single stage bevel gear transmission in presence of local damage. In: The 4th European conference on mechanism science, EUCOMES'2012, Santander (Spain), New trends in mechanism and machine science, mechanisms and machine science, vol 7, pp 337–345. https://doi.org/10.1007/978-94-007-4902-3 36

Molina Vicuna C (2009) Contributions to the analysis of vibrations and acoustic emissions for the condition monitoring of epicyclic gearboxes. Dissertation, the Faculty of Georesources and Materials Engineering of the RWTH Aachen University

Randall RB (1982) A new method of modelling gear faults. J Mech Des 104:259–267

Wright. (2005) Notes on design and analysis of machine elements. Department of Mechanical and Materials Engineering, The University of Western Australia

Post-buckling Analysis of Functionally Graded Materials Structures with Enhanced Solid-Shell Elements

A. Hajlaoui, E. Chebbi, E. Triki and F. Dammak

Abstract This paper presents a first-order solid-shell element for the post-buckling behavior of functionally graded material (FGM) structures based on the enhanced assumed strain (EAS) with five parameters. The EAS three-dimentional finite element formulation presented in this paper is free from shear locking and leads to accurate results for distorted element shapes. The transverse shear strain is formulated by the assumed natural strain (ANS) method, which ensures a constant distribution through the thickness and requires the introduction of shear correction factors. The transverse shear correction factors are calculated using a computational algorithm based on the static equilibrium and energy equivalence between the shear energy of the shell and the energy from three-dimentional theory. Material properties are varied continuously in the thickness direction according to different distributions. This finite element is used to study the post-buckling behavior of FGM structures and to investigate the influence of same parameters on post-buckling. Comparisons of numerical results among existing ones show the performance of the developed elements.

Keywords Solid-shell element · Post-buckling · Functionally graded
material · Shear correction factor

A. Hajlaoui (✉) · E. Chebbi · E. Triki · F. Dammak
Mechanical Modeling and Manufacturing Laboratory (LA2MP),
National School of Engineers of Sfax, University of Sfax,
B.P-1173-3038 Sfax, Tunisia
e-mail: abdhajlaoui@gmail.com

E. Chebbi
e-mail: chebbi.elouni@gmail.com

E. Triki
e-mail: emna_triki@yahoo.fr

F. Dammak
e-mail: fakhreddine.dammak@enis.rnu.tn

331

1 Introduction

Functionally graded materials (FGM) are now being used for the structural component in nuclear reactor manufacturing due to their high stiffness and excellent temperature resistance capacity. The thin-walled regions of the FGM structures subjected to in-plane loading may be prone to buckle. The studies of post-buckling of FGM structures by different theories attracted many researchers.

Two main steps must be taken to analyze the buckling and post-buckling of functionally graded plates and shells: the choice of plate theory and the choice of solution method. The plate theories can be classified into the following three categories: The classical plate theory (CPT), the First-order Shear Deformation Theory (FSDT) and the Higher order Shear Deformation Theories (HSDTs). Concerning the solution method of the aforementioned different theories, a variety of methods (analytical, numerical, differential quadrature, etc.) can be chosen.

Using the finite element method based on FSDT, (Ganapathi et al. 2006) studied the buckling of FG skew plates under compressive loadings. Park and Kim (2006) investigated the post-buckling and vibration of FG plates under thermal loadings. Reddy and Chin (1998) studied the dynamic response of FG cylinders and plates subjected to two different types of thermal loadings. Arciniega and Reddy (2007) analyzed the geometrically nonlinear of FG shells. Behjat et al. (2009) studied the static bending, free vibration and transient responses of FG piezoelectric cylindrical panels subjected to mechanical, thermal and electrical loadings. Using a discrete double director's shell element, static, free vibration, forced vibration geometric nonlinearity of FGM shell structures was studied by Wali et al. (2014, 2015), Frikha et al. (2017, 2016).

In our previous work, a list of finite element model based on different theories was developed in order to study the behaviors of composite and FGM plates and shells. Based on FSDT, (Hajlaoui et al. 2012) presented a solid-shell element with 5, 7 and 9 parameters to study the buckling behavior of structures with delaminations. Hajlaoui et al. (2015) extended this formulation to investigate the behavior of FGM structures under buckling loads. Hajlaoui et al. (2016) developed a higher order solid-shell element for static and buckling analysis of laminated composite structures based on the enhanced assumed strain (EAS). In this formulation, the assumed natural transverse shear strain is enhanced with two parabolic functions in terms of natural thickness coordinate. Hajlaoui et al. (2017) extend this formulation to the fully three-dimentional nonlinear dynamic analysis of FGM shell structures.

The aim of this paper is to extend the work of (Hajlaoui et al. 2015) to study the post-buckling behavior of functionally graded material (FGM) structures. As the finite element method is based on FSDT, shear correction factors are then introduced. Numerical results and discussions of the finite element model are investigated.

2 Functionally Graded Materials

In this paper, we consider an FGM shell structures made from a mixture of metal and ceramics and the composition varies continuously in the thickness direction. In fact, the Young's modulus $E(z)$, density $\rho(z)$ and Poisson's ratio $\nu(z)$ are assumed to vary through the shell thicknesses according to a power law distribution as

$$E(z) = (E_c - E_m)V_c + E_m, \rho(z) = (\rho_c - \rho_m)V_c + \rho_m, \nu(z) = (\nu_c - \nu_m)V_c + \nu_m \quad (1)$$

in which the subscripts m and c refer to metal and ceramic components, respectively. z is the thickness coordinate and $V_c(z)$ is defined by

$$V_c(z) = \left(\frac{1}{2} + \frac{z}{h}\right)^p \quad (2)$$

where *h is* the thickness of structure and p is the power law index.

3 Solid-Shell Finite Element Formulation

The developed solid-shell element is eight nodes hexahedral element with three degrees of freedom per node. The transverse shear strain is formulated by the assumed natural strain method (ANS). The enhanced assumed strain method consists in the enhancement of the compatible part of the Green-Lagrange strain tensor, $\mathbf{E}^c$, with an enhanced part $\tilde{\mathrm{E}}$ to have a total strain as follows

$$\mathbf{E} = \mathbf{E}^c + \tilde{\mathrm{E}} \quad (3)$$

3.1 Compatible Strains

The compatible part is arranged in (6×1) column matrix as follows:

$$\mathbf{E}^c = \left[E^c_{11}, E^c_{22}, E^c_{33}, 2E^c_{12}, 2E^c_{13}, 2E^c_{23}\right]^T \quad (4)$$

For the compatible part of the strain tensor, and to avoid shear locking, an assumed natural strain (ANS) method is used for the transverse shear strains E^c_{13}, E^c_{23} as proposed by Hajlaoui et al. (2012, 2015, 2016) where the transverse shear strains are evaluated at four mid-points of the element edges. Also, an ANS method is used for the thickness strains E^c_{33} as used in Hajlaoui et al. (2012, 2015, 2016). Then the compatible part of the Green-Lagrange strain tensor takes the following form:

$$\mathbf{E}^c = \mathbf{T}^{-T} \begin{bmatrix} \frac{1}{2}(g_{11} - G_{11}) \\ \frac{1}{2}(g_{22} - G_{22}) \\ \sum_{A=1}^{4} \frac{1}{4}(1 + \xi_A\xi)(1 + \eta_A\eta)\frac{1}{2}(g_{33}^A - G_{33}^A) \\ (g_{12} - G_{12}) \\ \frac{1}{2}[(1 - \eta)(g_{13}^B - G_{13}^B) + (1 + \eta)(g_{13}^D - G_{13}^D)] \\ \frac{1}{2}[(1 - \eta)(g_{23}^A - G_{23}^A) + (1 + \eta)(g_{23}^C - G_{23}^C)] \end{bmatrix} \tag{5}$$

where $\mathbf{T}$ is the transformation of the strain tensor from parametric coordinates to the local Cartesian coordinates, written as

$$\mathbf{T} = \begin{bmatrix} (t_{11})^2 & (t_{21})^2 & (t_{31})^2 & 2t_{11}t_{21} & 2t_{11}t_{31} & 2t_{21}t_{31} \\ (t_{12})^2 & (t_{22})^2 & (t_{32})^2 & 2t_{12}t_{22} & 2t_{12}t_{32} & 2t_{22}t_{32} \\ (t_{13})^2 & (t_{23})^2 & (t_{33})^2 & 2t_{13}t_{23} & 2t_{13}t_{33} & 2t_{23}t_{33} \\ t_{11}t_{12} & t_{21}t_{22} & t_{31}t_{32} & t_{11}t_{22} + t_{12}t_{21} & t_{11}t_{32} + t_{12}t_{31} & t_{21}t_{32} + t_{22}t_{31} \\ t_{11}t_{13} & t_{21}t_{23} & t_{31}t_{33} & t_{11}t_{23} + t_{13}t_{21} & t_{11}t_{33} + t_{13}t_{31} & t_{21}t_{33} + t_{23}t_{31} \\ t_{12}t_{13} & t_{22}t_{23} & t_{32}t_{33} & t_{12}t_{23} + t_{13}t_{22} & t_{12}t_{33} + t_{13}t_{32} & t_{22}t_{33} + t_{23}t_{32} \end{bmatrix} \tag{6}$$

$t_{ij} = \mathbf{G}_i.\mathbf{T}_j$ and $\mathbf{T}_j$ ($j = 1, 2, 3$) are a local orthonormal base vectors.

3.2 Enhanced Strains

The enhanced strain is assumed to be interpolated in a discontinuous way over element boundaries as follows

$$\tilde{\mathbf{E}} = \tilde{\mathbf{M}}\boldsymbol{\alpha}, \delta\tilde{\mathbf{E}} = \tilde{\mathbf{M}}\delta\boldsymbol{\alpha}, \Delta\tilde{\mathbf{E}} = \tilde{\mathbf{M}}\Delta\boldsymbol{\alpha} \tag{7}$$

where $\boldsymbol{\alpha}$ is the vector of the internal strain parameters. $\tilde{\mathbf{E}}$, $\delta\tilde{\mathbf{E}}$ and $\Delta\tilde{\mathbf{E}}$ are total, virtual and incremental enhanced Green-Lagrange strain tensor respectively. The crucial assumption of the EAS method is the enforcement of the orthogonality conditions for the assumed stress field $\tilde{\mathbf{S}}$ and the enhanced strain $\tilde{\mathbf{E}}$. These orthogonality conditions impose the following choice for the interpolation function matrix $\tilde{\mathbf{M}}$ to be expressed as follows

$$\tilde{\mathbf{M}} = \frac{\det\mathbf{J}_0}{\det\mathbf{J}}\mathbf{T}_0^{-T}\mathbf{M}_{\xi\eta\zeta}, \int_{-1}^{1}\int_{-1}^{1}\int_{-1}^{1}\mathbf{M}_{\xi\eta\zeta}d\xi d\eta d\zeta = 0 \tag{8}$$

where the subscript '$_0$' means evaluation at the center of the element in the natural coordinates and $\mathbf{J} = [\mathbf{G}_1, \mathbf{G}_2, \mathbf{G}_3]$ is the Jacobian matrix. The interpolation matrix $\mathbf{M}_{\xi\eta\zeta}$ is expression in terms of the parametric coordinates (ξ, η, ζ). In the numerical results, a five parameters matrix $\mathbf{M}_{\xi\eta\zeta}$ will be considered as follows

$$\mathbf{M}_{\xi\eta\zeta} = \begin{bmatrix} \xi & 0 & 0 & 0 & 0 \\ 0 & \eta & 0 & 0 & 0 \\ 0 & 0 & \zeta & 0 & 0 \\ 0 & 0 & 0 & \xi & \eta \\ 0 & 0 & 0 & 0 & 0 \\ 0 & 0 & 0 & 0 & 0 \end{bmatrix} \qquad (9)$$

After including interpolation functions for enhanced strain fields, we obtain the solid-shell element enhanced with five incompatible modes (C3D8S5). This solid-shell element is based on first-order shear deformation concept and requires the introduction of shear correction factors, see (Hajlaoui et al. 2015).

3.3 Weak Form and Linearization

The variational framework of the EAS method, which is based on the three-field variational functional, in Lagrange formulation, is written as

$$\Pi(\mathbf{u}, \tilde{\mathbf{E}}, \tilde{\mathbf{S}}) = \int_V \left[\psi(\mathbf{E}) - \tilde{\mathbf{S}} : \tilde{\mathbf{E}} - \mathbf{u}.\mathbf{F}_V \right] dV - \int_{\partial V_f} \mathbf{u}.\mathbf{F}_S dA = 0 \qquad (10)$$

where ψ is the strain energy function and $\mathbf{u}$, $\tilde{\mathbf{E}}$ and $\tilde{\mathbf{S}}$ are the independent tonsorial quantities which are: displacement, enhanced assumed Lagrange strain and assumed second Piola-Kirchhoff stress fields respectively. Vectors $\mathbf{F}_V$ and $\mathbf{F}_S$ are the prescribed body force and surface traction respectively. When invoking the classical orthogonality condition, $\int_V \tilde{\mathbf{S}} : \tilde{\mathbf{E}} \, dV = 0$, the number of independent variables in the original function is reduced to two $(\mathbf{u}, \tilde{\mathbf{E}})$. The weak form of this modified functional may be obtained as

$$W = \int_V \left[\delta\mathbf{E} : \mathbf{S} - \delta\mathbf{u}.\mathbf{F}_V \right] dV - \int_{\partial V_f} \delta\mathbf{u}.\mathbf{F}_S dA = 0 \qquad (11)$$

where $\mathbf{S}$ is the Piola-Kirchoff stress tensor given by $\mathbf{S} = \partial \psi / \partial \mathbf{E}$.

Equation (11) is a nonlinear equation that will be solved iteratively by the Newton–Raphson method. For this purpose, one needs the corresponding linearization

$$W + DW.(\Delta\mathbf{U}_n, \Delta\boldsymbol{\alpha}) = \begin{bmatrix} \delta\mathbf{U}_n & \delta\boldsymbol{\alpha} \end{bmatrix}^T \left(\begin{bmatrix} \mathbf{K} & L^T \\ L & H \end{bmatrix} \begin{Bmatrix} \Delta U_n \\ \Delta\boldsymbol{\alpha} \end{Bmatrix} + \begin{bmatrix} \mathbf{f}^{int} - \mathbf{f}^{ext} \\ \mathbf{h} \end{bmatrix} \right) = 0 \qquad (12)$$

where **L**, **H** and **K** are given by

$$L = \int_V \tilde{\mathbf{M}}^T \mathbb{C} B \, \mathrm{dV}, H = \int_V \tilde{\mathbf{M}}^T \mathbb{C} \tilde{\mathbf{M}} \, \mathrm{dV}, \mathbf{K} = \mathbf{K}_D + \mathbf{K}_G \tag{13}$$

with $\mathbb{C} = \frac{\partial^2 \psi}{\partial \mathbf{E} \partial \mathbf{E}}$ is the 6 × 6 three directional material tangent moduli, or elasticity tensor, and $\mathbf{K}_D$ is given by

$$\mathbf{K}_D = \int_V \mathbf{B}^T \mathbb{C} \, \mathbf{B} \, dV \tag{14}$$

$\mathbf{f}^{int}$, $\mathbf{f}^{ext}$ and **h**, in Eq. (12), are given by the following expressions

$$\mathbf{f}^{int} = \int_V \mathbf{B}^T \mathbf{S} \, dV, \mathbf{f}^{ext} = \int_V \mathbf{N}^T \mathbf{F}_V dV + \int_{\partial V_f} \mathbf{N}^T \mathbf{F}_S dA, \mathbf{h} = \int_V \tilde{\mathbf{M}}^T \mathbf{S} \, dV \tag{15}$$

$\mathbf{K}_G$ is the geometric stiffness matrix

$$\delta \mathbf{U}_n^T \mathbf{K}_G \Delta \mathbf{U}_n^T = \int_V \mathbf{S}^T . \Delta \delta \mathbf{E}^c dV \tag{16}$$

Relative to a couple of nodes (I, J)

$$\mathbf{K}_G^{IJ} = \int_V diag[\, G_{IJ} \quad G_{IJ} \quad G_{IJ} \,] dV \tag{17}$$

$$G_{IJ} = \mathbf{S}^T \mathbf{T}^{-T} \begin{bmatrix} N_{I,1} N_{J,1} \\ N_{I,2} N_{J,2} \\ \sum_{L=1}^{4} \tfrac{1}{4}(1 + \xi_L \xi)(1 + \eta_L \eta) N_{I,3}^L N_{J,3}^L \\ N_{I,1} N_{J,2} + N_{I,2} N_{J,1} \\ \tfrac{1}{2}\big[(1 - \eta)\big(N_{I,1}^B N_{J,3}^B + N_{I,3}^B N_{J,1}^B\big) + (1 + \eta)\big(N_{I,1}^D N_{J,3}^D + N_{I,3}^D N_{J,1}^D\big)\big] \\ \tfrac{1}{2}\big[(1 - \xi)\big(N_{I,2}^A N_{J,3}^A + N_{I,3}^A N_{J,2}^A\big) + (1 + \xi)\big(N_{I,2}^C N_{J,3}^C + N_{I,3}^C N_{J,2}^C\big)\big] \end{bmatrix} \tag{18}$$

The strain parameters $\Delta\boldsymbol{\alpha}$ must be eliminated from Eq. (12) at the element level. For this purpose, we use the static condensation procedure, which leads to the element tangent operator given by its classical partition into material and geometrical parts

$$\mathbf{K}_T = \big(\mathbf{K}_D - L^T H^{-1} L\big) + \mathbf{K}_G \tag{19}$$

and the residual vector

$$\mathbf{R} = L^T H^{-1} h + \mathbf{f}^{ext} - \mathbf{f}^{int} \tag{20}$$

The transverse shear strain of this sold-shell FSDT element is constant through the thickness and require the introduction of shear correction factors. The shear correction coefficient computation algorithm is based on the static equilibrium and energy equivalence between the shear energy of the shell and the energy from three-dimentional theory. In this algorithm, the coupling of membrane bending which is indispensable for FGM structures is taken into account. This coupling term is equal to zero only when we consider a material symmetry with respect to the mid-plane surface. For more details on this algorithm see (Hajlaoui et al. 2015).

4 Results and Discussion

In this study, the post-buckling load parameters are examined using an in-house nonlinear finite element program. In this section, we present several representative numerical simulations in order to illustrate an exceptionally good performance of the proposed solid-shell element.

4.1 Post-buckling of Cantilevered Beam

The first numerical example consists of a cantilevered beam under an end load N, as shown in Fig. 1. Maximum displacements for this test is given in Timoshenko and Gere (1961) when using analytic solution.

Fig. 1 Post-buckling response of cantilevered beam
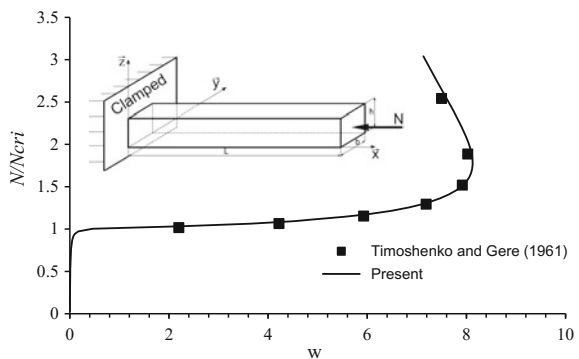
$$N_{cri} = k \frac{\pi^2 EI}{L} \qquad (21)$$

k is the factor accounting for the end conditions ($k = 0.25$; one end fixed, one end free). The numerical data for this example are: $E = 1200000$, $\nu = 0.3$, $L = 10$, $b = 1$ and $h = 0.1$.

The numerical results of the nondimensional post-buckling calculated using the present method are compared with those obtained by the analytic solution given by Timoshenko and Gere (1961). It can be found from Fig. 1 that the present model gives results in good agreement with analytic solution.

4.2 Post-buckling of FGM Cantilevered Beam: Parametric Studies

In this section, we study the effect of power law index (p) on the post-buckling response of a FGM cantilevered beam. The post-buckling response of FGM cantilevered beam, subjected to compressive mechanical loading is shown in Fig. 2. The numerical data for this example are: $E_c = 380$ GPa, $E_m = 70$ GPa, $\nu = 0.3$ $L = 10$, $b = 1$ and $h = 0.1$.

The nondimensional parameter is defined as:

$$\lambda = \frac{Nb^3}{E_c h^3} \qquad (22)$$

The post-buckling response decreases with increasing FGM power law index (p).

Fig. 2 Post-buckling response of cantilevered beam with different power law index (p)
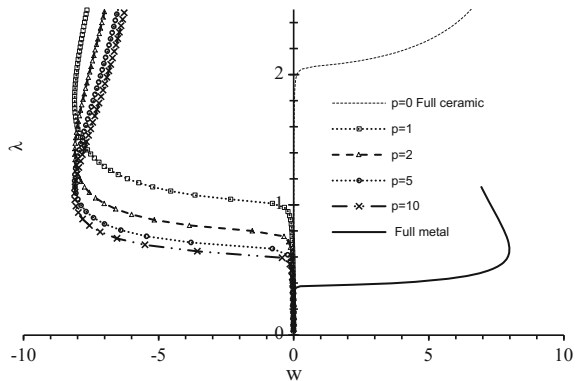
5 Conclusion

This paper presents a numerical investigation on the post-buckling response of FGM shell structures. The finite element formulation is based on the assumed natural strain and the enhanced strain method. The transverse shear correction factors are calculated using a computational algorithm based on the static equilibrium and energy equivalence between the shear energy of the shell and the energy from three-dimentional theory. Results of present formulations are verified by comparing the present results with those available in the literature. In addition, the present solid-shell model can be used in complex shells structures analysis, unlike the analytical formulation that can be employed only for smooth differentiable geometry of shell structures.

References

Arciniega RA, Reddy JN (2007) Large deformation analysis of functionally graded shells. Int J Solids Struct 44(6):2036–2052

Behjat B, Sadighi M, Armin A, Abbasi M, Salehi M (2009) Static, dynamic and free vibration analysis of functionally graded piezoelectric panels using finite element method. J Intell Mater Syst Struct 20(13):1635–1646

Frikha A, Dammak F (2017) Geometrically nonlinear static analysis of functionally graded material shells with a discrete double directors shell element. Comput Methods Appl Mech Engrg 315:1–24

Frikha A, Wali M, Hajlaoui A, Dammak F (2016) Dynamic response of functionally graded material shells with a discrete double directors shell element. Compos Struct 154:385–395

Ganapathi M, Prakash T, Sundararajan N (2006) Influence of functionally graded material on buckling of skew plates under mechanical loads. J Eng Mech 132(8):902–905

Hajlaoui A, Jarraya A, El Bikri K, Dammak F (2015) Buckling analysis of functionally graded materials structures with enhanced solid-shell elements and transverse shear correction. Compos Struct 132:87–97

Hajlaoui A, Jarraya A, Kallel-Kammoun I, Dammak F (2012) Buckling analysis of a laminated composite plate with delaminations using the enhanced assumed strain solid shell element. J Mech Sci Technol 26:3213–3221

Hajlaoui A, Triki E, Frikha A, Wali M, Dammak F (2017) Nonlinear dynamics analysis of FGM shell structures with a higher order shear strain enhanced solid-shell element. Lat Am J Solids Struct 14:72–91

Hajlaoui A, Wali M, Ben Jdidia M, Dammak F (2016) An improved enhanced solid shell element for static and buckling analysis of shell structures. Mech Ind 17:510

Park JS, Kim JH (2006) Thermal post buckling and vibration analyses of functionally graded plates. J Sound Vib 289(1–2):77–93

Reddy JN, Chin CD (1998) Thermo mechanical analysis of functionally graded cylinders and plates. J Therm Stresses 21(6):593–626

Timoshenko SP, Gere JM (1961) Theory of elastic stability, 2nd edn. McGraw-Hill, New York

Wali M, Hajlaoui A, Dammak F (2014) Discrete double directors shell element for the functionally graded material shell structures analysis. Comput Methods Appl Mech Eng 278:388–403

Wali M, Hentati T, Jaraya A, Dammak F (2015) Free vibration analysis of FGM shell structures with a discrete double directors shell element. Compos Struct 125:295–303

Wu TL, Shukla KK, Huang JH (2007) Post-buckling analysis of functionally graded rectangular plates. Compos Struct 81:1–10

Reliability Analysis of Random Aerodynamic Torque of Horizontal Axis Wind Turbine

Manel Tounsi, Moez Beyaoui, Kamel Abboudi, Nabih Feki, Lassaad Walha and Mohamed Haddar

Abstract This paper considers the reliability analysis of mechanical system, especially wind turbine system. Optimization of horizontal axis wind turbine performance is confronted by the aerodynamic complexities such as the instability of the energy source, randomness of loads. The objective of this work is to study the system reliability taking into account random input parameters of the aerodynamic part. It is assumed that the probability law distribution of random parameters is known. The influence of random input parameters on dynamic reliability is evaluated in this study. In order to improve product reliability, an efficient computational method based on the first- and the second-order reliability method (FORM/SORM) has been investigated. For more accuracy, results obtained by the proposed approximation methods are compared to Monte Carlo reference results. These three methods are developed in reliability approach to calculate the failure probability and the reliability index of the studied wind turbine system.

Keywords Reliability analysis · Random variable · Aerodynamic torque
FORM/SORM method

M. Tounsi (✉) · M. Beyaoui · K. Abboudi · N. Feki · L. Walha · M. Haddar
Mechanical Modeling and Manufacturing Laboratory (LA2MP), National School
of Engineers of Sfax, University of Sfax, B.P. 1173, 3038 Sfax, Tunisia
e-mail: manelt@yahoo.fr

M. Beyaoui
e-mail: moez.beyaoui@yahoo.fr

K. Abboudi
e-mail: kamalo1982@yahoo.fr

N. Feki
e-mail: fekinabih@gmail.com

L. Walha
e-mail: walhalassaad@yahoo.fr

M. Haddar
e-mail: mohamed.haddar@enis.rnu.tn

341

1 Introduction

Wind turbine power production depends on the interaction between the wind and the rotor. For this, the choice of design parameter is critical for optimizing wind turbine performance which is confronted by aerodynamic complexities such as instability of the energy source. The disposition of new designs wind turbine with increased reliability and reduced maintenance requirements is an important consideration for future development of wind turbines system. So, it is crucial to takes into account uncertainties in the design parameters (Soize et al. 2008; Hamel and Azarm 2011) of the aerodynamic torque.

In the literature, several researches have been developed to study dynamic model of rotating structures such as wind turbines system (Hiskens 2012; Ahmed 2013; Laina and Boumhidi 2015; Archana 2016). However, these studies do not consider the variability effect of uncertain parameters on system reliability approaches.

To improve the reliability prediction of the aerodynamic part of wind turbine, an efficient computational method based on first and second-order approximations FORM/SORM (Zhao and Ono 1999; Smolders 2010; Juan et al. 2015) has been discussed.

The main objective of this manuscript is to estimate the reliability index of the studied problem using the FORM/SORM approximations.

2 Aerodynamic Torque Model

The wind turbine system studied in this work is constituted by a rotor, a transmission power system, and a generator. The rotor is composed of three blades (Fig. 1) removed by an angle of 120° (Gebreslassie et al. 2013). The incoming wind energy attacks the blade.

The optimum design of the aerodynamic unit of a wind turbine can be achieved from considering uncertainties of design parameters. In this context, the aerodynamic torque expression is given by Eq. (1) (Rajakumar and Ravindran 2012).

$$dQ_{aero} = \frac{\rho_{air}}{2} n_p c W^2 (C_L \sin \phi - C_D \cos \phi) r dr \tag{1}$$

with ρ_{air} is the air density, n_p is the number of blades, c is the chord, W is the wind velocity, C_L and C_D represent respectively the lift and drag coefficient and ϕ is the inflow angle (Fig. 2).

The aerodynamic torque is obtained by integration of Eq. (1) from 0 to R (rotor radius).

The random parameters adopted in this work are presented in Table 1. For every parameter, the mean value, the standard deviation, and the distribution law are given.

Fig. 1 The three-bladed rotor

Wind flow

Direction of rotation
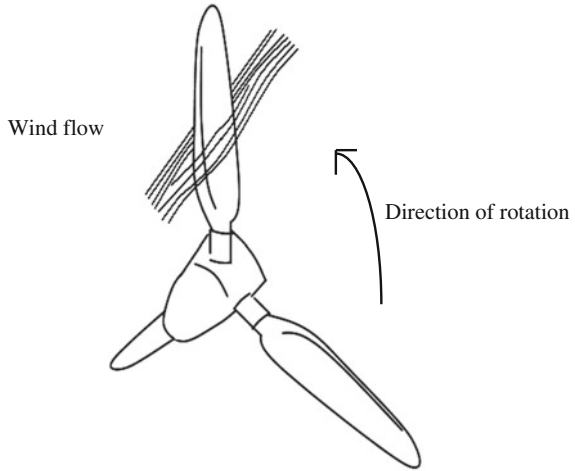
Fig. 2 Blade parameters
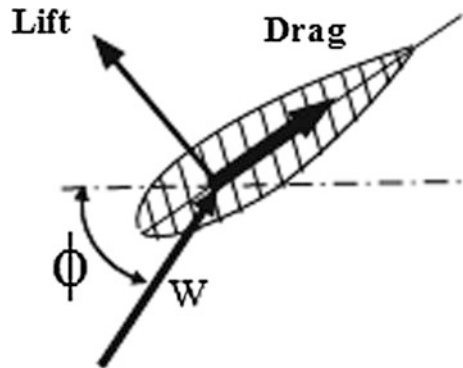
Table 1 Random variable of the system

Random variable	Distribution law	Mean	Standard deviation (%)
ρ_{air}	Normal	1.225 Kg/m^3	5
C	Normal	0.9 m	5
W	Normal	14 m.s^{-1}	5
ϕ	Normal	15°	5
C_L	Normal	0.6	5
C_D	Normal	0.14	5

Figure 3 presents the probability distribution of the wind velocity. It reacts according to the normal law with a mean velocity equal to 14 ms^{-1}.

Fig. 3 Law distribution of
wind velocity
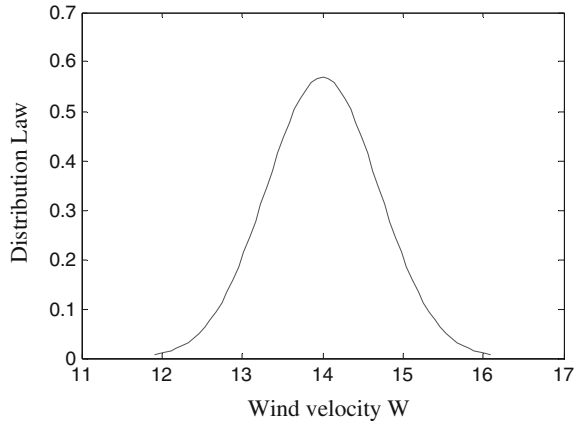
3 FORM/SORM Method

Reliability methods have been implemented to take into account uncertainties involved in the analysis of an engineering problem. The failure probability and the reliability index are used to quantify risks of failure. In this approach, the variables of the problem are modeled as random parameters. Random variables are grouped in a random vector X where $f_X(x)$ is the joint probability density function (PDF).

Reliability is defined as the probability of a performance function g(X) greater than zero $P\{g(X) > 0\}$. In other words, reliability is the probability that the random variables X are in the safe region which is defined by $g(X) > 0$. The probability of failure is defined as the probability $P\{g(X) < 0\}$. Also, it is defined as the probability that the random variables $g(X) < 0$. The probability of failure is evaluated by the integral given by Eq. (2).

$$P_f = P\{g(X) < 0\} = \int\limits_{g(x) < 0} f_x(x) dx \qquad (2)$$

The reliability is defined by

$$R = 1 - P_f = P\{g(X) > 0\} = \int\limits_{g(x) > 0} f_x(x) dx \qquad (3)$$

A failure surface is defined when g(X) = 0. So, several methods are used to resolve the probability integral. After calculating P_f, a reliability index may be obtained from the inverse transformation.

$$\beta = -\Phi^{-1}(P_f), \tag{4}$$

where $\Phi^{-1}(.)$ is the inverse of standard normal cumulative distribution function.

Two of the most commonly used reliability analysis methods such as the First-Order Reliability Method (FORM) and the Second-Order Reliability Method (SORM) are presented in this work. The basic idea of these methods is to ease the computational difficulties through simplifying the integrand $f_x(X)$ and approximating the performance function $g(X)$.

3.1 FORM Procedure

The name of First-Order Reliability Method (FORM) comes from the fact that the performance function $g(X)$ is approximated by the first-order Taylor expansion (linearization). The FORM method is an analytical approximation in which the reliability index is explained as the minimum distance from the origin to the limit state surface in the standardized normal space. Here, the performance function G is approximated by a linear function at the design point, accuracy problems take place when the performance function is strongly nonlinear (Fiessler et al. 1979; Tichy 1994).

The first step in this method consists on a transformation of the original space variable (X) into a standard Gaussian space (U).

$$G(U) = G(u^*) + \left(\frac{\partial G(U)}{\partial U_i}\right)_{|u^*} (U - u^*)^T \tag{5}$$

where u* are the coordinates of the design point MPP in the U-space.

The probability of failure is given by:

$$P_f(G(U) \leq 0) \cong \Phi\left(\frac{-mean_G}{\sigma_G}\right), \tag{6}$$

where $mean_G$ and σ_G are respectively the mean value and the standard deviation of the limit state function G (Fig. 4).

3.2 SORM Procedure

The second-order reliability method (SORM) has been established as an attempt to improve the accuracy of FORM. The SORM method is obtained by approximating the limit state surface in standardized normal space at the design point by a second-order surface (Fiessler et al. 1979).

The probability of failure according to SORM method is given by

$$P_f(G(U) \le 0) \cong \Phi(-\beta) \prod_{i=1}^{n} (1 - q_i\beta)^{-\frac{1}{2}}, \tag{7}$$

where q_i are the different individual curvatures at the design point MPP.

Since the approximation of the performance function in SORM is better than that in FORM (Fig. 5), SORM is generally more accurate than FORM.
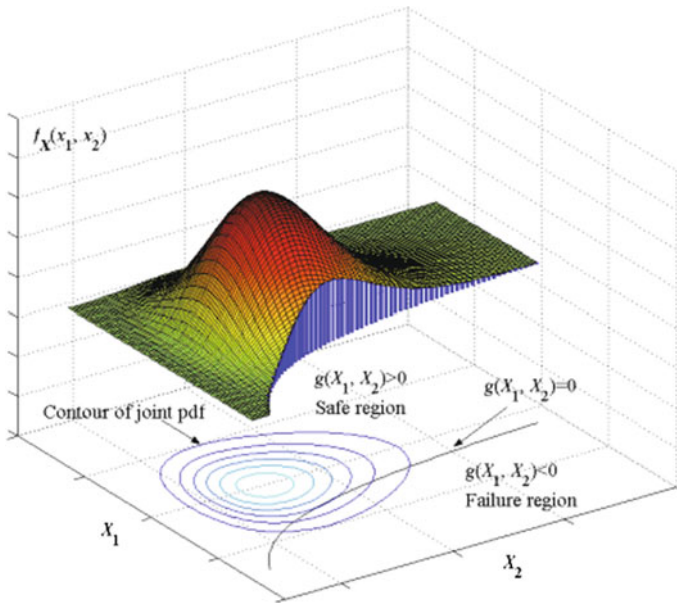
Fig. 4 Probability integration

Fig. 5 Comparison of FORM and SORM
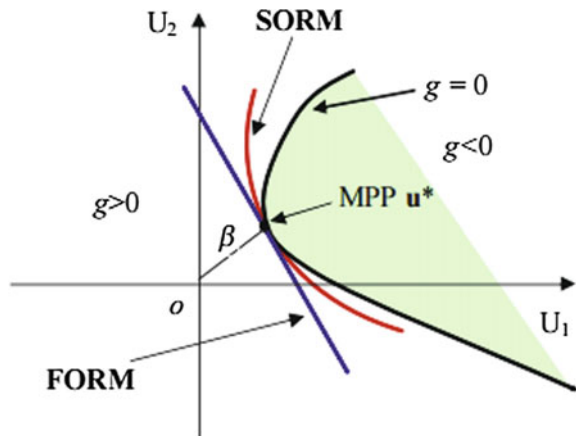
4 MC Simulation

The Monte Carlo simulation consists in performing random draws succession by law joint probability of the random vector, and counting the number of times the system is in the failure domain. The probability of failure is given by the following expression:

$$P_f = \frac{1}{N} \sum_{i=1}^{N} I_f(x_i) = E\left[I_f(x_i)\right],$$ (8)

where N is the number of Monte Carlo samples and If is the Indicator function expressed by:

$$I_f = \begin{cases} 1 & \text{si } G(X) \leq 0 \\ 0 & \text{si } G(X) > 0 \end{cases}$$ (9)

5 Results

The reliability analysis is doing under two cases. In the first case, only two random parameters are considered which are the wind velocity W and the inflow angle ϕ. In the second case, the four random parameters considered are the wind velocity W, the inflow angle ϕ, the lift C_L and the drag C_D coefficients.

According to Tables 2 and 3, it is clear that

- The reliability index obtained by approximation methods (FORM and SORM) gives a good accuracy with it issued by the Monte Carlo simulation.
- By increasing the number of random variables, the reliability index decreases and therefore the system is less reliable. For this, it is very interesting to take into account uncertainties in the modeling phase of design parameters of mechanical system.

Table 2 Reliability results for 2 random parameters

Reliability index β	
MC	2.4
FORM	2.3667
SORM	2.3667

Table 3 Reliability results for 6 random parameters

Reliability index β	
MC	0.03
FORM	0.0280
SORM	0.0281

6 Conclusion

The reliability analysis is an important part in wind turbine studies. Approximation methods based on the FORM and SORM algorithm are employed to estimate the reliability index. Results shown the efficiency of the adopted method in the reliability analysis compared to the reference results obtained by Monte Carlo simulation.

References

Ahmed WK (2013) Mechanical modelling of wind turbine: comparative study. Int J Renew Energy Res 3(1)

Archana T (2016) Mathematical modeling of wind energy system using two mass model including generator losses patil ashwini. Int J Emerg Trends Electr Electron 12(2)

Fiessler B, Neumann HJ, Rackwitz R (1979) Quadratic limit states in structural reliability. J Eng Mech 105(4): 661–676

Gebreslassie MG, Tabor GR, Belmont MR (2013) Numerical simulation of a new type of cross flow tidal turbine using OpenFOAM—part I: calibration of energy extraction. Renew Energy 50:994–1004

Hamel JM, Azarm S (2011) Reducible uncertain interval design by Kriging metamodel assisted multi-objective optimization. ASME J Mech Des 133:011002

Hiskens A (2012) Dynamics of type-3 wind turbine generator models. IEEE Transact Power Sys 27(1)

Juan GC, Natarajan A, Nikolay KD (2015) Effects of bearing configuration in wind turbine gearbox reliability. Energy Procedia 8:392–400

Laina R, Boumhidi I (2015) Control and modeling of wind turbines using genetic algorithms and support vector machines for regression. Int J Comput Netw Commun Secur 3(6):235–243

Rajakumar S, Ravindran D (2012) Iterative approach for optimising coefficient of power, coefficient of lift and drag of wind turbine rotor. Renew Energy 38:83–93

Smolders K (2010) Reliability analysis and prediction of wind turbine gearboxes. Eur Wind Energy Conf 4:2660–2670

Soize C, Capiez-Lernout E, Durand JF, Fernandez C, Gagliardini L (2008) Probabilistic model identification of uncertainties in computational models for dynamical systems and experimental validation. Comput Methods Appl Mech Eng 198:150–163

Tichy M (1994) First-order third-moment reliability method. Struct Saf 16:189–200

Zhao YG, Ono T (1999) A general procedure for first/second-order reliability method (FORM/SORM). Struct Saf 21:95–112

Topological Modeling of 2D Piezoelectric Truss Structure Using the MGS Language

Nourhene Abdeljabbar Kharrat, Régis Plateaux, Mariem Miladi Chaabane, Jean-Yves Choley, Chafik Karra and Mohamed Haddar

Abstract In this paper, we are interested in the change sustained by the topology transformation and in introducing the notion of variable topology of dynamics systems. We are also interested in using substitution to model complex patterns by applying the MGS language (General Modeling System). This later is applied to a 2D piezoelectric truss structure. In fact, the process has been validated since the modeling by using the KBR topological graph, and then by using MGS language, it shows the same result. The major interest in presenting this model of piezoelectric structure is that it contains both electrical and mechanical parameters, and this allows us to treat it as a mini-mechatronic system (actuator and sensor). Considering that any system which is complex is legible to be represented by a topological graph, and knowing that each component of the mechatronic system has its local behavior's law, so the process that applies to any mini-mechatronic system can be extended later to complex systems. This work highlights the importance of the MGS language, and it also makes the topological graph modeling more flexible. Moreover, we can do the modeling smoothly by changing the topological structure without modifying the behavior's law, but simply by modifying the topological structure.

Keywords Topological modeling · MGS language · Variable topology Piezoelectric truss structure · KBR topological graph

N. Abdeljabbar Kharrat (✉) · R. Plateaux · J. -Y. Choley
QUARTZ Laboratory, High Institute of Mechanic of Paris (SUPMECA),
3, rue Fernand Hainaut, 93407 Saint-Ouen Cedex, France
e-mail: nourhene.abdeljabbar@gmail.com

N. Abdeljabbar Kharrat · M. Miladi Chaabane · C. Karra · M. Haddar
Laboratory Mechanics, Modeling and Production, National Engineering
School of Sfax (ENIS), BP 1173-3038 Sfax, Tunisia

349

1 Introduction

Consumer requirements and technological development have both contributed to the appearance of systems named "Mechatronics". These systems coordinate multidisciplinary fields like mechanical engineering, electrical engineering, control engineering, computer sciences, and automation engineering. In order to be able to model these systems, many methodologies have been developed such as the MBSE (Model-Based Systems Engineering) and methods using SysML language specification. Unifying the modeling of mechatronic systems is the purpose of several works. A topological approach was proposed by Miladi et al. (2014) and used as a basis of unification for the modeling of mechatronic system. We are interested to use this topological approach for two reasons; the first refers to its ability to dissociate the topology and the behavior of the system in order to have a generic local model which allows the optimization of the global behavior. The second reason is the generic aspect for modeling of this approach (Plateaux 2012). So in this paper, the topological approach has been applied for the modeling of piezoelectric truss (truss structure).

In this work, we are interested in studying dynamic systems with variable topology, so the integration of changes is among the main goal at this work. The interest of the change of the structure of dynamic systems with variable topology is dedicated to shed light to the topology change through KBR topological graph. As a language allowing the application of this approach we use MGS (Miladi 2014; The MGS home page 2012; Spicher 2006; Cohen 2004).

MGS is a language devoted to modeling and simulating dynamic systems with a dynamic structure, developed in the IBISC (Laboratory for Computer Science, Integrative Biology and Complex Systems) of the University Of Every (France) (Spicher 2006). The data structure of MGS is based on topological collections witch are composed of elements with various dimensions.

The remaining of this paper is organized as follows. Section 2 is dedicated to introduce the topological approach and the topological modeling as well as our methodology of works among this paper. We present also systems of variable topology. Then, Sect. 3 is devoted to the application of the topological approach to the case of a two-bar piezoelectric structure. In addition, this section is dedicated to the modification studied after change of the two-bar piezoelectric structure. Our conclusions are summarized in Sect. 4.

2 State of the Art

2.1 Topological Approach

Topological approach was introduced by the graph theory integrated for the first time for the resolution of the problem known as "the bridges of Konigsberg"

by Euler (1741). Since the 1930s, the graph theory has known very significant developments on the theoretical level as well as on the practical level (communication networks, road networks, electric circuits) and has become an established branch of mathematics devoted to the study of system topologies. In overall, a graph allows representing the connections of a complex set by expressing the relationships between its components. Therefore, graphs are method that makes modeling a wide variety of problems by leading back to the study of nodes and arcs. In 1955, Roth (1955) has validated the work of Kron (1959) by applying algebraic topology on the networks and electric machine. Then, in 1966, Branin (1966) generalized to higher dimensions the work of Roth in electric networks and used the same topological structures to describe the physical behavior of multi-physics systems. So, he was placed in a perspective not necessarily electric by applying the inverse analogies which is proposed by Fireston (1933). From these works, Plateaux (2011) applied the topological graph KBR (Kron, Branin and Roth), for the modeling of complex systems. Thus this graph relates the topological structures of complexes of chains and cochains. The tensor behavior transforms the variables associated with 1-cochains in variables associated with 1-chains. Then, as shown in Fig. 1 the KBR topological graph allows getting any relationship between its elements whatever the unknown parameters and specifications of the studied systems. Also, it allows the distinction between the topological structure of the system and the associated physics. Since, Miladi (2014) applied a topological approach which is based on the concepts of topological collections and transformations. Then, these concepts were implemented using the MGS language (Miladi et al. 2014). The main advantage of this approach is that it allows associating to the same topological structure different physical parameters of type of flow and potential.

2.2 Systems with Variable Topology

A modular approach was introduced by Magos (2005) which was based on the energetic concept. He was interested in the modeling and analyzing of systems of a variable topology, whose dynamic depends on the discrete variables. He integrated

Fig. 1 KBR topological graph (Plateaux 2012)
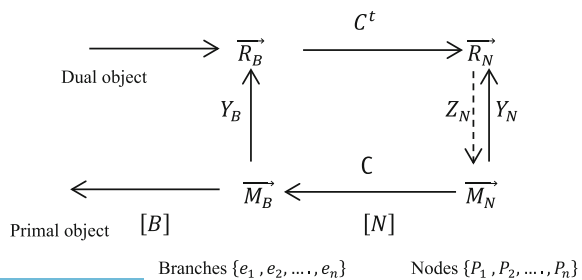
the notion of connectivity. Due to this notion, Magos carries out the study of modification for the dynamic graph and the change of fundamental matrix.

In this paper, we just first adapted the notion of variable topology to prove that MGS language is able to adapt this change easily. Second, we designate using this modular approach to validate that its works with mechatronics systems.

3 Case Study: Piezoelectric Structure

We consider the piezoelectric structure as a system with a variable topology. So we began with a presentation of the piezoelectric structure theory. Then, we proceeded the modeling of this case using MGS language and the topological approach along of application. Finally, we devoted the part of topology change to present the change of the structure by proceeding the same methodology using previously.

3.1 Presentation of the Piezoelectric Structure Theory

3.1.1 Converse and Direct Piezoelectric's Effect

Some materials have a piezoelectric substance that becomes electrically charged, when a mechanical stress is applied. Conversely, a mechanical deformation is produced when subjected to an electric field. To explain this, we have to look at the individual molecules that make up the crystal. Each molecule has a polarization which is called dipole; one end is more negatively charged and the other end is positively charged. Electrostatic balance being broken, the polarization appears: this presents the piezoelectric direct effect as illustrated in Fig. 2a. Also as shown in Fig. 2b there is a converse piezoelectric effect refers to a deformation that results from the application of an electric field.

For linear piezoelectric materials simultaneously submitted to a mechanical deformation process and an electrical polarization process, the constitutive equations are written in matrix form as follows:
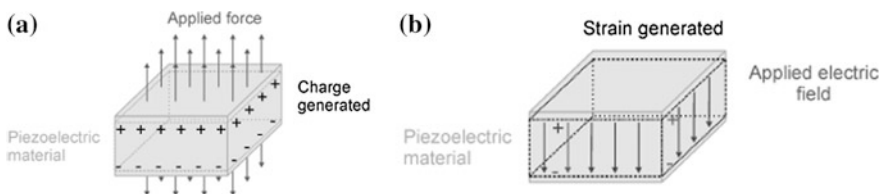
Fig. 2 Piezoelectric effect **a** direct piezoelectric effect, **b** converse piezoelectric effect
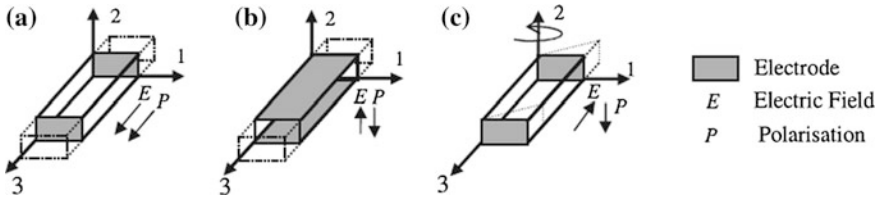
Fig. 3 The different coupling modes of a rectangular piezoelectric bar. **a** The longitudinal mode. **b** The transverse mode. **c** The shear mode (Spicher 2006)

$$\begin{cases} \{\sigma\} = [c^E]\{\varepsilon\} + [e]^T\{E\} \\ \{D\} = [e]\{\varepsilon\} + [\in^S]\{E\} \end{cases} \quad (1)$$

where $\{\sigma\} = \{\sigma_{11}, \sigma_{22}, \sigma_{33}, \sigma_{23}, \sigma_{13}, \sigma_{12}\}$: Stress vector (N/m^2), $\{\varepsilon\} = \{\varepsilon_{11}, \varepsilon_{22}, \varepsilon_{33}, \varepsilon_{23}, \varepsilon_{13}, \varepsilon_{12}\}$: Strain vector (m/m), $\{E\} = \{E_1, E_2, E_3\}$: Vector of applied electric field (V/m), $\{D\} = \{D_1, D_2, D_3\}$: Vector of electric displacement (C/m^2), $[c^E]$: Mechanical stiffness matrix for a constant electric field (Pa), $[e]$: Piezoelectric coupling coefficients matrix, (N/m/V), $[e]^T$ is the transposed, $[\in^S]$: Dielectric constant matrix for constant mechanical strain (F/m).

3.1.2 Main Piezoelectric Coupling Modes

The piezoelectric structures have several vibration modes. As shown in Fig. 3 there is a case which refers to the different main piezoelectric ceramic coupling modes of a rectangular bar.

4 Two-Bar Piezoelectric Truss Structure

4.1 Description of the Example

We consider a two-dimensional two-bar truss structure articulated to a rigid support in P_1 and P_2 and subjected to an external load $\overrightarrow{F}$ in P_0 presented in Fig. 4. This truss has only one piezoelectric bar which is bar 2.

Fig. 4 The two-bar piezoelectric truss
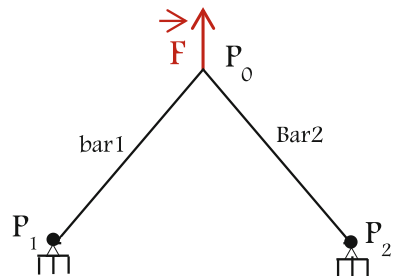
4.2 KBR Topological Graph

Three nodes and two arcs made a linear graph which refers to two-bar piezoelectric truss element. So we give an incidence matrix associated to this linear graph as shown in Fig. 5. We must determinate the KBR topological graph of a bar element in tension/compression and of a piezoelectric stack.

4.2.1 KBR Topological Graph for 2D Bar Element

The linear graph (a) of the bar element and its incidence matrix (b) are shown in Fig. 6. This topological structure allows us to create a displacement vector at the nodes which are provided by the incidence matrix (Fig. 7).

The transformation to the dual space for a bar element was linked to forces associated with nodes and branches. Due to the transpose of the incidence matrix, we effectuated the transformation of forces from internal of bars to external of nodes (Fig. 8).

Fig. 5 The two-bar piezoelectric truss. **a** Linear graph. **b** Incidence matrix

$$C = \begin{array}{c} \\ e_1 \\ e_2 \end{array} \begin{array}{ccc} P_0 & P_1 & P_2 \\ \begin{bmatrix} 1 & -1 & 0 \\ 1 & 0 & -1 \end{bmatrix} \end{array}$$
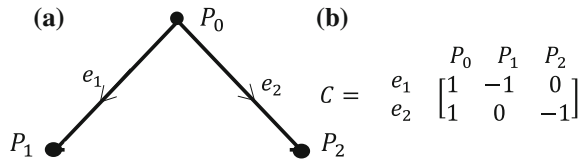
Fig. 6 The 2D bar element **a** Linear graph **b** Incidence matrix

$$C = \begin{array}{c} P_0 \\ P_1 \end{array} \begin{array}{c} e_1 \\ \begin{bmatrix} 1 \\ -1 \end{bmatrix} \end{array}$$
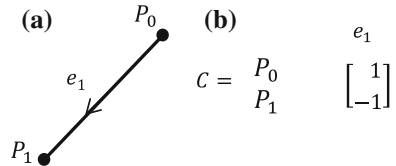
Fig. 7 Primal topological graph of displacements

$$\left\{ \overrightarrow{\Delta P_{e_1}} \right\} \xleftarrow{\quad [C] \quad} \left\{ \begin{array}{c} \left\{ \overrightarrow{\Delta P_{p_0}} \right\} \\ \left\{ \overrightarrow{\Delta P_{p_1}} \right\} \end{array} \right\}$$

Fig. 8 Dual topological graph of forces

$$\left\{ \overrightarrow{\tau_{e_1}} \right\} \xrightarrow{\quad [C]^t \quad} \left\{ \begin{array}{c} \left\{ \overrightarrow{\tau_{p_0}} \right\} \\ \left\{ \overrightarrow{\tau_{p_1}} \right\} \end{array} \right\}$$

We obtain the KBR topological graph of the bar element as shown in Fig. 9 by introducing the force–displacement relationship between the two dual spaces. The obtaining of any relationship between the elements of the graph and the determination of the unknowns of the system are allowed by the KBR topological graph.

4.2.2 KBR Topological Graph for 2D Piezoelectric Stack

The KBR graph of the piezoelectric stack is shown in Fig. 10.

Figure 11 refers to the KBR topological graph of a piezoelectric truss structure which is the combination of the KBR topological graph of a bar element (Fig. 9) and the KBR topological graph of a piezoelectric stack (Fig. 10).

Where $[K_2]_{\text{stack}} = \begin{bmatrix} (pA_1)/L_1 & 0 \\ 0 & A_1/L_1 \end{bmatrix} \begin{bmatrix} \in_{33} & e_{33} \\ -e_{33} & C_{33}^E \end{bmatrix}$

To obtain the KBR topological graph of the 2D piezoelectric truss structure of our study, we have to combine the two KBR topological graphs (Figs. 9 and 10). So refers to Fig. 11 we can have this KBR topological graph.

Fig. 9 KBR topological graph of a bar element

$$\{\overrightarrow{\tau_{e_1}}\} \xrightarrow{\quad [C]^t \quad} \left(\begin{matrix} \{\overrightarrow{\tau_{p_0}}\} \\ \{\overrightarrow{\tau_{p_1}}\} \end{matrix} \right)$$

$$[K_1] = \frac{E_1 A_1}{L_1} \begin{bmatrix} c^2 & cs \\ cs & s^2 \end{bmatrix}$$

$$\{\overrightarrow{\Delta P_{e_1}}\} \xleftarrow{\quad [C] \quad} \left(\begin{matrix} \{\overrightarrow{\Delta P_{p_0}}\} \\ \{\overrightarrow{\Delta P_{p_1}}\} \end{matrix} \right)$$
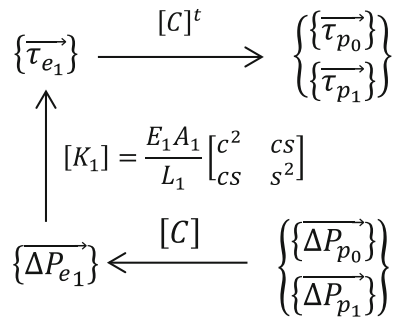
Fig. 10 KBR topological graph of a piezoelectric stack (Miladi et al. 2013)

$$\{\overrightarrow{\tau_{e_2}}\} \xrightarrow{\quad [C]^t \quad} \left(\begin{matrix} \{\overrightarrow{\tau_{p_0}}\} \\ \{\overrightarrow{\tau_{p_2}}\} \end{matrix} \right)$$

$$[K_2]_{stack}$$

$$\{\overrightarrow{\Delta P_{e_2}}\} \xleftarrow{\quad [C] \quad} \left(\begin{matrix} \{\overrightarrow{\Delta P_{p_0}}\} \\ \{\overrightarrow{\Delta P_{p_2}}\} \end{matrix} \right)$$
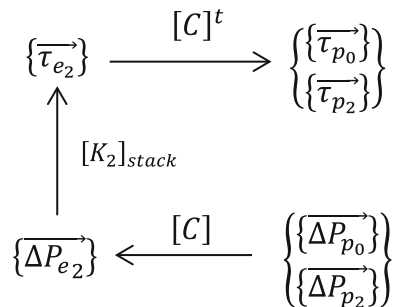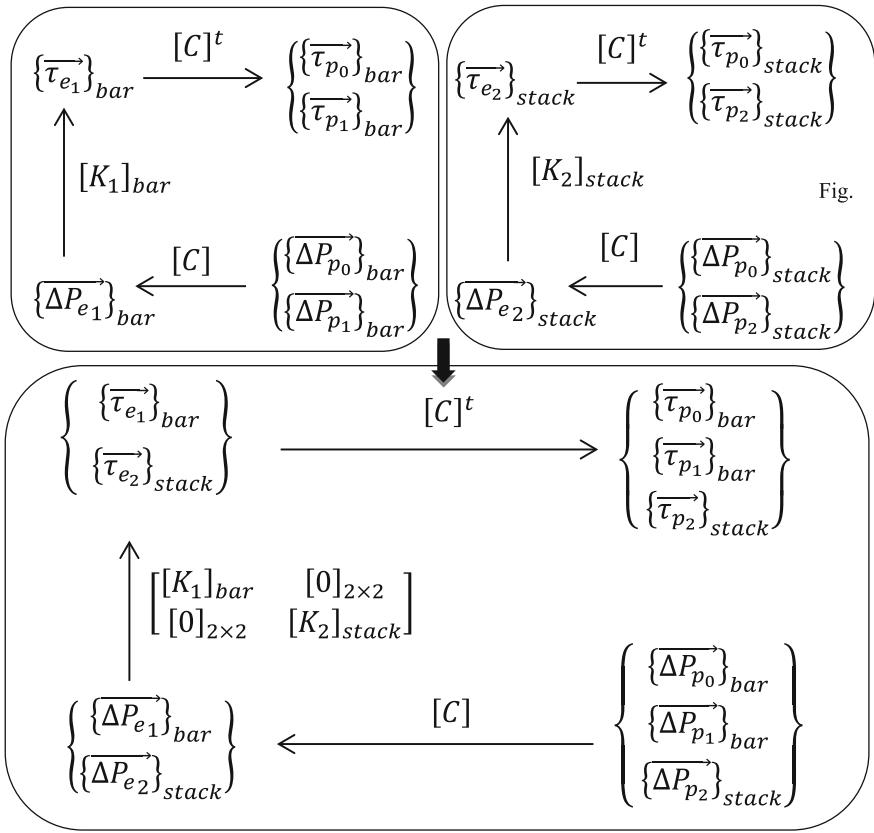
Fig. 11 KBR topological graph of a piezoelectric truss structure

4.3   MGS Modeling

Figure 12 presents the modeling steps of the two-bar piezoelectric truss. First of all, we introduce the definition of the cells representing the piezoelectric truss structure.

- 0-cells represent the nodes noted P_0, P_1 and P_2.
- 1-cells represent
    - The bar noted e_1
    - The piezoelectric bar noted e_2
    - The two electrical ground are noted e_{m1} and e_{m2} (the two nodes P_0 and P_2 are linked to the electrical ground)
    - The two frames noted e_{b1} and e_{b2}
    - The external load F noted e_f.

Fig. 12 Topological
structure after topological
change
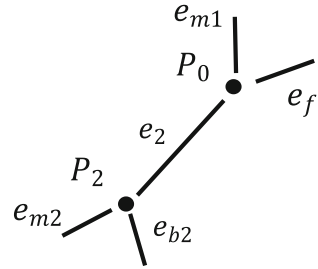
The 1-cells representing the piezoelectric stack element differ from those representing the frame, the external load and the electrical ground in that they are bounded by two nodes. Then, we define the functions of the piezoelectric variables and, we associate them with the corresponding k-cells. Finally, we generate the system of equations of the piezoelectric truss structure, taking into account that this system should be written in a format executable by other soft wares. In our case, the equations are written in MODELICA format, and we use Dymola as a solver. The generation of the system of equations is done by sweeping all the cells and defining the local behavior law of each cell.

- For 0-cells, we have $\sum_{j=1}^{N} \vec{F_j} = 0$ and/or $\sum_{j=1}^{N} I_j = 0$ where $\vec{F_j}$ and I_j represent

  respectively; the normal force and the electric current of each arc connected to the isolated node and N the number of concurrent arcs to the node.
- For 1-cells, they can present (i and j denote the ends of the arc)

  - The piezoelectric stack element in this case, we have

$$\begin{cases} \vec{F_i} + \vec{F_j} = \vec{0} \\ I_i + I_j = 0 \\ \vec{\Delta} P_{piez} = [K]_{piez} \overrightarrow{\tau_{piez-e}} \end{cases}$$

  - The frame, in this case, we have $\overrightarrow{F_i} + \overrightarrow{F_j} = 0$
  - The electrical ground, in this case we have $I_i + I_j = 0$.

5   Topological Modification

5.1   Description

We introduced in this part the case of the change of the piezoelectric truss structure. Therefore, the change in this work presents the elimination of the bar element noted e_1. For that, we have a two-dimensional piezoelectric bar structure articulated to a

rigid support in P_2 and subjected to an external load F in P_0 as presented in Fig. 12. This structure has only one piezoelectric bar. Figure 12 refers to the topological structure after topological change. We will use the same notions explained previously $(P_0, P_2 e_2, e_f, e_{b2}, e_{m1}, e_{m2})$.

5.2 KBR Topological Graph

The KBR topological graph of the system after the change of topological structure action conserves the KBR topological graph of the piezoelectric stack (Fig. 13).

Where, [K] refers to the general matrix of rigidity after the modification affecting to our system of study.

5.3 MGS Modeling

Figure 14 presents the modeling steps of the structure after topological change. We introduce the definition of the cells representing the piezoelectric structure.

- 0-cells represent the nodes noted P_0 and P_2
- 1-cells represent

    - The piezoelectric bar noted e_p
    - The two electrical ground noted e_{m1} and e_{m2}
    - The frame noted e_{b2}
    - The external load F noted e_f

Then, we precede the same strategy before the topological change.

Fig. 13 KBR topological graph of the system after change
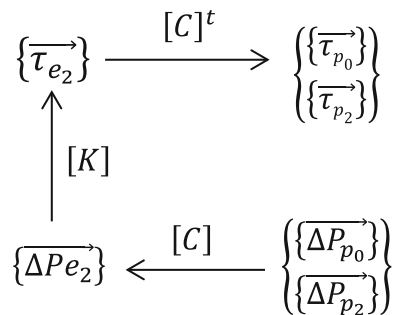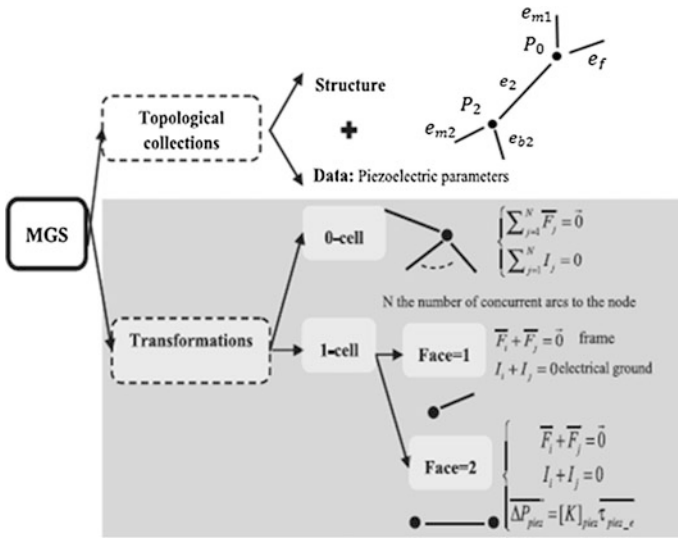
Fig. 14 Modeling principal steps of the piezoelectric structure (Miladi et al. 2013)

6 Conclusion

In this study, we presented the notion of changed structure for the modeling of mechatronic systems by using a topological approach on the basis of topological collections and transformations. This notion was applied in the case of piezoelectric truss structure.

The major advantage of using this approach is the separation of the topology (interconnection law) and the behavior laws (physics) of the studied system, which allows the formation of generic models. Therefore, we can create an MGS library by defining the local behavior laws of the different fields of mechatronic systems.

The perspective of this study is the application of the methodology of substitution of several patterns using the notions of Disconnection/Connection for the modeling of more complex systems.

References

Branin FH Jr (1966) The algebraic topological basis for network analogies and the vector calculus. In: Proceedings of the symposium on generalized networks, Polytechnic Institute of Brooklyn, pp 453–491

Cohen J (2004) Intégration des collections topologiques et des transformations dans un lan-gage fonctionnel, Every Val d'Essonne

Euler L (1741) Solutio problematisad geometriam situspertinentis. Commentarii academiaescientiarum petropolitanae, vol 8, pp 128–140

Firestone F (1933) A new analogy between mechanical and electrical systems. J Acoust Soc Am 4

Kron G (1959) A short course in tensor analysis for electrical engineers, Wiley, NY, Chapman & Hall, London, pp 250

Magos R (2005) Sur la modélisation des systèmes dynamiques à topologie variable: une formulation Hamiltonienne à ports paramétrée, Thèse de Doctorat, Lyon 1

Miladi M (2014) Modélisation géométrique et mécanique pour les systèmes mécatroniques, Thèse de Doctorat, École Nationale d'Ingénieurs de Sfax/ Institut Supérieur de Méca-nique de Paris (SUPMECA)

Miladi M, Plateaux, R, Choley JY, Karra C, Riviere A, Haddar M. (2012) Topologi-cal approach to solve 2D truss structure using MGS language. In: Mechatronics (MECATRONICS), 9th France-Japan & 7th Europe-Asia congress on and Re-search and education in mechatronics (REM). pp 437–444

Miladi M, Plateaux R, Choley JY, Karra C, Riviere A, Haddar M (2013) New topological approach for the modeling of mecatronic systems: application for piezoelec-tric structures. Eur J Comput Mech/Rev Eur de Méc Num 22:209–227

Miladi M, Plateaux R, Choley JY, Karra C, Riviere A, Haddar M (2014) Topological modeling of a one stage spur gear transmission. Chin J Mech Eng 27(5):900–908

Plateaux R (2011) Continuité et cohérence d'une modélisation des systèmes mécatroniques basée (s) sur une structure topologique. Thèse de doctorat, Institut Supérieur de Méca-nique de Paris (SUPMECA)

Roth JP (1955) An application of algebraic topology to numerical analysis: on the existence of a solution to the network problem. Proc Nat Acad Sci 41(7):518–521

Spicher A (2006) Transformation de collections topologiques de dimension arbitraire: appli-cation à la modélisation de systèmes dynamiques

The MGS home page (2012) web page http://www.ibisc.univer-evry.fr/~mgs

Developing Mathematical Models of Stress Concentration Factor Using Response Surface Method

Mohamed Makki Mhalla, Ahmed Bahloul and Chokri Bouraoui

Abstract The present paper consists first in developing mathematical models to predict stress concentration factor of a carbon fiber reinforced epoxy. Based on response surface method (RSM) a mathematical model has been determined, in which three factors with three levels are implemented. Carbon fiber content, fiber angle, and stress loading are chosen as the main input parameters in this study, which are very significant and rarely considered. The stress concentration factor is considered as output response which is evaluated through finite element study. Second, Minitab statistical package was used to analyze the numerical results and to investigate the effect and the interaction of different factors. An empirical relationship was developed based on the RSM approach for correlating the stress concentration factor with predominant process parameters. The proposed approach can be used as a powerful and an interesting method for engineering design, to determine the stress concentration factor behavior of a carbon fiber reinforced epoxy.

Keywords Stress concentration factor · Response surface methodology
Finite element method

1 Introduction

Carbon fiber reinforced epoxy is widely used in many industrial applications, such as stressed functional automotive parts and safety parts (sports and leisure). It received increasing attention in these applications due to their stiffness, toughness,

M. M. Mhalla (✉) · A. Bahloul · C. Bouraoui
Laboratoire de Mécanique de Sousse, Ecole Nationale d'Ingénieurs de Sousse,
Université de Sousse, Bp.264 Erriadh, 4023 Sousse, Tunisia
e-mail: mhallamaki@yahoo.fr

light weight, and their resistance to tensile loading. The presence of holes in composite structures is considered as the potential reason for crack initiation and growth location (Zitoune et al. 2005; Akay and Oregan 2004). This discontinuity in structures (hole, notch) leads to a high stress concentration around their edges. Also, the stress concentration is the site of initiation damage and it is causing a wide range of effects, such as stress or strain gradients. In this context, several works have dealt with the mechanical properties such as fiber ratio, diameter, length, orientation, and the stress loading which are of prime importance to the final properties of the composites materials (Tancrez et al. 2006; Thomason 1999).

The objectives of the present paper consist in

(i) Developing an analytical model for correlating the interactive and higher order influence of various parameters such as the carbon fiber content, fiber angle, and stress loading on stress concentration factor of composites materials using response surface methodology (RSM).

(ii) The RSM technique coupled with finite element method is used to investigate the effect between the different factors on the stress concentration factor of a carbon fiber reinforced epoxy.

(iii) Developing a mathematical approach for evaluating the stress concentration factor of a carbon fiber reinforced epoxy by taking into account the different parameters: (*) the carbon fiber content, (**) the fiber angle, and (***) the stress loading.

2 Response Surface Methodology

The main idea of the surface response method is to construct a polynomial approximation of the limit state function based on the results obtained by the design of experiments (DoE) method where a full factorial design plan is used (Myers and Montgomery 1995). It is a sequential experimentation strategy for building and optimizing the empirical model. Consequently, RSM is a collection of statistical and mathematical procedures that are useful for the analysis of problems, in which the objective is to optimize this response (Grum and Slab 2004; Oktem et al. 2005). In the RSM, the quantitative form of relationship between desired response and independent input variables could be written as

$$Y = f(X1, X2, X3 \ldots Xn) \pm \varepsilon \qquad (1)$$

X1, X2 … Xn are the independent input variables, where the response Y depends on them and the experimental error term, denoted as ε. The appearance of the response function is a surface as plotting the expected response of $G(\{x\})$. This

approximation of G({x}) will be proposed using the second order polynomial regression model, which called the quadratic model.

In the case of the quadratic response surface with three random variables, the response is represented as follows:

$$G(\{x\}) = a_0 + \sum_{i=1}^{n} a_i X_i + \sum_{i=1}^{n} a_{ii} X_i^2 + \sum_{i<1}^{n} a_{ij} X_i X_j \tag{2}$$

where a_i represents the linear effect of X_i, a_{ii} represents the quadratic effect of X_i^2 and aij reveals the linear-by-linear interaction between X_i and X_j. These coefficients of the mathematical model are determined by the regression tool. Then response surface G({x}) contains the cross product terms, linear terms, and squared terms. Using this quadratic mathematical model of G({x}) in this study is not only to locate regions of the desired target, but also to investigate over the entire factor space.

3 Finite Element Method

3.1 *Material*

The plate has been made from woven ply laminates (CFRP) with 2 mm of total thickness and $[\pm 45°]_{2s}$ of sequences. The specimen has eight woven ply with a thickness of 0.25 mm for each ply.

The material used in the present study was short carbon fiber reinforced epoxy. The length (L) and width (W) of plate are 250 and 25 mm respectively. A circular hole (5 mm) is drilled at the center of the panel.

3.2 *Simulation with Abaqus*

In this study, a simulation under "ABAQUS 6.12" software has been realized with a mesh-type shell hexagonal, continuum, refined and progressive around the hole (Fig. 1). To reduce the computation time with a good accuracy, we meshed only a quarter of the plate with a refined mesh around the hole and larger elsewhere. The fineness meshing is optimized in order to have a constant value of maximum stress.

Tests were carried out at different parameters such as: carbon fiber content, fiber angle, and stress loading. The carbon fiber content is selected to be between 45 and 55%, stress loading ranges from 100 to 140 MPa and fiber angle is considered to be between 45° and 65°.
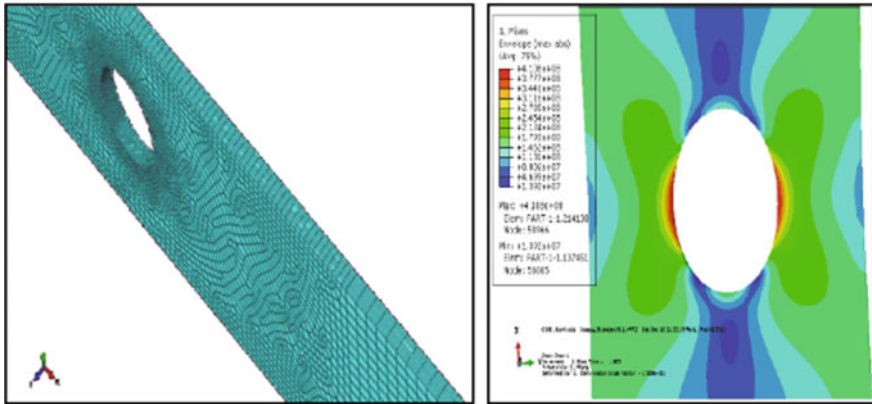
Fig. 1 Mesh of the plate with FEM

4 Results and Discussion

4.1 Development a Mathematic Model

In this section, the influence of both intrinsic parameters (carbon fiber content and fiber angle) and extrinsic parameters (stress loading) on the stress concentration factor has been investigated.

The response surface method coupled with the finite element results is implemented for predicting the mathematical relationships that link stress concentration factor as a function of the carbon fiber content, fiber angle, and stress loading.

The analytical expression, obtained from analyzing the influences of the various dominant parameters on the stress concentration factor is given by

$$
\begin{aligned}
Kt = {}& -0.44 + 0.00619\,\sigma + 0.0200\,\theta + 6.95\,Vf - 0.00008\,\sigma*\sigma - 0.000347\,\theta*\theta - \\
& 10.0\,Vf*Vf - 0.000064\,\sigma*\theta - 0.00103\,\sigma*Vf + 0.0370\,\theta*Vf
\end{aligned}
$$

(3)

In order to validate and check the accuracy of the constructed RS model, some verification points are generated. Figure 2 shows the verification point's results obtained using experiment and RS models.

The high value of R-squared (superior to 98.8%) indicated that the model was highly reliable in predicting the stress concentration factor. The results of the RS models are in a good correlation with experimental results and provide accurate and satisfactory results.

All the above consideration indicates an excellent adequacy of the developed empirical relationships.

Fig. 2 Model validation for stress concentration factor
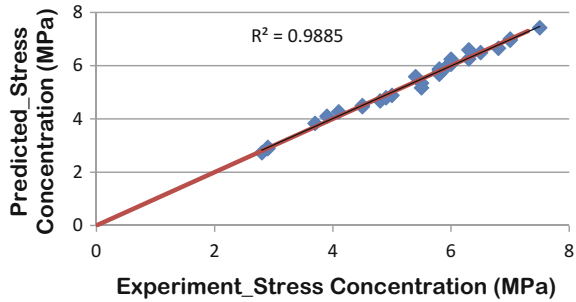
Fig. 3 Pareto chart of standardized effects on the stress concentration factor
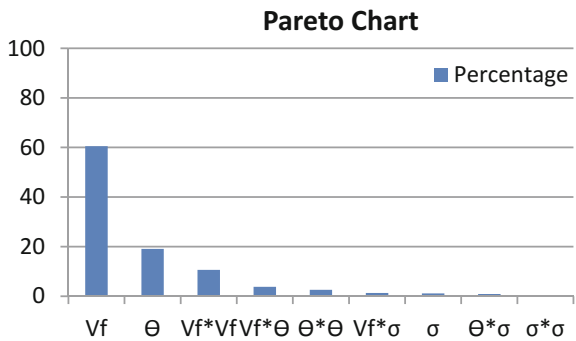
The Pareto chart indicates main and interaction effects considered statistically significant by ANOVA (Fig. 3).

As apparent, the carbon fiber content has the strongest effect of 59% on the stress concentration factor. The fiber angle contributes 20% on the stress concentration factor. From this analysis, it is confirmed that the effect of the stress loading was trivial, with a percentage contribution equals to 2.5% on the stress concentration factor. This observation is in good agreement with the previous results (Ceolho 2011), in which they have found that the effect of stress loading on the stress concentration factor was negligible on the composites materials.

4.2 Effect and Sensitivity Analysis of Input Factors

The main objective of the factorial experiments consists in studying the relationship between the response as a dependent variable and the different parameter levels. This approach helps to understand better how the change in the levels of each parameter can affect the response. It has been reported that the factorial experiments provide an opportunity to study not only the individual effects of each factor but also their interactions. The design required 27 experiments with three levels. The design was generated and analyzed using MINITAB 16.0 statistical package.
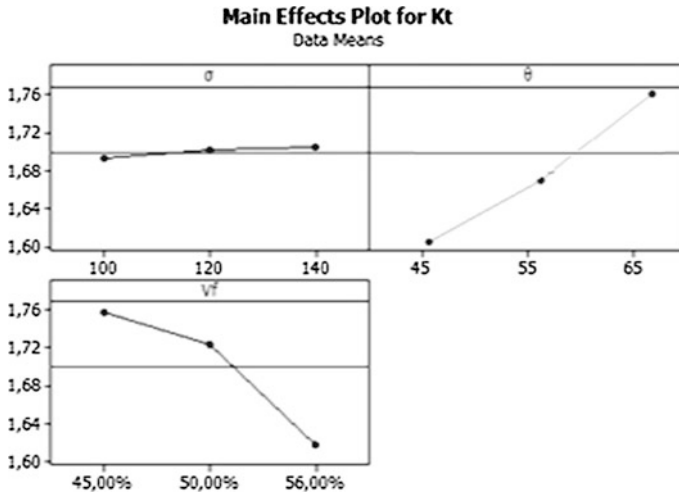
Fig. 4 Main effect plot of σ, θ and Vf on the value of the stress concentration factor

Carbon fiber content, fiber angle, and stress loading are chosen as the main input parameters in this study (Fig. 4):

It is observed that the carbon fiber content and the fiber angle have the highest significant effect of the stress concentration factor. Moreover, comparing with fiber angle and carbon fiber content, the effect of the stress loading is trivial. In conclusion, the optimal combination of different parameters to achieve minimal stress concentration factor is Vf = 55%, Θ = 45° et σ = 100 MPa.

4.3 Surface Response Results

In order to study the interaction of the three input variables on the stress concentration factor, the RSM is implemented. Three-dimensional plots were generated. The surface response plots were drawn for various combinations as shown in Figs. 5 and 6.

From Figs. 5 and 6, we can deduce the significant effect of the two factors Θ and Vf. on the stress concentration factor which is calculated using the surface response method.

An important decrease of the stress concentration factor is observed when the fiber content value decrease. Concerning the stress loading effects, it is observed that the stress concentration factor is not affected by the variation of the stress loading. Moreover, comparing with fiber angle and carbon fiber content, the effect of the stress loading is trivial.

Fig. 5 Response surface plots showing the effects of Vf and ϴ on the stress concentration factor
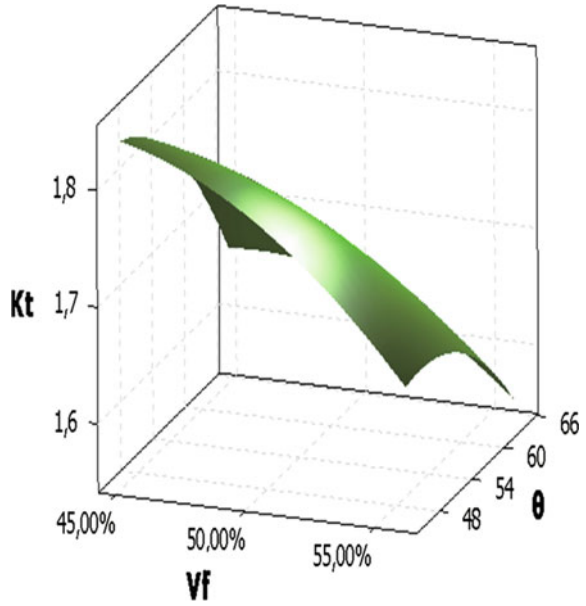
Fig. 6 Response surface plots showing the effects of Vf and σ on the stress concentration factor
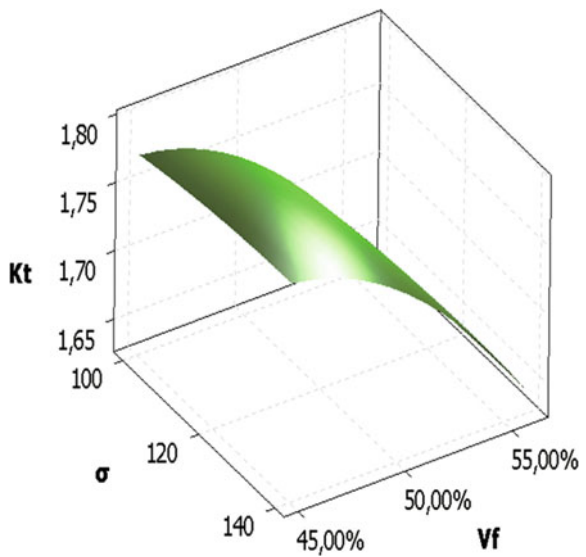
It is interesting to note that fiber content and fiber angle have a very significant effect on the stress concentration factor. For this reason, the highest values of the stress concentration factor occur in carbon fiber content of 55% and fiber content of 45°.

5 Conclusion

In this paper, the Response Surface Method (RSM) is used to calculate the performance function and their corresponding design points based on finite element results. The basic idea of this method is to approximate the system response by an explicit function of different variables. An empirical relationship was developed based on the RSM approach for correlating the stress concentration factor with predominant process parameters.

The following conclusions can be drawn:

Based on the finite element observations and response surface methodology, we can investigate the stress concentration factor of our material. This result can be used also, to characterize qualitatively the effect of the different fiber angle and fiber content modifications.

A minimum stress concentration factor of 6 was obtained under the condition of 45° fiber angle, 100 MPa stress loading and 55% carbon fiber content reinforced epoxy and that confirmed by RSM method.

This approach leads to improve the prediction models by taking into account the various parameters of: (i) fiber angle and (ii) fiber content and (iii) stress loading which are very significant and rarely considered. This observation clearly shows the capability of the prediction model to correctly take into account the statistical distribution of the input parameters in composite materials.

References

Akay M, Oregan DF (2004) Fracture behaviour of carbon fibre reinforced polyamide mouldings. Polym Test 14, 149–162.

Ceolho V (2011) Effects of stress loading and fiber angle on the mechanical properties of gfrp composites. Engenharia Térmica (Thermal Eng), vol 10, pp 03–06

Grum J, Slab JM (2004) J Mater Process Technol 155:2026–2032

Myers RH, Montgomery DH (1995) Response surface methodology. Wiley, USA

Oktem H, Erzurmlu T, Kurtaran H (2005) J Mater Process Technol 170:11–16

Tancrez JP, Pabiot J, Rietsch F (2006) Damage and fracture mechanisms in thermoplastic-matrix composites in relation to processing and structural parameters. Compos Sci Technol 56:725–731

Thomason JL (1999) The influence of fibre properties of the performance of carbon - fibre-reinforced polyamide 66. Compos Sci Technol 59:2315–2328

Zitoune R, Collombet F, Piquet R, Lachaud F, Pasquet P (2005) Experiment–calculation comparison of the cutting conditions representative of the long fiber composite drilling phase. Compos Sci Technol 65:455–466

Porous Shape Memory Alloy: 3D Reconstitution and Numerical Simulation of Superelastic Behavior

Shijie Zhu, Céline Bouby, Abel Cherouat and Tarak Ben Zineb

Abstract As a new class of metallic foam materials have attracted increasing interest in different fields of engineering. They are particularly versatile because of their interesting mechanical and physical properties: relative low density makes it possible to obtain a high stiffness/weight radio, existence of cavities results in the abilities of energy absorption and of damping, and also gives them thermal and acoustic insulation properties. As a well-known material for reversible inelastic deformation, shape memory alloys (SMA) have been paid attention on over last few years. They possess two important properties: superelasticity and shape memory effect. Cellular structures in SMAs are particularly interesting for their potential to provide superelasticity and shape memory effect in a lightweight material. In this work, 3D foam CAD structure of NiTi material is reconstituted using ellipsoid cell units. A "taking" and "placing" algorithm based on uniform distribution and normal distribution is adopted for the reconstitution process of Representative Volume Element (RVE). In the RVE, dimensions, positions, and orientations are all random. A constitutive model for shape memory alloy including phase transformation, martensitic reorientation and twins accommodation is used to simulate by the finite element analysis the superelastic behavior of the SMA foam. In order to show the efficiency of the proposed methodology, some applications are presented to simulate the compression of shape memory alloy foam. The effects of porosity, size,

S. Zhu · A. Cherouat (✉)
ICD/GAMMA3, University of Technology of Troyes, 12 rue Marie-Curie,
10010 Troyes, France
e-mail: abel.cherouat@utt.fr

S. Zhu
e-mail: shijie.zhu@utt.fr

C. Bouby · T. Ben Zineb
LEMTA, UMR 7563, Université de Lorraine, Vandœuvre-lès-Nancy, France
e-mail: celine.bouby@univ-lorraine.fr

T. Ben Zineb
e-mail: tarak.ben-zineb@univ-lorraine.fr

C. Bouby · T. Ben Zineb
LEMTA, UMR 7563, CNRS, Vandœuvre-Lès-Nancy, France

371

orientation, and ratio of long and axes short of the unit cell on the superelastic behavior of porous material are discussed.

Keywords Foam Shape Memory Alloy · Finite Element Analysis 3D Reconstruction · Superelastic behavior

1 Introduction

As a new class of materials, metallic foams have attracted increasing interest in different fields of engineering (Ashby et al. 2000; Deshpande and Fleck 2000; Gibson and Ashby 1999). This kind of materials is a cellular structure containing solid and gaseous phase, where the cavities occupy a certain percentage of the overall volume. Based on the morphology of their internal cells, metallic foams can be classified into open foams or closed foams. They are particularly versatile because of their interesting mechanical and physical properties: for example, the relatively low density makes it possible to obtain a high stiffness/weight radio, the existence of cavities results in the abilities of energy absorption and of damping, and also gives them thermal and acoustic insulation properties.

As a well-known material for reversible inelastic deformation, shape memory alloys (SMA) have been paid attention on over last few years (Otsuka and Wayman 1999). Thanks to the thermoelastic martensitic transformation, SMA materials possess two important properties: superelasticity and shape memory effect. It has become interesting if a kind of material combines both an attractive structure and an important behavior law. Thus, porous shape memory alloys have been an innovate kind of material in many engineering field. Cellular structures in SMAs are particularly interesting for their potential to provide superelasticity and shape memory effect in a lightweight material.

Lots of processes have been done to fabricate the material of SMA foams (Bansiddhi and Dunand 2011; Castrodeza et al. 2009). Besides, many experiences and characterizations have been done to understand the properties of SMA foams (Scalzo et al. 2009). However, the lack of numerical procedure of SMA foams sets up a barrier for their effective use. Not only experimental data of SMA foams, but also trusty numerical modeling for calculation of behavior law is needed to well predict the properties of this kind of materials. In particular, it would be satisfying to study the macroscopic behaviors of SMA foams with the use of their microstructure. There is no doubt that microstructural properties could influence macroscopic behaviors, which is necessary for designers, but it is still difficult to derive macroscopic behaviors from microstructure.

In this study, the macroscopic compressive superelastic behavior of SMA foams starting from their microstructure is tried to evaluate. The model of Duval and Chemisky (Chemisky et al. 2011; Duval et al. 2010) is used to predict the mechanical response of representative volume element of open-cell NiTi foams subjected to uniaxial compression. A foam structure of 3D reconstitution based on

the ellipsoid cell unit, by using a "taking" and "placing" algorithm based on uniform distribution and normal distribution (De Giorgi et al. 2010), is built to well simulate the real foam structure. Numerical simulations are presented in order to validate the proposed model for foam structures. The effects of porosity, size, orientation, and ratio of long axis and short axis of cell unit on the superelastic behavior of SMA foams are also studied numerically.

2 Shape Memory NiTi Behavior Modeling

In this paper, a constitutive model for shape memory alloy including phase transformation, martensitic reorientation, and twins accommodation (Chemisky et al. 2011; Duval et al. 2010) is used to simulate the superelastic behavior of the SMA foam. When a thermomechanical loading is applied in a shape memory alloy, the total macroscopic strain can be written as

$$\boldsymbol{\varepsilon} = \boldsymbol{\varepsilon}^e + \boldsymbol{\varepsilon}^{th} + \boldsymbol{\varepsilon}^T + \boldsymbol{\varepsilon}^{twin} = S{:}\boldsymbol{\sigma} + \boldsymbol{\alpha}\left(T - T_{ref}\right) + f.\bar{\boldsymbol{\varepsilon}}^T + f^{FA}.\bar{\boldsymbol{\varepsilon}}^{twin} \tag{1}$$

where $(\varepsilon^e, \varepsilon^{th}, \varepsilon^T, \varepsilon^{twin})$ are respectively the elastic strain, the thermal expansion strain, the inelastic strain due to martensitic transformation and the inelastic strain due to the accommodation of twins between martensite variants. S is the isotropic compliance tensor and σ is the mean stress tensor over the RVE. α is the isotropic thermal expansion tensor and T_{ref} is the reference temperature. f is the martensite volume fraction, $\bar{\boldsymbol{\varepsilon}}^T$ is the mean transformation strain tensor in martensite volume, f^{FA} is the formed self-accommodated martensite volume fraction and $\bar{\boldsymbol{\varepsilon}}^{twin}$ is the mean twins accommodation strain in twinned martensitevolume.

The Clausius–Duhem inequality can be written from the Gibbs free energy

$$-\frac{\partial G}{\partial \sigma}{:}\dot{\sigma} - \frac{\partial G}{\partial T}.\dot{T} - \frac{\partial G}{\partial V_k}.\dot{V}_k - \dot{\sigma}{:}\varepsilon - \overrightarrow{q}.\frac{\overrightarrow{grad T}}{T} \geq 0 \tag{2}$$

where V_k is an internal variable.

The Gibbs free energy potential G is chosen as follows:

$$\begin{aligned} G = U^A - TS^A + B(T - T_0)f - \frac{1}{2}\sigma{:}S{:}\sigma - \sigma{:}\alpha\Delta T - \sigma{:}\bar{\varepsilon}^T f - \sigma{:}\bar{\varepsilon}^{twin} f^{FA} \\ + \frac{1}{2}fH_\varepsilon\bar{\varepsilon}^T{:}\bar{\varepsilon}^T + \frac{1}{2}H_f f^2 + \frac{1}{2}f^{FA}H_{twin}\bar{\varepsilon}^{twin}{:}\bar{\varepsilon}^{twin} - C_v\left[\left(T - T_{ref}\right) - T\log\frac{T}{T_{ref}}\right] \end{aligned} \tag{3}$$

where U^A and U^M are the internal energy of the austenitic and martensitic phase, S^A and S^M are the entropy of the austenitic and martensitic phase, $B = -\Delta S = -(S^M - S^A)$, $T = \frac{\Delta U}{\Delta S} = \frac{U^M - U^A}{S^M - S^A}$ is the equilibrium temperature of transformation, H_ε, H_f and H_{twin} are proportionality factors, C_v is the heat flux for the RVE.

Therefore, driving force variables linked to internal variables are defined by:

- Transformation force linked to f:

$$F_f = \boldsymbol{\sigma} : \bar{\boldsymbol{\varepsilon}}^T + \zeta^{FA}\boldsymbol{\sigma} : \bar{\boldsymbol{\varepsilon}}^{twin} - B(T - T_{ref}) - \frac{1}{2}H_\varepsilon^T\bar{\boldsymbol{\varepsilon}}^T : \bar{\boldsymbol{\varepsilon}}^T - H_f f + \frac{1}{2}H_{twin}\zeta^{FA}\bar{\boldsymbol{\varepsilon}}^{twin}\bar{\boldsymbol{\varepsilon}}^{twin} - \lambda_0 - \lambda_1$$

$$(4)$$

- Orientation force linked to $\bar{\boldsymbol{\varepsilon}}^T$:

$$F_{\boldsymbol{\varepsilon}^T} = \boldsymbol{\sigma}' - fH_\varepsilon\bar{\boldsymbol{\varepsilon}}^T - \lambda_2 \tag{5}$$

- Twin accommodation force linked to $\bar{\boldsymbol{\varepsilon}}^{twin}$:

$$F_{\bar{\boldsymbol{\varepsilon}}^{tw}} = \boldsymbol{\sigma}' - H_{twin}\bar{\boldsymbol{\varepsilon}}^{twin} \tag{6}$$

where λ_0, λ_1 and λ_2 are Lagrange multipliers.

3 Numerical Analysis of Shape Memory NiTi Open-Cell Foams

3.1 3D Reconstitution of Foam Structure Using CAD Method

In order to build porous structure with random cell morphology, an ellipsoid shape in which two of the three axes are the same is used to define the foam pore as

- (x_0, y_0, z_0): are les coordinates of the ellipsoid center;
- a: is the length of the semi-major axis;
- b: is the length of the semi-minor axis;
- (α, β, γ): are the orientation angles of the ellipsoid (Euler angles).

Figure 1 shows the scheme of the geometric modeling of foams with random distributions of ellipsoidal cells. A "taking" and "placing" algorithm is adopted for the 3D reconstitution process. The process is accomplished by using the mathematical programming software MATLAB and the Abaqus/CAE. The basic principles of the algorithm are

- **Definition of RVE ellipsoids characteristics**: the cell dimension, position and orientation are defined with random distributions. The RVE chosen is a cube of $10 \times 10 \times 10$ mm.
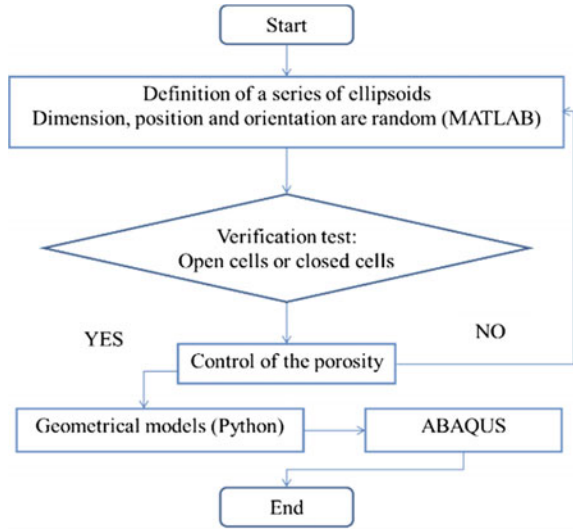
- **Verification test** (open cells or closed cells): In the process of generating metallic foam structure, at first, an ellipsoid cell unit is created in the cube of RVE, and then the following ellipsoids are examined whether they meet the conditions to form open cells or closed cells. Therefore, there are always two kinds of cell unit: the existing valid ellipsoids and the ellipsoid to verify. Here, a method of intersection checking is developed. Two conditions should be taken into consideration: first, the ellipsoid to verify must be intersected with at least one of the existing valid ellipsoids; second, the intersecting part of the two ellipsoids should not occupy a large part of the existing valid ellipsoid because of the foam structure authenticity.

- **Control of the porosity**: It is difficult to calculate exactly the porosity of open cells foam even if all the parameters of the ellipsoid cell units are known. The difficulty comes from the complexity of the intersections between two ellipsoids. To solve this problem, a statistical method is used to approximate the result of porosity. First, a point P with coordinate (x_p, y_p, z_p) is generated randomly inside the cube of RVE by uniform distribution. Then by geometrical transformation, the coordinates of P in the coordinate system of the existing valid ellipsoid and the equation for verification are (x_{ep}, y_{ep}, z_{ep}):

$$F_p = \frac{x_{ep}^2}{a^2} + \frac{y_{ep}^2}{b^2} + \frac{z_{ep}^2}{b^2} \tag{7}$$

If $F_p < 1$, then the point P is inside of the existing valid ellipsoid. In this way, we note the successful index S as 1, or we note S as 0.
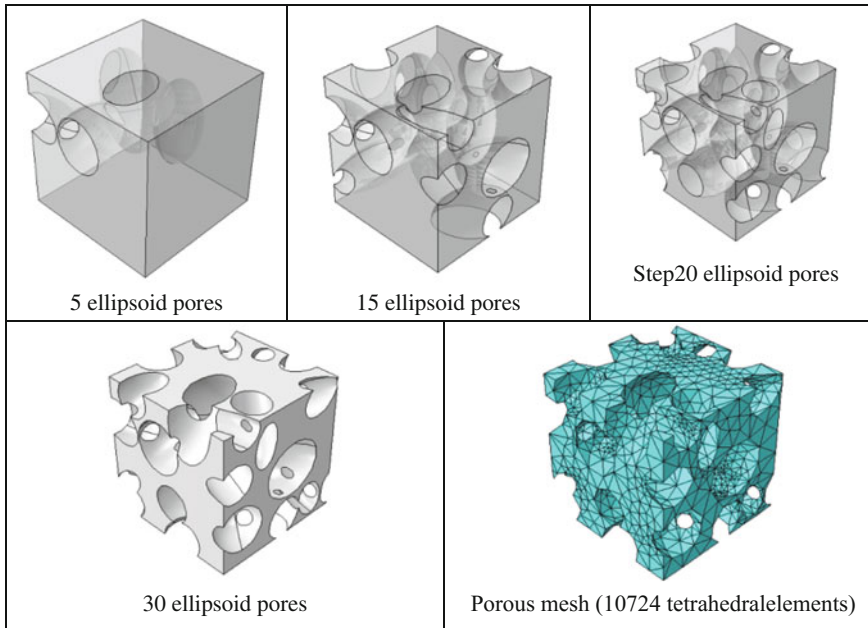
Fig. 2 Level steps of a foam CAD reconstitution and Porous structure mesh

– **Numerical models**: by using script Python in Abaqus/CAE, the process of generating of random distributions of ellipsoid cell pores is based on the flowchart program.

Figure 2 reports the level steps of a foam CAD reconstitution and foam mesh. The foam structure obtained by CAD reconstitution is transformed to a model with surface mesh (triangular elements) using Abaqus and Decimesh optimizer mesher. Optiform software is then used to mesh the 3D porous structure with tetrahedral finite elements.

3.2 Numerical Analysis of Superelastic Behavior

In this section, 3D cubic ($10 \times 10 \times 10$ mm^3) porous shape memory alloy with 60% porosity part is side-pressed between two planar tools, assumed infinitely long, which tend to flatten it. The assumed rigid tools are composed of both the moving upper plane through which the imposed vertical displacement is applied ($u = 1.5$ mm). The mechanical properties of the used NiTi SMAs material are

Table 1 Material parameters for NiTi SMA materials

Parameters	Value	Parameters	Value	Parameters	Value	Parameters	Value
$E(MPa)$	39500	ε_{comp}^{T}	0.044	r_f	0.25	$H_s(MPa)$	68.5
υ	0.3	$b_{dtrac}\left(\frac{MPa}{°C}\right)$	4.2	$F_{\bar{\varepsilon}^T}^{max}(MPa)$	220	α_0	0.01
$\alpha(°C^{-1})$	0	$b_{rtrac}\left(\frac{MPa}{°C}\right)$	7	$H_f(MPa)$	2	α_1	0.01
ε_{trac}^{T}	0.056	$M_s(°C)$	−80	$H_{\bar{\varepsilon}^T}(MPa)$	1635	α_{eps}	0.05
ε_{trac}^{TFA}	0.053	$A_f(°C)$	−2	$H_{twin}(MPa)$	25,000	n_{surf}	5
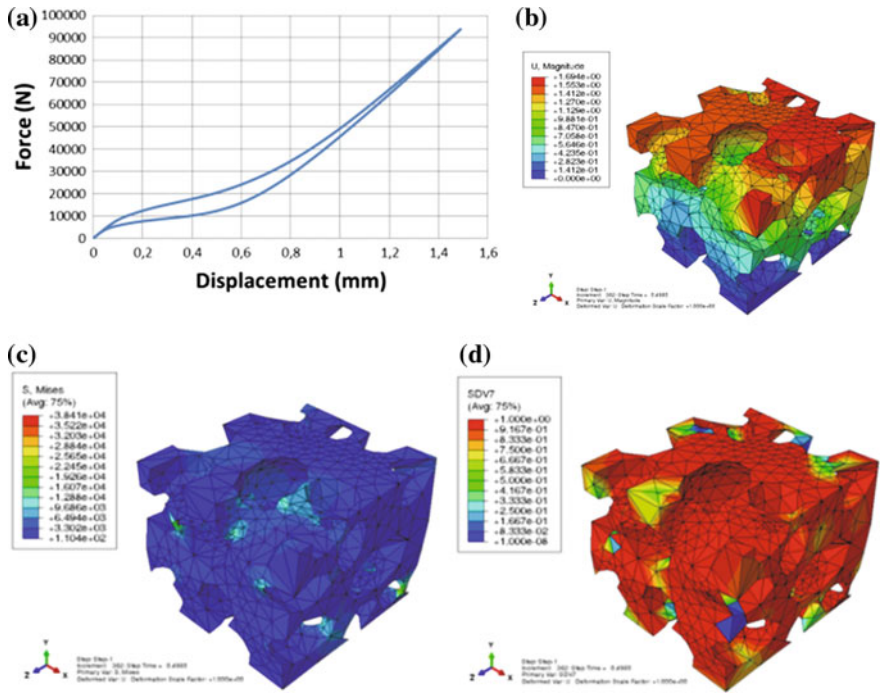
Fig. 3 **(a)** Force-displacement response **(b)** Displacement magnitude **(c)** Von Mises stress **(d)** Volume fraction of martensite for a compression displacement of 1.5 mm

given in Table 1. The predicted results obtained by the proposed methodology are given in Fig. 3 in term of the deformed mesh, the load versus displacement charge and discharge curve, the von Mises stress and the volume fraction of martensite for a displacement of the upper plane about 1.5 mm. One can see that at this compression level, almost all the areas of the RVE are transformed.

4   Parameters Effect Study

Considering the fact that the performance of porous materials can be affected by the pores shape, size, distribution, and orientation, different simulations are proposed to study these effects on the overall response of the material.

4.1   Porosity Effect

Figure 4 reveal the predicted compressive force-displacement curves and their areas for different porosity values, 0 (massive), 40, 60, 70 and 80% respectively. The obtained results show that the porosity of the porous material affects the mechanical properties of foam in term of stiffness, flexibility and damping (Table 2).

4.2   Size of Cell Unit Effect

In this example, three cell unit sizes of the long axis (a = 7.51, 3.76 and 2.50 mm) of porous shape memory alloy with 60% porosity are study numerically. Figure 5 shows the predicted force-displacement curves for different length values of a. The results in both charge and discharge procedures, show that when the length values of the long axis diminishes, which equals that the size of cell unit decreases, the elastic modulus and the plateau force both raise.
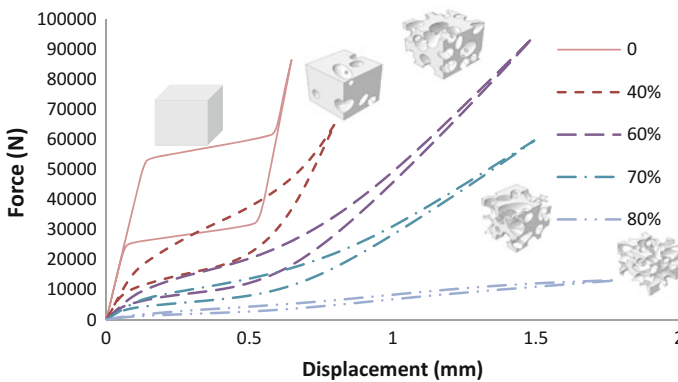
Fig. 4 Compressive force versus displacement for different porosities

Table 2 Important parameters for different porosities

Porosity	0	40%	60%	70%	80%
Elastic modulus (MPa)	395.0	175.5	88.5	61.3	18.2
Plateau force (kN)	54.9	16.2	10.1	5.9	1.4
Maximum displacement (mm)	0.65	0.8	1.5	1.5	1.8
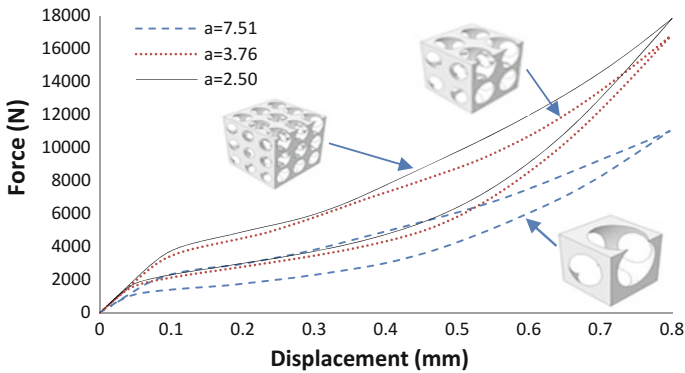
Fig. 5 Compressive force versus displacement for different size values
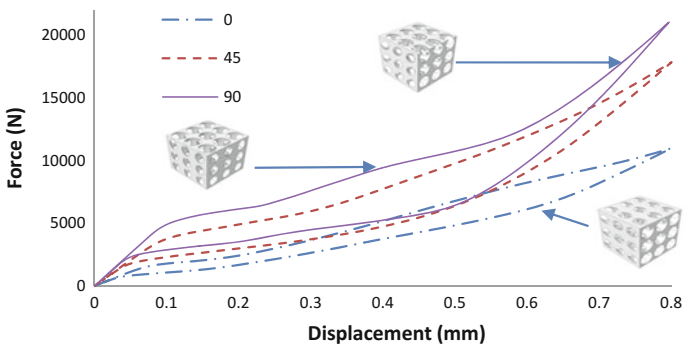
Fig. 6 Compressive force-displacement responses for different orientation values

4.3 Orientation of Cell Unit Effect

In terms of orientation of cell unit pore, the angles between the directions of long axis and the horizontal directions are defined by angleθ. Here a periodic model is used to neglect the effect of other parameters of porous shape memory alloy with 60% porosity. Figure 6 shows the numerical compressive force-displacement curves for different orientation values, θ = 0°, 45° and 90° respectively. From the
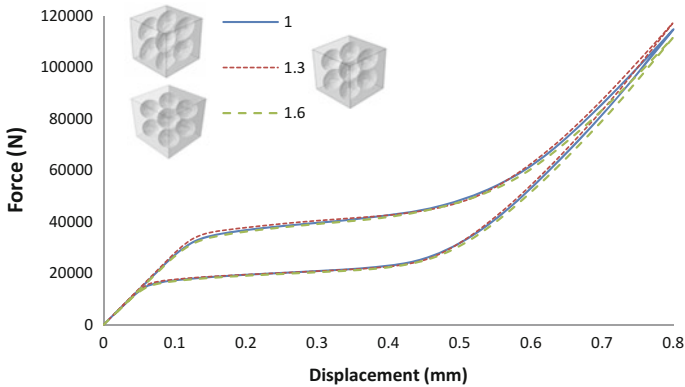
Fig. 7 Compressive force-displacement responses for different ratio of ratio r

results, one can tell that, in both charge and discharge procedures, the elastic modulus, and the plateau force are strongly affected by the orientation of cell unit pores.

4.4 Cell Unit Ratio Effect

In this section, the effect of the ratio of r = long axis/short axis is also studied. Figure 7 shows the obtained predicted force-displacement curves for different ratio values, r = 1 (sphere), r = 1.3 and r = 1.6 (ellipse) respectively. According to the results, the ratio of long axis and short axis does not have an apparent effect on the performance of SMA foams.

5   Conclusion

A study of 3D foam microstructure reconstitution is carried out. The foam structure, the porosity of which can be controlled, is well built on the basis of the ellipsoid cell unit with random dimension, position, and orientation. The obtained simulation results indicate that the porosity of foams is a crucial parameter to characterize SMA foams. With the foam porosity increasing, the elastic modulus, the plateau force, and the curve area diminish. The smaller size of cell unit there is in RVE, the more solid the material is. The larger orientation of cell unit there is in RVE, the more solid the material is. Moreover, the ratio of long axis and short axis does not much influence the performance of SMA foams.

References

Ashby MF, Evans T, Fleck, N A, Hutchinson JW, Wadley HNG, Gibson LJ (2000) Metal foams: a design guide. Elsevier

Bansiddhi A, Dunand DC (2011) Processing of NiTi foams by transient liquid phase sintering. J Mater Eng Perform 20:511–516

Castrodeza EM, Mapelli C, Vedani M, Arnaboldi S, Bassani P, Tuissi A (2009) Processing of shape memory CuZnAl open-cell foam by molten metal infiltration. J Mater Eng Perform 18:484–489

Chemisky Y, Duval A, Patoor E, Zineb TB (2011) Constitutive model for shape memory alloys including phase transformation, martensitic reorientation and twins accommodation. Mech Mater 43:361–376

De Giorgi M, Carofalo A, Dattoma V, Nobile R, Palano F (2010) Aluminium foams structural modelling. Comput Struct 88:25–35

Duval A, Haboussi M, Zineb TB (2010) Modeling of SMA superelastic behavior with nonlocal approach. Phys Proc 10:33–38

Fleck NA, Deshpande VS (2000) Isotropic constitutive models for metallic foams. J Mech Phys Solids 48:1253–1283

Gibson LJ, Ashby MF (1999) Cellular solids: structure and properties. Cambridge University Press

Otsuka K, Wayman CM (1999) Shape memory materials. Cambridge University Press

Scalzo O, Turenne S, Gauthier M, Brailovski V (2009) Mechanical and microstructural characterization of porous NiTi shape memory alloys. Metall Mater Trans A 40:2061–2070

Flexural Fatigue of Bio-Based Composites

H. Daoud, A. El Mahi, J.-L. Rebiere, M. Taktak and M. Haddar

Abstract The paper presents an investigation of the mechanical fatigue behavior of a bio-based composite with an interleaved natural viscoelastic layer. The material used is a unidirectional laminate with different orientations. It is composed of a GreenPoxy resin reinforced with long flax fibers. A viscoelastic layer made of natural rubber has been introduced at the middle layer of the laminate. Different configurations of unidirectional specimens were tested in static tests. The mechanical properties such as the characteristics at failure of the structures with and without natural rubber were determined and compared. The effect of the insertion of the viscoelastic layer in the studied composite on the stiffness, hysteresis loops and loss factors were investigated during cyclic fatigue tests. A comparison of the fatigue behavior of the composite with and without viscoelastic layer was made. The results show that the composite with an interleaved natural viscoelastic layer presents an interesting damping properties considering the high values of the loss factors obtained from cyclic fatigue tests.

Keywords Biocomposite · Flexural tests · Fatigue · Natural rubber

H. Daoud (✉) · A. El Mahi · J.-L. Rebiere
Acoustics Laboratory, Université Du Maine (LAUM) UMR CNRS 6613,
Av. O. Messiaen, 72085 Le Mans Cedex 9, France
e-mail: hajer.daoud.etu@univ-lemans.fr

A. El Mahi
e-mail: abderrahim.elmahi@univ-lemans.fr

J.-L. Rebiere
e-mail: jean-luc.rebiere@univ-lemans.fr

M. Taktak · M. Haddar
Laboratory of Mechanics Modeling and Production (LA2MP),
National School of Engineers of Sfax, University of Sfax,
BP N, 1173 - 3038 Sfax, Tunisia
e-mail: mohamed.taktak@fss.rnu.tn

M. Haddar
e-mail: mohamed.haddar@enis.rnu.tn

383

1 Introduction

The advanced researches in composite materials are now heading to bio-based structures. These types of materials are made from renewable and biodegradable resources, which can help to reduce the use of petro-chemical products.

Researchers are now more interested to investigate biocomposite materials. A comparison between the mechanical properties of composites reinforced with natural fibers with those reinforced with synthetic ones has been also studied by Hristozov et al. (2016), Wambua et al. (2003) and Monti et al. (2016). They have demonstrated that bio-based composites present relatively similar mechanical properties with synthetic ones such as glass.

Flax is one of the most studied natural fibers. Yan et al. (2014), Abdul Nasir et al. (2015), Bensadoum et al. (2016), Monti et al. (2016) and Liang et al. (2011) have investigated the mechanical and damping behavior of flax fiber reinforced composites. They have demonstrated that flax composites present several advantages such as their important specific mechanical properties, high damping behavior, and good thermal and acoustic insulation. Daoud et al. (2016) have investigated the dynamic properties of flax fibers reinforced composites. Their results show that this type of material presents very high damping properties. They have demonstrated also that the insertion of a viscoelastic layer of natural rubber could ameliorate these properties with a significant way.

In this area, the purpose of our work is to study the mechanical behavior of Flax/GreenPoxy composites with and without a viscoelastic layer. Experimental tensile and three-point bending tests were carried out to characterize the structure. Then cyclic fatigue in the bending tests has been also realized to follow the evolution of the mechanical properties during fatigue. The stiffness, hysteresis loops, and loss factors were studied. Moreover, the effect of inserting the viscoelastic layer on the mechanical properties of the parent materials has been investigated.

2 Materials

The composites studied in this work were produced using a bio-based epoxy resin (SR GreenPoxy 56/Green Pox 505 V2) manufactured by Sicomin reinforced by unidirectional long flax fibers (Flax Tape 200 LINEO) manufactured by LINEO. The laminates were produced by manual lay-up process at room temperature (20°C) with a pressure of 0.6 bar using vacuum molding process. The obtained plates were exposed at room temperature for at least one week to ensure the complete polymerization of the resin. Thus, test specimens were cut up with a diamond disc.

The value of the volume fraction was measured on different specimens from the values of the masses and volumes of samples extracted from several plates. The average was estimated between 38 and 45%. The porosity of the studied materials was determined by the comparison of the theoretical density of the composite and

Table 1 Dimensions of the specimens

	Length (mm)	Width (mm)	Thickness (mm)
Tensile tests	250	25	3.5
Bending tests	100	16	3.5

its measured one. Therefore, the values of the porosity were calculated to be between 2.5 and 7.5%.

Three orientations of unidirectional specimens (UD 0°, UD 45° and UD 90°) composed of eight plies were manufactured for the tensile tests. Moreover, different unidirectional specimens UD 0° were prepared for the static and cyclic fatigue loading in three-point bending tests. The dimensions of the different specimens are shown in Table 1.

3 Experimental Procedure

3.1 Tensil Tests

Flax fiber reinforced composite was characterized by uniaxial tensile loading of the unidirectional fiber specimens for the orientations 0°, 45°, and 90°. The tests were carried out using MTS universal traction equipped with a 100 kN load cell. The strains in the tensile direction were measured by mean of an extensometer with a gauge length of 50 mm. The tests were performed at room temperature according to the NF T57-101 standard with a displacement rate of 1 mm · min^{-1}.

The engineering modulus of the studied composite referred to the directions (1, 2) was measured in static tests: The longitudinal modulus E_1 and the Poisson's ratio v_{12} are measured from the tests on the specimens UD 0°. The transverse modulus E_2 is measured on the UD 90° specimen and the Shear modulus G_{12} could be obtained from the UD 45° specimens. This engineering modulus was calculated using the following equation where θ is the orientation of material in layer.

$$\frac{1}{E_x} = \frac{4}{E_1}\cos^4\theta + \frac{1}{E_2}\sin^4\theta + \left(\frac{1}{G_{12}} - 2\frac{v_{12}}{E_1}\right)\sin^2\theta\cos^2\theta \tag{1}$$

Figure 1 presents typical stress/strain curves obtained in static monotonic tensile tests performed for every kind of specimen (UD0°, UD45° and UD90°). It will be seen that samples UD-0° containing fiber aligned with the tensile direction exhibit a short linear elastic domain followed by a nonlinear part. Flax composite presents a nonlinear behavior, which is due to the morphology or the nonlinearity of the flax fibers. This kind of behavior is not observed for synthetic composites. The initial yield point, occurring for a very low deformation level and resulting in an important loss of stiffness, is visible on the stress/strain curves. In the case of UD45° and UD90°
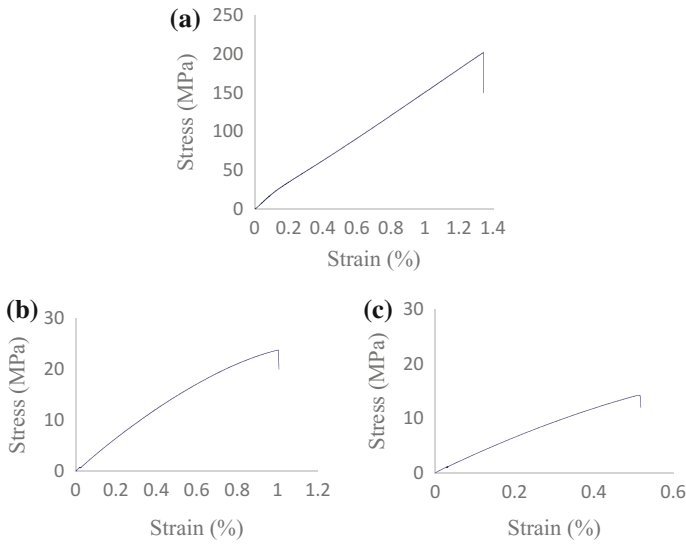
Fig. 1 Stress/strain curves of unidirectional Flax/GreenPoxy composite in tensile tests: **a** UD0°
b UD45° and **c** UD 90°

Table 2 Engineering modulus of flax fiber reinforced composite obtained in tensile tests

E_1 (GPa)	E_2 (GPa)	G_{12} (GPa)	v_{12}
22.2	3.2	1.33	0.32

Table 3 Tensile characteristics of flax fiber reinforced composites

Fiber orientation (°)	0°	45°	90°
Maximum stress (MPa)	200	22.4	14
Maximum strain (%)	1.3	1.0	0.55

specimens, the behavior is linear until the failure, which is a brittle type. In the linear part, different mechanical characteristics were measured with at least five specimens per configuration and reported in Table 2.

Table 3 below illustrates the values of the stresses and strains for the unidirectional specimens with different fiber orientations.

3.2 Flexural Bending Tests

Static and fatigue tests were carried using three-point bending tests for the unidirectional fiber specimens (UD0°). The tests were carried out using the standard hydraulic machine INSTRON. These specimens were tested according to the ASTM standard D790-86.

3.2.1 Static Results of Flax/GreenPoxy Composites

Flexural static tests have been conducted on unidirectional specimens UD 0° under displacement control with a constant rate of 2 mm · min^{-1}. Figure 2 shows the typical curve of stress/strain during the flexural test. The analysis of these results shows a short linear elastic domain followed by a nonlinear part. At the maximum load, a rapid drop has been seen in the load. A crack inside the composite was clearly visible. The values of the stiffness and fracture characteristics were obtained from the results of at least five test specimens. The obtained results are reported in Table 4.

3.2.2 Static Results of Flax/GreenPoxy with an Interleaved Viscoelastic Layer

In our previous studies (Daoud et al. 2016), a viscoelastic layer made of natural rubber (NR) has been introduced at the middle layer of the laminate in order to improve the damping properties of biocomposite. We have demonstrated that this layer can highly improve the dynamic behavior of the composite. In this study, the mechanical behavior of the structure with and without viscoelastic layer was investigated. Figure 3 shows the interposition of the stress/strain curves of the specimens in static bending tests. The maximum stress is about 135 MPa for the composite without natural rubber and it decreases to 85 MPa for the composite with

Fig. 2 Stress/strain curve of unidirectional Flax/GreenPoxy composite in three-point bending tests
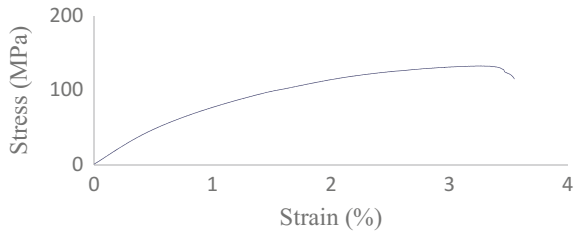
Table 4 Bending characteristics of flax fiber reinforced composites

Failure strain (%)	3.5
Failure stress (MPa)	135
Bending modulus (GPa)	10.2

Fig. 3 Stress/strain curves of unidirectional Flax/GreenPoxy composite with and without viscoelastic layer
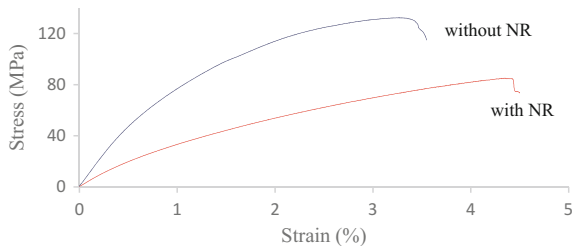
an interleaved natural viscoelastic layer. The figure shows also an important decrease on the slope of the composite with viscoelastic layer. This difference is due to the decrease of the rigidity and the strength of the composites.

3.2.3   Fatigue Results

The fatigue tests were performed on unidirectional specimens UD 0° having the same dimensions of the one used in static bending tests. They were conducted under displacement control using a sinusoidal waveform with a frequency of 5 Hz. The mean displacement is equal to 40% of the ultimate failure displacement in static tests ($d_m/d_u = 40\%$). The applied displacement level r (d_{max}/d_u) used is 55% where d_{max} is the maximum applied displacement in fatigue test. During this test, the displacement and the load were recorded up to 10,000 cycles.

Figure 4 shows a typical result of a fatigue test, which present the evolution of the maximum stress $\sigma_{max}/\sigma_{0max}$ as a function of the number of cycles using a semi-logarithmic scale (the maximum stress σ_{max} is referred to that obtained in the first cycle σ_{0max}). The results of the composite with and without viscoelastic layer have been presented in the same figure for comparison between the different materials.

For a given configuration, the loss of the rigidity, which is presented by the stress $\sigma_{max}/\sigma_{0max}$, is presented in two phases: the first one is a significant decrease in the first cycles, it could be associated to the initiation and the multiplication of the cracking of the resin and the fibers. This decrease is about 20% for the composite without natural rubber and 35% for the composite with an interleaved viscoelastic layer. This variation approves the fact that the viscoelastic layer decreases the strength of the composite. The second one, which is corresponding for almost the entire test, is characterized by a very slow decrease. It presents the stable propagations of the cracks during the test.

During these tests, 200 experimental points have been recorded for each cycle. The different hysteresis is then obtained from the experimental load and displacement data. Figure 5 presents the evolution of the obtained hysteresis with the
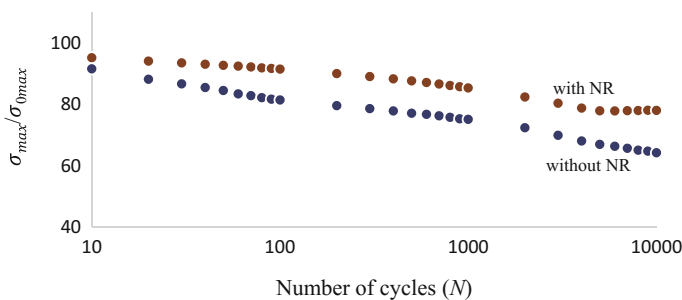
Fig. 4 Evolution of the stress ($\sigma_{max}/\sigma_{0max}$) versus number of cycles with and without viscoelastic layer
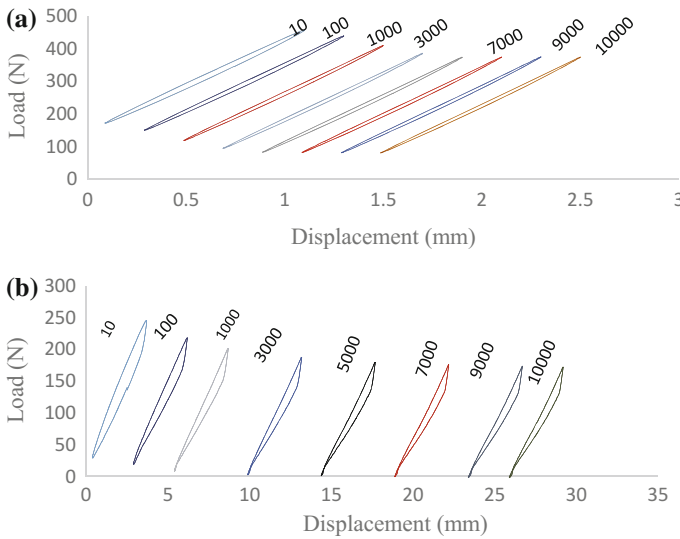
Fig. 5 Hysteresis loops for cyclic fatigue tests: **a** without NR and **b** with NR

number of cycles at 10, 100, 1000, 3000, 5000, 7000, 9000, and 10,000 cycles. The results with and without viscoelastic layer were discussed. The curves have been translated along the displacement axis in order to clarify the figure.

For the two configurations, while the number of cycle increases, the maximum load decreases and the area of the hysteresis cycles increases. This difference is due to the development of the damage governed by the degradation during the fatigue test of the laminates. Composites without a viscoelastic layer present a small area of the hysteresis loops (Fig. 5a) while those with an interleave layer of natural rubber presents a large area (Fig. 5b). A distortion of the hysteresis curves was also observed for the composite with viscoelastic layer. This distortion increases as the number of cycles increases. This variation can be explicated by the difference in the dynamic response on loading and unloading which is due to the viscoelastic layer's behavior.

The areas for the hysteresis loops present the dissipated energy E_d and the areas under the upper part of the curves represent the potential energy E_p. These quantities (E_d and E_p) have been calculated numerically using the trapezoid method.

Figure 6 shows the dissipated energy E_p as a function of the number of cycles for the composites with and without viscoelastic layer. For the different configurations, the dissipated energy decreases as the number of cycles increases. This decrease is presented by two phases: the first one is an important decrease in the first cycles (beginning of the damage in the composite structure) followed by the second one, which is characterized by a very slow decrease (stabilization). It was also observed that the compsoite with the viscoelastic layer dissipated more energy than this without this interleaved layer. This difference can reach the 100 mJ in the first cycles and it is around the 50 mJ for 10^4 cycles.
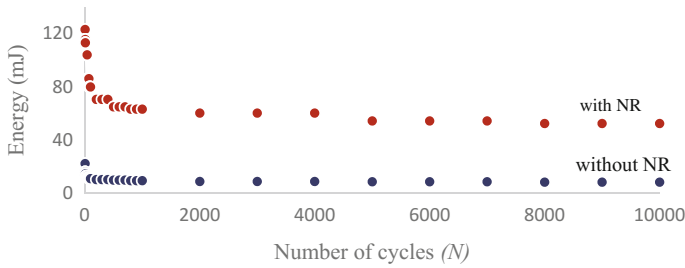
Fig. 6 Evolution of the dissipated energy as a function of the number of cycles with and without viscoelastic layer

The loss factor of the materials could be influenced by different processes such as the fiber/matrix interface, the damage, the porosities, the viscoelastic behavior of the different components constituting the structure. In this work, this factor is calculated in the cyclic fatigue tests as follows:

$$\eta = \frac{E_d}{2\pi E_p} \tag{2}$$

where E_d is the dissipated energy and E_p is the maximum potential energy.

Figure 7 shows the variation of the loss factor as a function of the number of cycles for the composite with and without the natural rubber. The curves present a decrease of this factor in the first cycles, and it becomes almost constant after a few hundred of cycles. Moreover, the composite with natural rubber presents very high values, which varies between 3 and 4% comparing with those without viscoelastic layer in which the maximum value of the damping is 1%. Therefore, this viscoelastic layer improves with a significant way the damping behavior of the structure.
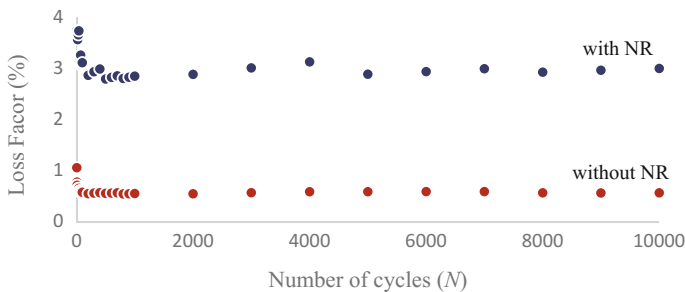
Fig. 7 Loss factor as a function of the number of cycles with and without viscoelastic layer

4 Conclusion

The mechanical properties of flax fibers reinforced composites under static and fatigue tests have been investigated. In the first part, different mechanical properties such as the characteristics at failure of the studied laminate structure were determined from tensile and bending static tests. The stiffness, hysteresis loops, and loss factors were also studied during cyclic fatigue tests. The results show a short linear elastic domain followed by a nonlinear part of Flax/GreenPoxy composite. In the second part, the effect of the insertion of a viscoelastic natural rubber on the mechanical behavior has been investigated. A comparison of the different properties with and without viscoelastic layer was made. This work brought interesting considerations regarding the damping behavior of the structure with an interleaved natural viscoelastic layer.

References

Abdul Nasir AA, Azmi AI, Khalil ANM (2015) Measurement and optimisation of residual tensile strength and delamination damage of drilled flax fibre reinforced composites. Measurement 75:298–307

Bensadoum F, Vallons KAM, Lessard LB, Verpoest I, Van Vuure AW (2016) Fatigue behaviour assessment of flax-epoxy composites. Compos A 82:253–266

Daoud H, Rebiere J-L, Makni A, Taktak M, El Mahi A, Haddar M (2016) Numerical and experimental characterization of the dynamic properties of flax fiber reinforced composites. IJAM S1758-8251. https://doi.org/10.1142/S175882511650068X

Daoud H, El Mahi A, Rebiere J-L, Taktak M, Haddar M (2016) Characterization of the vibrational behavior of flax fibre reinforced composites with an interleaved natural viscoelastic layer. Appl Acoust. https://doi.org/10.1016/j.apacoust.2016.12.005

Hristozov D, Wroblewski L, Sadeghian P (2016) Long-term tensile properties of natural fibre-reinforced polymer composites: Comparison of flax and glass fibres. Compos B 95:82–95

Liang S, Gning PB, Guillaumat L (2011) Comportement en fatigue des composites en lin/epoxy. JNC 17-Poitiers

Monti A, El Mahi A, Jendli Z, Guillaumat L (2016) Experimental and finite elements analysis of the vibration behaviour of a bio-based composite sandwich beam. Compos Part B 110:466–475. http://www.sciencedirect.com/science/article/pii/S1359836816320224

Monti A, El Mahi A, Jendli Z, Guillaumat L (2016) Mechanical behaviour and damage mechanisms analysis of a flax-fibre reinforced composite by acoustic emission. Compos Part A 90:100–110. http://www.sciencedirect.com/science/article/pii/S1359836816320224

Wambua P, Ivens J, Verpoest I (2003) Natural fires: can they replace glass in fibre reinforced plastics? Compos Sci Technol 63:1259–1264

Yan L, Chouw N, Jayaraman K (2014) Flax fibre and its composites. Rev Compos Part B 56:296–317

Mode I Fracture Energy of One-Component Polyurethane Adhesive Joints as Function of Bond Thickness for the Automotive Industry

Yasmina Boutar, Sami Naïmi, Taieb Daami, Salah Mezlini, Lucas F. M. da Silva and Moez Ben Sik Ali

Abstract The interfacial fracture of adhesively bonded structures is a serious issue for the widespread application of a variety of modern industries. For many manufacturing applications such as automotive structures, bond line thickness can vary considerably. This factor influences adhesively bonded joints performance. Therefore, its effect has to be examined experimentally and should be taken into consideration in the design of adhesive joints. Most of the results from the literature are for usual structural epoxy adhesives, which are usually formulated to perform in thin sections. However, polyurethane adhesives are designed to execute in thicker sections and might have a different behaviour as a function of adhesive thickness. In this study, an experimental procedure is undertaken to characterise the effect of different adhesive thicknesses between aluminium substrates on the mechanical behaviour of a one-component polyurethane adhesive. The mode I fracture toughness of the adhesive was measured using double cantilever beam (DCB) tests with various thicknesses of the adhesive layer ranging from 0.3 to 2 mm. The

Y. Boutar (✉) · S. Naïmi · T. Daami · S. Mezlini
Mechanical Engineering Laboratory, National Engineering School of Monastir,
Monastir University, Rue Ibn El Jazzar, 5000 Monastir, Tunisia
e-mail: jasmine.boutar@gmail.com

S. Naïmi
e-mail: sami.naimi@gmail.com

T. Daami
e-mail: daamitch@gmail.com

S. Mezlini
e-mail: salah.mezlini@gmail.com

L. F. M. da Silva
Faculdade de Engenharia, Departamento de Engenharia Mecanica,
Da Universidade Do Porto, Rua Dr. Roberto Frias, 4200-460 Porto, Portugal
e-mail: lucas@fe.up.pt

M. B. S. Ali
Automotive Industry- ICAR, Route de Monastir ZI Sidi Abdelhamid, 4003 Sousse, Tunisia
e-mail: moez.bensikali@icar-sa.com

393

fracture energy, G_{IC}, was found to be directed by the thickness of the adhesive layer. It increased linearly up to 1 mm adhesive thickness and then it decreases.

Keywords Fracture mechanics · Aluminium · Automotive industry Polyurethane · Double cantilever beam · Adhesive thickness

1 Introduction

The application of adhesively bonded joints in structural constituents for the automotive industry is widely known as an extremely valuable tool for mechanical design. This technic allows the production of connections that lead to lighter weight vehicles, fuel savings and reduced emissions. Nevertheless, the nature of adhesive connections does not allow it to replace all other connection techniques. A thoughtful use of it and the correct combination with other connection techniques can result in synergies that benefit the final product.

The main benefits are design flexibility, the opportunity for part consolidation and joining of dissimilar and/or new materials (Banea et al. 2014). Moreover, as reported by Banea and da Silva (2009), to predict the strength of adhesive joints perfectly, correct material data of adhesives is crucial. Hence, the investigation on the effect of bondline thickness on joint performance must be done and should be taken into consideration in the design of adhesive joints. In this context, the effect of the adhesive thickness has been investigated in the literature by studying the adhesive bonded joint fracture under mode I using double cantilever beam (DCB) joints (Ji et al. 2013; Hasegawa et al. 2015), tapered double cantilever beam (TDCB) joints (Kinloch et al. 1983; Kinloch and Shaw 1981; Lee et al. 2004), butt joints (Costa-Mattos et al. 2010; Naito et al. 2012), tubular butt joints (Castagnetti et al. 2011), or compact tension (CT) joints (Lee et al. 2004).

Furthermore, modern polyurethane adhesives are increasingly being used in structural joining applications as they present important advantages in terms of damping, impact, fatigue and safety which are critical factors in the automotive industry (Loureiro et al. 2010). However, most of the results from the literature regarding the effect of adhesive thickness are for typical structural epoxy adhesives, which are generally formulated to perform in thin sections, while polyurethane adhesives are designed to perform in thicker sections and might have a different behaviour as a function of the adhesive thickness. Therefore, it is important to know how polyurethane adhesive-bonded joints performance is affected by adhesive thickness. In this study, the effect of adhesive thickness on the mechanical behaviour of a structural one-component polyurethane adhesive designed for the automotive industry was investigated. The mode I fracture energy of the adhesive was measured using DCB tests with various thicknesses of the adhesive layer ranging from 0.3 to 2 mm.

2 Experimental Details

2.1 Material

The materials used in this study were an aluminium–copper alloy (see Table 1) and a one-component polyurethane adhesive (Table 2) (Boutar et al. 2016).

2.2 Specimens Manufacture

The DCB specimen was first standardised under (ASTM D 3433–99 2004) standard and now is included in the international standard (ISO 25217:2009 2009). The specimen consists of two beams bonded by an adhesive layer in which a pre-crack is previously introduced.

The DCB joint surfaces were grit blasted and degreased with acetone prior to the application of the adhesive. In order to ensure maximum strength, a primer treatment was applied on the surfaces and smoothed dried for about 15 min before the application of the adhesive (manufacturer recommendations). The specimen geometry and the loading are shown in Fig. 1.

The bondline thickness varied from 0.3 to 2 mm. Spacers Fig. 2a (calibrated steel bars C1 and C2) were inserted between the adherends before the application of the adhesive in order to control the bondline thickness. These spacers were removed after the adhesive was cured. A sharp pre-crack in the adhesive layer mid-thickness was assured using a razor blade Fig. 2b. A mould was used to guarantee the correct alignment of the adherends. The DCB joints were dried at room temperature (RT). The reticulation's time depends on adhesive thickness (Boutar et al. 2016). A dimensional verification was carried out with a calliper.

The horizontal distance from the tip of the razor blade to the point where the load is applied is called a_0, and known as the initial crack length. The knowledge of this

Table 1 Tensile properties of aluminium

Aluminium–copper alloys	
Yield strength (MPa)	≥ 190
Elongation at yield stress (%)	17
Poisson's ratio	0.33
Stiffness modulus (MPa)	26,500
Modulus of elasticity (MPa)	68,000

Table 2 Adhesive properties

Temperature (°C)	Young's modulus (MPa)	Tensile strength (MPa)	Tensile strain (%)
RT	2.15 ± 0.8	5.40 ± 0.15	230 ± 0.16
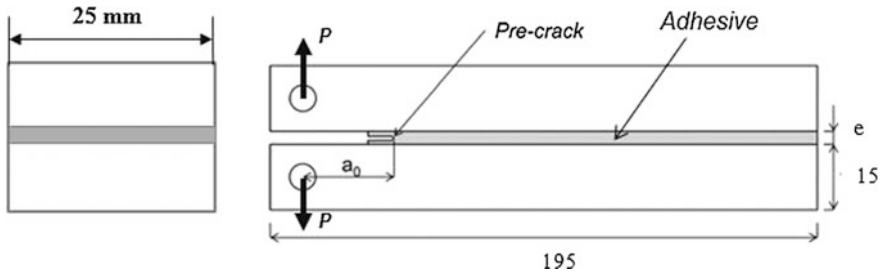
Fig. 1 DCB specimen geometry (dimensions in mm), e = 0.3, 0.5, 1 and 2 mm
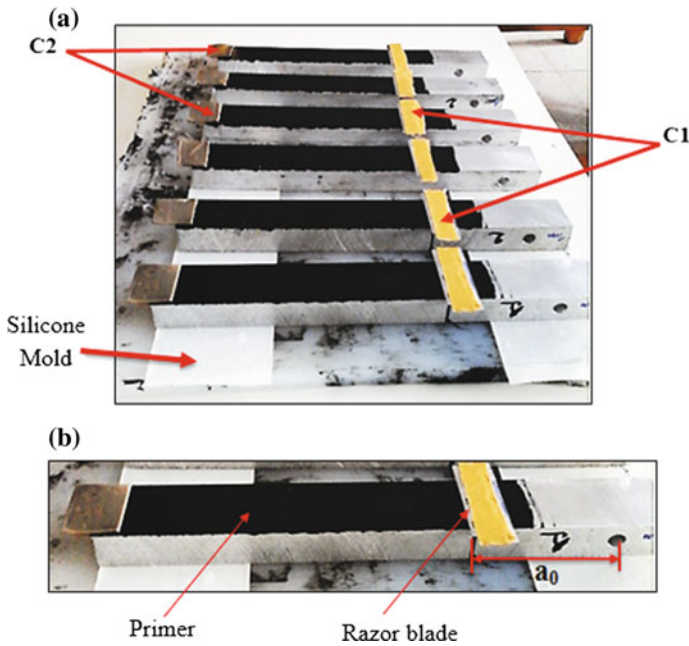
Fig. 2 Preparation of the specimens **a** configuration of the positioning of the substrates on the bonding device **b** preparation detail of the pre-crack

length is very important to obtain the crack propagation energy. For these tests, the value of a_0 was 50 mm, but each specimen was measured so that the a_0 value introduced in the calculations was as accurate as possible.

2.3 Test Method

Testing was conducted at RT using LLOYD 20 kN machine. Three joints were tested to failure for each adhesive thickness. Loads and displacements to failure were recorded. Figure 3 shows the DCB specimen test set-up.

It has been shown that for polymeric materials the ultimate properties vary with the strain rate (Banea et al. 2011; Carlberger et al. 2009; Martínez et al. 1998). For mode I loading, some authors indicated that the fracture toughness increases slightly with increasing strain rate (Carlberger et al. 2009), while others showed that the fracture energy is rate independent, (Sun et al. 2008). However, thicker ductile adhesive layers might present rate-dependent plasticity (Kinloch and Shaw 1981). Therefore, in order to avoid any influence of the strain rate on the results, the crosshead speed was set appropriately in order to produce a constant strain rate in the adhesive layer (1 min^{-1}) as established by Banea et al. (2015).
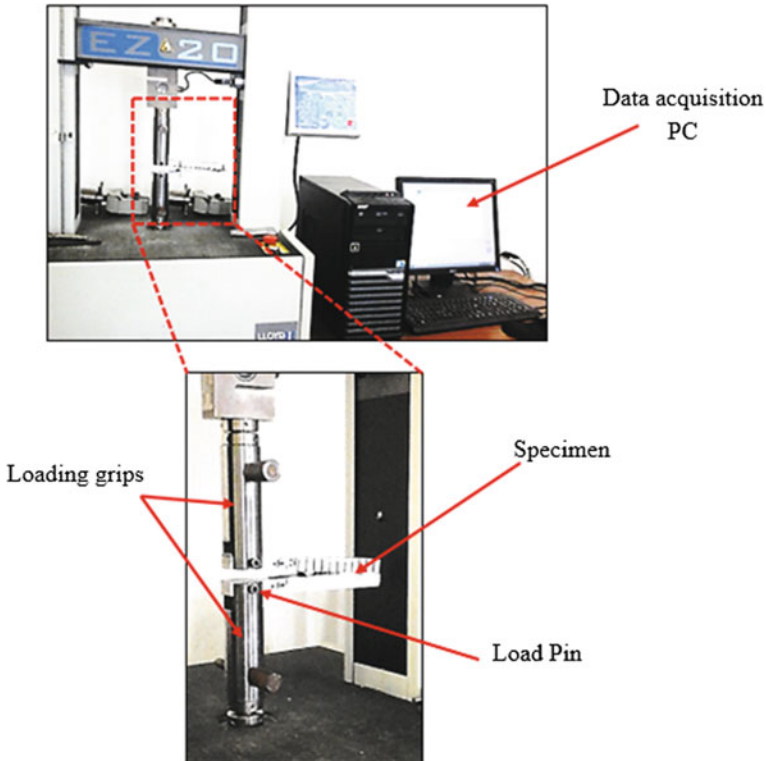
Fig. 3 DCB specimen test set-up

3   Results and Discussion

Representative experimental **P–δ** (Load/Displacement) curves of the DCB speci-
mens as a function of adhesive thickness are presented in Fig. 4. The strength
increases with increasing the thickness of the joint to a maximum observed with a
thickness of 1 mm and decreases for thicker bondlines. Furthermore, as we can see
for the four curves, after reaching a peak on the applied force it decreases pro-
gressively. This phenomenon is related, at first, to a start of the crack and then a
stage of crack propagation.

The geometrical parameters of the DCB test specimen used during the calcu-
lation of the fracture energy mode I are represented in Fig. 5.

The critical fracture energy in mode I, G_{IC}, was evaluated using the
compliance-based beam method. This method was developed by de Moura et al.
(2008). It does not require measuring the crack length during the test, because an
equivalent crack length is used, instead of the real crack length. The equivalent
crack can be obtained using the compliance defined in Eq. (1).

$$C = \frac{\delta}{P} = \frac{8}{bE_f}\left(\frac{a_{eq}}{h}\right)^3 + \frac{12}{5bG}\left(\frac{a_{eq}}{h}\right) \qquad (1)$$

E_f is a corrected flexural modulus to account for all phenomena affecting the P-δ
curve, such as stress concentrations at the crack tip and stiffness variability between
specimens;

Fig. 4 Representative experimental P-δ curves as a function of adhesive thickness

E_f was obtained using:

$$E_f = \left(C_0 - \frac{12(a_0 + |\Delta_I|)}{5bhG} \right)^{-1} \times \frac{8(a_0 + |\Delta_I|)^3}{bh^3} \tag{2}$$

a₀: Initial pre-crack;

G: Shear modulus of the adherends.

The initial compliance **C₀** is given by the expression (Blackman et al. 2003):

$$C_0 = \frac{8}{bE} \left(\frac{a_0 + \Delta_I}{h} \right)^3 \tag{3}$$

E is the Young's modulus of substrates
where Δ_I is a correction factor for crack length

$$\Delta_I = h \sqrt{\frac{E}{11G} \left[3 - 2 \left(\frac{\Gamma}{1+\Gamma} \right)^2 \right]} \tag{4}$$

with $\Gamma = 1.18 \frac{E}{G}$

The crack equivalent value is (Chaves et al. 2014):

$$a_{eq} = \frac{1}{6\alpha} A - \frac{2\beta}{A} \tag{5}$$

where the coefficients are:

$$\alpha = \frac{8}{bh^3 E_f}; \beta = \frac{12}{5bhG_{sub}}; \gamma = -C \tag{6}$$

$$A = \left(\left(-108\gamma + 12\sqrt{3\left(\frac{4\beta^3 + 27\gamma^2\alpha}{\alpha}\right)} \right) \alpha^2 \right)^{1/3} \tag{7}$$

Finally, using Irwin Kies expression:

$$G_{IC} = \frac{P^2}{2b} \frac{dC}{da} \tag{8}$$

G_{IC} can be obtained as fellow:

$$G_{IC} = \frac{6P^2}{b^2 h} \left(\frac{2a_{eq}^2}{E_f h^2} + \frac{1}{5G} \right) \tag{9}$$

Representative R-curves as a function of adhesive thickness are presented in Fig. 6. R-curves are used to identify the fracture energy from the plateau corresponding to the crack propagation.

The effect of adhesive thickness on the fracture energy, G_{IC} is presented in Fig. 7. It can be seen that the fracture toughness increased nearly linearly up to 1 mm adhesive thickness, while from 1 to 2 mm it decreases. Experience showed that when the adhesive has the ability to deform plastically, then plastic zone forms ahead of the crack tip creating a plastic zone (Papini et al. 1994).

The given results show that the adhesive fracture energy depends on the size of the plastic zone diameter (2rp), as expressed by Kinloch and Shaw (1981), in addition, the constraining effects of the two adherends control the plastic zone size (Ranade et al. 2014). Therefore, in this study, for the adhesive thickness less than
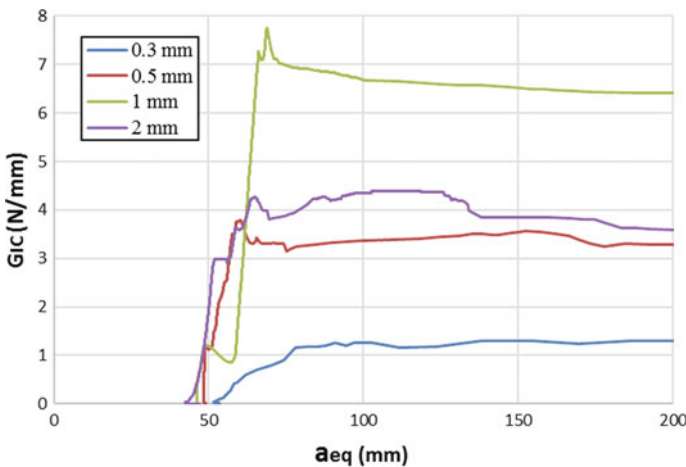
Fig. 6 Representative experimental R-curves as a function of adhesive thickness
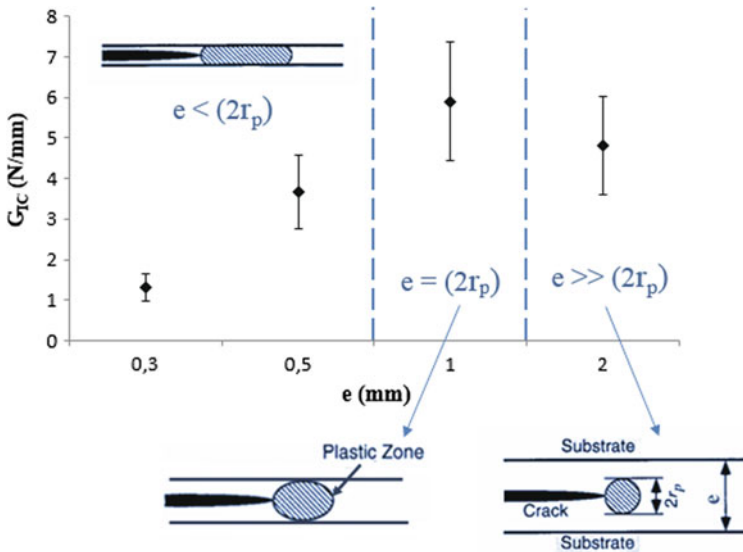
Fig. 7 G_{IC} as a function of adhesive thickness

1 mm, the increase of the adhesive layer induces an increase in the adhesive fracture energy due to the ability to generate plastic zones of increased sizes prior to fracture.

In this way, the plasticity spans the entire thickness of the adhesive, and the energy dissipated is proportional to the thickness. From 1 to 2 mm, G_{IC} decreased. This reduction might be explained by the fact that the amounts of defects such as microvoids are larger in thicker adhesive layers. On the other hand, it might due also to the fact that the effect of the adherends constraint is reduced for thick bondline.

4   Conclusion

This work demonstrates that the mode I fracture energy of a polyurethane one-component are sensitive to the adhesive thickness. In fact, the DCB testing procedure proves an increase in the G_{IC} value as the adhesive thickness increases until a thickness of 1 mm where G_{IC} reaches its maximum value. A decrease in the fracture energy was observed with the increase of the adhesive thickness from 1 to 2 mm. This result might be explained by the fact that at the head of the crack tip there is a formation of a plastic zone. Indeed, the size of this zone changes with the adhesive thickness allowing a proportional dissipation of the energy. On the other hand, defect-free joints with thicknesses equal or higher than 2 mm are difficult to fabricate and also are of less importance for practical applications.

References

ASTM D 3433 –99 (2004) Standard Test Method for Fracture Strength in Cleavage of Adhesives in Bonded Metal Joints. ASTM, 100 Barr Harb Drive, West Conshohocken, PA 19428–2959, United States 98:1–5. https://doi.org/10.1520/D3433-99R05

Banea MD, da Silva LFM (2009) Adhesively bonded joints in composite materials: an overview. J Mater Des Appl 223:1–18. https://doi.org/10.1243/14644207

Banea MD, da Silva LFM, Campilho RDSG (2015) The effect of adhesive thickness on the mechanical behavior of a structural polyurethane adhesive. J Adhes 91:331–346. https://doi.org/10.1080/00218464.2014.903802

Banea MD, da Silva LFM, Campilho RDSG, Sato C (2014) Smart adhesive joints: an overview of recent developments. J Adhes 90:16–40. https://doi.org/10.1080/00218464.2013.785916

Banea MD, de Sousa FSM, da Silva LFM et al (2011) Effects of temperature and loading rate on the mechanical properties of a high temperature epoxy adhesive. J Adhes Sci Technol 25:2461–2474. https://doi.org/10.1163/016942411X580144

Blackman BRK, Hadavinia H, Kinloch AJ, Williams JG (2003) The use of a cohesive zone model to study the fracture of fibre composites and adhesively-bonded joints. Int J Fract 119:25–46

Boutar Y, Naïmi S, Mezlini S et al (2016) Effect of adhesive thickness and surface roughness on the shear strength of aluminium one-component polyurethane adhesive single-lap joints for automotive applications. Int J Adhes Sci Technol 4243:1–17. https://doi.org/10.1080/01694243.2016.1170588

Carlberger T, Biel A, Stigh U (2009) Influence of temperature and strain rate on cohesive properties of a structural epoxy adhesive. Int J Fract 155:155–166. https://doi.org/10.1007/s10704-009-9337-4

Castagnetti D, Spaggiari A, Dragoni E (2011) Effect of bondline thickness on the static strength of structural adhesives under nearly-homogeneous shear stresses. J Adhes 87:780–803. https://doi.org/10.1080/00218464.2011.597309

Chaves FJP, da Silva LFM, de Moura MFSF et al (2014) Fracture mechanics tests in adhesively bonded joints: a literature review. J Adhes 90:955–992. https://doi.org/10.1080/00218464.2013.859075

Costa-Mattos HS, Monteiro AH, Sampaio EM (2010) Modelling the strength of bonded butt-joints. Compos Part B Eng 41:654–662. https://doi.org/10.1016/j.compositesb.2010.09.002

de Moura MFSF, Campilho RDSG, Gonçalves JPM (2008) Crack equivalent concept applied to the fracture characterization of bonded joints under pure mode I loading. Compos Sci Technol 68:2224–2230. https://doi.org/10.1016/j.compscitech.2008.04.003

Hasegawa K, Crocombe AD, Coppuck F et al (2015) Characterising bonded joints with a thick and flexible adhesive layer—Part 1: fracture testing and behaviour. Int J Adhes Adhes 63:124–131. https://doi.org/10.1016/j.ijadhadh.2015.09.003

ISO 25217:2009 (2009) Determination of the mode 1 adhesive fracture energy of structural adhesive joints using double cantilever beam and tapered double cantilever beam specimens. Int Stand. https://doi.org/10.5594/J09750

Ji G, Ouyang Z, Li G (2013) Effects of bondline thickness on mode-i nonlinear interfacial fracture of laminated composites: an experimental study. Compos Part B Eng 47:1–7. https://doi.org/10.1016/j.compositesb.2012.10.048

Kinloch AJ, Shaw SJ (1981) The fracture resistance of a toughened epoxy adhesive. J Adhes 12:59–77. https://doi.org/10.1080/00218468108071189

Kinloch AJ, Shaw SJ, Tod DA, Hunston DL (1983) Deformation and fracture behaviour of a rubber-toughened epoxy: 1. Microstruct Fract Stud Polym (Guildf) 24:1341–1354. https://doi.org/10.1016/0032-3861(83)90070-8

Lee D-B, Ikeda T, Miyazaki N, Choi N-S (2004) Effect of bond thickness on the fracture toughness of adhesive joints. J Eng Mater Technol 126:14. https://doi.org/10.1115/1.1631433

Loureiro AL, da Silva LFM, Sato C, Figueiredo MAV (2010) Comparison of the mechanical behaviour between stiff and flexible adhesive joints for the automotive industry. J Adhes 86:765–787. https://doi.org/10.1080/00218464.2010.482440

Martínez MA., Chocron IS, Rodríguez J et al (1998) Confined compression of elastic adhesives at high rates of strain. Int J Adhes Adhes 18:375–383. https://doi.org/10.1016/S0143-7496(98)00023-2

Naito K, Onta M, Kogo Y (2012) The effect of adhesive thickness on tensile and shear strength of polyimide adhesive. Int J Adhes Adhes 36:77–85. https://doi.org/10.1016/j.ijadhadh.2012.03.007

Papini M, Fernlund G, Spelt JK (1994) The effect of temperature on the strength of adhesive joints. Int J Adhes Adhes 14:185–190. https://doi.org/10.1016/0143-7496(92)90052-W

Ranade SR, Guan Y, Ohanehi DC et al (2014) A tapered bondline thickness double cantilever beam (DCB) specimen geometry for combinatorial fracture studies of adhesive bonds. Int J Adhes Adhes 55:155–160. https://doi.org/10.1016/j.ijadhadh.2014.08.006

Sun C, Thouless MD, Waas AM et al (2008) Ductile–brittle transitions in the fracture of plastically-deforming, adhesively-bonded structures. Part I: experimental studies. Int J Solids Struct 45:3059–3073. https://doi.org/10.1016/j.ijsolstr.2008.01.011

Scratch Resistance and Wear Energy Analysis of TiO$_2$ Coatings on 316L Stainless Steel

Hafedh Dhiflaoui and Ahmed Ben Cheikh Larbi

Abstract In this study, TiO$_2$ nanoparticles coatings were prepared on 316L stainless steel substrate by electrophoretic deposition (EPD) process. The morphology and composition were investigated, respectively. The influences of calcination temperature on the wear performance of coated films were also examined by scanning electron microscopy (SEM) and X-ray diffraction (XRD). A novel experimental process to improve the wear resistance was investigated. The energetic wear coefficients of wear were also studied. It was observed that the morphology and structure change with the heat treatment. The findings of scratch test showed that the calcined coating exhibited the ability to higher critical load. The relation between wear volume and dissipated cumulated energy was established for calcined and coated thin film, and the energetic wear coefficients of wear were deduced. The results prove that the heat treatment appreciably improves the wear resistance. Obviously, the calcined coating reduced the energetic wear coefficient, which enhanced the resistance to fretting wear.

Keywords TiO$_2$ coatings · Electrophoretic deposition · Adhesion Wear resistance

1 Introduction

At present, coating technology has found a wide array of applications. These include functional coating, decorative coating, industrial coating, thermal barrier coating, biomaterial coating, and others. Whatever the application is, the mechanical properties of the deposited coatings should be sufficient to satisfy the applications' requirements. Important mechanical properties include hardness, adhesion

H. Dhiflaoui (✉) · A. B. Cheikh Larbi
Université de Tunis, LMMP, 5 Av. Taha HUSSIN Monfleury, 1008 Tunis, Tunisia
e-mail: dhafedh@gmail.com

A. B. Cheikh Larbi
e-mail: ahmed.cheikhlarbi@gmail.com

strength, and coefficient of friction. The growing interest in powder coatings has opened new challenges toward the definition of new material formulations, which can improve film properties. There exist many methods for deposited powder coating, each of them has advantages and disadvantages. The most famous are plasma and flame spraying (Xu et al. 2014; Ali et al. 2011), electrophoretic deposition (De Riccardis et al. 2008; Dhiflaoui et al. 2016), sol-gel (Bayati et al. 2010), dipping method, and micro-arc oxidation (Pan et al. 2013).

Electrophoretic deposition is a simple and low-cost technique, which consists in the migration of the charged particles powder in suspension under the effect of an electric field. The particles will agglomerate and form a homogeneous layer at the surface of the substrate used as an electrode. This process has numerous advantages like its short processing time as well as its ability to control the surface morphology and the thickness of the coatings (Drevet et al. 2016). However, the electrophoretic deposition technique needs further heat treatment to remove volatile species from the films and to enhance their mechanical properties.

TiO_2 is an important inorganic material because of its good physical properties, which make it appropriate for coating applications. Also, coatings of TiO_2 enhanced tribological properties of metal surfaces (Wang et al. 2009; Comakli et al. 2014; Antony et al. 2016). The influence of TiO_2 coating on tribological properties of substrate material and the effect of process parameters on properties of TiO_2 oxide film in the scientific literature were shown (Fu et al. 2012; Mechiakh et al. 2010; Surowska et al. 2010).

Very few studies have studied the energetic approach in wear for TiO_2 coating elaborated by electrophoretic deposition. Therefore, this work aims at producing, for the first time, a nano-TiO_2 coating which studies the wear resistance by electrophoretic deposition.

In this study, thin films of TiO_2 were deposited on 316L stainless steel substrate by electrophoretic deposition method. Microstructure, adhesion, and wear properties were investigated.

2 Materials and Methods

2.1 Coating Preparation

The substrate used for the surface coating was a 316L stainless steel disk of 15 mm in diameter and 3 mm in thickness. Prior to deposition, the substrates were abraded and polished using silica paper up to 1200 grit size. The substrates were then cleaned ultrasonically in a diluted acetone bath for 25 min at 60 °C. The substrates were ultrasonically cleaned a second time in ethanol followed by rinsing in distilled water. This was done to ensure that the substrate surface was free from contaminants and acetone residues.

After preparing the substrates, deposition was then carried out. We used TiO$_2$ powder from Aldrich (Sigma-Aldrich Corporation, St. Louis, MO, USA) where 99.7% of the particles have dimensions less than 25 nm. The electrolyte solution is composed of a mixture of 0.06 g of TiO$_2$ nanopowder with 60 ml of absolute ethanol where 99.8%. An aluminum plate with a dimension of 20 × 15 mm^2 was used as a counter electrode (anode). Each electrode was submerged into the prepared media with a 1 cm distance. The suspensions were magnetically stirred for 5 min followed by 15 min ultrasonification, subsequently followed by 5 min of stirring. Optimized EPD was performed at an applied voltage of 30 V, for 5 min at room temperature. Finally, the deposited coatings were air dried for 24 h.

Some of the coatings were subjected to annealing at 850 °C for 2 h. Heating rate of 2.5 °C/min was used while cooling was allowed to take place naturally inside the furnace. A desirable temperature due to the possible transformation of the anatase phase in the TiO$_2$ particles will be converted to the rutile phase.

2.2 Characterization

The morphologies of the coatings surface were observed using a LaB6 scanning electron microscope (JEOL JSM 6460 LV) operating at 0–30 keV. This microscope is associated with an ultra-thin window Si (Li) detector for the energy dispersive X-ray analysis.

The phase composition of the samples was investigated using an X-ray diffractometer (Bruker D8 Advance). The X-ray pattern data were collected from 2θ = 20° to 70° using a monochromatic CuKα radiation with a step of 0.02° every 4 s. XRD analysis was carried out before and after the thermal treatment. The identification of phases was performed by using the Powder Diffraction Files (PDF) of the International Center for Diffraction Data (ICDD).

The TiO$_2$ coatings were subjected to a series of adhesion strength measurements using a scratch-tester type MST (CSM instruments, Switzerland) which was equipped with a Rockwell spherical diamond tip with a radius of 100 nm. A minimum of three scratches were made on the coatings. The scratch tests were performed by increasing continuously the normal load from 30 mN to 10 N. The loading speed was 0.5 N.s^{-1} and the track length was 5 mm.

The critical loads were recorded based on the scratch profile of the load–displacement graph. It was verified with an optical image of the scratch path since it was discovered that some failure modes can occur without a noticeable change in the scratch profile. Three values of critical loads were recorded and referred to as LC1, LC2, and LC3 in this study. LC1 indicates the failure characterized by trackside cracking, which appears to be cohesive in nature. LC2 is the load at which delamination on the trackside, accompanied by mild tensile cracking, is observed but not along the scratch path. This can also be typified by a mixture of adhesive and cohesive failure. Finally, LC3 is the load at which the coatings are delaminated along the scratch path.

Wear tests were done with a CSM micro-scratch tester, a spherical diamond Rockwell indenter, tangent the surface, having a tip radius of 50 μm, and a cone angle of 60°. After indentation, this indenter was carried out by a scratch at a constant normal load. The sensor system measured the normal and tangential forces in real time. For these tests, the normal force (Fn), the sliding speed (V), the number of cycles and the sliding distance (L) were being controlled. Each test was conducted for 500 cycles of repeated passages and the sliding amplitude (L) was equal to 3 mm with laboratory temperature equal to 22 °C and relative humidity of 46%. The normal loads were 1, 1.5, 2, 2.5, and 3 N, while the sliding velocities were 100, 200, and 300 μm/s.

3   Results and Discussions

3.1   PhysicoChemical and Structural Study

Figure 1 shows the XRD patterns before and after thermal treatment of TiO_2 thin films. Distinctive peaks, at $2\theta = 27.4°$, $36.1°$, $39.2°$, $41.2°$, $54.3°$, $56.6°$, $62.7°$, $64.07°$, and $69.04°$ corresponding to the (110), (101), (200), (111), (211), (220), (002), (310), and (301) planes, are observed. When the coating is heated, the intensities of anatase peaks decrease, while the intensities of the rutile peaks increases. Besides, at 850 °C, the anatase phase nearly transforms into the rutile phase.

The surface morphology of the untreated and the coated sample calcined at 850 °C are shown in Fig. 2. The as-deposited surface exhibits a smooth and uniform porous layer. Some small voids are present for the untreated coating, indicating a low density. By further increasing the annealing temperature to 850 °C, the coating becomes dense, homogenous in microstructure, and rather uniform in its

Fig. 1 The X-ray diffraction pattern of coating: **a** before and **b** after thermal treatment
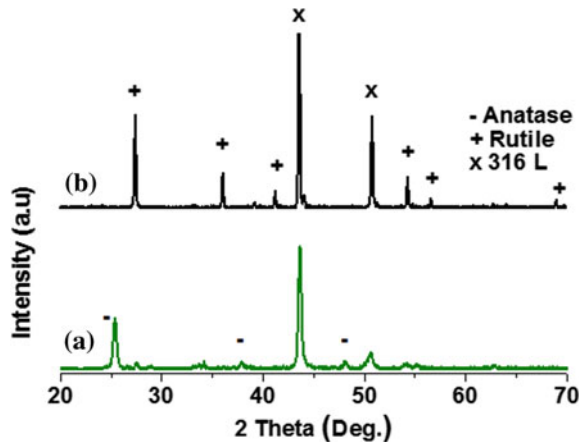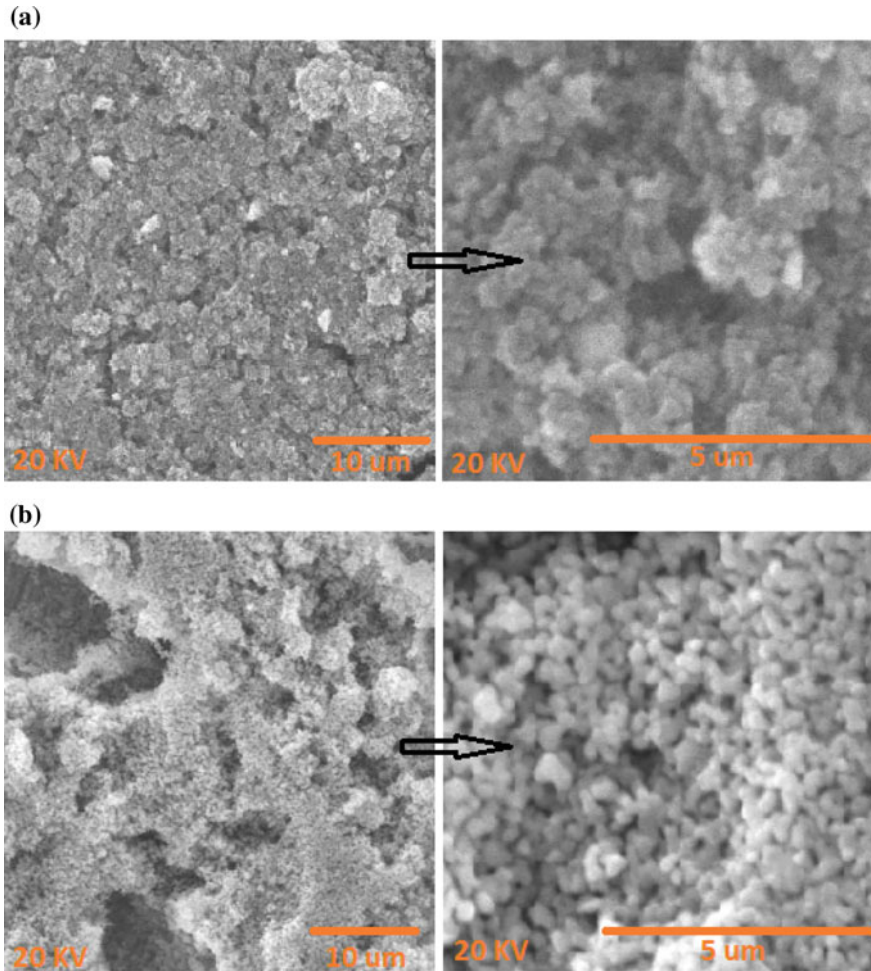
Fig. 2 SEM micrograph of the TiO₂ coating before (**a**) and after thermal treatment (**b**)

thickness with spheroids having diameters inferior to 100 nm. Such morphological transformation resulted from the rutile phase evolution.

3.2　Adhesion Strength Measurement

The evaluation of critical loads is typically performed with the addition of the information obtained from the analysis of the deformation response and the involved forces during and after the progressive scratch test mode. Figure 3 presents the scratch test result obtained on the TiO₂.

Fig. 3 Scratch-test study before and after thermal treatment
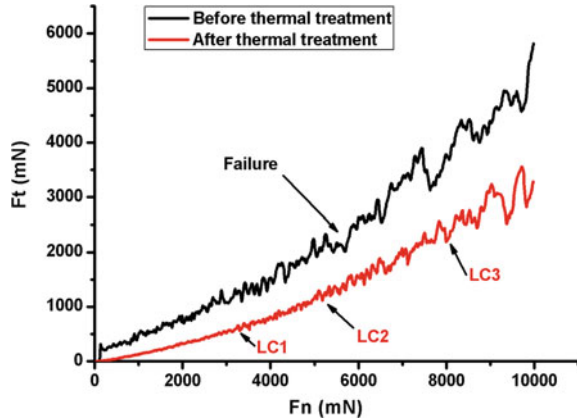
Table 1 Critical loads obtained by scratch test of the TiO$_2$ coatings

	Untreated		850 °C
LC1	5.6		3.22
LC2	–		5.08
LC3	–		7.99

The three critical loads LC1, LC2, and LC3 are identified. Their values are summarized in Table 1. In the case of the untreated coating (Fig. 3a), the friction force suddenly increases for a critical load LC1 = 5.6 N, which corresponds to the total remove of the coating observed. Before this critical load, the friction force of the coating remains very low which indicates the poor load-bearing capacity of the untreated coating. For the calcined coating (Fig. 3b), the friction–load curve is different with three critical loads meaning that the spallation of the coating occurs gradually. The first critical load LC1 = 3.22 N reveals the start of the coating cracking associated with its cohesive limit. The second critical load LC2 = 5.08 N indicates the start of the coating spallation linked to its adhesive limit. The total remove of the coating is then observed at LC3 = 7.99 N. The increase of the critical load associated with the adhesive limit clearly demonstrates that the heat treatment improves the coating adhesion to the substrate.

3.3 Adhesion Strength Measurement

The friction energy can activate numerous damage mechanisms, such as abrasion, oxidation, debris formation, and ejection. The wear resistance of the deposits was
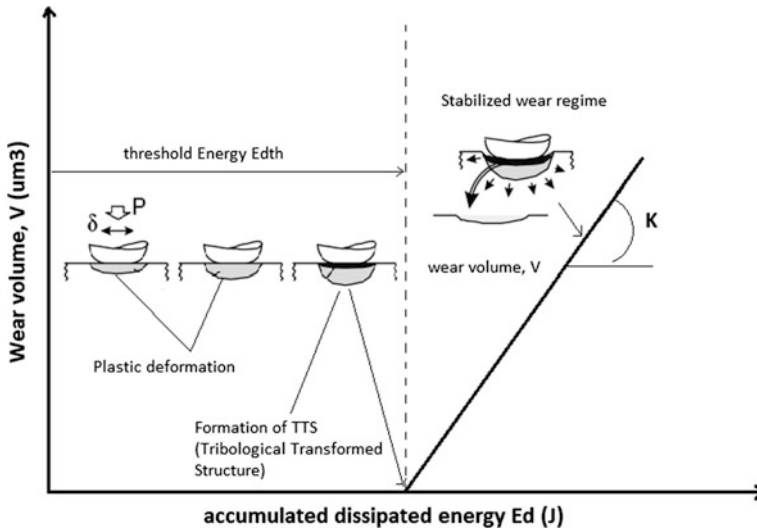
Fig. 4 Schematization of the wear process (Fouvry et al. 2001)

evaluated according to the evolution of the spent coating volume as a function of the energy dissipated by friction. These two parameters are linked by the relation.

$$V = K.E_t \tag{1}$$

K is called the energy coefficient of wear and is expressed in μm^3 of used material per joule dissipated in the contact. It can be noted that for coatings, the linear approximation does not cross the origin, but presents a small shift along the energy axis. This quantity is related to threshold energy Edth, required to first transform the structure before generating wear particles. During the incipient loading, the surface endures severe strain-hardening, which modifies the initial microstructure to a very hard phase called a tribologically transformed structure (TTS) Fig. 4.

The energy approach was applied to analyze two different coatings. Figure 5 compares the different wear energy coefficient, outlining a significantly higher wear resistance of the calcined coatings compared to the untreated coating. Results show that the coated coating provides an energetic wear coefficient of 51240 µm 3/J, while that of untreated sample was 105970 µm 3/J. Experimental findings reveal also that energetic wear coefficient decreases with increasing the calcination temperature. This result shows the good wear resistance of the coating treated at 850 °C.
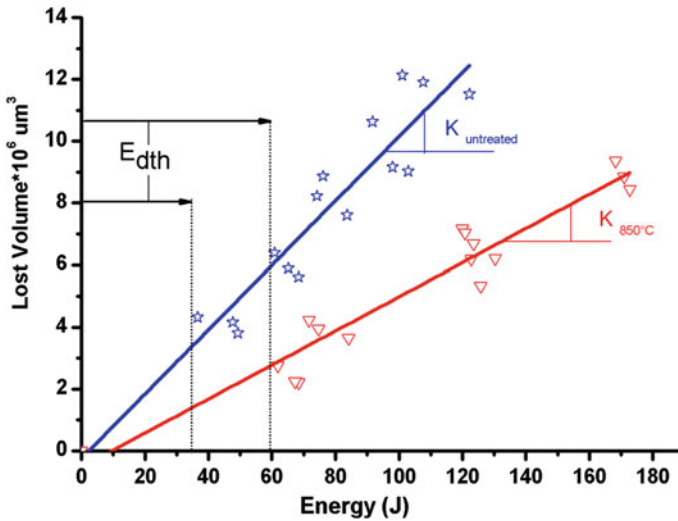
Fig. 5 Variation of the worn volume as a function of dissipated energy

4   Conclusion

This work attempt to study the heat treatment to the friction energy and wear resistance of the considered coatings, on the one hand, and to evaluate their scratch resistance, on the other. Surface observations demonstrated that the agglomerate spheroids/porous morphology play a dominant role in improving the TiO_2 coating adhesion properties. XRD results showed that the structure of the coating changes with the heat treatment temperature. Wear resistance can be described by the energetic wear coefficient deduced from the linear relation between the used volume and dissipated cumulated energy. Calcined coating improves the wear resistance of 316L stainless steel.

References

Ali R, Alkhateeb E, Kellner F, Virtanen S, Popovska-Leipertz N (2011) Chemical vapor Deposition of titanium based ceramic coatings on low carbon steel: characterization and electrochemical evaluation. Surf Coat Technol 205:5454–5463
Antony Vasantha Kumar C, Selwin Rajadurai J (2016) Influence of rutile (TiO_2) content on wear and microhardness characteristics of aluminium-based hybrid composites synthesized by powder metallurgy. Trans Nonferrous Met Soc China 26:63–73

Bayati MR, Zargar HR, Talimian A, Ziaee A, Molaei R (2010) Characterization of Al2O3–TiO$_2$ nano porous solar absorbers derived via MAO/sol-gel hybrid process. Surf Coat Technol 205:2483–2489

Çomakl O, Yetimb T, Çelik A (2014) The effect of calcination temperatures on wear properties of TiO$_2$ coated CP-Ti. Surf Coat Technol 246:34–39

De Riccardis MF, Carbone D, Piscopiello E, Antisari MV (2008) Electron beam treatments of electrophoretic ceramic coatings. Appl Surf Sci 254:1830–1836

Dhiflaoui H, Khlifi K, Cheikh larbi AB (2016) Effect of deposition parameters on electrophoretically deposited TiO$_2$. Res Rev: J Mater Sci (RRJOMS) 4

Drevet R, Ben Jaber N, Faure J, Tara A, Ben Cheikh Larbi A, Benhayoune H (2016) Electrophoretic deposition (EPD) of nano-hydroxyapatite coatings with improved mechanical properties on prosthetic Ti6Al4 V substrates. Surf Coat Technol 301:94–99

Fu T, Wen CS, Lu J, Zhou YM, Ma SG, Dong BH, Liu BG (2012) Sol-gel derived TiO$_2$ coating on plasma nitrided 316L stainless steel. Vacuum 86:1402–1407

Fouvry S, Kapsa Ph (2001) An energy description of hard coating wear mechanisms. Surf Coat Technol 138:141–148

Mechiakh R, Ben Sedrine N, Chtourou R, Bensaha R (2010) Correlation between microstructure and optical properties of nano-crystalline TiO$_2$ thin films prepared by sol–gel dip coating. Appl Surf Sci 257:670–676

Pan YK, Chen CZ, Wang DG, Lin ZQ (2013) Preparation and bioactivity of micro-arc oxidized calcium phosphate coatings. Mater Chem Phys 141:842–849

Surowska B, Bienia J (2010) Composite layers on titanium and Ti6Al4 V alloy for medical applications. JAMME 43:162–169

Wang D, Gordon PB (2009) Sol–gel coatings on metals for corrosion protection. Prog Inorg Coat 64:327–338

Xu Z, Dai J, Niu J, Li N, Huang G, He L (2014) Thermal shock behavior of platinum aluminide bond coat/electron beam-physical vapor deposited thermal barrier coatings. J Alloys Compd 617:185–191

Analysis of Double Reducer Stage Using Substructuring Method

Marwa Bouslema, Ahmed Frikha, Taher Fakhfakh, Rachid Nasri and Mohamed Haddar

Abstract Global dynamics of a coupled system are synthesized using a substructuring technique based on the transfer functions of the subsystems. In this chapter, the substructuring method was applied in transmission system. The Frequency-Based Substructuring (FBS) methods are considered to identify the dynamic behavior of a structural system. Impedance coupling technique is applied to a double reducer stage, which is based on the Frequency Response Functions (FRFs) of each substructure and constraint conditions in the connection coordinates. The FRF-based substructuring technique has been previously proposed for computing the vibration modes of complex structural system by coupling the FRF of each subsystem. The effect of damping on substructuring method was discussed. Finally, the coupling technique is validated by comparing the present results with the full system ones. The major interest of using this method is that it allows replacing each subsystem by another subsystem without repeating the computation of the full system.

Keywords Coupling method · Frequency response function
Frequency-based substructuring · Transmission system

M. Bouslema (✉) · A. Frikha · T. Fakhfakh · M. Haddar
Mechanical Modeling and Manufacturing Laboratory (LA2MP),
National School of Engineers of Sfax, University of Sfax,
B.P 1173-3038, Sfax, Tunisia
e-mail: marwa.bouslema@yahoo.fr

A. Frikha
e-mail: frikhaahmed@yahoo.fr

T. Fakhfakh
e-mail: tahar.fakhfakh@enis.rnu.tn

M. Haddar
e-mail: mohamed.haddar@enis.rnu.tn

R. Nasri
Applied Mechanics and Engineering, University of El-Manar II, 1002 Tunis, Tunisia
e-mail: rachid.nasri@enit.rnu.tn

1 Introduction

The complex mechanical structure object of this study is a multicomponent-assembled system. In many applications, such systems are so complex and the corresponding numerical models are so complicated that the global system resolution methods require much more CPU and calculus time. In order to simplify the analysis of such systems and safe computational time, many researchers were interested in the study of the substructuring method and component mode synthesis presented by Jetmundsen et al. (1988) and Craig and Bampton (1968).

The substructuring techniques such as coupling method were proposed in Liu and Ewins (2002) This method was introduced in order to reduce both the complexity of dynamical models and the size of computational models (Guyan 1965).

The basic idea of dynamic substructuring method consists of dividing the full system into subsystems. Each part can be analyzed separately. After that, an assembly procedure should be used in order to couple them together.

On the other hand, the base of this substructuring technique is the FRF representations which allow predicting the overall coupled system response.

According to D'Ambrogio and Fregolent (2008), this tool of substructuring makes the task of coupling or decoupling components easy such as using additional knowledge of interface characteristics.

Several approaches were proposed in the literature to solve the coupling method. Choi and Park (2002) applied the impedance coupling method in rotating systems based on the FRFs of each substructure to pumps. D'Ambrogio and Fregolent (2010) used the decoupling method for a torsional system. Jetmundsen et al. (1988) have described the FRF coupling method.

The global system is analyzed to be more difficult than the local dynamic behavior. In fact, when one substructure is replaced by another, the dynamic substructuring allows a rapid determination of the dynamic complete system. For more details, only the changed sub-part needs to be calculated. In addition, the use of FRF allows joining substructures of different types. Since most configurations can be used to produce the proper response, behavior function is needed for the coupling task. The objective of this work is to prove the two suggested analytical procedures; the results of substructure coupled method FRF are compared to ones from a full system model of the double reducer stage.

This chapter is structured as follows. The theoretical principals of FBS are described in sect. 2. Then, a description of the studied system is presented. Sect. 3 gives an explanation of the full system FRF and the coupling method FRF. Finally, a comparison between the FRF of the full system and the one of the coupling method for a double reducer stage is presented in sect. 4.

2 Theory of FBS

The objective of the FBS is interested in the dynamic behavior of a rigidly coupled system. This method is based on the FRF of the uncoupled subsystem. The FRF of the global system is obtained by combining the FRF of each component.

2.1 Frequency Response Functions (FRF)

The FRF coupling method was described in Bishop and Johnson (1960). The FRF of the subsystem can be expressed theoretically by considering the dynamic equations of motion in time domain. The motion equation of a damped linear subsystem is expressed by:

$$[M]\{\ddot{U}(t)\} + [C]\{\dot{U}(t)\} + [K]\{U(t)\} = \{F(t)\} \tag{1}$$

where $[M]$, $[K]$, and $[C]$ are the mass, stiffness, and damping matrices of subsystem, respectively. $\{U(t)\}$ and $\{F(t)\}$ represent the displacement and the excitation force, respectively.

The second step consists to determine the FRF of the subsystem by performing an FRF synthesis based on a mode shape and natural frequencies of the damped subsystem. The application of Fourier transformation on Eq. (1) leads to Choi and Park (2002):

$$H_{jk}(w) = \sum_{r=1}^{n} \frac{{}_r\Phi_{jr}\Phi_k}{w_r^2 - w^2 + j2\xi_r w_r w} \tag{2}$$

where $H_{jk}(w)$ is the steady-state displacement at coordinate j due to a harmonic force excitation at coordinate k, n is the number of Degrees of Freedom (DoFs). ${}_r\Phi_j$ is the mass-normalized eigenvector.

2.2 Substructure Coupling Method

The fundamental concept of this technique consists of using individual uncoupled component FRFs to construct the total system response via either an impedance computational equation.

The coupling problem is formalized mathematically in Liu and Ewins (2002) The receptance matrices of subsystems "A" and "B," used in the frequency-based substructuring method to couple the substructures, are expressed as in Jetmundsen et al. (1988) by:

$$
\begin{bmatrix} _A U_i \\ \dots\dots \\ _A U_c \end{bmatrix} = \begin{bmatrix} _A H_{ii} | _A H_{ic} \\ \dots\dots | \dots\dots \\ _A H_{ci} | _A H_{cc} \end{bmatrix} \begin{bmatrix} _A f_i \\ \dots\dots \\ _A f_c \end{bmatrix} \tag{3}
$$

$$
\begin{bmatrix} _B U_j \\ \dots\dots \\ _B U_c \end{bmatrix} = \begin{bmatrix} _B H_{jj} | _B H_{jc} \\ \dots\dots | \dots\dots \\ _B H_{cj} | _B H_{cc} \end{bmatrix} \begin{bmatrix} _B f_j \\ \dots\dots \\ _B f_c \end{bmatrix} \tag{4}
$$

Each structure can be divided into uncoupled DoF (index ''i'' for structure A and index ''j'' for structure B) and DoF that are coupled (index ''c'') namely the coupling DoFs. The subsystem A is rigidly connected to subsystem B at DoF c. The equation of motion is given by Eqs. (3) and (4). The coupled system FRF is developed according to Jetmundsen et al. (1988)

$$
\begin{bmatrix} H_{aa} & H_{ac} & H_{ab} \\ H_{ca} & H_{cc} & H_{cb} \\ H_{ab} & H_{bc} & H_{bb} \end{bmatrix} = \begin{bmatrix} _A H_{ii} & _A H_{ic} & 0 \\ _A H_{ci} & _A H_{cc} & 0 \\ 0 & 0 & _B H_{jj} \end{bmatrix}
$$
$$
- \begin{bmatrix} _A H_{ic} \\ _A H_{cc} \\ _B H_{ic} \end{bmatrix} \left[[_A H_{cc}] + [_B H_{cc}] \right]^{-1} \begin{bmatrix} _A H_{ic} \\ _A H_{cc} \\ _B H_{ic} \end{bmatrix}^T \tag{5}
$$

where $[_A H]$ and $[_B H]$ are the FRF matrices of substructures A and B, respectively. Subscript i and j represent internal DoFs and c denotes the coupling DoFs. The sub-matrices of the whole system were identified by Liu and Ewins (2002). Equation (5) is applied to calculate the coupling FRF of full system.

3   Model Description

A two-stage spur gear mechanism is considered in this chapter. The present system is formed by two subsystems rigidly connected in DoF c. Subsystem A is a torsional model with four DoFs with parameters concentrated as in Lin and Parker (2001). Gears are modeled by concentrated masses. The gear mesh stiffness is modeled by a linear spring and damping acting on the line of action of the meshing teeth. Shaft (2) is coupled to shaft (3) by a rigid coupling of inertia I_a. To verify the coupling technique, two methods are used which are the substructure coupled method and the full system FRFs.

3.1 Substructure Coupled Method Based on FRF

This method couples two subsystems as presented in Fig. 1. The coupling inertia is divided into two equal inertia (Gladwell 1964). A system which is an assembly of two subsystems rigidly connected to one DOF is studied.

Both subsystems A and B are modeled by discreet masses, linear springs, and viscous dampers. The subsystem can be presented by:

$$[M]\{\ddot{Q}\} + [C]\{\dot{Q}\} + [K]\{Q\} = \{F\} \tag{6}$$

where [M], [C], and [K] are respectively the global mass, damping, and stiffness matrices of the whole system. Q is the vector of DoFs, which is expressed by:

$$Q = [\theta(1,1) \quad \theta(1,2) \quad \theta(2,1) \quad \theta(2,2)] \tag{7}$$

The DOF of the subsystem can be partitioned into internal DOFs and coupling degree.

The mass matrix is expressed by:

$$[M] = diag\,[I(1,1),\,I(1,2),\,I(2,1),\,I(2,2)]. \tag{8}$$

The torsional stiffness and damping of the shaft are $k_{\theta(i,j)}$ and $c_{\theta(i,j)}$ where $(i,j = 1,2)$. The gear mesh stiffness [K] is expressed in Chaari et al. (2008)
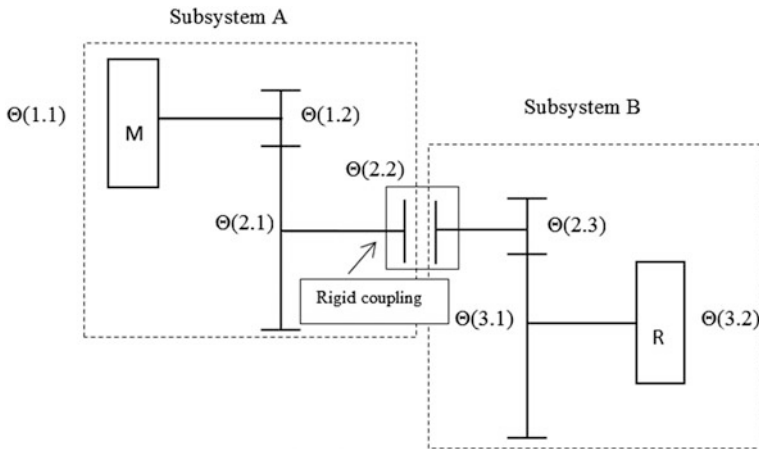
Fig. 1 A double reducer stage with rigid coupling

3.2 Full System FRF

The full system method consists to compute the overall system without partitioning into subsystems. The determination of dynamic behavior of the full system is expressed in FRFs. The DoFs of the full system is expressed by:

$$Q = [\theta(1,1) \quad \theta(1,2) \quad \theta(2,1) \quad \theta(2,2) \quad \theta(2,3) \quad \theta(3,1) \quad \theta(3,2)] \quad (9)$$

The mass matrix M is expressed by:

$$[M] = diag\,[I(1,1), I(1,2), I(2,1), I(2,2), I(2,3), I(3,1), I(3,2)] \quad (10)$$

The stiffness, mass, and damping matrices are determined using Lagrange formalism before applying the FRF method.

4 Numerical Applications

4.1 Validation of Substructuring Technique

To validate the performance of the FBS method in transmission system, the results of the coupling analysis are compared to ones from a full system model of the reducer stage gear. The frequency response function and the coupling methods are used to calculate the transfer functions of each subsystem and the global system one.

The studied case presents two subsystems having the same parameters for both stages of reducer. The values of these parameters are given in Table 1.

The coupled method FRF was calculated from the Eq. (5). The FRF receptance H presents the ratio displacement/force. The receptance of each subsystem in coupling method is investigated to be the same one as those used in the full system. In the first study, the damping is neglected. Figure 2 shows that the two curves are identical in both the frequency and the magnitude. The results using the impedance coupling method is in good agreement with those of the full system method. A good

Table 1 Parameters of the studied two-stage gear system

Torsional damping	$C\theta_i = 5.5 \times 10^{-2}$ (Nm s/rad)
Torsional shaft flexibilities	$K\theta_i = 10^5$ (Nm/rad)
Pressure angle	$\alpha 1 = \alpha 2 = 20°$
Teeth module	$m = 4 \times 10^{-3}$ (m)
Teeth number	$Z_1 = 30; Z_2 = 45; Z_3 = 30; Z_4 = 45$
Average mesh stiffness	$K_{1moy} = K_{2moy} = 4.8 \times 10^7$ (N/m)
Teeth width	$b = 3 \times 10^{-2}$ (m)
Inertia coupling	4.48×10^{-8}
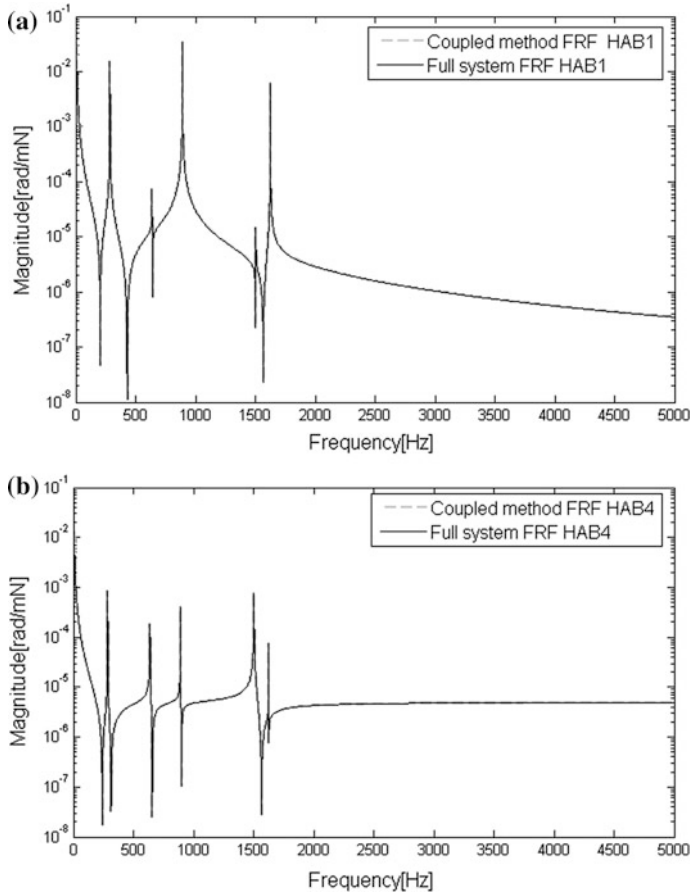
Fig. 2 Transfer function based on the coupled method and the full system: **a** FRF at the degree of motor, **b** at the coupling DoF

accuracy is observed between the natural frequencies obtained by the substructure coupling and those calculated by the full system FRF method.

4.2 Effect of Damping on Substructuring Method

A study is focused to analyze the effect of damping on substructuring method.

The corresponding numerical results are illustrated in Fig. 3. It appears that in Fig. 3a, b, the introducing of damping has a good agreement for the same frequency. Nevertheless, some difference appears in magnitude between the full system FRF curve and the coupled method FRF curve with different degree.
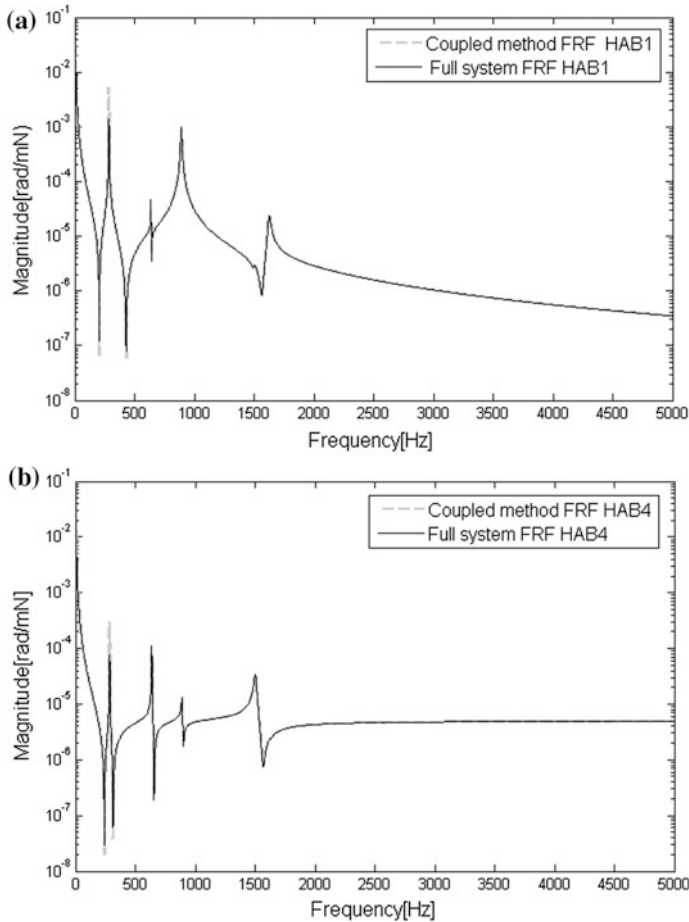
Fig. 3 Effect of damping on the substructuring method, **a** FRF at the degree of motor, **b** at the coupling DoF

The damping affects the difference which appears in magnitudes between the coupled method FRF and the full system FRF methods. This difference is due to the damping value, which is justified by the work of Irvine (2014). The exact frequency domain transfer function is contaminated with synthetic measured noise, which influences the robustness of the substructuring technique according to Per sjövall and Thomas Abrahamsson (2008). The measured noise is neglected in this study.

5 Conclusion

The substructuring method was tested in transmission system. The impedance coupling is presented to determine the vibration modes of complex structural system by using FRF of substructures. To verify the coupling procedures, the results were compared to those of the full system. It is observed that the natural frequencies obtained by the FRF of the global system and by the FRF of subsystem are in good agreement. But the difference that appears in magnitude is due to damping. The robustness of the adopted method will be the subject of the future work.

References

Bishop RED, Johnson DC (1960) The mechanics of vibration. Cambridge University Press, Cambridge

Chaari F, Baccar M, Abbes S, Haddar M (2008) Effect of spalling or tooth breakage on gear mesh stiffness and dynamic response of a one-stage spur gear transmission. Eur J Mech A/Solids 27:691–705

Choi BL, Park JM (2002) Application of the impedance coupling method and the equivalent rotor model in rotor dynamics. J Finite Elements Anal Des 441–832

Craig R, Bampton M (1968) Coupling of substructures for dynamic analysis. Am. Inst. Aero. Astro 1313–1319

D'Ambrogio W, Fregolent A (2008) Promises and pitfalls of decoupling procedures. In: Proceeding of 26th IMAC. Orlando, USA

D'Ambrogio W, Fregolent A (2010) The role of interface DoFs in decoupling of substructures based on the dual domain decomposition. Mech Syst Signal Process 24:2035–2048

Gladwell G (1964) Branch mode analysis of vibrating systems. J Sound Vib 41–59

Guyan R J (1965) Reduction of stiffness and mass matrices. AIAA J

Irvine T (2014) Notes on damping in FRF substructuring. Vib data

Jetmundsen B, Bielawa RL, Flannelly WG (1988) Generalized frequency domain substructure synthesis. J Am Helicopter Soc 55–64

Lin J, Parker RG (2001) Parametric resonance in two-stage gears from fluctuating mesh stiffness. Int J Gearing Transm 127–134

Liu W, Ewins DJ (2002) Substructure synthesis via elastic media. J Sound Vib 257(2):361–379

Per sjövall, Thomas Abrahamsson (2008) Substructure system identification from coupled system test data. Mech Syst Signal Process 22(1):15–33

Numerical Study of Water Waves Impact on Offshore Structure

Mohamed Ali Maâtoug and Mekki Ayadi

Abstract To understand the behavior of marine structures when submitted to the action of waves, it is necessary to assess the pressure field exerted on these structures. This chapter aims at dealing with the numerical modeling of the second-order wave forces acting on a marine structure in finite water depth. The numerical approach consists in using the finite difference method to compute the fully second-order Stokes wave problem applied to a three-dimensional domain with fixed vertical cylinder. To simplify the meshing task, the fluid domain has been decomposed into subdomains. To ensure the continuity of the transformations and the velocity of these transformations at the level of the contact zones of the subdomains, additional boundaries conditions are required. The results provided in this chapter are to expose the numerical results of the water wave impact on the offshore structure for different water depths and wave heights.

Keywords Second-order stokes wave · Pressure · Finite difference method Structure

Nomenclature

t Time variable
H Wave height
h_0 Water depth
T Wave period
L Wave length
P_0 Atmospheric pressure

M. A. Maâtoug (✉)
National Engineering School of Tunis, Tunis-El Manar University, Tunis, Tunisia
e-mail: ma.maatoug@gmail.com

M. Ayadi
Higher School of Sciences and Technologies of Hammam-Sousse,
University of Sousse, Sousse, Tunisia
e-mail: mekki.ayadi@enis.rnu.tn

P Exerted pressure
ϕ Potential flow
η Free surface elevation

1 Introduction

Marine structures design depends heavily on their behavior under the influence of environmental conditions such as water waves. The problem of water wave loads and motions is of great importance. Hence, to understand their behavior, it is necessary to know the forces applied on these marine structures. This can be achieved by assessing of pressure field that the waves exert. To achieve this objective, the nonlinear water waves problem is considered as one of the most important problems; the solving of this dilemma enables us to calculate the pressure loads (Maâtoug and Ayadi 2016). In this context, many research works in the field of fluid–structure interaction have been conducted. To obtain the wave forces acting on a cylinder under one wave condition, (Song et al. 2015) used the moving particle semi-implicit (MPS) method. They opted for a three-dimensional numerical wave tank to generate a second-order Stokes wave. Akimoto (2013), also, introduced a method based on the MPS method with modifications to simulate the flow around a planning. Lu et al. (2013) treated the impact of a triangular jet and the impact of a solitary wave on a vertical wall using the Smoothed Particle Hydrodynamics (SPH) method. A time domain method is employed to analyze interactions between water waves and a group of an array of cylinders. The first- and second-order velocity potential problems at each time step are solved through a finite element method (FEM) (Wang and Wu 2007). It is also worth mentioning that to predict high-order wave loads for a cylinder and monotower platform exposed to regular waves, Klepsvik (1995) solved the first-order problem using the computer program WaveAnalysisMIT (WAMIT) to obtain the added mass and wave damping. Then, he also used the superposition principle to find out the pitch response due to the second and higher order wave loads. Likewise, the volume-of-fluid method was into consideration to simulate wave impact on a box placed in the flow as a model for a container on the deck of an offshore floater (Kleefsman et al. 2004, 2005). Hu et al. (2011) used the computational fluid dynamics (CFD) flow code AMAZON-SC as a numerical wave tank (NWT) to study wave loading on floating bodies. The panel method has been widely used to simulate wave effects on fixed structures (Lee and Newman 2004; Peng et al. 2009) and ship responses (Islam et al. (2004)). The open source solvers such as OpenFOAM were also used in coastal and offshore engineering (Morgan and Zang 2011). To predict reflection and transmission of nonlinear water waves at a semi-submerged dock, Sulisz (2013) applied a theoretical approach. The solution was achieved analytically and by the method of matched eigenfunction expansions. The results show that the dock geometry has a significant effect on the nonlinear components of wave reflection and transmission. The reflection and transmission of nonlinear waves simultaneously increase with increasing dock width

for shallow water waves and decrease with increasing dock width for intermediate- and deep-water waves.

The main purpose of this work is to study numerically the water wave impact on an offshore structure using the finite difference method. The boundary value problem is formulated up to a second-order in wave steepness. To overcome the problem of nonlinearity of the fluid–structure contact zones, the space domain was decomposed into subdomains. To ensure the continuity of the transformations and the velocity of these transformations at the level of the contact zones of the sub-domains, additional boundaries conditions are required. Numerical results are exposed to show the impact of water waves on an offshore structure and to highlight the effects of changes in water depth and waves height on the exerted loads.

2 Problem Formulation

In this study, it is assumed that the fluid is inviscid, incompressible, and irrotational. Also, it is assumed that there is neither fluid–structure interaction (the structure is assumed to be rigid) nor shock waves (no wave reflection).

To simplify the meshing task, the fluid domain is decomposed into subdomains as shown in Fig. 1. These subdomains are taken as follows:

- $\Omega_1, \Omega_3, \Omega_6, \Omega_8$ have same dimensions: $L_1 \times L_1$.
- $\Omega_2, \Omega_4, \Omega_5, \Omega_7$ have same dimensions: $L_2 \times L_1$; L_2 is the structure diameter.
- $\Omega_9, \Omega_{10}, \Omega_{11}, \Omega_{12}$ have same dimensions.

The second-order boundary value problem is governed by the Laplace partial differential equation within the flow domain (Eq. 1)

$$\phi_{xx}^{(2)} + \phi_{yy}^{(2)} + \phi_{zz}^{(2)} = 0 \quad in \quad -h_0 < z < 0 \tag{1}$$
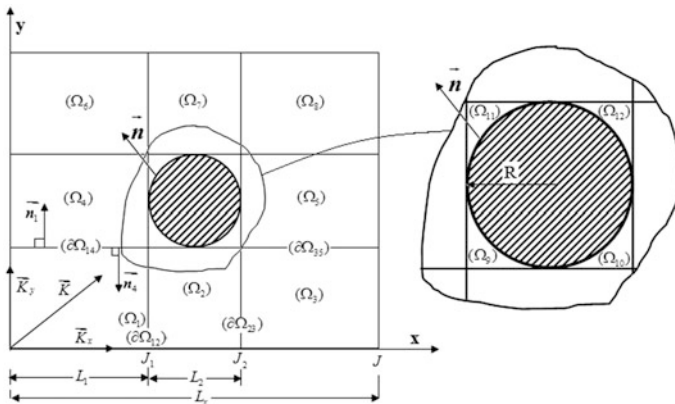
Fig. 1 Dimensional and positioning characteristics of the structure in the fluid domain

together with the nonlinear kinematic and dynamic boundary conditions, both applied at the free surface of the wave (Eqs. 2 and 3)

$$\phi_t^{(2)} + \frac{1}{2}\left[\left(\phi_x^{(1)}\right)^2 + \left(\phi_y^{(1)}\right)^2 + \left(\phi_z^{(1)}\right)^2\right] + g\eta^{(2)} + \eta^{(1)}\phi_{tz}^{(1)} = 0 \ at \ z=0 \qquad (2)$$

$$\eta_t^{(2)} + \phi_x^{(1)}\eta_x^{(1)} + \phi_y^{(1)}\eta_y^{(1)} - \phi_z^{(2)} - \eta^{(1)}\phi_{zz}^{(1)} = 0 \ at \ z=0 \qquad (3)$$

and the zero-vertical velocity condition at the bottom (Eq. 4),

$$\phi_z^{(2)} = 0 \quad at \quad z = -h_0 \qquad (4)$$

in addition, with the lateral boundary conditions (Eqs. 5–8)

$$\phi_x(0, y, z, t) = \phi_x(L_x, y, z, t) \qquad (5)$$

$$\phi_y(x, 0, z, t) = \phi_x(x, L_y, z, t) \qquad (6)$$

$$\eta(0, y, t) = \eta(L_x, y, t) \qquad (7)$$

$$\eta(x, 0, t) = \eta(x, L_y, t) \qquad (8)$$

the initial conditions (Eqs. 9 and 10)

$$\phi(x, y, z, 0) = \phi_0(x, y, z) \qquad (9)$$

$$\eta(x, y, 0) = \eta_0(x, y) \qquad (10)$$

and supplementary conditions on the boundaries of the subdomains in direct contact and the contact zones fluid–structure. These supplementary conditions reflect the continuity of the transformations and velocity of these transformations on the boundaries of the subdomains in direct contact. They are taken as:

$$\begin{cases} \phi_p - \phi_q = 0; & on \quad \partial\Omega_{pq} \\ \dfrac{\partial\phi_p}{\partial \boldsymbol{n}_p} + \dfrac{\partial\phi_q}{\partial \boldsymbol{n}_p} = 0; & on \quad \partial\Omega_{pq} \\ \dfrac{\partial\phi_p}{\partial \boldsymbol{n}} = 0 \end{cases} \qquad (11)$$

$\boldsymbol{n}_p$ and $\boldsymbol{n}_q$ are, respectively, the normal to the subdomains

(Ω_p) and (Ω_q)

$\boldsymbol{n}_q = -\boldsymbol{n}_p$ ($\boldsymbol{n}_p = \boldsymbol{x}$ or $\boldsymbol{y}$). $\boldsymbol{n}$ is the normal to the structure.

3 Finite Difference Discretization

The second-order finite difference and the Crank–Nicolson methods are adopted to discretize, respectively, the space and the time domains.

For the time discretization, the time step is taken as: $\Delta t = \frac{T}{N}$ for $0 \leq n \leq N$

For the spatial discretization of the subdomains, a grid of $J_1 \times J_1$ points is defined along the x-axis and the y-axis. Also, a grid of $J_2 \times J_2$ points is defined along the x-axis and the y-axis for the spatial discretization of the subdomains in contact with the structure. And along the z-axis, a grid of N_z points is defined. For each point of the spatial grid, the time-stepping variables η and ϕ are to be evolved.

For the fluid–structure, nonlinear contact zones are approached by performing a discretization of the angles delimited by the contact points between the fluid and the structure (Fig. 2). In this way, the discretization angles step is taken as: $\Delta\beta = \pi/2J_2$. Thus, an angular mesh point will be identified by the angle $\beta_l = l\Delta\beta$ for $0 \leq l \leq J_2 + 1$.

Each point of the angular mesh will form a segment with the opposite vertex of the square. This segment will then be discretized until we arrive to cover the entire subdomain (Fig. 3).

The discretization steps, $\Delta\beta_x(l)$ and $\Delta\beta_y(l)$, corresponding to the lth point of the angular mesh along, respectively, the x-axis and the y-axis will be taken as follows:

$$\begin{cases} \Delta\beta_x(l) = \dfrac{L_2}{2J_2}(1 - \cos(\beta_l)) \\ \Delta\beta_y(l) = \dfrac{L_2}{2J_2}(1 - \sin(\beta_l)) \end{cases} \quad \text{for} \quad 1 \leq l \leq J_2 + 1 \quad (12)$$

For each subdomain, a system of equations is obtained and is put in a matrix form. The preconditioning step then consists of solving a linear system of the form:

$$\mathbb{K}\begin{pmatrix} \eta^{n+1} \\ \phi^{n+1} \end{pmatrix} = \mathbb{F}^n \quad (13)$$

Fig. 2 Angular discretization of nonlinear zones

$\left(\dfrac{\eta^{n+1}}{\phi^{n+1}}\right)$ is a vector having the dimensions $J_1^2 + (N_z + 1)(J_1 + 1)^2$ for the case of
subdomains $\Omega_1, \Omega_3, \Omega_6, \Omega_8$, or of dimensions $J_1 J_2 + (N_z + 1)(J_1 + 1)(J_2 + 1)$ for the
case of subdomains $\Omega_2, \Omega_4, \Omega_5, \Omega_7$, or of dimensions $J_2^2 + (N_z + 1)(J_2 + 1)^2$ for the
case of subdomains $\Omega_9, \Omega_{10}, \Omega_{11}, \Omega_{12}$.

With the assumption of irrotational motion fluid, a velocity potential exists; this
should satisfy the continuity equation. Once the velocity potential ϕhas been
simulated numerically, the next step consists in deducing the velocity field from the
equation below:

$$\mathbf{v} = \nabla\phi \tag{14}$$

The pressure field associated with a progressive wave is determined from the
unsteady Bernoulli equation

$$\frac{1}{\rho}(P - P_0) = -\frac{\partial\phi}{\partial t} - \frac{1}{2}(\nabla\phi)^2 - gz \tag{15}$$

where, on the free surface $z = \eta;\ P = P_0$.

4 Numerical Results and Discussions

The computational results of the effects of the structure implantation in the fluid
flow domain showed that all the numerical results are for $N_z = J = 15$, $N = J + 1$ and
$T = 10$.

In the beginning of the climbing phase, the particles upstream of the structure are
animated by their optimal velocity; whereas, those which are downstream will be
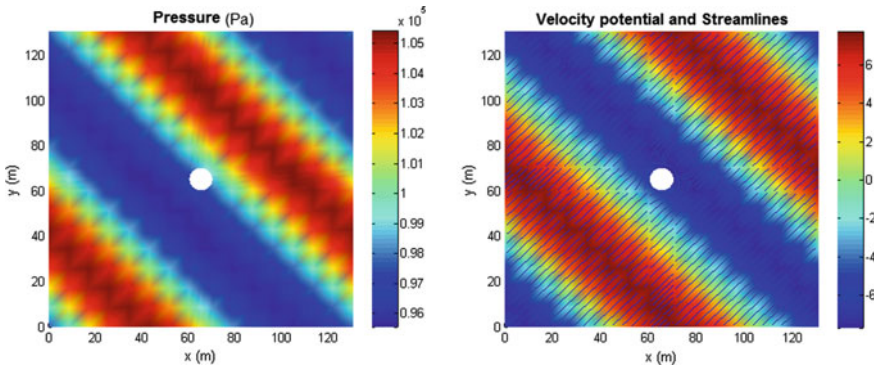
Fig. 4 Behavior of pressure, potential, and streamlines for: $n = 6$, $h_0/gT^2 = 0.01$, $H/gT^2 = 0.001$
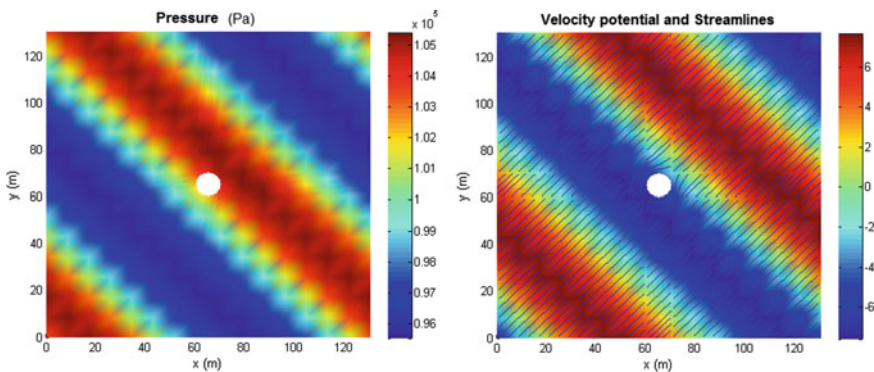
Fig. 5 Behavior of pressure, potential, and streamlines for: $n = 3$, $h_0/gT^2 = 0.01$, $H/gT^2 = 0.001$

subject to the refractive action caused by the structure. The deceleration is caused, at the same time, by the rise and contact with the structure (Fig. 4).

Closer to the crest, the actions of the structure and the slope unite to increasingly slow down the water uphill until it reaches its minimum on the crest of the wave (Fig. 5). The streamlines are deformed and the pressure increases remarkably with respect to a flow without the presence of the structure.

When the structure is in the middle of the crest, the flowing water reaches its minimum velocity, bypasses the structure, and exerts maximum pressure. Water is braked around the structure (Fig. 6).

In the beginning of the descent phase, the flowing water particles which are upstream of the structure will undergo the braking action on the part of the structure and those which are downstream will increase in speed as the slope decreases (Fig. 7).
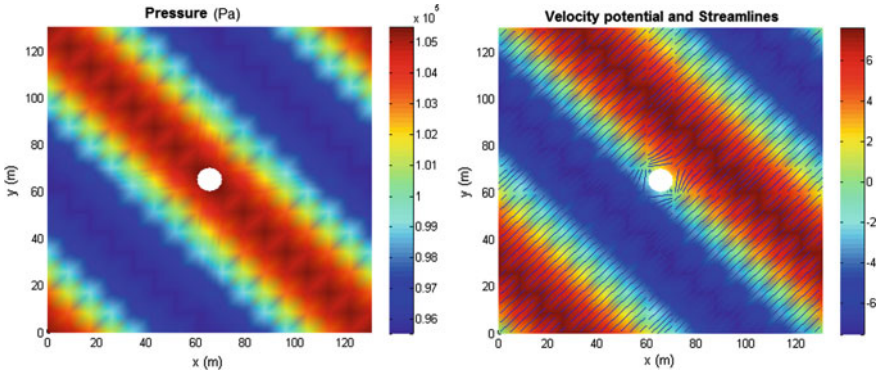
Fig. 6 Behavior of pressure, potential, and streamlines for: $n = 1$, $h_0/gT^2 = 0.01$, $H/gT^2 = 0.001$
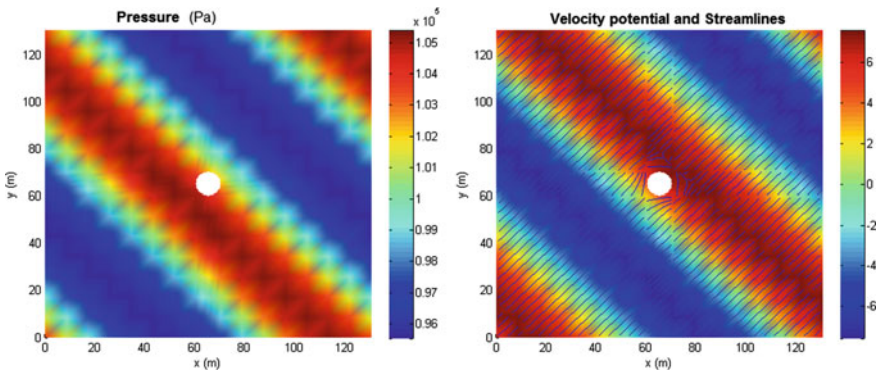
Fig. 7 Behavior of pressure, potential, and streamlines for: $n = 15$, $h_0/gT^2 = 0.01$, $H/gT^2 = 0.001$

It has been noticed that as the depth increases, the contribution of the structure to the braking of the water and consequently to the increase of the pressure, of course compared to a domain without structure, this will necessarily lead to an increase in the stresses exerted by the wave on the structure. For example, for a depth given by $(h_0/gT^2 = 0.01)$, it has been observed that the pressure exerted on the structure differs just a little from that exerted in a domain without structure (Fig. 8). For a depth given by the value $(h_0/gT^2 = 0.07)$ (zone close to the deep waters), the difference between the pressures exerted in both types of domains becomes increasingly important (Fig. 9). The same observation also applies to the depths given by $(h_0/gT^2 = 0.2)$, belonging to the deep-water validity domain (Fig. 10).
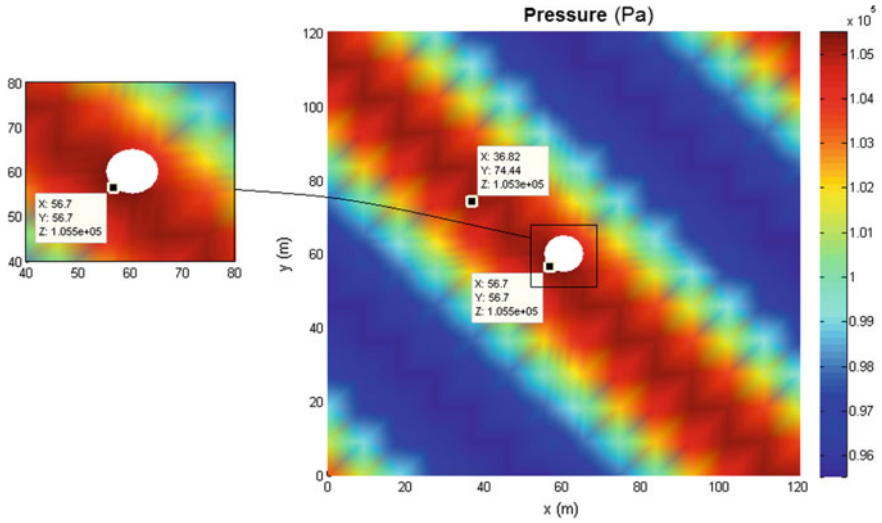
Fig. 8 Pressure exerted on the structure for: $n = 16$, $h_0/gT^2 = 0.01$, $H/gT^2 = 0.001$
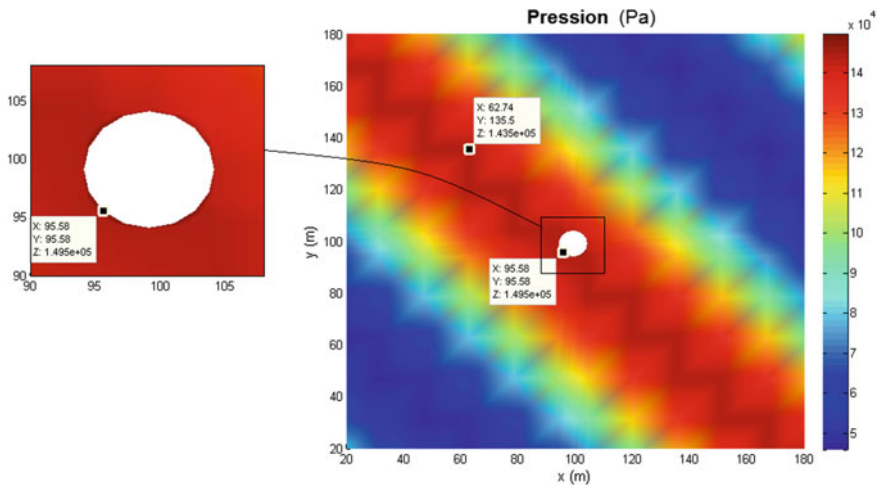
Fig. 9 Pressure exerted on the structure for: $n = 16$, $h_0/gT^2 = 0.07$, $H/gT^2 = 0.01$
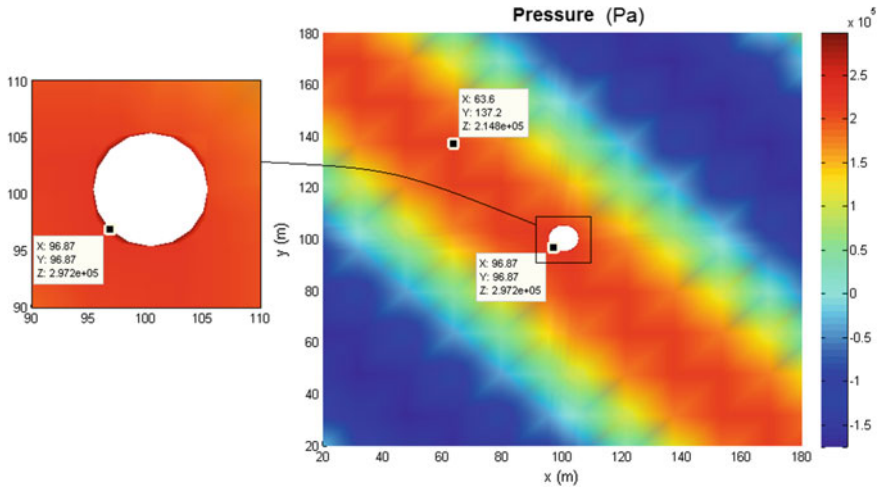
Fig. 10 Pressure exerted on the structure for: $n = 16$, $h_0/gT^2 = 0.2$, $H/gT^2 = 0.04$

5   Conclusions

An efficient computer has been, successfully formulated and implemented to numerically simulate the impact of the second-order Stokes wave on a structure using the finite difference method.

   The obtained numerical results showed the existence of a concordance between the effects of the flowing fluid on the structure and the effects of the latter on the fluid. In fact, the analysis of these numerical results showed that flow velocity was affected by the existence of the structure in the domain. It has been noticed that the particles have been slowed down and have been subjected to the refractive action caused by the structure, which necessarily caused the increase of the pressure exerted by the water waves on the structure.

References

Akimoto H (2013) Numerical simulation of the flow around a planing body by MPS method. Ocean Eng 64:72–79

Hu ZZ, Causon DM, Mingham CG, Qian L (2011) Numerical simulation of floating bodies in extreme free surface waves. Nat Hazards Earth Syst Sci 11:519–527

Islam MN, Islam MR, Baree MS (2004) Computation of ship responses in waves using panel method. J Naval Architect Marine Eng 1:35–46

Kleefsman KMT, Fekken G, Veldman A EP, Iwanowski B (2004) An improved volume-of-fluid method for wave impact problems. In: 14th international offshore and polar engineering conference, Toulon, France

Kleefsman KMT, Fekken G, Veldman AEP, Iwanowski B, Buchner B (2005) A Volume-of-Fluid based simulation method for wave impact problems. J Comput Phys 10:363–393

Klepsvik J (1995) Nonlinear wave loads on offshore structure. Master of science in ocean engineering. Massachusetts Institute of Technology (MIT)

Lee CH, Newman JN (2004) Computation of wave effects using the panel method. In: Chakrabarti S (ed) Numerical models in fluid-structure interaction. WIT Press, South Hampton

Lu XZ, Cherlfis JM, Pinon G, Rivoalen E, Brossard J (2013) Simulations numériques de l'impact de la houle sur une paroi verticale par la méthode SPH, 21ème Congrès Français de Mécanique, Bordeaux

Maâtoug MA, Ayadi M (2016) Numerical simulation of the second-order Stokes theory using finite difference method. Alexandria Eng J 55(3):3005–3013

Morgan GCJ, Zang J (2011) Application of OpenFOAM to coastal and offshore modelling. In: The 26th international workshop on water waves and floating bodies, Athens, Greece

Peng H, Qiu W, Spencer D (2009) Validation studies of panel-free method for wave-body interaction analysis. Int J Offshore Polar Eng 19:295–299

Song X, Shibata K, Koshizuka S (2015) MPS simulation of wave forces acting on a cylinder. In: 25th international ocean and polar engineering conference (ISOPE) Kona, Big Island, Hawaii, USA

Sulisz W (2013) Reflection and transmission of nonlinear water waves at a semi-submerged dock. Arch Mech 65(3):237–260

Wang CZ, Wu GX (2007) Time domain analysis of second-order wave diffraction by an array of vertical cylinders. J Fluids Struct 23:605–631

Comparative Investigation of Turbulence Modeling in Counterflowing Jet Predictions

Amani Amamou, Nejla Mahjoub Saïd, Philippe Bournot and Georges Le Palec

Abstract In this chapter, a comparison between a number of turbulent models is done in order to investigate turbulence modeling in a turbulent round jet flowing into a counterflow stream. For this purpose, three turbulence closure models are tested: Standard k-ε model, k-ε RNG model, and RSM model. The studied cases of jet-to-counterflow velocity ratios are ranging between $R = 3$ and $R = 15$. Velocity and concentration fields are predicted through the centerline velocity and dilution decay along the downstream jet axis. Predicted results are compared with available experimental data from the literature. It is found that the three tested models behave in a similar way in the first region, however, in the further region, a difference between curves from different models appears. This discrepancy seems to depend on the jet-to-current velocity ratio. The k-ε models are found to underestimate the experimental data, while the second-order closure model RSM is found to be the best model to predict the jet diffusion.

Keywords Counterflowing jet · Turbulence models · Velocity Concentration

A. Amamou (✉)
LGM, National Engineering School of Monastir, University of Monastir, Monastir, Tunisia
e-mail: amani.amamou@yahoo.fr

N. Mahjoub Saïd
LGM, Preparatory Institute for Engineering Studies, University of Monastir, Monastir, Tunisia
e-mail: nejla.mahjoub@fsm.rnu.tn

P. Bournot · G. Le Palec
IUSTI-UMR CNRS 7543, University of Aix-Marseille, Marseille, France
e-mail: philippe.bournot@univ-amu.fr

G. Le Palec
e-mail: georges.lepalec@univ-amu.fr

1   Introduction

The configuration of a turbulent round jet issuing into a stagnant or in a moving ambient has many applications in various fields of engineering. The presence of a moving ambient flow, especially in an opposing stream, enhances the mixing and the dispersion of the jet (Amamou et al. 2016). This feature seems to be essential in environmental engineering such as the discharging of wastewater in the sea. In this chapter, the configuration of a round jet submerged in a uniform counterflow stream is studied.

Turbulent free jet discharged into a uniform countercurrent may be divided into two distinct regions (Yoda and Fiedler 1996): the zone of flow establishment (ZFE), also known as the potential core, and the zone of established flow (ZEF). The first region is the near region from the jet exit and it represents a jet flow dominance zone. The ZEF is the far field region where the counterflow stream dominates. In this region, the interaction between the jet and the counterflow stream generates the deceleration of the jet fluid until the stagnation point where the jet is stopped. After reaching this point, the jet is deflected backward to approach asymptotically the counterflow velocity. The axial distance from the jet exit to the stagnation point is the jet penetration length (L_p). This peculiar length scale is found to depend on the jet-to-counterflow velocity ratio (R), where R is the ratio between the jet exit velocity and the counterflow velocity (Arendt et al. 1956). Rajaratnam (1976) reported two empirical relationships: $Lp = 2.4R$ and $Lp = 2.7R$ that link the penetration length to the jet-to-current velocity ratio. Similarly, Chan (1999) and Bernero (2000), from their experimental investigations, and recently Amamou et al. (2015a, b, 2016), through a numerical study, concluded that the constant of linearity is fallen between 2.5 and 2.7. The previous authors investigated the velocity and the concentration field of a counterflowing round jet using the second-order turbulence model RSM.

In order to predict the mixing behavior of a counterflowing jet, we should, first of all, choose the turbulence model which describes the best the flowfield. In this chapter, we propose to test three turbulence models; two first-order turbulence models (Standard k-εmodel and k-ε RNG model) and a second-order turbulence model (Reynolds stress model: RSM). Results from numerical tests are compared with the available experimental and analytical data for velocity and concentration field, respectively. A range of jet-to-counterflow velocity ratios between 3 and 15 is investigated.

2   Computational Procedure

For a turbulent, steady and incompressible fluid flow, the RANS equations, based on the Reynolds decomposition, are numerically solved.

2.1 Mathematical Formulation

The continuity (1), the momentum (2), and the passive scalar (3) conservation equations are presented in the Cartesian coordinates system as follows:

$$\frac{\partial U_i}{\partial x_i} = 0 \tag{1}$$

$$\frac{\partial}{\partial x_k}(U_k U_i) = -\frac{1}{\rho}\frac{\partial P}{\partial x_i} + \frac{\partial}{\partial x_k}\left[\nu\left(\frac{\partial U_i}{\partial x_k} + \frac{\partial U_k}{\partial x_i}\right) - \overline{u_i' u_k'}\right] \tag{2}$$

$$\frac{\partial}{\partial x_i}(U_i C) = \frac{\partial}{\partial x_i}\left(\Gamma\frac{\partial C}{\partial x_i} - \overline{u_i' c'}\right) \tag{3}$$

where i, k = 1, 2, 3 referring to x, y, and z, respectively. x_i and U_i are, respectively, the coordinate and the mean velocity in the i direction and C represents the passive scalar concentration. P, ρ, υ and Γ represent, respectively, the pressure, the fluid density, the kinematic viscosity, and the scalar diffusion coefficient. $\overline{u_i' u_k'}$ are the Reynolds stresses while, $\overline{u_i' c'}$ are turbulent fluxes terms.

Due to additional unknowns in the above system of equations, a closure turbulence model is required to solve this system. In this chapter, we propose to test three turbulence models: two first-order turbulence models (Standard k-ε model and k-ε RNG model) and a second-order turbulence model (RSM model).

For the Standard k-ε model, the turbulent kinetic energy and the dissipation of the turbulent kinetic energy equations are written, respectively, as follows (Wilcox 2006):

$$\frac{\partial(U_i k)}{\partial x_i} = \frac{\partial}{\partial x_k}\left[\left(\nu + \frac{\nu_t}{\sigma_k}\right)\frac{\partial k}{\partial x_k}\right] + G_k - \varepsilon \tag{4}$$

$$\frac{\partial(U_i \varepsilon)}{\partial x_i} = \frac{\partial}{\partial x_k}\left[\left(\nu + \frac{\nu_t}{\sigma_\varepsilon}\right)\frac{\partial \varepsilon}{\partial x_k}\right] + C_{\varepsilon 1}\frac{\varepsilon}{k}G_k - C_{\varepsilon 2}\frac{\varepsilon^2}{k} \tag{5}$$

where G_k is the production rate of turbulent energy whose expression is:

$$G_k = \nu_t\left(\frac{\partial U_i}{\partial x_k} + \frac{\partial U_k}{\partial x_i}\right)\frac{\partial U_i}{\partial x_k} \tag{6}$$

The turbulent kinematic viscosity is given by the following relation:

$$\nu_t = C_\mu\frac{k^2}{\varepsilon} \tag{7}$$

Table 1 Constants of k-ε turbulence models

Models	C_μ	$C_{\varepsilon 1}$	$C_{\varepsilon 2}$	σ_k	σ_ε	η_0	β
k-ε	0.09	1.44	1.92	1	1.3	–	–
k-ε RNG	0.085	1.42	1.68	0.718	0.718	4.38	0.012

In the k-ε RNG model, an additional term is considered in the dissipation of ε Eq. (5) and it is given as follows:

$$\frac{\eta(1-\eta/\eta_0)}{1+\beta\eta^3}\frac{\varepsilon G_k}{k} \tag{8}$$

with $\eta = \frac{Sk}{\varepsilon}$ and $S = \sqrt{2\,S_{ij}S_{ij}}$ where S_{ij} is:

$$S_{ij} = \frac{1}{2}\left(\frac{\partial u_i}{\partial x_j} + \frac{\partial u_j}{\partial x_i}\right) \tag{9}$$

Empirical constants of the k-ε models are tabulated in Table 1.

For the second-order turbulence model, the Reynolds stress model (RSM), the following equation is solved (Launder et al. 1975):

$$\underbrace{\frac{\partial}{\partial x_l}\left(U_l\overline{u_i'u_k'}\right)} = P_{ik} + D_{ik}^T + D_{ik}^\nu + \Pi_{ik} - \varepsilon_{ik} \tag{10}$$

where P_{ik}, D_{ik}^T, D_{ik}^ν, Π_{ik} and ε_{ik} are respectively, the stress production, the turbulent diffusion, the viscous diffusion, the pressure strain, and the dissipation rate. D_{ik}^T, Π_{ik} and ε_{ik} tensors are recommended to be modeled, while P_{ik} and D_{ik}^ν do not require any modeling.

The turbulent flux terms are expressed using the following form:

$$-\overline{u_k'c'} = \Gamma_t\frac{\partial C}{\partial x_i} \tag{11}$$

Γ_t is the turbulent diffusivity of mass and it is related to the turbulent eddy viscosity as:

$$\Gamma_t = \frac{\nu_t}{Sc_t} \tag{12}$$

where Sc_t is the turbulent Schmidt number with a value of 0.7 (Spalding 1971).
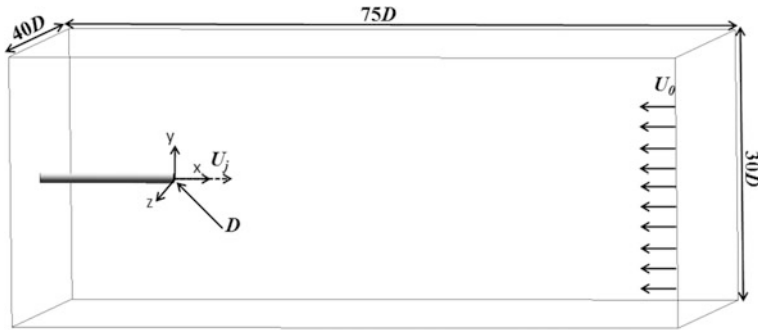
Fig. 1 Schematic of flow configuration

2.2 Flow Configuration and Boundary Conditions

The flow configuration of a circular water jet flowing horizontally into a uniform counterflow stream is sketched in Fig. 1. The dimension of numerical domain is $75D \times 30D \times 40D$ in x, y, and z directions, respectively, with D the inner diameter of jet nozzle. The origin of the Cartesian coordinate system is placed in the center of the jet exit.

At the jet exit ($x = 0$), initial conditions for velocity and concentration are set as U_j and C_j, respectively. While at the counterflow inlet ($x = 75D$), the velocity is specified as U_0 and zero concentration is imposed at this boundary. At $x = -15D$, zero gradient for all variables is prescribed at the outlet boundary of the resulting flow. The rest of the domain is set to wall.

2.3 Numerical Method

The resolution of the governing equations is carried out using the finite volume method (FVM), allowing the discretization of these equations using the first-order upwind scheme. The pressure–velocity coupling is performed by the SIMPLE algorithm (Patankar and Spalding 1972). A three-dimensional grid is elaborated with nonuniform, tetrahedral mesh refined in the vicinity of the nozzle jet exit. The resulting number of cells is about 750000 cells which are picked out after a careful grid independence investigation (Amamou et al. 2015a, 2016).

3 Results and Discussion

The choice of the appropriate turbulence model is based on a comparison between predicted results, obtained using the three different models already presented above, and available data extracted from the literature. Herein for the velocity field, experimental results are LDA measurements from Chan (1999) for $R = 3.1$, and from Bernero (2000) for the rest of velocity ratio cases. The jet fluid concentration data, measured with the laser-induced fluorescence (LIF) technique, are derived from Bernero (2000) and Lam and Chan's experiments (Lam and Chan 2002). Also, predicted results are compared to analytical model elaborated by Chan and Lam (1999).

3.1 *Velocity Field*

Figure 2 illustrates the centerline velocity decay along the jet axis at various jet-to-counterflow velocity ratios; $R = 3.1$, $R = 5$, $R = 7.5$, $R = 10$, and $R = 15$. For each velocity ratio, predicted centerline velocities (Uc/Uj) from the three turbulence models, namely the standard k-ε model, the k-ε RNG model, and the RSM model are shown in Fig. 2 together with previous experimental results. When the velocity ratio increases, the centerline velocity decay decreases, proving that the centerline velocity decay depends on the velocity ratio. It is clear that in the near-field region, predicted results from the different turbulence models are very close. Moving farther downstream, a small discrepancy between curves of various models appeared. This discrepancy is much more observed when the counterflow stream becomes stronger, in other words, when the velocity ratio is low ($R = 3.1$). Also, Fig. 2 shows a reasonabe agreement between experimental data and predicted results from RSM model, at all velocity ratios. However, first-order models exhibit an underestimation of the centerline axial velocity in the far field of the counterflowing jet which is accentuated at lower velocity ratio cases. From these results, we can conclude that the RSM model predict well the velocity field. Thus, it is recommended to test the validity of this model on the evolution of the passive scalar field to judge the use of the second-order turbulence model.

3.2 *Passive Scalar Field*

In order to achieve correspondence between velocity and concentration field, the centerline concentration decay is investigated, at the same previous range of jet-to-current velocity ratios and for the three tested turbulence models. To support predicted results, experimental and analytical data from previous investigations are included together in the same figure. Figure 3 introduces the normalized
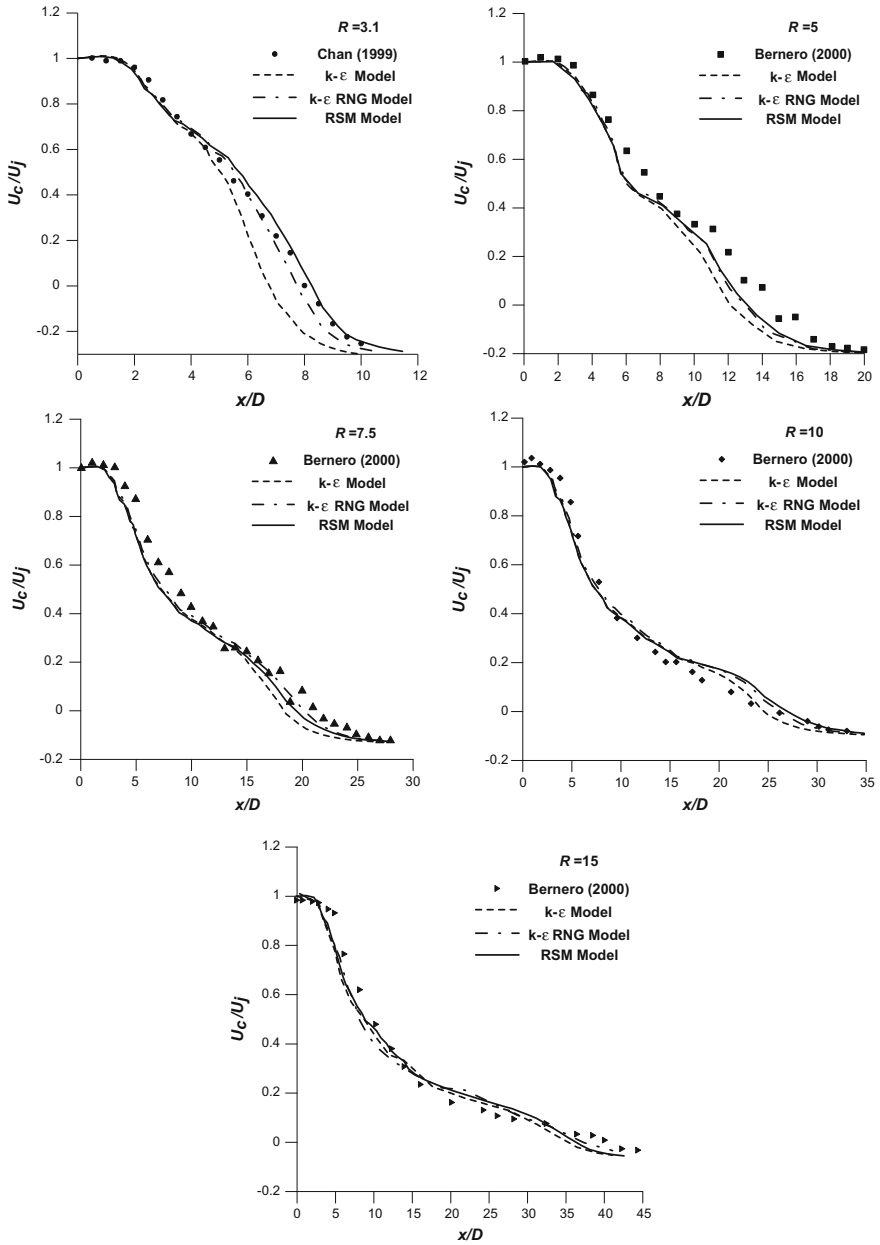
Fig. 2 Centerline velocity decay for different turbulence models
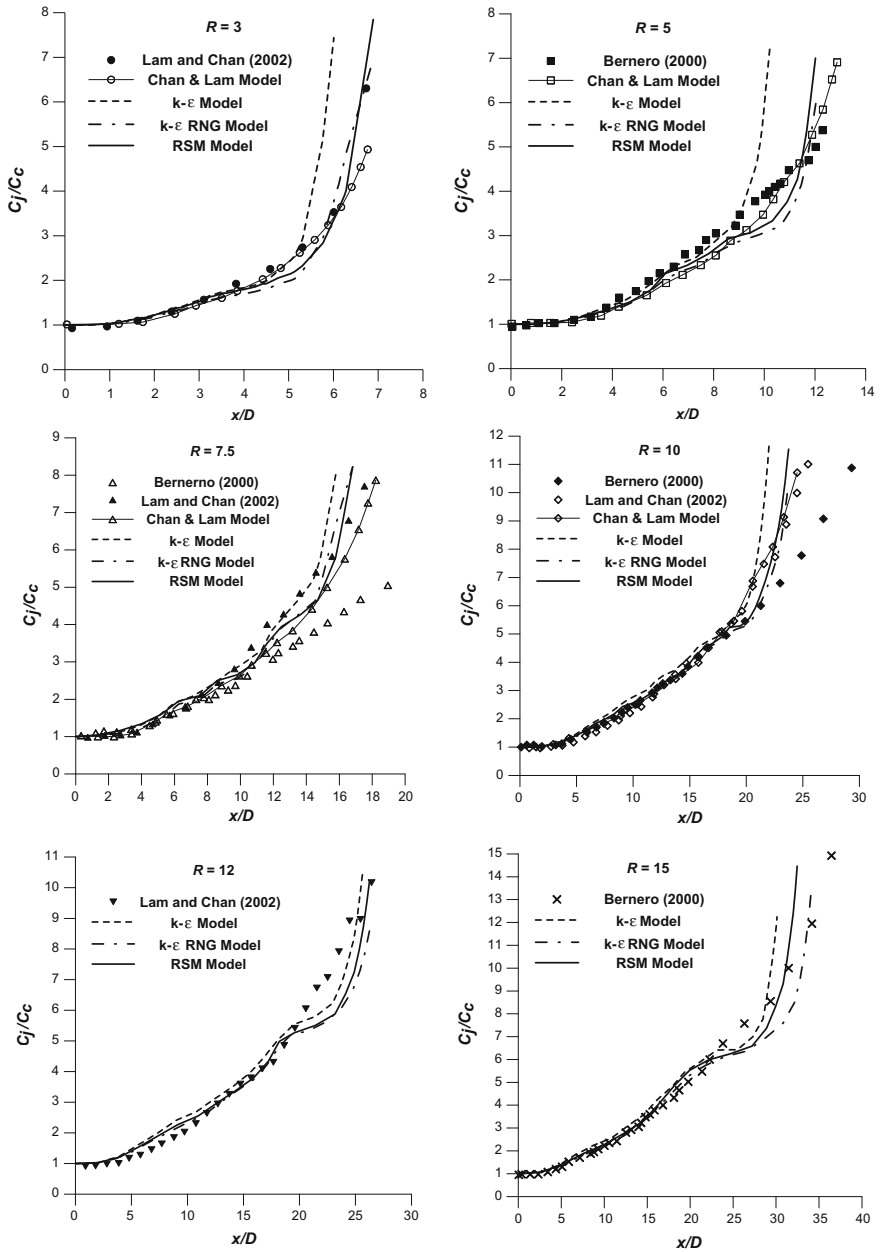
Fig. 3 Centerline dilution along the axial direction for different turbulence models
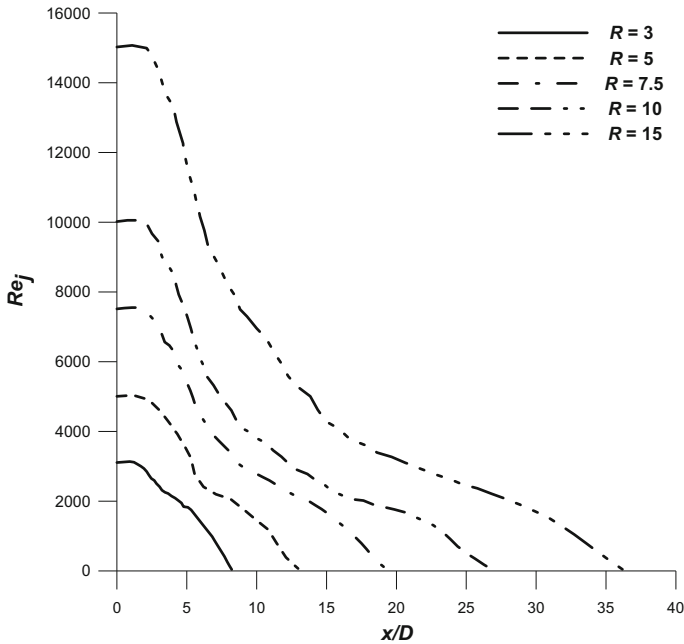
Fig. 4 Variation of the jet Reynolds number along the centerline jet axis

concentration (C_j/C_c) corresponding to different studied models compared to the Chan and Lam model obtained from their analytical investigation (Chan and Lam 1999) together with available measurements from Bernero (2000) and Lam and Chan (2002). Figure 3 shows that downstream of the jet exits, and the predicted centerline dilution maintains a constant value along roughly short region. This region becomes larger as well as the jet-to-counterflow velocity ratio increased. Further, a noticeable rise in the centerline dilution appears in the forward direction, near the stagnation zone. This is due to the attenuation of the concentration in the penetration zone (Amamou et al. 2016). Figure 3 exhibits a reasonabe argument between the predicted results and available literature data. Similar to the hydro-dynamic aspect which is previously presented in Fig. 2, the discrepancy between plots extracted from the three tested models lies in the forward farther region; where the flow instability becomes stronger due to the interaction between the jet flow and the opposing stream. It is obvious that the second-order model is the best to predict the centerline dilution data.

Once the closure turbulence model is picked out, a description of the down-stream variation in the jet Reynolds number (Re_j) along the centerline jet axis is performed. In Fig. 4, Re_j is plotted against axial positions normalized by the jet diameter D (x/D), for various jet-to-current velocity ratios. It is obvious that the jet Reynolds number decays in the same way as the centerline velocity decay. In fact, Reynolds number is characterized by a constant value in the potential core region

whose length rises with the increase of the jet-to-counterflow velocity ratio. Moving downstream further from jet injection, a drop of Re_j is observed along the downstream x-positions until it becomes zero corresponding to the position of the stagnation point. Similar to velocity and concentration field, Fig. 4 shows that the decay of the jet Reynolds number depends on the jet-to-current velocity ratio: Re_j decay increases as the ratio decreases.

4 Conclusion

A numerical investigation of a round turbulent jet issuing into a uniform counterflow stream is conducted using three turbulence closure models (Standard k-ε model, k-ε RNG model, and RSM

model). The centerline velocity and concentration decay are predicted at different jet-to-counterflow velocity ratios based on a comparison with the available data from previous researches. The discrepancy between tested computational models appears in the forward further region where the jet instability becomes stronger due to the interaction between the jet flow and the opposing stream. Based on those comparisons, the second-order RSM model is chosen to be the turbulence closure model.

References

Amamou A, Habli S, Mahjoub Saïd N, Bournot Ph, Le Palec G (2015a) Numerical study of turbulent round jet in a uniform counterflow using a second order Reynolds stress model. J Hydro-environ Res 9:482–495

Amamou A, Habli S, Mahjoub Saïd N, Bournot Ph, Le Palec G (2015b) Computational study of mixing behavior of a turbulent jet issuing in a uniform counterflow at low velocity ratios. J Turbul 17(2):237–251

Amamou A, Habli S, Mahjoub Saïd N, Bournot Ph, Le Palec G (2016) Computational study of mass and heat transport in a counterflowing turbulent round jet. Appl Thermal Eng 105: 724–736

Arendt J, Babcock HA, Schuster JC (1956) Penetration of a jet into counterflow. J Hydraul Div Proc ASCE 82:1038-8-11

Bernero S (2000) A turbulent jet in counterflow. PhD thesis, Technical University of Berlin

Chan HC (1999) Investigation of a round jet into a counterflow. PhD thesis, University of Hong Kong

Chan HC, Lam KM (1999) The concentration field of a circular jet in a counterflow. In: Proceedings of the 28th IAHR congress, Graz, Austria, vol 342, pp 22–27

Lam KM, Chan HC (2002) Time-averaged mixing behavior of circular jet in counterflow: velocity and concentration measurements. J Hydraul Eng 128(9):861–865

Launder BE, Reece GJ, Rodi W (1975) Progress in the development of a Reynolds-stress turbulent closure. J Fluid Mech 68:537–566

Patankar SV, Spalding DB (1972) A calculation procedure for heat, mass and momentum transfer in three dimensional parabolic flows. Int J Heat Mass Transf 15:1787–1806

Rajaratnam N (1976) Turbulent jets. Elsevier Scientific Publishing Company, Amsterdam, The Netherlands

Spalding DB (1971) Concentration fluctuations in a round turbulent free jet. J Chem Eng Sci 26:95–107

Wilcox DC (2006) Turbulence modeling for CFD, 3rd edn. DCW Industries, Inc

Yoda M, Fiedler HE (1996) The round jet in a uniform counterflow: flow visualization and mean concentration measurements. Exp Fluids 21(6):427–436

Structural Sources Localization in 2D Plate Using an Energetic Approach

Ahmed Samet, Mohamed Amine Ben Souf, Olivier Bareille,
Tahar Fakhfakh, Mohamed Ichchou and Mohamed Haddar

Abstract This paper is concerned with the localization of structural forces acting in 2D plate at medium and high frequency ranges, through an inverse method based on energy quantities. An energy-based method, called simplified energy method (MES), has already been proposed to predict the energy density field repartition for structural–acoustic problems in mid- and high-frequency ranges. In order to illustrate but also to present one of the applications of this method, this paper presents a formulation to solve inverse structural problems. The main novelty of this paper is to localize the vibration sources in plates, thanks to experimental data of energy densities. The injected forces localization was obtained in the mid–high-frequency range. Experimental investigation was performed to test the validity of the presented technique using different positions of the shaker and measurement points. The experimental results show that the IMES method has an excellent performance in localizing the input forces.

A. Samet (✉) · M. A. B. Souf · T. Fakhfakh · M. Haddar
Laboratoire de Mécanique, Modélisation et Productique (LA2MP), École Nationale
d'Ingénieurs de Sfax, 3038 Sfax, Tunisia
e-mail: samet.ahmed14@hotmail.com

M. A. B. Souf
e-mail: bensouf.mohamedamine@gmail.com

T. Fakhfakh
e-mail: tahara.fakhfakh@gmail.com

M. Haddar
e-mail: mohamed.haddar@enis.rnu.tn

A. Samet · M. A. B. Souf · O. Bareille · M. Ichchou
Laboratoire de Tribologie et Dynamique des Systèmes (LTDS), École Centrale Lyon,
36 venue Guy de Collongue, 69134 Écully Cedex, France
e-mail: Olivier.Bareille@ec-lyon.fr

M. Ichchou
e-mail: mohamed.ichchou@ec-lyon.fr

1 Introduction

The localization of input sources acting on plate from operating measurements is an important topic in the structural engineering. However, the direct measurements of sources often reveal complications to perform. As a result, an indirect process for estimating the exciting sources is employed to solve this problem. The problem considered here can apply also in some application in structural health monitoring (SHM). In other words, the damage in the structure leads to a modification in the distribution of the vibration energy. Thus, the position and the size of the damage can be detected.

Several researches have been done and published in the literature in order to localize the vibration sources. For example, the force analysis technique (FAT) is an alternative experimental method developed by Pezerat and Guyader (1995, 2000). It consists of obtaining the input load through the vibration displacement distribution on the structure. Still, other approaches have been used in the literature in order to localize the exciting load. The finite element method (FEM) is one of them. It has been used by Ibrahim et al. (1996) to estimate the forces applied at measured and unmeasured positions in the structure through data about the possible force locations. This method was also used by Corus and Balmes (2004) to identify the vibration sources applied to the structure by a compressor. The Kalman filter method has also been developed to estimate the input load (Liu et al. 2000). This method has been used by Ji and Liang (2000) to estimate a time-wise variation rod force source on the rod end with free boundaries.

In the range of medium and high frequencies, numerical methods as the finite element method and the boundary element method present limits when the frequency is increased.

For this reason, the energy methods based on energy quantities are often used. Among these methods is the simplified energy method. The direct theory formulation has been applied in various domains including beam (Ichchou et al. 2001), membrane and plates (Ichchou and Jezequel 1996), and acoustic applications (Besset et al. 2010). The inverse energy flow method IMES has been developed for acoustical application (Hardy et al. 2002) and structures (Chabchoub et al. 2011), as an indirect predictive tool.

The main novelty of this paper is the application of the IMES localization technique for a $2D$ plate, in order to localize the exciting sources through an experimental measurement of the energy density field.

First, the assumption of the simplified energy method will be reviewed; the energetic and the inverse formulation will be presented in Sec. 2. Next, the experimental setup and validation will be presented to validate the proposed IMES technique in Sect. 3.

2 Simplified Energy Method

2.1 Assumptions

The simplified energy method is a vibro-acoustic approach at medium and high frequencies, based on the description of two local energy quantities. The first one is the total energy density W defined as a sum of the potential energy density and the kinetic energy density. The second energy variable $\overrightarrow{I}$ presents the energy flow inside the system. The energy flow balance in a local region can be written as follows:

$$\overrightarrow{\nabla} \cdot \overrightarrow{I} + P_{diss} = P_{inj}, \tag{1}$$

where $\overrightarrow{\nabla}$ is the gradient operator, P_{diss} is the local dissipated power density, and P_{inj} is the local input density.

MES adopts the same damping model as that in SEA. It has been discussed in the literature (Lyon 2014) and can be expressed as follows:

$$P_{diss} = \eta \omega W, \tag{2}$$

where η is the hysteretic damping factor and ω is the circular frequency. Thus, the energy flow balance can be written as follows:

$$\overrightarrow{\nabla} \cdot \overrightarrow{I} + \eta \omega W = P_{inj}. \tag{3}$$

The MES propagative waves are characterized by a simple equation depending on the energy density W and energy flow $\overrightarrow{I}$ such that

$$\overrightarrow{I} = c \cdot \omega \overrightarrow{n}, \tag{4}$$

where c is the group velocity. This expression is valid in the far field for outing traveler waves and for undamped system.

2.2 Energetic Formulation

The MES formulation used the assumption of the noncorrelation of the propagating waves. In the following, the derivation the MES energetic formulation is done considering the n-dimensional (nD) space. So, in the case of 2D plates, the following equation will be considered with $n = 2$. Considering symmetrical waves, it corresponds to the propagating fields from a point source s in (nD) space.

Therefore, their fields depend only on the distance r between the source s and the measurement point m. The energy balance can then be written as follows:

$$\frac{1}{r^{n-1}} \frac{\partial}{\partial r} \left(r^{n-1} \overrightarrow{I} \right) + \eta \omega W \overrightarrow{n} = 0. \tag{5}$$

In addition, this equation can also be written considering only W, such that

$$\frac{1}{r^{n-1}} \frac{\partial}{\partial r} \left(r^{n-1} W \right) + \eta^2 \omega^2 W \overrightarrow{n} = 0. \tag{6}$$

The solutions of this equation in terms of energy density and active intensity are expressed by G and $\overrightarrow{H}$, respectively:

$$G(r) = \frac{1}{\gamma_0 c} \frac{e^{-\eta \omega r}}{r^{n-1}}; \quad \overrightarrow{H}(r) = \frac{1}{\gamma_0} \frac{e^{-\eta \omega r}}{r^{n-1}} \overrightarrow{u_r}, \tag{7}$$

where γ_0 is the solid angle of the considered space (2 for $1D$, 2π for $2D$, and 4π for $3D$ space), r is the distance between the source s and the measurement point m and $\overrightarrow{u_r}$ is the unit vector from m to s.

The total energy field is constructed by the superposition of a direct field P_{inj} (primary source) coming from the input power in the system surface Ω and a reverberant field σ (secondary sources) coming from the fictitious sources localized in the system boundaries $\partial\Omega$, as shown in Fig. 1:

$$W(m) = \int_{\Omega} P_{inj}(s)G(s,m)d\Omega + \int_{\partial\Omega} \sigma(p)G(p,m)\overrightarrow{u_r} \cdot \overrightarrow{n} \, d\Omega. \tag{8}$$

Finally, W can be expressed, thanks to an operator K.

$$(W) = K(P_{inj}, \sigma). \tag{9}$$

Thus, the matrix formulation of Eq. (8) can be written as follows:

$$\{W\} = [S] \cdot \{P_{inj}\}, \tag{10}$$

Fig. 1 Source description
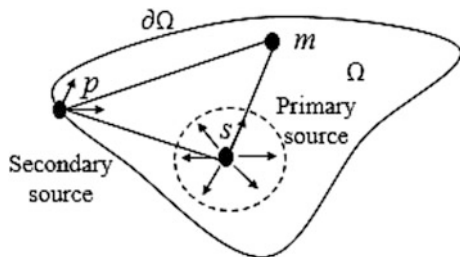
where $\{W\}$ is the energy density field and $[S]$ is the (n_s, n_m) matrix sensitivity operator. Let us recall that n_s is the number of sources and n_m is the number of measurements.

2.3 Inverse Formulation

The inverse simplified energy method will be presented in this section. The sources will be detected, thanks to measurements made on the system. In this paper, the localization IMES technique on $2D$ plate is applied. Thus, the MES Eq. (10) is discretized to provide the following matrix:

$$\left\{ \begin{array}{c} W_1 \\ \vdots \\ W_{n_m} \end{array} \right\} = \left[\begin{array}{ccc} S_{11} & \cdots & S_{1n_s} \\ \vdots & \ddots & \vdots \\ S_{n_m 1} & \cdots & S_{n_m n_s} \end{array} \right] \cdot \left\{ \begin{array}{c} P_1^{inj} \\ \vdots \\ P_{n_s}^{inj} \end{array} \right\}. \tag{11}$$

The IMES aims to invert Eq. (11). The injected power in the plate can then be localized through the knowledge of a set energy densities within the structure. Then, the IMES formulation is expressed as follows:

$$\{P_{inj}\} = [S]^+ \cdot \{W\}, \tag{12}$$

where $+$ is the pseudoinverse. In the next parts, the validation of this technique of sources localization with experimental tests for different positions of sources will be presented. In addition, a parametric study of the sensors repartition effect will be investigated.

3 Results and Discussion

This section deals with experimental tests for different positions of the shaker and number of measurements in order to validate the ability of the IMES technique to localize the structural load.

3.1 Experimental Setup

The system of measurement consists of a scanning Polytec laser vibrometer head connected to a data post-processing. The used structure here is a (1 m × 1 m) square plate of thickness $h = 0.014$ m. The plate is attached with an elastic string to simulate free boundary condition, as shown in Fig. 2.
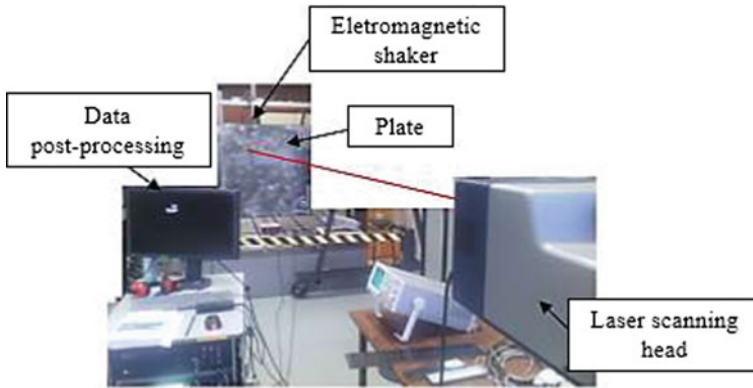
Fig. 2 Experimental setup
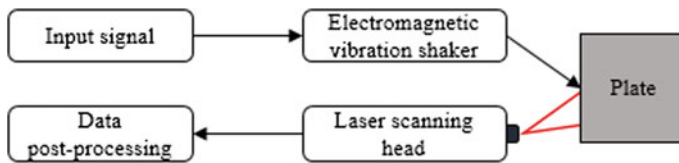
Fig. 3 Schematic of the experimental signal flow

The schematic of the experimental signal flow is shown in Fig. 3. The excitation signal is input into the vibration shaker, which transmits vibrations to the plate. The Polytec PSV-400 optical scanning laser head is used to measure the out plan velocity component of the plate, which is transferred to the vibration analyzer to study the vibration characteristic of the plate.

3.2 Experimental Validation

This section deals with an experimental validation of this technique for different positions of the shaker for the purpose to study the ability of the IMES localization technique to identify the input sources.

The electromagnetic vibration shaker is placed behind the plate, roughly in the location $(X, Y) = (0.32$ m, 0.53 m$)$ for position 1 and $(X, Y) = (0.35$ m, 0.04 m$)$ for position 2. The laser scanning head is placed at 4.8 m from the plate to measure the velocities on a selected surface of $(1$ m $\times$ 1 m$)$. In this test, the scanning surface is divided into $n_m = 100$ points as shown in Fig. 4:

- 10 points in the x-direction separated by $d_x = 0.1$ m.
- 10 points in the y-direction separated by $d_y = 0.1$ m.
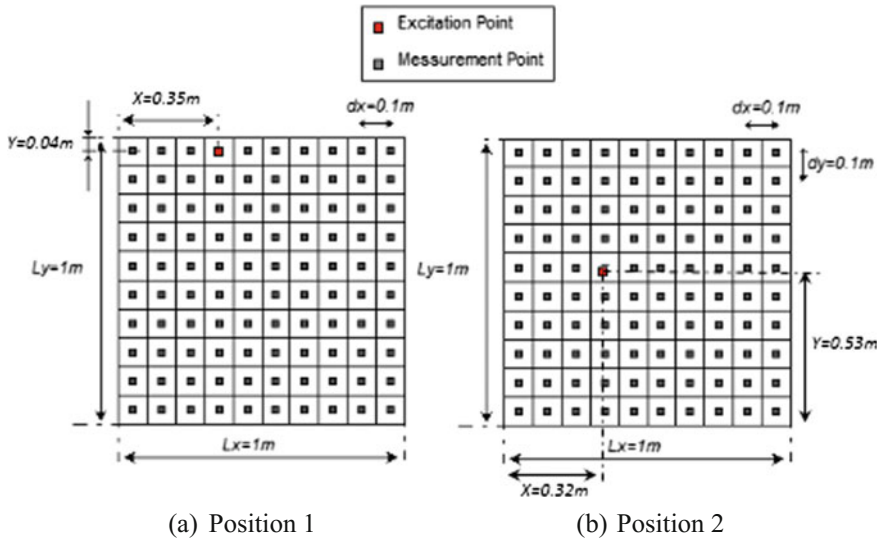
Fig. 4 Grid of measurement for $n_m = 100$

The aim of the plate velocity field measurement is to give a reference for force localization. The plate velocity field was measured with a scanning Polytec laser vibrometer at each point of the grid as presented in Fig. 4. Let us recall that the density energy field W is calculated from the measured velocities.

The results presented in this section are computed for a frequency center around $f_c = 1500$ Hz for the two positions of shaker. Figure 5 shows an example of the frequency response of the velocity at a point ($X = 0.3$ m, $Y = 0.85$ m) in the plate.

As shown below, it is clear that the modal density becomes high from 700 Hz. Thus, at frequency center higher than 700 Hz, one considers that the modal overlap is sufficiently high and the MES assumptions are valid for the validation of this experiment.
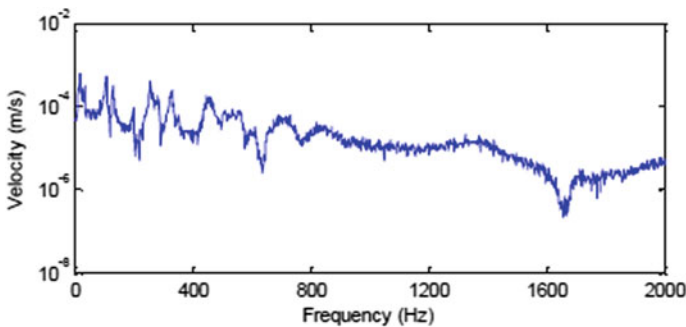
Fig. 5 Velocity (m/s) at point ($X = 0.3$ m, $Y = 0.85$ m)

(a) Position 1   (b) Position 2
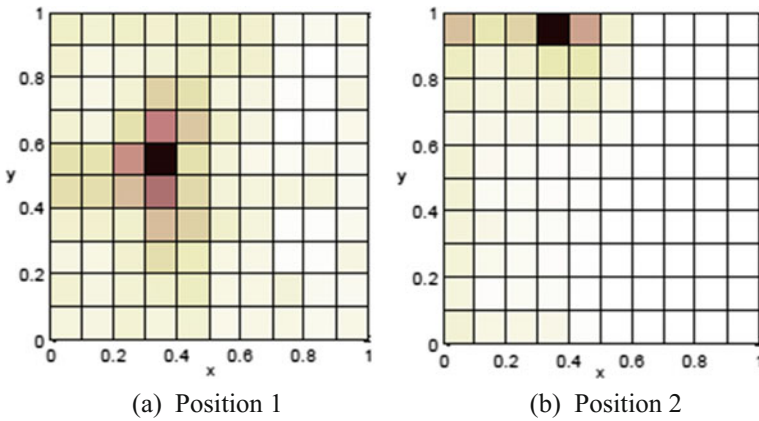
Fig. 6 IMES experimental source-location extraction

Figure 6 displays the source location from the measured data showing that the force applied by the different shaker positions clearly appears to be in the exact location. Furthermore, the case of position 2 seems to indicate that the near-field waves due to the boundary proximity do not disturb the location identification. This confirms the validation of the presented method.

3.3 Sensors Distribution Effect

After the validation of the technique of localization IMES, in this section, the influence of sensors repartition on the localization of the input sources will be investigated. In this application, the number of measurements n_m is changed for the two positions of the shaker and the results are presented in Figs. 7 and 8.

As seen below, a good localization of the two-shaker position is observed in Figs. 7 and 8 for the different number of measurements. For example, for a few

(a) $n_m = 36$ (b) $n_m = 100$ (c) $n_m = 784$
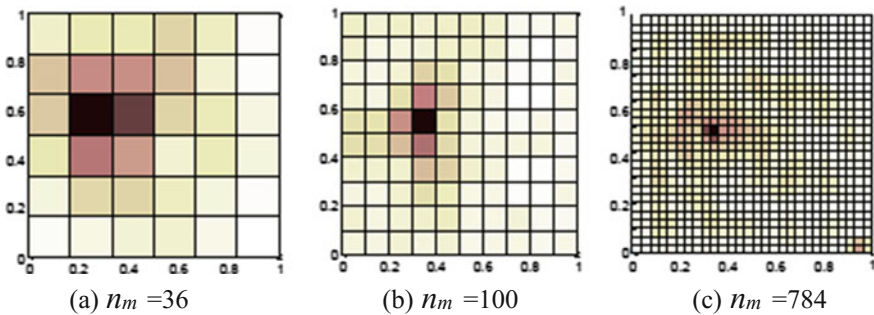
Fig. 7 IMES experimental source-location extraction for position 1

(a) $n_m = 36$ (b) $n_m = 100$ (c) $n_m = 784$
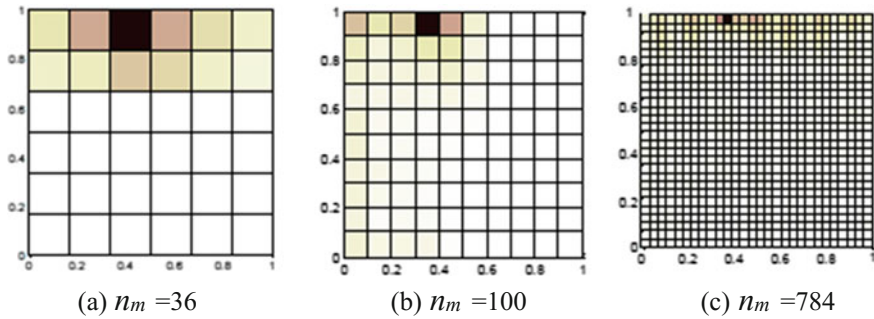
Fig. 8 IMES experimental source-location extraction for position 2

Table 1 Shaker position location for different n_m numbers

	$n_m = 36$		$n_m = 100$		$n_m = 784$	
	X (m)	Y (m)	X (m)	Y (m)	X (m)	Y (m)
Position 1	0.24	0.58	0.35	0.55	0.33	0.52
Position 2	0.41	0.08	0.35	0.05	0.36	0.53

measurement points $n_m = 36$, the estimated loads obtained by the IMES localization technique appear near to the exact positions.

Table 1 summarizes the estimated shaker location for the different number of measurements. It appears that the precision of shaker position increases when the number of measurements increases. Moreover, in this experiment, a good position of the shaker is obtained for a higher number of measurements, precisely for n_m upper to 100.

Finally, this section confirmed that the present method has an excellent performance in estimating the input forces.

4 Conclusion

The objective of this paper was to localize the vibration sources acting in $2D$ plate in mid- and high-frequencies by means of the energy density measurement. Several experimental test cases involving different positions of shaker and measurement points were considered. The obtained results confirm that the proposed approach exactly localizes the excitation force with a low density of measurement points. In the future works, the IMES method should be developed for structural health monitoring (SHM) application to detect the damage in the structure. Moreover, the detection of the position and size of the damage using IMES method is currently being investigated.

References

Besset S, Ichchou MN, Jezequel L (2010) A coupled BEM and energy flow method for mid-high frequency internal acoustic. J Comput Acoust 18(1):69–85

Chabchoub MA, Besset S, Ichchou MN (2011) Structural sources identification through an inverse mid-high frequency energy method. Mech Syst Signal Process 25(8):2948–2961

Corus M, Balmes E (2004) A priori verification of local FE model based on force identification. In: Proceedings of ISMA

Hardy P, Jezequel L, Ichchou MN (2002) Absorption coefficient and energy flow path identification by means of inverse local energy method. J Acoust Soc Am 112(5):2320 2320

Ibrahim SR, Fregolent A, Sestieri A (1996) Structural force identification at unmeasured locations. In: Proceedings-SPIE the international society for optical engineering. SPIE International Society for Optical

Ichchou MN, Jezequel L (1996) Letter to the editor: comments on simple models of the energy flow in vibrating membranes and on simple models of the energetic of transversely vibrating plates. J Sound Vib 195(4):679–685

Ichchou MN, Le bot A, Jezequel L (2001) A transient local energy approach as an alternative to transient sea: wave and telegraph equations. J Sound Vib 246(5):829–840

Ji CC, Liang C (2000) A study on an estimation method for applied force on the rod. Comput Methods Appl Mech Eng 190(8):1209–1220

Liu JJ, Ma CK, Kung IC, Lin DC (2000) Input force estimation of a cantilever plate by using a system identification technique. Comput Methods Appl Mech Eng 190(11):1309–1322

Lyon RH (2014) Theory and application of statistical energy analysis. Elsevier

Pezerat C, Guyader JL (1995) Two inverse methods for localization of external sources exciting a beam. Acta Acustica 3(1):1–10

Pezerat C, Guyader JL (2000) Force analysis technique: reconstruction of force distribution on plates. Acta Acustica 86(2):322–332

A CAD Assembly Management Model: Mates Reconciliation and Change Propagation

Ameni Eltaief, Borhen Louhichi, Sébastien Remy and Benoit Eynard

Abstract Nowadays, companies are developing more and more collaborative projects, and hence the need to exchange data with many partners, contractors, subcontractors, suppliers, and customers. So, to establish successful collaborations, they must ensure the relevance, coherence, and especially the security of exchanged data. But the Computer-Aided Design (CAD) systems still have gaps that need to be corrected in order to improve the productivity of the design process: they offer few solutions to maintain data consistency within the digital model. Adding to that poor management of changes, the user has to manage the consequences of each change manually. This research explores the role of mates' assembly, as defined in CAD systems, as a key to maintaining the links between parts in the assembly. In this work, we propose the CAD Assembly Management Model that is based on reference elements, in order to maintain mates between CAD entities when a part is modified by a partner and then reinserted into the assembly CAD, and then propagate changes.

Keywords CAD assembly · Change propagation · Mates · Reference element

A. Eltaief (✉) · B. Louhichi
LMS, ENISo, Université de Sousse, 4023 Sousse, Tunisia
e-mail: ameni.eltaief@yahoo.fr

B. Louhichi
e-mail: borhen.louhichi@etsmtl.ca

S. Remy
UMR UTT/CNRS 6281 ICD-LASMIS, UTT, CS 42060,
10004 Troyes, France
e-mail: sebastien.remy@utt.fr

B. Eynard
UMR UTC/CNRS 7337 Roberval, UTC, CS 60319,
60203 Compiègne Cedex, France
e-mail: benoit.eynard@utc.fr

459

1 Introduction

A Digital Mock-Up (DMU) is a geometric representation of an object or a set of objects in 3D, usually performed on computer in order to design them, analyze, and simulate their behavior. It is used to understand a product before it exists physically (really), including a virtual prototyping. The development process of the DMU involves a variety of expertise that gathers multiple partners that are often geographically dispersed. A CAD assembly is multiple components and/or sub-assemblies combined into a single environment. Different relationships, which determine component behavior in the assembly, are created. These relationships can range from simple constraint-based relationships that determine a component's position in the assembly, to advanced relationships such as adaptability. So each component of the assembly is linked and constrained with other components and consequently those links have a significant importance to maintain the CAD data coherence. But the design is not limited to the development phase. Product definition may go through several changes to improve and refine continuously the design, during its life cycle. The changes that are defined as shape changes or modifications that affect the fitting, the function, the material, or size parameters are designated as technical changes. Thus, our model (CAD Assembly Management Model) is based on assembly mates. The CAD Assembly Management Model enables a CAD assembly to be reconciled after parts modification and assists the user in propagating the modifications made.

This paper is organized as follows: In the next section, a review of related literature is presented. The framework and algorithms developed, to provide a CAD Assembly Management Model, are detailed in the third section. Finally, conclusions and perspectives for this work are provided.

2 Review of Related Literature

In the context of the CAD assembly management, Fouda et al. (2001) proposed a precedence graph generation system for product components, in order to improve CAD assembly management. He has harnessed the associations between components, described physical contacts and the order of insertion as well as relative motion and stability. Also, a fast assembly system was proposed by Li et al. (2010), based on TAFs (typical assembly features). The mechanism is mainly based on the assembly features and also on the possible constraints between them. It enables first reducing the complexity of the assembly process, and moreover to effectively manage its components. However, the SCAP (Security Content Automation Protocol) capable of creating a geometric and technological mock-up using various assemblies' components was developed by Mascle et al. (1997). It consists of four modules: the first module is the module which assigns a signature to each one of the assembly components; it also describes its assembling priority, its materials, etc.;

the second module assigns each component a signature to decipher the number of its instances in the assembly and how those instances are dispatched (in a circular fashion, linear, etc.); the third module is responsible for specifying the process used to assemble the component (welding, gluing, etc.); and the fourth one is to identify subassemblies and their instances. Concerning the product and assembly relationships management in the concurrent engineering and product life cycle management (PLM) domain, a novel approach to integrate assembly process engineering information and knowledge in the early phases of the product development process have been developed by Demoly et al. (2011). Their approach—called Skeleton geometry-based Assembly Context Definition (SKL-ACD)—enables the control of the product modeling phase by introducing skeleton entities consistent with the product relationships and the assembly sequence planning information. The NSM (Neutral Skeleton Model) can be developed from Part 42 of ISO 10303 STEP (2003), and also from neutral modeling commands that were defined in previous macro-parametric studies (ISO 10303-11 1994; Choi et al. 2002; Mun et al. 2003). The macro-parametric approach is proposed in order to exchange parametric CAD model data among commercial CAD systems. A neutral reference model about representation and propagation of engineering change information in collaborative product development is developed by Hwang et al. (2009). In the same context of changes propagation, Louhichi and Rivest (2012, 2014) proposed an approach which first considers the associations between the initial work package objects and the modified work package objects, and then the associations between the modified work package objects and the DMU, where the evolution of these objects (modified) is spread to the DMU. On the other hand, Yin et al. (2014) used topology faces as basic processing units and focused on the constraint relation between topology faces to develop a method for change propagation analysis from aircraft to assembly tooling. Eger et al. (2007) focused on the question of how designers can be made aware of the impact of a proposed change before they commit. It discusses the links between the product, process, and people domains that interact during product development, listing limiting factors that make change implementation risky and lead to increased change cost. His research paper called "engineering change analysis during ongoing product development" presents a tool to evaluate change proposals during ongoing design processes where the state of the development of parts is taken into account. The last is the work of Krishna (2009), which presents a framework to automate the identification of affected parts due to an EC (engineering change) and to document how the components are affected. It lists all the components that are affected by an EC along with their features. The attribute–component and component–component relationships are captured during the design phase and are used to identify the affected parts. This literature review presented allowed us to discover the (Krishna 2009) model where he presented a system for automating the identification of affected parts, after an EC (engineering change). This system enumerates all components that are affected by the change, as well as their characteristics. Indeed, we can learn a great deal from the method used in this aspect, and apply it later on our work because the identification of the affected parts is a fundamental step that precedes the propagation of the changes. In the same

context, the tool developed by Eger et al. (2007) to describe a tree of propagation of changes is also very beneficial. However, the approach proposed by Louhichi and Rivest (2014) seems to be a purely mathematical approach.

3 Proposed Approach: The CAD Assembly Management Model

In an efficient design framework, a component or a subassembly would be extracted from the CAD assembly, modified, and then reinserted in the assembly. The consistency and the coherence between the mPart and the iAssembly would be easily maintained. We aim at propagating change to the CAD assembly while maintaining consistency and coherence, and especially while conserving the mates existing in the assembly. But no warranty exists when new version of the part conserves its initial mate entities intact, so that the topological entities are not inalienable or permanent, whence come to the idea of creating permanent elements that are able to hold out and resist to modification. Subsequently, we chose to work with the reference element; each mate entity (geometric entity) will be represented by a reference element, and like that even if the real entities are modified or updated, the corresponding reference elements are constantly undamaged. So the mate is still valid. Therefore, the reinsertion of the modified part is easy and fluent. As a result, the assembly reconciliation is also becoming trivial and the rest is to propagate the changes to the whole assembly. The assembly management model operating mechanism is composed of four steps, as introduced earlier:

(1) Capturing the initial mates (between the iPart and the rest of the assembly parts) and creating the reference elements: modifying the mates;
(2) Comparing iPart and the mPart and detecting the modifications;
(3) Reconciling the mates between the mPart and the iAssembly and recognizing the necessary modifications;
(4) Propagating changes in order to obtain an mAssembly and maintaining the CAD data consistent and coherent (Fig. 1).

3.1 Modifying the Mates

3.1.1 The Coherence Maintaining Algorithm

In order to really carry out necessary changes (creation of the reference elements and editing the mates), we developed an algorithm called coherence maintaining algorithm (Fig. 2). This algorithm enables us to read through all mates of a component and manage them easily. It is dedicated to maintain the assembly
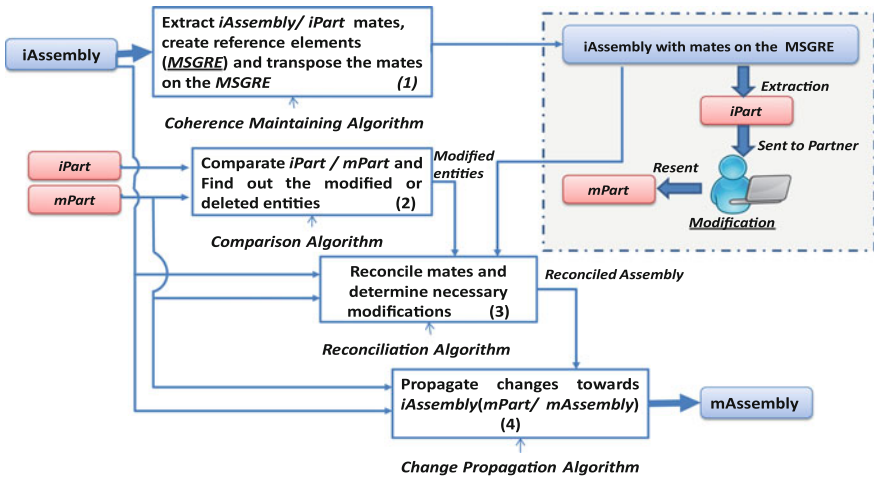
Fig. 1 General algorithm of the proposed approach
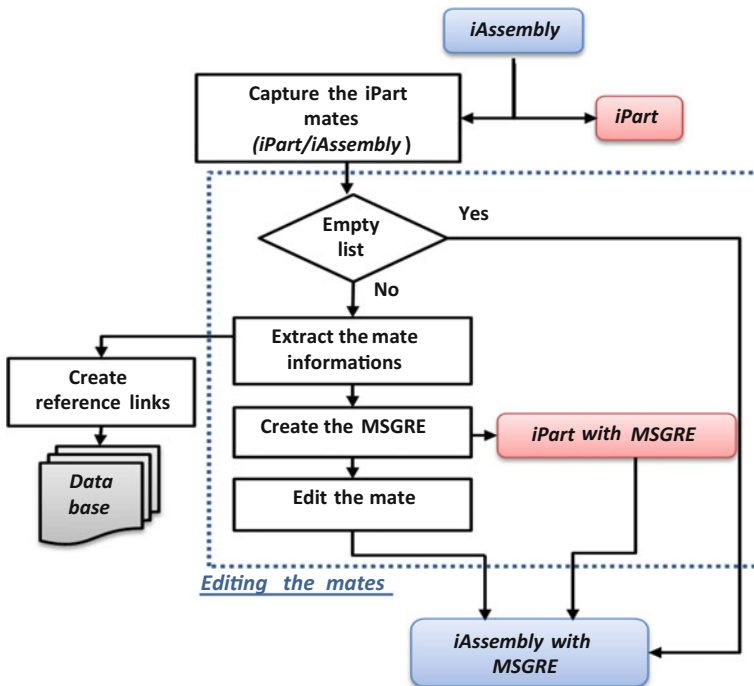
Fig. 2 Coherence maintaining algorithm (CMA)

associations and its consistency. The system inputs are iPart, which will be adapted, modified, or ameliorated, and the iAssembly. Thereby the mates, in whom the iPart is engaged, are captured via the coherence maintaining algorithm (CMA) as the first step, and then MSGRE are created before updating and editing the mates. For each captured mate, some important information is extracted such as

- Mate types,
- Mate entities,
- Mate parameters, and
- Concerned parts.

We note that the algorithm creates also *reference links* between the real mate entities extracted and the corresponding MSGRE created. Those links are saved in a *Data Base* in order to use them later on. And finally the MSGRE created are transposed on the mates, and we obtain the modified mate.

3.1.2 Minimum and Sufficient Geometric Reference Elements (MSGRE)

In order to conserve consistency, we choose to work on mates and to preserve the links between different components of the assembly. In fact, small modifications have to be done. Since real geometric or topologic entity mates are going to be substituted by *"Minimum and Sufficient Geometric Reference Elements"* called MSGRE, the MSGRE are defined as the set of geometric reference elements that can replace a real topologic entity, while keeping the same constraint that it had previously with other entities intact. It means that, if we remove this geometric entity of the assembly and replace it by these MSGRE, the assembly remains valid as well as the existing mates. We must note that this change will depend greatly on the nature and type of the mates that the real topologic entities are involved in. In some cases, even the type of the mate will change. The defined MSGRE are situated below:

- *Planar face*: A plane (the plane coinciding with the face);
- C*ylindrical face*: An axis (the cylinder axis);
- *Conical face*: An axis (the cone axis);
- *Spherical face*: A point (the center of the sphere);
- *Edge*: An axis (the axis coinciding with the edge);
- *Circular edge*: A point (the center of the circular edge).

To better explain the notion of the MSGRE an illustrative example is exposed (Fig. 3). The example shows that the planar faces engaged in a mate are substituted by a reference plane and the edges are substituted by axes. The MSGRE are created and the mate's entities are now permanent elements. The new mate entities can resist to modifications. Thus, the assembly coherence is maintained.
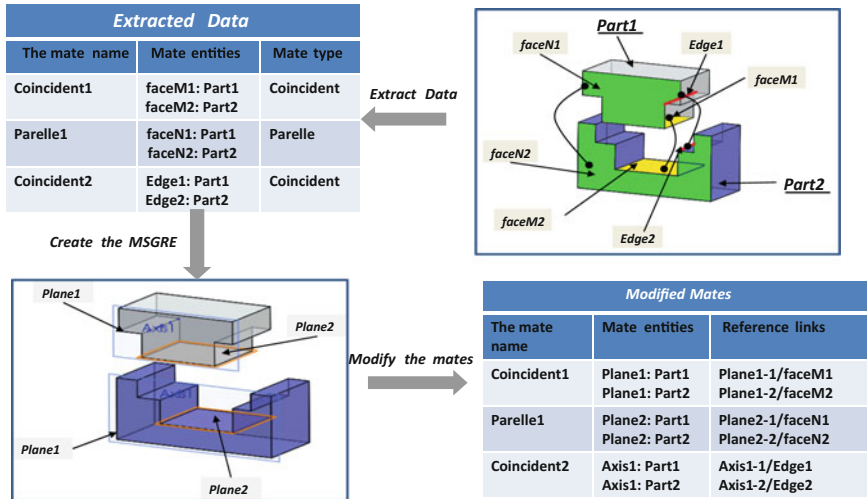
Fig. 3 Creating the MSGRE and modifying the mates

3.2 Comparing the iPart and the mPart

After editing the mates, creating the MSGREs and conserving the reference links between the real topological entities and their MSGREs previously created, we can now modify the iPart. It can be modified by the user or sent to a partner for adjustment. This section presents the algorithm enabling automatic comparison between iPart entities and entities of the mPart followed by an identification of the deleted or modified one. For this, we must recognize, for each face of the iPart, its corresponding face in the mPart, which is not a trivial task. Our ***comparison algorithm*** (Fig. 4) determines the characteristics of the CAD part (iPart). The last algorithm extracts *the topological and geometrical data* of the part:

- Topological Data:

  – Vertices, and
  – Edges,
  – Faces.

- Geometrical Data:

  – Surface of faces,
  – Lengths of edges, and
  – Coordinate of vertices.

While comparing those results extracted from the CAD model (iPat/mPart), the affected topologic entities are determined.

Fig. 4 Comparison between iPart and mPart
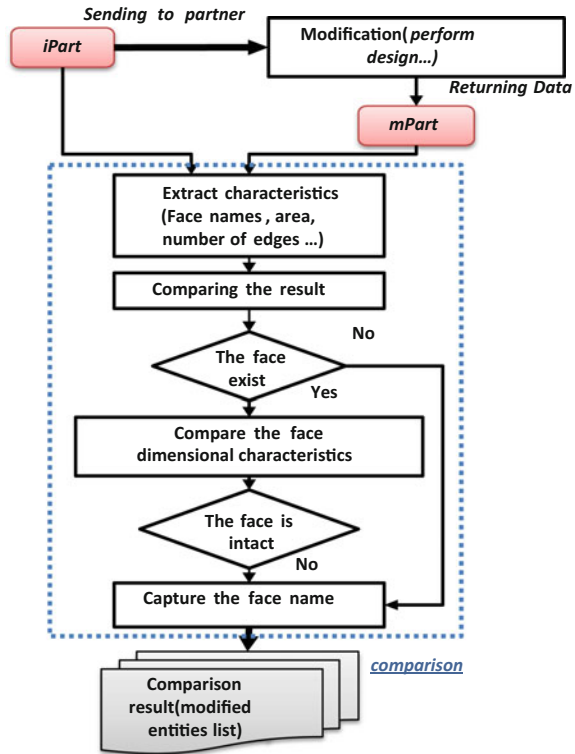
3.3 Reconciliation of the Mates

Since we have conserved the mates before editing the iPart, by creating permanent elements (MSGRE) that replace the real topologic entities, the reconciliation of the mates between the modified part (mPart) and the initial assembly (iAssembly) is becoming a feasible task. As the mates' entities now are represented by the created MSGREs, which remain intact even after the part modification, the mates remain valid (Fig. 3). As much as the mPart has different links and relationships with its neighbor's part and the rest of the assembly in general, any change that affects it will certainly require other parts change and especially the part, which was in direct contact with the affected faces (the faces that were lost or modified). Thus, an update must be done. Up to now, this update is done manually by the user or the designer. But we aim to make this step done automatically; our assembly management model will detect the features of the other parts that must be modified as a consequence to the iPart modifications and as far as, it detects even the sketches which need to be edited. In dead after comparing the tow version of the part in question (the mPart and the iPart) and detecting the modification that occurs (The previous step), for each detected entity (topologic entity), we associate the corresponding entity. An entity corresponds to another means that any modification that

affects the first must propagate to second and vice versa. We inspire the proposal of sketches detection from the work of Duhwan et al. concerning the skeleton model who considers the data of the skeleton model as basic and fundamental geometry for CAD modeling.

3.4 Change Propagation

Propagating changes to the mAssembly is the final step of the proposed in management model. Several solutions can be considered to help users make the changes required to obtain coherent associations and geometry between the mPart and the mAssembly. Therefore, we choose to work on solving a determined number (five scenarios) of change modification as it exists as an infinity of change modification scenarios (Fig. 5).

After editing the iPart, propagating the change to rest of the assembly is required. Normally, the propagation is done manually by the designer. All parts having a relationship with the one that has been modified must be updated. We aim to automate these propagations, which is not an easy or simple task. In this paper research, a tool of change *propagation*, which allows solving many scenarios of modifications, is developed. It represents the last step of the **CAD Assembly Management Model**. Subsequently, five scenarios are defined. The five scenarios identified are mainly based on the change propagation algorithm (Fig. 6). It is essentially developed on the principle of *correspondence associations* between entities of the different linked components of the assembly. It allows to easily propagating changes that affect a part of the assembly to the rest of the assembly parts, depending on the scenario of the modification that occurred; each affected

Fig. 5 Mates reconciliation algorithm
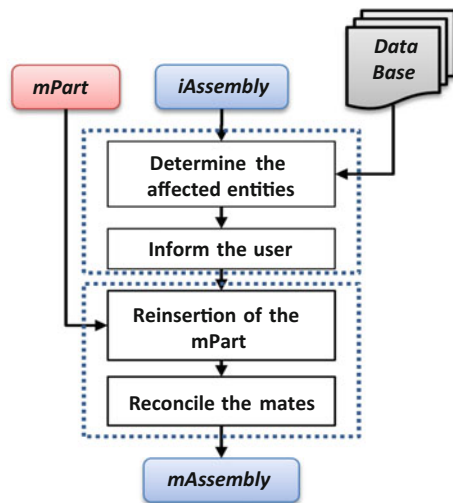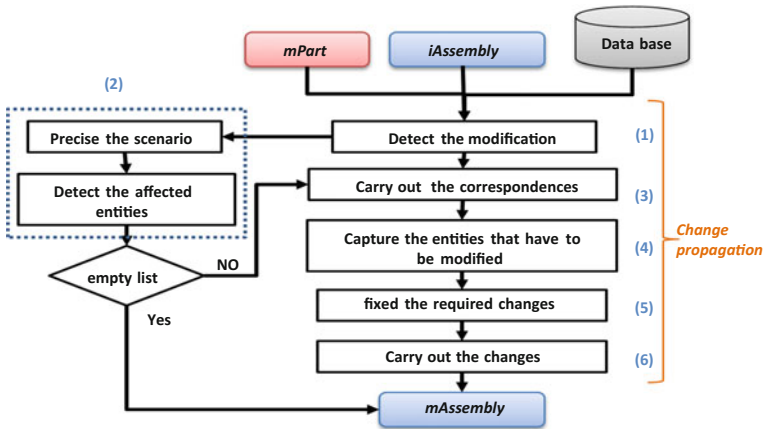
Fig. 6 Change propagation developed algorithm

entity of the part in question has its *corresponding entity*. As a result, the change propagation will affect only the entity concerned. The five scenarios defined are as follows:

- *Scenario1*: Section modification;
- *Scenario2*: Dimension modification;
- *Scenario3*: Sketch modification (sketch segments);
- *Scenario4*: Fillet, Chamfer, and Draft; and
- *Scenario5*: Linear or circular repetitions parameters modification.

4 Illustration and Validation

Our model is called a CAD Assembly Mates Management Model (CAD-A3M) which is mainly based on reference element that we used to maintain consistency of the CAD assembly and reconcile its mates and it is composed basically of four parts:
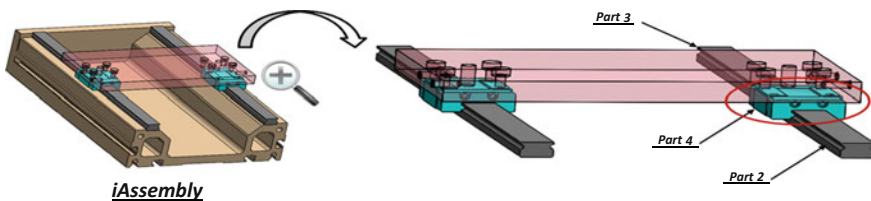
Fig. 7 iAssembly of the validation example

- Reference elements creation and editing the mates;
- Modifying the part and comparing it with the original;
- Reconciling the mates; and
- Change propagation.

To illustrate our CAD management model, we choose to work on the linear table (iAssembly) based on linear guidance containing a cylindrical form. But it is known that this kind of shapes is delicate and needs manufacturing precisions to decrease the risks, increase the stability, and the security we have to change the solution. So we choose to change the shape of our linear guidance to become a dovetail. The part in question, which will stand for modification, is the Part 4 shown in Fig. 7.
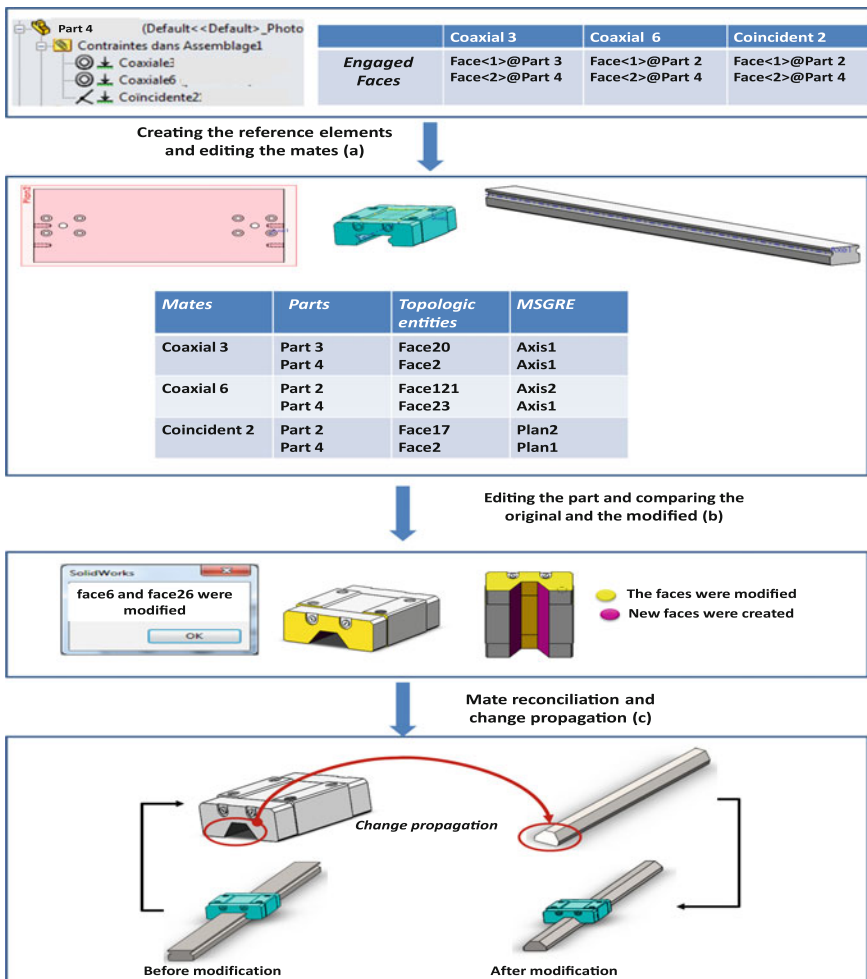
Fig. 8 Illustrative example

In the first step, the initial mates, between the iPart (Part 4 in our validation example) and the iAssembly, are extracted (saved in the Data Base: an Excel spreadsheet), as well as the topologic entities engaged in. This step consists of scanning the various assembly mates to identify the entities in the iAssembly and in the iPart that are concerned in the next steps. The second step is to create the corresponding Minimum and Sufficient Geometric Reference Elements (MSGRE). Each entity captured during the first step has its corresponding MSGRE as is shown in Fig. 8 (part (a)) using the CMA (Fig. 2). This step is essential for the transposition of initial mates toward the mPart. The comparison result, between two versions of Part entities (initial and modified), is shown with more details in Fig. 8 (part (b)). The third step consists of reconciling the associations between the mPart and the mAssembly. This step is becoming trivial as we the initial mates have been transposed. The user is alerted with a message indicating which entities have been modified or deleted and which entities are most likely to be modified. We provide the user with decision-making support, enabling him/her to make the changes as required obtaining consistent associations and geometry. An annotation is placed on each of them. Change propagation is the last and the most important step and it is done using the change propagation developed algorithm (Fig. 6). So the corresponding modification scenario is captured first and then the related associations are determined, in order to easily spread necessary changes to the whole assembly.

5   Conclusion

In this paper, we presented a mates management model that facilitates collaborative design by maintaining coherence between CAD elements. First, it detects the initial mates between the part to modify and the rest of the assembly, detect the geometric (reel) entities, and then create the corresponding reference element for each entity; and finally, we edit this to obtain a mate between low reference elements instead of reel elements or entities. Then we are now able to modify the model. Afterward, the second step is to compare the modified part with the original one and detects the modified or deleted entities. Our model third step is to reconcile the mates; the notion of the reference elements will make it very easy and fluent. And finally, the most important part of our work is to propagate changes to the whole CAD assembly. The last is the real objective of our model in order to facilitate the data exchange, reduce and minimize the user or designer role, and especially conserve the information consistency. As a conclusion, our CAD management mates model is a model that enables designer to save time and money, reduce errors, facilitate data exchange, collaborative design, and partners collaboration while maintaining the coherence, consistency, and security.

References

Choi G, Mun D, Han S (2002) Exchange of CAD part models based on the macro-parametric approach. Int J CAD/CAM l2(1):13–21

Demoly F, Toussaint L, Eynard B, Kiritsis D, Gomes S (2011) Geometric skeleton computation enabling concurrent product engineering and assembly sequence planning. Comput Aided Des 43(12):1654–1673

Eger T, Eckert C, Clarkson PJ (2007) Engineering change analysis during ongoing product development. In: International conference on engineering design, Iced'07 28–31 August 2007, Cité des sciences et de l'Industrie, Paris, France

Fouda P, Danloy J, L'Eglise T, De Lit P, Rekiek B, Delchambre A (2001) A heuristic to generate a precedence graph between components for a product family. In: International symposium on assembly and task planning (ISATP2001), 29 May

Hwang J, Duhwan M, Soonhung H (2009) Representation and propagation of engineering change information in collaborative product development using a neutral reference model. Concurr Eng (SAGE Journals)

ISO 10303-11 (1994) Industrial automation systems and integration—product data representation and exchange—Part 11: Description methods: the EXPRESS language reference manual, Geneva, Switzerland. International Organization for standardization (ISO)

ISO 10303-42 (2003) Industrial automation systems and integration—product data representation and exchange— art 42: Integrated generic resource: geometric and topological representation, Geneva, Switzerland. International Organization for Standardization (ISO)

Leilei Y, Dunbing T, Yuyun K, Sheng L (2014) Topology face–based change propagation analysis in aircraft assembly tooling design. Proc Inst Mech Eng Part B: J Eng Manuf (SAGE Journals)

Li GD, Zhou LS, An LL, Ji JF, Tan CB, Wang ZG (2010) A system for supporting rapid assembly modeling of mechanical products via components with typical assembly features. Int J Adv Manuf Technol 46:785–800

Louhichi B, Rivest L (2012) Management of associations within digital mock-ups for improved collaboration, PLM12: product lifecycle management: towards knowledge-rich enterprises. In: The IFIP WG5.1 9th international conference on product lifecycle management, 9th–11th July, École de Technologie Supérieure, Montreal, Canada. ISBN: 978-2-921145-82-4

Louhichi B, Rivest L (2014) Maintaining consistency between CAD elements in collaborative design using association management and propagation. Comput Ind 65:124–135

Mascle C, Jabbour T, Maranzana R (1997) Assembly features for mechanical product data. In: Proceedings of the IEEE international symposium on assembly and task planning (ISATP'97) —towards flexible and agile assembly and manufacturing, 7–9 August

Mun D, Han S, Kim J, Oh Y (2003) A set of standard modeling commands for the history-based parametric approach. Comput Aided Des 35(13):1171–1179

Reddi K, Young M (2009) A framework for managing engineering change propagation. Int J Innovation Learn 6(5)

Mechanical Performance of Doum Palm Fiber-Reinforced Plater Mortars

Naiiri Fatma Zahra, Zbidi Fayrouz, Allegue Lamis and Zidi Mondher

Abstract Due to the need to reducing the cost of construction and minimizing the environmental impact in producing, a Doum palm fiber has been used as a reinforcement for plater mortar. The objective of this work is to study the mechanical properties of plater mortar reinforced with varying length and mass fraction of Doum palm fiber. However, naturel fiber have been affected by the Alkali environment of mortar, to avoid this problem an alkali treatment of fiber with sodium hydroxide solution of 1% concentration has been used in order to reduce the effect of alkali attack. In this framework, five-fiber contents (0.5%, 1%, 1.5%, 2%, and 2.5%) by weight and three types of fibers (powder fibers, mixture fibers, and long fibers) have been used. The experimental investigation depicts an improvement of flexural strength for a fibers content equal to 1% for powder fibers and mixture fibers and 0.5% for long fibers. This improvement is due to the alkali treatment which removes the impurities in the fibers. For compressive strength, for 2% of treated Doum Plam fiber, it increase about 4.41%, 9.57%, and 1.26% respectively for powder, mix, and long fibers. Only samples with treatment fibers show an enhanced flexural and compressive strength. Thus, the alkaline treatment is a suitable choice to avoid fiber degradation in the alkali environment.

N. F. Zahra (✉) · Z. Fayrouz · A. Lamis · Z. Mondher
Laboratoire de génie mécanique, Ecole Nationale d'Ingénieurs de Monastir,
5000 Monastir, Tunisia
e-mail: fatma.naiiri@gmail.com

Z. Fayrouz
e-mail: zbidifayrouz@gmail.com

A. Lamis
e-mail: lamis.allegue@gmail.com

Z. Mondher
e-mail: mondherzidi@gmail.com

Keywords Doum palm fiber · Flexural strength · Compressive strength Sodium hydroxide treatment · Alkali environment

1 Introduction

The use of fibers in plater mortar as reinforcement become widely used, thanks to their capacity to limit and control crashing both at young age and under mechanical stresses.

Several types of vegetable fibers in various sizes have been incorporated into plater mortar. These fibers have been used as a reinforcement for composites in order to provide an economical aspect as well as high technical products. Thanks to their reduced cost, availability, and optimal mechanical performance beside synthetic fibers; lignocellulose fibers present a potential use as reinforcement (Tolêdo et al. 2003; de Silva et al. 2010).

Many works have been completely devoted the durability broken of natural fibers in cementitious environment. The fiber treatment represents a solution to alleviate the environmental chemicals aggressive (Tonoli et al. 2013; Barra et al. 2012).

Another solution to avoid fibers degradation is to limit matrix alkalinity through reducing the PH of the cementitious matrix using pozzolanic materials (de Souza Rodrigues et al. 2006).

Among another solution, an alkali treatment is commonly used to clear the surface of fibers. Several researchers have verified the interfacial adhesion improvement of the fiber to cement matrix with alkali treatment (Van de Weyenberg et al. 2006; Fayrouz 2014).

The aim of this work is to contribute to the valorization of the Doum palm fiber, characterized by their lower cost and their biodegradability.

The fiber content was varied from 0 to 2.5% weight percent to observe its effect on the mechanical properties.

2 Materials

2.1 Doum Palm Fiber

The tested fibers have been extracted from the Doum palm tree. That tree belongs to the family of the monocotyledons, like the graminy and musaces. The leaf is composed of folioles on which it grows the leafstalks. The obtained fibers length varies according to the tree type, its form, and its age.

Doum palm is planted in most of the main roads in rural and urban areas. They are used as decorative plants in public and private parks. Production of fibers from these leaves will convert the unused wasted leaves to renewable source materials and low-cost natural fibers that will be incorporated in plater mortar mixes.

The obtained fiber varies according to the method of extraction.

2.1.1 Fibers Extraction

The palm fibers used in this work are harvested in Monastir from a Doum palm tree. The used part of Doum palm is the leafstalks.

The extraction of the fiber was made in several steps. First, we cut the palm leafstalks; subsequently, they were crushed using a grinder made in mechanical engineering laboratory.

From this extraction method, we obtain a mixture of different lengths of fiber.

The following figure presents the different parts of Doum palm leaf (Fig. 1).

To study the effects of the fiber size on the mechanical properties of plater mortar, we choose to use three types of fiber:

- Powder fibers with average length 1 mm.
- Mixture fibers with average length 10 mm.
- Long fibers with average length 18 mm.

Fig. 1 Doum palm leaf
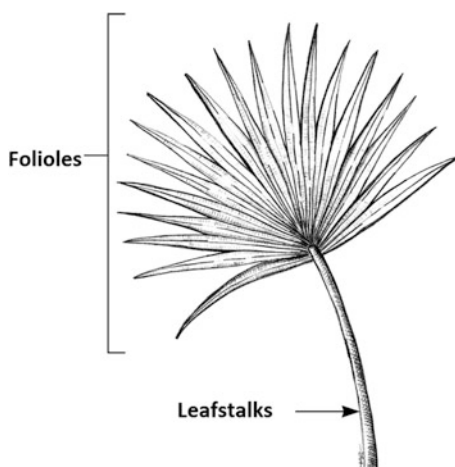
2.1.2 Fiber Treatment

The treatment of Doum palm fibers was performed by NaOH solution immersion. The Doum palm fibers were immersed in sodium hydroxide for 1 h at a temperature 105 °C. Then the fibers were rinsed many times to eliminate the excess of residual soda and followed with a bleaching of the fiber with sodium chloride. The use of sodium hydroxide removes a certain amount of lignin, waxes, and fats from the outer surface of the fiber (Fayrouz 2014).

Table 1 shows the three varieties of extracted fibers.

2.2 Mix Proportion

The fiber-reinforced plater mortar was tested in comparison with the control mix that had a ratio of 0.5:1 plater to sand (P: S) with W/P + S ratio of 0.6 (W: Water, S: Sand, P: Plater).

Various mix designs were prepared by altering the proportion of weight percentage of fiber to the binder at 0, 0.5, 1, 1.5, 2, and 2.5%.

2.3 Specimens Fabrication

In order to prepare specimens of 40 × 40 × 160 mm, we used the method recommended by Mokhtar (2013) for all fiber-reinforced plater mortar mixes. The weight percentage has been varied from 0.5 to 2.5% with a step of 0.5%.

An automatic mortar mixer with maximum capacity 5 L was used to produce the mortar composites.

The composites are obtained by mixing the sand, the water, and the plater with different ratios of treated and untreated palm fiber. The composites obtained are presented in Fig. 2.

Table 1 Abbreviations of the three varieties of extracted fibers

Fiber	Fiber properties
PNT	Untreated powder fiber
PT	Treated powder fiber
MNT	Untreated mixture of two types of fiber
MT	Treated mixture of two types of fiber
LNT	Untreated long fiber
LT	Treated long fiber
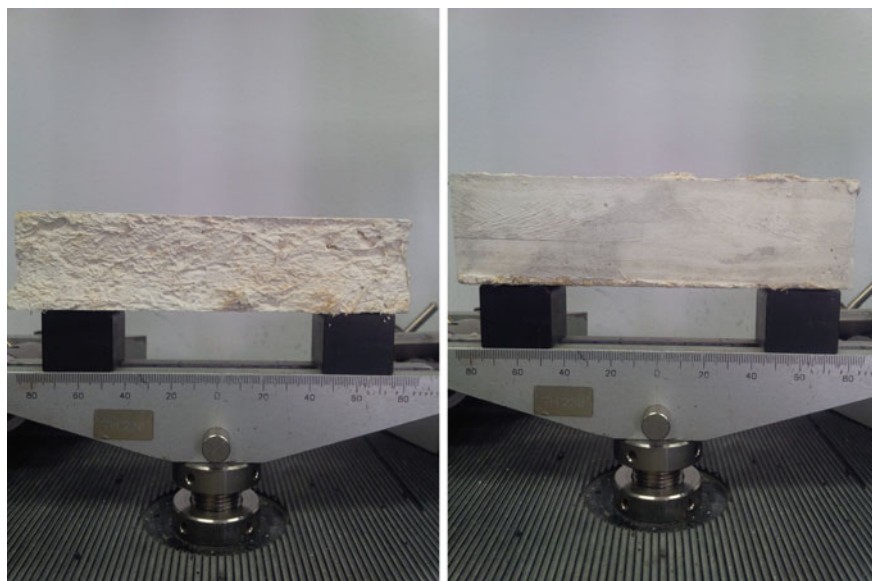
Fig. 2 Compression and flexion specimens

2.4 Test Program

After demolding, the specimens were cured until the date of test in the laboratory under normal climatic condition: Temperature $T = 20 \pm 2$ °C and relative humidity RH = $65 \pm 5\%$.

Three-point bending test and compressive test were conducted for 7 days, 28 days, and 1 year of curing in accordance to standard ASTM C109 (2012), with an average of three samples of $40 \times 40 \times 160$ mm for each trail, using a Lloyd Instrument tensile test machine of capacity 5 KN.

In the three-point bending test, the distance between the support was 10 cm.

A deflection rate of 0.1 mm/s for flexural test and 0.02 mm/s for compressive test was used for all tests.

3 Results and Discussions

3.1 Effect of the Treatment on the Diameter of Fibers

The equivalent diameter is determined from a series of fiber measurements with a profile projector on a batch of 100 fibers for each type.

The fibers having an alkaline treatment has a diameter less than those untreated because treatment eliminates residues of gummy material (Table 2).

Table 2 Physical properties of Doum palm fiber

Fiber	Diameter (μm)
Untreated leafstalk	307 ± 37.38
Treated leafstalk	287.4 ± 39.54

Table 3 Mecanical properties of Doum palm fiber

Fiber	Stress (MPa)	Tensile modulus (GPa)	Strain (%)
Untreated leafstalk	249.70 ± 8.95	6.34 ± 1.44	2.54 ± 0.44
Treated leafstalk	266.37 ± 9.23	7.83 ± 2.37	2.94 ± 0.34

3.2 Tensile Strength Results on the Doum Palm Fibers

The presented properties of fibers are calculated based on a randomly chosen sample of 10 fibers of 20 mm length. The resulting data of tensile strengths are presented in Table 3.

From the data presented in Table 3, we observe that treatment for 1 h in 1% sodium hydroxide solution concentration results in a rise in the tensile strength; this may be related to the increase in the degree of arrangement of the cellulose and the decrease of the lignin content in the fibers. By eliminating the lignin in fibers after treatment, the crystallinity increases which favors the improvement of the mechanical properties.

3.3 Mechanical Properties of Composites

3.3.1 Compressive Strength

All the presented results are for plater mortar tested after 1 year according to the standard ASTM C109. Compressive strength is one of the properties relative to building material. The variation of the compressive strength of the specimens as a factor of the powder fibers content is shown in Fig. 3. It is noticed from Fig. 3 that the compressive strength decreases for certain high percentage because the packing of fiber becomes difficult at high fiber content.

Figures 3, 4, and 5 show the evolution of the compressive strength of the plater mortars reinforced with, respectively, powder fiber, mix fiber, and long fiber as a function of fiber ratio cited above.

The addition of untreated fiber does not provide any improvement in the compressive strength. For 1% of treated Doum palm fibers, the compressive strength increases about 4.41%, 9.57%, and 1.26%, respectively, for powder, mix, and long fibers.

Thus, the decrease in compressive strength is a result of the poor fibers/matrix adhesion and the increase of the porosity in the matrix due to the air entrainment.

Fig. 3 The effect of the incorporation of powder fiber in mortar mix on the compressive strength
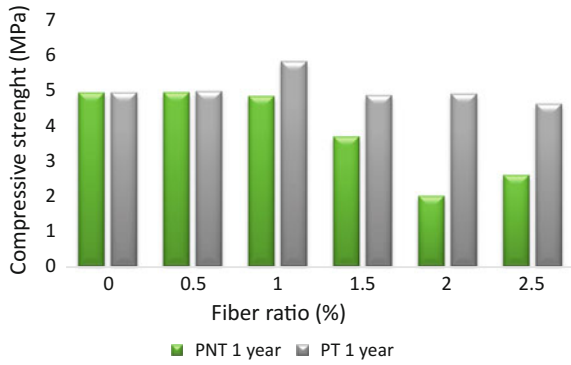
Fig. 4 The effect of the incorporation of mix fiber in mortar mix on the compressive strength
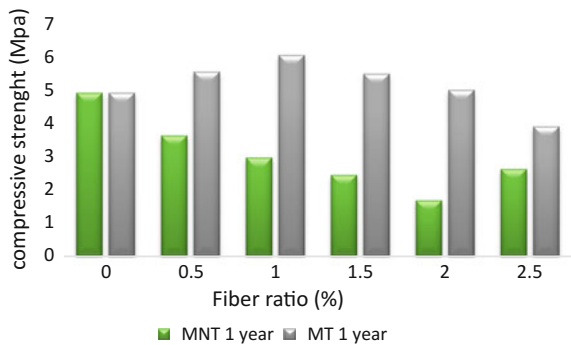
Fig. 5 The effect of the incorporation of long fiber in mortar mix on the compressive strength
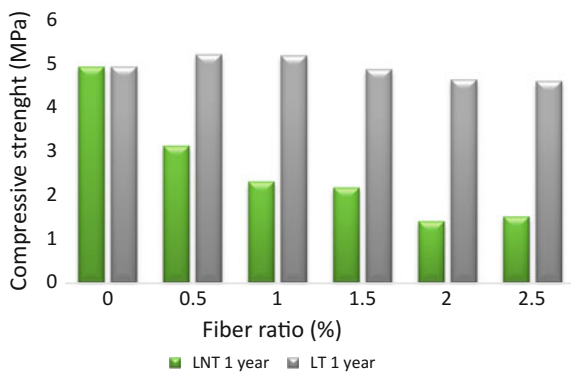
The maximum compressive strength was obtained for three types of fibers for percentage of fibers 1%. The fiber-reinforced plater mortars were more porous and less resistant than the plater mortar without fibers because they were made with more water. The alkaline treatment of three types of fibers does not decrease the

performance in compression of palter mortar; on the other hand, the addition of untreated fibers decreases the compressive properties of palter mortar. This shows the efficiency of the treatment and the improvement of adhesion fiber matrix.

3.3.2 Flexural Strength

Figures 6, 7, and 8 present the result of flexural test for three types of fiber. The flexural strength increases with lower fiber contents and decreases with higher fiber content; this is due to poor distribution of the fiber with the matrix and the excess quantity of fibers.

The treatment of fibers with NaOH entails change on the flexural strength for the same fibers ratio. The chemical treatment improves the interfacial adhesion between matrix and fibers.

The treatment removes the impurity on the surface of the fibers so it becomes uniform and the tensile strength become too high. These changes contribute to a better contact between fibers and matrix to obtain a greater flexural strength.

Fig. 6 The effect of the incorporation of powder fiber in mortar mix on the flexural strength
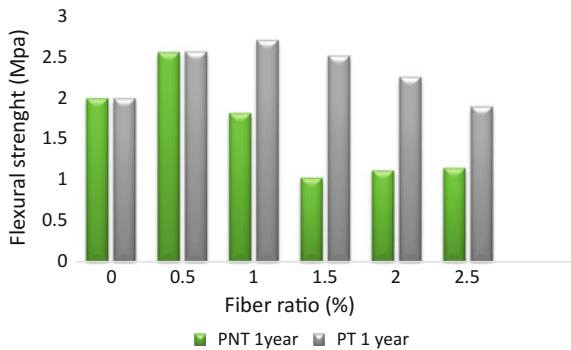
Fig. 7 The effect of the incorporation of mix fiber in mortar mix on the flexural strength
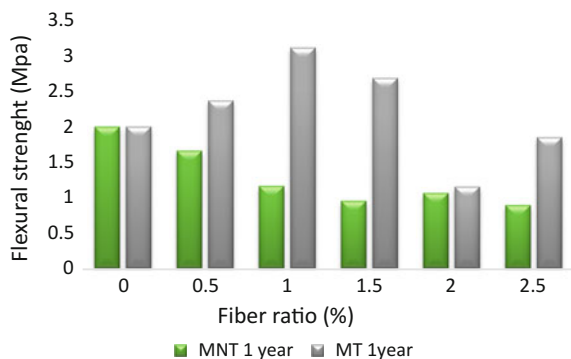
Fig. 8 The effect of the incorporation of long fiber in mortar mix on the flexural strength
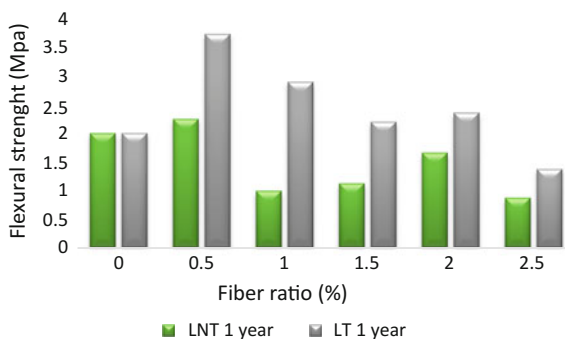
The higher flexural strength is obtained for Doum palm fiber ratio 1% for the treated powder, mix fibers, and 0.5% for treated long fibers.

4 Conclusion

This paper presents the results of an experimental investigation on the mechanical properties of the plater mortar reinforced with Doum palm fibers.

In the context to clarify the effect of alkali treatment on composite properties, a comparison has been carried out between composites reinforced by untreated fiber and treated fiber for 1 h in 1% NaOH solution.

The treatment with NaOH solution cleans the fibers by removing impurities and eliminating the weak boundary, which improves its flexural and compressive strength compared to the reference composites by the amelioration of the fiber-matrix adhesion.

Better performance is achieved with the addition of a low percentage of Doum palm fibers in the plater mortar, with 1% mass fraction of treated powder and mix fibers and 0.5% for treating long fibers; but for the other mass fraction, they have no impact on the composite mechanical properties.

Based on this study, it can be concluded that addition of treated Doum palm fibers in plater mortars improves the flexural and compressive strength more than untreated Doum palm fibers.

References

ASTM D7357-07 (2012) Standard specification for cellulose fibers for fiber reinforced concrete. ASTM International, West Conshohocken, PA

Barra B et al (2012) Effects of methane cold plasma in sisal fibers. Key Eng Mater 517:458–468

de Silva FA et al (2010) Physical and mechanical properties of durable sisal fiber-cement composites. Constr Build Mater 24:777–785

de Souza Rodrigues C et al (2006) Porosity and water permeability of rice husk ash-blended cement composites reinforced with bamboo pulp. J Mater Sci 41:6925–6937

Fayrouz Z (2014) thèse de doctorat. Université of Monastir, Etude des matériaux composites à base des fibres du palmier doum

Tonoli GHD et al (2013) Processing and dimensional changes of cement based composites reinforced with surface-treated cellulose fibres. Cem Concr Compos 37:68–75

Mokhtar R (2013) Magister, Contribution à l'Etude de la durabilité de mortier de plâtre à base de sable de dunes renforcé par des fibres de palmier dattier, University Kasdi Merbah Ourgla

Tolêdo et al (2003) Development of vegetable fibre–mortar composites of improved durability. Cem Concr Compos 25:185–196

Van de Weyenberg I et al (2006) Improving the properties of UD flax fibre reinforced composites by applying an alkaline fibre treatment. Compos Appl Sci Manuf. 37:1368–1376

Experimental and Analytical Analysis of Particle Damping

Marwa Masmoudi, Stéphane Job, Mohamed Slim Abbes, Imed Tawfiq and Mohamed Haddar

Abstract Particle damping is an emerging technology among passive devices for furnishing high damping of structural vibration, particularly in harsh environment, through the use of granular particles filled within an enclosure. In this work, we investigate experimentally the effect of acceleration amplitude, mass ratio, volume package, and type of material on the dynamic behavior of the particle damping to yield a thorough understanding of the attenuation mechanism played within such dampers. Experimental trials are realized within a rigid enclosure attached to a shaker and partially filled with particles. An analytical model based on the inelastic bouncing ball model (IBBM) is also developed in order to describe the nonlinear behavior of particle dampers. Our measurements reveal that the loss factor only relies on the total mass of the incorporated grains and on the driving magnitude. Further scaling of the loss factor, for all measurements, by the mass ratio led to a universal curve dependent only on the acceleration magnitude. A good agreement between the analytic model and the experimental results was verified.

Keywords Vibration suppression · Particle damping · Granular media

1 Introduction

Active and passive damping techniques are known method of attenuating vibration in most structural control application. Active control devices are not easy to implement as they present some costly prerequisites, in terms of environment preparation and power consumption. Due to these limitations, choosing passive

M. Masmoudi (✉) · M. S. Abbes · M. Haddar
Mechanics Modeling and Production Research Laboratory (LA2MP),
National Engineering School of Sfax (ENIS), B.P, 1173, 3038 Sfax, Tunisia
e-mail: masmoudi.marwa@gmail.com

M. Masmoudi · S. Job · I. Tawfiq
Quartz Laboratory, Supméca, 3 rue Fernand Hainaut, 93400 Saint-Ouen, France
e-mail: stephane.job@supmeca.fr

damping techniques is often a preferable solution. Among numerous passive damping devices, particle dampers which are receptacles or structural voids partially or totally filled with granules are an attractive alternative due to their advantages in a harsh environment (elevated temperature, cryogenic environment) over traditional approaches, e.g., viscoelastic materials. Particle dampers offer high damping by absorbing the kinetic energy of the structure and convert it into heat, through momentum transfer between moving particles and vibrating wall. Their performances mainly count on the capacity of the particles they are filled with to redistribute the energy of a harmonic motion among many degrees of freedom and over a broad frequency range.

Particle dampers technic present the natural evolution of the single-mass impact damper technic that refers to only a single body in a cavity. Particle dampers exhibit much greater damping effectiveness on vibrating structure than impact dampers. Furthermore, it includes the elimination of excessive noise and consequential damage of the cavity occurred by an impact damper. Studies achieved during the last years have demonstrated the effectiveness and potential application of particle dampers for controlling structural vibration. Paget (1973) described the first functional application of an impact damper, where it is used to attenuate the vibrations of turbine blades. Since a lot of fields are catching up and relying on particle dampers on their industries. Aerospace sector is the leader in this regard (Simonian et al. 2008; Panossian 2002; Ehrgott et al. 2009), automotive (Xia et al. 2011) and Chem Petroleum (Velichkovich and Velichkovich 2001) industries are more involved as well in the last decade. Many efforts were devoted to identify particle damper's features, making it a promising subject of study. Previous particle damper characterizations have adopted the use of a single-particle impact damper model to estimate the effectiveness of these devices (Araki et al. 1985; Yokomichi et al. 1996; Papalou 1993; Papalou and Masri 1996, 1998; Trigui et al. 2009). Currently, the discrete element method is highly adopted for particle damping analysis (Simonian 1995; Chen et al. 2001). This is due to the fact that DEM method keeps the track of all particles' motions within the host structure allowing the possibility to determine interactions between them (i.e., particles/particles and particles/host structure). Once interactions are well described, associated dissipated energy resulting from these interactions can be evaluated. Despite all these efforts, some aspects of this passive particle damping method are yet a mystery to analyze. A deeper understanding of experimental and numerical results can be achieved once having a protocol describing this technic's behavior.

In the present work, series of measurement relying on a granular damper were carried out using different material types and different volume package. The primary objective of this work is to identify characterizing elementary mechanisms in order to provide a thorough understanding of this emerging technology. The secondary objective is to develop a straightforward model to predict particle damping behavior. A good agreement between experimental and analytical results was checked.

2   Experimental Trials

The apparatus used for this experiment consists of a particle damper device attached directly to the shaker. The particle damper is a cylindrical cavity made of Plexiglas (Young's module = 3.1e9 Pa, density = 1190 kg/m^3), with interior dimensions of: diameter = 0.035 m, height = 0.04 m, and a mass equal to 0.3468 kg. A shaker connected to a function generator via a power amplifier is used to provide the exciting forces for the device defined below. A BK 4514 accelerometer is placed above the receptacle to measure its acceleration. A BK 8230-001 force sensor is placed between the shaker and the damper for the accurate excitation force sensor measure. Each of force sensor and accelerometer are related to acquisition chain, which discretizes their signal. A schematic of the experimental setup is shown in Fig. 1. The signal used to excite the structure is a sinusoidal excitation. Two types of granules are used; glass sphere (Young's module = 210e9 Pa, density = 7850 ± 0.1 kg/m^3) and steel sphere (Young's module = 69e9 Pa, density = 2630 ± 0.30 kg/m^3).

A set of measurement was carried out with this device by varying several parameters: different excitation level from 0.2 to 8g, different granules volume and different types of granular (as described in the below table). It is important to note that even at the maximum filling volume a clear gap remains between the top of the container and the top of the granular layer. The driving frequency f_1 used in experiments is equal to 166 Hz (Table 1).

This experimental method consists in determining the loss factor at the driving frequency

$$\eta_1 = \frac{E_{diss}}{2\pi E_{el}} \tag{1}$$

We attempt to measure the excitation force and the acceleration of the device. These measures will be introduced later into MATLAB Software for analysis. A synchronous detection method is used to extract fundamental experimental signals from noisy measured ones. After determining each of the excitation amplitude

Fig. 1 Schematic of the experimental setup
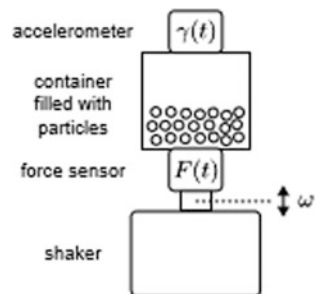
Table 1 Granular volume characterization for both steel and glass particle

Filling volume (L)	Steel (R = 1.07 ± 0.01)		Glass (R = 0.95 ± 0.03)	
	Mass (kg)	Number	Mass (kg)	Number
0.0074	0.0344	862	0.0117	1234
0.0111	0.0516	1293	0.0176	1851
0.0148	0.0688	1724	0.0235	2468
0.0185	0.0860	2155	0.0293	3085
0.0221	0.1032	2586	0.0352	3702
0.0258	0.1204	3017	0.0411	4319
0.0295	0.1377	3448	0.0470	4936
0.0332	0.1549	3879	0.0528	5553
0.0369	0.1721	4310	0.0587	6170

(F_1, γ_1) and phase angle (ϕ_F, ϕ_γ) for both of acceleration and force signals. Then the elastic energy of system is computed based on the following formula

$$E_{el} = \frac{1}{2} F_1 \delta_1 \cos(\phi_1^z - \phi_1^F) \tag{2}$$

The dissipated energy of the device is donated by:

$$E_{diss} = \pi F_1 \delta_1 \sin(\phi_1^z - \phi_1^F) \tag{3}$$

F_1 and γ_1 correspond to the fundamental component of the Fourier series at the driving frequency

$$F_1 e^{j\phi_1^F} = (1/nT_1) \int_0^{nT_1} F(t) e^{-j\omega_1 t} dt \tag{4}$$

$$\gamma_1 e^{j\phi_1^\gamma} = (1/nT_1) \int_0^{nT_1} \gamma(t) e^{-j\omega_1 t} dt \tag{5}$$

Thus the loss factor is expressed by:

$$\eta_1 = \tan(\phi_1^z - \phi_1^F) \tag{6}$$

Figures 2a, b, and 3a, b represent each of the elastic energy and the dissipated energy involved in the system. We note that the elastic energy increases as a parabolic form with the driving acceleration, which was expected, because the stored energy in the system evolves as the square of the excitation velocity. And now, concerning the dissipated energy, it depends heavily on excitation amplitude and granular volume embedded in the container. The formation of the dissipated energy is due to the motion of particles within the system. At the beginning, the dissipated energy is around zero for amplitude excitation loser than 1g and this can

be explained by the grain immobility. Beyond of 1g, the dissipated energy follows an increasing curve versus the amplitude excitation which is related to the difference between velocities at the instant of impact. Energy dissipation increases when particles collide with the plate with greater velocities and an opposite way.

Figures 2c and 3c represent the dynamic behavior of a cylindrical particle damper for each of glass and steel particles. It has been shown that the loss factor relies strongly on the amplitude of excitation and on percentage of changes in the granular volume. The loss factor evolution presents characterizing information; with value nearly null for excitation amplitude less than 1g (all grains are in contact with the container). Above 1g the loss factor increases with the driving magnitude until reaching the maximum attenuation at 2.5g for both steel and glass particle (i.e., the energy dissipated per cycle increases more important than the stored energy). As the excitation amplitude is increased more than 2.5g, the loss factor decreases progressively as the amplitude of acceleration increases (i.e., the energy dissipated per cycle increases lower than the stored energy).

Fig. 2 Experiments with glass particle. **a** elastic energy, **b** dissipated energy, **c** loss factor as a function of normalized acceleration for 9 different filling volumes
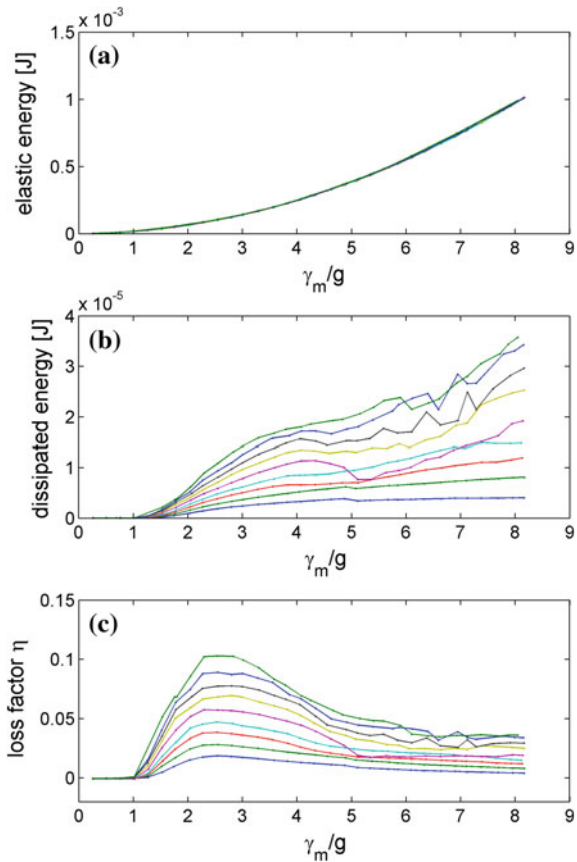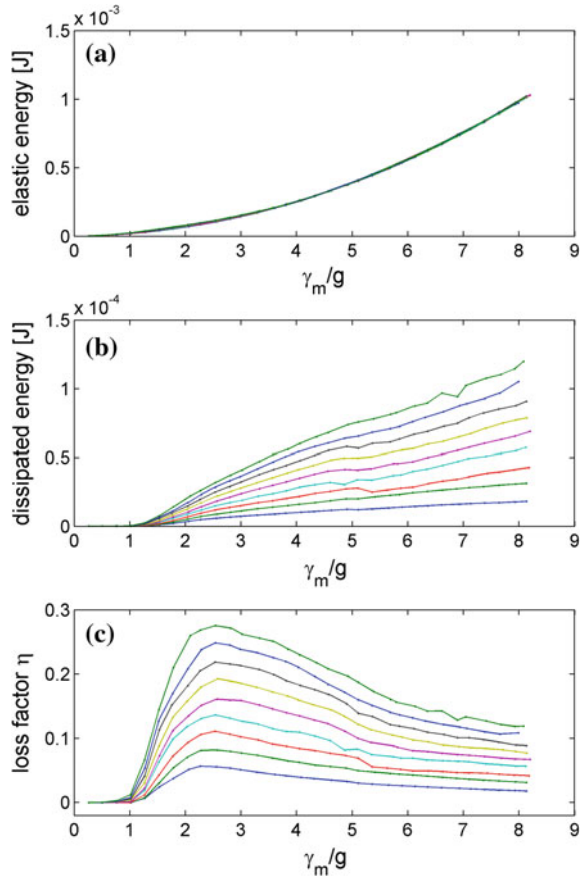
In this part, a parametric study approach was followed to identify which are the parameters that influence the loss factor evolution.

Figure 4 shows the maximum damping rate of each of glass and steel grains depending on the mass. It is clear that the maximum damping rate changes linearly depending on the grain mass, illustrating the proportional relationship between the damping rate and the mass of the grains. The damping factor is proportional to the ratio of the mass of grains introduced normalized by the mass of the empty box. Accordingly, a single curve that characterizes all the curves of the reduced damping factor was produced (see Fig. 5). The link of the loss factor with the mass of the grains has been carried out by Friend and Kinra (2000) and Marhadi and Kinra (2005). It is worth mentioning that our investigation corroborates their prediction at small mass ratio $\eta \propto mg/M \leq 1$, but fails to represent our results at greater values. This discrepancy can be explained by the distinction between our systems and protocols.

This figure also shows that the number of particles is not directly impacting the loss factor value. Analysis came to the fact that the maximum damping factor for the same amount of mass with different radius values is the same. In our case the

Fig. 4 Maximum loss factor versus ration between particle mass and enclosure mass for steel and glass particle
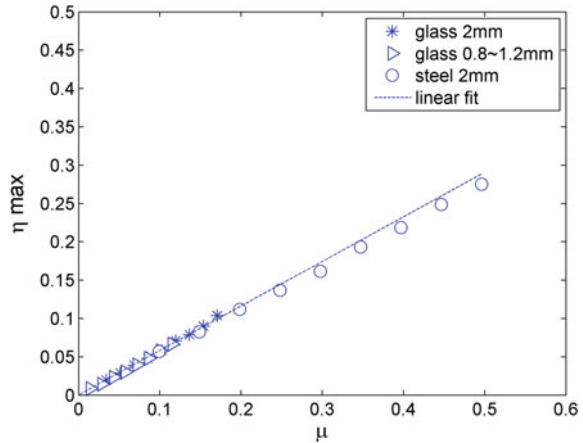
Fig. 5 Reduce Loss factor versus amplitude excitation for all granular volume for each of glass and steel particle
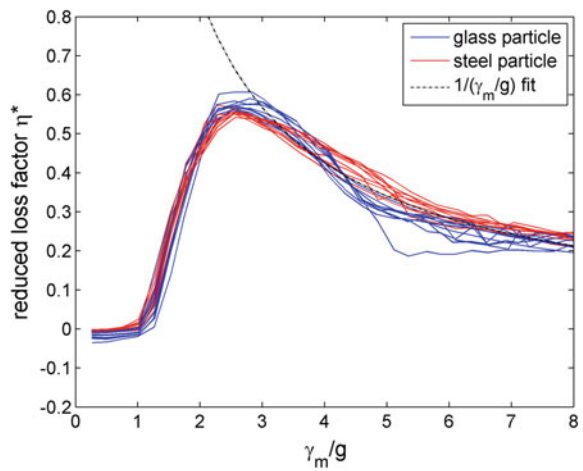
number of particles has almost grown 8 times when changing the radius keeping the same mass; Results confirm that the damping factor is still the same, which allows us to conclude that the number of particles is not a driving factor for the dissipation mechanism.

Figure 5 represents a unique and universal curve which characterizes the damping provided by each of the glass and steel particles which only depend on the nondimensional acceleration magnitude γ 1/g. These master curves are impacted neither on the material of the particles nor on the number of particles. The obtained results allow us to conclude that the number of particles is not a driving factor for the dissipation mechanism, meaning that dissipation of the system is not primarily managed by viscoelastic contacts (friction and inelastic collisions) between the particles. The dissipation process is linked to the redistribution of the vibrational energy among all grains. The increase in loss factor with the increase of the

introduced mass into the housing is linked to the kinetic energy stored by the grains when taking off the container which corresponds to the dissipated energy during the collision between the particles and the container.

3 Analytical Model

The investigation of the trajectory of a single equivalent inelastic particle vibrated on a plate, well known as the inelastic bouncing ball model (IBBM) furnishes the feature of the dynamics of vibrated grains in a simplified form (Mehta and Luck 1990; Pastor et al. 2007). In turn, this simple model can describe the energy dissipation mechanism implicated in a particle damper.

At this point, ensuing the IBBM model, we assume a set of noncohesive grains disposed on a vibrating plate oscillating at angular frequency $\omega_1 = 2\pi f_1$; (mass $M \gg m_g$)

$$z(t) = z_1 \sin \omega_1 t \quad \omega_1 = 2\pi f_1 \tag{7}$$

$$v(t) = z_1 \omega_1 \cos \omega_1 t = v_1 \cos \omega_1 t \tag{8}$$

$$\gamma(t) = -z_1 \omega_1^2 \sin \omega_1 t = -\gamma_1 \sin \omega_1 t \tag{9}$$

Once the acceleration of the plate exceeds the gravity, when it rises up, the particles can detach from the plate and start to bounce periodically on the plate.

In effect, the moment of takeoff t_d occurs when $\gamma_d = \gamma(t_d) = -g$

$$t_d = (1/\omega_1) \arcsin(g/\gamma_1) \tag{10}$$

The position and the velocity of the particle at the instant of the detachment are donated by:

$$z_d = z(t_d) = z_1 g/\gamma_1 = g/\omega_1^2 \tag{11}$$

$$v_d = v(t_d) = v_1 \left[1 - (g/\gamma_1)^2\right]^{1/2} \tag{12}$$

The granular layers leave the plate and its center of mass tracks a parabolic flight

$$z_f(t) = -gt^2/2 + v_d t + z_d \tag{13}$$

$$v_f(t) = -gt + v_d \tag{14}$$

$$\gamma_f(t) = -g \tag{15}$$

The highest position reached by the granular packing is equal to

$$z_f^m = z_f(t_f^{\max}) = v_d^2/2g + z_d \tag{16}$$

The particle collides with the plate at the instant t_c after his flight time τ_f;

$$z_f(t_c) = z(t_c), \text{ i.e. } -g\tau_f^2/2 + v_d\tau_f + z_d = z_1 \sin \omega_1(t_d + \tau_f) \tag{17}$$

The numerical resolution of Eq. 5 shows that $\tau_f \simeq 2v_d/g \pm 10\%$ for $\gamma_1 \gg 3g$, see Fig. 6.

Furthermore, the particle comes to the plan after the duration of flight τ_f with a speed $v_c = v_f(\tau_f)$; $v_c = -v_d$ for high amplitude excitation ($\gamma_1 \geq 3g$).

As a consequence, the relative velocity between the grains and the plate is

$$v_r = v_c - v(t_c) \text{ is } v_r \cong -v_1[1 + \cos(\omega_1(t_d + \tau_f))] \text{ for } \gamma_1 \geq 3g \tag{18}$$
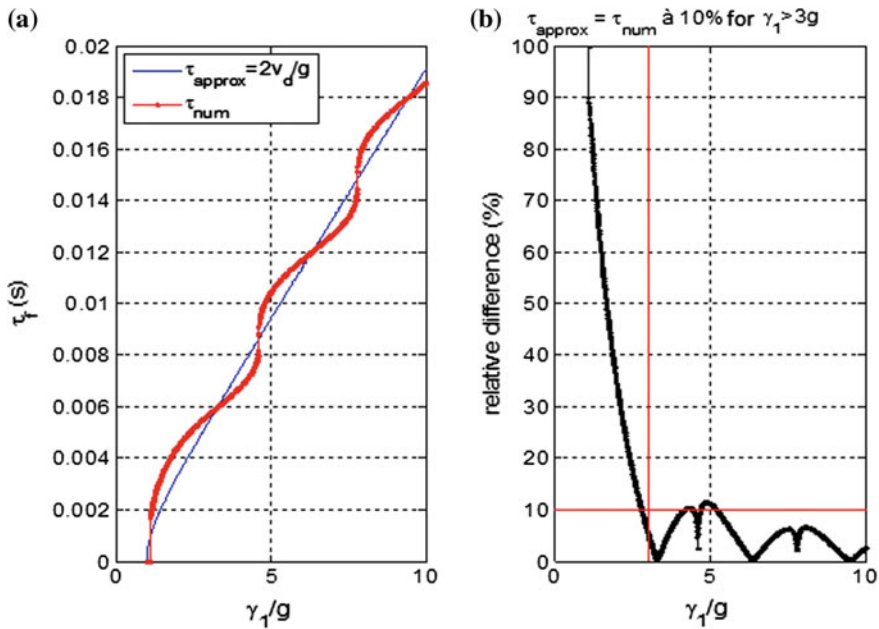
Fig. 6 a Duration of the gravitational flight τ_f between two collisions with the vibrating plate, as a function of the acceleration: numerical solution of Eq. 5 (red) versus the approximations $\tau_f = 2v_d/g$ (blue)

The impact of the noncohesive grains with the plate can be modeled by a perfectly plastic collision (McNamara and Young 1992). Then, the dissipated energy per cycle is expressed by:

$$E_d = (T_1/\tau_f)m_r v_r^2/2 \tag{19}$$

The term T_1/τ_f traduces the energy dissipated per collision into dissipation per cycle $T_1/\tau_f \cong \pi g/\gamma_1$ for $\gamma_1 \geq 3\,g$.

The kinetic energy of the plate

$$E_k = M v_1^2/2 \tag{20}$$

We finally determine the loss factor as $\eta_1 = E_d/2\pi E_k = (m_g/M)\eta_*^1$

$$\eta_*^1 \cong (\frac{g}{2\gamma_1}) \times \{1 + \cos \omega_1 (t_d + \tau_f)\}^2 \text{ for } \gamma_1 \geq 3g \tag{21}$$

$$\eta_*^1 = 0 \, \gamma_1 \leq g \tag{22}$$

The discrete set of driving amplitudes ($\gamma_1/g \simeq 4.6, 7.8, 10.6\ldots$) at which the loss factor tends to zero corresponds to cases where the collision velocity exactly matches the velocity of the plate, $v_r = 0$.

In the case of a large ensemble of particles, the multiple and delayed interactions with the plate desynchronize the dynamics of individual particles and prevent the cancelation of the attenuation, consistently with the description provided in Windows-Yule et al. (2015). In this case, the loss factor Eq. 7 is bounded by

$$\eta_*^1 \cong 2g/\gamma_1 \text{ for } \gamma 1 > 3g \tag{23}$$

Equations 21 and 23 are shown in Fig. 7.

Fig. 7 Representation of the reduced loss factor versus the driving acceleration
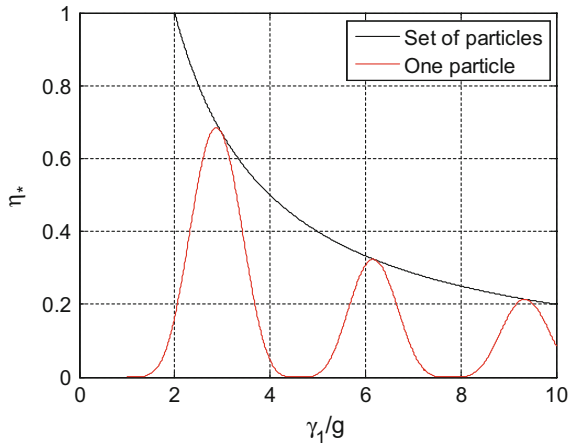
4 Conclusion

In this paper, we present an experimental device intended to characterize the dynamic behavior of particle damping. Additional parameters have been explored to provide an enhanced understanding of the attenuation mechanisms involved in particle dampers which is based on the inelastic collapses phenomena. We have developed a simple analytical model based on the IBBM description apt to describe the experimental setup. Our analysis generously anticipates the evolution of the loss factor determined experimentally.

References

Araki Y, Yokomichi I, Inoue J (1985) Impact dampers with granular materials (2nd report, both sides impact in a vertical oscillating system). Bull Japan Soc Mech Eng 28(241):1466–1472

Chen T, Mao K, Huang X, Wang MY (2001) Dissipation mechanisms of non-obstructive particle damping using discrete element method. In: Proceedings of SPIE international symposium on smart structures and materials: damping and isolation, vol 4331, March, Newport Beach, CA, pp 294–301

Ehrgott R, Panossian HV, Davis G (2009) Modeling techniques for evaluating the effectiveness of particle damping in turbomachinery. In: 50th AIAA/ASME/ASCE/AHS/ASC structures, structural dynamics and material conference, Palm Springs

Friend RD, Kinra VK (2000) Particle impact damping. J Sound Vib 233:93–118

Marhadi KS, Kinra VK (2005) Particle impact damping: effect of mass ratio, material, and shape. J Sound Vib 283:433–448

McNamara S, Young WR (1992) Inelastic collapse and dumping in a one-dimensional granular medium. Phys Fluids A 4:496

Mehta A, Luck JM (1990) Novel temporal behavior of a nonlinear dynamical system: the completely inelastic bouncing ball. Phys Rev Lett 65(4):393

Paget A (1973) Vibration in steam turbine bucket sand damping by impact. Engineering 143: 305–307

Panossian HV (2002) Non-obstructive particle damping experience and capabilities. Proc SPIE 4753:936–941

Papalou A (1993) Analytical and experimental studies of impact dampers. Ph.D. dissertation for University of Southern California, Civil Engineering Department

Papalou A, Masri SF (1996) Response of impact dampers with granular materials under random excitation. Earthq Eng Struct Dyn 25:253–267

Papalou A, Masri SF (1998) An experimental investigation of particle dampers under harmonic excitation. J Vib Control 4:361–379

Pastor JM, Maza D, Zuriguel I, Garcimartín A, Boudet JF (2007) Time resolved particle dynamics in granular convection. Physica D 232(2):128

Simonian SS (1995) Particle beam damper. In: Proceedings of SPIE conference on passive damping, SPIE, vol 2445, SPIE, San Diego, CA, 1995, pp 149–160

Simonian SS, Camelo VS, Sienkiewicz JD (2008) Disturbance suppression using particle dampers. In: 49th AIAA/ASME/ASCE/AHS/ASC structures, structural dynamics and material conference, Schaumburg

Trigui M, Foltete E, Abbes MS, Fakhfakh T, Bouhaddi N, Haddar M (2009) An experimental study of a multi-particle impact damper. Proc Inst Mech Eng Part C: J Mech Eng Sci 223(9):2029–2038

Velichkovich AS, Velichkovich SV (2001) Vibration-impact damper for controlling the dynamic drillstring conditions. Chem Petrol Eng 37:213–215. https://doi.org/10.1023/A:1017650519261

Windows-Yule CRK, Rosato AD, Thornton AR, Parker DJ (2015) Resonance effects on the dynamics of dense granular beds: achieving optimal energy transfer in vibrated granular systems. New J Phys 17(2):023015

Xia Z, Liu X, Shan Y (2011) Application of particle damping for vibration attenuation in brake drum. Int. J. Veh Noise Vibr 7:178–194. https://doi.org/10.1504/IJVNV.2011.040573

Yokomichi I, Araki Y, Jinnouchi Y, Inoue J (1996) Impact dampers with granular materials for multibody system. J Pressure Vessel Technol 118:95–103

Seeded Planetary Bearing Fault
in a Helicopter Gearbox—A Case Study

Linghao Zhou, Fang Duan, Elasha Faris and David Mba

Abstract Helicopters have been extensively employed as a versatile tool in modern society, thus guaranteeing operation safety and flightworthiness has always been our top-tier concerns. However, many accidents indicate that current helicopter health and usage monitoring system (HUMS) are not accurate and effective enough to fulfil this goal, especially for detecting an imminent planetary bearing fault (CAA Authority 2006). To study this case and address such issues, an experiment was undertaken with a special rig, comprising of real helicopter main gearbox (MGB) and dynamometer as a variable load. Defects of different sizes were seeded at the outer race of bearings inside second epicyclic planetary module. Vibration signals of different test conditions (input speed, load and defect sizes) were recorded for post-processing. Measured vibration data contains overwhelming background noise and planetary gear meshes, making it cumbersome to identify the bearing defect. Various signal processing techniques are applied to identify the bearing defect, including signal pre-whitening, gear/bearing signal separation, kurtogram, envelope analysis, high-order spectral analysis and so on. The comparative results suggest that certain combinations of aforementioned methods are more effective than single process techniques. One case of successful detection is demonstrated in this paper. This study potentially benefits improving HUMS effectiveness and supports helicopter maintenance decision-making.

Keywords Planetary bearing · Seeded defect · HUMS
Advanced signal processing · Fault diagnosis

L. Zhou (✉) · F. Duan · D. Mba
School of Engineering, London South Bank University, SE1 0AA London, UK
e-mail: zhoul7@lsbu.ac.uk

E. Faris
School of Mechanical, Automotive and Aerospace Engineering, Coventry University,
Coventry, UK
e-mail: ac1027@coventry.ac.uk

495

1 Introduction

Helicopters have been extensively employed as a versatile tool in modern society. They are distinctively different than other type of aircrafts due to their unique capabilities of direct taking off and landing, as well as performing some other flight regimes, e.g. hovering to fulfil special needs during operation. These specialties come from the structure of helicopters' dynamic system. As a crucial component for both dynamic drive train system and powertrain system in a helicopter, main rotor gearbox (MGB) functions in reducing high driving speed generated from engines, through a couple of complex epicyclic modules (Mba et al. 2011). MGB outputs reduced speed but large torque to drive main rotors, as well as transmitting power to other accessory components to make the helicopter operate as a whole.

However, the costs for being able to fly freely are large speed reducing the rate, and a constant change of loading zones for planetary bearings and gears, resulting in excessive heat, noise and contact among all the rotating components, making MGB prone to components wear and causing failure. Additionally, the overwhelming operational noise interferes the diagnosis regarding planetary rotating components.

As early as 1980s, the UK government started to encourage researchers and engineers to investigate the development of helicopter Health and Usage Monitoring System (HUMS), which is a combination of various sensors, alarms and condition indicators (CI) generated from processing sensor data to reflect helicopter health state (Land 2001). It was till 1986, the very unfortunate North Sea major accident which had caused nearly 50 casualties due to drivetrain malfunctioning, really accelerated HUMS progress (Larder 1999). Since 90s from last century, HUMS has been actively installed in helicopters. Evident suggests that applying HUMS shows positive results of decreasing helicopter accident rates, reducing maintenance cost and improving aircrafts' flightworthiness (JHSIT Team 2013). Nevertheless, tragic helicopter crashes still remind researchers that HUMS system accuracy and efficacy needs improvement. Especially, through analysing retrieved MGBs, HUMS did not give out accurate warnings to incipient fault happened planetary bearings/gears set (See Fig. 1), and thus these faults propagated towards

Fig. 1 Recovered epicyclic planetary module from a crash (AIBN 2016)

Fig. 2 Illustration of planetary carrier and gear/bearing sets (Greaves et al. 2013)
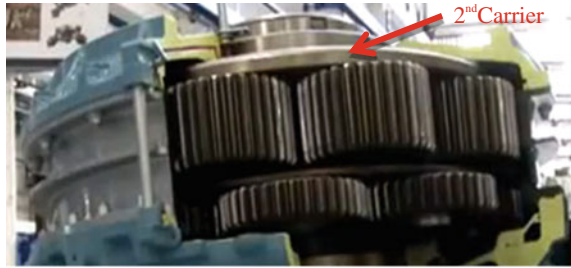
epicyclic case of MGB and eventually cause mechanical failure such as rotor imbalance, MGB disassembly, leading to catastrophic crashes (Department of Transport 2011).

The reasons for ineffective HUMS diagnosis include, but not limited to:

- Extremely strong operational noise, resulting in low signal-to-noise ratio.
- Dominating signals generated by gear meshes mask fault-related bearing signals.
- Different from simulation tests using the anchored signal bearing rig, planetary bearings also rotate with a carrier which drives the main rotor. This mechanism makes signal transmission path more complex, and more difficult to find fault-related resonances, especially if there is only one faulty bearing with incipient fault.
- HUMS CIs are generated mainly from statistical manipulation; the disadvantages of such indicators are that signals tend to not having predictable or stable statistical terms, thus the indication might not be accurate, e.g. kurtosis increases first but decreases as defects enlarging (Fig. 2).

2 Signal Processing Techniques

As stated in the previous section, too many factors could have hindered HUMS from successful fault detection. Monotonous CI-based detection method could be improved with introducing advanced signal processing techniques which contribute in dealing with problems and obstacles in the diagnosis of bearing defects.

Through literature review, I summarise those signal processing techniques into mainly three categories, namely signal separation techniques, signal enhancement techniques and fault signature extraction techniques, based on what each of them is excelling at. I will thus discuss these techniques in the following pages.

2.1 Signal Separation Techniques

Techniques listed in this paper are limited to those applied for analysis. The reader is referred to Randall and Antoni's work (2011) for a detailed review of other signal separation techniques.

2.1.1 Cepstrum Editing

Cepstrum is invented in 1960s (Bogert 1963) for speech analysis. Randall has made a thorough study on the history and applications of Cepstrum analysis (Randall 2016). Recent years more researchers are showing interests in Cepstrum editing and applied this technique in condition monitoring and fault diagnosis because its ability of suppressing targeted frequency components along with their harmonics (Randall and Smith 2016). Cepstrum is a term created from 'spectrum'; it is defined as Inverse Fast Furrier Transform (IFFT) of the estimated spectrum of raw signal x[n] in logarithm form. The equation is,

$$Cepstrum = IFFT\{\log(FFT(x[n]))\} \tag{1}$$

Editing Cepstrum was used to be applied in conjunction with complex value. Recently a real-Cepstrum editing pre-whitening method has been proposed (Randall and Smith 2016) since fault amplitude modulation matters more than phase in some case. The data domain of Cepstrum is 'quefrency' in unit of n samples, with lower quefrency range indicating higher frequency range. This feature brings convenience in processing data containing bearing fault-induced high-frequency resonances. Borghesani et al. (2013) proposed an efficient method by applying an exponential window in the form of $W(n) = e^{-an}$, where a is a parameter selected based on your choice of frequencies to be suppressed and n is simply discrete data length. This window functions in a way that passing low quefrency but suppressing higher quefrency components, thus separates fault-induced high-frequency resonances from repetitive gear frequencies and harmonics.

2.1.2 SANC and DRS

Self-adaptive noise cancellation (SANC) and Deterministic Random Separation (DRS) are compared very often because their core theory is very much alike, i.e. different correlation length of periodic signals (gear-related) and random signals (bearing-related and noise). Periodic signals have longer autocorrelation length than that of random signals. Through this key point, properly chosen delayed signal could be used to compare with the original signal and imitate the predictable components from the original signal. The part that cannot be predicted will be separated as more 'random' signal.

With that being introduced, SANC was first invented, previously for denoising speech using an adaptive filter. Adaptive filters could adaptively adjust filter coefficients iteratively based on different algorithms embedded, i.e. Least Mean Square (LMS), Kalman Filter and Recursive Least Squares (RLS). Different adaptive methods determine stop condition for ultimate outcome. It would be optimum when the final separation results from a subtly chosen delay where periodic signals are still correlated, but random signals are not, hence they can be separated iteratively.

The side effect of reliable results from SANC is relatively tedious work of choosing delays, convergence factors for filters to adapt and filter length. Antoni and Randall (2004a, b) developed a novel method to provide another perspective of solution, which is Deterministic and Random Separation (DRS) method. With the same core theory applied, this method approaches separation in faster and easier way of introducing FFT. First, divide the raw signal into several equal-length sections, then apply a fine selected delay to each section. The following equation is then adopted from the concept of Frequency Response Function:

$$FRF(f) = \frac{E\{D(f)d(f)\}}{E\left(|D(f)|^2\right)} \qquad (2)$$

where $D(f)$ is a spectrum of each section, while $d(f)$ is that of delayed section. E represents expectation operator. This method provides fast calculation in calculating stable frequency responses while using multiple averaging to suppress unstable frequency components instead of adaptive algorithms. The trade-offs for such superior features are requirement of no-smear in frequency domain and perhaps larger filter length. Also in practice, SANC provides more reliable results when speed fluctuations cannot be fully handled. Antoni and Randall (2011) have made a detailed study on both SANC and DRS method including suggestions on choosing parameters.

2.2 Signal Enhancement Techniques: NCS

Separation techniques are designed to separate deterministic signals with nondeterministic signals. The fact that random noise also consists part of nondeterministic signals make it reasonable to apply some other enhancing techniques to improve SNR. Neighbour coefficient shrinking (NCS) rule combined with complex dual-tree wavelet transform (CDTWT) is discovered to fulfil this goal. CDTWT is recently studied to address the problems of traditional real discrete wavelet transform (DWT) such as oscillation, aliasing, shift variance and so on. Due to CDTWT's better accuracy of representing singularities, Wang and his group (2010) proposed a new way for denoising with NCS method. NCS has a long history of being developed as a denoising rule. Due to page limitation, the author will not invest

more contents on the application of NCS, because of its nature of heavily mathematical involvement. Detailed information of NCS and CDTWT could be found in Selesnick et al. (2005).

2.3 Fault Signature Extraction Techniques: Envelope Analysis, Kurtogram

Most commonly, bearing defects, e.g. bearing outer race defect, inspires faulty signal when rolling elements rotate across the crack surface. Despite such signal's spikey nature, it is too weak to be detected directly. However, bearing structures are prone to amplify such bearing signals to form a cyclostationary (Antoni and Randall 2004a, b) high-frequency resonance. Thus an indirect way of retrieving diagnosis information inspired by faulty bearings is by analysing high-frequency resonances.

Although not first developed for such purpose, Envelope Analysis is indeed capable of demodulating signals in high-frequency band, and by analysing the envelope that are amplitude modulated by faulty bearing signal, fault frequency components can thus be extracted and adopted for diagnosis. For many years, Envelope Analysis has been established as benchmark method for bearing fault detection. In Bonnardot's research (2005), the detailed graphic explanation of Envelope analysis using Hilbert Transform (HT) demodulation is demonstrated.

With all the advantages of Envelope Analysis, one drawback is the simple difficulty of determining suitable demodulation band, i.e. finding the right structural resonances of bearings. That's where Kurtogram weighs in. The idea of Kurtogram comes from the question of how to properly illustrate Spectral Kurtosis (SK), which is essentially kurtosis of complex envelope of signals in different frequency bands buried in raw signals (Antoni and Randall 2004a, b).

$$K(f) = \frac{\left\{ |X(t,f)|^4 \right\}}{\left\{ |X(t,f)|^2 \right\}^2} - 2 \tag{3}$$

where $X(t, f)$ is a complex envelope of the signal band passed around centre frequency f. It is desired to demonstrate SK at different centre frequency, as well as different frequency bandwidth Δf. Thus Kurtogram is developed, as a function of $(f, \Delta f)$. Kurtogram provides optimum centre frequency along with corresponding frequency band for envelope demodulation, where the hidden impulsive signatures that are related to bearing defects are extracted from strong noises. Now Kurtogram has been widely adopted when dealing with hidden spikey signals or addictive noise removal.
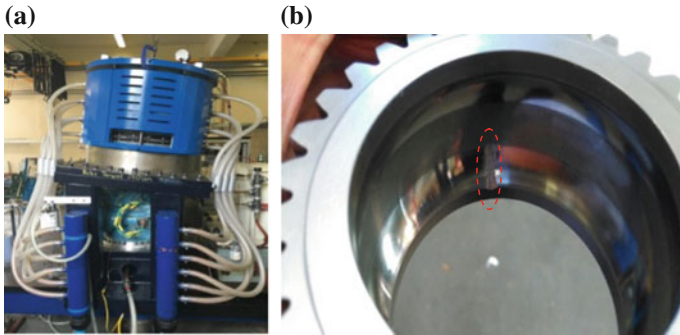
Fig. 3 Illustration of test rig (**a**) and illustration of major defect (**b**)

Table 1 Test condition summary

Fault type	Input speed (RPM)	Load (kW)	Sampling rate (Hz)	BPFO (Hz)
Major	14000	100, 180	25600	59.34
	16000	100, 180	25600	68.25

3 Seeded Bearing Defect Tests with Commercial MGB

In order to validate aforementioned techniques, and also investigate on real vibration data collected from commercial-available operational MGB, seeded bearing defect tests were undertaken with a special designed MGB rig. The rig is illustrated in Fig. 3a.

On top was a cylindrical dynamometer, worked as an adjustable load. Beneath the load was the tested MGB, model Super Puma SA 330. This MGB consists of two epicyclic modules. We planted major and minor outer race defect at second epicyclic planetary bearing. Four accelerometers of which two of them are triaxial were installed at epicyclic module case and input module to collect vibration data. A major defect is demonstrated in Fig. 3b

The test conditions for major defect test are summarised in Table 1, noted that minor defect test had exact same conditions. Bearing ball pass frequency of outer race (BPFO) calculated as fault frequency indicator is also included.

In this paper, because of page limitations, only processing results of a major fault, 16000 rpm with 180 kW load test are demonstrated.

4 Results and Discussions

In the following pages, processing results using a combination of several techniques introduced before are demonstrated and discussed.
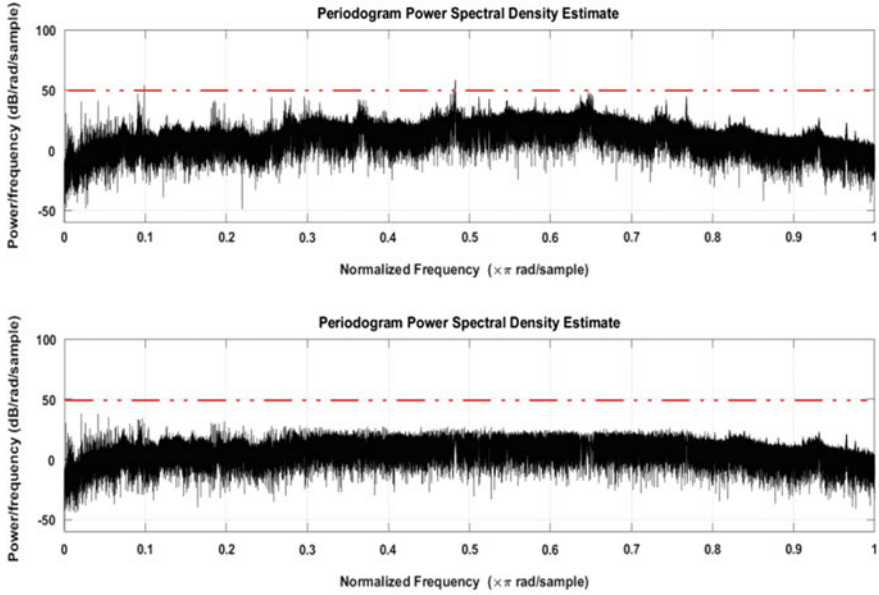
Fig. 4 Separation results of SANC

Figure 4 demonstrates the separation results using SANC techniques in power spectral density graph (PSD). It is quite evident that strong, repetitive spectral spikes which are believed to be related with gear meshes in upper graph are significantly eliminated.
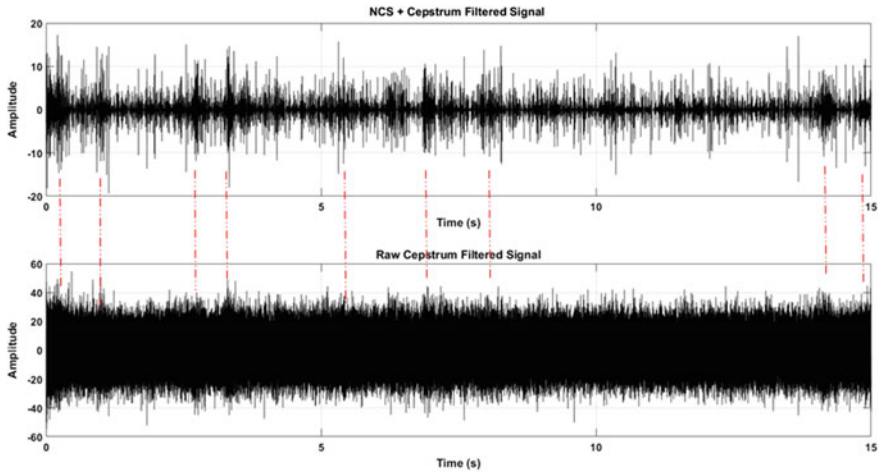
Fig. 5 Denoising results using NCS

After Cepstrum editing, NCS was applied and drastically reduced non-spikey random noises. Result is shown in Fig. 5, where upper graph is reconstructed signal after NCS, in comparison with the signal before NCS.

With the aid of Kurtogram, a proper frequency band was chosen for demodulation. Spectral analysis was then performed on squared envelope for fault frequency capture. In comparison, the result of the major defect is shown beneath result of processing data from healthy bearing tested under the same condition, see Fig. 6.
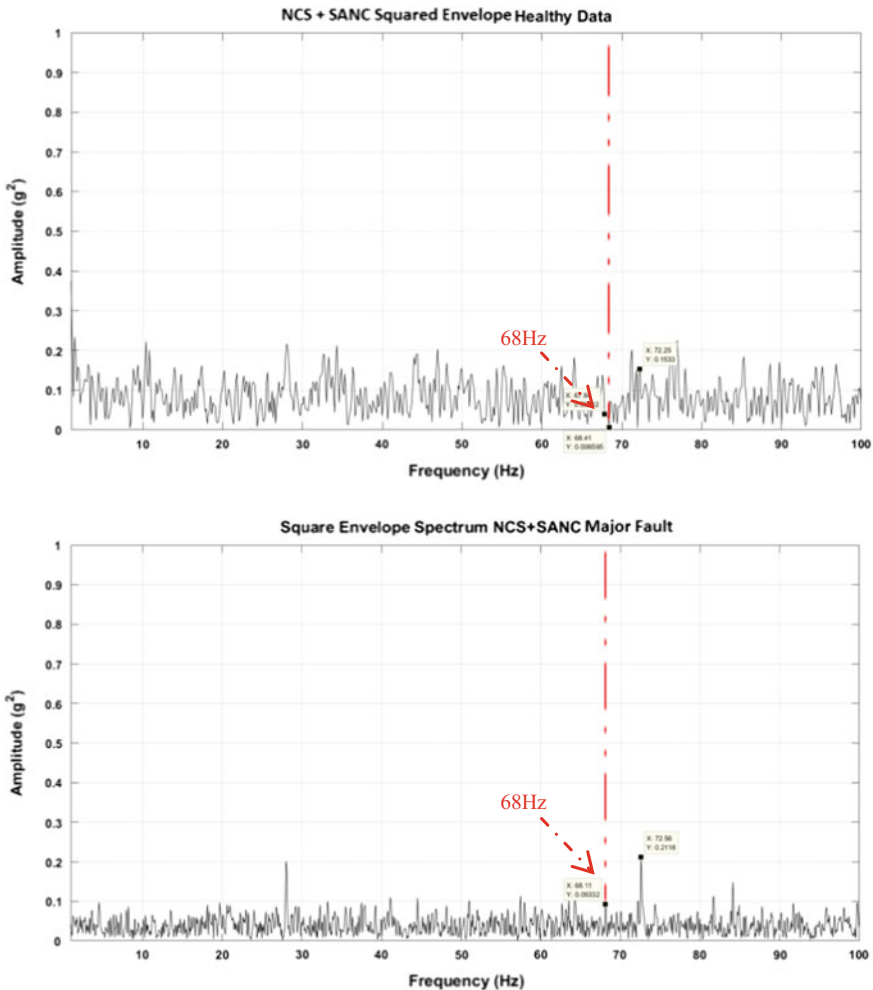
Fig. 6 Envelope analysis of healthy (**a**) and major fault (**b**)

Figure 6 demonstrates that after processing, frequency components around calculated 68 Hz BPFO, which is an indicator of outer race bearing fault, is distinctively standout in major fault condition compared with healthy condition.

5 Conclusion

This paper describes the importance of MGB, introduces HUMS' historical impact and needs for improvement. To make accurate defect diagnosis, several signal processing techniques are studied and validated using commercial helicopter operational MGB. Finally, processing has successfully extracted fault-related frequency components. In future, more study will be focused on enlarging the pool of processing techniques, especially for boosting weak non-stationary signals and denoising, hence improving effective SNR.

References

Accident Investigation Board Norway (2016) Preliminary report on accident at Turoy, near Bergen, Norway on 29 April 2016, involving airbus helicopters h225, LN-OJF. https://www.aibn.no/Aviation/Investigations

Antoni J, Randall RB (2004a) Unsupervised noise cancellation for vibration signals: Part I—evaluation of adaptive algorithms. Mech Syst Signal Process 18(1):89–101

Antoni J, Randall RB (2004b) Unsupervised noise cancellation for vibration signals: Part II—a novel frequency-domain algorithm. Mech Syst Signal Process 18(1):103–117

Authority CA (2006) CAP 753Helicopter vibration health monitoring (VHM) guidance material for operators utilizing VHM in rotor and rotor drive systems of helicopters, 1st edn

Bechhoefer E, Kingsley M (2009) A review of time synchronous average algorithms. In: Annual conference of the prognostics and health management society, San Diego, CA, pp 24–33

Bogert BP, Healy MJ, Tukey JW (1963) The quefrency alanysis of time series for echoes: cepstrum, pseudo-autocovariance, cross-cepstrum and saphe cracking. In: Proceedings of the symposium on time series analysis, vol 15, pp 209–243

Bonnardot F, El Badaoui M, Randall RB, Daniere J, Guillet F (2005) Use of the acceleration signal of a gearbox in order to perform angular resampling (with limited speed fluctuation). Mech Syst Signal Process 19(4):766–785

Borghesani P, Pennacchi P, Randall, RB, Sawalhi N, RicciR (2013) Application of cepstrum pre-whitening for the diagnosis of bearing faults under variable speed conditions. Mech Syst Signal Process 36(2):370–384

Department for Transport (2011) Report on the accident to Aerospatiale (Eurrocopter) AS332 L2 Super Puma, registration G-REDL 11 nm NE of Peterhead, Scotland, on 1 April 2009. Air Accident Investigation Branch, Aldershot, UK, 2/2011

Fyfe KR, Munck ED (1997) Analysis of computed order tracking. Mech Syst Signal

Greaves M, Elasha F, Mba D et al (2013) VHM vibration health or alternative monitoring technologies for helicopters, EASA.2012.OP.13, UK

International Helicopter Team (2013) Health and usage monitoring system toolkit. http://www.ihst.org/portals/54/Toolkit_HUMS.pdf

Land JE (2001) HUMS—the benefits-past, present and future. In: Aerospace conference, 2001, IEEE proceedings, vol 6. IEE, pp 3083–3094

Larder AD (1999) Helicopter HUM/FDR: benefits and developments. In: Annual forum proceedings—American Helicopter, vol 55. American Helicopter Society, pp 1839–1846

Mba D, Place S, Rashid H, Lim CK (2011) Helicopter main gearbox loss of oil performance optimization—HELMGOP. Final report No. EASA, 5

McFadden PD, Toozhy MM (2000) Application of synchronous averaging to vibration monitoring of rolling element bearings. Mech Syst Signal Process 14(6):891–906

Randall RB (2016) A history of cepstrum analysis and its application to mechanical problems. Mech Syst Signal Process

Randall RB, Antoni J (2011) Rolling element bearing diagnostics—a tutorial. Mech Syst Signal Process 25(2):485–520

Randall RB, Smith WA (2016) New cepstral methods for the diagnosis of gear and bearing faults under variable speed conditions. In: ICSV23 conference, Athens

Selesnick IW, Baraniuk RG, Kingsbury NC (2005) The dual-tree complex wavelet transform. IEEE Signal Process Mag 22(6):123–151

Večeř P, Kreidl M, Šmíd R (2005) Condition indicators for gearbox condition monitoring systems. ActaPolytechnica 45(6)

Wang Y, He Z, Zi Y (2010) Enhancement of signal denoising and multiple fault signatures detecting in rotating machinery using dual-tree complex wavelet transform. Mech Syst Signal Process 24(1):119–137

Study of the Anti-fingerprint Function: Effect of Some Texture Properties on the Finger Contact Area

Meriem Belhadjamor, Saoussen Belghith and Salah Mezlini

Abstract Recently, anti-fingerprint surfaces have attracted wide attention due to their self-clean and esthetic performances. The surface texture is a determinant parameter that governs such properties. In this paper, the anti-fingerprint function of microstructured surfaces has been investigated. We have studied the effect of some topographic parameters on the mechanical behavior of the finger contact. Our analysis is mainly focused on the effect of the pitch value and the aspect ratio of the surface patterns on the anti-fingerprint function. A numerical approach has been employed to model dry contacts between the human fingertip and differently microstructured surfaces. The fingertip was modeled taking into account the topography of the finger skin (finger ridges) and the mechanical properties of the finger tissues. Results indicate that the pitch value has a critical effect on the anti-fingerprint function particularly for low aspect ratio surfaces. This highlights the relevance of the texture properties on the surface functionality.

Keywords Numerical model · Finger contact mechanics · Microstructures Anti-fingerprint property

1 Introduction

The design of functional surfaces still remains a great challenge from a research and technological standpoints. Surfaces that achieve self-clean and anti-fingerprint functions are, among others, of interest for different applications such as touch

M. Belhadjamor (✉) · S. Belghith · S. Mezlini
Laboratoire de Génie Mécanique, École Nationale d'Ingénieurs de Monastir,
Université de Monastir, Rue Ibn Eljazzar, 5019 Monastir, Tunisia
e-mail: meriem.belhadjamor@gmail.com

S. Belghith
e-mail: belghith.saoussen@gmail.com

S. Mezlini
e-mail: salah.mezlini@gmail.com

507

screens, optical lenses, packages, and textiles. Various researches have been done to build an anti-fingerprint function using different materials (Peng and Bhushan 2016; Bhushan and Muthiah 2013; Wu et al. 2011). It was proved that this function is dependent on the surface wettability, namely, the hydrophobic and the oleophobic properties (Siriviriyanun and Imae 2014). These properties are, in turn, achieved by lowering the surface energy and introducing the functional topography. The surface roughness and texture are important factors that govern the surface functionalities (Belhadjamor et al. 2016a, b). The influence of different topographic parameters such as the pitch value on the wetting behavior has been studied. Great effect of this parameter was shown especially for low aspect ratio surfaces (Grewal et al. 2014). The aspect ratio (AR) of the surface structures is the ratio of the pattern height to the pattern width.

On the other hand, the mechanical behavior of the contact between the finger and the touch surface (i.e., finger contact) was proven to govern the fingerprinting process (Scruton et al. 1975; Kent 1981). Experimental evidence proves that the stained area with fingerprints is the area of the finger contact. Such area is dependent on the touch load since the two surfaces into contact are rough. In our previous work, we have reviewed the physics of fingerprints and the different issues related to the anti-fingerprint function (Belhadjamor et al. 2016a, b). The evaluation of the fingerprint property is an important issue that has attracted a lot of attention. It was always restricted to the examination of the surface wettability against water, hexadecane, oleic acid (Siriviriyanun and Imae 2014), and/or artificial fingerprint liquid (Wu et al. 2011). However, it was found that the mechanical behavior of the finger contact was always overlooked. Indeed, none of the existing studies have measured the touched area nor analyzed the effect of the surface topography of this area.

In this work, we have studied the mechanics of the finger contact to evaluate the anti-fingerprint function of structured surfaces. A bi-dimensional numerical model of the finger contact has been performed. In the aim to highlight the effect of the pitch parameter on the anti-fingerprint function, the evolution of the touch area for high and low aspect ratio structured surfaces have been analyzed. Results show that the pitch value has a critical effect on the anti-fingerprint function. This effect was shown to be closely related to the patterns aspect ratio.

2 Numerical Model of the Finger Contact

A finite element model of a two-dimensional dry finger contact was developed using the commercial FE software package ABAQUS/Standard. Figure 1 illustrates the geometry of the model, parts, dimensions, and boundary conditions. The fingertip model is bio-inspired from the multilayered structure and the mechanical properties of the human finger. It approximates the structure and the shape of a typical male index finger. It is represented by an elliptical form with major and minor axes 20 and 14 mm (Wu et al. 2004). The fingertip is supposed to be
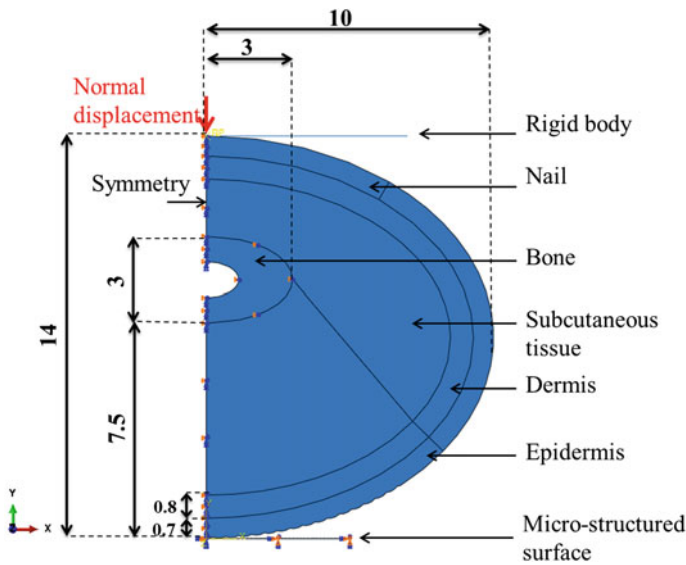
Fig. 1 Geometry of the model, dimensions (mm), and boundary conditions

composed of epidermis, dermis, subcutaneous tissue, bone, and nail. The thicknesses of the epidermis and dermis layers are taken 0.7 mm (Whitton and Everall 1973) and 0.8 mm (Hendriks et al. 2004), respectively. Meso-scaled ridges were introduced on the finger skin to model the fingerprint. The width and the height of ridges are assumed to be, respectively, 0.45 mm and 0.05 mm (Shao et al. 2010).

The nail and the bone are supposed linear elastic materials, whereas, the finger skin is assumed to be composed of multilayered visco-elastic tissue (Holt et al. 2008; Kim et al. 2008; Amaied et al. 2015). Both elastic and visco-elastic material parameters of different tissues are shown in Table 1 (Shao et al. 2009). The viscous material properties of the epidermis, dermis, and the subcutaneous tissues are described by Prony series (See Table 1). It is a range of three parameters, the shear relaxation modulus ratio g_i, the bulk relaxation modulus ratio k_i, and the relaxation

Table 1 Elastic and Prony series parameters relative to the fingertip tissues

	Elastic properties (Shao et al. 2009)		Prony series (Amaied et al. 2015)		
	E (MPa)	υ	g_i	k_i	τ_i (s)
Epidermis	0.08	0.48	0.0332	0	1.29
Dermis	0.05	0.48	0.0282	0	17.68
Subcutaneous tissue	0.024	0.48	0.0183	0	2412
Nail	170	0.3	–	–	–
Bone	17000	0.3	–	–	–

time τ_i. These parameters were determined by the mean of the in vivo creep tests (Amaied et al. 2015).

Due to the symmetry of the model, a half of the fingertip was modeled and a symmetry condition was applied. The bottom of the structured surface was fixed. The fingertip was loaded against the rough surface with a normal displacement of 1.3 mm.

Different microstructured surfaces were simulated by this model. These surfaces were considered as an elastic material with Young's modulus of 72 GPa and Poisson's ratio (υ) of about 0.3. The penalty formulation was used in the interface between the finger skin and the tested surface (friction's coefficient 0.2) and that between the rigid body and the nail (friction's coefficient 0.2). The contact modeling has employed surface-to-surface discretization and the finite sliding contact algorithm. Low aspect ratio microscaled periodic patterns (AR = h/w = 1:2) with different pitch values were simulated (See Fig. 2). These surfaces are described by the height (h = 1 μm), the width (w = 2 μm), the pattern radio (r = 500 nm) and

Fig. 2 Geometry of the microstructured surfaces, width (w = 2 μm), height (h = 1 and 5 μm), and pitch (p = 3, 5 and 11)
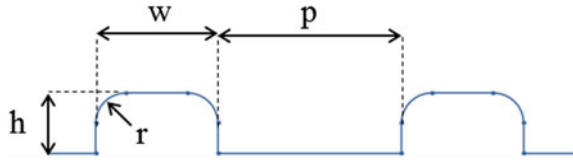
Fig. 3 Model meshing, magnification of the contact zone
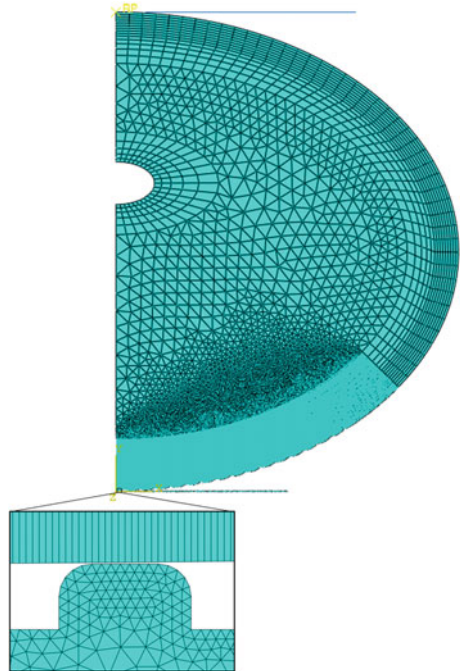
the pitch (p = 3, 5 and 11 μm). High aspect ratio surface (AR = 5:2) was also simulated. This surface has the same topographic parameter values as the other surfaces except the height h = 5 μm and the pitch (p = 11 μm).

Figure 3 depicts the meshing of the finite element finger contact. Linear Plane strain elements in the implicit mode were imposed. Structured 4-node linear quadrilateral elements were applied to mesh the multilayered skin, the nail and the bone. Free 3-node triangular elements were used for the subcutaneous tissues discretization. Near contact zone, finer elements were required to ensure an accurate contact conditions and a reliable measurement of the contact area. The fingerprint ridges were meshed using an element with a size of 0.1 μm. A total of 1,027,785 elements are utilized to mesh the fingertip. 3-node linear plane strain triangular elements were used to mesh the microstructured surfaces. A fine mesh was applied on the surface patterns with an element size of 0.15 μm. The total number of elements in the surface is 576,259.

3 Results and Discussion

3.1 Effect of the Surface Pitch on the Finger Contact Mechanics

The contact load resulted from a normal displacement of 1.3 mm reach a value of about 25 mN regardless of the surface microstructure. In fact, this load is governed by the mechanical properties of the fingertip since it is much softer than the microstructures. Compared with the literature, the load value agrees well with that numerically measured in the literature (Shao et al. 2010). In the current model, which is a half of a 2D fingertip, the contact load is equal to 50mN in the entire 2D configuration. This load was shown to be equivalent to the typical touch load which is about 0.5 N in the 3D configuration.

Figure 4 illustrates the deformed shape and the strain distributions of the fingertip in contact with two microstructured surfaces having different pitch values. Figure 4a shows a fingertip loaded against a surface with a pitch value of 3 μm. Figure 4b presents a finger contact in the case of higher pitch value equal to 11 μm. As a validation point for the model, the strain distribution and the order of values agree with the results reported in the literature (Amaied et al. 2015). The strain distribution on the finger is approximately the same regardless of the pitch value. The subcutaneous tissue between the bone and the skin has undergone the maximum deformation. This tissue is less rigid and more viscous than the other tissues which explain this result. In this zone, which is far from the contact regions, the strain value is roughly the same for the two surfaces. The magnified views show the fingerprint-microstructures interface. The finger skin into contact with micropatterns has undergone more deformation than the skin between patterns. It can be a priori expected from these figures that increasing the pitch value increases the area
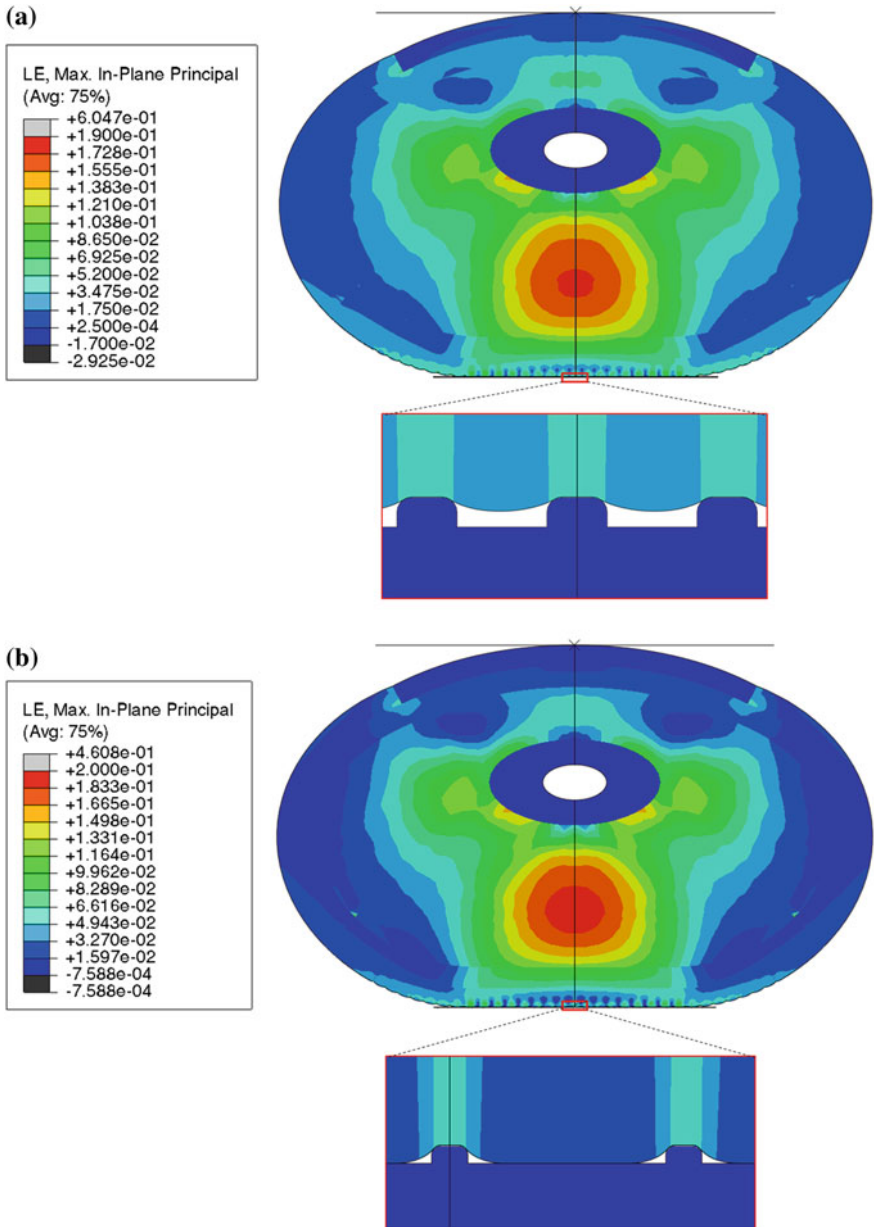
Fig. 4 The deformed shapes and the strain distributions for fingertip in contact with microstructured. **a** p = 3 μm, **b** p = 11 μm

of the finger contact. Indeed, for high pitch value, the finger skin contacts the bottom surface between micropatterns. Therefore, it is necessary to evaluate the contact area for different pitch values in order to highlight this effect.

The developed model enables the measurement of the real area (A_r) of the finger contact using the field output CNAREA or the history output CAREA. The real area has been normalized by the apparent area (A_a). Figure 5 presents the evolution of the contact ratio (A_r/A_a) versus the contact load for surfaces having different pitch values. Since the two surfaces into contact are rough, the increase of the applied load leads to an increase of the real area into contact. This increase is governed by the deformation of the finger skin coming into contact with the microstructures. Comparing the evolution of the contact ratio of surfaces with different pitch values, the increase of the pitch from 3 to 5 µm decreases the real contact area. In fact, when increasing the pitch within the same length (apparent contact area), the number of surface patterns decreases. Therefore, the number of contact zones (i.e., contact density) for a pitch of 5 µm is lower than for a pitch value of 3 µm. As shown in inserts of Fig. 5, over a length of 20 µm, when the pitch value is equal to 3 µm the fingerprint touch four patterns, whereas, with a pitch value equal to 5 µm, only three patterns are touched. It can be so deduced from these results that increasing the pitch value enhances the anti-fingerprint function since the contaminated area is reduced. But regarding the evolution of the contact ratio in the case of a very high pitch value of 11 µm, another issue was highlighted. In this example, the increase of the pitch value increases the touched area. This result was justified by the fact that the finger skin touches the bottom of the surface. Thus, as exhibited in the insert of Fig. 5, even though the number of patterns into contact is reduced, the touched area in the bottom of the surface is very important. It is concluded from these results that increasing the pitch value is an interesting strategy to design anti-fingerprint surface but very high values must be avoided. It can be expected that from a critical pitch value, which is, in this case, less than 11 µm, the positive effect of increasing the pitch is inverted.

Fig. 5 Evolution of the contact ratio (A_r/A_a) with increasing contact load. Inserts show a length of about 20 µm of the finger contact
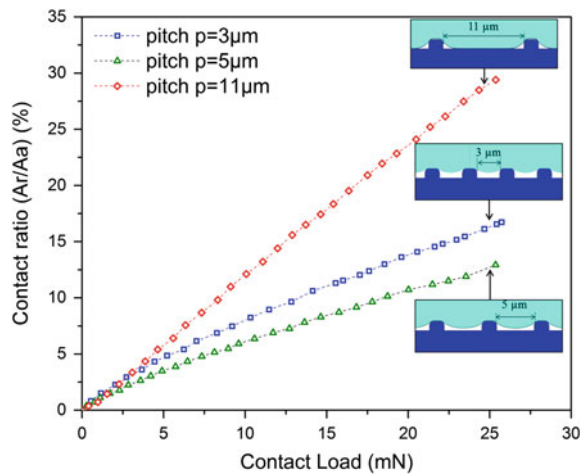
Fig. 6 The deformed shape of the finger contact under the touch load for **a** low aspect ratio 1:2 and **b** high aspect ratio 5:2. Dimensions (µm)
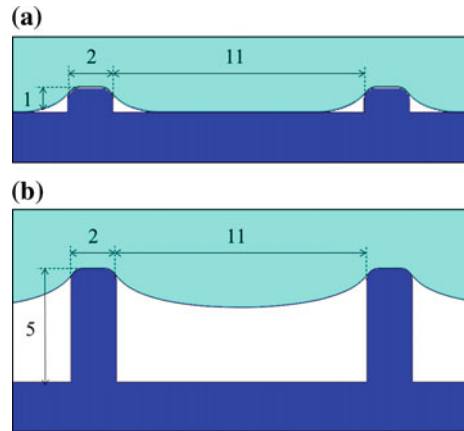
3.2 Effect of the Pattern Aspect Ratio

Figure 6 shows the deformed shapes of the finger contact subjected to a typical touch load for low and high aspect ratio surfaces that have a high pitch value (p = 11 µm). It can be noted that for high aspect ratio patterns the finger skin does not touch the bottom of the surface and the contact occurs only on the top of the microstructures. Interestingly, even though the surfaces have high pitch values the contact area is dramatically reduced. The measured contact area for the high aspect ratio surface does not exceed 9% of the apparent area versus more than 30% for low aspect ratio. It can be deduced that the study of the effect of the pitch value on the anti-fingerprint function must be made taking into account the patterns aspect ratio. The coupling of a high pitch value and a high aspect ratio patterns can be a relevant strategy to construct anti-fingerprint function.

However, it is important to note that very high aspect ratio patterns have poor mechanical durability against pressure, abrasion, and wear. The design of anti-fingerprint surfaces will depend on the trade-off between mechanical durability and touch ability. In conclusion, the effect of the pitch value must be analyzed correlated with the patterns aspect ratio taking into account the surface material and the application.

4 Conclusion

In this work, we have developed a finite element model of a contact between a human fingertip and microstructured surfaces. The static mechanical behavior of the finger contact has been investigated. The real area of the contact has been numerically assessed to evaluate the anti-fingerprint function. The effect of the pitch value on this function has been analyzed in the case of low aspect ratio structures.

The increase of the pitch parameter decreases the contact density and thus reduces the touched area by the fingertip. However, from a critical pitch value, this increase results in enlargement of the real finger contact area. To avoid such negative effect, high aspect ratio microstructures can be employed. The design of a functional anti-fingerprint topography requires an optimal compromise between the finger contact areas, mechanical durability, and wetting properties.

References

Amaied E, Vargiolu R, Bergheau JM, Zahouani H (2015) Aging effect on tactile perception: experimental and modelling studies. Wear 332–333:715–724. https:\\doi.org\10.1016/j.wear.2015.02.030

Belhadjamor M, Belghith S, Mezlini S (2016a) Finite element modeling of RMS roughness effect on the contact stiffness of rough surfaces. Tribol Ind 38:392–401

Belhadjamor M, El Mansori M, Belghith S, Mezlini S (2016b) Anti-fingerprint properties of engineering surfaces: a review. Surf Eng. https:\\doi.org\10.1080/02670844.2016.1258449

Bhushan B, Muthiah P (2013) Anti-smudge screening apparatus for electronic touch screens. Microsyst Technol 19:1261–1263. https:\\doi.org\10.1007/s00542-013-1856-2

Grewal HS, Cho I-J, Oh J-E, Yoon E-S (2014) Effect of topography on the wetting of nanoscale patterns: experimental and modeling studies. Nanoscale 6(24):15321–15332. https:\\doi.org\10.1039/c4nr04069d

Hendriks FM, Brokken D, Oomens CWJ, Baaijens FPT (2004) Influence of hydration and experimental length scale on the mechanical response of human skin in vivo, using optical coherence tomography. Skin Res Technol 10:231–241. https:\\doi.org\10.1111/j.1600-0846.2004.00077.x

Holt B, Tripathi A, Morgan J (2008) Viscoelastic response of human skin to low magnitude physiologically relevant shear. J Biomech 41:2689–2695. https:\\doi.org\10.1016/j.jbiomech.2008.06.008

Kent T (1981) Latent fingerprints and their detection. J Forensic Sci Soc 21:15–22. https:\\doi.org\10.1016/S0015-7368(81)71368-9

Kim SW, Shim JK, Zatsiorsky VM, Latash ML (2008) Finger inter-dependence: linking the kinetic and kinematic variables. Hum Mov Sci 27:408–422. https:\\doi.org\10.1016/j.humov.2007.08.005

Peng S, Bhushan B (2016) Mechanically durable superoleophobic aluminum surfaces with microstep and nanoreticula hierarchical structure for self-cleaning and anti-smudge properties. J Colloid Interface Sci 461:273–284. https:\\doi.org\10.1016/j.jcis.2015.09.027

Scruton B, Robins BW, Blott BH (1975) The deposition of fingerprint films. J Phys D Appl Phys 8:714–723. https:\\doi.org\10.1088/0022-3727/8/6/016

Shao F, Childs THC, Barnes CJ, Henson B (2010) Finite element simulations of static and sliding contact between a human fingertip and textured surfaces. Tribol Int 43:2308–2316. https:\\doi.org\10.1016/j.triboint.2010.08.003

Shao F, Childs THC, Henson B (2009) Developing an artificial fingertip with human friction properties. Tribol Int 42:1575–1581. https:\\doi.org\10.1016/j.triboint.2009.02.005

Siriviriyanun A, Imae T (2014) Anti-fingerprint properties of non-fluorinated organosiloxane self-assembled monolayer-coated glass surfaces. Chem Eng J 246:254–259. https:\\doi.org\10.1016/j.cej.2014.02.066

Whitton JT, Everall JD (1973) The thickness of the epidermis. Br J Dermatol 89:467–477. https:\\doi.org\10.1111/j.1365-2133.1973.tb03007.x

Wu JZ, Donga RG, Rakheja S, Schopper AW, Smutza WP (2004) A structural fingertip model for simulating of the biomechanics of tactile sensation. Med Eng Phys 26:165–175. https:\\doi.org \10.1016/j.medengphy.2003.09.004

Wu LYL, Ngian SK, Chen Z, Xuan DTT (2011) Quantitative test method for evaluation of anti-fingerprint property of coated surfaces. Appl Surf Sci 257:2965–2969. https:\\doi.org\10. 1016/j.apsusc.2010.10.101

Online Identification of Road Profile Variation Using a Constant Piecewise Function

Maroua Haddar, S. Caglar Baslamisli, Fakher Chaari and Mohamed Haddar

Abstract Road profile estimation has become an indispensable tool for improved route planning and enhanced design of active suspensions. Performances requirements, such as increasing ride comfort and improving the driving maneuverability, depend on the road unevenness. The core idea is to use vehicle dynamics to get information about road perturbation and isolates passengers from vibrations. Online estimation of geometric variation of the road was investigated in this paper based on the operational calculus method and algebraic approach. The estimator equations are derived from a predictor scheme which was used to approximate this unknown signal variation by a piecewise constant function. The major interest of this technique is that it allows using minimum numbers of mechanical sensors and few parameters for tuning. Accurate approximations were obtained from the measurement of sprung mass and un-sprung mass vertical displacements. Numerical results with MATLAB/Simulink environment were used for investigating the effectiveness of the proposed technique for fast prediction.

Keywords Road profile · Online estimation · Piecewise function

M. Haddar (✉) · F. Chaari · M. Haddar
Mechanics, Modeling and Production Laboratory (LA2MP), Mechanic Department,
National Engineering School of Sfax (ENIS), BP 1173, 3038 Sfax, Tunisia
e-mail: HADDAR.marwaGEM1@gmail.com

F. Chaari
e-mail: Fakher.chaari@gmail.com

M. Haddar
e-mail: Mohamed.haddar@enis.rnu.tn

S. C. Baslamisli
Department of Mechanical Engineering, Hacettepe University, 06800 Beytepe,
Ankara, Turkey
e-mail: Caglar.baslamisli@gmail.com

517

1 Introduction

For the last few decades, extensive research has been dedicated to the study of the variability of the real road profile which plays a key role in the vehicle dynamics. Maintenance of electromechanical items on the one hand and ride comfort on the other is influenced by time-varying characteristics of this exogenous input. Several prediction methods have been developed in order to collect the precise information about road serviceability. Researchers have worked on creating the most convenient observer implementation method with the cheapest instrumentation cost.

General Motors Profilers (GMP) established the inertial speed profiler (Spangler and Kelly 1964). A reference was created fro the relative error of accelerations collected data and the pavement area. Meanwhile, the application task of this technique is very hard due to practical reasons. Longitudinal Profile Analyzer (LPA) was established by researchers such as Imine et al. (2006). Here, the drawback is that the integration of this device on a real vehicle is practically impossible.

Recently, Fauriat et al. (2016) and Doumiati et al. (2011) were focused on the design of observers such as the Extended Kalman filter for estimating the road profile. Meanwhile, a sliding mode approach (Imine et al. 2006), a numerical optimization technique (Harris et al. 2010), and an algorithm with Jump diffusion estimator were proposed by Li et al. (2016) which produce better results than Kalman filters. Another method is the Youla Kucera parameterization (or Q-parametrisation) used by Tudon-Martinez et al. (2015). The cited estimators have different complexity in modeling; more precisely, they present rather difficult tasks for tuning parameters of observer.

The present paper makes the first attempt to investigate the identification of road variation based on operational calculus theory. The inverse model is developed in Laplace domain. This new algebra design methodology is easy to be implemented as discrete linear filters. Using this approach, the estimator equation can be precisely modeled using fewer parameters and with straightforward tuning.

The organization of the paper is as follows. Section 2 describes the motion equations of quarter car model. Section 3 gives a simple description of estimator approach. A comparison between real road and estimated road is discussed in Sect. 4. Finally, conclusions are drawn in Sect. 5.

2 Description of the System and Road Input

2.1 Quarter Car Model

The motion equations of passive quarter car system are given below:

$$m_s\ddot{z}_s + d_s(\dot{z}_s - \dot{z}_u) + k_s(z_s - z_u) = 0 \tag{1}$$

$$m_u\ddot{z}_u - d_s(\dot{z}_s - \dot{z}_u) - k_s(z_s - z_u) + k_t(z_u - z_r) = 0 \tag{2}$$

m_s is the sprung mass which represents the body of the car. m_u is the un-sprung mass. k_s is the suspension stiffness. d_s represents suspension damping and k_t is the tire stiffness. The road variation is denoted by z_r (Fig. 1).

2.2 Random Road Model

In this study, a stationary random road profile is analyzed. The power spectral density (PSD) is used to describe the trajectory of a vehicle which moves with a constant speed V

$$G_q(n) = G_q(n_0)\left(\frac{n}{n_0}\right)^{-2}, \tag{3}$$

where n is the spatial frequency, n_0 is reference spatial frequency and $G_q(n_0)$ represent the PSD at n_0 (m^3).

We use a relationship "Eq. (4)" between the spatial frequency n, *spatial* angular frequency $\Omega(rad/m)$, the vehicle speed $V(m/s)$, the angular velocity $\omega(rad/s)$ and

Fig. 1 Quarter car model
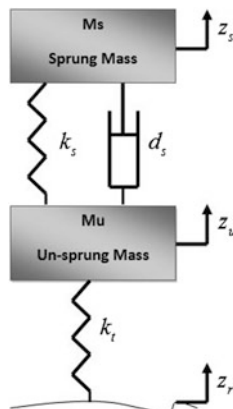
the time frequency f, in order to give an expression of the road roughness in the frequency domain "Eq. (5)"

$$\begin{cases} \omega = 2\pi f = 2\pi V n \\ \Omega = 2\pi n \end{cases} \tag{4}$$

$$G_q(f) = G_q(n_0)n_0^2 \frac{V}{f^2} \tag{5}$$

According to the theory of random vibration signals and the procedure of generation of time signals of profile given by He et al. (2008), a transfer function $H(s)$ can be obtained from "Eq. (5)". The expression of this transfer function from white noise signal to power spectral density in Laplace domain can be written as

$$H(s) = \frac{\sqrt{G_q(\Omega_0)V}}{\omega_0 + js} \tag{6}$$

ω_0 is the lowest cut-off angular frequency.

From "Eq. (6)" and passing from Laplace domain to the time domain, the random road excitation is characterized by a constant of roughness that is given by

$$\dot{z}_r(t) = -2\pi V n_0 z_r(t) + 2\pi \sqrt{G_0 V} w(t) \tag{7}$$

where $z_r(t)$ is the random road displacement, G_0 is the road roughness coefficient and $w(t)$ represents a white noise signal whose power spectral density is equal to 1.

3 Estimator Design

A suitable approximation of the road profile with a constant function ϕ is presented here. This function is a linearly identifiable constant (Fliess and Sira Ramirez 2003–2008).

From "Eq. (1)" and "Eq. (2)", a linear combination of the sprung mass and the un-sprung mass accelerations is obtained

$$m_s \ddot{z}_s + m_u \ddot{z}_u = -k_t(z_u - z_r) \tag{8}$$

The model given by "Eq. (4)" can be written

$$\frac{m_s}{k_t} \ddot{z}_s + \frac{m_u}{k_t} \ddot{z}_u + z_u = \phi \tag{9}$$

In the following, we approximate $z_r(t)$ by a constant function ϕ in a short windows of time [t − L, t]. This estimation horizon L should be quite small and

positive. Among different methods available for the identification of piecewise functions, the classic rules of operational calculus are used in this paper

Step1: applying the Laplace transformation in Eq. (9).

Step2: Multiplying both sides of the equation by $\frac{d^2}{d^2s}$ for canceling out initial conditions.

Step3: Getting rid of the positive power by multiplying both sides on the left by s^{-3}.

Step4: Passing from Laplace domain to the operational area according to operational calculus rules (Mikusiński 1967).

This yields three pure integrating actions which are easy to implement

$$z_r(\sigma) = \frac{60}{L^5} \int_{t-L}^{t} a_1(L^2 - 6\sigma L + 6\sigma^2)z_s(\sigma) + a_2(L^2 - 6\sigma L + 6\sigma^2)z_u(\sigma)$$
$$+ \frac{1}{2}(L-\sigma)^2 \sigma^2 z_u(\sigma)d\sigma \tag{10}$$

with $a_1 = \frac{m_s}{k_t}$ and $a_2 = \frac{m_u}{k_t}$.

From "Eq. (10)", it can be seen that only from the measured responses of vertical displacements, we can obtain an approximation of the road profile variation. This online estimation can be easily implemented as discrete linear filters.

4 Results of Simulation

In this section, we use a random road class A and a vehicle speed of 15 km/h. System parameters are given in Table 1.

A comparison between estimated road and real road in time and frequency domain is depicted in Figs. 2 and 3. The displayed results in time domain show that the estimated road approximates finely the real signals. However, a persistent delay and a difference in amplitude exist due to the low-pass filtering process applied to the measured signals.

The estimation of roughness in frequency domain is acceptable Fig. 3. But, it can be clearly seen that the filtering process has a marked effect in the high

Table 1 Parameters of Suspension system

Parameters	Description	Value
m_s	Sprung mass	285 kg
m_u	Un-sprung mass	41 kg
k_s	Spring stiffness	17900 N/m
d_s	Damping constant	535 N/(m/s)
k_t	Tire stiffness	19125 N/m
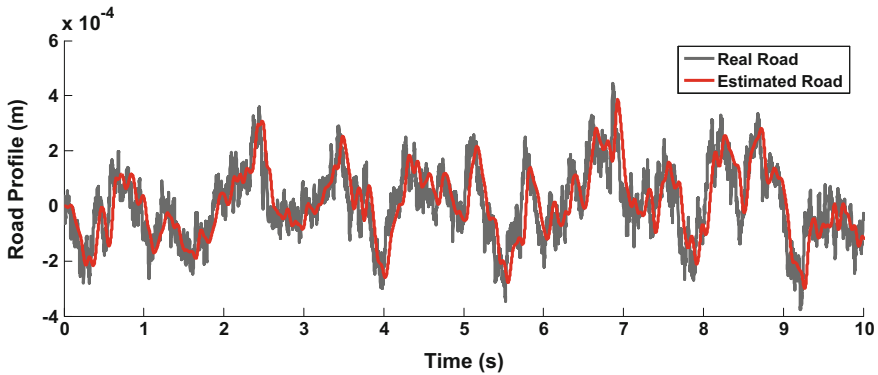
Fig. 2 Time response of random rode profile
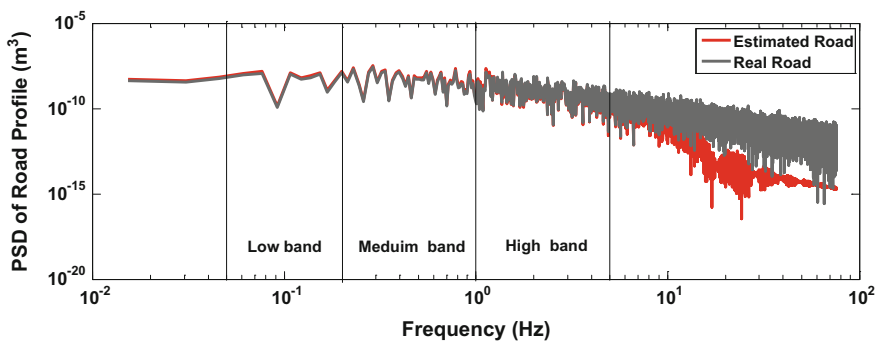
Fig. 3 Power spectral density of two road profiles

frequency band. This phenomenon can be observable in other works (Fauriat et al. 2016). The vehicle speed and mechanical characteristic could have a significant effect on the quality of estimation in high frequency.

Next, the estimated road profile is taken as an input excitation of the vehicle quarter car model simulator and compared to numerical responses with real road excitation Figs. 4, 5. The comparison between signals is made in the time domain. The smoothing effect causes discrepancy between signals. However, one notes that the relative error (in Table 2) is acceptable and the signals are quite similar.
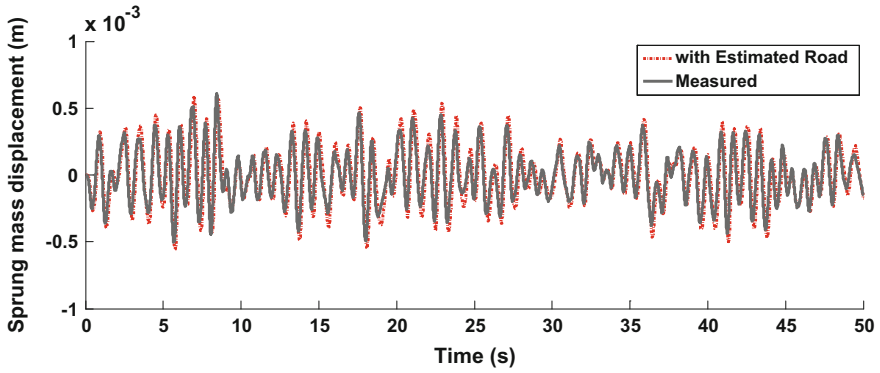
Fig. 4 Time response of Sprung mass displacement
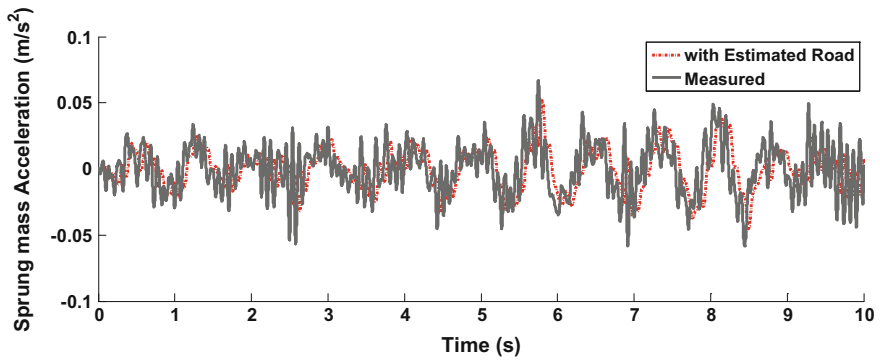
Fig. 5 Time response of Sprung mass acceleration

Table 2 Comparison between the RMS

RMS criteria	True profile	Estimated profile	Relative error (%)
Sprung mass	1.9 E-04	2.2 E-04	9
Sprung mass acceleration	0.0174	0.0134	22.7

5 Conclusion

In this work, we introduced a new predictive method that uses pure integrating actions to identify the variation of random road profile. This new design of estimator is easy to be implemented as discrete linear filters and we use very few parameters for tuning. Further improvements could be made to the technique by taking sprung mass uncertainty and the calibration of the window of integration method into consideration.

References

Doumiati M, Victorino A, Charara A et al (2011) Estimation of road profile for vehicle dynamics motion: experimental validation. In: Proceedings of the 2011 American control conference. http://doi.org/10.1109/ACC.2011.5991595. Source: IEEE Xplore

Fauriat W, Mattrand C, Gayton N, Beakou A, Cembrzynski T (2016) Estimation of road profile variability from measured vehicle responses. Veh Syst Dyn. http://doi.org/10.1080/00423114.2016.1145243

Fliess M, Sira-Ramirez H (2003) An algebraic framework for linear identification. ESAIM Control Optimiz. Calculus Variat. http://doi.org/10.1051/cocv:2003008

Fliess M, Sira-Ramirez H (2008) Closed-loop parametric identification for continuous-time linear systems via new algebraic techniques. In: Garnier H, Wang L (eds) Continuous-time model identification from sampled data. Springer. http://doi.org/10.1007/978-1-84800-161-9_13

Harris NK, González A, OBrien EJ, McGetrick P (2010) Characterisation of pavement profile heights using accelerometer readings and a combinatorial optimisation technique. J Sound Vib. http://doi.org/10.1016/j.jsv.2009.09.035

He L, Qin G, Zhang Y, Chen L (2008) Non-stationary random vibration analysis of vehicle with fractional damping. In: 2008 international conference on intelligent computation technology and automation (ICICTA), vol 2. IEEE, pp 150–157. http://doi.org/10.1109/ICICTA.2008.348

Imine H, Delanne Y, M'sirdi NK (2006) Road profile input estimation in vehicle dynamics simulation. Veh Syst Dyn. http://doi.org/10.1080/00423110500333840

Li Z, Kalabić UV, Kolmanovsky IV, Atkins EM, Lu J, Filev DP (2016) Simultaneous road profile estimation and anomaly detection with an input observer and a jump diffusion process estimator. In: American control conference (ACC). IEEE, pp 1693–1698. http://doi.org/10.1109/ACC.2016.7525160

Mikusiński J (1967) Operational calculus, vol 8. CUP Archive

Tudon-Martinez JC, Fergani S, Sename O, Martinez JJ, Morales-Menendez R, Dugard L (2015) Adaptive road profile estimation in semiactive car suspensions. IEEE Trans Control Syst. http://doi.org/10.1109/TCST.2015.2413937

Cathodic Protection System by Imposed Current for a Vedette

Issam Hemdana, Habib Dallagi, Bechir Sabri and Chiheb Zaoui

Abstract This article deals with the method of cathodic protection by imposed current. This technique reduces the rate of corrosion of a metallic material in the presence of an aqueous medium. Corrosion, its causes, its effects as well as the solution to combat this phenomenon, has been established in this paper. Indeed, the technique of protection by imposed current has been studied extensively in this work. The study and installation of a cathodic protection system imposed on-board the vedette, it is possible to determine the need for a DC current. This study ensures a good protection of the hull and a better location of the anodes. An imposed current regulation system has been studied. This system consists of measuring the potential of the boat's hull by the reference electrode. With reference to this voltage value, the controller imposes the necessary current injected at the anode to maintain a fixed protection potential. In order to validate this study, simulations results under PSIM software dealing with protection of the hull of the vedette is finally presented.

I. Hemdana (✉) · H. Dallagi · B. Sabri · C. Zaoui
U.R Automation and Robotics Marine (ARM), Naval Academy, Tunis, Tunisia
e-mail: issamhemdana@gmail.com

H. Dallagi
e-mail: habib.dallagi@ept.rnu.tn

B. Sabri
e-mail: bechir.sabri@yahoo.fr

C. Zaoui
e-mail: chiheb.zaoui@gmail.com

1 Introduction

Corrosion is an interaction between a metallic material and its environment that causes degradation of the material. Corrosion causes changes in the properties of the materials leading to a malfunction of the technical system in which it participates (Benard et al. 1991; Ahmad 2006). At room temperature, the phenomenon usually results from the combined action of an aqueous medium and the oxygen of the air. The corrosion of a metal is not an intrinsic property, but depends on a large number of parameters, including those related to the aggressive environment. The term "marine corrosion" thus covers all physicochemical and mechanical interactions between materials and the marine environment (Eliades et al. 2003). Protection against this degradation (corrosion), which must be considered from the conception of the system, and the choice of materials are also intimately linked to the specificity of the environment. In fact, corrosion is a destructive phenomenon that alerts and destroys any unprotected metal structure (Grosgogeats et al. 2001; Gopalakrishnan et al. 2012). This is even more pronounced for an immersed structure, such as a ship whose shell is subjected to all the known mechanisms of corrosion in an aqueous medium such as: electrochemical corrosion linked to the presence of the electrolyte, corrosion by the aggressive anions present in seawater, corrosion by differential aeration due to the heterogeneous distribution of oxygen in sea water, corrosion by biosolids and the aggressive substances they produce, Abrasion caused by the movement of water on the hull and the solid particles it contains (Ogden 2015; Guyonnet et al. 1993). This particularly serious phenomenon has pushed researchers and engineers to look at it to study and provide solutions. Different methods of protection have been studied and tried, the most effective method is that introduced for the first time around 1788 by the Englishman Davy who developed the first cathodic protection. Two types of cathodic protection are distinguished: the first is Sacrificial Cathodic Protection (SCP), which consists in placing blocks of less noble metals than steel (Zinc, Aluminum, etc.) on the structure to be protected (Roche 2015). The major disadvantage is that it is necessary to regularly replace these anodes which will oxidize and therefore destroy themselves. The second is the Imposed Current Cathodic Protection (ICCP) where platinum (and therefore stainless) current injection anodes are placed on the hull. By injecting a sufficient current into the water, the electrochemical potential of the damaged zone is artificially lowered to its passivation range. However, this method requires the use of a direct current source in the vessel (Roche 2015; Kim and Nho 2005). In this paper we are interested in the method (ICCP). In the first part we will study the different types of corrosion and their causes and effects. The method of determination of the potential of metal electrodes and the steel protection threshold will also be treated in order to analyze the diagrams of POURBAIX. Then the minimum protection conditions will be established from the protective current density. The principle of cathodic protection by imposed current and the equipment necessary to realize this system have been dealt with in the second part. Next, we will be interested in the realization of withdrawal and its different compositions to

arrive at the various anodes with imposed current. The calculation of the necessary current and the installation of the anodes on the 27 m vedette are carried out to ensure a good protection of the hull.

2 Processes and Effects of Corrosion

2.1 Chemical Corrosion (Dry)

This type of corrosion represents 3% of the cases of corrosion, it is manifested only by a chemical reaction without creation of an electric current (Ogden 2015; Roche 2015; Kim and Nho 2005). It involves in most cases a gas, for example oxygen

$$2Fe + O_2 \rightarrow FeO \tag{1}$$

This reaction translates the natural return to the most stable state of iron in the form of oxide (ore).

2.2 Electrochemical Corrosion (Galvanic or Wet)

This type of corrosion accounts for 97% of corrosion. It is characterized by the appearance of an electric current, outside any external source, due to a displacement of electrons within the metal mass between regions which are brought to different potentials. The corrosion of a metal such as iron is the result of a process which can be schematized by Eq. (2) (Roche 2015; Kim and Nho 2005)

$$Fe \rightarrow Fe^{2+} + 2e^- \tag{2}$$

Conservation of the neutrality of the medium requires that the electrons emitted by the dissolution reaction (2) be consumed in a second reaction which may be for example

$$2H^+ + 2e^- \rightarrow H_2 \tag{3}$$

$$\frac{1}{2}O_2 + H_2O + 2e^- \rightarrow 2OH^- \tag{4}$$
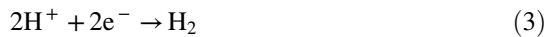
These last two reactions (3) and (4) are related to the nature of the medium with which the material is in contact (electrolyte) (Ogden 2015).

2.3 Potential of Metal Electrodes

The exchanges of electric current at the metal–electrolyte interface are governed by differences in potential. With each chemical reaction there corresponds a so-called electrode potential that can be determined by the Nernst equation (Barral et al. 2003; Chambre syndicale de la recherche et de la production du pétrole et du gaz naturel and Comité des techniciens 1986)

$$E = E_0 + \frac{0.058}{n} \ln C, \tag{5}$$

where E_0: corresponds to the standard potential of the electrochemical reaction whose value is known for several materials and can be easily found (Chambre syndicale de la recherche et de la production du pétrole et du gaz naturel and Comité des techniciens 1986). By convention, the standard potential of the reaction (5) is taken equal to zero. n is the number of electrons transferred in the half reaction and C is the concentration of the ions passed in solution. The influence of these parameters in the state of a metal is shown schematically in the Pourbaix diagrams (potential-pH diagrams) (Pourbaix 1963).

2.4 Choice of Cathodic Protection

The choice of the method of protection is not easy because no method is universally applicable; the choice is made on the one hand depending on the environment and on the other hand, according to economic considerations. These include not only the initial cost of implementation, but also the cost of maintenance such as replacement of corroded parts and in some cases renewal of protection. The following methods can be cited: coatings by noble metals; Standard coatings and cathodic protection (Ogden 2015; Guyonnet et al. 1993). The method most commonly used industrially is cathodic protection, which is generally inexpensive and efficient over a long period when this technique is controlled and accompanied by a good knowledge of the surrounding conditions (Grosgogeats and Brugirard 2001; Gopalakrishnan et al. 2012; Ogden 2015; Guyonnet et al. 1993).

2.5 Minimum Condition of Protection

In this paper, we aim to ensure the hull of a headlight against corrosion using the cathodic protection by imposed current, to do this we must first determine the protection potential.

Based on the NERNST equation, we find the potential for protecting iron in seawater. The oxidation reaction: $Fe \rightarrow Fe^{2+} + 2e^-$, the standard iron protection
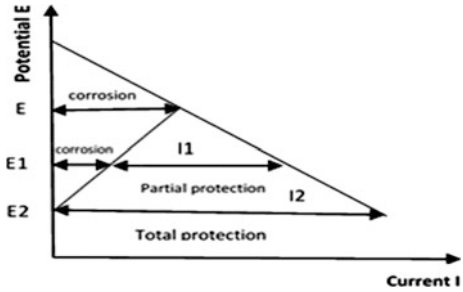
potential: $E_0/ENH = -0.44$ V, the limit concentration of ions Fe^{2+} is $C = 10^6$, the number of electrons transferred in the half reaction is $n = 2$, which gives us the standard protection potential

$$E_{prot} = -0.44 + \frac{0.058}{n} \log 10^{-6} = -0.61 V/ENH \tag{6}$$

To reach the potential corresponding to the threshold of the cathodic protection, the whole surface of the object must be traversed by a current expressed in current density (A/m^2). This situation is described in Fig. 1.

Under free corrosion conditions, the metal structure has a mixed corrosion potential E and corrodes at a rate proportional to the corrosion. If the cathodic polarization is applied so that the potential of the structure decreases to E1 by the applied current I1, then the object is partially protected, since the corrosion rate has decreased and is corrosion-prone. If the external current is increased to I2 so that the potential drops to E2 (corresponding to the reversible potential of the anodic reaction), then the anodic dissolution will be stopped. The structure is then under cathodic protection. As a result, the initial current density (necessary for polarization up to the protection threshold) is often distinguished from the repolarization current density in the event of degradation of the protective capacity of the calcareous deposit (Roche 2015). When the cathodic protection is applied in conjunction with a coating, the current requirement calculations must take a degradation coefficient which generally varies over time. The resistance opposed to the current by the electrolyte must be evaluated.

3 Cathodic Protection by Imposed Current

3.1 Principle

The imposed current (or withdrawal) design uses a direct current electric power source which delivers in a circuit comprising: an overflow (or anodic mass), the electrolyte (soil or water) and the structure to be protected. The positive pole of the

source is connected to the weir while the negative pole is connected to the structure to be protected. The current from the outlet flows through the electrolyte and then enters the structure, thus creating a potential reduction down to the immunity potential of the metal to be protected Fig. 2 (Roche 2015).

Figure 3 shows the required equipment for the installation of a cathodic protection by imposed current (or by withdrawal): an on-board current generator (G), a
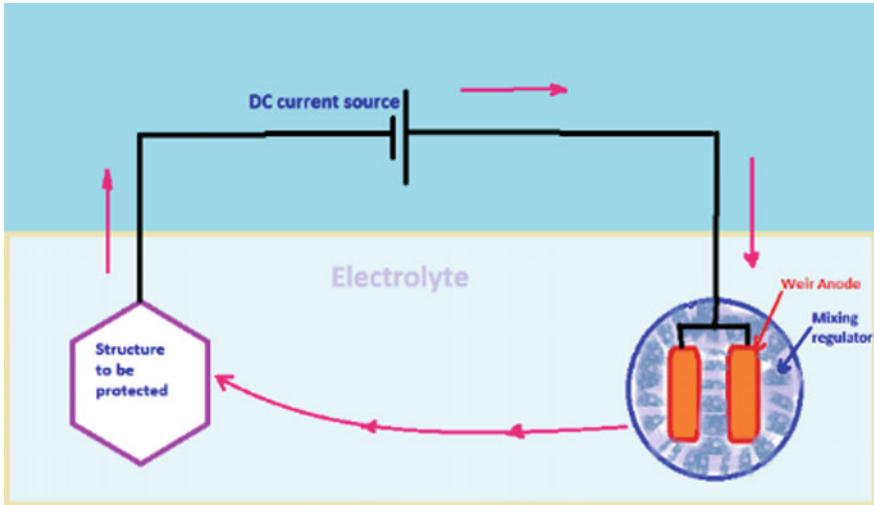
Fig. 2 Circuit diagram of cathodic current protection
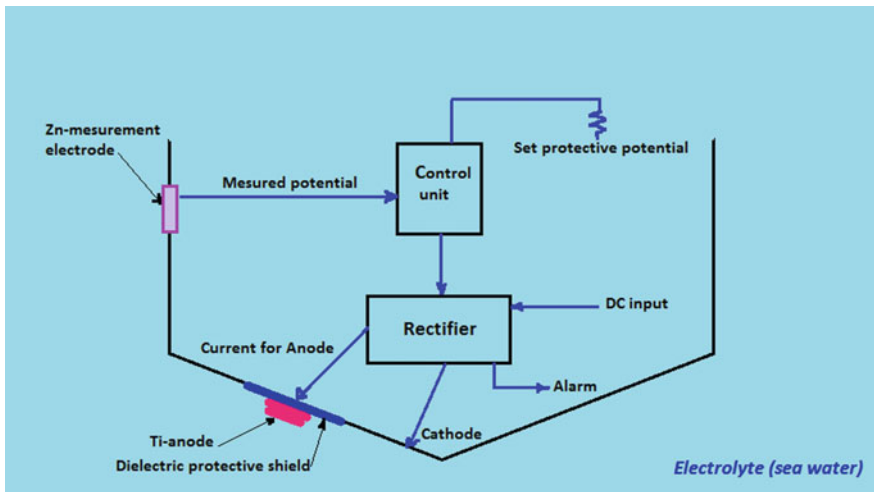
Fig. 3 Schematic diagram of a current protection imposed on a ship

current rectifier (R), an ammeter and a control voltmeter, an automatic or manual current regulator (C), a reference electrode, and an energizing anode.

3.2 Realization of Racking

In this part, we will discuss the method of implantation of the filling station to ensure proper operation leading to protection against corrosion.

Cathodic protection is defined by the following parameters: first, the protective current density, which is the intensity per unit area, depends essentially on: the quality of the insulation of the coating and the aggressiveness of the surrounding environment. Second, the characteristics of the generator are defined below. The flow rate of the current generator I is defined by the law of ohm: $I = U/R$ where: U the voltage of the DC generator and R is the resistance of the circuit. Voltage U is in the low voltage category (TBT) where the voltage is usually 48 V, but in some cases it can reach 120 V DC. The generators used can operate in several modes depending on the need, either at constant current or at constant voltage. Under certain conditions, it is possible to control the instrument with a reference value taken from a permanent reference electrode. The resistance of the circuit is generally conditioned by the resistance of the anode mass. It is therefore advantageous to obtain for this anodic mass as little resistance as possible in order to avoid losses (Jellali 2008).

3.3 Establishment of Filling Stations

The establishment of a filling station must take account of the following practical criteria: possibility of occupation of the ground, low resistivity ground, risk of flooding, or drainage of the water on the ground that can penetrate the filling station, availability and cost of power supply, ease of access for maintenance, and human monitoring. A tapping station comprises at least: a power source, a weir, connecting cables, auxiliary electrical equipment.

The source of energy may be: local distribution network, solar panels, associated with electric batteries in buffer (night operation), generators, turbo-generators, thermoelectric generators, batteries with limited life a few years. The weir is a mass of electrically conductive material whose role is to inject the current into the medium where the structure to be protected is located. Its contact resistance to the ground must be as low as possible and its mass is determined to have the desired longevity. The most commonly used materials are: connecting cables must not carry metal sheaths. The cable cross-section must be determined in relation to the allowable voltage drop (ohm law), the temperature rise, and the mechanical stresses. The auxiliary electrical equipment consists essentially of breaking, protection, and measuring devices. In addition to the elementary filling station, it is common to

install certain devices allowing: automatic control of the potential of the structure protection; the limitation of intensity. This applies in particular to the lock gates, the doors of the vedette and the drawings on railway tracks in service (where the rail is used as an anode); the counting of the operating time. It is a device that counts. The commonly used information is: on-off. Consider the following block diagram which represents an automatic regulation of the current to be injected by the tapping station, complete with a simulation Fig. 4.

4 Implementation of the System on Board of a Boat

In this part, a practical application will be proposed ensuring the cathodic protection of a vedette Fig. 5, using the imposed current protection method.
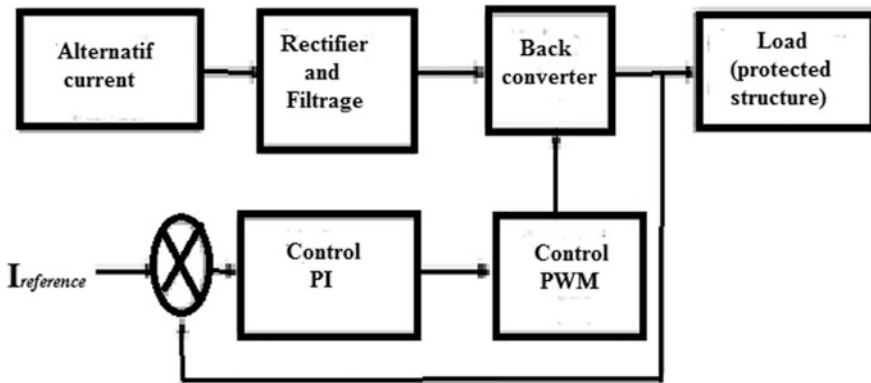
Fig. 4 Single filling station
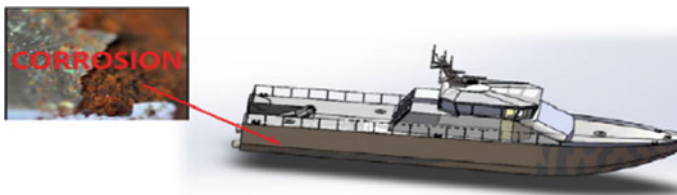
Fig. 5 The prototype vedette

4.1 Vedette Specifications

Overall length: 26.5 m, length between PP: 23.52 m, width at livet: 5.8 m, hollow in the middle: 3.2 m, draft medium: 1.2 m, surface of the hull: 135.72 m^2 and cruising speed: 15 nd.

4.2 Calculation of Parameters Involved in Protection

The star on which one is going to apply the system sails in the Mediterranean, so the middle is the sea water. The total area to be protected is: $S_T = 135.72$ m^2. For the density of protection, one will take $D_p = 40$ mA/m^2. So the current requirement for protection is: $I_{prot} = S_T D_p$ from where $I_{prot} = 135.72 \times 40 \times 10^{-3} = 5.4$ A.

4.3 Diagrams of the System for Controlling the Intensity of the Anodes

Figure 6 show the principle of current control system consisting in measuring the potential of the shell by the reference electrode. Referring to this voltage value, the controller will provide the required current (which will be generated by the generator and injected to the anode) to keep the protection potential −850 mV.

The Ωm is used to measure the resistance between two terminals. To measure the resistance, the power source is disconnected and, instead of the source, the first Ωm is placed between the + and - terminals and the second between the other
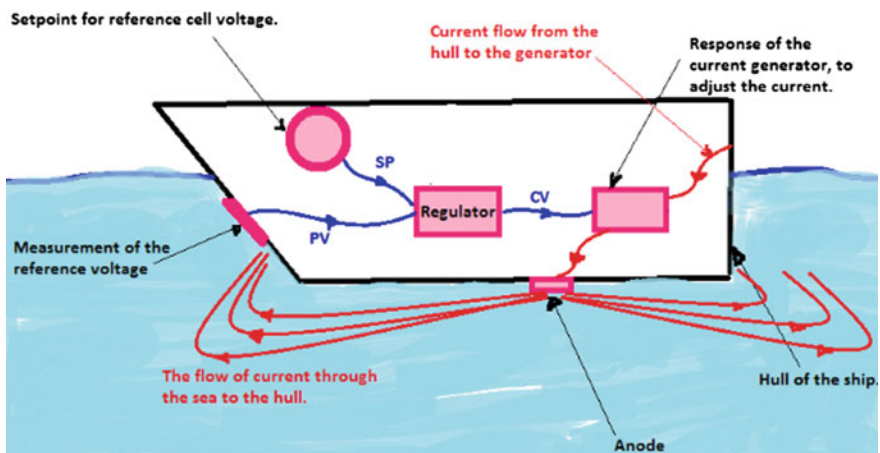
Fig. 6 Principle of current control system

terminal + and the − (checking the continuity of the current). Figure 7 shows the schematic diagram of the imposed current system.

The negative terminal (−) is connected to the cathode which is represented here by the shell of the vedette and the positive (+) terminal is connected to the anode (in this case it is a Titanium anode). The current required to keep the protective potential of the hull (Fig. 8).
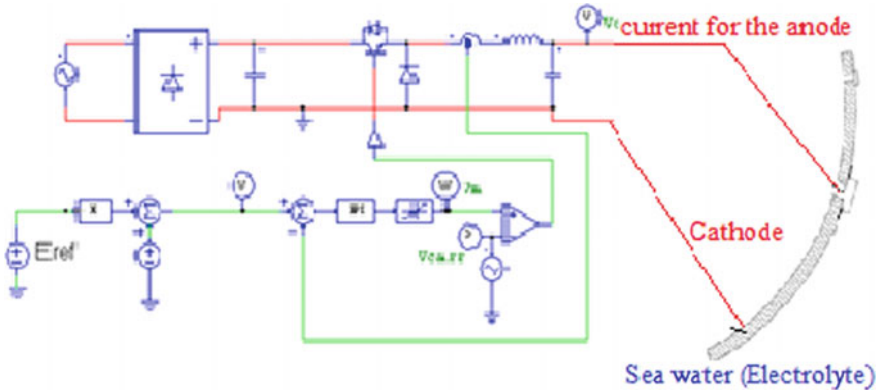
Fig. 7 Schematic diagram of the imposed current system
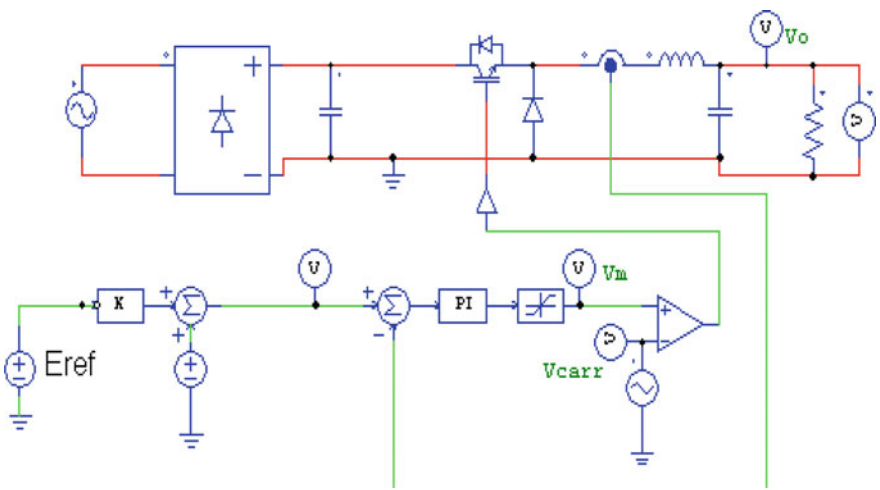
Fig. 8 Automatic regulation of the imposed current

4.4 Numerical Simulations

To validate our study concerning the cathodic protection of the hull by imposed current, tests were carried out by numerical simulation under the software PSIM. Indeed, three values of the voltage of the reference electrode.

It can be seen from Fig. 9 that the current injected into the protection anode is equal to 2.6 A, which is the same as the reference current.

Figure 10 shows that the current injected into the protection anode is equal to 2.7 A, which is the same as the reference current.

It can be seen from Fig. 11 that the current injected into the protection anode is equal to 2.8 A which is the same as the reference current. This simulation allows us

Fig. 9 Imposed current ($E_{ref} = -900$ mV)
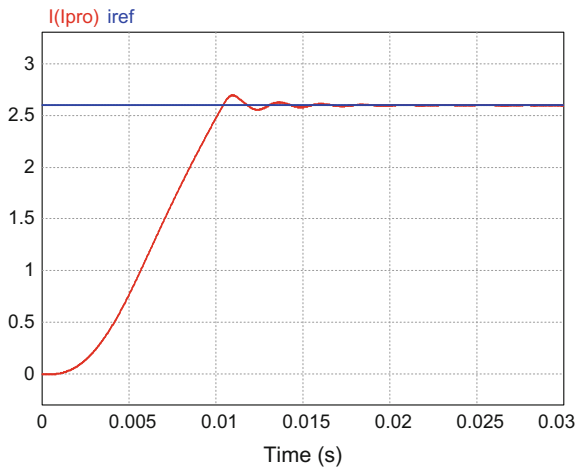
Fig. 10 Imposed current $E_{ref} = -850$ mV
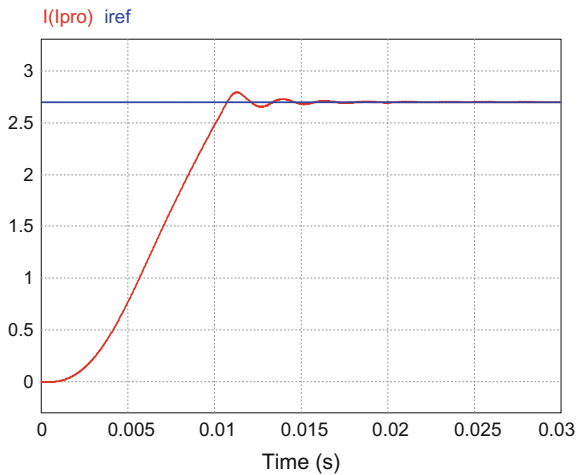
to impose the current necessary to keep the potential −850 mV (protection potential). From experiments carried out with the reference electrodes, it is deduced that there is a relation between the imposed current and the potential of the protection required by the reference electrode in the form

$$I = a\,E_{ref} + b \tag{7}$$

So if the potential measured by the electrode decreases, the imposed current increases and vise versa. For $E_{ref} = -900$ mV the measured current is 2.6 A, for $E_{ref} = -850$ mV the measured current is 2.7 A and for $E_{ref} = -800$ mV the measured current is 2.8 A.

4.5 Choice of Anodes and Their Positions

In order to install the anodes on the hull and ensure a good distribution, it is necessary to determine the center of gravity of the hull. To carry out this task, the software AUTOCAD will be used (Fig. 12).

Fig. 11 Current imposed as a function of de $E_{ref} = -800$ mV
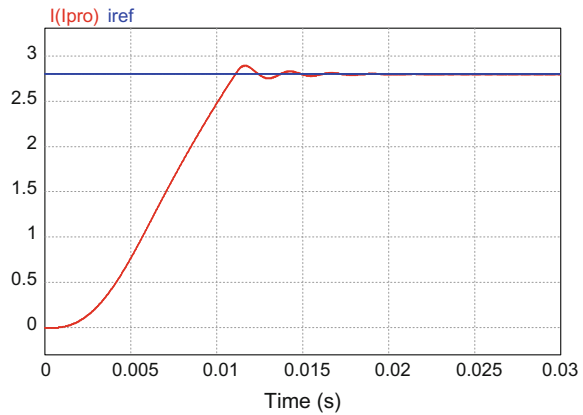
Fig. 12 Position of the anode on the hull

Thus one can install the anodes (one on the starboard side and the other on the port side) on the hull at the point of coordinates

$$(X = 11,005 \text{ m}, \ Y = 0,606 \text{ m})$$

4.6 System with Temperature Control

The resistivity of sea water, ρ (Ωm), is a function of the salinity of sea water and temperature. In the open sea, salinity does not vary significantly and temperature is the main factor. The relationship between resistivity and temperature at a salinity of 30–40‰ is shown in Fig. 13.

In coastal areas, particularly at river mouths and in closed bays, salinity varies considerably. It is recommended that the design of PC systems in such locations is based on resistivity measurements reflecting the annual mean value and the variation of resistivity with depth. In temperate regions (annual mean surface water temperature from 7 to 12 °C), the resistivity of 0.30 and 1.3 Ωm is recommended as reasonably conservative estimates for the calculation of anode resistance in sea water and marine sediments, respectively, and depth independent. Lower values should be documented by actual measurements, taking into account seasonal variations in temperature. In our case, the average temperature of the sea water varies between 13 and 28 °C depending on the season (Chambre syndicale de la recherche et de la production du pétrole et du gaz naturel and Comité des techniciens 1986) (Fig. 14).

From the data measurements it is evident that the cathodic current increases as the temperature of the solution increases. The increase in temperature decreases the solubility of the dissolved oxygen with a subsequent decrease in the rate of

Fig. 13 Resistivity of seawater as a function of temperature
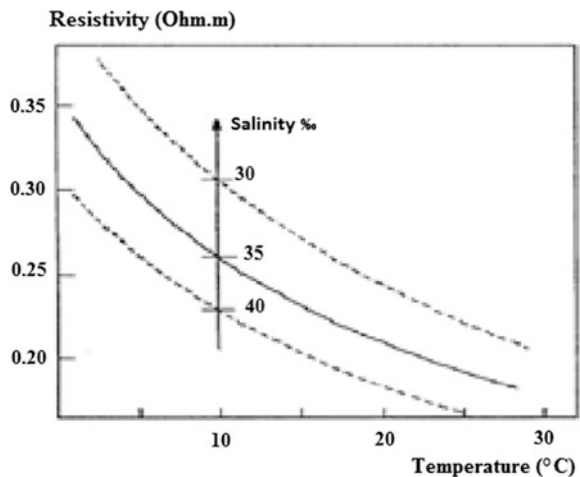
Fig. 14 Function of the resistivity of seawater as a function of temperature

$$y = 0.5123x^{-0.313}$$
$$R^2 = 0.9798$$
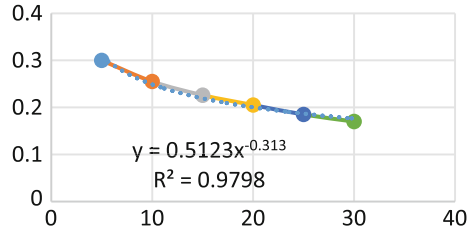
Fig. 15 Cathodic current as a function of sea water temperature

$$y = -0.008x^3 + 0.66x^2 - 17.1x + 148$$
$$R^2 = 1$$
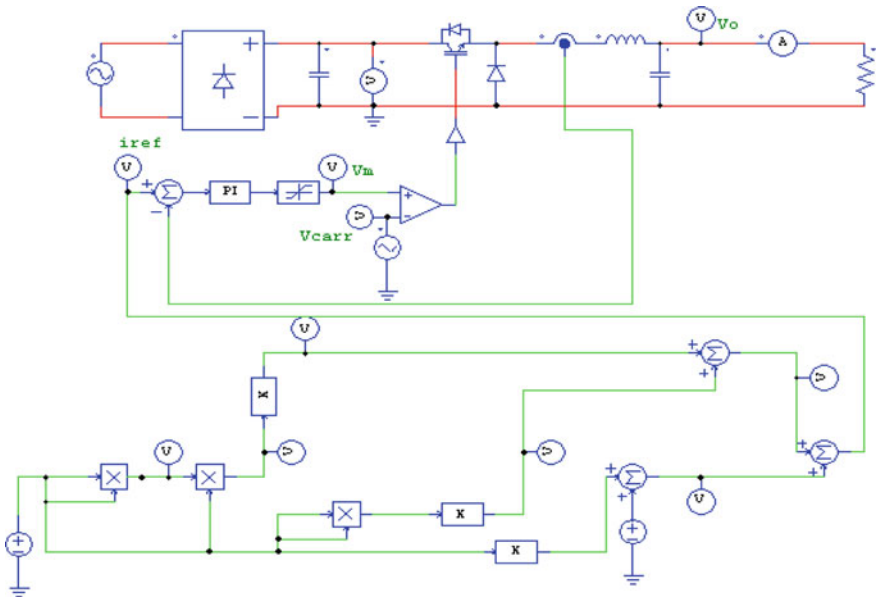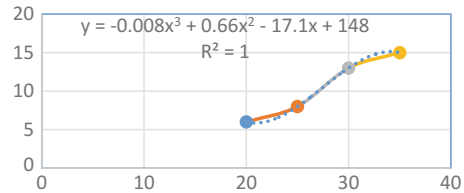
Fig. 16 Circuit for regulating current as a function of temperature

diffusion of the oxygen at the surface of the cathode, thus the corrosion rate decreases (Fig. 15).

Sea water temperature is one of the parameters that influences the phenomenon of corrosion. A relationship between temperature and the current imposed has been established by exploiting practical results. This relation is governed by the relation $I = f(T)$. Figure 16 gives the block diagram of the regulation of the current imposed when the temperature change (Figs. 17 and 18).

Fig. 17 Current required for protection for T = 20 °C
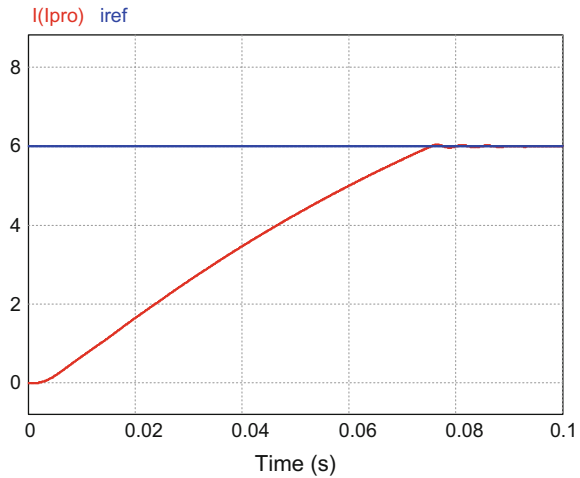
Fig. 18 Current required for protection for T = 25 °C
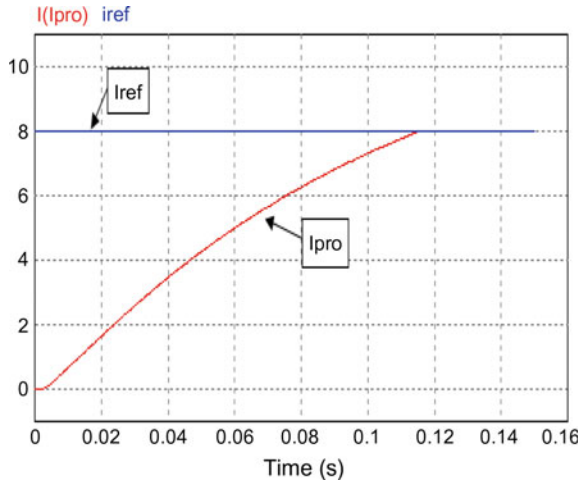
If the design of the PC includes the use of cables for electrical continuity, requirements to the electrical continuity check will be defined in the design report of the PC system. It is recommended that the product of the shunt resistor and the current demand (or current output for a non-welded anode) does not exceed 10% of the design driving the voltage. In no case the resistance through a continuity cable exceeds 0.1Ω. For anodes intended for cathodic protection, special provisions are required to ensure electrical continuity. We must therefore equip our headliner with detection alarms in the event of a power failure, or in case of over-tension: when the current density exchanged on the surface of the structure is greater than that required for its protection.

5 Conclusion

The cathodic protection is an effective method of combating the corrosion of structures and equipment placed in a sufficiently conductive electrolyte. However, a certain number of installation rules must be followed and experience is essential and requires the use of specialized engineering companies, qualified and, if possible, certified personnel. In particular, for the imposed current system it is necessary to take more precautions view that this technique requires a lot of maintenance, attention and a regular follow-up in order to ensure a good protection for a long duration.

No one can deny that the cost of the imposed current system is high compared with other means of protection and that its installation is more complicated, but this does not prevent it from being the most effective method of protecting large areas. It is for this reason that this technique has been chosen by choosing as an anode: the titanium anode (C-Max) in the form of a disk installed in the center of the hull (a port and a starboard) to give the total of a protective current equal to 5.4 A and with reference electrodes Cu/Cu-SO$_4$.

References

Ahmad Z (2006) Principles of corrosion engineering and corrosion control. Elsevier, Amsterdam, pp 293–344

Barral G, Le Gorrec B, Montella C (2003) Notions élémentaires sur les cellules électrochimiques. pp 11

Benard J, Michel A, Philibert J, Talbot J (1991) Métallurgie générale. Masson, Paris

Chambre syndicale de la recherche et de la production du pétrole et du gaz naturel, Comité des techniciens (1986) La protection Cathodique: guide pratique. pp 8

Eliades G, Eliades T, Brantley W, Watts D (2003) Dental materials in vivo. Quintessence Book, Carol Stream

E Ogden (2015) YACHTS: les phénomènes de corrosion. pp 183–188

Gopalakrishnan J, Agnihotri G, Deshpande DM (2012) J Inst Eng India Ser 93:259. https://doi/org/10.1007/s40031-012-0033-9

Grosgogeats B, Brugirard J (2001) Les essais de corrosion des biomatériaux: leurs usages, leurs limites, leurs fondements. Matériaux et Tech 5–6:15–27

Guyonnet J, Gregoire G, Joniot-Champion S, et al (1993) Electrogalvanisme buccal et sa pathologie. Moyens et protocoles d'expérimentation. Encyclopédie Médico-Chirurgicale 23063D10: pp 6

Jellali R (2008) Elaboration de revêtements antifouling par photoréticulation d'oligoisoprènes fonctionnalisés: étude de leurs activités antibactériennes, antifongiques et antialgales. Thése de Doctorat de l'université de Maine

Kim I-D, Nho E-C (2005) Module-type switching rectifier for cathodic protection of underground and maritime metallic structures. IEEE Trans Ind Elect 52(1):181–189

Pourbaix M (1963) Atlas d'équilibres électrochimiques. Gauthier-Villars, Paris

Roche M (2015) L'essentiel sur la protection cathodique, pp 1–14

Vibration Analysis of a Nonlinear Drivetrain System in the Presence of Acyclism

Ahmed Ghorbel, Moez Abdennadher, Lassâad Walha, Becem Zghal and Mohamed Haddar

Abstract Drivetrain vibrations are a great concern in the automotive industry, once they are related to many Noise, Vibration and Harshness (NVH) phenomena. An automobile drivetrain system generally consists of the following main components: engine, clutch, gearbox, disk brake, and transmission shafts. This paper represents a nonlinear dynamic model for each drivetrain components in the presence of the acyclism phenomena (cyclostationary regim). This model is simulated by 18 degrees of freedom. The governing nonlinear time-varying motion equation formulated is resolved by the analytic Runge–Kutta method. The dynamic responses of the clutch and the single-stage helical gear reducer are investigated in the idle engine regime. The results are presented in the time and time-frequency domain by using the Wigner-Ville distribution. The dynamic behavior study of the system, comes to confirm the significant influence of the engine excitation (torque and speed fluctuation), particularly in the case of the gasoline engine acyclism condition.

Keywords Dynamic behavior · Engine acyclism · Clutch · Gearbox Disk brake

A. Ghorbel (✉) · M. Abdennadher · L. Walha · B. Zghal · M. Haddar
Laboratory of Mechanics Modeling and Production, National School
of Engineering of Sfax, University of Sfax, Sfax, Tunisia
e-mail: gh.ahmed.enis@gmail.com

M. Abdennadher
e-mail: moez.abdennadher@gmail.com

L. Walha
e-mail: walhalassaad@yahoo.fr

541

1 Introduction

Drivetrain is considered as the most important generator of noise and vibration in the vehicle. For that purpose, a drivetrain vibration analysis was addressed by many researchers.

In most studies on drivetrain dynamic behavior so far, the system modeled as a simple model such as the model of Templin P. and the model of Bemporad A., which they used a model with only two degrees of freedom (Templin and Egardt 2009; Bemporad et al. 2001). More detailed and coupled models are investigated in the literature (van Berkel et al. 2014; Caruntu et al. 2016; Ahmed et al. 2017). Other research works interested in modeling and analyses clutches and reducers with spur or helical teeth, without modeling a mechanism of braking (Walha et al. 2011; Koos 2014). In addition, most researches works studied the clutch and gearbox separated. Driss et al. (2007) studied a clutch model which contains 11 degrees of freedom with three types of nonlinearity. Furthermore, Walha et al. (2009) treated a model of helical gear system with two floors. The experimental observations of Fosberry and Holubecki on a model of disk brake (Fosberry and Holubecki 1961), show that the vibration of the disk are much more important than the brake calipre, from where the importance of studying the effect of vibration of the disk, especially when it is coupled by another system like a reducer. Khabou et al. (2014) studied the influence of the friction phenomenon generated by a disk brake on the dynamic behavior of a single gear stage. On the other side, the load condition variation can also be considered a significant source of excitation. In this context, Khabou et al. (2011) investigated a spur gear dynamic behavior in the case of engine acyclism condition.

In this paper, a nonlinear automobile driveline model with 18 degrees of freedom was proposed. The dynamic behaviors of the clutch and the geared system were investigated in the presence of the acyclism phenomena.

2 Dynamic Drivetrain Model

The dynamic behavior study of a vehicle driveline requires analysis of the main subsystems and components. In this part, we are interested in modeling of the different elements. The kinematic layout of the driveline system is shown in Fig. 1.

2.1 Combustion Engine Modeling

In the idle engine regime, the acyclism is essentially due to the thrust of the gases.

Under low load the combustion moment expression of the gasoline engine with four cylinders is given by Ligier and Baron (2002).
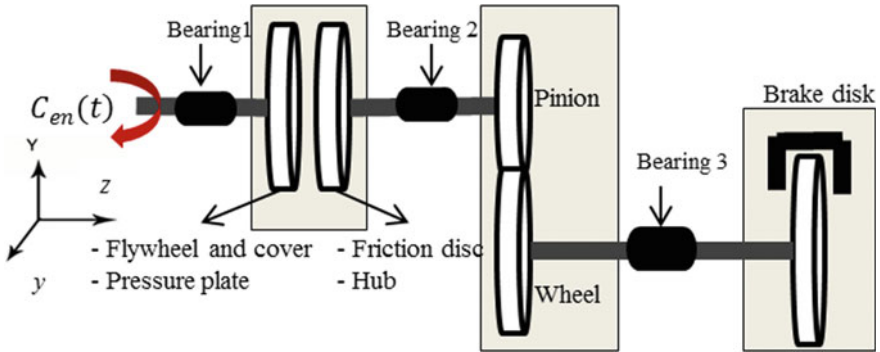
Fig. 1 Vehicle driveline model
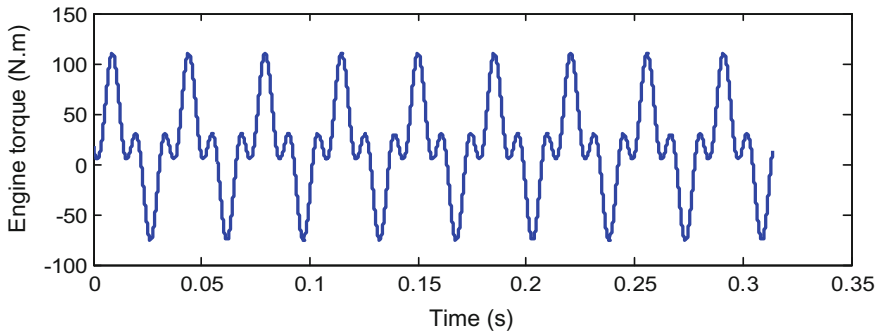
Fig. 2 Engine torque

$$C_{en}(t) \approx C_{vg4} = \overline{C_{m4}} + \frac{P_{max}}{68.4} V_{cyl}(0.32 \sin(2\alpha_c) - 0.21 \sin(6\alpha_c)) \qquad (1)$$

The adopted acyclism model lead to the following rotational speed function:

$$\Omega(t) = \Omega_{10}\left(1 + \sum_n \rho_n(\Omega_{10}) \sin(n\Omega_{10}t + \varphi_n)\right) \qquad (2)$$

Figure 2 shows the fluctuation of the engine torque of the selected gasoline engine with an idling speed (850 rpm).

2.2 Clutch Modeling

Modeling a vehicle clutch is effectuated by a torsional model with a nonlinear function. This is due to dry friction. The friction torque $\tilde{T}_f(\dot{\delta})$ is a nonlinear function which depends on the relative velocity $\dot{\delta}$. The equation of the friction torque is given by: Duan and Singh (2005, 2006)

$$\tilde{T}_f(\dot{\delta}) = \bar{\mu}(\dot{\delta}) \cdot \mu_D \cdot P \cdot A \cdot R \tag{3}$$

where P is the pressure, A is the surface area of contact, and R is the mean radius of that surface. $\mu(\dot{\delta})$ is the coefficient of friction that depends on the relative velocity.

The developed dynamic model is shown in Fig. 3. I_1 represents the torsional inertia of flywheel and cover. I_2 is the inertia of the pressure plate and I_3 represents the friction disk inertia. I_4 is the inertia of the hub of the clutch.

2.3 Gearbox Modeling

The periodic variation of the gear mesh stiffness is another excitation source of the system and it is generated by the time-varying teeth number in contact. A dynamic torsional model of a single gear stage is presented in Fig. 4.

The transmission mechanism is effectuated by helical gears. The toothed wheels are assumed rigid body and the bearings are modeled by linear stiffness. I_p and I_w
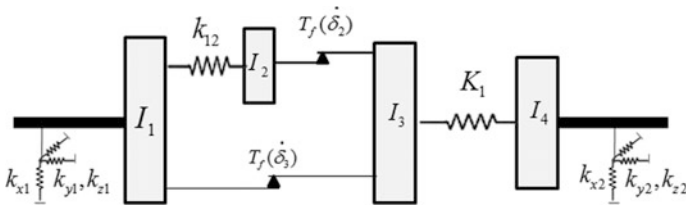
Fig. 3 Dynamic model of the clutch

Fig. 4 Dynamic model of the helical gear stage
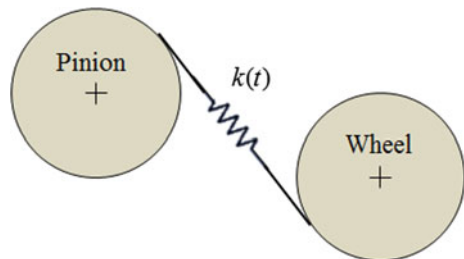
are respectively the inertia of the pinion and wheel. The gear mesh is modeled by linear stiffness acting on the line of action.

2.4 Disk Brake Modeling

The proposed model includes the respective torsional and tangential motions of the disk and pad. Figure 5 shows the mechanism of a disk brake system, where I_d, m_d are respectively the inertia and the mass of the rigid disk, and I_{p1} and m_{p1} represents inertia and mass of the pad. The parameters k_f and k_t represent the linear and torsional stiffness of the pad. F_{st} is the static force applied on the pad.

2.5 Equation of Motion

Applying the Lagrange formulation will lead to the equation of motion with 18 degrees of freedom given by

$$[M]\{\ddot{q}\} + [C]\{\dot{q}\} + [K_G]\{q\} = \{F_0(t)\} + \left\{\vec{F}(q)\right\} \tag{4}$$

where the vector of degrees of freedom defined by

$$\{q\} = \{x_1 \quad y_1 \quad z_1 \quad x_2 \quad y_2 \quad z_2 \quad x_3 \quad y_3 \quad z_3 \quad z_g \quad \theta_1 \quad \theta_2 \quad \theta_3 \quad \theta_4 \quad \theta_p \quad \theta_w \quad \theta_d \quad \theta_g\}$$
$$\tag{5}$$

Fig. 5 Dynamic model of the brake disk
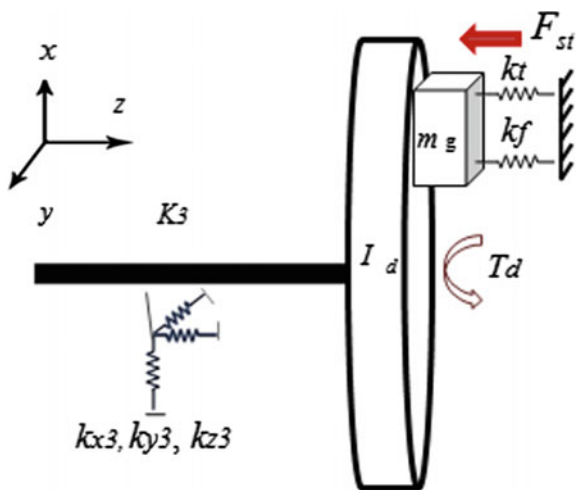
x, y, and z are the bearing displacements. z_g is the pad vibration. θ is the angular displacement of the wheel and gears following the direction.

$[M]$ represents the global mass matrix and it can be defined by

$$[M] = diag\left(m_{b1}, m_{b1}, m_{b1}, m_{b2}, m_{b2}, m_{b2}, m_{b3}, m_{b3}, m_{b3}, m_{p1}, \atop I_1, I_2, I_3, I_4, I_p, I_w, I_d, I_{p1}\right) \tag{6}$$

$[K_G]$ is the stiffness matrix and can be written as follows:

$$[K_G] = [K_e(t)] + [K], \tag{7}$$

where $[K_e(t)]$ is the linear time-varying mesh stiffness matrix.

$[K]$ is the constant stiffness matrix which consists of the bearings stiffness matrix $[K^b]$ and the shafts stiffness matrix $[K_{sh}]$, and can be written by

$$[K] = diag\left([K^b], [K^{sh}]\right) \tag{8}$$

For reasons of simplicity, the viscous damping is assumed proportional to the mass and the stiffness matrix.

$$[C] = \lambda[M_G] + \eta[\tilde{K}_G] \tag{9}$$

$[\tilde{K}_G]$ is the average rigidity matrix, independent of time. λ and η are determined experimentally.

The linear excitation vector is expressed by

$$\{F_0(t)\} = \{0, 0, P, 0, 0, 0, 0, F_T, -F_{st}, F_{st}, C_{en}(t), 0, 0, 0, 0, 0, -(T_d + T_{br}), T_{br}\} \tag{10}$$

The nonlinear excitation vector is defined by

$$\{\vec{F}(q)\} = \{F_{Tx2/3}, F_{Ty2/3}, 0, -F_{Tx2/3}, -F_{Ty2/3}, 0, 0, 0, 0, 0, -T_f(\dot{\delta}_3), -T_f(\dot{\delta}_2), (T_f(\dot{\delta}_2) + T_f(\dot{\delta}_3)), 0, 0, 0, 0, 0\} \tag{11}$$

The terms $F_{Tx2/3}$ and $F_{Ty2/3}$ are the tangential forces applied by the second block on the third block following the direction x and y and can be expressed as follows:

$$F_{Tx2/3} = -\mu_D \cdot P \cdot A \cdot \frac{\dot{x}_2 - \dot{x}_1}{\|\dot{x}_2 - \dot{x}_1\|}, \tag{12}$$

$$F_{Ty2/} = -\mu_D \cdot P \cdot A \cdot \frac{\dot{y}_2 - \dot{y}_1}{\|\dot{y}_2 - \dot{y}_1\|} \tag{13}$$

The Coulomb friction theorem is applied to the modeling of tangential braking forces F_T and torque T_{br}

$$F_T = \mu \cdot F_{st}, \tag{14}$$

$$T_{br} = r \cdot F_T, \tag{15}$$

where μ is the friction coefficient and r represents the distance between the pad and the center of the disk.

3 Simulation Results

Nonlinear Runge–Kutta method was used to solve the motion equation. Smoothed Wigner-Ville time-frequency method is used to analyze the nonstationary behavior of the time signal. Table 1 lists typical values of parameters used for simulation studies.

Figure 6 shows the temporal shape the nonlinear tangential forces applied on clutch disk along the x and y directions. The signs of these two forces show a

Table 1 Values of parameters for numerical studies of the drivetrain system

Parameters	Values
Engine speed (tr/mn)	$\Omega = 850$
Clutch parameters	$P = 8 \times 10^4$ N/m, $A = 0.025$ m^2, $R = 0.07$ m
Masses (kg)	$m_1 = 5$, $m_2 = 1.17$, $m_3 = 0.8$, $m_4 = 0.2$, $m_d = 7.5$, $m_g = 0.2$
Inertias (kg m^2)	$I_1 = 0.02$, $I_2 = 12 \times 10^{-3}$, $I_3 = 8 \times 10^{-4}$, $I_4 = 2 \times 10^{-4}$
Torsional stiffness (N m/rad)	$k_{12} = 8 \times 10^4$, $K_1 = 1.75 \times 10^4$, $K_2 = K_3 = K_4 = 1 \times 10^5$
Bearing stiffness (N/m)	$k_{xi} = k_{yi} = k_{zi} = 10^8$
Number of teeth	$Z_{12} = 18$, $Z_{21} = 26$
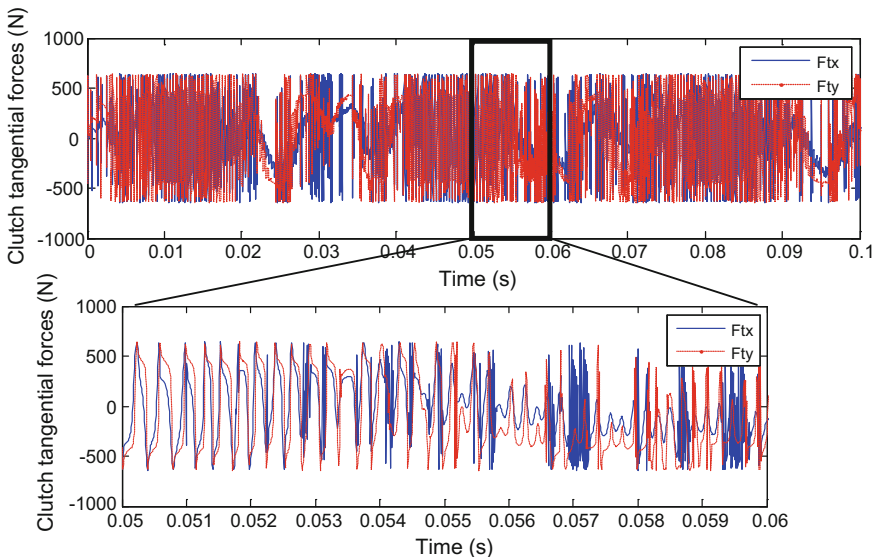
Fig. 6 The clutch tangential force along *x* and *y* directions
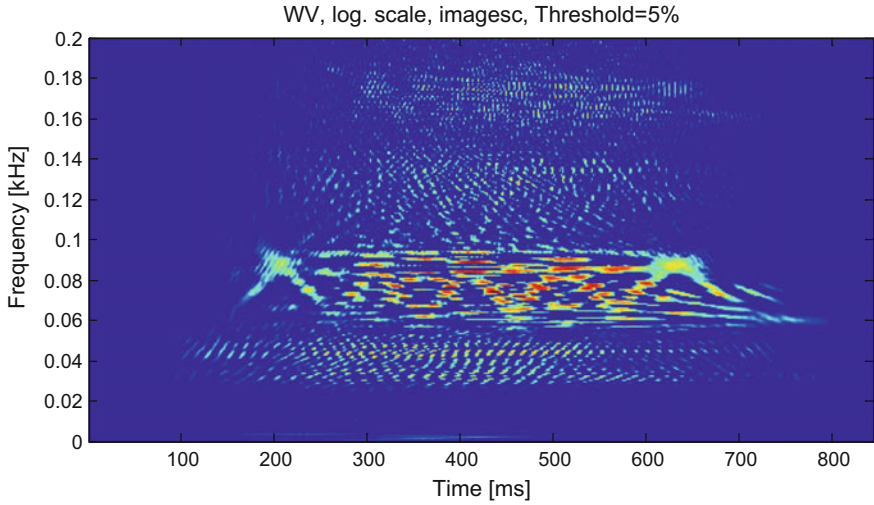
Fig. 7 Wigner–Ville distribution of the tangential force along x direction
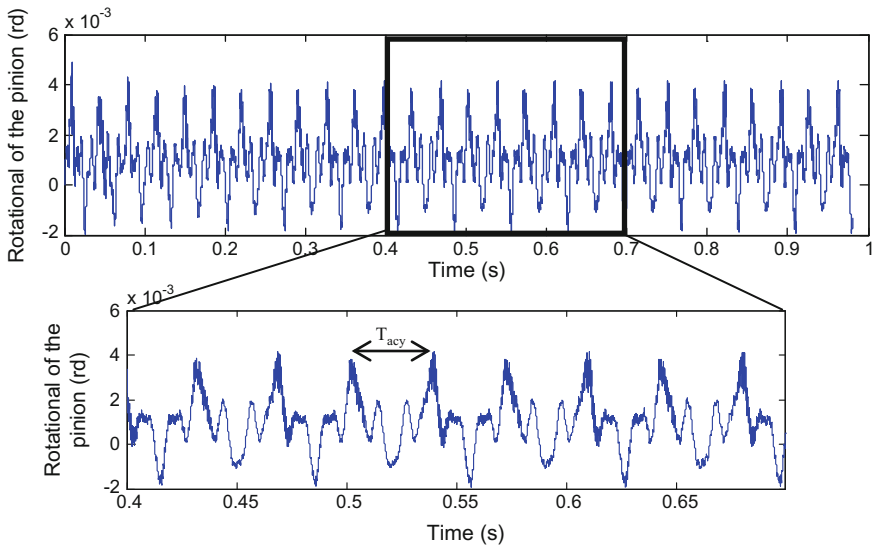
Fig. 8 Time responses of the pinion

variation of period over time. This variation is due to the acyclism phenomena of the excitation torque.

The period of the meshing stiffness which excites the system is not constant. In order to describe the evolution of the frequency, a time-frequency map is drawn based on Wigner-Ville distribution. Figure 7 represents the time-frequency map of the tangential force only along x direction.

Figure 8 shows the rotational vibration of the pinion. This response is time-varying and periodic with T_{acy} ($2.\pi/\Omega_{10}$) as the period and its fluctuation is proportional to loading conditions.

4 Conclusion

In this paper, a nonlinear dynamic drivetrain model is detailed to investigate the dynamic behavior of the system and the influence of the acyclism phenomena. The nonlinearity of the studied system takes its origin from the friction model in the clutch system. The dynamic responses of the tangential forces of the clutch and the transmission error of the helical geared system are investigated using an appropriate Runge–Kutta algorithm. The simulation results show the meaningful effect of the torque and speed fluctuation due to acyclism phenomena in the vibration behavior of the system.

References

Bemporad A, Borrelli F, Glielmo L, Vasca F (2001) Optimal piecewise-linear control of dry clutch engagement. In: IFAC workshop advances in automotive control, IFAC, pp 33–38

Caruntu CF, Lazar M, Di Cairano S (2016) Driveline oscillations damping: a tractable predictive control solution based on a piecewise affine model. Nonlin Anal Hybrid Syst 19:168–185

Driss Y, Fakhfakh T, Haddar M (2007) Effect of eccentricity on a clutch system under a harmonically varying normal load. J Fail Anal Prev 7(2):127–136

Duan C, Singh R (2005) Transient responses of a 2-dof torsional system with nonlinear dry friction under a harmonically varying normal load. J Sound Vib 285:1223–1234

Duan C, Singh R (2006) Dynamics of a 3dof torsional system with a dry friction controlled path. J Sound Vib 289:657–688

Fosberry RA, Holubecki Z (1961) Disc brake squeal: its mechanism and suppression. Technical report, motor industry research association, Warwickshire, England

Ghorbel A, Abdennadher M, Zghal B, Walha L, Haddar M (2017) Modal analysis and dynamic behavior for analytical drivetrain model. J Mech 1–17

Khabou MT, Bouchaala N, Chaari F, Fakhfakh T, Haddar M (2011) Study of a spur gear dynamic behavior in transient regime. Mech Syst Signal Process 25(8):3089–3101

Khabou MT, Ksentini O, Jarraya A, Abbes MS, Chaari F, Haddar M (2014) Influence of disk brake friction on the dynamic behaviour of a directly coupled spur gear transmission. Multidiscip Model Mater Struct 10(2):146–162

Koos VB (2014) Fast and smooth clutch engagement control for dual-clutch transmissions. Control Eng Pract 22:57–68

Ligier JL, Baron E (2002) Acyclisme et vibrations: applications aux moteurs thermiques et aux transmissions. Analyses avancées et expérimentales, vol 2. Technip Ophrys Editions

Templin P, Egardt B (2009) An LQR torque compensator for driveline oscillation damping. In: Control applications, (CCA) & intelligent control, (ISIC). IEEE, pp 352–356

van Berkel K, Hofman T, Serrarens A, Steinbuch M (2014) Fast and smooth clutch engagement control for dual-clutch transmissions. Control Eng Pract 22:57–68

Walha L, Driss Y, Fakhfakh T (2009) Effect of manufacturing defects on the dynamic behaviour for a helical two-stage gear system. Mécanique Ind 10:365–376

Walha L, Driss Y, Khabou MT, Fakhfakh T, Haddar M (2011) Effects of eccentricity defect on the nonlinear dynamic behavior of the mechanism clutch-helical two stage gear. Mech Mach Theor 46(7):986–997

Calibration and Correction of the Beam Solar Radiation Models Using High Temporal Resolution Measurements

Ismail Loghmari and Youssef Timoumi

Abstract The conversion of the Direct Normal solar Irradiance (DNI) energy into thermal or electrical energy is performed by concentrating solar power systems. They use the received solar radiation to expose an industrial working fluid to high temperature. A good knowledge of the availability of the DNI in the place of settlements of a solar power plant plays a crucial role in the design of solar collectors and the optimization of operations within the industrial applications. In regions where no solar radiation measurements are available, the modeling of the DNI is commonly adopted to determine the solar radiation potential of the site. However, the DNI models could predict the direct solar radiation with high uncertainty. This paper presents a performance analysis of three DNI clear sky models: Ineichen, Iqbal, and Solis models to predict the Direct Normal Irradiance. The performance analysis conducted in our study consisted of validation and calibration of these models using 10 min resolution measurements performed in a southern Tunisian region (Tataouine). The purpose of our research is to improve the accuracy of the DNI model prediction and to offer more reliable estimations. The results of the sub-hourly statistical validation of these models show that the Iqbal model achieves the lowest uncertainty of prediction. After performing calibration with the in situ measurements, The results show that, the uncertainty of estimation, represented by the relative root mean square error (rmse%), has been generally reduced by 3%. For a high DNI intensity, the lowest errors are recorded by the corrected Solis model (rmse% = 6.2%) while, for a low DNI intensity, it reaches 25.6% which is recorded by the corrected Iqbal model.

Keywords Direct normal irradiance · Clear sky model · Linear correction
Desert region

I. Loghmari (✉) · Y. Timoumi
Mechanical Engineering Laboratory, University of Monastir, Monastir, Tunisia
e-mail: yesine@live.fr

Y. Timoumi
e-mail: Youssef.Timoumi@enim.rnu.tn

1   Introduction

To limit the fossil fuel consumption and their negative impacts on the environment, the exploitation of solar energy for industrial applications becomes more and more a worldwide demand.

The Direct Normal Irradiance (DNI) is used by concentrating solar power systems in order to convert it into thermal power. Therefore, the knowledge of the availability of DNI in a specific region plays a crucial role to perform a reliable estimation of the performance of concentrating solar energy systems. A high-quality DNI database such as measurement database is rarely available in a specific potential site and for all the desired years. This implies the need to create predicting solar radiation models in the targeted regions.

In desert regions, where most days of the year have clear sky conditions, the DNI clear sky models are likely used to predict the DNI. Indeed, many models have been developed in the literature (Energer and Mills 2015; Ineichen 2016) to estimate the DNI in regions where no measurements are available. These models can predict instantaneously the DNI using meteorological and atmospheric parameters as inputs to the models. So, in order to conduct a high-quality sub-hourly estimation of the DNI, the atmospheric input parameters should also be presented with high-quality sub-hourly resolution. Unfortunately, most of the relevant atmospheric input parameters are presented with low-quality values such as daily or monthly averages (Sengupta et al. 2015). As results, these models could predict the DNI without enough accuracy. Therefore, they generally require calibrations and corrections in order improve their accuracy of prediction. These corrections are usually based on developing correlating equations between the modeled and the measurement databases. The correlation equation could be a simple ratio between the model and the measurements (Gueymard 2009), a first-order polynomial equation (Beyer et al. 2009) or a third-order polynomial equation as suggested by Mieslinger et al. (2014). Most of the proposed correction methods are based on developing a unique equation between the modeled and measurement databases in order to conduct the calibration procedure. In this study, we corrected the models by means of multiple developing equations that take into account the intensity of the DNI intensity during the day.

2   DNI Computation

The clear sky models use atmospheric, meteorological, and geographic parameters as inputs in order to perform an instantaneous computation of the direct normal solar radiation (DNI) throughout the day.

We selected three of the best and largely used clear sky models in order to compute and evaluate the DNI. The choice of the simplified Solis (Ineichen 2008); Ineichen and Perez (2002) and Iqbal (Wong and Chow 2001) models was based on

Table 1 Input parameters of the clear sky models

Input parameter	Resolution/value	Sources
aod	Daily average	NASA (2016) database
Ta	Daily average	Meteorological station
Rh	Daily average	Meteorological station
W	Daily average	Atwater equation (Atwater and Ball 1976)
loz	Average value of 340 DU	Ineichen (2006)
TL	Monthly average	Soda (2016) database
am	Instantaneous	Kasten equation (Kasten 1965)

the availability of input parameters in the desired region and their simplicity of implementation. The aerosol optical depth (aod), the air mass (am), the Link Turbidity (TL), the Ozone column (loz), the Water vapor column (W), the ambient temperature (Ta) and the relative humidity (Rh) are required to implement these models. In Table 1, we summarized the sources from where we captured these input parameters.

3 Clear Sky Model Evaluation

To evaluate the three developed clear sky models, we compared their results with the measurements of a high-quality first class Kipp and Zonen CHP1 Pyrheliometer performed in Tataouine (Tunisia) desert region. 20 days, covering all the seasons of the year, have been selected to evaluate the models.

In order to perform a reasonable study of the accuracy of clear sky models to compute DNI over the journey, we conducted a discrete evaluation of the models based on the DNI intensity during the day:

Based on a sub-daily comparative study between the results of the models and the experimental values, we have chosen three DNI intervals to validate the clear sky models: High DNI intensity (DNI $\leq$ 600 W/m^2), medium DNI intensity (601 $\leq$ DNI $\leq$ 800 W/m^2) and low DNI intensity (801 $\leq$ DNI $\leq$ 1100 W/m^2).

The relative root mean square error (rmse%) was used in our study to evaluate our models. It is computed as follows (Inman et al. 2013):

$$\text{rmse\%} = \frac{1}{\sqrt{N}} \sqrt{\sum_{i=1}^{N} e_i^2} / \text{DNI}_{\text{mes, i}} \times 100 \tag{1}$$

N Represents the number of measurements.
e_i is the single calculus error described as follows:
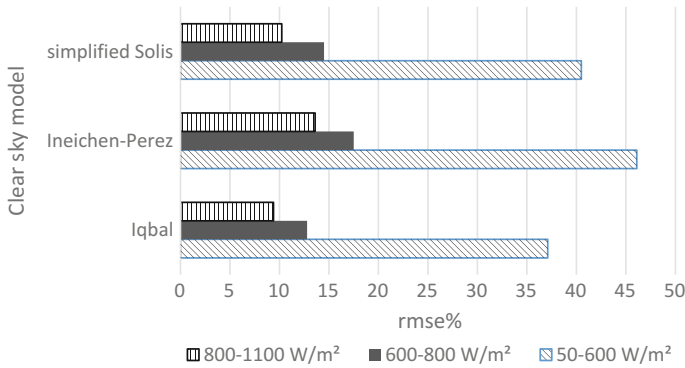
Fig. 1 The root mean square error rmse% recorded by clear sky models at every DNI interval

$$e_i = DNI_{pred, i} - DNI_{mes, i} \tag{2}$$

$DNI_{pred,i}$ is the model calculated or predicted DNI value.
$DNI_{mes,i}$ is the corresponding measured value.
$\overline{DNI_{mes, i}}$ is the average value of the measured DNI.

In Fig. 1, we presented the evaluation results of our three clear sky models for each interval.

The results of the evaluation presented in Fig. 1 show that the accuracy of the three clear sky models increases with the DNI intensity. The Ineichen-Perez model has the lowest accuracy for all the DNI intervals. The Iqbal model is the most accurate model to estimate DNI for all intervals.

The results of the evaluation show that the accuracy of the models are generally low. Meanwhile, it is very clear to see that estimating the low DNI intensity using clear sky models is not appropriate. These results could be explained by the fact that the atmospheric input parameters are not sufficiently precise or with high quality.

In order to reduce the uncertainty of DNI prediction, we carried out a study of calibration and correction of these models using in situ measurement.

4   Reducing the DNI Prediction Uncertainty: Correction of Clear Sky Models

4.1   Correction Method

In order to reduce the DNI prediction uncertainty, a transformation or a correction is applied to the value of DNI predicted by clear sky models. The correction consists

of performing a linear transformation of DNI values predicted by each model (Beyer et al. 2009).

The expression of the corrected DNI is presented by Eq. (3) (Beyer et al. 2009).

$$DNI_{corrected} = a \cdot DNI_{model} + b \qquad (3)$$

where

$$a = \sigma(DNI_{measure})/\sigma(DNI_{model}) \cdot r \qquad (4)$$

$$b = \overline{DNI_{measure}} - a \cdot \overline{DNI_{model}} \qquad (5)$$

$DNI_{measure}$ and DNI_{model} represent respectively the DNI measured and computed by the clear sky model. $\overline{DNI_{measure}}$ and $\overline{DNI_{model}}$ represent their corresponding mean average values.

"r" stands for the correlation coefficient and $\sigma(DNI)$ is the standard deviation of DNI.

4.2 Evaluation of the Post Corrected Clear Sky Models

Eight clear sky days have been selected in order to compute the correlation coefficients. a and b were developed for the two different DNI intervals

- $50 \leq DNI \leq 700$ W/m^2
- $DNI \geq 700$ W/m^2

Table 2 summarizes the values of a and b for each interval.

After applying the linear correction for each clear sky model, the same evaluation procedure as the one conducted in Sect. 3, has been performed to the corrected clear sky models. Table 3 presents a comparative study of the results of the DNI prediction by clear sky models before and after correction.

The results presented in Table 3 shows that, on average, the rmse% errors have been reduced by 3%. The corrected Solis model has recorded the best accuracy, at the highest DNI intensity interval, with an error that reaches 6.2%. However, for

Table 2 The correcting correlation coefficient a and b developed for each clear sky model

Clear sky model	$50 \leq DNI \leq 700$ W/m^2		$DNI \geq 700$ W/m^2	
	a	b	a	b
Simplified solis	0.8	95.78	0.4937	464.45
Iqbal	0.8121	68.715	0.535	419.94
Ineichen-Perez	0.715	188.29	0.437	527.91

Table 3 Comparative study of the relative root mean square error (rmse%) recorded by the three clear sky models before and after applying linear correction (rmse% before correction—rmse% after correction)

Clear sky model	DNI interval	rmse% before correction (%)	rmse% after correction (%)
Simplified solis	$50 \leq DNI \leq 700$ W/m^2	30.2	27.3
	$DNI \geq 700$ W/m^2	10.9	6.2
Iqbal	$50 \leq DNI \leq 700$ W/m^2	27.88	25.6
	$DNI \geq 700$ W/m^2	9.82	6.46
Ineichen-Perez	$50 \leq DNI \leq 700$ W/m^2	35.24	26.4
	$DNI \geq 700$ W/m^2	14	6.66

low DNI intensity, the lowest error is recorded by the corrected Iqbal model, it amounts 25.6%.

These results show that in order to perform Direct normal radiation prediction using low-quality input parameters, it is recommended to use the corrected simplified Solis model Eq. (6) only when the DNI is higher than 700 W/m^2, i.e., at noon.

$$DNI = 0.4937.DNI\_solis + 464.47 \tag{6}$$

$$DNI\_solis = I_0 exp(-\tau_b/sin(h)^b) \tag{7}$$

I_0 is the extraterrestrial solar radiation (1367 W/m^2)
H is the solar elevation (rad)

The coefficient b is given by the following expression:

$$b = b_1 ln(w) + b_0$$

where
w is the water vapor column

$$b_1 = 0.00925.aod_{700}^2 + 0.0148.aod_{700} - 0.0172$$

$$b_0 = -0.7565.aod_{700}^2 + 0.5057.aod_{700} + 0.4557$$

The coefficient τ_b is computed as follows:

$$\tau_b = t_{b1}.aod_{700} + t_{b0} + t_{bp} \cdot ln(p/p_0)$$

where

$$t_{b1} = 1.82 + 0.056 \cdot \ln(w) + 0.0071 \cdot \ln^2(w)$$

$$t_{b0} = 0.33 + 0.045\ln(w) + 0.0096 + \ln^2(w)$$

$$t_{bp} = 0.0089.w + 0.13$$

P   is the air pressure

p_0 is the standard air pressure

aod_{700} is the aerosol optical depth for the 700 nm electromagnetic wave length.

However, it is not recommended to predict the DNI for low intensity of DNI (sun is close to the horizon) using clear sky models even after applying corrections. This could be caused by the fact that during this period of the day (sunrise or sunset), the air mass (path of the sunlight through the atmosphere) is relatively high, so the effect of the atmospheric parameter such as aod and/or w on the direct solar radiation is more important and hence more uncertain.

Therefore, in order to effectively estimate the low DNI intensity, it is not recommended to use low-quality input parameters such as average values of aerosol optical depth and water vapor column, etc.

5 Conclusion

In this paper, we have conducted a sub-hourly performance analysis study of three DNI clear sky models. It consists of validating and calibrating these models using the in situ measurements. The purpose is to find the best predicting model that offers the highest accuracy of prediction when it uses low-quality atmospheric input parameters.

The first conclusion is that all the DNI clear sky models perform very well when the DNI is at high intensity (DNI $\geq$ 700 W/m^2). However, when the sun is close to the horizon (low DNI intensity), it is not suitable to compute the DNI using a clear sky model with low-quality input parameter.

The second conclusion is that even after improving the clear sky model's accuracy by applying linear correction and calibration; the uncertainty of low DNI prediction persists relatively high. Therefore, in order to achieve a good accuracy of low-intensity DNI prediction, it is advisable to use good quality atmospheric input parameters before applying any calibration or correction of the clear sky models.

References

Journal Article

Atwater MA, Ball JT (1976) Comparison of radiation computations using observed and estimated precipitable water. J Appl Meteorol 15:1319–1320

Engerer NA, Mills FP (2015) Validating nine clear sky radiation models in Australia. Sol Energy 120:9–24

Ineichen P (2006) Comparison of eight clear sky broadband models against 16 independent data banks. Sol Energy 80:468–478

Ineichen P (2008) A broadband simplified version of the Solis clear sky model. Sol Energy 82:758–762

Ineichen P (2016) Validation of models that estimate the clear sky global and beam solar irradiance. Sol Energy 132:332–344

Ineichen P, Perez R (2002) A new airmass independent formulation for the Linke turbidity coefficient. Sol Energy 73(3):151–157

Inman RH, Pedro HT, Coimbra CF (2013) Solar forecasting methods for renewable energy integration. Prog Energy Combust Sci 39(6):535–576

Kasten F (1965) A new table and approximation formula for the relative optial air mass. Archiv für Meteorologie, Geophysik und Bioklimatologie, Serie B 14(2):206–223

Mieslinger F, Ament K, Chhatbar K, Meyer R (2014) A new method for fusion of measured and model-derived solar radiation time series. Energy Procedia 48:1617–1626

Wong LT, Chow WK (2001) Solar radiation model. Appl Energy 69(3):191–224

Online Document (no DOI available)

Beyer HG, Martinez JP, Suri M, Torres JL, Lorenz E, Müller SC, Hoyer-Klick C, Ineichen P (2009) Management and exploitation of solar resource knowledge: ca contract no. 038665—D 11.3.2009 report on benchmarking of radiation products. http://www.mesor.org/docs/MESoR_Benchmarking_of_radiation_products.pdf (accessed 01 Jan 2017)

Gueymard C, Wilcox S (2009) Spatial and temporal variability in the solar resource: assessing the value of short-term measurements at potential solar power plant sites. In solar 2009 conference proceedings. May 11–16, Buffalo, New York, Boulder, CO: ASES

NASA (2016). http://giovanni.sci.gsfc.nasa.gov/giovanni (accessed 01 Jan 2017)

Sengupta M, Habte A, kurtz S, Dobos A, Wilbert S, Lorenz E, Stoffel T, Renné D, Myers D, Wilcox S, Blanc P, Perez R (2015) Best practices handbook for the collection and use of solar resource data for solar energy applications. Technical report NREL/TP-5DT (accessed 01 Jan 2017)

Soda (2016). http://www.soda-is.com/eng/index.html (accessed 01 Jan 2017)

Collapse Analysis of Longitudinally Cracked HDPE Pipes

M. A. Bouaziz, M. A. Guidara, M. Dallali, C. Schmitt, E. Haj Taieb and Z. Azari

Abstract High-density polyethylene (HDPE) is one of the most widely used materials in fluid transport networks due to its good resistance to wear and corrosion, ease of installation, and low cost. However, HDPE is a flexible material and therefore more vulnerable to scratches and other types of damage during transport and installation. Therefore, accurate prediction of crack initiation pressure in damaged pipes is a very important point in the safety analysis of HDPE piping systems. In this study, a new semi-empirical formulae, which predicts this critical pressure, is developed. The cracking pressure depends on the mechanical characteristics of the material and the geometric parameters (pipe geometry and defect size). A parametric study based on numerical simulations was established in order to quantify the influence of each parameter on the cracking pressure. The pressures calculated by the proposed formulae in a HDPE pipe having a superficial defect are in good agreement with the burst pressure determined experimentally for the same geometry.

Keywords HDPE pipe · Crack initiation pressure · Damaged pipes
Parametric study

M. A. Bouaziz (✉) · M. A. Guidara · M. Dallali · E. H. Taieb
Laboratoire de Mécanique des Fluides Appliqués, Génie des Procédés et Environnement,
Ecole Nationale d'Ingénieurs de Sfax, Université de Sfax, BP 1173, 3038 Sfax, Tunisia
e-mail: mohamedali.bouaziz@gmail.com

M. A. Guidara
e-mail: gem3_guidara@yahoo.fr

M. A. Bouaziz · M.A. Guidara · M. Dallali · C. Schmitt · Z. Azari
Laboratoire de Biomécanique, Polymères et Structures (LaBPS), Ecole Nationale
d'Ingénieurs de Metz, 57070 Metz, France

559

1   Introduction

The preoccupation of pipe network operators is to avoid breaks that pose a potential threat because of their economic and social impact. In addition, repairing defects and premature pipe's replacement entails considerable financial losses. Therefore, the residual strength evaluation of pipes with defects should be as accurate as possible and based on confirmed experimental and numerical methods. Over the past 40 years, such an analysis has been based on so-called empirical formulas developed by the Battelle Memorial Institute (BMI). These formulas are used in the calculation procedures of almost all normative documents in different industries. Many studies have been performed on cracked metal pipes based on burst test results or finite element analysis results (A. N. S. Institute 1991; Miller 1988; Staat 2004, 2005; Kiefner et al. 1973). Some methods of estimating the critical dimensions of cracks have been developed from the flow limit or elastic limit or from the combination of the yield strength and the tensile strength such as Kiefner et al. (1973) and Staat (2004). However for polymeric materials, the existing models are not sufficient hence the need to make improvements. In this context, we propose a simplified formulation to determine the crack initiation pressure in a high-density polyethylene pipe with a surface defect. This critical pressure depends essentially on the geometric parameters, including the geometry of the pipe and the default size. A parametric study is carried out based on numerical results from a finite element calculation campaign. The numerically calculated fracture pressures and those given by the proposed formulation will be compared to experimentally determined bursting pressures (Guidara et al. 2015).

2   Methodology

In this study, the crack initiation pressure is defined as the minimum loading level involving the initiation of the crack. This condition is verified when the integral J, computed numerically in the vicinity of a preexisting defect, exceeds the value of the resistance to cracking J_{Ic} (toughness). On the one hand, the cracks initiation pressure depends on the material's mechanical characteristics (law of behavior and toughness) and on the other hand it is strongly linked to the geometrical parameters, in particular the pipe geometry and the size of the defect. The studied material is HDPE PE100 used for drinking water supply (Bouaziz et al. 2015). Therefore, based on the characterization carried out on this material, the study focuses on geometrical parameters (Ben Amara et al. 2015).

The pipes fracture under pure pressure loads is analyzed generally by applying the formula allowing to calculate the main stress as a function of the geometrical parameters of the structure. In the case of a cylindrical pipe free of any defect charged only under internal pressure, this equation is

$$\sigma_{\theta\theta} = \frac{pr_i}{e} \tag{1}$$

This formulation is valid only for thin-walled pipes. In general, thick-walled pipes are characterized by a wall thickness that exceeds 1/20 of the pipe diameter. In this case, the circumferential stress is calculated according to the Lamé equations (Westergaard 1952; Eringen 1967; Timoshenko and Goodier 1970).

$$\sigma_{\theta\theta} = \frac{r_i^2 p}{r_e^2 - r_i^2} \left(1 + \frac{r_e^2}{r^2} \right) \tag{2}$$

In this study, the crack initiation pressure in a flawless pipe is deduced from Eq. (2). The crack is initiated when the hoop stress on the mean radius $(r = (r_i + r_e)/2)$ reaches the material elastic limit. Flawless HDPE pipe cracking pressure is

$$p_{Max} = \sigma_y \frac{\frac{r_e^2}{r_i^2} - 1}{1 + \frac{4r_e^2}{(r_e + r_i)^2}} \tag{3}$$

This formulation is limited to flawless pipes. A defect in the wall of the pipe causes a change in the stress state. Locally high stress concentration occurs in the vicinity of the defect. The presence of a defect makes the formulation of the distribution of constraints complex, hence the use of numerical resolution methods, in particular the finite element method (FEM). This method requires a developed expertise and a long characterization process. For these reasons, charts and pre-defined formulas are widely preferred by designers and operators. In this context, we establish a new formulation allowing to define the critical pressure as a function of the tube geometry as well as the size of the preexisting defect in the structure.

3 Formulation

The pipe geometry is characterized through "r_i", "r_e" and "e" the internal and external radius and the wall thickness, respectively. The defect size is characterized by crack depth "a" and crack length "c" as shown in Fig. 1.

The first step of this study is devoted to the influence of the size of the defect on the priming pressure. For this purpose, only one pipe geometry is considered: 125 mm outside diameter and 12 mm thickness. The crack initiation pressure for a longitudinal defect on the outer surface (Fig. 1) is calculated numerically for five defect lengths (35, 50, 100, 125, and 250 mm). For each crack length, the depth was varied between 2 mm and 10 mm. Twenty-seven numerical simulations were performed to represent the cracking pressure variation as a function of the defect depth and length, Fig. 2. Finite element simulation was performed using the
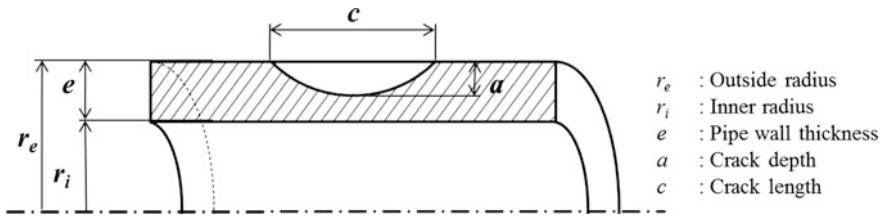
Fig. 1 Pipe with longitudinal defect
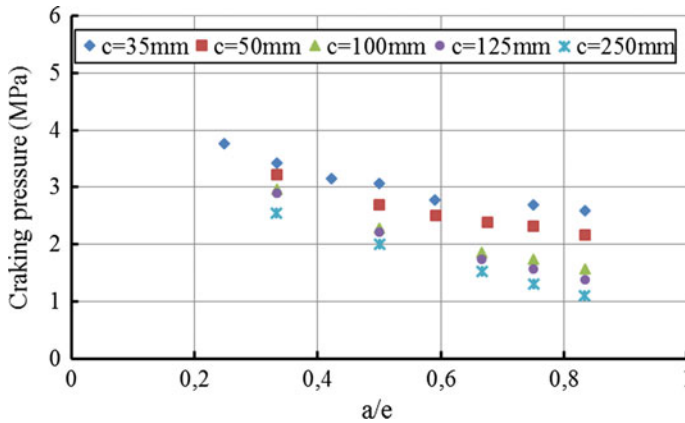
Fig. 2 Variation of the cracking pressure as a function of the ratio a/e

ABAQUS (FEA). Cracked pipes were modeled as a 20 mm closed ends pipe. Symmetric conditions were fully used. Only a quarter of the model was studied in order to reduce the computation time. The specimen was loaded with an internal pressure uniformly distributed over the entire inner surface of the model. The quarter of the specimens were meshed by HyperMesh using C3D20 which is a second order element consisting of 20 nodes. The numerically calculated cracking pressure is plotted as a function of the ratio of the defect depth to the pipe wall thickness "a/e".

For a constant defect length (c fixed), we find that the priming pressure decreases with the increase of the depth of the crack and also decreases with the increase of the length of the defect, "c". This result is entirely consistent with the literature (Benhamena et al. 2010, 2011). The cracking pressure converges to a single value which is the crack initiation pressure in a crack-less pipe (Eq. (3)).

The cracking pressure as a function of "a/e" is expressed using the function $f(x) = A(1 - \beta\sqrt{x})$. The calculated numerical values can be interpolated with the following function:

$$p_{cracking}(a/e) = A(1 - \beta\sqrt{a/e}), \tag{4}$$

where A and β are interpolation parameters and $(\beta \geq 0)$.

When a/e tends to zero, the pipe is assumed to be perfect and has no defect. The priming pressure p_{Max} is calculated by the Eq. (3)

$$\lim_{a/e \to 0} \left(p_{amorçage}(a/e) \right) = A = p_{Max} \tag{5}$$

The interpolations of the numerical points are shown in Fig. 3. The coefficient β is determined for the different studied defect lengths. The coefficients of determination R^2 for the interpolation functions are satisfactory, and are very close to 1.

The β value depends on the defect length "c". Therefore, it shows the effect of "c" on the approximation function of the cracking pressure (3). Table 1 and Fig. 4 shows calculated β coefficients for the five studied defect lengths. A large variation is observed when "c" is less than the pipe diameter, in contrast to the relatively long cracks where the coefficient β continues to increase gradually to near 1, for extremely high "c" values. Based on this finding, it is assumed that in the case of relatively long cracks the effect of crack length becomes minor in comparison with depth's one. For this reason, we limit our study to cracks whose length does not exceed twice the diameter of the pipe. In the following, the defect length "a" will be associated to the outer pipe radius "r_i" and will be introduced in the approximation of the priming pressure function by the dimensionless term "$c/4r_i$".

In Fig. 5, the variation of β as a function of $(c/4r_i)$ is interpolated by the function $f(x) = 1/\sqrt{1 + \alpha/x}$; Where α is an interpolation coefficient. The best interpolation for the numerical points gives a value of $\alpha = 0.31$ for a coefficient of determination $R^2 = 0.992$.
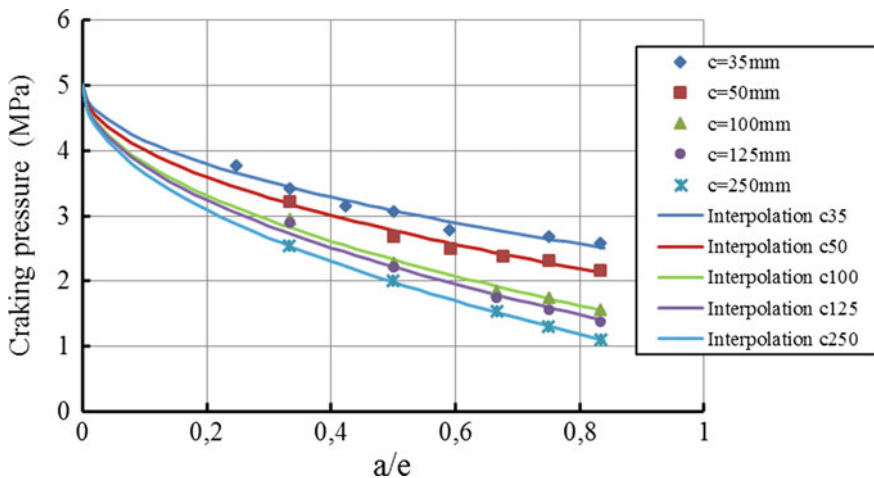
Fig. 3 Interpolation of numerical results

c (mm)	35	50	100	125	250
β	0.546	0.629	0.754	0.786	0.853
R^2	0.987	0.995	0.997	0.997	1

Table 1 Interpolation coefficient β as a function of c
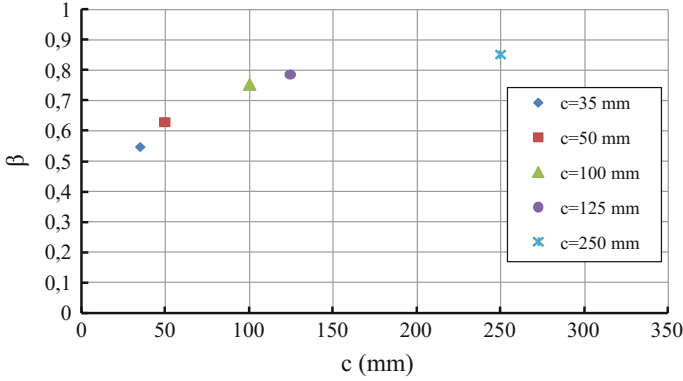
Fig. 4 β variation as a function of the length of the defect
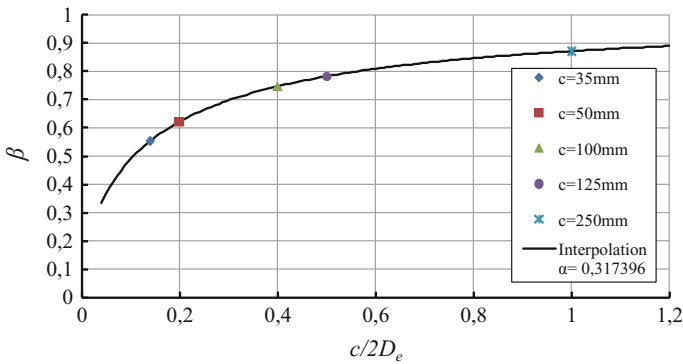
Fig. 5 Interpolation of β variation as a function of $(c/4r_e)$

Thus β is written as follows:

$$\beta(c/4r_e) = \frac{1}{\sqrt{1 + \frac{0.31}{c/4r_e}}} \tag{4}$$

We propose a new formulae which gives the crack initiation pressure of an existing crack on the outer wall of a HDPE PE100 pipe. This pressure is also considered as the maximum allowable pressure. The model takes into account the geometry of the pipe and the defect size in addition to the material properties.

$$p_{cracking}(a, c, r_e, e) = p_{Max}\left(1 - \sqrt{\frac{a/e}{1 + \frac{0.31}{c/4r_e}}}\right) \qquad (6)$$

This developed formulation is based on a numerical study involving only one pipe diameter. It is therefore necessary to check the validity of this equation for other diameters.

4 Validation

In this part of the parametric study, we are interested in the effect of the pipe geometry (diameter) on the cracking initiation pressure of an already existing longitudinal crack on its external wall. The ratio of thickness to defect depth was set to 0.5 ($a/e = 0.5$) and we studied three lengths of defects ($c = 50$ mm, $c = 125$ mm, and $c = 250$ mm). The numerically calculated cracking pressures for the six treated diameters are shown in Fig. 6.

We interpolate the numerical results for the different values of "c" with the function of Eq. (7) by fixing "a" and "c" and tacking the diameter of the pipe as a unique variable.

$$p_{cracking}(a, c, r_i, r_e, e) = \sigma_y \frac{\frac{r_e^2}{r_i^2} - 1}{1 + \frac{4r_e^2}{(r_e + r_i)^2}}\left(1 - \sqrt{\frac{a/e}{1 + \frac{\alpha}{c/4r_e}}}\right), \qquad (7)$$

where "α" is the interpolation coefficient.

It is noted that the developed model gives a fairly accurate approximation of the cracking pressure with a slight variation in the interpolation coefficient, Fig. 7.
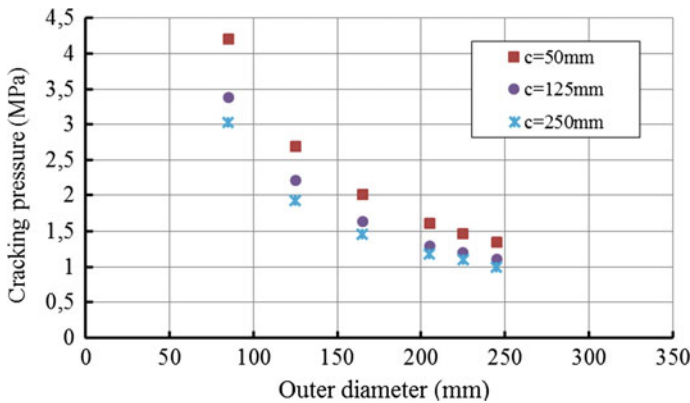
Fig. 6 Effect of pipe's diameter on cracking pressure
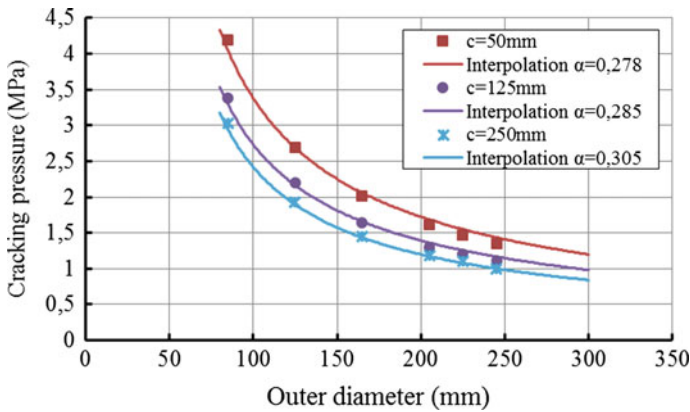
Fig. 7 Cracking pressure variation interpolation as a function of diameter

Indeed, "α" slightly varies from 0.278 to 0.305, without major effect on the approximation function of the cracking pressure.

Now coefficient "α" previously calculated can be corrected thanks to the three new values. An average of the fourth value of "0.3" is retained. The final equation estimating the maximum inside pressure for a PE100 pipe with a surface crack can be written as follows:

$$p_{cracking}(a, c, r_i, r_e, e) = \sigma_y \frac{\frac{r_e^2}{r_i^2} - 1}{1 + \frac{4r_e^2}{(r_e + r_i)^2}} \left(1 - \sqrt{\frac{a/e}{1 + \frac{0.3}{c/4r_e}}}\right) \quad (8)$$

5 Comparison with Burst Tests

The cracking pressures given by the developed formula will be compared to the experimentally determined burst pressures. The burst tests were performed on pipes HDPE PE100 with superficial defect in the pipe axial direction (Guidara et al. 2015). The experimental test was reproduced numerically by using the EF model to calculate the cracking pressure, while maintaining the same test conditions (pipe size, size, and position of the defect, loading speed, boundary conditions). The studied geometry is a pipe with an outside diameter of 125 mm and a thickness of 12 mm containing a longitudinal defect on its outer surface of length "c" and depth "a". Different sizes of the defect are treated (Table 2). The crack initiation pressures determined numerically and those given by the proposed formula as well as the experimentally determined burst pressures are summarized in Table 2 and shown in Fig. 8.

Table 2 Burst pressure versus crack initiation pressure

a (mm)	2	4	6	8	10
a/e	0.167	0.333	0.5	0.667	0.833
c (mm)	25	34.87	42.14	48	52.91
$P_{bursting}$ (MPa) experimental	[5.36; 5.11]	[4.58; 4.84; 4.81]	[4.25; 4.03; 4.1]	[3.52; 3.59; 3.58]	[3.11]
$P_{cracking}$ (MPa) formula	3.9	3.417	2.8	2.4	2.167
$P_{cracking}$ (MPa) numerical	3.98	3.37	2.88	2.45	2.06
Δ_1 (%)	2	1.25	2.83	2.07	4.72
Δ_2 (%)	25.88	28.02	32.24	32.73	30.43
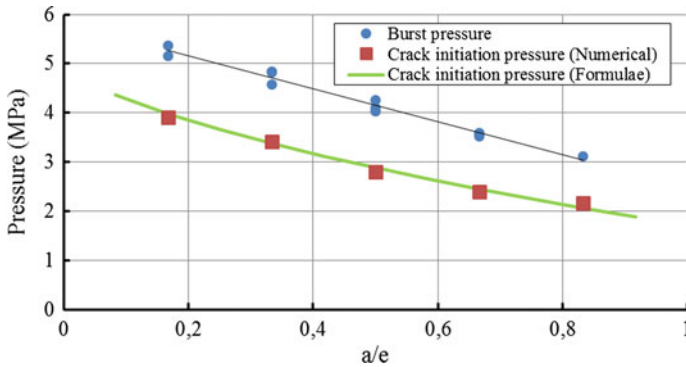
Fig. 8 Comparison between burst pressure and crack initiation pressure

The values given by the formula are in good agreement with the numerically calculated cracking pressure with an error Δ_1 which does not exceed 5%. The cracking initiation pressures are lower than the burst pressures with an offset Δ_2 varying between 25 and 33%.

6 Conclusion

In the present study, a new simplified formulae is proposed to estimate the crack initiation pressure in a PE100 PEHD pipe with a surface defect. The cracking pressure is the minimum loading level involving the initiation of the crack. It depends on the material mechanical characteristics and the geometrical parameters (pipe geometry and size of the defect). The pressures given by the proposed formula are in perfect agreement with numerically calculated priming pressure values. The

cracking pressures are less than the burst pressures with a slightly variable offset. This offset comes from the crack propagation phase. Indeed, the initiation of the crack is followed by a propagation phase of the crack on the ligament remaining until the total bursting. The advantage of the proposed formula lies in its simplicity since its application requires only knowledge of the elasticity limit of the material and the geometrical parameters of the pipe and the size of the defect.

References

A. N. S. Institute (1991) Manual for determining the remaining strength of corroded pipelines: a supplement to ASME B31 code for pressure piping

Ben Amara M, Pluvinage G, Capelle J, Azari Z (2015) Crack tip opening angle as a fracture resistance parameter to describe ductile crack extension and arrest in steel pipes under service pressure. Phys Mesomech 18(4):355–369

Benhamena A, Bouiadjra B, Amrouche A, Mesmacque G, Benseddiq N, Benguediab M (2010) Three finite element analysis of semi-elliptical crack in high density poly-ethylene pipe subjected to internal pressure. Mater Des 31(6):3038–3043

Benhamena A, Aminallah L, Bouiadjra B, Benguediab M, Amrouche A, Benseddiq N (2011) J integral solution for semi-elliptical surface crack in high density poly-ethylene pipe under bending. Mater Des 32(5):2561–2569

Bouaziz MA, Guidara MA, Schmitt C (2015) Failure analysis of HDPE pipe for drinking water distribution and transmission. Design and modeling of mechanical systems—II, pp 407–414. In: Proceedings of the sixth conference on design and modeling of mechanical systems, CMSM'2015, March 23–25, Hammamet, Tunisia

Eringen W (1967) Mechanics of continua. Wiley, New York

Guidara MA, Bouaziz MA, Schmitt C, Capelle J, Haj Taïeb E, Azari Z, Hariri S (2015) Structural integrity assessment of defected high density poly-ethylene pipe: Burst test and finite element analysis based on J-integral criterion. EFA 57:282–295

Kiefner J, Maxey W, Eiber R, Duffy A (1973) Failure stress levels of flaws in pressurized cylinders. In: ASTM STP, vol 536, Philadelphia, pp 461–481

Miller A (1988) Review of limit loads of structures containing defects. Int J Press Vessel Pip

Staat M (2004) Plastic collapse analysis of longitudinally flawed pipes and vessels. Nucl Eng Des

Staat M (2005) Local and global collapse pressure of longitudinally flawed pipes and cylindrical vessels. Int J Press Vessel Pip

Timoshenko S, Goodier J (1970) Theory of elasticity. New York

Westergaard H (1952) Theory of elasticity and plasticity

Cutting Modeling of Ti6Al4V Alloy When Using a TiAlN-Coated Insert

Kallel Cherif Mouna and Bouaziz Zoubeir

Abstract A better understanding of coating is required to increase productivity and tool life in especially dry cutting conditions of difficult to cut materials. In this work, in order to evaluate the performance of coated TiAlN cutting tool during orthogonal cutting of Titanium Ti6Al4V alloys, a 2D finite element modeling using the commercial code ABAQUS/Explicit is developed. Lagrangian approach has been adopted. Different cutting conditions have been defined, cutting tool geometry (coated TiAlN et uncoated tool) has been changed in the order to validate numerical model results. An acceptable correlation between numerical results and those of the literature is obtained in terms of chip morphology, cutting forces, feed forces, and temperature distribution. Numerical results have highlighted the effect of coated TiAlN tool on temperature distribution at tool-chip-workpiece interfaces, on chip morphology and its geometry, as well as cutting and feed forces. We can conclude that the FEM employed in this study gives significant information about tool coating effects on machining difficult to cut materials.

Keywords Numerical model · Coated TiAlN tool · Cutting · Ti6Al4V

1 Introduction

In recent years, the demand of titanium alloys especially Ti6Al4V alloy has increased in automotive, aerospace sector because of their excellent properties such as high strength to weight ratio, low density, high toughness, and good corrosion resistance. Also, the demand has increased for biomedical equipment due to his excellent bio-compatibility (Cottrell and Byrne 2008). However, this alloy exhibit

K. C. Mouna (✉) · B. Zoubeir
Applied Fluid Mechanics, Process Engineering Environment,
National Engineering School of Sfax, Sfax University, BP 1173, 338 Sfax, Tunisia
e-mail: mounacherif1124@gmail.com

B. Zoubeir
e-mail: zoubeir.bouaziz@enis.rnu.tn

serrated chip formation and is deemed to be difficult to cut for several reasons such as: (i) low conductivity (ii) high chemical reactivity with cutting tool materials at elevated temperatures (iii) low elasticity modulus (iv) work hardening. So, at the tool-chip-workpiece interfaces, the cutting tool is exposed to several thermo-mechanical phenomena and tribological conditions, producing intense dynamic friction, chemical reaction, and high cutting temperature, leading up to an accelerated tool wear (Attanasio et al. 2010).

To increase productivity of Ti6Al4V alloy and to improve machined surface quality, it is necessary to increase the cutting speed which affects drastically the tool wear in the case of dry orthogonal cutting of difficult to cut materials. To overcome this problem, it is mandatory to improve cutting tool materials, especially coatings (Bouzakis et al. 2009). Indeed, coatings can act as a protective layer and thermal barrier (Kone et al 2011; Krajinovic et al 2016).

Many researchers (Kone et al 2011; Krajinovic et al 2016) have been reported in their work, that using coated cutting tools in machining can affect the temperature distribution at chip-tool-workpiece interfaces, which strongly impact of chip formation process, surface integrity of machined surface and tool wear. For more understanding, the behavior of coatings is important to study their impact during cutting process and their use in optimal conditions. For this purpose, many researchers focused on developing numerical models to simulate orthogonal cutting process. These approaches applied essentially to the Finite Element Method (FEM) and help to predict many important information which are difficult to gather experimentally such as plastic strain, strain rate, stress, and temperature distribution at tool-workpiece contact. In fact, those approaches are used to reduce the number of experimental tests which being still costly and time consuming. However, modeling cutting process is usually a complex task because the large elasto-visco-plastic deformation, the diversity of the thermo-physical phenomena and the severe tribological conditions involved.

The aim of this study is to compare between the TiAlN-coated tool and the uncoated tungsten carbide tool inserts performance during dry turning conditions of the Ti6Al4V alloy. A FE model is developed is this work and validated in terms of chip morphology, cutting, and feed forces by comparison with experimental results obtained thanks to works of authors in the literature. Different cutting conditions have been defined, cutting tool geometry has been changed in the order to validate numerical model results.

2   Finite Element Model

Recently, several researchers had a great interest to use a 2D finite element model in the case of orthogonal cutting, because is easier to simulate as well as this can be adequate. So, to construct the 2D FE model in orthogonal cutting of Ti6Al4V alloy, especially in dry conditions, a Lagrangian formulation with Explicit integration scheme is adopted using the commercial code ABAQUS version 6.10. A plane
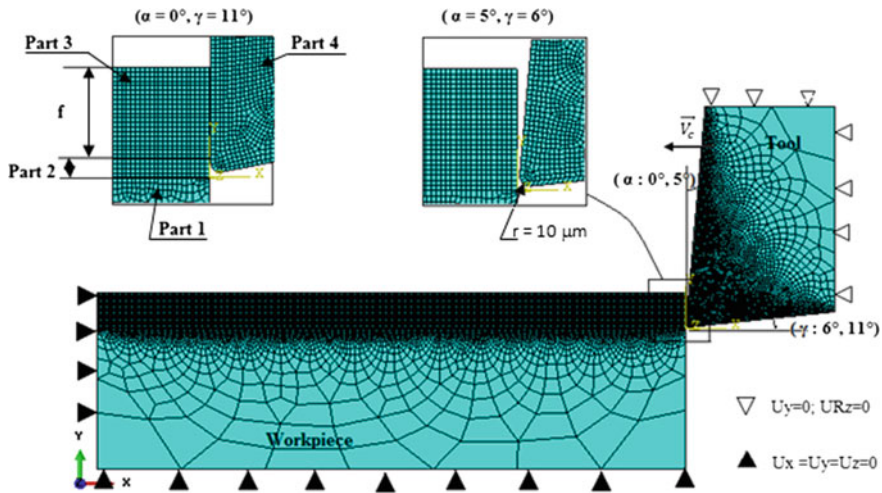
Fig. 1 Initial geometries, mesh and boundary conditions of the model

strain condition in assumed and a coupled temperature-displacement analysis is developed by using quadrilateral four-node elements type CPE4RT with reduced integration. In addition, "relax stiffness" is integrated in element type to minimize the hourglass treatment approach and reduce its effects for gathering physical results (Barge 2005; Mabrouki et al 2016).

The initial geometries, mesh, and boundary conditions of workpiece and cutting tools are shown in (Fig. 1). The geometric model follows the multipart model proposed by (Mabrouki et al 2008). This model compromised four geometrical parts: (Part 1) is the remaining area of workpiece after cutting, (Part 2) is the material separation band, (Part 3) represents the zone of workpiece will transferred as chip during cutting. And finally, (Part 4) is the tool. Two cutting tool geometry has been used: for uncoated carbide tool (WC/Co) the edge radius is 5 μm, while for TiAlN-coated carbide tool, the edge radius is 10 μm and thickness of coating layer is 5 μm. The workpiece is fixed while the cutting speed is applied to the cutting tool during turning process. A minimum element size 5μm is considered both in the chip (Part 3) and separation zone (Part 2).

The thermo-visco-plastic Johnson–Cook constitutive law (Johnson and Cook 1983) is the most popular model adopted in cutting process. This model is widely used to describe the material behavior which their flow stress is highly influenced by temperature and high strain rate. In fact, this law describes the equivalent plastic flow stress of material with strain, strain rate, and temperature by the following expression (1):

$$\bar{\sigma} = \underbrace{\left[A + B.\bar{\varepsilon}^n\right]}_{Elasto-plastic} \underbrace{\left[1 + C.\ln\left(\frac{\dot{\bar{\varepsilon}}}{\dot{\bar{\varepsilon}}_0}\right)\right]}_{Viscosity} \underbrace{\left[1 - \left(\frac{T - T_0}{T_m - T_0}\right)^m\right]}_{Softening}, \qquad (1)$$

where $\bar{\sigma}$ is the equivalent flow stress (MPa), A, B, C, m and n are material constants parameters, $\bar{\varepsilon}$ is the equivalent plastic strain, $\dot{\bar{\varepsilon}}$ is the equivalent plastic strain rate (s^{-1}), $\dot{\bar{\varepsilon}}_0$ is the reference equivalent plastic strain rate (s^{-1}), T, T_0 and T_m are, respectively, the workpiece temperature (°C), the reference absolute temperature (°C) and the melting temperature (°C).

In order to model the chip segmentation in orthogonal cutting, a damage-based model (Johnson and Cook 1985) was used and coupled to the thermo-visco-plastic JC law(1). This damage model takes into account the sensitivity to strain rate, temperature and stress triaxiality. It includes a damage initialization criterion and a damage propagation. In current work, the workpiece material is assumed to be homogenous during cutting its behavior is described by the J-C constitutive law (1) and J-C ductile fracture law. The tool material behavior law must take into consideration physical and thermal aspects that may occur during cutting process. For that, the substrate of the tool and TiAlN coating are considered deformable and modeled by an elastic law. The mechanical and thermal material properties of Titanium Ti6Al4V, WC/Co and TiAlN coating are taken from (Zhang et al. 2011; Sima and Ozel 2010). The set of J-C parameters used for simulation is given by Seo et al. (2005) and Wang and Shi et al. (2013).

It should be noticed that the simple Coulomb friction model was used in the current work which has been widely used in cutting simulation (Calamaz et al. 2008; Zhang et al 2015). The assumed friction coefficient value used in all FE calculations is 0.15. The thermal conductance at chip-tool-workpiece interfaces was kept as a constant value of 46000 W/m²K (Zhang et al. 2011).

3   Results and Discussion

This section provides a FE validation by comparison with experimental results obtained thanks to works of (Sima et Ozel 2010) and FE analysis of chip morphology, cutting forces, and temperature distribution on tool rake face as well as inside of the cutting tool for different cutting conditions and different tool materials and geometries.

3.1 Chip Morphology Analysis

The captured chip images and predicted chip morphology are show in (Table 1). Generally, there is a quite correlation. Serrated chip were observed throughout all investigations of numerical simulation.

Table 2 reports a comparison between geometric results achieved by both numerical and experimental chips for various cutting conditions when h_1 is the average minimum serrated chip thickness, h_2 is the average maximum serrated chip thickness and p_t is the pitch between two successive chip segment crests. The degree of serration decreases while pitch of serrated chips increases with decreasing cutting speed and increasing uncut chip thickness and decreasing tool rake angle.

3.2 Forces Analysis

The measured forces obtained thanks to the work (Sima and Ozel 2010), and the predicted forces are reported in (Fig. 2). For both inserts of material tools (Uncoated WC/C0 and TiAlN-coated WC/C0), cutting forces increases with increasing uncut chip thickness or decreasing rake angle and decreased with increasing cutting speed and increasing rake angle. It is reported in literature that cutting forces is usually affected by the tribological conditions at the tool-chip contact. In fact, at higher cutting speed, the temperature increases at the chip-tool interface and tends to thermal softening of titanium Ti6Al4V leading to decrease in cutting forces. The correlation between cutting tool geometry and temperatures distribution is highlighted in the follow subsection.

3.3 Temperature Analysis

This part is focused on the temperature analysis of the tool rake face surface and in the interior of the cutting tool. Regarding the evolution of temperature fields into the both geometries of the cutting tool reported in (Table 3), the highest temperatures are calculated at the chip-tool rake face contact. while inside the tool, temperature decreases towards the interior. A comparison between two different materials of the tool shows that the predicted temperature at the tool rake face surface are highest for the TiAlN-coated tool, similar to finding of several researchers (Grzesik and Nieslony 2004; Grzesik et al 2005; Kone et al 2011; Krajinovic et al 2016). The main reason for this is that the TiAlN coating exhibits a lower thermal conductivity than the WC/Co substrate of the tool. As a consequence, the higher temperature fields inside the cutting tool are less wide for the TiAlN-coated tool than for the uncoated tool. A higher thermal conductivity of the WC/Co substrate helps the heat energy at tool-chip contact to transmit and entering the tool.

Table 1 The comparison of chip morphology between simulated serrated chip and chips images (Sima et Ozel 2010) for different cutting conditions
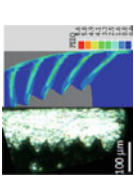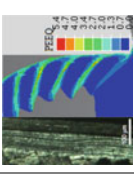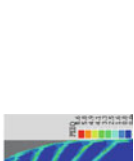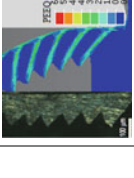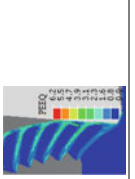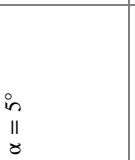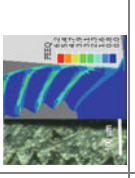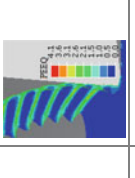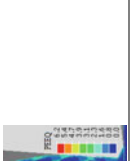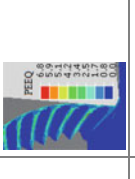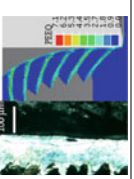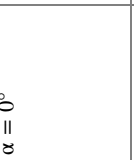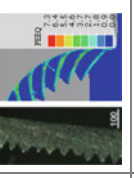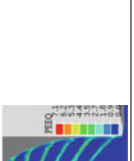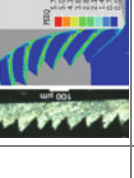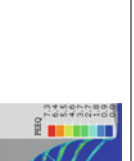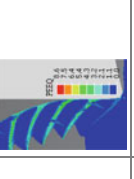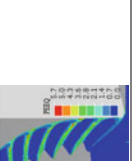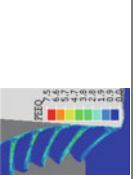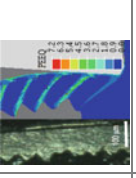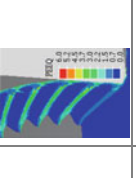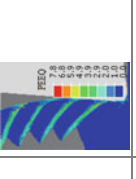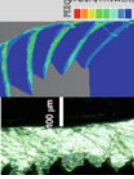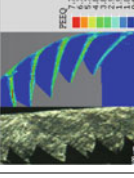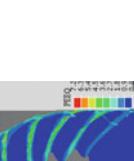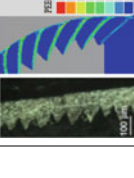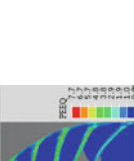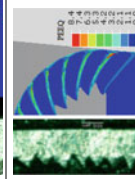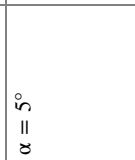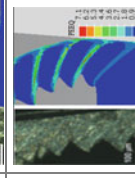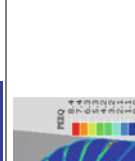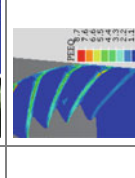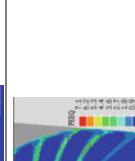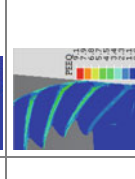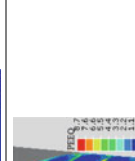
Table 2 Comparison between experimental chip thickness (Sima and ozel 2010) and numerical predicted

Rake angle	Cutting tool	Vc m/min	Feed	Experimental			Simulation		
				h_1	h_2	p_t	h_1	h_2	p_t
$\alpha = 0°$	Uncoated WC/Co	121.9	0.076	0.095	0.133	0.05	0.085	0.102	0.031
			0.1	0.13	0.192	0.07	0.11	0.158	0.068
			0.127	0.104	0.177	0.09	0.121	0.162	0.07
		240.8	0.1	0.087	0.16	0.08	0.094	0.142	0.059
			0.127	0.102	0.186	0.095	0.104	0.166	0.079
	TiAlN-coated	121.9	0.1	0.137	0.182	0.075	0.095	0.138	0.056
			0.127	0.14	0.216	0.1	0.121	0.176	0.068
$\alpha = 5°$	Uncoated WC/Co	121.9	0.127	0.156	0.23	0.089	0.124	0.165	0.06
	TiAlN-coated	121.9	0.1	0.102	0.158	0.073	0.101	0.135	0.051
		121.9	0.127	0.12	0.208	0.08	0.126	0.17	0.058

When comparing the numerical results of both material tools summarized in (Table 3), it can be seen that the location as well as the value of the higher temperature evolves during a simulation.

The cause of this, that titanium Ti6Al4V alloy exhibits saw tooth chip (evolution of serrated chip formation of the initiation phase to final phase) causing a discontinuous contact leading to a variation of the contact length. As a consequence, a fluctuation of the temperature occurs at the tool rake face surface as follow in Fig. 3.

The temperature distributions along the cutting tool rake face surface for both materials tool (uncoated WC/Co et TiAlN-coated WC/Co) and at the same cutting conditions (Vc = 240 m/min and feed f = 0.1 mm) are shown in Fig. 3. It is observed that the higher value of temperature is obtained for the TiAlN-coated tool and for zero rake angle.

With respect to time turning simulation, Fig. 4a, b shows temperatures inside the tool along the path starting at point A and finishing at point B. The lowest surface temperature is for the uncoated WC/Co tool while it is highest for TiAlN-coated WC/Co tool with a difference exceed of almost 60°C in the case of rake angle 0° and 120°C in the case of rake angle 5°. For both materials tool and for each cutting conditions, the temperature calculated decreases towards the interior of the cutting tool. The temperature in the TiAlN-coated tool drops significantly at a depth of 5 µm decreases by almost 151°C in the case rake angle 0° and 186°C in the case of rake angle 5°. While the temperature in the uncoated tool at a depth of 5 µm decreases slightly by 17°C for rake angle 0° and 9° for rake angle 5°. The temperatures in the substrate is higher for the uncoated tool than the TiAlN-coated tool
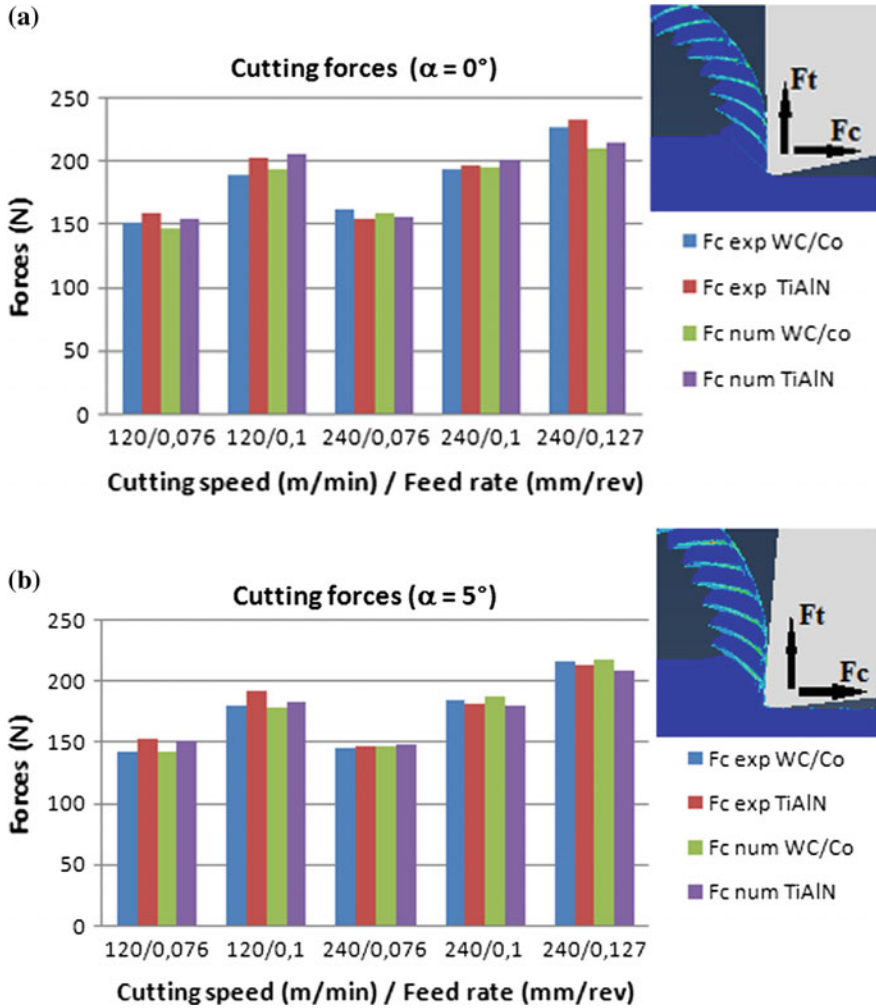
Fig. 2 The comparison of cutting forces during cutting: **a** rake angle 0°, **b** rake angle 5°

beyond 0.002 mm of the tool surface in the case of zero rake angle and beyond 0.0035 mm of the tool surface in the case of 5° rake angle. We can conclude that TiAlN coating with low thermal conductivity plays a role as thermal shield.

Table 3 The comparison between temperature calculated for different tool materials and geometry. Figures shows the evolution of temperature fields inside the cutting tool at the same cutting time for feed rate 0.1 mm and cutting speed Vc = 240 m/min
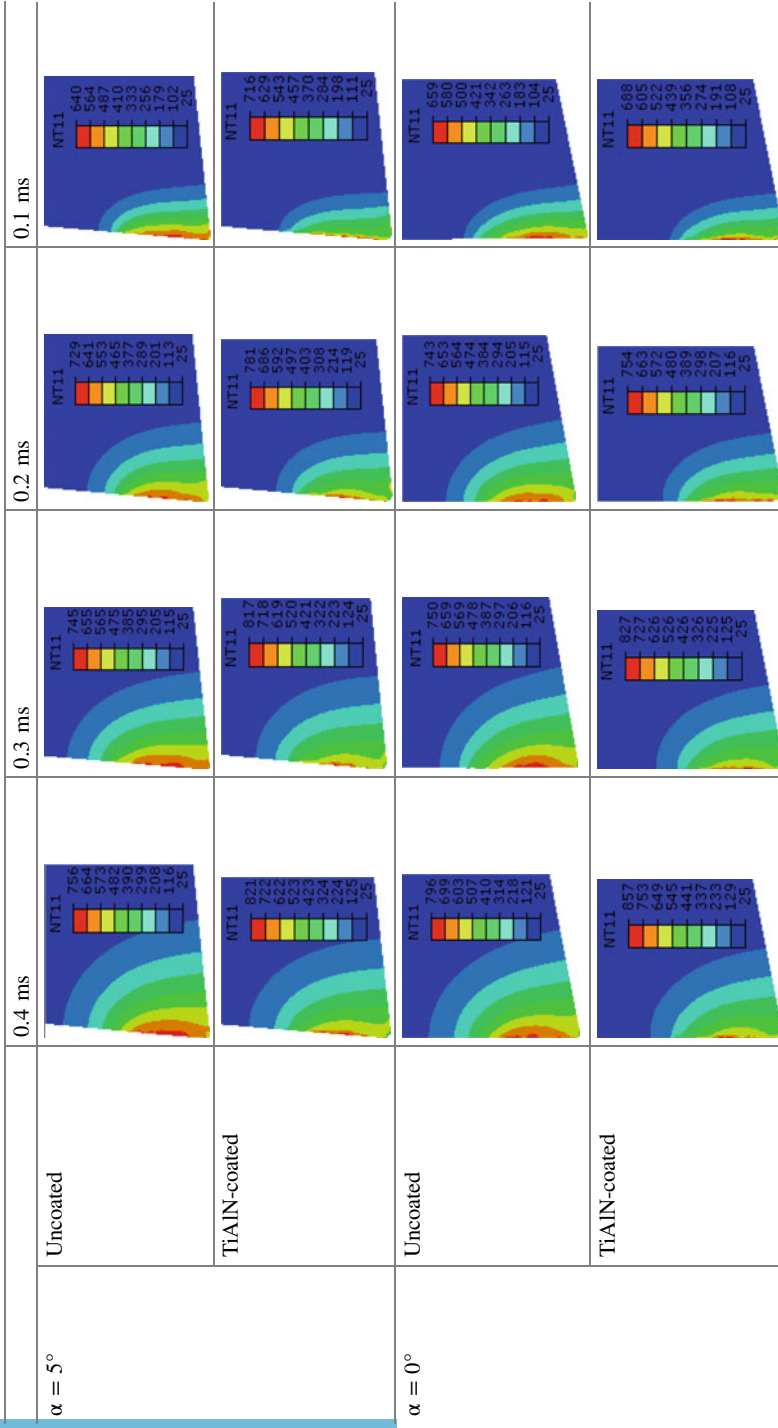
Fig. 3 Temperature
distribution after 0.38 ms of
turning time along the rake
face of the two investigated
material cutting tools: **a** for
rake angle 0° and **b** for rake
angle 5°. Gray lines are the
approximately limits of
contact zone
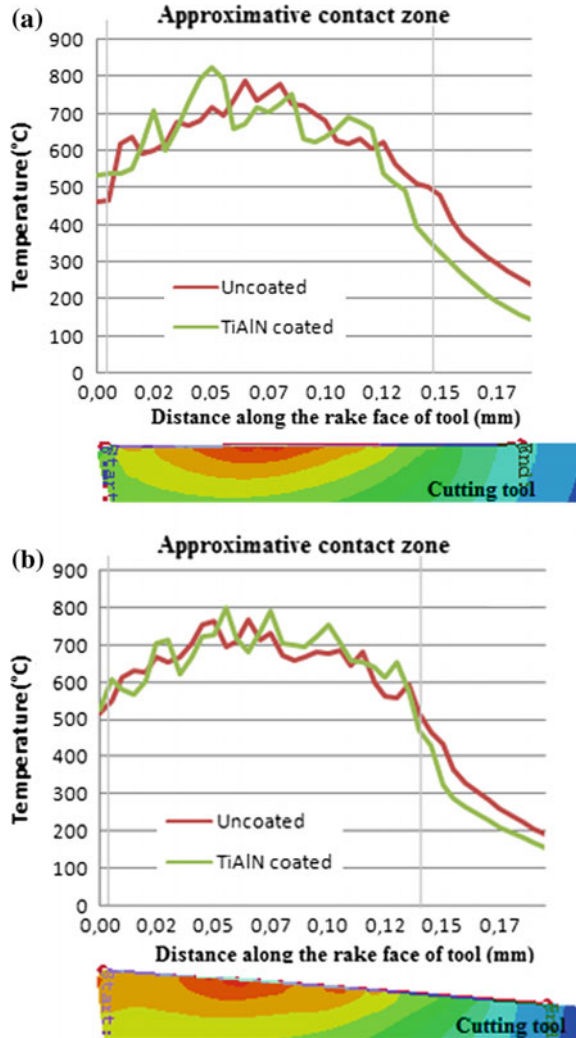
4 Conclusion

In this work, 2D FE Lagrangian turning model for uncoated and TiAlN-coated
cutting tools is presented. This model has highlighted the effect of TiAlN coating on
chip morphology and its geometry, as well as cutting forces. We can conclude that
the FEM employed in this study gives significant informations about tool coating
effects on machining Titanium Ti6Al4V alloy.

Fig. 4 Temperature distribution after 0.38 ms of turning time in the interior of cutting tool for both materials along the path (AB): **a** for rake angle 0° and **b** for rake angle 5°. Gray lines indicate the thickness of the TiAlN coating layer (5 μm)
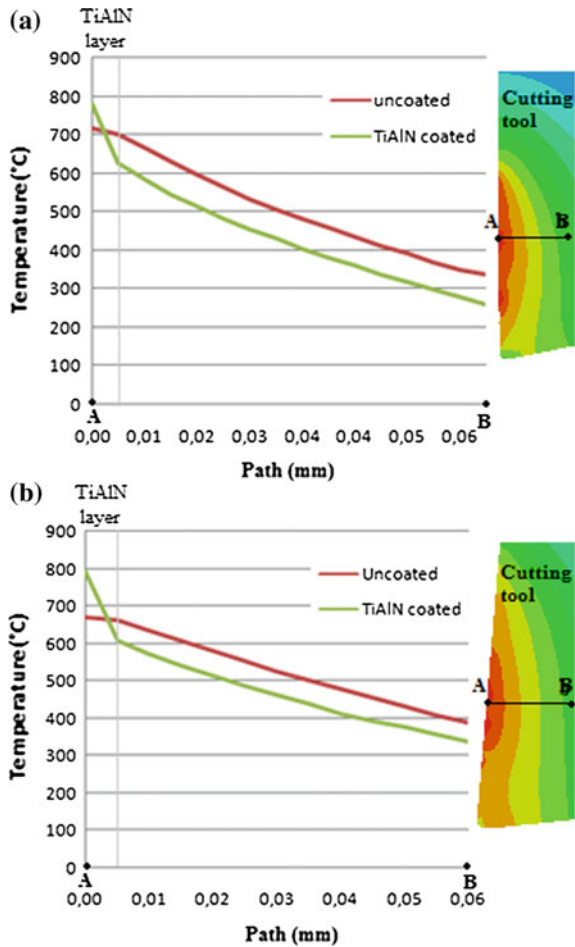
- Coated tool minimized the cutting forces compared to uncoated tool at positive rake angle (α = 5°). The cutting forces increase with increasing uncut chip thickness or decreasing rake angle.
- The temperature distribution along the rake face and inside the tool appear dependent to cutting conditions, tool geometry and material. The temperatures increase as uncut chip thickness increases, or cutting speed increases and decreases as rake angle increases.
- The numerical results show that TiAlN coating serve as thermal barrier. In fact, the temperature calculated in the substrate is reduced.

References

Attanasio A, Ceretti E, Fiorentino A, Cappellini C, Giardini C (2010) Investigation and FEM-based simulation of tool wear in turning operations with uncoated carbide tools. Wear 269:344–350

Barge M, Hamdi H, Rech J, Bergheau J-M (2005) Numerical modelling of orthogonal cutting: influence of numerical parameters. J of Mat Proces Tech 164–165:1148–1153

Bouzakis KD, Skordaris G, Gerardis S, Makrimallakis G, Pappa M, Lill E, M'Saoubi R (2009) Ambient and elevated temperature properties of TiN, TiAlN and TiSiN PVD films and their impact on the cutting performance of coated carbide tools. Surf Coat Technol 204:1061–1065

Calamaz M, Coupard D, Girot F (2008) A new material model for 2D numerical simulation of serrated chip formation when machining titanium alloy Ti6-Al-4V. Int J Mach Tools Manuf 48(3–4):275–288

Cotterell M, Byrne G (2008) Dynamics of chip formation during orthogonal cutting of Titanuim alloy Ti6Al4V. CIRP Ann 57:93–96

Grzesik W, Nieslony P (2004) Physics based modelling of interface temperatures in machining with multilayer coated tools at moderate cutting speed. Int J Mach Tools Manuf 44:889–901

Grzesik W, Bartoszuk M, Nieslony P (2005) Physics based modelling of temperature distribution in the cutting zone in turning process with differently coated tools. J Mater Process Technol 164–165:1204–1211

Johnson G, Cook W (1983) A constitutive model and data for metals subjected to large strains, high strain rates and high temperatures. Procceedings of the Seventh International symposium on Basllistics, the Hague, the Netherlands: 541–547

Johnson G, Cook W (1985) Fracture characteristics of three metals subjected to various strains, strain rates, temperatures and pressures. Eng Frac Mec 21(1):31–48

Kone F, Czarnota HB, Nouari M (2011) Finite element modeling of the thermo-mechanical behavior of coating under extreme contact loading in dry machining. Surf Coat Technol 205:3559–3566

Krajinovic I, Daves W, Tkadletz M, Teppernegg T, Klünsner T, Schalk N, Mitterer C, Tritremmel C, Ecker W, Czettl C (2016) Finite element study of the influence of hard metal tool loading during milling. Surf Coat Technol 304:134–141

Mabrouki T, Girardin F, Asad M, Rigal JE (2008) Numerical and experimental study of dry cutting for an aeronautic aluminium alloy (a2024-t351). Int J Mach Tools Manuf 48(11): 1187–1197

Mabrouki T, Courbon C, Zhang Y, Rech J, Nélias D, Asad M, Hamdi H, Belhadi S, Salvatore F (2016) Some insights on the modelling of chip formation and its morphology during metal cutting operations. Comptes Rendus Mecanique 344:335–354

Seo S, Min O, Yang H (2005) Constitutive equation for Ti-6Al-4 V at high temperatures measured using the SHPB technique. Int J Impact Eng 31:735–754

Sima M, Ozel T (2010) Modified material constitutive models for serrated chip formation simulations and experimental validation in machining of titanium alloy Ti-6Al-4 V. Int J. Mach Too Manuf 50:943–960

Wang X, Shi J (2013) Validation of Johnson-Cook plasticity and damage model using impact experiment. Int J Impact Eng 60:67–75

Zhang Y, Mabrouki T, Nelias D, Gong YD (2011) Chip formation in orthogonal cutting considering interface limiting shear stress and damage evolution based on fracture energu approach. Fin Ele Anal Des 47:850–863

Zhang Y, Outerio JC, Mabrouki T (2015) On the selection of Johnson-cook constitutive model parameters for Ti-6Al-4V using three types of numerical models of orthogonal cutting. Procedia CIRP 31:112–117

Turbulent-Heated Plane Compressible Jet Emerging in a Directed Co-Flowing Stream

Amel Elkaroui, Mohamed Hichem Gazzah, Nejla Mahjoub Saïd, Philippe Bournot and Georges Le Palec

Abstract In this present work, we have studied the directed co-flow effects on mean and turbulent flow properties of a turbulent heated plane jet with variable density discharging into a directed co-flowing stream. The first order k-εturbulence model is applied and has been compared with the existing experimental data. The Finite Volume Method (FVM) is used to discretize governing equations. First of all, it is found that predicted results are in satisfactory agreement with the experimental findings. Moreover, the numerical results of the mean and turbulent quantities has been presented and discussed in this work. The major interest of presenting this model is that to show the importance of the directed co-flow with a positive angle, which is enhancing the mixing. Furthermore, a qualitative analysis of the air entrainment would suggest that the higher inlet hot air jet temperature affect more the lateral in flow of air into the jet and jet lateral expansion is augmented when the inlet hot air jet temperature increases. Therefore, the increase of the inlet hot air jet temperature decreases faster the axial mean velocity and thus more entrainment air is required.

A. Elkaroui (✉)
LGM, National Engineering School of Monastir, University of Monastir,
5000 Monastir, Tunisia
e-mail: amel.karoui@hotmail.fr

M. H. Gazzah
Electronics and Microelectronics Laboratory, Faculty of Science of Monastir,
University of Monastir, Monastir, Tunisia
e-mail: hichem.gazzah@fsm.rnu.tn

N. M. Saïd
LGM, Preparatory Institute for Engineering Studies, University of Monastir,
Monastir, Tunisia
e-mail: nejla.mahjoub@fsm.rnu.tn

P. Bournot · G. Le Palec
IUSTI, Aix-Marseille University, UMR CNRS 7543 Marseille, France
e-mail: philippe.bournot@univ-amu.fr

G. Le Palec
e-mail: georges.lepalec@univ-amu.fr

581

1 Introduction

The development of free jet is well known and many works has treated this type of
flow, this abundance take the attention of many researchers, both numerically and
experimentally. The turbulent jets with variable density are involved in various
industrial systems, such as the turbulent diffusion flames. Otherwise, we can see the
practical importance the secondary flow. So, many researchers were interested to
study turbulent jets discharged in a co-flow. Indeed, Gaskin et al. (2001) studied the
axisymmetric and the plane jet in co-flow. Through a numerical study, they showed
on the one hand, that the turbulent velocity flux consisting of a portion due to the
excess jet velocity and a portion due to the turbulent co-flow velocity which is
carried by a velocity approximately equal to the top hat velocity. On the other hand,
the entrainment into this flow is driven by the jet excess velocity and the modified
entrainment function allows for the change in entrainment from the strong jet to the
weak jet. They showed also that the same functional relationship for the entrain-
ment is applied for an axisymmetric and a plane jet in a co-flow. Finally it is better
that this modification is due to clustering of eddies distorting the boundary between
turbulent and irrotational fluid. The presence of the constant depends of the addi-
tional entrainment in the weak jet case. The predicted mean properties agree with
the experimental results. However, for the axisymmeric jet an allowance can be
made for a finite duct size.

A strongly advected jet in a co-flow was studied by Davidson and Wang (2002).
Their experimental works describe the behavior of a strongly advected jet (weak jet)
in a co-flowing ambient fluid. Indeed, the results presented are discussed in the
context of recent observations about the importance of large-scale eddy motions in
defining the mean behavior of weakly advected jets and plumes. In addition, the
experiments provide information on the contrasts between the mixing processes in
the weakly advected and strongly advected co-flowing jet regions, and their
influence on the mean behavior of these flows. Concentration fluctuation statistics
from both regions are presented and implications for the application of the
entrainment assumption in the strongly advected region are discussed.

A numerical study of the scalar fields in turbulent round jet with co-flowing
stream was conducted by Gazzah et al. (2004). They studied numerically, the
influence of co-flow on a turbulent binary gas mixing using the first- and the
second-order turbulence closure models. They found that the comparisons between
recently published experimental results and mean mixture fraction, the scalar

turbulent fluctuation, and the jet spreading rate, feature reasonably good agreements. Also they mainly showed that the co-flow reduces the jet spreading rate on then one hand, but on the other hand increases the mixing efficiency.

Imine et al. (2005) have studied the effects of directed co-flow on a non-reactive turbulent jet with variable density. In this study, the effects of a directed co-flow on the process of mixture jet with variable density have been investigated numerically. The results obtained indicate that the directed co-flow with positive angles enhances considerably the mixing. Also, the prediction of the present calculation agrees reasonably well with the very recent experimental study in the case of non-directed co-flow (α = 0°). The introduction of a directed co-flow with positive angles made it possible to obtain very good performance of mixing and improve the mixing process more in order to ensure a good combustion. For that according to results obtained, it was noticed that in far field the influence of the directed co-flow persists in both axial and radial directions.

Directed co-flow effects on local entropy generation in turbulent heated round jets have been treated by Gazzah and Belmabrouk (2014). They show that the total entropy production rate increases in three cases: the increase of the hot air jet temperature at the inlet, the decrease of the co-flow velocity, and the increase of deviation angles.

Nevertheless, in the current study, we have to predict the effect of directed co-flow on turbulent plane jet with variable density. The closure of the averaged equations governing the problem, in the turbulent regime is carried out using the first-order model k–ε. We also adopted a numerical method for solving the system of equations associated with the boundary conditions imposed. This system is actually obtained through the Finite Volume Method (FVM) of Patankar (1980). First, we compare our numerical findings with Sarh experimental results (1990). Then, we will study a turbulent heated plane jet into co-flowing air in various directions between −10° and +10°. Moreover, we will analyze the influence of the directed co-flow on various physical parameters such as the mean and turbulent quantities.

2 Problem Formulation

The turbulent flow is two-dimensional and steady. The fluid, with variable density, is assumed to obey the ideal gas law: $P = \rho r T$. Then, the averaged equations governing the flow with variable density using Favre-averaged quantities (2014) are reduced to

$$\frac{\partial \rho U_j}{\partial x_j} = 0 \tag{1}$$

$$\frac{\partial}{\partial x_j}\left(\rho U_i U_j\right) = \rho g_i - \frac{\partial P}{\partial x_i} - \frac{\partial}{\partial x_i}\left(\overline{\rho u_i'' u_j''}\right) + \frac{\partial}{\partial x_j}\left[\mu\left(\frac{\partial U_i}{\partial x_j} + \frac{\partial U_j}{\partial x_i}\right) - \frac{2}{3}\mu\frac{\partial U_k}{\partial x_k}\delta_{ij}\right] \quad (2)$$

$$\frac{\partial}{\partial x_j}\left(\rho T U_j\right) = \frac{\partial}{\partial x_j}\left(\frac{\lambda}{C_P}\frac{\partial T}{\partial x_j}\right) - \frac{\partial}{\partial x_j}\left(\overline{\rho t'' u_j''}\right) \quad (3)$$

With $\tau_{ij} = \left[\bar{\mu}\left(\frac{\partial U_i}{\partial x_j} + \frac{\partial U_j}{\partial x_i}\right) - \frac{2}{3}\bar{\mu}\frac{\partial U_k}{\partial x_k}\delta_{ij}\right]$ is the tensor of viscous constraints.

$\overline{\rho u_i'' u_j''} = -\mu_t\left(\frac{\partial U_i}{\partial x_j} + \frac{\partial U_j}{\partial x_i}\right) + \frac{2}{3}\rho k\delta_{ij}$ is the Reynolds tension.

δ_{ij} is the Kronecker symbol $\delta_{ij} = 1$ if i = j, 0 if not.

$\overline{\rho u_i'' t''} = -\frac{\mu_t}{\sigma_t}\frac{\partial T}{\partial x_i}$ is the turbulent flow temperature.

To obtain a closed equations system, the first-order standard $k - \varepsilon$ model is considered. In this model, the equations of the kinetic energy of turbulence (k) and its rate of dissipation (ε) can be shown as

$$\frac{\partial}{\partial x_j}\left(\rho U_j k\right) = \frac{\partial}{\partial x_j}\left((\mu + \frac{\mu_t}{\sigma_k})\frac{\partial k}{\partial x_j}\right) - \overline{\rho u_i'' u_j''}\frac{\partial U_i}{\partial x_j} - \beta g\overline{\rho t''^2} - \rho\varepsilon \quad (4)$$

$$\frac{\partial}{\partial x_j}\left(\rho U_j \varepsilon\right) = \frac{\partial}{\partial x_j}\left((\mu + \frac{\mu_t}{\sigma_\varepsilon})\frac{\partial\varepsilon}{\partial x_j}\right) + C_{\varepsilon 1}P_k\frac{\varepsilon}{k} - C_{\varepsilon 2}\rho\frac{\varepsilon^2}{k} \quad (5)$$

With $\mu_t = \rho C_\mu\frac{k^2}{\varepsilon}$ the turbulent viscosity This model requires the use of the following empirical constants (2014)

$$\sigma_k = 1,\ \sigma_\varepsilon = 1.3,\ C_{\varepsilon 1} = 1.44,\ C_{\varepsilon 2} = 1.92,\ C_\mu = 0.09,\ \sigma_t = 0.7,\ \Pr_t = 0.70$$

3 Boundary Conditions

A compressible and a non-isothermal air jet flowing out vertically from a plane nozzle with outside thickness H/2. The jet is discharging into a directed co-flowing stream as shown in Fig. 1. In this figure, x and y denote the longitudinal and the transverse distances, respectively.

In simulations, the boundary conditions are imposed on the jet with a uniform velocity U_j, and a temperature T_j. The jet is evolving, in a moving uniform directed co-flow velocity U_{co}.
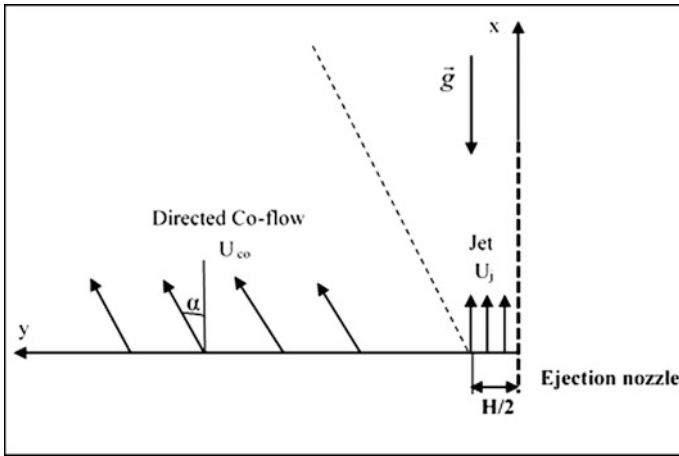
Fig. 1 Geometric configuration

The foregoing system of equations is completed with the following boundary conditions:

$$x = 0: \begin{cases} 0 < y < H/2: U = U_j; V = 0; T = T_j; k = 10^{-3} U_j^2; \varepsilon = \dfrac{C_\mu k^{3/2}}{0.03 H} \\ y \geq H/2: U = U_{co}; v = 0; T = T_a; k = 0; \varepsilon = 0 \end{cases}$$

$$x > 0: \begin{cases} y = 0: V = 0; \; \dfrac{\partial \Phi}{\partial y} = 0 \; \text{ where } \Phi = U, T, k, \varepsilon \\ y \to \infty: U = U_{co}; \dfrac{\partial V}{\partial y} = 0; T = T_a; k = 0; \varepsilon = 0 \end{cases}$$

4 Numerical Solution Method

The equations are solved by the Finite Volume Method (FVM) with a staggered grid as described by Patankar (1980) is used for the numerical resolution of the transport equations of momentum, energy, turbulent kinetic energy, and its dissipation rate are discretized through this equation: $A_P \Phi_P = \sum\limits_{nb} A_{nb} \Phi_{nb} + \Phi_P,$.

Where, the subscripts nb designates neighbors which means $(i+1, j)$, $(i-1, j)$, $(i, j+1)$ and $(i, j-1)$. This method was used in previous work of Gazzah and Belmabrouk (2014) and successfully adopted for numerical stability reasons compared to other methods using a non-staggered grid discretization.

The mesh used is not uniform and gradually extends according to the longitudinal and transversal directions. A non-uniform mesh, refined near of the jet exit and the symmetry axis has been adopted in numerical simulation. Indeed, the distance between two successive nodes obeys the following relationship:

$\Delta X_i = \alpha \Delta X_{i-1}$ and $\Delta X_j = \alpha \Delta X_{j-1}$. The grid with 110×130 nodes in axial and longitudinal directions respectively allows to obtain a satisfactory accuracy.

5 Results and Discussion

This study based on a detailed comparison between a computational results and an experimental measurements conducted by Sarh (1990) is carried out for the case a heated turbulent plane jet with variable density. The effects of a directed co-flow with positive and negative angles are examined. Two inlet jet temperature ($T_j = $ 320 K, $T_j = 500$ K) was taken. The jet is ejected from a plane nozzle with a velocity $U_j = 18$ m/s emerging into the co-flowing air with a velocity $U_{co} = 1.2$ m/s.

Figure 2 shows the evolution of the centerline longitudinal velocity $\left((U_j - U_{co})/(U_c - U_{co})\right)^2$ as a function of the normalized distance x/H for $T_j = $ 320 K, $T_j = 500$ K, and $\alpha = -10°, 0°, +10°$. First of all, it is seen that the velocity agree well with the experimental data of Sarh (1990) in the case of non-directed co-flow ($\alpha = 0°$) and $T_j = 320$ K. Moreover this figure shows also the effects of the directed co-flow. The major effects of the directed co-flow with positive angle ($\alpha = +10°$) is that the centerline axial velocity decreases faster, than the non-directed co-flow ($\alpha = 0°$). However, in the case of the negative directed co-flow ($\alpha = -10°$) it decreases more slowly than in the case ($\alpha = 0°$). Therefore, a jet with positive directed co-flow tends to entrain the ambient air more rapidly than the others cases.

Fig. 2 Directed co-flow effects on the axial evolution of the centerline longitudinal velocity
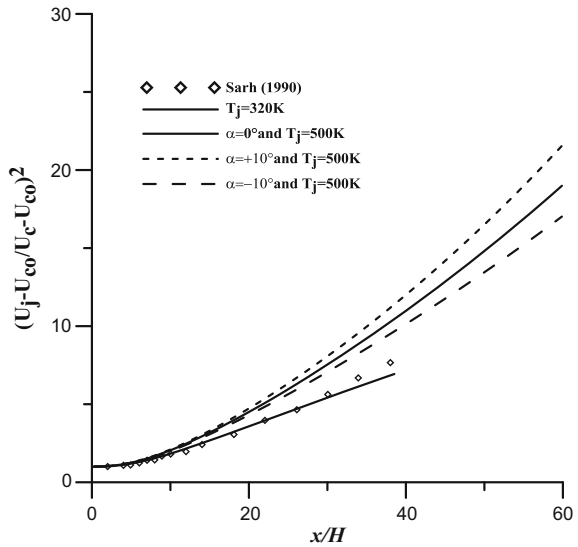
Figure 3 exhibits the axial evolution of the dimensionless centerline temperature $(T_j - T_a)^2 / (T_c - T_a)^2$ as a function of the normalized distance x/H for different jet temperature (T_j = 320 K, T_j = 500 K) and different deviation angles ($\alpha = -10°$, $0°$, $+10°$). The axial mean temperature is an important parameter to characterizing the jet mixing. The predicted results indicate a reasonable agreement with the experimental data of Sarh (1990) for the case of non-directed co-flow ($\alpha = 0°$) and T_j = 320 K. Figure 3 shows also the effect of directed co-flow. The mean temperature has the same behavior as the mean velocity.

The axial evolution of the centerline turbulent intensity $u'/(U_c - U_{co})$ is represented in Fig. 4. A reasonably agreement is observed with the experimental data of Sarh (1990) in the case of non-directed co-flow ($\alpha = 0°$) and for T_j = 320 K. Moreover, it is noticeable that for co-flow with a positive deviation ($\alpha = +10°$), the centerline of turbulent intensity increases faster than that in the case of non-directed co-flow ($\alpha = 0°$). Then, more turbulent mixing has been obtained. However, for a negative deviation ($\alpha = -10°$), the centerline of turbulent intensity decreases slowly than the non-directed co-flow.

The axial evolution of the centerline temperature fluctuation intensity $t'/(T_j - T_c)$ is presented in Fig. 5 for Tj = 320 K, Tj = 500 K, and for three deviation angles ($\alpha = -10°$, $0°$, $+10°$).

The computed results are overpredicted compared with the experimental data of Sarh (1990) for the case of non-directed co-flow ($\alpha = 0°$) and T_j = 320 K. In the case of T_j = 500 K and for different deviation angles ($\alpha = -10°$, $0°$, $+10°$), it is noticeable that with positive co-flow the asymptotic value of the centerline temperature fluctuation intensity decreases faster than the others cases. The reason for

Fig. 3 Directed co-flow effects on the axial evolution of the centerline turbulent intensity
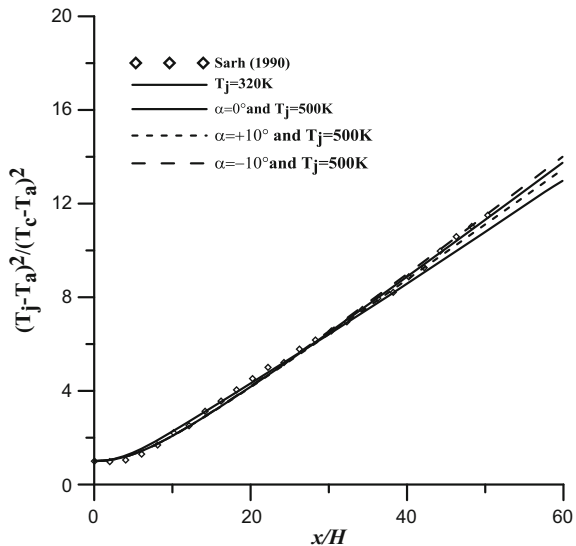
Fig. 4 Directed co-flow effects on the axial evolution of the centerline turbulent intensity
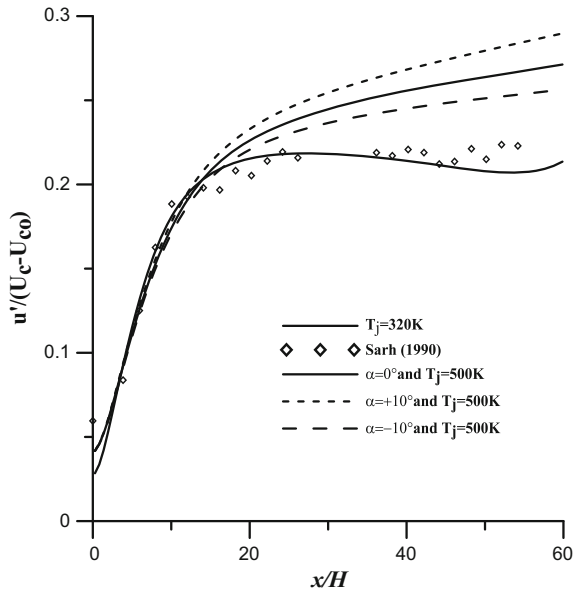
Fig. 5 Directed co-flow effects on the axial evolution of the centerline temperature fluctuation intensity
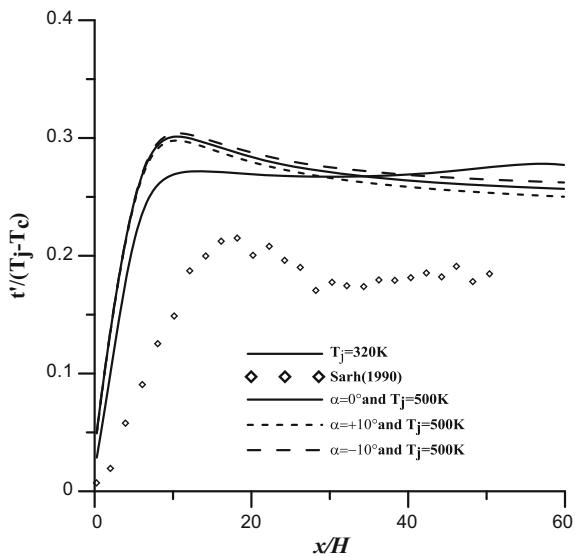
this peculiarity is may be related to the above mentioned behavior of the mean temperature decay and the increase of air entrainment in this case.

Figure 6 represents the axial evolution of the amount of air entrainment with two inlet hot air jet temperatures (T_j = 320 K, T_j = 500 K) and for the same co-flow velocities (U_{co} = 1.2 m/s). It is shown that the inlet hot air jet with T_j = 500 K

Fig. 6 Directed co-flow effects on the axial evolution of the entrainment air for different inlet jet temperature
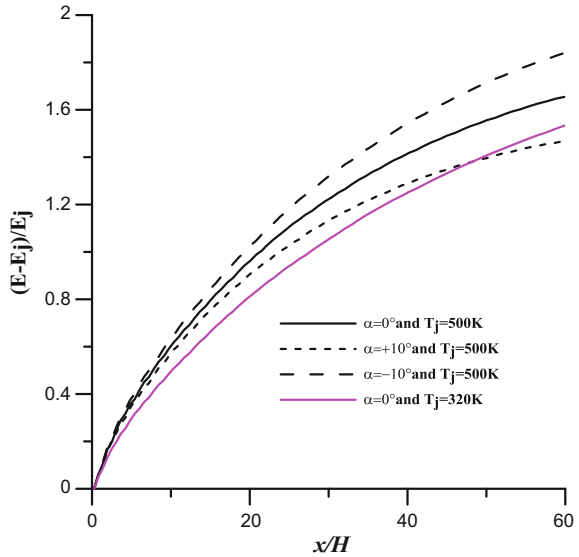
entrain more air than the case of $T_j = 320$ K at any given axial location. A qualitative analysis would suggest that the higher inlet hot air jet temperature affects more the lateral in flow of air into the jet and jet lateral expansion is augmented when the inlet hot air jet temperature increases. Therefore, the increase of the inlet hot air jet temperature decreases faster the axial mean velocity and thus more entrainment air is required.

6   Conclusion

In this present work, we numerically studied a turbulent plan heated jet with variable density taking into account the effects of a directed co-flow with positive and negative angles. Numerical simulations are carried out using the first order k-εturbulence model. A good agreement is noted with the experimental data of Sarh (1990). The major effect of the positive co-flow deviation angles causes a rapid decrease of the mean axial velocity and temperature and consequently an increase in air entrainment.

References

Davidson MJ, Wang HJ (2002) Strongly advected jet in a coflow. J Hydraul Eng 128:742–752
Gaskin S, Wood IR (2001) the axisymmetric and the plane jet in a coflow. J Hydraul Res 39:451–458

Gazzah MH, Belmabrouk H, Sassi M (2004) A numerical study of the scalar field in turbulent round jet with co-flowing stream. Comput Mech 34:430–437

Gazzah MH, Belmabrouk H (2014) Directed co-flow effects on local entropy generation in turbulent heated round jets. Comput Fluids 105:285–293

Imine B, Saber-Bendhina A, Imine O, Gazzah MH (2005) Effects of a directed co-flow on a non-reactive turbulent jet with variable density. Heat Mass Transf 42:39–50

Patankar SV (1980) Numerical heat transfer and fluid flow. Hemisphere Publishing, Washington DC

Sarh B (1990) Contribution à l'étude des jets turbulents à masse volumique variable et des flammes turbulentes de diffusion. Thèse de doctorat à l'Université Pierre et Marie Curie Paris

Effects of Starting Time and Impeller Geometry on the Hydraulic Performance of a Centrifugal Pump

Kchaou Nouha, Elaoud Sami, Chalghoum Issa and Bettaieb Noura

Abstract Due to the lack of studies that investigate the transient behavior of centrifugal pumps during starting and stopping periods, this paper provides a numerical study to predict the variation of the dynamic behavior of the flow during the starting period of a centrifugal pump by considering an actual motor torque. The numerical study is based on the characteristic method of specified time intervals taking the pressure head and the flow rate as two dependent variables. After developing the continuity and motion equations, a study based on the pump motor equation was carried out in order to determine the impeller angular velocity variation during the starting time. The numerical obtained results have shown that the pressure increase is more important in the case of a relatively short starting time compared to a long one. These results have shown a good agreement with those obtained by experiment. In this study, the influence of the impeller geometry on the pressure head and flow rate is also investigated. The obtained results have shown a dependency of the pump dynamic behavior with the impeller geometry during the starting periods.

K. Nouha (✉) · E. Sami · C. Issa · B. Noura
Research Laboratory "Applied Fluid Mechanics, Process Engineering and Environment"
Engineering School of Sfax, BP'W'3038 Sfax, Tunisia
e-mail: nouha.kchaou@enis.tn

E. Sami
e-mail: elaoudsa@yahoo.fr

C. Issa
e-mail: chalghoumissa@yahoo.fr

B. Noura
e-mail: noura.bettaieb@enis.tn

1 Introduction

Pumps are one of the most complex fluid machine which converts mechanical energy to hydraulic energy. Depending on the specific speed, pumps are divided into three categories: centrifugal, mixed flow and axial flow pumps. In this study, we are interested in centrifugal pumps to transfer a liquid from a source to a required destination. The choice of this type of pumps is based on their significant advantages taking into consideration our application. Going with this choice, we need to investigate the centrifugal pump behavior and its governing parameters. Up to now, studies have been done just on the steady-state characteristics of turbo machinery. However, there are no many advanced studies about pumps behavior under unsteady conditions. In fact, the transient performance during starting period of a pump under unsteady conditions has been assumed to be identical with the steady-state performance. However, when the changing rate of the operational point exceeds a certain limit, the pump cannot respond quickly enough to follow along its steady-state characteristics curves, thus resulting in a considerable change in transient behavior (Tsukamoto and Ohashi 1982). Then, selecting a centrifugal pump to transfer fluid in pipelines is very critical. In fact, when the pump is accelerating very rapidly, the pressure and flow rise can be excessively high. This rise can damage the pipelines system and be the cause of danger to the operator. Therefore, we will investigate the transient behavior of a centrifugal pump during its starting period and the parameters that influence on the flow rate and pressure variation during starting transient. It has been demonstrated that three factors can influence on the dynamic behavior of a pump during its starting transient, which are the mass of water in the pipeline, the valve opening percentage and the starting time (Saito 1982). The majority of studies assumed a linear variation of the angular velocity during starting transient. However, in this work, we will analyze the effect of those parameters based on the actual speed variation and the motor torque considering the geometry and the parameters of the used hydraulic installation.

In addition, we will investigate the effect of the impeller diameter and the blades geometry on the flow rate and the head evolution.

2 Fundamental Equations

2.1 Fluid Governing Equations

2.1.1 Equation of Motion

The basic equation of motion applied on the control volume shown in Fig. 1 is given by

Fig. 1 Velocity triangles and applied forces in the rotating impeller
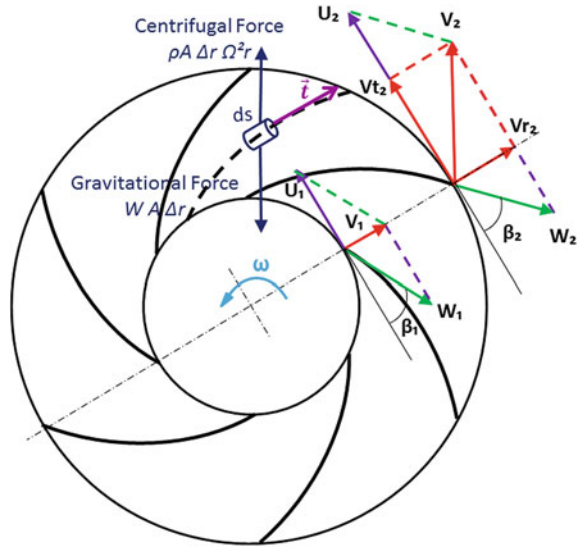
$$dm(\Gamma_{relative} + \Gamma_{driving} + \Gamma_{coriolis})\vec{t} = [p(s) - p(s+ds)]dS, \tag{1}$$

where $\Gamma_{relative}$ is the relative acceleration, $\Gamma_{driving}$ is the driving acceleration, $\Gamma_{coriolis}$ is the Coriolis acceleration and $p(s)$ and $p(s+ds)$ is the pressure applied on the upstream and the downstream surface. After neglecting unimportant terms and simplifying the equation of motion (1) in a reference frame rotating with the impeller as shown in Fig. 1, we obtain the following equation:

$$\frac{1}{A}\frac{\partial Q}{\partial t} + g\frac{\partial H}{\partial r} + \lambda\frac{Q|Q|}{2D_h A^2} - r\Omega^2 = 0, \tag{2}$$

where A is the impeller passage section, Q is the fluid discharge, H is the head, λ is the Darcy Weisbach friction coefficient and D_h is the hydraulic diameter of the section A. It should be noted that the term $r\Omega^2$ is an extra term comparing to water hammer equations for conduit flow. This extra term is resulting on the centrifugal force of the rotating impeller. In addition, we assumed that the blade angle β is equal to 90°.

2.1.2 Continuity Equation

Considering the mass instability due to compressibility of the fluid and the elasticity of the passage material, we will derive the continuity equation. Under the sited assumptions, the basic continuity equation in the rotating reference related to the impeller is given by

$$\frac{\partial \rho}{\partial t} + \rho \, div \vec{W} = 0, \tag{3}$$

where ρ is the fluid density. After simplifying the basic continuity equation, we found the following equation:

$$\frac{\partial H}{\partial t} + \frac{C^2}{gA}\frac{\partial Q}{\partial r} = 0, \tag{4}$$

where C is the pressure wave speed.

The fluid governing Eqs. (2) and (4) will be used for the numerical computation to study the fluid discharge and head variation during the starting transient in the hydraulic installation described in Fig. 2. For this purpose, we need the impeller angular velocity variation during the starting transient. Therefore, we will use, in the following paragraph, an analytic method to determine the transient pump equation.

2.2 Pump Governing Equations

During the starting time, the pump provides besides of the acceleration torque, a torque Tf to overcome the friction of fluid that circulate in the system and the friction of the rotating parts. Reaching the steady state, no torque is needed for acceleration. Torque is needed only to overcome the frictional losses. Therefore, the governing equation for mechanical model can be expressed as following:

$$(I_M + I_P)\frac{d\Omega}{dt} + T_f = T_m - T_r, \tag{5}$$

Fig. 2 Hydraulic installation
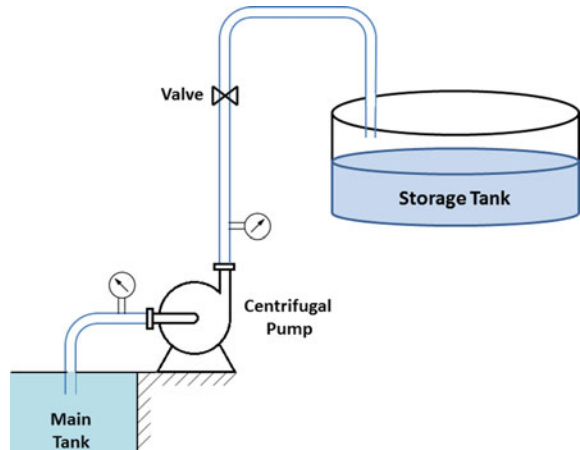
where I_M is the inertia of the motor, I_P is the inertia of the propeller including the rotating water inertia, is the propeller angular velocity, T_m is the motor torque and T_r is the resistant hydrodynamic torque. The resistant hydrodynamic torque depends on the propeller angular speed and the flow rate Menon (2014) and given by:

$$T_r = k_1 \Omega^2 + k_2 \Omega Q. \tag{6}$$

To calculate the hydrodynamic torque coefficients, we used the pump power characteristic curve. If the motor torque Tm is known as a mathematical function of speed it may be possible to integrate it numerically with the purpose of obtaining the impeller angular velocity variation. The motor torque equation is given by

$$T_m = \frac{3p}{w_s} \frac{r_2}{g} \frac{V_s^2}{\left(r_s + \frac{r_2}{g}\right)^2 + (l_s w_s + l_2 w_s)^2}, \tag{7}$$

where p is the motor poles number, r_2, r_s, l_2, l_s is the resistance and the inductance of the rotor and the stator, V_s is the supply voltage, w_s is stator frequency and g is the sliding coefficient. Knowing the motor torque equation and the resistant torque, we can obtain numerically the propeller angular velocity variation. In the following, we will derive ordinary differential equations associated with the flow velocity and the pressure using the characteristic method.

3 Numerical Analysis

In this section, we will derive the characteristic equations in order to reduce our partial differential Eqs. (2) and (4) to a system of ordinary differential equations grouped and identified as C + and C− equations

$$C^+ \begin{cases} \frac{gA}{C} dH + dQ + JA dt - r\Omega^2 A dt = 0 \\ dr = +C dt \end{cases}, \tag{8}$$

$$C^- \begin{cases} -\frac{gA}{C} dH + dQ + JA dt - r\Omega^2 A dt = 0 \\ dr = -C dt \end{cases}, \tag{9}$$

where $J = \lambda \frac{Q|Q|}{2 D_h A^2}$ is the head loss by impeller length unit.

The ordinary differential Eqs. (8) and (9) are numerically solved in order to determine the flow and the head at any interior point of the pump (Chalghoum et al. 2016). In order to get the complete solution, we need to define the boundary conditions in the different junctions. For the pipelines calculations, we use the same approach with removing the term related to the pump angular velocity.

As has been previously stated, the characteristic equations depend on the pump angular velocity. Therefore, we need the impeller speed variation in order to obtain
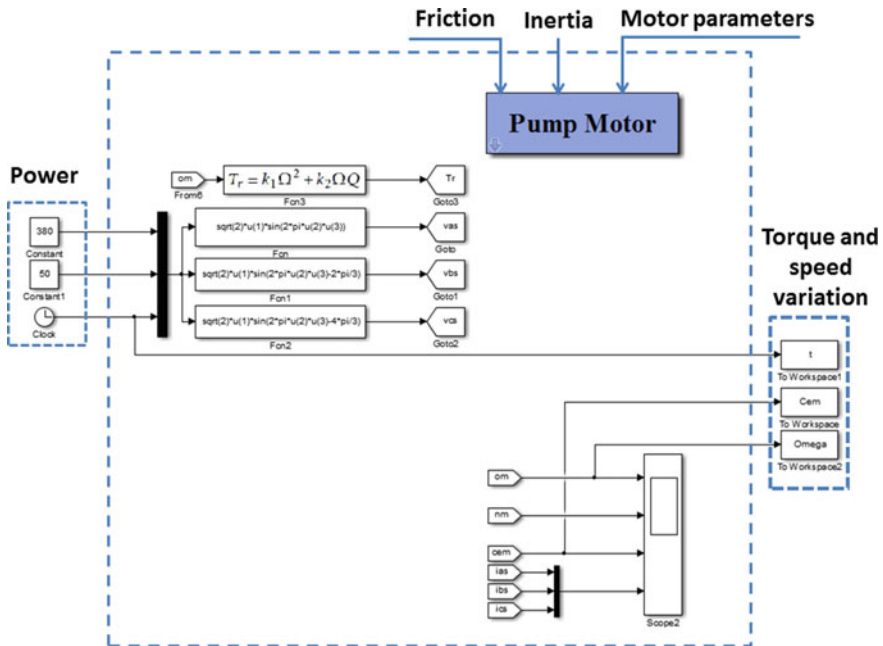
Fig. 3 Motor torque and impeller speed numerical calculation

the head and the discharge variation. A numerical calculation was done to model the motor torque taking into consideration the friction of the system, the total inertia and the hydraulic resistant torque. This numerical study covers all the possible configurations of the hydraulic installation as demonstrated in Fig. 3.

As a first step, we consider the hydraulic test facility (TE-83) studied by (Chalghoum et al. 2016). In this case, Figure represents the angular velocity variation as function of time.

The pump impeller speed increase due to the applied motor torque. The rotational speed of the pump encounters some fluctuations at the beginning of the transient response. After the transient time, the angular velocity stabilized at 2900 rpm.

4 Results and Analysis

4.1 Steady-State Response Analysis

According to the given hydraulic installation configuration used in the test facility TE-83, the transient angular velocity varies as shown in Fig. 4 during a startup period equals to 0.3 s. Considering this rotational speed variation, we will validate
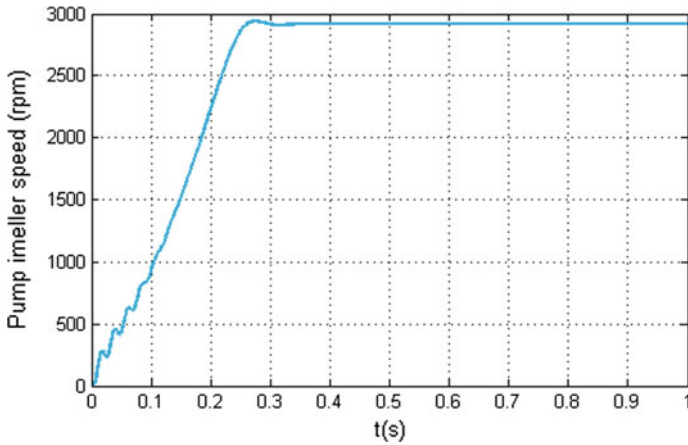
Fig. 4 Pump Impeller speed variation for I = 0.0053 kg.m^2
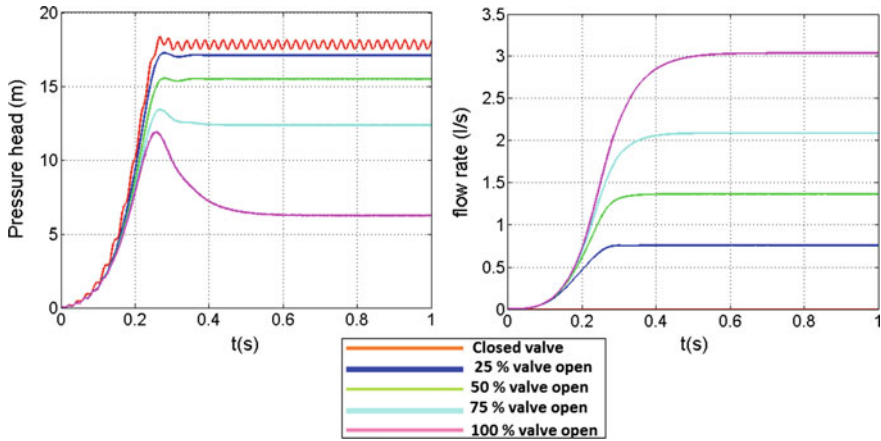
Fig. 5 Pressure head and discharge evolution for different valve opening positions

the steady-state characteristic curve as a first step. Figure 5 shows the head and the flow rate variation for different opening positions of the valve.

Fixing the valve position, the head pressure and the flow rate steady-state values correspond to the operating point. By gathering all the operating points we obtain the characteristic curve. Figure 6 shows a comparison between the experimental characteristic curve and numerical modeled curve. The slight difference between the two curves is due to the negligence of the pump volute shape (Saito 1982).

As a second step, we will investigate the parameters that effect the pump steady-state performance. The steady-state curve of the pump depends on the pump angular velocity, the suction and exit diameter, the blade curve, the blade width, the
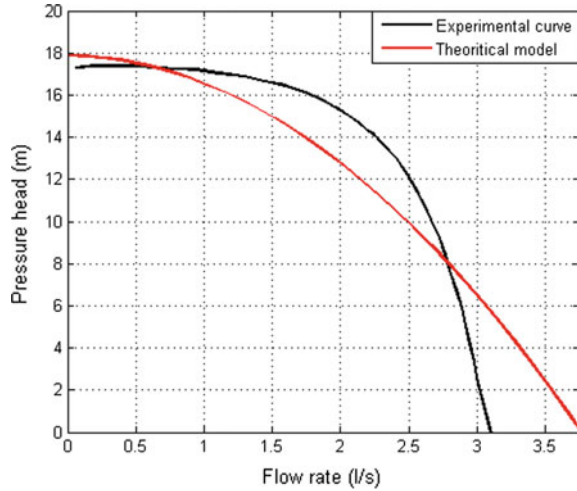
pump pressure losses and the volute shape. In the following, we will investigate the
effect of some parameters on the characteristic curve from the sited above.

4.1.1 Pump Impeller Diameter

Figure 7 illustrates the effect of the pump impeller diameter on the steady-state
behavior. The flow rate and the head variations are proportional to the impeller
diameter variation. This variation follows the affinity law (Menon 2014).

4.1.2 Blade Width

The blade width varies linearly from its maximum value b1 corresponding to the
inner diameter to its minimum value b2 corresponding to the outer diameter.
Figure 8 shows the effect of the blade width on the pump characteristic curve.

The blade width is an important parameter that largely influence on the pump
performance as shown in Fig. 7. In fact, the impellers of different width are used for
low or high capacity performance.

4.2 Transient Response Analysis

During the starting period of the pump, the pressure evolution is affected by the
mass of water in the pipe, the opening position of the valve and the starting time.
Using the transient behavior of the angular velocity shown in Fig. 4 and varying the

Fig. 7 Effect of the impeller diameter on the pump characteristic curve for N = 2900 rpm and I = 0.0053 kg.m²
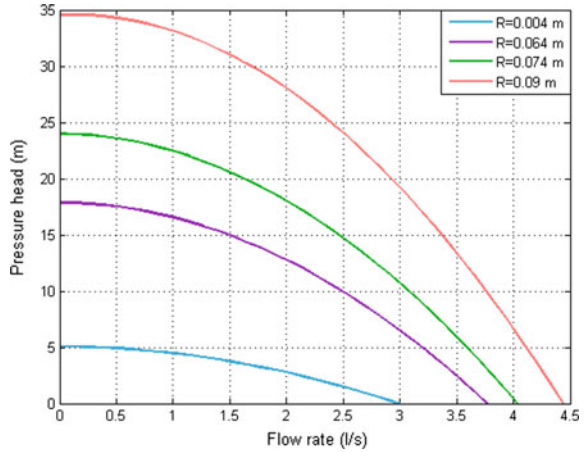
Fig. 8 Effect of the blade width on the pump characteristic curve for N = 2900 rpm and I = 0.0053 kg.m²
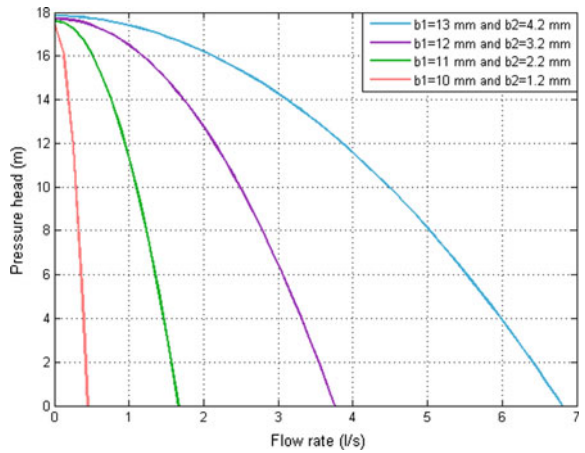
time startup shows that the increase of the startup time causes the decrease of the pressure head during starting transient as demonstrated in Fig. 9.

Finally, we investigate the effect of the width variation on the transient behavior and we conclude that the blade width cause a large increase in the pressure head pick as shown in Fig. 10.

Therefore the optimum configuration is to choose a maximum startup period by fixing the system inertia avoiding then the head pick during the transient startup. In fact, to transfer a liquid from a source to a required destination, a fast response is not needed. So a starting period equal to 0.5 s is adequate for our application. Especially, the steady head value is not function of the starting period. Also, we need to consider the adequate blade width based on Fig. 10.

Fig. 9 Effect of the starting time on the pressure evolution
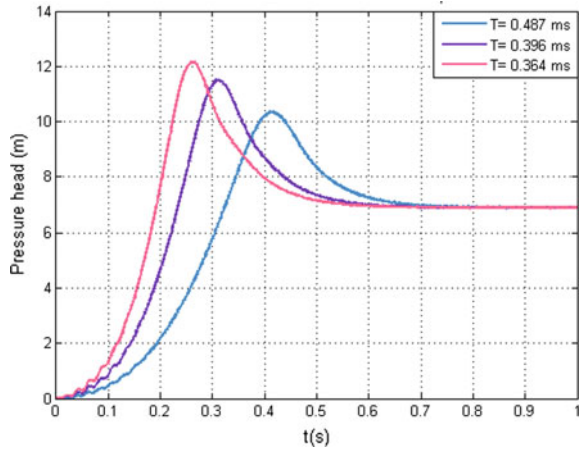
Fig. 10 Effect of the blade width variation on the pressure evolution
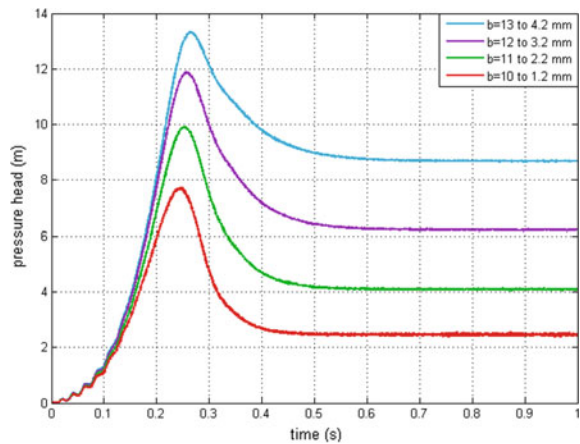
5 Conclusion

In this paper, the transient behavior of a given centrifugal pump has been analyzed. A numerical study was developed in order to show the effect of the angular speed variation of the pump impeller on the discharge and pressure head transient variation. Therefore, a numerical calculation was done to obtain the impeller speed variation for a given hydraulic installation knowing the friction, the inertia, and the resistant torque.

After validating the pump characteristic curve, we demonstrated the startup time and the opening valve position effect on the transient behavior. Additionally, we consider a linear variation of the blade width in order to show the effect of the maximum and the minimum value of the blade width on the transient behavior.

References

Chalghoum I, Elaoud S, Akrout M, Taieb EH (2016) Transient behavior of a centrifugal pump during starting period. Appl Acoust 109(2016):82–89. https://doi.org/10.1016/j.apacoust.2016.02.007

Menon ES (2014) Transmission pipeline calculations and simulations manual. Prentice, 1st edn. Hall, Englewood Cliffs, N.J

Saito S (1982) The transient characteristics of a pump during startup. Bull JSME 1982 201 (25):372–9. https://doi.org/10.1299/jsme1958.25.372

Tsukamoto H, Ohashi H (1982) Transient characteristics of a centrifugal pump during starting period. ASME J Fluids Eng 1982:104(1). https://doi.org/10.1215/1.3240859

Effect of the Volute Diffuser Shape on Pressure Pulsations and Radial Force in Centrifugal Pumps

Issa Chalghoum, Noura Bettaieb and Sami Elaoud

Abstract Centrifugal pump is a major cause of pressure perturbations in hydraulic installations. The internal geometry of this turbomachine and its running conditions affect excessively the magnitude of these excitations. In the present study, a numerical investigation is conducted to analyze the influence of the volute diffuser type on flow characteristics in centrifugal pumps with the same impeller under wide range of flow rate. An unsteady numerical analysis was carried out in order to study the strong interaction between blade and tongue with two different geometries of the volute. The main objective is to analyze the characteristics of pressure and force fluctuations inside the pump. For tangential diffuser shape, the pressure fluctuation amplitudes are greater than that in the case of a radial diffuser. Based on the fast Fourier transform (FFT), the spectral analysis was performed on the pressure fluctuation signals in frequency domain under running condition for two volute at different monitoring points in the pump. The time frequency characteristics of these pressure fluctuations were affected greatly by both volute type and measurement locations in each diffuser. However, simulation results were compared with the available experimental data, and an acceptable agreement was obtained. The results obtained in this work can provide a useful reference for designing the type of volute diffuser in pump.

Keywords Unsteady flow characteristics · Tangential diffuser · Radial diffuser Pressure fluctuation

I. Chalghoum (✉) · N. Bettaieb · S. Elaoud
Research Laboratory "Applied Fluid Mechanics, Process Engineering and Environment"
Engineering School of Sfax, BP'W'3038, Sfax, Tunisia
e-mail: chalghoumissa@yahoo.fr

N. Bettaieb
e-mail: noura.bettaieb@enis.tn

S. Elaoud
e-mail: elaoudsa@yahoo.fr

603

1 Introduction

A centrifugal pump is composed mainly of two important parts, the impeller and the volute. Together, these two components specify the characteristics performance of pumps. In addition, the volute geometry is an important key in the creation of pressure pulsations inside the pump. To adapt the various types pipelines installation, the volute shape is designed in different types. The strong impeller-volute interaction is a major source of generating high amplitude pressure pulsations and flow-induced vibrations, Brennen (1994). In recent years, the use of CFD (computational fluid dynamics) software is highly increased for studying and analyzing the unsteady flow field behavior inside pumps, Dawes et al. (2001) and Zhang et al. (2009). Several studies were conducted on the geometric parameters of pumps in order to control and reduce the pressure pulsation amplitude and radial forces. Spence and Amaral Texeira (2009) investigated the effects of various pump geometries (blade tip clearance, shroud-to-casing radial clearance, vane arrangement and sidewall clearance) by means of experimental and numerical ways. He found out, on the one hand, that increasing the gap between the impeller and the volute is an effective method to lower the amplitude of pressure pulsation. On the other hand, this method may have harmful effects on the efficiency pump, Yang et al. (2014). As for impeller–volute interaction, many studies, Dwayne et al. (2005) and Zhu et al. (2007), demonstrate that the impeller blade geometry has an impact on unsteady pressure pulsations. Moreover, many researchers have numerically studied, the unsteady pressure characteristics inside centrifugal pumps, such as in the work of (Mosallem 2008) and (Majidi 2005). However, only few authors have conducted research about the effect of diffuser shapes type on unsteady pressure fluctuation. Torabi and Nourbakhsh (2011) studied, numerically, the effects of the volute geometry variation on radial forces. They found that the gap between the impeller and the tongue affects the radial force. The obtained results indicated that a 6% reduce in the gap increases the maximum value of the static pressure by 50% around the impeller exit. Recently, Parrondo et al. (2011) and Keller et al. (2014) developed an acoustic model to analyze the pump internal sound field at the blade-passing frequency. They found that the sound field could be reasonably characterized by a dipole-like source located at the tongue region. This mode was also used to determine the ideal sound sources that generate the equivalent of the acoustic field to the sound emission by fluid-dynamic blade–tongue interaction at different flow rates.

In this study, two different diffuser types of volute were designed to study, numerically, their effect on pressure fluctuation and radial force features of centrifugal pump, with the same impeller geometry. First, a comparison between numerical and experimental characteristic curves with the base volute configuration is presented. Later, results of the use of two different diffuser types are presented and a comparison for these cases is conducted. Computational methods are applied to compute the pump performance, radial force, and pressure pulsation characteristics

by mounting 9 monitoring points on the impeller and volute walls. Finally, a comparison between the effects of different volute shapes on the centrifugal pump are carried out and discussed.

2 Numerical Simulation

2.1 Pump Geometry

To investigate the influence of the volute diffuser shape on the performance and pressure pulsations of the centrifugal pump, two different diffuser shapes, including radial and tangential diffusers, are designed for the purpose of this work. Figure 1 presented a 3D view of these diffusers while the geometry of the impeller geometry remains the same in both designs. The main geometric characteristics of the impeller are illustrated in Table 1.

2.2 Solution Parameters

In order to be consistent with the experimental method, total pressure at pump inlet is specified as an inlet boundary condition. The mass flow is chosen as an outlet of

Fig. 1 Sketch of the pump mesh **a** with radial diffuser **b** with tangential diffuser
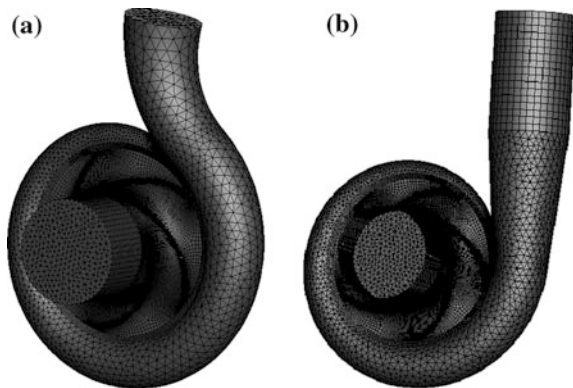
Table 1 Main characteristics of impeller

Impeller	Value
Inlet diameter	0.150 m
Outlet diameter	0.4084 m
Inlet width	0.0859
Outlet width	0.0420 m
Blade number	5

the pump. All the physical pump walls are modeled as a no slip condition. The turbulent flow is solved using shear stress transport (SST) model, the accuracy of this model was validated in many reported research (Chalghoum et al. 2016). For steady-state numerical calculation, a multiple frame reference (MFR) approach is applied in order to couple the rotation and stationary domains (impeller and volute).

The results of the steady calculation are taken as the initial flow field in unsteady flow calculation. For unsteady calculation, transient rotor–stator interface is set to connect impeller and volute parts. The predicted pump performance curve for both steady and unsteady calculation was obtained by changing the flow rate values.

3 Analysis of Numerical Results

3.1 Experimental Validation of the CFD Simulations

To approve the accuracy of the obtained numerical results, Fig. 2 shows a comparison of the experimental and the numerically predicted performance curve of the pump using steady and unsteady computation. The unsteady results are plotted after averaging the obtained values of a whole cycle. As it can be seen from Fig. 2, the external characteristics curve from the unsteady model exhibits good agreement with the experimental results for a wide range of operating flow rates ($0.5Q_n$, 0.8 Q_n, Q_n, and $1.2Q_n$).

At the nominal flow rate Q_n, the difference between the experimental and the numerical head curve is about 0.3 m, which corresponds to an error less than 0.6%. In addition, for the numerical performance curve obtained with the steady state computation, the calculation error is much larger compared to unsteady and experimental results. At the rated condition, the calculation error is about 7.9%. These errors increase due to the disability of the steady computation to capture

Fig. 2 Experimental and numerical head characteristic of the pump
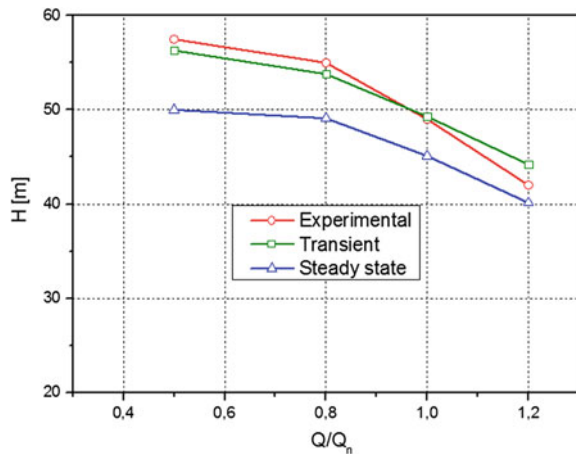
some additional flow instabilities. However, the unsteady numerical analysis is used to capture the complex phenomena and to treat them at off-nominal conditions, which yields to a high calculation precision with this method.

3.2 Design of Volutes with Different Diffuser Shapes

3.2.1 Head Curve

Figure 3 is a comparison between the head curve, obtained from CFD calculations, in both cases of radial and tangential diffusers. It can be noticed that the head obtained with the radial diffuser is slightly lower than in the case of the tangential diffuser. At nominal flow rate and at high flow rates, the radial diffuser gives a slightly higher head.

3.2.2 Transient Head Fluctuations

Figure 4 shows the total head variations over one impeller revolution for two diffuser shapes under nominal flow rates conditions. It can be noticed that there are different wave peaks and troughs, and the value of each peak and trough varies. The explanation for the peaks appearance in unsteady head is that the number of impeller blades is five. The appearance of the latter phenomenon is mainly due to the presence of unsteady and complex flow field inside the pump. For radial diffuser types, the amplitude variation of the total head curve is smaller than when a tangential diffuser is used.

Fig. 3 Head curve for radial and tangential diffuser
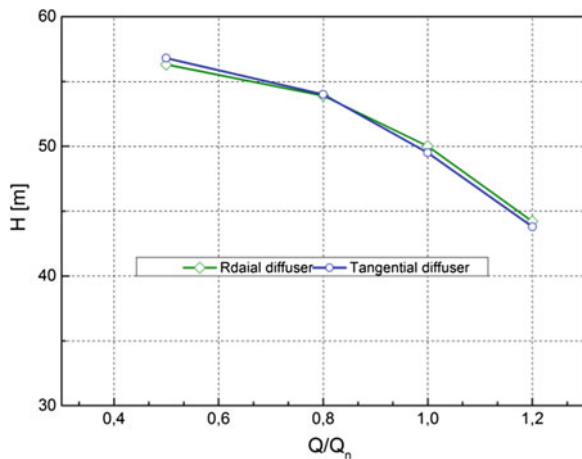
Fig. 4 Temporal evolution of
the nominal transient head
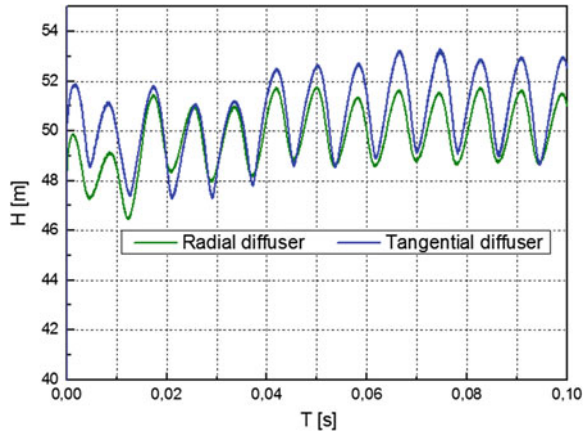
3.2.3 Radial Force

In this section, the magnitude of the radial force (steady and unsteady components) was computed by means of a full integration of the pressure distribution around the impeller's periphery (Fig. 5a, b). According to the results of Fig. 5a, the magnitude of the steady component of the radial force changes with pump flow rate values. It is observed that the radial force magnitude reaches a minimum value at the nominal condition for both diffuser shapes. This force is especially high outside nominal flow rate. The time evolution of the unsteady radial force is presented in Fig. 5b for both diffusers. According to the results of Fig. 5b, the magnitude of the unsteady components of the radial force changes periodically with times.

The results indicated that a higher pulsation of the radial force is expected for a pump with tangential diffuser.

3.2.4 Unsteady Pressure Pulsations

To investigate the effect of the diffuser shape on unsteady pressure pulsation characteristics, pressure signals in the pump are achieved using nine measurement points (Fig. 6).

All simulations are conducted at nominal condition. These points are located at impeller passage (four points) and at volute wall (five points). Figure 7 shows the monitored pressure fluctuation during five-impeller rotation. The two diffuser shapes present a similar dependence between distribution of pressure amplitude and measurement locations in pump. It can be seen that the pressure amplitude increases gradually from Pi1 to Pi4 (inlet to outlet of the impeller). As observed from Fig. 7, the interactions between the impeller and volute have increasing effects as the impeller radius increases. For radial diffuser shape, the pressure fluctuation curves for the first three measurement points (Pi1, Pi2, and Pi3) are flat, but from monitor

Fig. 5 Steady and unsteady radial force for radial and tangential diffuser
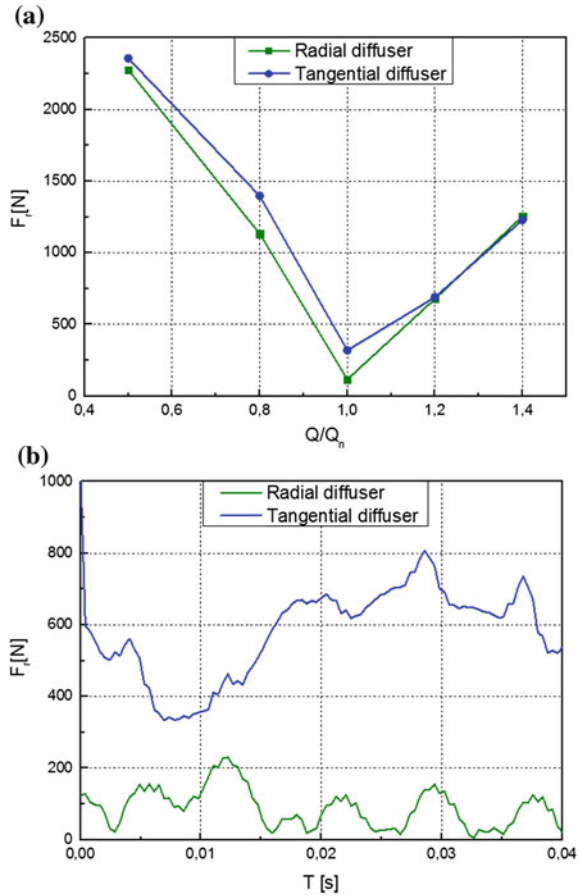
Pi4 peaks start appearing. These peaks appear with large amplitudes on each measurement points for tangential diffuser. Therefore, it is concluded that the rotor–stator interactions have more effects on the impeller for a pump with tangential volute than on a pump with a radial diffuser. In general, pressure fluctuation amplitudes, at all monitor points in an impeller, are higher and more important for a tangential diffuser than a radial diffuser.

It is indicated that the pressure fluctuations are dominant at all points at the rotation frequency ($f_r = 24.48$ Hz). For the tangential diffuser, the amplitudes of pressure fluctuations at nominal flow rate were much larger than in the case of a radial diffuser. For both diffuser types of volute, the maximum pressure pulsation is reached at the exit of the impeller (Pi4) on the location near the volute tongue zone, in which the interaction between blade and volute tongue have more and more important. Figure 7 indicates that the amplitude of pressure fluctuations at all measurement locations for tangential volute is larger than in the case of a radial diffuser.
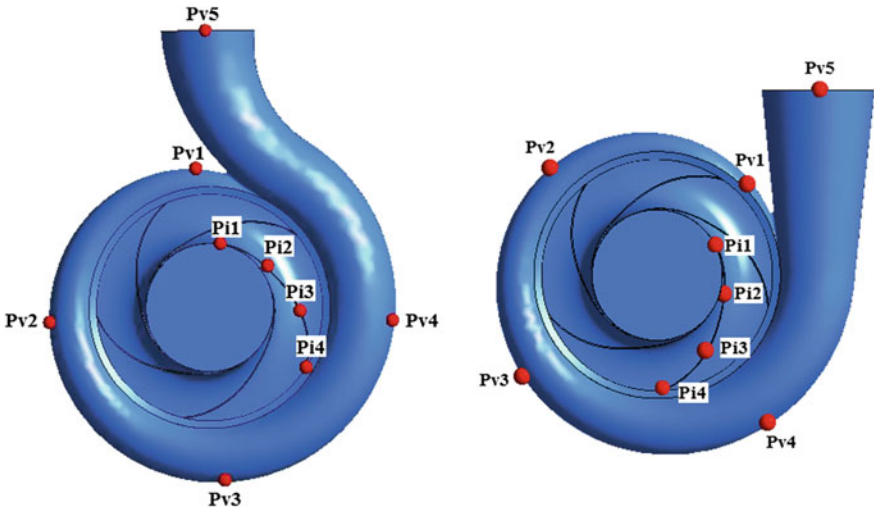
Fig. 6 Pump scheme with location of the measurement points
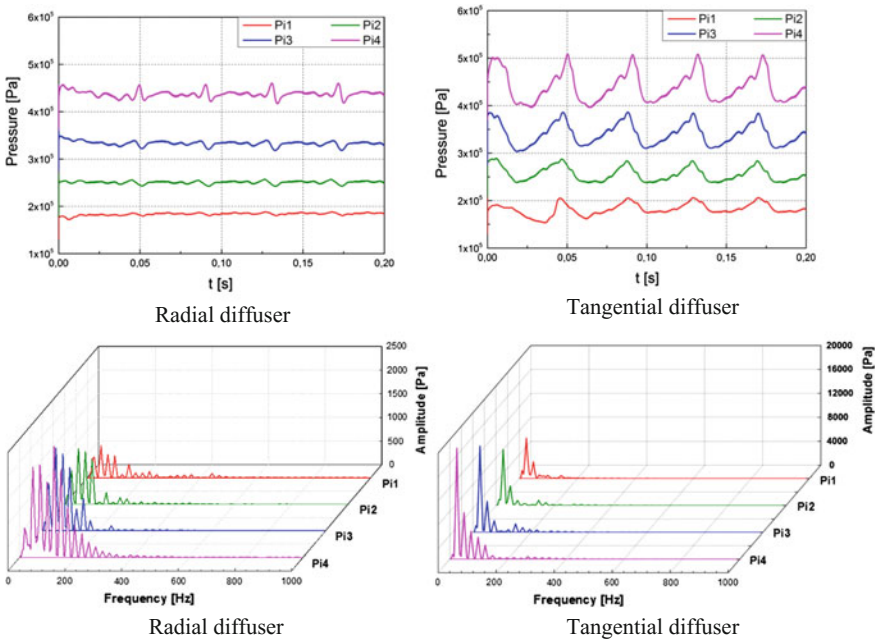
Fig. 7 Pressure fluctuation at the impeller in time and frequency domain curves

Radial diffuser   Tangential diffuser
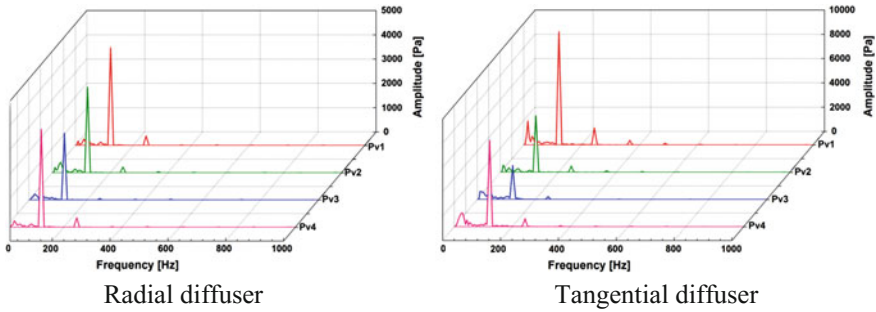
Fig. 8 Pressure fluctuation at the volute wall in frequency domain curves

For both diffuser types, the results demonstrate that the pressure fluctuations dominate at the blade-passing frequency ($f_{BPF} = z \times f_r = 122.49$ Hz) at all locations. For the two diffuser types, Fig. 8 indicates that the maximum pressure fluctuations are reached on location Pv1, which is relatively close to the volute tongue. The amplitude of the pressure fluctuation at the blade-passing frequency significantly increases in the tangential diffuser when compared to the radial diffuser case. The pressure fluctuations registered around the volute wall are strongly dependent on the volute diffuser geometry.

4 Conclusion

In this study, the effect of the volute diffuser on global and local performance curves was investigated using unsteady numerical simulation. The influence of the volute diffuser shape on the performance, radial force, and pressure pulsations in a centrifugal pump is studied using a numerical method. Furthermore, an analysis of the pressure fluctuation in time and frequency domains for both diffuser types of volute was performed. The magnitude of the total radial force and pressure fluctuation on the impeller was estimated for both diffuser shapes under rated condition. Moreover, the pressure pulsation signals are computed by mounting nine measurement points on the impeller and volute walls. The pressure spectrum characteristics are obtained by FFT analysis. Based on pump performance characteristics obtained using radial and tangential diffuser shape, a slightly difference was observed. At nominal flow rate, the amplitude of the unsteady radial force obtained using tangential diffuser is greatest than for the radial diffuser. It is observed that the pressure pulsation amplitudes at the impeller are increased by utilizing the tangential diffuser shape.

References

Brennen CE (1994) Hydrodynamics of pumps. Concept ETI/Oxford University Press, Oxford, UK

Chalghoum I, Kanfoudi H, Elaoud S, Akrout M, Ridha Z (2016) Numerical modeling of the flow inside a centrifugal pump: influence of impeller-volute interaction on velocity and pressure fields. Arab J Sci Eng 14(11):4463–4476. https://doi.org/10.1007/s13369-016-2157-8

Dawes WN, Dhanasekaran PC, Demargne AA, Kellar WP, Savill AM (2001) Reducing bottlenecks in the CAD-to-mesh-to-solution cycle time to allow CFD to participate in design. ASME J Turbomach 123:552–557. https://doi.org/10.1115/1.1370162

Dwayne AB, Steven LC, David RD (2005) Vortex shedding from a hydrofoil at high reynolds number. J Fluid Mech 531:293–324. https://doi.org/10.1017/S0022112005004076

Keller J, Parrondo J, Barrio R, Fernández J, Blanco E (2014) Effects of the pump-circuit acoustic coupling on the blade-passing frequency perturbations. Appl Acoust 72:150–156. https://doi.org/10.1016/j.apacoust.2013.06.009

Majidi K (2005) Numerical study of unsteady flow in a centrifugal pump. ASME Turbo Expo 2004: Power for Land, Sea, and Air (5):805–814. https://doi.org/10.1115/GT2004-54099

Mosallem MM (2008) Numerical and experimental investigation of beveled trailing edge flow fields. J Hydrodyn 20(3):273–279

Parrondo J, Pérez J, Barrio R, González J (2011) A Simple acoustic model to characterize the internal low frequency sound field in centrifugal pumps. Appl Acoust 72:59–64. https://doi.org/10.1016/j.apacoust.2010.08.005

Spence R, Amaral Texeira J (2009) A CFD parametric study of geometrical variations on the pressure pulsations and performance characteristics of centrifugal Pump. Comput Fluids 38 (6):1243–1257. https://doi.org/10.1016/j.compfluid.2008.11.013

Torabi R, Nourbakhsh SA (2011) Hydrodynamic design of the volute of a centrifugal pump using CFD ASME-JSME-KSME joint fluids engineering conference, Hamamatsu, Shizuoka, Japan, vol 24–29, pp 423–427. https://doi.org/10.1115/AJK2011-06077

Yang SS, Liu HL, Kong FY, Xia B, Tan LW (2014) Effects of the radial gap between impeller tips and volute tongue influencing the performance and pressure pulsations of pump as turbine. ASME J Fluids Eng 136(5):054501. https://doi.org/10.1115/1.4026544

Zhang W, Yu YC, Chen HX (2009) High performance computing and applications. Springer, German, pp 571–578

Zhu BS, Lei J, Cao SL (2007) Numerical simulation of vortex shedding and lock-in characteristics for a thin cambered blade. ASME J Fluids Eng 129(10):1297–1305

Multi-criteria Decision-Making Approaches for Facility Layout (FL) Evaluation and Selection: A Survey

Mariem Besbes, Roberta Costa Affonso, Marc Zolghadri, Faouzi Masmoudi and Mohamed Haddar

Abstract Facility Layout Problem (FLP) is concerned to arrange facilities efficiently within the available floor area in order to operate in an efficient way. So, the aim of this paper is to provide a survey related to the criteria that affect the effectiveness of a facility layout. The design criteria can be classified according to the previous research into two categories which are qualitative and quantitative indicators. Then, this paper presents a review of different Multi-Criteria Decision-Making (MCDM) techniques that have been proposed in the literature to pick the most suitable layout design. These methods are particularly suitable to deal with complex situations, including various criteria and conflicting goals which need to be optimized simultaneously. The review serves as a guide to those interested in how to evaluate and select the most appropriate layout which can handle an expanded range of manufacturing companies. Finally, we present a discussion followed by a conclusion.

Keywords Multi-criteria decision-making · Facility layout evaluation
Facility layout design selection · Survey

M. Besbes (✉) · R. C. Affonso · M. Zolghadri
Quartz-Supmeca, 93407 Saint-Ouen, France
e-mail: mariem.besbes@supmeca.fr

R. C. Affonso
e-mail: roberta.costa@supmeca.fr

M. Zolghadri
e-mail: marc.zolghadri@supmeca.fr

M. Besbes · F. Masmoudi · M. Haddar
University of Sfax, LA2MP-ENIS, B.P 1173, 3038 Sfax, Tunisia
e-mail: faouzi.masmoudi@enis.run.tn

M. Haddar
e-mail: mohamed.haddar@enis.rnu.tn

1 Introduction

The layout problem is concerned with finding the most efficient arrangement of the facilities with the available floor area, evaluating the layout design alternatives and selecting the most appropriate design as illustrated in Fig. 1. The layout design problem can have a significant impact on the overall effectiveness of the manufacturing systems. Hence, it has been an active research area for several decades. A lot of research has been dedicated to present the different approaches for the generation of layout. Detailed review is provided by Kusiak and Heragu (1987), Meller and Gau (1996), Singh and Sharma (2006), Drira et al. (2007) and Nordin and Lee (2016). However, no research has been found to survey the multi-criteria layout evaluation and selection approaches through a literature review since except (Lin and Sharp 1999). The aim of this proposed study is to present a survey about the criteria and the techniques considered by the decision-makers for evaluating and selecting the most appropriate layout. Hence, we will study the part B as shown in Fig. 1. This paper is organized as follows: Sect. 2 describes the evaluating criteria. Section 3 provides an overview of the multi-criteria decision approaches. An analysis of the current and future trends is discussed in Sect. 4 followed by a conclusion.

2 Overview of the Evaluating Criteria

In this section, we summarize the principal criteria found in the collected papers for the evaluation and selection of a new configuration among a set of available alternatives. These criteria can be classified into two categories: quantitative and qualitative.
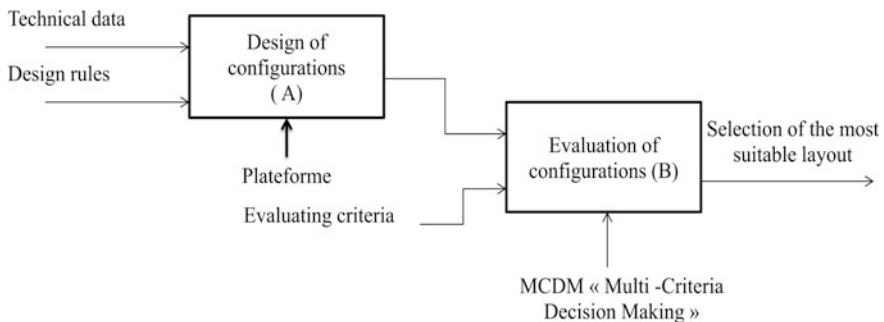
Fig. 1 Conceptual framework of facility layout problem

2.1 Quantitative Criteria

Distance is the most popular criterion considered by the designer for the evaluation of configurations. It was determined by the sum of the products of flow volume and rectilinear distance between the centroids of two facilities as shown in Eq. 1. There is two ways for measuring the distances: distance between Input/Output (I/O) points or centroid to centroid. The main objective function for facility layout problem is to minimize the material handling cost according to the travelled distance because handling work adds to cost but does not increase value to products; consequently any unnecessary movements should be avoided.

$$Cost = \sum_i \sum_j f_{ij} * d_{ij} \qquad (1)$$

Note that: f_{ij} is the material flow between the facilities i and j.

d_{ij} is the distance between facilities.

Adjacency of facilities is highly suggested due to some factors such as noise, vibration, luminosity, sharing of operators or tools and flow exchange density or frequency. It was determined by the sum of all positive relationships between adjacent facilities as shown in Eq. (2).

$$Adjacency = \sum_i \sum_j r_{ij} * l_{ij} \qquad (2)$$

Note that r_{ij} is the closeness rating and l_{ij} is the contact perimeter length between facilities i and j.

Shape ratio is defined as the maximum of the depth-to width and width-to-depth ratio of the smallest rectangle that completely encloses the facilitate (Aiello et al. 2006, 2012)

Space consists of five types (Lin and Sharp 1999): space for production machinery and material handling equipment, space for storage, space for personal needs aisle space for material and personal movement and free space. Hence, the production area include value added area and non-value added area (Raman et al. 2009). It can be overused when there is not enough space for future activity or underused when the shop floor are not fully used. To examine the effectiveness of layout design, we should calculate the space utilization rate as follows (Suo 2012):

$$R_s = \frac{\sum_i A_i}{\sum_i A_i + \sum_j B_j} \qquad (3)$$

Note that A_i is the area of department i where equipment i is sitting and B_j is the unusable space.

Products indicators are associated to throughput time, product earliness, product lateness, and product blocked time. Ben cheikh (2015, 2016) defined the throughput

time as the period required for a single product to be produced. The product earliness is calculated when the product is finished before its due date. However, the product lateness is computed when the product is finished after its due date. These indicators are evaluated using event simulation software like Arena, Witness, ProModel. Product blocked time is the waiting time for the product in the queue until loaded on the machine to be processed.

Resources indicators are related to machine utilization, the number of machine, and the number of operators that are used in a configuration.

Work in process is the set of unfinished items waiting for further processing in a queue or buffer storage. Optimal configuration aims to minimize work in process. In fact, it requires storage space and cost. It affects the production rates by slowing at bottlenecks.

2.2   Qualitative Criteria

Flexibility is defined as the ability of the company to adapt to changes in its environment. In fact, flexibility is the ability to achieve a variety of tasks under a wide range of operating conditions. We find several type of flexibility:

Volume flexibility is defined as the ability to function profitably at different production volumes. This can be done by changing the number of facilities for example.

Routing flexibility is described as the ability of a product to change path during the production process.

Expansion flexibility is defined as the ease of increasing the production capacity of a production system. It can be quantified by the number of free space locations with good shape factors or usable area (Raman et al. 2009).

Accessibility has been defined by Yang and Hung (2007) as the material handling and operators paths. While designing the layout, we should save enough space within or along the contours of the departments to allow the movement of materials and personnel. Moreover, all servicing and maintenance points should be readily accessible. For example, equipment should not be placed against a wall in such a manner that necessary maintenance cannot easily be carried out.

Human issues cluster involves several aspects. First, it is related to the ease of supervision control and communication between workers by the elimination for example of hidden corners. Second, other criteria that are related to environment, safety, security of operators should be taken into account.

Layout reconfigurability presents a facilitating level of rearrangement and/or alteration of facilities to respond to new situations (Abdi 2009). The five main criteria of layout reconfigurability are convertibility, modularity, mobility, reconfiguration speed and scalability.

All of the criteria are not explained in the text. However, a survey of different criteria that are used in the literature to evaluate different layouts is provided in

Table 1 A summary of evaluating criteria and techniques for facility layout evaluation and selection

Authors	Shang (1993)	Abdul-Hamid et al (1999)	Yang et al (2000)	Yang and Kuo (2003)	Abdi (2005)	Ertay et al (2006)	Rahimi (2007)	Yang and Hung (2007)	Kuo et al(2008)	Abdi (2009)	Singh and Singh (2011)	Maniya and Bhatt (2011)	Shahin and Poormostafa (2011)	Lateef-UR and Ateekh-UR(2013)	Shokri et al(2013)	Vencheh et al.(2013)	Al-Hawari et al. (2014)	Ben cheikh et al (2015)	Ben cheikh et al (2016)	Wang et al. (2016)
A				✓		✓		✓	✓			✓	✓			✓	✓			✓
B				✓		✓		✓	✓			✓	✓			✓	✓			✓
C				✓		✓		✓	✓			✓	✓			✓	✓			✓
D	✓	✓	✓	✓		✓	✓	✓	✓		✓	✓	✓			✓	✓	✓		✓
E				✓				✓	✓			✓	✓			✓	✓			✓
F				✓				✓	✓			✓	✓			✓	✓			✓
G																	✓			
H		✓																		
I																		✓	✓	
J																✓				
K					✓	✓	✓				✓									
L	✓											✓	✓				✓		✓	
M															✓			✓	✓	
N															✓			✓	✓	
O	✓		✓									✓	✓							✓
P															✓			✓	✓	
Q																				✓
R					✓															
S		✓	✓					✓												
T				✓							✓									
U	✓			✓							✓									
V				✓																
W							✓				✓									

Legend

A	Distance	I	Reconfiguration time	Q	Number of machines and number of operators
B	Adjacency score	J	Productive area utilization	R	Material handling vehicle utilization and handling cost
C	Shape ratio	K	Quality	S	Productivity
D	Flexibility	L	Human issues clus-	T	Layout reconfigurability
E	Accessibility	M	Throughput time	U	Cost
F	Maintenance	N	Products indicators	V	Reliability
G	Closeness gap value cluster	O	Work in Process	W	Flow
H	Process capacity	P	Machine utilization		

Table 1 wherein 23 criteria are tabulated in columns A to w in order to give a background for the designers.

3 Multi-Criteria Analysis Techniques

While the multi-objective optimization techniques search for new solutions in solution space, multi-criteria analysis techniques consider limited number of pre-determined alternatives and discrete preference ratings (Tzeng and Huang 2011). In this section, we present the most frequently used techniques such Analytic Hierarchy Process (AHP), Analytic Network Process (ANP) and Technique for Order of Preference by Similarity to Ideal Solution (TOPSIS) and others.

3.1 Analytic Hierarchy Process

The Analytical Hierarchy Process (AHP) is a multi-criteria decision making tool developed by Saaty (1980). It can be used for both qualitative and quantitative MCDM problems. The decision problem is structured hierarchically with different levels. AHP method uses a simple paired comparison of criteria, to measure the weights of the components of the hierarchical structure, and finally to rank the alternatives in the decision. In the case of facility layout problem, Abdi (2005) applied AHP to evaluate and select the most appropriate layout. The alternative layouts are defined based on serial, parallel and hybrid configurations of three machines. The AHP hierarchy consists of four evaluating criteria and eleven sub-criteria of which the relative importance ratings were calculated based on decision-makers requirements. Ben Cheikh et al. (2016) developed an AHP-based decision making approach to select one configuration among a set of available alternatives. Configurations were evaluated based on operational and strategic indicators. AHP is used in (Abdul-Hamid et al. 1999) for the layout selection problem with respect to three criteria and ten sub-criteria in order to evaluate transfer line, group technology and functional layout against these criteria. In order to overcome the inherent uncertainty in the judgements of experts at the pair-wise comparison of selection attributes, Abdi (2009) uses fuzzy AHP to solve facility layout problem.

Some research applied integrated AHP approaches to evaluate the performance of layout and select the most suitable one. Among these articles, we find (Yang and Kuo 2003; Ertay et al. 2006) which integrate AHP and Data Envelopment Analysis (DEA). DEA is used to evaluate Decision Making Units (DMU) (Cooper et al. 2011). Each DMU convert m inputs to produce n outputs. The approach proposed by Vencheh et al. (2013) combines AHP and Nonlinear Programming (NLP) to deal with the layout selection and evaluation problem. In Shokri et al. (2013), an integrated AHP-VIKOR methodology is developed to solve facility layout design

problem. A computer-aided layout-planning tool is used to generate a number of alternatives layouts as well as their quantitative data.

3.2 Analytical Network Process

Analytical network process (ANP), which was developed by (Saaty 1996), is a more general form of the AHP used in multi-criteria decision analysis. AHP structures a decision problem into a hierarchy with objective, criteria, sub-criteria and alternatives, while the ANP structures it as a network. ANP is used for the first time in (Al-Hawari et al. 2014) to select the best layout based on dependent and independent criteria.

3.3 Technique for Order of Preference by Similarity to Ideal Solution

Technique for Order of Preference by Similarity to Ideal Solution (TOPSIS), which was developed by Hwang and Yoon (1981), is a powerful technique in dealing with multi-criteria decision making problems. It is based on choosing the best alternative having the shortest distance from the positive-ideal solution and the farthest distance from the negative-ideal solution. Yang and Hung (2007) applied TOPSIS and fuzzy TOPSIS to solve facility layout problem. The proposed methodology is applied to an IC packaging company. Wang et al. (2016) developed an integrated Simple Additive Weighing (SAW), TOPSIS and Grey Relational Analysis (GRA) for solving optimal facility layout design selection problem.

3.4 Other Techniques

Many other approaches were presented to solve facility layout problem such as PROMETHEE (Lateef-UR and Ateekh-UR 2013), ELECTRE (Ateekh-Ur and Babu 2009), Grey Relational Analysis (GRA) (Yang and Hung 2007), and Preference Selection Index (PSI) (Maniya and Bhatt 2011). (Maniya and Bhatt 2011) use PSI for the selection of optimal facility layout design alternative among given alternative. The main advantage of the PSI method is that there is no relative importance between facility layout design selection attributes. (Yang and Hung 2007) evaluate the layout with respect to three quantitative and three qualitative criteria by developing Grey Relational Analysis.

4   Discussion and Conclusion

In this paper, we presented a literature review about evaluating criteria and multi-criteria decision-making techniques for facility layout problem. First of all, it was found that distance is the most widely adopted criterion to examine the effectiveness of layouts followed by adjacency. There are other several criteria for evaluating configurations such as space, work flow and material handling cost. We cannot find a general model for all companies. Indeed, the criteria and configuration alternatives can distinct from a firm to another because of differences in product types, process flow, available technologies, economical conditions and decision-makers requirements. Besides, the feasible layouts may differ from a planning period to another.

To overcome the difficulties in selection of alternatives among a set of predetermined alternatives, researchers use a multi-criteria decision-making such as AHP, TOPSIS. These approaches share common characteristics of conflict among objectives, criteria and sub-criteria and incomparable units. Based on literature review, it was observed that AHP is the most prevalent approach for selection of the best layout due to its mathematical simplicity and flexibility. However, the main drawback is the subjectivity of judgments of experts. As a final remark, this survey can be used as a background for designers for the evaluation of layout.

Futures research may be interested in the problem of generating configurations. In fact, the commercial software available to reinforce the facility layout problems are currently restricted.

References

Abdi MR (2005) Selection of layout configuration for reconfigurable manufacturing system using the AHP. ISAHP, Honolulu

Abdi MR (2009) Layout configuration selection for reconfigurable manufacturing systems using the fuzzy AHP. Int J Manuf Technol Manag 17(1/2):149–165. https://doi.org/10.1504/IJMTM.2009.023783

Abdul-Hamid YT, Kochhar AK, Khan MK (1999) An analytic hierarchy process approach to the choice of manufacturing plant layout. Proc Inst Mech Eng Part B 213:397–406

Aiello G, Enea M (2006) Galante G (2006) A multi-objective approach to facility layout problem by genetic search algorithm and Electre method. Robot Comput-Integr Manuf 22:447–455. https://doi.org/10.1016/j.rcim.2005.11.002

Aiello G, Scalia GL, Enea M (2012) A multi objective genetic algorithm for the facility layout problem based upon slicing structure encoding. Expert Syst Appl 39:10352–10358. https://doi.org/10.1016/j.eswa.2012.01.125

Al-Hawari T, Mumani A, Momani A (2014) Application of the analytic network process to facility layout selection. J Manuf Syst 33(4):488–497. https://doi.org/10.1016/j.jmsy.2014.04.006

Ateekh-Ur and Babu (2009) Evaluation of reconfigured manufacturing systems: an AHP framework. Int J Product. Qual Manag 4(2):228–246. https://doi.org/10.1504/IJPQM.2009.023189

Ben Cheikh S, Hajri-Gabouj S, Darmoul S (2015) Reconfiguring manufacturing systems using an analytic hierarchy process with strategic and operational indicators. Ind Eng Oper Manag (IEOM). https://doi.org/10.1109/IEOM.2015.7093890

Ben Cheikh S, Hajri-Gabouj S, Darmoul S (2016). Manufacturing configuration selection under arduous working conditions: A multi-criteria decision approach. In: Proceedings of the 2016 International Conference on Industrial Engineering and Operations Management Kuala Lumpur, Malaysia, Mar 8–10

Cooper WW, Seiford LM, Zhu J, Cooper WW, Seiford LM (2011) Data envelopment analysis: history, models, and interpretations. Handbook on data envelopment analysis. Springer, US, pp 1–39

Drira A, Pierreval H, Hajri-Gabouj S (2007) Facility layout problems: a survey. Ann Rev Control 31(2):255–267. https://doi.org/10.1016/j.arcontrol.2007.04.001

Ertay T, Ruan D, Tuzkaya UR (2006) Integrating data envelopment analysis and analytic hierarchy for the facility layout design in manufacturing systems. Inf Sci 176(3):237–262. https://doi.org/10.1016/j.ins.2004.12.001

Hadi-Vencheh A, Mohamadghasemi A (2013) An integrated AHP–NLP methodology for facility layout design. J Manuf Syst 696 32(1):40–45

Hwang CL, Yoon K (1981) Multiple attribute decision making: Methods and applications. Springer, NewYork

Kuo Y, Yang T, Huang GW (2008) The use of grey relational analysis in solving multiple attribute decision-making problems. Comput Ind Eng 55(1):80–93. https://doi.org/10.1016/j.cie.2007.12.002

Kusiak A, Heragu SS (1987) The facility layout problem'. Eur J Oper Res 29(3):229–251. https://doi.org/10.1016/0377-2217(87)90238-4

Lateef-Ur R, Ateekh-Ur R (2013) Manufacturing configuration selection using multicriteria decision tool. Int J Adv Manuf Tech 65(5–8):625–639. https://doi.org/10.1007/s00170-012-4201-5

Lin LC, Sharp GP (1999) Quantitative, and qualitative indices for the plant layout evaluation problem. Eur J Oper Res 116:118–138. https://doi.org/10.1016/S0377-2217(98)00046-0

Maniya KD, Bhatt MG (2011) An alternative multiple attribute decision making methodology for solving optimal facility layout design selection problems. Comput Ind Eng 61:542–549. https://doi.org/10.1016/j.cie.2011.04.009

Meller RD, Gau K (1996) The facility layout problem: Recent and emerging trends and perspectives. J Manuf Syst 15(5):351–366. https://doi.org/10.1016/0278-6125(96)84198-7

Nordin NN, Lee L-S (2016) Heuristics and metaheuristics approaches for facility layout problems: a survey. Pertanika J Sch Res Rev PJSRR 2(3):62–76

Rahimi N (2007) Outil d'aide à la décision pour l'aménagement des ressources de production d'une entreprise d'assemblage de cartes électroniques (pcba, "grande variété, faible volume"), Dissertation, université du Québec à Montréal

Raman D, Nagalingam SV, Lin GCI (2009) Towards measuring the effectiveness of a facilities layout. Robot Comput-Int Manuf 25/191–203. https://doi.org/10.1016/j.rcim.2007.06.003

Saaty TL (1980) The analytic hierarchy process. McGraw-Hill, New York

Saaty TL (1996) Decision making with dependence and feedback: the analytic net-work process. RWS Publications, Pittsburgh, PA

Shahin A, Poormostafa M (2011) Facility layout simulation and optimization. An integration of advanced quality and decision making tools and techniques. Mod Appl Sci 5(4):95. https://doi.org/10.5539/mas.v5n4p95

Shang JS (1993) Multi-criteria facility layout problem: an integrated approach. Eur J Oper Res 66(3):291–304. https://doi.org/10.1016/0377-2217(93)90218-C

Shokri H, Ashjari B, Saberi M, Yoon JH (2013) An integrated AHP. VIKOR methodology for facility layout design. Ind Eng Manag Sys 12(4):389–405. https://doi.org/10.7232/iems.2013.12.4.389

Singh SP, Sharma RRK (2006) A review of different approaches to the facility layout problems. Int J Adv Manuf Technol 30:425–433. https://doi.org/10.1007/s00170-005-0087-9

Singh SP, Singh VK (2011) Three-level AHP-based heuristic approach for a multi-objective facility layout problem. Int J Prod Res 49(4):1105–1125. https://doi.org/10.1080/00207540903536148

Suo X (2012) In: Aziz FA (ed.) Facility layout, manufacturing system [en línea]. ISBN: 978-953-51-0530-5

Tzeng G-H, Huang JJ (2011) Multiple attribute decision making: methods and applications. CRC Press, Boca Raton, FL

Wang P, Zhu Z, Wang Y (2016) A novel hybrid MCDM model combining the SAW, TOPSIS and GRA methods based on experimental design. Inf Sci 345(1):27–45. https://doi.org/10.1016/j.ins.2016.01.076

Yang T, Su CT, Hsu YR (2000) Systematic layout planning: A study on semiconductor wafer fabrication facilities. Int J Oper Product Manag 20(11):1360–1372. https://doi.org/10.1108/01443570010348299

Yang T, Kuo CA (2003) A hierarchical AHP/DEA methodology for the facilities layout design problem. Eur J Oper Res 147(1):128–136. https://doi.org/10.1016/S0377-2217(02)00251-5

Yang T, Hung CC (2007) Multiple-attribute decision making methods for plant layout design problem. Robot Comput Int Manuf 23:126–137. https://doi.org/10.1016/j.rcim.2005.12.002

Effect of the Radial Flow and Average Molecular Weight on the Surface Defect in PDMS Extrusion

M. Ketata, A. Ayadi, Ch. Bradai and N. Elkissi

Abstract This study examines the role of both a radial flow created at the entrance of the die and the average molecular weight of polymer, on the appearance and development of the sharkskin defect. To do so, three linear polydimethylsiloxanes (PDMS) of different viscosities and molecular weights were considered. A convergent radial flow was created at the entrance zone by imposing a rod upstream the die. It was found, that when the radial flow is well established in the entrance zone (i.e., for very low gaps between the bottom of the rod and the plane of the die) the onset of sharkskin defect can be translated to higher flow rate. As the influence of molecular weight of polymer, it was shown that the extrusion of lower molecular weight PDMS can delay the occurrence of sharkskin instability. Besides, it was remarked that the morphology of the extrudate associated to the trigger of surface defect is not affected with the presence of radial flow in the entrance region or with the molecular weight of the extruded polymer.

Keywords Radial flow · Molecular weight · Polydimethylsiloxane Sharkskin defect

M. Ketata (✉) · Ch. Bradai
LASEM National Engineering School of Sfax, B.P. W3038, Sfax, Tunisia
e-mail: ketata_manel@yahoo.fr

Ch. Bradai
e-mail: abdelhak.ayadi@gmail.com

A. Ayadi
CFDTP National Engineering School of Sfax, B.P. W3038, Sfax, Tunisia
e-mail: chedly20412517@gmail.com

N. Elkissi
Laboratory of Rheology and Process, UMR, 5520—UJF—38041 Grenoble Cedex 9, France
e-mail: nadia.elkissi@ujf-grenoble.fr

623

1 Introduction

Many processing operations with synthetic polymers are still disturbed by extrusion instabilities. These instabilities can affect the surface or the whole volume of the extruded material. Industrially, the surface instability also called as sharkskin is the most embarrassing instability as it concerns the whole family of linear polymers and it comes at low flow rates.

In the literature, there are three possible interpretations of the origin of sharkskin defect: The first one which is known as exit stick-slip considers that the surface instability is due to a periodic slip boundary condition at the die (Vinogradov and Malkin 1980; Ramamurthya 1988; Barone et al. 1998). The second interpretation has been proposed by Cogswell (1977) and Migler et al (2002). They hypothesized that the surface melt fracture at the die exit is due to high extensional stresses developed at this location caused by a sudden change of the velocity profile of polymer melt from a parabolic shape inside the die region to an almost plug profile as it emerges from the die. Allal et al (2005) have found that the magnitude of the stretch stresses and the stresses of the transition low slip-strong slip are similar which can explain the near-simultaneous occurrence of both phenomena.

In fact, several parameters influence the development of sharkskin defect: temperature, die geometry, upstream geometry, molecular structure.

Regarding the molecular effects, it seems that the critical stress for the onset of sharkskin decreases by increasing the average molecular weight M_w (Vlachopoulos and Alam 1972; Goyal et al. 1997). Conversely, other researchers have shown a weak dependence on Mw (Kazatchkov et al. 1999; Fujiyanna et al. 2002)

In the present work, we are interested in the influence of convergent radial flow imposed upstream the die and the average molecular weight of the extruded polymer on the appearance and evolution of sharkskin instability.

2 Experimental Facilities

2.1 Fluids Used

Three linear polydimethylsiloxanes (PDMS) are tested in this study. These polymers have the advantage of being transparent and melted at room temperature, and, thus, heat application is not necessary to perform extrusion.

The rheological characterization of these PDMS has been reported by Ketata et al. (2017). The least viscous PDMS the density of which is 0.978 posses a molecular weight M_w of 396000 g/mol, a polydispersity of 2.37 and a plateau viscosity at 23 °C η_0 of 1180 Pa.s. The second considered PDMS the density of which is 0.978 posses a molecular weight of 479000 g/mol, a polydispersity of 3.01 and a plateau viscosity at 23 °C η_0 of 2630 Pa.s. The most viscous PDMS which

density is 0.978 posses a molecular weight of 958000 g/mol, a polydispersity of 2.94 and a plateau viscosity η_0 of 29000 Pa.s at a temperature of 23 °C.

2.2   Experimental Apparatus

The tested fluid is held in a reservoir and forced to flow through a capillary die by a flux of pressurized nitrogen (Fig. 1). The experiments are run under constant pressure condition and are performed at room temperature.

The mentioned reservoir is achieved of transparent Plexiglass. Its internal diameter is 20 mm and its height is 100 mm. A die made of extruded aluminum, 2 ± 0.03 mm in diameter and 1 ± 0.05 mm in length is fixed to the end of the reservoir. To obtain a radial flow at the entrance of the die, a stainless steel rod, 10 mm in diameter, is introduced in the reservoir. The gap width of the radial flow is the field between the extremity of the rod and the plane of the die. Finally, the extruded fluid is directly timed and weighed and then the average mass flow rate is evaluated.

Fig. 1 Experimental set up
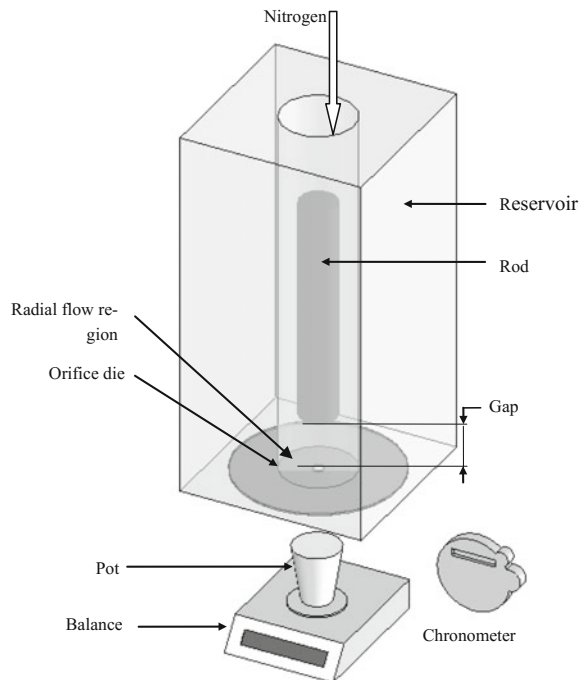
3 Results

3.1 *Effect of Radial Flow on the Surface Defect*

Figure 2 displays the variation of the imposed pressure drop as a function of the measured mass flow rate for the three PDMS melts flowing through the orifice die $(D = 2\,\text{mm}, \ L/D = 0.5)$, with and without rod at the entrance zone. The onset of sharkskin instability is indicated by arrows on the flow curves.

Figure 2 shows that for the three PDMS, the surface defect is triggered almost or the same flow rate value for extrusion through gaps greater than 1 mm. For gaps less than 1 mm, experiments with the PDMS-3 show that more the gap is essenced more the critical flow rate of the occurrence of sharkskin is higher. In fact the critical flow rate of the onset of sharkskin defect associated to the extrusion of PDMS-3 through the gap 0.15 mm $(1.8\ 10^{-3}\ \text{g/s})$ is almost 2.5 more important than the average critical flow associated to the extrusion through gaps superior to 1 mm.

Figure 3 exhibits photographs corresponding to the triggering of sharkskin defect of the three PDMS extruded through different gap width of radial flow.
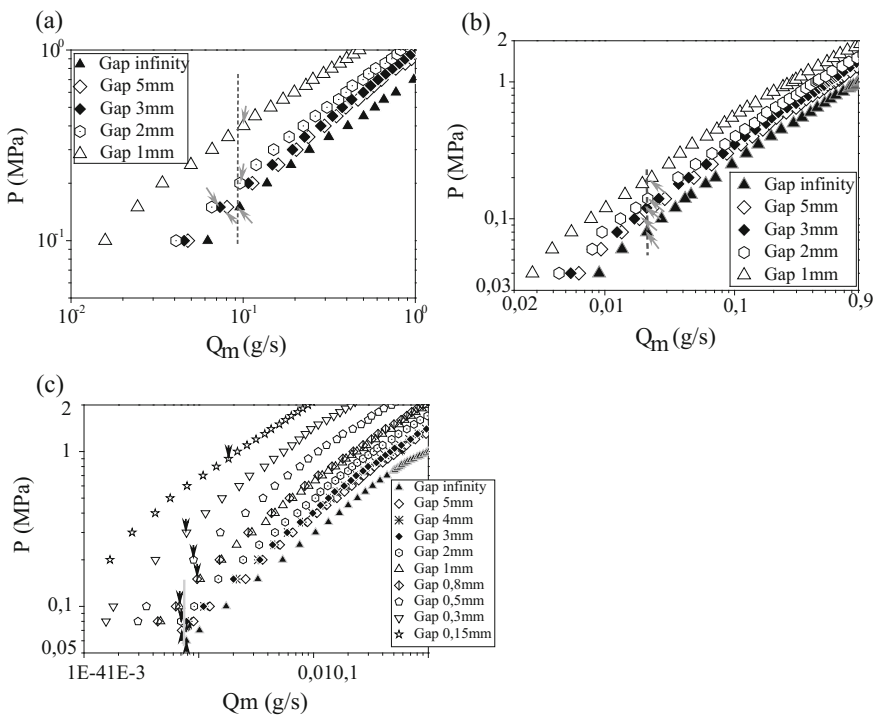
Fig. 2 Flow curves obtained through different gaps at low pressure **a** for PDMS-1, **b** for PDMS-2, **c** for PDMS-3

(a)

Gap infinity
P=0,15 MPa
Q_m=9,5$10^{-2}$ g/s

Gap 3mm
P=0,15 MPa
Q_m=7,3$10^{-2}$ g/s

Gap 1mm
P=0,3 MPa
Q_m=7$10^{-2}$ g/s

(b)

Gap infinity
P=0,08 MPa
Q_m= 2 10^{-2} g/s

Gap 3 mm
P=0,12 MPa
Q_m= 2,1 10^{-2} g/s

Gap 1 mm
P=0,12 MPa
Q_m= 2,3 10^{-2} g/s

(c)

Gap infinity
P=0,06 MPa
Q_m= 7,6 10^{-4} g/s

Gap 1 mm
P=0,1 MPa
Q_m= 7 10^{-4} g/s

Gap 0,3 mm
P=0,3 MPa
Q_m= 9,2 10^{-4} g/s

Gap 0,15 mm
P=0,9 MPa
Q_m= 1,8 10^{-3} g/s
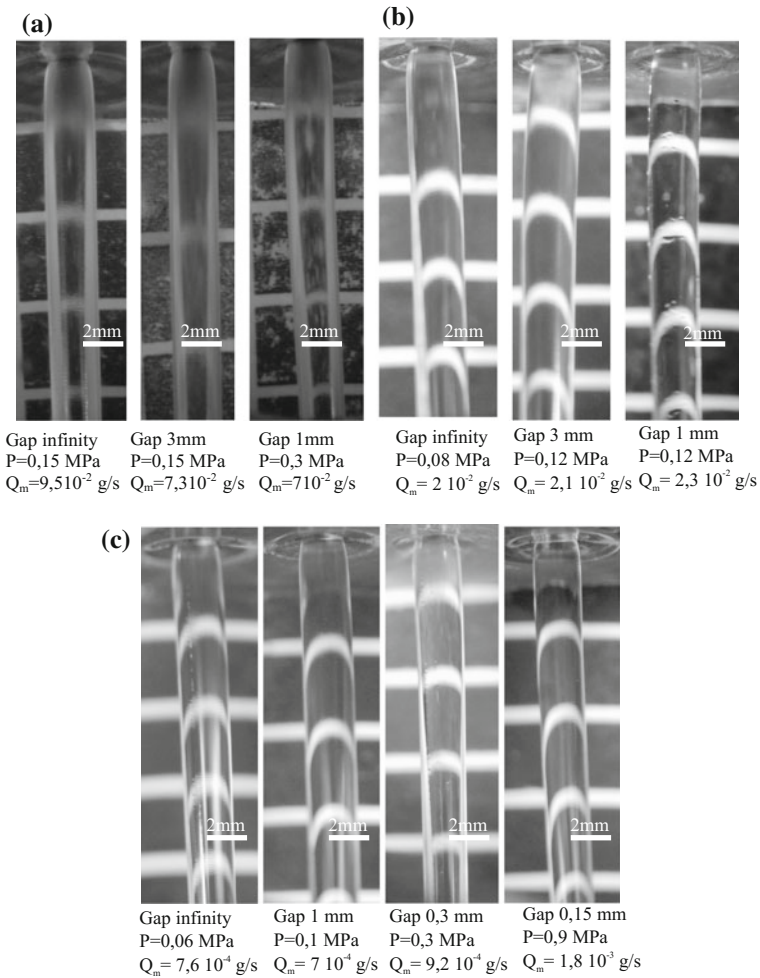
Fig. 3 Photographs associated to the onset of sharkskin defect **a** of PDMS-1, **b** of PDMS-2, **c** of PDMS-3

We remark in this figure (Fig. 3) that the morphology of the extrudate associated to the onset of sharkskin defect is not very affected with the presence of radial flow in the entrance region: it is almost the same translucency and sense of cracking.

Therefore, the radial flow "well" imposed upstream the die can affect only the triggering of the surface instability.

The delay of the occurrence of sharkskin defect can be explained by the state of stresses in the entrance region caused by the imposition of the radial flow upstream the die. In fact, in a previous study (Ayadi et al. 2011; Elgasri et al. 2011), it was demonstrated that the decrease of the gap width of radial flow increases shear with regard to elongation upstream the contraction. Thus, for a well-established radial
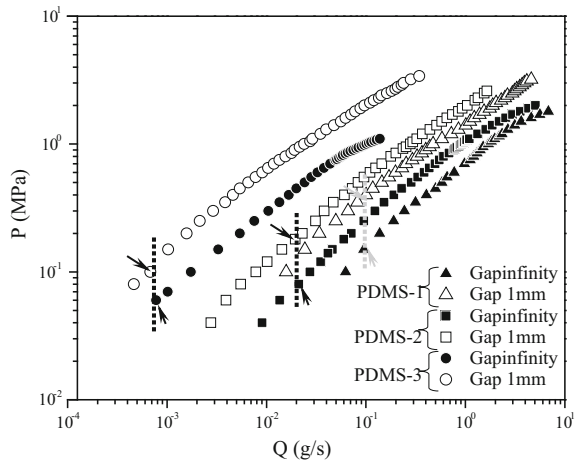
flow (the case of very low gap), shear is dominant and elongation is less pronounced. That causes the translation of the appearance of surface defect to higher flow rate, i.e., when the critical elongational stress is reached.

3.2 Effect of Molecular Weight on the Surface Defect

Figure 4 displays the variation of the imposed pressure drop as a function of the measured mass flow rate for the three PDMS melts flowing through the capillary die $(D = 2mm; L/D = 0.5)$, with and without rod at the die entrance.

What can be observed in Fig. 4 is that the onset of sharkskin instability can be translated to higher flow rate with the extrusion of PDMS possessing low molecular weight. This can be associated to the mobility of the chain of the extruded polymer. In other words, with a lower molecular weight, the chain mobility is decreased and as a consequence the critical stretch stress of the appearance of the surface defect is early reached.

Besides, we note that there is no significant effect of molecular weight on the extrudate morphology (Fig. 3).

4 Conclusion

Three linear PDMS were used to study the effect of geometry entrance and molecular structure on their surface melt fracture behavior. It was found that the occurrence of sharkskin defect can be delayed with the extrusion of PDMS possessing low molecular weight as with the extrusion through small gaps of radial

flow. In fact, the effect of the radial flow was associated to shear enhanced with regard to the elongation upstream the contraction. This interpretation comforts the literature (Cogswell 1977; Migler et al 2002) which associates the trigger of surface melt fracture to high extensional stresses developed at the die exit.

References

Allal A, Lavernhe A, Vergnes B, Marin G (2005) Relation entre structure moléculaire et défaut de peau de requin pour les polymères linéaires à l'état fondu. Rhéologie 8:31–43

Ayadi A, Elgasri S, Mezghani A, Castro M, Elhaouani F (2011) Effect of radial flow in the die entrance region on gross melt fracture of PDMS extrudate. J Non Newtonian Fluid Mech 166:661–666

Barone IK, Plucktaveesak N, Wang SQ (1998) Interfacial molecular instability mechanism for sharkskin phenomenon in capillary extrusion of linear polyethylene. J Rheol 42:4

Cogswell FN (1977) Stretching flow instabilities at the exit of extrusion dies. J Non-Newt Fluid Mech 2:37–47

Elgasri S, Ayadi A, Elhalouani F (2011) Effect of die geometry on helical defect during extrusion of PDMS across a radial flow upstream the contraction. J Non-Newt Fluid Mech 166:1415–1420

Fujiyanna M, Kitajima Y, Inata H (2002) Rheological properties of polypropylenes with different molecular weight distribution characteristics. J Appl Polym Sci 84(12):2128–2141

Goyal SK, Kazatchkov IB, Bohnet N, Hatzikiriakos SG (1997) Influence of molecular weight distribution on the rheological behavior of LLDP resins. In: Proceedings of the Antec'97-Plastics saving planet earth, conference, 1–3:1076-80

Kazatchkov IB, Bohnet N, Goyal SK, Hatzikiriakos SG (1999) Influence of molecular structure on the rheological and processing behavior of polyethylene resins. Polym Eng Sci 39(4):804–815

Ketata M, Ayadi A, Elkissi N, Bradai Ch (2017) Effect of rheological and physical properties on mitigation of melt fracture instability during extrusion of polymer melts through a radial flow die. Rheol Acta 56:341–350

Migler KB, Son Y, Qiao F, Flynn K (2002) Extensional deformation, cohesive failure and boundary conditions during sharkskin melt fracture. J Rheol 46(2):383–400

Ramamurthya V (1988) Exmidate impularities and the polymer-metal interface connection. In: Proceedings of 10th international. congress rheology, Sydney

Vinogradov GV, Malkin AYa (1980) Rheology of polymers. Springer, p 764

Vlachopoulos J, Alam M (1972) Critical shear for polymer melt fracture. Polym Eng Sci 12(3):184

DSC Investigation on Entropy and Enthalpy Changes in Ni-Rich NiTi Shape Memory Alloy at Various Cooling/Heating Rates

Boutheina Ben Fraj, Slim Zghal and Zoubeir Tourki

Abstract The aim of this work is to experimentally investigate the effect of the cooling/heating rate on both entropy and enthalpy changes during the phase transformation of the Ni-rich NiTi Shape Memory Alloy (SMA). The thermal analysis was performed at zero stress using the Differential Scanning Calorimetry (DSC) technique. From the obtained calorimetric results, it was found that the transformation temperatures are considerably sensitive to the cooling/heating rate variation, mainly the finish temperature of the forward martensitic transformation (M_f). Accordingly, it was shown that enthalpy and entropy changes, during the phase transformation process, are strongly affected by the change of this parameter. Based on Gibbs fundamental equation, the evolution of the Gibbs free energy change was also discussed. The findings of this study can be useful to predict the evolution of the critical stress–temperature diagram. Indeed, the enthalpy change describes the evolution of the diagram slopes as function of the cooling/heating rate which allows to limit each occurred transformation domain and defines the material mechanical behavior whether superelasticity or shape memory.

Keywords DSC · Cooling/heating rate · NiTi SMA · Entropy · Enthalpy

B. B. Fraj (✉) · Z. Tourki
Mechanical Laboratory of Sousse (LMS), National Engineering School
of Sousse ENISo, University of Sousse, 4023 Sousse, Tunisia
e-mail: bfb.ingmec@gmail.com

Z. Tourki
e-mail: zbrtourki@gmail.com

S. Zghal
Laboratory of Multifunctional Materials and Applications (LaMMA),
Faculty of Sciences of Sfax, University of Sfax, BP 1171, 3000, Sfax, Tunisia
e-mail: salim_zghal@yahoo.fr

631

1 Introduction

When we talk about NiTi shape memory alloy (SMA), it is unavoidable to cite its two famous superelastic and shape memory effects. These two unique properties are vitally based on the martensitic transformation between both high and low temperature phases, austenite and martensite, respectively. This phase transformation occurs under a thermal and/or mechanical loading.

First of all, to investigate the NiTi SMA thermomechanical behavior, the determination of its transformation temperatures is necessary. These transformation temperatures have a key role in the NiTi thermal characterization since they indicate the beginning and the end of each phase transformation, forward (A-M) and reverse (M-A). They are usually noted by: M_s, M_f, A_s, and A_f, respectively. Based on previous research works, it was frequently proved that these NiTi thermal properties are considerably influenced by chemical composition (Wang et al. 2015), heat treatment temperature (Sadiq et al. 2010), cooling media (Motemani et al. 2009), cooling/heating rate (Nurveren et al. 2008; Ben Fraj and Tourki 2016), and manufacturing process (Wang et al. 2013; Laplanche et al. 2017). This dependence of the transformation temperatures to the above-cited parameters is often attributed to the variation of the microstructural behavior.

From thermodynamic point of view, numerous previous studies have proved that the variation in NiTi transformation behavior affects the Gibbs free energy change (ΔG) which is mainly the function of enthalpy and entropy changes, ΔH and ΔS respectively. It has been reported that entropy change is greatly dependent on M_f (Natalia and Sergey 2015). Moreover, it has been experimentally shown that both enthalpy and entropy changes are strongly influenced by the chemical composition (Khalil-Allafi and Amin-Ahmadi 2009). They decrease with the increase of the Ni content in binary NiTi SMA. However, the effect of the cooling/heating rate on the NiTi thermodynamic behavior is not yet discussed and well understood in literature.

In this paper, the effect of the cooling/heating rate on the transformation temperatures is experimentally investigated. From the obtained calorimetric results, the relationship between this parameter and both entropy and enthalpy changes is studied. Consequently, the dependence of the Gibbs free energy change to the cooling/heating rate variation is discussed.

2 Material and Experimental Method

The NiTi SMA was supplied by Baoji Rare Titanium-Nickel Co. Ltd., China. The chemical composition of this material is given in Table 1. All samples were cut from the same NiTi hot-rolled bar and the weight of each one is about 12 mg. The samples were heat treated at 650 °C for 1 h and cooled in air. After annealing, samples were polished using a waterproof sand paper and then rinsed with ethanol.

Table 1 The chemical composition of the NiTi alloy (wt%)

Elements	Value
Ni	55.89
H	0.001
N	0.002
O	0.048
C	0.041
Ti	Balance
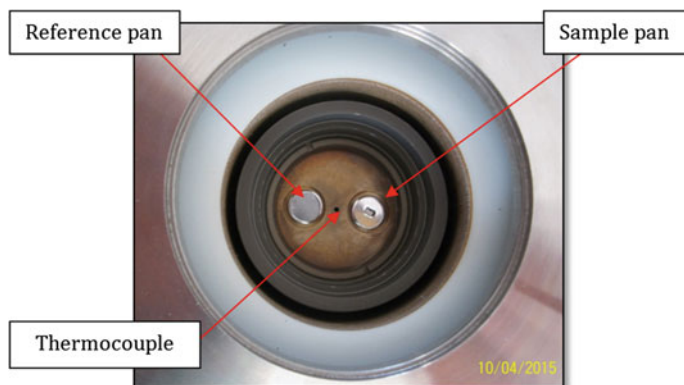
Fig. 1 DSC experimental setup

To characterize the thermal behavior of this material, the measurements were performed using a differential scanning calorimeter DSC 4000/Perkin Elmer with an accuracy of $\pm$ 0.1 °C. The samples were encapsulated in an aluminum specimen pans. A matching empty specimen pan with crimped lid was used as the reference (Fig. 1). The NiTi specimens were treated at various heating and cooling rates, from 5 °C/min to 20 °C/min, under a constant nitrogen flow rate of 20 ml/min. All the DSC tests consisted of a complete cooling and heating cycle. For each sample, the thermal cycle was repeated twice to ensure the reproducibility of the material response.

3 Results and Discussion

The DSC curves of the tested specimens at various cooling and heating rates are presented in Fig. 2a, b, respectively. Under cooling, the forward transformation (A-M) is observed to be exothermic. However, during heating, the reverse one (M-A) presents an endothermic reaction.

The austenitic and martensitic start and finish temperatures (A_s, A_f, M_s, and M_f, respectively) have been determined by the intersection of a base line and the tangent

Fig. 2 Calorimetric curves for different cooling/heating rates; **a** during cooling, **b** during heating
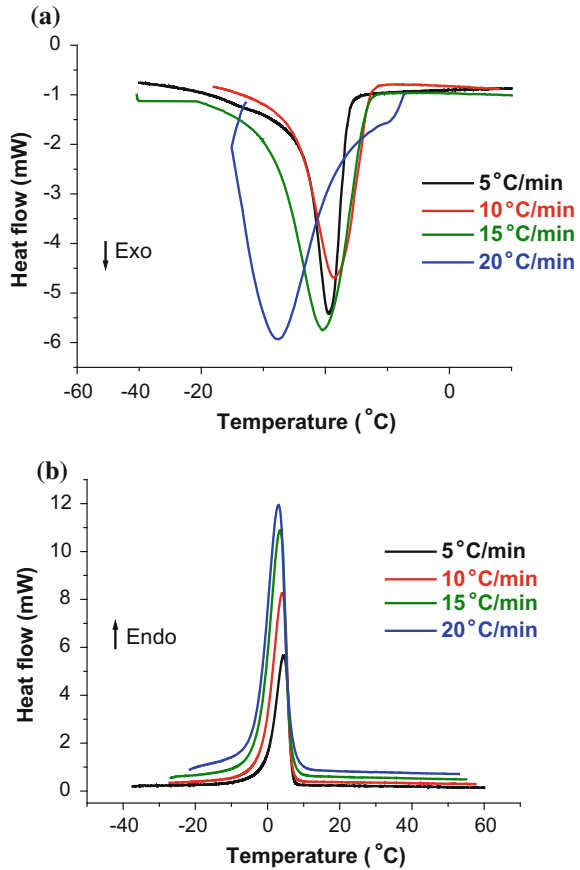
to a peak, as described in the standard ASTM-F2004-00. For each proposed cooling/heating rate, the transformation temperatures are summarized in Table 2 and then plotted in Fig. 3.

According to Fig. 3, it can be observed that the onset transformation temperatures, M_s and A_s, are not highly sensitive to the increase of the cooling/heating rate. However, for the finish transformation temperatures, calorimetric results show that A_f remains stable during heating process at different heating rates whereas M_f significantly decreases with the increasing of the cooling rate. It can be concluded

Table 2 The transformation temperatures of the NiTi at various cooling/heating rates

Cooling/heating rate (°C/min)	Transformation temperatures (°C)			
	A_s	A_f	M_s	M_f
5	−0.96	6.7	−16.23	−23.18
10	−2.43	6.82	−14.20	−26.52
15	−3.42	6.56	−13.85	−29.26
20	−4.25	6.97	−16.91	−35.18

Fig. 3 The transformation temperatures as function of the cooling/heating rate
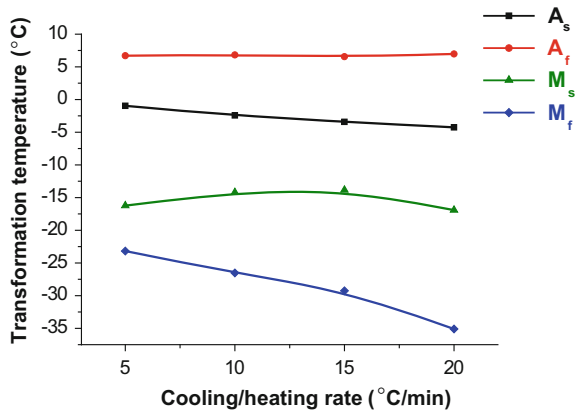
from these results that the temperature M_f is the most influenced transformation temperature by the variation of the cooling/heating rate.

The decrease of M_f leads to the increase of the hysteresis width expressed frequently by (A_f-M_f) which leads to deduce that the increase of the cooling/heating rate is able to decelerate the phase transformation process. Based on the microstructural study of Nurveren et al. 2008, this variation of the transformation temperatures with the cooling/heating rate is directly related to the reduction of the Ni_4Ti_3 precipitates proportion in the matrix which promotes the increase of both dislocation density and resistance to martensitic transformation.

The observed variation of the NiTi thermal properties affects certainly its thermodynamic behavior. Hence it is necessary to study the relationship between the cooling/heating rate and the thermodynamic properties. Hence, both entropy and enthalpy changes as function of the cooling/heating rate will be discussed.

We recall that

$$\Delta S = \frac{\Delta H}{T_0} \tag{1}$$

with

- ΔS: The entropy change during the full transformation cycle
- ΔH : The enthalpy change during the full transformation cycle. It is the average of the two enthalpies calculated during both forward and reverse transformations (the areas bounded by the peak and the base line from calorimetric curves given in Fig. 2).
- T_0 is the thermodynamical equilibrium temperature. Below this temperature, the martensitic phase is stable while above it the stable phase is the austenitic one. It may be estimated as

Table 3 Enthalpy change, equilibrium temperature, and entropy change as function of the cooling/heating rate

Cooling/heating rate (°C/min)	ΔH (mJ)	T_0 (°C)	ΔS (mJ/°C)
5	81.58	−4.76	−17.13
10	83.73	−3.69	−22.69
15	138.6	−3.64	−38.07
20	162.56	−4.97	−32.7

$$T_0 = \frac{M_s + A_f}{2} \tag{2}$$

For each proposed cooling/heating rate, ΔH, T_0 and ΔS are calculated and presented in Table 3. T_0 seems almost unchanged, it is not remarkably influenced by the increase of the cooling/heating rate. It is obvious to obtain this result since this temperature is expressed as function of M_s and A_f, which, in their tour, are not influenced by this parameter as proved in Fig. 3.

Fig. 4 Enthalpy (**a**) and entropy (**b**) changes as function of the cooling/heating rate
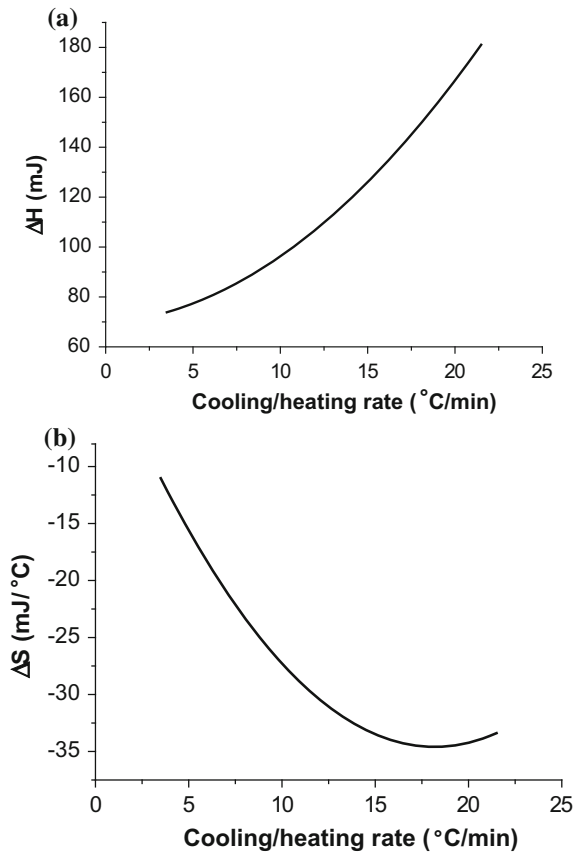
Fig. 5 Gibbs free energy changes as function of temperature for different cooling/heating rate: **a** 5 °C/min, **b** 20 °C/min
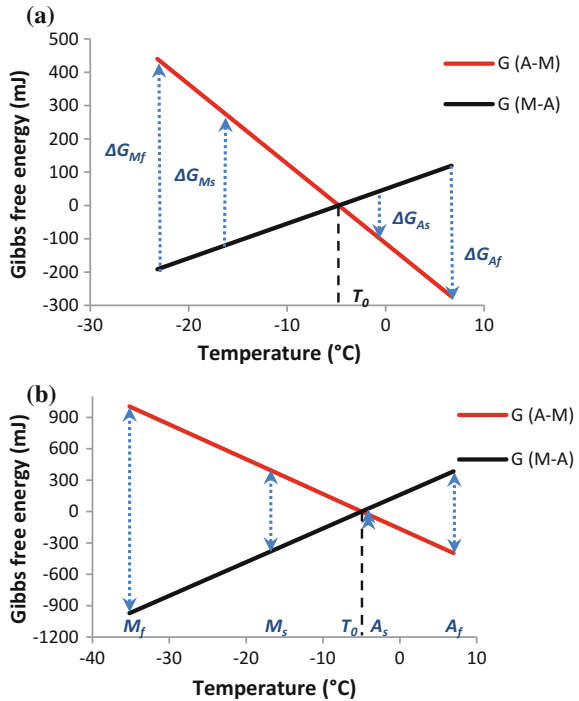
Figure 4a, b evinces that ΔH increases and ΔS decreases with the increase of the cooling/heating rate. The observed enthalpy tendency has been explained by the existence of the dislocations associated with high cooling/heating rates which generate an internal stress state and restrict the transformation process (Nurveren et al. 2008).

From the obtained results, the study of the Gibbs free energy change ΔG becomes easy using the Eq. (3)

$$\Delta G = \Delta H - T.\Delta S = \Delta H \left(1 - \frac{T}{T_0} \right) \tag{3}$$

T is the absolute temperature. At $T = T_0$, $\Delta G = 0$ which means that the Gibbs free energies of both martensite and austenite phases (G_{A-M} and G_{M-A}, respectively) are equal at this temperature.

In order to describe the variation of the Gibbs free energy as function of the cooling/heating rate, G_{A-M} and G_{M-A} are calculated and plotted in Fig. 5a, b for 5 °C/min and 20 °C/min, respectively. In each transformation temperature, we indicate the Gibbs free energy change ΔG. Below T_0, ΔG is positive, however above this temperature it will negative. It is clearly seen that the increase of the cooling/heating rate strongly affects the Gibbs free energy evolution. At 20 °C/min, ΔG_{Mf} heavily increases by the decreasing of the temperature M_f.

Here, it should be noted that following the obtained calorimetric data, we can determine numerous parameters which considered very useful in the modeling of the NiTi thermodynamic behavior during the NiTi phase transformation process. Indeed, it is very helpful to exploit these findings in the models which takes into account the cooling/heating rate, usually noted $\dot{T}$.

4   Conclusion

Based on calorimetric analysis, the influence of the cooling/heating rate on the thermodynamic properties of the Ni-rich NiTi SMA was investigated in this study. The main obtained findings are summarized as follows:

(1) M_f is strongly decreased by the increase of the cooling rate, which causes the increase in the width of the corresponding thermal hysteresis. This tendency leads to decelerate the phase transformation process.
(2) During the phase transformation process, the enthalpy changes ΔH increases and the entropy changes ΔS decreases by increasing the cooling/heating rate. However, the equilibrium temperature T_0 was not affected by variation.
(3) The Gibbs free energy change ΔG is also influenced by the cooling/heating rate. It heavily increases with the decrease of the temperature M_f.

References

Ben Fraj B, Tourki Z (2016) Influence of cooling and heating rates on the thermal properties of Ni-Ti shape memory alloy. In: 23rd International federation of heat treatment and surface engineering congress, Savannah, Georgia, USA, pp 481–486

Khalil-Allafi J, Amin-Ahmadi B (2009) The effect of chemical composition on enthalpy and entropy changes of martensitic transformations in binary NiTi shape memory alloys. J Alloy Compd 487:363–366

Laplanche G, Birk T, Schneider S, Frenzel J, Eggeler G (2017) Effect of temperature and texture on the reorientation of martensite variants in NiTi shape memory alloys. Acta Mater. https://doi.org/10.1016/j.actamat.2017.01.023

Motemani Y, Nili-Ahmadabadi M, Tan MJ, Bornapour M, Rayagan Sh (2009) Effect of cooling rate on the phase transformation behavior and mechanical properties of Ni-rich NiTi shape memory alloy. J Alloy Compd 469:164–168

Natalia R, Sergey B (2015) Entropy change in the B2- > B19' martensitic transformation in TiNi alloy. Thermochim Acta 602:30–35

Nurveren K, Akdogan A, Huang WM (2008) Evolution of transformation characteristics with heating/cooling rate in NiTi shape memory alloys. J Mater Process Technol 196:129–134

Sadiq H, Wong MB, Al-Mahaidi R, Zhao XL (2010) The effects of heat treatment on the recovery stresses of shape memory alloys. Smart Mater Struct 19(035021):1–7

Wang X, Amin-Ahmadi B, Schryvers D, Verlinden B, Humbeeck JV (2013) Effect of annealing on the transformation behavior and mechanical properties of two nanostructured Ti-50.8at.%. Mater Sci Forum 738–739:306–310

Wang X, Verlinden B, Humbeeck JV (2015) Effect of post-deformation annealing on the R-phase transformation temperatures in NiTi shape memory alloys. Intermetallics 62:43–49

On the NiTi SMA Thermal Behavior
at Various Heat Treatment Conditions

Boutheina Ben Fraj, Slim Zghal and Zoubeir Tourki

Abstract In this paper, the relationship between the heat treatment temperature and the phase transformation behavior in the Ni-rich NiTi Shape Memory Alloy (SMA) was experimentally investigated. The characterization of the thermoelastic martensitic transformation at zero stress was performed based on differential scanning calorimetry (DSC) experiments. It was shown that the R phase behavior is extremely affected by the increase of the heat treatment temperature. For the samples heat treated below 650 °C, the R phase appears in both forward and reverse transformations. However, it completely disappears above this heat treatment temperature. Moreover, it was reported that the NiTi thermal behavior and mainly the transformation temperatures are strongly influenced by the heat treatment temperature change. By increasing this parameter, the austenitic finish temperature (A_f) is considerably decreased while the martensitic one (M_f) is increased which greatly affects the thermal transformation hysteresis. Accordingly, the effect of the this thermal behavior on the NiTi diagram phase was discussed. The obtained findings were largely in line with previously published studies.

Keywords DSC · Heat treatment temperature · NiTi SMA · Transformation hysteresis · Diagram phase

B. B. Fraj (✉) · Z. Tourki
Mechanical Laboratory of Sousse (LMS), National Engineering
School of Sousse ENISo, University of Sousse, 4023 Sousse, Tunisia
e-mail: bfb.ingmec@gmail.com

Z. Tourki
e-mail: zbrtourki@gmail.com

S. Zghal
Laboratory of Multifunctional Materials and Applications (LaMMA),
Faculty of Sciences of Sfax, University of Sfax, BP 1171, 3000 Sfax, Tunisia
e-mail: salim_zghal@yahoo.fr

1   Introduction

The thermomechanical behavior of the NiTi shape memory alloy (SMA) is based on a phase transformation mechanism carried out between austenite A (high temperature phase) and martensite M (low temperature phase). This phase transformation process is mainly governed by the transformation temperatures which define the start and the finish of the forward transformation (A-M) during cooling and the reverse transformation (M-A) during heating; M_s, M_f, A_s, and A_f, respectively. Under specific conditions, the phase transformation process (A $\leftrightarrow$ M) can be carried out through an intermediate phase known as rhombohedral phase, denoted R phase in this paper, which resulting a multistage phase transformation (A $\leftrightarrow$ R and R $\leftrightarrow$ M) (Duerig and Bhattacharya 2015).

Under stress-free state, the transformation temperatures may be easily determined through thermal analysis such as the differential scanning calorimetry (DSC) (Fig. 1a). In the case of the thermomechanical loading, they are correlated with the critical stresses to form the stress–temperature diagram phase in which the NiTi properties are exhibited for different mechanical loadings at various temperatures, especially the superelastic effect (SE) and the shape memory effect (SME) as shown in Fig. 1b. The critical stresses define the path of the stress-induced phase transformation process.

Fig. 1 **a** Typical NiTi DSC curve, **b** Simplified critical stress–temperature diagram
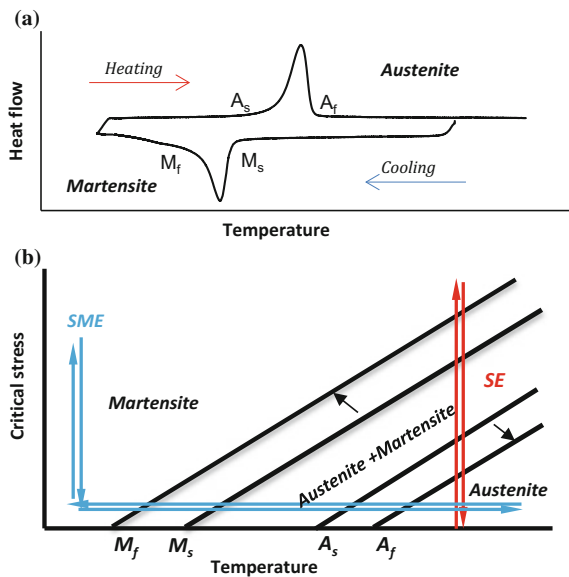
Based on previous investigations, it has been experimentally demonstrated that many factors can alter the NiTi thermal behavior such as the heat treatment temperature and duration (Sadiq et al. 2010; Khaleghi et al. 2013; Wang et al. 2015), cooling media and cooling/heating rate (Motemani et al. 2009; Ben Fraj and Tourki 2016), manufacturing process (Sczerzenie et al. 2011; Wang et al. 2013), Ni content in the matrix (Kim 2002; Allafi and Ahmadi 2009) and the grain size (Kazemi-Choobi et al. 2011).

For that, the dependence of the thermal behavior of a Ni-rich NiTi SMA with the heat treatment temperature (noted HTT in this paper) is experimentally investigated in this study. The thermal characterization is performed using the DSC technique. The sensitivity of the transformation temperatures, R phase behavior, and thermal transformation hysteresis is also discussed. Moreover, based on the obtained findings, the influence of this parameter on the stress–temperature diagram evolution will be studied.

2 Material and Experimental Method

The NiTi SMA was supplied by Baoji Rare Titanium-Nickel Co. Ltd., China. The chemical composition of this material is given in Table 1. All samples were cut from the same NiTi hot rolled bar, the weight of each one is between 8 and 15 mg. These samples were heat treated at various temperatures, from 450 °C to 700 °C, for 1 h and then cooled in air. After annealing, samples were polished using a waterproof sand paper and then rinsed with ethanol.

In order to characterize the thermal behavior of this material, the measurements were performed using a differential scanning calorimeter DSC 4000/Perkin Elmer with an accuracy of ± 0.1 °C. The samples were encapsulated in an aluminum specimen pan. A matching empty specimen pan with crimped lid was used as the reference. The imposed cooling/heating rate was 5 °C/min with a constant nitrogen flow rate of 20 ml/min. All the DSC tests consisted of a complete cooling and heating cycle. For each sample, the thermal cycle was repeated twice to ensure the reproducibility of the material response.

Table 1 The chemical composition of the NiTi alloy (wt%)

Elements	Value
Ni	55.89
H	0.001
N	0.002
O	0.048
C	0.041
Ti	Balance

3 Results and Discussion

In Fig. 2a, for HTT = 450 °C, the DSC thermogram shows that the R phase is occurred during both forward and reverse transformations, each one presents two peaks which indicate the A-R-M and the M-R-A paths, respectively. By increasing the HTT to 500 °C, the superposition between the R phase and the austenitic peaks is clearly seen under heating. During the forward transformation, the martensitic peak is less flattened than that obtained in previous thermogram. At HTT = 550 °C, the R phase peak is completely superposed with the austenitic one. It is present only during the cooling path with a small peak which tends to be superposed with the martensitic one at HTT = 600 °C. With the raising of the HTT to 650 °C, only a one stage transformation A-M and M-A are observed. Accordingly, the HTT range of 600–650 °C may be considered as the critical range in which the total disappearance of the R phase, in the phase transformation process, is recorded. The corresponding thermogram to HTT = 700 °C evinces the stabilization of the last obtained result.

Based on the obtained calorimetric results, the high influence of the HTT on the transformation temperatures is clearly observed. So, in order to understand this effect, the austenitic and martensitic finish temperatures, A_f and M_f, were determined by the intersection of a base line and the tangent to a peak, as described in the standard ASTM-F2004-00. These transformation temperatures are summarized in Table 2 and plotted in Fig. 3 for various proposed HTT.

As shown in the above results, the finish transformation temperatures are heavily influenced by the increase of the HTT when M_f increases by almost 27 °C and A_f

Fig. 2 The NiTi DSC thermogrammes for different HTT
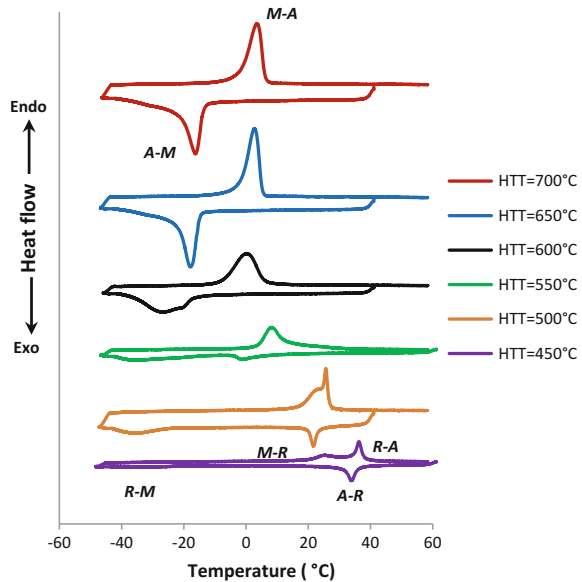
Table 2 A_f and M_f for different HTT

HTT (°C)	Transformation temperatures (°C)	
	A_f	M_f
450	38.59	−48.34
500	27.21	−43.44
550	18.06	−42.52
600	6.68	−41.54
650	5.75	−21.6
700	5.88	−21.25

Fig. 3 Transformation temperatures as function of HTT
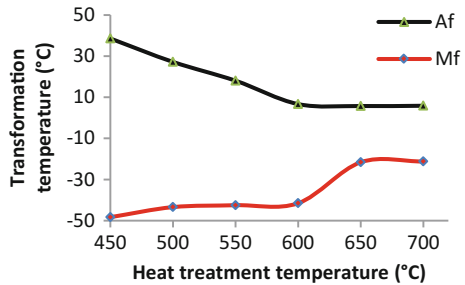
decreases by about 33 °C. It should be noted that from a microscopic point of view, these transformation behavior changes are attributed to the evolution of the Ni_4Ti_3 precipitates, developed during the heat treatment. It has been reported that both size and shape of these precipitates increase by increasing the HTT which is able to reduce the dislocation density and promote the transformation process (Nurveren et al. 2008; Capeck and Kubasek 2014). This change in the precipitation process causes the decrease of the Ni content in the matrix which alters the transformation temperatures (Sehitoglu et al. 2000; Allafi et al. 2002).

These changes in these material properties affect obviously the thermal transformation hysteresis which is expressed by the difference (A_f-M_f) (Zhang et al. 2012). The evolution of the hysteresis width with the HTT variation is illustrated in Fig. 4. It decreases considerably by about 60 °C.

Fig. 4 Transformation hysteresis width as function of the HTT
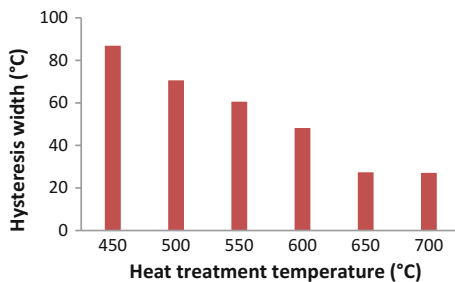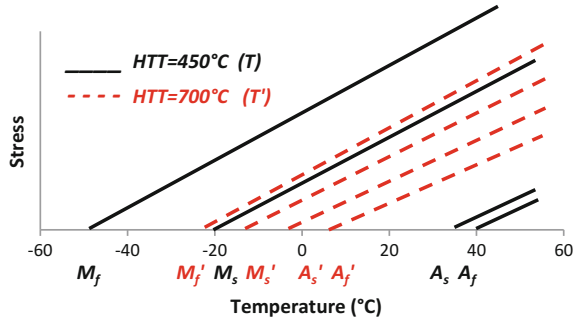
According to the obtained transformation temperatures at zero stress, we present schematically the stress–temperature diagrams corresponding to the lower and higher proposed HTT, 450 °C and 700 °C (Fig. 5). In these diagrams, the evolution of the critical stresses is not considered. The curve slopes ($d\sigma/dT$) are supposed equal. The different domains corresponding to the phase transformation process (defined in Fig. 1b) are strongly affected by the increase of the HTT which highly affects the superelasticity and the shape memory aspects of the NiTi alloy. This result can be useful to predict the temperature range in which occur these NiTi thermomechanical properties.

4   Conclusion

In this paper, the influence of the heat treatment temperature on the NiTi thermal properties was experimentally investigated using a DSC analysis. The main findings are summarized as follows:

(1) The R phase occurs during the phase transformation cycle until a HTT of 600 °C. Above this temperature, it eventually disappears and the single stage transformations A-M and M-A take place.
(2) The finish transformation temperatures are strongly influenced by increasing the HTT, M_f increases while A_f decreases.
(3) The hysteresis width is heavily decreased with the increase of the HTT. Accordingly, the stress–temperature diagram is affected which is useful to predict the evolution of the superelasticity and the shape memory effect of the NiTi alloy.

References

Allafi KJ, Dlouhy A, Eggeler G (2002) Ni4Ti3-precipitation during aging of NiTi shape memory alloys and its influence on martensitic phase transformations. Acta Mater 50:4255–4274

Allafi KJ, Ahmadi AB (2009) The effect of chemical composition on enthalpy and entropy changes of martensitic transformations in binary NiTi shape memory alloys. J Alloy Compd 487:363–366

Ben Fraj B, Tourki Z (2016) Influence of cooling and heating rates on the thermal properties of Ni-Ti shape memory alloy. In: 23rd International federation of heat treatment and surface engineering congress, Savannah, Georgia, USA, pp 481–486

Capek J, Kubasek J (2014) Influence of temperature of the short-period heat treatment on mechanical properties of the NiTi alloy. Mater Eng 21:11–15

Duerig TW, Bhattacharya K (2015) The influence of the R-phase on superelastic behavior of NiTi. Shap Mem Superelasticity 1:153–161

Kazemi-Choobi K, Khalil-Allafi J, Abbasi-Chianeh V (2011) Study of the precipitation of Ni4Ti3 particles during aging of Ni-rich NiTi shape memory wires using in-Situ electrical resistance measurement. In: 3rd International conference on manufacturing engineering ICME, Tehran, Iran

Khaleghi F, Khalil-Allafi J, Abbasi-Chianeh V, Noori S (2013) Effect of short-time annealing treatment on the superelastic behavior of cold drawn Ni-rich NiTi shape memory wires. J Alloy Compd 554:32–38

Kim Y (2002) Fatigue properties of the Ti-Ni base shape memory alloy wire. Mater Trans 7:1703–1706

Motemani Y, Nili-Ahmadabadi M, Tan MJ, Bornapour M, Rayagan Sh (2009) Effect of cooling rate on the phase transformation behavior and mechanical properties of Ni-rich NiTi shape memory alloy. J Alloy Compd 469:164–168

Nurveren K, Akdogan A, Huang WM (2008) Evolution of transformation characteristics with heating/cooling rate in NiTi shape memory alloys. J Mater Process Technol 196:129–134

Sadiq H, Wong MB, Al-Mahaidi R, Zhao XL (2010) The effects of heat treatment on the recovery stresses of shape memory alloys. Smart Mater Struct 19(035021):1–7

Sczerzenie F, Paul D, Belden C (2011) Comparison of inclusions in cold drawn wire and precursor hot-rolled rod coil in VIM-VAR Nickel-Titanium alloy. JMEPEG 20:752–756

Sehitoglu H, Karaman I, Anderson R, Zhang X, Gall K, Maier HJ, Chumlyakov Y (2000) Compressive response of NiTi single crystals. Acta Mater 48:3311–3326

Wang X, Amin-Ahmadi B, Schryvers D, Verlinden B, Humbeeck JV (2013) Effect of annealing on the transformation behavior and mechanical properties of two nanostructured Ti-50.8at.%. Mater Sci Forum 738–739:306–310

Wang X, Verlinden B, Humbeeck JV (2015) Effect of post-deformation annealing on the R-phase transformation temperatures in NiTi shape memory alloys. Intermetallics 62:43–49

Zhang Y, Jiang S, Zhao Y, Tang M (2012) Influence of cooling rate on phase transformation and microstructure of Ti − 50.9%Ni shape memory alloy. Trans Nonferrous Met Soc China 22:2685–2690

Multiobjective Constrained Optimization of Sewing Machine Mechatronic Performances

Najlawi Bilel, Nejlaoui Mohamed, Affi Zouhaier and Romdhane Lotfi

Abstract Sewing is one of the most commonly used manufacturing processes in the world. In the textile industry, development of sewing machines with optimal performances has found a great attention during recent years. Therefore, this work deals with the multiobjective design optimization of a sewing machine viewed as a mechatronic system. The mechatronic model of the machine is developed based on the coupling the needle-bar-and-thread-take-up-lever (NBTTL) dynamic model and the DC motor model. Based on the mechatronic model, the DC motor current and its fluctuation are minimized, simultaneously, in order to minimize the load on the motor and the machine vibration. The multiobjective imperialist competitive algorithm (MOICA) is used to solve this problem. The obtained results are presented as a Pareto front, since the two objective functions are shown to be contradictory. Out of the solutions presented in the Pareto front, the designer can choose the one with the best compromise for his application.

Keywords Multiobjective optimization · Dynamic analysis · MOICA Mechatronic system · Pareto front

N. Bilel (✉) · N. Mohamed · A. Zouhaier
LGM, ENIM, University of Monastir, Monastir, Tunisia
e-mail: najlawibilelali@gmail.com

N. Mohamed
e-mail: nejlaouimohamed@gmail.com

A. Zouhaier
e-mail: zouhaier.affi@enim.rnu.tn

R. Lotfi
Department of Mechanical Engineering,
American University of Sharjah, Sharjah, UAE
e-mail: lotfi.romdhane@gmail.com

1 Introduction

Textile industry and its applications in many industrial fields have a great attention in recent years. To improve the quantity and the quality of textile products, several engineering applications were used. Optimization of the design of sewing machines, in order to improve their performances, is one of the fields that several researchers are addressing. In particular, the design of the NBTTL mechanism is one of the most important studies in this area (Ebrahimi and Payvandy 2014). This mechanism consists of a four-bar linkage and a slider-crank mechanism driven by the same crank (Najlawi et al. 2015).

Several studies deal with the dimensional synthesis of four-bar mechanisms. Matekar et al. (2011) presented the optimization of a four-bar mechanism with the differential evolution algorithm. Affi et al. (2007) developed a multiobjective optimization of a motor-driven four-bar system. They consider the mechanism and the driving motor as one mechatronic system. The objectives were the minimization of the motor torque and its fluctuation. Najlawi et al. (2016a) optimized the NBTTL mechanism design to minimize the angular velocity ratio of the coupler.

Other works dealt with the design of slider-crank mechanisms. Ebrahimi and Payvandy (2014) minimized the needle velocity, in the case of the NBTTL mechanism, in order to decrease the heat caused by friction between the needle and the fabric in the penetration zone. However, the reduction of the needle velocity in the penetration zone may affect the amount of the required needle force (Najlawi et al. 2016b). This force depends on the transmission angle of the slider-crank mechanism. Najlawi et al. (2016c) developed a multiobjective optimization strategy to minimize the tracking error, the needle jerk, and the transmission angle index of the NBTTL mechanism.

In this work, the sewing machine is treated as a mechatronic system. Indeed, the dynamic behavior of the NBTTL cannot be studied without taking into account the dynamic behavior of the actuator. Therefore, the mechatronic model has to include the design parameters of the mechanism and the design parameters of the DC motor driving the system. Based on the MOICA and the mechatronic model, a multiobjective optimization is conducted in order to optimize two performances, i.e., the maximum current drawn by the motor and its fluctuation. In Sect. 2, the NBTTL mechanism is presented and modeled. In Sect. 3, the optimization algorithm is presented and the obtained results are discussed. Some concluding remarks are summarized in Sect. 5.

2   The Mechatronic Model of the NBTTL Mechanism

2.1   *The NBTTL Mechanism*

The sewing machine is presented in Fig. 1. The NBTTL mechanism, used in sewing machines, consists of a slider-crank mechanism and a four-bar mechanism driven by the same crank (Fig. 2). The thread take-up lever mechanism is the four-bar linkage OABC. During the formation of a loop, the take-up lever eye D pulls the upper thread vertically. The goal is to generate a given path of the point D. OEF represents the slider-crank mechanism in which point F denotes the needle. The role of the thread take-up lever in the stitch formation process is to ensure appropriate thread feeding. The function of the needle, which is fixed to the needle bar, is to penetrate the fabric. The rotation of the input link (OA) is transmitted to the needle bar through the coupler link EF. The displacement of the needle bar is represented by the distance 'S'.

To analyze the dynamic behavior of the mechatronic device, it is necessary to derive the dynamic model of each of the components of the system, i.e., the NBTTL mechanism and the DC motor. The coupling of these two models leads to the mechatronic model of the sewing machine.
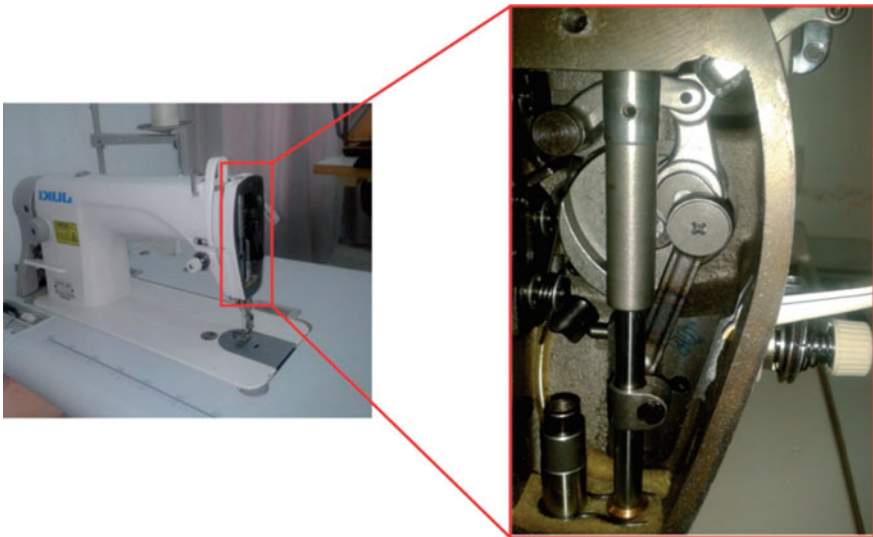
Fig. 1 The NBTTL of a sewing machine
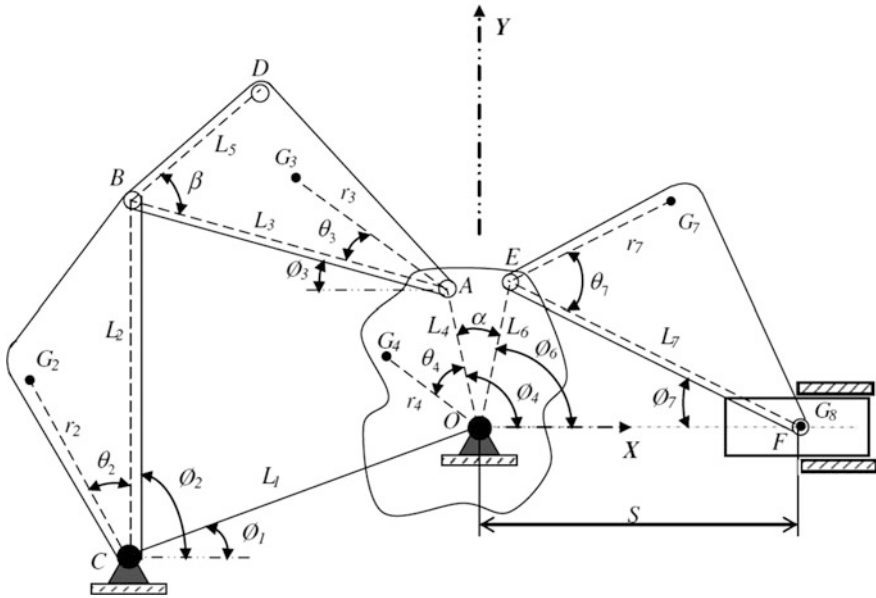
Fig. 2 The NBTTL mechanism parameters

2.2 The NBTTL Dynamic Model

A schematic of the NBTTL mechanism containing all the geometric parameters, is shown in Fig. 2. The angle ϕ_4 is the input variable of the NBTTL mechanism. The Lagrange's equation describing the motion of the mechanism can be written as

$$T_{me} = \frac{d}{dt}\left(\frac{\partial K}{\partial \phi_4}\right) - \frac{\partial K}{\partial \phi_4} + \frac{\partial P}{\partial \phi_4} + \frac{\partial D}{\partial \phi_4}, \tag{1}$$

where T_{me}, K, P and D denote, respectively, the driving torque applied to the crank, the kinetic energy, the potential energy and the dissipative energy of the system. For more details, see (Najlaoui et al. 2017).

Replacing all these quantities by their expressions as a function of the mechanism parameters yields the following expression for the input torque of the mechanism:

$$T_{me} = A\dot{\phi}_4 + \frac{1}{2}\frac{dA}{\phi_4}\phi_4^2 + B, \tag{2}$$

where the expressions of A, and B are given in (Najlaoui et al. 2017).
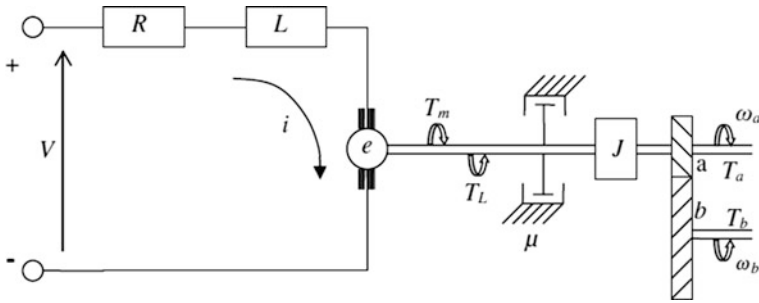
Fig. 3 The DC motor system

Table 1 Motor parameters (Najlaoui et al. 2017; Affi et al. 2007)

R (Ω)	L (H)	K_m (Nm/a)	K_g (V.s)	J (Kg.m2)	T_L (Nm)	μ (Nms)
0.4	0.05	0.678	0.678	0.056	0.0	0.226

2.3 The DC Motor Model

In this section, we present the electromechanical model of the DC motor system. The different characteristics of the electrical motor are presented in Fig. 3.

The characteristics of the motor used in this work are given in Table 1.

It's shown in Najlaoui et al. (2017), Affi et al. (2007) that the dynamic model of DC motor can be given by

$$T_b = nK_m i(t) - nT_L - n^2 \mu \dot{\phi}_4 - n^2 J \ddot{\phi}_4 \tag{3}$$

T_b, R, L, n, K_m, K_g, J, T_L and μ are respectively the motor torque the armature resistance, the inductance, The ratio of the geared speed-reducer, the motor torque constant, the motor voltage constant, the moment of inertia of the rotor, the constant mechanical load torque and the viscous damping at the bearings friction.

2.4 The Mechatronic System Model

For a mechatronic system, the torque given by the DC motor (Eq. (3)) should be equal to the torque needed by the mechanical system (Eq. (2)). Therefore, we have

$$nK_m i(t) - nT_L - n^2 \mu \dot{\phi}_4 - n^2 J \ddot{\phi}_4 = A\ddot{\phi}_4 + \frac{1}{2}\frac{dA}{d\phi_4}\dot{\phi}_4^2 + B \tag{4}$$

At the steady state, the velocity of the crank is assumed to be constant. With this assumption the second order derivative of ϕ_4 in Eq. (4) becomes zero and all the first derivatives of ϕ_4 in Eq. (3) are constant. Therefore, solving Eq. (4) for $i(t)$, yields

$$i(t) = \frac{1}{nK_m} \left(\frac{1}{2} \frac{dA}{d\phi_4} \dot{\phi}_4^2 + B + nT_L + n^2 \mu \dot{\phi}_4 \right) \tag{5}$$

This equation gives the mechatronic model of the motor-driven NBTTL system at a steady state. It gives the current required to maintain a constant crank speed. It presents also the first objective function that should be minimized. Indeed, minimizing the current at a constant voltage correspond to the minimization of the machine consumed energy.

The second objective function to be minimized is the DC motor current fluctuation. Indeed, this fluctuation is a source of overload and overheating in the motor and can generate the machine vibration (Najlaoui et al. 2017; Affi et al. 2007).

From Eq. (5) we can write

$$\frac{di(t)}{dt} = \frac{1}{nK_m} \left\{ \frac{1}{2} \dot{\phi}_4^2 \frac{d}{dt} \left(\frac{dA}{d\phi_4} \right) + \frac{dB}{dt} \right\} \tag{6}$$

See Najlaoui et al. (2017) for more details.

3 Optimization of the Design of the Mechatronic System

In what follows, the design variables of the mechatronic system will be optimized. The search domain of each design variables is given in Najlaoui et al. (2017). The optimization problem can be defined as minimizing simultaneously the DC motor current $i(t)$ of the mechatronic system and its fluctuation $\frac{di(t)}{dt}$. Hence, the multi-objective design optimization of the mechatronic system can be formulated as:

$$\text{Minimize} \begin{cases} i(t)|_{\max} = \max \left(\frac{1}{nK_m} \left[\frac{1}{2} \frac{dA}{d\phi_4} \dot{\phi}_4^2 + B + n^2 \mu \dot{\phi}_4 + nT_L \right] \right) \\ \left. \frac{di(t)}{dt} \right|_{\max} = \max \left(\frac{1}{nK_m} \left[\frac{1}{2} \dot{\phi}_4^2 \frac{d}{dt} \left(\frac{dA}{d\phi_4} \right) + \frac{dB}{dt} \right] \right) \end{cases} \tag{7}$$

$$\text{Subject to:} \begin{cases} 2[\max(L_1, L_2, L_3, L_4) + \min(L_1, L_2, L_3, L_4)] \\ \quad < L_1 + L_2 + L_3 + L_4 \quad (C1) \\ \phi_4^i - \phi_4^{i+1} < 0 \quad (C2) \\ TE = \max|C_{Dd}(\phi_4) - C_{Dx}(\phi_4)| \le 0.1 \quad (C3) \\ 30\text{mm} \le S \le 62\text{mm} \quad (C4) \\ DP \in D(DP) \quad (C5) \end{cases} \tag{8}$$

– Constraint (C1) is the Grashof law, which ensures that the input crank of the
   thread take-up lever can make a complete rotation.
– Constraint (C2) ensures that the input variable ϕ_4 is increasing with time.
– Constraint (C3) avoids the thread breakage during the stitch forming process.
– Constraint (C4) defines the range of motion of the needle (Najlawi et al. 2015).
– Constraint (C5) represents the search domain D(DP) of the different design
   parameters DP (Najlaoui et al. 2017).

To solve this optimization problem (Eqs. (7) and (8)), the Multiobjective
imperialist competitive algorithm (MOICA) (Najlawi et al. 2016d) will be used.

The MOICA method is a recently introduced stochastic optimization strategy
inspired from the socio-political process of imperialist competition. Figure 4 shows
the flowchart of the MOICA. This algorithm starts by a random generation of initial
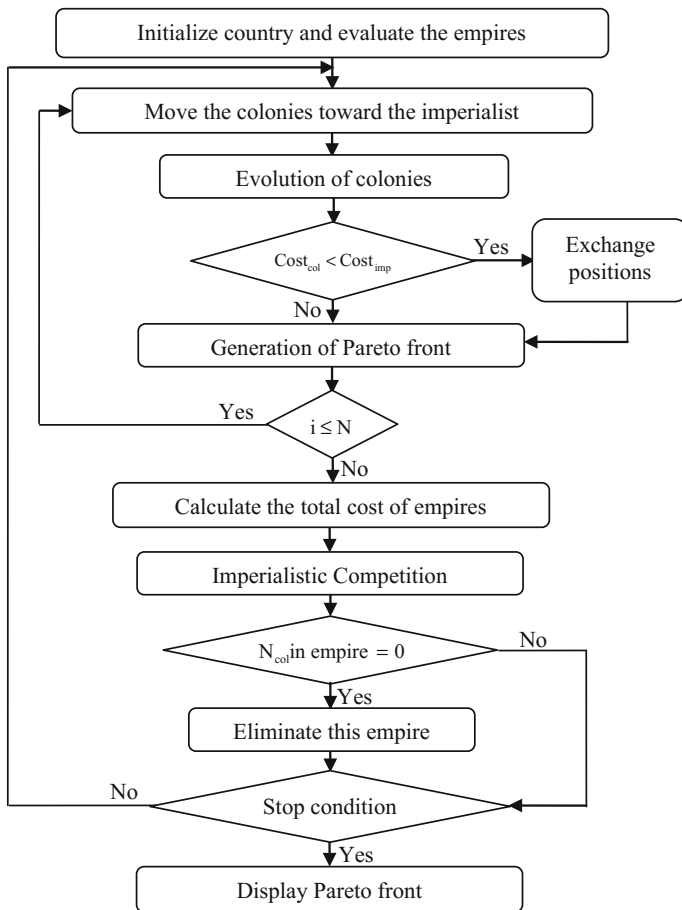
Fig. 4 The MOICA flowchart

Table 2 The MOICA parameters

Number of countries	Number of imperialists	Assimilation coefficient β	Crossover probability	Mutation probability
500	50	1.2	0.9	0.1

countries. The most powerful country is called "imperialist" and the remaining countries are considered as "colonies". Each initial empire is composed of one imperialist and several colonies. After forming initial empires, colonies start moving towards the relevant imperialist. In each empire, the crossover and the random replacement mutation operators enhance the colonies with a new one that can have more power and eventually constitute imperialists. In this case, the colony and the imperialist permute positions. Then, non-dominated imperialists are kept in an archive based on the fast non-dominated sorting approach (Najlawi et al. 2016d). This archive represents the Pareto front. Based on their power, any non-competitive empire will collapse. Finally, the MOICA algorithm stops when only one empire remains. The used MOICA parameters are given in Table 2.

4 Results and Discussion

In this section, we will present the results of the multiobjective design optimization defined by Eq. (7) under the constraint presented by Eq. (8). Using the MOICA algorithm, the Pareto front can be determined to find the optimal non-dominated solutions (Fig. 5).
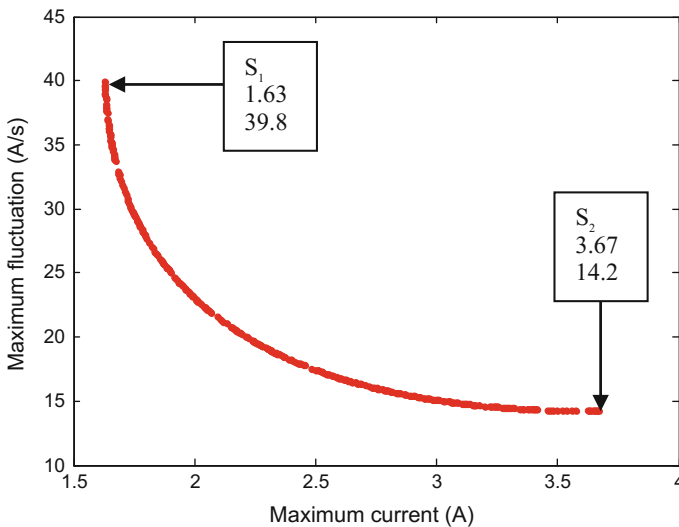
Fig. 5 Optimal design of the mechatronic system

Table 3 DP value of optimized solutions S_1 and S_2

DP	S_1	S_2	DP	S_1	S_2	DP	S_1	S_2
$L_1(mm)$	33.41	29.21	$\theta_4(°)$	5.11	0.79	$m_2(kg)$	0.061	0.063
$L_2(mm)$	31.89	33.04	$\theta_7(°)$	356.41	6.59	$m_3(kg)$	0.065	0.067
$L_3(mm)$	28.11	25.74	$\alpha(°)$	19.64	17.33	$m_4(kg)$	0.074	0.081
$L_4(mm)$	19.56	16.87	$\phi_1(°)$	27.03	23.91	$m_7(kg)$	0.061	0.071
$L_5(mm)$	24.01	26.11	$\beta(°)$	29.17	31.01	$m_8(kg)$	0.067	0.066
$L_6(mm)$	21.73	17.36	$r_2(mm)$	11.25	15.23	$I_2(kg.m^2)$	0.37E-4	0.38E-4
$L_7(mm)$	27.41	23.55	$r_3(mm)$	12.04	11.89	$I_3(kg.m^2)$	0.37E-4	0.37E-4
$\theta_2(°)$	358.76	5.89	$r_4(mm)$	0	0	$I_4(kg.m^2)$	0.38E-4	0.39E-4
$\theta_3(°)$	7.43	359.02	$r_7(mm)$	13.87	13.58	$I_7(kg.m^2)$	0.41E-4	0.39E-4

Fig. 6 Variation of the current of solutions S_1 and S_2
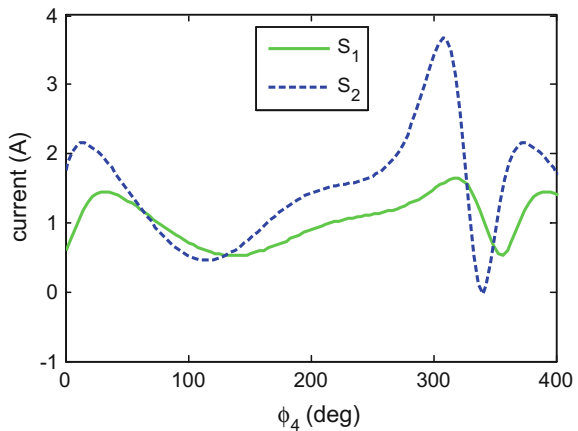
In Fig. 5, each non-dominated solution represents an optimal design vector of the mechatronic system with the corresponding values of the objective functions. One can note that the mechatronic system having the minimum of $i(t)|_{max}$, has the maximum of the current fluctuation $\frac{di(t)}{dt}\big|_{max}$ and vice versa. Table 3 presents the design vectors of the optimal solutions S_1 and S_2 taken from the Pareto front.

For the selected optimal solutions S_1 and S_2, the variation of the current as a function of the input angle ϕ_4, is presented in Fig. 6. One can remark that the solution S_1 presents the advantage of having the minimum of the maximum current value. In fact, the solution S_1 has a reduction of the maximum of current by about 55% compared to the solution S_2.

Figure 7 presents the current fluctuation as a function of the input crank angle. One can note that the optimal solution S_2 presents the advantage of having the minimum current fluctuation. The design parameters vector of the solution S_2 can minimize the current fluctuation by 64% compared to the solution S_1.

Fig. 7 Current fluctuation of solutions S_1 and S_2
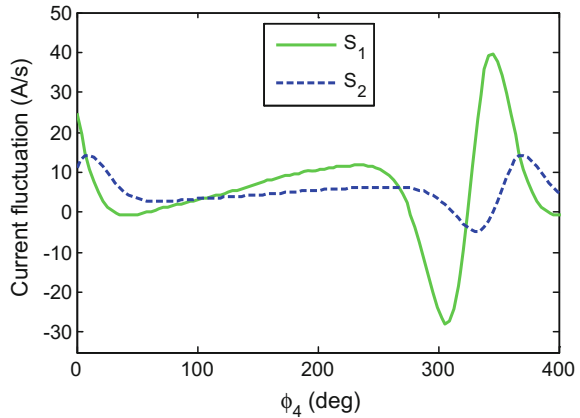
5 Conclusion

The study dealt with the modeling and the optimization of a sewing machine viewed as a mechatronic system. The mechatronic model that regroups the NBTTL mechanism dynamic parameters and the driving DC motor parameters was developed. The optimization problem was conducted and the DC motor current and its fluctuation were minimized simultaneously by using the MOICA method. The optimal solutions were presented as a Pareto front. The two extreme solutions from the Pareto front were shown to minimize one of the objective functions at the cost of a high value of the second one. This contradiction between the two objective functions requires from the designer more effort to choose the best solution for his application.

References

Affi Z, EL-Kribi B, Romdhane L (2007) Advanced mechatronic design using a multi-objective genetic algorithm optimization of a motor-driven four-bar system. Mechatronics 17:489–500

Ebrahimi S, Payvandy P (2014) Optimization of the link drive mechanism in a sewing machine using imperialist competitive algorithm. Int J Cloth Sci Technol 26:247–260

Matekar SB, Gogate GR (2011) Optimum synthesis of path generating four-bar mechanisms using differential evolution and a modified error function. Mech Mach Theor 52:158–179

Najlawi B, Nejlaoui M, Affi Z, Romdhane L (2015) Optimal design of the needle bar and thread take up lever mechanism using a multi-objective imperialist competitive algorithm. In: 10th international symposium on mechatronics and its applications (ISMA), 2015, Sharjah. https://doi.org/10.1109/ISMA.2015.7373463

Najlawi B, Nejlaoui M, Affi Z, Romdhane L (2016a) Multi-objective design optimization of the NBTTL mechanism. International conference on acoustics and vibration (ICAV 2016), Hammamet, Tunisia

Najlawi B, Nejlaoui M, Affi Z, Romdhane L (2016b) Optimization of the NBTTL mechanism using MOICA method. International conference on mechanics and energy, 22–24 Dec 2016, Hammamet, Tunisia

Najlawi B, Nejlaoui M, Affi Z, Romdhane L (2016c) Multi-objective robust design optimization of a sewing mechanism under uncertainties. J Intell Manuf. https://doi.org/10.1007/s10845-016-1284-0

Najlawi B, Nejlaoui M, Affi Z, Romdhane L (2016d) An improved imperialist competitive algorithm for multi objective optimization. Eng Optim 48:1823–1844

Najlaoui B, Nejlaoui M, Affi Z, Romdhane L (2017) Mechatronic design optimization of the mechanism in a sewing machine. Proc IMechE, Part C: J Mech Eng Sci. https://doi.org/10.1177/0954406216687786

Numerical Study of a Gas Jet Impinging on a Liquid Surface

Rim Ben Kalifa, Nejla Mahjoub Saïd, Hervé Bournot and Georges Le Palec

Abstract The present study introduces a numerical model for one of the most important fluid–fluid interaction problems in industrial engineering applications, mainly a gas jet impinging perpendicularly onto a liquid interface. A better understanding of the process of the interaction of this type of flow was performed using the Reynolds Stress Model (RSM). The Volume Of Fluid (VOF) method is employed to follow the deformation of the liquid surface. The results from the numerical tests are comparable with those presented by Muñoz (Appl Math Model 36:2687-2700, 2012) and it is found that computational results agreed well with experimental data. The obtained numerical results provide useful insight and a better understanding of the highly complex flow encountered in such processes. Moreover, we propose to examine the effect of the nature of the liquid on the development of the global flow. Dynamic characters of liquid surface such as the presence of the cavity and the formation of the wave were displayed.

R. B. Kalifa (✉)
LGM, National Engineering School of Monastir, University of Monastir,
Monastir, Tunisia
e-mail: rimbenkalifa@yahoo.fr

N. Mahjoub Saïd
LGM Preparatory Institute for Engineering Studies, University of Monastir,
Monastir, Tunisia
e-mail: nejla.mahjoub@fsm.rnu.tn

H. Bournot · G. Le Palec
IUSTI, IUSTI Laboratory, University of Aix-Marseille, UMR CNRS 7543,
Marseille, France
e-mail: georges.lepalec@univ-amu.fr

1   Introduction

For more than half a century (Gaunter et al. 1970), the phenomenon of an air jet impinging normally onto a deformable liquid surface plays important role in many industrial applications because they control bath mixing, chemical reaction kinetics, energy consumption, foaming slag formation, heat and mass with the slag and the molten steel.

Based on the experimental observations, three different modes of jet impingement on a liquid surface have been identified by Molloy (1970): First, dimpling mode (LFR), secondary, Splashing mode (HER) and finally, Penetrating mode.

The instability of the cavity at higher jet-impact velocity was also reported by Cheslak et al. (1969). Experiments were performed using an air jet on a water surface. They compared their experimental results with predictions from a theory similar to that from Banks and Chandrasekhara (1963). It was shown that the change in the vertical momentum of a jet impinging on a liquid surface is equal to the weight of displaced fluid. The depth and diameter of the cavity are predicted and it was found that the cavity had a paraboloid shape.

Understanding the effects of a gas jet impinging on a liquid surface would give more insight into the process behavior. Many of researchers have traced the effects of the main parameters. Koria and Lange (1984) carried out an experimental study on an impinging air jet on a water surface. They give more importance to examine the Oxygen pressure, lance distance, and the number of nozzles.

Eletribi et al. (1997) described the evolution of surface deformation. The interface between air and liquid is subjected to four different forces: the impingement force of the jet, the shear force associated to the flow of gas along the surface, the surface tension force, and the pressure force due to the induced recirculatory flow in the bath. The surface tension force increases with the surface area. It is found that the higher the gas velocity, the higher the jet pressure force, the higher the recirculatory flow induced force and the shear force.

More recently, an unsteady simulation of a planar air jet impinging onto a deformable liquid surface is present by Muñoz-Esparza et al. (2012). The objective of their study is to simulate the fluid dynamics phenomena. The VOF (Volume of Fluid) method is used due to the existence of two different immiscible phases and separated by just one interface. The analysis of the velocity and Reynolds stress fields highlights the turbulence transport mechanisms from the air jet towards the water flow.

A CFD modeling of gas jet impinging onto the liquid surface was carried out using the commercial code FLUENT. All the numerical simulation concerning this problem is modeled using the volume of fluid technique (VOF). Nguyen and Evans (2006) used a standard k-ε turbulence model and the VOF model in a 2D axisymmetric geometry formulation.

From the available literature, very few researches have been interested to the behavior of the interaction of plane jet impinging onto fluid surface. The present study is devoted to the numerical investigation of the impingement of a plane gas

jet onto a water surface. The results from the numerical tests are comparable with those presented by Muñoz-Esparza et al. (2012). This study analyzes the structure of the flow in both phases in the case of an impinging jet on the liquid surface for different nature of the liquid (Water and Gasoline).

2 Numerical Study

2.1 Governing Equations

The Reynolds-averaged Navier–Stokes equations are computationally solved, for an unsteady and incompressible turbulent fluid. The governing equations including the continuity (1) and the momentum (2) are written in the Cartesian coordinates as follows:

$$\frac{\partial \rho}{\partial t} + \frac{\partial (\rho u_i)}{\partial x_i} = 0 \tag{1}$$

$$\frac{\partial (\rho u_i)}{\partial t} + \frac{\partial}{\partial x_j}(\rho u_j u_i) = -\frac{\partial \overline{P}}{\partial x_i} + \frac{\partial}{\partial x_j}\left[\mu\left(\frac{\partial u_i}{\partial x_j} + \frac{\partial u_i}{\partial x_i}\right) - \rho\overline{u_i' u_j'}\right] + \rho g + S_{i,s}, \tag{2}$$

where i, j = 1, 2, 3 referring to x, y and z respectively, u_i and x_i are the mean velocity and the coordinate in the i direction, respectively. P represents the mean pressure. The terms $\overline{u_i' u_j'}$, products of the velocity fluctuations, are the Reynolds stresses which serve as the nonlinear term of the momentum equation. To fully characterize the fluctuating functions and variables developing in a similar complex three-dimensional flow, we introduced the Reynolds Stress Model (RSM).

The introduction of RSM leads to the resolution of the following equation:

$$\underbrace{\frac{\partial}{\partial x_k}(u_k \overline{u_i' u_j'})}_{C_{ij}} = -\underbrace{\frac{\partial}{\partial x_k}\left[\overline{u_i' u_j' u_k'} + \frac{1}{\rho}\overline{p'\left(\delta_{kj} u_i' + \delta_{ik} u_j'\right)}\right]}_{D_{ij}^T} - \underbrace{\left[\overline{u_i' u_k'}\frac{\partial u_j}{\partial x_k} + \overline{u_j' u_k'}\frac{\partial u_i}{\partial x_k}\right]}_{P_{ij}} + \phi_{ij} + \varepsilon_{ij},$$

$$\tag{3}$$

where the symbols Cij, Pij, Gij, D_{ij}^T and ϕ_{ij} denote, respectively, the convective term, the turbulent diffusion, the viscous diffusion, the stress production, the buoyancy production, the pressure strain, and the dissipation term (Wilcox 1998).

2.2 Multiphase Flow Modeling

The interaction between the liquid phase (water) and the gas phase (air) was carried out using the volume of fluid model (VOF) (Hirt and Nichols 1981).

In the continuity Eq. (1), the velocity field is shared by air and water, which means that there is a continuous velocity of these phases through the interface. We distinguished that in the momentum Eq. (2), the interaction between air and water is modeled by $S_{i,s}$ which is the surface tension.

To follow this interface, this method uses scalar functions representing the volume fraction of each fluid in each computational cell. The interface is calculated with the following equation:

$$\frac{\partial(\alpha_2\rho_2)}{\partial t} + \frac{\partial(\alpha_2\rho_2 u_i)}{\partial x_i} = s_2 \tag{4}$$

s_2 is the source of phase 2 (air phase), ρ_2 is the density of air, and α_2 is the volume fraction of air; where v is the volume of fluids ($v = v_1 + v_2$), v_1 and v_2 are respectively the volume of phase 1 and 2. The volume fraction of the primary phase $(\alpha_1 = v_2/v_1)$ is calculated by the following expression: $\sum_{i=1}^{2} \alpha_i = 1$.

2.3 Flow Configuration and Boundary Conditions

Figure 1 exhibits the calculation domain in the case of impinging jet on a liquid surface. The jet nozzle with a width (e) of 5 mm is modeled. The jet Reynolds number, Re, is based on the nozzle slit and the inlet velocity v_j. In the present study, the Reynolds number value of 2000, 3000, and 5000 are measured. The thickness of the water layer is $3 \times e$, and the distance with the nozzle outlet close to $h = 6 \times e$. Three types of boundary conditions were used to describe the flow field: The condition of the nozzle jet is essential in predicting the centerline velocity and the shear stress. A uniform jet velocity profile was specified at the jet exit "v_j". The boundary condition for the upper part of the domain was choice Zero gradient for all variables was prescribed at the position (corresponding to $y = 120 \times e$). The rest of the domain was wall where the no-slip boundary conditions were imposed and with zero roughness.

Fig. 1 Schematic of the model geometry
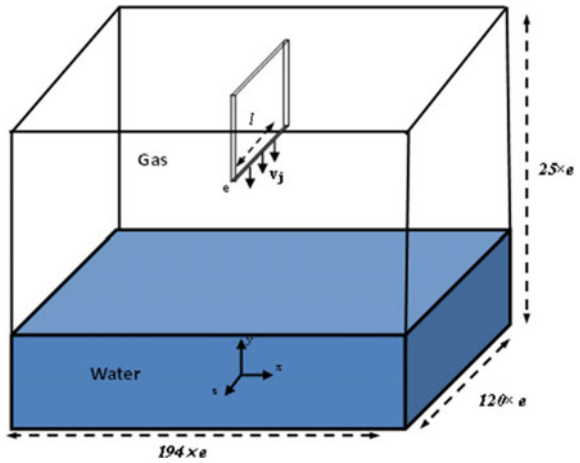
3 Results and Discussion

3.1 Validation of the Numerical Code

A comparison between experimental data, outcome from the study of Muñoz-Esparza et al. (2012), and computational results obtained by numerical simulation is shown in Fig. 2. This figure introduces the profiles of the velocity magnitude $\left(\sqrt{u^2 + v^2}/v_j \right)$ normalized by the jet velocity "v_j" along the axial direction for $y/e = 5$. The goal of this analysis is to validate the RSM models by compared with the experimental study.

It is detected that the axial distributions of the velocity magnitude present a Gaussian shape towards the jet axis. The distributions of computational mean velocity magnitude are almost coincident with experimental ones. These agreements are present in the shear layer ($-1 \leq x/e \leq 1$). In this region, numerical results produce the same values with the experiments, and therefore, more important gradients through the shear layer. The experimental data given by Muñoz-Esparza et al. (2012) are provided with the results obtained with the RSM models.

3.2 Hydrodynamic Phenomena

This section is focused on various hydrodynamic phenomena associated with the impingement of a gas jet onto a liquid surface, namely the development of the gas jet, the formation of a cavity at the liquid surface and the generation of droplets from this cavity due to the interactions with the jet.
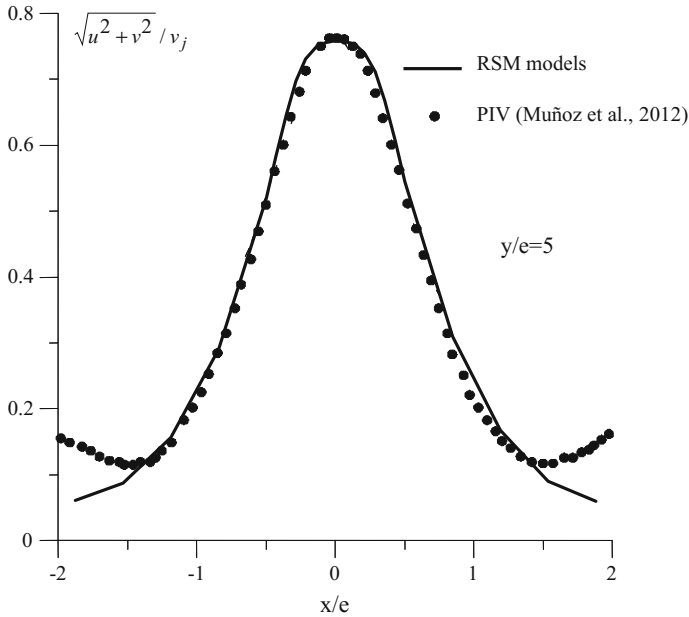
Fig. 2 Axial profile of the velocity magnitude at x/d = 5 for Re = 2000

Fig. 3 The mean flow streamline pattern in the case of HFR (Re = 3000)
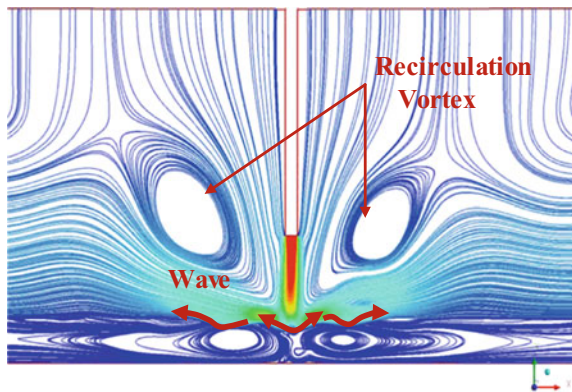
Figure 3 we shall discuss vortex dynamics in the case of air jet impinging on a liquid surface in the case of Splashing mode "HFR" (for a Reynolds number Re = 3000). In order to render the interface and the flow visualization more visible, the streamlines schematic of this configuration is given in this figure.

First, it is clear from the streamline pattern that the jet penetrates into the water causes a small cavity. After that, Fig. 3 also identifies a stagnation zone that extends to a radial location defined by the spread of the jet. The air jet is deflected into the deformed surface flow. When a gas jet impinges on a liquid surface, the liquid

surface is deformed vertically and horizontally. The balance of the dynamic pressure and the opposing force (buoyancy) from the liquid mainly affects the horizontal movement. The surface tension and the shear stress from the deflected gas flow produce an interfacial deformations behavior. This deformation of the surface also contributes to generate of a significant amount of the wave. It appears that the surface layer accelerated under the air stress, surface waves were generated. We observe that the recirculation region attached to the wave cause the departure of the formation of a new recirculation vortex in the water surface. Thus, the liquid phase is, eventually, blown up from below by the nascent recirculation vortex. The air phase is characterized by a ring-shaped vortex slightly away from the interface air/water that is responsible for large structure dynamics in the outer layer. The air flow is directed toward the gas plumes, entrained, lifted and finally the flow is re-attached after a small recirculation zone (Fig. 3).

In Fig. 4, the evolution of the kinetic energy at different locations (for $x/e = 3, 4, 5, 6$ and 8) is examined. For $x/e = 3$, the jet starts to feel the presence of the water presenting a peak close to the liquid film and, moreover, has a wide lobe due to the shear layer. This higher level of turbulent kinetic energy was attributed to the presence of the deformation surface. The result shows that the energy transfer-taking place from the wave to the turbulence leads to an intensification of the streamwise vortices determined previously in Fig. 3. For the two last plane ($x/e = 6$ and $x/e = 8$), the shape of the kinetic energy profile is similar and with a single peak. The results show an attempt to decreasing of the turbulence further away the centerline jet.
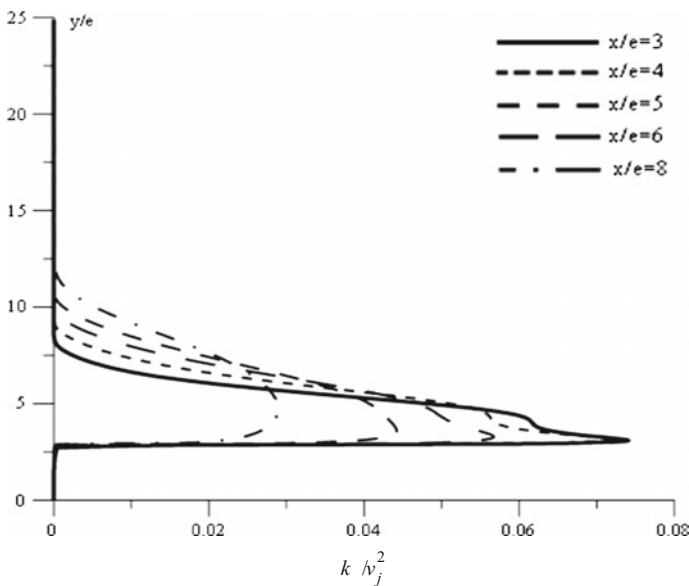
Fig. 4 The turbulent kinetic energy distribution in the surface wave

3.3 Effect of Nature of the Liquid

As we have seen, the impinging jets are used in many technological applications where mixing is important (mass transfer or heat): burning, heating or cooling surface and they are responsible for mixing and transfer of mass in the reactors. This section presents the different phenomena to configuration of plane air jet impinging on a flammable liquid (Gasoline) at the ambient temperature. The properties of the liquid used in this section are listed in Table 1. This table shows that the Gasoline have a lower surface tension than the water.

Once touching the liquid surface, the gas is deviated and the surface is deformed by the creation of a cavity. To a relatively high jet velocity, Re = 5000, when the jet flow is important, the large pressure force resulting from the airflow causes a well-developed cavity. The cavity length is defined as the length scale at which gravity and surface tension forces. From the numerical tests, the cavity length is around 5.2 × e for the water/air system and around 4.6 × e for the gasoline/air system. For a water case (Fig. 5), the surface is deformed by the creation of a small cavity, therefore, the pressure force due to the circulatory flow causes a raised dimple and beyond this region, a periodic train of waves propagating.

The action of the gas/liquid interface has two effects, which generate deformations of the surface and the presence of the wave. We are interested in instantaneous

Table 1 Properties of liquid used in the numerical simulation

Liquid type	Density (Kg/m^3)	Kinematic viscosity (kg/mms^{-1})	Surface tension (Kg/s^2)
Water	998.2	0.1	0.074
Gasoline	684	0.5	0.02
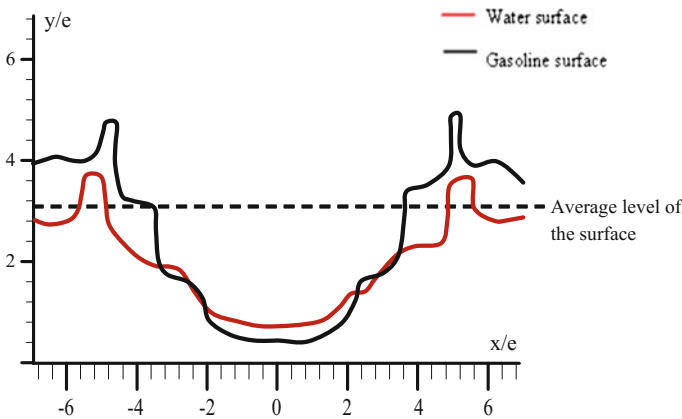
Fig. 5 Cavity depth as a function of nature of the liquid

(a) Gasoline surface
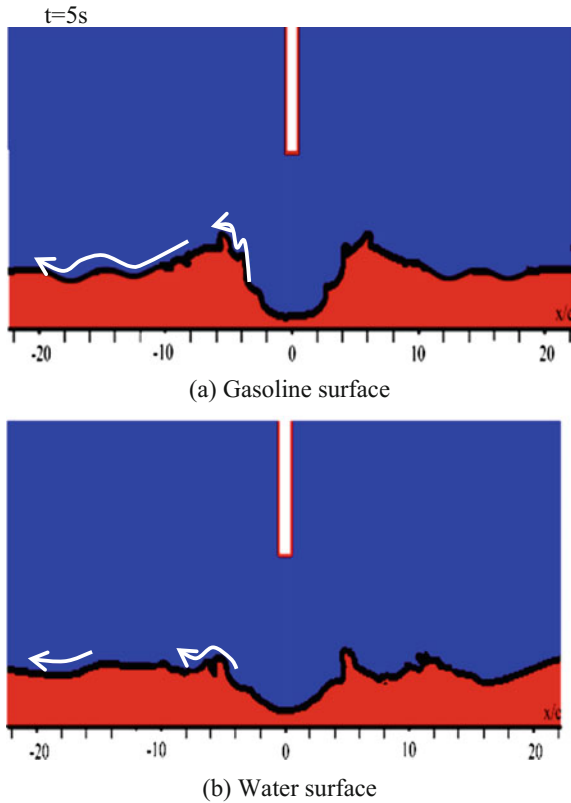
(b) Water surface

phenomena generated by the change of the nature of the liquid. The evolution of the free surface at t = 5 s, for the different nature of liquid and at high Reynolds numbers (Re = 5000) is plotted in Fig. 6a, b.

The impact of a gas jet onto a water surface will produce a liquid surface cavity less deep and wider than the gasoline case. A remarkable perturbation that form on the sides of the cavity (case of gasoline surface) suggests that the surface tension associated to the interface between air and liquid is important parameters. This instability results from the competitive effects of the inertia forces and the pressure forces.

Another major difference between the two liquid surfaces is that the amplitude of the waves for the gasoline surface in the x-direction become weaker compared with the water surface case further away from the centerline jet.

4 Conclusion

A numerical investigation, which examined a gas jet impingement on a liquid surface, was conducted in this paper. Impinging gas jet on liquid surface was modeled using RSM model with a Cartesian coordinate over a range of flow rates (Re). The dynamic behavior of the liquid surface was solved using the VOF method.

First, a good agreement between the numerical predictions and the experimental results of Muñoz-Esparza et al. (2012) was found.

The study is focused on various hydrodynamic phenomena associated with the impingement of a gas jet onto a liquid surface, namely the development of the gas jet, the formation of a cavity at the liquid surface. Large turbulence intensity observed near free surfaces, produces a turbulent pressure field, which would, in principle, be able to generate a large eddies further away the interface air–water. Next, the study is focused on various hydrodynamic phenomena associated with the impingement of a gas jet onto a liquid surface. The results highlight that the air jet penetration rate is more important for the case of gasoline surface. In addition, the surface of gasoline is dominated by an irregular wave pattern than the other case.

References

Banks RB, Chandrasekhara DV (1963) Experimental investigation of the penetration of a high-velocity gas jet through a liquid surface. J Fluid Mech 15:13–34

Cheslak FR, Nicholls JA, Sichel M (1969) Cavities formed on liquid surfaces by impinging gaseous jets. J Fluid Mech 36(01):55

Eletribi S, Mukherjee DK, Prasad V (1997) Experiments on liquid surface deformation upon impingement by a gas jet. Proc ASME Fluids Eng Div 244:235–247

Gaunter JW, Livingood JNB, Hrycak P (1970) Survey of literature on flow characteristic of a single turbulent jet impinging on a flat plate, NASA TN D-5652

Hirt CW, Nichols BD (1981) Volume of fluid (VOF) method for the dynamics of free boundaries. J Comput Phys 39(1):201–225

Koria SC, Lange KW (1984) A new approach to investigate the drop size distribution in basic oxygen steelmaking. Metall Trans B 15(1):109–116

Molloy NA (1970) Impinging jet flow in a two-phase system the basic flow pattern. J Iron Steel Inst 208(10):943–950

Muñoz-Esparza D, Buchlin JM, Myrillas K, Berger R (2012) Numerical investigation of impinging gas jets onto deformable liquid layers. Appl Math Model 36:2687–2700

Nguyen AV, Evans GM (2006) Computational fluid dynamics modelling of gas jets impinging onto liquid pools. Appl Math Model 30(11):1472–1484

Wilcox DC (1998) Turbulence modeling for CFD, DCW Industries, Inc., La Canada, Cal., USA

Modeling and Simulation of Transients in Natural Gas Pipelines

Sabrine Trabelsi, Ezzedine Hadj-Taieb and Sami Elaoud

Abstract The simulation of natural gas transmission pipelines has been studied by many workers. To simulate one-dimensional transient flow in natural gas pipeline, the continuity and momentum equations must be solved simultaneously. This creates a set of nonlinear partial differential equations, which are complex and cumbersome. The numerical solution, by the method of characteristics of the general equations governing the transient state, is then developed by introducing an inertial factor. A computer programme was developed to study the transient flow in a system of pipelines with a constant pressure upstream and imposed downstream consumption.

Keywords Gas transmission · Transient flow · Method of characteristics

1 Introduction

Natural gas flows in pipelines can be numerically modeled by different methods similar to those of liquid flows. In this paper, we direct research towards the study of transient flows in gas pipes using numerical method. To keep this analysis simple, most of them assumed that flow is steady in the pipeline. The fluctuations in demand as well as the operation of system controlling devices such as valves, compressors, and pressure regulators bring about disturbance in the pipeline.

Evidently, the analysis of unsteady-state conditions owing to dependence of variables to time and space is much more difficult than that of steady state where its

S. Trabelsi (✉) · E. Hadj-Taieb · S. Elaoud
Research Laboratory "Applied Fluid Mechanics, Process Engineering and Environment",
Engineering School of Sfax, BP'W'3038, Sfax, Tunisia
e-mail: sabrine.trabelsi@enis.tn

E. Hadj-Taieb
e-mail: Ezed.Hadj@enis.rnu.tn

S. Elaoud
e-mail: elaoudsa@yahoo.fr

parameter is only depended to space. The investigation of such transient phenomena enables the gas transmission operators to control and monitor any changes in the gas pressure, temperature, and flow rate. Numerical methods previously used to solve this system of linear partial differential equations include the method of lines (Tentis et al. 2003), the finite difference, the finite volume, the finite volume with total variation diminishing (TDV) (Zhou and Adewumi 2000), finite element, the method of characteristics (MOC), and a variety of explicit and implicit finite difference schemes (Heath and Blunt 1969). Neglecting the inertia term in the momentum equation will result in loss of accuracy of the simulation results. In order to compensate for the exclusion of the inertia term from the momentum equation, (Yow 1972) introduced the concept of *inertia multiplier* to partially account for the effect of the inertia term in the momentum equation. (Wylie et al. 1974) simulated transients in natural gas pipelines in accordance with the concept of the inertia multiplier. Rachford and Dupont (1974) have demonstrated that calculations based on the concept of inertia multiplier will sometimes yield very misleading results. In the present study, the inertia term in the momentum equation is fully included. The governing equations, together with an equation of state, constitute a non-homogeneous hyperbolic system of first-order quasi-linear partial differential equations. The (MOC) is used to solve this system. The numerical solution of this set of non-homogeneous quasi-linear hyperbolic partial differential equations is not trivial.

2 Hypotheses

The following assumptions are considered: Unidirectional flow, flow is isotherm, expansion of pipe wall will be neglected, the pipe has a constant slope over any particular reach, the equation of state is given by $p = z\rho RT$ in which z the compressibility factor considered constant over the range of a single problem, the friction factor is a function of wall roughness and Reynolds number and the change in kinetic energy along a pipe is unimportant and may be neglected.

3 Mathematical Formulation

3.1 Transient Pipeline Gas Flow Model

The governing equations describing the general one-dimensional compressible flow through a pipeline under isothermal conditions are the conservation of mass (or continuity), momentum and an equation of state relating the pressure, the mass rate
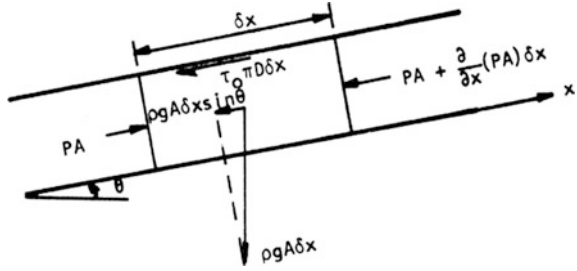
of flow and the temperature. For a general pipe as shown in Fig. 1, these hyperbolic
partial differential equations are (Wylie and Streeter 1978)

$$\frac{C^2}{A}\frac{\partial M}{\partial x} + \frac{\partial p}{\partial t} = 0 \tag{1}$$

$$\frac{\partial p}{\partial x} + \frac{pg}{C^2}\sin\theta + \frac{fC^2 M|M|}{2DpA^2} + \frac{\alpha^2}{A}\frac{\partial M}{\partial t} = 0 \tag{2}$$

$$\frac{p}{\rho} = ZRT \tag{3}$$

where C is the acoustic wave speed, A is the cross-sectional area of the pipe, M is
the mass rate of flow, p is the absolute pressure, g is the acceleration of gravity, f is
the friction factor, D is the pipeline diameter, α is the inertial, θ is the angle the pipe
makes with the horizontal measured positive for increasing elevation in the +x
direction, ρ is the mass density, Z is the gas compressibility factor, R the gas
constant, and T the absolute temperature.

The continuity Eq. (1) and the equation of motion (2) are used to derive the
transient algebraic equations by the method of characteristics. Before undertaking
these derivations we will examine steady-state relations in pipes.

3.2 Steady-State Equations

For steady-state isothermal flow, transient terms are null (terms with $\partial/\partial t$), thus
Eq. (1) becomes

$$\frac{dM}{dx} = 0 \Rightarrow M = cte \tag{4}$$

For constant M Reynolds number is constant which makes f a constant. X is now
the only independent variable, and Eq. (2) becomes

$$dp + \left(\frac{pg}{C^2} \sin\theta + \frac{fC^2 M^2}{2 Dp A^2} \right) dx = 0 \tag{5}$$

This equation may be integrated between limits, from $x = 0$, $p = p_1$ to $x = \Delta x$, $p = p_2$

$$\frac{p_1^2 + fB^4 M^2 /2gDA^2 \sin\theta}{p_2^2 + fB^4 M^2 /2gDA^2 \sin\theta} = e^s \tag{6}$$

In which $s = 2g\Delta x \sin\theta/B^2$. After solving for p_2^2

$$p_2^2 = \left(p_1^2 - \frac{fB^2 M^2}{DA^2} \Delta x \frac{e^s - 1}{s} \right) / e^s \tag{7}$$

This equation can be written under the following form:

$$p_1 - p_2 = \frac{fB^2 M^2 \Delta x}{(p_1 + p_2)DA^2} \frac{e^s - 1}{s} + \frac{p_2^2}{p_1 + p_2}(e^s - 1) \tag{8}$$

4   Resolution of Transient Gas Flows in Pipes by the Method of Characteristics

The linear combination of both Eqs. (1) and (2) gives the following system (Wylie and Streeter 1978):

$$C^+ : \begin{cases} \dfrac{\alpha^2}{A} \dfrac{dM}{dt} + \dfrac{\alpha}{C} \dfrac{dp}{dt} + \dfrac{pg}{C^2} \sin\theta + \dfrac{fC^2 M^2}{2Dp A^2} = 0 \\ \dfrac{dx}{dt} = \dfrac{C}{\alpha} \end{cases} \tag{9}$$

$$C^- : \begin{cases} \dfrac{\alpha^2}{A} \dfrac{dM}{dt} - \dfrac{\alpha}{C} \dfrac{dp}{dt} + \dfrac{pg}{C^2} \sin\theta + \dfrac{fC^2 M^2}{2Dp A^2} = 0 \\ \dfrac{dx}{dt} = -\dfrac{C}{\alpha} \end{cases} \tag{10}$$

Thereby, the system shown in Eqs. (9) and (10) can be integrated over a grid of characteristics like those shown in Fig. 2, along C^+ and C^- Along lines RP and SP respectively, in the rank $0 \leq t \leq T$, $0 \leq x \leq L$. Assuming a linear approximation, the slopes of the lines satisfy the condition shown in Eq. (11).
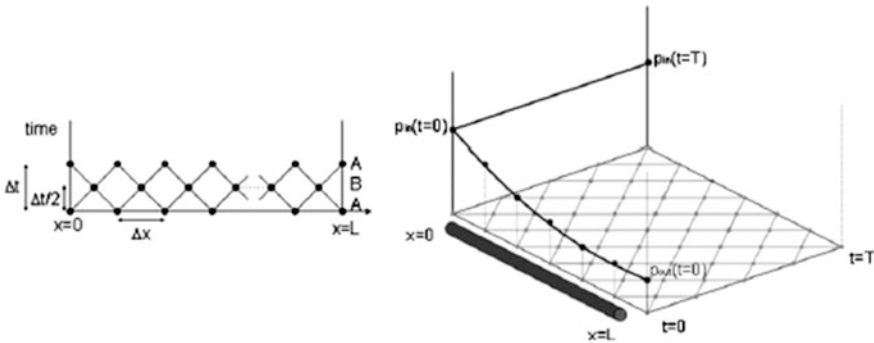
Fig. 2 Numerical scheme for the method of characteristics

$$\pm C \leq \frac{\Delta x}{\Delta t} \tag{11}$$

In order to get a consistent numerical scheme, it is necessary that Δx and Δt to be linked by means of Eq. (11) so that the numerical integration of the equations was carried out over the characteristic curves. In such a case, the system shown in both Eqs. (9) and (10) becomes respectively the one shown in Eqs. (12) and (13).

$$C^+ : p_P - p_R + \frac{\alpha C}{A}(M_P - M_R) + \frac{p_P^2}{p_P + p_R}(e^s - 1) +$$
$$+ \frac{fC^2 \Delta x}{2(p_P + p_R)DA^2}(M_P|M_P| + M_R|M_R|)\frac{(e^s - 1)}{s} = 0 \tag{12}$$

$$C^- : p_P - p_S - \frac{\alpha C}{A}(M_P - M_S) + \frac{p_P^2}{p_P + p_S}(e^s - 1) +$$
$$+ \frac{fC^2 \Delta x}{2(p_P + p_S)DA^2}(M_P|M_P| + M_S|M_S|)\frac{(e^s - 1)}{s} = 0 \tag{13}$$

In these equations a "second-order" evaluation of friction is used, averaging the flow at P and at A or B. The absolute value signs are inserted so that the equations are valid for flow in the reverse direction. Another approximation for the friction term is

$$M^2 = \frac{M_P|M_P| + M_R|M_R|}{2} \tag{14}$$

Equations (12) and (13) are solved simultaneously for interior sections of a pipe and they are used individually with the appropriate boundary conditions. Newton's iterative method, the boundary conditions and Eqs. (12) and (13) allow the determination of flow parameters (pressure and the mass rate of flow) at $t_0 + \Delta t$

Evaluation of inertial Multiplier α

Yow, who developed the concept of the inertial multiplier, made an extensive analysis of the relation of the value of α to error, based on gas flow in a single horizontal pipe with sine wave variation of input boundary conditions.

$$\alpha^2 = 1 - (\sigma m h)^2/3\, p_d + \psi \sqrt{p_d \left[1 + (\sigma m \omega^*)^2\right]}/m\,\omega^*\,\Delta q \qquad (15)$$

The inertial multiplier may change during the course of the transient. In fact, several time zones may be set up in advance, allowing the time increment to be adjusted. Interpolations are not needed, as shown in the computer programme, since for each reach of length Δx_i

$$\alpha_i = \frac{B\Delta t}{\Delta x_i} \qquad (16)$$

And α becomes a subscribed quantity for each reach.

5   Application and Results

As an application, we deals with a pipeline consisting of five reaches, or five separate pipes in series (Fig. 3) each of a single reach. Constant pressure control is used upstream and specified flow is given downstream. The pipeline has changes in elevation at each section.

As the flow demand consists of two linear segments, α is calculated for the two time zones, indicated in Fig. 4.

The programme uses Eq. (7) to solve for downstream steady-state pressure for each reach.

After steady-state and transient printout is provided for, the transient loop consists of three parts, each a Newton–Raphson solution. The upstream boundary condition has only PP(6) to determine, and the interior sections solve for MP(I) and
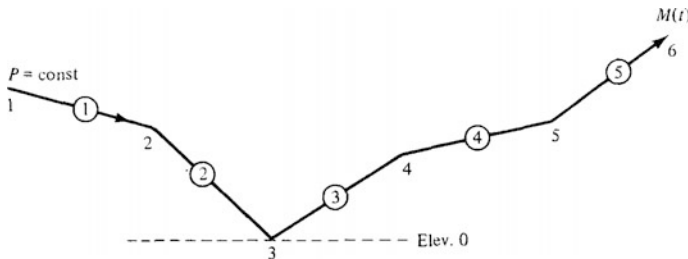
Fig. 3 Gas installation with 5 pipelines in series

Fig. 4 Consumption curve at node 6
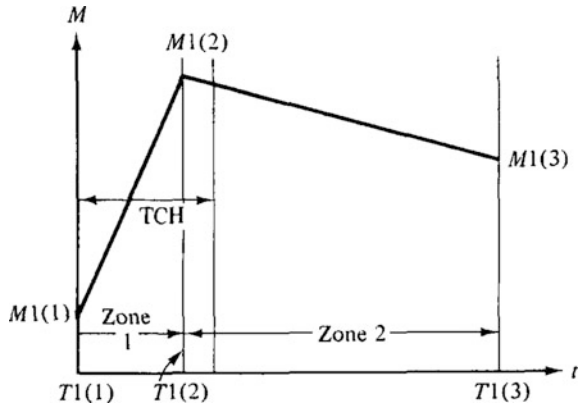
PP(I), I = 2, 5. Each iterative solution is started by a linear extrapolation of the two previous values of the variables, e.g.,

MP(1) = 2 M(1)–MO(1)

MO(1) is one step before M(1). The Newton–Raphson method then improves this estimate by calculating a correction Δp or ΔM.

After simulation, we obtain the curves of evolution of the pressure and the mass flow rate for each node.

Gradual opening manoeuver

The downstream valve is opened gradually, and then we show in Figs. 5, 6 the evolution of the pressure and mass flow rate generated by this perturbation.

Snap closure manoeuver

In this case, an abrupt closure was performed downstream (M (6) = 0), and then we show in Figs. 7, 8 the evolution of the pressure and mass flow rate generated by this perturbation.

Severe transient conditions are created from a downstream valve's stroking. At $t = 0-$, steady-state flow is established (pipeline length and diameter are 50500 m and 2 m respectively) with inlet gas mass flux of four slug/s, at $t = 0+$, the
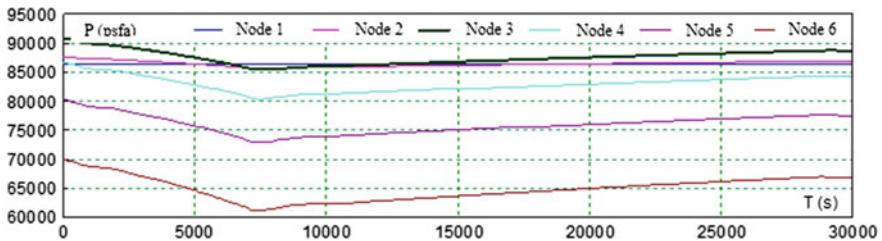
Fig. 5 Evolution of pressures
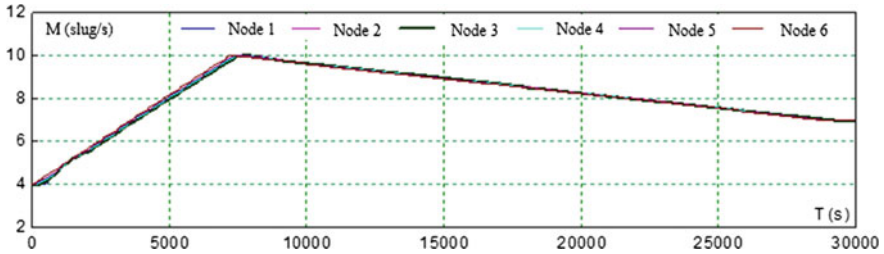
Fig. 6 Evolution of mass flow rates
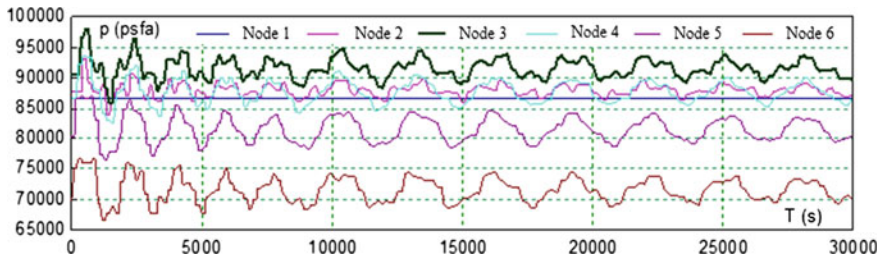
Fig. 7 Evolution of pressures
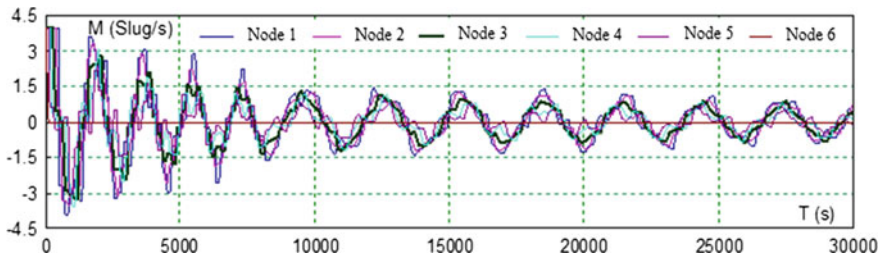
Fig. 8 Evolution of mass flow rates

downstream valve is closed instantaneously, thus setting the gas mass flux at the outlet equal to zero, while the inlet mass flux is maintained at its original value. The pipe compressibility factor is set to 1.04 mm and temperature is about 520 °F. Multiple lines show the mass flow rate waves while traveling backwards along the pipeline after the valve stroking, it decreases from one node to another until it cancel at node 6. Whereas for the pressure it varies in a random way, increases at the level of the first nodes and then it relapses.

6 Conclusion

In this study, the numerical solution of the transient natural gas flow in rigid pipelines has been presented. This problem is governed by coupled two linear partial differential equations; the momentum and continuity equations. The numerical method used to solve these equations is the method of characteristics. This method is simple, straightforward, and without convergence problem. The occurrence of pressure oscillations in the different sections of the pipe was analyzed due to the compression wave created by the rapid closure of downstream valve. In this case, the pressure may reach excessive values due to the mass accumulation effect caused by the delay of the upstream valve closure. The figures presented show the perfect concordance of the numerical results obtained by the method of characteristics (M.O.C).

References

Dorao* CA, Fernandino M (2011) Simulation of transients in natural gas pipelines, Elsevier. J Nat Gas Sci Eng. https://doi.org/10.1016/j.jngse.2011.01.004

Ebrahimzadeha E, Shahrakb MN, Bazooyar B (2012) Simulation of transient gas flow using the orthogonal collocation method, Elsevier. Chem Eng Res Design. https://doi.org/10.1016/j.cherd.2012.02.018

Gonzàlez AH et al (2008) Modeling and simulation of a gas distribution pipeline network. Appl Math Model. https://doi.org/10.1016/j.apm.2008.02.012

Hai W, Xiaojing L, Weiguo Z (2011) Transient flow simulation of municipal gas pipelines and networks using semi implicit finite volume method, Elsevier. Engineering Procedia. https://doi.org/10.1016/j.proeng.2011.05.034

Heath MJ, Blunt JC (1969) Dynamic simulation applied to the design and control of a pipeline network. J Inst Gas Eng 9:261–279

Rachford HH Jr, Dupont T (1974) A fast, highly accurate means of modeling transient flow in gas pipeline systems by variational methods. Soc Pet Eng J 15:165–178

Streeter VL, Wylie EB (1970) Natural gas pipeline transients. Soc Pet Eng J 75:357–364

Taylor TD, Wood NE, Power JE (1962) A computer simulation of gas flow in long pipelines. Soc Pet Eng J Trans AIME 225:297–302

Tentis E, Margaris D, Papanikas D (2003) Transient gas flow simulation using an adaptive method of lines, Elsevier. https://doi.org/10.1016/S1631-0721(03)00106-2

Wylie EB, Streeter VL (1978) Fluid transients. Mac Graw-Hill Company, New York

Wylie EB, Stoner MA, Streeter VL (1971) Network system transient calculation by implicit methods. Soc Pet Eng J 3:356–362

Wylie EB, Streeter VL, Stoner MA (1974) Unsteady natural gas calculation in complex piping systems. Soc Pet Eng J 10:35–43

Yow W (1972) Numerical error in natural gas transient calculations. ASME Trans Ser D 94: 422–428

Zhou J, Adewumi MA (2000) Simulation of transients in natural gas pipelines using hybrid TVD schemes. Int J Numer Methods Fluids

Damage Analysis of Flax Fibre/Elium Composite Under Static and Fatigue Testing

M. Haggui, A. El Mahi, Z. Jendli, A. Akrout and M. Haddar

Abstract Due to their eco-friendly, bio-degradability characteristics and good mechanical properties, natural fibre composite has become a good alternative in many composite applications such as automotive, aerospace and furniture construction. The present study deals with the mechanical properties of flax fibre reinforcement associated to Elium which is a thermoplastic resin. First, the composite prepared by liquid infusion was subjected to quasi-static tensile loading and cyclic tensile test to investigate macroscopic damage behaviour. Second, a three-point static and fatigue bending test were performed to failure. In case of fatigue test, the hysteresis loops was used as a measure for stiffness degradation, energy dissipation and loss factor. Many configuration of laminate were prepared for experimental work. The flax/Elium composite has shown a promising solution that could be integrated in many industrial applications thanks to its short time needed for manufacturing by infusion and its good mechanical characteristics.

M. Haggui (✉) · A. El Mahi
LAUM – Laboratoire d'Acoustique de l', Université du Maine,
Avenue Olivier Messiaen, 72085 Le Mans Cedex 9, France
e-mail: Mondher.Haggui.Etu@univ-lemans.fr

A. El Mahi
e-mail: abderrahim.elmahi@univ-lemans.fr

M. Haggui · A. Akrout · M. Haddar
LA2MP – Laboratoire de Mécanique, Modélisation et Productique,
Ecole Nationale d'Ingénieurs de Sfax, BP 1173, 3038 Sfax, Tunisia
e-mail: ali_akrout2005@yahoo.fr

M. Haddar
e-mail: mohamed.haddar@enis.rnu.tn

M. Haggui · A. Akrout · M. Haddar
Université de Sfax, Sfax, Tunisia

Z. Jendli
ESTACA'Lab – Pôle Mécanique des Matériaux Composites et Environnement,
Parc Universitaire Laval-Changé, Rue Georges Charpak, BP-76121,
53061 Laval Cedex 9, France
e-mail: zouhaier.jendli@estaca.fr

681

1   Introduction

The application of polymer composites reinforced with natural fibres has substantially increased in the last few years, especially in sectors such as the automotive, aerospace, sport, leisure and packaging. Due to their reduced cost, eco-friendly and higher bio-degradability, biocomposites represent an important incentives for use (Wambua et al. 2003). Flax fibres associated to thermoplastic polymer are widely used in recent researches.

There are many factors that can influence the performance of bicomposites. In general, high fibre volume fraction induces high performance of the composites (Ku et al. 2011). Therefore, the increase in fibre strength leads to an increase in tensile properties (Baley et al. 2006). The processing method is also an important factor having impact on mechanical properties and interfacial characteristics of the composites. Thus, suitable processing techniques and parameters must be carefully selected in order to produce the optimum composite.

Many authors studied the mechanical behaviour in static and cyclic loading in composite. Monti et al. (2016) studied the damage mechanism for five types of flax fibre laminate specimens subjected to static tensile test. For each category of broken specimens microscopic and macroscopic analyses of the failure modes and mechanisms were performed. Generally, matrix microcracking and fibre/matrix debonding are the first registered microscopic defects. Then, these defects multiply and merge to form transverse cracks. Aslan (2013) investigated the damage mechanism of flax fibre polyethylene terephthalate (LPET) commingled composites by acoustic emission analysis. Shah (2015) studied the damage evolution in static and fatigue tests of jute, hemp and flax composites. He emphasized that the complex nonlinear behaviour of these materials comes essentially from the specificity of the natural fibres behaviour. The analysis of the flax composites microstructure, made by Coroller et al. (2013), shows a high bundle content.

El Mahi et al. (1995) studied the stiffness degradation and the identification of damage mechanisms under static and fatigue test applied to cross-ply carbon fibre laminate. The first stage of damage is induced by matrix cracking in the 90° plies. These matrix cracks develop in the fibre direction and extend across the laminates. Idriss et al. (2013) investigated three-point bending fatigue test applied to sandwich using a glass fibre laminates as a skin. The results showed significant stiffness degradation along the first cycles followed by a gradual decrease until rapid drop in stiffness due to failure.

The purpose of this study is to investigate the mechanical behaviour of flax fibre/Elium composite subjected to static and fatigue loading. In first time we deal with static tensile testing to evaluate mechanical properties and cyclic tensile tests to quantify the stiffness degradation. Second static and fatigue three-point bending

tests until failure were performed to analyze damage during lifetime. Hysteresis loop was used to evaluate energy dissipation and loss factor.

2　Material and Experimental Setup

2.1　Material

The composite developed in this work is based on a 200 g/m^2 continuous unidirectional dry Flax Tape reinforcement developed by the company LINEO. The resin is the new thermoplastic called Elium made by ARKEMA. This resin is an acrylic activated by peroxide (Arkema Technical specification of the Elium$^®$ 150 resin: Viscosity Brookfield LVF #2, 60 rpm 100 mPa.s). Its fluidity makes it particularly interesting in manufacturing by infusion unlike other thermoplastic which need a complicate thermo-compression method.

　Flax fibres dried in an oven for about 1 h at 110 °C. This conditioning cycle has a good compromise between drying of the fibres and conservation of mechanical properties (Baley et al. 2012). The dried plies are positioned manually to the desired stacking sequence directly on a plane and previously waxed smooth mould. The fibres are coated with a tissue and a draining medium comprising a micro-perforated film. The assembly is then placed in a waterproof cover, attached to the mould by suitable mastic. The vacuum is achieved by a pipe inserted in the device and connected to a spiral duct outlet. The arrival of resin is provided by an inlet pipe, allowing a front advanced resin. Before the infusion, the maximum vacuum is maintained for a period of about 5 h to allow degassing. The infusion is then performed at a 0.4 bar depression. Once the performance is fully impregnated, the inlet of resin is cut-off and the vacuum is maintained until the ambient temperature under the exothermic peak. The plate is then removed from the mould, and conditioned at ambient temperature for at least one week. The fibre volume fraction measured was about 38% and the void content was in range of 5%.

2.2　Experimental Setup

Tensile tests (Fig. 1a) were carried out with a tensile machine equipped with a 100 kN load cell. The strains in the tensile direction were measured by mean of an extensometer. The tensile specimens have rectangular geometries (25 mm × 250 mm × 1.5 mm) and they are formed by four-ply of flax fibres. All prepared configuration were tested under uniaxial loading, according to the standard test method ASTM D3039/D3039M.

　The specimens were tested in three-point bending (Fig. 1b) test according to ASTM D790-86 standard. In static tests the loading was performed at rate of

Fig. 1 Experimental set up: **a** Tensile test. **b** Three-point bending test
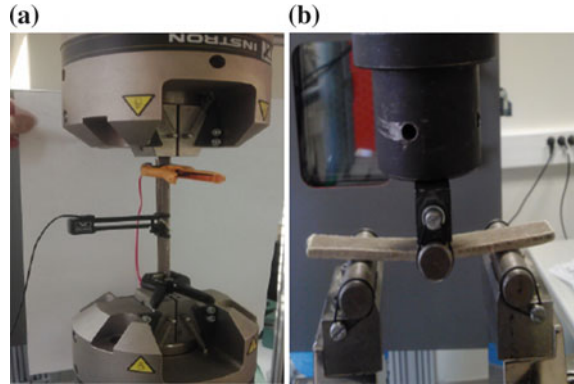
5 mm/min. The fatigue tests were carried on at controlled displacement using a sinusoidal waveform with a 5 Hz frequency. The bending specimens are cross-ply laminates $[0_3/90_3]_s$ and have rectangular geometries (15 mm × 125 mm × 4.5 mm). A constant mean displacement d_{mean} was applied during tests equal to 50% of displacement at static testing failure. The maximum amplitude of load was equal to 60% of displacement at failure.

3 Results and Discussion

3.1 Tensile Test Analysis

The macroscopic stress–strain response (Fig. 2) is developed in three consecutive phases: first linear phase corresponds to elastic and reversible behaviour of the composite material, then a second, nonlinear phase, is associated to the initiation of damage mechanisms and a last linear and relatively inelastic phase, is conditioned by the intensification and spread of damage phenomena preceding the rupture of specimen. A slight inflexion occurs at a strain value of about 0.4% from which the apparent stiffness seems increase slightly. The mechanical properties of the UD composite are shown in Table 1.

In order to evaluate and quantify the macroscopic damage in tow configuration of specimens, quasi-static cyclic tensile tests was carried on the Flax/Elium composite. Figure 3 shows the stress/strain response with periodic amplification of the maximal stress.

The hysteresis loops slope decreases with cycle charge–discharge progress until the material final rupture. This effect symbolizes the damage growth in the composite material (Fig. 4). Moreover, the area of the hysteresis loops increases progressively, indicating the presence of the viscosity within the material. We can see in figure that the hysteresis loops in the cross-ply curves has a higher area compared
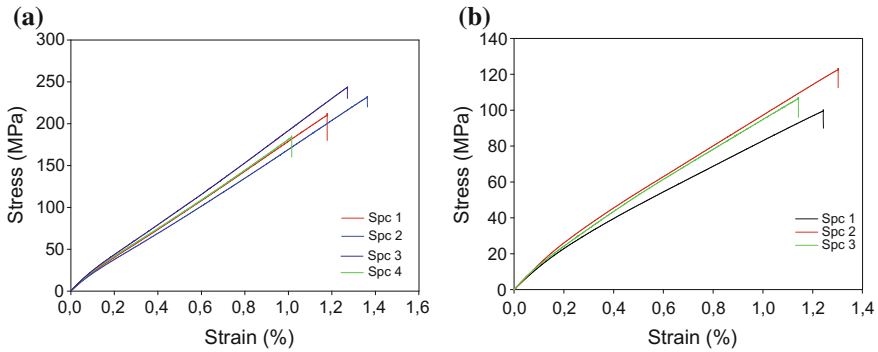
Fig. 2 Tensile test stress–strain curves for **a** UD-0°; **b** [0/90]$_S$

Table 1 Mechanical properties of the UD composite

Elastic properties		Strength properties	
Components	Value	Components	Value
E_L (GPa)	23	σ_{Lrupt} (MPa)	210
E_T (GPa)	3.2	σ_{Trupt} (MPa)	7.5
E_{LT} (GPa)	13.3	σ_{LTrupt} (MPa)	115
ν_{LT}	0.35		
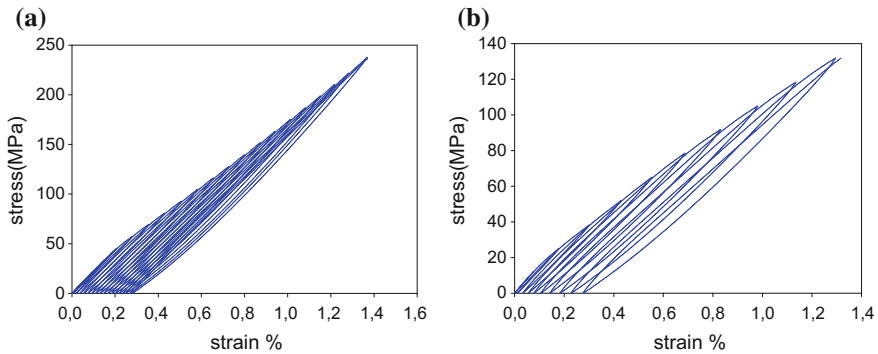
Fig. 3 Stress/strain response under quasi-static cyclic tensile test: **a** UD-0°; **b** [0/90]$_s$

to the case of UD°. Therefore, we deduce that the dissipated energy during test is greater for the cross-ply laminate and the damage in it is attempted quickly.

The maximum stress continues to increase after each load bearing but little change with the deformation.

The stiffness degradation of the composite (Fig. 5) is evaluated by the macro-scopic damage scalar parameter (Eq. 1). E_0 and E_d are respectively the Young's modulus of the virgin and damaged composites. The latter is estimated each cycle of loading.
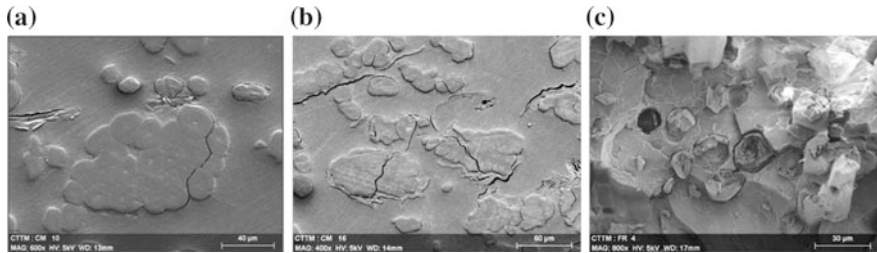
Fig. 4 SEM observations of flax/Elium composite. **a** Safe specimen micrograph. **b** Specimen loaded to 50% of UTS. **c** Specimen at failure. Monti et al. (2016)
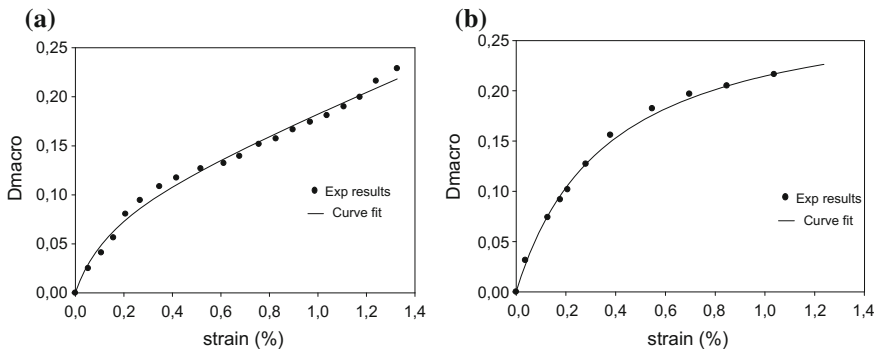
Fig. 5 The composites progressive stiffness degradation: **a** UD0°; **b** [0/90]$_s$

$$D_{macro} = 1 - \left(\frac{E_d}{E_0}\right) \tag{1}$$

The damage kinetic under cyclic tensile test is more pronounced in the first cycles and then recedes gradually until the rupture of the specimen. This is mainly due to the accumulation of the different mechanisms noted in the first stage such matrix microcracking and fibre/matrix debonding and then fibres breakage in the second stage. In Fig. 5a we notice an increase of the damage parameter from a strain value of about 0.5% meaning the effect of stiffening mechanisms during this phase. Several authors, Monti (2016) and Shah (2015), consider the hypothesis of reorientation of cellulose microfibrils driven through a "stick-slip" mechanism.

3.2 Static Bending Test

Static three-point bending test was carried on to investigate the mechanical behaviour of the cross-ply laminate [0$_3$/90$_3$]$_s$ such as stiffness, failure load, failure

Fig. 6 Three-point static bending test $[0_3/90_3]_s$
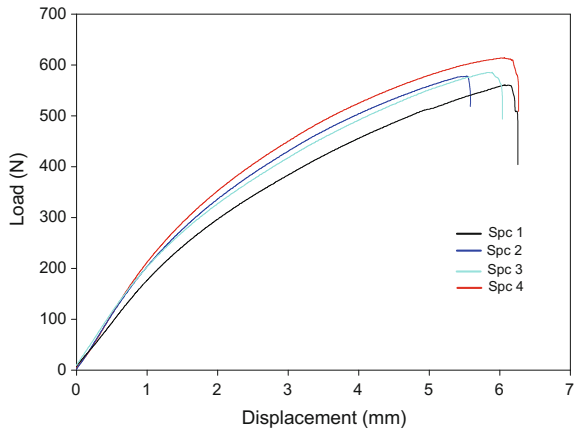
Table 2 Flexure characteristics for $[0_3/90_3]_s$ Flax/Elium composite

Parameters	Value
Stiffness (N/mm)	218
Failure load (N)	604
Failure displacement (mm)	6
Flexure Modulus (GPa)	15.8

displacement and flexure modulus. The results are given in Fig. 6. load versus displacement curve allows to distinguish three stage: First a little linear part followed by a nonlinear one in which we notice a transverse microcracking in the 90° layers and a last quasi-linear part characterized by the damage propagation until a fragile fracture. Tables 2 illustrate the flexure characteristics of composite.

3.3 Fatigue Bending Test

3.3.1 Stiffness Degradation

The specimens are loaded in bending and then subjected to cyclic fatigue when the load is sufficiently high, the plastic deformation and damage take place, and the curve of the load vs the displacement get the form of a loop, due to hysteresis, that is explained by the loss of energy during cyclic loading.

During fatigue test, the evolution of the load as a function of the number of cycles was recorded and given in Fig. 7. The curve shows the evolution of the maximum load in depending on the number of fatigue cycles. The maximum load F_{max} is obtained in the first cycle F_{0max}.

The stiffness degradation in the specimens occurs in two phases. In first time, we notice a slow decrease in rigidity. Then, it becomes rapid in the second phase from
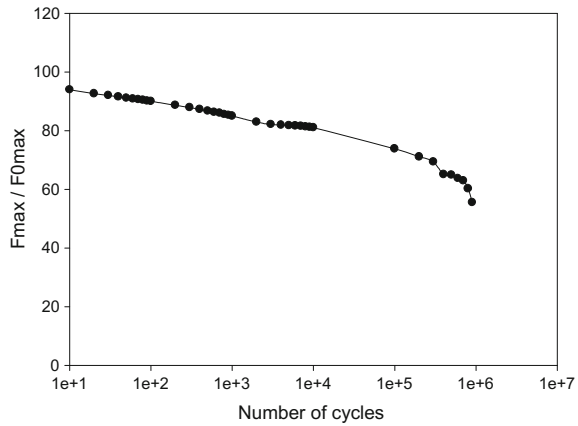
10^4. This effect could be explained by the microcracking and damage initiation. The two parts of the curve could be associated with the multiplication of the transverse cracking, which appears in the 90° layers, and propagation of delamination at the interface between the 0° and the 90° layers. The failure of the composite takes place up to 9×10^5 cycles.

3.3.2 Energy Dissipation

The fatigue test was evaluated throw the evaluation of two type of energy one is dissipated energy E_d which consists on the area enclosed by hysteresis loop (Fig. 8). The other one is the maximum stored potential energy E_p given by the area under the loading part of the hysteresis loop. To evaluate the dissipation energy and the maximum potential energy, numerical trapezoidal summation of area was used (Idriss et al. 2013).

$$E_d = \frac{1}{2} \sum_{i=1}^{n} (d_{i+1} - d_i)\{[f(d_{i+1}) + f(d_i)] - [g(d_{i+1}) + g(d_i)]\} \qquad (2)$$

$$E_p = \frac{1}{2} \sum_{i=1}^{n} (d_{i+1} - d_i)[f(d_{i+1}) + f(d_i)] \qquad (3)$$

The dissipate energy versus number of cycles is presented in Fig. 9: viscoelastic behaviour of the matrix, fibre-matrix friction and microcracks are the main mechanisms leading to the dissipation of energy in the composites. The curve (Fig. 8) shows a high decrease of energy at the first cycles and it becomes relatively constant in the last cycles to failure.

The evaluation of the two types of energy leads to know about the evolution of the loss factor which is given by
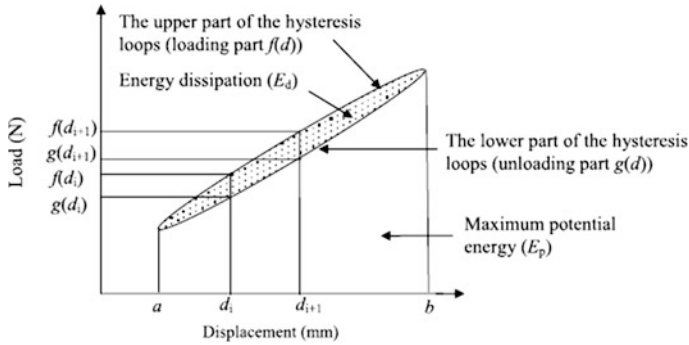
Fig. 8 Maximum potential energy (E_p) and dissipated energy (E_d)

Fig. 9 Energy dissipation E_d (mJ) versus number of cycles
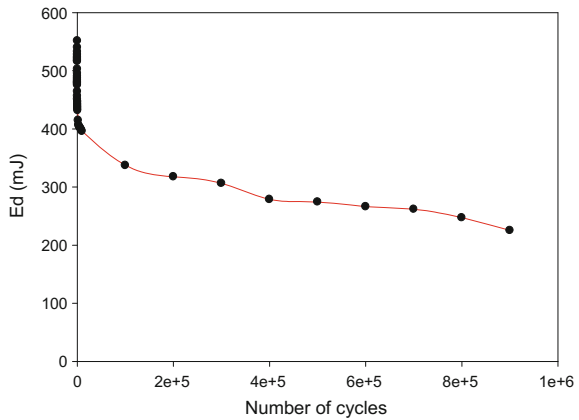
$$\eta = \frac{E_p}{2\pi E_d} \tag{4}$$

Figure 10 shows that the loss factor is constant during the first cycles of fatigue and then it increases in high rate from 10000 cycles due to the creation of microcracking. This allows concluding that the loss factor could be an appropriate indicator of damage accumulation in fatigue tests.

4 Conclusion

The present study highlights the characteristic of an eco-composite based on thermoplastic liquid resin and flax fibres. The infusion technique allows preparing multiple samples during a very short time compared to thermocompression.
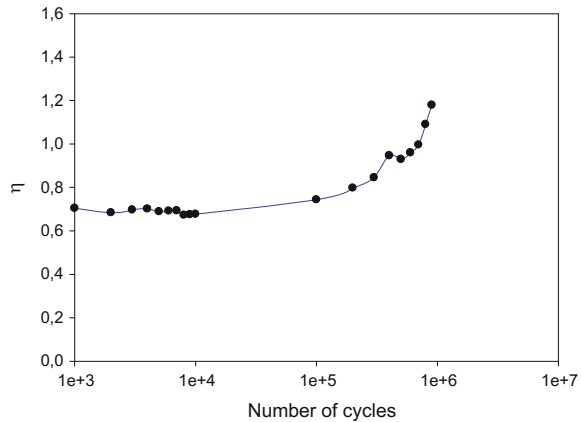
Mechanical testing carried on different configurations of specimens shows a non-linear response, essentially due to the specific behaviours of the two phases Flax fibre and the Elium resin. Fatigue bending tests showed significant stiffness degradation in the earlier part of fatigue life and then a gradual decrease was observed until a rapid drop in stiffness due to failure. Many damage mechanisms take place along loading to failure: matrix microcracking, fibre/matrix debonding, delamination and fibres breakage. In order to more clarify the damage mechanisms impact on the behaviour and understand the physical origin of the stiffening phenomena in the UD° composite, it appears necessary to achieve experimental investigations at the fibres local scale. This could be obtained by analysis of microscopic observations (SEM) coupled to an acoustic emission monitoring during tests. Finally, in view of the results presented above, the Flax–Elium composites would be suitable solution for many industrial applications.

References

Aslan (2013) Investigation of damage mechanism of flax fibre LPET commingled composites by acoustic emission. Compos: Part B 54:289–297

Baley C, Perrot Y, Busnel F, Guezenoc H, Davies P (2006) Transverse tensile behaviour of unidirectional plies reinforced with flax fibres. Mater Lett 60:2984–2987

Baley.C, Le Duigou A, Bourmaud A, Davies P (2012) Influence of drying on the mechanical behaviour of flax fibres and their unidirectional composites. Compos: Part A 43:1226–1233

Coroller G, Lefeuvre A, Le Duigou A, Bourmaud A, Ausias G, Gaudry T, Baley C (2013) Effect of flax fibres individualisation on tensile failure of flax/epoxy unidirectional composite. Compos: Part A 51:62–70

El Mahi A, Berthelo J-M, Brillaudb FJ (1995) Stiffness reduction and energy release rate of cross-ply laminates during fatigue tests. Compos Struct 30:123–130

Idriss M, El Mahi A, Assarar A, El Guerjouma.R (2013) Damping analysis in cyclic fatigue loading of sandwich beams with debonding. Compos: Part B 44:597–603

Ku H, Wang H, Pattarachaiyakoop N, Trada M (2011) A review on the tensile properties of natural fiber reinforced polymer composites. Composites: Part B 42:856–873

Monti A (2016) Elaboration et caractérisation mécanique d'une structure composite sandwiche à base de constituants naturels. Dissertation, University of Maine

Monti A, El Mahi A, Jendli Z, Guillaumat L (2016) Mechanical behaviour and damage mechanisms analysis of a flax-fibre reinforced composite by acoustic emission. Compos: Part A 90:100–110

Shah DU (2015) Damage in biocomposites: stiffness evolution of aligned plant fibre composites during monotonic and cyclic fatigue loading. Composites: Part A:160–168

Wambua P, Ivens J, Verpoest I (2003) Natural fibres: can they replace glass in fibre reinforced plastics? Compos Sci Technol 63:1259–1264

Measurement of Thermal Contact Resistance Across Cylinder Head Gasket

Saoussen Belghith, Salah Mezlini and Hedi Belhadj Salah

Abstract In order to accurately estimate the temperature reached in the cylinder block and cylinder head gasket of an internal combustion engine, an experimental investigation of the thermal contact resistance (TCR) across cylinder head gasket is performed. TCR has been calculated for contact pressure up to 42 MPa which corresponds to the clamping pressure of the gasket. Different sections (inter-cylinders, oil, and water ribs) with different law behavior have been retained. The temperature evolution has been recorded using thermocouples immerged in the measurement device. The heat flux has been calculated using this temperature evolution. The TCR has been deduced using Fourier law. Results show that the TCR decreases with increasing the load and tends toward a constant value for various sections of the gasket. In addition, TCR values are more important for the inter-cylinder's section which will result in greater values of temperature near inter-cylinder's section on the cylinder block .

Keywords Thermal contact resistance · Experimental investigation Cylinder head gasket

1 Introduction

Heat transfer in internal combustion engine has a great influence on the temperature reached on the cylinder block and cylinder head gasket. Especially, temperature values at the top of the cylinder block have an influence on the lifetime of the piston segmentation.

S. Belghith (✉) · S. Mezlini · H. Belhadj Salah
LGM, ENIM, Av. Ibn ElJazzar, 5019 Monastir, Tunisia
e-mail: belghith.saoussen@gmail.com

S. Mezlini
e-mail: salah.mezlini@gmail.com

H. Belhadj Salah
e-mail: hedi.belhadjsalah1@gmail.com

693

The cylinder head gasket ensures the seal between cylinder block and cylinder head with regard to coolants, combustion gasses, and engine oil. They also transmit the force between the cylinder head and the cylinder block, which has a considerable influence on the stresses and deformation in all the components of the system.

The heat transfer in these joints has a crucial influence on the temperatures reached in the cylinder head and in the cylinder block. In particular, the temperatures reached on the cylinders of the internal combustion engines have an impact on the lifetime of the segmentation and pistons.

In order to accurately estimate temperatures in the cylinder head/gasket/cylinder block assembly, we try to assess the overall thermal resistance opposed by the joint to the thermal transfer between the cylinder head and the cylinder block. Such resistance consists of the intrinsic joint resistance and the thermal contact resistance (TCR). The latter has an effect on the temperature distribution at low contact pressures particularly the pressure of the joint clamping.

Many previous studies have measured TCR across contacting surfaces. In fact, measurement of the TCR between solids in static contact consists of creating a unidirectional heat flow perpendicular to the contact surface. The temperature jump at the interface is determined from the temperatures measured on the solids using thermocouples (Rosochowska et al. 2003, 2004; Zhang et al. 2010; Singhal et al. 2005; Howard 1975). Indeed, (Rosochowska et al. 2003, 2004; Zhang et al. 2010) measured the TCR at the interface of the workpiece and the forging tool. In particular (Rosochowska et al. 2003, 2004) evaluated the TCR for samples of small thicknesses in dry contact under an axial pressure greater than their elastic limit. The evolution of the TCR was determined as a function of the load for several types of samples with different roughness. The authors found that TCR decreases as a function of pressure and increases as a function of roughness. (Zhang et al. 2010) measured the TCR between samples in lubricated contact. Results also show a decrease in the TCR as a function of the pressure and the temperature at the interface. While an increase in the latter is observed as a function of the thickness of the lubricant.

In our previous work, a numerical study of the thermo-mechanical behavior of the cylinder head gasket contacts has been conducted (Belghith et al. 2011). The roughness of the contacting surfaces has been taken into account and a homogenization technique has been used (Belghith et al. 2013). In this paper, we report an experimental study of TCR across various specimens of the cylinder head gasket. First, the experimental device designed to measure the TCR has been presented. Second, we describe different tested samples. Finally, the obtained results have been analyzed and TCR has been calculated as a function of the applied load.

2   Experimentation

2.1   Description of the Device

Measurement of TCR is generally made by creating an unidirectional heat flux across contacting surfaces. The heat flux is determined using temperature evolution in zones that doesn't contain flux constriction (Merrill and Grimella 2011).

For this achievement, a device was designed and manufactured (Fig. 1). This device is composed of two heating cylinders (2). These cylinders were heated by means of two heating cartridges (12). The temperature control was ensured by using two autotransformers (Fig. 2).

The insulation of the heating cylinders was ensured by two Teflon isolators (1) with a thermal conductivity of 0.23 W/m °C. On the one hand, these parts allowed the insulation of the two upper and lower bases and avoided the heat evacuation toward the compression system (tensile machine). On the other hand, it enabled the lateral insulation of the two heating cylinders. Teflon was retained because of its quality of insulation coupled with its good mechanical strength.

The lateral insulation was also ensured by the vermiculite with a thermal conductivity of 0.045 W/m°C. The used vermiculite has a granular form which fills the external cover (7). This cover was surrounded by glass wool with a thermal

1- Teflon isolator
2- Heating cylinder
3- Resistance cover
4- The bottom heating cylinder cover
5- Bottom cover
6- Top cover
7- External cover
8- Guide pillar
9- Nut M10
10- The top heating cylinder cover
11- Clamping screw
12- Heating cartridge
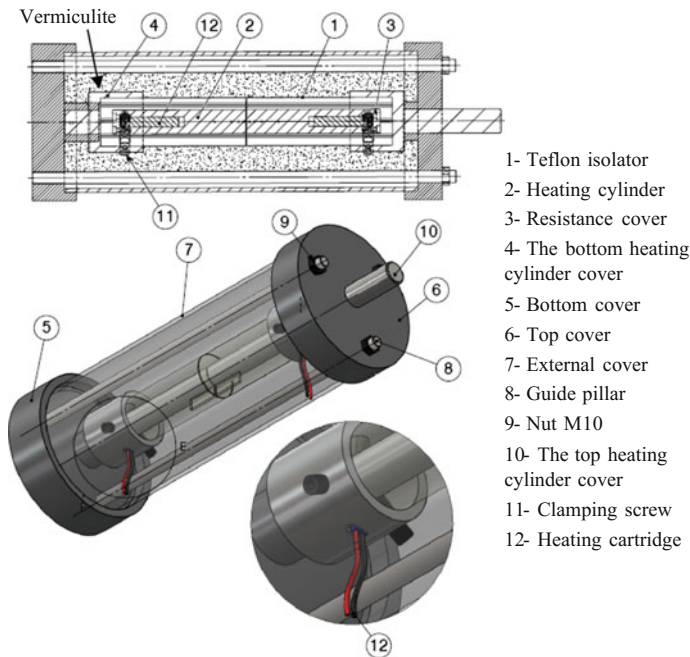
Fig. 1 Shematic representation of the TCR measurement device
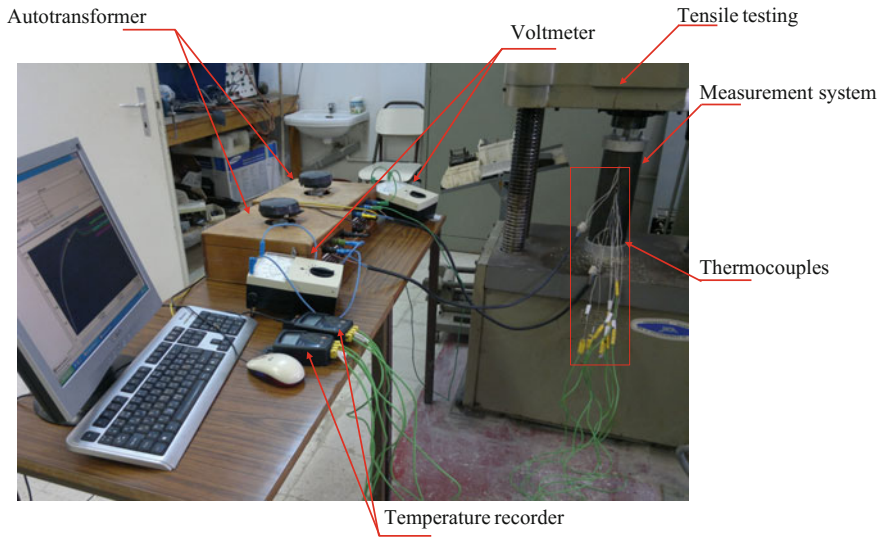
Fig. 2 Experimental test bench

conductivity of 0.036 W/m °C. The isolation precautions were made in order to have a one-way heat flux.

The two heating cylinders were centered by three clamping screws (11). The two upper and lower parts were secured by the two covers (5) and (6) in addition to the guide columns (8).

In order to apply a controlled force, the designed device was installed upon a tensile machine. The applied force was varied from 2000 to 3500 N. The associated pressure was deduced using the Eq. (1):

$$P = \frac{F}{S} \tag{1}$$

where:

F   the applied force (N)
S   the sample's section (mm^2)

Figure 2 represents a test bench containing a measurement designed device, the temperature recorder, and the autotransformer.

The designed device makes it possible to test relatively small sections. The diameter of the heating cylinder is 20 mm. The tested section was centered between the heating cylinders. Therefore, the desired load was applied and the temperature was recorded by the mean of thermocouples immersed upon the two heating cylinders. Four thermocouples were attached to the inner side of each cylinder. TCR opposed by the gasket to the two heating cylinders can be calculated knowing

the thermocouple locations, the two heating cylinder conductivities, the sample dimensions, and conductivity.

2.2 Sample Presentation

Test samples were cut from four layers cylinder head gasket by a laser cutting. Different sections related to a gasket body, inter-cylinders, oil rib, and water rib were cut (Fig. 2). These sections were placed between the two heating cylinders. The temperature evolution was recorded under different pressures. It should be noted that four samples were tested for each type of sections (Fig. 3).

3 Results

The temperature evolutions have been recorded in different locations of the heating cylinders using thermocouples immerged in these locations (Fig. 4). The distance between thermocouples and samples' surfaces is detailed in Fig. 4.

Figure 5a and b show the recorded temperature for the inter-cylinder samples as a function of time in the upper and lower cylinders, respectively, for different pressures. The pressure has been applied when the temperature tends to stabilize. The steady state couldn't be perfectly achieved because the holding time of the compression machine must not exceed 20 min at the same pressure for safety reasons.

The experimental measurements have been used to evaluate the TCR. For monodirectional heat flux, the TCR is given by the Fourier law (Bardon 1972):
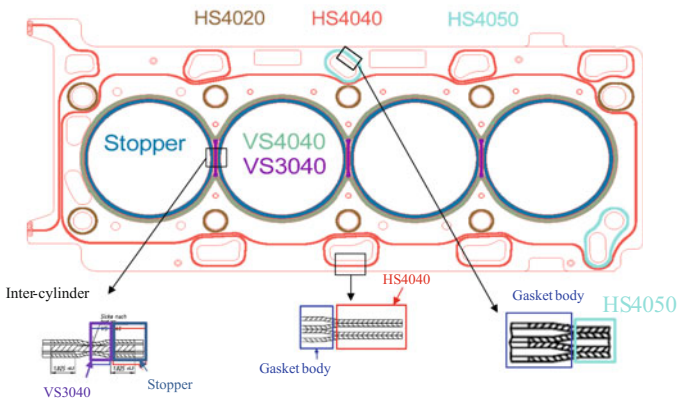
Fig. 3 Tested section of the cylinder head gasket
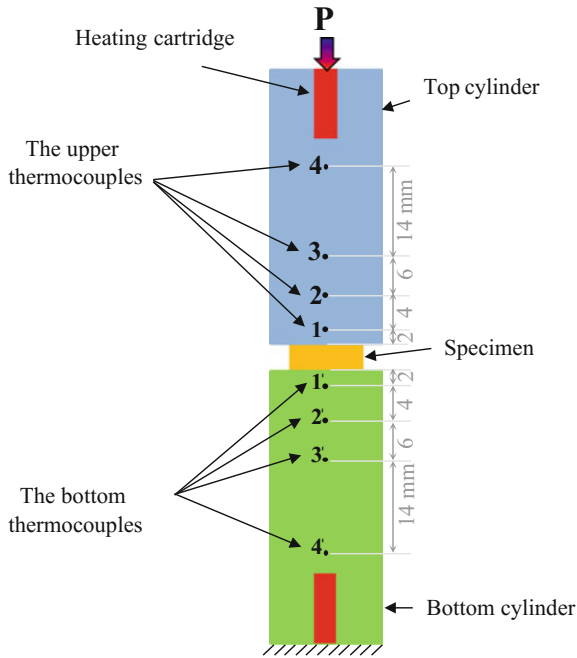
Fig. 4 Thermocouple layout
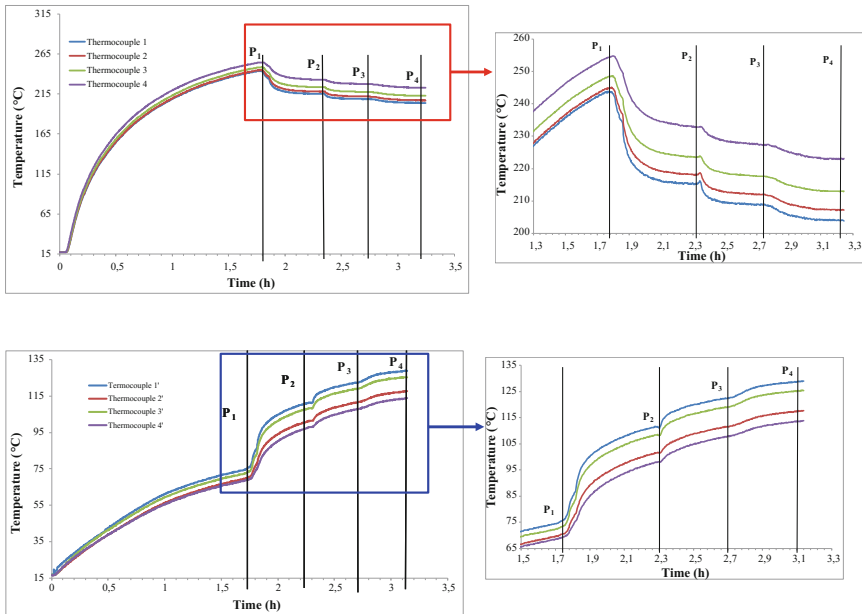
Fig. 5 Temperature evolution results for thermocouples of: **a** the upper cylinder; **b** the bottom cylinder

$$RTC = \frac{\Delta T_{44'}}{\Phi_{mean}} - \frac{e_1}{\lambda_1} - \frac{e_2}{\lambda_2} - \frac{e_s}{\lambda_s} \tag{2}$$

where:

e_1 Distance between the lower surface of the upper heating cylinder and the thermocouple 4.

e_2 Distance between the upper surface of the lower heating cylinder and the thermocouple 4'.

e_s Sample thickness.

λ_1 et λ_2 Thermal conductivity of the upper and lower heating cylinders respectively.

Λ_s Thermal conductivity of the sample.

$$\Delta T_{44'} = T_4 - T_{4'} \tag{3}$$

$$\Phi_{mean} = \frac{1}{2}\left(\Phi_{upper} + \Phi_{lower}\right) \tag{4}$$

$$\Phi_{upper} = \frac{(d_{12} \times \Phi_{12} + d_{23} \times \Phi_{23} + d_{34} \times \Phi_{34})}{d_{12} + d_{23} + d_{34}} \tag{5}$$

Where: d_{ij} (mm): distance between thermocouples i et j.

$$\phi_{12} = \frac{T_2 - T_1}{\left(\frac{e_{12}}{\lambda_1}\right)} \tag{6}$$

$$\phi_{23} = \frac{T_3 - T_2}{\left(\frac{e_{23}}{\lambda_1}\right)} \tag{7}$$

$$\phi_{34} = \frac{T_4 - T_3}{\left(\frac{e_{34}}{\lambda_1}\right)} \tag{8}$$

The lower heat flux Φ_{lower} has been calculated using the same approach.

TCR has been determined as a function of the pressure for inter-cylinders, HS4040 and HS4050 sections as presented in Fig. 6. This figure shows that, for the same samples, TCR values have a large dispersion especially at low pressure. TCR decreases as a function of the contact pressure and tends to stabilize at a pressure of 30 MPa for the HS4040 and HS4050 samples. However, for the inter-cylinder section the stabilized TCR value is reached at 50 MPa. This is due to the higher stiffness of the inter-cylinder zone and more precisely the stopper.
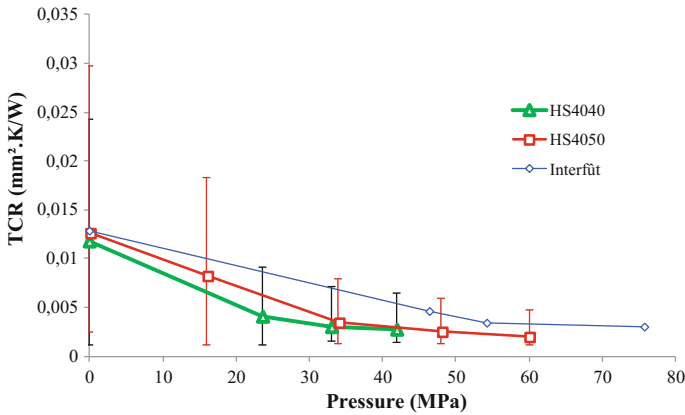
Fig. 6 TCR evolution as a function of applied pressure for cylinder head gasket sections

4 Conclusion

In this work, we have prepared an experimental device to evaluate the TCR across cylinder head gasket of an internal combustion engine. Our study has been focused on the thermal behavior of three zones: inter-cylinders, oil, and water ribs. An omnidirectional heat flux has been calculated from temperature evolutions across different samples. TCR has been deduced as a function of load. Interestingly, results show large dispersions of the TRC especially at low contact pressure. Dispersions tend to stabilize quickly for fluid ribs but slowly for inter-cylinder zone. Additionally, TCR values are more important for the inter-cylinder's section. We can so conclude that heat transfers are inhibited in this zone which will result in greater values of temperature near inter-cylinder's section on the cylinder block.

References

Bardon JP (1972) Introduction à l'étude des résistances thermiques de contact. Rev Gen Therm 11:429–447

Belghith S, Mezlini S, BelhadjSalah H, Ligier J-L (2011) Modélisation du comportement thermomécanique des éléments Gasket: application au joint de culasse, CMSM'2011, session orale. Sousse, Tunisie

Belghith S, Mezlini S, BelhadjSalah H, Ligier J-L (2013) Thermo-mechanical modelling of the contact between rough surfaces using homogenization technique. Mech Res Commun 53:57–62

Howard JR (1975) An experimental study of heat transfer through periodically contacting surfaces. Int J Heat Mass Trans 19:367–372

Merrill CT, Grimella SV (2011) Measurement and prediction of thermal contact resistance across coated joints. Exp Heat Transf 24:179–200

Rosochowska M, Balendra R, Chodnikiewicz K (2003) Measurments of thermal contact conductance. J Mater Process Technol 135:204–210

Rosochowska M, Chodnikiewicz K, Balendra R (2004) A new method of measuring thermal contact conductance. J Mater Process Technol 145:207–214

Singhal V, Litke PJ, Black AF, Garimella SV (2005) An experimentally validated thermo-mechanical model for prediction of thermal contact conductance. Int J Heat Mass Transf 48:5446–5459

Zhang XZ, Zhang LW, Xing L (2010) Study of thermal interfacial resistance between TC11/glass lubrication/K403 joint. Exp Therm Fluid Sci 34:48–52

Ultra-Thin Films Effects on the Dynamic Behaviour of Three-Layer Laminated Plate

A. Ghorbel, A. Akrout, B. Bouzouane, M. Abdennadher,
T. Boukharouba and M. Haddar

Abstract In this paper, a dynamic study is carried out for a new laminated glass plate which contains two elastic skins, a viscoelastic core and two adhesives films supposed to be ultra-thin layers; and which can be used for the assembly of the laminated structure. In this case, the coupling between all layers is modelled by taking into account the interfacial shear stresses. Hence, by mixing the Kirchhoff and Mindlin plate's theories respectively for the two skins and the viscoelastic core with a dynamic behaviour rule for the two ultra-thin films, the displacement field in the laminate can be derived. Here, the finite element method is used for discretizing the laminate energy functional allow obtaining a complex dynamic equation. Also, the dynamic modal recombination method is adopted for calculating the vibratory responses of the studied structure. Then, the aim of this work is to determine the effect of the interfacial shear stress on the dynamic behaviour of the laminated plate.

Keywords Lamination effect · Ultra-thin adhesive film · Modal recombination method

A. Ghorbel · A. Akrout (✉) · M. Abdennadher · M. Haddar
LA2MP—Mechanics, Modelling and Production Research Laboratory,
Engineering National School of Sfax, University of Sfax, Sfax, Tunisia
e-mail: ali_akrout2005@yahoo.fr

A. Ghorbel
e-mail: amenighorbel2@gmail.com

M. Abdennadher
e-mail: moez.abdennadher@gmail.com

M. Haddar
e-mail: mohamed.haddar@enis.rnu.tn

B. Bouzouane · T. Boukharouba
LMA—Advanced Mechanics Research Laboratory, Houari Boumediene Sciences
and Technology University, Alger, Algeria
e-mail: bbouzouane@yahoo.fr

T. Boukharouba
e-mail: t.boukha@gmail.com

1 Introduction

Laminated plates are extensively used in many applications such as the ship-building, the aerospace and automobile industries. Vibration control is an important issue in those various domains. Several researchers have studied the dynamic behaviour of the sandwich plate in order to improve their technical performance.

The standard laminate widely presented in the literature is composed of two elastic skins and a viscoelastic core. See for example, (Assaf et al. 2010; Hammami et al. 2005). However, Akrout et al. (2008) has developed a model which contains two elastic glass layers assembled with an ultra-thin adhesive film. Based on both, the ultra-thin film Inter-facial shear model and the sandwich plate model, a new dynamic model of laminated glass is created in this paper which is composed of two glass layers and a PVB core joined with two ultra-thin adhesive films. The dynamic model of this laminated glass plate is derived by mixing the Kirchhoff (1850) and Mindlin (1951) plate theories and a specific behaviour law for the films.

In this study, numerical simulations investigating the effect of the interfacial shear stress on the laminate dynamic behaviour is presented. Free and forced laminate vibration responses such as the eigenfrequencies values and the physical displacement are determined using the finite element and the modal recombination methods.

2 Dynamic Model

In this study, the laminated model is composed of two skins of glass and a core of PVB in the middle. The laminate layers are joined with two adhesive ultra-thin films as presented in Fig. 1.

For the dynamic equation, kinematic hypotheses are considered. Therefore, the presence of the adhesive ultra-thin films in the plate is modelled by both the shear stress and the discontinuity of displacement at the layer interfaces. Besides, the two
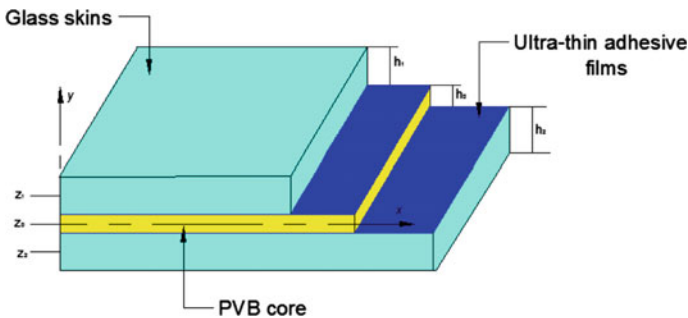
Fig. 1 Laminated plate with ultra-thin films

skins and the core conform respectively to the Kirchhoff and Mindlin plate theories. Consequently, under these considerations, the corresponding displacement field in the laminate can be expressed as follows:

- x-direction

$$
u_0 = \frac{-[u_{\tau 1}] + [u_{\tau 2}]}{2} + u_m + z\varphi_x - \frac{z_1 + z_2}{2}\beta_x
$$
$$
u_1 = \frac{[u_{\tau 1}] + [u_{\tau 2}]}{2} + u_m + \frac{h_0}{2}\varphi_x + \left(z - \frac{z_1 + z_2}{2}\right)\beta_x \tag{1}
$$
$$
u_2 = -\frac{[u_{\tau 1}] + [u_{\tau 2}]}{2} + u_m - \frac{h_0}{2}\varphi_x + \left(z - \frac{z_1 + z_2}{2}\right)\beta_x
$$

- y-direction

$$
v_0 = \frac{-[v_{\tau 1}] + [v_{\tau 2}]}{2} + v_m + z\varphi_y - \frac{z_1 + z_2}{2}\beta_y
$$
$$
v_1 = \frac{[v_{\tau 1}] + [v_{\tau 2}]}{2} + v_m + \frac{h_0}{2}\varphi_y + \left(z - \frac{z_1 + z_2}{2}\right)\beta_y \tag{2}
$$
$$
v_2 = -\frac{[v_{\tau 1}] + [v_{\tau 2}]}{2} + v_m - \frac{h_0}{2}\varphi_y + \left(z - \frac{z_1 + z_2}{2}\right)\beta_y
$$

- z-direction

$$
w(x, y, z) = w(x, y) \tag{3}
$$

where $u_i, v_i, (i = 0, 1, 2)$ and w represent the in-plane and the transversal displacement of the laminate, respectively. $[u_{\tau i}]$ and $[v_{\tau i}], (i = 1, 2)$ are the shear interfacial displacements due to the presence of the films. u_m and v_m represent the average longitudinal displacement. (φ_x, φ_y) and (β_x, β_y) are the Mindlin and Kirchhoff deflection rotations, respectively. $z_i, (i = 1, 2)$ is the average plane slope of the skin 'i'.

Then, the discretization of the laminate energy functional by the finite element gives, after minimization, the following equation:

$$
\left(([K_{re}] + j[K_{im}]) - \omega^2[M]\right)\{U\} = \{F\} \tag{4}
$$

where $([K_{re}] + j[K_{im}])$ and $[M]$ are respectively is the complex stiffness matrix and the mass matrix of the structure. $\{U\}$ represent the nodal displacement vector. $\{F\}$ is the nodal external force vector distributed on the plate upper surface as shown in Fig. 2. ω is the angular frequency.

3 Results

In this section, the dynamic behaviour of the designed plate is investigated. Hence, a modal approach is adopted in order to reduce the matrix system size. The physical and geometrical features of the laminate are given as:

- Two glass skins: $h_1 = h_2 = 0.004$ m, $\rho = 2500$ kg/m^3, $\nu = 0.22$, E = 7.2 × 10^4 MPa
- PVB core: $h_0 = 0.001$ m, $\rho = 1068$ kg/m^3, $\nu = 0.4981$, E = 2.8 × 10^4 + j 3.74 × 10^4 MPa, G = 0.94 × 10^4 + j 1.25 × 10^4 MPa.
- Two types of adhesive films: Araldite ($k_{film} = 1.362$ × 10^7 N/mm^3), Epoxy ($k_{film} = 1.1$ × 10^{4}N/mm^3).
- Plate dimensions: (1 m, 1 m) in plane (x, y).
- A mesh of 10 × 10 linear quadrilateral finite elements is adopted in the numerical simulation. Note that, the laminate finite element developed in this work presents 11 degrees of freedom at each node.

3.1 Numerical Validation

By assuming null values to the stiffness of the film, the configuration of laminate becomes a standard sandwich and the obtained results from the FE simulation can be compared to the results based on the FE model developed by Assaf (1991) for the standard sandwich.

Table 1 presents the first 10 eigenfrequencies obtained from both FE models for the same structure. We can see that the two models give almost identical values. Hence, the finite element model developed in this work is validated.

Fig. 2 Laminated glass plate subjected to a normal external loading
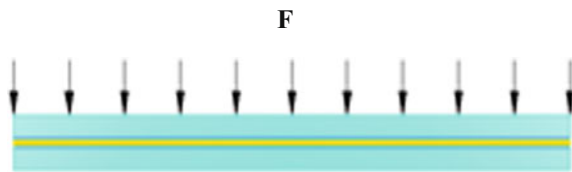
Table 1 Validation of the FE model

Mode	Eigenfrequencies of standard sandwich based on the FE developed				
	In this work	By Assaf (1991)	Mode	In this work	By Assaf (1991)
1	86.745	86.745	6	361.12	361.12
2	184.75	184.75	7	440.30	440.31
3	184.75	184.75	8	440.30	440.31
4	273.00	273.00	9	595.82	595.83
5	359.48	359.48	10	646.64	646.65

3.2 Ultra-Thin Films Effects on the Laminate Behaviour

As a next step, the dynamic responses are established by modal recombination in order to calculate the nodal displacement vector (Hammami et al. 2005):

$$\{U(\omega)\} = [\psi_1 \quad \cdots \quad \psi_N] \left\{ \begin{array}{c} \lambda_1(\omega) \\ \vdots \\ \lambda_N(\omega) \end{array} \right\} \tag{5}$$

where

$$\lambda_i(\omega) = \frac{f_i(\omega)}{m_{ii}\left[(\omega_i^2 - \omega^2) + 2j\sum_{k=1}^{N} \xi_{ik}\omega_i^2\right]} \tag{6}$$

$[\psi_1 \quad \cdots \quad \psi_N]$ is the modal basis of the structure. $\lambda_i(\omega)$, $(i = 1 \ldots N)$ represent the modal variables. $f_i(\omega)$, m_{ii}, ξ_{ik} are respectively the generalized force, mass and damping. $j = \sqrt{-1}$ is the imaginary unit.

In order to analyse the ultra-thin adhesive films effects on the laminated plate dynamic behaviour, we present in Fig. 3 the nodal displacement in the laminate centre for three different cases of laminated structure. It is observed that the vibration amplitude is reduced and a little shift to the right for all picks due to
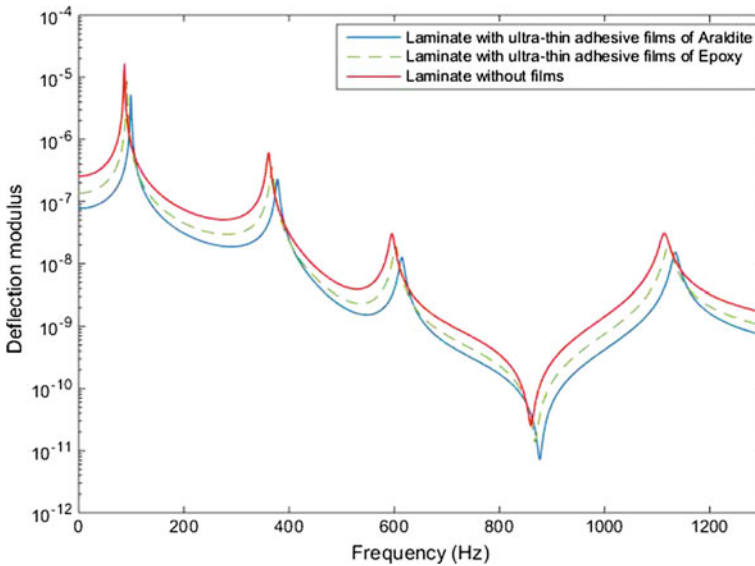
Fig. 3 Ultra-thin films effects on the nodal displacement in the laminate centre

the presence of the ultra-thin adhesive films compared to the one without films. Moreover, the dynamic response depends on the adhesive films stiffness. In fact, the increasing of the films stiffness improves considerably the deflection modulus of the plate. Therefore, by taking into account the shear interfacial stress the dynamic behaviour of the laminate can be much improved.

In this figure, some eigenfrequencies didn't appear in the frequency-displacement evolution due to the viscoelastic structural damping of the PVB core.

Also, by considering the same dimension of the laminate with respect to x and y direction, some eigenfrequencies are equal for two consecutive modes (e.g. modes 2 and 3).

Finally, when another node is considered, we observe additional picks corresponding to other different eigenfrequencies (inverse modes) as presented in Figs. 4, 5.
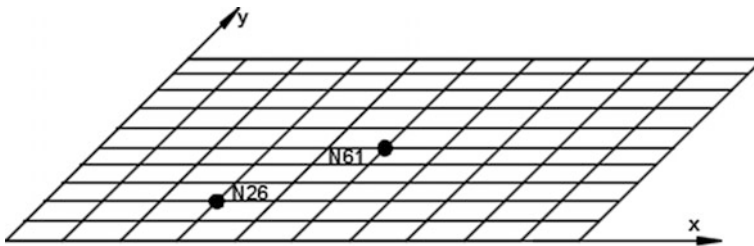
Fig. 4 Considered nodes for dynamic response calculation
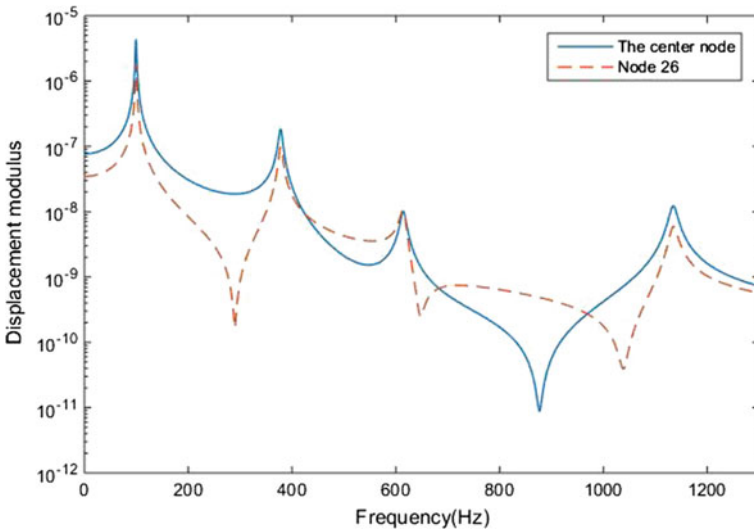
Fig. 5 Nodal displacements of a laminate with ultra-thin films of araldite in two nodes: the centre (node 61) and node 26

4 Conclusion

This paper deals with an original numerical model for predicting the dynamic behaviour of a laminate which contains two elastic skins, a viscoelastic core and two adhesive ultra-thin films at the interfaces. Therefore, a new dynamic model is highlighted by considering some kinematic hypothesis which combines the Kirchhoff and Mindlin plate's theories with a specific behaviour law for the adhesive ultra-thin films. Hence, the finite element model is validated by comparing the eigenfrequencies calculated in the case of a laminate with null stiffness values of the films to those corresponding to the standard sandwich structure. Numerical results show the ultra-thin film's effects on the dynamic responses. Moreover, the laminated plate vibratory behaviour depends on the ultra-thin adhesive films stiffness.

References

Akrout A, Hammami L, Tahar MB, Haddar M (2008) Inter-facial shear effects of ultra-thin film on laminated glass plate dynamical behaviour. Proc Mech E, Part C: J Mech Eng Sci 222:1421–1433

Assaf S (1991) Modélisation par la méthode des éléments finis du comportement vibratoire des poutres et plaques sandwiches - Métal matériaux viscoélastiques. Doctoral thesis, University of Technology of Compiegne, France

Assaf S, Guerich M, Cuvelier P (2010) Vibration and acoustic response of damped sandwich plates immersed in a light or heavy fluid. Comput Struct 88:870–878

Hammami L, Zghal B, Fakhfakh T, Haddar M (2005) Modal approach for dynamical analysis of sandwich plates. Int J Comput Appl Technol 24(4):203–211

Kirchhoff GR (1850) Uber dasgleichgewicht und die bewegung einer elastischen scheibe. J Reine Angew Math 40:51–88

Mindlin RD (1951) Influence of rotary inertia and shear on flexural motions of isotropic, elastic plates. J Appl Mech 18:31–38

Assembly Sequence Generation Based on the CAD Model Simplification

Riadh Ben Hadj, Imen Bel Hadj, Moez Trigui and Nizar Aifaoui

Abstract At present, Computer-Aided tools are at the heart of the product development cycle. These tools can accelerate and make more efficient the design and simulation tasks. However, there is no commercial aid tool for the assistance in the assembly/disassembly tasks. In this context, many approaches and methods are proposed in which feasible assembly/disassembly sequences can be generated. Amongst the limitations of those approaches is the considerable processing time. In this paper, we propose an approach for the simplification of the product CAD model in order to generate Assembly Sequences (AS). The developed approach, which is automatic and integrated to CAD system, begins by the identification and the elimination of standard components (such as screws, nuts, keys, etc.) present in the model. Then a simplified AS is carried out using a collision analysis. Finally, the global AS is obtained by inserting the eliminated elements into the final AS using a case-based algorithm which contains a census of the different standard component types. This developed case-based algorithm allows, according to the type, the identification of the assembly direction and the chronological order of the eliminated standard component.

Keywords Assembly sequence · CAD model · Simplification
Integrated design

R. Ben Hadj (✉) · I. Bel Hadj · M. Trigui · N. Aifaoui
Mechanical Engineering Laboratory, National Engineering School of Monastir,
University of Monastir, Av. Ibn Eljazzar, 5019 Monastir, Tunisia
e-mail: riadh.bhadj@gmail.com

I. Bel Hadj
e-mail: imenne.belhadj@gmail.com

M. Trigui
e-mail: moez.trigui@gmail.com

N. Aifaoui
e-mail: nizar.aifaoui@gmail.com

711

1 Introduction

Assembly and disassembly tasks are important parts in the mechanical products life cycle. In effect, it reflects the effectiveness of the product design. In order to develop an aid tool for the designer, a multitude of assembly and disassembly approaches were proposed in the literature. The first developed approaches were nonintegrated to CAD system in which various methods were adopted to generate and optimize assembly sequences such as genetic algorithms, ant colony optimization, simulated annealing, etc. (Rashid et al. 2011). Actual approaches are integrated into CAD environment which improves its efficiency and automation. These approaches, which can be associated with heuristic methods (Kedher et al. 2015), generally adopt a geometric reasoning based on interferences analysis (Liu et al. 2013) and (Yu and Wang 2013), knowledge-based algorithms (Wu et al. 2013) and (Kashkoush and ElMaraghy 2015) or subassemblies generation (Belhadj et al. 2016). Regardless approach type, Assembly Sequence Planning (ASP) is considered as a NP-hard problem (Ibrahim et al. 2015), in which the complexity increases with the number of assembly components. Thus, the processing time of a complex mechanical product can be very long, especially with geometric reasoning based approach. Therefore, it should be useful to reduce as possible assembly components to be treated.

In this paper, we present an approach for the assembly CAD model simplification in order to generate AS. The first step is the identification and the elimination of standard components present in the model. As second step, a collision analysis is performed in order to generate a Simplified Assembly Sequence (SAS). The final step is the insertion of the eliminated elements into the final AS using a case reasoning algorithm.

In the following sections, a presentation of the CAD model exploration and simplification process is carried out. Then, the SAS generation process is presented and the standard components insertion method is explained. Finally, a computer implementation is presented and a validation example is treated in order to demonstrate the efficiency of the developed approach.

2 Proposed Approach

A mechanical product is a set of components assembled together with a large number of connectors and fastening elements (screws, nut, washer, stud, etc). These elements are standard and universally used. After treating and analyzing several mechanisms, we noted that standard components represent the large part of an assembly's elements. Therefore, these points were highlighted:

- Standard elements are more numerous than the nonstandard ones. Figure 1 shows an example of eight bolts (32 standard components) used to fix the two
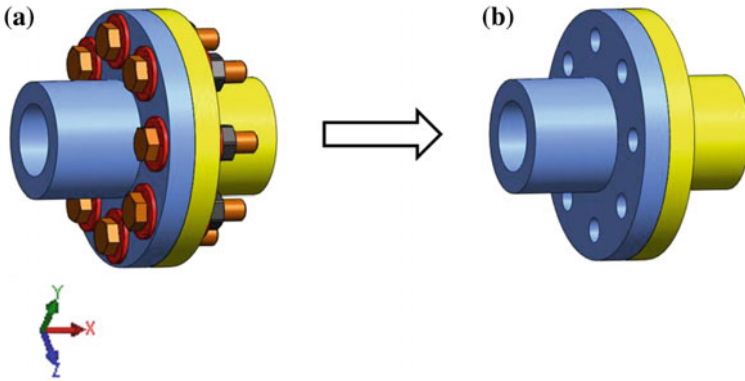
Fig. 1 Assembly CAD model: **a** initial model, and **b** simplified model

components (1) and (2). The assembly of the 32 elements is ensured in the same
manner.

- These elements can be categorized in order to be assembled according to the
  same direction. In the example shown in Fig. 1, eight screws and eight washers
  form a group of components to be assembled according to the direction (+x),
  and eight nuts and eight washers to be assembled according to the direction
  (−x).
- Standard elements are always assembled directly after/before their host
  components.

2.1 CAD Model Exploration and Simplification Process

Based on our previous works (Ben Hadj et al. 2015a), the AS algorithm explores
the CAD model in order to extract all useful data for the AS generating. Among
these data, the algorithm gets the component origin (from toolbox library or not)
and by using its nomenclature, the type of the component can be identified. If the
explored component was identified as a standard element, it will be hidden in the
assembly model and therefore eliminated. Figure 1 illustrates an example of a CAD
model simplification.

2.2 Assembly Sequence Generation

Once the CAD is simplified, the assembly sequence generation is carried out
through two steps: the first one is the generation of a Simplified Assembly
Sequence (SAS) based on a collision analysis of the simplified CAD model. The

second one is the insertion of the standard elements into the SAS using a knowledge-based reasoning algorithm.

2.2.1 SAS Generation

The simplified assembly sequence is generated by the exploitation of the relationships matrix and a collision analysis between components (Ben Hadj et al. 2015b). According to volumes, areas, and relationship numbers, the AS algorithm assigns to each component a score. Respecting a decreasing order of those scores, the algorithm searches a free assembly path for each component.

Figure 2 shows an example of a "mechanical rigid coupling" demonstrating the insertion of standard elements in order to carry out the final assembly sequence. After the elimination of the standard parts and performing the collision analysis, the generation of the SAS is performed. In this example, the component (1) must be assembled first, then the component (3), and finally the component (5) (Fig. 2a).

2.2.2 Standard Components Insertion

Once the SAS is generated, the standard components can be inserted in order to get the assembly sequence. In this procedure, a standard components types census is carried out, and for each type one, an appropriate algorithm is developed. In Fig. 3, the screws assembly algorithm is presented as an example. This algorithm searches for every screw, its related components in the SAS in order to identify its chronological order.
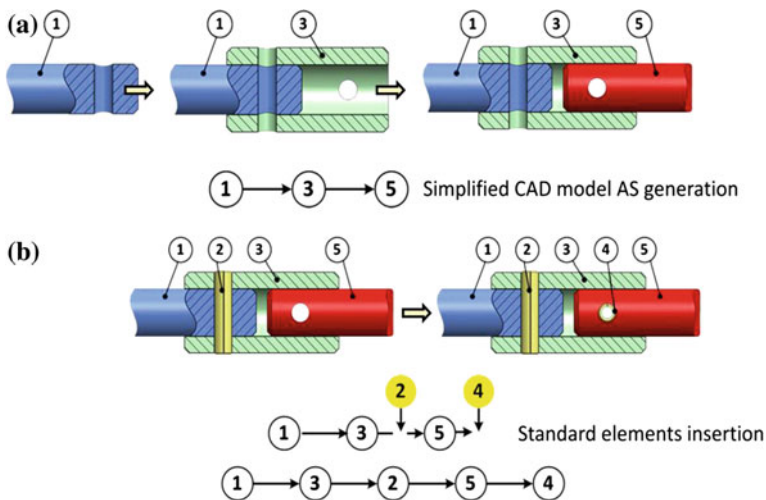
Fig. 2 "Mechanical rigid coupling" example

Fig. 3 Screws assembly
algorithm

```
Procedure Screws_assembly(N : Integer, Cs : Component, Assemb_list : String array)
    Variables
        i, j, k, p : Integer
    Begin
        i ← 0
        p ← 0
        while i < Size(Cs.Relations) Do
            p ← p + 1
            For j = 1 To Size(Cs.Relations) do
                If Assemb_list(p) = Cs.Relations(j) Then
                    i ← i + 1
                End If
            End For
            If p = Size(Cs.Relations) − 1 AND Cs.Type = « Bolt » Then
                p ← p + 1
                For k = p + 1 To N − 1 do
                    Assemb_list (k + 1) ← Assemb_list (k)
                End For
                Assemb_list (p) ← Cs.Name
            Else If p = Size(Cs.Relations) AND Cs.Type = « Screw » Then
                p ← p + 1
                For k = p + 1 à N − 1 Do
                    Assemb_list (k + 1) ← Assemb_list (k)
                End For
                Assemb_list (p) ← Cs.Name
            End If
        End While
        Dir_comps_rev(Cs)     // Identification process of the Cs's assembly directions.
    End
```

Fig. 4 Assembly direction
example

Contact surface and its normal vector

Revolution axis
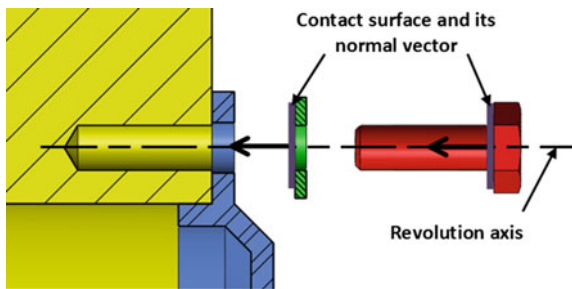
For the "Mechanical rigid coupling" example, the algorithm uses a database, to identify the mounting order of the pins (2) and (4), and insert them on the AS (Fig. 2b).

2.2.3 Standard Components Assembly Directions

By analyzing the assembly mates and the contact surfaces between the standard element and its support, assembly directions are identified. Excepting mechanical keys, these elements have a revolution shape which coincides with the host component.

The revolution axis represents the only direction in which the standard can be assembled or disassembled. In addition, there is a bearing surface between the element and its support. Therefore, the sense and the direction of assembly are done by the normal vector of the contact surface as presented in the example of Fig. 4.

3 Validation Example

To demonstrate the efficiency of the developed approach, we propose the treatment of a "hydraulic pump" presented in the Fig. 5. The CAD model is imported via a computer interface which is the data processing implementation of the developed approach (Fig. 6).

The simplified assembly sequence of the "hydraulic pump" is presented in Table 1. At this stage, the developed algorithm browses the non-assembled components and identifies its types. According to types, the chronological order and assembly direction are known. In the case of the shaft seal (19), the algorithm checks at first if the component is unassembled. Then, it inspects the list of the
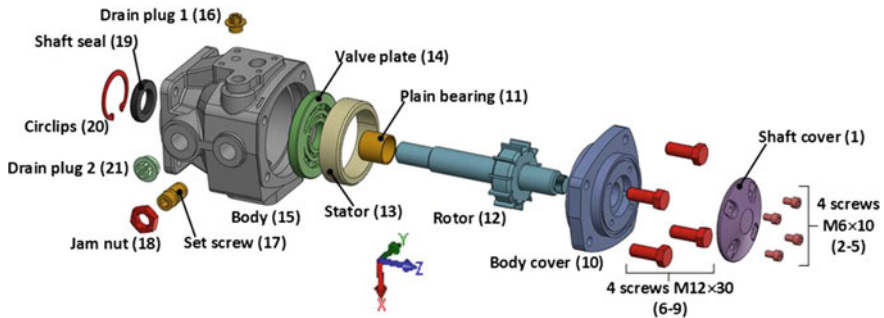
Fig. 5 Hydraulic pump CAD model
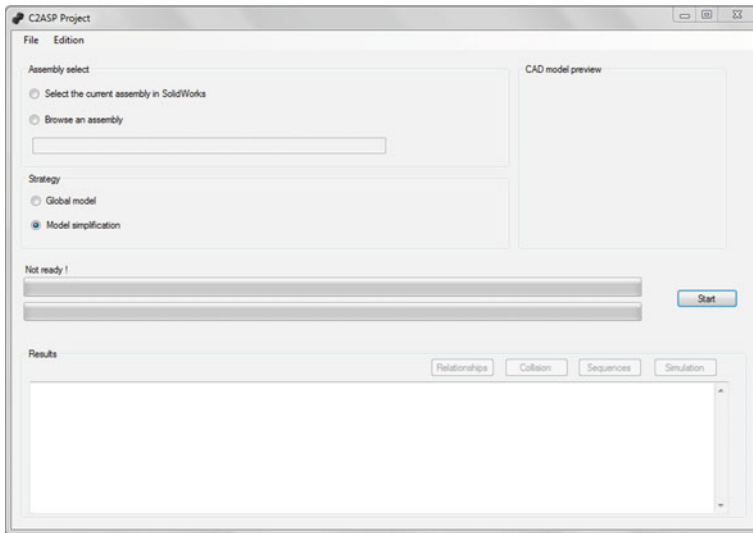
Fig. 6 Data-processing interface

Table 1 "Hydraulic pump" simplified assembly sequence

Assembly order	Component	Assembly direction
1	Body (15)	
2	Rotor (12)	[0, 0, −1]
3	Plain bearing (11)	[0, 0, 1]
4	Valve plate (14)	[0, 0, −1]
5	Stator (13)	[0, 0, −1]
6	Body cover (10)	[0, 0, −1]
7	Shaft cover (1)	[0, 0, −1]
8	Drain plug 2 (21)	[0, 1, 0]
9	Drain plug 1 (16)	[1, 0, 0]

Table 2 "Hydraulic pump" complete assembly sequence

Assembly order	Component	Assembly direction
1	Body (15)	
2	Rotor (12)	[0, 0, −1]
3	Plain bearing (11)	[0, 0, 1]
4	Shaft seal (19)	[0, 0, 1]
5	Circlips (20)	[0, 0, 1]
6	Valve plate (14)	[0, 0, −1]
7	Stator (13)	[0, 0, −1]
8	Set screw (17)	[0, 1, 0]
9	Jam nut (18)	[0, 1, 0]
10	Body cover (10)	[0, 0, −1]
11	Screw M12 × 30 (6)	[0, 0, −1]
12	Screw M12 × 30 (7)	[0, 0, −1]
13	Screw M12 × 30 (8)	[0, 0, −1]
14	Screw M12 × 30 (9)	[0, 0, −1]
15	Shaft cover (1)	[0, 0, −1]
16	Screw M6 × 10 (2)	[0, 0, −1]
17	Screw M6 × 10 (3)	[0, 0, −1]
18	Screw M6 × 10 (4)	[0, 0, −1]
19	Screw M6 × 10 (5)	[0, 0, −1]
20	Drain plug 2 (21)	[0, 1, 0]
21	Drain plug 1 (16)	[1, 0, 0]

assembled components in order to insert this element into the final assembly sequence according to this reasoning:

Step 1: Component (15): not related to (19) ⇒ The developed algorithm continuously to scroll through the list.
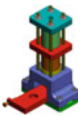
Step 2: Component (12): related to (19) ⇒ (19) is a seal ⇒ (19) is related to 2 components and must be assembled in last ⇒ The developed algorithm continuously to scroll through the list.

Step 3: Component (11): related to (19) ⇒ (19) is a seal ⇒ (19) is related to two components which are assembled ⇒ Execute assembly direction identification process ⇒ Insert (19) just after (11) in the final assembly sequence.

After a few iterations, the final assembly sequence of the whole assembly model is obtained (Table 2). The elapsed time for the generation of this assembly sequence is equal to only 47 min (2820 s). However, the processing time for the treatment of the entire assembly model is equal to 2 h and 21 min (8460 s). By using the simplification approach, 1 h and 34 min of calculation was gained which corresponds to a percentage of computational earned time equal to 66.7%.

4   Conclusion

In this paper, an AS approach based on the simplification of the product CAD model is presented. The aim is to reduce the number of parts by removing standard elements before the assembly sequence generation process. Based on a case reasoning algorithm, these elements are then automatically inserted. The developed method offers a considerable gain in calculation time. Table 3 presents the processing time for some concrete examples and the gained time percentage. This method not only allows the treatment of more complex assemblies but also contributes in AS feasibility. In the future work, an improvement of the proposed approach can be carried out by taking into account the stability of the components during the assembly process and the subassemblies detection.

Table 3 Gained processing time for some concrete examples

Mechanism model	Total components	SC	Entire model processing time	Simplification method processing time (min)	Gained processing time (%)
	15	9	42 min	19	54.8
	29	16	1 h 14 min	41	44.6
	14	6	1 h 52 min	11	90.2

References

Belhadj I, Trigui M, Benamara A (2016) Subassembly generation algorithm from a CAD model. Adv Manuf Technol 87:2829

Ben Hadj R, Trigui M, Aifaoui N (2015a) Toward an integrated CAD assembly sequence planning solution. J Mech Eng Sci Part C 229–16:2987–3001

Ben Hadj R, Trigui M, Aifaoui N (2015b) Integrated CAD Approach for generating assembly sequence plans based on collision study results. Design and modeling of mechanical systems—II. In: Proceedings of the sixth conference on design and modeling of mechanical systems, CMSM' 2015. March 23–25. Hammamet, Tunisia

Ibrahim I, Ibrahim Z, Ahmad H et al (2015) An assembly sequence planning approach with a rule-based multi-state gravitational search algorithm. Int J Adv Manuf Technol 79:1363

Kashkoush M, ElMaraghy H (2015) Knowledge-based model for constructing master assembly sequence. J Manuf Syst 34:43–52

Kheder M, Trigui M, Aifaoui N (2015) Disassembly sequence planning based on a genetic algorithm. J Mech Eng Sci Part C 229(12):2281–2290

Liu X, Liu Y, Bihong X (2013) A converse method-based approach for assembly sequence planning with assembly tool. Int J Adv Manuf Technol 69:1359–1371

Rashid MFF, Hutabarat W, Tiwari A (2011) A review on assembly sequence planning and assembly line balancing optimisation using soft computing approaches. Int J Adv Manuf Technol 59:335–349

Wu M, Zhao Y, Wang C (2013) Knowledge-based approach to assembly sequence planning for wind-driven generator. Math Prob Eng 2013

Yu J, Wang C (2013) A max–min ant colony system for assembly sequence planning. Int J Adv Manuf Technol 67:2819–2835

In-Plane Strength Domain Numerical Determination of Hollow Concrete Block Masonry

Friaa Houda, Hellara Laroussi Myriam, Stefanou Ioannis, Karam Sab and Abdelwaheb Dogui

Abstract Masonry wall is a composite structure formed by units linked vertically and horizontally by mortar. One of the interests in this paper is composed of hollow concrete blocks. Generally, in structural analysis of masonry wall, the determination of the limit strength presents a challenge, due to the complexity and the heterogeneity of his constituent materials. In the present paper, a numerical homogenization is used for the estimation of the strength domain of an in-plane loaded masonry by accounting for the failure of its blocks. The determination of this domain was based on a rigorous definition of the microstructure in three-dimensions, on convex analysis and on the kinematical approach in the frame of limit analysis theory. A three-dimensional periodic basic cell with a nonlinear material behavior is used. Periodic boundary conditions have been imposed on the lateral boundary of the unit cell by matching the degrees of freedom of pairs of nodes.

Keywords Masonry · Homogenization method · Numerical simulations Strength domain · Periodic cell

1 Introduction

Masonry is a composite material made of bricks or blocks joined by mortar. The numerical simulation of such structure is extremely difficult because of the large number of influential factors such as anisotropy, variety of material properties, and

F. Houda (✉) · H. L. Myriam · A. Dogui
Laboratoire de Génie Mécanique, Ecole Nationale d'Ingénieurs de Monastir,
Université de Monastir, Monastir, Tunisie
e-mail: houda.frea@hotmail.com

S. Ioannis · K. Sab
Laboratoire Navier (École des Ponts Paris Tech, IFSTTAR, CNRS), Université Paris-Est,
École des Ponts Paris Tech, 6 et 8 avenue Blaise Pascal, 77455 cedex 2 Marne-la-Vallée,
France

dimensions of units and mortar. Recently, in numerical simulation, more interest has been made on the determination of the mechanical behavior of this complex structure in failure (Cecchi et al. 2007; Portioli et al. 2014; Fernando et al. 2012; Thamboo and Dhanasekar 2016). The failure can be studied either by continuum or discrete-type models (micro and macro). In micro-modeling, the blocks and mortar are defined by continuum element, with explicitly defined joint (interface) while, in macro-modeling masonry is represented as one material with different material properties. The latter method is based on simplified analytical approaches or on homogenization. Each method has advantages and disadvantages. Macro-modeling, does not make any distinction between joints and units. Many others use this method to simulate masonry structure (Pelà et al. 2011). The main aim of this approach is to define the mechanical properties of an equivalent homogeneous material. Generally, the most available macro-modeling, describe the elastic linear behavior of brickwork, but the inelastic behavior of masonry structure is studied in fewer works. On the other hand, this method usually requires many mechanical parameters to be set, which need a lot of costly experimental complain on masonry wallettes and the analysis of different texture need a new calibration of model parameters. Mirco-modeling is the most utilized approach to study masonry structure (Lourenço and Rots 1997; Lotfi and Shing 1994; Drougkas et al. 2016). In the latter method, brick and mortar joints are presented by continuum elements; however, the unit-mortar interface is represented by discontinuous elements. The computational effort of this approach is proportional to the number of elements that consist of the structure so that its applicability is limited to small wallettes. Homogenization represents a fair compromise between micro- and macro-modeling. The mechanical parameter of an equivalent continuum structure are derived from those constituents (bricks or blocks and mortar) Pietruszczak (1991), Luciano and Sacco (1997) Milani (2011), proposed a homogenization approach to determine a lower bond of the strength domain of masonry. Buhan (de Buhan and de Felice 1997), based on kinematic approach and under plane stress condition have determined in closed-form the strength domain with the use of Coulomb interface. Massart (2005) and Zucchini and Lourenço (2007) considered, in addition, the brittle behavior of masonry structure elements in the frame of damage mechanics theory. The limitation of homogenization approach is related to the nonlinearity analysis. In any case, a huge number of mechanical parameter mentioned before is needed and those parameters are not always available or easy to determine. For those reasons, limit analysis with homogenization technique is still the most powerful structural analysis tool to study masonry behavior at collapse. Nevertheless, the strength domain in the abovementioned approaches does not have an analytical closed-form expression. Stefanou et al. (2015) pursue the results of de Buhan and de Felice (1997) and derive analytically the overall strength domain of masonry wall using a kinematic limit analysis approach in three-dimensions, whereas the exact formulation of the unit cell problem is not reducible to plane strain or stress (Sahlaoui et al. 2011).

This paper focuses on determining the strength domain of in-plane loaded masonry wall formed by hollow block connected with frictional interfaces of finite thickness (mortar).

2 Homogenized Strength Domain with Kinematic Approach

Masonry represents a composite structure formed by units and mortar. Which are really periodically arranged. Thanks to this periodicity, the entire wall can be considered as a repetition of a basic cell (elementary cell) as shown in Fig. 1. This repetitive cell Y describes the geometry of the whole structure Ω. In addition, if the structure is a running bond pattern, it can be easily checked that the elementary cell is rectangular.

To define the macroscopic (or average) mechanical properties for periodic arrangement of units and mortar, homogenization method can be used both in elastic and inelastic domain which leads to many simplifications of the numerical models adopted for studying entire wall, especially in inelastic case. In this paper, numerical homogenization is used in order to determine the overall in-plane strength domain of running bond masonry structure formed by hollow blocks joined by mortar. A kinematic limit analysis method is used following three-dimensional stress and kinematic field. The basic idea of homogenization method consists in defining averaged quantities representing the macroscopic stress Σ and macroscopic strain.

Let the heterogeneous structure to be studied occupy the domain $\Omega = w$ x]$-t/2$, $t/2$[where w C R^2 is the middle surface and t is his thickness. The geometry of hollow concrete is presented in Fig. 2. Because of its periodicity, this structure can
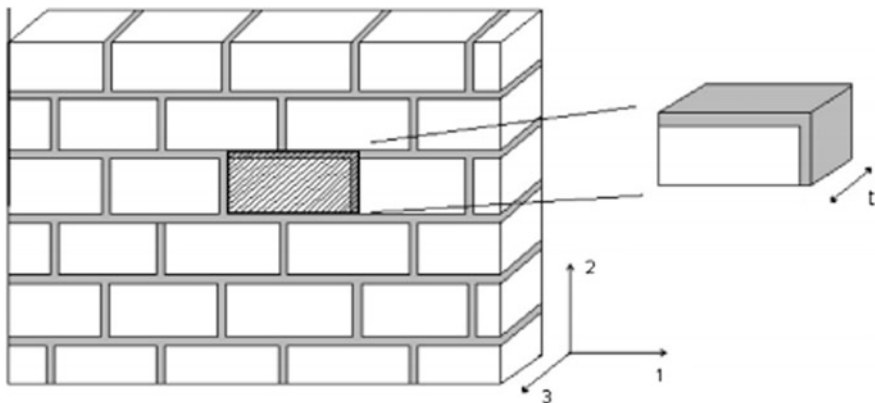
Fig. 1 The running bond masonry geometry and the unit cell chosen

Fig. 2 The hollow block geometry (mm)
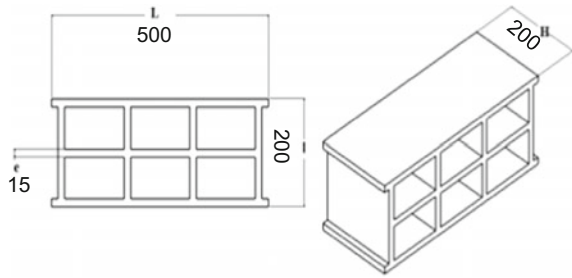
be represented by a basic cell which can repeat the wall by periodically translating in direction 1 and 2 (Fig. 1), and its size is small compared with the size of the whole structure and large comparing with the size of heterogeneities. The basic cell chosen occupy the domain $Y = A \times]-t/2, t/2[$ where $A \subset R^2$, the boundary ∂Y of Y is decomposed into three parts $\partial Y = \partial Y_1 \cup \partial Y_3^+ \cup \partial Y_3^-$ with $\partial Y_3^\pm = \{\pm \frac{t}{2}\}$. We remarque that this wall may be regarded as a periodic plate in its plane whose thickness and the size of the periodic in the plane are of the same order as shown in Fig. 1.

The homogenization of periodic plate has been studied in different cases: constitutive material with elastic behavior, elasto-plastic or rigid plastic. The homogenization of elastic plate have been studied by many others such as Caillerie et al. (1984). The homogenization method used to define the strength domain of tridimensional periodic heterogeneous structure has been initially introduced by Suquet (1983) for continuous medium. In their work Sab (2003) and Bouregeous et al. (1998) have proposed in an independent way to substitute the periodic tridimensional structure in the plane by a homogeneous Love-Kirchhoff plate whose homogenized macroscopic strength domain is determined from the resolution of an auxiliary problem on a 3D basic cell. This procedure is a generalization to the limit analysis of the work of Caillerie et al. (1984) on thin elastic plates. Let $N = (N_{\alpha\beta}(x_1 x_2))$ the macroscopic in-plane (membrane) stress field resultants for the homogenized plate with $(x_1 x_2) \in w$ and $\alpha, \beta = 1, 2$, $M = (M_{\alpha\beta}(x_1 x_2))$ the macroscopic out-of-plane (flexural) stress field resultants, $D = (D_{\alpha\beta}(x_1 x_2))$ the in-plane strain rate field, $\chi = (\chi_{\alpha\beta}(x_1 x_2))$ the out-of-plane strain rate field and $V = (V_i(x_1 x_2))$ the plate velocity field with $D_{\alpha\beta} = 1/2 (V_{x,\beta} + V_{\beta,\alpha})$ and $\chi_{\alpha\beta} = - V_{3,\alpha\beta}$. Then the convex strength domain can be determined by solving an auxiliary limit analysis problem over the unit cell Y. The in-plane strength domain of the symmetric second order in-plane stress tensor $\Sigma = (\Sigma_{\alpha\beta})$ is defined by a convex closed domain $G^\Sigma(y)$. This domain is defined by a positive homogeneous function of degree one, called support function and defined as:

$$\Pi(d) = \sup\{\sigma: d, \sigma \in G^\Sigma\} \Leftrightarrow G^\Sigma = \{\sigma | \sigma: d \leq \Pi(d), \forall d\} \tag{1}$$

with $\sigma = (\sigma_{ij})$ the stress tensor and i, j = 1, 2 and $d = (d_{ij})$ denotes a strain rate tensor and: represents double contraction. According to a static definition of the G^{Σ}, $\Sigma \in G^{\Sigma}$, if there exists a Y-periodic stress field of the 3D unit cell verifying:

$$
\begin{cases}
\sigma(y) \in G(y), \forall y \in Y \\
\langle \sigma_{\alpha\beta} \rangle = \Sigma\alpha\beta \\
div\sigma = 0 \; on \; Y \\
\sigma \cdot n \; skew - periodic \; on \; \partial Y_1 \\
\sigma \cdot e_3 = 0 \; on \; \partial Y_3^{\pm}
\end{cases}
\tag{2}
$$

The kinematic definition of G^{Σ} is as follows:

$$
G^{\Sigma} = \{\Sigma = (\Sigma_{\alpha\beta}) | \Sigma : D \leq \Pi^{\Sigma}(D), \forall D = (D_{\alpha\beta})\}
\tag{3}
$$

where Π^{Σ} is the support function of G^{Σ} and it is given by:

$$
\Pi^{\Sigma}(D) = \inf_{v \in KA(D, 0)} \{\langle \Pi(\nabla \otimes^s v) \rangle\}
\tag{4}
$$

with KA is the set of cinematically admissible velocity field of the unit cell.

3 Numerical Homogenization

3.1 Geometry

The structure to be studied is a running bond masonry made of identical parallelepipedic hollow blocks separated by horizontal continuous bed joints and alternative vertical head joints. Let Y be the chosen unit cell (Fig. 3) of size b in the horizontal direction 1(length), a in the vertical direction 2(height), and t is the third direction (thickness), e_h is the thickness of the horizontal joint and e_v is the thickness of the vertical one.

The limit analysis problem with 3D unit cell has been solved with ABAQUS finite elements software. In Table 1, we resume the dimensions of the unit cell in mm:

Fig. 3 The unit cell chosen geometry
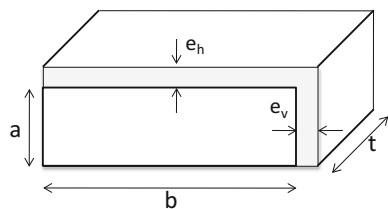
Table 1 Dimensions of unit cell (mm)

Parameters	Value
a	200
b	500
t	200
e_h	5
e_v	5

Table 2 Mechanical parameters (Stefanou Stefanou et al. 2015)

Parameters	Blocks	Mortar
Coulomb cohesion (MPa)	4.3	0.35
Coulomb friction angle	30°	40°
Elastic modulus (MPa)	6740	1700
Poisson ratio	0.17	0.05

3.2 Material

The masonry wall is composed of blocks and mortar considered as two different materials. Blocks and mortar are geomaterials, usually described by Coulomb failure Criterion. But, the numerical treatment of Coulomb yield surface with Abaqus finite elements software can provoke problems related to the non-smoothness of this Criterion. Therefore, elasto-plastic simulation with perfectly plastic Drucker-Prager materials (no hardening) obeying the normality rule, was performed for both blocks and mortar. The Drucker-Prager failure criterion has the following form:

$$\sigma \in G \Leftrightarrow f(\sigma) \le 0 \text{ with } f(\sigma) = q - p\beta - k \tag{5}$$

where $p = \frac{1}{3} tr(\sigma)$ is the hydrostatic, $S = \sigma - pI$ is the deviatoric stress, $q = \sqrt{\frac{3}{2} s : s}$, c > 0 is the Drucker-Prager cohesion and β is the friction angle with $(c, \beta) = (c^J, \beta^J)$ in the joints and $(c, \beta) = (c^B, \beta^B)$ in the blocks. According to Salençon (1990), the Drucker-Prager interface yield strength coincides with Mohr-Coulomb one given by:

$$\tau + \sigma \tan \rho - c' \le 0 \tag{6}$$

with σ is the normal components of $\sigma \cdot n$, $\sigma = n \cdot (\sigma \cdot n)$, τ is its shear component $|\sigma \cdot n - \sigma n|$, ρ is the Mohr-Coulomb friction angle such as $\frac{3 \sin \rho}{\sqrt{3 + \sin^2 \rho}} = \tan \beta$ and $c' = \frac{c \tan \rho}{\tan \beta}$ is the Mohr-Coulomb cohesion. The parameters used in numerical simulation analysis are resumed in Table 2 for both blocks and mortar.

$$\Sigma_2 = -(1+\xi)\,\Sigma$$

$$\Sigma_1 = (1-\xi)\,\Sigma$$

Θ
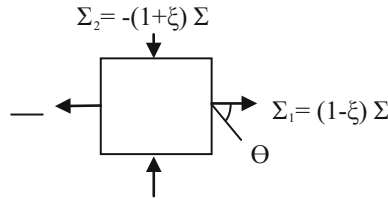
Fig. 4 Load to be studied
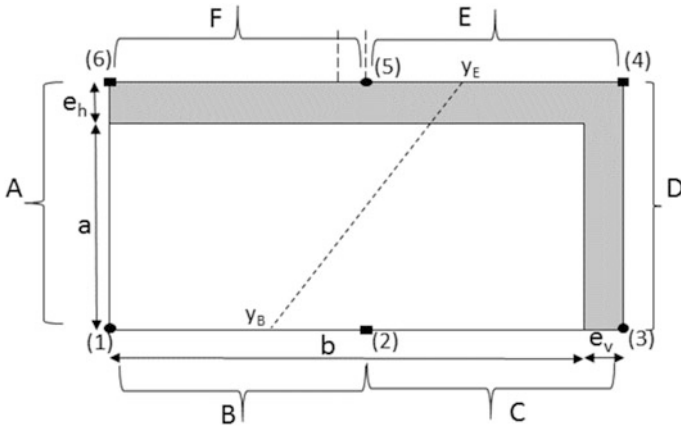
Fig. 5 Section of the unit cell along the middle plane of the masonry and notation of its interactions with the adjacent cells

3.3 Boundary Conditions

In this paper, we study two cases of loading, one is uniaxial compression normal to the bed joints and the other is uniaxial tension normal to the head joints as shown in Fig. 4.

The in-plane stress may be expressed as follows:

$$\Sigma = \begin{pmatrix} \cos 2\theta - \xi & -\sin 2\theta \\ -\sin 2\theta & -\cos 2\theta - \xi \end{pmatrix},\ \Sigma > 0 \tag{7}$$

The maximum value of $\Sigma = \Sigma^{\mathrm{max}}$ such that $\Sigma \in G^{\Sigma}$, can be determined for certain value of θ and ξ is non-dimensional real parameter varying between -1 and 1, and θ is the angle of the principal axis with respect to bed joints direction (direction 1) as shown in Fig. 4. In the frame of perfect associate elasto-plasticity, failure will occur when $\Sigma = \Sigma^{\mathrm{max}}$. Periodic boundary conditions have been imposed on the lateral boundary of the unit cell by matching the degrees of freedom of pairs of nodes. In Fig. 5 A, B, C, D, E, F are the six faces of the boundary of the unit cell. Notice that the geometry of the elementary cell remains invariant to translations by

vectors joining node (5) with node (1) or (3) and vectors joining node (4) with node (6) or (2). Consequently, face E should be matched by periodicity conditions with face B, face D should be matched with face A and face F with face C. Hence, the periodic conditions at the unit cell are:

$$v(y_E) - v(y_B) = D \cdot (y_E - y_B) = \begin{pmatrix} \dfrac{b+e_v}{2}D_{11} + (a+e_h)D_{12} \\ \dfrac{b+e_v}{2}D_{12} + (a+e_h)D_{22} \\ 0 \end{pmatrix}$$

$$v(y_D) - v(y_A) = D \cdot (y_D - y_A) = \begin{pmatrix} b+e_v D_{11} \\ b+e_v D_{12} \\ 0 \end{pmatrix} \tag{8}$$

$$v(y_F) - v(y_C) = D \cdot (y_F - y_C) = \begin{pmatrix} -\dfrac{b+e_v}{2}D_{11} + (a+e_h)D_{12} \\ -\dfrac{b+e_v}{2}D_{12} + (a+e_h)D_{22} \\ 0 \end{pmatrix}$$

These equations are implemented in periodic boundary conditions so these conditions become linear relations between the nodal degree of freedom of the lateral boundary of Y. In Abaqus, we use "Equation" to insert these relations and loading parameters D. Notice that, in numerical simulation in static condition there is no need to distinguish between velocities and displacements, and strains from strain rates.

4   Results and Discussion

Numerical simulations of the 3D unit cell were done by increasing ε until the ultimate load that corresponds to $\Sigma = \Sigma^{\max}$. The unit cell is meshed with tetrahedral elements type with quadratic interpolation (C3D10), because of the geometrical specificity of the structure due to the presence of holes. A convergence mesh study is carried out and the adopted one is with a number of elements 15699 and three layers of elements on the thickness of joints as shown in Fig. 6.

In Fig. 7, we represent the contour of minimum principal stress in MPa developed in a 3D unit cell for the case of uniaxial compression normal to the bed joints ($\xi = 1$, $e_v = e_h = 5$ mm).
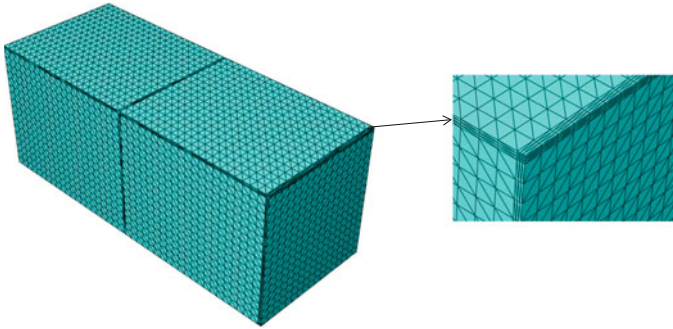
Fig. 6 Mesh adopted in numerical simulation
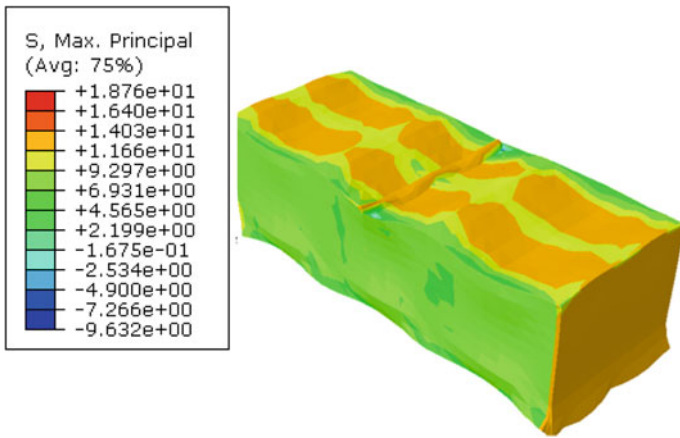
Fig. 7 Contour of S min principal of uniaxial compression
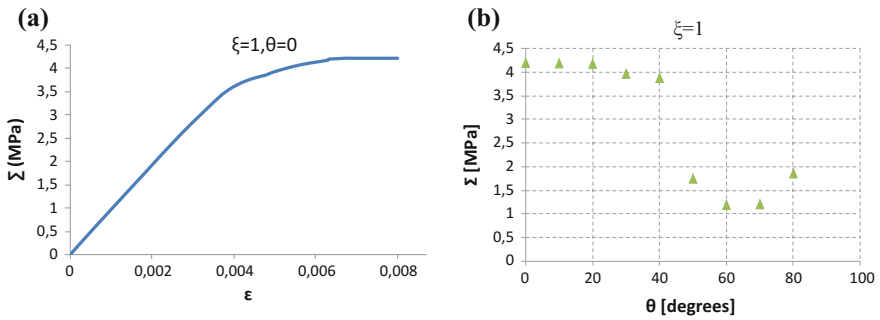
Fig. 8 Strain-Stress curve (**a**), strength domain (**b**)
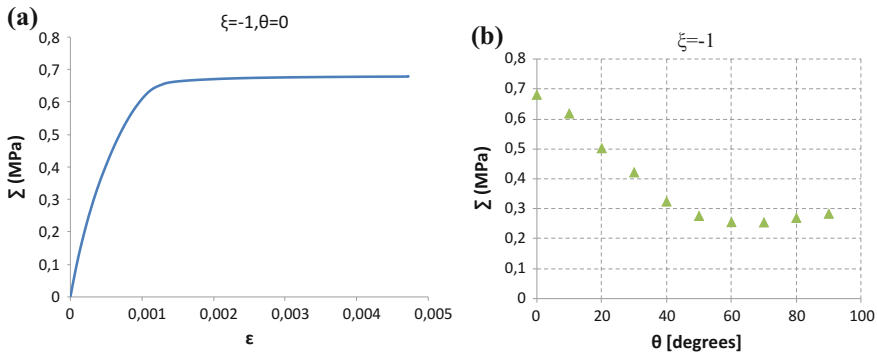
Fig. 9 Strain-Stress curve (**a**), strength domain (**b**)

The analysis of the results shows that the failure of the wall occurred by plastifying the horizontal joints and it propagates through the blocks. We notice the appearance of bending at the level of holes. The equivalent plastic strain in the block is not uniform, it is maximum at the center and quasi-zero at the extremities. The overall stress components $\Sigma_{\alpha\beta} = <\sigma_{\alpha\beta}>$ are computed by averaging the stress values measured at the Gauss points. As shown in Fig. 8a, the ultimate stress Σ^{max} is obtained as the asymptotic value of Σ for increasing ε. The ultimate uniaxial compressive strength is equal to $\Sigma_{22} = -2\Sigma^{max}$. In this case of uniaxial compression, the numerical strength domain is plotted for different values of the angle θ (Fig. 8b). According to this study, we find that the failure of the structure in the case of uniform uniaxial compression in the plane is related to the resistance of the blocks rather to the resistance at the masonry for this type of loading.

The ultimate stress Σ^{max} is obtained as the asymptotic value of Σ for increasing ε. The ultimate uniaxial compressive strength is equal to $\Sigma_{11} = 2\Sigma^{max}$ (Fig. 9)

For tensile tests, failure always occurs at the joints for all the values of θ. For $\theta = 0$, the plasticity of the horizontal joints is done by shear, on the other hand, the vertical joints failed in tension. For the loading of $\theta = 45\pm$, the plasticity of the joints takes place by pure shear in the two joints. For $\theta = 90\pm$, we have failure of the horizontal joints in tension.

5 Conclusion

In this paper, we have applied a numerical homogenization scheme based on the kinematic approach, for certain geometrical and mechanical parameters, to determine the in-plane strength of masonry structure formed by hollow blocks periodically arranged in space and connected with mortar. In this analysis, a three-dimensional unit cell is used which is composed of blocks and mortar considered as two different materials. Blocks and mortar are geomaterials, described by

the Coulomb failure Criterion. Two cases of loading are presented, one is uniaxial compression normal to the bed joints and the other is uniaxial tension normal to the head joints. Periodic boundary conditions have been imposed on the lateral boundary of the unit cell by matching the degrees of freedom of pairs of nodes. Two modes of failure are observed: failure in the interface joints for the cases of load which favor shear and failure of blocks in the case of compression.

References

Bourgeois S, Débordes O, Patou P et al (1998) Homogénéisation et plasticité de plaques minces Homogeneisation et plasticite de plaques minces. Rev Eur des Éléments Finis. https://doi.org/10.1080/12506559.1998.11690464

Caillerie D, Ciarlet G, Ciarlet PG et al (1984) Thin Elastic Period Plates 6:159–191

Cecchi A, Milani G, Tralli A (2007) A Reissner-Mindlin limit analysis model for out-of-plane loaded running bond masonry walls. 44:1438–1460. https://doi.org/10.1016/j.ijsolstr.2006.06.033

de Buhan P, de Felice G (1997) A homogenization approach to the ultimate strength of brick masonry. J Mech Phys Solids 45:1085–1104. https://doi.org/10.1016/S0022-5096(97)00002-1

Drougkas A, Roca P, Molins C (2016) Nonlinear micro-mechanical analysis of masonry periodic unit cells. Int J Solids Struct 80:193–211

Fernando L, Vélez R, Magenes G, Michael C (2012) International Journal of Architectural Heritage : Conservation, Analysis, and Restoration Dry Stone Masonry Walls in Bending—Part I : Static Tests. 3741. https://doi.org/10.1080/15583058.2012.663059

Lotfi HR, Shing PB (1994) Interface model applied to fracture of masonry structures. J Struct Eng 120:63–80

Lourenço P, Rots JG (1997) Multisurface interface model for analysis. J Eng Mech 660–668

Luciano R, Sacco E (1997) Homogenization technique and damage model for old masonry material. Int J Solids Struct 34:3191–3208. https://doi.org/10.1016/S0020-7683(96)00167-9

Massart TJ (2005) Mesoscopic modeling of failure in brick masonry accounting for three-dimensional effects. Eng Fract Mech 72(72):1238–1253. https://doi.org/10.1016/j.engfracmech.2004.09.007

Milani G (2011) Simple lower bound limit analysis homogenization model for in- and out-of-plane loaded masonry walls. Constr Build Mater 25:4426–4443. https://doi.org/10.1016/j.conbuildmat.2011.01.012

Pelà L, Cervera M, Roca P (2011) Continuum damage model for orthotropic materials: application to masonry. Comput Methods Appl Mech Eng 200:917–930. https://doi.org/10.1016/j.cma.2010.11.010

Pietruszczak S (1991) A mathematical description of macroscopic behaviour of brick masonry

Portioli F, Casapulla C, Gilbert M, Cascini L (2014) Limit analysis of 3D masonry block structures with non-associative frictional joints using cone programming. Comput Struct 143:108–121. https://doi.org/10.1016/j.compstruc.2014.07.010

Sab K (2003) Yield design of thin periodic plates by a homogenization technique and an application to masonry walls. Comptes Rendus Mec 331:641–646. https://doi.org/10.1016/S1631-0721(03)00144-X

Salençon J (1990) An introduction to the yield desing theory and its application to soil mechanics. Europ J Mech Solids 21:715–746

Sahlaoui R, Sab K, Heck J (2011) Comptes Rendus Mecanique yield strength of masonry-like structures containing thin adhesive joints: 3D or 2D-interface model for the joints? Comptes Rendus Mec 339:432–438. https://doi.org/10.1016/j.crme.2011.03.018

Stefanou I, Sab K, Heck JV (2015) Three dimensional homogenization of masonry structures with building blocks of finite strength: a closed form strength domain. Int J Solids Struct 54:258–270. https://doi.org/10.1016/j.ijsolstr.2014.10.007

Suquet P (1983) Analyse limite et homogénéisation. C R Acad Sci Paris série II 296:1355–1358

Thamboo JA, Dhanasekar M (2016) Nonlinear finite element modelling of high bond thin-layer mortared concrete masonry. Int J Mason Res Innov 1:5. https://doi.org/10.1504/IJMRI.2016.074727

Zucchini A, Lourenço PB (2007) Mechanics of masonry in compression: results from a homogenisation approach. Comput Struct 85:193–204. https://doi.org/10.1016/j.compstruc.2006.08.054

Definition and Classification of Collaborative Network: MCDM Approaches for Partner Selection Problem

Souhir Ben Salah, Wafa Ben Yahia, Omar Ayadi and Faouzi Masmoudi

Abstract The quick environment development make impossible that an enterprise, working individually, can respond to market opportunities. For this reason, more and more firms are aware and motivated to improve their offer and competitiveness by means of collaboration, through sharing competencies and resources. Thus, the purpose of this paper is to describe, through a literature review, the key concepts related to a Collaborative Network (CN) and to provide a classification of networks. Furthermore, the key issue of the CN is the selection of the right partners, which is performed based on several, sometimes conflicting, quantitative, and qualitative criteria. Thus, this task is considered, in the literature, as a Multi Criteria Decision Making (MCDM) problem. Therefore, the second objective of this research is to survey this area by identifying the frequently used criteria, in strategic and tactical management level, as well as the MCDM approaches.

Keywords Collaborative network · Partner selection criteria · MCDM approaches

1 Introduction

Nowadays, organizations, especially the Small and Medium sized Enterprises (SME), seek to explore new organizational models and to adopt new business models to remain competitive in the turbulent market. Therefore, they are exceeding

S. Ben Salah (✉) · W. Ben Yahia · O. Ayadi · F. Masmoudi
Mechanics, Modelling and Production Research Laboratory (LA2MP),
National Engineering School of Sfax (ENIS), Sfax University, 1173-3038 Sfax, Tunisia
e-mail: souhirbensalah@hotmail.com

W. Ben Yahia
e-mail: wafa.benyahia@hotmail.fr

O. Ayadi
e-mail: omar.ayadi@yahoo.fr

F. Masmoudi
e-mail: masmoudi.fawzi@gmail.com

733

their organizational boundaries to collaborate with partners in order to quickly respond to market opportunities while assuring fast response time and competitive prices (Azevedo et al. 2017). Indeed, the collaboration becomes a hot topic and it receives considerable attention in recent years.

Collaboration relationships consists of a combination of multiple skills, which can help enterprises access complementary resources, share risks, reduce transaction costs, increase productivity, and enhance profit performance as well as competitive advantage over time (Cao and Zhang 2011).

The success of such a CN strongly depends on its composition. In this context, finding the suitable partners is an important issue and it is the key step in the formation of any collaboration. Further, the decision on which partner should be selected for each task depends not only on operational characteristics such as cost, quality, etc., but also on financial situation, capability to work in collaboration with other partners and even past performance in collaborative processes. Several researchers have investigated the Partner Selection (PS) criteria in different context. The PS problem is considered as a Multi Criteria Decision Making (MCDM) problem. A number of approaches have proposed to solve this problem.

This paper provides a literature review that covers the concept of CN. It addresses first, the different concepts of a collective work and second the large variety of network forms. Subsequently, the PS problem is studied by presenting some of the evaluation and selection criteria as well as the different MCDM techniques used by authors. Therefore, this paper targets readers who are interested in the basic terms of collaboration in order to design and manage collaborative relationships.

The remainder of this paper is organized as follows: the definition of the concept of the CV and the classification of the important terms of a collective work are presented in Sect. 2. Section 3 presents the different forms of the CN. Section 4 presents the two important issue of the PS problem, which are PS criteria and the MCDM approaches. Finally, Sect. 5 draws the conclusion of this work and proposes future research directions.

2 Collaborative Network Concept

The concept of CN is largely studied by Camarinha-Matos et al. since 1998. They have analyzed its evolution across the time. The CN is defined as *an organization of a variety of entities (e.g., organizations and people) that are largely autonomous, geographically distributed, and heterogeneous in terms of their: operating environment, culture, social capital, and goals. Nevertheless, these entities collaborate to better achieve common or compatible goals, and whose interactions are supported by a computer network* (Camarinha-Matos and Afsarmanesh 2005).

Several studies introduce the collaboration by specifying different types and levels of collaboration in terms of the level of commitment or degree of sharing between the partners. In fact, according to Montarnal (2017), the degree of sharing in a CN is what the partners decide to have in common when working together.

The most important levels of a collective work are cooperation, coordination, and collaboration. These terms are often used by researchers in an interchangeable manner without clearly distinguishing them from each other. Thus, in an attempt to clarify the existing ambiguity in the literature, the following definitions are proposed.

2.1 Cooperation

Cooperation can be defined as working together to achieve compatible goals. Indeed, the cooperative work involves not only communication, information exchange, and alignment of activities, but also sharing resources (Camarinha-Matos et al. 2009). Cooperation is achieved by division of some labor among participants. Each participant perform their part of the job, in a quasi-independent manner. However, there exists a common plan, which is not defined jointly but rather designed by a single entity that can be the coordinator or the administrator of the network. Further, members engaged in a cooperative strategy act autonomously in order to achieve first their own objectives and second the whole network goals (Ben Yahia 2015).

Cooperative alliances have attracted increasing research interest. For instance, Adenso-Díaz et al. (2014) have approved that cooperation among firms in the running of logistics operations is an interesting way of reducing costs and gaining efficiency. However, they are asserted that, because of the increase in complexity in the coordination of the cooperation, there is a limit to the number of partners that can effectively cooperate. Also, Wei et al. (2012) have looked for the success factors of a cooperative relationship. They have demonstrated from their study that information integration and trust are the most important conditions to improve the performance of partners working cooperatively.

2.2 Coordination

Coordination has been widely considered as one of the key drivers of collective work. It can be defined as the act of making all members of the network involved to harmonize their efforts to reach an arrangement for a goal (Ben Yahia 2015). Coordination is mainly concerned with information sharing functions, interaction between parts, and it refers to a more direct and active cooperation (Hammer 2006). Further, collective work within the framework of coordination is characterized by a specified workflow and information exchange in a manner that allows to apply Just-In-Time systems (JIT) and Electronic Data Interchange (EDI) between and among entities (Camarinha-Matos et al. 2009).

Compared to cooperation, decisions within a group of companies working in coordination are taken in interactive and join manner (Hammer 2006). As a result,

coordination permits partners working in an information and communication environment to ensure complete, correct, timely, and full information.

Several studies show that the network coordination plays a critical role in integrating different entities and can improve the whole CN performance. However, managing uncertainties and complexities to coordinate network, in the global competition, is a challenging task. For this reason, Shukla et al. (2014) and Arshinder and Deshmukh (2007) have developed a mechanism, based on several factors, by which coordination can be achieved between partners. In fact, from their point of view, the use of a coordination mechanism allows to increase efficiency and effectiveness in the operations and the actors and improve the performance of CN.

2.3 Collaboration

Collaboration has been recognized as the most form of a collaborative work which requires a greater level of involvement and interaction and includes joint activities and teamwork (Hammer 2006). It is a process in which actors share information, responsibilities, and resources to jointly plan, implement, and evaluate a set of activities in order to achieve a common goal and jointly generating value (Camarinha-Matos et al. 2009). This concept implies a group of entities to enhance the capabilities of each other. It also implies sharing risks, losses, and rewards, which if desired by the group can also give to an outside observer the image of a joint identity. Collaboration involves mutual trust and engagement of participants to solve a problem together.

As opposed to cooperation and coordination, the collaboration is a collective working situation where tasks and goals are common on the strategic plan as well as on the tactical plan. Each member of the group works on the same points to finally satisfy the end customer requirements (Piquet 2009).

Several studies (Cao and Zhang 2011; Divine 2014; Ramanathan and Gunasekaran, 2014; Long 2016) show that the collaboration between networks partners can reduce costs and response time, leverage resources, and improve innovation. Thus, the success of the network's collaboration will improve the confidence of CN partners to improve their performance further to achieve high profit.

In the field of CN management, there is an overlap in the order of the different concepts of collective work as well as the meaning of each one. However, according to Ayadi (2014), there is a common agreement that the highest level of the collective work is the collaboration, in which partners work, jointly at strategic and operational levels, the whole project and share information, resources, risks, responsibilities, losses, and gains. Indeed, networks' collaboration is, currently, the topic of interest for many researchers and practitioners.

3 Types of Collaborative Network

The classification and perceptions of a CN vary significantly. Drawing on networks literature, it is possible to classify them according to the structure or the nature of linkages between members (Simatupang and Sridharan 2002). Another classification is proposed by Camarinha-Matos et al. (2009) based on the nature of interaction and strategy of collaboration of network entities. Each type of network is described below in terms of the two criteria already cited.

3.1 Classification of Networks in terms of the Nature of Linkages Between Members

Basically, there are three types of networks: the horizontal, vertical, and lateral network. The type of network is mainly decided by the collaboration scenario and the attributes of the participants (Chan and Zhang 2011). Each type is defined below according to (Simatupang and Sridharan 2002; Roach 2010; Ben Yahia 2015):

- **Vertical Network**

It is a form of collaborative arrangement between two or more heterogeneous enterprises, which are related because the output of one organization is an input for another. In other words, the entities share their resources and responsibilities to serve similar end customer. The competencies of these firms and their activities are therefore different and complementary. Vertical collaboration problems include the well-known news vendor problem, issues of risk pooling, coordinated demand forecasting, coordinated pricing, and coordinated lot sizing.

- **Horizontal Network**

It is an association of two or more homogeneous companies positioned at the same level in a CN. They may be unrelated or competing firms and they have close competence fields. This form of collaboration is especially beneficial to SME who are mainly interested in increasing their capacities (inventory, production, resources, etc.) in order to penetrate markets they would otherwise be unable to enter. However, the engagement in horizontal network presents a unique challenge, namely the management of an opportunistic behavior among competing entities.

- **Lateral Network**

It is an association of companies adopting both vertical and horizontal collaboration form. This type of network aims to increase the flexibility of the actors through the combination and the share of their capabilities.

The benefits of such collaboration forms rest largely on the opportunities to achieve superior capabilities and performance over the long-term and to generate significant economic advantages. However, according to Roach (2010) vertical associations tend to be more common than horizontal ones because they offer substantial opportunities for buyers and sellers to cooperate through information sharing, distribution, and producing complementary products. Moreover, researchers, applying network theory, have largely focused on the vertical and lateral arrangements such as suppliers, manufacturing organizations, distributors, and intermediaries (Taghipour and Frayret 2012; Pan and Nagi 2013; Mousavi et al. 2014; Sarrafha et al. 2015; Montarnal 2017). Therefore, further research in horizontal collaboration form, which represents a relatively neglected area of study, would contribute to the development of a framework that help practitioners for managing a set of homogeneous firms who cooperate to gain access to external complementary resources.

3.2 Classification of Networks in terms of the Nature of Collaboration Strategy

A large variety of CNs have emerged depending on the nature of relationship between partners as well as their collaboration strategy. The most important forms of collaboration are the Virtual Enterprises, the Virtual Organizations, the Virtual Breeding Environment, and the Supply Chain Network. Each collaboration form is defined as follows:

- *Virtual Enterprise (VE)*

It is a temporary alliance of enterprises that come together to share skills and resources (Camarinha-Matos et al. 2009). In other words, a VE is a tactical combination of core competencies (Binder and Clegg 2007), to better respond to opportunities emerging from a new market.

From the point of view of Binder and Clegg (2007), a VE presents a unified face to externals. Indeed, companies keep their autonomous behaviors and can participate in other VEs simultaneously for more power and maturity.

Zhao et al. (2006) argue that the VE is a basic organization form to achieve agile manufacturing.

- *Virtual Organization (VO)*

Camarinha-Matos et al. (2009) considered that the VE is a particular case of VO. They define the VO as a set of independent organizations (legally) that are integrated by sharing resources and core competencies in order to achieve a particular mission/goal. The VO will dissolve once their mission or objective has accomplished.

Typically, there are four stages in the life cycle of a VE and VO: *creation, operation, evolution, and dissolution* (Camarinha-Matos et al. 2005; Sadigh et al. 2014). A detailed description of each stage can be found in studies already cited.

- ● *Virtual Breeding Environment (VBE)*

It represents an association of firms and their related supporting institutions, that have both the will and the potential to cooperate with each other (Camarinha-Matos et al. 2009). According to Romero and Molina (2010), the VBE is a long-term strategic alliance of enterprises. The VBE concept mainly focuses on creating an adequate environment for the establishment of cooperation agreements, common interoperable infrastructures, common operation principles, common ontologies, and mutual trust among members.

The creation of a VBE aims to offer the necessary conditions (e.g., human, financial, social, infrastructural, and organizational) to support the rapid configuration of VE/VO that will be established when a collaboration opportunity arises. Indeed, Afsarmanesh and Camarinha-Matos (2005) are asserted that an efficient creation of VOs/VEs is the main purpose for the existence of the VBEs, which is considered as necessary context in order to improve the preparedness of its members for joining potential virtual organizations.

- ● *Supply Chain Network (SCN)*

It is a stable long-term network of connected and interdependent enterprises that are cooperatively working together. Each of them have clear roles in the manufacturing value chain, covering all steps from initial product design and the procurement of raw materials, through production, shipping, distribution, and warehousing until a finished product is delivered to a customer. The level of stability of these entities is being challenged, leading to dynamic supply chains where the participants can change more often (Camarinha-Matos et al. 2009).

Finally, these different variants of CNs represent a major trend in which enterprises and professionals seek complementarities and joint activities to allow them to participate in competitive business opportunities and in new markets.

4 Partner Selection Problem

In recent years, the literature is very rich with studies dedicated to VE/VO configuration. Several authors (Crispim and Pinho De Sousa 2010; Sadigh et al. 2014; Dao et al. 2014) asserted that the success of VE/VO highly depends on the creation stage, in which the suitable partners should be selected. Hence, the PS problem is a fundamental (Wu and Barnes 2013) and crucial (Kafa et al. 2015) issue as it contributes significantly to overall VE/VO performance. It consists of evaluating

and selecting the partners, who have the required skills in order to fully meet customer requirements.

From the point of view of Büyüközkan and Güleryüz (2016), the PS is a common problem businesses frequently face in their everyday operations. Therefore, they argued that this task should be managed with care as it is a critical decision that can affect their operational success.

The PS problem, which can be named as supplier selection in literature if it is a purchase process, has been attracting a lot of research attention. For instance, the Shevtshenko et al. (2015)'s study proposed a novel process of Partner Network initiation, which covers the aspects of composing the members and introduces the business processes classifier for enterprises partners. The purpose of this study is to enable a faster commencement of new projects or VE/VO configuration for the price proposal preparation.

Wu and Barnes (2013) divided the PS process into four phases: *criteria formulation*, *qualification*, in which appropriate partners are identified, followed by *final selection*, in which a final choice is made from among suitably qualified partners. The last phase is *application feedback* in which the decision-makers (DMs) evaluate the members in order to improve the effectiveness of the network by ensuring that the most suitable partners are selected at all times.

Subsequently, it is argued in the literature, that the PS problem is not a simple optimization problem. In fact, many researchers (Lee et al. 2015; Büyüközkan and Güleryüz 2016; Lin 2009; Azadnia et al. 2014) considered the PS as an MCDM problem since the decision-makers aim to choose the best alternative based on several conflicting criteria. Recently, a volume of literature has been written concerning this topic in terms of evaluation and selection criteria as well as the methods which are proposed to solve this complex problem.

4.1 Partner Selection Criteria

The most important issue of any decision-making problem is choosing the suitable set of evaluation criteria. The literature is very rich with studies dedicated to PS criteria. Indeed, Dickson's study (1966) represents a reference of the majority of researchers dealing with PS problem. He identified 23 criteria for evaluation of the performance of companies and he considered that quality, delivery, and performance history are the most important criteria. Actually, the criteria considered in PS are situation-specific and each network DMs should develop its own selection criteria when facing with finding potential members.

Following the hierarchical CN management, there are two levels of decision-making in the PS problem: Strategic and tactical. Thus, the PS criteria are different at these two levels.

Strategic criteria should evaluate the organizations' characteristics and their positions in the market in order to obtain a reliable network as well as long-term relationships among companies. In fact, Lee et al. (2015) used four main evaluation

criteria, namely the general management capability perspective (financial status and reputation, etc.), manufacturing capability perspective (product diversity, quality control, etc.), collaboration capability perspective (delivery reliability and after sales service), and agility perspective (IT infrastructure, delivery flexibility, etc.). Also, Geum et al. (2013) relied on technology strength, Research and Development (R&D) openness, R&D linkage, and collaboration effects to identify strategic R&D partners.

Tactical criteria should relate to the evaluation of operational performance and competitive priorities of members in order to achieve the customer satisfaction. For instance, Xiang (2012) selected 14 most frequently considered criteria representing five major aspects of operational performance, which are delivery, quality, flexibility, cost, and innovation. In addition, the uncertainties are mostly found in the tactical stage in terms of demand, supply quantities, logistics operations, etc. Therefore, Esmaeilikia et al. (2014) argued that a flexible SC is able to be quickly adaptable in the presence of uncertainties. Indeed, they identified several tactical flexibility measures such as volume flexibility, delivery flexibility, operational decision flexibility, processes flexibility, etc.

4.2 MCDM Approaches

The MCDM approaches are recognized for their advantages in dealing with challenges that do not only involve high levels of uncertainty, but also conflicting objectives and numerous dimensions (Büyüközkan and Güleryüz 2016). These techniques have a methodological framework that aims to provide to DMs (experts) a knowledgeable recommendation amid a set of alternatives (i.e., actions, solutions) while being evaluated by multiple criteria (i.e., attributes, objectives). However, it has limitations in dealing with the imprecise and vague nature of linguistic assessment. Therefore, it is better to make the assessment and selection problems under fuzzy conditions.

From the analysis of studies (Ho et al. 2010; Govindan et al. 2013; Yadav and Sharma 2015), the MCDM techniques have been applied in both individual and integrated ways. The most popular individual approaches are Analytic Hierarchy Process (AHP), Analytic Network Process (ANP), and Technique for Order Preference by Similarity to Ideal Solution (TOPSIS). Further, the current studies mainly used the integrated approaches for PS. In fact, it is noticed that the integrated AHP approaches are more prevalent. For instance, Shukla et al. (2014), Taylan et al. (2015), Beikkhakhian et al. (2015), Garg (2016) and Alizadeh et al. (2016) applied both AHP and TOPSIS techniques to solve a selection problem in different decision fields. In addition, Mathematical Programming (MP) techniques, such as Data Envelopment Analysis (DEA), Multi-Objective Programming (MOP), Goal Programming (GP), are extensively used, especially where the decision problem is formulated mathematically. Indeed, Ho et al. (2010) argued that the integrated AHP-GP approach is the most popular.

5   Conclusion and Perspectives

CNs are recognized, by both academia and industry, as an efficient solution for survival of enterprises in the current fast-changing environment conditions. In this paper, we present a literature review on this research area including the concept of the CN, the different forms of networks and the PS problem.

Through a literature analysis, we note that, in spite of the effort of several authors, there are no effective or proven methodologies to support the managers in designing and managing the CN. Furthermore, we observe that there is a gap in some research area. In fact, a little attention is given to case study research with enterprises that are involved in a horizontal CN. In addition, the PS problem, in the tactical decision level, is not well-studied. Therefore, these findings can serve as a foundation for such future studies. It is also worth to develop a decision-making framework to support the partners' evaluation and selection to establish such collaboration for a specific business opportunity.

References

Adenso-Díaz B, Lozano S, Garcia-Carbajal S et al (2014) Assessing partnership savings in horizontal cooperation by planning linked deliveries. Trans Res Part A Policy Pract 66:268–279. https://doi.org/10.1016/j.tra.2014.05.013

Afsarmanesh H, Camarinha-Matos LM (2005) A framework for management of virtual organization breeding environments. Collab Netw Breed Environ 23:35–48. https://doi.org/10.1007/s10278-009-9220-x

Alizadeh S, Salari Rad MM, Bazzazi AA (2016) Alunite processing method selection using the AHP and TOPSIS approaches under fuzzy environment. Inter J Mining Sci Technol 26 (6):1017–1023. https://doi.org/10.1016/j.ijmst.2016.09.009

Arshinder KA, Deshmukh SG (2007) Coordination in supply chains: an evaluation using fuzzy logic. Prod Plan Cont 18(5):420–435. https://doi.org/10.1080/09537280701430994

Ayadi O (2014) Modélisation et optimisation des performances de réseaux d'entreprises manufacturières. Dissertation, University of Sfax

Azadnia AH, Saman MZM, Wong KY (2014) Sustainable supplier selection and order lot-sizing: an integrated multi-objective decision-making process. Inter J Prod Res 53:383–408. https://doi.org/10.1080/00207543.2014.935827

Azevedo A, Faria J, Ferreira F (2017) Supporting the entire life-cycle of the extended manufacturing enterprise. Robot Comput Integr Manuf 43:2–11. https://doi.org/10.1016/j.rcim.2016.05.009

Beikkhakhian Y, Javanmardi M, Karbasian M et al (2015) The application of ISM model in evaluating agile suppliers selection criteria and ranking suppliers using fuzzy TOPSIS-AHP methods. Exp Syst Appl 42:6224–6236. https://doi.org/10.1016/j.eswa.2015.02.035

Ben Yahia W (2015) Multi-objective optimization for collaborative planning in supply chain. Dissertation, University of Sfax

Binder M, Clegg B (2007) Enterprise management: a new frontier for organisations. Inter J Prod Eco 106(2):409–430. https://doi.org/10.1016/j.ijpe.2006.07.006

Büyüközkan G, Güleryüz S (2016) A new integrated intuitionistic fuzzy group decision making approach for product development partner selection. Comp Indus Eng 102:383–395. https://doi.org/10.1016/j.cie.2016.05.038

Camarinha-Matos LM, Afsarmanesh H (2005) Collaborative networks: a new scientific discipline. J Intel Manuf 16:439–452. https://doi.org/10.1007/s10845-005-1656-3

Camarinha-Matos LM, Afsarmanesh H, Ollus M (2005) Ecolead : a holistic approach to creation and management of dynamic virtual organizations. In: Collaborative networks and theri breeding environments, pp 3–16

Camarinha-Matos LM, Afsarmanesh H, Galeao N et al (2009) Collaborative networked organizations—concepts and practice in manufacturing enterprises. Comp Indus Eng 57 (1):46–60. https://doi.org/10.1016/j.cie.2008.11.024

Cao M, Zhang Q (2011) Supply chain collaboration: impact on collaborative advantage and firm performance. J Op Manage 29(3):163–180. https://doi.org/10.1016/j.jom.2010.12.008

Chan FTS, Zhang T (2011) The impact of collaborative transportation management on supply chain performance: a simulation approach. Exp Sys App 38(3):2319–2329. https://doi.org/10.1016/j.eswa.2010.08.020

Crispim J, Pinho De Sousa J (2010) Partner selection in virtual enterprises. Inter J Prod Res 48 Jan 2015, 683–707. https://doi.org/10.1080/00207540802425369

Dao SD, Abhary K, Marian R (2014) Optimisation of partner selection and collaborative transportation scheduling in virtual enterprises using GA. Exp Sys App 41(15):6701–6717. https://doi.org/10.1016/j.eswa.2014.04.030

Dickson GW (1966) An analysis of vendor selection systems and decisions. J Purch 2:5–17

Divine L (2014) La collaboration virtuelle : Proposition d'un modèle, d'une mesure et d'une méthode d'aide au management d'entités virtuelles. Dissertation, University of Paris

Esmaeilikia M, Fahimnia B, Sarkis J et al (2014) Tactical supply chain planning models with inherent flexibility: definition and review. Annals Op Res 1–21. https://doi.org/10.1007/s10479-014-1544-3

Garg CP (2016) A robust hybrid decision model for evaluation and selection of the strategic alliance partner in the airline industry. J Air Trans Manage 52:55–66. https://doi.org/10.1016/j.jairtraman.2015.12.009

Geum Y, Lee S, Yoon B et al (2013) Identifying and evaluating strategic partners for collaborative R&D: index-based approach using patents and publications. Technovation 33(6–7):211–224. https://doi.org/10.1016/j.technovation.2013.03.012

Govindan K, Rajendran S, Sarkis J et al (2013) Multi criteria decision making approaches for green supplier evaluation and selection: a literature review. J Clean Product. https://doi.org/10.1016/j.jclepro.2013.06.046

Hammer A (2006) Enabling successful supply chain management: coordination, collaboration, and integration for competitive advantage. Dissertation, University of Mannheim

Ho W, Xu X, Dey PK (2010) Multi-criteria decision making approaches for supplier evaluation and selection: a literature review. Europ J Op Res 202(1):16–24. https://doi.org/10.1016/j.ejor.2009.05.009

Kafa N, Hani Y, Mhamedi AEL (2015) An integrated sustainable partner selection approach with closed-loop supply chain network configuration. In: 15th IFAC symposium on information control in manufacturing, pp 1885–1890

Lee J, Cho H, Kim YS (2015) Assessing business impacts of agility criterion and order allocation strategy in multi-criteria supplier selection. Exp Sys App 42(3):1136–1148. https://doi.org/10.1016/j.eswa.2014.08.041

Lin RH (2009) An integrated FANP-MOLP for supplier evaluation and order allocation. App Mathe Model 33(6):2730–2736. https://doi.org/10.1016/j.apm.2008.08.021

Long Q (2016) A novel research methodology for supply network collaboration management. Inf Sci 331:67–85. https://doi.org/10.1016/j.ins.2015.10.035

Montarnal A (2017) Deduction of inter-organizational collaborative business processes within an enterprise social network. Dissertation, Federal University of Toulouse

Mousavi SM, Bahreininejad A, Musa SN et al (2014) A modified particle swarm optimization for solving the integrated location and inventory control problems in a two-echelon supply chain network. J Intel Manuf. https://doi.org/10.1007/s10845-014-0970-z

Pan F, Nagi R (2013) Multi-echelon supply chain network design in agile manufacturing. Omega 41(6):969–983. https://doi.org/10.1016/j.omega.2012.12.004

Piquet A (2009) Guide pratique du travail collaboratif : Théories, méthodes et outils au service de la collaboration. LUSSI department

Ramanathan U, Gunasekaran A (2014) Supply chain collaboration: impact of success in long-term partnerships. Inter J Prod Res 147(PART B):252–259. https://doi.org/10.1016/j.ijpe.2012.06.002

Roach G (2010) Horizontal networks and collaborative marketing in the Tasmanian wine industry. In: 5th international conference of the academy of wine business research, pp 1–9

Romero D, Molina A (2010) Virtual organisation breeding environments toolkit: reference model, management framework and instantiation methodology. Prod Plan Control 21. https://doi.org/10.1080/09537280903441963

Sadigh BL, Arikan F, Ozbayoglu et al (2014) A multi-agent system model for partner selection process in virtual enterprise. Procedia Comput Sci 36:367–372. https://doi.org/10.1016/j.procs.2014.09.007

Sarrafha K, Habib S, Rahmati A et al (2015) A bi-objective integrated procurement, production, and distribution problem of a multi-echelon supply chain network design: a new tuned MOEA. Comput Op Res 54:35–51. https://doi.org/10.1016/j.cor.2014.08.010

Shevtshenko E, Poljantchikov I, Mahmooda K et al (2015) Collaborative project management framework for partner network initiation. Procedia Eng 100:159–168. https://doi.org/10.1016/j.proeng.2015.01.354

Shukla R, Garg D, Agarwal A (2014) An integrated approach of fuzzy AHP and fuzzy TOPSIS in modeling supply chain coordination. Prod Manuf Res 2(1):415–437. https://doi.org/10.1080/21693277.2014.919886

Simatupang TM, Sridharan R (2002) The collaborative supply chain. Inter J Logist Manage 13

Taghipour A, Frayret JM (2012) Dynamic mutual adjustment search for supply chain operations planning co-ordination. Inter J Prod Res, 1–25. https://doi.org/10.1080/00207543.2012.737952

Taylan O, Kabli MR, Saeedpoor M et al (2015) Commentary on construction projects selection and risk assessment by fuzzy AHP and fuzzy TOPSIS methodologies. Appl Soft Comput 36:419–421. https://doi.org/10.1016/j.asoc.2015.05.051

Wei HL, Wong CWY, Lai KH (2012) Linking inter-organizational trust with logistics information integration and partner cooperation under environmental uncertainty. Inter J Prod Eco 139(2):642–653. https://doi.org/10.1016/j.ijpe.2012.05.036

Wu C, Barnes D (2013) Partner selection in agile supply chains: a fuzzy intelligent approach. Prod Plan Cont 25:821–839. https://doi.org/10.1080/09537287.2013.766037

Xiang T (2012) Les coopérations en réseau pour optimiser la performance de l'entreprise: L'exemple du réseau logistique en Chine. Dissertation, University of Aix-Marseille

Yadav V, Sharma MK (2015) Application of alternative multi-criteria decision making approaches to supplier selection process. Intel Tech Eng Manage 723–743. https://doi.org/10.1007/978-3-319-17906-3_27

Zhao F, Hong Y, Yu D (2006). A multi-objective optimization model of the partner selection problem in a virtual enterprise and its solution with genetic algorithms. Int J Adv Manuf Technol 28(11):1246–1253. http://doi.org/10.1007/s00170-004-2461-4

Supply Chain Risk Management, Conceptual Framework

Faiza Hamdi, Faouzi Masmoudi and Lionel Dupont

Abstract Nowadays, global speedy transformations have required the company to investigate on risk supply chain management. The goal of this investigation is to overcome their around insecure conditions. The objective of this paper is to present supply chain risk management area. In this context, we propose a conceptual framework of the supply chain risk management process. This process involves basically four sequential steps: identification of risk, analyzing of risk, evaluate of risk, and control and monitoring of risk. Further, we recap the different sets of risk and we present the frequent techniques that used to measure risk in the literature review of supply chain risk management. After that, we synthesize some works based on the approach of resolution. Finally, analyzes and potential areas for future research will be presented. This paper contributes to current risk management literature by providing an efficient gait to manage risk which makes company to mitigate the negative effect of risk.

Keywords Supply chain risk management · Risk sets · Conceptual framework process

F. Hamdi (✉)
Unité de recherche de Logistique, Gestion Industrielle et Qualité (LOGIQ), Institut Supérieur de Gestion Industrielle de Sfax, Université de Sfax, Sfax, Tunisia
e-mail: faiza_isgi@yahoo.fr

F. Masmoudi
Laboratoire de recherche de Mécanique, Modélisation et Production (La2MP), Département de Génie Mécanique, École Nationale d'Ingénieurs de Sfax, Université de Sfax, Sfax, Tunisia
e-mail: masmoudi.fawzi@gmail.com

F. Hamdi · L. Dupont
École des Mines d'Albi-Carmaux, Centre de Génie Industriel (CGI), Université de Toulouse, Toulouse, France
e-mail: lionel.dupont@mines-albi.fr

745

1 Introduction

The current business environment is characterized by the globalization of the market, outsourcing of some activities. This mutation offers many benefits to the firms in term of efficiency and effectiveness, but they can also make supply chains more brittle and can increase risks of supply chain disruption. Historic and recent events have proven the need to identify and find strategies to mitigate risks. Among the disruption: the case of Ericson company which loss $400 million due to a fire at a Phillips semiconductor plant in 2000. This event leads to disruption in supply chain production. The earthquake, tsunami, and the subsequent nuclear crisis at a power plant that happens in Japan in 2011 caused Toyota's production to drop by 40,000 vehicles, costing $72 million in profits per day (Pettit et al. 2013). This event showed how one event can disrupt many elements of global supply chains, including supply, distribution, and communications. In October 2011, Thailand flooding affected disruption in delivery of hard disk to the computer company. In order to find some strategies to mitigate and minimize the negative effect of these events, several types of research have been investigated in the area of supply chain risk management. The objective of management of supply chain risk is to ensure that product and materials get to the right place and at the right time. In fact, the company who manage supply chain risk than its competitors do can gain a competitive advantage.

The remainder of this paper is organized as follows. Section 2 provides definitions of supply chain risk. Section 3 present supply chain risk set. Section 4 treat SCRM definitions. Section 5 present SCRM process. Modeling techniques are presented in Sect. 6. Then SCRM approaches. After that, we present some analysis and recommendations and finally conclusion.

2 Definitions of Supply Chain Risk

There are vast researches that have addressed the risk of supply chain definitions. The objective of this section is to present some definitions of the present concept Zsidisin (2003) define supply chain risk as the probability of an incident associated with inbound supply from individual supplier failures or the supply market occurring, in which its outcomes result in the inability of the purchasing firm to meet customer demand or cause threats to customer life and safety. Jüttner et al. (2003) define supply chain risk as any risks for the information, material and product flows from original suppliers to the delivery of the final product for the end user. Whereas Wagner and Bode (2006) considered the negative deviation from the expected value of a certain performance measure, resulting in negative consequences for the focal firm. As for Bogataj and Bogataj (2007) considered supply risk as the potential variation of outcomes that influence the decrease of value added at any activity cell in a chain. Ellis et al. (2010), proposed other definition of supply

risk as an individual's perception of the total potential loss associated with the disruption of the supply of a particular purchased item from a particular supplier. More recently Ho et al. (2015) considered supply risk as the likelihood and impact of unexpected macro-and/or micro-level events or conditions that adversely influence any part of a supply chain leading to operational, tactical, or strategic level failures or irregularities.

3 Risk Supply Chain Sets

The area of supply chain risk management recognizes a diverse set of risks that firms face everyday. The objective here is to present and recap the taxonomy of risk set. Among the classification which proposed by Tang (2006) who divided risk of supply chain into two categories: operational risk and disruptions risks. The first one related to inherent uncertainties such as in products demand, supply and all types of costs. As for the second can be raised by natural disasters like earthquakes, floods, hurricanes, and terrorist attacks. Goh et al. (2007) considered two sets of risk in the supply chain: the internal risk that contains supply, demand, and trade credit risks, and external risks that arise from the interactions amongst the supply chain and their environment, comprising international terrorism and natural disasters. Regarding to Waters (2007) how considered two sets of risks such as: controllable risk and incontrollable risk. Tang and Tomlin (2008) supposed that the risk can be divided into strategic risk and tactical risk.

Chopra and Sodhi (2004) classified supply chain risks into nine sources such as disruptions, delay, systems, forecast, intellectual property, procurement, receivables, inventory, and capacity. Hallikas et al. (2004) considered that the risk of the supply chain can take many forms such as strategy, operations, supply, customer relations, asset impairment, competition, reputation, financial markets, fiscal and regulatory requirements, and legal. Christopher and Peck (2004) gathered risk of supply chain sources in five groups: process, control, demand, supply, and environment. Whereas Kar (2010) classified risk in systematic risk, demand uncertain and supply uncertain and non-systematic risk.

Punniyamoorthy et al. (2013) categorized risk of supply chain according to their sources such as side, demand side, manufacturing side, logistics side, information, and environment risks. Hantsch and Huchzermeier (2013) divided risks into procurement risk, production risk, sales risk, financial market risk, risk specific to the production network, political/legal risk, and other risks. Recently, Giannakis and Papadopoulos (2015) proposed a specific classification for supply chain and they focused on the risk of sustainability of supply chain, which can be Environmental endogenous (Environmental accidents, Pollution, Energy consumption …), and Environmental exogenous (Natural disasters, Healthy, and safe working environment …)

4 Supply Chain Risk Management

Effective supply chain risk management (SCRM) is an essential key to a successful company. Chen et al. (2013) define Supply chain risk management is a collaboration between partners to deal with risks and uncertainties in logistics-related activities in the supply chain. Ho et al. (2015) Define supply chain risk management as an interorganizational collaborative endeavor utilizing quantitative and qualitative risk management methodologies to identify, evaluate, mitigate, and monitor unexpected macro-and micro-level events or conditions, which might adversely impact any part of a supply chain.

Yang (2011) proposed a specific definition of maritime supply chain risk management as a process of making and carrying out decisions that will minimize the adverse effects of accidental losses. They are based also on the risk assessment methods involving cooperation and communication between all members involved in maritime supply chain activities.

We turn next to how firms manage their supply chain risk management process. In this context, the firm must identify their internal and external environments.

5 Supply Chain Risk Management Process

The majority of research agree that the main stages of supply chain risk management (SCRM) involve five sequential steps: risk identification, assessment, analysis, treatment, and monitoring. Different classifications have been proposed in the literature review to define SCRM process. For example, Sinha et al. (2004) consider five steps to mitigate risk (1): identification risk (2) assessment risk (3) plan and implement risk (4) conduct failure mode and effect analysis and (5) continuous amelioration. Kleindorfer and Saad (2005) gathered supply chain risk management steps into three stages: first, determine sources of risk and vulnerabilities, then assessment risk and finally mitigate risk. As for Sodhi et al. (2012) recapitulated SCRM process in four steps: risk identification, risk assessment, risk mitigation, and finally responsiveness to risk incidents (Fig. 1).

Fig. 1 Risk matrix

Impact		Low	Medium	high
	high	Medium	High	High
	Medium	Low	Meduim	High
	Weak	Low	Low	Meduim
		Low	Medium	high
		Probability		

Here, we provide an approach to manage risk in the supply chain as presented in (Fig. 2). In fact, the process of supply chain risk management must begin with the identification of internal and external risks. In this stage, Enterprise must establish and classify the different set of risk. There exist several risk classifications in the SCRM literature. A commonly preferred risk classification is based on the 'sources of risk.' The common sources of risk are 'internal and external risk.' Then, it is
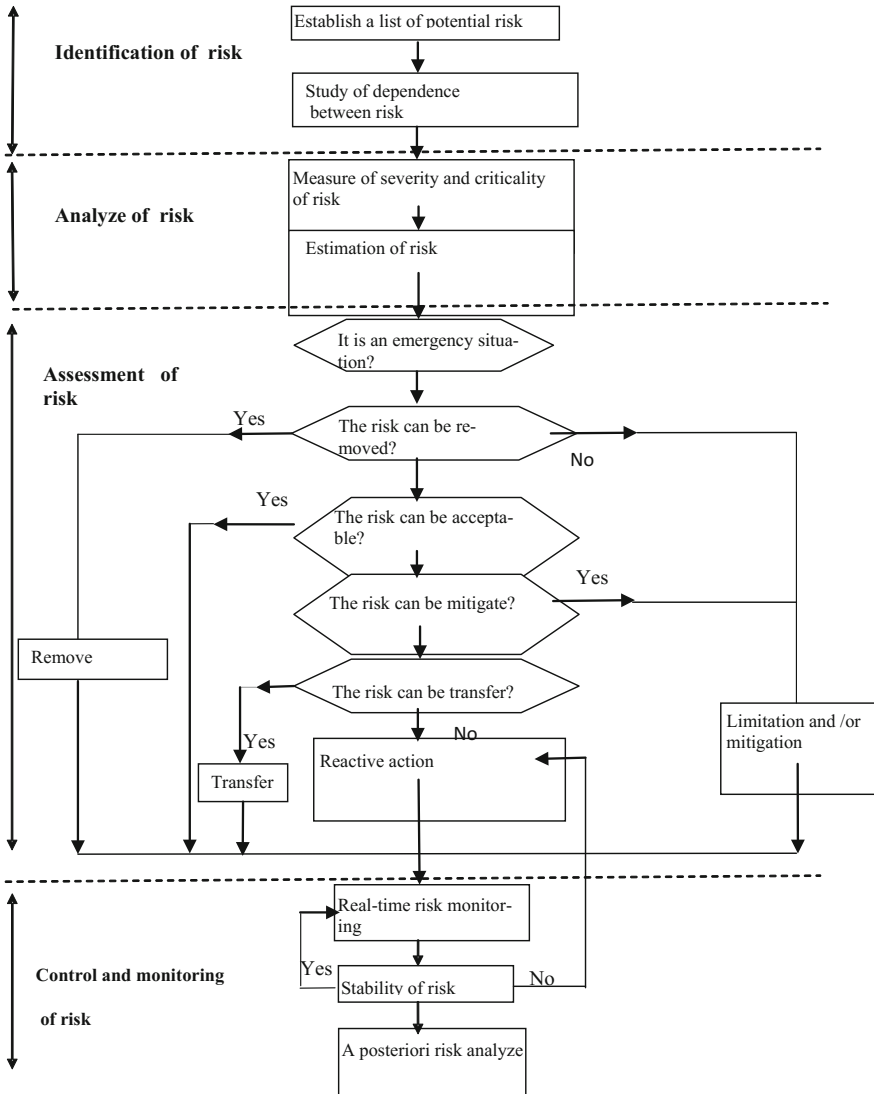
Fig. 2 Supply chain risk management process

recommended to study the interdependence between the different risks. Here, we mention they exist different methods to identify all plausible risk in supply chain among we cite Brainstorming, quest method, historic data, Pareto analysis.

The second step of SCRM process concern risk analysis. In this stage, the decision maker must prioritize risk by threat (prioritization can be measured by likelihood and consequences). In a risk analysis step, three questions make up the basis of the analysis: what can go wrong? How likely is it to happen? What are the consequences? The aim here is to determine the risk that can make supply chain vulnerable in a structured and systemic way. In fact, the objective of risk analysis stage is to helps firms to better understand the point of occurrence of each set of risk and its consequences, which in turn aids them to develop a shared awareness of different types of risk and their potential effects on different supply chain partners.

Different techniques can be used to analyze risk include FMEA. This method aims to categorize failure, evaluate their effects, and then analyze their causes on the system. AHP (Analytic hierarchy process) can be used also in this step. This technique aims to prioritize the existent risk.

The following step is about assessment step, here we distinguish between the different set of risk and then we give the importance for the major risk. Risk evaluated in terms of the likelihood of probability of the risk and the severity of the consequence. Risk matrix can be used to rank which risk to mitigate, which risk to eliminate and which risk to transfer as mention on Fig. 2. Choudhary and Shankar (2014) considered the step of assessment of supply chain risk must become during the new product development process due to the growing uncertainty in supply chains.

Zsidisn (2003) proposed some useful suggestions to mitigate and reduce the upstream risks among: establishing buffer stock and enhancing inventory management, avoiding single sourcing and using alternative sources of supply, utilizing supply contracts to manage the fluctuation in sourcing price and adopting quality initiatives to implement comprehensive quality management.

Jüttner et al. (2003), Kleindorfer and Saad (2005) considered that risk sharing mechanism refers to the formal policies and arrangements (ex, agreements, and contracts) through which supply chain partners share the obligations and duties for mitigating SCRs and dealing with the consequences of the SCRs in their supply chains.

Managers usually select the proper mitigation strategies based on several factors, such as the nature of the risk, origin of the risk, and company resources. In this context, efficient mitigation of supply chain risk can help minimize supply chain cost and improve customer satisfaction.

The objective of the risk matrix is to categorize risk events by the probability of occurrence (horizontal axis) and impact (vertical axis) at a given risk. The manager focuses first on the event that attains high levels on both axes. The upper right quadrant of the matrix, and suggest potential countermeasures for risk mitigation. The focus on off-diagonal quadrants involves either loss mitigation or risk mitigation and the lower left quadrant is where risk and loss acceptance is considered.

The last step refers to risk monitoring and control. The objective is to ensure the execution of risk action and evaluation their effectiveness in reducing and mitigating risk. Continuous monitoring of risks is recommended in this stage.

6 Risk Modeling

Within the literature on supply chain risk management, many researches have investigated in the area. Each work has the specific manner to model and treat risk.

In practice, different risk measure is used. A traditional risk measure like the variance, which was suggested for quantifying the risk. However, the variance presents some limitations. Others papers choose random parameters to model risk. This can be fixed or estimated via time series analysis. Others papers integrate the notion of fuzzy to model uncertainty. Some other based on the developing stochastic models and a probabilistic model. This method is available for the complex situations.

More recently, we find some papers integrate quantitative techniques to model risk such as the value at risk, conditional value at risk (Sawik 2011, 2013, 2014), miss the target Choudhary and Shankar (2014) and so on … some other papers recourse to simulation which considers as a natural tool for evaluating the impact of disruptions in complex supply chains.

There exists an abundant set of factors, which would give rise to supply chain disruptions. However, there is lack of research measuring the correlations between risk factors and corresponding risk types, or the probability of occurrence of particular risk types associated with their factors. In this context, practice case study is necessary to quantify and estimate such correlation and dependence and concentrate on creating a method to assess the probabilities of occurrence of some specific risk sets.

7 SCRM Approaches

In the past decade, a number of qualitative and quantitative methods have been developed and applied to manage supply chain risks management. The objective of this section is to present some works in the present problem. Wang et al. (2012) used fuzzy AHP to evaluate the risk of implementing different green initiatives in the fashion industry. Samvedi et al. (2013) combined fuzzy AHP and fuzzy TOPSIS approaches to model risk in the supply chain. He (2017) investigated the impact of supply or demand risk reduction on the CLSC's financial and environmental performances. They used game-theoretical models to analyze equilibrium between the recycling price decision and the remanufacturing.

Song et al. (2017) used a rough weighted decision-making and trial evaluation laboratory (DEMATEL) approach to evaluate and analyze sustainable supply chain

management (SSCM) risk factor as well as extract interrelationships. Rao et al. (2016) investigated the problem of supplier selection under multi sources procurement for a type of divisible goods (such as coal, oil, and natural gas). Mavia et al. (2016) investigated supplier selection under supply chain risk management. They used Shannon entropy for weighing criteria and fuzzy TOPSIS for ranking suppliers.

Mathematical programming models have been developed in this area, including multistage stochastic programming model, multiobjective stochastic programming model, mixed integer programming model stochastic, mixed integer nonlinear programming model.

8 Analyses and Recommendations

A most of paper has been carefully treated a variety of risk such as inventory risk, quality risk, delay risk, disruption risk, etc. Researches concentrate only on the major problem and they studied each risk isolated. Hence the internal dependence are seldom studied in the literature. Field and case studies are necessary to investigate and estimate such correlation between risks.

A common drawback is that the majority of papers did not apply their models in the practical case study. In contrast, they limited on a simple simulated data to validate the effectiveness and efficiency of their models. Thus, it is better to use real data.

A lack of studies, which focus on robustness and resilience. In this case, Asbjørnslett (2009) defined resilience which is referred to the ability of supply chain to return to a new stable or desirable situation after the impact of risk.

Based on the literature review, we mention that they have several papers, which focus on SCRM strategies, and they have a lack of studies, which concentrate on creating proactive and reactive strategies to manage risk.

Further research is necessary to integrate quantitative techniques to estimate and quantify the risk that firm can meet in their supply chain. Here, we propose to use value at risk and conditional value at risk to estimate risk. VaR techniques is widely used in the financial industry, but in the supply chain, they still limited. This technique allows calculating a financial portfolio's range of most and least probable gains or losses overtime. Extremely high or low portfolio gains and losses are rare but still possible. Hence, they represent a best-case or worst-case scenario.

We show also lack of studies which combine between supply chain risk and green supply chain and sustainability.

9 Conclusion

With the globalization and externalization of activities of supply chains, the importance of supply chain risk management (SCRM) has grown significantly. Still, although both researchers and practitioners fully approve on its importance, most of the firms pay very limited attention to SCRM. In fact, companies should not just effectively manage the existing risks. In contrast, professionals SCRM should go beyond risk minimization and be active in justifying costly risk mitigation strategies. In addition, they must find the effectiveness and adequate SCRM measures. In this paper, we presented an overview of SCRM area. First, available definitions of supply chain risk and classifications of risk are synthesized. Then, we proposed a conceptual framework of the supply chain risk management process. After that, we cited some works related to the area. Finally, we proposed some analysis and recommendations for future research.

References

Asbjørnslett BE (2009) Assessing the vulnerability of supply chains. In: Zsidisin GA, Ritchie B (eds) Supply chain risk. Springer, pp 13–33

Bogataj D, Bogataj M (2007) Measuring the supply chain risk and vulnerability in frequency space. Int J Prod Eco 108:291–301

Chen J, Sohal A, Prajogo DI (2013) Supply chain operational risk mitigation: a collaborative approach. Int J Prod Res 51:2186–2199. https://doi.org/10.1080/00207543.2012.727490

Chopra S, Sodhi M (2004) Managing risk to avoid supply chain breakdown. MIT Sloan Manag Rev 46(1):53–62

Choudhary D, Shankar R (2014) A goal programming model forjoint decision making of inventory lot-size, supplier selection and carrier selection. Comput Ind Eng 71:1–9

Christopher M, Peck H (2004) Building the resilient supply chain. Int J Logist Manag 15(2):1–13

Ellis SC, Henry RM, Shockley J (2010) Buyer perceptions of supply disruption risk: a behavioral view and empirical assessment. J Oper Manag 28(1):34–46

Giannakis M, Papadopoulos T (2015) Supply chain sustainability: a risk management approach. Int J Prod Eco. https://doi.org/10.1016/j.ijpe.2015.06.032

Goh M, Lim JY, Meng F (2007) A stochastic model for risk management in global supply chain networks. Eur J Op Res 182(1):64–173

Hallikas J, Karvonen I, Pulkkinen U, Virolainen VM, Tuominen M (2004) Risk management processes in supplier networks. Int J Prod Eco 90(1):47–58

Hantsch M, Huchzermeier A (2013) Identifying, analyzing, and assessing risk in the strategic planning of a production network: the practical view of a German car manufacturer. J Manage Control 24:125–158

He Y (2017) Supply risk sharing in a closed-loop supply chain. Int J Prod Eco 183:39–52

Ho W, Zheng T, Yildiz H, Talluri S (2015) Supply chain risk management: a literature review. Int J Prod Res 53(16):5031–5069. https://doi.org/10.1080/00207543.2015.1030467

Jüttner U, Peck H, Christopher M (2003) Supply chain risk management: outlining an agenda for future research. Int J Logist Res App 6:197–210

Kar K (2010) Risk in supply chain management. https://business-fundas.com/2010/riskin-supply-chainmanagement/

Kleindorfer PR, Saad GH (2005) Managing disruption risks in supply chains. Prod Op Manage 14 (1):53–68

Mavia Rk, Gohb M, Mavi NK (2016) Supplier selection with Shannon entropy and fuzzy TOPSIS in the context of supply chain risk management. Procedia Social Behav Sci 235:216–225

Pettit TJ, Croxton KL, Fiksel J (2013) Ensuring supply chain resilience: development and implementation of an assessment tool. J Bus Logist 34:46–76

Punniyamoorthy M, Thamaraiselvan N, Manikandan L (2013) Assessment of supply chain risk: scale development and validation. Benchmarking: An Int J 20(1):79–105

Rao C, Xiao X, Goh M, Zheng J, Wen J (2016) Compound mechanism design of supplier selection based on multi-attribute auction and risk management of supply chain. Comput Ind Eng. https://doi.org/10.1016/j.cie.2016.12.042

Samvedi A, Jain V, Chan FTS (2013) Quantifying risks in a supply chain through integration of fuzzy AHP and fuzzy Topsis. Int J Prod Res 51:2433–2442

Sawik T (2011) Selection of supply portfolio under disruption risks. Omega 39:194–208

Sawik T (2013) Selection of resilient supply portfolio under disruption risks. Omega 41:259–269

Sawik T (2014) Optimization of cost and service level in the presence of supply chain disruption risks: Singlevs multiple sourcing. Comput Op Res 51:11–20

Sinha PR, Whitman LE, Malzahn D (2004) Methodology to mitigate supplier risk in an aerospace supply chain. Supply Chain Manag Int J 9(2):154–168

Sodhi MS, Son BG, Tang CS (2012) Researchers' perspectives on supply chain risk management. Prod Op Manag 21(1):1–13

Song W, Ming X, Liu H-C (2017) Identifying critical risk factors of sustainable supply chain management: a rough strength-relation analysis method. J Clean Prod. https://doi.org/10.1016/j.jclepro.2016.12.145

Tang CS (2006) Perspectives in supply chain risk management. Int J Prod Econ 103(2):451–488

Tang CS, Tomlin B (2008) The power of flexibility form mitigating supply chain risks. J Prod Eco 116(1):12–27

Wagner SM, Bode C (2006) An empirical investigation into supply chain vulnerability. J Purchasing Supply Manag 12(6):301–312

Wang X, Chan HK, Yee R, Rainey, D (2012) A two-stage fuzzy-AHP model for risk assessment of implementing green initiatives in the fashion supply chain. Int J Prod Eco 135:595–606

Waters D (2007) Supply chain risk management: vulnerability and resilience in logistics. Kogan Page limited, London

Yang YC (2011) Risk management of Taiwan's maritime supply chain security. Safety Sci 49:382–393

Zsidisin GA (2003) A Grounded definition of supply risk. J Purchas Supply Manag 9:217–224

Numerical Analysis of a Segmented Wind Turbine Blade Using the Substructure Method

Majdi Yangui, Slim Bouaziz, Mohamed Taktak and Mohamed Haddar

Abstract The wind turbine blade segmentation development remains a tough challenge for constructors to reduce the blade manufacturing and transport cost. In this paper, numerical analysis is developed in order to study the dynamic characteristics of a segmented wind turbine blade assembled with a spar. The spar and the blade segments are assimilated to a shell structure with different homogeneous and isotropic materials. Accordingly, the three nodes triangular shell element DKT18 is adopted to model the blade. To reduce the problem size the Craig–Bampton substructure method is applied. This study covers the effects the of twist angle on the blade natural frequencies. To validate the accuracy and reliability of the proposed substructuring approach, numerical results obtained from the present study were compared with those determined by modal analysis using ABAQUS software. Results showed that the blade natural frequencies are not monotonically varying with respect to the twist angle which must be investigated to be well above the wind turbine system frequencies.

M. Yangui (✉) · S. Bouaziz · M. Taktak · M. Haddar
Mechanics, Modeling and Production Laboratory (LA2MP), Mechanic Department,
National School of Engineers of Sfax, University of Sfax, BP.1173, 3038 Sfax, Tunisia
e-mail: yanguimajdi@gmail.com

S. Bouaziz
e-mail: slim.bouaziz1@gmail.com

M. Taktak
e-mail: mohamed.taktak@fss.rnu.tn

M. Haddar
e-mail: mohamed.haddar@enis.rnu.tn

755

1 Introduction

Wind turbine blade is considered as the most important component in the wind energy extraction performance. Natural frequencies of the wind turbine components must be investigated during the design process where they must above the wind turbine system frequencies (McKittrick et al. 2001). In order to extend the blade life cycle, many researchers investigate their dynamic characteristics. Maalawi and Negm (2002) presented an optimization model for the design of a wind turbine blade in order to make an exact placement of the blade natural frequencies to avoid resonance. By dint of its several merits such as the accuracy and reliability of results, the Finite Element Method was the most widely used to study the wind turbine blade dynamic behavior. To reduce the vibration and noise, the geometric complexities of the blade have been increased. A precise analysis of such structures requires shell model. Modal analysis was investigated by Dokainish and Rawtani (1972) using a flat triangular element to study the effects of the twist angle on the pretwisted cantilever plate vibration characteristics. Leissa et al. (1981) investigated the impact of rotating speed, pretwist angle, and stagger angle on the shell type blades natural frequencies. Likewise, Sinha and Turner (2011) applied a thin shell theory to study the dynamic characteristics of a pretwisted blade subjected to a centrifugal load. Due to the increase of the blade size, many segmentation techniques were proposed by Saldanha et al. (2013) and Broehl (2014) to reduce the manufacturing and transportation costs. A reliable meshing of the segmented blade structure requires several elements, resulting very large matrices. Reducing the size of the problem becomes obvious to reduce the computing times. The Craig–Bampton methodology is used extensively to recharacterize large finite element models into a set of relatively small matrices containing mass, stiffness and mode shape information. The method formulation is the most often used for assembled structures that have a common interface.

The three-node triangular shell element DKT18 which has six degrees of freedom per node was adopted in this paper to model the segmented blade structure. To reduce the problem size, the substructure method is used. To validate the accuracy and reliability of the proposed method, the present study results were compared with those obtained by modal analysis using ABAQUS software. The influences of the twist angle on the blade natural frequencies were investigated.

2 The Global Blade Model

The blade consists of five segments assembled together on a steel spar as shown in Fig. 1. The three-node triangular shell element DKT18 is used to model the blade segments and the spar structures. The spar was assimilated to a cylindrical shell of length L_s = 550 mm and thickness h_s = 3 mm. The blade model has a length
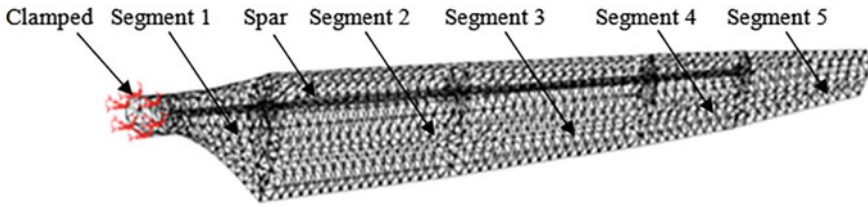
Fig. 1 Segmented wind turbine blade model

Table 1 The blade segments and the spar material properties

Parameters	Elastic modulus (GPa)	Poisson's ratio	Density (kg/m3)
Blade segments	2.4	0.3879	1070
Spar	210	0.3	7850

L_b = 700 mm and thickness h_b = 3 mm. The blade segments and spar material properties are presented in Table 1.

3 Modal Analysis Using Substructure Method

In this section, a modal analysis of the proposed segmented wind turbine blade is performed to obtain their natural frequencies. Because of the blade structure complexity, the substructure method is used to reduce the problem size. Therefore, the segmented blade dynamic characteristics can be obtained rapidly. This method is based on dividing the entire structure into different parts (substructures) examined separately. It uses as basis vectors the static modes and normal modes with the fixed interface. For any substructure k under consideration, the undamped equations of motion are presented as

$$[M^k]\{\ddot{Q}^k\} + [K^k]\{Q^k\} = \{F^k\} \tag{1}$$

where $[M^k]$ and $[K^k]$ are the mass and the stiffness matrices for the total Degree Of Freedom (DOFs). $\{Q^k\}$ and $\{F^k\}$ presents the global displacements vector and the force vector respectively.

$\{Q^k\}$ is partitioned as:

$$\{Q^k\} = \begin{Bmatrix} Q_e^k \\ Q_i^k \end{Bmatrix} = \begin{bmatrix} L_e^k & 0 \\ 0 & I \end{bmatrix} \begin{Bmatrix} Q_e \\ Q_i^k \end{Bmatrix} \tag{2}$$

where $\{Q_i^k\}$ includes the interior DOFs which are to be eliminated and $\{Q_e^k\}$ includes the exterior DOFs that are in physical contact with the other substructures.

$[L_e^k]$ is a Boolean localization matrix relating the assembled exterior DOFs of the global domain represented by $\{Q_e\}$ to the substructure exterior DOFs $\{Q_e^k\}$.

Reordering the mass and stiffness matrices depending on the DOFs repartition, they are rewritten as

$$[M^k] = \begin{bmatrix} M_{ee}^k & M_{ei}^k \\ M_{ie}^k & M_{ii}^k \end{bmatrix} \tag{3}$$

$$[K^k] = \begin{bmatrix} K_{ee}^k & K_{ei}^k \\ K_{ie}^k & K_{ii}^k \end{bmatrix} \tag{4}$$

Consequently, the equation of motion of all substructures N can be assembled in a primal way as

$$[M_g]\{\ddot{Q}_g\} + [K_g]\{Q_g\} = \{F_g\} \tag{5}$$

where

$$[M_g] = \begin{bmatrix} \hat{M}_{ee} & \hat{M}_{ei}^{(1)} & \cdots & \hat{M}_{ei}^{(N)} \\ \hat{M}_{ie}^{(1)} & \hat{M}_{ii}^{(1)} & & 0 \\ \vdots & & \ddots & \\ \hat{M}_{ie}^{(N)} & 0 & & \hat{M}_{ii}^{(N)} \end{bmatrix}, \text{ with } \begin{array}{l} \hat{M}_{ee} = \sum\limits_{k=1}^{N} L_e^{k^T} M_{ee}^k L_e^k \\ \hat{M}_{ie}^{(k)} = M_{ie}^k L_e^k \\ \hat{M}_{ei}^{(k)} = L_e^{k^T} M_{ei}^k \end{array} \tag{6}$$

$$[K_g] = \begin{bmatrix} \hat{K}_{ee} & \hat{K}_{ei}^{(1)} & \cdots & \hat{K}_{ei}^{(N)} \\ \hat{K}_{ie}^{(1)} & \hat{K}_{ii}^{(1)} & & 0 \\ \vdots & & \ddots & \\ \hat{K}_{ie}^{(N)} & 0 & & \hat{K}_{ii}^{(N)} \end{bmatrix}, \text{ with } \begin{array}{l} \hat{K}_{ee} = \sum\limits_{k=1}^{N} L_e^{k^T} K_{ee}^k L_e^k \\ \hat{K}_{ie}^{(k)} = K_{ie}^k L_e^k \\ \hat{K}_{ei}^{(k)} = L_e^{k^T} K_{ei}^k \end{array} \tag{7}$$

$$\{Q_g\} = \left\{ Q_e \quad Q_i^{(1)} \quad \cdots \quad Q_i^{(N)} \right\}^T \tag{8}$$

$$\{F_g\} = \left\{ \hat{F}_e \quad F_i^{(1)} \quad \cdots \quad F_i^{(N)} \right\}, \text{ with } \hat{F}_e = \sum\limits_{k=1}^{N} L_e^{k^T} F_e^k \tag{9}$$

The static modes are computed as follows:

$$\begin{aligned} \{Q_i^k\} &= -[K_{ii}^k]^{-1}[K_{ie}^k]\{Q_e^k\} \\ &= [\Phi_C^k]\{Q_e^k\} \end{aligned} \tag{10}$$

The normal modes are also calculated with Eq. (11):

$$\left(\left[K_{ii}^{k}\right] - \omega_{r}^{2}\left[M_{ii}^{k}\right]\right)\left\{\varphi_{N}^{k}\right\} = \{0\} \tag{11}$$

A transformation matrix is then established with these last modes and used to formulate the generalized coordinate's vector in the physical domain under the following form:

$$\left\{\begin{array}{c} Q_{e}^{k} \\ Q_{i}^{k} \end{array}\right\} = \left[\begin{array}{cc} I & 0 \\ \Phi_{C}^{k} & \Phi_{N}^{k} \end{array}\right]\left\{\begin{array}{c} Q_{e}^{k} \\ \Gamma_{N}^{k} \end{array}\right\} \tag{12}$$

where Φ_{N}^{k} and Γ_{N}^{k} are the truncated set of fixed interface normal modes and the truncated set of generalized modal coordinates, respectively.

In order to reduce the primal assembled system, the Craig-Bampton reduction matrix $[R_{CB}]$ is defined as

$$Q_{g} \approx \left[\begin{array}{cccc} I & 0 & \cdots & 0 \\ \Phi_{C}^{1}L_{e}^{1} & \Phi_{N}^{1} & & 0 \\ \vdots & & \ddots & \\ \Phi_{C}^{N}L_{e}^{N} & 0 & & \Phi_{N}^{1} \end{array}\right]\left\{\begin{array}{c} Q_{e} \\ \Gamma_{N}^{1} \\ \vdots \\ \Gamma_{N}^{N} \end{array}\right\} = [R_{CB}]\{\Gamma\} \tag{13}$$

Incorporating this last equation into Eq. (5), we find

$$[R_{CB}]^{t}[M_{g}][R_{CB}]\{\ddot{\Gamma}\} + [R_{CB}]^{t}[K_{g}][R_{CB}]\{\Gamma\} = [R_{CB}]^{t}\{F_{g}\} \tag{14}$$

4   Results and Discussion

The studied blade model is subdivided into six substructures. Several same nodes are shared at each boundary between these different components. Thus, different substructures own the same movement on the interface depending on the interface continuity.

4.1   Validation Test

Modal analysis was achieved to verify the segmented blade natural frequency using the substructure method and ABAQUS software. The obtained natural frequencies are presented in Table 2.

From this table, it can be noted that the results show a good agreement between the two calculation methods. So, the blade structure complexity has not degraded the computation accuracy. Figure 2 presents the first five mode shapes.

Table 2 Segmented blade natural frequencies

N° Mode	Natural frequencies (Hz)		Diff (%)
	Substructure	ABAQUS	
1	14.36	14.49	0.89
2	23.47	23.64	0.72
3	92.31	91.52	0.85
4	186.82	190.04	1.69
5	211.26	209.63	0.77

1st mode (1st flapwise mode) F=14.49 Hz   2nd mode (1st edgewise mode) F=23.64 Hz

3rd mode (2nd flapwise mode) F=91.52 Hz   4th mode (1st torsinal mode) F=190.04 Hz

5th mode (2nd edgewise mode) F=209.63 Hz
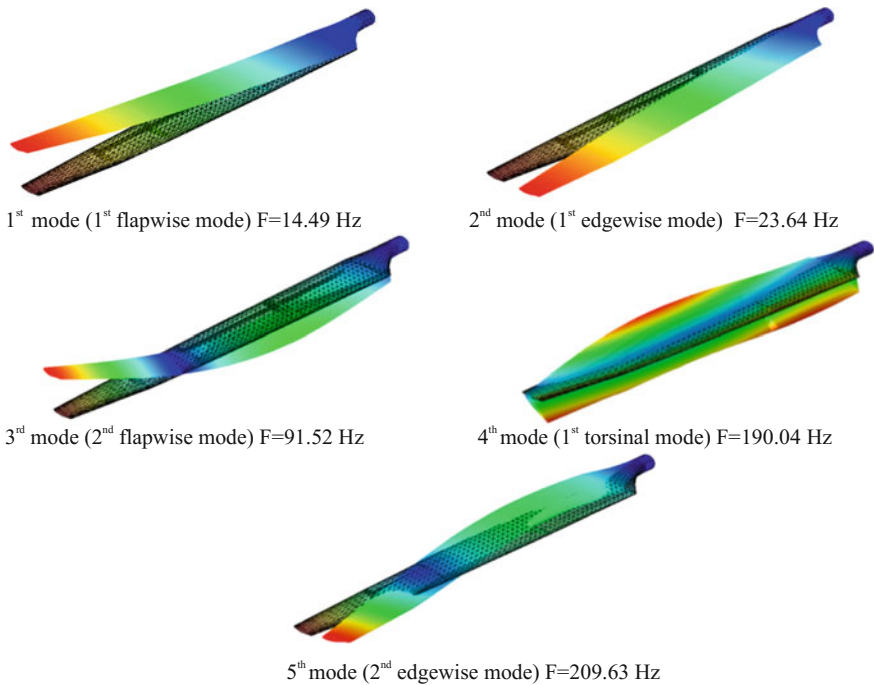
Fig. 2 Wind turbine blade deformed shapes

4.2 The Twist Angle Impact

To improve the blade vibration performance, the impact of the twist angle from 0°
to 45° as presented in Fig. 3 on the natural frequencies is studied.

Results in Fig. 4 represent the first five natural frequencies relative to the twist
blade angle. It is clearly observed that natural frequencies are not monotonically
varying with respect to the twist angle. Accordingly, the blade twist angle must be
investigated during the design process where the blade natural frequencies must be
well above the wind turbine system frequencies.
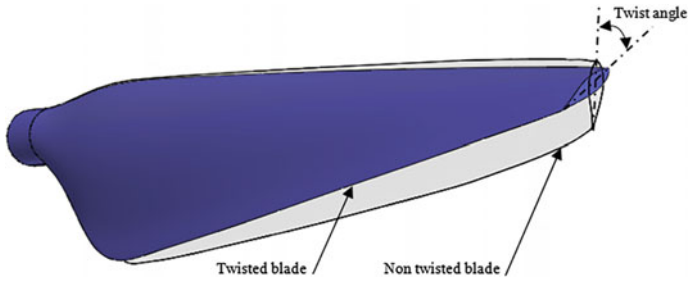
Fig. 3 Twisted blade design
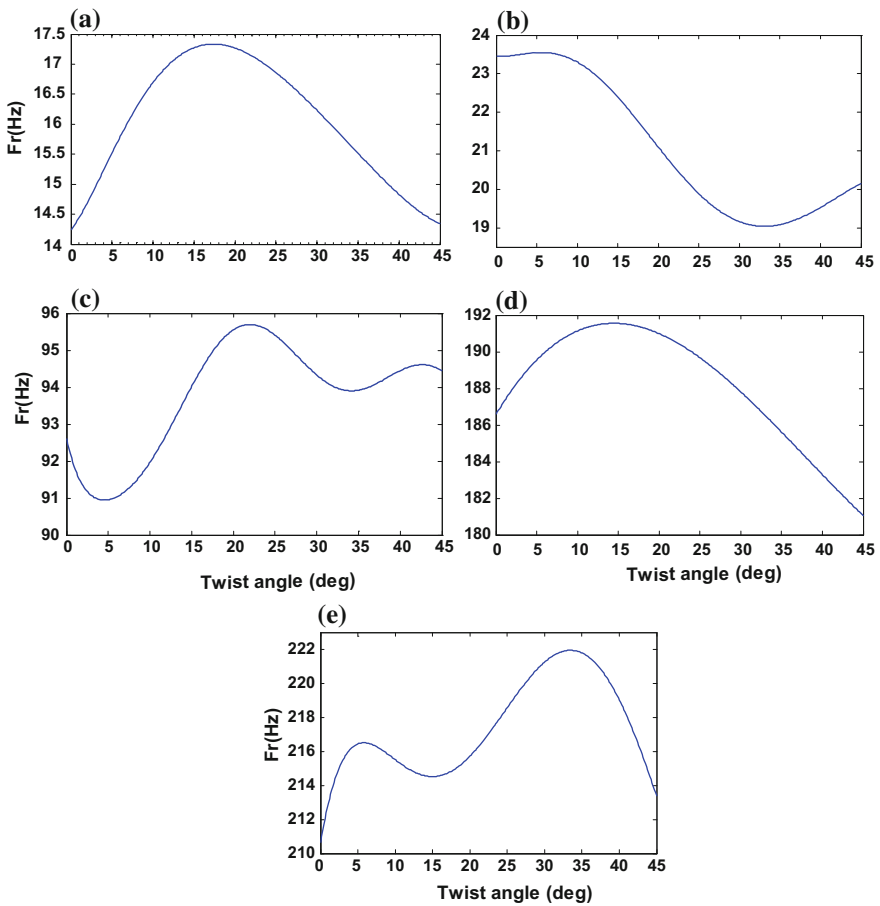
Fig. 4 The blade natural frequencies variation versus the twist angle: **a** 1st natural frequency; **b** 2nd natural frequency; **c** 3rd natural frequency; **d** 4th natural frequency; **e** 5th natural frequency

5   Conclusion

In this study, a twisted segmented wind turbine blade assembled with a spar was modeled using the three-node triangular shell element DKT18. The twist angle effects on the natural frequencies and mode shapes of the segmented blade were investigated using the finite element method. The substructure method was adopted to reduce the computing time. Modal analysis using ABAQUS software was established to validate the proposed method. Results show that the substructure method has not degraded the computation accuracy. Moreover, the pretwist angle has a non-monotonically relationship with natural frequencies.

The method presented in this study can be used to evaluate the vibration characteristics of rotating segmented blade with a complex shape. However, this study was limited to the twist angle effects. Therefore, this research can be extended taking into account the aerodynamic and the rotation speed effects.

References

Broehl J (August, 2014) Wind energy innovations: segmented blades. http://www.navigantresearch.com/blog/. Accessed 11 Jan 2017

Dokainish MA, Rawtani S (1972) Pseudo-static deformation and frequencies of rotating turbomachinery blades. AIAA Journal 10(11):1397–1398

Leissa AW, Lee JK, Wang A (1981) Rotating blade vibration analysis using shells. In: ASME 1981 international gas turbine conference and products show. American Society of Mechanical Engineers, pp V004T13A005–V004T13A005

Maalawi KY, Negm HM (2002) Optimal frequency design of wind turbine blades. J Wind Eng Ind Aerodyn 90(8):961–986

McKittrick LR, Cairns DS, Mandell J, Combs DC, Rabern DA, Van Luchene RD (2001) Analysis of a composite blade design for the AOC 15/50 wind turbine using a finite element model. Sandia national laboratories report

Saldanha FA, Rao VV, Christopher J, Adhikari R (August, 2013) Investigations on concepts for modularizing a horizontal axis wind turbine blade. In: ASME 2013 international design engineering technical conferences and computers and information in engineering conference. American Society of Mechanical Engineers, pp V008T12A003–V008T12A003

Sinha SK, Turner KE (2011) Natural frequencies of a pre-twisted blade in a centrifugal force field. J Sound Vib 330(11):2655–2681

Proposition of Eco-Feature: A New CAD/PLM Data Model for an LCA Tool

Raoudha Gaha, Abdelmajid Benamara and Bernard Yannou

Abstract Today, the environmental problems become serious and they are highlighted in regulations frameworks. Then, the use of Life cycle assessment (LCA) tools, for assessing products environmental impacts, is necessary, till Computer Aided Design (CAD) phase, for manufactures aiming at guarding their market places. Required LCA data (processes) can be provided from CAD and Product Life Management integrated systems (CAD/PLM), which became a necessity for industries to manage easily their data. In this paper, we propose a new CAD data model oriented ecodesign which we name "Eco-feature", based on the exploration of CAD/LCA systems to extract possible features life cycle scenarios, in order to select the most ecological one. Hence, firstly, we present the state of the art of researches aiming at connecting CAD/PLM systems to LCA tools. Secondly we present our new approach and describe its advantages. Finally, we present a case study to valid the new proposed concept.

Keywords CAD · PLM · Ecodesign · Eco-feature · Scenarios

1 Introduction

Design stage is very critical as many decisions impacting the downstream development activities, the product cost and environmental impact are made in this stage. Today, energy, resources and environmental problems become more and more

R. Gaha (✉) · A. Benamara
Laboratoire de Génie Mécanique, Ecole Nationale D'Ingénieurs de Monastir, Monastir, Tunisia
e-mail: raoudha.gaha@gmail.com

A. Benamara
e-mail: abdel.benamara@enim.rnu.tn

B. Yannou
Laboratoire de Génie Industriel, Ecole Centrale de Paris, Châtenay-Malabry, France
e-mail: bernard.yannou@centralesupelec.fr

763

serious. That's why they are highlighted in regulations frameworks such as WEEE (European Union 2003).

Over the years, numerous "Design for environment (Dfe)" concepts/methods and tools have been developed in order to increase the environmental conscious efficiency at the design stage, and reduce the total impact of the product (Leibrecht 2005; Capelli 2006; Mathieux et al. 2005; Mathieux and Roucoules 2007; Morbidoni 2012), etc. These researches highlight the necessity of the Life Cycle Modelling (LCM) for the environmental assessment. PLM systems are the source of required LCA data in mostly developed works.

In this paper we present firstly the state of the art of connecting CAD/PLM systems to an environmental assessment tool. Secondly, based on these connections, we propose the based-scenarios concept of eco-feature. Finally we present a case study to valid the proposed model.

2 Analysis of Connecting CAD/PLM Systems to LCA Tools

2.1 Product Life Management Systems (PLM)

Product lifecycle management is a comprehensive information system that coordinates all aspects of a product from initial concept to its eventual retirement. It contains data about different stages of a product development process; analysis and design stages, manufacturing, product launch, distribution, quality assurance, in-service maintenance and spare parts provisions. It supports the management of a portfolio of products, processes and services from initial concept, through design, launch, production and use to final disposal. They co-ordinate products, project and process information throughout new product introduction, production, service and retirement among the various actors who must collaborate to bring the concept to finish product.

2.2 Eco-Designing with CAD/PLM: State of the Art

For assessing environmentally a CAD model, a Life Cycle Assessment (LCA) tool requires Life Cycle Data (LCD) (from cradle to grave). However, CAD systems can only offer geometric data which is insufficient. Then, the use of PLM systems, which supplies necessary data for an LCA especially about processes, is present in most researches aiming at eco-designing in CAD phase. Among these works we find (Mathieux and Roucoules 2007; Segonds et al. 2011; Rio et al. 2013; Rio 2012).

In the literature realized in our previous work (Gaha et al. 2013), we have identified that the extracted data from CAD/PLM systems and required by an LCA tool are provided from features; such as the "DEMONSTRATOR" developed by (Mathieux et al. 2005). This prototype tool binds CATIA(a CAD software) and EIME (an LCA software). CATIA is connected to a Product Life Management (PLM) system that extracts all data provided by different used features. The established system then selects necessary LCA data and transfers them to EIME to calculate and show the environmental impact. Also, (Jain 2009) use the integration between PLM and CAD presents a plugin (Eco-fit) designed for 3DSmax using the Eco-indicator99 (EI99), an eco-assessment methodology and database designed to evaluate CAD-based products. There is also "EcoCAD" presented by Cappelli et al. (2007), which is based on the analysis of the tree structure of a CAD project composed of assemblies, subassemblies, parts, and features. The lake of these works is that only one scenario is environmentally evaluated. Computer aided sustainable tool "CAST Tool" presented by Morbidoni et al. (2011) provide a prototype with an open access database, allowing products to be evaluated regardless of the CAD or LCA systems used. Benefits are essentially due to selecting more than one production process, introducing lifecycle scenarios and extracting the right amount of geometrical and non geometrical data from the CAD data structure and PLM databases. "CAST Tool" overcomes many weaknesses such as the single scenario introduced where the evaluation of different possible scenarios is available. However, the evaluation is post modelling that is realized on a final part where modifications are difficult to implement, especially when it is a complex part. This explains the need for a real time evaluation tool.

From the overview of last works presented for connecting CAD/PLM systems to an LCA tool, we generated four major gaps; first, it was noted that the majority of the tools and methodologies presented, realize environmental assessments to a final part (post-modeling assessment), hence, modifications become a hard task to the designer when it is the case of a complex part. Second, the objective of these works was essentially the extraction of necessary data relative to a single Life Cycle (LC) scenario of the final part; where CAD/PLM systems are able to provide more LC scenarios for the part. Finally, works using this integration are interested only in the manufacturing phase, although products can be impacting in other phase such as use or end of life (EOL). This led us to propose a real time data model that can overcome these gaps. The approach proposed can provide Environmental Evaluation (EE) till features attribution. It is based on scenarios provided by CAD/PLM integration.

3 Approach for Eco-Designing in CAD Phase Based on PLM Systems

The approach proposed can provide Environmental evaluation (EE) till features attribution. It is based on scenarios provided by CAD and PLM (Product Life Management) integration. CAD/PLM systems can provide information about different LC processes because PLM systems can include the requirements phase, analysis and design stages, manufacturing, product launch, distribution, quality assurance, in service maintenance and spare parts provisions. As deduced previously, CAD feature is the source of data. Hence, we propose to extract its related data till its attribution from CAD/PLM system as shown in Table 1.

CAD/PLM can offer different types of data which can be used to generate possible LC scenarios. These scenarios can include necessary LCA data and then environmentally evaluated, in order to choose the most ecological one till feature's selection as mentioned in Fig. 1. The environmental impact is calculated with CML method because it is a method which respects the normation procedure of environmental assessment (Cao et al. 2002). In this method, environmental impacts are calculated by four steps: classification; characterisation; normation and assessment. The graphic representation is with End-points Impacts (Resources, Human Health and Eco-system damages) in a Single Score. This allows the non environmental expert designer to understand Environmental Impacts (EIs).

A CAD feature can involve different machining scenarios with different parameters such as selecting machine tool, cutting tool, energy consumption, etc. It may also carry other types of data when it is developed in an integrated CAD/PLM (Gaha et al. 2014b). Provided data will allow assessing all scenarios proposed in order to select the most ecological one. Proposed alternative scenarios can be shown with their Environmental Impact (EI) simply.

Enriching a classic CAD feature with LCA data led us to propose the concept of "*Eco-feature*", which is a classic CAD feature that can be environmentally assessed. It is a new CAD data model oriented eco-design. A model of the Eco-feature is presented in Fig. 2, which shows that *Eco-feature* is a special type of feature that we have assigned processes such as material production, transport and landfill. The way, how to generate these entities from a CAD model is described in (Gaha 2014). In the next section we present a case study to valid this proposed concept.

Table 1 CAD feature data from CAD/PLM system	Information systems	Related data
	CAD	Forms
		Dimensions
		Materials
		Volumes
	PLM	Production process
		Materials
		Choice of « make or buy »
		Thermal or surface treatments
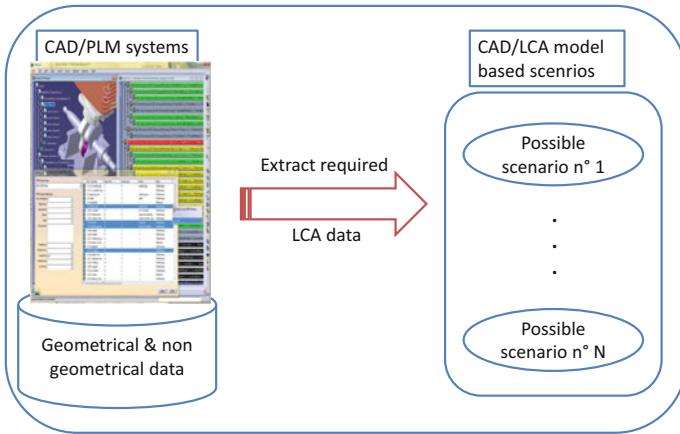
Fig. 1 Proposed CAD/LCA based scenarios model extracted from CAD/PLM systems
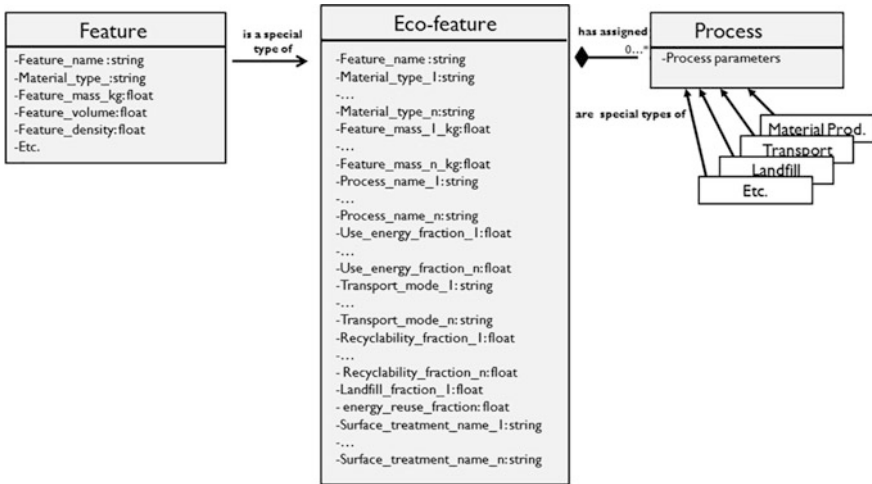
Fig. 2 The model of Eco-feature

4   Validation of the Proposed Concept on a Case Study

From the study realized in our previous work (Gaha et al. 2014a) we consider the basin mixer as a case study. The environmental assessment shows that the use phase is the most impacting stage in the life cycle of the product. The related CAD feature to this stage is the hole of water injection (Fig. 3). By applying the concept of Eco-feature to this classic feature (the hole) we obtain different possible scenarios, each one has different environmental evaluation result from the other.

Fig. 3 The feature hole case study of the basin mixer
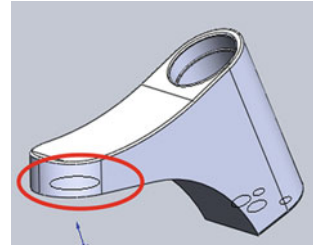
Table 2 Hole data related to material, use and transport phases

Phase	Scenario 1		Scenario 2	
Raw material	Material: brass	Weight: 0.025 kg	Material: brass	Weight: 0.0125 kg
Transport	Mean: truck < 16t	Weight: 0.025	Mean: truck < 16t	Weight: 0.0125
Use	Water: 36000 kg		Water: 54000 kg	

Table 3 Hole data related to manufacturing and end of life phases

Phase	Scenario 1		Scenario 2		Scenario 3	
Manufacturing	Process:	Drilling	Process:	Turning	Process:	Drilling NC
	Temps:	4mn20	Time:	4mn15	Time:	3mn50
	Energy:	0.0045 Kw	Energy:	0.0055 Kw	Energy:	0.005 Kw
	% waste recovery	50%	% waste recovery	60%	% waste recovery	80%
End of life	% waste recycling	50%	% waste recycling	60%	% waste recycling	80%

To generate the Eco-feature we consider 2 scenarios, where raw material (RM), use (U) and transport (T) phases are in relation and 3 scenarios for manufacturing (M) and end of life (EoL) phases. These scenarios are presented in Tables 2 and 3. The data used is provided by the company which collaborates in this work (AMS 2011).

We obtain then 6 life cycle possible scenarios for the Eco-hole, which are presented in Fig. 4. The LCA tool "Bilan Produit" (Ademe 2008) gives the result of comparison of their environmental evaluation in Fig. 5. Hence compared to present methodologies and tools including environmental aspects, it is a real time environmental assessment methodology. It is also a life cycle based scenarios methodology, where possible life cycle scenarios are evaluated and environmentally

Fig. 4 Possible life cycle scenarios of the hole case study of the basin mixer
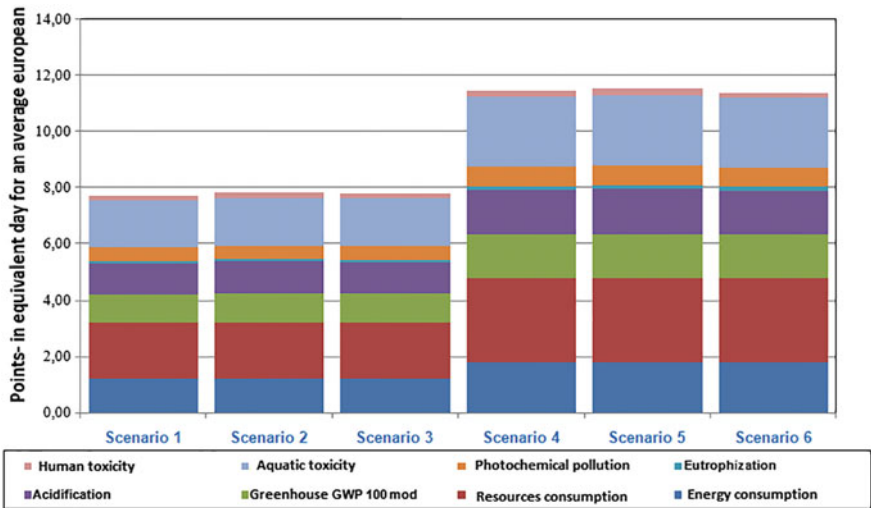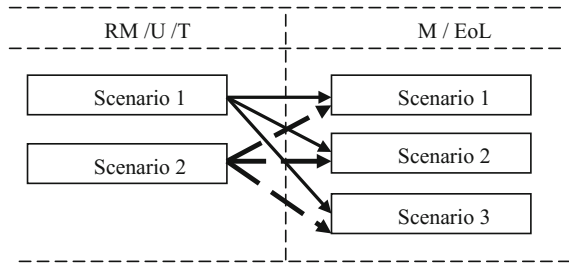
Fig. 5 Comparison of the environmental impacts of possible life cycle scenarios of the hole

compared. However existent methodologies in terms of environment present only one assessed scenario.

5 Conclusion

This paper presents the eco-feature concept which is a LCA data model rxtracted from CAD/PLM system. It is obtained from an enrichment Semantics of classical features of CAD systems by the three information Concerning the geometry, the material and the manufacturing process. A geometry-material-process combination of Manufacturing constitutes a life scenario for an eco-feature. Different scenarios can be generated for the same feature. The different scenarios are the inputs for an LCA tool. The result obtained guide CAD designer to choose the most ecological

one. The approach proposed is applied to a feature of a basin mixer (hole) to valid its brings to ecodesign.

References

AMS (2011) Ateliers Mécaniques du Sahel, rapport de fabrication du mitigeur de lavabo Carthage

ADEME, Bilan Produit (2008). http://www.ademe.fr/bilanproduit/ Manuel Bilan Produit (2008)/ Eco-invent, Swiss centre for life cycle inventories, 2009. http://www.ademe.fr/bilanproduit

Cao HJ, Liu F, He Y, Zhang H (2002) Study on model set based process planning strategy for green manufacturing. Jisuanji Jicheng Zhizao Xitong/Comput Integr Manuf Syst (China) 8 (12):978–982

Capelli F (2006) Integration of LCA and eco-design guideline in a virtual cad framework. In: The 13th edition of the CIRP international conference on life cycle engineering. Leuven

Cappelli F, Citti P, Delogu M, Pierini M (2007). Strumento informatico integrato in ambiente cad per l'analisi preventiva degli impatti ambientali dei processi/prodotti in fase di produzione. Atti del XXXVI Convegno Nazionale AIAS

European Union (2003) Directive 2002/96/EC of the 27 January 2003 on waste electrical and electronic equipment (WEEE)

Gaha R, Benamara A, Yannou B (2013) A feature-based methodology for eco-designing parts on detail phase. In Design and Modeling of Mechanical Systems. Springer, Berlin, Heidelberg. ISO 690, pp. 645–654

Gaha R (2014) Eco-conception et CAO Paramétrique, Thèse de Doctorat à l'école nationale d'ingénieurs de Monastir

Gaha R, Bnamara A, Yannou B (2014a) Eco-design of a basin mixer in geometric modeling phase. Key Eng Mater 572:7–11

Gaha R, Yannou B, Benamara A (2014b) A new eco-design approach on CAD systems. Int J Precis Eng Manuf 15(7):1443–1451

Jain P (2009) Design of an interactive eco-assessment GUI tool for computer aided product design. Doctoral dissertation, Indian Institute of Technology

Leibrecht S (2005) Fundamental principles for CAD based ecological assessments (9 pp). Int J Life Cycle Assess 10(6):436–444

Mathieux F, Roucoules L (2007) Connecting CAD and PLM systems with ecodesign software: current experiences and future opportunities. In: International conference on engineering design (ICED'07)

Mathieux F, Roucoules L, Lescuyer L, Bouzidi Y (2005) Opportunities and challenges for connecting environmental assessment tools and CAD software. In: Proceedings of LCM 2005-innovation by life cycle management

Morbidoni A (2012) The ecodesign issue: proposal for a new approach, methodology and tools. Doctoral dissertation, Università Politecnica delle Marche

Morbidoni A, Favi C, Germani M (2011) CAD-integrated LCA tool: comparison with dedicated LCA software and guidelines for the improvement. Glocalized Solut Sustain Manuf 2001:569–574

Rio M (2012) A l'interface de l'ingénierie et de l'ana lyse environnementale :fédération pour une écoconception proactive, thèse de doctorat à l'université technologique de Troyes

Rio M, Reyes T, Roucoules L (2013) Toward proactive (eco)design process: modeling information transformations among designers activities. J Clean Prod 39:105–116

Segonds F, Maranzana N, Véron P, Aoussat A (2011) Collaborative reverse engineering design experiment using PLM solutions. Int J Eng Educ 27(5):1037–1045

Effects of Pretextured Surface Topography on Friction and Wear of AA5083/AISI52100 Materials' Pair

F. Elwasli, S. Mzali, F. Zemzemi, A. Mkaddem and S. Mezlini

Abstract This paper covers the study of the effect of surface topography on tribological behavior in the early stage of repetitive sliding under dry condition. Reciprocating sliding tests were conducted on AA5083 sample against smooth AISI52100 ball bearing. Unidirectional polishing was adopted for the surface preparation of AA5083 samples. Experiments were performed at a pressure of 200 MPa for a maximum number of 1000 cycles. The sliding velocity and the sliding track were kept constant at 50 mm/s and 15 mm, respectively. Evolution of friction coefficient as a function of the sliding distance was monitored. Wear was characterized using scanning electron microscope (SEM), energy-dispersive X-ray spectroscope (EDS), and profilometer. Experimental results have shown that the friction coefficient as well as wear mechanisms, significantly, depends on the initial surface topography. Particular focus was put in the study of the effect of the mean

F. Elwasli (✉) · S. Mzali · S. Mezlini
LGM, Ecole Nationale d'Ingénieurs de Monastir, Université de Monastir,
Avenue Ibn Aljazzar, 5019 Monastir, Tunisia
e-mail: elwaslifatma@gmail.com

S. Mzali
e-mail: mzalislah@laposte.net

S. Mezlini
e-mail: salah.mezlini@gmail.com

F. Zemzemi
LMS, Ecole Nationale d'Ingénieurs de Sousse, Université de Sousse,
BP 264 Sousse Erriadh, 4023 Sousse, Tunisia
e-mail: fzemzemi@gmail.com

A. Mkaddem
Engineering College, Faculty of Engineering, University of Jeddah,
PO Box 80327, 21589 Jeddah, Saudi Arabia
e-mail: amkaddem@uj.edu.sa; ali.mkaddem@ensam.fr

A. Mkaddem
MSMP-EA7350, Arts et Métiers ParisTech, Rue Saint Dominique BP. 508,
51006 Châlons-en-Champagne, France

771

absolute profile slope Δ_a. Results showed that the mean absolute profile slope Δ_a played a major role in friction and wear.

Keywords Reciprocating sliding tests · Pretextured surface · Wear · Friction

1 Introduction

In recent years, much attention has been focused on the development of new surfaces that dispose of a high wear resistance. Several technics were used such as diamond-like carbon (DLC) coatings, MoS_2 coatings, and surface texturing (Cha and Erdemir 2015; Ibatan et al. 2015; Ronkainen et al. 2007). It has commonly been assumed that surface preparation plays a major role in controlling friction and wear (Al-Samarai 2012; Blau 2008; Meine et al. 2002a, 2002b; Stickel et al. 2015). Thus, a good comprehension of the relation between initial surface roughness and the tribological behavior is a key factor for reducing friction and wear.

Many researches have been devoted to analyze the effect of normalized roughness parameters on tribological behavior. Generally, authors use the average roughness R_a and the root mean square roughness R_q to describe the surface roughness. Recently, authors pointed out the influence of other roughness parameters such as Kurtosis S_{ku}, Skewness S_{sk}, and reduced valley depth S_{vk} on the tribological behavior (Sedlaček et al. 2009, 2012). They found that, under lubrication condition, the friction is smaller for the negative S_{sk} and the higher S_{ku} and S_{vk}. Thus, under the lubricated condition and based on roughness parameters, the prediction of the tribological behavior is possible.

The effect of the mean absolute profile slope Δ_a was investigated by Menezes et al. (2015). They have studied the roughness of the harder material during the pin-on-plate sliding test using Al–Mg/080 M40. They found that the friction is more for higher surface slope. This is explained by the fact that to climb a high slope asperity, a high force is required.

In addition, Golchin et al. (2015) have shown that the ploughing action of asperities of the harder surface increases the high mean absolute profile slope Δ_a. This result is in agreement with results obtained by Elwasli et al. (2015) and Mezlini et al. (2008). They found that the shape of asperities plays an important role in the material removal.

The purpose of this paper is to enhance comprehension of the tribological behavior of a rough surface of AA5083 plate during the repetitive sliding test. Investigation of the effect of surface roughness on the tribological behavior has been conducted. The sensitivity of the friction coefficient and wear was studied for different configurations. Spatial focus was made on the effect of the average roughness R_a and the mean absolute profile slope Δ_a of AA5083 plates on the friction and wear, which were studied.

2 Experimental Procedures

2.1 *Sample Preparation*

The AA5083 samples were prepared by the unidirectional polishing. For that, three abrasive papers of P50, P80, and P400 grit sizes were used. The average roughness R_a and the mean absolute profile slope Δ_a for three textures are summarized in Table 1. The samples were grounded by P50, P80, and P400 and are denoted G_{50}, G_{80}, and G_{400}, respectively.

The measurement of roughness parameters was performed via a Taylor-Hobson Surtronic S series tester. The analysis of the obtained information was conducted by Talyprofile (Gold) software. Specimens employed are $40 \times 40 \times 8$ mm^3 in dimensions.

2.2 *Friction Test*

Reciprocating ball-on-flat tests were conducted to investigate the friction and wear performances of polished AA5083 surfaces sliding against the AISI52100 ball bearing steel with a diameter 10 mm (Fig. 1). Experimental tests were realized through the device whose technical specifications were presented in (Guezmil et al. 2016a, b).

Experiments have been performed perpendicular to the unidirectional grinding marks. During the tests, the ball was fixed and the AA5083 specimen was continuously animated with reciprocating motion. The test conditions were a reciprocating speed of 50 mm/s and a reciprocating slide length of 15 mm. The total number of reciprocating cycles was 1000. All tests were performed under a dead weight of 1 N representing an apparent contact pressure of 200 MPa.

All test series were conducted at room temperature under dry conditions and repeated three times under the same conditions. Details of the experiment are presented in Table 2.

By means of a piezoelectric friction transducer, the friction force was measured continuously. The apparent friction coefficient μ_{App} is calculated as the tangential-to-normal force ratio. The wear of the ball and the sample was inspected using scanning electronic microscope (SEM). In addition, the worn ball was investigated using energy-dispersive X-ray spectroscopy (EDS).

Table 1 Average roughness parameters

	G_{50}	G_{80}	G_{400}
SiC paper	P50	P80	P400
R_a (μm)	4.98	3.31	0.45
Δ_a (°)	3.9	12.9	5.3

Table 2 Experimental test conditions

Test conditions	
Normal force F_N	1 N
Contact pressure	200 MPa
Sliding track d	15 mm
Sliding speed V	50 mm/s
Body	AA5083
Counter body	Ball; R = 5 mm; AISI52100
Maximum number of cycles	1000
Environment	Dry
Temperature	Room temperature
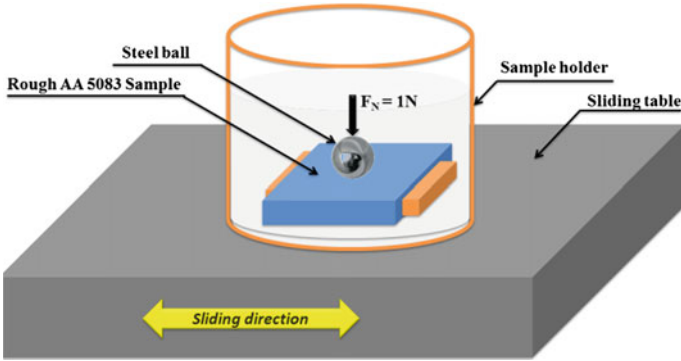
Fig. 1 Schematic presentation of reciprocating sliding test

After the sliding test, measures of wear track were realized through Taylor-Hobson Surtronic S series tester. The profiles were taken in four positions perpendicularly to wear track.

3　Results and Discussion

3.1　Friction Evolution

The effect of number of cycles on the friction evolution was investigated (Fig. 2). The lowest friction coefficient was recorded for the first few cycles. The increase in the sliding cycle provokes a sharp increase (D_I) and then a decrease (D_{II}) in apparent friction coefficient until reaching a steady state (D_{III}). When comparing the friction coefficient of different configurations, it can be noticed that G_{80} presents the highest value followed by G_{400} and then G_{50}. Furthermore, the amplitude of oscillation of G_{80} was the highest for the first few cycles, and it gets reduced when it reached the steady state.

Fig. 2 Friction coefficient versus number of cycles
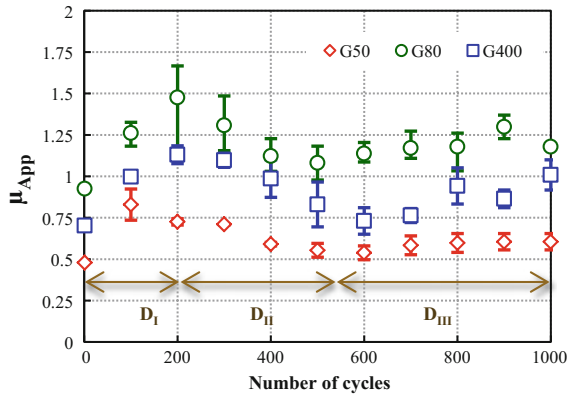
The most widely used roughness parameter to characterize the surface is the average roughness (R_a) (Sedláček et al. 2012). However, experimental results prove that the R_a cannot predict the tribological behavior. Comparing friction coefficient for different configuration after 1000 cycles, it can be illustrated that G_{50} and G_{80} that have a comparable value of R_a show dissimilar values of friction coefficient μ_{App}. In addition, G_{50} and G_{400} that have different R_a show comparable values of friction coefficient μ_{App}. Actually, surface topographies could be significantly different and have similar or even the same R_a (Menezes et al. 2009). Then, R_a is insufficient to predict the friction behavior. However, experimental results show a dependency friction coefficient of Δ_a. In fact, when the ball slides over a surface characterized by sharp peaks, higher shear stress is required to deform asperities. The high energy dissipated in deforming high asperities provokes the increase of friction coefficient (Gualtieri et al. 2011).

3.2 Worn Surface State

The microscopic inspections performed on wear tracks revealed that the initial surface topography was totally distorted (Fig. 3). It is worth noting that new grinding marks parallel to the sliding direction show up and replace the perpendicular grinding marks. Those abrasive marks are caused by the severe plastic deformation of the surface's peaks. This provokes the debris generation on and around of wear tracks. G_{80} configuration presents the highest track width and the most pronounced abrasive marks compared to other configurations. In addition, G_{50} shows the smallest track width.

G_{80} is characterized by the highest Δ_a, which is contrary to G_{50} that have the smallest Δ_a. Then, the material behavior can be attributed to the value of Δ_a. In fact, high Δ_a leads to severe shear failure (Menezes et al. 2008) and plastic deformation, which provokes asperities destruction and debris generation. In
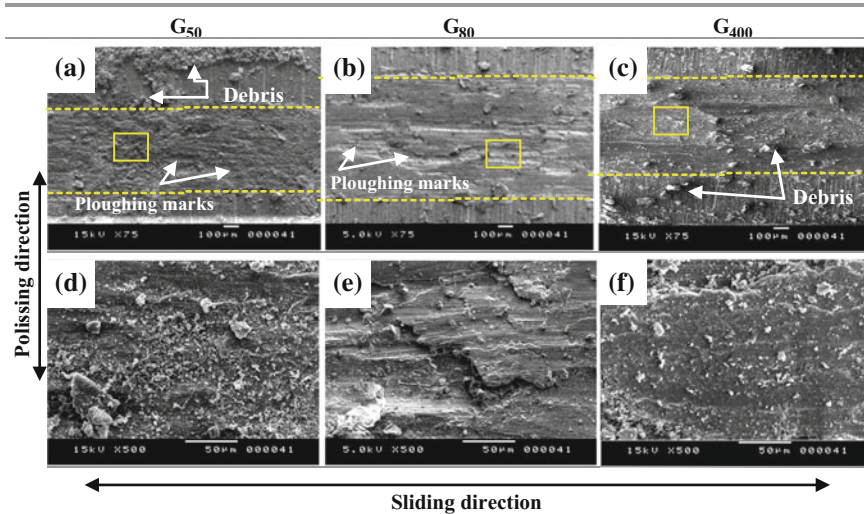
Fig. 3 SEM micrographs **a**, **b** and **c** wear tracks after 1000 cycles, and **d, e** and **f** enlarged view, respectively

addition, the entrapped wear debris in the contact zone gives rise to the generation of abrasive marks parallel to the sliding direction.

3.3 Wear Signature on the Friction Ball

The worn surface of the steel ball was examined by both SEM and EDS. Microscopic observations Fig. 4a–c reveal the presence of a transfer layer on balls for the three configurations. The EDS analyses (Fig. 4d–f) reveal the existence of Al and Mg on the worn surface of the ball. Al and Mg are originated from AA5083 sample.

The observed result demonstrates that material transfer occurred between the mating materials. This is due to the high adhesion tendency of the aluminum (SafaraNosar and Olsson 2013). As it can be noted from SEM observations, there are no ploughing marks on the ball surface. The tribo-layer protects the ball from abrasive wear. Consequently, the contact pairs changes. The contact is no longer AISI52100/AA5083 but it become AA5083/AA5083.

3.4 Crater Area Versus Number of Cycles

In order to evaluate the variation of wear scar for different configurations, the crater area S- was measured. Figure 5 presents the evolution of the average values of
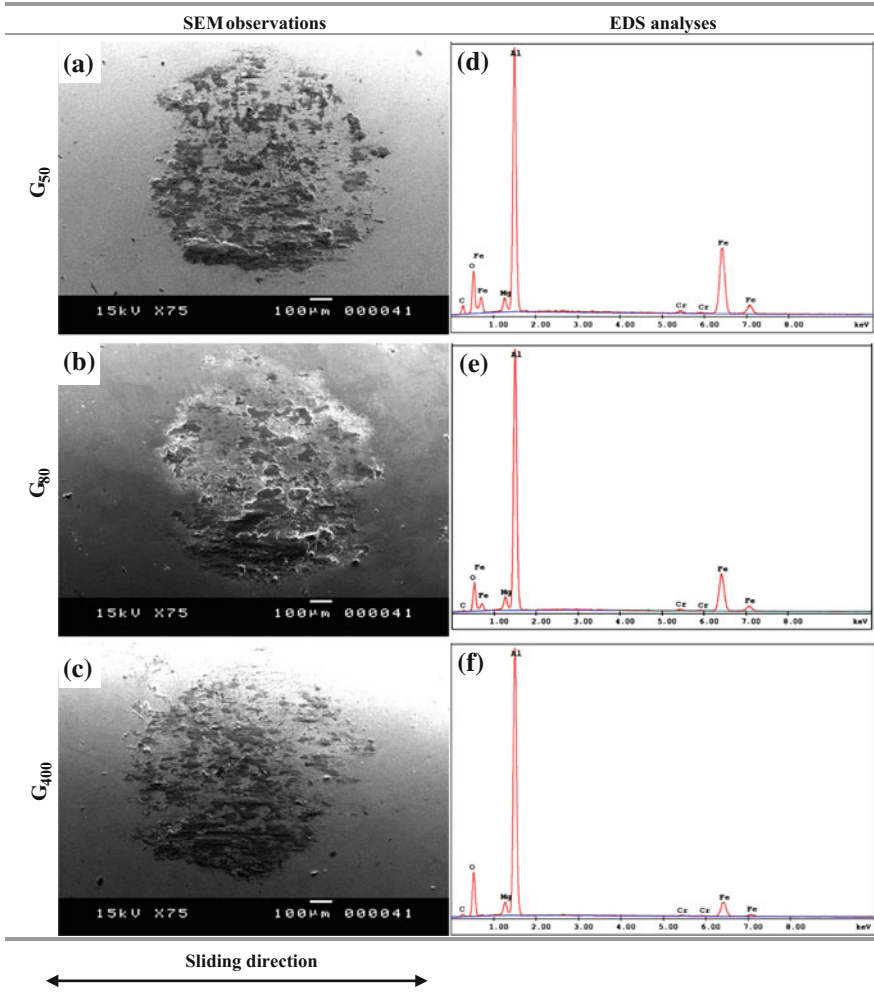
Fig. 4 **a**, **b** and **c** cSEM micrographs and **d, e** and **f** EDS analysis of steel ball after 1000 cycles

Fig. 5 Evolution of crater area with the number of cycles
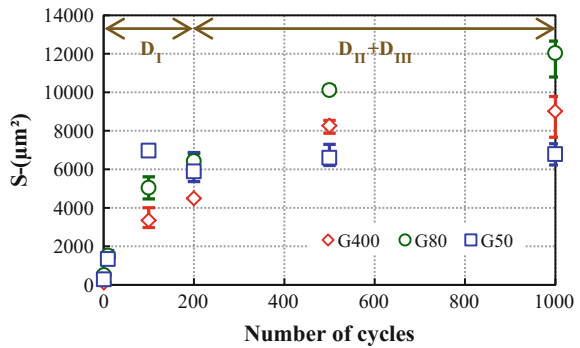
crater area S- for different textures as a function of the number of cycles. For the first few cycles (D_I), a sharp growth in the crater area was observed. Then, the slope decreases and finally levels off ($D_{II} + D_{III}$). This behavior can be attributed to the transition of wear mechanism from abrasive to adhesive wear. In fact, during D_I, a direct contact between AISI ball and the AA5083 sample exists, and the main wear mechanism is abrasion. In this case, a quick removal of high peaks acquires. Then, in D_{II} and D_{III}, the adhesive wear dominates. As it was shown by EDS analyses (Fig. 3), AA5083 is transferred and covered the steel ball.

As it was demonstrated by SEM observation, the largest crater area was observed for the G_{80} texture followed by G_{400} and then G_{50}. This behavior is associated to the increase in the mean slope of the profile. According to Golchin et al. (2015), the increase in the mean slope of the profile leads to the rise of abrasive wear contribution in the total wear of the polymeric materials.

4 Conclusion

The present research investigates the effect of the textured surface on tribological behavior. Reciprocated sliding test for the pair AISI52100/AA5083 was conducted. From experimental results, the following conclusions can be drawn:

- Tests depicted the dependence of friction coefficient on the textured surface.
- Analysis prove that R_a is insufficient to predict the friction behavior. Contrary, Δ_a present a significant effect on friction coefficient, the friction coefficient is as high as Δ_a increases.
- SEM observation and crater area measurement reveal that the higher is Δ_a, the larger is the wear track width.
- EDS analyses demonstrate that material transfer occurred between the mating materials. The presence of aluminum in the steel ball surface reduces the contribution of the abrasive wear mechanism.

References

Al-Samarai RA, (2012) Evaluate the effects of various surface roughness on the tribological characteristics under dry and lubricated conditions for Al-Si alloy. JSEMAT 02:167–173. https://doi.org/10.4236/jsemat.2012.23027

Blau PJ (2008) Friction science and technology: from concepts to applications, 2nd edn. CRC Press. https://doi.org/10.1007/s13398-014-0173-7.2

Cha SC, Erdemir A (2015) Coating technology for vehicle applications. Springer. https://doi.org/10.1007/978-3-319-14771-0

Elwasli F, Zemzemi F, Mkaddem A, Mzali S, Mezlini S (2015) A 3D multi-scratch test model for characterizing material removal regimes in 5083-Al alloy. Mater Des 87:352–362. https://doi.org/10.1016/j.matdes.2015.07.121

Golchin A, Friedrich K, Noll A, Prakash B (2015) Influence of counter surface topography on the tribological behavior of carbon- filled PPS composites in water. Tribo Int 88:209–217. https://doi.org/10.1016/j.triboint.2015.03.023

Gualtieri E, Pugno N, Rota A, Spagni A, Lepore E, Valeri S (2011) Role of roughness parameters on the tribology of randomly nano-textured silicon surface. J Nanosci Nanotechno 111:9244–9250. https://doi.org/10.1166/jnn.2011.4296

Guezmil M, Bensalah W, Mezlini S (2016a) Effect of bio-lubrication on the tribological behavior of UHMWPE against M30NW stainless steel. Tribo Int 94:550–559. https://doi.org/10.1016/j.triboint.2015.10.022

Guezmil M, Bensalah W, Mezlini S (2016b) Tribological behavior of UHMWPE against TiAl6V4 and CoCr28Mo alloys under dry and lubricated conditions. J Mech Behav Biomed Mater. 63:375–385. https://doi.org/10.1016/j.jmbbm.2016.07.002

Ibatan T, Uddin MS, Chowdhury MAK (2015) Recent development on surface texturing in enhancing tribological performance of bearing sliders. Surf Coat Technol 272:102–120. https://doi.org/10.1016/j.surfcoat.2015.04.017

Meine K, Schneider T, Spaltmann D, Santner E (2002a) The influence of roughness on friction: part I. The influence of a single step. Wear 253:725–732. https://doi.org/10.1016/S0043-1648(02)00159-X

Meine K, Schneider T, Spaltmann D, Santner E (2002b) The influence of roughness on friction: part II. The influence of multiple step. Wear 253:733–738

Menezes PL (2015) Surface texturing to control friction and wear for energy efficiency and sustainability. Int J Adv Manuf Technol 85:1385–1394. https://doi.org/10.1007/s00170-015-8058-2

Menezes PL, Kishore, Kailas SV (2008) On the effect of surface texture on friction and transfer layer formation—a study using Al and steel pair. Wear 265:1655–1669. https://doi.org/10.1016/j.wear.2008.04.003

Menezes PL, Kishore, Kailas SV, Bobji MS (2009) Influence of inclination angle of plate on friction, stick-slip and transfer layer—a study of magnesium pin sliding against steel plate. Tribo Int 267:476–484. https://doi.org/10.1016/j.triboint.2009.12.028

Mezlini S, Tkaya MB, El Mansori M, Zahouani H, Kapsa P (2008) Correlation between tribological parameters and wear mechanisms of homogeneous and heterogeneous material. Tribol Lett 33:153–159. https://doi.org/10.1007/s11249-008-9403-5

Ronkainen H, Laukkanen A, Holmberg K (2007) Friction in a coated surface deformed by a sliding sphere. Wear 263:1315–1323. https://doi.org/10.1016/j.wear.2007.01.103

SafaraNosar N, Olsson M (2013) Influence of tool steel surface topography on adhesion and material transfer in stainless steel/tool steel sliding contact. Wear 303:30–39. https://doi.org/10.1016/j.wear.2013.02.015

Sedlaček M, Podgornik B, Vižintin J (2009) Influence of surface preparation on roughness parameters, friction and wear. Wear 266:482–487. https://doi.org/10.1016/j.wear.2008.04.017

Sedlaček M, Podgornik B, Vižintin J (2012) Correlation between standard roughness parameters skewness and kurtosis and tribological behaviour of contact surfaces. Tribo Int 48:102–112. https://doi.org/10.1016/j.triboint.2011.11.008

Stickel D, Fischer a, Bosman R (2015) Specific dissipated friction power distributions of machined carburized martensitic steel surfaces during running-in. Wear 330–331:32–41. https://doi.org/10.1016/j.wear.2015.01.010

Solidworks—Matlab Coupling for Disassembly Plan Generation in a CAE Environment

Imen Belhadj, Riadh Ben Hadj, Moez Trigui, Nizar Aifaoui and Abdelmajid BenAmara

Abstract Nowadays, mechanical products which respond to customer requirements become more and more complex. Concurrent engineering environment requires that various computer-aided tools be used concurrently for design, analysis, and validation of complex product. Computer-aided design (CAD) and computer-aided engineering (CAE) tools should have the capacity of integration or easy interoperability. However, many of them are often unconnected systems that are not intended for collaborative use. Engineering designers and analysts tend to use specific CAD software for design and other CAE software for analysis. Consequently, the triplet (Cost/Delay/Quality) of a complex product cannot be improved. In this paper, a disassembly plan (DP) generation based on a coupling between Solidworks and Matlab is detailed. Base on an encapsulation of parts into a subassemblies bloc, the proposed approach aims to automatically integrate the both softwares in a concurrent engineering context in order to identify and generate a feasible and optimal DP. A comparative example is presented in order to highlight the feasibility and efficiency of the proposed approach.

Keywords Concurrent engineering · Interoperability · CAD model
Disassembly plan · Subassembly · Encapsulation

1 Introduction

In the context of current globalization, improving competitiveness remains a major challenge for manufacturing enterprises. This challenge will be reached by the use of innovative processes which ensure a better triplet (Cost/Delay/Quality). Actually, mechanical products which respond to customer requirements become more and more complex. Therefore, the design process has undergone major changes and the

I. Belhadj (✉) · R. Ben Hadj · M. Trigui · N. Aifaoui · A. BenAmara
Mechanical Engineering Laboratory, National Engineering School of Monastir,
University of Monastir, Av. Ibn Eljazzar, 5019 Monastir, Tunisia
e-mail: imenne.belhadj@gmail.com

781

use of computer-aided engineering (CAE) tools, such as idealization and finite element analysis (Lee 2005; Hamdi et al. 2012; Corriveau et al. 2009), tolerance analysis and synthesis (Ghali et al. 2017), cost analysis and green design (Gaha et al. 2016), etc. become essential in the development of the life cycle of a mechanical product. Hence, the integration of the different phases constituting an industrial CAD–CAE process grows to be a necessity according to Lee (2005).

Among the CAE tasks, the assembly and disassembly planning (AP/DP) becomes an important task in the validation of the design solutions regarding the complexity of the modern products. In the literature the AP/DP integration concept in a CAD–CAE environment has been widely discussed but with a low integration level. Ben Hadj et al. (2015) has developed an ASP generation tool based on CAD assembly data named 'Computer Aided Assembly Sequence Plan (C2ASP) to generate ASP. C2ASP is divided into two mains steps. The first one is the extraction of the CAD assembly data. To identify all possible obstacles during the components' displacement, an interference analysis process is performed in the second step. Based on a mobility matrix definition for every part on mobility constraints, a new representation model of disassembly directions, starting from geometric and assembly CAD data has been proposed by (Issaoui et al. 2015). The model gives information about the mobility state of a given part (particularly the wearing parts) during disassembly sequencing by updating its mobility matrix. The proposed model has been implemented under Open Cascade platform. In order to bypass the AP/DP combinatory problem of mechanism with an important number of parts, (Kheder et al. 2017) presented an automated disassembly sequence planning approach based on ant colony algorithm. The developed method permits the generation of an optimal and feasible disassembly sequence planning of a product from its CAD representation. In this approach, several criteria have been introduced, such as part volume, tool change, disassembly directions, and the maintainability of wearing part. Many other investigations of DSP by ACO in the context of recycling or part reuse were developed (Shu-Kai et al. 2013).

In the same context, Belhadj et al. (2016) proposed a new method to identify subassemblies in order to generate an optimal and feasible DSP of complex products. The proposed approach is implemented using the Matlab software. In the same way, Swaminathan and others (Swaminathan and Barber 1996; Gupta and Krishnan 1998; Su 2007) used a case-based reasoning method, based on existing cases or experiences, to identify subassemblies. Popa et al. (2012) presented a comparative study between the main CAD–CAE softwares having the ability to automate AP and DP generation in perspective. According to the authors, the results of the study will be used in order to propose a simulation platform that will contain the main function and facilities needed to AP and DP analysis.

This paper in mainly included in the same way with the authors cited above. The objective is to bypass the low integration level between CAD–CAE softwares in AP/DP generation context. The proposed approach aims to develop an interoperability method between Matlab and Solidworks softwares to identify and simulate a generated DSP based on the subassembly identification procedure. The remaining part of this paper is organized as follows: First, the data extraction and relationship

method based on the CADLAB Plug-in is detailed. Then, a transfer procedure from Solidworks to Matlab is presented in order to automatically convert the extracted data to Matlab variables. The output is a set of identified subassemblies. This result is transferred again to Solidworks to generate the interference matrix of sub-assemblies along the three directions (X, Y, and Z). Afterward, an interoperability loop is performed to generate and simulate the DP of the subassemblies. An illustrative example is dealt with in all sections of this paper in order to explain the different stages of the proposed approach and to highlight its feasibility and efficiency.

2 Proposed Approach

Figure 1 shows the strategy of the proposed interoperability approach. The treatment is done by looping three steps: CAD assembly attributes extraction using the developed SolidWorks CADLab plug-in. These data can be edited on Excel in order to be used elsewhere or treated subsequently by Matlab. The results obtained by Matlab will be transferred to CADLab plug-in and so on. The stop condition is the generation of an optimal and feasible DP of subassemblies.

In order to explain the proposed approach, an illustrative example is introduced. The treated example, found in the literature (Ben Hadj et al. 2015), is a pneumating crimping tool consisting of 18 parts joined by six screws and six nuts (Fig. 2). This mechanism is chosen in order to compare and validate the proposed approach.
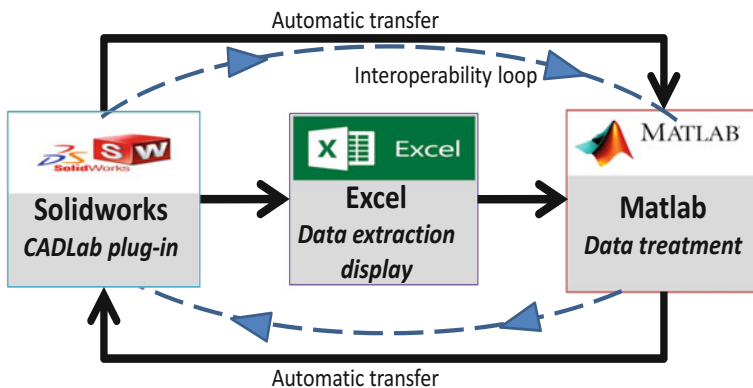
Fig. 1 Overview of the CAD–CAE interoperability approach
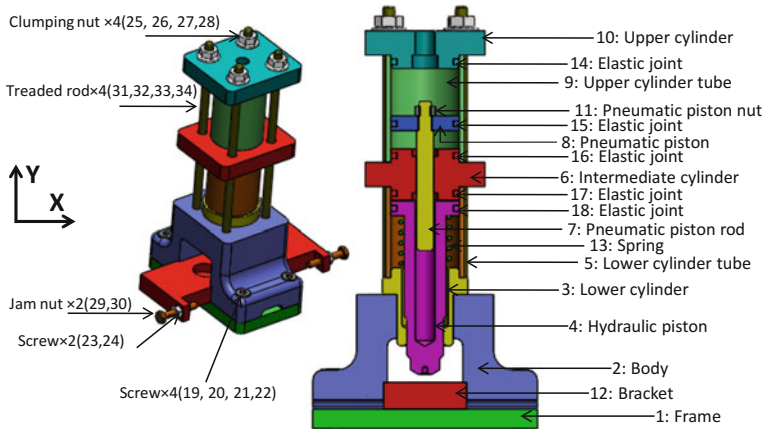
Fig. 2 CAD model of the pneumatic crimping tool and nomenclature of each part

2.1 CADLab for Data Extraction and Generation Process

A CAD assembly model encloses a large quantity of data which can be useful in AP/DP integrated application. The extraction of these data is only possible by the exploitation of the API of the CAD system. CADLab is an intergrated plug-in devoted to extract data from a CAD assembly which are divided into two types of data:

- The collected data which include both: the attributes of each component (mass properties, topological, and geometrical data) and the assembly constraints' attributes (mate types, mate entities, etc.).
- The generated data enclose a variety of matrices which are obtained through several integrated algorithms (Adjacency matrix, contact all direction matrices, interference matrices) which are detailed in Belhadj et al. (2016).

Figure 3 shows the interface of the CADLab plug-in integrated to SolidWorks. Figure 4 illustrates the collected data relative to the illustrative example such as: components number, component's attributes and an example of coaxial constraint types between the two parts.

2.2 Edition of the Extracted Data

All the extracted data can be displayed using Excel software in order to analyze them. These data can be transferred elsewhere for other treatment. Figure 5 illustrates the contact matrices in the three directions (X, Y, and Z) for the treated example.
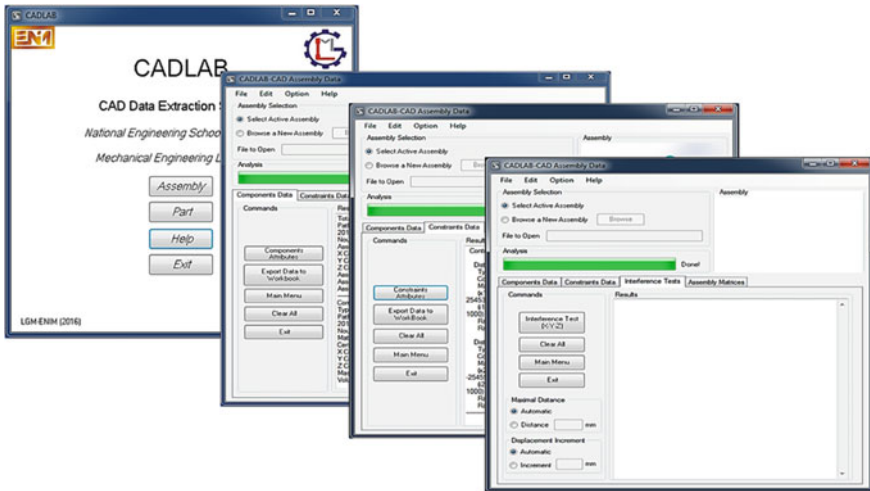
Fig. 3 CADLab plug-in interface to extract and generate data

2.3 Data Treatment

Once the extracted and generated CAD data are accomplished, the Matlab treatment process begins. This process is composed of three stages:

• **Base part research**: A base part can be defined as a central component on which most parts will be assembled. In order to identify the base part list, a fitness function is used. The goal is to identify parts having a maximum number of contacts, a higher volume, and the biggest boundary surface. These parts can constitute initiating elements of subassemblies. For a part p, the score of the objective function is calculated the following equation.

$$Ftp = \alpha \cdot Tc + \beta \cdot Vp/Vt + \gamma \cdot Sp/St \tag{1}$$

where: α, β, and γ represent the weight coefficients, Tc: represents the total contact between part p and other parts in the assembly; Vm represents the volume of part p; Vt represents the total volume of parts; Sp represents the border surface of part p; St: represents the total surface of parts.

For the treated example the identified base part set is [2, 4, 5, 6, 7, 9]. Each recognized base part should be an initiator of a subassembly group.

• **Subassemblies research (SR)**: The SR algorithm can be started once the identification of the base parts list is performed. It begins by browsing all connections between all base parts and removing them. Then, it browses all connections with other parts to identify subassemblies. The output of the SR step is a list of subassemblies. For the treated example, the list of the identified subassemblies is represented by Fig. 6.
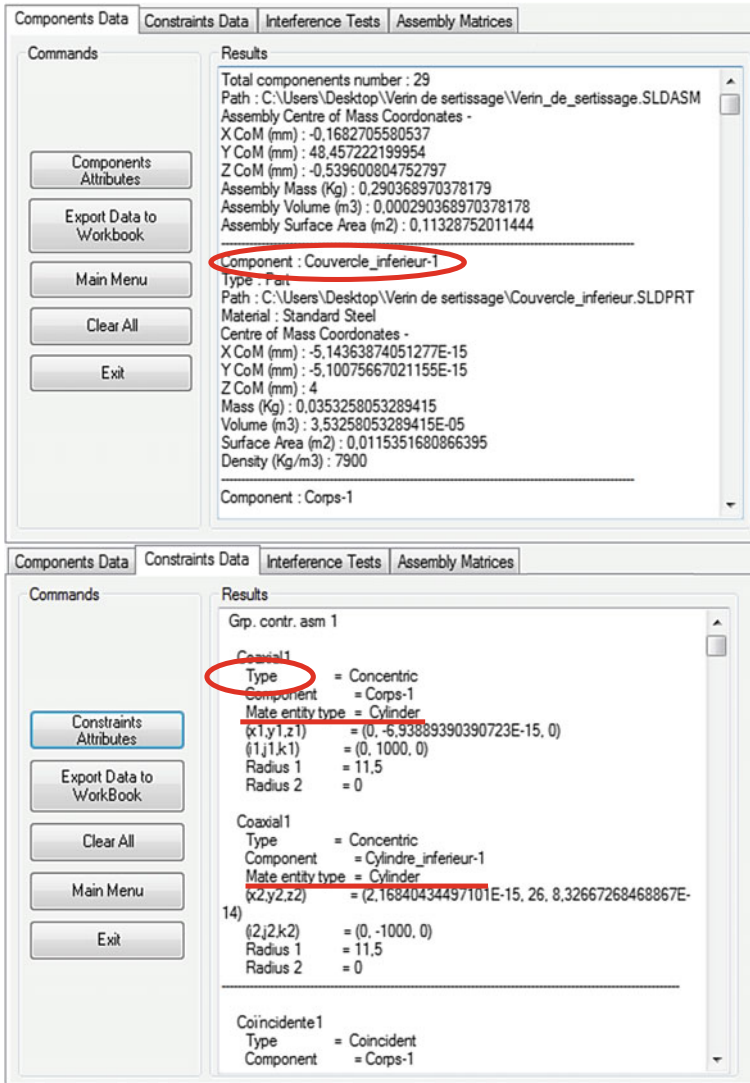
Fig. 4 Extracted constraints' data relative to the illustrative example

- **Disassembly plan generation of the subassemblies**: The DP algorithm starts by generating an Interference Matrix of subassemblies [IMS]. Its size is equal to ($p \times p$) where p represents the numbers of subassemblies. The IMS(i, j) element's associate to the k-axis is introduced as follows: If the subassembly i does not interfere with another subassembly j in the direction of the k-axis, the subassembly i can be disassembled freely from the subassembly j in the direction of the k-axis; in this case the value of IMS(i, j) = 0. If the subassembly

(a)

	5	6	7	8	9	10	13	12	2	1	4	3	11	14	15	16	17	18
5	0	1	0	0	0	0	0	0	0	0	1	1	0	0	0	0	1	1
6	1	0	1	0	1	1	0	0	0	0	0	0	0	0	0	1	1	0
7	0	1	0	1	0	0	0	0	0	1	0	1	0	0	0	0	0	0
8	0	0	1	0	1	0	0	0	0	0	0	0	1	0	1	0	0	0
9	0	1	0	1	0	1	0	0	0	0	0	0	0	1	1	1	0	0
10	0	1	0	0	1	0	0	0	0	0	0	1	0	0	0	0	0	0
13	0	0	0	0	0	0	0	0	1	1	0	0	0	0	0	0	0	0
12	0	0	0	0	0	0	0	0	1	1	0	0	0	0	0	0	0	0
2	0	0	0	0	0	0	0	1	0	1	0	1	0	0	0	0	0	0
1	0	0	0	0	0	0	0	1	1	0	0	0	0	0	0	0	0	0
4	1	0	1	0	0	0	1	0	0	0	0	1	0	0	0	0	0	0
3	1	0	0	0	0	0	1	0	1	0	1	0	0	0	0	0	0	1
11	0	0	0	1	1	0	0	0	0	0	0	0	0	0	0	0	0	0
14	0	0	0	0	1	1	0	0	0	0	0	0	0	0	0	0	0	0
15	0	0	0	1	1	0	0	0	0	0	0	0	0	0	0	0	0	0
16	0	1	0	0	1	0	0	0	0	0	0	0	0	0	0	0	0	0
17	1	1	0	0	0	0	0	0	0	0	0	0	0	0	0	0	0	0
18	1	0	0	0	0	0	0	0	0	0	1	0	0	0	0	0	0	0

Adjency Matrix

(b)

	5	6	7	8	9	10	13	12	2	1	4	3	11	14	15	16	17	18
5	0	1	0	0	0	0	0	0	0	0	1	1	0	0	0	0	1	1
6	1	0	1	0	1	1	0	0	0	0	0	0	0	0	0	1	1	0
7	0	1	0	1	0	0	0	0	0	1	0	1	0	0	0	0	0	0
8	0	0	1	0	1	0	0	0	0	0	0	0	0	1	0	0	0	0
9	0	1	0	1	0	1	0	0	0	0	0	0	0	1	1	1	0	0
10	0	1	0	0	1	0	0	0	0	0	0	1	0	0	0	0	0	0
13	0	0	0	0	0	0	0	0	1	0	0	0	0	0	0	0	0	0
12	0	0	0	0	0	0	0	0	1	0	0	0	0	0	0	0	0	0
2	0	0	0	0	0	0	0	1	0	0	0	1	0	0	0	0	0	0
1	0	0	0	0	0	0	0	0	0	0	0	0	0	0	0	0	0	0
4	1	0	1	0	0	0	1	0	0	0	0	1	0	0	0	0	0	0
3	1	0	0	0	0	0	0	0	1	0	1	0	0	0	0	0	0	1
11	0	0	1	0	0	0	0	0	0	0	0	0	0	0	0	0	0	0
14	0	0	0	0	1	1	0	0	0	0	0	0	0	0	0	0	0	0
15	0	0	0	1	1	0	0	0	0	0	0	0	0	0	0	0	0	0
16	0	1	0	0	1	0	0	0	0	0	0	0	0	0	0	0	0	0
17	1	1	0	0	0	0	0	0	0	0	0	0	0	0	0	0	0	0
18	1	0	0	0	0	0	0	0	0	0	1	0	0	0	0	0	0	0

Contact Matrix (X)

(c)

	5	6	7	8	9	10	13	12	2	1	4	3	11	14	15	16	17	18
5	0	1	0	0	0	0	0	0	0	0	1	0	0	0	0	0	0	0
6	1	0	0	0	1	1	0	0	0	0	0	0	0	0	0	1	1	0
7	0	0	0	1	0	0	0	0	0	0	0	0	1	0	0	0	0	0
8	0	0	1	0	0	0	0	0	0	0	0	0	1	0	1	0	0	0
9	0	1	0	0	0	1	0	0	0	0	0	0	0	0	0	0	0	0
10	0	1	0	0	1	0	0	0	0	0	0	1	0	0	0	0	0	0
13	0	0	0	0	0	0	0	0	1	1	0	0	0	0	0	0	0	0
12	0	0	0	0	0	0	0	0	1	1	0	0	0	0	0	0	0	0
2	0	0	0	0	0	0	0	1	0	1	0	1	0	0	0	0	0	0
1	0	0	0	0	0	0	0	1	1	0	0	0	0	0	0	0	0	0
4	0	0	0	0	0	0	1	0	0	0	0	1	0	0	0	0	0	0
3	1	0	0	0	0	0	1	0	1	0	1	0	0	0	0	0	0	1
11	0	0	1	1	0	0	0	0	0	0	0	0	0	0	0	0	0	0
14	0	0	0	0	1	0	0	0	0	0	0	0	0	0	0	0	0	0
15	0	0	0	1	0	0	0	0	0	0	0	0	0	0	0	0	0	0
16	0	1	0	0	0	0	0	0	0	0	0	0	1	0	0	0	0	0
17	0	1	0	0	0	0	0	0	0	0	0	0	0	0	0	0	0	0
18	0	0	0	0	0	0	0	0	0	0	1	0	0	0	0	0	0	0

Contact Matrix (Y)

(d)

	5	6	7	8	9	10	13	12	2	1	4	3	11	14	15	16	17	18
5	0	1	0	0	0	0	0	0	0	0	1	1	0	0	0	0	1	1
6	1	0	1	0	1	1	0	0	0	0	0	0	0	0	0	1	1	0
7	0	1	0	1	0	0	0	0	0	1	0	1	0	0	0	0	0	0
8	0	0	1	0	1	0	0	0	0	0	0	0	0	1	0	0	0	0
9	0	1	0	1	0	1	0	0	0	0	0	0	0	1	1	1	0	0
10	0	1	0	0	1	0	0	0	0	0	0	1	0	0	0	0	0	0
13	0	0	0	0	0	0	0	0	1	0	0	0	0	0	0	0	0	0
12	0	0	0	0	0	0	0	0	1	0	0	0	0	0	0	0	0	0
2	0	0	0	0	0	0	0	1	0	0	0	1	0	0	0	0	0	0
1	0	0	0	0	0	0	0	0	0	0	0	0	0	0	0	0	0	0
4	1	0	1	0	0	0	1	0	0	0	0	1	0	0	0	0	0	0
3	1	0	0	0	0	0	0	0	1	0	1	0	0	0	0	0	0	1
11	0	0	1	0	0	0	0	0	0	0	0	0	0	0	0	0	0	0
14	0	0	0	0	1	1	0	0	0	0	0	0	0	0	0	0	0	0
15	0	0	0	1	1	0	0	0	0	0	0	0	0	0	0	0	0	0
16	0	1	0	0	1	0	0	0	0	0	0	0	0	0	0	0	0	0
17	1	1	0	0	0	0	0	0	0	0	0	0	0	0	0	0	0	0
18	1	0	0	0	0	0	0	0	0	0	1	0	0	0	0	0	0	0

Contact Matrix (Z)

Fig. 5 Pneumatic crimping tool assembly matrices. **a** Adjacency, **b** x-axis contact, **c** y-axis contact and **d** z-axis contact

i that moves in the direction of the k-axis has interference with another sub-assembly j, then the subassembly j that moves in the direction of the k-axis will, in turn, has interference with the subassembly i; in this case the value of IMS(i, j) = 1. The [IMS] matrices are generated using the CADLab plug-in which is done by playing automatically the interoperability loop from Matlab to Solid-Works and vice versa (Fig. 1).

Figure 7 shows the method of simplification and generation of DP subassemblies from [IMs] matrix. In fact, when all elements of the line or column corresponding to a subassembly are equal to 0 then the subassembly can be disassembled freely in the direction of the (+y) axis (if the line is equal to 0) or (−y) axis (if the column is equal to 0). If in the same time tow subassemblies having a line or

Fig. 6 Subassembly list of the treated example
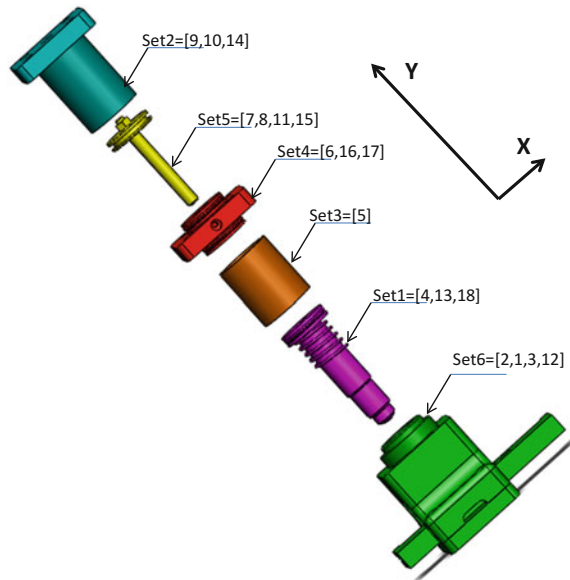
column equal to 0, the decision is carried out by comparing the scores of the objective function corresponding to the associate's base part. In fact, in the industrial practices, the disassembly process starts by dismantling parts having the smaller volume or surfaces, i.e., having the smaller value of the objective function. Once a subassembly is disassembled, its corresponding line, and column are removed from [IMS]. A new square matrix [IMS] is then generated. This procedure is repeated until all subassemblies are dismantled.

3   Results and Discussion

The computer programming of the proposed approach is carried out using both platforms: SolidWorks© CAD system using its API (Application Programming Interfaces) and Matlab© (Matrix Laboratory). The CADLab plug-in is the responsible tool to collect and generate all useful data.

The output of the implemented system is organized in a list three results: a base parts set, a list of subassembly groups and a DP including the disassembly sequence of subassemblies with the inherent directions.

Based on the developed approach, the planner intervention is more reduced. As much as possible using the developed approach. The obtained results are encouraging.
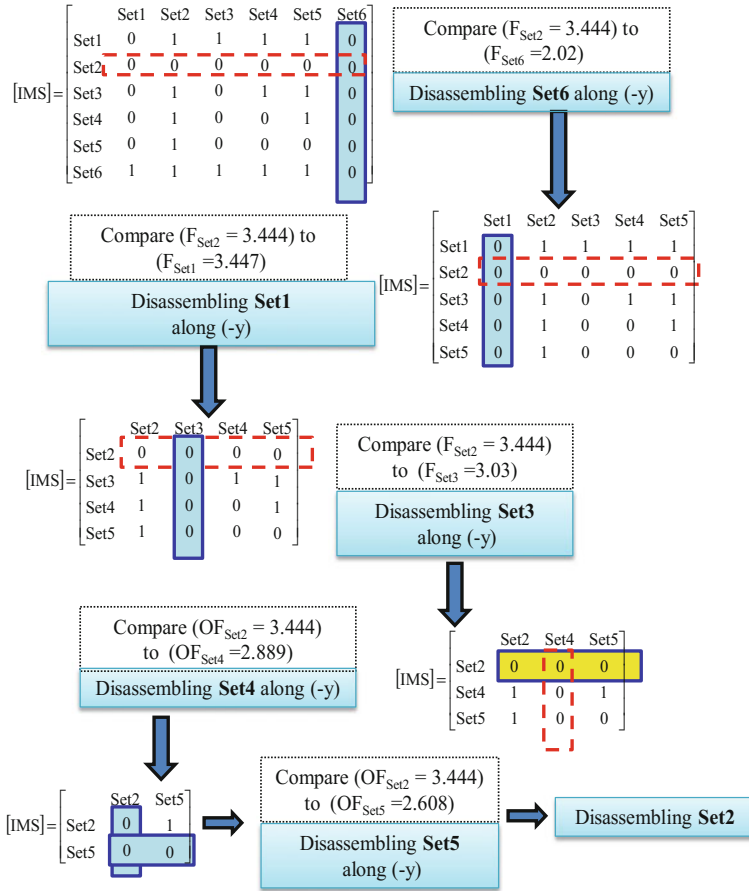
Fig. 7 DP generation of the subassemblies

4 Conclusion

In this paper, a concurrent engineering approach to generate automatically the DP of complex product based on subassemblies is detailed. The developed approach begins by identified all subassemblies with respect to the assembly' constraints and component's attributes generated by a CADLab application which is integrated into SolidWorks. An interference matrix of components and of the subassemblies was generated by playing an interoperability loop from Matlab to SolidWorks and vice versa. A simplification method applied to the subassembly interference matrix was performed in order to generate the DP of subassemblies and then the DP of each subassembly. An illustrative example, chosen from the literature, was treated in order to highlight the efficiency if the proposed approach.

In the future work, a more complex product will be treated in order to validate the proposed approach. This work considers that each part is disassembled with a translation movement along one direction. However, in some cases, it is necessary to consider more than one dismounting direction with a rotation motion.

References

Belhadj I, Trigui M, Benamara A (2016) Subassembly generation algorithm from a CAD model. Int J Adv Manuf Technol 87:2829–2840

Ben Hadj R, Trigui M, Aifaoui N (2015) Toward an integrated CAD assembly sequence planning solution. Proc Inst Mech Eng Part C J Mech Eng Sci 229(16):2987–3001

Corriveau G, Guilbault R, Tahan A (2009) Genetic algorithms and finite element coupling for mechanical optimization. Adv Eng Softw 41(1):422–426

Gaha R, Yannou B, Benamara A (2016) Selection of a green manufacturing process based on CAD features. Int J Adv Manuf Technol 87:1335–1343

Ghali M, Tlija M, Aifaoui N, Pairel E (2017) A CAD method for tolerance allocation considering manufacturing difficulty based on FMECA tool. Int J Adv Manuf Technol. https://doi.org/10.1007/s00170-016-9961-x

Gupta S, Krishnan V (1998) Product family-based assembly sequence design methodology. IIE Trans 30(10):933–945

Hamdi M, Aifaoui N, Benamara A (2012) CAD model simplification using a removing details and merging faces technique for a FEM simulation. J Mech Sci Technol 26(11):3539–3548

Issaoui L, Aifaoui N, Benamara A (2015) Solution space reduction of disassembly sequences generated automatically via computer aids. Proc Inst Mech Eng Part C J Mech Eng Sci 229(16):2977–2986

Kheder M, Trigui M, Aifaoui N (2017) Optimization of disassembly sequence planning for preventive maintenance. Int J Adv Manuf Technol. https://doi.org/10.1007/s00170-016-9434-2

Lee SH (2005) A CAD–CAE integration approach using feature-based multi-resolution and multi-abstraction modelling techniques. Comput Aided Des 37:941–955

Popa C, Paraplala L, Constantin R, Cotet C (2012) Contact identification for assembly/disassembly process in CAD–CAE software. In: Proceedings of the 23rd international DAAAM symposium, vol. 23, no. 1, pp 613–616

Shu-Kai F, Fan C, Yang JH, Liu KR (2013) Disassembly and recycling cost analysis of waste notebook and the efficiency improvement by re-design process. J Clean Prod 39:209–219

Su Q (2007) Computer aided geometric feasible assembly sequence planning and optimizing. Int J Adv Manuf Technol 33(1/2):48–57

Swaminathan A, Barber KS (1996) An experience-based assembly sequence planner for mechanical assemblies. IEEE Trans Robot Autom 12(2):252–266

Numerical Study of Wall Horizontal Turbulent Jet of Freshwater in a Homogeneous Co-flow Stream of Saltwater

Syrine Ben Haj Ayech, Nejla Mahjoub Saïd, Philippe Bournot and Georges Le Palec

Abstract The disposal of effluents in nature and more particularly in the sea is a very frequent practice. The discharge of wastewater into a receiving environment such as seawater is generally in the form of a turbulent jet. The efficiency of the dispersion of the jet depends on its characteristics of mixing with the ambient environment and when the latter is in motion, it is significantly modified. This paper investigates a numerical study about buoyant wall turbulent jet in co-flow stream. A light fluid of freshwater is injected horizontally and tangentially to a plane wall into homogenous moving environment of saltwater. Since the domain temperature is assumed to be constant, the density of the mixture is a function of the salt concentration only. The mathematical model is based on the finite volume method and reports on an application of standard turbulence model k-ε for steady flow with densimetric Froude number of 11 and Reynolds number of 3800. The aim of this work is to predict the influence of the co-flow stream on the dispersion of the jet and the mixing processes between freshwater jet and ambient saltwater. The concentration contours, the cling length, and the central trajectory of the jet are determined. It is found that the jet behavior depends on the co-flow-to-jet velocity ratio.

Keywords Wall jet · Co-flow stream · Turbulence · Buoyancy
Cling length

S. B. H. Ayech (✉)
LGM, National Engineering School of Monastir, University of Monastir, 5000 Monastir, Tunisia
e-mail: ayechsyrine@hotmail.com

N. M. Saïd
LGM, Preparatory Institute for Engineering Studies, University of Monastir, Monastir, Tunisia
e-mail: nejla.mahjoub@fsm.rnu.tn

P. Bournot · G. Le Palec
IUSTI, UMR CNRS 7543, Aix-Marseille University, Marseille, France
e-mail: georges.lepalec@univ-amu.fr

791

1 Introduction

Thermal and hydrodynamic processes that occur in nature and technology often cause flows where the density varies greatly. These flows are found in different industrial applications, linked to energy and propulsion. The variation in density can be caused either by wide temperature differences or chemical reactions within the flow, or by mixing several flows of different compositions. It appears necessary to understand the effects induced by density variations on turbulent flows and develop models able to predetermine. In this context, several numerical (Birch 1978; Imine et al. 2006) works have been devoted.

The influence of the co-flows surrounding on the turbulent jets with variable density was the object of many studies. In order to reduce the turbulence intensities on the nozzle edges or to have good boundary conditions for modeling, a co-flow is often used. An analytical study on the jets with co-flow has been investigated by Abramovich (1963). He showed the presence of three essential areas: initial, principal, and transition areas. Mesnier (2001) investigated three turbulent jets, including helium, air, and CO_2 jets exiting with 40 m/s velocity in a low-velocity air co-flow. He was concerned to study density and nozzle geometry effects on jet structure. Antoine et al. (2001) performed measurements in turbulent water jet flowing with an injection velocity equal to 10 m/s and emerging in a low-velocity co-flow water ($R = u_{co}/u_0 = 0.05$). They showed that co-flow reduces the jet spreading rate by approximately 30% from the free jet.

A numerical study have been carried out to determine the behavior of a buoyant laminar wall jet in uniform moving stream in its various zones (Ben Haj Ayech et al. 2014), because the relative intensity of the buoyancy forces with respect to the inertia forces can cause the flow from the regime of the inertial jet to that of plume through the transitional regime. Huai et al. (2010) conducted a numerical simulation on a three-dimensional horizontal buoyant jet ejected tangentially to an adiabatic plate in medium at rest. The horizontal buoyant wall jet can be divided into three regions: initial region, wall jet region, and free jet region. The initial region is the region where the maximum velocity keeps constant, and the one behind the wall jet region is the free jet region. The centerline trajectory of the jet shows that the wall buoyant jet clings to the floor and slips for some distance before it lifts off, and the position where the centerline leaves wall is closer to the nozzle. Recently, Ben Haj Ayech et al. (2016) conducted a numerical study on a configuration of a turbulent plane jet ejected vertically and tangentially to a heated plate subjected to a constant temperature. The aim of this work is to predict the spreading and mixing behavior of isothermal and non-isothermal turbulent wall jet with co-flowing stream.

In most cases, the designer wishes to use a new configuration that ensures rapid mixing of the jet with the co-flow. In the current study, we used a configuration of a turbulent buoyant jet ejected horizontally and tangentially to a plate subjected to a constant temperature. The aim of this work is to predict the influence of the co-flow stream on the mixing processes between freshwater jet and ambient saltwater. Results are presented for velocity ratios varying between 0 and 0.2.

2 Problem Formulation

2.1 Assumptions

A turbulent jet with a discharge velocity u_0, temperature T_0, and density ρ_0 issues out from a rectangular nozzle, tangentially to a flat plate subjected to a constant temperature T_p. The jet is discharged into the static ambient water T_∞, the temperature, the density ρ_∞ and a uniform velocity u_{co}. The flow is assumed to be incompressible, steady and satisfies the Boussinesq approximation. A Cartesian coordinate system may be used, with x being the longitudinal position (or main flow) and y being the lateral distance (wall-normal direction), originating from the nozzle. We also assume that the width of the nozzle is very large in relation to its thickness, so that the problem can be considered as two-dimensional; the flow regime is assumed to be turbulent, and the thermophysical properties vary as a function of the mass concentration. Since the domain temperature is assumed to be constant, density gradients are functions of the mass concentration (salinity) only.

2.2 Governing Equations

The Reynolds-averaged Navier–Stokes (RANS) equations are computationally solved. The continuity (1) and the conservation of momentum Eq. (2) are given in the Cartesian coordinates system as follows:

$$\frac{\partial \overline{u_i}}{\partial x_i} = 0 \qquad (i = 1, 2, 3) \tag{1}$$

$$\overline{u_i}\frac{\partial \overline{u_j}}{\partial x_j} = -\frac{1}{\rho}\frac{\partial \overline{p}}{\partial x_i} + \frac{\partial}{\partial x_j}\left(\nu\frac{\partial \overline{u_i}}{\partial x_j} - \overline{u_i'u_j'}\right) - \frac{\rho - \rho_\infty}{\rho_\infty}g, \tag{2}$$

where i, j = 1, 2, 3 and x_i refer to x and y, respectively. $\overline{u_i}$ is the mean velocity in the i direction. ρ, p, and ν represent the pressure, the density, and the kinematic viscosity, respectively. $\overline{u_i'u_j'}$ are known as the Reynolds stresses. To study dilution features of the co-flowing wall jet, the averaged transport equation of a concentration (3) is given by

$$\overline{u_i}\frac{\partial \overline{C}}{\partial x_i} = \frac{\partial}{\partial x_i}\left(D\frac{\partial \overline{C}}{\partial x_i} - \overline{u_i'C'}\right), \tag{3}$$

where C corresponds to the tracer concentration with D as its diffusion coefficient which is assumed to be constant. Similar to the Reynolds stresses terms, $\overline{u_i'C'}$ is the concentration turbulent flux. The obtained Reynolds-averaged equations introduce an additional number of unknowns which require a closure turbulence model to

solve the system of equations. Herein, the k-ε model is used for all computations, and its representative equation is as follows:

$$\overline{u_j}\frac{\partial k}{\partial x_j} = \frac{\partial}{\partial x_j}\left[\left(\nu + \frac{\upsilon_T}{\sigma_k}\right)\frac{\partial k}{\partial x_j}\right] + G_k + G_b - \varepsilon \tag{4}$$

$$\overline{u_i}\frac{\partial \varepsilon}{\partial x_i} = \frac{\partial}{\partial x_i}\left[\left(\nu + \frac{\upsilon_T}{\sigma_\varepsilon}\right)\frac{\partial \varepsilon}{\partial x_i}\right] + C_{\varepsilon 1}\frac{\varepsilon}{k}(G_k + C_{\varepsilon 3}G_b) - C_{\varepsilon 2}\frac{\varepsilon^2}{k} \tag{5}$$

The terms G_k and G_b, which appear in these latter transport equations, represent, respectively, the kinetic turbulence energy production term (k) and the production term due to buoyancy.

$$G_k = \left(-\rho\overline{u_i'u_j'}\frac{\partial \overline{u_j}}{\partial x_i}\right) \tag{6}$$

$$G_b = \left(g\beta\frac{\upsilon_T}{Pr_t}\frac{\partial T}{\partial x_i}\right), \tag{7}$$

where β is the coefficient of thermal expansion.

According to the Boussinesq hypothesis, the Reynolds shear stress is related to mean quantities through the following equation:

$$-\overline{u_i'u_j'} = \nu_t\left(\frac{\partial \overline{u_i}}{\partial x_j} + \frac{\partial \overline{u_j}}{\partial x_i}\right) - \frac{2}{3}k\delta_{ij}, \tag{8}$$

where ν_t and δ_{ij} are, respectively, the turbulent viscosity and the Kronecker symbol, which is worth 1 if i = j if not 0.

The turbulent mass flux is given by the following relationship:

$$\overline{u_i'C'} = -D_t\frac{\overline{\partial C}}{\partial x_i} \tag{9}$$

The turbulent mass diffusivity coefficient D_t is related to the turbulent viscosity v_t via the turbulent Schmidt number Sc_t.

$$D_t = \frac{v_t}{Sc_t} \tag{10}$$

The two constants Pr_t and Sc_t, which appear in these expressions, designate, respectively, the turbulent Prandtl number whose default value is 0.85 and the turbulent Schmidt number which is of the order of unity.

The Eddy viscosity ν_T is related to k and ε through the Kolmogorov–Prandtl relations as:

$$\upsilon_T = C_\mu \frac{k^2}{\varepsilon} \tag{11}$$

The empirical constants used in the system of Eqs. (4) and (5) are the constant standard averaged-Reynolds-number model k-ε:

$$c_\mu = 0.09, \ c_{\varepsilon1} = 1.44, \ c_{\varepsilon2} = 1.92, \ c_{\varepsilon3} = 1.0, \ \sigma_k = 1.0 \text{ and } \sigma_\varepsilon = 1.3$$

It is known that the model k-ε is based on hypotheses which are valid only for flows with high Reynolds numbers. In such flows, the predominance of viscous effects in a very thin area immediately through contact with the wall is negligible. However, the wall boundary represents a region where the velocity changes from the no-slip condition at the wall to its free flow value. The variation is usually the largest in the near-wall region, and hence strongest, gradients are found here. Thus, one of the most common engineering problems is computing wall turbulent flows. So, the turbulent wall jet is solved with k-ε model associated with a wall function which takes account of the viscous zone adjacent to the wall, enabling us to calculate the characteristics of the flow starting at the wall.

To treat the boundary conditions in the presence of a wall boundary, the parameters characteristics of the jet are estimated by wall functions (Belcaid et al. 2015).

2.3 Boundary Conditions

When solving the governing equations, appropriate initial and boundary conditions (Fig. 1) needed to be applied. Hence, the following conditions were taken into account.

The initial velocity of jet corresponds to the mean velocity of discharges flow rate: This condition is applied to compute mass flow into the domain and fluxes of momentum and concentration. The no-slip boundary conditions at the wall: $u = v = 0$ and isothermal wall condition are adopted. The boundary conditions of the turbulent kinetic energy and its dissipation rate at the wall used are the modified standard wall functions of Launder and Spalding models (Belcaid et al. 2015).

Fig. 1 Scheme of coordinates system and boundary conditions
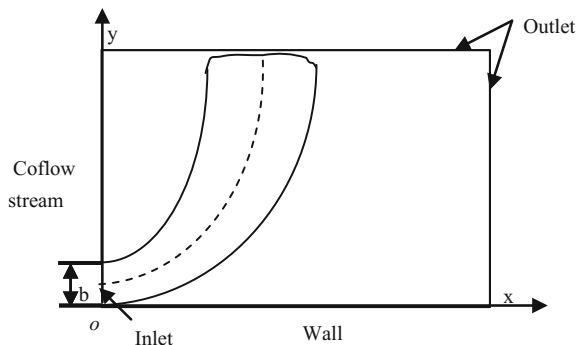
Table 1 Boundary and initial conditions

Boundary conditions	Velocity	Turbulent kinetic energy	Dissipation rate
Nozzle section	u = u0, v = 0	$k_0 = 10^{-3}u_0^2$	$\varepsilon = k_0^{3/2}/0.5b$
Co-flow Section	uco, v = 0	$k = 0.05u_{co}^2$	$\varepsilon = k_0^{3/2}/0.2l_{co}$
Wall	u = 0, v = 0	$P_k = \frac{\tau_p^2}{\rho k C_\mu^{1/4}\sqrt{ky}}$	$\varepsilon = \frac{C_\mu^{3/4}k^{3/2}}{ky}$
Outlet	$\frac{\partial u}{\partial y} = 0$	$\frac{\partial k}{\partial n} = 0$	$\frac{\partial \varepsilon}{\partial n} = 0$

Outlet boundary regarding the flow at outlet section as a fully developed turbulent flow leads to the second class of boundary conditions for u, v, k, and ε, i.e., the gradients perpendicular to the boundary are zero (Table 1).

The following table summarizes the boundary conditions (Belcaid et al. 2015): with l_{co} is the section of the co-flow stream.

2.4   Numerical Resolution

A computer code is developed with the aim of resolving the RANS equations. The discretization of the governing equations is done through the finite volume method using the first-order upwind scheme. The coupling between pressure and velocity variables is achieved via the SIMPLE algorithm using the staggered grid. Convergence occurs when the residual is reduced to a value below 10^{-5}, for each equation.

3   Results and Discussion

3.1   Validation of Numerical Results

The study is based on a detailed comparison between computational results and experimental measurements conducted by Wygnanski et al. (1992) using the same boundary conditions for a wall jet in a medium at rest $r = u_{co}/u_0 = 0$. The profile of the longitudinal velocity is plotted in function of the transverse position (y) in Fig. 2 at downstream location ($x/b = 20$) for an inlet Reynolds number equal to 7500. It is noticed that the obtained result and the experimental data are in close agreement in all regions of the flow.

3.2   The Concentration Contours

In this work, the freshwater is injected from the nozzle outlet with initial density in the same geometric and dynamic terms, i.e., for the same thickness of the nozzle

Fig. 2 Lateral evolution of the longitudinal velocity at $x/b = 20$ for $Re = 7500$ and $r = u_{co}/u_0 = 0$
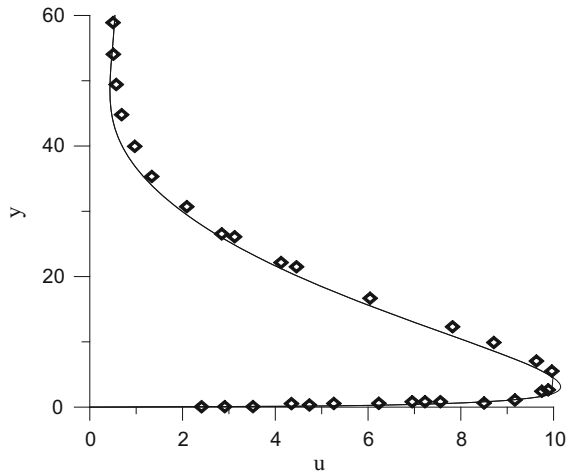
(b = 7.62 mm), and the same uniform velocity ($u_0 = 0.5$ m/s) into a co-flowing stream. The behavior of the jet at the outlet of the nozzle is also conditioned by the initial density gradient between the jet and the ambient saline medium $\Delta\rho = \rho - \rho_0$, where ρ_0 is the freshwater jet density at the nozzle, and ρ_∞ is the density of ambient fluid (saltwater) $\rho_0 < \rho_\infty$.

Since the flow is generated by both momentum and buoyancy, the rate between momentum and viscous forces is defined by the Reynolds number while the Froude number defines the rate between buoyancy and momentum. At the source, these numbers are defined by $Re = \frac{u_0 b}{v}$ and $Fr = \sqrt{\frac{u_0^2 \rho_\infty}{gb(\rho_\infty - \rho_0)}}$.

During its rising as a result of buoyancy forces, the plume takes a curved form due to the combined effect of the horizontal component of momentum and the gravity. When a jet is injected horizontally from a nozzle with a certain momentum, it begins to ascend vertically as if the buoyancy forces predominate the inertia forces. In this work, a turbulent wall jet is ejected in moving ambient water (co-flow stream) for a fixed Froude number (in the same initial momentum flux, i.e., initial velocity u_0, and buoyancy flux, i.e., initial density gradient between mixture injection fluid and ambient fluid) by varying the co-flow stream velocity.

During its development, the jet moves downstream of the outlet over a distance quite short under the effect of its initial momentum, accompanied by a high vertical elevation. In the second region, the buoyancy effect becomes greater and the flow spreads vertically and laterally. Even if the flow is ejected in static ambient water (external medium at rest) R = 0 or in weak co-flow stream $R \le 0.03$ Fig. 3a, the jet leaves from the wall nearest of the nozzle. For these low velocity ratios, the buoyancy forces are important and the co-flow stream effects are negligible. For strong velocity ratio ($R \ge 0.05$) (Fig. 3b and c), the buoyancy and co-flow effects are no longer negligible. Results show that the co-flow stream intervenes to make raise the flow at further downstream location from the jet exit. It is concluded that
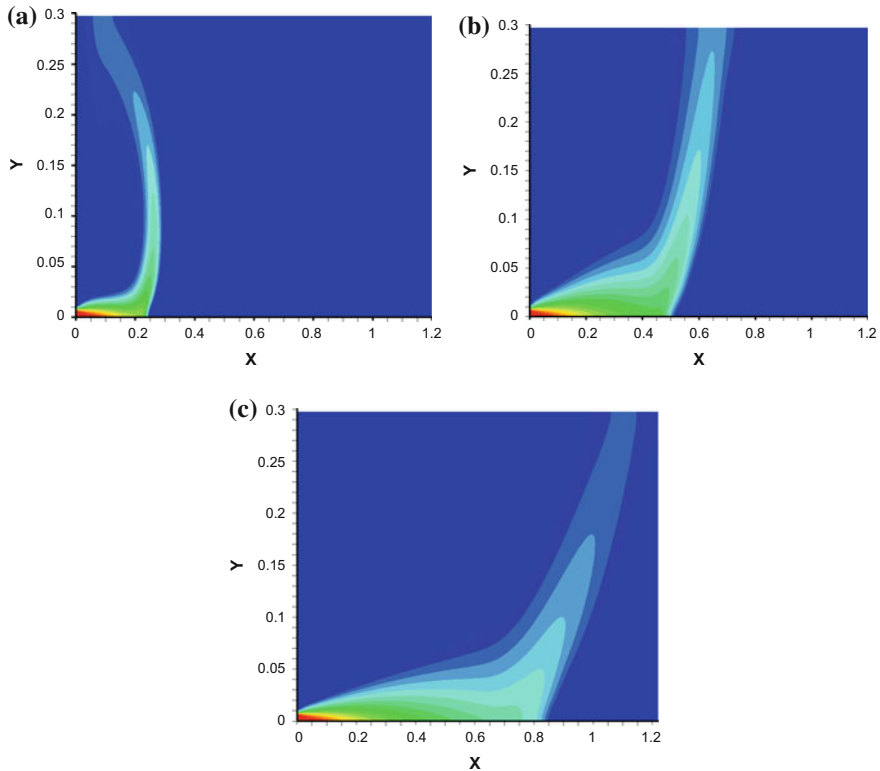
Fig. 3 The concentration contours for $Fr = 11$ and for different co-flow velocity ratios: **a** $R = 0.03$, **b** $R = 0.05$, and **c** $R = 0.2$

the presence of co-flow stream ensures larger mixing zone of the jet with the ambient fluid and prevents a return flow of the jet toward the injection source and therefore improves dilution.

3.3 Cling Length and Jet Trajectory

Outgoing from the nozzle, the jet seeps into the external medium and the mixing process with ambient fluid starts. During its flow, the jet clings to the bottom for some distance. At the level of that boundary, the jet is submitted to frictional forces that brake the flow and decrease its kinetic energy. When this later becomes sufficiently weak, the flow is dominated by the positive buoyancy generated by initial density gradient $\Delta\rho$. Thus, the jet leaves the bottom and rises to surface as a free jet. The distance between the nozzle and the position where the trajectory leaves the floor is L. In Fig. 4, we are interested to examine the influence of the co-flow stream

Fig. 4 Cling length for different velocity ratios
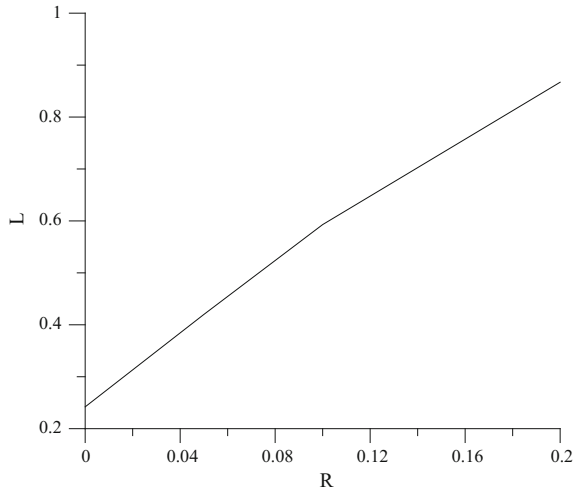
Fig. 5 Co-flow velocity effects on the jet trajectory
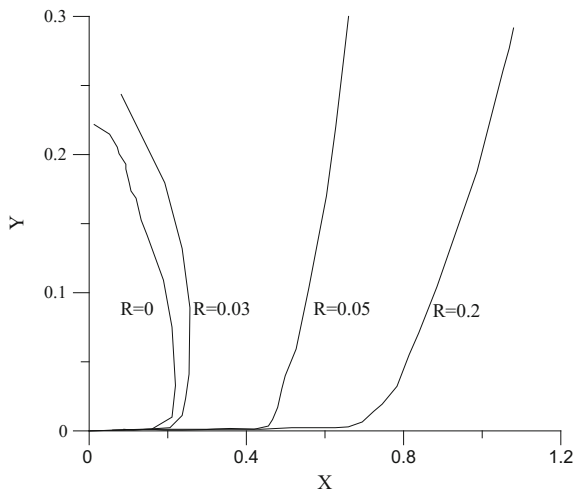
on the cling length. Results show that this distance increases linearly, and the wall buoyant jet clings to the floor and slips for some distance before it lifts off, and the position that the jet leaves wall is closer to the nozzle for weaker velocity ratio. We notice that the stronger co-flow stream is, the more important the cling length L is.

The average behavior of the jet discharged into moving saltwater is characterized by a curved form caused by the initial flow of buoyancy created by the difference in density between the effluent (freshwater) and the ambient saltwater. These observations are supported by the central trajectory of the jet (Fig. 5), which shows that the bending curvature of the jet is large in absence of co-flow stream (R = 0) or with weak co-flow velocity ratios $R \leq 0.03$. When the flow is ejected into the ambient fluid with strong co-flow velocity $R \geq 0.05$, the jet evolves with some little deviation by moving toward the free surface (outlet boundary), away from the jet exit.

4   Conclusion

In this work, a numerical investigation of wall horizontal turbulent jet of freshwater in an ambient fluid (saltwater) is considered by using the k-ε models. The analysis focuses essentially on the influence of the co-flow stream (ambient fluid) effects on the jet behaviors such as concentrations contours, the central trajectory of the jet, and especially its cling to the wall.

Results show that the jet clings to the wall and depends strongly on co-flow stream: The weaker the co-flow velocity ratio is, the weaker its cling to the wall is.

It is also showed that, in order to ensure good jet dilution and effective mixing between jet freshwater and saltwater, a strong co-flow velocity should be used.

References

Abramovich GN (1963) The theory of turbulent jets. MIT Press, Cambridge, MA

Antoine Y, Fabrice L, Michel L (2001) Turbulent transport of a passive scalar in a round jet discharging into a co-flowing stream. J Mech B Fluid 20:275–301

Belcaid A, Le palec G, Draoui A (2015) Numerical and experimental study of Boussinesq wall horizontal turbulent jet of fresh water in a static homogeneous environment of salt water. J Hydrodyn 27: 604–615

Ben Haj Ayech S, Habli S, Mahjoub Saïd N, Bournot H, Le Palec G (2014) Effect of the coflow stream on a plane wall jet. Heat Mass Transf 50:1685–1697

Ben Haj Ayech S, Habli S, Mahjoub Said N, Bournot H, Le Palec G (2016) A numerical study of a plane turbulent wall jet in a coflow stream. J Hydro-Environ Res 12:16–30

Birch AD, Brown DR, Dodson MG, Thomas JR (1978) The turbulent concentration field of a methane jet. J Fluid Mech 88:431

Huai W, Li Z, Qian Z, Zeng Y, Han J (2010) Numerical simulation of horizontal buoyant wall jet. J Hydrodyn 22:58–65

Imine B et al (2006) Study of non-reactive isothermal turbulent asymmetric jet with variable density. Comput. Mech 38:151–162

Mesnier B (2001) Studies on the development of turbulent jets with variable density in axisymmetric and asymmetric geometries (In French). PhD thesis, Orleans University, Orleans, France

Wygnanski I, Katz Y, Horev E (1992) On the applicability of various scaling laws to the turbulent wall jet. J Fluid Mech 234:669–690

Collaborative Inventory Management in Tunisian Healthcare Sector

Mouna El Arbi, Ahmed Amine Karoui, Malek Masmoudi and Omar Ayadi

Abstract Drug shortages are the most complex and critical existing problems in public hospitals; this is due to different causes like deficiencies in the supply chain of medicines and parallel trade. This problem is costly for hospitals because it can affect patient's safety. For this, hospitals have to find solutions to protect their patients and to provide drugs in the right amount at the right time. Among solutions, which help to resolve these problems, there is the collaborative supply chain. Collaborative supply chain is-based on the interaction and collaboration between organizations in order to achieve a common goal and obtain mutual benefit. This study extends research to show the impact of collaboration between hospitals on reducing the drug shortages problem. In addition, we will investigate the importance of collaboration within horizontal supply chain, by presenting different strategies, such as placing orders in different dates, standardization of orders dates and group purchasing organization and seeing the impact of each strategy on solving the drug shortages in Tunisian healthcare sector.

Keywords Drug shortage · Collaboration · Horizontal supply chain

M. El Arbi (✉) · O. Ayadi
Mechanics Modelling and Production Research Laboratory (LA2MP),
National School of Engineers of Sfax (ENIS), Sfax University,
BP 1173, 3038 Sfax, Tunisia
e-mail: Mouna_arbi55@yahoo.fr

O. Ayadi
e-mail: Omar.ayadi@yahoo.fr

A. A. Karoui · M. Masmoudi
University of Lyon, 42023 Saint-Etienne, France
e-mail: AhmedAmineKaroui@outlook.com

M. Masmoudi
e-mail: Malek.masmoudi@univ-st-etienne.fr

A. A. Karoui · M. Masmoudi
LASPI, IUT de Roanne, University of Saint Etienne, Jean Monnet, 42000, 42334
Saint-Etienne, France

801

1 Introduction

As any organization, the hospital has to practice the best supply chain management, which participates to organize its activities and reach its goals. The main objective of the hospital is to satisfy the needs of its patient and realize a good quality of service. In hospitals, there are internal pharmacies, which are responsible to provide drug and pharmaceutical products to respond to patient's needs. According to (Trouiller 2013), the role of hospital pharmacies is to warrant the management of pharmaceutical products and executing the operations of (selection, procurement, preparation, quality control, storage, distribution, and dispensing) so it is necessary to use the best practices and methods that help pharmacies to satisfy the patients need and achieve the goals of hospitals.

To satisfy its patient need's, the hospital pharmacy has to provide pharmaceutical product in the right amount at the right time, so the shortage of drug is not allowed. Unfortunately, the drug shortages problem is very frequent in most hospital pharmacies around the world. According to the literature, many countries suffer from this problem like Canada (Boyle 2012), the European Union (Weerdt et al. 2015), Saudi Arabia (Al-ruthia et al. 2016) and Tunisia. The reasons for the drug shortages problem differ from one country to another. Among this reasons, we find the shortages of raw materials (Golembiewski 2012), the production problems (Alshehri and Alshammari 2016). In other side, there is the variation of demand, the bad process of production, also because the drug production is concentrated in the emerging countries. These last causes are cited in the world report of **Barbara Casassus** following a declaration signed by 45 European patient, consumer, and healthcare professional organizations (Casassus 2014).

Among the solutions that can help hospitals to solve the drug shortage problems, there is the collaborative supply chain management. According to (Hassan 2005) the different sector's companies (agriculture, industrial, health care etc.) have to cooperate and build a mutual supply chain, rather than working isolated.

This study extends research to show the impact of collaboration between hospitals on reducing the drug shortages. Our framework is about horizontal collaborative supply chain for Tunisian hospitals. According to (Simatupang and Sridharan 2002) the horizontal collaborative supply chain is the alliance between competitors companies, working in the same activity sector, to share their own information or resources.

Based on the collected data from the hospital of Habib Bourguiba, which is located in Sfax (Tunisia), we will present some statistics about drug shortages, then we will identify the reasons of this problem, and we will demonstrate the importance of collaborative supply chain management to reduce the drug shortages in hospitals.

2 Problem Description

Table 1 presents statistics from real data corresponding to Habib Bourguiba hospital in Sfax. In this table, the hospital orders are-classified into two types: monthly orders (Mo) and additional ones (Add). Considered orders correspond to the period from April 2015 to March 2016. For each month, we have the number of ordered drug types, the number of types of drug not delivered and the satisfaction percentage. We can see the frequent unavailability of medicines in hospital and this due to the non-satisfaction of their orders by the Tunisian central pharmacy (PCT), which is the unique drug supplier.

For example, for the month of April, the hospital pharmacy of Habib Bourguiba hospital ordered 184 types of drug. Among these drugs, there are 31 kind, which were-not-received with total quantity requested, so the dissatisfaction percentage was 16.85%. In other side, the quantity received of 22 types of drug, was lower than 80% of the total quantity needed, with a dissatisfaction percentage of 11.96%. For the worst case, 14 types of drug were not available in the drug inventory of the PCT.

We can see from these values that the PCT did not satisfy all the quantities of medicines requested by hospitals, and this is due to many reasons. This dissatisfaction of hospitals orders can causes a drug shortage problem in hospital pharmacies.

The objective of this study is to find solutions to solve the problem of orders dissatisfaction by the PCT, and consequently to not have a drug shortages in hospitals. For this reason, we propose that hospitals coordinate with each other's and place their orders in different dates. In this case, the PCT will not have an overload. Moreover, the hospitals can exchange drug between them in order to avoid shortages. In the next section, we will show the importance of collaborative supply chain to mitigate the impact of drug shortage problem and to help hospitals to satisfy their patient's needs. The following collaborative issues are-discussed: placing drug orders in different dates, standardization of order dates and group purchasing organization.

3 Placing Orders in Different Dates

According to the collecting data, Tunisian hospitals place their drug orders at the beginning of each month, which result an overload of the PCT. Then the PCT cannot satisfy all the orders at the same time. For this, we propose that cooperative hospitals, place their orders in different dates for reducing the drug shortages and reducing the load of the PCT.

Table 1 Statistics of orders satisfaction in Habib Bourguiba Hospital of Sfax

Month	Type	Nb Ref	NbLivQt < 100%	Satisfaction < 100%	NbLivQt < 80%	Satisfaction < 80%	NbLivQt < 50%	Satisfaction < 50%	NbLivQt < 30%	Satisfaction < 30%	NbLivQtNul	% drug satisf null
Apr-15	Mo	184	31	16.85	22	11.96	22	11.96	20	10.87	14	7.61
Apr-15	Add	7	3	42.86	3	42.86	2	28.57	2	28.57	1	14.29
May-15	Add	5	2	40.00	2	40.00	1	20.00	1	20.00	1	20
June-15	Mo	181	35	19.34	27	14.92	24	13.26	23	12.71	19	10.50
June-15	Add	15	9	60.00	9	60.00	6	40.00	6	40.00	5	33.33
Sept-15	Mo	172	29	16.86	21	12.21	19	11.05	16	9.30	16	9.30
Sept-15	Add	5	3	60.00	3	60.00	3	60.00	3	60.00	2	40.00
Oct-15	Mo	197	40	20.30	33	16.75	29	14.72	27	13.71	23	11.68
Oct-15	Add	5	3	60.00	3	60.00	3	60.00	3	60.00	3	60.00
Oct-15	Add	14	9	64.29	9	64.29	9	64.29	9	64.29	9	64.29
Nov-15	Mo	230	34	14.78	24	10.43	21	9.13	21	9.13	18	7.83
Dec-15	Mo	275	55	20.00	39	14.18	25	9.09	25	9.09	21	7.64
Jan-16	Mo	196	35	17.86	31	15.82	27	13.78	25	12.76	25	12.76
March-16	Mo	225	50	22.22	42	18.67	32	14.22	28	12.44	25	11.11

Reducing the drug shortages:

Collaborative SC of hospitals will ensure that no stock shortages occur in the group. Consequently, even if a hospital in the group suffer of shortage problem, before the end of the month (and therefore before the next order), it would be possible for him to borrow the necessary quantity from his collaborators.

Different scenarios are-considered in order to test the impact of placing ordersin different dates on shortage levels. Two parameters are considered:

- The number of hospitals working in collaboration
- Hospitals shortage dates if they work individually

Table 2 shows the details of different illustrative scenarios.

The performance indicator that is-proposed for these scenarios is the percentage of coverage of a hospital by its partners during the period of its drug shortage. This indicator is-noted I_A and it is-calculated as follow:

$$I_A = \frac{\sum_i^N Q_{ri}}{C_A \times d_A} \times 100, \tag{1}$$

where Nis the number of hospitals in collaboration, C_A is the daily consumption of one drug of hospital A, d_A is the predicted drug shortage date of hospital A, Q_{ri} is the quantity of drug that exists in the stock of other hospitals during the drug shortage period of hospital A.

The table above show that for 83.33% of network members who have a drug shortage, the coverage percentage exceeded 100% of their needs. The coverage's percentage are very high except in two cases, that of scenario 3, which coverage percentage for one of the two hospitals is 33.33% and another in Scenario 5 the coverage percentage is 63% for one of the three hospitals. In fact, for the first case, it is a collaboration between only two hospitals. With a drug shortage of these two hospitals before 10 days of their next orders, one of them is covered at 108% of its need, and the other, Which has a high daily consumption compared to its partner, is covered at 33.33% for a period of more than 3 days.

Scenario 5 represents, it is a collaboration between three hospitals. The three hospitals fall out of stock before 10 days of their next orders. The result, one will be covered at 143.75% of its necessity, the other will be covered at 196% of its necessity and the last one, always the one which has a relatively high daily consumption, will be covered to 63% of its necessity. In Scenario 4, the coverage percentage reach the 1235.21% considering collaboration between three hospitals.

Reducing the load of the PCT:

With the current situation of the Tunisian pharmaceutical network, all hospitals place their orders at the beginning of each month to the PCT. The demand is very high because all hospitals place their orders at the same time, also there are certainly fluctuations in the demand of hospitals, and so often, the PCT breaks down and

Table 2 Example of collaboration scenarios for replenishment dates

Scenario	Network member	Ordered Qt	Days without shortage	Shortage period (di)	Daily consumption	Required Qt for no short.	Remain. Qt at the begin of short. period of a partner	Remain. Qt until the end short. period of a partner	% shortage cover by partners
1	2	1000	24	6	41.67	250.02	458.33	416.67	139.99
		700	28	2	25.00	50.00	475.00	350.00	833.34
2	2	800	25	5	32.00	160.00	576.00	352.00	159.09
		700	22	8	31.82	254.55	381.82	254.55	138.29
3	2	900	20	10	45.00	450.00	675.00	270.00	33.33
		500	20	10	25.00	250.00	375.00	150.00	108.00
4	3	1000	23	7	43.47	304.29	260.00	173.91	172.64
							782.61	608.70	
		800	25	5	32.00	160.00	576.00	512.00	473.03
							384.00	192.00	
		500	27	3	18.51	55.53	444.44	333.33	1235.21
							222.22	148.15	
5	3	1000	20	10	50.00	500.00	500.00	50.00	63.00
							1000.00	550.00	
		800	20	10	40.00	400.00	800.00	440.00	143.75
							400.00	40.00	
		500	20	10	25.00	250.00	500.00	275.00	196.00
							250.00	25.00	

Table 3 Distribution of supply dates in the framework of a spontaneous collaboration

Parameters	Hosp. 1A	Hosp. 2B	Hosp. 3C	Hosp. 4D	Hosp. 5E
Drug. 1	7	25	1	19	13
Drug. 2	1	13	7	25	19
Drug. 3		11		1	21
Drug. 4	22	1	8		15
Drug. 5	1		8	15	22
Drug. 6	15	8	22	1	
Drug. 7	13	7	25	19	1
Order number	5	6	5	4	6

cannot satisfy the orders of its customers. The advantage of our purpose is that orders will be spaced in time, so the PCT will have time to control its stock level and fill it if there are low quantities of certain drugs.

We have demonstrated that coordination between hospitals on purchasing dates has many advantages such as avoiding the risk of drug shortage and reducing the load of the PCT. Now, we will illustrate this kind of collaboration based on a group of five hospitals and seven kinds of drug which are used by at least one of the network members. Each hospital that uses a drug should order it once a month.

The Table 3 show the distribution of supply dates in the framework of a spontaneous collaboration:

With spontaneous management like that shown in the example above, even with only seven drugs, a hospital in the group may have to order at six different dates per month, which is not at all profitable for him. If the number of drugs increases, a hospital may have to order more than 6 times per month and this will generate high delivery costs. In the next section, we propose to standardize the order dates to reduce the number of orders for each hospital in the network.

4 Standardization of Orders Dates

The first operation that must be done to reduce the number of orders is to choose five standard order dates for the network members, this ensures that a hospital in the group places only five orders per month.

For the previous example, we propose the following dates as standard ordering dates 1, 8, 16, 21, 26, as shown in the Table 4 no hospital in the group exceeds 5 order dates.

It is-noted also, that the total number of trips to the PCT for the hospital group has decreased from 26 to 20 trips.

The delivery costs for hospitals working individually are-much-less, than the delivery costs when hospitals are working with the form of collaboration, presented above. To show this, we will compare between two cases as below:

Table 4 Example of assigning dates after standardization

Parameters	Hosp. 1A	Hosp. 2B	Hosp. 3C	Hosp. 4D	Hosp. 5E
Drug. 1	8	26	1	21	16
Drug. 2	1	16	8	26	21
Drug. 3		8		1	21
Drug. 4	21	1	8		16
Drug. 5	1		8	16	21
Drug. 6	16	8	21	1	
Drug. 7	16	8	26	21	1
Order number	4	4	4	4	4

Table 5 Example of quantity dimensions to be-ordered by a network group

	Drug. 1	Drug. 2	Drug. 3	Drug. 4	Drug. 5	Drug. 6	Drug. 7
Hosp. 1	150	100	0	220	145	90	100
Hosp. 2	170	80	180	150	0	90	14
Hosp. 3	90	50	0	100	60	100	90
Hosp. 4	200	150	240	0	210	150	180
Hosp. 5	250	180	290	270	260	0	180

Table 6 Delivery costs of hospitals working individually

	Hosp. 1	Hosp. 2	Hosp. 3	Hosp. 4	Hosp. 5
Orders number	3	3	2	4	4
Unit cost	2	2	2	2	2
Distance PCT	100	80	70	90	85
Delivery cost	600	480	280	720	680

Case 1: individual work

Table 5 presents an illustrative example in which we have the dimensions of the monthly quantities of seven drugs to be ordered by five hospitals working individually.

To estimate the delivery costs in this case, the distances traveled during deliveries are-fixed for each hospital and a unit cost for each unit of distance is-estimated.

The orders number is-calculated based on the data in the table above and fixing a maximum dimension constraint supported by the transport means: Dmax = 350. Table 6 presents an example of hospitals working individually.

Table 7 Delivery costs of hospitals working together

	Hosp. 1A	Hosp. 2B	Hosp. 3C	Hosp. 4D	Hosp. 5E
Orders number	4	4	4	4	4
Unit cost	2	2	2	2	2
Distance PCT	100	80	70	90	85
Delivery cost	800	640	560	720	680

Case 2: collaborative work

In Table 7 we will present an example of hospitals working together:

- Starting from Table 7, we notice that delivery cost increases compared to the first case by about 20% in total. Consequently, the delivery cost also increases. Therefore, it is important to find a solution to minimize the delivery cost. The solution that we propose is the group purchasing organization.

5 Group Purchasing Organization (GPO)

To reduce the delivery cost, it is necessary to decrease the number of orders to the PCT. For this, we propose as solution the group purchasing organization. This solution will enable to: Optimize the delivery costs and to reduce the number of means of transport used within the group.

We developed an algorithm whose objective is to give a planning of orders that will minimize the number of monthly deliveries for a group of collaborating hospitals.

This algorithm will have as inputs: The monthly quantities of drugs to be-ordered by each hospital in the group (transformed into their corresponding dimensions), the maximum dimension, which can-be-delivered by the means of transport available to them and standard order dates within the group. As result, it will determines an orders plan, which is based on the concept of group purchasing organization; it will indicates the order dates for each network member, which reduce the delivery costs.

The first constraint of this algorithm is the capacity of the means of transport; in addition, it is necessary to respect a constraint of dates. In fact, it is necessary that orders for a given drug will-be-placed on different dates.

Algorithm notations and variables:
$i = 1, 2, …, I$: date notation; $j = 1, 2, …, J$: drug notation. S_i is the size of drugs ordered at date i. V_i is the number of journeys to the PCT at a date i. D_{max} is the maximum dimension that can be transported. D_{ij} is the size of the quantity ordered at date i of drug j. $N_i = S_i/D_{max}$.

From the quantities of drugs indicated in Table 5, we determine the optimal trips number to the PCT as follow: $E\left(\frac{\sum\sum D_{ij}}{D_{max}}\right) + 1 = $ (14 trips). When the algorithm

Table 8 The dates of placing drug orders by the hospital group

	Drug. 1	Drug. 2	Drug. 3	Drug. 4	Drug. 5	Drug. 6	Drug. 7
Hosp. 1	Date 4	Date 1		Date 2	Date 3	Date 3	Date 2
Hosp. 2	Date 3	Date 4	Date 3	Date 3		Date 4	Date 3
Hosp. 3	Date 1	Date 5		Date 4	Date 2	Date 2	Date 1
Hosp. 4	Date 2	Date 2	Date 4		Date 4	Date 1	Date 4
Hosp. 5	Date 5	Date 3	Date 5	Date 1	Date 5		Date 5

reached this value, we found the following schedule of drug orders as shown in Table 8:

We can see from the table above, that on the same date hospitals can place several orders for different types of medicines. Consequently, the number of trips decreases from 16 (the trips number calculated according to the capacity constraint of the transport means and before the application of the algorithm), to 14➜ a gain of 12.5%.

Algorithm steps:
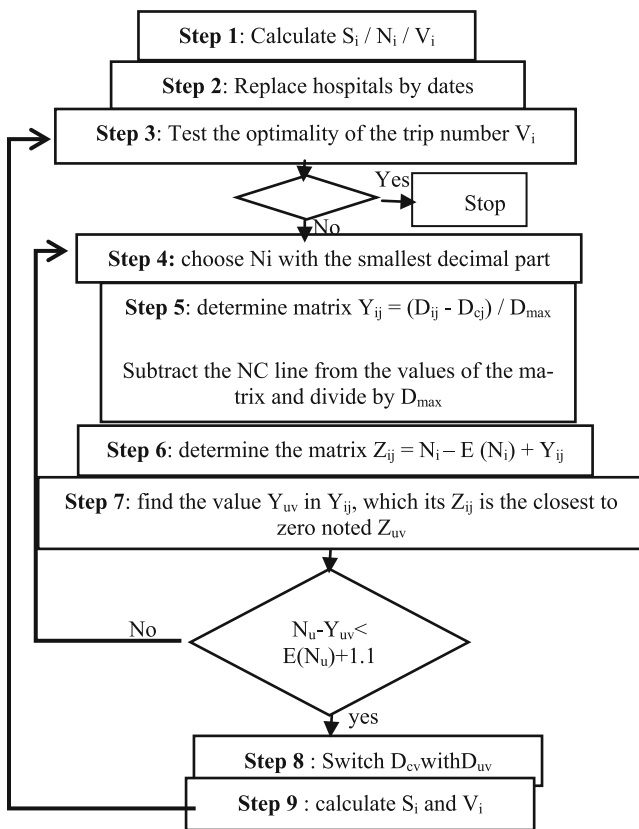
6 Conclusion and Perspectives

Our objective in this study is to show the importance of collaborative supply chain to help organizations to achieve their objectives and controlling their related costs. Based on the case of Tunisian hospital pharmacies, we have proposed a set of highly related and complementary strategies. We started by the strategy of placing orders in different dates, which allowed 83.33% of hospitals that have a problem of drug shortage to be covered to more than 100% of their needs. We have also proposed the standardization of order dates which helped hospitals to reduce the number of orders and the strategy of group purchasing organization which allowed a gain of 12.5% on the total number of delivery and therefore on transport costs. However, the idea of borrowing medicines from network members was not well studied, which can be a good solution for hospitals to not have a drug shortages problem. For future work, we propose an information system that helps hospitals to share data about forecast consumption and the stock level at the end of each period. In addition, it will classify the concerned members according to a set of criteria like the delivery cost. Therefore, the hospital, which has a drug shortage problem, will choose the best solution between borrowing drugs from his partners and placing a new order to the PCT.

References

Al-ruthia YS et al (2016) Shortage of psychotropic medications in community pharmacies in Saudi Arabia: causes and solutions. Saudi Pharm J. https://doi.org/10.1016/j.jsps.2016.10.013

Alshehri S, Alshammari A (2016) Drug supply shortages in pharmacies: causes and solutions case study in King Khaled Eye Special Hospital. Int Bus Manag (Medwell Journals) 10 (12):2453–2459

Boyle K (2012) Drug shortages : canadian strategies for a complex. Healthc Manag Forum 2012 25:S48–S52. https://doi.org/10.1016/j.hcmf.2012.07.017

Casassus B (2014) Health professionals say that a coordinated response is needed to protect patients in European. The Lancet 385(9975):1279–1280. https://doi.org/10.1016/S0140-6736(15)60667-5

Golembiewski J (2012) Drug shortages in the perioperative setting: causes, impact, and strategies. J PeriAnesthesia Nurs 27(4):286–292. https://doi.org/10.1016/j.jopan.2012.05.005

Hassan MD (2005) Engineering supply Chains as systems as systems. Syst Eng 9(1) https://doi.org/10.1002/sys.20042

Simatupang TM, Sridharan R (2002) The collaborative supply chain. Int J Logistics Manag 13 (1):15–30. https://doi.org/10.1108/09574090210806333

Trouiller P (2013) Appui technique pour l'amélioration de la gestion et de l'organisation des pharmacies hospitalières. Guide d'organisation et de fonctionnement de la pharmacie hospitalière, Maroc

Weerdt E, Simoens S, Hombroeckx L et al (2015) Causes of drug shortages in the legal pharmaceutical framework. Regul Toxicol Pharmacol 71(2):251–58. https://doi.org/10.1016/j.yrtph.2015.01.005

On the Role of Activation Volume Parameter in Heterogeneous Deformation of Zr-Based Metallic Glasses

M. Belkacem and T. Benameur

Abstract We report activation volume measurements of Zr-based Bulk Metallic Glasses (BMGs) through nanoindentation tests. Monotonic and cyclic nanoindentation loadings are carried out at rates ranging from 250 to 2500 μN/s and at ambient temperature. The quantitative analysis of the activation volume parameter is determined using depth variation at constant load. In particular, the effect of loading rates on the activation volume of metallic glass is studied. Under quasi-static cyclic loading, series of measurement revealed that activation volume depending on the number of cycles and the loading rates. Indeed, a significant increase in the order of 96% of activation volume at 250 μN/s is determined. Furthermore, a quantitative analysis in terms of the plastic yield criterion for improving the identification of the shear band initiation key parameter in the BMGs is developed. Both the Von Mises and Mohr Coulomb constitutive description of plastic yield criterion were used in the calculation of the activation volume parameter. The numerical results based on Mohr Coulomb criterion are three to four times higher than the Von Mises criterion.

Keywords Metallic glass · Nanoindentation · Shear band · Activation volume · Von Mises · Mohr Coulomb

1 Introduction

In 1960, the first metallic glass (or amorphous metal) was synthesized by rapid quenching from the liquid state at very high rates (10^6 K/s) (Klement et al. 1960). Contrary to the crystalline counterparts, this process prevents atoms to be organized

M. Belkacem (✉) · T. Benameur
Laboratory of Mechanical Engineering, National School of Engineers of Monastir,
Av. Ibn El Jazzar, 5019 Monastir, Tunisia
e-mail: madihabelkacem@gmail.com

T. Benameur
e-mail: t.benameur@enim.rnu.tn

813

in a crystalline order, leading to an ill-defined atomic structure. Afterwards, in 1980 (Inoue et al. 1988), bulk metallic glasses (BMGs), whose thickness can reach 10 cm, were developed. Below the glass transition temperature, T_g, their mechanical properties are characterized by high strength (2000 MPa for Zr-based BMGs), large elastic strain (∼2%), low elastic modulus, and high toughness. The very high strength is a promising property for structural applications of bulk metallic glasses. However, the absence of macroscopic plastic deformation is a main disadvantage of bulk metallic glasses. BMGs presented a brittle mechanical behavior under tensile loading. Yet, investigations have shown micro plasticity events in BMGs. Indeed, the deformation mechanism is related to the formation of shear bands. Under tensile test, at ambient temperature, BMGs presented an elastic-brittle behavior when fracture occurs without plastic flow (Leamy et al. 1972). Under compression, tests show that the mechanical behavior is perfect elastoplastic (Bruck et al. 1996), and the plastic deformation is associated to the generation of a large number of shear bands. When free volume is retained, local shearing and dilatation of a group of atoms occur under stress, initiating the formation of thin shear bands.

So far, instrumented nanoindentation was widely used to investigate the individual shear band event. In that respect, shear band initiation can be estimated by the measurement of the activation volume through the nanoindentation tests (Champion and Nowak 2008). It is an important parameter that makes it possible to approach the mechanisms of deformation of the metallic glasses that intrinsically depends on the volume of STZ (Shear Transformation Zone). Indeed, in nanoindentation, serrations (pop-ins) are observed in load-displacement curves (Schuh et al. 2002; Greer et al. 2004). The activation volume is defined as the variation, with the applied stress, of the energy barrier of the thermally activated process controlling shear band formation (Thurieau et al. 2015; Perrière et al. 2013). In addition, the activation volume is calculated using depth variation at constant load (Thurieau et al. 2015; Perrière et al. 2013). In this study, cyclic nanoindentation tests in quasi-static and incremental solicitation are conducted for Zr-based BMGs. The objectives of this work are to calculate the activation volume of a Zr-based bulk metallic glass and to shed further light on the influence of Mohr Coulomb plasticity criterion in the quantitative evaluation of the activation volume in order to examine the shear band initiation in Zr-based BMGs.

2 Experimental Details

The metallic alloys used in this study $Zr_{60}Cu_{20}Al_{10}Ni_{10}$, $Zr_{65}Cu_{15}Al_{10}Ni_{10}$, and $Zr_{50}Cu_{40}Al_{10}$ (in at. %) BMG were prepared by arc-melting a mixture of pure elements with purities ranging from 99.9 to 99.99% and under a purified argon atmosphere. The amorphicity was checked using a monochromatic X-ray diffractometer. The nanoindentation experiments were conducted, at room temperature, using Triboindenter (Hysitron). This system is connected to a digital instrument

D3100 AFM. The load and depth resolutions are 1 nN and 0.04 nm, respectively. Tests were made with a pyramidal diamond Berkovich indenter (E = 1141 GPa, $\nu = 0.07$) with a total included angle of 142.3° and a finite tip radius of 100 nm. Prior to testing, fused silica was used as a reference for the calibration of the area function. Monotonic and cyclic loading were conducted at different loading rates ranging from 250 to 2500 µN/s. Nanoindentation tests were performed under maximum load of 3750 µN as well as incremental cyclic loading experiments with a load varying from 1000 to 6000 µN. Ten tests were repeated and the results were presented within standard deviation of less than 5%. A dwell period of 120 s was imposed to correct for the thermal drift in the system.

3   Results and Discussion

During cyclic nanoindentation, at varying loading rates, pile-ups were observed. Figure 1 shows the formation of shear bands during quasi-static cyclic nanoindentation test for $Zr_{50}Cu_{40}Al_{10}$. The indent image by atomic force microscopy (AFM) shows semicircular shear bands around the indent (a Berkovich tip has been employed) at different loading rates of 250, 500, and 2500 µN/s and constant load of 3500 µN. The indents surface, obtained after 10 cycles loading, decrease about 28% when the loading rate increase from 250 to 2500 µN/s. The decrease suggests that elastic recovery increases significantly at higher loading rate.

Instrumented nanoindentation was used for the characterization of metallic glasses. Typical example of loading-unloading curve variation, at applied force of 350 mN, is given in Fig. 2. From nanoindentation curves, the hardness H and the Young modulus E are estimated according to the model of Oliver and Pharr (1992). For $Zr_{60}Cu_{20}Ni_{10}Al_{10}$ at strain rate of 0.05 s^{-1}, H is 6.25 GPa and E is 110 GPa. Many studies analyzed the load-displacement curve of BMGs exploring serrations

Fig. 1 AFM images of indents in $Zr_{50}Cu_{40}Al_{10}$ at different loading rate of 250, 500, and 2500 µN/s and at constant load of 3500 µN
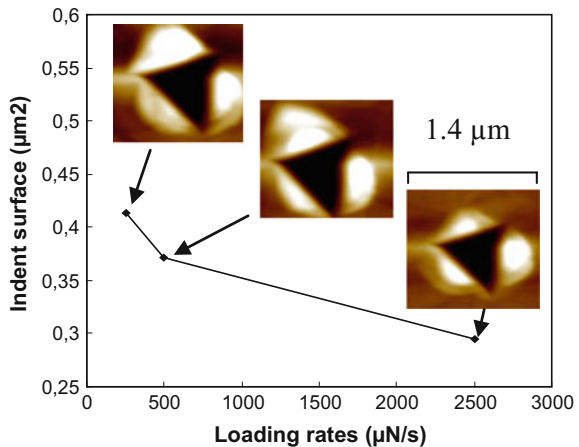
(or *pop-ins*) formation. Figure 3 shows the load-displacement curves of $Zr_{60}Cu_{20}Ni_{10}Al_{10}$, during loading phase, at different strain rates of 0.02, 0.05, and 0.1 s^{-1}. At low strain rates, the loading curve presented many serrations of rapid displacement at constant load. But, this phenomenon disappear for high strain rates (0.1 s^{-1}). Schuh et al. (2002) suggested that the disappearance of pop-in at high loading rates was caused by the kinetic limitation on the nucleation of shear bands. The formation of pop-ins is associated to the activation of shear band events. This relationship is explored for a wide range of metallic glasses, from thin films to bulk.

Furthermore, the activation volume of Zr-based MGs can be determined using nanoindentation data based on the method proposed by Perrière et al. (2013)and Thurieau et al. (2015). The activation volume can be obtained from the depth variation at constant load. The variation of the depth with time, at constant load, was plotted with a logarithm function in Fig. 4. The depth is defined by:

$$h_{fit} = A + B \cdot \ln(t) \qquad (1)$$

Fig. 2 Load as a function of depth in monotonic nanoindentation of $Zr_{60}Cu_{20}Ni_{10}Al_{10}$ at strain rate of 0.05 s^{-1}. The maximum load $F_{max} = 350$ mN
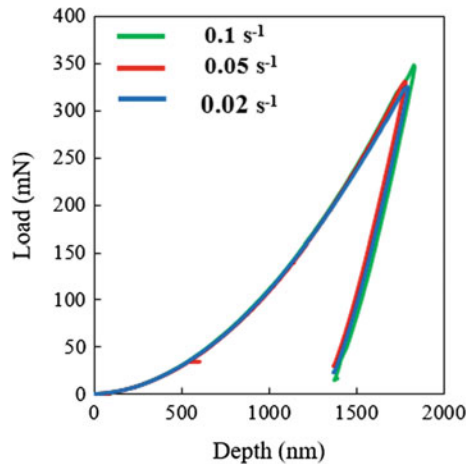
Fig. 3 Load as a function of depth obtained for $Zr_{60}Cu_{20}Al_{10}Ni_{10}$ at a loading of 3500 μN/s and at different strain rates. Curves are offset from the origin for clear viewing. The effect of the loading rate on bursts formation is highlighted
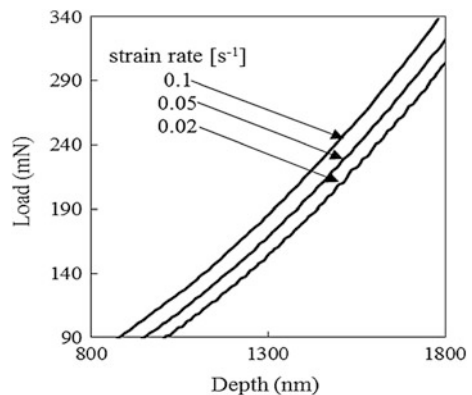
Fig. 4 Depth as a function of time at constant load for $Zr_{50}Cu_{40}Al_{10}$. Δh is the maximum depth parameter starting at 75.1 min
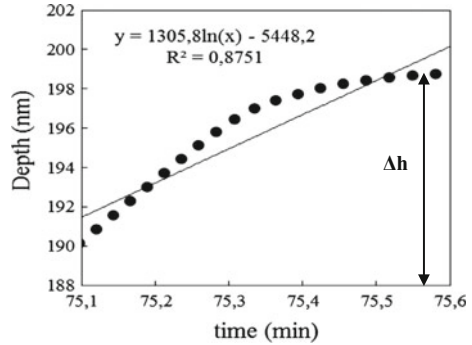
The shear rate is assumed as (Dubach et al. 2007):

$$\dot{\gamma} = \dot{\gamma}_0 \exp\left(-\frac{Q - \tau V}{KT}\right) \tag{2}$$

where $\dot{\gamma}$ is the shear rate, $\dot{\gamma}_0$ is a constant, Q is the activation free energy for the elementary deformation mechanism, τ is the applied shear stress, K is the Boltzmann constant, and T is the temperature.

Therefore, the activation volume, V, controlling initiation of shear bands in the localized deformation process was given by:

$$V = KT\left(\frac{\partial \ln(\dot{\gamma})}{\partial \tau}\right) = MKT\left(\frac{\partial \ln(\dot{\varepsilon})}{\partial \sigma}\right) \tag{3}$$

where M is the Taylor factor of the order of $\sqrt{3}$ (Perrière et al. 2013; Champion et al. 2008). M relates the macroscopic applied stress σ, to the shear stress τ, in a Von Mises plasticity criterion.

In nanoindentation, with Berkovich tip, the stress is given by:

$$\sigma = \frac{F_{\max}}{3.3 \times 24.5 \times h^2} \tag{4}$$

Moreover, the strain rate is calculated as:

$$\dot{\varepsilon} = \frac{1}{h} \cdot \frac{dh}{dt} \tag{5}$$

where h is the indentation depth. Thus, the activation volume can be rewritten through formula transformation of the Eqs. (4) and (5) as (Thurieau et al. 2015):

$$V = -\frac{MKT \times 3.3 \times 24.5}{2 \times F_{max}} \cdot h_0^2 \times \left(\frac{(\ln(\frac{t_i}{t_f}) \cdot h_0)}{\Delta h} - 1\right) \tag{6}$$

where h_0 is the initial depth. Note that this equation is valid only if the yielding criterion used is the Von Mises criterion. In Fig. 5, the activation volume varies with Δh is shown for $Zr_{50}Cu_{40}Al_{10}$. Where Δh is the maximum depth variation during constant load Fmax = 1878 μN for Δt = 4 s. For Δh = 4 nm, the activation volume V = 0.124 nm^3.

Moreover, to quantify the variation of activation volume of $Zr_{50}Cu_{40}Al_{10}$ in each cycle, both, quasi-static and incremental cyclic loading are conducted. The influence of the number of cycles on the activation volume measurements were examined at loading rates of 250–2500 μN/s (Fig. 6). For incremental cyclic loading, the measurements are conducted at applied force ranging from 1000 to 6000 μN. Figure 6a shows that activation volume is independent of loading rate at

Fig. 5 Activation volume variation as a function of Δh at loading rate of 2500 μN/s
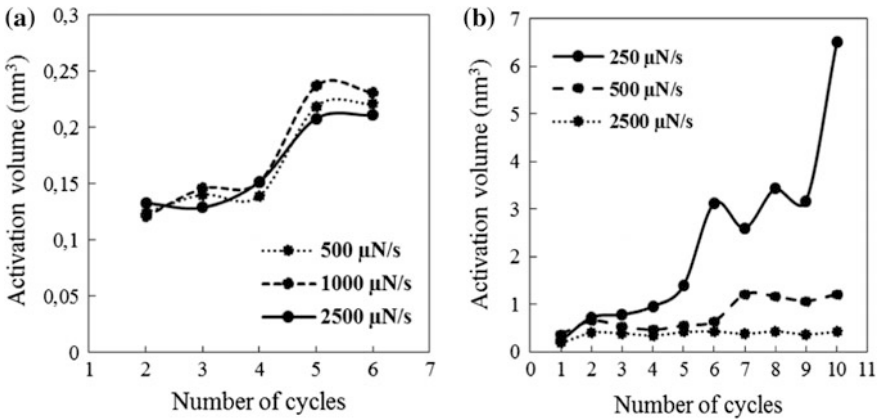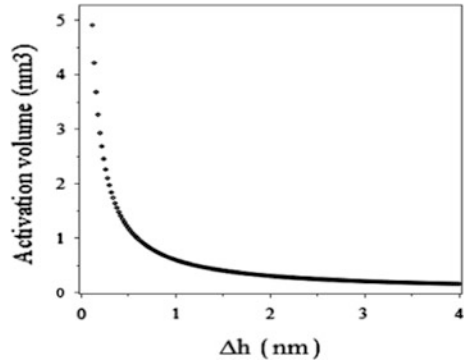
Fig. 6 Activation volume variation as a function of number of cycles at **a** incremental cyclic loading, **b** quasi-static cyclic load at different loading rates
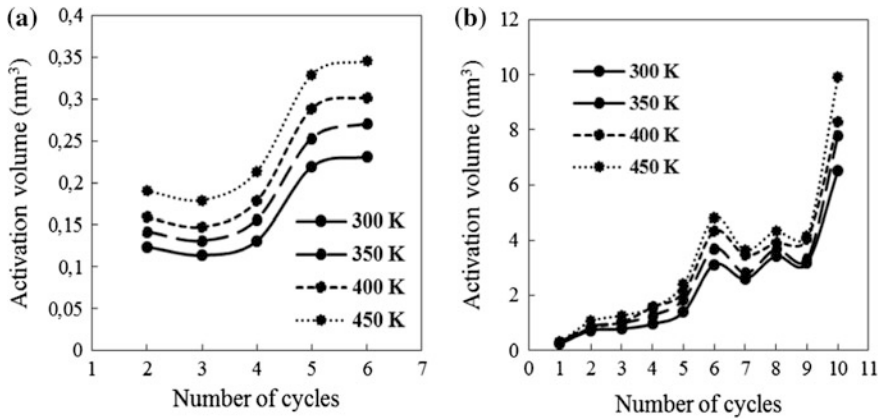
Fig. 7 Activation volume variation as a function of number of cycles at **a** incremental cyclic loading, **b** quasi-static cyclic load at different temperatures

ambient temperature. However, for quasi-static cyclic loading, at loading rate 250 μN/s, the activation volume V increases by 96.5% from 0.231 to 6.503 nm^3.

Furthermore, for both quasi-static and incremental cyclic loading, the effect of temperature is examined. For $Zr_{50}Cu_{40}Al_{10}$, Fig. 7 shows the variation of Activation volume as a function of the number of cycles and temperature for the quasi-static cyclic loading (Fig. 7a) and the incremental cyclic loading (Fig. 7b). The activation volume increases with the increase of temperature.

Vaidyanathan et al. (2001) have shown that Mohr Coulomb criterion adequately models the deformation mechanism of Zr-based BMGs. Indeed, experimental studies of nano- and microindentation show that the load-depth response with a Mohr Coulomb criterion is the most appropriate, suggesting the influence of a normal stress component. In addition, Zhang et al. (2003) demonstrated that deformation in bulk metallic glass follows a Mohr Coulomb criterion rather than the Von Mises criterion. The Mohr Coulomb criterion, which is sensitive to the local normal stress, is written by:

$$\tau_c = k_0 + \alpha \sigma_n \tag{7}$$

where τ_c is the shear stress, k_0 and α are constants, $\alpha = 0.13$ (Vaidyanathan et al. 2001) and σ_n is the normal stress. In that respect, a comparison between the Von Mises and Mohr Coulomb criterion is established in order to examine the influence of the normal stress on the activation volume. Figure 8a, b illustrate the significant higher values of activation volume observed with Mohr-Coulomb constitutive law description for $Zr_{50}Cu_{40}Al_{10}$. Based on the Mohr Coulomb criterion, the activation volume is rewritten by:
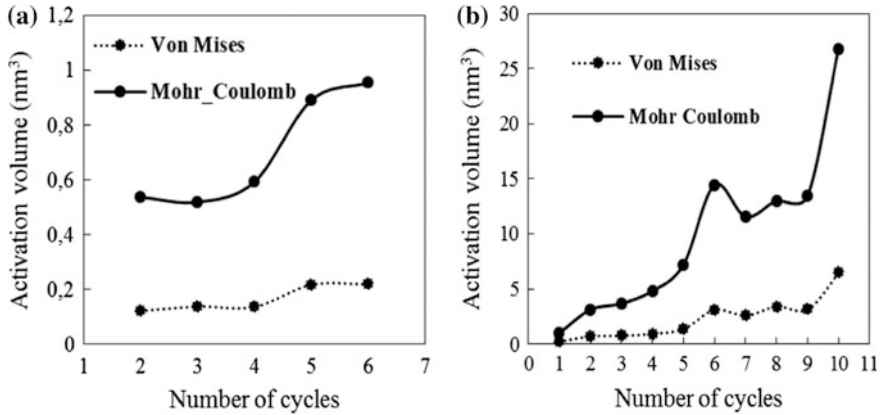
Fig. 8 Activation volume considering the Von Mises and Mohr Coulomb criterion at **a** incremental cyclic loading, **b** quasi-static cyclic loading

Table 1 Comparison of the activation volume, AV, for different metallic glasses, the effect of yielding criterion is highlighted

References	Metallic glasses	AV_Von Mises (nm^3)	AV_Mohr Coulomb (nm^3)
Thurieau et al. (2015)	$Mg_{65}Cu_{12.5}Ni_{12.5}(Ce_{75}La_{25})10$	0.1–0.8	–
Perrière et al. (2013)	$Zr_{57}Cu_{20}Al_{10}Ni_8Ti_5$	0.205	–
Perrière et al. (2013)	$Zr_{58.4}Cu_{24.5}Al_{6.4}Ni_{6.7}Sn_4$	0.194	–
Perrière et al. (2013)	$Zr_{50.3}Cu_{29.8}Al_{7.5}Ni_{8.1}Sn_{0.3}W_4$	0.17	–
Perrière et al. (2013)	$Zr_{50}Cu_{50}$	0.190	–
Perrière et al. (2013)	$Zr_{48}Cu_{48}Sn_2W_2$	0.189	–
Perrière et al. (2013)	$Zr_{44}Cu_{44}Al_8Sn_2W_2$	0.167	–
Present results	$Zr_{60}Cu_{20}Al_{10}Ni_{10}$_Monotonic	0.106–0.573	0.482–2.691
Present results	$Zr_{65}Cu_{15}Al_{10}Ni_{10}$_Monotonic	0.156–0.52	0.701–2.341
Present results	$Zr_{50}Cu_{40}Al_{10}$_Monotonic	0.124–0.182	0.536–0.867
Present results	$Zr_{50}Cu_{40}Al_{10}$_Incremental	0.124–0.231	0.536–0.956

$$V = -\frac{KT \times 3.3 \times 24.5}{2 \times \alpha \times F_{max}} . h_0^2 \times \left(\frac{(\ln(\frac{t_i}{t_f}).h_0)}{\Delta h} - 1 \right). \tag{8}$$

However, (Argon 1978) has proposed a theory of the plastic deformation in metallic glasses below their glass transition temperature T_g. This is based on shear transformation zones, STZs, which are thermally activated. Hence, many authors have established measurements of activation volume in order to identify the plastic deformation of bulk metallic glasses (Thurieau et al. 2015; Perrière et al 2013).

Moreover, these measurements are calculated assuming Von Mises criterion constitutive description. All the results deduced from Mohr Coulomb criterion are listed in Table 1 in comparison with the results obtained by Von Mises criterion. The measurements obtained in this work are in good agreement with the data reported in the literature assuming Von Mises plasticity criterion. However, it is clearly seen that the activation volume parameter shows three to four times higher values when accurate Mohr Coulomb constitutive description of mechanical behavior of BMGs is applied.

4   Conclusions

Nanoindentation measurements were carried out on Zr-based metallic glasses. Monotonic and cyclic loading at rates ranging from 250 to 2500 µN/s and at ambient temperature were designed.

The quantitative analysis of the activation volume was deduced from depth variation at constant load. Under quasi-static cyclic loading, a series of measurement revealed that the activation volume depends on the number of cycles and the loading rates. Furthermore, both the Von Mises and Mohr-Coulomb constitutive description of plastic yield criterion were applied in the calculation of the activation volume. The results obtained using Mohr Coulomb criterion are two to three times higher than those obtained based on Von Mises criterion.

References

Argon AS (1978) Plastic deformation in metallic glasses. Acta Mater
Bruck HA, Rosakis AJ, Johnson WL (1996) The dynamic compressive behavior of beryllium bearing bulk metallic glasses. J Mater Res 11(2):503–511
Champion Y, Nowak S (2008) Activation volume in fine grained metals from stress relaxation and nano-indentation. Mater Sci Forum 584–586:399–404
Champion Y, Langlois C, Guérin S, Duhamel C (2008) Analysis of ductility of nanostructured copper prepared by powder metallurgy. Eng Fract Mech 75:3624–3632
Dubach A, Dalla Torre FH, Loffer JF (2007) Deformation kinetics in Zr-based bulk metallic glasses and its dependence on temperature and strain-rate sensitivity. Philos Mag Lett 87: 695–704
Greer AL, Castellero A, Madge SV, Walker IT, Wilde JR (2004) Nanoindentation studies of shear banding in fully amorphous and partially devitrified metallic alloys. Mater Sci Eng 375–377:1182–1185
Inoue A, Ohtera K, Kita K, Masumoto T (1988) New amorphous Mg-Ce-Ni alloys with high strength and good ductility. Jpn J Appl Phys 27:L2248–L2251

Klement W, Willens RH, Duwez P (1960) Non-crystalline structure in solidified gold-silicon alloys. Nature 187:869. https://doi.org/10.1038/187869b0

Leamy HJ, Chen HS, Wang TT (1972) Plastic flow and fracture of metallic glass. Metall Trans 3:699

Oliver WC, Pharr GM (1992) An improved technique for determining hardness and elastic modulus using load and displacement sensing indentation experiments. J Mater Res 7:1567

Perrière L, Nowak S, Brossard S, Thai MT, Blétry M, Champion Y (2013) Nanoindentation study of chemical effects on the activation volume controlling shear band initiation in metallic glasses. Scripta Mater 8:183–186

Schuh CA, Nieh TG, Kawamura Y (2002) Rate dependence of serrated flow during nanoindentation of a bulk metallic glass. J Mater Res 17(7):1651–1654

Thurieau N, Perrière L, Laurent-Brocq M, Champion Y (2015) Activation volume in heterogeneous deformation of $Mg_{65}Cu_{12.5}Ni_{12.5}$ $(Ce_{75}La_{25})_{10}$ metallic glass. J Appl Phys 118:204–302

Vaidyanathan R, Dao M, Ravichandran G, Suresh S (2001) Study of mechanical deformation in bulk metallic glass through instrumented indentation. Acta Mater 49:3781–3789

Zhang ZF, Eckert J, Schultz L (2003) Difference in compressive and tensile fracture mechanisms of $Zr_{59}Cu_{20}Al_{10}Ni_8Ti_3$ bulk metallic glass. Acta Mater 51:1167–1179

Inhomogeneous Wave Correlation for Propagation Parameters Identification in Presence of Uncertainties

Ramzi Lajili, O. Bareille, M.-L. Bouazizi, M.-N. Ichchou
and N. Bouhaddi

Abstract In order to achieve more realistic structural parameter identification, it is inevitable to account for uncertainties. The present paper proposes a stochastic identification process to identify propagation parameters such as the wavenumber, the damping loss factor, and the wave attenuation, in presence of uncertainties. The proposed stochastic identification process combines, in a wave propagation framework, the Inhomogeneous Wave Correlation method with the Latin Hypercube Sampling method. It is compared to the identification process combining the Mc Daniel method and the Latin Hypercube Sampling method which are considered as reference for structural identification and uncertainty propagation, respectively. An isotropic beam example is considered and identification is done from

R. Lajili (✉) · O. Bareille · M.-N. Ichchou
Laboratory of Tribology and Dynamics of Systems (LTDS),
Ecole Centrale de Lyon, 36 Avenue Guy de Collongues, 69130 Ecully, France
e-mail: ajiliramsis@gmail.com

O. Bareille
e-mail: olivier.bareille@ec-lyon.fr

M.-N. Ichchou
e-mail: mohamed.ichchou@ec-lyon.fr

R. Lajili
National School of Engineers of Tunis (ENIT), University of Tunis El Manar,
BP 37, Le Belvedere, 1002 Tunis, Tunisia

R. Lajili · M.-L. Bouazizi
Research Unit of Structural Dynamics, Modelling and Engineering of Multi-Physics,
Preparatory Engineering Institute of Nabeul (IPEIN), 8000 M'rezgua, Nabeul, Tunisia
e-mail: mohamedlamjed@gmail.com

N. Bouhaddi
Department of Applied Mechanics, FEMTO-ST Institute, CNRS/UFC/ENSMM/UTBM,
University of Bourgogne Franche-Comté, 25000 Besançon, France
e-mail: noureddine.bouhaddi@univ-fcomte.fr

M.-L. Bouazizi
Mechanical Department, College of Engineering, Prince Sattam Bin Abdulaziz University,
Al-Kharj, KSA, Saudi Arabia

823

Frequency Response Functions computed at several measurement points which coordinates are supposed to be the uncertain parameters. The effects of uncertainties on parameter identification are evaluated through statistical quantifications of the variability of the identified parameters. Obtained results show that all identified parameters are affected by uncertainties, except damping.

Keywords Structural identification · Inhomogeneous wave correlation Uncertainties · Latin hypercube sampling · Wavenumber · Damping

1 Introduction

Structural identification forms an ever growing emphasis in engineering applications. Since modal identification approaches reach their limits in mid and high frequencies where great modal density exists, other identification methods based on the wavenumber space (k-space) analysis are introduced in the literature Ichchou et al. (2008a). The most frequently used methods are the Mc Daniel method (McDaniel and Shepard 2000a) and the Inhomogeneous Wave Correlation (IWC) (Berthaut et al. 2005) method. For each frequency, the Mc Daniel method adjusts iteratively the wavenumber and the damping, starting from neighboring-frequencies wavenumbers. The efficiency of the Mc Daniel method with respect to the modal approach was proved in (McDaniel and Shepard 2000b) one-dimensional application consisting of a freely suspended beam. Its extension, later (Ferguson et al. 2002), to a two-dimensional application was based on a Continuous Fourier Transform (CFT) and a least square minimization in order. Correlating vibratory fields with inhomogeneous waves is the principle of the IWC method. It permits to build a frequency and direction-dependent dispersion equation from a space vibratory field. In the literature, Berthaut et al. (2005) and Ichchou et al. (2008b) proved the ability of the IWC method to identify accurately structural parameters of isotropic and aniso-tropic ribbed panels and plates. The authors illustrated the dependence of the loss factor on the wave direction and its independence on boundary conditions, geometry and source location. IWC application was extended in Ichchou et al. (2008a) to honeycomb beams and panels identification at wide frequency band and, then, in (Inquiété 2008) to a quasi-isotropic laminated composite plate identification. Rak et al. (2008) applied both Mc Daniel and IWC methods to identify the damping of a homogeneous beam covered with viscoelastic layers. Non-reliable IWC identification was obtained since identified loss factor was negative. In Chronopoulos et al. (2013), the IWC method was compared with the Wave Finite Element Method (WFEM) for propagation characteristics identification of a composite panel. The IWC method identification was based on the vibratory data measured by the experimental configuration and was compared to the Wave Finite Element Method (WFEM) estimation. Cherif et al. (2015) used the IWC method to identify accurately the damping of orthotropic honeycomb panels, based on experimental and numerical results. The accuracy of the method was proven through its comparison to other

classical methods such as the 3 dB method, the decay rate method and the power input method.

To achieve realistic identification, it is inevitable to account for uncertainties. Quantifying and propagating uncertainties permits to evaluate them, impact and obtain an agreement between design models and experimental analyses. Focusing on parametric uncertainties (e.g., geometrical parameters, loading forces) and according to probabilistic modeling, random variables are used to quantify the variability of affected parameters. Stochastic methods allow propagating uncertainties to evaluate the stochastic impact of uncertain input parameters on output responses if direct problems are considered and inversely if inverse problems are considered. Several stochastic methods are introduced in the literature. The most commonly used methods are the sample-based ones. The Monte Carlo Simulations (Fishman 1996; Rubinstein and Kroese 2008) and the Latin Hypercube Sampling (LHS) (McKay et al. 1979; Helton and Davis 2003) are frequently used. Based on successive deterministic evaluations, the LHS method permits to reduce the prohibitive computational time required by the MCS method without a significant loss of accuracy. It allows reducing the number of samples by partitioning the variability space into regions of equal probability and selecting one sampling point in each region.

The originality of this work lies in proposing a stochastic identification process, which combines the above-cited parameter identification methods (IWC and Mc Daniel) with the LHS uncertainty propagation method. The effect of uncertainties on parameter identification is evaluated through statistical quantifications of the variability of the identified parameters of an isotropic beam example.

2 Theoretical Backgrounds

2.1 Mc Daniel Method

Let's consider a harmonic displacement field which depends on space coordinates:

$$u = \Re\left\{Ue^{-i\omega t}\right\} \tag{1}$$

where $\Re\{\}$ Refers to the real part and U to the displacement amplitude.

The Mc Daniel method consists of solving the linear differential equation of motion of the neutral axe or surface of the structure which takes the form

$$-\omega^2 U + \mathcal{L}\{U\} = 0 \tag{2}$$

where $\mathcal{L}\{\}$ is a linear operator containing the displacement derivatives with respect to the space coordinate x.

Taking into account boundary conditions:

$$\mathcal{L}_b\{u\}|_{(x=x_b)} = \Re\{Be^{-i\omega t}\} \tag{3}$$

where x_b represents boundaries and B is complex valued, the solution of Eq. (2) is expressed as

$$U(x) = \sum_{n=1}^{N}\left\{F_n e^{ik_n x} + B_n e^{ik_n(L-x)}\right\} \tag{4}$$

where N is the number of different waves. Each wave n is characterized with a wavenumber k_n of complex value containing positive real and imaginary parts and an amplitude F_n or B_n according to forward or backward propagation, respectively, and computed using boundary conditions.

The wavenumber is computed according to the type of the propagated wave through the structure. It is, in fact, expressed, in the flexural, longitudinal, and torsion wave case, respectively, as

$$k_f = \sqrt[4]{\frac{\rho A\omega^2}{E(\omega)(1-i\eta(\omega))I}},\ k_l = \sqrt{\frac{\rho\omega^2}{E(\omega)(1-i\eta(\omega))}},\ k_t = \sqrt{\frac{\rho\omega^2}{G(\omega)(1-i\eta(\omega))}} \tag{5}$$

where $E(\omega)$ and $G(\omega) = E(\omega)/2(1+\nu)$ are the real parts of the Young and shear modulus, respectively, ρ is the mass density, I the inertia moment, A the area of the transversal section and $\eta(\omega)$ the material loss factor.

The loss factor depends on the wavenumber and can consequently be identified by

$$\eta_f = \left|\frac{\Im\{k_f^4\}}{\Re\{k_f^4\}}\right|,\ \eta_i = \left|\frac{\Im\{k_i^2\}}{\Re\{k_i^2\}}\right| \tag{6}$$

where $\Im\{.\}$ and $\Re\{.\}$ correspond respectively to the imaginary and real parts. The index i can refer to the indexes l or t according to the specific cases longitudinal and torsion, respectively.

To verify the validity of the initially supposed wavenumber, it is compared to the obtained wavenumber through the error function defined as

$$\varepsilon^2(k) = \sqrt{\frac{\sum_{m=1}^{M}\rho(x_m)|U^{mes}(x_m,\omega) - U(x_m,\omega)|^2}{\sum_{m=1}^{M}\rho(x_m)|U(x_m,\omega)|^2}} \tag{7}$$

where M is the number of considered measurement points, $\rho(x_m)$ the coherence function and $U^{mes}(x_m,\omega)$ and $U(x_m,\omega)$ are the measured and real wave fields,

respectively. To minimize this error, an optimization algorithm varying the wavenumber is implemented.

2.2 Inhomogeneous Wave Correlation (IWC) Method

The IWC method uses a harmonic field $U(x, y)$, calculated either from a harmonic excitation or from a temporal Fourier transform

$$u(x, y, t) = \int\limits_{0}^{+\infty} U(x, y)e^{-i\omega t}d\omega \tag{8}$$

The principle of the IWC method is to compute propagation parameters, such as the wavenumber k and the wave attenuation γ, by correlating the vibratory field $u(x, y, \omega)$ of the structure with an inhomogeneous wave

$$u_{IWC} = e^{-ik(\theta)(1 + i\gamma(\theta))(x\cos(\theta) + y\sin(\theta))} \tag{9}$$

where θ is the wave direction.

The correlation is performed through an IWC criterion defined as

$$IWC(k_{IWC}, \gamma_{IWC}, \theta) = \frac{\left|\iint_S u.\bar{u}_{IWC}dxdy\right|}{\sqrt{\iint_S u.\bar{u}.dxdy \times \iint_S u_{IWC}.\bar{u}_{IWC}.dxdy}} \tag{10}$$

where $\bar{u}_{IWC}$ is the complex conjugate of the wave u_{IWC}. This criterion represents the wave (u_{IWC}) contribution in the field $u(x, y, \omega)$ or also the ratio of the energy carried by the wave by the total energy contained in the field. Maximizing the IWC correlation criterion leads to optimizing the wavenumber and damping identification.

According to the works performed in Berthaut (2004) on plate structures, for a zero fixed damping $(\gamma_0 = 0)$ (undamped wave) and direction $(\theta_0 = 0)$, the wavenumber k_0 is calculated for a maximal IWC criterion. Then, the damping γ_0 is computed. For the initial obtained couple (k_0, γ_0), an iterative algorithm is implemented to calculate the couples (k_i, γ_i) for a finite set of directions θ_i. The couple (k_i, γ_i) being calculated, they are sorted and the damping values which correspond to vanishing waves, which don't transport energy, $\gamma(\theta_i) > 1$ are eliminated. If the correlation criterion is very low meaning that the wave transport very small energy, the corresponding couple (k_i, γ_i) is also eliminated. The final step consists in varying the frequency band of study and identifying the wavenumber $k(\theta, \omega)$ and the damping $\gamma(\theta, \omega)$ for each frequency iteration.

For numerical discrete analysis, integrals in Eq. (10) are replaced by weighted discrete sums:

$$IWC(k, \gamma, \theta) = \frac{\left|\sum_M \rho_i u . \bar{u}_{IWC} S_i\right|}{\sqrt{\sum_M \rho_i |u|^2 S_i \cdot \sum_M \rho_i |u_{IWC}|^2 S_i}} \tag{11}$$

where S_i is the elementary surface of the structure corresponding to the measurement point i and M is the number of measurement points.

3 Analytical-Numerical Model of an Isotropic Beam

We propose to compute numerically the harmonic displacement field $U(x, t)$ of an isotropic clamped-free beam with a membrane loading applied on its free extremity: $F = F_0 e^{i\omega t}$. The geometrical and mechanical properties of the beam are presented in Table 1. Damping is introduced into the system using a complex Young modulus given by $E = E_0(1 + i\eta)$ where η is the structural loss factor.

If a membrane loading is considered, the equation of motion, also called the wave propagation equation, is expressed as:

$$-ES\frac{\partial^2 U(x, t)}{\partial x^2} + \rho S \frac{\partial^2 U(x, t)}{\partial t^2} = F(x, t) \tag{12}$$

where $U(x, t)$ refers to beam membrane deformation when x is the longitudinal direction. E is the Young modulus, ρ the density, and S the cross section.

The solution of Eq. (12) takes the form

$$U(x, t) = u(x)e^{i\omega t} \tag{13}$$

where ω is the angular frequency and $u(x) = A_1 e^{-ikx} + A_2 e^{ikx}$.

The longitudinal wave Eq. (14) is a sum of traveling (incident) wave moving in the $-x$ sense and deflected wave moving in the $+x$ sense. A_1 represents thus the incident wave coefficient while A_2 stands for the reflected wave coefficient. These unknown constants can be evaluated in terms of the physical boundary conditions.

Computing the constants A_1 and A_2 according to the clamped-free beam configuration (clamped boundary: $U(x = 0, t) = 0$. Free boundary: $ES\frac{\partial U(x = L, t)}{\partial x} = -F_0 e^{i\omega t}$) leads to the following expression of the harmonic displacement field

$$u(x_j) = \frac{F_0}{iESk_l(e^{-ikL} + e^{ikL})} e^{-ikx_j} - \frac{F_0}{iESk_l(e^{-ikL} + e^{ikL})} e^{ikx_j} \tag{14}$$

Table 1 Geometrical and mechanical properties of the isotropic beam

Parameters	b (m)	h (m)	v	E_0 (GPa)	ρ (kg m^{-3})	F_0 (N)
Value	0.029	0.015	0.29	210	7800	10

This longitudinal wave case implies defining the wavenumber as $k(\omega) = \omega/c_\varphi$ where $c_\varphi = \sqrt{E/\rho}$ is the wave (or propagation) velocity. The wave attenuation γ, representing the spatial damping, is related to the structural damping loss factor η by $\eta = (2c_g/c_\varphi)\gamma$, where c_g is the group velocity defined as $c_g = \partial\omega/\partial k$. Consequently, $c_g = \omega/k = c_\varphi$ and $\eta = 2\gamma$.

We propose to identify the wavenumber, the wave attenuation, the damping loss factor, and the phase velocity. The IWC method is applied and compared to the Mc Daniel method.

3.1 Deterministic Identification

Figure 1 illustrates the variation of the wavenumber and the phase velocity according to frequency computed using the IWC method and the Mc Daniel method.

The approximations obtained using the IWC method are in agreement with those obtained by the Mc Daniel method. Figure 2 shows the variation of the wave attenuation and the damping loss factor according to frequency.

Some oscillations affect the IWC estimations at low frequencies, this disadvantage of the method is also mentioned in Berthaut (2004) and Inquiété (2008). The authors demonstrated the IWC method accuracy at mid and high frequencies when high modal overlap occurs and thus energy is distributed in all propagation directions. Nevertheless, at low frequencies, when low modal overlaps occur, the IWC method reaches its limits.

As shown in Fig. 3, the errors of the IWC estimations of the wavenumber and the wave attenuation are small at high frequencies. More accurate results are obtained for the identified wavenumber while more oscillations affect the identified wave attenuation, especially at low frequencies.

The IWC identification method proves its efficiency, with respect to the reference Mc Daniel method. It is important to note that this efficiency is independent of
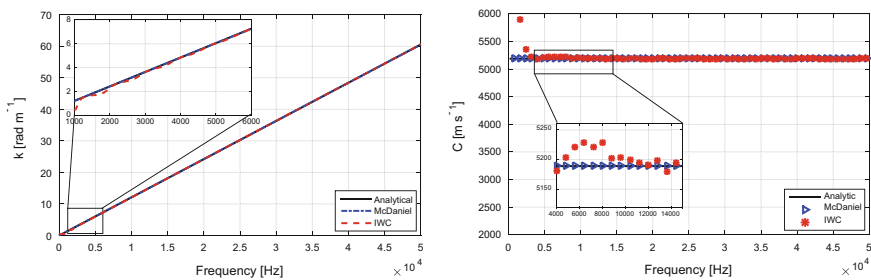
Fig. 1 Wavenumber and phase velocity variation according to frequency, computed using the Mc Daniel method and the IWC method
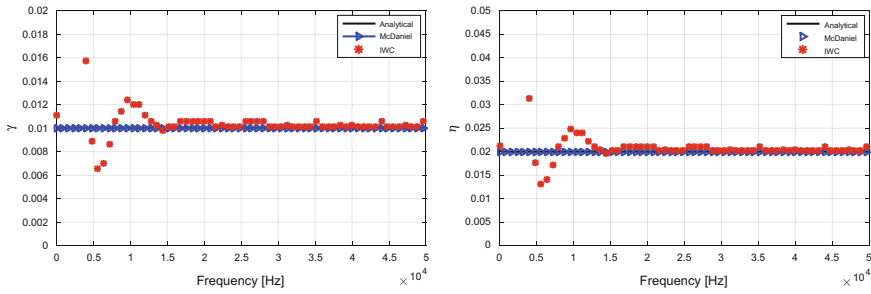
Fig. 2 Wave attenuation and damping loss factor variations according to frequency, computed using the Mc Daniel method and the IWC method
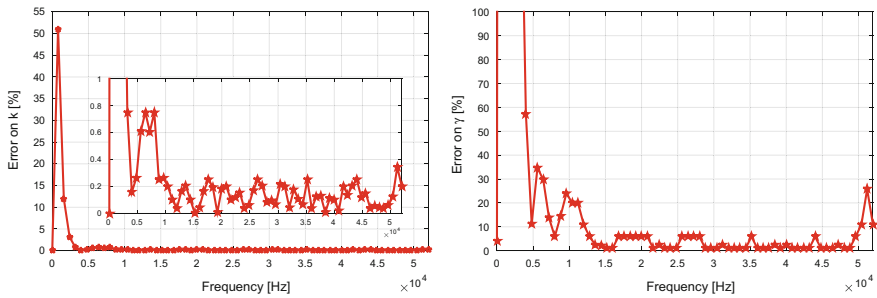
Fig. 3 Errors on wavenumber and wave attenuation computed using the IWC method with respect to those computed using the Mc Daniel method

the applied boundary conditions. In fact, several configurations of boundary conditions are studied but for clarity, only the membrane loading configuration is illustrated here.

3.2 Identification in Presence of Uncertainties

Measurement point's coordinates are supposed to be uncertain; their variability is modeled by random variables. The measurement point's vector is thus expressed as

$$x_s = x(1 + \delta_x \xi) \tag{15}$$

where x is the vector containing the mean coordinates of the measurement points, δ_x is the dispersion value and ξ is a normal random variable.

In presence of uncertainties, a stochastic identification process combines uncertainty propagation with parameter identification. In the present paper, the LHS method could be combined with either the Mc Daniel method or the IWC method.

Thousand samples of random variable are considered. Thousand successive deterministic simulations are thus generated. At final, several post-processing quantities are computed, such as mean, extreme statistics, standard deviation, and dispersion. The LHS method permits to reduce the CPU computational time required by the MCS method, for 10,000 samples, by 90.04%, without a significant loss of accuracy.

Figure 4 illustrates the mean, the envelope (extreme statistics), the standard deviation, and the dispersion (standard deviation/mean) of the stochastic identified wavenumber.

A very good agreement is obtained between the Mc Daniel method and the IWC method. The envelope and the standard deviation of the wavenumber variability (Fig. 4b–c) increase with frequency. Since the mean and the standard deviation increase similarly, a nearly constant dispersion is obtained (Fig. 4d). Note that for a given dispersion value 5% on the stochastic input parameter leads to a nearly 5% of dispersion of the identified wavenumber.

The quantification of the damping loss factor variability through statistical evaluations is illustrated in Fig. 5. Contrary to the wavenumber, the damping is not affected by uncertainties. This can be deduced from perfect superposition of the mean, maximal and minimal curves (Fig. 5a), and the null standard deviation and dispersion (Fig. 5b).
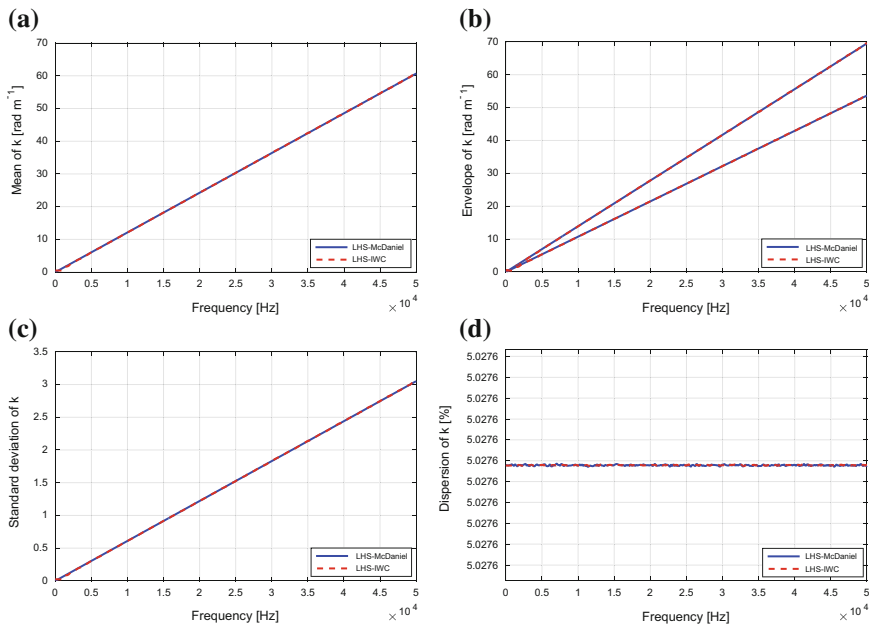
Fig. 4 **a** Mean, **b** envelope, **c** standard deviation, and **d** dispersion of the wave number computed using the identification process combining the LHS method with the Mc Daniel method and the IWC method for $\delta_x = 5\%$
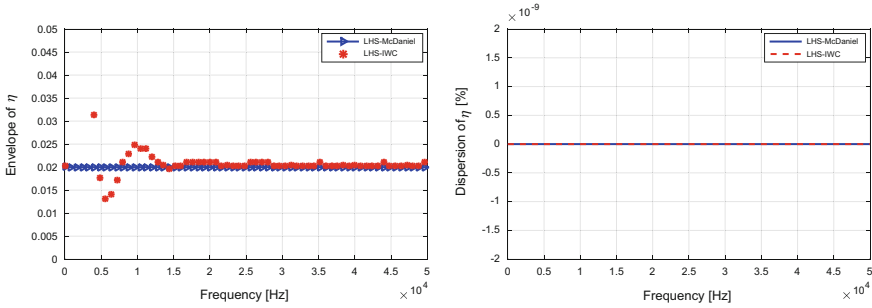
Fig. 5 **a** Envelope and **b** dispersion of the damping loss factor computed using the identification process combining the LHS method with the Mc Daniel method and the IWC method for $\delta_x = 5\%$

Berthaut et al. (2005) and Ichchou et al. (2008b) illustrated that the loss factor doesn't depend on boundary conditions, nor on geometry, nor on source location. The independence on geometry is proved in this work since damping is not affected by the randomness of the coordinates of the measurement points.

4   Conclusion

To achieve more realistic structural identification, uncertainties were then taken into account. To analyze their effect on identified parameters, a stochastic identification process combining the LHS uncertainty propagation method with the IWC method is proposed and compared to the identification process combining the LHS method with the Mc Daniel method. Statistical evaluations illustrated the effect of uncertainties on the identified wavenumber. Nevertheless, no stochastic effect was found on the damping loss factor. This result agrees with the already demonstrated geometry-independence of the damping, in the literature.

In spite of efficiency of the IWC method at high frequencies and its independence on the boundary and loading conditions, inaccurate estimations are obtained at low frequencies. This inaccuracy results from oscillatory estimations. In future works, it should be interesting to improve the IWC method with special concentration on low-frequency identification.

References

Berthaut J (2004) Contribution à l'identification large bande des structures anisotropes—Application aux tables d'harmonie des pianos. PhD thesis: Ecole Centrale de Lyon, France.
Berthaut J, Ichchou MN, Jezequel L (2005) K-space identification of apparent structural behavior. J Sound Vib 280:1125–1131

Cherif R, Chazot J-D, Atalla N (2015) Damping loss factor estimation of two-dimensional orthotropic structures from a displacement field measurement. J Sound Vib 356:61–71

Chronopoulos D, Troclet B, Bareille O, Ichchou M (2013) Modeling the response of composite panels by a dynamic stiffness approach. Compos Struct 96:111–120

Ferguson NS, Halkyard CR, Mace BG, Heron KH (2002) The estimation of wavenumbers in two dimensional structures. In: Proceedings of ISMA II, pp 799–806

Fishman GS (1996) Monte Carlo: concepts, algorithms, and applications. Springer-Verlag, New York

Helton JC, Davis FJ (2003) Latin hypercube sampling and the propagation of uncertainty in analyses of complex systems. Reliab Eng Syst Saf 81:23–69

Ichchou MN, Berthaut J, Collet M (2008a) Multi-mode wave propagation in ribbed plates: part I, wavenumber-space characteristics. Int J Solids Struct 45:1179–1195

Ichchou MN, Bareille O, Berthaut J (2008b) Identification of effective sandwich structural properties via an inverse wave approach. Eng Struct 30:2591–2604

Inquiété G (2008) Numerical simulation of wave propagation in laminated composite plates. PhD thesis: Ecole Centrale de Lyon, France

McDaniel JG, Dupont P, Salvino L (2000a) A wave approach to estimating frequency-dependent damping under transient loading. J Sound Vib 231(2):433–449

McDaniel JG, Shepard WS (2000b) Estimation of structural wave numbers from spatially sparse response measurements. J Acoust Soc Am 108(4):1674–1682

McKay MD, Beckman RJ, Conover WJ (1979) A comparison of three methods for selecting values of input variables in the analysis of output from a computer code. Technometrics 2:239–245

Rak M, Ichchou MN, Jan H-S (2008) Identification of structural loss factor from spatially distributed measurements on beams with viscoelastic layer. J Sound Vib 310:801–811

Rubinstein RY, Kroese DP (2008) Simulation and the Monte Carlo method, 2nd edn. Wiley

Experimental and Numerical Study on Force Reduction in SPIF by Using Response Surface

Badreddine Saidi, Laurence Giraud-Moreau, Atef Boulila, Abel Cherouat and Rachid Nasri

Abstract The single point incremental forming process is an emerging process which presents an alternative to the conventional sheet-metal forming processes like stamping and drawing. It is particularly suitable for prototyping and low production thanks to its flexibility and low cost. The objective of this paper is to study the incremental forming of titanium grade2 and AISI 304L stainless steel sheets. The forming force of sheet titanium grade2 and 304L steel parts formed by single point incremental process depends on different parameters (tool path, tool size, materials and shape, friction, etc.). During the process, considerable forces can occur which must be controlled to ensure the safe use of the CNC milling machine. The aim of this paper is to study the effect of different process parameters on the maximal force. Experimental and numerical studies are performed. An optimization method based on the use of an experimental design and response surface method is used to minimize the forming force.

B. Saidi
ISET Radés département de Génie Mécanique, Avenue de France, Radès, Tunisia
e-mail: badreddinesaidi@yahoo.fr

B. Saidi · L. Giraud-Moreau (✉) · A. Cherouat
Institut Charles Delaunay-UMR CNRS 6281-GAMMA3, Université de Technologie de
Troyes, 12 rue Marie Curie-CS 42060, 10004 Troyes Cedex, France
e-mail: laurence.moreau@utt.fr

A. Cherouat
e-mail: abel.cherouat@utt.fr

A. Boulila
Institut National des Sciences Appliquées et de Technologie, Centre Urbain Nord, BP 676,
1080 Tunis Cedex, Tunisia
e-mail: atef.boulila@gmail.com

B. Saidi · R. Nasri
Ecole Nationale d'Ingénieurs de Tunis, MAI, BP 37, 1002 Tunis Le Belvédère, Tunisia
e-mail: rachidnasri2003@yahoo.fr

835

1 Introduction

The single point incremental forming presented in Fig. 1 is a new forming process perfectly suited for prototyping and small volume production. It is a very flexible process which has received great attention from the engineering community (Ambrogio et al. 2004; Duflou et al. 2007; Saidi et al. 2015; Thibaud et al. 2012). The forming force is an important parameter of this process which must be controlled to ensure the preservation of the tooling and the machinery, the safe use of the CNC milling machine or the industrial robot (Saidi et al. 2016; Shanmuganatan and Senthil Kumar 2014). The forming force value is particularly important when ASTM grade2 titanium or stainless 304L steel sheets are used. The aim of this study is to optimize input process parameters in order to minimize the maximal forming force.

An experimental study based on a Taguchi orthogonal experimental design (Table 1) is conducted (Thibaud et al. 2012). The influence of three input parameters (material (Rm), punch diameter (dp), and steps size (Δz)) on the forming force is analyzed. Numerical simulations of the incremental forming process are realized. Comparison of numerical and experimental results is realized to validate the numerical approach. A response surface methodology is used to obtain the optimal combination of input process parameters allowing to minimize the forming force. Comments on the quality of the parts, phenomena associated with the forming (Duflou et al. 2007; Gate et al. 2016) are given.

Fig. 1 Single point incremental sheet forming process (SPIF)
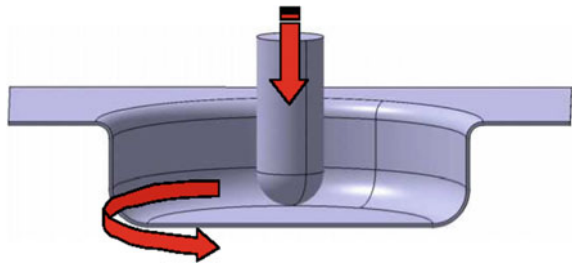
Table 1 Taguchi Experimental design L4

Input parameters	A: Rm (N/mm^2)	B: dp (mm)	C: ΔZ (mm)
E1	650	10	0.5
E2	650	15	1
E3	350	10	1
E4	350	15	0.5

2 Experimental Setup

During the last decades, most of the researchers have concentrated their works on aluminum alloys. In this work, two other materials are studied: ASTM grade2 titanium and 304L stainless steel. Sheets have a thickness of 0.5 mm.

The platform used for the experiment is a 4-axis Spinner MFG 850 milling machine (Kurra and Regalla 2014; Saidi et al. 2015), which is shown in Fig. 2. The device is fixed on a multicomponent FN7325 force sensor which measures the evolution of the forming forces during the process. The experimental device of the single point incremental forming process is presented in Fig. 3.
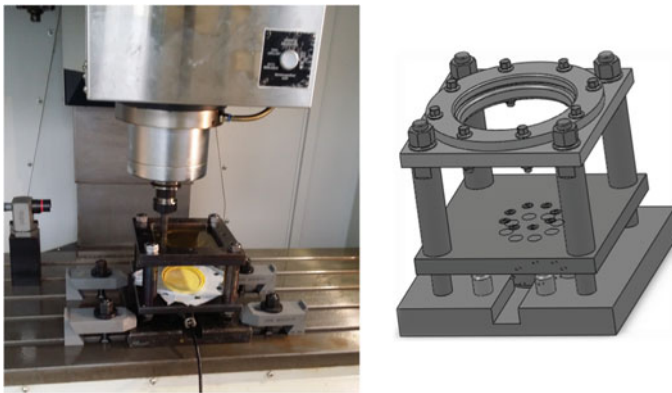
Fig. 2 Spinner 4-axis CNC vertical milling machine
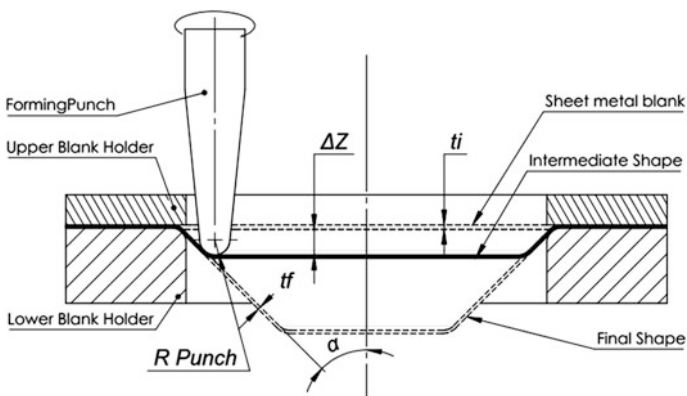
Fig. 3 Single point incremental sheet forming experimental device

3 Experimental Results

The experimental design was performed with (L4) Taguchi orthogonal array three factors (Azaouzi and Lebaal 2012). The three experimental design factors are as follows:

- Materials parameter (maximum tensile strength of material noted **Rm**),
- Tool punch diameter (**dp**), and
- Incremental tool displacement (**Δz**).

In this study, we consider two types of material with Rm = 350 MPa for T40 and Rm = 650 MPa for 304L (Table 2). For the spherical tool punch diameter, we

Table 2 Mechanical characteristics of materials

	E (GPa)	Rpo.2 (MPa)	Rm (MPa)	A (%)
T40	100	210	350	20
304L	210	350	650	50

(a) E1-304L-10-0.5

(b) E1-304L-15-1

(c) E1-T40-10-1

(d) E1-T40-15-0.5
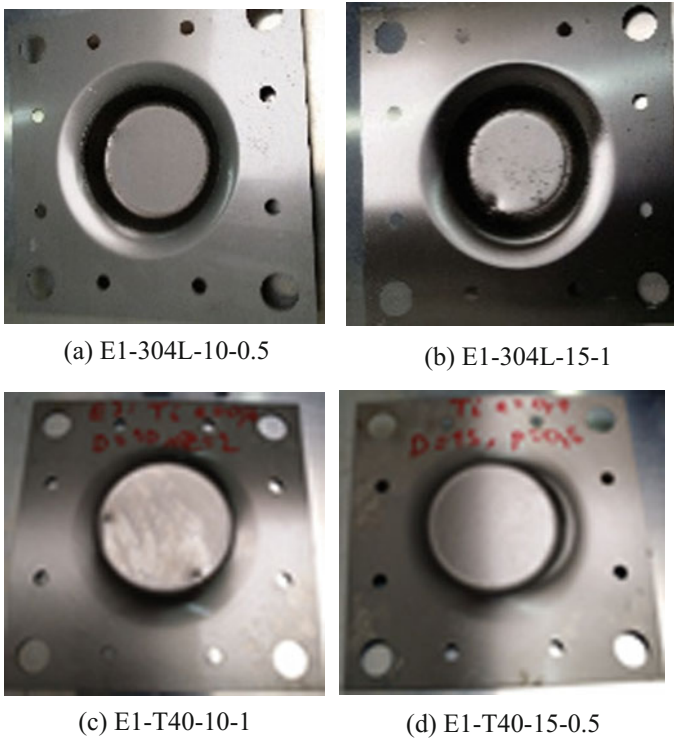
Fig. 4 Experimental shapes for different experimental design cases
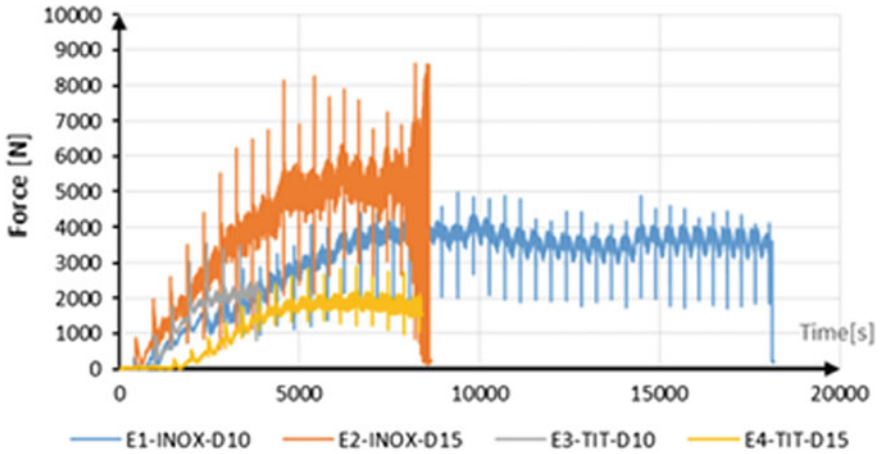
Fig. 5 Force versus time for different shape design cases

consider two values: dp = 10 mm and dp = 15 mm. For the incremental tool displacement, two values are considered: 0.5 and 1 mm. The others process factors are assumed to be fixed at the optimum value such as the rotational speed, the feed rate, the lubricant, the sheet thickness, the depth, and the angle (α) (Fig. 4).

The initial sheet metal is cut by laser into a 300×300 mm^2 size, with using suitable diameter punches of 10 and 15 mm with hardness 55HRC made of X160CrMoV12 steel (Palumbo and Brandizzi 2012). Four experimental design cases were considered and simulated numerically. The average experimental response curve represented by the tool force versus time is illustrated in Fig. 5 for each experimental design. The maximum force is estimated at 5554 N for the E1-304L-15-1 case and at 3966 N for the E1-304L-10-0.5 case. For the E1-T40-10-1 and E1-T40-15-0.5 cases, the maximum force is about 2000 N (see Table 3).

Table 3 Experimental design of Taguchi L4 and forming force responses

	A: Δz (mm)	B: dp (mm)	C: Rm (N/mm^2)	F_{Exp} (N)	F_{num} (N)
E1	0.5	10	650	3966	1360
E2	1	15	650	5554	1520
E3	1	10	350	1794	920
E4	0.5	15	350	1856	875

4 FEM Simulation

This section is dedicated to the validation of the proposed methodology to simulate the single point incremental sheet forming. A three-dimensional finite element analysis (FEA) has been performed using the finite element solver ABAQUS. The numerical model uses linear quadrilateral sheet elements in modeling the initial sheet and rigid finite element to model the tools. The elastoplastic behavior with isotropic hardening model is used to characterize the sheet behavior (Thibaud et al. 2012). The stress–strain material hardening parameters of the sheet are obtained using tensile tests. The predicted deformed sheet and the iso-value of the von Mises stress for the different shape design are shown in Fig. 6.

We can notice that the design shape strongly affects the stress distribution. The maximum stress is estimated of 900 MPa for the shape design E1-304L-10-0.5 and E1-304L-15-1 and of 445 MPa for the shape design E1-T40-10-1 and E1-T40-15-0.5. The predicted force versus time for different shape design cases is presented in Fig. 7. The same trend is observed as in the experimental case.

(a) E1-304L-10-0.5

(b) E2-304L-15-1

(c) E3-T40-10-1

(d) E4-T40-15-0.5
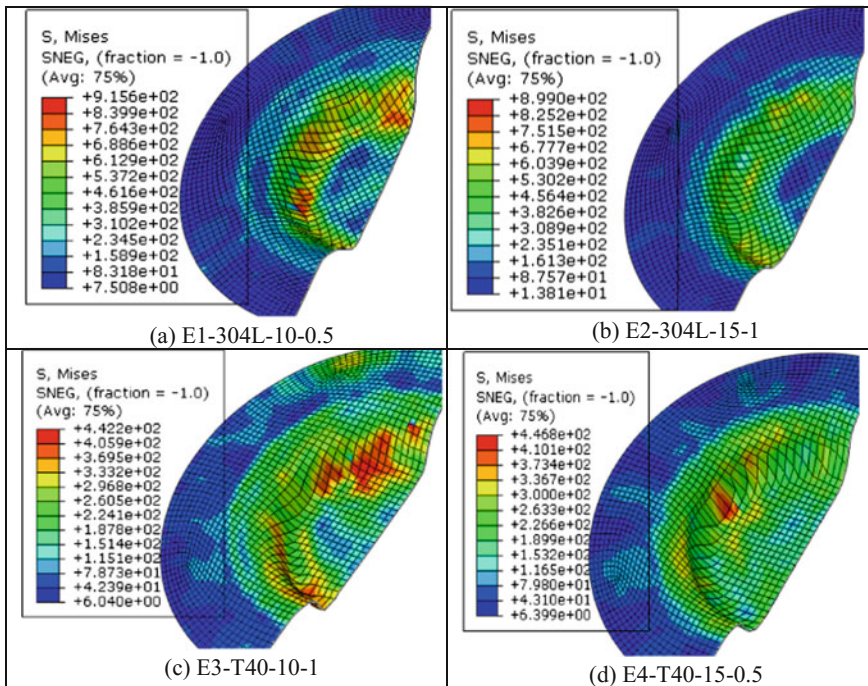
Fig. 6 von Mises stress distribution in sheet for different shape design cases
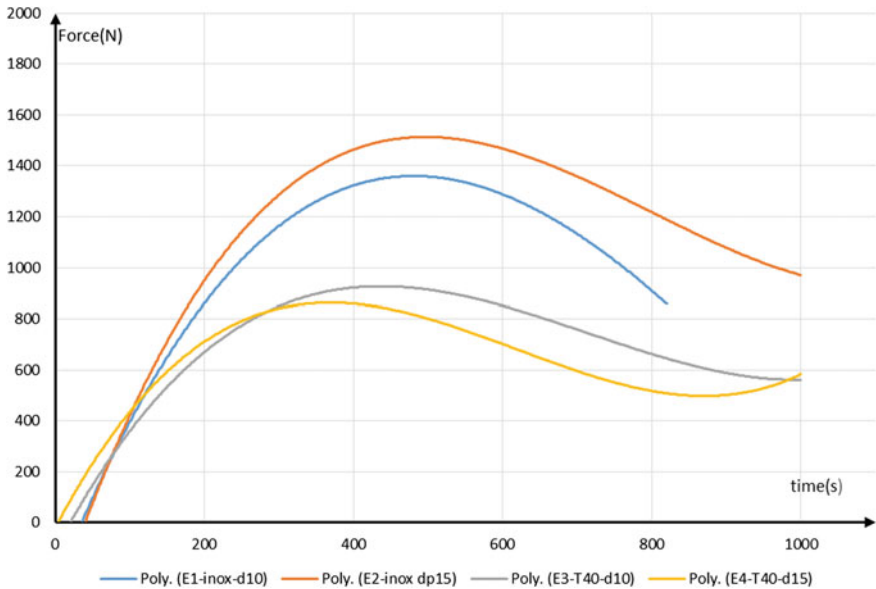
Fig. 7 Predicted force versus time for different shape design cases

5   Design Optimization

The aim of the surface plot is to predict the optimum values of forming force. The 3D response surface plots, which are the material chosen (Rm fixed as 500 MPa), are useful in understanding both interaction properties between the punch diameter (**dp**) and the increment punch displacement (**Δz**) and effect on the forming force. Table 3 presents the obtained results of estimated parameters. The response surface
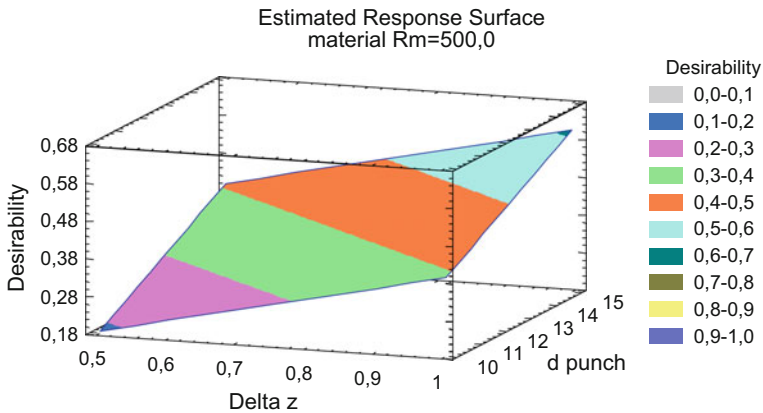
Fig. 8 Experimental force response surface (Rm = 500 MPa)
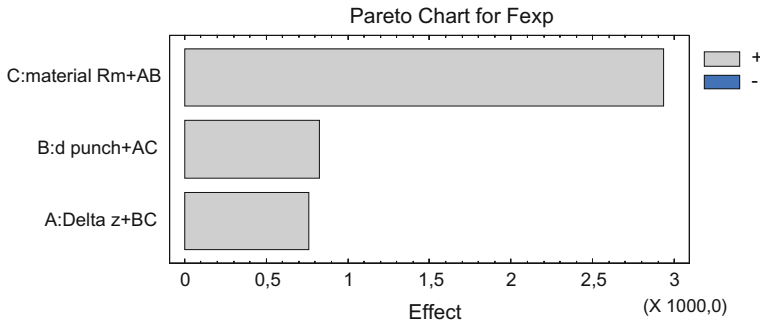
Fig. 9 Pareto chart of effect parameters on F_{exp}

Table 4 Estimated values of input factors on forming force

	Estimated values	
	F_{num}	F_{exp}
Average	2031.75	3292.5
Case A: $\Delta z + BC$	166.5	763.0
Case B: $dp + AC$	264.5	825.0
Case C: $Rm + AB$	1125.5	2935.0

plots in Figs. 8 and 10 and Pareto chart in Figs. 9 and 11 of experimental and numerical results (Saidi et al. 2016; Bahloul et al. 2014).

The desirability function through in this analysis determines the combination of experimental factors, which simultaneously optimize several responses. It does so by minimizing a desirability of experimental and numerical force function. In our study, the obtained parameters are evaluated by the probability value with 95% confidence level. With Taguchi's method, the parameters effects are given in
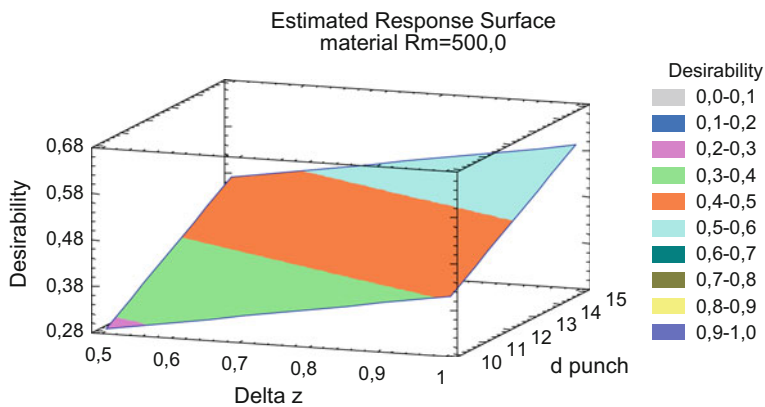
Fig. 10 Input factors effects on numerical force response surface (Rm fixed)

Table 5 Experimental and numerical optimum factors

Factor	Low	High	Optimum experimental	Optimum numerical
Δz (mm)	0.5	1.0	0.5	0.52
dp (mm)	10.0	15.0	10.00	10.54
Force (N)			1051.96	1414.23
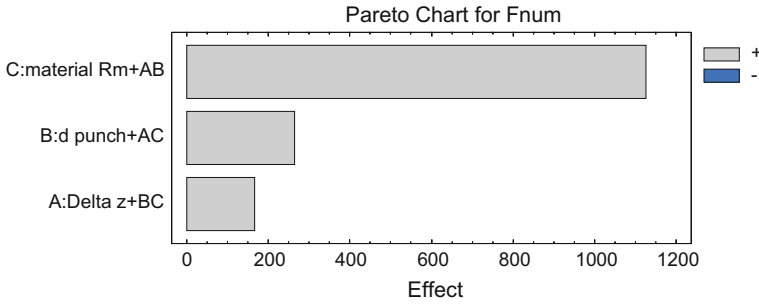
Fig. 11 Pareto chart of effect parameters on F_{num}

Table 4. The 3D response surfaces show the forming force variation with respect to the punch diameter and the increment size tool displacement (Figs. 8 and 10). We can see from these figures that the increase in the tool diameter (**dp**) and the increment tool displacement (**Δz**) increase the force forming force. The results of the selected material (Rm is chosen) are presented in Table 5. Pareto Charts given in Figs. 9 and 11 show each of the estimated effects and interactions.

6   Conclusion

The Taguchi's method of experimental design applied to optimize the forming force is proposed by using response surface methodology. The mechanical characteristic of the material has a significant factor on the forming force of single point incremental sheet forming. The numerical study shows that the increment tool displacement and the spherical punch diameter also have a great effect on the final sheet part (stress distribution, sheet shape and thickness, and forming force). The proposed numerical methodology can be used to optimize the single point incremental sheet forming process.

References

Ambrogio G, Costantino I, De Napoli L, Filice L, Fratini L, Muzzupappa M (2004) Influence of some relevant process parameters on the dimensional accuracy in incremental forming: a numerical and experimental investigation. J Mater Process Technol 153–154(November):501–507. https://doi.org/10.1016/j.jmatprotec.2004.04.139

Azaouzi Mohamed, Lebaal Nadhir (2012) Tool path optimization for single point incremental sheet forming using response surface method. Simul Model Pract Theor 24(May):49–58. https://doi.org/10.1016/j.simpat.2012.01.008

Bahloul R, Arfa H, BelHadjSalah H (2014) A study on optimal design of process parameters in single point incremental forming of sheet metal by combining box-behnken design of experiments, response surface methods and genetic algorithms. Int J Adv Manuf Technol 74(1–4):163–185. https://doi.org/10.1007/s00170-014-5975-4

Duflou J, Tunçkol Y, Szekeres A, Vanherck P (2007) Experimental study on force measurements for single point incremental forming. J Mater Process Technol 189(1–3):65–72. https://doi.org/10.1016/j.jmatprotec.2007.01.005

Gatea S, Hengan O, McCartney G (2016) Review on the influence of process parameters in incremental sheet forming. Int J Adv Manuf Technol 87(1–4):479–499. https://doi.org/10.1007/s00170-016-8426-6

Kurra S, Regalla SP (2014) Experimental and numerical studies on formability of extra-deep drawing steel in incremental sheet metal forming. J Mater Res Technol 3(2):158–171. https://doi.org/10.1016/j.jmrt.2014.03.009

Palumbo G, Brandizzi M (2012) Experimental investigations on the single point incremental forming of a titanium alloy component combining static heating with high tool rotation speed. Mater Des 40(September):43–51. https://doi.org/10.1016/j.matdes.2012.03.031

Saidi B, Boulila A, Ayadi M, Nasri R (2015) Experimental force measurements in single point incremental sheet forming SPIF. Mech Ind 16(4):410. https://doi.org/10.1051/meca/2015018

Saidi B, Giraud-Moreau L, Abel C (2016) Optimization of the single point incremental forming process for titanium sheets by using response surface. In: Saanouni K (ed) MATEC web of conferences 80. pp 10011. https://doi.org/10.1051/matecconf/20168010011

Shanmuganatan SP, Senthil Kumar VS (2014) Modeling of incremental forming process parameters of al 3003 (o) by response surface methodology. Procedia Eng 97:346–356. https://doi.org/10.1016/j.proeng.2014.12.258

Thibaud S, Ben Hmida R, Richard F, Malécot P (2012) A fully parametric toolbox for the simulation of single point incremental sheet forming process: numerical feasibility and experimental validation. Simul Model Pract Theor 29(December):32–43. https://doi.org/10.1016/j.simpat.2012.07.004

Identification of Control Chart Deviations and Their Assignable Causes Using Artificial Neural Networks

Souha Ben Amara, Jamel Dhahri and Nabil Ben Fredj

Abstract In case of complex processes, the identification of out-of-control states, observed on control charts, and their specific assignable causes are very complicated tasks. To overcome these difficulties artificial intelligence techniques have been used. Among these methods, the artificial neural networks can develop intelligence by using process data without need to expert opinion. This paper proposes an original method for process monitoring based on control chart exploration using artificial neural networks applicable for high batch size production requiring high sampling frequency. The developed approach helps to identify the out-of-control states and the corresponding process defects that lead to their occurrences. Attention is given to three most frequently observed cases in industrial practices: shifts, ascending and descending trends, and cyclic phenomena. The developed neural networks use back propagation algorithm and one hidden layer. A real industrial case of study was used to evaluate the recognition and identification performances of the developed artificial neural networks. Results have shown excellent recognition rates that reached percentages of identification of both process deviations and assignable causes higher than 90%.

Keywords Statistical process control · Control charts
Artificial neural networks

S. B. Amara (✉) · J. Dhahri · N. B. Fredj
Laboratoire de Mécanique, Matériaux et Procédés,
Ecole Nationale Supérieure d'Ingénieurs de Tunis, Tunis, Tunisia
e-mail: souhabenamara@yahoo.fr

J. Dhahri
e-mail: jameldhahri@yahoo.fr

N. B. Fredj
e-mail: benfredjnabil@gmail.com

1 Introduction

Statistical process control (SPC) refers to a set of methods used to monitor and improve industrial processes through the setting of several tools such as the control charts (CC). These graphical techniques are widely used to first detect any shift in the process which can lead to an out-of-control situation, and thus resulting on the generation of a high percentage of non-conforming parts. A correct exploration of these charts would then make the identification of the assignable causes of the observed shifts possible and, therefore, act to correct them in time (Montgomery 2009).

The level of reaching these two main objectives depends widely on the process complexity. Indeed, because complex processes are generally controlled by a large number of parameters, the identification of the assignable causes of an observed out-of-control situation on a CC remains complicated.

Moreover, the recognition of the out-of-control situation itself is not evident and requires in many cases the opinion of an SPC expert. This is because several overlapping patterns corresponding to several process states that are generally observed on the CC makes the distinction between controlled and out-of-control situations difficult. To overcome these difficulties and avoid the requirement to the expert opinion, research works have been conducted to develop artificial intelligent methods that help reaching the objectives described above. Even though several approaches were used to develop these methods, i.e., expert system (Evans and Lindsay 1998), fuzzy logic (Chen and Liang 2016; Kaya et al. 2017), Bayes theory (Song et al. 2017; Atoui et al. 2016), artificial neural networks (ANN) is the only approach that can develop intelligence by using process data without need to expert opinion (Zorriassatine et al. 1998). The exhaustive review works of Psarakis (2011), Woodall (2016) concluded that in spite of the high potential that has this technique, its application in SPC is hampered by the lack of reliable databases required for the ANN training and generalization. Therefore, more efforts have to be made to promote the use of this technique in SPC and to evaluate accurately the advantages that may result from its application.

In this paper, attention is given to the development of ANNs capable of recognizing three types of CC out-of-control states: shifts, ascending and descending trends, and cyclic phenomena, and identifying their assignable causes. An industrial case of study is used to evaluate the recognition and identification performances of the developed ANNs.

2 Methodology and Databases Preparation

2.1 Methodology

In this section, the developed methodology for intelligent system development using ANN to help exploring CC is introduced. Databases inputs and outputs definitions and codification used for ANN training and generalization are explained and the method developed to identify the positions of the samples means on the CC is detailed.

2.2 Identification of the Positions of Samples Means and Ranges

In order to eliminate the scale effects of the specification being controlled using CC, normalized CC are used in this investigation. For these charts, averages are set to zero and standard deviations are fixed to one. Therefore, the upper and lower control chart limits (UC Land LCL) are fixed to plus and minus three respectively. To do so, the following expressions are given for chart:

- The mean value of the ith sample $\overline{X}_i$ is normalized as follows:

$$\overline{X}_i \rightarrow Z_i = \frac{\overline{X}_i - \overline{X}}{\sigma_{\overline{X}}} \tag{1}$$

- The control chart limits are normalized as shown by Eqs. (2) and (3)

$$LCS = \overline{\overline{X}} + 3\sigma_{\overline{x}}; \quad LCI = \overline{\overline{X}} - 3\sigma_{\overline{x}} \tag{2}$$

As $\overline{\overline{Z}} = 0 \, and \, \sigma_Z = 1$;

$$LCI = -3; \quad LCI = 3 \tag{3}$$

Therefore, in case of $LCI \leq \overline{X}_i \leq LCS$ implies that $-3 \leq \overline{X}_i \leq 3$.

2.3 Investigated Out-of-Control States

In this paper, attention is given to three types of CC out-of-control states: shifts, ascending and descending trends, and cyclic phenomena. Indeed, according to Apley (2012), these states are the most frequently observed cases in industrial practices. Moreover, as the distinction between shifts and trends is usually

confusing, it is important to evaluate the ability of the developed ANN to distinguish between these two out-of-control states.

2.4 Databases Generation

Review of published research works dealing with the application of ANNs to SPC reveals that the average size of the database used for training varies between dozens (Pham and Oztemel 1993) and millions of data (Anagun 1998) depending on production type, process stability and sampling frequency and reliability.

The developed approach in this paper is applicable for high batch size production requiring high sampling frequency to qualify and control the process and for variables SPC. The set of information that should be contained in the database and the corresponding data treatments are given by Fig. 1. It is important to notice that the recognition of the causes of the out-of-control states is data consuming rather than the identification of the out-of-control state itself. Indeed, the same process defect may conduct to several out-of-control situations and a particular out-of-control state may have several causes. Therefore, in order to develop ANNs that are able to consider these confusing situations, big sizes databases are particularly required in these cases. In this work, sampling results $(\overline{X}_i, R_i)$ are twice normalized: the first normalization is realized according to Eq. (1) and the second normalization is made to have a data set varying between -1 and $+1$. These normalized data are used for the ANN input layer.
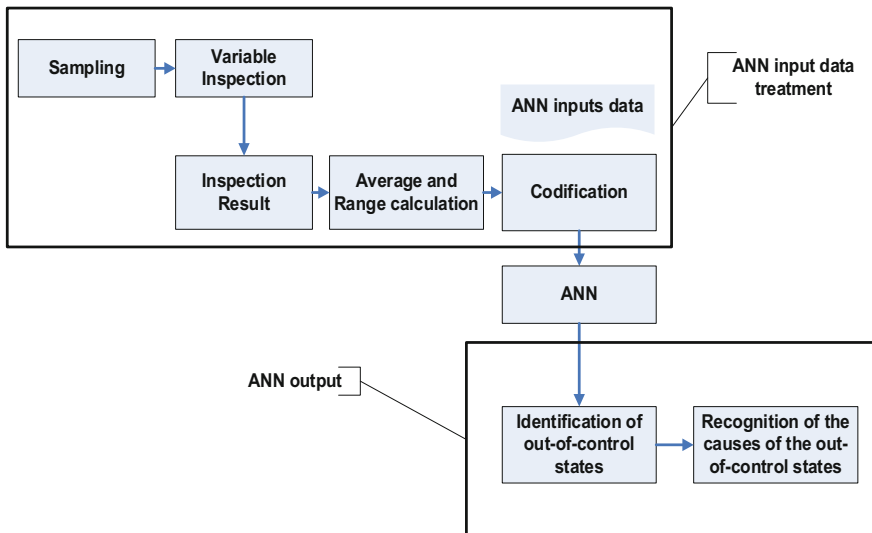
Fig. 1 Databases used for the ANN input and output

Concerning the output data including the out-of-control state and its associated process defects are codified. A binary code was selected for the out-of-control states and an 8 bits hexadecimal codification was used for the assignable causes.

2.5 Developed ANNs Architecture

In this work, ANNs with a single hidden layer using the back propagation algorithm are developed. The number of neurons in the hidden layer equals the value of the window size (WS) used in the CC for the out-of-control state recognition.

2.6 Identification of Assignable Causes

It is established that coding of the data used for training neural networks significantly affects their performances (Yu and Xi 2009; Aparisi and Sanz 2010). Moreover, Guh and Hsieh (1999) noted that adequate coding facilitates the convergence of neural networks. This same rule also applies to the coding of data used by Bayesian networks Weidl et al. (2005), Dhafr et al. (2006); Alaeddini and Dogan (2011) and that the outputs of the networks are strongly affected by the used coding.

The literature shows that this codification takes the form of normalization in the case of quantitative variables. In the case of qualitative inputs, the bibliography does not indicate any particular coding rules. In this study, a binary code specific to each combination of causes generating a particular out-of-control state has been developed (Fig. 2).

In this investigation, even though the applied coding took the form of arborescence of causes as shown in Fig. 2, the direct relation case-effects are not considered. The main advantage form using this strategy is the possibilities that it offers to integrate new causes when they are identified. This technique relies on facts without seeking to establish the logical sequences that would require the opinion of the expert.

The practical implementation of the proposed codification given by Fig. 2, requires the recording of quality problems encountered as well as the corrections that have been made to fixed these problems. These registrations are done in a systematic way in most companies. The statistical master of the processes who wishes to apply the approach developed in this study will have to relate the quality problem encountered in the production line to the specific pattern observed on the control chart (Fig. 3).

It is important to notice, that the use of control charts is to prevent the occurrence of quality problems. Therefore, it becomes necessary to identify the type of out-of-control state that is likely to occur and to fix it before its occurrence.
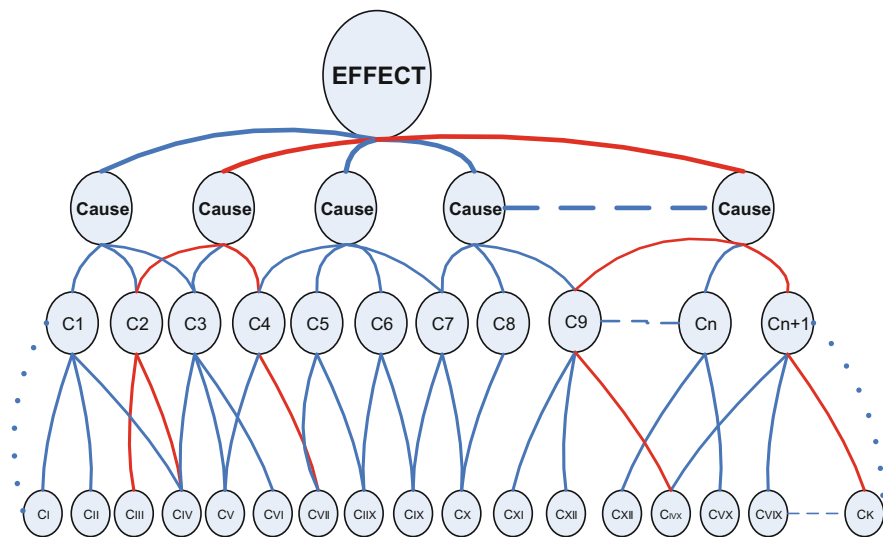
Fig. 2 Codification used for the qualitative variables (C: cause)
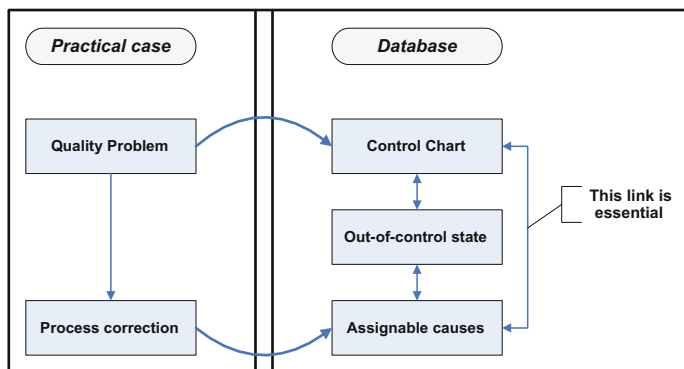
Fig. 3 Relation quality problems, out-of-control states and control charts

3   Industrial Case Study

The industrial case studied consists of the preparation of the clay slurry for the manufacture of ceramic products. The manufacturing process begins with a preparation of the slurry, which then passes through molding, drying, enameling, and finally firing in the furnace. A key specification to ensure quality is to maintain
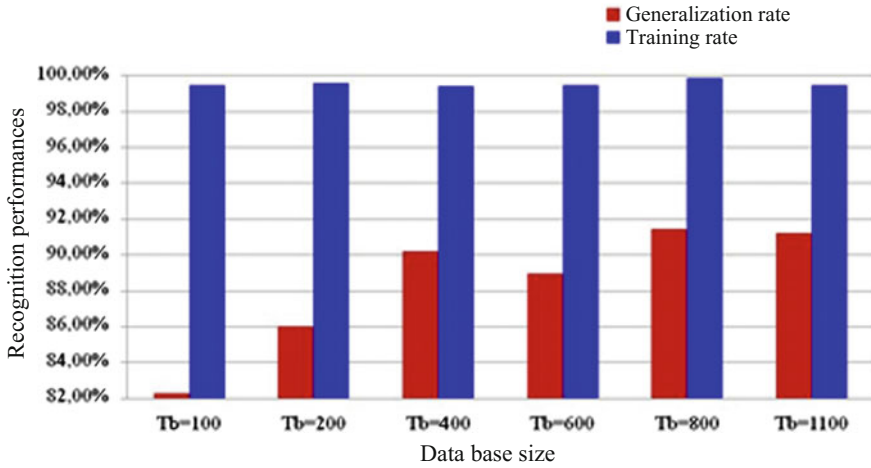
Fig. 4 Accuracy of the out-of-control state identification

the viscosity of the slurry at a predefined level by the specification. This parameter (viscosity) is monitored for 17 h, with a sampling frequency corresponding to half an hour. This makes it possible to construct control charts of type ($\overline{X}_i$, R_i) of 34 points. Each point on the CC represents the average of three measurements taken on a sample with a size n = 3. The number of CC constructed is 1580. The total number of observations is 1580 × 3 × 34 = 161160 measurements. The basis of assignable cause data consists of 46 possible causes capable of generating one or more the out-of-control states cited in the introduction.

Figure 4 shows the existence of thresholds associated with the number of data used for the training of ANNs for which the recognition percentages of the out-of-control states variate little. These thresholds are of capital importance from an industrial point of view. These thresholds indicate the size of the database that will be needed to be available before implementing the approach developed in this study. These thresholds seem to be dependent on the type of the out-of-control state detected on the chart.

Concerning the generalization data, it should be noted that the developed networks are able to distinguish between ascending or descending phenomena with no particular specification between a trend and a shift.

Concerning the recognition of the causes associated with the various out-of-control states, Fig. 5 shows significant high convergence rates (>80%). This is the main finding of the current study, which has enabled the development of a tool helping the exploitation of the control charts used in SPC. The developed tool uses the process data without any need to the opinion of the expert.
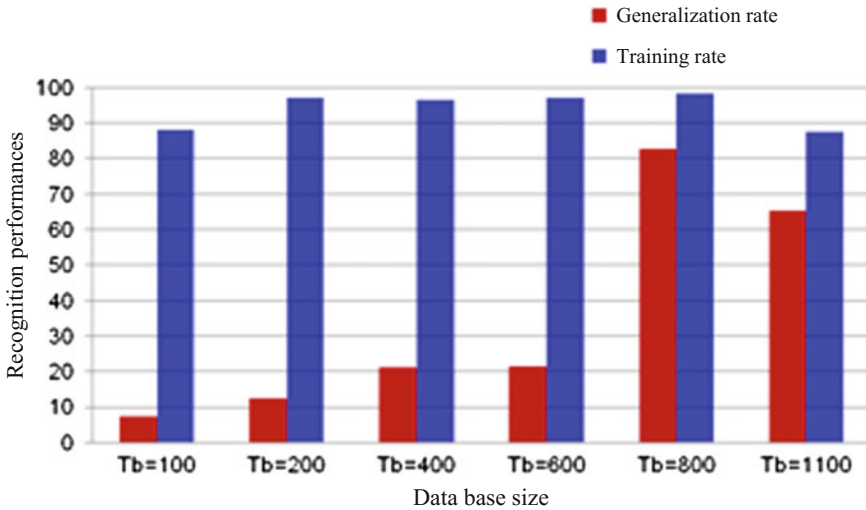
Fig. 5 Accuracy of the out-of-control state causes identification

4 Conclusion

In this study, particular attention has been paid to the problem of exploiting the control charts used in SPC. A tool to support this exploitation based on neural networks has been developed. The main results can be summarized as follows:

- The developed networks have quite high levels of recognition of upward or downward tendencies without specification of the precise type of the out-of-control state (shift or trend) (>90%).
- A recognition rate of the assignable causes to the investigated out-of-control states as high as 80% was recorded as a mean value associated with 480 charts used for the validation tests of the approach developed in this study.

The main advantage of the approach is that it is based on structured data rather than expert opinion, which is often absent in many industrial cases.

References

Alaeddini A, Dogan I (2011) Using bayesian networks for root cause analysis in statistical process control. Expert Syst Appl 38:11230–11243

Anagun AS (1998) A neural network applied to pattern recognition in statistical process control. Comput Ind Eng 35(1):185–188

Aparisi F, Sanz J (2010) Interpreting the out-of-control signals of multivariate control charts employing neural networks. World Acad Sci Eng Technol 61

Apley DW (2012) Posterior distribution charts: bayesian approaches for graphically exploring a process mean. Technometrics 54(3):293–307

Atoui MA, Verron S, Kobi A (2016) A bayesian network dealing with measurements and residuals for system monitoring. Trans Inst Measur Control 38(4):373–384

Chen J, Liang Y (2016) Development of fuzzy logic-based statistical process control chart pattern recognition system. Int J Adv Manuf Technol 86(1):1011–1026

Dhafr N, Ahmad M, Burgess B, Canagassababady S (2006) Improvement of quality performance in manufacturing organizations by minimization of production defects. Robot Comput-Integr Manuf 22:536–542

Evans JR, Lindsay WM (1998) A framework for expert system development in statistical quality control. Comput Ind Eng 14(3):335–343

Guh RS, Hsieh YC (1999) A neural network based model for abnormal pattern recognition of control charts. Comput Ind Eng 36:97–108

Kaya IM, Erdoğan M, Yildiz C (2017) Analysis and control of variability by using fuzzy individual control charts. Appl Soft Comput 51:370–381

Montgomery DC (2009) Statistical quality control: a modern introduction, 6th edn. Wiley, New York

Psarakis S (2011) The use of neural networks in statistical process control charts. Qual Reliab Eng Int 27(5):641–650

Pham DT, Oztemel E (1993) Control chart pattern recognition using combinations of multi-layer perceptions and training vector quantization networks. In: Proceedings of the institution of mechanical engineers, part I: J Syst Control Eng 207(2):113–118

Song H, Xu Q, Yang H, Fang J (2017) Interpreting out-of-control signals using instance-based bayesian classifier in multivariate statistical process control. J Commun Statist—Simul Comput 46(1):53–77

Weidl G, Madsen AL, Israelson S (2005) Applications of object-oriented Bayesian networks for condition monitoring, root cause analysis and decision support on operation of complex continuous processes. Comput Chem Eng 29:196–209

Woodall WH (2016) Bridging the gap between theory and practice in basic statistical process monitoring. Qual Eng. https://doi.org/10.1080/08982112.2016.1210449

Yu JB, Xi LF (2009) A neural network ensemble-based model for on-line monitoring and diagnosis of out-of-control signals in multivariate manufacturing processes. Expert Syst Appl 36: 909–921

Zorriassatine F, TannockJ DT (1998) A review of neural networks for statistical process control. J Intell Manuf 9:209–224

Optimization of Machining Process During Turning of X210Cr12 Steel Under MQL Cooling as a Key Factor in Clean Production

M. Nouioua, M. A. Yallese, R. Khettabi, A. Chabbi, T. Mabrouki and F. Girardin

Abstract For better surface quality and production efficiency in mechanical manufacturing, operators need to make a good choice of cutting parameters such as depth of cut, cutting speed, feed rate and also the cooling condition that affects not only product quality, but also respects the ecological aspect and preserves environment. In the current work, an experimental study has been carried out in order to evaluate the influence of cutting parameters on surface roughness, when turning of X210CR12 steel using multilayer-coated carbide insert with various nose radius. The ANOVA analysis has been performed to determine the effect of cutting conditions on Ra. The results have been analyzed using S/N ratios, mean effect graphs, and 3D response surface plots. The results indicate that the cutting insert nose radius and the feed rate are the mainly affecting factors on surface roughness. Confirmatory experiments have been established after Taguchi's optimization. It has been found that the MQL is an interesting way to minimize lubricant quantity, protect operator health and environment with keeping better machining quality.

M. Nouioua (✉) · M. A. Yallese · R. Khettabi · A. Chabbi
Mechanical Engineering Department Mechanics and Structures Research Laboratory (LMS),
University of 8th May 1945, P.O. Box 401, 24000 Guelma, Algeria
e-mail: nouiouamourad25@yahoo.fr

M. A. Yallese
e-mail: yallese.m@gmail.com

R. Khettabi
e-mail: riad.khettabi@uqtr.ca

A. Chabbi
e-mail: amel_chabbi@yahoo.fr

T. Mabrouki
Université de Tunis El Manar, Ecole Nationale d'Ingénieurs de Tunis (ENIT),
1002 Tunis, Tunisia
e-mail: Tarek.Mabrouki@yahoo.fr

F. Girardin
Laboratoire Vibrations Acoustique, INSA-Lyon, 25 bis avenue Jean Capelle,
69621 Villeurbanne Cedex, France
e-mail: francois.girardin@insa-lyon.fr

855

1 Introduction

Actually, number of research studies have been established using the MQL technique in order to minimize the lubricants consumption while ensuring best quality of manufactured products. An experimental study carried out by Rahim et al. (2015) qualify that the minimum quantity lubrication "MQL" as a sustainable cooling technique using a synthetic lubricant. The effectiveness of this technique has been justified according to the variation of the temperature and the cutting speed in chip formation during the machining of AISI 1045 steel by an uncoated carbide tool. A reduction of the cutting temperature was observed, along with much reduced cutting forces and improved chip formation under MQL than those of the dry machining. MQL research literature, so far, indicate that the MQL technique has proved its efficiency. Allowing for reduction in lubricant use (50–90%) (Dixit et al. 2012), energy consumption, better performance, and environment protection.

The present study investigates the MQL efficiency compared to dry and wet machining during turning of X210Cr12 steel using multilayer-coated tungsten carbide insert (grade GC4215 (ISO P15-CVD coated carbide) at different nose radius (r, mm), in order to identify the effect of different cutting parameters on surface roughness. The tests are designed according to Taguchi's L_{18} $(2^1 \times 3^4)$ orthogonal array, signal-to-noise ratios (S/N), 3D response surface plots, mean effect plots and the ANOVA analysis were performed to determine the contribution of cutting conditions on surface roughness (Ra, μm). Taguchi's confirmatory tests have been established after optimizing machining parameters.

2 Design of Experiment

2.1 Tools

The experimental conditions and cutting parameters are set according to different aspects such as (the workpiece material, the machine tool, cutting tool, and lubrication mode). In this experimental work, the tests are carried out using a conventional lathe "TOS TRENCIN" model SN-40. The workpiece material is the X210Cr12 steel. The diameter (d) and length (l) of the workpiece are respectively 80 mm and 330 mm. The surface roughness measurements have been taken directly after each test using a roughness-meter (Mitutoyo Surftest SJ-201) which consists of a diamond tip (probe).

2.2 Procedure

The experimental design has been conceived in order to study the influence of cutting setting on the obtained surface quality. The tests have been considered using a five-factor orthogonal array TAGUCHI L_{18}. Four of these factors have three levels (3^4) namely the cutting speed (Vc; 180, 250, and 350 m/min), the feed rate (f; 0.08, 0.12, and 0.16 mm/rev), the nose radius variation (r; 0.4, 0.8, and 1.6 mm) and cooling condition (C; dry, wet, and MQL). Concerning the depth of cut only two levels (2^1) were adopted (ap; 0.15, 0.3 mm). The set is organized by the Taguchi's L_{18} ($2^1 \times 3^4$). For the cooling condition (C), the turning tests have been performed under traditional lubrication mode, dry machining and MQL technique using a synthetic oil with a flow rate of 120 ml/h and a pulverization air pressure of 6 bar. The different defined parameters were shown in Table 1.

The combination of the different parameters of the orthogonal array L_{18} with the measured values of the surface roughness (Ra) and it S/N ratios are shown in Table 2. Each test in this table is related to a set of cutting conditions such as

Table 1 Factors and levels used in the experimental plan

Level	ap (mm)	Vc (m/min)	f (mm/rev)	r (mm)	Cooling condition
01	0.15	180	0.08	0.4	Dry
02	0.30	250	0.12	0.8	Wet
03	–	350	0.16	1.6	MQL

Table 2 L_{18} ($2^1 \times 3^4$) orthogonal array experimental data

No	Cutting parameters					Ra/S/N	
	ap	Vc	f	r	C	Ra (µm)	S/N (dB)
1	0.15	180	0.08	0.4	DRY	0.87	1.21
2	0.15	180	0.12	0.8	WET	0.62	4.15
3	0.15	180	0.16	1.6	MQL	0.54	5.35
4	0.15	250	0.08	0.4	WET	0.91	0.82
5	0.15	250	0.12	0.8	MQL	0.77	2.27
6	0.15	250	0.16	1.6	DRY	0.75	2.50
7	0.15	350	0.08	0.8	DRY	0.55	5.19
8	0.15	350	0.12	1.6	WET	0.58	4.73
9	0.15	350	0.16	0.4	MQL	1.29	−2.21
10	0.30	180	0.08	1.6	MQL	0.43	7.33
11	0.30	180	0.12	0.4	DRY	1.55	−3.81
12	0.30	180	0.16	0.8	WET	0.77	2.27
13	0.30	250	0.08	0.8	MQL	0.51	5.85
14	0.30	250	0.12	1.6	DRY	0.41	7.74
15	0.30	250	0.16	0.4	WET	1.27	−2.08
16	0.30	350	0.08	1.6	WET	0.39	8.18
17	0.30	350	0.12	0.4	MQL	0.73	2.73
18	0.30	350	0.16	0.8	DRY	1.02	−0.17

cutting speed, depth of cut, feed rate, and nose radius combined with a lubrication condition.

The values of roughness represent the mean of three measured values for each test. The surface roughness is selected in order to study the influence of the different cutting parameters on the material's machinability (X210Cr12 steel). Similarly, it could be possible to investigate the efficiency of MQL technique for an environment-friendly ecological machining.

2.3 Taguchi Design

Taguchi method allows us to evaluate inputs parameters and identify the optimal cutting combination to obtain the desired quality. It uses the signals-to-noise (S/N) ratio to analyze targets by an optimization function. There are three main function characteristics used to evaluate the performance, which are smaller-the-better, nominal-the-best, and larger-the-better.

For smaller-the-better, the S/N ratio is calculated by Eq. (1)

$$S/N = -10 \log \frac{1}{n} \left(\sum_{i=1}^{n} y_i^2 \right) \tag{1}$$

For nominal-the-best, the S/N ratio is calculated by Eq. (2)

$$S/N = 10 \log \frac{\overline{y}}{S_y^2} y \tag{2}$$

For larger-the-better, the S/N ratio is calculated by Eq. (3)

$$S/N = -\log \frac{1}{n} \left(\sum_{i=1}^{n} \frac{1}{y_i^2} \right) \tag{3}$$

In the current investigation, the surface roughness is a factor to be minimized. In this case the S/N ratio should be calculated using Eq. (3), that correspond to a smaller-the-better approach, in order to obtain the optimum combination of cutting parameters for best surface quality.

3 Results and Discussions

3.1 Signal-to-Noise (S/N) Analysis

Currently, the experts always search to improve the surface state, to obtain the high precision and the reliability and good functioning of the mechanical systems. The

Table 3 S/N response for surface roughness

Level	A-ap	B-Vc	C-f	D-r	E-C
1	2.67	2.75	4.76	−0.56	2.11
2	3.12	2.85	2.97	3.26	3.01
3		3.08	0.94	5.97	3.55
Delta	0.45	0.32	3.82	6.53	1.44
Rank	4	5	2	1	3

S/N ratio for every cutting combination result is calculated using Eq. (3) and presented in Table 1.

The optimal level of each process parameter is the one with the Signal-to-Noise ratio that presented in shaded cells of Table 3. In majority cases a greater S/N ratio corresponds to better quality characteristics. The Fig. 1 represent the S/N graphics used for performance evaluation. According to S/N analysis in Fig. 1, the optimal
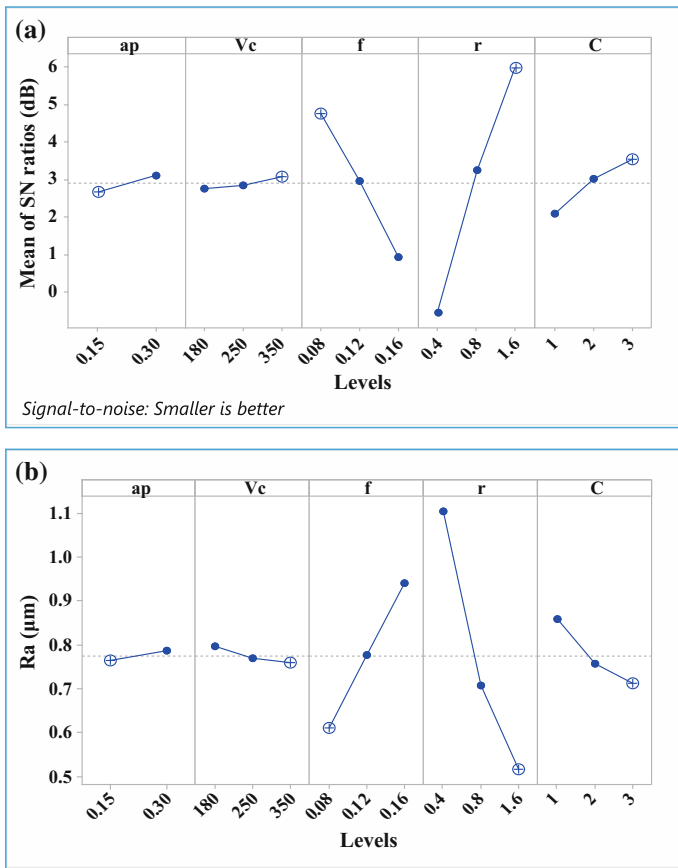
Fig. 1 Main effect plots **a** Mean of S/N ratio for Ra **b** Effects of cutting factors on Ra
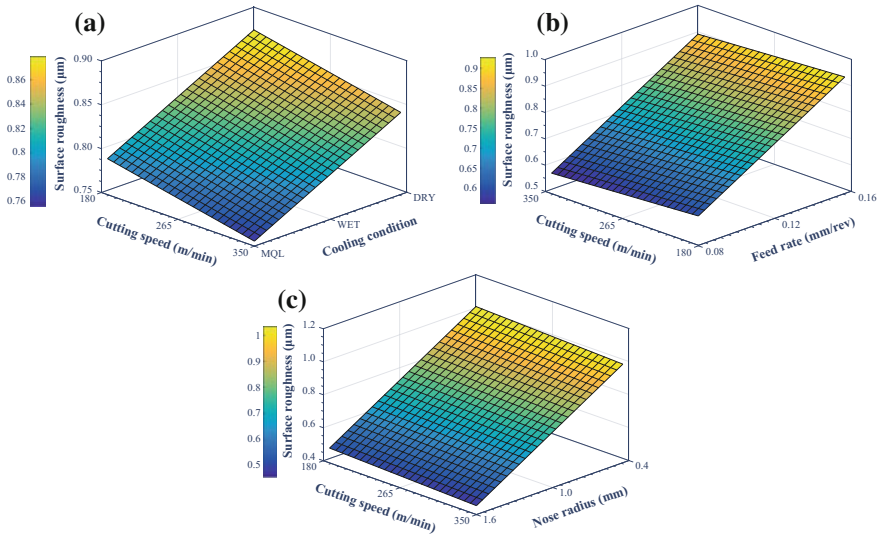
Fig. 2 Effect of cutting parameters on surface roughness

cutting parameters combination were indicated as "$A_1B_3C_1D_3E_3$". Which are 0.15 mm of depth of cut (ap, level 1), 350 m/min of cutting speed (Vc, level 3), 0.08 mm/rev of feed (f, level 1), a large nose radius 1.6 mm. The Fig. 2 illustrate the estimated response on 3D surface plots, that are drawn using the developed RSM model through MATLAB software, for evaluating responses by cutting settings variation. Figure 2b shows the effect of feed rate under cutting speed variation on surface roughness. As illustrated, it can be observed clearly that the surface roughness increases along with an increase of feed rate. However, a best surface quality obtained at high speed and low feed. The use of large feed rate results a worst surface roughness, because at large feed rates the distance between peaks and valleys of the feed marks is much more important. However, at high speeds; the generated temperature in the cutting zone leads to improve the surface quality due to the softening of workpiece material (Sarıkaya and Güllü 2014; Suresh et al. 2012).

Figure 2c illustrates the qualitative effect of large tool nose radius, with which the roughness has undergone an important improvement, also, a better surface quality obtained at high level of cutting speed. The use of large nose radius improves the surface roughness by the crushing of the asperities. These observations justify the use of low feeds and cutting inserts with a large nose radius (r = 0.8–1.6 mm) for the finishing process where a low roughness is desired.

Figure 2a illustrates that the MQL cooling with 120 ml/min of flow rate provide better surface quality as compared to dry and conventional machining.

3.2 ANOVA Analysis

The analysis of variance "ANOVA" is used as a tool to interpret the output data, in order to display the influence of the input parameters given by starting with a series of experimental results while respecting the design of experiment method for the machining process. Many indicators can be found in the tables of variation analysis like the degree of Freedom "DF", the sum of squares "SS" and the F values that can be used for the qualitative comprehension of the effects related to the factors. A high F value means that the effect of a given factor is high in regards to the variation error, the most important factor given affects the process response. In the same way, a weak P-value is a statistical signification of the source of the corresponding response. The analysis was performed for a confidence level of 95%.

From Table 4, and as we have previously noticed that the nose radius is the parameter with the biggest impact on the surface roughness by a contribution of 58.45%, followed by the feed rate and the cooling condition with contributions 17.76 and 3.68% respectively. Similar results were found by Meddour et al. (2015) and Bouzid et al. (2014).

Figure 3 shows the interaction effect due to cooling condition and nose radius variation, it can be observed clearly that the surface roughness is mainly improved under MQL cooling according to S/N ratio values indicated in the graph (Fig. 3). From a radius of 0.4–1.6 mm the surface roughness has undergone an important improvement.

3.3 Confirmation Experiments

In Taguchi method, optimization is verified by confirmation experiments that used to validate the predicted performance characteristics under the selected optimal levels of cutting parameters. In this study the optimal levels are indicated as "$A_1B_3C_1D_3E_3$" for Ra, these two combinations are used for the prediction of optimal surface roughness. The estimated outputs using the optimal levels of the design parameters can be calculated as (Eq. 4)

$$Ra_{pre} = T_{Ra_{exp}} + (\overline{A_1} - T_{Ra_{exp}}) + (\overline{B_3} - T_{Ra_{exp}}) + (\overline{C_1} - T_{Ra_{exp}}),$$
$$+ (\overline{D_3} - T_{Ra_{exp}}) + (\overline{E_3} - T_{Ra_{exp}}) \tag{4}$$

Table 4 ANOVA analysis for response factors

Variation of source	DF	SS	MS	F-Value	P-value	Cont. %
ap	1	0.002	0.002	0.05	0.83	0.12
Vc	2	0.004	0.002	0.05	0.95	0.23
f	2	0.33	0.163	3.6	0.08	17.76
r	2	1.08	0.537	11.84	0.004	58.45
C	2	0.07	0.338	0.75	0.51	3.68
Error (e)	8	0.36	0.045			19.75
Total	17	1.84				100.00

Fig. 3 Interactions effect plot of cooling condition and Nose radius
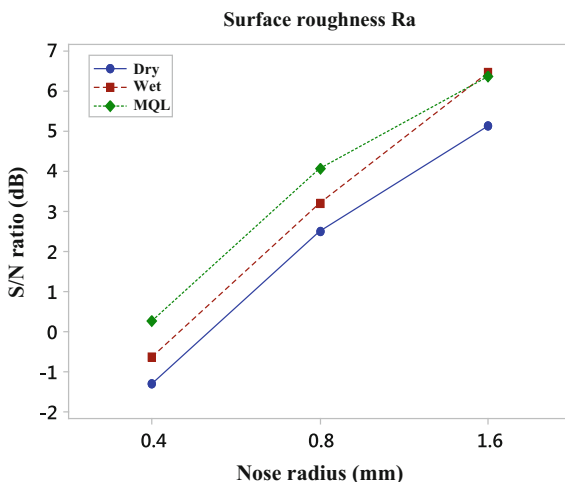
where
$T_{Ra_{exp}} = 0.776, \overline{A_1} = 0.76, \overline{B_3} = 0.76, \overline{C_1} = 0.61, \overline{D_3} = 0.52, \overline{E_3} = 0.71$
Hence $Ra_{pre} = 0.256 \,\mu m$.

The confidence interval for predicted optimal process is employed in order to verify the quality characteristics of the confirmation experiment, using the Eq. (5) (Roy 1990):

$$CI = \sqrt{F_{(0.05, 1, \vartheta_e)} \cdot V_e \cdot \left(\frac{1}{n_{eff}} + \frac{1}{n_{ver}} \right)}, \qquad (5)$$

where $F_{(0.05, 1, \vartheta_e)}$ is the F value at 0.05 level of significance (95% confidence), ϑ_e is the DOF of error, V_e is the variance of error, n_{ver} is confirmatory trial number (Eq. 6).

$$n_{eff} = \frac{N(total\,trial\,number)}{(1 + total\,DOF\,of\,P\,factors)} \qquad (6)$$

The confidence interval for the surface roughness is given as follows:

$F_{0.05;\,(1,\,8)} = 5.3177$ (from F table), $V_e = 0.0454$, and $n_{eff} = 1.8$, so the calculated CI were $= 0.504$.

The predicted surface roughness is $Ra_{pre} = 0.256 \,\mu m$.

$\left| Ra_{pre} - CI \right| < Ra_{pre} < \left| Ra_{pre} + CI \right|$, i.e., $0.2481 < Ra_{pre}(\mu m) < 0.752$.

If the prediction error $\left| Y_{pre} - Y_{exp} \right|$ is within the confidence interval, in this case, the optimal cutting parameters combination for Ra are valid. From Table 5, it can be observed that the optimization protocol for Ra was achieved at 95% confidence using the Taguchi method.

Table 5 Confirmation experiments results using Taguchi method

Response	Difference	Optimization
Ra (µm)	$Ra_{Exp} - Ra_{pre} = 0.064$	$0.064 < 0.504 = $ successful

4 Conclusion

The present study investigates the MQL performance during turning of the X210Cr12 steel compared to dry and wet machining using the Taguchi method which is based on signal-to-noise ratio in order to obtain the optimal cutting settings. It was concluded that

1. The obtained results proved that the Taguchi method is an optimization technique that simplify the experimental protocol to highlight the effects of factors on the responses that can implemented successfully in turning researches to obtain the desired quality.
2. From ANOVA results, the tool nose radius is the most significant parameter on surface roughness with a contribution 58.45% followed by feed rate, the use of large nose radius improves the surface roughness. Low feeds and cutting inserts with a large nose radius (r = 0.8–1.6 mm) are useful for finishing process where a low roughness is desired.
3. The confirmation results were obtained using the optimal setting factors at confidence level of 95% and verified successfully through Taguchi method.
4. Minimum quantity lubrication (MQL) machining can be qualified as a green machining process when the optimization is considered.

References

Bouzid L, Yallese MA, Chaoui K, Mabrouki T, Boulanouar L (2014) Mathematical modeling for turning on AISI 420 stainless steel using surface response methodology. Proc IMechE Part B J Eng Manuf 1–17

Dixit US, Sarma DK, Davim JP (2012) Environmentally friendly machining. Springer Science and Business Media

Meddour I, Yallese MA, Khattabi R, Elbah M, Boulanouar L (2015) Investigation and modeling of cutting forces and surface roughness when hard turning of AISI 52100 steel with mixed ceramic tool: cutting conditions optimization. Int J Adv Manuf Technol 77(5–8):1387–1399

Rahim EA, Ibrahim MR, Rahim AA, Aziz S, Mohid Z (2015) Experimental investigation of minimum quantity lubrication (MQL) as a sustainable cooling technique. Procedia CIRP 26:351–354

Roy RK (1990) A primer on the Taguchi method. Van Nostrand Reinhold, New York, USA

Sarıkaya M, Güllü A (2014) Taguchi design and response surface methodology based analysis of machining parameters in CNC turning under MQL. J Clean Prod 65:604–616

Suresh R, Basavarajappa S, Gaitonde VN, Samuel GL (2012) Machinability investigations on hardened AISI 4340 steel using coated carbide insert. Int J Refract Metals Hard Mat 33:75–86

High Strain-Rate Tensile Behaviour of Aluminium A6063

M. Khlif, L. Aydi, H. Nouri and Ch. Bradai

Abstract The growing demand for more fuel-efficient vehicles to reduce energy consumption and air pollution is a challenge for the automotive industry. The aluminium alloy can replace steels and copper in this industry. In this framework, we are interested in studying the behaviour at high strain rate. Dynamic tensile tests are conducted on aluminium alloy (AA) 6063 using a split-Hopkinson tension bar and a sensing block system to validate the testing technique and to investigate the strain-rate effect on the material's stress–strain behaviour and failure mode. We present the experimental procedures and results discussing the constitutive response of the alloy at strain rates up to approximately 1500 s^{-1}. We tested two different specimen sizes at a wide range of actuator velocities to achieve the desired strain rates. Results show that the yield strength, ultimate strength and failure strain were dependent on strain rate. We fitted the data to the Johnson-Cook (JC) constitutive model and the resulting parameters are comparable to published results in similar work.

Keywords Aluminium alloy · High strain-rate · Tensile behaviour

1 Introduction

Many testing techniques have been used to extract data under dynamic conditions. Each serves a range of strain rates and provides a specific type of information. Some of the techniques commonly used include servo-hydraulic systems, tensile and compression split Hopkinson bar (SHB), flywheel facilities, and drop weight systems (Reyes et al. 2006). For this we have developed a machine for the dynamic

M. Khlif (✉) · L. Aydi · H. Nouri · Ch. Bradai
LASEM (Analysis Laboratory of the Electro-Mechanical Systems), National School of Engineers of Sfax Tunisia (ENIS), BP. 1173, 3038 Sfax, Tunisia
e-mail: khlifmohamed@yahoo.fr

865

tensile test at high deformation, similar to the Hopkinson bar system which consists of an input bar and a sensing block system (Khlif et al. 2008).

In his tests, these metals showed increasing degree of strain-rate sensitivity higher than 500–1500 s^{-1}. Tests on AA6063—and AA6063 recycled showed measurable strain-rate sensitivity in tension at the high strain rates, although similar tests in compression showed essentially no strain-rate sensitivity.

2 Experimental Setup

A schematic of the sensing block system that was used in this study is shown in Fig. 1. This apparatus is composed of three parts. The first part represents the shock generating system used to excite the input bar. It includes a striker that projectile the end part of the incident bar. The shock receiving system represents the second part. It is composed of an incident bar which receives the shock excitation generated by the striker and transmits the corresponding strain wave to the specimen located between the incident bar and the sensing block. The incident bar is instrumented in order to measure the force. The choice of a long bar enables us to solve the waves superposition problem (incident and reflected waves) and to measure the loading force for a dynamic test. Moreover, the transmitting incident wave from the bar is transmitted to the specimen. This wave is finally received by the sensing block which is composed of a sensing receiver and a base block. A strain gauge located at the sensing receiver measures the corresponding transmitted stress wave. Due to the important relative large mass of the base block, the stress wave moving from the sensing receiver is dissipated after some reflect ions between the bases block upper surfaces.

2.1 Calculation of Response in Test Specimen

This section aims to present the relations necessary to calculate the response the test specimen.
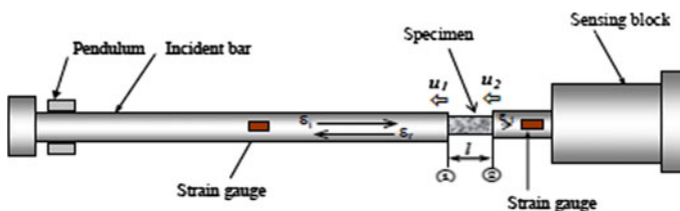
Fig. 1 Schematic of experimental setup
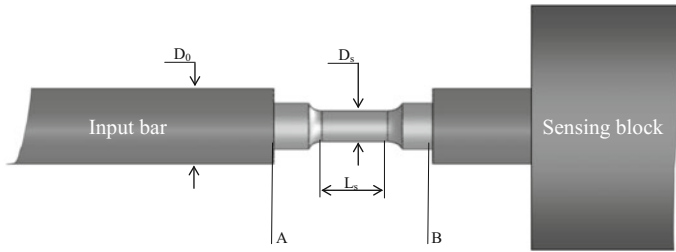
Fig. 2 Schematic view of sensing block system

In order to determine the response, that is the stress and strain state, of the specimen, only two strain gauges mounted on the incident bar and on the sensing block are necessary (Fig. 2). The signals from the strain gauges are resistance changes of the metal filament that is converted to voltage changes through a connected Wheatstone bridge (Kolsky 1953).

As the tensile stress wave propagates towards the end of the incident bar and the specimen, the strain in the incident bar will be measured by strain gauge 1 and is referred to as the incident strain, ε_I. When the stress wave reaches the end of bar, it will partly be reflected back, and partly transmitted to the specimen. The reflected strain measured by strain gauge 1 is denoted the reflected strain, ε_R, while the transmitted strain measured by strain gauge 2 is denoted the transmitted strain, ε_T.

For the relations stated below, subscript s denotes specimen, subscript 0 refers to the sensing block, A is cross-sectional area, E is Young's modulus, Ls is the length of the gauge section of the specimen, C_0 is the wave propagation velocity and t is time (Chen et al. 2009).

The stress in the specimen is found by dividing the force at point B (or at point A) by the cross-sectional area of the specimen

$$\sigma_s = \frac{F_s}{A_s} = \frac{E_0 A_0}{A_s} \varepsilon_T \tag{1}$$

By assuming that all strains in the specimen take place in the gauge section, the strain in the specimen is calculated as

$$\varepsilon_s = \frac{C_0}{L_s} \int_0^t (-\varepsilon_T - (\varepsilon_I + \varepsilon_R)) dt = -2 \frac{C_0}{L_s} \int_0^t \varepsilon_R dt \tag{2}$$

The corresponding strain rate is simply the time derivative of the strain state

$$\dot{\varepsilon}_s = \frac{\partial \varepsilon_s}{\partial t} = -2 \frac{C_0}{L_s} \varepsilon_R \tag{3}$$

Table 1 Chemical compositions of the AA6063

Element	Si	Mg	Fe	Mn	Cn	Ti	Al
Wt%	0.440	0.480	0.170	0.030	<0.01	0.01	Balance
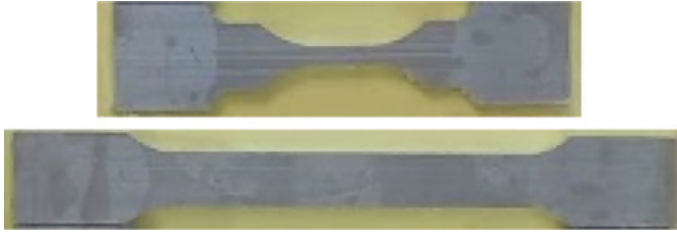
Fig. 3 Geometry of the specimen

2.2 Material and Specimen Geometry

AA6063 is heat treatable, work-hardening Al–Mg alloys. The alloys are commonly used for automobile structural or body inner panels. The nominal compositions of the alloys tested are listed in Table 1. The nominal sheet thicknesses available for AA6063 were 3 mm

Currently, there is no standardized specimen geometry for TSHB testing and specimen design became a significant aspect of the current research. The objective was to design a specimen that follows the mechanical response of a standard ASTM specimen, while meeting the requirements for specimens used in dynamic experiments.

Two requirements for a TSHB specimen are a small gauge length to reduce ring-up time and inertial effects, as well as a geometry that results in a uni-axial stress state (Fig. 3).

3 Experimental Results

Tests were conducted at nominal strain rates of approximately 3×10^{-3} s^{-1} (quasi-static), 500, 1000 and 1500 s^{-1}. The tests conducted at 23 °C considered all strain rates.

Three specimens were tested at each set of conditions. The test conditions and results from all tests are summarized in curve. Only the median stress–strain responses for each set of test conditions are shown in the following sections, and are shown only for a single loading pulse. The remainder of the data is given in the paper.

Fig. 4 Stress–Strain response for quasi-static test
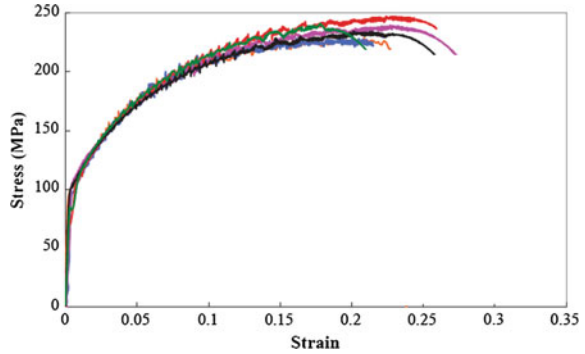
Fig. 5 Stress–Strain responses at high strain rate
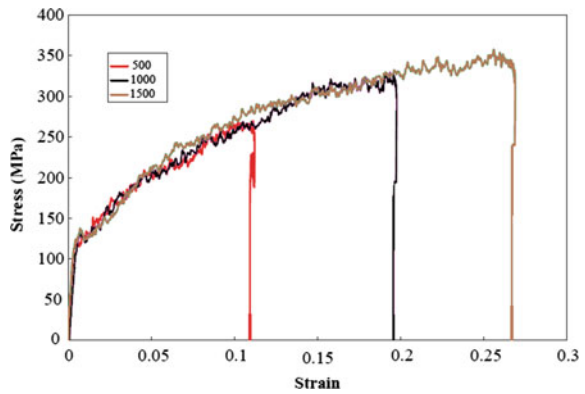
Figure 4 show the resulting stress–strain curves at ambient temperature for alloy tested AA6063 (quasi-static test). In Fig. 5, it is seen that AA6063 exhibits a mild increase in flow stress at higher strain rates. For example, at 5% strain, the flow stress of 3 mm thick AA6063 is approximately 203 MPa at a nominal strain rate of 500 s^{-1}, compared to approximately 185 MPa at a strain rate of 3×10^{-3} s^{-1}.

However, while this increase occurred for the change in strain rate from quasi-static to TSHB regimes (six orders of magnitude), the change in flow stress in the range between 500–1500 s^{-1} was negligible. The thinner 1 mm material shows very similar behaviour. The flow stress at 5% strain increases from approximately 195 MPa at 3×10^{-3} s^{-1} to approximately 206 MPa at 500 s^{-1}. This behaviour is expected since it has been shown that the flow stress has a logarithmic dependence on strain rate for aluminium alloys. The difference in flow stress between the two thicknesses under quasi-static conditions can be attributed to differences in the raw mechanical processing experienced by the 1 mm thick sheet during cold rolling.

4 Conclusion

Tensile tests on aluminium alloy relevant for application in automotive crash components were carried out over a wide range of strain rate, and the stress–strain behaviour and plastic anisotropy were established. Two tests techniques were used to obtain the data. In the low-to-medium strain-rate range a tensile test machine was applied. While a new device sensing block system was used for high strain rates. The tests show that AA6063 exhibit only slight sensitivity to the strain rate, and could probably be modelled as rate-insensitive with good accuracy.

References

Chen Y, Clausen AH, Hopperstad OS, Langseth M (2009) Stress-strain behavior, of aluminium alloys at a wide range of strain rates. Int J Solids Struct 46:3825–3835

Khlif M, Grolleau V, Masmoudi N, Bradai C, Rio G (2008) Development of a new test ing method for polymer materials at high strain rate. J Theor Appl Mech 38(3)

Kolsky H (1953) Stress waves in solids. Clarendon Press, Oxford

Reyes Aa, Hopperstad OS, Lademo O-G, Langseth M (2006) Modeling of extured aluminum alloys used in a bumper system: material tests and characterization. Comput Mater Sci 37: 246–268

Pump Failure: Effect of Wall Elasticity on Pressure Fluctuations

Noura Bettaieb, Issa Chalghoum, Elaoud Sami and Ezzeddine Hadj Taieb

Abstract The mechanical behaviour of the pipe wall material plays a major role in determining the pressure response of a fluid system during transient events. In regards to the behaviour of plastic pipes, such pipes have been widely used in water supply networks. This paper investigates and compares, numerically, the pressure response of a polyethylene high density (HDPE) pipe and a rigid steel pipe in case of exposure to transient events. The governing equations of the system are two coupled nonlinear hyperbolic partial differential equations, continuity, and momentum. The classical water hammer theory was used in the numerical modelling. The initiation of the hydraulic transients in the network was caused by a sudden centrifugal pump failure. The numerical resolution of the pressure-discharge equations is performed using the method of characteristics. The pressure fluctuations in polyethylene pipelines were found to be delayed in time compared to rigid pipes. The delayed wave celerity in polymeric pipeline is an asset for damping transient waves over time.

Keywords Hydraulic transient · Centrifugal pump · Polyethylene PEHD
Wave celerity · Steel pipe

N. Bettaieb (✉) · I. Chalghoum · E. Sami · E. H. Taieb
Research Laboratory "Applied Fluid Mechanics Process Engineering and Environment"
Engineering School of Sfax, BP'W'3038 Sfax, Tunisia
e-mail: noura.bettaieb@enis.tn

I. Chalghoum
e-mail: chalghoumissa@yahoo.fr

E. Sami
e-mail: elaoudsa@yahoo.fr

E. H. Taieb
e-mail: Ezed.Hadj@enis.rnu.tn

871

1 Introduction

The analysis of Water Hammer events is a mandatory stage for designing hydraulic installations. Choosing pipe materials, selecting wall thickness and the convenient protection devices against surge, are the first steps for designing water pipeline systems. Under the assumption of a linear elastic behaviour and a quasi-steady state friction loss, many researchers have undertaken this subject since last century such as Fox (1977), Chaudhry (1987), Almeida and Koei (1992), Wylie et al. (1993). The hydraulic fluctuations are governed by a set of two partial derivative equations, continuity, and motion equations. The solution of this system yields to the evolution of pressure and discharge along the pipeline networks. However, these perturbations occur accidentally (pump failure or pipe rupture) or voluntarily (valve closure, pump startup). Operations of rotary machines, mainly centrifugal pumps, may lead to severe changes in pressure heads. As a remedy, modelling transient fluctuations caused by power loss of centrifugal pumps has been a priority for researchers, (Streeter and Wylie 1967; Afshar and Rohani 2008; Rohani and Afshar 2010). However, as mentioned earlier, the modelling of these events was based on the assumptions of linear elastic behaviour. Although this assumption is considered relatively accurate in cases of describing transient events in concrete or metal pipes, it relatively over estimates pressure responses in cases of plastic pipes. In recent years, Polymer pipes such as polyvinyl chloride (PVC) and polyethylene (PE) have been widely used in urban water supply networks. This is due to the low cost price in comparison with the high-resistant operating properties. Ferry (1970) and Riande et al. (2000) have shown that these plastic materials exhibit a viscoelastic mechanical behaviour. This behaviour affects the pressure response of the pipeline in case of exposure to transient events. Covas et al. (2004, 2005) have shown that the viscoelastic behaviour of polyethylene pipes results in a considerable attenuation of pressure wave oscillations. This effect was also been confirmed by Soares et al. (2008) in the case of PVC pipes. In recent years, (Apollonio et al. 2014) gave a set of parameters describing the creep function in a single-pipe system. Evangelista et al. (2015) investigated experimentally the transmission and reflection of pressure waves within branched polyethylene pipes. When interpreting the results, they tested the efficacy of the viscoelastic model. They found a strong agreement between the numerical and experimental results.

However, in the previous research work, the viscoelastic model was applied only for ducts with a small diameter and in small pumping stations.

In what follows, the transient events are initiated by power loss of a centrifugal pump feeding a downstream reservoir. The numerical resolution of the governing PD equations, momentum and continuity, was performed by the method of characteristics MOC. Pressure fluctuations along the pipe were investigated for two different pipe materials, steel and HDPE pipe using the linear elastic model. The response in time of both materials was compared.

2 Mathematical Model

Modelling transient flows in closed pipes is based essentially on the continuity and momentum equations. The mathematical model can be adapted from the one developed in Wylie et al. (1993).

2.1 PD Equations

$$\frac{\partial H}{\partial t} + \frac{C^2}{gA}\frac{\partial Q}{\partial x} = 0 \tag{1}$$

$$\frac{\partial Q}{\partial t} + gA\frac{\partial H}{\partial x} + \frac{\lambda Q|Q|}{2DA} = 0, \tag{2}$$

where Q is the fluid discharge, H is the head, C is the pressure wave celerity, ρ is the fluid density, λ is the coefficient of friction, A is the cross-sectional area of the pipe, D is the circle pipe diameter, t is the time and x is the distance along the pipe.

2.2 Wave Celerity Expression

Chauhdry (1987) has developed an expression for the wave speed in rigid conduits. This expression depends mainly on the bulk modulus of elasticity and density of the fluid.

$$C = \sqrt{\frac{\Delta p}{\Delta \rho}} = \sqrt{\frac{K}{\rho}} \tag{3}$$

However, in elastic pipes, the wave speed depends also upon the elastic properties of the pipe wall and the external constraint. Thus, its expression would be:

$$C = \sqrt{\frac{K}{\rho[1 + (K/E)\psi]}}, \tag{4}$$

where ψ is a non-dimensional parameter, its value depends on the properties of the conduit, and E is the Young's modulus of elasticity of the pipe wall. For a thick walled elastic pipe, anchored against longitudinal movement throughout the length, the expression of ψ could be approximated with:

$$\psi = 2(1+\upsilon)\frac{R_o^2 + R_i^2}{R_o^2 - R_i^2} - \frac{2\upsilon R_i^2}{R_o^2 - R_i^2}, \tag{5}$$

where R_o and R_i are the outside and the internal radius of the conduit, D is the diameter, e is the wall thickness and υ is Poisson's ration of the pipe wall material.

3 Numerical Solution

To simulate pressure and discharge fluctuations, during transient events in pipelines, a variety of numerical approaches have been introduced in literature. The most commonly used numerical method is the Method of characteristics (MOC).

3.1 Method of Characteristics

The simplicity of the MOC method, nevertheless its effective performance, is a major reason for adopting this method in solving transient events in hydraulic networks. MOC is used to transform the PD system of Eqs. (1) and (2) into a set of ordinary differential equations system integrated numerically without difficulties (Fox 1977).

Specifying a time interval $\Delta t = \Delta x / C$, the integration along the characteristic lines, presented on Fig. 1, yields to:

$$H_{Pi} = C_P - BQ_{Pi} \tag{6}$$

$$H_{Pi} = C_M + BQ_{Pi}, \tag{7}$$

where $\quad C_P = H_{i-1} + BQ_{i-1} - RQ_{i-1}|Q_{i-1}|, \quad C_M = H_{i+1} - BQ_{i+1} + RQ_{i+1}|Q_{i+1}|$
$B = \frac{C}{gA}$ and $R = \frac{\lambda \Delta x}{2gDA^2}$.

Fig. 1 Characteristic lines
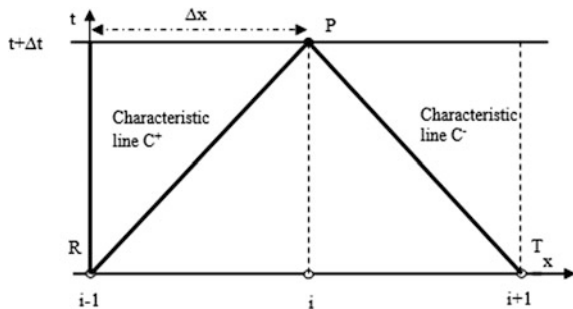
The head and discharge flow at any interior sections of the pipe and at each time step is given by

$$H_{Pi} = \frac{C_P + C_M}{2} \tag{8}$$

$$Q_{Pi} = \frac{(C_P - C_M)}{2B} \tag{9}$$

3.2 Boundary Conditions

3.2.1 Pump Failure at the Upstream End

The shutting down of a centrifugal pump cannot be considered an instantaneous operation. One of the solutions to delay the shutting down time is to introduce a flywheel to the shaft of the pump. In this case, it is necessary to present the axial torque equation (Frelin 2002).

$$I\frac{d\omega}{dt} = T_{motor} - T_{resistant} \tag{10}$$

The resistant torque of the pump is known for different values of the rotational speed. At the disjunction, the motor torque is switched off, Eq. (10) would be:

$$I\frac{d\omega}{dt} = -T_{resistant}, \tag{11}$$

where I is the moment of inertia of the rotating masses around a rotating axis, T_{motor} is the motor torque, ω is the rotational speed, and $T_{resistant}$ is the resistant torque. Several methods were been used to integrate this equation in order to determine the pump speed variation. These methods depend on the expression of the resistant torque in term of the speed.

3.2.2 Constant-Level Reservoir at the Downstream End

The head at a constant level reservoir is given by

$$H_{P_{N+1}} = H_0, \tag{12}$$

where H_0 is the constant level of the fluid in the reservoir. Using Eq. (6), the discharge at the entrance of the reservoir is given by

$$Q_{P_{N+1}} = \frac{(C_P - H_{P_{N+1}})}{B} \qquad (13)$$

4   Results and Discussion

The hydraulic network considered herein is shown on Fig. 2. The installation consists of a pump lifting water from level B to level R through a cylindrical pipe. A sudden disconnection of the drive motor of the pump causes the initiation of transient events.

The characteristic of the centrifugal pump are presented in Table 1. The total inertia I is the sum of the inertia of the rotating masses, including the fluid, around a rotating axis.

A check valve was installed downstream the pump to prevent the reverse back flow. To examine the response of the pipe wall elasticity, two different materials were used in the numerical simulation. Table 2 contains the properties of the pipelines.

Figure 3 represents the value of the torque for different discharges of the pump. The resisting torque could be approximated by

$$T_{resis\ tan\ t} = a_1 \omega^2 + a_2 \omega\, Q, \qquad (14)$$

where $a_1 = 0.02\ \text{Kg m}^2$ and $a_2 = 5.236\ \text{Kg m}^{-1}$.

The head-discharge characteristic curve of the pump, at the steady state speed $\omega_0 = 1500$ rpm, is presented on Fig. 4. The curve $H = f(Q)$ could be approximated by a second-order polynomial function:

Fig. 2 Water supply installation (Frelin 2002)
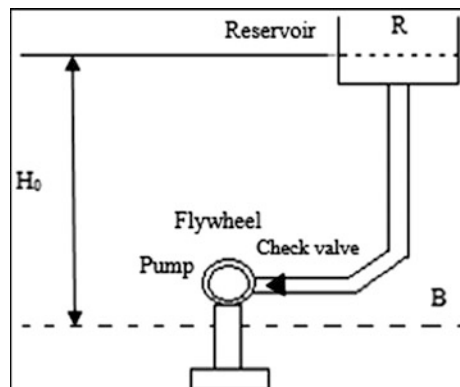
Table 1 Characteristics of the centrifugal pump

Parameter	Value
Head	27 m
Discharge flow	0.3 m^3/s
Rotational speed	1500 rpm
Moment of inertia	20 kg m^2

Table 2 Characteristics of the hydraulic installation

Parameter	Steel	HDPE
Inner diameter	0.7 m	0.69 m
Wall thickness	16×10^{-3} m	55×10^{-3} m
Length	700 m	700 m
Friction coefficient	0.02	0.012

Fig. 3 Torque versus Discharge of the pump
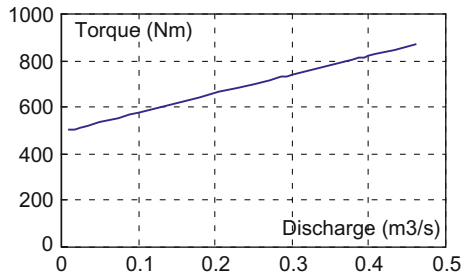
Fig. 4 Characteristic curve of the pump
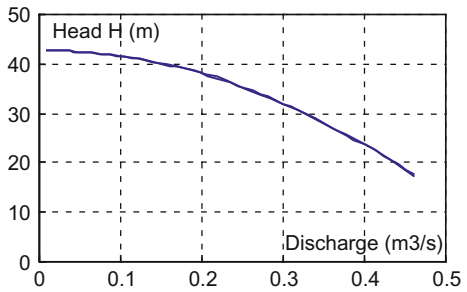
$$H = a_0\omega^2 - b_0 Q^2, \tag{15}$$

where $a_0 = 4.05$ and $b_0 = 120$.

The rotational speed is first determined by integrating equation (11).

$$\int_{\omega_i}^{\omega_f} \frac{d\omega}{a_1\omega^2 + a_2\omega\, Q_i} = -\frac{1}{I}\int_{t_i}^{t_f} dt \tag{16}$$

ω_i is known from previous time step $t = t_i$. Assuming that the flow rate Q_i remains constant during the time interval $t_f - t_i = \Delta t$, the rotational speed ω_f would be (Abramowitz 1965):

$$\omega_f = \frac{a_2 Q_i}{\left(a_1 + \frac{a_2 Q_i}{\omega_i}\right) \exp\left(\frac{a_2 Q_i}{I}(t_f - t_i)\right) - a_1} \tag{17}$$

The discharge is given by Eq. (18) and the head is obtained by using the compatibility along the negative characteristic line, Eq. (7).

$$Q_{P1} = \frac{-B + \sqrt{B^2 + 4b_0\left(a_0\omega_f^2 - C_M\right)}}{2b_0} \tag{18}$$

The numerical results drawn as a function of time on Figs. 5 and 6 are, respectively, the discharge at the entrance of the reservoir and the head downstream the check valve. The results, for the rigid steel pipe, were validated with literature using the graphical method of Bergeron (Bergeron 1950).

After disjunction of the drive motor, a negative pressure wave travels along the pipe until it reaches the downstream end. As the wave celerity is equal to $C = 1227\,\text{m/s}$, the time needed for the pressure wave to reach the downstream reservoir is $t = L/C = 0.5704\,\text{s}$. At this instant, the discharge at the entrance of the reservoir begins to decrease. In the pipe, a region of depression is developed for some time as it can be seen from Fig. 6. The positive reflected pressure wave travelling from the end of the pipe will cause the pressure to rise. Immediately after the check valve closure, the pressure downstream rises reaching a value of $H = 43\,\text{m}$. The pressure at different sections of the pipe is presented on Fig. 7. The maximum value is located downstream the pump. Even though the amplitude decreases from one section to another, the pressure wave within the same section is slightly damped over time.

However, when a HDPE pipe was used in numerical calculations a remarkable damping of the pressure was observed downstream the pump and for at different sections of the pipe, Fig. 8. The pressure response of both materials is presented on Fig. 9.

For the plastic HDPE pipe, only one peak of pressure is reached within 20 s, Fig. 9, while almost six peaks are reached in the case of the rigid steel pipe. This

Fig. 5 Discharge fluctuation at the entrance of the reservoir
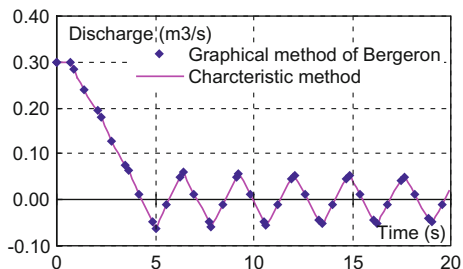
Fig. 6 Head fluctuation downstream the pump
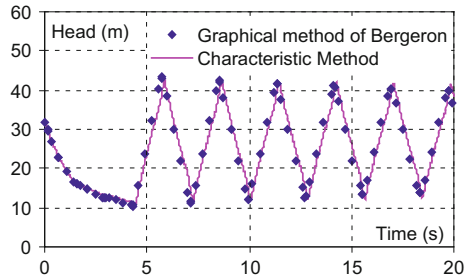
Fig. 7 Head fluctuation at different sections of the pipe: steel pipe
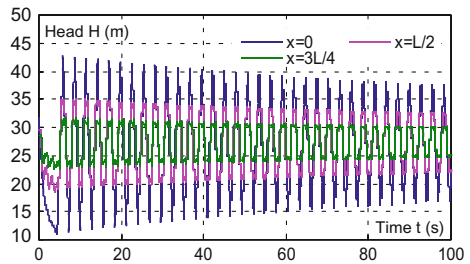
Fig. 8 Head fluctuation at different sections of the pipe: HDPE pipe
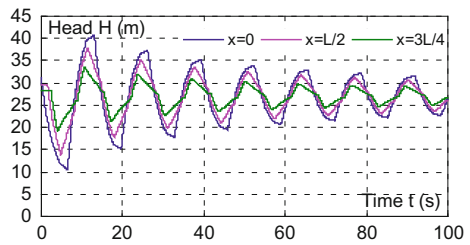
Fig. 9 Head fluctuation downstream the pump
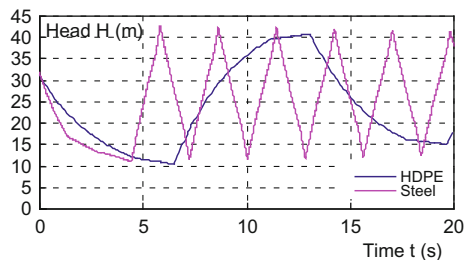
delay in the response of the HDPE pipe is due to the difference in the wave celerity. As mentioned earlier, the time needed for the pressure wave to reach the upstream reservoir is equal to $t = L/C$. As the value of the wave celerity in HDPE is very low compared to steel pipes, $C = 213$ m/s, the period for the reflection of the wave is almost six times higher than the with the case of rigid steel pipe.

5   Conclusion

The pressure response of two different material types in a hydraulic system, exposed to transient events, was investigated. The network considered in the numerical calculation consists of a centrifugal pump feeding an upstream reservoir through a cylindrical pipe. The transient was initiated due to a sudden disjunction of the drive motor of the pump. A linear elastic behaviour of the pipe wall was adopted. The method of characteristics was used to solve the set of partial differential equations governing the systems. In the case of rigid steel pipe, the fluctuations were found to be very excessive in different section in the conduit. Nevertheless, the amplitude is slightly damped over time. However, a different pressure response was found in the case of plastic polyethylene pipe. The pressure pulsation was remarkably damped over time.

References

Abramowitz M, Stegun IA (1965) Handbook of mathematical functions. National Bureau of Standards, Washington, D.C

Afshar MH, Rohani M (2008) Water hammer simulation by implicit method of characteristic. Int J Press Vessels Pip 85(12):851–859

Almeida AB, Koeile E (1992) Fluid transients in pipe networks. Computational Mechanics Publications, Elsevier Applied Science, Amsterdam

Apollonio C, Covas DIC, de Marinis G, Leopardi A, Ramos HM (2014) Creep functions for transients in HDPE pipes. Urban Water J. 11(2):160–166

Bergeron L (1950) Du coup de bélier en hydraulique au coup de foudre en électricité. Dunod

Chaudhry HM (1987) Applied hydraulic transients. Van Nostrand Reinhold, NewYork

Covas DIC, Stoianov I, Mano J, Ramos HM, Graham N, Maksimovic C (2004) The dynamic effect of pipe-wall viscoelasticity in hydraulic transients: Part I—Experimental analysis and creep characterization. J Hydraul Res 42(5):517–531

Covas DIC, Stoianov I, Mano J, Ramos HM, Graham N, Maksimovic C (2005) The dynamic effect of pipe-wall viscoelasticity in hydraulic transients: Part II—Model development, calibration and verification. J Hydraul Res 43(1):56–70

Evangelista S, Leopardi A, Pignatelli R, de Marinis G (2015) Hydraulic transients in viscoelastic branched pipelines. ASCE J Hydraul Eng. ISSN 0733-9429/04015016(9)

Ferry JD (1970) Viscoelastic properties of polymers, 2nd edn. Wiley, New York

Fox JA (1977) Hydraulic analysis of unsteady flow in pipe networks. The Macmillan Press LTD., London

Frelin M (2002) Coups de bélier. Les techniques de l'Ingénieur BM 4(176):1–27

Riande E, Díaz-Calleja R, Prolongo MG, Masegosa RM, Salom C (2000) Polymer viscoelasticity: stress and strain in practice. Marcel Dekker Inc, New York

Rohani M, Afshar MH (2010) Simulation of transient flow caused by pump failure: Point-Implicit Method of Characteristics. Ann Nucl Energy 37(12):1742–1750

Soares AK, Covas DIC, Reis RLF (2008) Analysis of PVC pipe-wall viscoelasticity during water hammer. J Hydraul Eng 134(9):1389–1394. doi:10.1061/(ASCE)0733-9429

Streeter VL, Wylie EB (1967) Hydraulic transients. McGraw-Hill Book Company, New York

Wylie EB, Streeter VL, Suo L (1993) Fluid transients in system. Prentice Hall, New Jersey

Numerical Modeling of Hot Incremental Forming Process for Biomedical Application

Manel Sbayti, Riadh Bahloul and Hedi Belhadjsalah

Abstract The selection of a suitable technique for manufacturing of a specific product represents a complex issue, especially for the biomedical field. Single point incremental forming (SPIF) process presented an alternative manufacturing means in producing biomedical parts characterized by the need of patient-specific geometry. In addition, the titanium alloy Ti–6Al–4V is one of the most frequently used materials for biomedical application. Due to its poor-room-temperature formability, deformation under high temperature is needed. In this context, the present work aims at proving the feasibility of the hot incremental forming of titanium alloy Ti–6Al–4V denture base by finite element simulations. The effects of the forming temperature on the material failure and more particularly on the geometric accuracy of the final product were investigated. The comparison between the final deformed geometry predicted numerically and the target one obtained from CAD modeling is conducted. Therefore, a good agreement has been obtained and significant improvements in terms of geometric accuracy have been reached employing the SPIF at elevated forming temperature.

M. Sbayti (✉) · R. Bahloul · H. Belhadjsalah
Mechanical Engineering Laboratory, National Engineering School,
University of Monastir, Avenue Ibn El Jazzar, 5000 Monastir, Tunisia
e-mail: manelasbayti@gmail.com

R. Bahloul
e-mail: bahloul_riadh@yahoo.fr

H. Belhadjsalah
e-mail: hedi.belhadjsalah1@gmail.com

1 Introduction

The technology of incremental sheet forming (ISF) is suitable for prototyping, customized components and small-batch production due to its flexibility and low tool effort (Arfa et al. 2013). It was primarily applied in the automobile (Lievers et al. 2004) and aerospace's industry (Hussain et al. 2013). However, there are other branches with an important potential for the technology, such as the biomedical field (Araújo et al. 2014; Lu et al. 2016).

Among biocompatible metallic materials, titanium, and its alloys, such as Ti–6Al–4V are increasingly used in biomedical applications due to their excellent mechanical properties as well as good corrosion resistance. When implanted into human bodies, Ti–6Al–4V remains essentially unchanged in appearance. Consequently, it is often used as a biomaterial for the dental application (Elias et al. 2008).

However, Ti–6Al–4V possesses low formability at room temperature. Hot working of this alloy might be an alternative for formability enhancement (Seshacharyulu et al. 2000). Multiple techniques based on the different heating methods for warm ISF process were recently developed and introduced in the technical literature (Magnus 2016; Mohammadi et al. 2015). It was shown that by using hot ISF process, the formability of difficult-to-form materials among them Ti–6Al–4V titanium alloy can be significantly improved (Fan et al. 2010; Mosecker et al. 2013). Among these techniques, a laser is considered as a heating device which has been applied by Duflou et al. (2007) and Göttmann et al. (2011) in order to form Ti–6Al–4V alloy. Fan et al. (2010) used an electrical resistance heating to well form the titanium alloy and to reduce the surface roughness. A direct current (DC) was passed through the tool to the sheet while allowing for a significant temperature increase in the contact zone between the tool and the sheet.

A hybrid mixed double-sided incremental forming method for forming Ti–6Al–4V sheets has been proposed by Valoppi et al. (2016). The influence of the electrical process parameters on microstructure, micro-hardness, and surface roughness of the formed parts are investigated. Sbayti et al. (2016) studied the feasibility of manufacturing customized Ti–6Al–4V hip prostheses by the application of the hot ISF process. The aim of their study is to develop reliable numerical models for the finite element simulations of the process. The effect of the main processing parameters, namely the forming temperature and the punch diameter on the geometric accuracy and the failure of the final product are investigated.

The objective of the present work is to characterize the formability of Ti–6Al–4V alloys by means of the hot incremental forming. This process was used in the biomedical fields for manufacturing a dental prosthesis. FE simulations of Hot ISF applied to an upper denture base have been carried out using ABAQUS FE program.

2 Finite Element Aspects and Material Modeling

The accuracy of finite element method (FEM) in numerical simulations of metal forming processes depends both on the constitutive laws used and their material parameters identification. In order to simulate the SPIF process, the temperature-dependent physical, and mechanical properties of the material are taken into consideration in the current simulations.

2.1 Material Properties

The sheet material used in these numerical simulations represents the Ti–6Al–4V titanium alloy. The mechanical and thermophysical properties of this metal employed for the workpiece are summarized in Table 1.

The parameters for the Johnson–Cook (J–C) constitutive model of a biomedical grade Ti–6Al–4V alloy were determined for the numerical modeling of its deformation in the warm SPIF process. So, the J–C flow stress is proposed as the applied material model for the workpiece in this study. It considers simple forms of empirical relations of stress as a function of strain, strain rate, and temperature as follows:

$$\sigma_f = \left(A + B \cdot \bar{\varepsilon}_{pl}^n \right) \cdot \left[1 + C \cdot \ln\left(\frac{\dot{\bar{\varepsilon}}}{\dot{\varepsilon}_0}\right) \right] \cdot \left[1 - \left(\frac{T - T_{room}}{T_m - T_{room}}\right)^m \right], \tag{1}$$

where, A, B, C, n, and m are the constants of material, $\dot{\bar{\varepsilon}}$ is the strain rate which is normalized with respect to a reference strain rate $\dot{\varepsilon}_0$ (1 s^{-1}). T_{room} represents the ambient temperature and T_m is the melting temperature of the material equal to 1604 °C. The parameter n takes into account the strain hardening effect and the both coefficients m and C model the thermal softening effect and the strain rate sensitivity, respectively. Damage model proposed by J–C is used in conjunction with J–C yield model. According to J–C damage law, the general formulation of the fracture strain at critical damage can be written as:

Table 1 Thermo-physical parameters of material (Tuğrul et al. 2010)

Material parameters of Ti–6Al–4V sheet	Values
Density ρ [Kg/m³]	4430
Poisson's ratio υ	0.22
Young's modulus E [MPa]	E(T) = 0.7412T + 113375
Thermal expansion α [1/°K]	8.9E-6
Heat conductivity λ [W/(m °C)]	$\lambda(T) = 7.039\ e^{0.0011T}$
Specific heat C_p [N/(mm² °C)]	$C_p(T) = 2.24\ e^{0.0007T}$

Table 2 Constants of the Johnson-Cook constitutive model and failure parameters for the Ti–6Al–4V alloy

A (MPa)	B (MPa)	C	n	m	D_1	D_2	D_3	D_4	D_5
460	1450	0.08	1.31	0.85	−0.09	0.25	−0.5	0.014	3.87

$$\bar{\varepsilon}_f = [D_1 + D_2.\exp(D_3\eta)] \times \left[1 + D_4.\ln\left(\frac{\dot{\bar{\varepsilon}}}{\dot{\bar{\varepsilon}}_0}\right)\right] \times \left[1 + D_5.\left(\frac{T - T_{room}}{T_m - T_{room}}\right)\right], \qquad (2)$$

where $D1$, $D2$, $D3$, $D4$, and $D5$ are respectively, designated by the initial failure strain, the exponential factor, the triaxiality factor, the strain rate factor, and the temperature parameter. The term η defines the ratio of the hydrostatic pressure to the effective stress.

The identified J–C parameters relative to the titanium alloy Ti–6Al–4V are illustrated in Table 2.

2.2 Finite Element Model Description

As the SPIF process involves large material deformation without the presence of the dies, the suitable algorithm should be employed in conjunction with the FEA. In this numerical approach, a three-dimensional modeling described by a thermo-elasto-viscoplastic material model is proposed for the simulation of the SPIF process, which can characterize both mechanical and geometrical responses. The numerical computations were performed by using dynamic explicit FEA code (ABAQUS software).

2.3 Geometrical Model and Tool Trajectory Generation

Based on the scanned shape of an existing custom-made denture as presented in Fig. 1b, the tool path has been generated to produce simultaneously two identical denture base parts. The forming strategy consists of a single forming stage, where the tool traces along a sequence of contour lines with a vertical increment step size (Δz = 0.02 mm) in between. In all simulations, the tool diameter is maintained fixed at a constant value and equal to 10 mm. The initial shape of the titanium alloy sheet Ti–6Al–4V has been considered square having a size of 120 mm × 120 mm and a thickness of 0.5 mm. Concerning the thermal loading, the entire sheet is subjected to different uniform temperature values. As shown in Fig. 1a, the sheet was clamped in its peripheral contour in such manner that all degrees of freedom (three rotations and three translations) are zero. A backing plate is placed underneath the sheet to support the part.
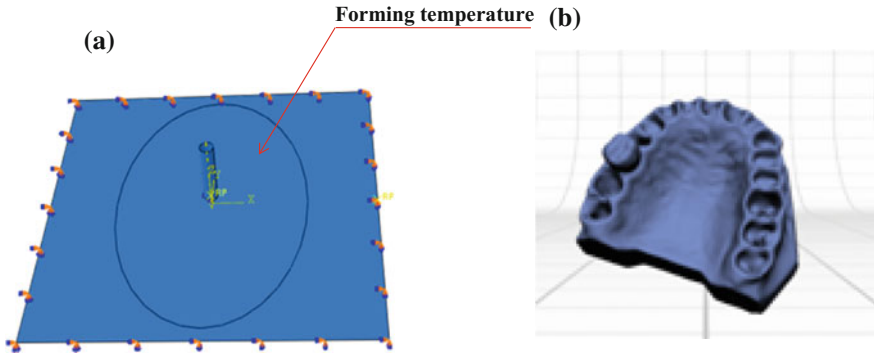
Fig. 1 **a** Numerical model used for FEA simulations in initial position of sheet material and tool, and **b** Geometrical model (STL file)

2.4 Friction Model

Modeling the interaction between the tool and the sheet is one of the most important considerations necessary to simulate the incremental forming process correctly. The punch and the backing plate are modeled by adopting the assumption of an analytical rigid body hypothesis, while the sheet material is considered as elastic–plastic object. Since in the experiments the sheet was flooded with lubricant, the contact properties at the interface between the sheet and the contact area with the punch are defined by the Coulomb's friction model expressed as follows:

$$\tau_{fric} = \mu P, \tag{3}$$

where τ_{fric} is the friction shear stress, μ the friction coefficient, and P the normal contact pressure at the interface. Friction conditions between the forming tool and the sheet metal part have been accounted by considering sliding friction with a small relatively friction coefficient equal to $\mu = 0.15$.

A fraction of dissipated energy converted into heat has been taken into account. So, the rate of frictional energy dissipation is given by the following equation:

$$q_{fric} = \eta \dot{\gamma} \tau_{fric} = \eta \dot{\gamma} \mu P, \tag{4}$$

where $\dot{\gamma}$ is the slipping rate and η the fraction of dissipation energy converted into heat. The value of the last parameter used in the contact algorithm is: $\eta = 0.5$.

2.5 Finite Element Meshing

In the FE model, eight-node thermally coupled brick elements (C3D8RT), with trilinear displacement and temperature with reduced integration and hourglass control are applied in the fully coupled thermal analysis to model the initial blank. In the numerical calculations, the sheet was meshed in three layers in the thickness direction to take into account of the bending effects and the global size of elements is 0.8 mm × 0.8 mm. In this way and for each node both displacements and rotations (i.e., 6° of freedom for each node) are taken into account. Furthermore, the element is subjected to both tractions and bending moments at each step of the deformation path.

3 Results and Discussion

Figure 2a shows the damage distribution at room temperature extrapolated in the center of finite elements presented in form of iso-values. So, the scalar damage variable is modeled by the stiffness degradation (SDEG) during the forming process. It can be retained herein that SDEG = 1.0 means that the corresponding elements failed and the appearance of cracks occurred. Thus, in this case, maximum damage reaches the critical value. According to these results, the critical damage appears at ambient temperature since the SDEG value is very close to 1. As observed in Fig. 2a, highest damage iso-values are located at the failure regions detected in the contact zone between punch and sheet. As it can be expected, the part is completely damaged at Ti = 20 °C after describing some succeeding contours by the punch movement, because as we have cited that the Ti–6Al–4V titanium alloy has a very poor formability at room temperature.
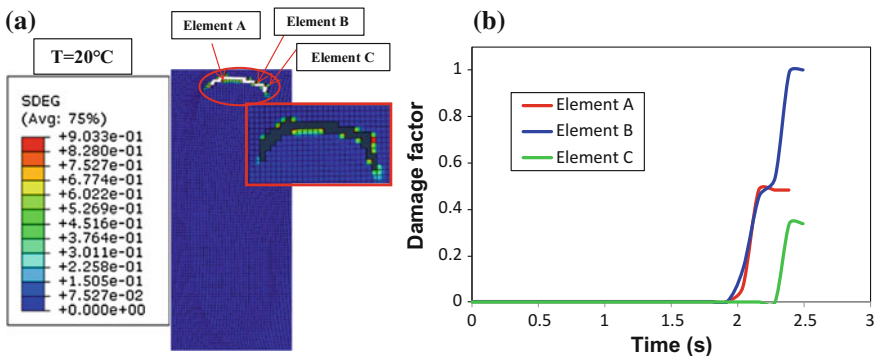
Fig. 2 **a** Damage distribution factor at temperature T = 20 °C, **b** Damage variation versus time at three particular finite elements

Figure 2b present the mechanical response associated with the damage variable evolution monitored in three elements A, B, and C around the failed area. It can be observed from these curves, that the damage values are initially negligible during
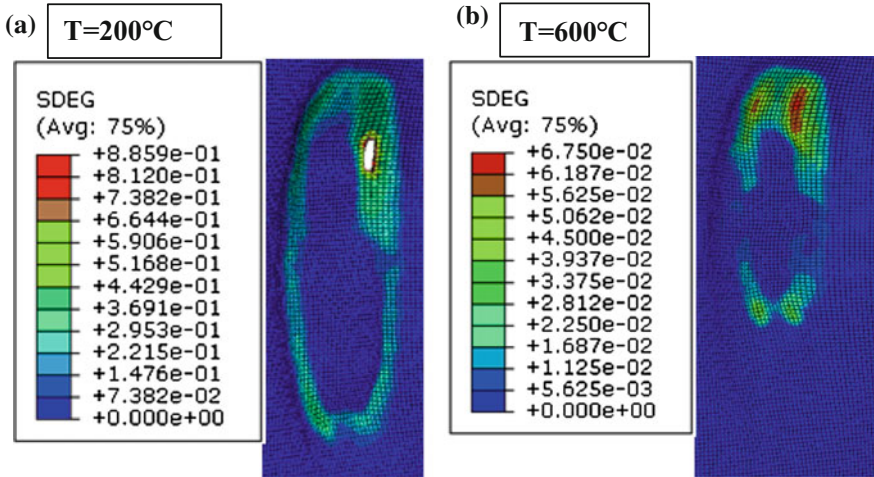
Fig. 3 Damage distribution at different temperatures: **a** T = 200 °C and **b** T = 600 °C
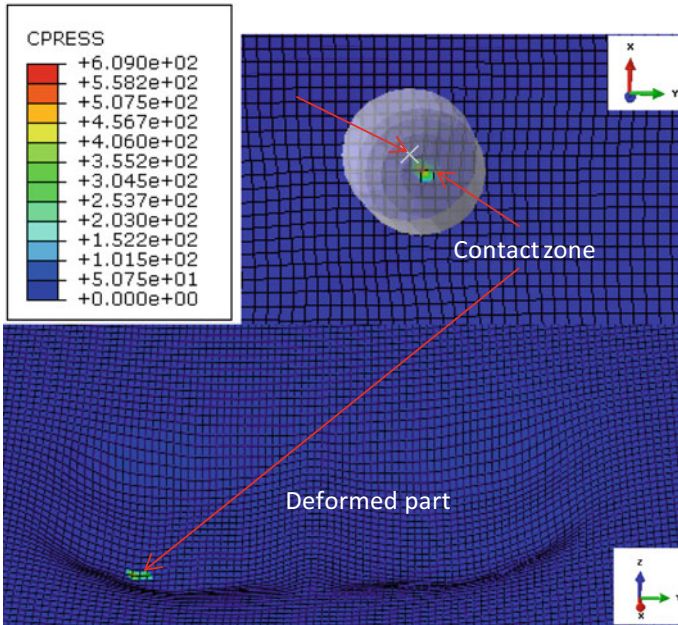
Fig. 4 The distribution of the contact pressure under the forming tool at T = 600 °C

Fig. 5 Distribution of the
equivalent plastic strain fields
at T = 600 °C
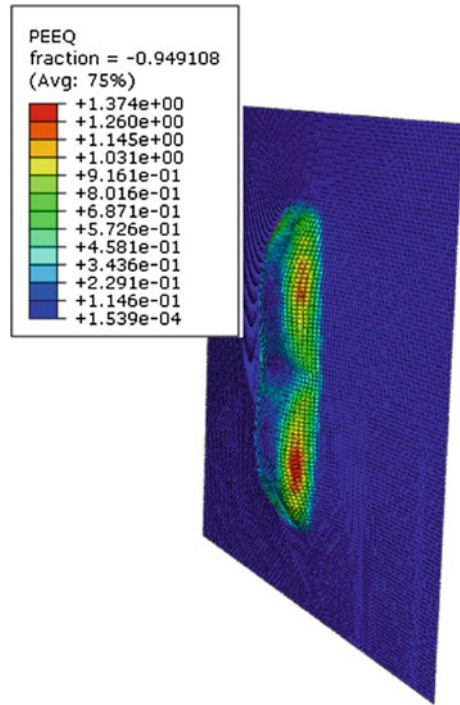
the first contours. This is due to the low accumulated plastic strain deformation on the deformed sheet material. However, the failure begins just after 2 s of the computation step time, corresponding to very severe hardening rate and damage induced within the material. These last output variables are functions of the plastic deformation generated in the formed zones of the part and which depends evidently on the stress intensity.

Figure 3a, b show the evolution of the accumulated damage defined by stiffness degradation SDEG for two forming temperatures T = 200 °C and T = 600 °C. As illustrated in Fig. 3a, there are some removed damaged elements at T = 200 °C. Under these heating conditions, there will be an improvement in the material formability and that the maximum value of damage decreases remarkably when comparing the obtained results with the last simulation. At the end of sheet incremental forming operation with a heating temperature value of T = 600 °C, the maximum SDEG values decrease again, they are very close and do not exceed 0.0675. Hence, we prove that the forming temperature has a significant effect on the mechanical behavior of the Ti–6Al–4V part.

From studying the distribution of the contact pressure between the sheet metal and the tool, it has been observed that after the tool passed the node, no contact is developed between the tool and the node in subsequent forming steps. This is because the tool is mostly in contact with the sheet in the contour area rather than

(a)

(b)
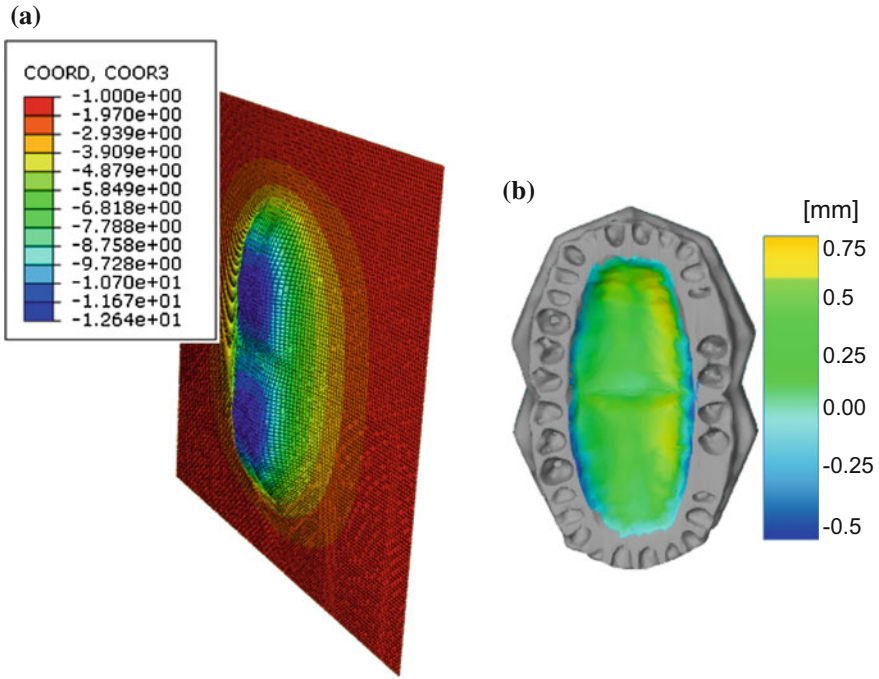
Fig. 6 3D iso-values at T = 600 °C of **a** The displacement along Z-axis, **b** The geometrical deviation of the finished part

the base region and there is always a forward and slightly inward offset between the compact contact zone and the center of the forming tool (Fig. 4).

The deformation of the sheet is in a stepwise fashion with an incremental increase per contour. Figure 5 shows the equivalent plastic strain in the part at the end of the incremental forming operation. It was noticed that, due to the wall angle inclination of the deformed geometry, the maximum plastic strains are localized in the lateral area. At the final forming step, this deformation reached a value of 1.374.

The final achieved geometry of the blank after forming can be seen in Fig. 6a where the part is well-formed with the final desired depth. In order to make a comparison with theoretical geometrical model generated by computer-aided design (CAD), the dimensional control of the deformed part was performed with GOM ATOS inspect software environment. The relative error representing the difference between the numerically predicted depth and desired one of is illustrated in Fig. 6b. It allows to show the well-formed denture base made by the warm SPIF technology with a maximum geometric deviation of the order of 0.75 judged to be acceptable.

4   Conclusion

In this work, by evaluating FE simulation of hot SPIF process for Ti–6Al–4V sheet, the feasibility of manufacturing customized titanium dental prosthesis by using the ISF approach is studied and the particular issues and possible solutions were discussed. The conclusions of this work may be summarized as follows:

(1) ISF of denture base by using Grade 5 titanium sheets is a feasible solution and it shows clearly the potential for real medical application.
(2) First results show promise and the process seem to be satisfactory for the application of dental prosthesis.
(3) The geometrical deviation of the finished part at T = 600 °C predicted by GOM ATOS inspect software environment is improved compared to the ones formed at low temperature.
(4) Further development is still needed to evaluate the effect of the majority of process parameters on the formability of the part to optimize these parameters for the experimental study.

References

Araújo R, Teixeira P, Montanari L et al (2014) Single point incremental forming of a facial implant. Prosthet Orthot Int 38:369–378. https://doi.org/10.1177/0309364613502071

Arfa H, Bahloul R, BelHadjSalah H (2013) Finite element modeling and experimental investigation of single point incremental forming process of aluminum sheets: influence of process parameters on punch force monitoring and on mechanical and geometrical quality of parts. Int J Mater Form 6:483–510. https://doi.org/10.1007/s12289-012-1101-z

Duflou JR, Callebaut B, Verbert J, De Baerdemaeker H (2007) Laser assisted incremental forming: Formability and accuracy improvement. CIRP Ann Manuf Technol 56:273–276. https://doi.org/10.1016/j.cirp.2007.05.063

Elias CN, Lima JHC, Valiev R, Meyers MA (2008) Biomedical applications of titanium and its alloys. pp 1–4

Fan G, Sun F, Meng X et al (2010) Electric hot incremental forming of Ti–6Al–4V titanium sheet. Int J Adv Manuf Technol 49:941–947. https://doi.org/10.1007/s00170-009-2472-2

Göttmann A, Diettrich J, Bergweiler G et al (2011) Laser-assisted asymmetric incremental sheet forming of titanium sheet metal parts. Prod Eng 5:263–271. https://doi.org/10.1007/s11740-011-0299-9

Hussain G, Khan HR, Gao L, Hayat N (2013) Guidelines for tool-size selection for single-point incremental forming of an aerospace alloy. Mater Manuf Process 28:324–329. https://doi.org/10.1080/10426914.2012.700151

Lievers WB, Pilkey AK, Lloyd DJ (2004) Using incremental forming to calibrate a void nucleation model for automotive aluminum sheet alloys. Acta Mater 52:3001–3007. https://doi.org/10.1016/j.actamat.2004.03.002

Lu B, Ou H, Shi SQ et al (2016) Titanium based cranial reconstruction using incremental sheet forming. 361–370. https://doi.org/10.1007/s12289-014-1205-8

Magnus CS (2016) Joule heating of the forming zone in incremental sheet metal forming: Part 2. Int J Adv Manuf Technol. https://doi.org/10.1007/s00170-016-9008-3

Mohammadi A, Vanhove H, van Bael A et al (2015) Formability enhancement in incremental forming for an automotive aluminium alloy using laser assisted incremental forming. Key Eng Mater 639:195–202. https://doi.org/10.4028/www.scientific.net/KEM.639.195

Mosecker L, Göttmann A, Saeed-Akbari A et al (2013) Deformation mechanisms of Ti–6Al–4V sheet material during the incremental sheet forming with laser heating. Key Eng Mater 549:372–380. https://doi.org/10.4028/www.scientific.net/KEM.549.372

Sbayti M, Ghiotti A, Bahloul R et al (2016) Finite element analysis of hot single point incremental forming of hip prostheses. https://doi.org/10.1051/matecconf/201

Seshacharyulu T, Medeiros SC, Frazier WG, Prasad YVRK (2000) Hot working of commercial Ti–6Al–4V with an equiaxed α–β microstructure: materials modeling considerations. Mater Sci Eng A 284:184–194. https://doi.org/10.1016/S0921-5093(00)00741-3

Tuğrul Ö, Sima M, Srivastava AK (2010) Finite element simulation of high speed machining Ti–6Al–4V alloy using modified material models. Trans NAMRI/SME 38:49–56

Valoppi B, Sanchez Egea AJ, Zhang Z et al (2016) A hybrid mixed double-sided incremental forming method for forming Ti–6Al–4V alloy. CIRP Ann Manuf Technol 65:309–312. https://doi.org/10.1016/j.cirp.2016.04.135

A Polynomial Chaos Method for the Analysis of the Dynamic Response of a Gear Friction System

Ahmed Guerine and Abdelkhalak El Hami

Abstract In this paper, we propose a new approach for taking into account uncertainties based on the projection on polynomial chaos method. The new approach is used to determine the dynamic response of a one-stage spur gear system modeled by eight degrees of freedom in the presence of friction coefficient between teeth that admits some dispersion. Therefore, it becomes necessary to take this uncertainty into account in the stability analysis of gear system to ensure robust predictions of stable and instable behaviors. The simulation results are obtained by the polynomial chaos approach for the dynamic analysis of a one-stage spur gear system with the uncertainty associated with friction coefficient on the teeth contact. The proposed approach is an efficient probabilistic tool for uncertainty propagation. The polynomial chaos results are compared with Monte Carlo simulations. The main results of the present study show that the polynomial chaos may be an efficient tool to take into account the dispersions of the friction coefficient of a one-stage spur gear system.

Keywords Spur gear system · Uncertainty · Friction coefficient
Polynomial chaos

1 Introduction

The study and analysis of the dynamic behavior with nonlinear systems are a major interest in the industrial sector. Thus, they allow overcoming the areas of instability and reducing vibration levels.

A. Guerine (✉) · A. El Hami
Laboratory Optimization and Reliability in Structural Mechanics LOFIMS,
National Institute of Applied Sciences of Rouen, BP 08,
76801 Saint Etienne du Rouvray Cedex, France
e-mail: ahmedguerine@gmail.com

A. El Hami
e-mail: abdelkhalak.elhami@insa-rouen.fr

The mechanisms of transmission by gear tooth contacts are characterized by the presence of friction coefficient that affects the vibration and noise of these systems. Parameter estimation is an important problem because many parameters simply cannot be measured physically with good accuracy, such as the friction coefficient, especially in the real-time application (Blanchard et al. 2009, 2010). Therefore, it becomes necessary to take into account these uncertainties to ensure the robustness of the analysis (Guerine et al. 2014, 2015a, b, 2016a, b, c, 2017; Guerine and El Hami 2016; Beyaoui et al. 2016). Several methods are proposed in the literature. Monte Carlo (MC) simulations are a well-known technique in this field (Fishman 1996). Parallel simulation (Papadrakakis and Papadopoulos 1999) and proper orthogonal decomposition (Lindsley and Beran 2005) are some solutions proposed to circumvent the computational difficulties of the MC method. polynomial chaos (PC) gives a mathematical framework to separate the stochastic components of a system response from the deterministic ones. The PC method has been shown to be considerably more efficient than Monte Carlo in the simulation of systems with a small number of uncertain parameters.

The main originality of the present paper is that the uncertainty of the gear friction system in the dynamic behavior study of one stage gear system is taken into account. The main objective is to investigate of the capabilities of the new method to determine the dynamic response of a spur gear system subject to uncertain friction coefficient. So, an eight degree of freedom system modeling the dynamic behavior of a spur gear system is considered. The polynomial chaos results are compared with Monte Carlo simulations.

2 One Stage Spur Gear System

The dynamic model of the one-stage gear system is represented in Fig. 1. This model is composed of two blocks. Every block is supported by a flexible bearing which the bending stiffness is k_1^x and the traction-compression stiffness is k_1^y for the first block, k_2^x and k_2^y for the second block.

The wheels (11) and (22) characterize, respectively, the drive and driven gears. The two shafts (1) and (2) admit some torsional stiffness k_1^θ and k_2^θ.

Angular displacements of every wheel are noticed by $\theta_{(1,1)}$, $\theta_{(1,2)}$, $\theta_{(2,1)}$ and $\theta_{(2,2)}$. Besides, the linear displacements of the bearing noted by x_1 and y_1 for the first block, x_2 and y_2 for the second block, are measured in the plan which is orthogonal to the wheel axis of rotation.

3 Polynomial Chaos Method

In this section, we propose a new methodological method based on the projection on polynomial chaos. This method consists in projecting the stochastic desired solutions on a basis of orthogonal polynomials in which the variables are Gaussian
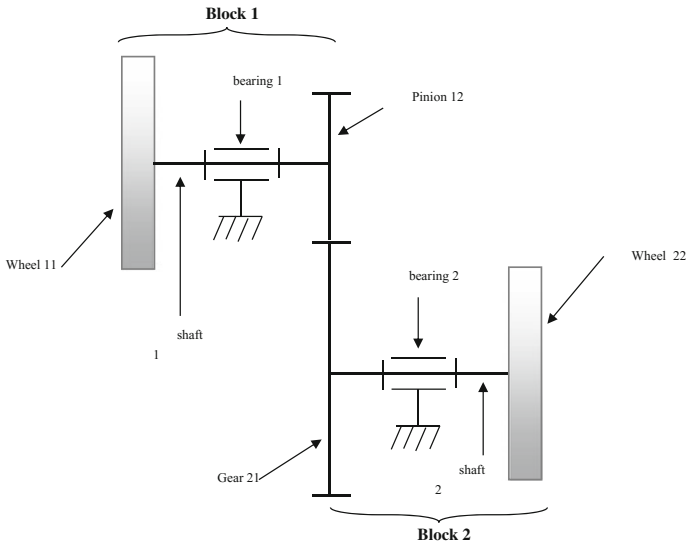
Fig. 1 Model of the one stage gear system

orthonormal. The properties of the base polynomial are used to generate a linear system of equations by means of projection. The resolution of this system led to an expansion of the solution on the polynomial basis, which can be used to calculate the moments of the random solution. With this method, we can easily calculate the dynamic response of a mechanical system.

4 Equations of Motion

The differential equations describing the dynamic behavior of our system (Fig. 1) are obtained using Lagrange formalism. These equations are represented as follows:

$$
\begin{cases}
m_1 \ddot{x}_1 + k_1^x x_1 + s^\alpha k(t)\langle L^\delta\rangle\{Q\} = \left(F_f^1 - F_f^0\right)s^\alpha \\
m_1 \ddot{y}_1 + k_1^y y_1 + c^\alpha k(t)\langle L^\delta\rangle\{Q\} = -\left(F_f^1 - F_f^0\right)c^\alpha \\
m_2 \ddot{x}_2 + k_2^x x_2 - s^\alpha k(t)\langle L^\delta\rangle\{Q\} = -\left(F_f^1 - F_f^0\right)s^\alpha \\
m_2 \ddot{y}_2 + k_2^y y_2 - c^\alpha k(t)\langle L^\delta\rangle\{Q\} = \left(F_f^1 - F_f^0\right)c^\alpha \\
I_{(1,1)}\dot{\theta}_{(1,1)} + k_1^\theta \Theta_1 = Cm \\
I_{(1,2)}\dot{\theta}_{(1,2)} - k_1^\theta \Theta_1 + r_{(1,2)}^b k(t)\langle L^\delta\rangle\{Q\} \\
\qquad\qquad = Cf_{12}^1(t) - Cf_{12}^0(t) \\
I_{(2,1)}\dot{\theta}_{(2,1)} + k_2^\theta \Theta_2 - r_{(2,1)}^b k(t)\langle L^\delta\rangle\{Q\} \\
\qquad\qquad = -Cf_{21}^1(t) + Cf_{21}^0(t) \\
I_{(2,2)}\dot{\theta}_{(2,2)} + k_2^\theta \Theta_2 = 0
\end{cases}
\tag{1}
$$

where $s^\alpha = \sin(\alpha)$ and $c^\alpha = \cos(\alpha)$ and $r^b_{(1,2)}$, $r^b_{(2,1)}$ represent the base gears radius $\Theta_1 = (\theta_{(1,1)} - \theta_{(1,2)})$ and $\Theta_2 = (\theta_{(2,1)} - \theta_{(2,2)})$

$\{Q(t)\}$ is the vector of the model generalized coordinates, it is in the form:

$$\{Q(t)\} = \begin{bmatrix} x_1 & y_1 & x_2 & y_2 & \theta_{(1,1)} & \theta_{(1,2)} & \theta_{(2,1)} & \theta_{(2,2)} \end{bmatrix}^T \tag{2}$$

$F_f^1(t)$ and $F_f^0(t)$ are the first and the second friction force corresponding to the first and the second pair in contact.

$Cf_{12}(t)$ and $Cf_{21}(t)$ are the friction torque on the first spur gear (12) and the second spur gear (21).

5 Numerical Simulation

The friction coefficient is supposed random variable and defined as follows:

Fig. 2 Mean value of $x_1(t)$ $\sigma_\mu = 4\%$
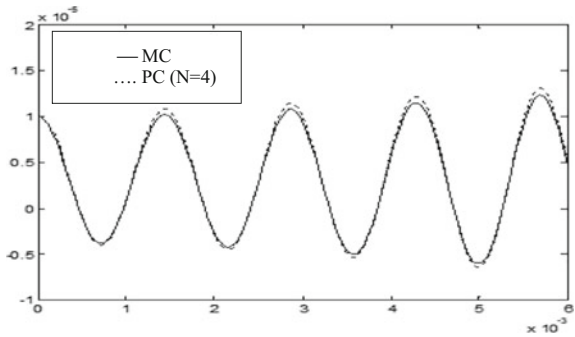
Fig. 3 Variance of $x_1(t)$ $\sigma_\mu = 4\%$
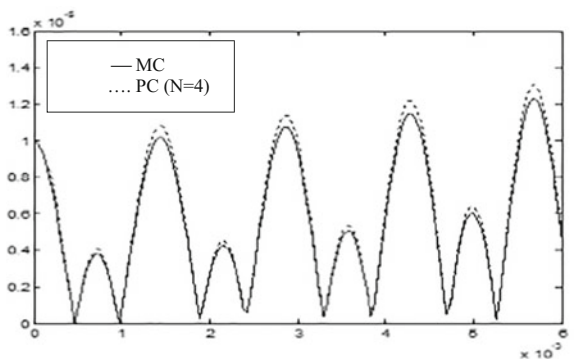
Fig. 4 Mean value of $x_1(t)$ $\sigma_\mu = 7\%$
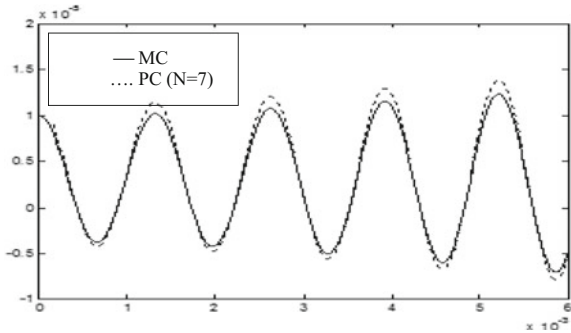
Fig. 5 Variance of $x_1(t)$ $\sigma_\mu = 7\%$

$$\mu = \mu_0 + \sigma_\mu \xi \tag{3}$$
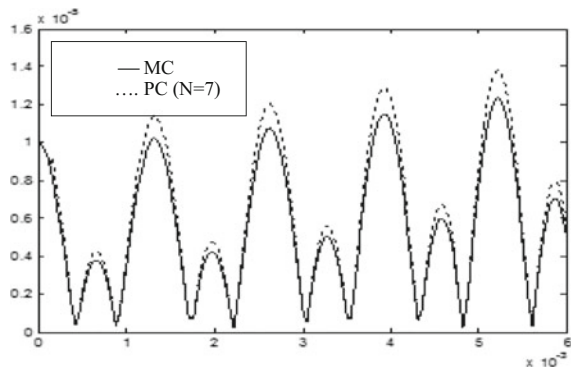
where ξ is a zero mean value Gaussian random variable, μ_0 is the mean value and σ_μ is the standard deviation of this parameter.

The mean value and the variance of the dynamic component of the linear displacement of the first bearing in two directions, x and y, have been calculated by the polynomial chaos method. The obtained results are compared with those given by the Monte Carlo simulations with 1000 simulations. The results are plotted in Figs. 2 and 3 for $\sigma_\mu = 4\%$ and in Figs. 4 and 5 for $\sigma_\mu = 7\%$.

These figures show that the obtained solutions oscillate around the Monte Carlo simulations reference solution. It can be seen that for small standard deviation $\sigma_\mu = 4\%$, the polynomial chaos solutions in fourth-order polynomial provides a very good accuracy as compared with the Monte Carlo simulations. When the standard deviation increases the error increases.

6   Conclusion

An approach based on the PC method has been proposed to study the dynamic behavior of one-stage gear system in the presence of friction coefficient between teeth that admits some dispersion. The polynomial chaos method has been used to determine the dynamic response of this system. The efficiency of the proposed method compared with the Monte Carlo simulation. The main results of the present study show that the polynomial chaos may be an efficient tool to take into account the dispersions of the friction coefficient.

References

Beyaoui M, Guerine A, Walha L, El Hami A, Fakhfakh T, Haddar M (2016) Dynamic behavior of the one-stage gear system with uncertainties. Struct Eng Mech 58(3):443–458

Blanchard E, Sandu A, Sandu C (2009) Parameter estimation for mechanical systems via an explicit representation of uncertainty. Int J Comput Aided Eng Comput 26:541–569

Blanchard E, Sandu A, Sandu C (2010) Polynomial chaos-based parameter estimation methods applied to vehicle system. Proc. Inst Mech Eng Part K J Multi-Body Dyn 224:59–81

Fishman GS (1996) Monte carlo, concepts, algorithms and applications, 1st edn. Springer

Guerine A, Driss Y, Beyaoui M, Walha L, Fakhfakh T, Haddar M (2014) A polynomial chaos method for the analysis of uncertain spur gear system. In: Mechatronic systems: theory and applications, pp 89–97

Guerine A, El Hami A, Walha L, Fakhfakh T, Haddar M (2015a) A perturbation approach for the dynamic analysis of one stage gear system with uncertain parameters. Mech Mach Theory 92:113–126

Guerine A, El Hami A, Fakhfakh T, Haddar M (2015b) A polynomial chaos method to the analysis of the dynamic behavior of spur gear system. Struct Eng Mech Int J 53:819–831

Guerine A, El Hami A, Walha L, Fakhfakh T, Haddar M (2016a) A polynomial chaos method for the analysis of the dynamic behavior of uncertain gear friction system. Eur J Mech A/Solids 59:76–84

Guerine A, El Hami A, Walha L, Fakhfakh T, Haddar M (2016b) Dynamic response of a spur gear system with uncertain parameters. J Theor Appl Mech 54(3):1039–1049

Guerine A, El Hami A, Walha L, Fakhfakh T, Haddar M (2016c) Dynamic response of a Spur gear system with uncertain friction coefficient. Adv Eng Softw. https://doi.org/10.1016/j.advengsoft.2016.05.009

Guerine A, El Hami A (2016) Uncertainty analysis of one stage gear system using interval analysis method. In: 2016 4th IEEE international colloquium on information science and technology (CiSt), pp 670–674

Guerine A, El Hami A, Walha L, Fakhfakh T, Haddar M (2017) Dynamic response of wind turbine gear system with uncertain-but-bounded parameters using interval analysis method. Renew Energ 113:679–687

Lindsley NJ, Beran PS (2005) Increased efficiency in the stochastic interrogation of an uncertain nonlinear aeroelastic system. In: International forum on aeroelasticity and structural dynamics, Munich, Germany, June

Papadrakakis M, Papadopoulos V (1999) Parallel solution methods for stochastic finite element analysis using Monte Carlo simulation. Comput Methods Appl Mech Eng 168:305–320

Sensitivity Analysis of Backlogging Cost in Multi-item Capacitated Lot-Sizing Problem

Hanen Ben Ammar, Omar Ayadi and Faouzi Masmoudi

Abstract In this paper, a multi-item capacitated lot-sizing problem (MI-CLSP) with backlogging is considered. The problem is formulated as bi-objective optimization model with two conflicting objectives. The first one aims to minimize the total cost composed of production, setup, and backlogging costs and the second one aims to minimize the total inventory level. Augmented epsilon-constraint method is adopted when solving this problem in order to find the set of Pareto-optimal solutions. The goal of this study is to investigate the effect of variation in the backlogging cost on optimal Pareto solutions of the MI-CLSP. Several numerical examples with different demand typology are tested. The different sensitivity analyses show a considerable effect of the variation in the backlogging cost on the set of Pareto-optimal solutions. This investigation offers to the decision-makers a global visibility on the influence of variation on the backlogging cost on the optimal solutions of a MI-CLSP.

Keywords Lot-sizing problem · Multi-objective optimization · Production planning · Backlogging cost parameter · Augmented epsilon-constraint

1 Introduction

The lot-sizing problem "LSP" has been the subject of significant amount of research in the past five decades, starting with the seminal paper of Wagner and Whitin (1958) on the uncapacitated LSP. The capacitated lot-sizing problem "CLSP",

H. Ben Ammar (✉) · O. Ayadi · F. Masmoudi
Mechanics, Modeling and Production Research Laboratory, National Engineering
School of Sfax (ENIS), Sfax University, Route de Sokra B.P.1173, 3038 Sfax, Tunisia
e-mail: hanen.benammar@enis.tn

O. Ayadi
e-mail: omar.ayadi@yahoo.fr

F. Masmoudi
e-mail: faouzi.masmoudi@enis.rnu.tn

which is a production planning problem, consists in deciding the quantity to produce for each item at each time period in order to satisfy the demands with minimal cost while facing a finite capacity constraint (Absi and Kedad-Sidhoum 2008). In an industrial context, multiple constraints may complicate the problem such as the finite capacity constraint. In fact, this limitation can lead to the impossibility to satisfy the total customer's demands when there is not sufficient capacity. The quantity of unsatisfied demand is referred to as «shortage on demand». Shortages are often assumed in lot-sizing problems and the amount of unsatisfied demand can be either lost or back-ordered.

Several researchers dealing with the capacitated lot-sizing problem with shortage have been reported in the literature. Aksen et al. (2003) introduced a profit maximization version of the well-known Wagner and Whitin model for the deterministic uncapacitated single-item LSP with lost sales. Absi and Kedad-Sidhoum (2007) developed a multi-item capacitated lot-sizing problem "MI-CLSP" with setup time and safety stock in which demand can be totally or partially lost. To solve their developed model, they proposed a fast combinatorial separation algorithm within a branch-and-cut framework. Subsequently, Absi and Kedad-Sidhoum (2008) extended the above model by considering the shortage cost. Absi and Kedad-Sidhoum (2009) proposed a MI-CLSP with setup times, safety stock deficit costs, and demand shortage costs. To solve their model, a Lagrangian relaxation of the resource capacity constraints was firstly proposed, and then the induced subproblem was solved using a dynamic programming algorithm.

Recently, Hajipour et al. (2015) addressed the MI-CLSP with setup times, safety stocks, and demand shortages plus lost sales and backorder considerations for different production methods. The developed model attempted to simultaneously minimize three conflicting objective functions: minimizing the total production costs; leveling the production volume in different production periods; and producing a solution which is as close as possible to the just-in-time level. Two novels meta-heuristic algorithms called multi-objective vibration damping optimization (MOVDO) and a multi-objective harmony search algorithm (MOHSA) were developed to solve the proposed model.

In the above literature, most of the researchers assumed backlogging cost as a high-penalty cost. However, in real life, backlogging cost parameter is variable from a case to another.

In this paper, a multi-item capacitated lot-sizing problem (MI-CLSP) with backlogging is addressed, which is a special variant of CLSP. The considered problem consists of generating an optimized production plan of N items over a finite planning horizon with respect to the capacity constraints. In fact, the consideration of backlogging is crucial in order to make the problem closer to reality. The purpose of this work is to examine the effect of variation in backlogging cost on the Pareto-optimal solutions of the addressed problem.

The remainder of the paper is organized as follows. Mathematical formulation of the addressed problem is presented in Sect. 2. Section 3 describes the used

resolution method. The description of the developed numerical examples is detailed in Sect. 4. In Sect. 5, the computational results are described and discussed. Finally, Sect. 6 draws the conclusion of this study.

2 Mathematical Formulation

The considered model is a bi-objective optimization model for the (MCLSP) with backlogging that generates an optimized production plan over a finite planning horizon with respect to the capacity constraints. The planning horizon is divided into a set of time period. The demand for each product is assumed to be known and is to be satisfied at the end of each planning period. In case of shortage, the unsatisfied demand is backlogged. The proposed model aims at simultaneously minimizing the total cost and the total inventory level.

The following assumptions are considered:

- Demand for each item is assumed to be deterministic
- Inventory and backlogging quantities are null at the initial period of the planning horizon
- Inventory and backlogging quantities are determined at the end of each planning period
- Inventory and backlogging quantities are null at the end of the planning horizon

To formulate this model, the following notations are considered:

Indices and Set Indexes:

t   period index, $t = 1,…, T$
i   item index, $i = 1,…, N$

Parameters

$D_{i,t}$ Demand of item type i in period t
c_i Unit production cost of item type i
bc_i Unit backlogging cost of item type i per unit of period
s_i Unit setup cost of item type i
st_i Setup time of item type i
v_i Required time to produce a unit of item type i
C_t Available capacity in period t (in time units)
$M_{i,t}$ Maximum production level of item type i in period t

Decision variables

$X_{i,t}$ Production quantity of item type i in period t (lot size)
$I_{i,t}$ Inventory quantity of item type i at the end of period t
$B_{i,t}$ Backlogging quantity of item type i at the end of period t
Z_{it} Binary setup variable. $Z_{it} = 1$ if the resource is setup for item type i in period t, and 0 otherwise

TC   Total Cost
I   Total Inventory Level

The formulation of the mathematical model is presented next:

$$\text{Min TC} = \sum_{t=1}^{T} \sum_{i=1}^{N} \left[(c_i X_{i,t}) + (s_i Z_{i,t}) + (bc_i B_{i,t}) \right] \tag{1}$$

$$\text{Min I} = \sum_{t=1}^{T} \sum_{i=1}^{N} I_{i,t} \tag{2}$$

$$X_{i,t} + I_{i,t-1} + B_{i,t} = D_{i,t} + I_{i,t} + B_{i,t-1} \quad \forall t = 1 \dots T; \ i = 1 \dots N; \tag{3}$$

$$\sum_{i=1}^{N} \left(v_i X_{i,t} + st_i Z_{i,t} \right) \leq C_t \quad \forall t = 1 \dots T \tag{4}$$

$$X_{i,t} \leq M_{i,t} Z_{i,t} \quad \forall t = 1 \dots T; \ i = 1 \dots N \tag{5}$$

$$X_{i,t}, I_{i,t}, B_{i,t} \geq 0 \quad \forall t = 1 \dots T; \ \forall i = 1 \dots N \tag{6}$$

$$Z_{i,t} \in \{0, 1\} \quad \forall t = 1 \dots T; \ i = 1 \dots N \tag{7}$$

In this formulation, the first objective function (1) attempts to minimize the total cost, including production, setup, and backlogging costs and the second objective function (2) tries to minimize the total inventory level over the planning horizon. Constraints (3) represent the flow balance equation between inventories, production, backlogs, and demand. The production capacity in each period is provided by constraints (4). Constraints (5) are the setup and production linkage. The decision variables domains are specified by constraints (6) and (7).

3 Description of the Resolution Method

Several solutions methods have been developed in the literature to solve the multi-objective optimization problem (MOOP) (Miettinen 1999). The epsilon-constraint method is considered among the well-known methods that dealing with MOOP and finding a Pareto-optimal fronts (Mavrotas 2009). In this work, a modified version on the conventional epsilon-constraint is adopted to generate a set of Pareto-optimal solutions. In this section, first, the epsilon-constraint method is described and then the augmented epsilon-constraint is presented.

3.1 Epsilon-Constraint Description

The epsilon-constraint method developed by Chankong and Haimes (1983) is a non-dominated method to find Pareto-optimal fronts for MOOP. In the epsilon-constraint method, one of the objective functions is chosen as the main objective function to be optimized and the other objective functions are incorporated as constraints part of the model by according some allowable levels to each of them. By varying the value of the ε_i, the set of the Pareto-optimal solutions is generated. The transformed problem is formulated as follows:

$$\text{Minimize } f_1(x)$$
$$\text{Subject to } f_i(x) \leq \varepsilon_i \quad \forall i = 2 \ldots N;$$
$$x \in X$$

where N is the number of objective functions.

3.2 Augmented Epsilon-Constraint Description

The epsilon-constraint method has various advantages among the weighting method. Nevertheless, in spite of its advantages, three points above its implementation that needs more attention (Mavrotas 2009).

(1) The determination of the range of the different objective functions over the efficient set.
(2) The guarantee of the efficiency of the provided Pareto solutions.
(3) The increased solution time for problems dealing with more than two objectives.

In order to overcome these three issues, a modified version of the ordinary epsilon-constraint method named augmented epsilon-constraint is used. In this method, the inequality of the objective functions constraints is transformed to equality constraints by incorporating positive slack or surplus variables. Then the principal objective function is augmented by these surplus or slack variables. Therefore, the new problem becomes:

$$\text{Minimize } \left(f_1(x) + \delta \times \left(\frac{s_1}{r_1} + \frac{s_2}{r_2} + \cdots + \frac{s_N}{r_N} \right) \right)$$
$$\text{Subject to } f_i(x) + s_i = \varepsilon_i \quad \forall i = 2 \ldots N;$$

$s_i \in R^+$, $x \in X$, Where N is the number of objective functions
Where δ is a small number usually between 10^{-3} and 10^{-6}. The r_i represent the range of the ith objective function and is calculated from the payoff table. This

payoff table is determined from the individual optimization of each objective. The maximum and the minimum values of each objective function are calculated from individual optimization. Then the range of each objective function is obtained by subtracting its maximum and minimum values.

4 Tests Description

The goal of this study is to investigate the influence of variation in the backlogging cost on the optimal solutions of the previously presented model. The unit backlogging cost is defined by the following equation:

$$bc_i = \alpha \times h_i \tag{8}$$

where α is a positive constant and h_i represents the unit holding cost of item i.

Two main cases will be studied. Each of these two cases contains three examples. In each Case, four item types (item 1, item 2, item 3, and item 4) and different demand trend are considered. The considered planning horizon is composed of six time periods. The demands of different items are supposed to be deterministic and to be satisfied over a finite planning horizon while facing finite capacity. These two cases have the same number of decisions variables and constrains.

Case 1: The first case represents a production system where the demand of each time period doesn't exceed the available capacity. In this first case, three numerical examples will be studied, where the only difference is the demand trend. As shown in Table 1, for the first example, the demand of different items has an increasing trend and for the second example, a decreasing trend is considered as presented in Table 2. Table 3 provides the third example which presents the example with random variation of demand trend.

Case 2: The second case corresponds to a production system where the demand of some time period exceeds the available capacity. As with the first case, three numerical examples are studied, where only the demand typology changes. As described in Table 4, in the first example, the demand has an increasing trend and in the second example it has a decreasing demand trend as reported in Table 5. Table 6 the random variation of third example demand.

Table 1 Demand of different items with increasing trend

Case 1. Example 1						
Demand of	T1	T2	T3	T4	T5	T6
Item 1	50	55	60	65	70	75
Item 2	60	65	70	75	80	85
Item 3	65	70	75	80	85	90
Item 4	55	60	65	70	75	80

Table 2 Demand of different items with decreasing trend

Case 1. Example 2						
Demand of	T1	T2	T3	T4	T5	T6
Item 1	80	75	70	65	60	55
Item 2	85	80	75	70	60	65
Item 3	80	75	70	65	60	55
Item 4	95	90	85	80	75	70

Table 3 Demand of different items with random variation trend

Case 1. Example 3						
Demand of	T1	T2	T3	T4	T5	T6
Item 1	69	72	97	70	84	72
Item 2	66	97	100	76	89	73
Item 3	69	77	77	84	69	77
Item 4	77	67	64	70	64	80

Table 4 Demand of different items with increasing trend

Case 2. Example 1						
Demand of	T1	T2	T3	T4	T5	T6
Item 1	70	75	80	85	90	95
Item 2	60	65	70	75	80	85
Item 3	75	80	85	90	95	100
Item 4	65	70	75	80	85	90

Table 5 Demand of different items with decreasing trend

Case 2. Example 2						
Demand of	T1	T2	T3	T4	T5	T6
Item 1	90	85	80	75	70	65
Item 2	85	80	75	70	60	65
Item 3	95	90	85	80	75	70
Item 4	95	90	85	80	75	70

Table 6 Demand of different items with random variation trend

Case 2. Example 3						
Demand of	T1	T2	T3	T4	T5	T6
Item 1	91	82	98	98	71	83
Item 2	96	54	99	74	96	51
Item 3	56	64	58	90	90	93
Item 4	96	77	99	57	98	97

A sensitivity analysis is carried out by considering the different numerical examples described above. During the examination of the effect of variation in the backlogging cost parameter on the optimal total cost and total inventory level, three different values of constant α are adopted, $\alpha = 2$, 5 and 10.

5   Results and Discussion

The main purpose of the different sensitivity analysis is to provide the decision maker a visibility on the effect of varying the backlogging cost on the optimal total cost and the optimal total inventory level while facing a different demand trend. These different sensitivity analyses are based on the variation of the backlogging cost in the multi-item capacitated lot-sizing model. The detailed method in Sect. 3 is used to generate the set of Pareto-optimal solutions for each of the described examples in Sect. 4 and for each value of the backlogging cost parameter α.

5.1   Sensitivity Analysis of Case 1

Sensitivity analyses corresponding to the first studied case are detailed below.

The influence of variation of the value of α on the optimal solutions for each studied example of the first case are given in Figs. 1, 2, and 3. It is observed that as the value of backlogging cost parameter α increase, the optimal total cost and the optimal total inventory level increase. Moreover, as the value of the parameter α increases, the obtained optimal solutions becomes close to the optimal solutions without backlogging. Based on this sensitivity analysis, it was concluded that for increasing demand trend, the total cost and total inventory level are lowly sensitive to variation in backlogging cost. However, for decreasing demand trend, the total optimal cost and total inventory level are highly sensitive to change in backlogging cost. Note that also for the third example when the demand has a random variation pattern, the optimal solutions are significantly sensitive to the variation of the backlogging cost.
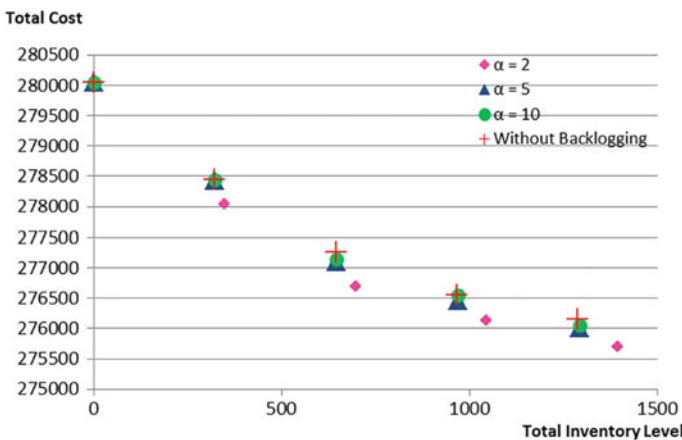
Fig. 1 The non-dominated front of objective functions for the Case 1. Example 1
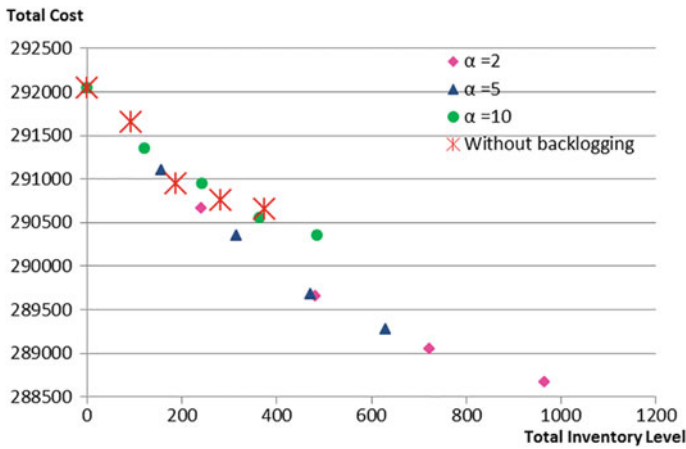
Fig. 2 The non-dominated front of objective functions for the Case 1. Example 2
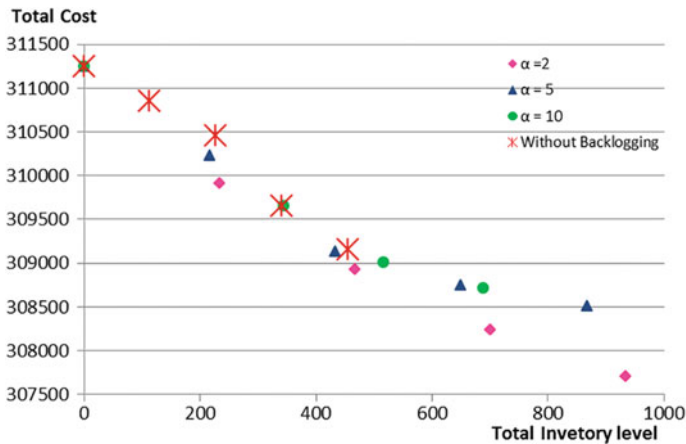
Fig. 3 The non-dominated front of objective functions for the Case 1. Example 3

5.2 Sensitivity Analysis of Case 2

For this second studied case, the effect of variation of the backlogging cost parameter α on the optimal solutions is different from an example to another. From Figs. 4, 5, and 6, it is shown that the total cost and the total inventory level increase with the increase of the value of the backlogging cost parameter α. From Figs. 4 and 6, it is seen that for increasing demand pattern and random demand variation, as the value of parameter α increases, as the total cost and the total inventory level become close to the optimal total cost and the optimal total inventory without backlogging. However, for the decreasing demand pattern, it is observed that the
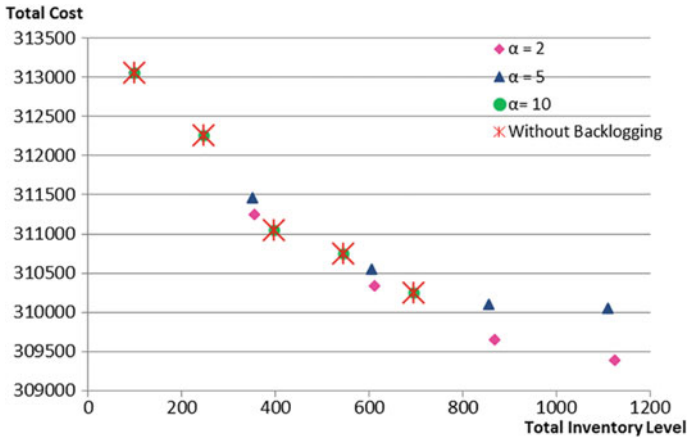
Fig. 4 The non-dominated front of objective functions for the Case 2. Example 1

number of the obtained Pareto-optimal solutions decreases with the increase in the value of the backlogging cost parameter α, as shown in Fig. 5. Based on the conducted sensitivity analyses, it is concluded that for increasing demand trend, the optimal total cost is lowly sensitive to the change in the backlogging cost while the optimal total inventory level is significantly sensitive. From Fig. 5, it is noted that for the decreasing demand trend case, the optimal total cost as well as the optimal inventory level are highly sensitive to the variation in the backlogging cost. Finally, from Fig. 6, it is concluded that the optimal solutions for studied example are highly sensitive to the change in the backlogging cost.
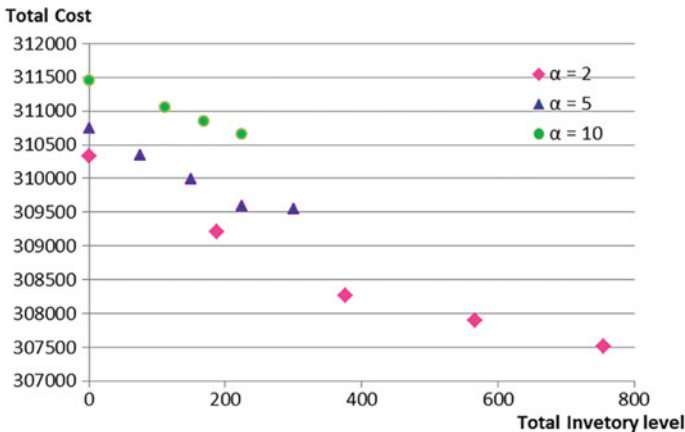
Fig. 5 The non-dominated front of objective functions for the Case 2. Example 2
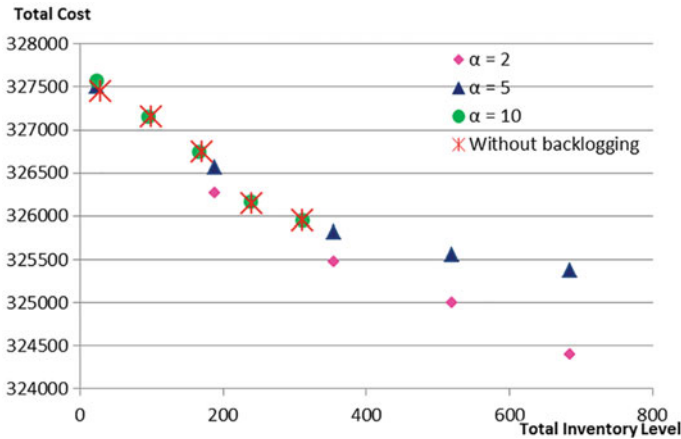
Fig. 6 The non-dominated front of objective functions for the Case 2. Example 3

6 Conclusion

In this paper, an investigation of backlogging cost effect on the optimal solutions of a bi-objective multi-item capacitated lot-sizing model is proposed. The considered model attempts to minimize simultaneously the total cost including production, setup, and backlogging costs and the total inventory level. Several numerical examples are studied and augmented epsilon-constraint method is applied to solve the developed examples. Based on the results of the different sensitivity analysis performed, it is shown that for the studied examples, the optimal total cost and the optimal total inventory level increase as the backlogging cost increases. However, this variation in the backlogging cost has impact differently on the optimal total cost and the optimal total inventory level for each demand trend. The main contribution of this study is to provide decision-makers with a global visibility on the influence of variation in the backlogging cost on optimal solutions of the considered problem that helps them during the planning development process.

References

Absi N, Kedad-Sidhoum S (2007) MIP-based heuristics for multi item capacitated lot-sizing problem with setup times and shortage costs. RAIRO—Oper Res 41(2):171–192

Absi N, Kedad-Sidhoum S (2008) The multi-item capacitated lot-sizing problem with setup times and shortage costs. Eur J Oper Res 185(3): 1351–1374. https://doi.org/10.1016/j.ejor.2006.01.053

Absi N, Kedad-Sidhoum S (2009) The multi-item capacitated lot-sizing problem with safety stocks and demand shortage costs. Comput Oper Res 36(11): 2926–2936. https://doi.org/10.1016/j.cor.2009.01.007

Aksen D, Altinkemer K, Chand S (2003) The single-item lot-sizing problem with immediate lost sales. Eur J Oper Res 147(3): 558–566. https://doi.org/10.1016/S0377-2217(02)00331-4

Chankong V, Haimes Y (1983) Multi-objective decision making theory and methodology. Elsevier Science, New York

Hajipour V, Kheirkhah A, Tavana M, Absi N (2015) Novel Pareto-based meta-heuristics for solving multi-objective multi-item capacitated lot-sizing problems. Int J Adv Manuf Technol 80(1–4): 31–45. https://doi.org/10.1007/s00170-015-6993-6

Mavrotas G (2009) Effective implementation of the E-constraint method in multi-objective mathematical programming problems. Appl Math Comput 213(2): 455–465. https://doi.org/10.1016/j.amc.2009.03.037

Miettinen K (1999) Nonlinear multiobjective optimization. Kluwer Academic Publishers, Boston

Wagner HM, Whitin TM (1958) Dynamic version of the economic lot size model. Manag Sci 5: 89–96

Effect of the Radial Flow on the Volume Defect in Polydimethylsiloxane Extrusion Using PIV the Technique

M. Ketata, A. Ayadi, Ch. Bradai and S. Ben Nasrallah

Abstract The present work aims to investigate the influence of flow geometry on volume instability associated to a linear polydimethylsiloxane (PDMS). To do so, a convergent radial flow is created at the die entrance. Particle Image Velocimetry (PIV) recordings performed under unstable flow regime, in the capillary rheometer, characterized with the new entrance zone, show a new pattern of streamlines above the die: elongational stresses are less pronounced; furthermore elongational stresses, as well as shear stresses, tend to concentrate near the lip of the capillary die. Photographs of extrudate strands obtained at the die exit, depict a new morphology of defect which appears with a well-established radial flow. These results lead to the agreement the correlation between the gross melt fracture and the flow instability at the entrance zone, as well as the importance of elongational and shear components linked to the upstream flow in the appearance and the development of volume distortion.

Keywords PDMS · Radial flow · PIV · Gross melt fracture
Elongational and shear components

M. Ketata (✉) · Ch. Bradai
LASEM National Engineering School of Sfax, B.P. W3038, Sfax, Tunisia
e-mail: ketata_manel@yahoo.fr

Ch. Bradai
e-mail: chedly20412517@gmail.com

A. Ayadi
CFDTP National Engineering School of Sfax, B.P. W3038, Sfax, Tunisia
e-mail: abdelhak.ayadi@gmail.com

S. Ben Nasrallah
National Engineering School of Monastir, Monastir, Tunisia
e-mail: sassi.bennasrallah@enim.rnu.tn

911

1   Introduction

Nowadays, many processing operations with synthetic polymers are still disturbed by extrusion instabilities. These instabilities can affect the surface, at low flow rates, or the whole volume of the extruded material, at higher flow regimes. Optical observations, such us birefringence (Muller and Vergnes 1996; Legrand and Piau 1998; Goutille et al. 2003), laser doppler velocimetry (Rothstein and McKinley 2001) and particle image velocimetry (Nigen et al. 2003), have shown that the onset of gross melt fracture is accompanied by upstream instability which may occur when the elongational stress exceeds a critical condition. On the other hand, this instability has been correlated with secondary flow (vortex) instability and it has been reported that volume distortion is initiated by the periodic discharge of vortex into the main stream (Meh 1997; Rudy 2002; Combeaud 2004).

In fact, several attempts have been made to mitigate upstream instability by modifying the geometry of the die entrance. This can be done by the extrusion through a conical entrance (Bagley and Schreiber 1961; Combeaud 2004) by introducing porous media just before the die (Legrand and Piau 1998; Goutille et al. 2003) to diminish elongational components or by imposing a convergent radial flow at the die entrance in order to raise shear deformations compared to those of elongation at the entrance region (Ayadi et al. 2011; Elgasri et al. 2011).

In the present work, the geometry of the die entrance is modified by imposing a convergent radial flow. Thus, we investigate the effect of the new entry flow on the appearance and the development of the wavy melt fracture defect. To do this, a series of extrusion experiments using a capillary rheometer is performed. Besides PIV method was used to cutch velocity fields of radial flow.

2   Experimental Facilities

2.1   Fluid Used

The tested material is a linear PDMS marketed under the name Pure Silicone Fluid (PSF) 20 000 000 Cst. This polymer has the advantage of being transparent and melted at room temperature, and thus heat application is not necessary to perform extrusion. PDMS is also known for its thermal, chemical and mechanical stability.

The rheological characterization of the considered PDMS has been reported by Ketata et al. (2017). It has a molecular weight of 958000 g/mol, a polydispersity of 2.94, and a plateau viscosity η_0 of 29000 Pa.s at a temperature of 23 °C.

2.2 *Experimental Apparatus*

The tested fluid is held in a reservoir and forced to flow through a capillary die by a flux of pressurized nitrogen (Fig. 1). The experiments are run under constant pressure condition and are performed at room temperature. The mentioned reservoir is achieved of transparent Plexiglass. Its internal diameter is 20 mm and its height is 100 mm. To obtain a radial flow at the entrance of the capillary die, a stainless steel rod, 10 mm in diameter, is introduced into the reservoir. The gap width of the radial flow is the field between the extremity of the rod and the plane of the die. The different gaps used in this study were 1 mm and ∞ (without the rod). Furthermore, to reduce considerably the diffused light and then to ensue PIV experiments, the die, 2 ± 0.03 mm in diameter and 1 ± 0.05 mm in length, is made of anodized aluminum and the rod is painted in matt black. Finally, the extruded fluid is directly timed and weighed and then the average mass flow rate is evaluated.
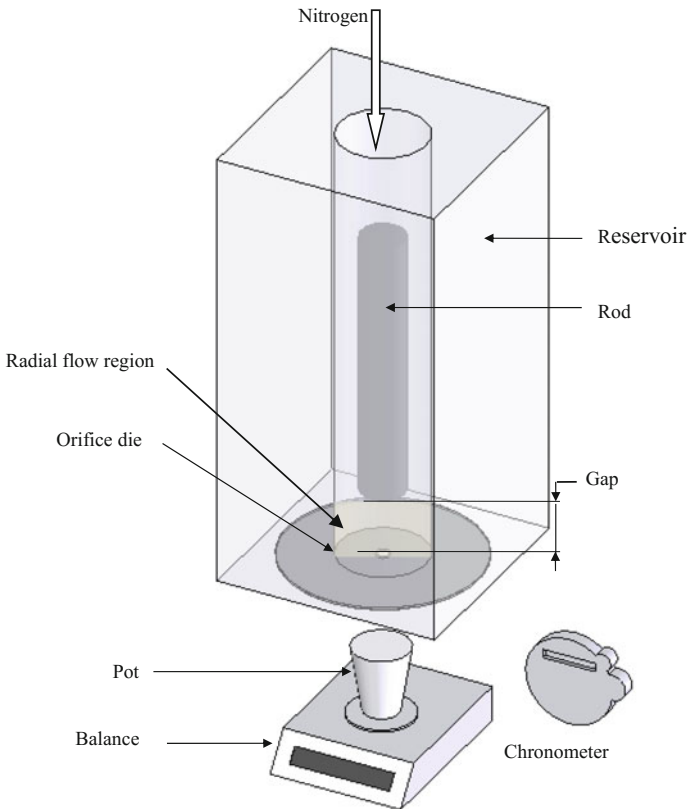
Fig. 1 Experimental set up

It should be specified that, in a previous study (Ketata et al. 2017), it was found that the die deformation increases linearly with imposed pressure with a characteristic slope of about $3.310^{-2}MPamm^{-1}$. This can affect the value of the adjusted gap and the shape of flow curves (at the zone of high pressure). Therefore, the flow curve associated to gaps 1 mm is corrected considering the estimated slope.

2.3 Visualization

To identify and visualize the extrusion defects at the exit of the die, a digital camera Nikon D 200 equipped with a variable focal lens 18/70, is placed just outside the die to film the extrudate.

For the observation of the flow upstream, a laser Nd-YAG double pulsed (30 mJ per pulse), of the wavelength of 532 nm was used. The laser light sheet is focused into the center of the die using a half-cylindrical lens. The fluid motion is followed with a double frame CCD camera Dantec Dynamics Flow Sense 4 M (2048 × 2048 as resolution) coupled to two spacers in total 48 mm length. A minisynchronizer is adopted for synchronization between the camera and the laser (Fig. 2).

The PDMS is seeded with micro-spheres of polyamide in order to conduct the particle image velocimetry (PIV) measurements. The main diameter of these particles is 20 μm. They are used at a mass fraction of about 0.03% in weight. This quantity is necessary for flow observations and velocity measurements and it is not enough to modify the flow characteristics or the behavior of the test fluid.

Fig. 2 PIV configuration
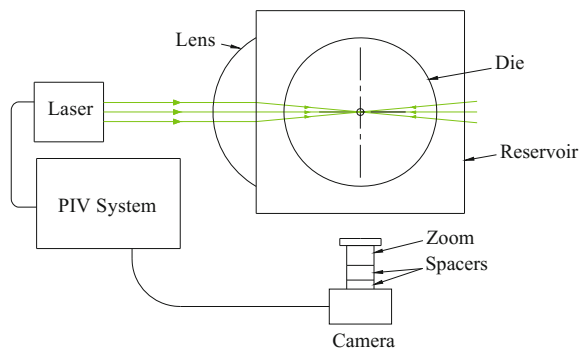
Table 1 The times intervals between two images for different zones over the orifice die	Around the centerline	Non-Newtonian vortex
	10000 μs (for stable regime)	67612 μs
	8000 μs (for instable regime)	

The upstream flow is examined with large interrogation areas of 128×128 pixels. Interrogation windows are overlapped by 50% to increase the number of interrogation areas and thus to obtain more information of the displayed region. The times intervals between two images (Δt) are chosen so that the maximal displacement (Δx) of the particles do not exceed the interrogation edge, in order to improve the quality of image processing (Eqs. (1)–(2)). Therefore, several time intervals, presented in Table 1, were chosen based on the speed of the flow area to be viewed.

$$Q_v = V_{max}.S = \frac{V_{max}}{2}\pi R^2 = \frac{\Delta x}{2\Delta t}\pi R^2 \tag{1}$$

$$\Rightarrow \Delta t = \frac{\Delta x \, \rho \, \pi \, R^2}{2 \, Q_m} \tag{2}$$

where Q_v: is the Volume flow rate, V_{max} is the maximal flow velocity, R is the radius of the area which the fluid flows through it, ρ is the density of the tested polymer, Δx is the maximal displacement of particles and Δt. is the time between two consecutive images.

Visualization of unstable flow is performed with a laser frequency of 6 Hz. This later is adjusted as the determined frequency of the gross melt fracture defect is 5.8 Hz for the gap infinity (Ketata et al. 2017). We note that a laser frequency of 2 Hz is adapted for visualization of stable flow and recirculation zones as they are characterized by slow flow velocity.

3 Results

3.1 Flow Curves and Observations at the Die Exit

Figure 3 shows the flow curves of the PDMS extruded through the capillary die, with and without rod at the die entrance. The gaps used are 1 mm and ∞ (corresponding to experiments without the rod).

What can be seen in Fig. 3 is that the flow curves obtained are continuous. For a constant mass flow rate, the total pressure drop is increased when the gap is reduced. Note that the strand photographs show the three known aspect defects (surface, helical, and chaotic morphology) for all gaps.

3.2 PIV Results

Vector maps obtained for the PDMS extruded through the three configurations (without rod and gaps and 1 mm) show that the flow just above the orifice die is basically symmetrical (Fig. 4a and d). For the extrusion without rod (Fig. 4a), we remark that from D, the flow is clearly influenced by the presence of the
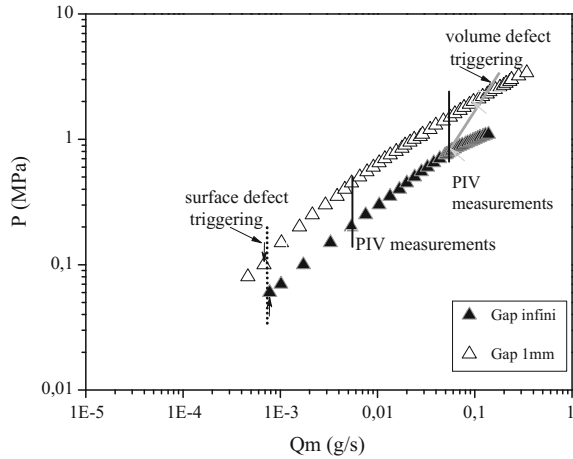
downstream contraction, this influence is more and more crucial as the fluid moves toward the orifice entrance. We remark also that for a constant flow rate, the average flow velocity is almost the same with or without radial flow imposed in the entrance zone. In addition, it seems that for the two used gaps, the vortices are present at the corners of the reservoir. The estimated angle between the main flow and the secondary flow takes successively the values 135° and 137° for gaps infinity and 1 mm.

Vector maps obtained in Fig. 5 show that the flow just above the capillary die is basically nonsymmetrical. For a constant flow rate, the average flow velocity is almost the same with the presence or not of the rod at the die entrance.

As a consequence of the radial flow the radial flow in the upstream zone, a new stress distribution is established: elongational stresses are less pronounced besides elongational stresses as well as shear stresses tend to concentrate near the lip of the capillary die (Fig. 5d). The associated defect is no longer concerns the whole volume of the extruded strand of the polymer, but rather, the volume of the external layer of this one (Fig. 5f). In addition, we note that for the two used gaps, vortices seem to be present at the corners of the reservoir. The estimated angle between the main flow and the secondary flow takes successively the values 135° and 148° for gaps infinity and 1 mm.

We remark also that the triggering of the helical instability is not accompanied by destabilization of the vortices, i.e., no discharge of vortices is observed when the helical defect occurs (Fig. 5b).
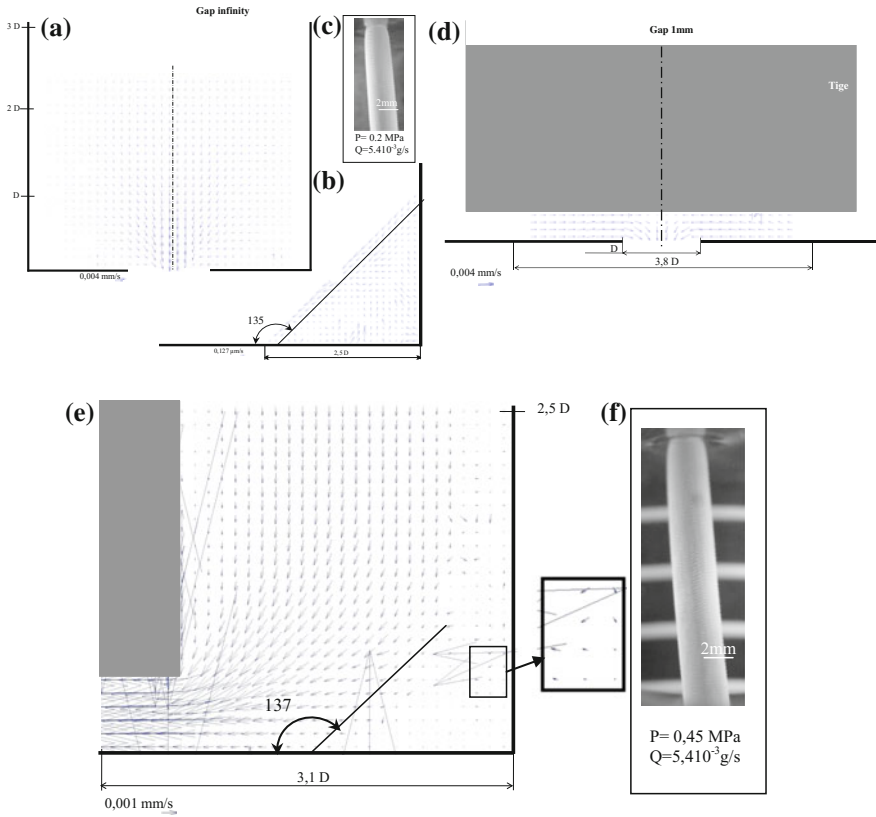
Fig. 4 Velocity maps describing the flow in the entrance zone for the PDMS extruded at 5.5×10^{-3} g/s through gaps infinity and 1 mm
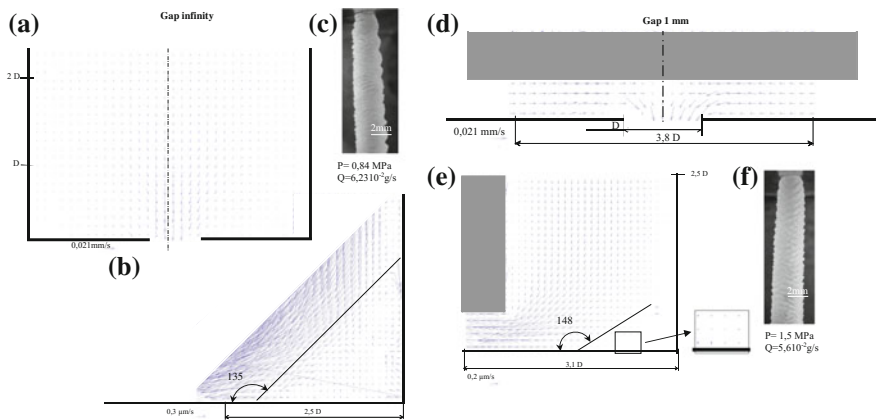
Fig. 5 Velocity maps describing the flow in the entrance zone for the PDMS extruded at 6×10^{-2} g/s through gaps infinity and 1 mm

4 Conclusion

The effect of radial flow imposed upstream the die on gross melt fracture behavior of extruded polymer was studied. The flow in the entrance zone of the die has been investigated using PIV. Vector maps obtained show that when the flow instability above the die, which is linked to elongation deformation, concerns the entire volume at the entrance of the die, the defect concerns the entire volume of the extruded strand of the polymer. In contrast, when the flow instability above the die, which is linked to deformations of radial flow, concerns the region near closely the lip of the die, the associated defect concerns only the external layer of the extruded strand of the polymer. Moreover, we can say that volume instability can be associated with the elongational component more than to the destabilization of the vortices which the size is independent of the flow rate.

References

Ayadi A, Elgasri S, Mezghani A, Castro M, Elhaouani F (2011) Effect of radial flow in the die entrance region on gross melt fracture of PDMS extrudate. J Non Newtonian Fluid Mech 166:661–666

Bagley EB, Schreiber HP (1961) Effect of die entry geometry on polymer melt fracture and extrudate distortion. Trans Soc Rheol 5:341

Combeaud C (2004) Study of volume instabilies in extrusion of polypropylene and polystyren. Dissertation, University of Paris

Elgasri S, Ayadi A, Elhalouani F (2011) Effect of die geometry on helical defect during extrusion of PDMS across a radial flow upstream the contraction. J Non-Newtonian Fluid Mech 166:1415–1420

Goutille Y, Majesté JC, Tassin JF, Guillet J (2003) Molecular structure and gross melt fracture triggering. J Non-Newtonian Fluid Mech 111:175–198

Ketata M, Ayadi A, Elkissi N, Bradai Ch (2017) Effect of rheological and physical properties on mitigation of melt fracture instability during extrusion of polymer melts through a radial flow die. Rheol Acta 56:341

Legrand F, Piau J-M (1998) Spatially resolved stress birefringence and flow visualization in the flow instabilities of a polydimethylsyloxane extruded through a slit die. J Non-Newtonian Fluid Mech 77:123–150

Meh M (1997) Private communication

Muller R, Vergnes B (1996) Validity of the stress optical law and application of birefringence to polymer complex flows. In: Piau J-M, Agassant JF (ed) Rheology for polymer processing. Elsevier

Nigen S, El Kissi N, Piau J-M, Sadun S (2003) Velocity field for polymer melts extrusion using particle image velocimetry stable and unstable flow regimes. J Non-Newtonian Fluid Mech 112:177–202

Rothstein JR, McKinley GH (2001) The axisymmetric contraction expansion: the role of extensional rheology on vortex growth dynamics and the enhanced pressure drop. J Non-Newtonian Fluid Mech 98:33–63

Rudy KM (2002) Engineering techniques, processed plastics and composites, AM3657

Tribological Behavior of HDPE Against Stainless Steel on the Presence of Bio-Lubricants

A. Salem, M. Guezmil, W. Bensalah and S. Mezlini

Abstract In this paper, the tribological behavior of the high-density polyethylene (HDPE) against the M30NW stainless steel was studied. A reciprocating pin-disk tribometer was used to conduct wear tests under dry and lubricated conditions. Two lubricants were used including saline solution (NaCl 0.9%) and nigella sativa oil. The disulfide of molybdenum (MoS_2) was used as an additive to the retained lubricants. The coefficient of friction and the wear volume measured on HDPE were studied. The morphological characterization of the polymer disks and metallic pins was carried out. It is found that the use of the saline solution and nigella sativa oil as lubricants increases the tribological performance of M30NW/HDPE pair. The addition of 2 wt% of MoS_2 to both lubricants does not show a significant decrease of the wear volume of HDPE comparatively to dry conditions. The performance of the nigella sativa oil was related to its adsorption ability to the stainless steel surface. The mechanism of nigella sativa oil adsorption on the M30NW surface is presented and discussed.

Keywords HDPE · Bio-lubricants · Tribological behavior

A. Salem (✉) · M. Guezmil · W. Bensalah · S. Mezlini
Laboratoire de Génie Mécanique (LGM), Ecole National d'Ingénieur de Monastir,
Université de Monastir, Rue Ibn Eljazzar, 5019 Monastir, Tunisie
e-mail: amirasalem0302@gmail.com

M. Guezmil
e-mail: manelguezmil@yahoo.fr

W. Bensalah
e-mail: walidbensalah@gmail.com

S. Mezlini
e-mail: salah.mezlini@gmail.com

1 Introduction

The high-density polyethylene (HPDE) is characterized by an excellent biocompatibility and considered as one of the thermoplastics which have a good mechanical property. The HDPE is used as acetabular cups for the total hip replacement implants (Zhil et al. 2009). Wear debris of polymer during use can cause the osteolysis (Robert et al. 1992). To increase the lifetime of the hip joint the tribological performance must be improved.

To achieve this objective, several researchers have tried different lubricants such as: Hyaluronic acid (HA) (Zhang et al. 2007), human serum (Borruto 2010), demineralized water, and polyethylene glycol (PEG) (Kobayashi et al. 2014).

For our part, we propose using bio-lubricants due to their biocompatibility and to their good tribological behavior. In this context, we will focus our study on the nigella sativa oil because it has a good tribological behavior and many medicinal applications (Guezmil et al. 2016; Gharby et al. 2015; Aftab et al. 2013; Periasamy et al. 2016).

The solid lubricants such as graphite and molybdenum disulfide MoS_2 are also used for hip joint (Fouad and Elleithy 2011). To reduced friction for an automotive engine, this lubricant is used (Tang and Li 2014). It is noted that molybdenum disulfide is used in medicine. It can have an influence on a variety of applications like biomedical; cancer therapy and medical friction-reduction coatings (Wu et al. 2011).

In this paper, we study the tribological properties of extruded HDPE against M30NWstainless steel. To undertake wear tests, a pin-disk tribometer has been used under dry and lubricated conditions. As lubricants, we have used nigella sativa oil and a saline solution. The two retained solutions are mixed by 2 %wt of MoS_2 and used as lubricants. The ultimate aim of this research is to study the friction coefficient, the wear volume and to examine the morphology and wear mechanism of HDPE under different conditions (dry and lubricant).

2 Experimental Details

2.1 Materials

In this work, we have used high-density polyethylene HDPE disks Ø30 × 10 mm. They were machined from a cylindrical bar extruded by 30 mm diameter acquired from Tunisian industry 2MTI with a shore hardness D: of 64 SH D. Besides, we have used M30NW stainless steel pins (<0.06% C, 21% Cr, 9.5% Ni, 4% Mn, 2.2% Mo, and 0.4% N). They are supplied from C2F implants-France Company (Tunisian factory). They have hemispherical shape with 10 mm diameter and with a micro-hardness of 440 ± 20 $HV_{0.5}$ (Fig. 1).
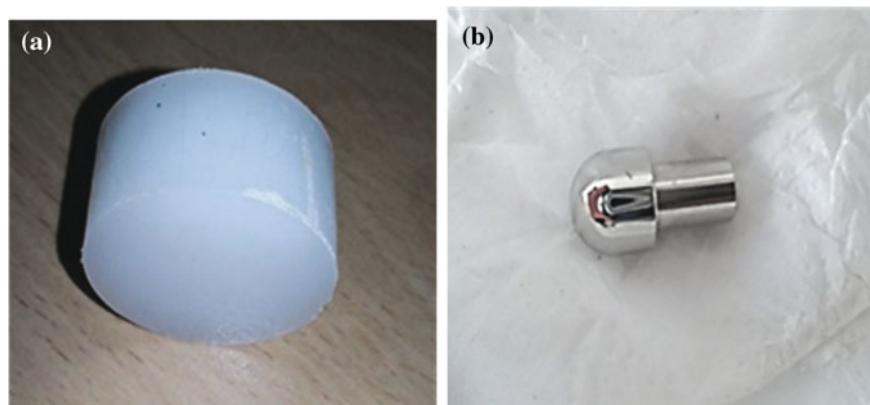
Fig. 1 Photographs of **a** HDPE disk and **b** stainless steel pin

We have used as lubricants saline solution (0.9% NaCl in purified water) and nigella sativa oil. This oil is pure and obtained by cold pressure extraction. It is used for pharmaceutical and cosmetic applications. The saline solution is an injectable sterile isotonic solution.

2 wt% of MoS_2 was added to these two lubricants, mixed for 3 h in an ultrasonic bath. In most cases, the concentration is less than 3%, and the concentration of MoS_2 dispersed in the oil could be between 0.1 and 60% (Lansdown 1999).

The molybdenum disulfide powder (MoS_2) has a density of 4800 kg/m^3 at 20 °C and 0.75 µm particle sizes.

2.2 Methods

2.2.1 Wear Test

A pin-disk tribometer was used at room temperature to analyze the wear performance of the HDPE disks (Fig. 2). Before tests, the surface of disks was polished using abrasive papers up to #4000 and then cleaned by acetone. The average roughness (Ra) is 0.06 ± 0.01 µm for the pin and 0.15 ± 0.03 µm for the HDPE disk.

The tests were carried out under reciprocating sliding conditions. The used velocity is 30 mm/s with 30 mm stroke. The sliding speed in a hip joint varies between 0 and 50 mm/s (Widmer et al. 2001). We have used 20 N as applied load (Borruto 2010). So it gives as a contact pressure of 58 MPa. Each test took 15,000 cycles and it corresponds to 450 m as a total sliding distance. The load cell measures the tangential force (Fig. 2).
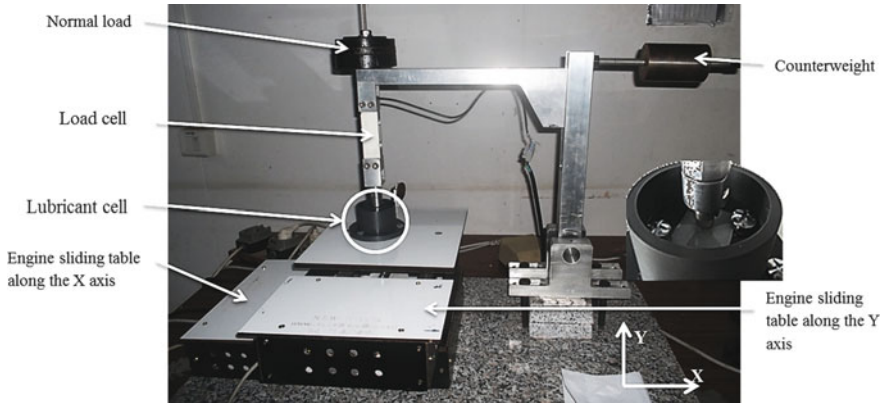
Fig. 2 The pin-disk tribometer

2.2.2 Morphological Characterization Techniques

To observe wear scratches generated on HDPE disks and the damage of the pins surfaces, we used an optical microscope. To quantify the wear volume of the HDPE, the 2D profilometer was used.

3 Results and Discussion

3.1 Friction Behavior

Figure 3 shows the friction coefficient of the disks of HDPE against stainless steel pins under dry and lubricated conditions as a function of number cycles.

With using those lubricants, we mention that the friction coefficient decreases about 65% from the dry test with saline solution and about 90% with nigella sativa oil.

Under dry conditions, we note the highest friction coefficient which can be explained by the significant change of the morphology in the contact. That means it can be caused by the generation and the crushing of debris. In fact, under dry condition, the materials in contact become more susceptible to degradation due to heat. So, the combination of contact pressure and heat causes chemical and morphological modifications for both materials. This phenomenon makes the generation of debris easier and increases the surface roughness. For the disk, the average roughness passed from 0.15 to 0.6 µm.

With regard to the saline solution, we can mention that the decrease of the friction coefficient can be caused by the use of the water as a solvent. In fact, the water decreases the warm-up and lubricates the contact which was observed by
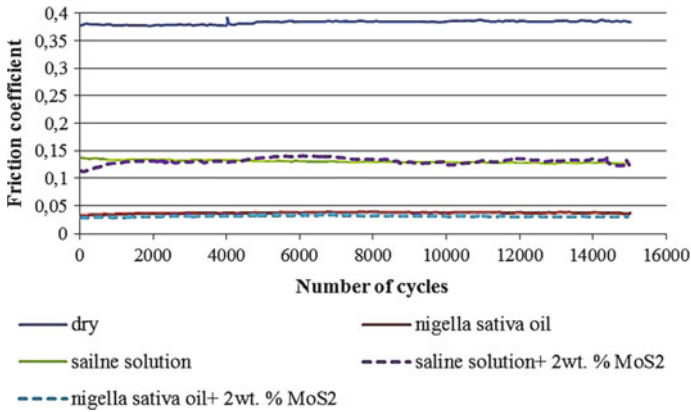
Fig. 3 Friction coefficient for HDPE extruder against stainless steel pins for dry and different lubricants used as a function of number of cycles

Borruto (2010). According to Wang et al. (2009) and Yan et al. (2007) it can be caused by the formation of a passive layer on the stainless steel under the action of the chlorine ions (Cl^-) and it has around 15–20 nm as thickness.

The lowest friction coefficient is for the nigella sativa oil. According to Reeves et al. (2015), this results is due to the chemical composition of the oil and specially to its fatty acid content. These results were confirmed by Guezmil et al. (2016) which mentioned that the friction coefficient decrease greatly compared to the saline solution and dry conditions with vegetable oils.

Figure 3 shows also the effect of the addition of the MoS_2 to the nigella sativa oil and to the saline solution for the contact of stainless steel pins against extruded HDPE. For the experiment with saline solution with 2 wt% MoS_2, the friction coefficient slightly increased and presented more fluctuation compared to the test without MoS_2. The result of an experiment with nigella sativa oil with or without 2 wt% MoS_2 was almost the same. However, the addition of nigella sativa oil to 2 wt% MoS_2 decreases the friction coefficient when compared to a saline solution with 2 wt% MoS_2. These results are in agreement with those of Zhang et al. (2015) and Koshy et al. (2015), They showed in their works that the addition of MoS_2 in the vegetable oil decrease the friction coefficient and produce a good lubricating performance.

3.2 Wear Behavior

Wear volume was measured using a 2D profilometer. The profile obtained gives the depth and the width of the wear scar, so it provides information about the wear.
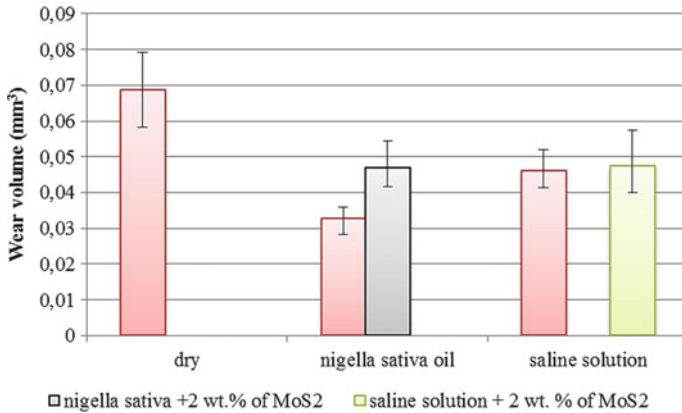
Fig. 4 Variation of wear volume of HDPE extruded for dry and different lubricants conditions at completion of tests

Figure 4 shows the variation of wear volume of HDPE for dry and different lubricants conditions at the completion of the tests. The highest wear volume is recorded for dry test. As can be seen, wear decreases about 33 and 52% compared to the dry test, respectively for saline solution and nigella sativa oil. As remarked with the friction coefficient, the used vegetable oil produces the lowest wear volume.

However, the addition of 2 wt% of MoS_2 in saline solution and nigella sativa oil increases equally the wear volume.

3.3 Morphological Examination

Figure 5 gives the optical microscopies of wear tracks generated of HDPE for a dry, saline solution, nigella sativa oil, 2 wt% of MoS_2 mixed respectively, with saline solution and nigella sativa oil at the completion of the tests. These figures show different morphologies between the tests.

These figures show that the damage is more noticeable and more pronounced plastic deformation is observed for dry tests. Figure 5a and b; illustrate that the surface of the HDPE presents stripes and delamination which accompanied with an increase of roughness. This changing in the morphology can be a result of the increasing of the temperature at the contact stainless steel/HDPE (Yousif et al. 2010).

On the other hand Fig. 5c and d show a change in morphology when a saline solution is applied on the contact surface of the polymer. This phenomena of decrease damage in presence of lubricant have been shown previously by Yousif
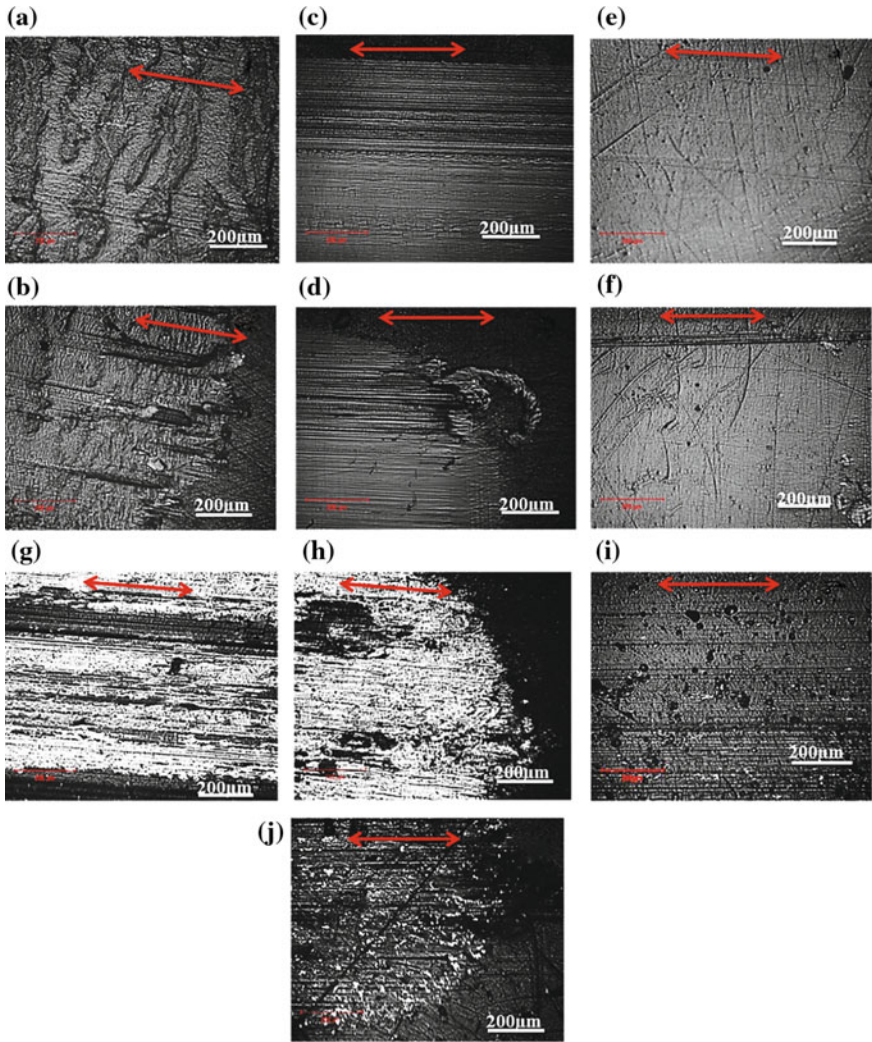
Fig. 5 Optical microscopies of wear tracks generated of HDPE samples for **a**, **b** dry; **c**, **d** saline solution; **e**, **f** nigella sativa oil; **g**, **h** saline solution +2 wt% MoS_2 and **i**, **j** nigella sativa oil + 2 wt % MoS_2 at completion of tests. Red arrow indicates the sliding direction

et al. (2010). In fact, the use of saline solution reduces damage and the scratches are less deep. Looking at Fig. 5d, it should be noted that the debris of polymer are detached and transported to the end of the track. This supposes the formation of a transfer film in the pin/polymer interface.

Looking at Fig. 5e and f, wear has considerably decreased; the wear grooves and the limits of the track are absent.

However, the use of MoS_2 as an additive to the saline solution and nigella sativa oil modifies the HDPE morphology compared to the tests without solid lubricant which viewed in Fig. 5g, h and i, j. Comparing Fig. 5c, d with Fig. 5g, h and Fig. 5e, f with Fig. 5i, j; it is found that the wear track width increase by using MoS_2. In the case of the saline solution (Fig. 5g, h), the MoS_2 seems to be more present in the contact. In fact, compared to the saline solution with MoS_2, the nigella sativa oil with 2% of MoS_2 gives a less damaged surface (Fig. 5i, j). The tribological behavior is preserved and these results go well with those analyzed previously.

The Fig. 6 shows the optical microscopies of worn pin surfaces with different conditions at the completion of the tests. From these figures, it can be mentioned that the degradation of the pins is more important for the dry test (Fig. 6a and b), moderate for saline solution (Fig. 6c) and the lowest when using nigella sativa oil (Fig. 6d).

The dry condition (Fig. 6a and b) highlights the phenomenon of adhesion of polymer on the stainless pins. The increase in the friction coefficient and the wear volume can be explained by the thick layer of adhesion presented in the worn surfaces.

As previously discussed, compared to the virgin lubricants (Fig. 6c and d), the addition of MoS_2 to saline solution and vegetable oil shows more deep stripes (Fig. 6e and f). In fact, this increase may be attributed to the limits of the
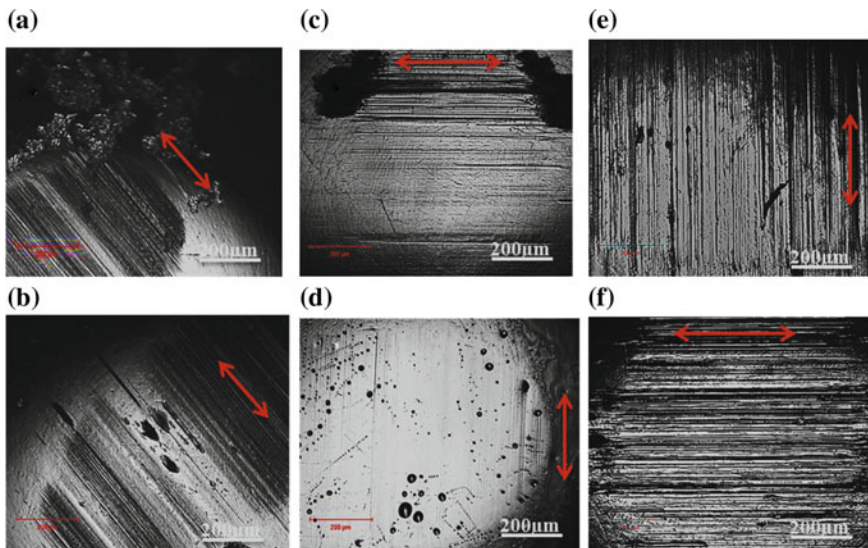
Fig. 6 Optical microscopies of a worn pin surface for **a**, **b** dry; **c** saline solution, **d** nigella sativa oil **e** saline solution +2wt% MoS_2, **f** nigella sativa oil + 2 wt% MoS_2 at completion of tests

Table 1 The composition of nigella sativa oil on fatty acids (ISO5508COI/T.20/DOCN °24)

Fatty acid	Nigella sativa oil
Myristic acid (C14:0)	0.33
Palmitic acid (C16:0)	17.05
Palmitoleic acid (C16:1)	1.1
Stearic acid (C18:0)	2.76
Oleic acid (C18:1)	24.76
Linoleic acid (C18:2)	50.06
Linolenic acid (C18:3)	0.28
Arachidic acid (C20:0)	0.12
Behenic acid (C22:0)	1.9
Others	Rest

insolubility of MoS_2 as an additive in deionized water (Fan et al. 2015) and in lubricating oils (Yu et al. 2000).

The remarkable decrease of friction and wear using the vegetable oil as a lubricant can be explained to their composition on fatty acids. According to Mannekote and Kailas (2012) the tribological behavior depends to the fatty acids. In fact, most vegetable oils are characterized by long chains of fatty acid: They contain carboxylic group at the end (Cheenkachorn 2013). The carboxylic group has a capacity to tie to the metal surface and generate a dense film which conducts to the decrease of the wear and friction (Loehlé et al. 2015).

According to Kalin et al. (2006) and Reeves et al. (2015) the degree of saturation of the oil molecules is related to the wear performance. Table 1 gives the composition of nigella sativa oil. It shows a high amount of unsaturated acids; especially for linoleic and oleic acids.

The existence of a correlation between the wear behavior and the presence of the fatty acids in the nigella sativa oil can be explained by the decrease of the friction coefficient and wear volume. This result is mentioned by Reeves et al. (2015). These authors have demonstrated that the natural oils with high oleic acid percentages maintain high tribological behavior. In fact, the oleic acid creates a denser monolayer which protects the metallic surfaces from wear (Fig. 7).

The molecules of the fatty acid form the hydrogen bonds with the oxides or hydroxides surface (Fig. 7 left). As well, the dissociation of fatty acid molecules onto carboxylate proton (H^+) and anion ($R\text{-}COO^-$), conduct to a chemical reaction with the atoms of iron surface. The formation of an iron carboxylate with a monodentate form is caused by this reaction (Fig. 7 right). Furthermore, the carboxylic acids form bonds with both oxygen atoms of the carboxyl group which given bidentate bonds on the surface iron atoms (Fig. 7 right) (Simic and Kalin 2013).
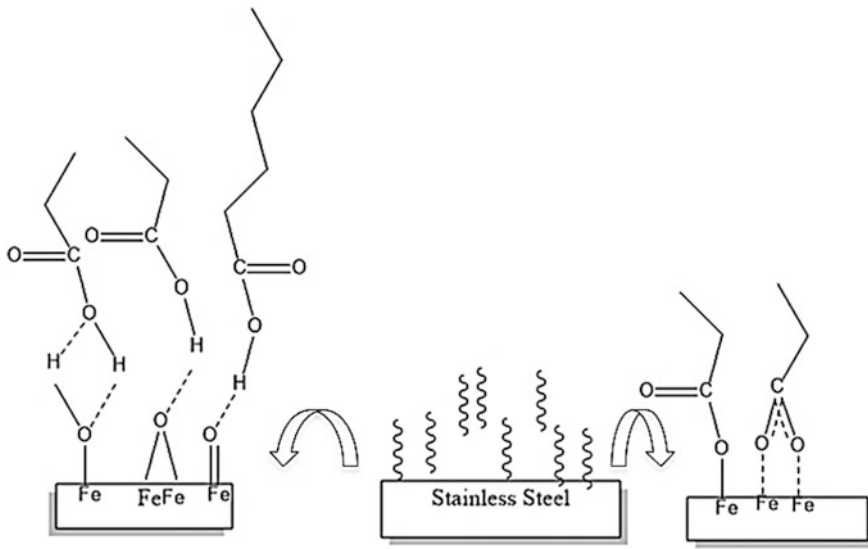
Fig. 7 Schematic presentation of fatty acid adsorption onto the steel surface: hydrogen bonds with the surface oxides/hydroxides and some form iron carboxylates

4 Conclusion

This study deals with the tribological behavior of extruded HDPE against M30NW stainless steel. Experiments were carried out under dry and lubricated conditions for 15000 cycles. The MoS_2 was mixed with both lubricants namely the saline solution and nigella sativa oil. The main conclusions from this study are as follows:

Nigella sativa oil demonstrated the best tribological behavior in terms of friction coefficient and wear volume compared to the others conditions. In fact, with nigella sativa oil the friction coefficient decreased compared to the dry and saline solution about 90% and 70%, respectively.

The use of the MoS_2 as an additive to the lubricants contributes to a decrease for the wear tribological behavior.

The dry test was characterized by adhesive wear according to the morphological examination. However, saline solution and nigella sativa oil are characterized by moderate and lowest wear volume, respectively.

The highest performance of nigella sativa oil in terms of the tribological behavior can be explained by the capacity of its fatty acids to create monolayer which protects the metallic surfaces from wear.

References

Aftab A et al (2013) Review on therapeutic potential of N igella sativa: a miracle herb. Asian Pac J Trop Biomed 3(5):337–352

Borruto A (2010) A new material for hip prosthesis without considerable debris release. Med Eng Phys 32:908–913

Cheenkachorn K (2013) A study of wear properties of different soybean oils. Energy Procedia 42:633–639

Fan X et al (2015) MoS2 actuators: reversible mechanical responses of MoS2-polymer nanocomposites to photons. Nanotechnology 26:1–11

Fouad H, Elleithy R (2011) High density polyethylene/graphite nano-composites for total hip joint replacements: Processing and in vitro characterization. J Mech Behav Biomed Mater 4:1376–1383

Gharby S et al (2015) Chemical investigation of Nigella sativa L. seed oil produced in Morocco. J Saudi Soc Agric Sci 14:172–177

Guezmil M, Bensalah W, Mezlini S (2016) Effect of bio-lubrication on the tribological behavior of UHMWPE against M30NW stainless steel. Tribol Int 94:550–559

Kalin M et al (2006) The lubrication of DLC coatings with mineral and biodegradable oils having different polar and saturation characteristics. Surf Coat Technol 200:4515–4522

Kobayashi M, Koide T, Hyon S (2014) Tribological characteristics of polyethylene glycol (PEG) as a lubricant for wear resistance of ultra-high-molecular-weight polyethylene (UHMWPE) in arti fi cial knee join. J Mech Behav Biomed Mater 38:33–38

Koshy CP, Rajendrakumar PK, Thottackkad MV (2015) Evaluation of the tribological and thermo-physical properties of coconut oil added with MoS 2 nanoparticles at elevated temperatures. Wear 330–331:288–308

Lansdown A.R. (1999) Use in oils and greases. In: Dowson D (ed) Molybdenum disulphide lubrication, 1st edn, Elsevier

Loehlé S et al (2015) Mixed lubrication of steel by C18 fatty acids revisited. Part I: toward the formation of carboxylate. Tribol Int 82:218–227

Mannekote JK, Kailas SV (2012) The effect of oxidation on the tribological performance of few vegetable oils. J. Mater. Res. Technol 1(2):91–95

Periasamy VS, Athinarayanan J, Alshatwi AA (2016) Anticancer activity of an ultrasonic nanoemulsion formulation of Nigella sativa L. essential oil on human breast cancer cells. Ultrason Sonochem 31:449–455

Reeves CJ et al (2015) The influence of fatty acids on tribological and thermal properties of natural oils as sustainable biolubricants. Tribol Int 90:123–134

Robert AC et al (1992) Polyethylene debris-induced osteolysis and loosening in uncemented total hip arthroplasty: a cause of late failure. J Arthroplasty 7(3):285–290

Simic R, Kalin M (2013) Adsorption mechanisms for fatty acids on DLC and steel studied by AFM and tribological experiments. Appl Surf Sci 283:460–470

Tang Z, Li S (2014) A review of recent developments of friction modifiers for liquid lubricants (2007–present). Curr Opin Solid State Mater Sci 18(3):119–139

Wang J, Yan F, Xue Q (2009) Tribological behavior of PTFE sliding against steel in sea water. Wear 267:1634–1641

Widmer MR et al (2001) Influence of polymer surface chemistry on frictional properties under protein-lubrication conditions: implications for hip-implant design. Tribol Lett 10(1):111–116

Wu H et al (2011) Biocompatible inorganic fullerene—nanoparticles produced by pulsed laser ablation in water. ACS Nano 5(2):1276–1281

Yan Y, Neville A, Dowson D (2007) Tribo-corrosion properties of cobalt-based medical implant alloys in simulated biological environments. Wear 263:1105–1111

Yousif BF, Alsofyani IM, Yusaf TF (2010) Adhesive wear and frictional characteristics of UHMWPE and HDPE sliding against different counterfaces under dry contact condition. Tribol Mater Surf Interfaces 4(2):78–85

Yu L, Zhang P, Du Z (2000) Tribological behavior and structural change of the LB film of MoS2 nanoparticles coated with dialkyldithiophosphate. Surf Coat Technol 130:110–115

Zhang M et al (2007) A novel ultra high molecular weight polyethylene—hyaluronan microcomposite for use in total joint replacements. II. Mechanical and tribological property evaluation. J Biomed Mater Res A 18–26

Zhang Y et al (2015) Experimental evaluation of MoS2 nanoparticles in jet MQL grinding with different types of vegetable oil as base oil. J Clean Prod 87:930–940

Zhil TV, Oliveira MSA, Ferreira JAF (2009) Relative influence of injection molding processing conditions on HDPE acetabular cups dimensional stability. J Mater Process Technol 209:3894–3904

Collective Dynamics of Disordered Two Coupled Nonlinear Pendulums

K. Chikhaoui, D. Bitar, N. Bouhaddi, N. Kacem and M. Guedri

Abstract The effect of disorder on the collective dynamics of two coupled non-linear pendulums is investigated in this paper. The disorder is introduced by slightly perturbing the length of some pendulums in the nearly periodic structure. A generic discrete analytical model combining the multiple scales method and a standing-wave decomposition is proposed and adapted to the presence of disorder. The proposed model leads to a set of coupled complex algebraic equations which are written according to the number and positions of disorder in the structure. The impact of the disorder on the collective dynamics of two coupled pendulums structure is analyzed through the frequency responses and the basins of attraction. Results show that, in presence of disorder, the multimode solutions are enhanced and the multistability domain is wider. The disorder introduced by reducing the length of one pendulum favors modal localization on its response. In practice, the

---

K. Chikhaoui · D. Bitar · N. Bouhaddi · N. Kacem (✉)
UMR 6174, CNRS/UFC/ENSMM/UTBM, Department of Applied Mechanics,
Université Bourgogne Franche-Comté, FEMTO-ST Institute, 25000 Besançon, France
e-mail: najib.kacem@femto-st.fr

K. Chikhaoui
e-mail: khaoula.chikhaoui@femto-st.fr

D. Bitar
e-mail: diala.bitar@femto-st.fr

N. Bouhaddi
e-mail: noureddine.bouhaddi@femto-st.fr

M. Guedri
National High School of Engineers of Tunis, University of Tunis,
5 Avenue Taha Hussein, BP 56, Bâb Manara, Tunis, Tunisia
e-mail: mohamed.guedri@isetn.rnu.tn

K. Chikhaoui · M. Guedri
Preparatory Engineering Institute of Nabeul, 8000 M'Rezgua, Nabeul, Tunisia

M. Guedri
Technical and Vocational Training Corporation, College of Technology at Makkah,
Mecca, Kingdom of Saudi Arabia

energy localization generated by disorder is suitable for several engineering applications such as vibration energy harvesting.

Keywords Collective dynamics · Near-periodicity · Coupled nonlinear pendulum · Disorder · Multimode solutions · Basins of attraction Modal localization

1   Introduction

Under the hypothesis of perfect periodicity, many works provided interesting insights in the behavior of periodic linear and nonlinear structures (Nayfeh 1983; Lifshitz and Cross 2003; Bitar et al. 2015; Manktelow et al. 2011). However, engineering systems are in reality affected by imperfections and the near-periodic term is, therefore, more adequate to characterize their arranging. In the literature, Kissel (1988), for instance, studied the effect of disorder in one-dimensional periodic structure. He proved that disorder allows wave attenuation and normal mode localization in the frequency range close to the attenuation bands of the associated perfectly periodic structure. A statistical analysis of the disorder effect on the dynamics of coupled one-dimensional periodic structures using the Monte Carlo method was performed by Pierre (1990). The effect of the disorder is evaluated through localization factor statistics reflecting the exponential decay of the vibration amplitude. Moreover, Koch (2003) combined a continuous Timoshenko beam model, the Monte Carlo method and a first-order perturbation approach to study the effects of the randomness of flexible joints on the free vibrations of simply supported periodic trusses. These works have shown that the normal modes of the near-periodic structures are localized in the region, where the periodicity is perturbed.

Coupled pendulums chain is an example of periodic structures that has been the purpose of several types of research in the literature. Recently, energy localization in coupled pendulums array under simultaneous external and parametric excitations has been investigated by Jallouli et al. (2017) using a nonlinear Schrodinger equation. The study proved that adding an external excitation increases the existence region of solitons. Bitar et al. (2016) investigated the collective nonlinear dynamics of perfectly periodic coupled pendulum structure under primary resonance using multiple scales method and standing-wave decomposition. In presence of disorder, Tjavaras and Triantafyllou (1996) studied the effect of nonlinearities on the forced response of two disordered pendulums. Results showed the high sensitivity of the structure to small parametric variations and the modal localization generated by the disorder. Moreover, Alexeeva et al. (2000) proved that the impurity introduced by increasing the length of one pendulum in a coupled parametrically driven damped pendulums to chain significantly expands the stability domain. By decreasing the length, solitons are pushed producing an effective partition of the chain. Hai-Quing and Yi (2006) studied the effect of mass impurity

on nonlinear modes localization in a damped coupled nonlinear pendulums array under parametric excitation. It was also proven, in (Chen et al. 2002; Zhu et al. 2003) that disorder introduced by increasing or decreasing one pendulum length results in attracting or repelling a breather, respectively.

The main purpose of this paper is to investigate the effect of disorder on the collective dynamics of two coupled pendulums chain. The length of one pendulum is in fact perturbed. Disorder effect is shown through the frequency responses computation in generalized coordinates. The analysis of the basins of attractions illustrates the robustness of the multimode solutions against disorder. It is performed in terms of attractors and bifurcation topologies, around a chosen frequency in the multistability domain.

2 Model

A generic structure of N coupled nonlinear pendulums is considered, Fig. 1. The pendulums are of identical mass m and viscous damping coefficient c. They are coupled by linear springs of stiffness k and excited by an external force $f\cos(\Omega t)$ each one. The structure is nearly periodic since some pendulums lengths are perturbed.

Two hypotheses are considered here: the linear coupling is very weak and the perturbations are supposed to be very small. Therefore, the eigenfrequencies are supposed to be equal: $\omega_n = \omega_0 = \sqrt{g/l}$, where l is the nominal length.
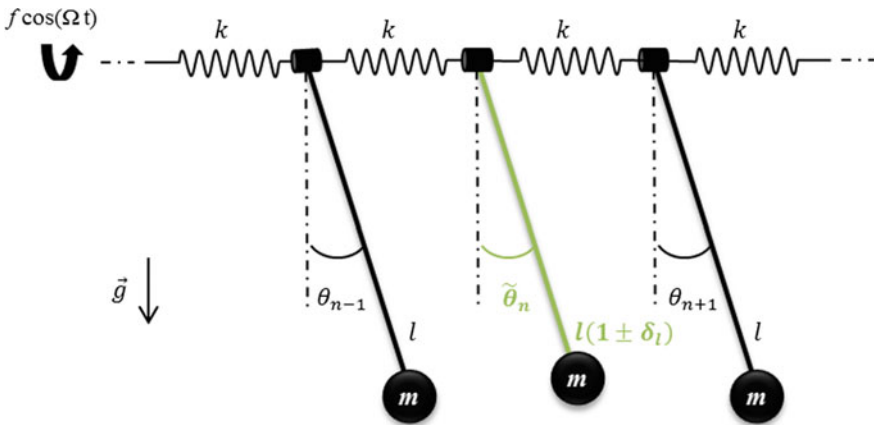
Fig. 1 Scheme of disordered nonlinear coupled pendulums

The equation of motion of the nth pendulum is expressed as

$$\ddot{\phi}_n + \frac{c}{m}\dot{\phi}_n + \omega_n^2\phi_n + \frac{k}{ml_n^2}(2\phi_n - \phi_{n-1} - \phi_{n+1}) - \frac{g}{6l_n}\phi_n^3 = \frac{f}{ml_n^2}\cos(\Omega t) \quad (1)$$

If the nth pendulum is perturbed, ϕ_n is replaced by ϕ_n and $l_n = l(1\pm\delta_l)$, where δ_l is the introduced perturbation.

To solve Eq. (1), the multiple scales method is applied. The single time variable t is thus replaced by an infinite sequence of independent time scales $(T_i = \varepsilon^i t)$, where ε is a small dimensionless parameter. The scaled equation of motion the nth pendulum is thus expressed as follows

$$\begin{aligned}
\ddot{\phi}_n + \varepsilon\frac{c}{m}\dot{\phi}_n + \omega_n^2\phi_n + \varepsilon\frac{k}{ml_n^2}(2\phi_n - \phi_{n-1} - \phi_{n+1}) \\
- \varepsilon\frac{g}{6l_n}\phi_n^3 = \varepsilon\frac{f}{ml_n^2}\cos(\Omega t),
\end{aligned} \quad (2)$$

where the excitation frequency $\Omega = \omega_0 + \varepsilon\sigma$, with σ the detuning parameter.

The solution of Eq. (2) can generally be given by a formal power series expansion $\phi_n = \sum_i \varepsilon^i \phi_{in}$. Up to the first order, one obtains an equation of the form

$$\begin{aligned}
\frac{\partial^2\phi_{1n}}{\partial t^2} + \omega_0^2\phi_{1n} + \frac{c}{m}\frac{\partial\phi_{0n}}{\partial t} + 2\frac{\partial^2\phi_{0n}}{\partial t\partial T} + \frac{k}{ml_n^2}\left(2\phi_{0n} - \phi_{0(n-1)} - \phi_{0(n+1)}\right) \\
- \frac{g}{6l_n}\phi_{0n}^3 = \frac{f}{2ml_n^2}exp[i(\omega_0 t + \sigma T)].
\end{aligned} \quad (3)$$

Projecting the displacement of the nth pendulum on standing-wave modes with slowly varying amplitudes $(\sin(nq_m), q_m = m\pi/(N+1), m = 1\ldots N)$ (Lifshitz and Cross 2003; Bitar et al. 2015, 2016), for boundary conditions $\phi_0 = \phi_{N+1} = 0$, leads to:

$$\phi_n = \underbrace{\sum_{m=1}^{N} A_m \sin(nq_m)exp(i\omega_0 t) + c.c.}_{\phi_{0n}} + \varepsilon\phi_{1n} \quad (4)$$

Substituting Eq. (4) into Eq. (3) leads to N equations of the form

$$\frac{\partial^2\phi_{1n}}{\partial t^2} + \omega_0^2\phi_{1n} = \sum_{m=1}^{N}\left(m^{th}\ secular\ terms\right)e^{i\omega_0 t} + other\ terms \quad (5)$$

The multiple scales method requires vanishing the secular terms. Projecting the response on the standing-wave modes leads to the generic complex equation of the mth amplitude A_m

$$2i\omega_0 \frac{\partial A_m}{\partial T} + i\omega_0 \frac{c}{m}A_m + \frac{k}{ml_n^2}[2A_m - G_m\cos(q_m)]$$

$$+ S\frac{2}{N+1}\frac{k}{ml_n^2}\sum_{n=1}^{N}\sin(nq_m)\sum_{x=1}^{N}\cos(nq_x)\sin(q_x)(A_x - \tilde{A}_x) \qquad (6)$$

$$- \frac{g}{8l_n}\sum_{j,k,l}A_jA_kA_l^*\Delta_{jkl,m}^{(1)} = \frac{1}{(N+1)}\frac{f}{ml_n^2}\exp(i\sigma T)\sum_{n=1}^{N}\sin(nq_m),$$

where $\Delta_{jkl,m}^{(1)}$ is the delta function defined in terms of the Kronecker deltas (Lifshitz and Cross 2003; Bitar et al. 2015). G_m and S depend on the number and the positions of the perturbed pendulums in the structure. Under perfect periodicity, $G_m = 2A_m$ and $S = 0$. If the concerned pendulum is perfect but the adjacent is perturbed, $G_m = A_m + \tilde{A}_m$, where $\tilde{A}_m$ refers to the perturbed amplitude. In this case, $S = -1$ or $S = +1$ if the perturbed pendulum is, respectively, the previous or the next. When the concerned pendulum is perturbed and his neighbors are perfect, $\tilde{A}_m$ replaces A_m in Eq. (6), $G_m = 2A_m$ and $S = 0$.

To solve the obtained complex equations, a Cartesian form of the amplitude is introduced: $A_m = (a_m + ib_m)exp(i\sigma T)$. Accordingly, to each complex Eq. (6) correspond two algebraic equations obtained for the real and imaginary parts of the amplitude A_m. Consequently, $2N(p+q+d)$ algebraic equations are obtained, where p is the number of perturbed pendulums, q the number of perfect pendulums neighbors of the perturbed ones and $d = 1$ if the structure contains perfect pendulums having perfect neighbors and 0 otherwise.

3   Numerical Example

A nearly periodic structure of two coupled nonlinear pendulums is considered here. The length of the first pendulum is perturbed by $\delta_l = 2\%$, such as $l_1 = l(1 - \delta_l)$. The design parameters of the structure are listed in Table 1 (Bitar et al. 2016).

$2N(p+q+d) = 8$ algebraic equations are generated in this case ($p = 1$, $q = 1$, $d = 0$). However, if the perfectly periodic structure is considered, 4 algebraic equations are obtained.

Figure 2 illustrates the amplitudes of the responses of the associated perfectly periodic structure in generalized coordinates.

Table 1   Design parameters of the two coupled pendulums structure

Parameters	m (kg)	l (m)	k (N m)	c (kg s^{-1})	f (N m)	ω_0 (rad s^{-1})
Values	0.25	0.062	9.10^{-4}	0.16	0.01	12.58
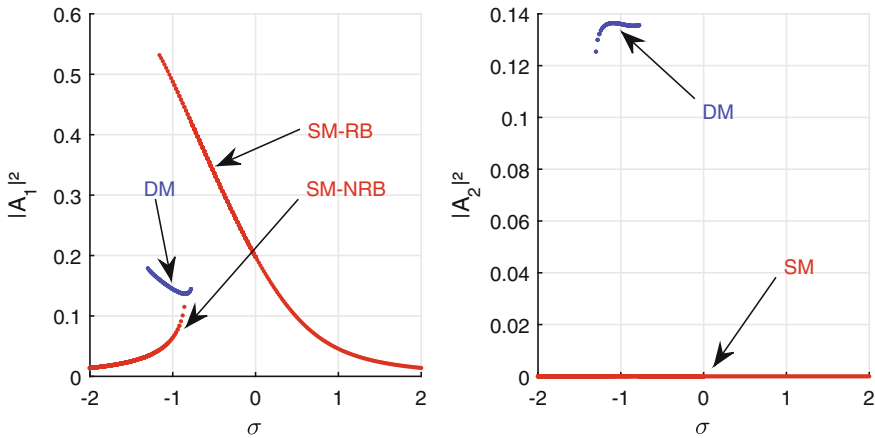
Fig. 2 Amplitudes of the pendulums responses in generalized coordinates, under perfect periodicity

The collective dynamics generates modal interactions between the pendulums responses. Up to three stable solutions exist at several frequencies in the multi-stability domain and are classified as Single (SM) and Double mode (DM) solutions. The null trivial solution of the second amplitude generates the only SM branch presented by red curve, which corresponds to the two SM branches in the first amplitude: a resonant branch (SM-RB) and a non-resonant branch (SM-NRB). The coupling between the pendulums generates the DM branches, presented by blue curves. The bifurcation topology transfer results in the correspondence between the amplitudes in term of bifurcation points and branch types. This phenomenon is more finely illustrated through the basins of attraction, which are plotted in the Nyquist plane $\left((a_1)_0, (b_1)_0\right)$ for a fixed detuning parameter $\sigma = -1$ and initial conditions $(a_2)_0 = (b_2)_0 = 0.25$, Fig. 3. Two and three attractors correspond to the generated stable solutions, for the second and the first amplitudes, respectively.

The analysis of the basins of attraction shows the correspondence between the DM branches for the two responses amplitudes. However, when the amplitude of the first pendulum response jumps between the SM-RB and SM-NRB, the amplitude of the second pendulum response is stabilized on the SM. The DM attractors are the most robust, since they dominate the basins of attraction with 60.9% of the total area. However, the contributions of the SM-RB and the DM attractors are quantified by 15.7% and 23.4%, respectively.

As illustrated in Figs. 4 and 5, introducing disorder results in adding other stable solutions. The Multistability domain is thus wider. More stable solutions are, in fact, added to the amplitude of the first pendulum response than to the amplitude of the second pendulum response. DM solutions are enhanced in both cases. Modal localization is more important on the SM-RB for the first pendulum response.
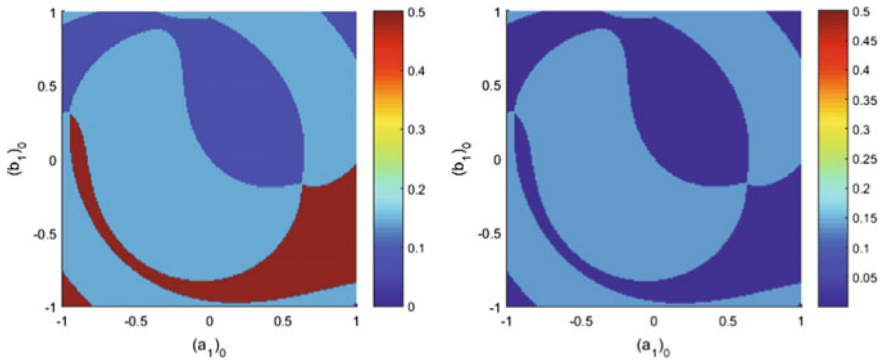
Fig. 3 Basins of attraction of the amplitudes of the pendulums responses, under perfect periodicity, in the Nyquist plane $\left((a_1)_0, (b_1)_0\right)$ for $\sigma = -1$ and $(a_2)_0 = (b_2)_0 = 0.25$, ■ SM-RB, ■ SM-NRB, ■ DM, ■ SM.
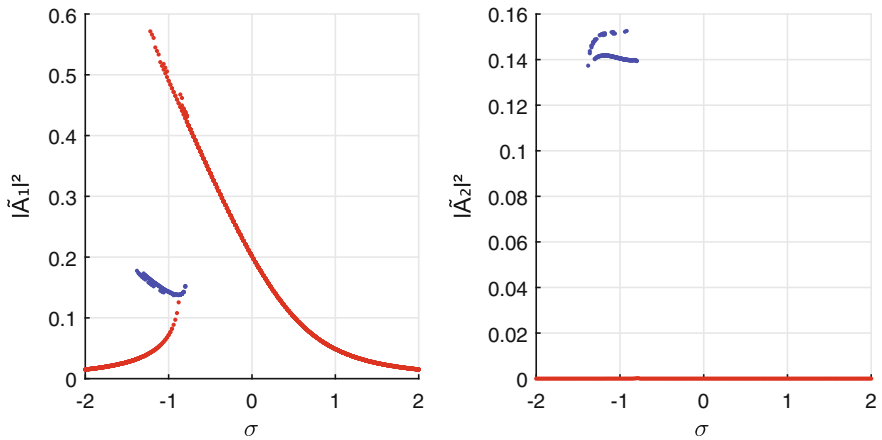
Fig. 4 Amplitudes of the first pendulum responses in generalized coordinates, for $l_1 = l(1 - \delta_l)$

However, few additional stable solutions are detected on the branches DM and SM-NRB of the amplitude of the second pendulum response.

The robustness of the basins of attractions against perturbation is illustrated through Figs. 6 and 7.

The attractors of the additional stable solutions, in the basins of attraction showed in Figs. 6 and 7, are distinguishable through colors which slightly differ from the initially defined colors for the same type of attractor. The attractors of the DM remain the most robust since they dominate the basins with 59.6% of their size. The size of the attractors of the SM-RB of the first pendulum response increases,
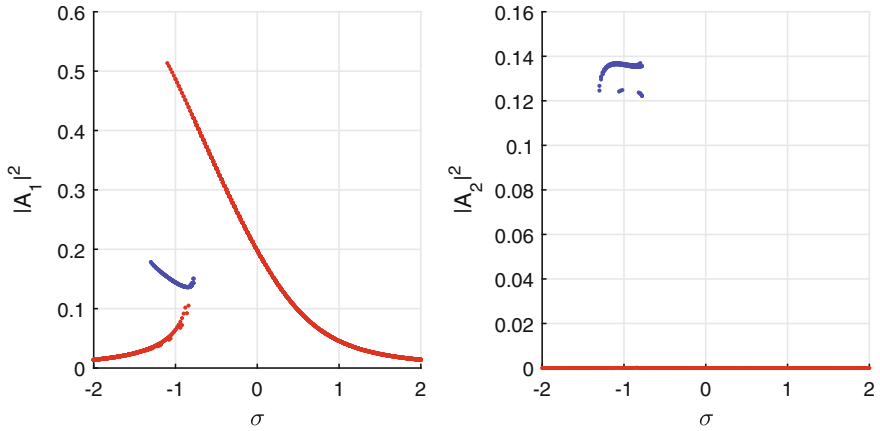
Fig. 5 Amplitudes of the second pendulum responses in generalized coordinates, for $l_1 = l(1 - \delta_l)$
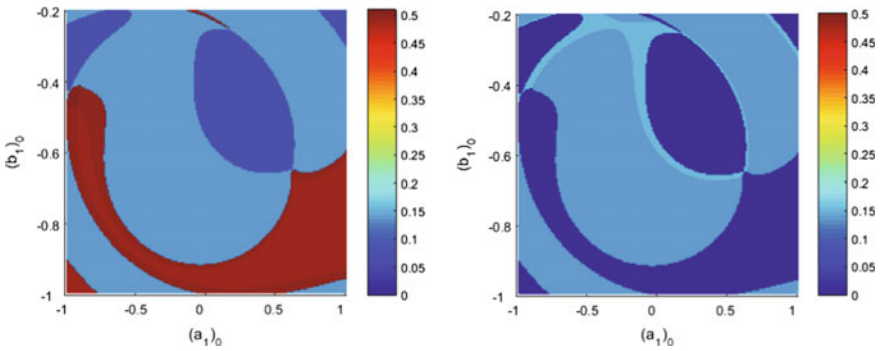
Fig. 6 Basins of attraction of the amplitudes of the first pendulum responses in the Nyquist plane $\big((a_1)_0, (b_1)_0\big)$ for $\sigma = -1$, $(a_2)_0 = (b_2)_0 = 0.25$ and $l_1 = l(1 - \delta_l)$
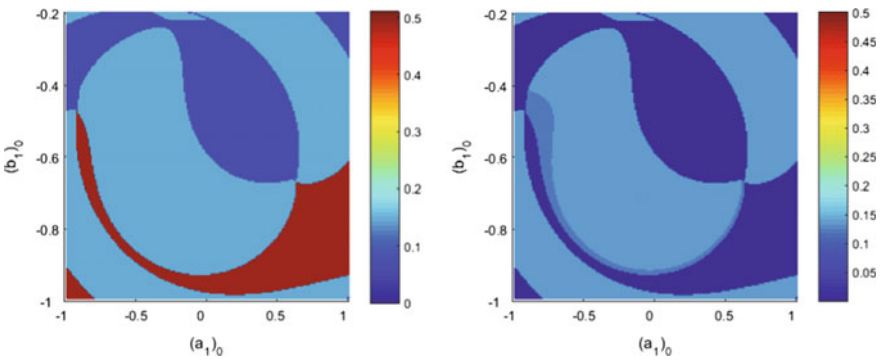
Fig. 7 Basins of attraction of the amplitudes of the second pendulum responses in the Nyquist plane $\big((a_1)_0, (b_1)_0\big)$ for $\sigma = -1$, $(a_2)_0 = (b_2)_0 = 0.25$ and $l_1 = l(1 - \delta_l)$

when introducing the perturbation, from 15.7 to 23.4%. The SM-RB attractors become more robust than those corresponding to the SM-NRB.

It can be concluded that introducing disorder results in enhancing the stability of the system. The perturbation introduced by reducing the length of one pendulum favors modal localization on its response.

4   Conclusion

Modal localization in disordered two coupled nonlinear pendulums was investigated through the robustness analysis of the collective dynamics against slight parametric perturbation.

The obtained results prove that in presence of disorder, the stability of the nearly periodic structure is enhanced and a modal localization is generated. In fact, more multimode solutions are generated by the collective dynamics and interactions between pendulums. The multistability domain is wider. These advantages allow considering the proposed model as a preliminary tool for more realistic nonlinear periodic structure design. In practice, the disorder can be functionalized in such nonlinear periodic structures in order to generate energy localization suitable for several engineering applications such as mass sensing in micro and nanotechnology, energy scavenging or trapping applications, vibration energy harvesting and bandgaps widening for vibroacoustic applications.

Only two degrees of freedom structure is considered in this paper. The extension of the study to large-size periodic structures will be the subject of future work.

References

Alexeeva NV, Barashenkov IV, Tsironis GP (2000) Impurity-induced stabilization of solitons in arrays of parametrically driven nonlinear oscillators. Phys Rev Lett 84(14)

Bitar D, Kacem N, Bouhaddi N, Collet M (2015) Collective dynamics of periodic nonlinear oscillators under simultaneous parametric and external excitations. Nonlinear Dynam 82:749–766

Bitar D, Kacem N, Bouhaddi N (2016) Investigation of modal interactions and their effects on the nonlinear dynamics of a periodic coupled pendulums chain. IJMS. doi:10.1016/j.ijmecsci.2016.11.030

Chen W, Hu B, Zhang H (2002) Interactions between impurities and nonlinear waves in a driven nonlinear pendulum chain. Phys Rev Lett 64:134302

Hai-Quing X, Yi T (2006) Parametrically driven solitons in a chain of nonlinear coupled pendula with an impurity. Chin Phys Lett 23(6):15–44

Jallouli A, Kacem N, Bouhaddi N (2017) Stabilization of solitons in coupled nonlinear pendulums with simultaneous external and parametric excitations. Commun Nonlinear Sci Numer Simulat 42:1–11

Kissel GJ (1988) Localization in disordered periodic structures. Ph.D. thesis, Massachusetts Institute of Technology

Koch RM (2003) Structural dynamics of large space structures having random parametric uncertainties. IJAV 8(2):95–103

Lifshitz R, Cross MC (2003) Response of parametrically driven nonlinear coupled oscillators with application to micromechanical and nanomechanical resonator arrays. Phys Rev Lett B 67:134302

Manktelow K, Leamy MJ, Ruzzene M (2011) Multiple scales analysis of wave interactions in a cubically nonlinear monoatomic chain. Nonlinear Dynam 63(1–2):193–203

Nayfeh AH (1983) The response of multidegree-of-freedom systems with quadratic non-linearities to a harmonic parametric resonance. JSV 90(2):237–244

Pierre C (1990) Weak and strong vibration localization in disordered structures: a statistical investigation. JSV 139(l):111–132

Tjavaras AA, Triantafyllou MS (1996) Non-linear response of two disordered pendula. JSV 190(1):65–76

Zhu Y, Chen W, Lu L (2003) Experiments on the interactions between impurities and solitary waves in lattice model. Sci China G 46(5)

Experimental Investigation on the Influence of Relative Density on the Compressive Behaviour of Metal Mesh Isolator

Fares Mezghani, Alfonso Fernandez Del Rincon,
Mohamed Amine Ben Souf, Pablo Garcia Fernandez, Fakher Chaari,
Fernando Viadero Rueda and Mohamed Haddar

Abstract Vibrations, considered one of the major problems in the engineering applications, are analyzed to predict their detrimental effects on the equipment and structures. The metal mesh isolator, named also metal rubber, has become widely applied to mitigate the disturbing vibration due to its special production techniques. Metal rubber is a kind of novel style porous damping material that is manufactured via a process of wire-drawing, weaving and compression moulding. This paper investigates the influence on the compression and dissipative behaviour of the metal mesh isolator provided by the relative density. The mechanical properties of five metal mesh samples with cylindrical geometry and with different relative density are obtained from a quasi-static cyclic compression test. The loading-unloading results of the five samples, subjected to a constant compression level, show the strong dependence exerted by the relative density over the compressive properties. Experimental analysis indicated that the porosity affects the stiffness but has an opposite effect regarding the loss factor. By increasing the ratio between the isolator's and wire's densities, the nominal stiffness increases, but the reduction of loss factor is obvious.

Keywords Metal mesh isolator · Quasi-static compression test
Relative density · Stiffness · Loss factor

F. Mezghani (✉) · M. A. Ben Souf · F. Chaari · M. Haddar
Laboratory of Mechanics, Modeling and Production, National School of Engineering of Sfax,
University of Sfax, Sfax, Tunisia
e-mail: fares.mezghani@gmail.com

F. Mezghani · A. F. Del Rincon · P. G. Fernandez · F. V. Rueda
Laboratory of Structural and Mechanical Engineering, Superior Technical School of
Industrial Engineering and Telecommunications, University of Cantabria, Santander, Spain

1 Introduction

Metal mesh isolator, named also metal rubber (Chen et al. 2002; Jiang et al. 2005), is a form of a metallic mesh that is made through a process of wire-drawing, weaving and moulding into any geometric shape by compression. Metal rubber is a kind of a novel intelligent damping material due to its outstanding properties including the significant damping capacity, low density and excellent mechanical resistance in large temperature ranges. Therefore, the mechanical proprieties make the metal isolator particularly suitable for many applications.

The metal mesh is widely used in vibration control engineering applications such as metal mesh damper of inertial platform (Wang and Pei 2004), isolation mounting of instruments in the aeronautics (Jiang et al. 2003) and damper for fuel nozzles in gas engines (Ma et al. 2008). Childs (1978) reviewed the high-pressure fuel turbo-pump rotor-dynamic problem and carried out test rigs performed on metal mesh bearing damper in efforts to eliminate the instability in the space shuttle main engine. Zarzour and Vance (2000) investigated the applied feasibility of bearing support made of metal mesh dampers in series to squirrel cage and showed that metal mesh bearing damper can be widely used in the turbo-machinery to attenuate vibration levels. Furthermore, the complete properties allow this material to be used in sound absorption (Haoyu and Yifeng 2009; Wu et al. 2009).

A number of quasi-static experimental tests have attempted to investigate the mechanical behaviour of metal mesh isolator in order to obtain information and exploit their potential. The effects of the mesh structure on the static properties of MR dampers are studied experimentally (Wang et al. 2010). The static stiffness and the damping of the metal mesh are mainly affected by wire dimension and typical coil size, by, its material properties and its relative density obtained from the manufacturing layout (Ma et al. 2015; Zhang et al. 2013). Hong et al. (2013) characterized the hysteresis behaviour of metal rubber particles (MRP) through a quasi-static experiment. Hysteresis loops were obtained by compressing a layer of MRP using an electrically driven uniaxial testing machine. Macro and microscopic compression deformation mechanisms of porous wire metallic in the cold stamping direction were investigated by Zuo et al. (2005). The compressed loading and unloading curves could be divided into three distinct stages.

The objective of the present paper is to analyse the influencing factors on the global mechanical compression proprieties of commercial metal mesh isolators. Metal damper samples with different relative densities have been produced and subjected to quasi-static compression loading. The main goal has been dedicated to obtain experimental results related to the loss factor and the stiffness, and to establish guidelines between these properties and the relative density.
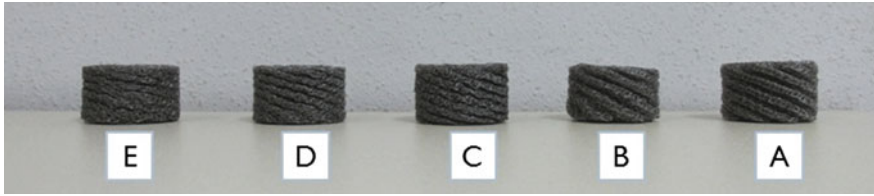
Fig. 1 Five models of isolators
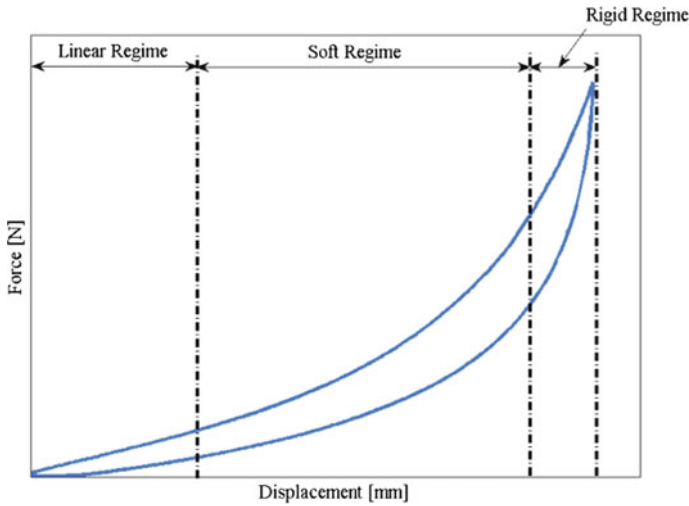
Fig. 2 Three regimes of the hysteresis loop

2   Quasi-static Compression Tests

Quasi-static cyclic compression tests were carried out to investigate the mechanical proprieties of metal mesh isolator. Hysteresis loops were obtained by compressing a specimen of metal damper using a uniaxial test machine. Five models of metal mesh samples (Fig. 1) with cylindrical geometry and different relative densities have been produced, with each model composed by nine specimens following the same manufacturing process. The relative density has been defined as the ratio between the density of the core and the density of the porous material samples.

As illustrated in Fig. 2, the compressed loading and unloading curves could be divided into three distinct regimes. At the beginning of the loading curve, there is a linear regime. Here the wires in the metal mesh solid behave as linear springs under small compression.

At higher levels, the force rises gradually with the deformation when the contact state between wires moves from non-contact to slip and stick. The loading curve enters into a long soft regime. At high deformations, the percentage of wires in stick
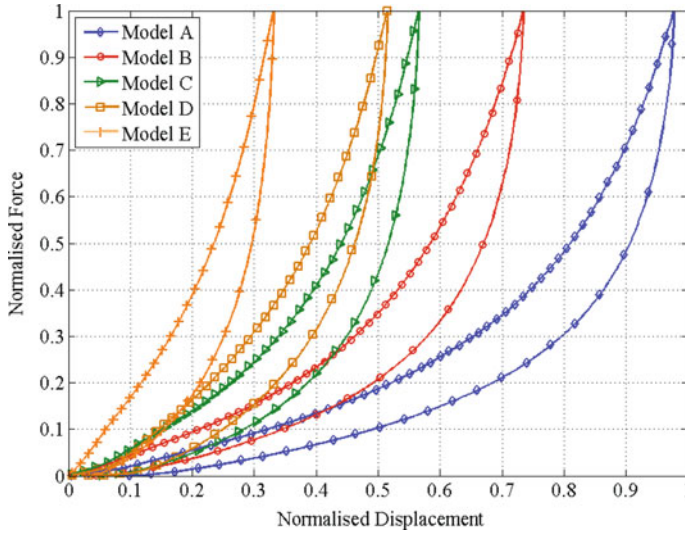
Fig. 3 Loading-unloading curve

Table 1 Maximum deformation on each metal mesh model

Model	Maximum deformation (mm)
A	11.7257
B	8.8084
C	6.7878
D	6.1781
E	3.9745

contact status increases and the deformation rises rapidly for small variation of load within the rigid regime.

The loading-unloading curves of the five metal mesh models, subjected to a constant compression level, are shown in Fig. 3. The results show the significant influence exerted by the relative density over the compressive properties of the metal mesh models.

From the model A to model E, it is apparent that the increase in the relative density leads to smaller linear, soft and rigid regimes. Meanwhile, the maximum deformation drops, with increasing the percentage of the wires stick contact status. The maximum deformation related to each model is listed in Table 1.

3 Stiffness and Loss Factor

Overall mechanical proprieties, in particular, the stiffness and the loss factor, of metal mesh isolator with different relative density can be obtained using experimental theory (Ma et al. 2016; Zhang et al. 2013). The stiffness is calculated from the gradient of the compression the hysteresis loop on the loading part. The energy dissipation coefficient, namely loss factor, is an important parameter of damping capacity from the perspective of energy dissipation.

The stiffness K of the metal mesh is defined as displacement under compression loading X caused by compression force F and can be expressed by the following equation:

$$K = \frac{F}{X}$$

The loss factor η is given by the following relation:

$$\eta = \frac{\Delta W}{\pi U}$$

where

ΔW is the dissipated energy in one load-unload cycle, is the difference between the areas under the loading and unloading curves (Fig. 4a).

U is the maximum energy stored in a cycle can be obtained from the area under the middle line of the hysteresis loop (Fig. 4b)

The nominal stiffness and loss factor for each metal mesh model is given in Fig. 5. The stiffness variation, in normalized values, for the five isolators with
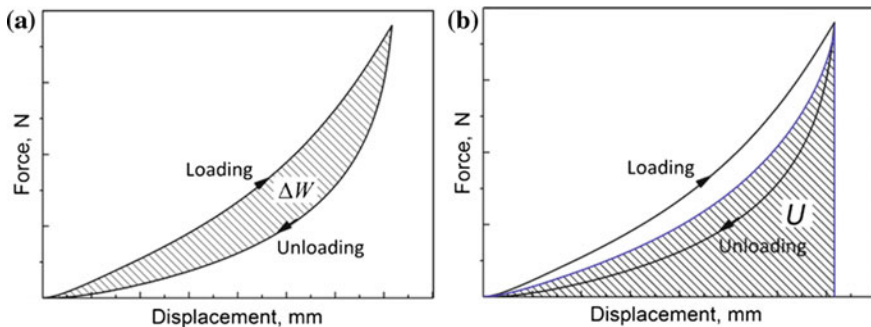
Fig. 4 Graphical Representation of: **a** energy dissipated ΔW and **b** energy stored U
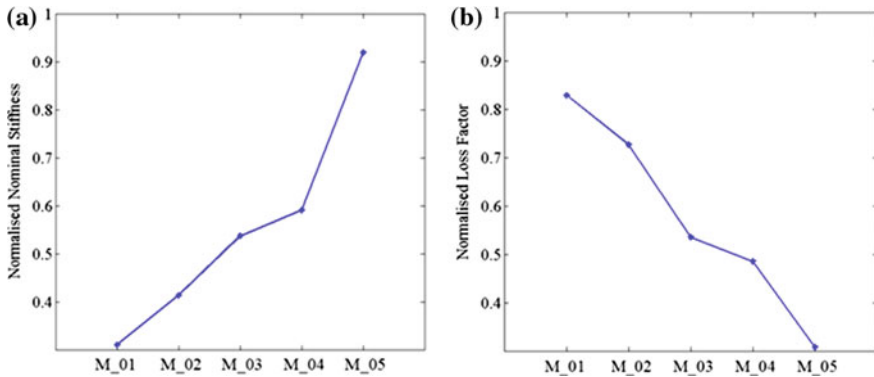
Fig. 5 Influence of the relative density on; **a** the stiffness and **b** the loss factor

different relative density is shown in Fig. 5a. The increase of the ratio between the isolator's and wire's densities provides an increase in the nominal stiffness. The loss factor has an opposite behaviour compared to the stiffness one, with the magnitude decreasing for higher values of relative density (Fig. 5b). This phenomenon has been established in metal mesh dampers made from other base materials (Zhang et al. 2013).

4 Conclusion

Metal mesh isolator is widely used as shock isolator for extreme environments, but the overall understanding of the mechanical behaviour is empirical. Quasi-static cyclic compression tests have been carried out to investigate the influence of the relative density on the stiffness and damping. With more sticking and less non-contact interactions, the stiffness increases, while the loss factor diminished. The results show the effectiveness in enhancing the mechanical properties of metal mesh damper by refining the manufacturing parameters affecting relative density, such as the compression moulding force, the mass and diameters of the wires.

References

Chen YQ, Guo BT, Zhu ZG (2002) The investigation of the stiffness characteristics and the stress-strain relation of metal rubber. J Aerosp Power 17(4):416–420

Childs DW (1978) The space shuttle main engine high-pressure fuel turbopump rotordynamic instability problem. J Eng Power 100:48–57

Haoyu MYHJL, Yifeng L (2009) Theoretical analysis on sound absorption characteristics of metal rubber. J Beijing Univ Aeronaut Astronaut 5:035

Hong J, Chen L, Ma Y, Tomlinson GR, Rongong JA (2013) Hysteretic properties of metal rubber particles. Proc Inst Mech Eng Part C J Mech Eng Sci 227(4):693–702

Jiang H, Xia Y, Ao H, Yan H (2003) Research on the application of special metal rubber components used in aeroengine. Gas Turbine Exp Res 16(3):1–5

Jiang H, Yu-Hong X, Hong-rui A et al (2005) Lifetime of metal rubber isolator with different vibration amplitudes. J Central South Univ Technol (English Edition) 12(2):181–185

Ma Y, Wang H, Li H et al (2008) Study on metal rubber materials characteristics of damping and sound absorption. In: ASME turbo expo 2008: power for land, sea, and air. American Society of Mechanical Engineers, pp 477–486

Ma Y, Zhang Q, Zhang D, Scarpa F, Liu B, Hong J (2015) The mechanics of shape memory alloy metal rubber. Acta Mater 96:89–100

Ma Y, Zhang Q, Zhang D, Scarpa F, Gao D, Hong J (2016) Size-dependent mechanical behavior and boundary layer effects in entangled metallic wire material systems. J Mater Sci 1–16

Wang JM, Pei TG (2004) Research on nonlinear characteristic of a new type of metal rubber damper for inertial platform. J Astronaut 25:256–311

Wang H, Rongong JA, Tomlinson GR, Hong J (2010) Nonlinear static and dynamic properties of metal rubber dampers. Energy 10:1

Wu G, Ao H, Jiang H, Izzheurov EA (2009) Calculation of resonant sound absorption parameters for performance evaluation of metal rubber material. Sci China Ser E Technol Sci 52(12):3587–3591

Zarzour M, Vance J (2000) Experimental evaluation of a metal mesh bearing damper. ASME J Eng Gas Turbine Power 122(22):326–329

Zhang D, Scarpa F, Ma Y, Boba K, Hong J, Lu H (2013) Compression mechanics of nickel-based superalloy metal rubber. Mater Sci Eng, A 580:305–312

Zuo H, Chen YH, Bai HB, Sun H (2005) The compression deformation mechanism of a metallic Rubber. Int J Mech Mater Des 2(3–4):269–277

Anisotropic Study of Behavior of Titanium Alloy Thin Sheets Using Identification Strategy

Amna Znaidi, Olfa Daghfas, Rym Harbaoui and Rachid Nasri

Abstract The objective of this work is to provide an operational model for the numerical simulation of the shaping processes by plastic deformation of thin plates made of Titanium alloy. Hence, the importance of developing a general framework of elastoplastic orthotropic models (initial orthotropy and isotropic hardening) based on the choice of an equivalent stress, a law of hardening for the development of a strategy of identification of the model from an experimental database. At this level, the identification of the constitutive parameters involved in the laws of behavior of the materials represents an important step in this work. A new identification strategy accompanied by its validation using the criterion of Barlat will be proposed. Numerical simulation can be a very useful tool for titanium alloy. Mainly due to its use in orthopedic surgery; Titanium is of great interest because of its elasticity modulus very close to that of the bone.

Keywords Anisotropy · Identification strategy · Off-axis testing
Lankford coefficient · Titanium alloy

A. Znaidi (✉) · O. Daghfas · R. Harbaoui · R. Nasri
LR-MAI-ENIT, National School of Engineers of Tunis, University Tunis El Manar,
BP37 Le Belvedere, 1002 Tunis, Tunisia
e-mail: amna.znaidi@laposte.net

O. Daghfas
e-mail: daghfasolfa@yahoo.fr

R. Harbaoui
e-mail: rym.harbaoui@gmail.com

R. Nasri
e-mail: rachid.nasri@enit.rnu.tn

A. Znaidi
IPEIEM, University Tunis El Manar, BP244 CP, 2092 Tunis, Tunisia

1 Introduction

To describe the plastic behavior of the material, it is necessary to clarify two concepts, the load surface related to a plasticity criterion and the evolution of anisotropy (Znaidi 2004), to indicate the conditions of plastic flow.

The objective of this work is to provide a model for the numerical simulation of forming processes. The idea is to study the plastic deformation of thin metal sheets in Ti40. Hence, the importance of developing a general framework for elastoplastic orthotropic models (initial orthotropic and isotropic hardening) is based on the choice of an equivalent stress, a hardening law and a plastic potential (Znaidi et al. 2015; Ben Mohammed et al. 2014) using an experimental database (Toussaint et al. 2008) for the model of the identification strategy.

This database consists of various hardening curves from various tests (interpreted as homogeneous) and their Lankford coefficients. These plates are obtained from a hot-rolling process. At this point, the identification of constitutive parameters of the material behavior laws is an important step. A new identification strategy with its validation using the criterion of Barlat will be presented, aiming to provide better accuracy compared to the studies using the criterion of Hill (Daghfas et al. 2015).

2 Anisotropic Elastoplastic Constitutive Laws

This work is limited to plastic orthotropic behavior. Models are formulated for standard generalized materials with an isotropic hardening described by an internal hardening variable, a law of evolution and an equivalent deformation. The material is initially orthotropic and remains orthotropic; isotropic hardening is assumed to be captured by a single scalar internal hardening variable denoted by α. In particular, we will assume that the elastic range evolves homothetically, the yield criterion is then written as follows:

$$f(\overline{\boldsymbol{\sigma}}^D, \alpha) = \sigma_c(\overline{\boldsymbol{\sigma}}^D) - \sigma_s(\alpha) \tag{1}$$

where $\sigma_s(\alpha)$ is the hardening curve

$\boldsymbol{\sigma}^D$ is the deviator of the Cauchy stress tensor (incompressible plasticity).
The function $\sigma_c(\overline{\boldsymbol{\sigma}}^D)$ satisfies the following condition

$$\sigma_c(a\overline{\boldsymbol{\sigma}}^D) = a\sigma_c(\overline{\boldsymbol{\sigma}}^D) \text{ for all } a > 0 \tag{2}$$

We introduce the angle θ which defines the orientation of $\boldsymbol{\sigma}^D$ in the deviatory plan and we define the off-axis angle ψ (angle which defines the orientation of the

loading directions with respect to the preferred direction of the material) as the following:

$$\overline{X}_1 = \left|\boldsymbol{\sigma}^D\right| \cos\theta, \ \overline{X}_2 = \left|\boldsymbol{\sigma}^D\right| \cos\theta \ \cos 2\Psi \ \text{and} \ \overline{X}_3 = \left|\boldsymbol{\sigma}^D\right| \cos\theta \ \sin 2\Psi \qquad (3)$$

Using the special setup of the space deviators, any type of criterion can be written in this form:

$$f(\theta, 2\psi) = \left|\overline{\boldsymbol{\sigma}}^D\right| / \sigma_s(\alpha) \qquad (4)$$

3 Results and Discussions

In this section, we focus on the phenomenology of the plastic behavior; especially the modeling of the plasticity and the hardening based on experimental data represented as families of hardening curves and Lankford coefficient data.

As a hardening function a Ludwick law is used:

$$\sigma_s = \sigma_0 + k\varepsilon^n \qquad (5)$$

where σ_0 is the stress for $\Psi = 0°$, k and n are the hardening coefficients.

And as a plasticity criterion the model of Barlat is used:

$$\sigma_c^m = \left|q_1 - q_2\right|^m + \left|q_2 - q_3\right|^m + \left|q_1 - q_3\right|^m. \qquad (6)$$

where q_1, q_2, and q_3 are the eigenvalues of the tensor q and m is the shape coefficient.

$$\sigma_c(q) - \sigma_s(\alpha) \leq 0 \quad \text{Where } \mathbf{q} = \mathbf{A}(a_i): \boldsymbol{\sigma} \quad \text{thus } \mathbf{q} = \sigma\mathbf{A}(a_i): \mathbf{a} \qquad (7)$$

A is the 4th order orthotropic tensor defined by anisotropy coefficients a_i and the hardening curve σ_s (α) (Table 1).

Knowing that the coefficient n is the same for all tests as demonstrated at the beginning of this work, by convention we choose n for traction in direction $\psi = 00°$ as a reference. For n = 0.9833, we present different values of k and σ_0 (Table 2).

For this strategy, the algorithm SIMPLEX is used, by minimizing the squared difference between the experimental and the theoretical results.

	Ψ	σ0	K	N
Table 1 Identification of the constants of hardening law for different tractions tests	0°	475.8334	352.2032	0.9833
	45°	468.4109	383.6323	0.9401
	90°	441.1489	422.1194	0.7233

In Fig. 1, the experimental hardening curves(exp) and the curve identified from a model (ident) using an average value of n are represented. For tensile tests, the models (ident) give a clear fit between the theoretical and experimental results.

Our second identification step amounts to determining the coefficients of anisotropy (f, g, h, n) and the shape coefficient m (Table 3), considering the non-quadratic criterion of Barlat.

Using the identified anisotropic coefficients, we represent in Fig. 2, the evolutionary developments of Lankford coefficient and the of the anisotropy based on off-axis.

We find good agreement (Fig. 2) between the experimental results of Lankford ratio and those from the model identified using the criterion of Barlat.

Table 2 Identification of the constant hardening law for fixed n

Ψ	σ_0	K
0°	474.5914	355.2603
45°	471.0220	391.4340
90°	480.3606	434.0709

Fig. 1 Identification of the hardening curve: $\Psi = 00°$
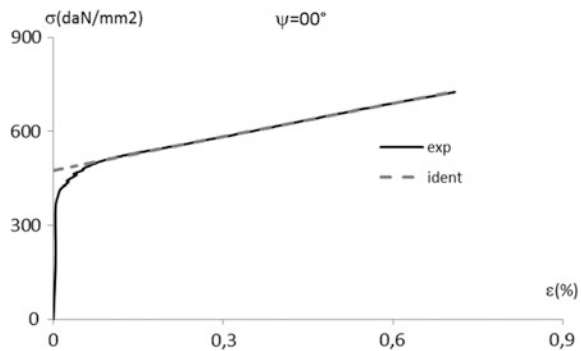
Table 3 Identification of anisotropic coefficients and a shape coefficient m

F	G	H	N	M
0.2854	0.2064	0.335	0.8921	6.9584

Fig. 2 Evolution of Lankford coefficient
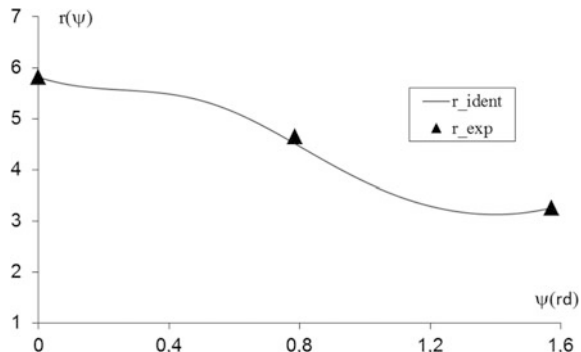
4 Conclusion

In this work, we show that following this identification strategy various results can be extracted. This identification has focused both on the plastic material parameters of the constitutive law and the Lankford coefficient. Thus, with the plastic behavior model: Ludwick Law and Barlat criterion, five parameters are identified.

A validation by comparing model/to experimental data was performed.

The model using the criterion of Barlat is in a good agreement with experimental results relating to Lankford coefficients.

References

Ben Mohamed A, Znaidi A, Baganna M, Nasri R (2014) The study of the hardening precipitates and the kinetic precipitation. its influence on the mechanical behavior of 2024 and 7075 aluminum alloys used in aeronautics. Applied condition monitoring, vol 2. Springer, pp 219–228

Daghfas O, Znaidi A, Nasri R (2015) Anisotropic behavior of mild steel subjected to isotropic and kinematic hardening. In: 6th international conference on advances in mechanical engineering and mechanics (ICAMEM2015) ID: 12. Hammamet (Tunisia)

Toussaint F, Tabourot L, Ducher F (2008) Experimental and numerical analysis of the forming process of a CP titanium scoliotic instrumentation. J Mater Process Technol 197

Znaidi A (2004) Plasticity orthotrope in large deformation, PhD thesis at the Faculty of Sciences of Tunis

Znaidi A, Daghfas O, Gahbiche A, Nasri R (2016) Identification strategy of anisotropic behavior laws: application to thin sheets of aluminium A5. J Theoret Appl Mech 54(4):1147–1156. Warsaw. https://doi.org/10.15632/jtam-pl.54.4.1147-2015

Biomechanical Approach for the Development and Simulation of a Musculoskeletal Model of the Ankle

E. Ederguel, S. Bennour and L. Romdhane

Abstract Estimation of individual muscle forces during human movement can provide insight into neural control and tissue loading and can thus contribute to improved diagnosis and management of both neurological and orthopaedic conditions. Direct measurement of muscle forces is generally not feasible in a clinical setting, and non-invasive methods based on musculoskeletal modeling should, therefore, be considered. The current state of the art in clinical movement analysis is that resultant joint torques can be reliably estimated from motion data and external forces (inverse dynamic analysis). The purpose of this paper consists in developing and simulating a biomechanical model of the lower limb, more precisely, of the foot during its movement. In this paper, we are interested in the calculation of the ankle joint. First, we have studied the muscular length variation as a function of the variation of the flexion angle. Then, we focus on the determination of the muscular force produced by muscles and involved in the flexion movement and the foot extension. Finally, we have cited the findings and the interpretations appropriate to the results obtained.

E. Ederguel · S. Bennour · L. Romdhane (✉)
Mechanical Laboratory of Sousse (LMS), National Engineering School of Sousse,
University of Sousse, BP264 Erriadh, 4023 Sousse, Tunisia
e-mail: lotfi.romdhane@gmail.com; lromdhane@aus.edu

E. Ederguel
e-mail: ebtissemederguel@gmail.com

S. Bennour
e-mail: sami.bennour@gmail.com

L. Romdhane
Mechanical Engineering Department, American University of Sharjah, PO Box 26666,
Sharjah, United Arab Emirates

1 Introduction

The low limb is responsible of the stabilization and the mobility of the human body; thanks to its articulation and its muscular system. In particular, the ankle is an important articulation for the human walk. To overcome some of its pathologies, it needs a rehabilitation, which aims to reestablish the muscular efforts. Nowadays, there is no instrument that can measure these efforts produced by a person while doing any action. But, a biomechanical model can estimate it based on measurable values (Zhu et al. 1999; Winter 2009). In the recent years, many researches on the domain of medical engineering had a progress. So, robots (Exoskeleton, robotic low limb, machine of rehabilitation, etc.) (Seddiki et al. 2007; Riener et al. 2005; Williams et al. 2004) and substitutions of rehabilitation like prosthesis and orthosis were invented to overcome some of these pathologies (Badr 2013; Gong et al. 2016).

In this paper, the main objective is to determine the muscular force produced by each muscle responsible for the bending and extension of the foot. The muscular-skeletal model of the foot is established to estimate the variation of the muscular force and to determinate the variation of the longer of each muscle during this movement (Scott et al. 1991). The results obtained will be very helpful especially in such domains like rehabilitation of members (Zabaleta et al. 2007) and sportive acts (Viel 2003). For example, the therapist can compare the variation of normal muscles' forces and lengths with the abnormal ones. Then, he can easily detect the pathologic muscles and do the adequate exercises to overcome this pathology or to reinforce the muscles.

Most of researches establish the biomechanical model of muscles in isometric case (Sami 2012; Rochcongar 2004). That s means that they study the comportment of muscles while they are stretched at a constant speed. In our work, we take on consideration the importance of the velocity and its effect on the variation of the total muscular force.

2 Calculation of the Muscular Length

The articulation of ankle, concerned in our study, is so flexible; thanks to its rich muscular system. Bending and extension are the most important movements of the ankle during human walking (Guillaume 2010). Figure 1 shows the bending angle considered:

2.1 Modelling Methodology

In order to validate our model, we will follow these steps shown in Fig. 2:
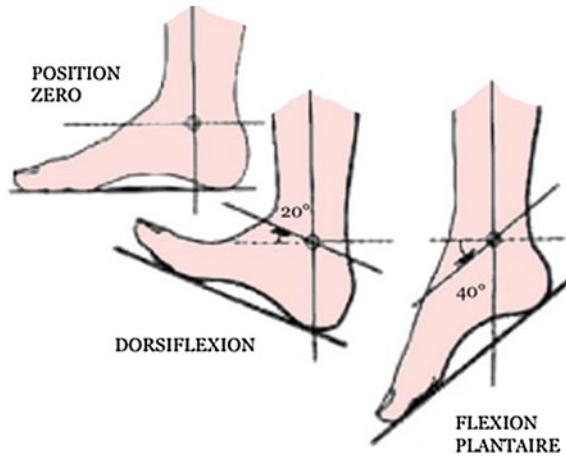
Fig. 1 Flexion-extension movement
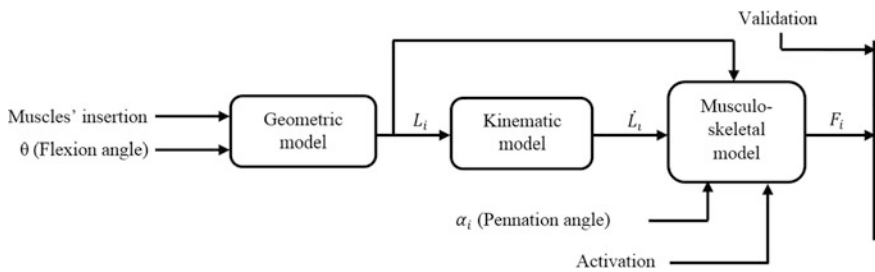
Fig. 2 Modelling methodology

2.2 Calculation of the Muscular Length

We focus on the calculation of the fibre's longer of flexor muscles. We consider the reference R(o, x, y) to the shank the fixed element. Let z be the axis of the ankle in the sagittal plane around which the movement of bending and extension is made.

- Extension case

The foot is said in extension if it is pushed down. The followed configuration represents a flexor muscle which is connected to the foot and the shank articulated between them by the ankle modelled by a pivotal relation (Fig. 3).

With: I: Insertion point of muscle; A: Application point of muscle; a: Distance between the insertion point and the origin which is the ankle; b: Distance between the application point and the origin which is the ankle; L: Muscle's longer; θ: Bending angle.

Fig. 3 Flexor muscle's model
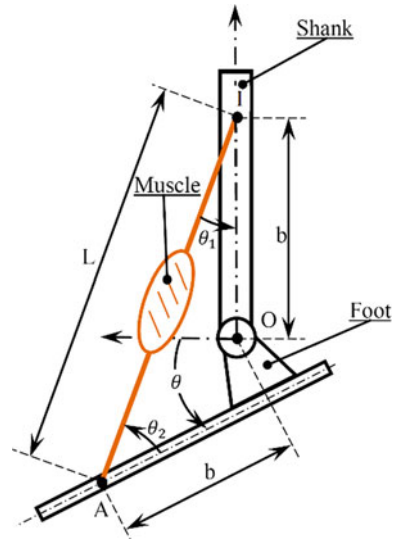
$$\frac{\pi}{2} + \theta + \theta_1 + \theta_2 = \pi \qquad (1)$$

$$\Rightarrow \theta + \theta_1 + \theta_2 = \frac{\pi}{2}$$

$$a^* \sin \theta_1 = b^* \sin \theta_2 \qquad (2)$$

$$a^* \cos \theta_1 + b^* \cos \theta_2 = L \qquad (3)$$

- Flexion case

The foot is said in flexion if it is upward. The flexor muscles contract to achieve this action. In Fig. 4 the flexor muscle is represented in case of the foot is upward.

This geometric is given in the following equation:

$$\frac{\pi}{2} - \theta + \theta_1 + \theta_2 = \pi \qquad (4)$$

We obtain then two functions, which rely on the muscles' longer to the bending angle:

$$L = f_1(\theta) = a^* \sqrt{1 - \frac{a^{2*}(\cos \theta)^2}{a^2 + b^2 - 2^* a^* b^* \sin \theta}} + b^* \sqrt{1 - \frac{b^{2*}(\cos \theta)^2}{a^2 + b^2 - 2^* a^* b^* \sin \theta}}, \ active \ muscle \qquad (5)$$

Fig. 4 Extensor muscle's model
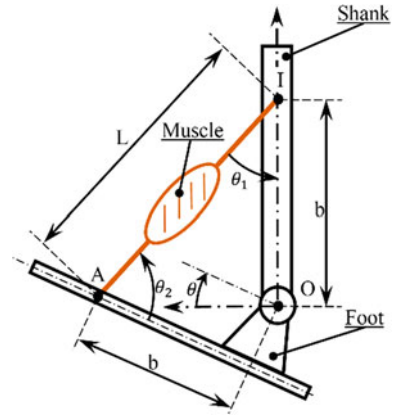
$$L = f_2(\theta) = a^* \sqrt{1 - \frac{a^{2*}(\cos\theta)^2}{a^2 + b^2 + 2^*a^*b^* \sin\theta}} + b^* \sqrt{1 - \frac{b^{2*}(\cos\theta)^2}{a^2 + b^2 + 2^*a^*b^* \sin\theta}}, \; passive \; muscle \tag{6}$$

2.3 Cinematic Calculation of the Ankle Articulation

If we derive the system of equations above, we obtain the following relation:

$$\dot{L} = \frac{\partial f}{\partial \theta} * \dot{\theta} \tag{7}$$

$$\dot{L} = \left(-\frac{b\left(\frac{2a^3 b \cos(\theta)^3}{(a^2 - 2ab \sin\theta + b^2)^2} - \frac{2a^2 \cos\theta \sin\theta}{a^2 - 2ab \sin\theta + b^2}\right)}{2\left(1 - \frac{a^2 \cos(\theta)^2}{a^2 - 2ab \sin\theta + b^2}\right)^{\frac{1}{2}}} - \frac{a\left(\frac{2ab^3 \cos(\theta)^3}{(a^2 - 2ab \sin\theta + b^2)^2} - \frac{2b^2 \cos\theta \sin\theta}{a^2 - 2ab \sin\theta + b^2}\right)}{2\left(1 - \frac{b^2 \cos(\theta)^2}{a^2 - 2ab \sin\theta + b^2}\right)^{\frac{1}{2}}} \right) \dot{\theta}, \; active \; muscle \tag{8}$$

$$\dot{L} = \left(\frac{b\left(\frac{2a^3 b \cos(\theta)^3}{(a^2 + 2ab \sin\theta + b^2)^2} + \frac{2a^2 \cos\theta \sin\theta}{a^2 + 2ab \sin\theta + b^2}\right)}{2\left(1 - \frac{a^2 \cos(\theta)^2}{a^2 + 2ab \sin\theta + b^2}\right)^{\frac{1}{2}}} + \frac{a\left(\frac{2ab^3 \cos(\theta)^3}{(a^2 + 2ab \sin\theta + b^2)^2} + \frac{2b^2 \cos\theta \sin\theta}{a^2 + 2ab \sin\theta + b^2}\right)}{2\left(1 - \frac{b^2 \cos(\theta)^2}{a^2 + 2ab \sin\theta + b^2}\right)^{\frac{1}{2}}} \right) \dot{\theta}, \; passive \; muscle \tag{9}$$

So, we have had this form:

$$\dot{L} = J\dot{\theta} \tag{10}$$

where $\dot{L}$ and $\dot{\theta}$ represent the time derivatives of L and θ. This tells us that the end velocity is equal to the Jacobean, J, multiplied by the joint angle velocity (Bernard 2005).

3 Biomechanical Model

Due to its reliability to the muscle biology in reality described in Fig. 5, we choose to adopt the Zajac model that is differentiated from the Hill model by the angle of pennation α (Serdar et al. 2014; Scott 1991). In this model, the tendon is schematized by a spring characterized by its elasticity. Since the muscle has actually a viscoelastic character (Zajac 1989a, b), it has been modelled by an elastic element and another viscous one as shown in the Fig. 6.

Fig. 5 Macroscopic architecture of a muscle
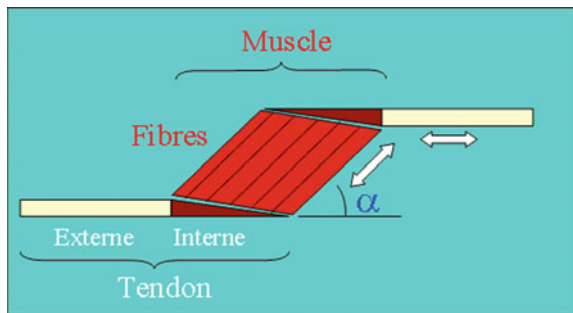
Fig. 6 Zajac model (Sami 2012)
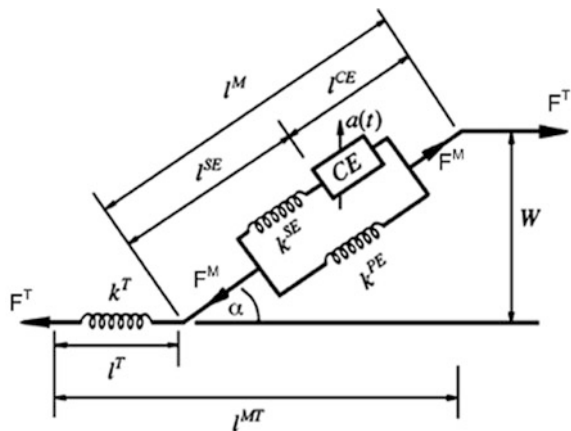
Muscle strength depends on three main parameters, which are: activation, deformation and rate of contraction. Taking into account human physiology and influential variables, the determination of muscular effort follows in the formula below:

$$F = F_{\max} \left[a(t)f(\varepsilon)f_c(v) + f_p(\varepsilon) \right] \qquad (11)$$

With: F muscular effort; $F_{\max}$ maximum muscle force; $a(t)$ activation of the muscle; $f(\varepsilon), f_p(\varepsilon)$ muscle deformation forces; $f_c(v)$ the contraction speed function (Joe 2005; Chalfoun et al. 2004).

3.1 The Activation's Effect

The activation is an Electromyogram signal from the brain. It commands muscles to achieve the desired action. It varies between 0 to 1. We study the variation of the muscular effort in different activations to show the effect of the activation on this effort. Figure 7 illustrates the total muscular force in deferent rates of activation:

The previous curves show that the total force is proportional to the activation. It attends its maximum for the maximum activation ($a = 1$). When the muscle is not activated ($a = 0$), only the passive force is involved.

3.2 The Deformation's Effect

The muscular deformation affects the muscular strength according to the two equations below:

Fig. 7 Activation influence on the muscles' length

$$f(\varepsilon) = \exp\left[-\left(\frac{(\varepsilon+1)^{0.96343\left(1-\frac{1}{ia}\right)}-1}{0.35327(1-ia)}\right)^2\right], \text{ if } ia < 1 \tag{12}$$

$$f(\varepsilon) = \exp\left[-\left(2.727277 \ln (\varepsilon+1)\right)^2\right], \text{if } ia = 1 \tag{13}$$

With: $\varepsilon = \frac{L-l_0}{l_0}$ Muscular deformation; L Muscle's length: l_0 Optimal muscle's length (in resting muscle case) and ia Index of constant muscular architecture that represents the ratio muscle fibres and the muscle length with $ia = \frac{L_f}{L}$ while $0 < ia < 1$ (Joe 2005; Chalfoun et al. 2004) (Fig. 8).

In the lower limb case, the muscles are very thin compared to their lengths. The thickness of the muscles is about 1/5 of their length. For this paper, we adopt in our calculation that ia is a constant and is equal to 0.2. When the muscular fibres expand, the passive force reacts according to Eq. 14 (Joe 2005; Chalfoun et al. 2004):

$$f(\varepsilon) = b_1 e^{b_2 \varepsilon} - b_1 \tag{14}$$

3.3 The Effect of the Contraction's Rate

The muscular force exerted on movement depends on the muscle contraction rate concerned. The function that connects force to velocity is expressed by Eq. (15):

$$f_c(v) = \beta_1 + \beta_2 \arctan(\beta_3 + \beta_4 v) \tag{15}$$

With: $\beta_1 = 1.52$, $\beta_2 = -0.97$, $\beta_3 = 0.6$ and $\beta_4 = 20$ (Joe 2005; Chalfoun et al. 2004).

4 The Simulation's Results

In this paper, we focus on the bending and extension movements of the foot. So, we study the muscles which participate in this movement. Table 1 illustrates the insertion coordination of these muscles and its maximum strengths:

Table 1 Coordination of the insertion responsible of flexion-extension of the ankle

Muscles	Abbreviation	Role	Insertion points (I)		Application points (A)		Maximum strength (N) Sami (2012)	Optimal length (mm)
			X	Y	X	Y		
Tibial anterior	TA	Flexor	−20	340	150	−50	360	425.4
Long extensor of Hallux	EXTALL	Flexor	−20	340	150	−50	110	403.6
Long toe extender	EXTORT	Flexor	−40	230	60	−50	340	481
Long fibular	LF	Extensor	0	400	260	−40	343	435.6
Short fibular	CF	Extensor	0	200	−70	−30	160	240.4
Long flexors of the toes	FLECHORT	Extensor	30	300	−90	−40	145	360.5
Hallux flexor	FLECHALL	Extensor	10	260	−90	−40	227	326.9
Tibial posterior	TP	Extensor	−30	380	−160	−70	475	468.4
Triceps sural	TS	Extensor	−30	440	−180	−90	1700	550.8

Fig. 9 Muscles flexors in flexion
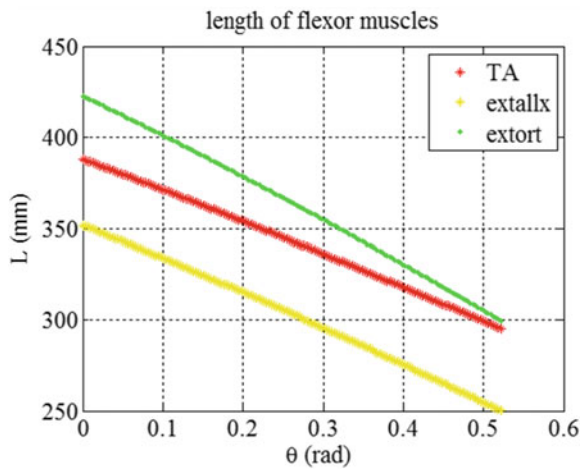
4.1 Variation of Muscles' Length

If the foot is pushed up or down, the length of the muscles which are responsible for this movement change. Some muscles are contracted and the others are iterated. Figures 9 and 10 represent the variation of the length of the flexors and the extensors in flexed foot case.

Fig. 10 Muscles extensors in flexion
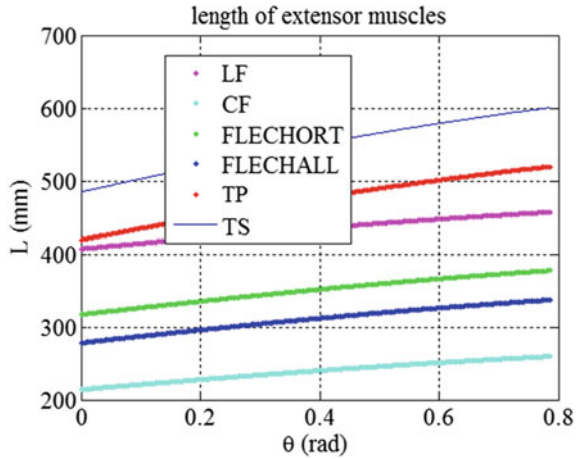
Fig. 11 Muscles flexors in extension
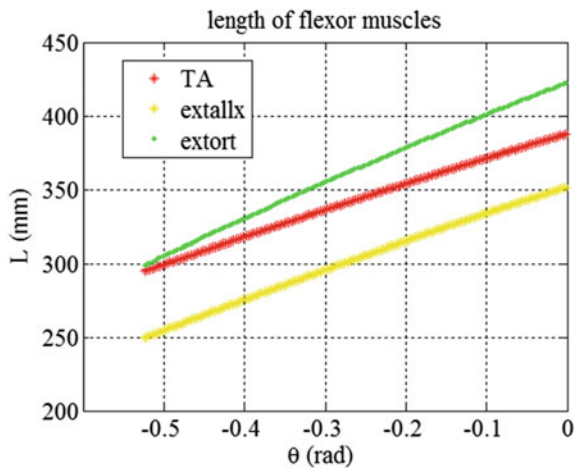
Figures 11 and 12 illustrate the variation of flexors' length and extensors' length in case of extended foot:

These curves show the evolution of the muscles length during the flexion and extension of the foot. In flexion case, the extensors' muscular lengths increase as the flexors' ones decrease. The flexors are active so they contract to rise up the foot and the extensors expand to make the movement more flexible. In extension case, the extensors' muscular lengths decrease to push the foot down while the flexors' ones increase to stabilize this movement. So, the flexion and the extension movements are symmetric.

Fig. 12 Muscles extensors in extension
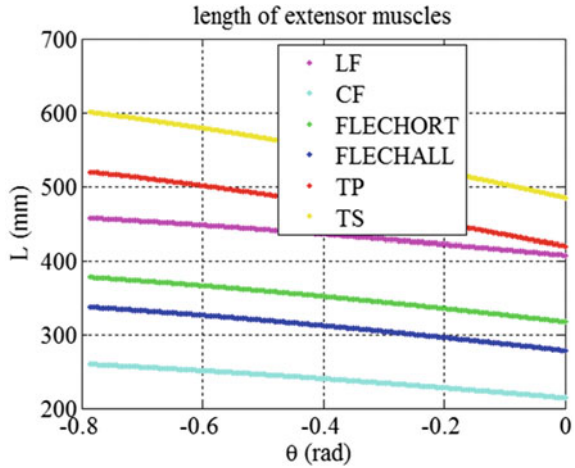
Fig. 13 Behavior of flexor muscles in flexion
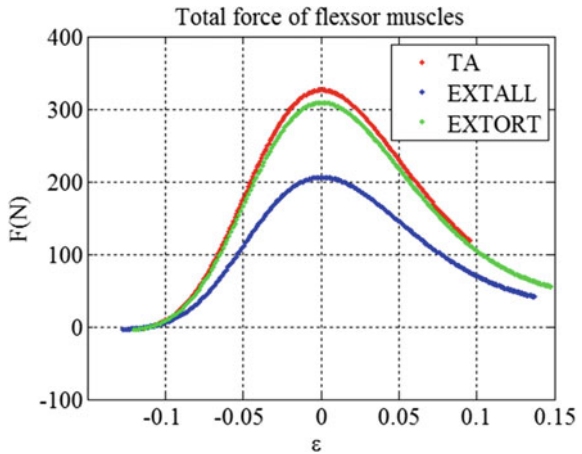
4.2 Variation of Muscles' Effort

● Flexion case

To push the foot up or down, some muscles produce an effort more important. They are called the active muscles. The Figs. 13 and 14 show the variation of the muscular force of flexors and extensors in case of flexed foot:

● Extension case

The Figs. 15 and 16 show the variation of the muscular force of flexors and extensors in case of extended foot:

Fig. 14 Behavior of extensor muscles in flexion
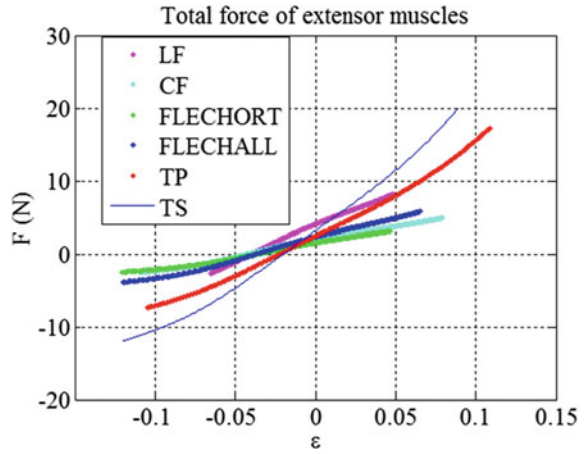
Fig. 15 Behavior of flexor muscles in extension
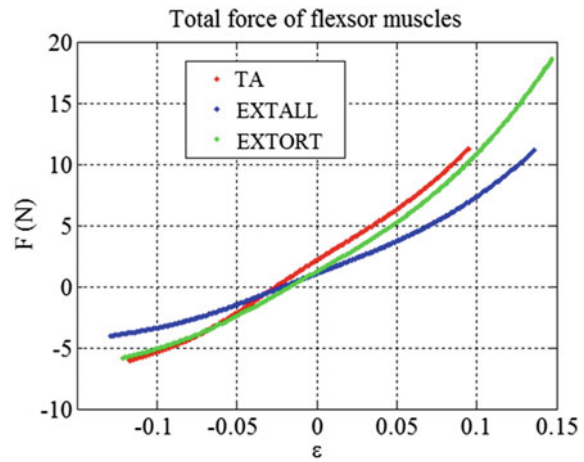
Fig. 16 Behavior of extensor muscles in extension
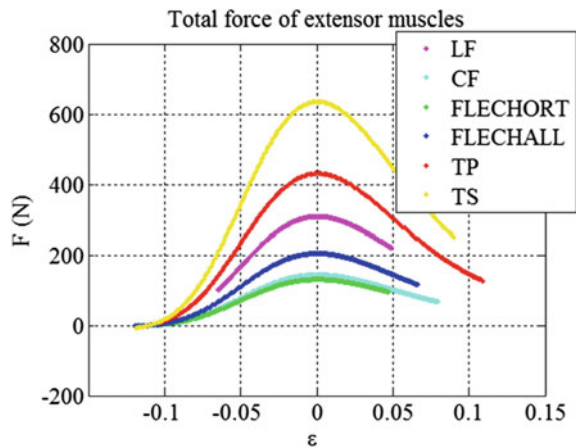
The extension of the foot is ensured by the relaxation of the flexor muscles and the activation of the extensors. In flexion case, the flexors are the active ones. When the deformation is negative, the curves show that the active muscles contract by producing a maximum force at zero deformation. So, when the muscle is contracted, only the active force is generated. If the muscular length exceeds this length, the curve of the total force sums both the active and the passive force. The force tends to increase when the deformation ε increases. The flexor force is almost zero.

5   Conclusion

In this paper, we have established the muscular-skeletal model of muscle. Thus, we studied the variation of the muscular length with the variation of the flexion's angle. We took on consideration only the longitudinal elongation because it is the most important in flexion and extension cases. So, the other elongations are neglected during this movement. Then, we estimated the muscular forces produced by each muscle responsible for the flexion and the extension of the foot. The result obtained could be closer to the reality if our model were three dimensional. Also, they can be ameliorated if we adopted experimental values of the muscles' activation. The validation of the model could be experimental and not only based on theoretical results.

References

Badr ME (2013) Les arthrodèses de la cheville (A propos de 08 cas). Thèse de doctorat de l'université sidi Mohammed Benabdellah faculté de médecine et de pharmacie

Bernard B (2005) Introduction à la Robotique. Cours à Université Louis Pasteur de Strasbourg ´ IUP Technologies Avancées des Sciences du Vivant

Chalfoun J, Renault M, Younes R, Ouezdou FB (2004) Muscle forces prediction of the human hand and forearm system in highly realistic simulation. Iros, Japan

Gong C, Peng Q, Zhao G, Haoyong Y (2016) Mechanical design and evaluation of a compact portable knee–ankle–foot robot for gait rehabilitation. Mech Mach Theor 103:51–64

Guillaume N (2010) Des données anatomiques à la simulation de la locomotion bipède: Application à l'Homme, au Chimpanzé, et à Lucy. Thèse de doctorat de l'université Renne 2

Joe C (2005) Prédiction des efforts musculaires dans le système main avant-bras: Modélisation, simulation, optimisation et validation. Thèse de doctorat de l'université de Versailles Saint-Quentin-en-Yvelines

Riener R, Frey M, Bernhardt M, Nef T, Colombo G (2005) Human centred rehabilitation robotics. IEEE International Conference in Rehabilitation Robotics, pp. 319–324

Rochcongar P (2004) Evaluation isocinétique des extenseurs et fléchisseurs du ge-nou en médecine du sport: revue de la littérature. Anales de réadaptation et de médecine physique 47:274–281

Sami B (2012) Contribution au Développement d'une Plateforme Robotisée pour la Rééducation Fonctionnelle. Thèse de doctorat de l'École Nationale d'Ingénieurs de Monastir

Seddiki L, Guelton K, Moughamir S, Mansouri B, Zaytoon J (2007) Modélisation T-S et commande Hinf d'une machine de rééducation des membres inférieurs. Journal Européen des Systèmes Automatisés, RSJESA 41(2):199–218

Serdar G, Andreas M, Ellen K (2014) The generalized Hill model: A kinematic approach towards active muscle contraction. J Mech Phys Solids 72:20–39

Scott SH, Winter DA (1991) A comparison of three muscle pennation assumptions and their effect on isometric and isotonic force. J Biomech 24:163–167

Viel E, Esnault M (2003) Récupération du sportif blessé. De la rééducation en chaîne fermée au stretching en chaîne musculaires, Edition Masson

Williams II RL, Snyder B, Albus JS, Bolstelman RV (2004) Seven- DOF cable-suspended robot with independent metrology. Comptes rendus – ASME IDETC/CIE Mech. and Robotics Conference, (Salt Lake City, États-Unis)

Winter DA (2009) Biomechanics and motor control of human movement. Wiley Inters. Publ., 4th Ed., New York, 143p

Zabaleta H, Bureau M, Eizmendi G, Olaiz E, Medina J (2007) Perez M (2007) Exoskeleton design for functional rehabilitation in patients with neurological dis-orders and stroke. Reh. Robotics, IEEE ICORR

Zajac FE (1989a) Determining muscle's force and action in multi-articular movement. Exercise and Sport Siences Reviews 17:187–230

Zajac FE (1989b) Muscle and tendon: properties, models, scaling, and application to biomechanics and motor control. Crit Rev Biomed Eng 17:359–411

Zhu Y, Chen JX, Xiao S (1999) 3D knee modelling and biomechanical simulation. Comput Sci Eng 82–87

Cooling of Circuit Boards Using Natural Convection

Ahmed Guerine, Abdelkhalak El Hami and Tarek Merzouki

Abstract In this paper, we study the air cooling of circuit boards populated with multiple integrated circuits using natural convection. The simulation and the modeling results of the model are obtained by digital software Comsol Multiphysics. The results then accurately describe the heat transport and temperature changes. From such simulations, it is also possible to derive accurate estimations of the film coefficients. The objective is to determine the evolution of the temperature and the flow of the velocity of the fluid. The results show that the temperature of the ICs (the heat sources) increases considerably under a constant heating load from the components. The temperature increase of the sources varies from 30 K for the lowest IC up to 90 K at the top IC. For the velocity of the fluid, the circuit board contributes a large amount of cooling power on its backside, although the thermal conductivity is quite small.

Keywords Circuit boards · Comsol Multiphysics · Natural convection

A. Guerine (✉) · A. E. Hami
Laboratory Optimization and Reliability in Structural Mechanics LOFIMS,
National Institute of Applied Sciences of Rouen, BP 08-76801 Saint Etienne
Du Rouvray Cedex, France
e-mail: ahmedguerine@gmail.com

A. E. Hami
e-mail: abdelkhalak.elhami@insa-rouen.fr

T. Merzouki
LISV, University of Versailles Saint-Quentin, 78140 Vélisy, France
e-mail: tarek.merzouki@uvsq.fr

1 Introduction

This example models the air cooling of circuit boards populated with multiple integrated circuits (ICs), which act as heat sources. Two possible cooling scenarios are shown in Fig. 1: vertically aligned boards using natural convection, and horizontal boards with forced convection (fan cooling). In this case, contributions caused by the induced (forced) flow of air dominates the cooling. To achieve high accuracy, the simulation models heat transport in combination with the fluid flow.

A common technique is to describe convective heat flux with a film-resistance coefficient, h. The heat-transfer equations then become simple to solve. However, this simplification requires that the coefficient is well determined which is difficult for many systems and conditions.

An alternative way to thoroughly describe the convective heat transfer is to model the heat transfer in combination with the fluid flow field. The results then accurately describe the heat transport and temperature changes. From such simulations, it is also possible to derive accurate estimations of the film coefficients. Such models are somewhat more complex but they are useful for unusual geometries and complex flows. The following example models the heat transfer of a circuit board assembly using the Heat Transfer Module's Conjugate Heat Transfer
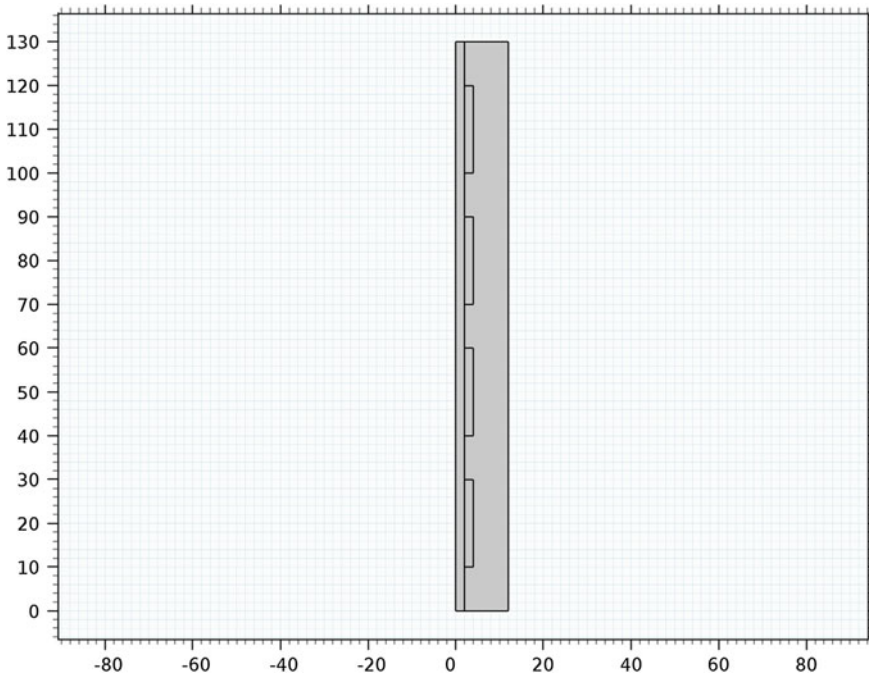
Fig. 1 The modeled geometry in 2D

predefined multiphysics coupling. The modeled scenario is based on work published by Ortega (2002).

FR4 circuit board material (Bailey 2003; Agyenim et al. 2009; Akhilesh et al. 2005) and silicon are used as the solid materials composing the circuit board system. The model treats air properties as temperature dependent.

2 Model Definition

This example models the natural convection. The simplified model considers the 2D cross section, from the board's backside to the next board's backside, through the center of a row of ICs. Figure 1 depicts the 2D geometry.

The model makes use of the Conjugate Heat Transfer predefined multiphysics coupling with a stationary study to set up the simulation. The heating rate per unit volume in the solid is 0.83 MW/m^3. It is 2/3 of the real heat power in order to represent the lateral average heating power (that is, taking into account the open slots between the ICs).

Due to heating of the fluid, deviations occur in the local density, ρ, compared to the inlet density, $\rho 0$. This results in a local buoyancy force defined using the Gravity feature in the Single Phase Flow interface.

3 Boundary Conditions

The top and bottom boundaries are open boundaries with given external air temperature. In addition, no-slip conditions at the surfaces of the board and the ICs are applied. You should also set the lateral boundaries periodic with respect to temperature, making the temperatures equal on both boundaries at every value. Finally, the models apply continuity of temperature and heat flux at all interior boundaries.

4 Results and Discussion

The results (Fig. 2) show that the temperature of the ICs (the heat sources) increases considerably under a constant heating load from the components. Note that the temperature increase of the sources varies from 30 K for the lowest IC up to 90 K at the top IC. This is a result of the thermal "footprint" of the heat sources.

Another interesting result is that the circuit board contributes a large amount of cooling power on its backside, although the thermal conductivity is quite small. This is apparent in the result plots as a temperature rise in the fluid at the right-hand boundary (that is, the backside of the next board in the stack) (Fig. 3).
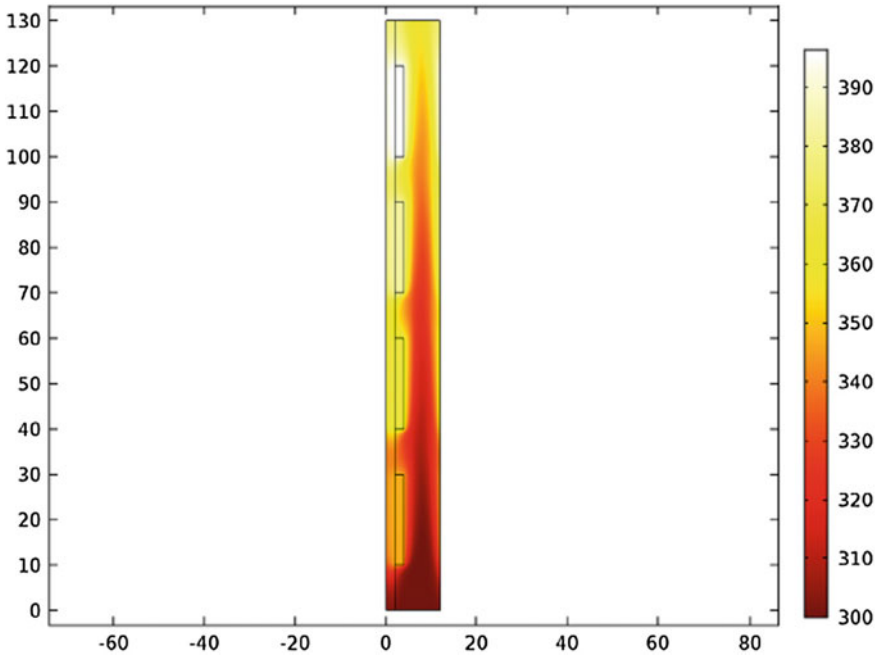
Fig. 2 Temperature distribution
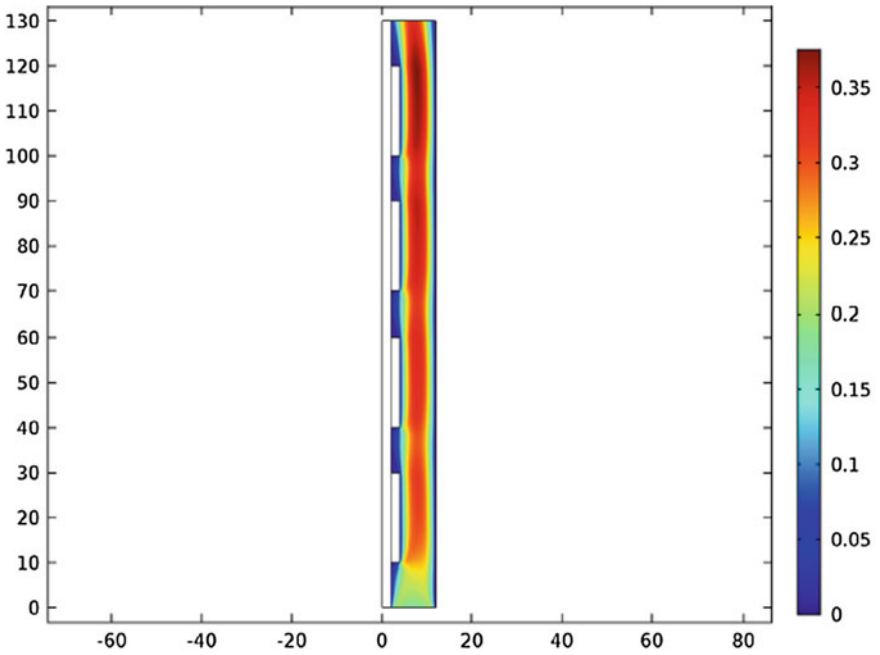
Fig. 3 Velocity magnitude (m/s)

5   Conclusion

In this paper, we have studied the air cooling of circuit boards populated with multiple integrated circuits using natural convection. The simulation and the modeling of the model were done by Comsol Multiphysics. The results show that the temperature of the ICs (the heat sources) increases considerably under a constant heating load from the components.

References

Agyenim F, Eames P, Smyth M (2009) A comparison of heat transfer enhancement in a medium temperature thermal energy storage heat exchanger using fins. Sol Energy 83:1509–1520

Akhilesh R, Narasimhan A, Balaji C (2005) Method to improve geometry for heat transfer enhancement in PCM composite heat sinks. Int J Heat Mass Trans 48:2759–2770

Bailey C (2003) Modeling the effect of temperature on product reliability. Proceedings of 19th IEEE SMITHERM Symposium

Ortega A (2002) Air cooling of electronics: a personal perspective 1981–2001. Presentation material, IEEE SMITHERM Symposium

Effect of Gravity of Carrier on the Dynamic Behavior of Planetary Gears

Ayoub Mbarek, Ahmed Hammami, Alfonso Fernandez Del Rincon, Fakher Chaari, Fernando Viadero Rueda and Mohamed Haddar

Abstract This work investigates the effect of gravity of carrier on the dynamic behavior of back to back planetary gears in a stationary condition. A tridimensional lumped parameter model is developed in order to study this phenomenon. The gravity of carriers has an effect on the distance between gears and it is included in the model through sun-planets and ring-planets mesh stiffness which influence on the dynamic response of gear. Numerical results are correlated with the experimental results obtained from a back-to-back planetary gear test bench, this test bench is composed of two identical planetary gears sets: reaction gear, where the ring is free and test gear where the ring is fixed. They are connected through two rigid shafts. A fix external load was applied through an arm attached to the free reaction ring. Data Acquisition System acquired signals from accelerometers mounted on the carrier and the ring. The signal processing was achieved using LMS Test.Lab software.

A. Mbarek (✉) · A. Hammami · F. Chaari · M. Haddar
Laboratory of Mechanics, Modeling and Production (LA2MP),
National School of Engineers of Sfax, BP1173–3038 Sfax, Tunisia
e-mail: ayoubmbarekenit@gmail.com

A. Hammami
e-mail: ahmed.hammami2109@gmail.com

F. Chaari
e-mail: fakher.chaari@gmail.com

M. Haddar
e-mail: mohamed.haddar@enis.rnu.tn

A. Mbarek · A. F. Del Rincon · F. V. Rueda
Department of Structural and Mechanical Engineering, Faculty of Industrial
and Telecommunications Engineering, University of Cantabria,
Avda de Los Castros S/N, 39005 Santander, Spain
e-mail: alfonso.fernandez@unican.es

F. V. Rueda
e-mail: fernando.viadero@unican.es

1 Introduction

Planetary gears are excellent mechanisms for power transmission seen their high load transmission ability and their compactness. Nevertheless, planetary gears have many drawbacks due to assembling and manufacturing error. Effect of gravity of carriers on planetary gear could be one of these drawbacks, many works have been established in order to study the effect of gravity of carrier. Hammami et al. (2014) used a torsional model to study the effect of the carrier on load sharing and they correlated the numerical results with experimental load-sharing behavior. Guo and Keller (2012) studied the effect of parameters combined gravity, bending input torque and clearance on the load-sharing horizontal wind turbine. They validated their experimental results with tridimensional model planetary gear.

Guo and Parker (2014) studied planetary gear dynamic under gravity; they established that gravity of carrier could be the fundamental source of vibration. Zhai et al. (2016) investigated the effect of carrier assembly error on the dynamic characteristics of wind turbine gearbox. They showed that the effect on the z-axis gearbox on the vibrations of dynamic transmission error response of the system is worse than other axis error cases. Guo and parker (2010) showed that gravity will disrupt the symmetry of the planets and cause tooth wedging under certain conditions.

Qiu et al. (2015) developed a rotational translational-axial lumped parameter model of the spur planetary gear taking into account the effect of gravity; tooth separation, backside contact and bedplate tilt, they concluded that load-sharing characteristics change with these parameters. All these works studied the gravity of carrier on the load-sharing behavior.

Inalpolat and Kahraman (2009) proposed a mathematical model in order to study modulation sidebands leading in planetary gear, the analytical results obtained are correlated with experimental results. Hammami et al. (2016) studied the effect of changing load conditions on the dynamic behavior of planetary gear in a stationary condition and they are neglected the effect of the carrier.

In this work, an investigation of the effect gravity of carrier in dynamic behavior will be presented. The system equation is solved by a direct numerical algorithm based on the Newmark scheme.
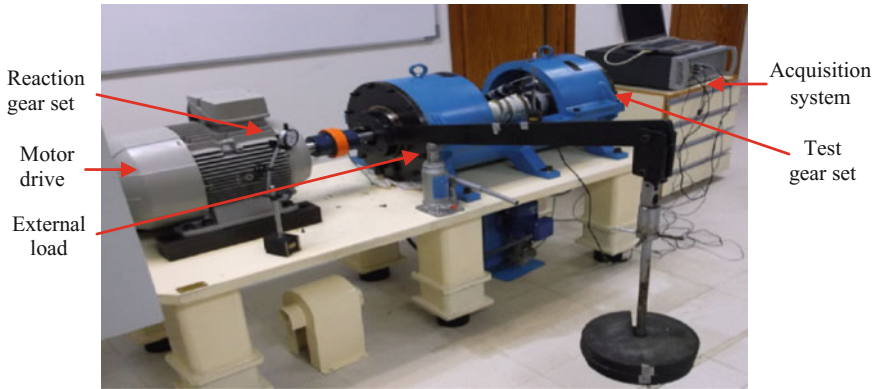
Fig. 1 Experimental test bench

2 Description of the Test Bench

Tests are carried out using test bench developed at the University of Cantabria in Spain and shown in Fig. 1. This test bench composed of two identical planetary gear reaction gear, where the ring is free and test gear where the ring is fixed. The numbers of planets in each stage are three. They are connected through two rigid shafts, inner shaft called sun shaft and external shaft called carrier shaft and motor drive. This test bench is well described in (Hammami et al. 2015, 2014). The external load is obtained by the adding mass on the arm which is fixed on the free ring. Accelerometers are mounted on the reaction and the test ring as well as on the reaction and test carrier.

Data obtained are transferred to the acquisition system 'LMS test lab.'

3 Numerical Model

A numerical model referred to the experimental test bench is presented (Fig. 2). It is a tridimensional model based on that developed of Karray et al. (2016). The model composed with two-stage planetary gear the components of each stage are the carrier (c) the ring (r) the sun (s) and the planets (p1, p2, p3). The planet set are supposed as identical and equally spaced.

These components are modeled as rigid bodies with mass m_{ij}, inertia I_{ij}.each components is supported by bearing with stiffness kb_{ijk}, where i = c, r, s, p1, p2, p3; j = r, t. in direction k = x, y, z, φ, Ψ,θ

For each stage, the ring gear and the sun gear are respectively linked to the three planets via mesh stiffness K_{rpt1}, K_{rpt2}, K_{rpt3} and K_{spt1}, K_{spt2}, K_{spt3} for the test gear and K_{rpr1}, K_{rpr2}, K_{rpr3} and K_{spr1}, K_{spr2}, K_{spr3} for the reaction gear.
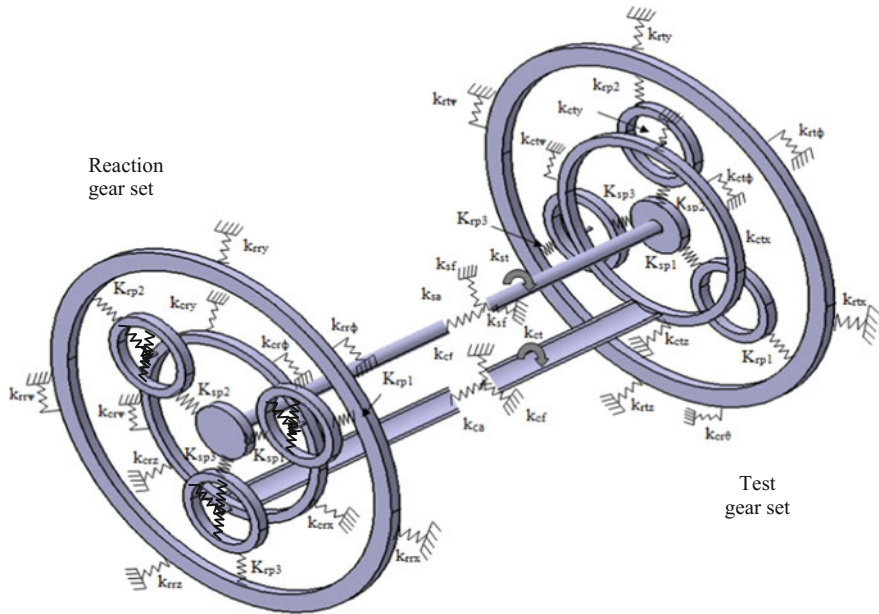
Fig. 2 Numerical model

The two-stage planetary gear sets are connected through sun's shaft and carrier's shaft. Each shaft is characterized, respectively, by axial stiffness k_{sa} k_{ca}; flexural stiffness k_{sf} k_{cf} and torsional stiffness k_{st} k_{ct}.

The equation of motion of this model is:

$$M\ddot{q} + C\dot{q} + (K_b + K_e(t))q = F(t) + T,\qquad(1)$$

where q is the vector degree of freedom, M is the mass matrix, C damping matrix, K_b is the bearing, and shaft stiffness matrix, $K_e(t)$ is the time-varying stiffness matrix, F(t) is the excitation force due to the rotation of the carrier and T is the external force vector applied to the system.

4 Numerical and Experimental Results

The computation of dynamic response in presence of gravity of carrier is done according to Fig. 2. The gravity of carriers introduces a variation on the distances between sun-planets and ring planets during the running of the system. Then, the values of gear mesh stiffness decrease as the distances between gears. Figure 3 shows the evolution of gear mesh stiffness ring-planets during one period of rotation of carrier with effects of gravity of carrier.
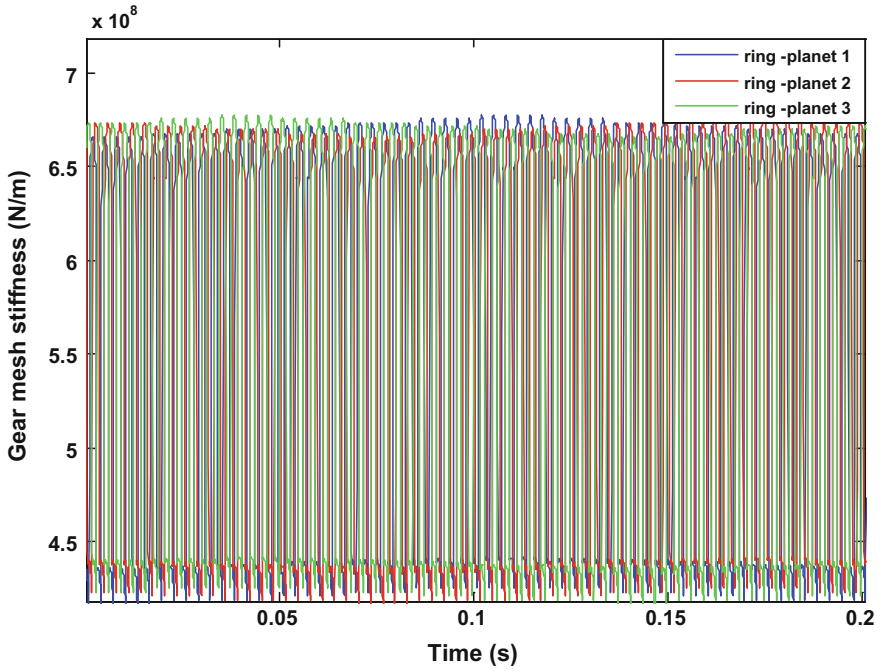
Fig. 3 Ring-planet mesh stiffness
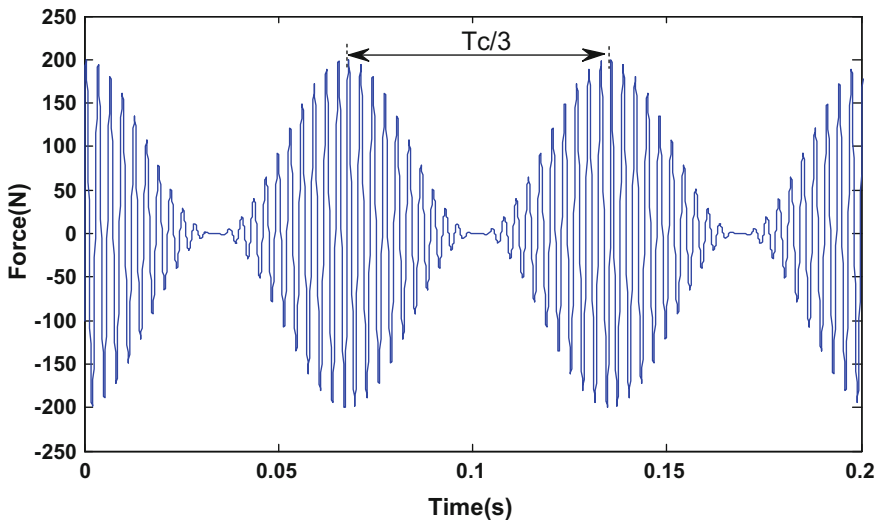
Fig. 4 Force due to rotation of carrier on the test ring in one period of rotation of carrier
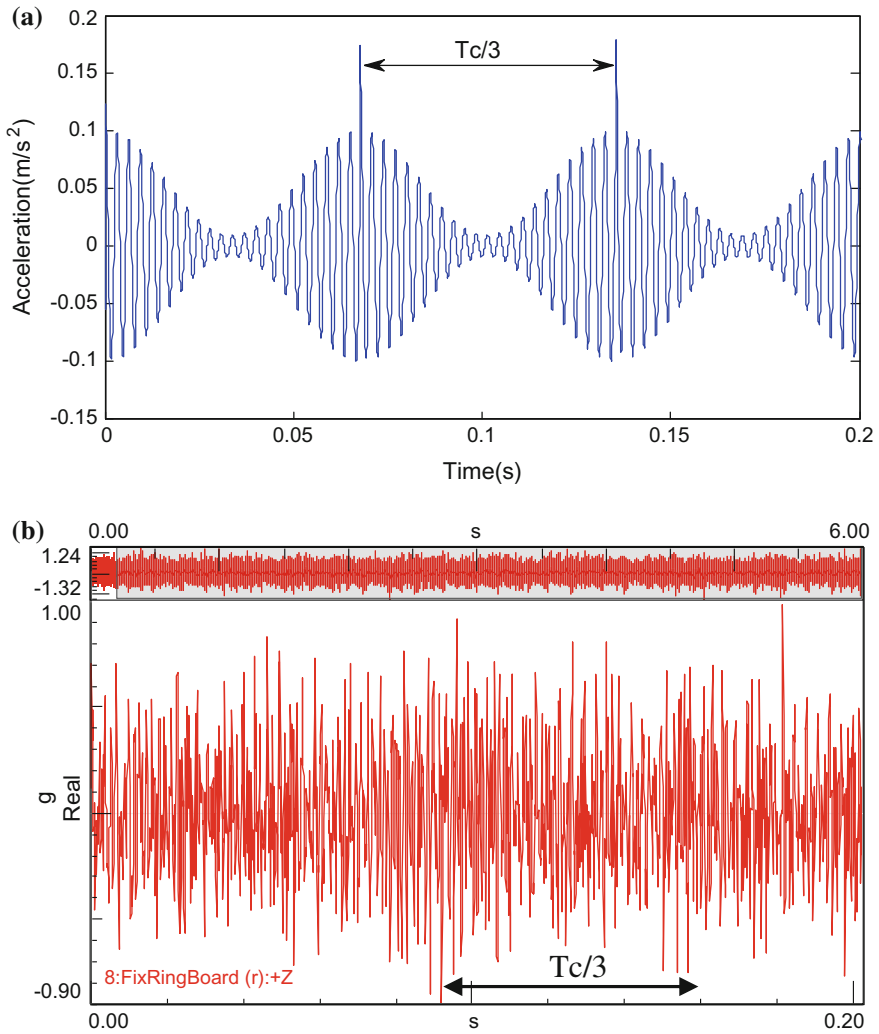
Fig. 5 Time response of the test ring in one rotation of carrier **a** Numerical **b** experimental

Results presented are obtained for the input rotational speed of motor 1498.5 rpm, and an external load 100 Nm. An external force due to the rotation of carrier with period $T_c/3 = 0.2027$ s exited the mechanical system. T_c is the period of rotation of the carrier. This force is explained by the effect of the individual passage of each planet near to the accelerometer. Figure 4 shows the evolution of the exited force on the test ring:

Figure 5 shows acceleration on test ring issued from simulation and experiments during one period of rotation of the carrier.
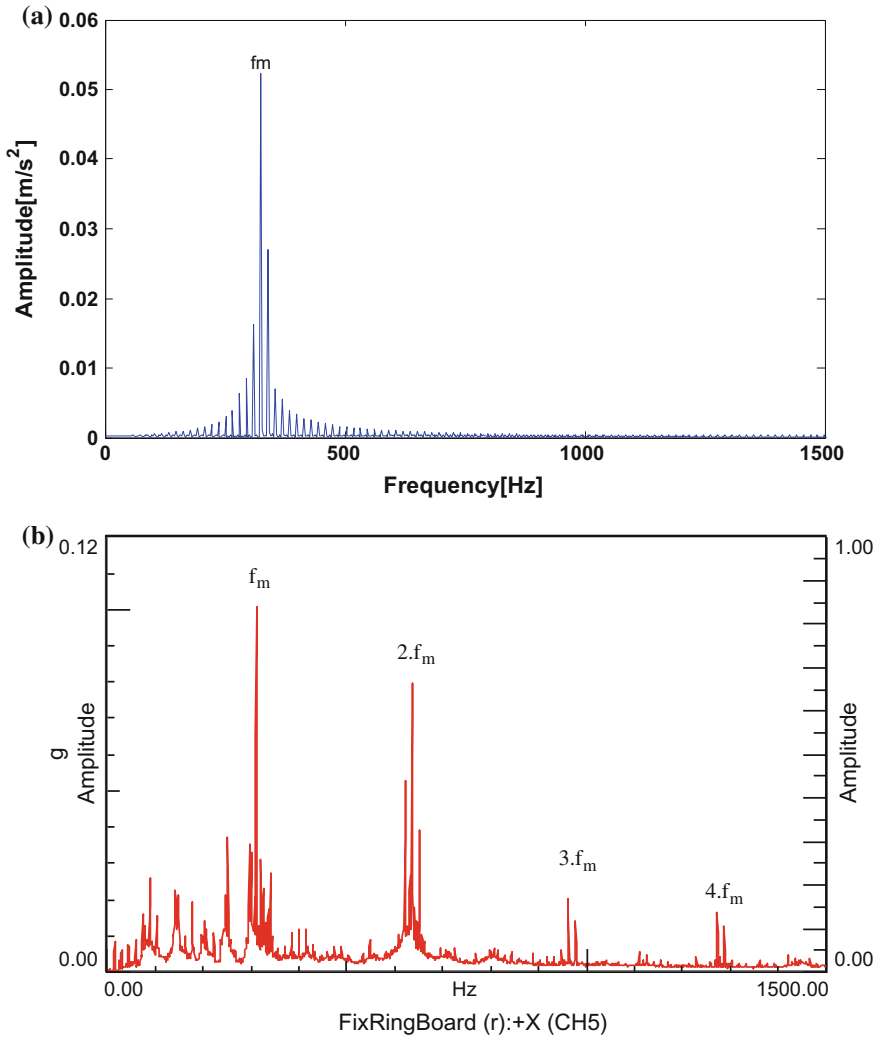
Fig. 6 Spectra of acceleration on the test ring: Numerical (**a**) Experimental (**b**)

The signal extracted on the reaction ring repeats three times, the modulation of amplitude is defined by the force due to rotation of the carrier. Figure 6 shows the spectra of acceleration on the reaction ring measured on the test ring The spectra of dynamic component of the fixed ring is dominated by mesh frequency (320.66 Hz) and its harmonics. Also sidebands appear on these spectra on the 3.n.fc (n: integer) and m.fc (m: integer). Numerical results obtained are correlated with the experimental results.

Figure 7 shows a zoom around the meshing frequency f_m; the influence of the gravity of the carrier on the dynamic behavior of planetary gear is well noticed
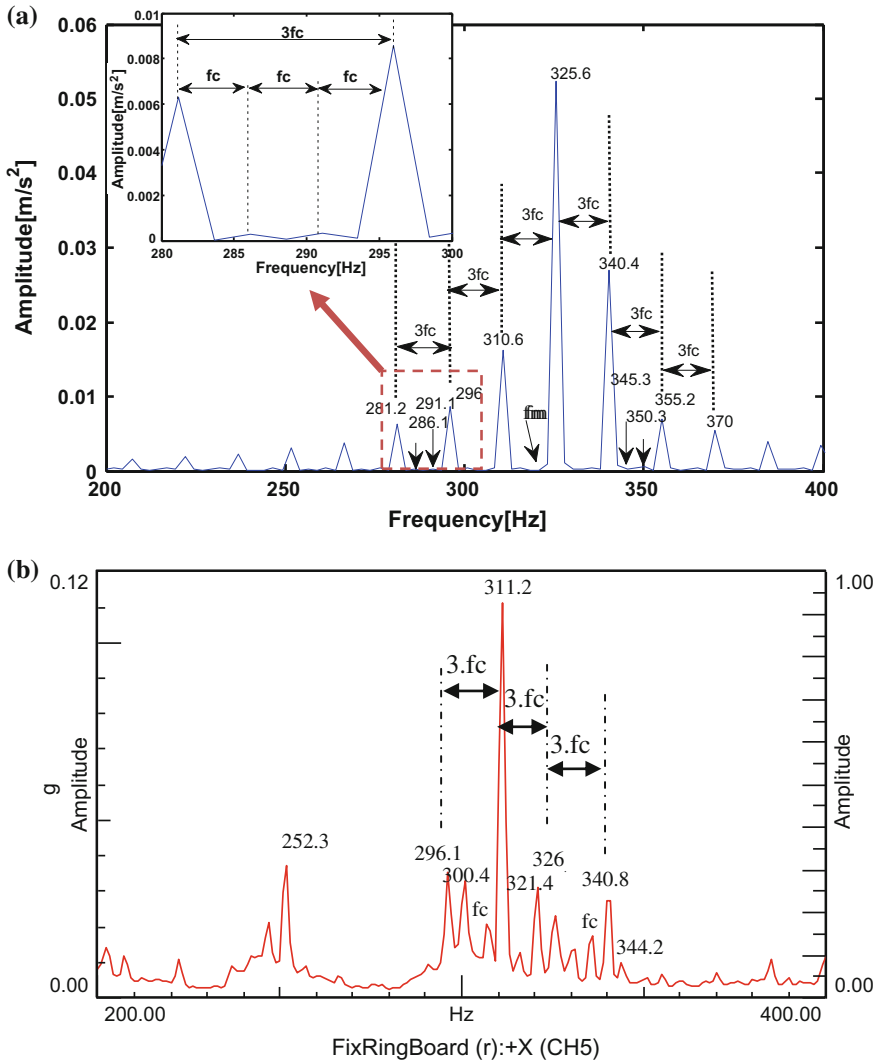
Fig. 7 Response spectrum of the test ring on the first harmonic of the mesh stiffness: Numerical (**a**) and Experimental (**b**)

through the appears of sidebands with frequency fc and corresponding to the effect of gravity of carrier which has the same frequency of rotation, this frequency appears in the response spectrum of the test ring along of the frequency axis. For example, the frequency appears in 281.2, 286.1, 345.3, and 350.3 as mentioned on Fig. 7.

5   Conclusion

This paper, based on the tridimensional model investigates the influence of the gravity of carrier on the dynamic response planetary gear.

The gravity of carriers is included in the model through sun-planets and ring planet mesh during the running of the system which is excited also by dynamic force due to the rotation of the carrier. The influence of the gravity of the carrier on the dynamic behavior planetary gear is well noticed through the apparition of the sidebands with frequency f_c and corresponding to the effect of gravity of carrier which has the same frequency of rotation. This frequency appears along of the frequency axis in both numerical and experimental results.

Future investigation will be focused on the effects of gravity of carrier in non-stationary operations.

References

Guo Y, Parker RG (2010) Dynamic modeling and analysis of a spur planetary gear involving tooth wedging and bearing clearance nonlinearity. Eur J Mechanics-A/Solids 29(6):1022–1033

Guo Y, Keller J, LaCava W (2012). Combined effects of gravity, bending moment, bearing clearance, and input torque on wind turbine planetary gear load sharing. American Gear Manufacturers Association Technical Paper, 12FTM05

Guo Y, Keller J, Parker RG (2014) Nonlinear dynamics and stability of wind turbine planetary gear sets under gravity effects. Eur J Mech-A/Solids 47:45–57

Hammami A, Del Rincon, AF, Chaari F, Santamaria MI, Rueda FV, Haddar M (2014) Springer International Publishing Switzerland 2015 M. Haddar et al (ed.), Multiphysics Modelling and Simulation for Systems Design and Monitoring, Applied Condition Monitoring 2

Hammami A, Del Rincon AF, Rueda FV, Chaari F Haddar M (2015) Modal analysis of back-to-back planetary gear: experiments and correlation against lumped-parameter model. J Theor Appl Mech, 53

Hammami A, Del Rincon AF, Chaari F, Santamaria MI, Rueda FV, Haddar M (2016) Effects of variable loading conditions on the dynamic behaviour of planetary gear with power recirculation. Measurement 94:306–315

Inalpolat M, Kahraman A (2009) A theoretical and experimental investigation of modulation sidebands of planetary gear sets. J Sound Vib 323(3):677–696

Karray M, Feki F, Khabou MT, Chaari F, Haddar M (2016). Modal analysis of gearbox transmission system in Bucket wheel excavator. J Theor Appl Mech pl.55.1

Qiu X, Han Q, Chu F (2015) Load-sharing characteristics of planetary gear transmission in horizontal axis wind turbines. Mech Mach Theor 92:391–406

Zhai H, Zhu C, Song C, Liu H, Bai H (2016) Influences of carrier assembly errors on the dynamic characteristics for wind turbine gearbox. Mech Mach Theor 103:138–147

Prediction of the Position Error of the Uncertain 3-UPU TPM Using Interval Analysis

S. El Hraiech, A. H. Chebbi, Z. Affi and L. Romdhane

Abstract This paper deals with the prediction of the 3-UPU translational parallel manipulator position error caused by the design parameter uncertainties. An algorithm, based on the interval analysis is developed and used to estimate the distribution of the position error within the robot workspace. As a result, we represented the distribution of the position error in different sections of the workspace and we showed that the minimum of the position error is located in the neighborhoods of base center. In general, the minimum position error is reached for higher sections of the workspace. Moreover, the effect of each design parameter uncertainty on the manipulator precision at different sections of the workspace is discussed. At the extreme points of the workspace, the most influent design parameters on the position error are the leg position angles and the radius of the base and the platform uncertainties. The actuator lengths uncertainties are supposed constant and have no effect on the platform position error.

Keywords Prediction · Position error · Krawczyk · Uncertainties

S. El Hraiech (✉) · A. H. Chebbi · Z. Affi
LGM, National Engineering School of Monastir, University of Monastir,
Monastir, Tunisia
e-mail: safa_el_hraiech@hotmail.fr

A. H. Chebbi
e-mail: ahmed.h.chebbi@gmail.com

Z. Affi
e-mail: zouhaier.affi@gmail.com

L. Romdhane
Mechanical Engineering Department, American University of Sharjah,
PO Box 26666, Sharjah, United Arab Emirates
e-mail: lotfi.romdhane@gmail.com

1 Introduction

The 3-UPU is a parallel manipulator that has been the subject of diverse studies as a translational or a rotational robot. The main advantage of this structure is its simplicity. The accuracy of parallel robot is generally altered by the design parameters uncertainties. The parameters uncertainties generate unavoidable accuracy error of parallel robot. In practice, the precision error limit should be known in advance and the designer works on its minimization. This error can be predicted using several methods such as the linearization methods, probabilistic methods, and interval analysis methods. To predict the precision limits, due to the robot design parameters uncertainties, some studies used the probabilistic method (Schade 1981; Lee et al. 1993; Wang et al. 2011) used the probability distribution theory to analyze the effect of design parameters uncertainties on the pose error of the parallel manipulator. A probabilistic approach is developed by Rao and Bhatti Rao and Bhatti (2001) to represent the kinematic and dynamic parameters uncertainties to compute the kinematic and dynamic reliabilities of the manipulator.

To avoid the probabilistic aspect of the robot accuracy, the interval method can be used (Merlet 2009; Pickard et al. 2016). This method uses interval functions and numbers. Each uncertain input parameter is considered as an interval number and also the outputs will be intervals. The study of Wu and Rao (2004) represents an application of interval analysis for modeling tolerances and clearances in linkages. By using this method, it is possible to identify the upper and the lower bounds of the parameters' response (Rao and Berke 1997; Rao et al. 1998) compute all solutions of the inverse kinematics problem of robotic mechanisms using the interval analysis. The major drawback of the interval method is the overestimation of the error bounds due to the wrapping and dependency effect (Jaulin et al. 2001). To avoid this overestimation, recent works have used an interval linearization method called the Krawczyk operator. The results given by this method are more effective as the parameters intervals are small enough (Tannous et al. 2014).

In this work, we propose an algorithm based on the Krawczyk method to predict the position error of the 3UPU in the workspace. The rest of this paper is organized as follows: In Sect. 2, we present the description of the manipulator structure and its kinematic modeling. In Sect. 3, we present the proposed algorithm and the obtained results. Finally, in Sect. 4, some concluding remarks are presented.

2 Architecture of the Manipulator

2.1 Structure of the Manipulator

The 3-UPU translational manipulator is composed of three kinematic chains with extensible legs, connecting the base to the platform (Varedi et al. 2009). Each chain is composed of an universal-prismatic-universal joint. The universal joint is
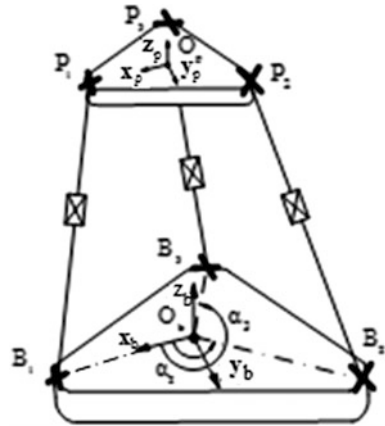
constituted by two revolute joints with concurrent axes. The centers of the universal joint fixed on the moving platform are P_1, P_2, P_3. The centers of the universal joint fixed on the base are B_1, B_2, B_3. The kinematic chains are placed at $2\pi/3$ to each other (Fig. 1).

2.2 Modeling of the 3-UPU Robot

Let r_b and r_p be respectively the radius of the base and the moving platform. B_k and P_k are denoted respectively the centers of the universal joints connected to the base and the platform (k = 1, 2, 3). The position of the platform in the reference system R_b can be expressed by:

$$\mathbf{O_bO_p} = \mathbf{O_bB_k} + \mathbf{B_kP_k} + \mathbf{P_kO_k}, \text{k} = 1, 2, 3 \tag{1}$$

$$\mathbf{x} = \mathbf{b_k} + \mathbf{I_k} - \mathbf{Qp_k} \tag{2}$$

where:

$\mathbf{b_k}$ is the position vector of B_k in R_b, $\mathbf{p_k}$ is the position vector of P_k in R_p, $\mathbf{I_k}$ be the vector defined by the points B_k and P_k

$$\mathbf{x} = \mathbf{O_bO_p} = [\text{x y z}]^T \tag{3}$$

$\mathbf{Q}$ is the rotation matrix that takes $\mathbf{R_p}$ to $\mathbf{R_b}$. Since the 3-UPU manipulator has only translations, the rotation matrix $\mathbf{Q}$ is constant. $\mathbf{Q}$ can be considered as the identity $(\mathbf{Q} = \mathbf{I_3})$

According to Eq. (1), the inverse kinematic model is expressed by:

$$l_k = \sqrt{\left(\left(x - (r_b - r_p).\cos(\alpha_k) \right)^2 + \left(y - (r_b - r_p).\sin(\alpha_k) \right)^2 + z^2 \right)} \qquad (4)$$

where

l_k is the length of the k-th actuator, α_k is the angular position of the k-th leg. The vector of design parameters of the 3-UPU manipulator is given by:

$$\mathbf{p} = [r_b, r_p, \alpha_1, \alpha_2, \alpha_3] \qquad (5)$$

3 The Prediction Error

3.1 The Krawczyk Operator

In this section, an analytical model has been proposed to express the upper and lower bounds of the position error as a function of design parameters and their uncertainty ranges. Interval method is implemented in order to predict the pose error of the manipulator using the Matlab library INTLAB (Rump 1999).

The design parameters nominal values (DPNV) and their uncertainties are defined by an interval vector [$\mathbf{p}$].

$$[\mathbf{p}] = \left[\tilde{r}_{b - \Delta r_{bmin}}^{+ \Delta r_{bmax}}, \tilde{r}_{p - \Delta r_{pmin}}^{+ \Delta r_{pmax}}, \tilde{\alpha}_{1 - \Delta \alpha_{1max}}^{+ \Delta \alpha_{1min}}, \tilde{\alpha}_{2 - \Delta \alpha_{2max}}^{+ \Delta \alpha_{2min}}, \tilde{\alpha}_{3 - \Delta \alpha_{3max}}^{+ \Delta \alpha_{3min}} \right] \qquad (6)$$

where: $\tilde{x}$ is the nominal value of the corresponding design parameter and Δx_{max} and Δx_{min} are the upper and lower uncertainties values.

The Krawczyk method used the quadratic form of Eq. (7)

$$l_k^2 - \left(\left(x - (r_b - r_p).\cos(\alpha_k) \right)^2 + \left(y - (r_b - r_p).\sin(\alpha_k) \right)^2 + z^2 \right) = 0 \qquad (7)$$

The system of equations given above takes the form of $f(\mathbf{p}, \mathbf{x}) = 0$. Let $(\tilde{\mathbf{x}}, \tilde{\mathbf{p}}) = 0$ be the solution of this equation corresponding to the design parameters nominal values. Thus, by using the concept of the Krawczyk operator, the prediction of the position error of the manipulator is obtained. This solution takes the form of an interval vector $[\mathbf{x}]$.

The solution of $f(\mathbf{p}, \mathbf{x}) = 0$ can be computed by the Krawczyk. For this goal, the Krawczyk operator can be written as follows:

$$\mathbf{K}_{\mathbf{f}, [\mathbf{p}]}([\mathbf{x}]) = \tilde{\mathbf{x}} - (\mathbf{C}.[\mathbf{X}] - \mathbf{I}).([\mathbf{x}] - \tilde{\mathbf{x}}) - [\mathbf{Y}] \tag{8}$$

where:

$$[\mathbf{X}] = [\mathbf{f}_v](\mathbf{p}, \mathbf{x}) \tag{9}$$

$$[\mathbf{Y}] = \mathbf{C}.[\mathbf{f}](\tilde{\mathbf{p}}, \tilde{\mathbf{x}}) + \mathbf{C}.[\mathbf{A}].([\mathbf{p}] - \tilde{\mathbf{p}}) \tag{10}$$

$$[\mathbf{A}] = [\mathbf{f}_p](\mathbf{p}, \tilde{\mathbf{x}}) \tag{11}$$

$$\mathbf{C} = \mathrm{mid}([\mathbf{X}])^{-1} \tag{12}$$

where $\mathbf{C}$ is a preconditioning nonsingular matrix (Tannous et al. 2014)

3.2 The Proposed Algorithm

The 3-UPU error prediction algorithm is developed in Fig. 2. The position error is calculated at each point of the workspace. This error can be expressed by:

$$\Delta E_p = \mathrm{Max}\left(\left|\mathbf{x}_{k, j\,\mathrm{max}} - \tilde{\mathbf{x}}_{i, j}\right|, \left|\mathbf{x}_{k, j\,\mathrm{min}} - \tilde{\mathbf{x}}_{k, j}\right|\right) \tag{13}$$

where: $\tilde{\mathbf{x}}_{k, j}$ correspond to the nominal value of the position of the platform along x, y, and z axis respectively. $\mathbf{x}_{k, j\mathrm{max}}$ and $\mathbf{x}_{k, j\mathrm{min}}$ correspond to the maximum and the minimum value of the first, second and the third line of the interval vector [x] obtained by the interval analysis method.

3.3 Distribution of the Position Error in the Workspace

For the following case study, the numerical DPNV of the 3-UPU robot are shown in Table 1.

The uncertainties of the parameters are approximated to 0.1% of their nominal values of parameters. This uncertainty regroups all sources of imperfections.

In this section, the desired workspace of the actuator is defined by:

$$-150 \leq x, y(\mathrm{mm}) \leq 150 \text{ and } 100 \leq z(\mathrm{mm}) \leq 400 \tag{14}$$

Using the proposed algorithm in Fig. 2 and with considering fixed lengths uncertainties $(\Delta l_{k\mathrm{max}} = \Delta l_{k\mathrm{min}} = 0.01 \text{ mm}, k = 1, 2, 3)$, we represent the distribution of the position error over different sections of the workspace (Fig. 3).

Fig. 2 The 3-UPU error prediction algorithm
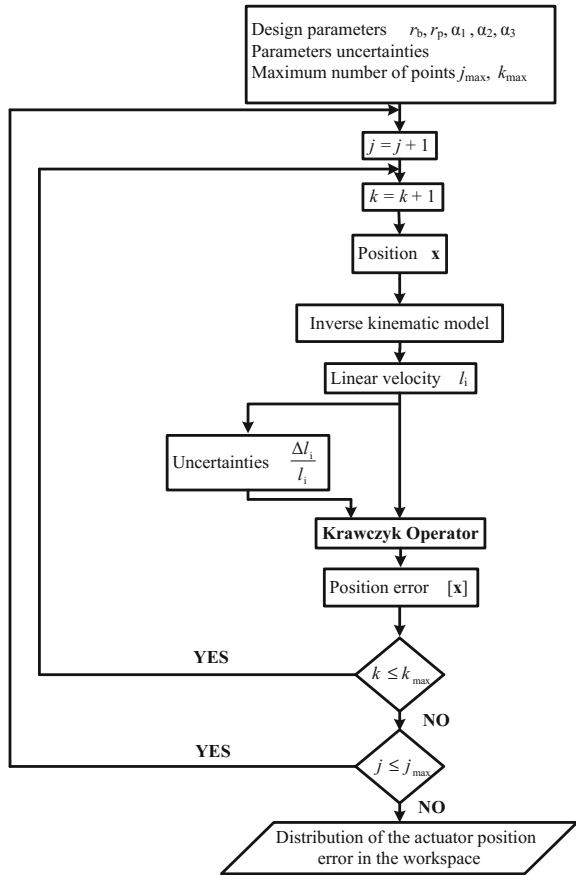
Table 1 The manipulator design parameters nominal values

Parameters	Value
r_b	300 mm
r_p	50 mm
α_1	0°
α_2	120°
α_3	240°

Figure 3 shows that, in different sections, the minimum of the position error is obtained when the position of O_p is at the neighborhood of the center of the workspace (x = 0, y = 0). The maximum error values are located at the extreme zones. One can note that, with the same nominal values and uncertainties, the magnitude of the position error decreases when the platform moves away from the (O, z_b) axis. Moreover, in general, the minimum of position errors are reached for higher section of the workspace.
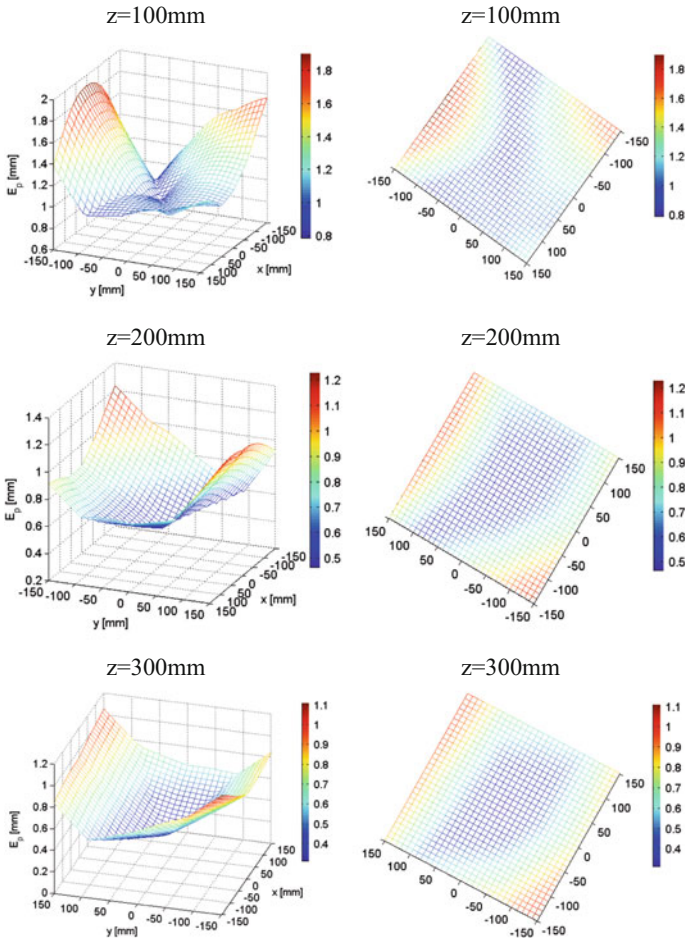
Fig. 3 Distribution of the position error

For a given section of the workspace (z = 100 mm), the effect of each design parameter on the position error can vary as a function of the platform nominal position. As long as we move away from the center of the workspace (x = 0, y = 0), the platform position becomes more sensitive to the leg position angles uncertainties and less sensitive to the radius of the base and the platform uncertainties. The effect of the actuator lengths uncertainties still limited (Fig. 4)

In what follows, the effect of each design parameter uncertainty on the manipulator precision at different sections of the workspace where x = 0 and y = 0 will be discussed. Table 2 presents the quantification of the effect of each design parameter uncertainty. The robot position error depends highly on the radius of the base and the platform uncertainties (more than 95%). The effect of the legs positions angles uncertainties does not exceed 2.6% at this region of the workspace.

(a) $\Delta\alpha_{1+}\Delta\alpha_{2+}\Delta\alpha_3$

(b) $\Delta r_{b+}\Delta r_p$
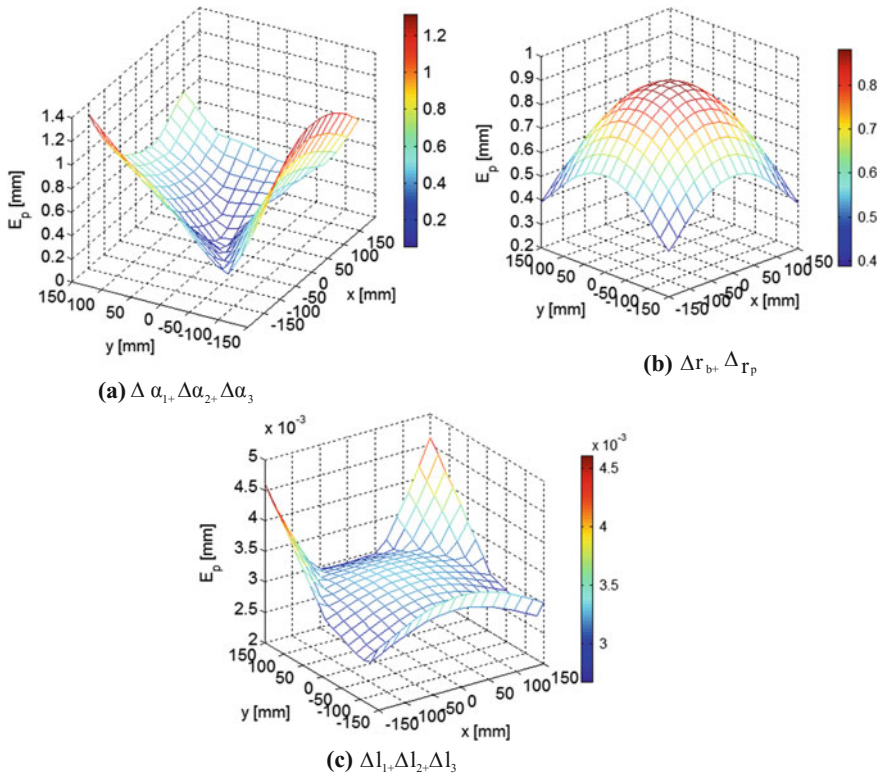
(c) $\Delta l_{1+}\Delta l_{2+}\Delta l_3$

Fig. 4 Contribution of the parameters uncertainties in the workspace

Table 2 The contribution of design parameters uncertainties in the position error

Section	Contribution of $\Delta r_b + \Delta r_p$	Contribution of $\Delta\alpha_1 + \Delta\alpha_2 + \Delta\alpha_3$	Contribution of $\Delta l_1 + \Delta l_2 + \Delta l_3$
z = 100 mm	98.3%	1.3%	0.4%
z = 200 mm	97.4%	1.9%	0.7%
z = 300 mm	96.4%	2.6%	1%

Moreover, this effect is proportional to the workspace section altitude. The influence of the actuator lengths uncertainties can be neglected (less than 2%).

Table 3 shows that, at the extreme points of the workspace (x = 150, y = −150 mm), the critical design parameters that can influence the magnitude of the position error are the leg position angles and the radius of the base and the platform uncertainties. The lengths uncertainties have no effect.

Table 3 The contribution of design parameters uncertainties in the position error

Section	Contribution of $\Delta r_b + \Delta r_p$	Contribution of $\Delta\alpha_1 + \Delta\alpha_2 + \Delta\alpha_3$	Contribution of $\Delta l_1 + \Delta l_2 + \Delta l_3$
z = 100 mm	22.8%	76.9%	0.3%
z = 200 mm	27.2%	72.5%	0.3%
z = 300 mm	28.9%	70.7%	0.4%

4 Conclusion

This work deals with the prediction of the 3-UPU translational robot position error caused by the design parameters uncertainties. An algorithm, based on the Krawczyk method is developed and used to predict the distribution of the position error within the robot workspace. We have shown that the minimum of position errors are located at the neighborhood of base center. Moreover, the minimum position error is reached for higher sections of the workspace.

References

Jaulin L et al (2001) Applied interval analysis with examples in parameter and state estimation robust control and robotics. Springer, ISBN 978-1-4471-1067-5

Lee SJ, Gilmore BJ, Ogot MM (1993) Dimensional tolerance allocation of dynamic mechanical systems through performance an and sensitivity analysis. ASME J Mech Des 115:392–402

Merlet J-P (2009) Interval analysis for certified numerical solution of problems in robotics. Int J Appl Math Comput Sci 19:399–412

Pickard J, Carretero JA, Merlet J-P (2016) Accounting for tolerances in the design parameters of the 3-RRR: advances in robot kinematics. Grasse, France

Rao SS, Bhatti PK (2001) Probabilistic approach to manipulator kinematics and dynamics. Reliab Eng system safety 72:47–58

Rao SS, Berke L (1997) Analysis of uncertain structural systems using interval analysis. AIAA J 35:727–735

Rao RS, Asaithambi A, Agrawal SK (1998) Inverse kinematic solution of robot manipulators ing interval analysis. ASME J Mech Des 120:147–150

Rump S (1999) INTLAB INTerval Laboratory, In: Cendes T (Ed.) Developments in reliable computing, Kluwer Academic Publishers, Dordrecht, pp. 77–104, Available via WIT eLibrary (http://www.ti3.tu-harburg.de/rump/)

Schade GR (1981) Probabilistic models in computer automated slider-crank function generator design". ASME J Mech Des 103:835–841

Tannous M, Caro S, Goldsztejn A (2014) Sensitivity analysis of parallel manipulators using an interval linearization method. Mech Mach Theory 71:93–114

Varedi SM, Daniali HM, Ganji DD (2009) Kinematics of an offset 3-UPU translational parallel manipulator by the homotopy continuation method. Nonlin Anal Real World Appl 10:1767–1774

Wang N et al (2011) Error sensibility analysis of 3-UPU parallel manipulator based on probability distribution. Mech Autom Control Eng 15–17 July, Hohhot, China

Wu W, Rao SS (2004) Interval approach for the modeling of tolerances and clearances in mechanism analysis. ASME J Mech Des 126:581–592

Influence of Stress Concentration Factor on the Evolution of the Strain Energy Release Rate at High Temperature in Highly Ductile Carbon Fibers Reinforced Thermoplastic Structures

M. Chabchoub, B. Vieille, C. Gautrelet, M. Beyaoui, M. Taktak, M. Haddar and L. Taleb

Abstract This work was aimed at investigating the influence of stress concentration factor on the evolution of the strain energy release rate J in 5-harness satin weave carbon fabrics reinforced Polyphenylene sulphide (PPS) structures at 120 °C (higher than the transition temperature T_g). The studied angle-ply (AP) laminates are characterized by a highly ductile behavior. For this purpose, the load separation method, as well as the compliance method, are applied in order to determine the strain energy release rate J for different crack length over specimen width ratios a/W. A fractographic analysis was conducted to understand the chronology of damage mechanisms which significantly depends on the enhanced PPS matrix ductility and toughness at $T > Tg$. An acoustic emission (AE) technique was used to investigate the correlation between the energy released during translaminar cracking and the cumulative AE energy/events for different stress concentration factors. Fibers breakage appears to be not very energetic from the AE standpoint. Finally, blunting is instrumental in increasing the strain energy release rate in specimens with low-stress concentration factors, due to large plastic deformations at the crack tip.

M. Chabchoub (✉) · B. Vieille · L. Taleb
Groupe de Physique des Matériaux UMR 6634 CNRS, Department of Mechanical
Engineering, National Institute of Applied Sciences of Rouen, 76801
St Etienne du Rouvray, France
e-mail: Manel.Chabchoub@insa-rouen.fr

M. Chabchoub · M. Beyaoui · M. Taktak · M. Haddar
Laboratory of Mechanics, Modelling and Production, Department of Mechanical
Engineering, National School of Engineers of Sfax, Route Soukra, 3038 Sfax, Tunisia

C. Gautrelet
Laboratoire de Mécanique de Normandie (LMN),
Department of Mechanical Engineering, National Institute
of Applied Sciences of Rouen, 76801 St Etienne du Rouvray, France

1 Introduction

In recent years, researchers have become greatly interested in using
thermoplastic-based (TP) composites for aeronautical applications as they are
characterized by important mechanical properties and processing advantages. When
it comes to investigating the fracture behavior and damage tolerance of
high-performance TP composites, the fracture toughness is an important parameter
because it represents the ability of the material to resist to fracture. The fracture
toughness and the strain energy release rate highly depend on matrix nature
especially at high temperature (Vieille et al. 2013a, b; Vieille and Albouy 2015;
Cowley and Beaumont 1997) as well as the reinforcement architecture. Indeed, the
fracture toughness is more significant in woven-ply laminates than the UD-ply
laminates (often more than 4–5 times) (Karaoglan et al. 1997; Bibo and Hogg
1996).

1.1 Evaluation of Strain Energy Release Rate in Ductile Composite Materials

In ductile materials, the fracture toughness is often studied using the J-resistance
curve from the J-integral as plastic deformations dominate the crack tip. The
J-integral can be expressed using its energy rate interpretation (Rice 1968):

$$J = -\frac{1}{B}\frac{dU_p}{da} \tag{1}$$

where U_p is the potential energy for the cracked body, B denotes the specimen
thickness and a is the crack length.

Researchers have proposed many experimental techniques to determine
J-integral. The multispecimen technique was the earliest one. First introduced by
Begley and Landes (1972) and based on the energy rate interpretation form, the
multispecimen technique requires multiple specimens to generate the energy versus
crack length record (Sharobeam and Landes 1991). Sumpter and Turner (1976)
have expressed the strain energy released J as a function of two constants η_{el} and η_{pl}
by separating J into elastic and plastic parts:

$$J = J_{elastic} + J_{plastic} = \eta_{el}.\frac{A_{el}}{B.b} + \eta_{pl}.\frac{A_{pl}}{B.b} \tag{2}$$

where A_{el} and A_{pl} are the elastic and plastic parts of the area under the load-displacement record respectively. b is the length of the uncracked ligament. η-factors depend on the crack length over specimen width ratio a/W, loading conditions, and specimen geometry.

It is not a question here to give a comprehensive review of the methods commonly used to determine η-factors, but it is relevant to briefly present the load separation method which can be considered as one of the most important methods used for determining η_{pl}-factor from a single load-displacement record for each crack length. Initially proposed by Ernst et al. (1979) and adapted by Sharobeam and Landes (1993) in the case of ductile materials, this method assumes that the applied load F can be expressed as a product of two independent functions: a geometry-dependent function $G\left(\frac{a}{W}\right)$ and a deformation-dependent function $H\left(\frac{\Delta_{pl}}{W}\right)$. Therefore, it is possible to write:

$$F = G\left(\frac{a}{W}\right).H\left(\frac{\Delta_{pl}}{W}\right) \tag{3}$$

Sharobeam and Landes introduced the separation parameter which can be expressed as follow (Sharobeam and Landes 1993):

$$S_{ij} = \frac{F(a_i)}{F(a_j)}\Big|_{\Delta_{pl}} = \frac{G\left(\frac{a_i}{W}\right).H\left(\frac{\Delta_{pl}}{W}\right)}{G\left(\frac{a_j}{W}\right).H\left(\frac{\Delta_{pl}}{W}\right)} = \frac{G\left(\frac{a_i}{W}\right)}{G\left(\frac{a_j}{W}\right)} \tag{4}$$

where $F(a_i)$ represents the applied load to a tested specimen (i) with a crack length a_i and $F(a_j)$ represents the applied load to a reference specimen (j) with a crack length a_j. Finally, according to Sharobeam and Landes, it is possible to assume that for a given material in the separable region, the separation parameter S_{ij} is given by a power law as follow (Sharobeam and Landes 1991):

$$S_{ij} = A\left(\frac{b_i}{W}\right)^m \quad \text{with } m = \eta_{pl} \tag{5}$$

For more details about the load separation method, one can refer to Sharobeam and Landes (1991), Cassanelli et al. (2003), Wainstein (2003), Wainstein (2004).

1.2 Correlation Between AE Energy and Strain Energy Release Rate

To characterize damage mechanisms and investigate their evolution in FRPs, many in situ and nondestructive evaluation techniques have been implemented. Acoustic Emission (AE) techniques are often used to detect the onset and growth of microscopic failure in composite materials (Albouy and Vieille 2014; Dickinson and Fletcher 2009). Sause et al. have recently shown that the quantification of matrix cracking, interfacial failure and fiber breakage in UD-ply orthotropic carbon/epoxy laminates can be evaluated by interpretation of the obtained distributions of acoustic emission signals types in terms of fracture mechanics (Sause et al. 2012). Considering the idea initially proposed by Ndiaye et al. (2000), the cumulative acoustic energy W_{AE} of an AE-signal can be associated with the critical strain energy release rate G_{Ic} in the case of stable mode I crack growth as follows (Sause et al. 2009):

$$W_{AE} = \beta(c_L^2).G_{Ic}.\Delta A \qquad (6)$$

where the proportionality constant $\beta(c_L^2)$ is a linear function of the cracked materials squared longitudinal sound velocity c_L^2, and ΔA represents the crack surface area. In other words, it means that the release of acoustic emission energy in FRPs is expected to be proportional to the mechanical energy release when damage grows within the materials.

2 Materials and Experimental Setup

2.1 Materials

The studied composite materials are carbon fabric reinforced laminates consisting of a semicrystalline high-performance PPS supplied by the Ticona company (Vieille and Albouy 2015; Vieille and Aucher 2011; Vieille et al. 2013a, b, 2014; Albouy and Vieille 2014). The woven-ply prepreg, supplied by SOFICAR, consists of 5-harness satin weave carbon fiber fabrics (T300 3 K 5HS) whose volume fraction is 50%. The prepreg plates are hot pressed according to angle-ply stacking sequences [(±45)]₇. The glass transition temperature of the C/PPS laminates studied in the present work is about 107 °C.
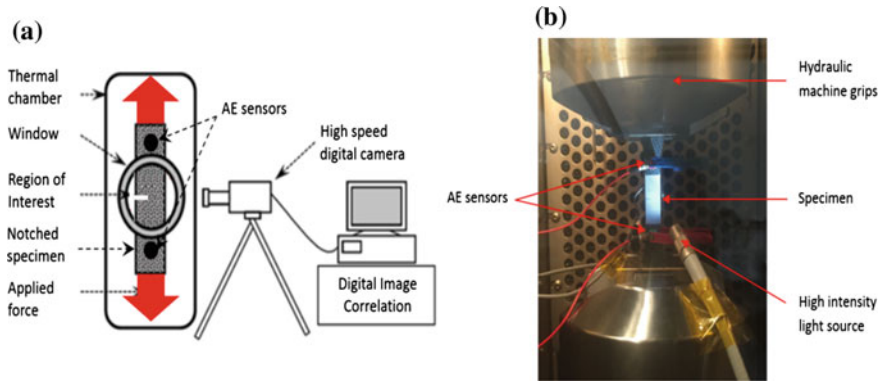
Fig. 1 **a** Schematic representation of the DIC technique **b** Experimental setup

2.2 Methods and Experimental Set-up

2.2.1 Mechanical Testing

Single-Edge Notch (SEN) specimens were subjected to monotonic tensile loadings at 120 °C (see Fig. 1b), by means of a MTS 810 servo-hydraulic testing machine equipped with a 100 kN capacity load cell (Vieille and Albouy 2015; Vieille and Aucher 2011; Vieille et al. 2013a, b, 2014; Albouy and Vieille 2014). SEN specimens have a given ratio a/w representing the ratio of the initial crack length over the specimen width. In addition, damage mechanisms have been discussed by means of fractographic analyses.

2.2.2 Acoustic Emission

The acoustic emission activity was monitored during monotonic tensile tests. The AE signals were detected using two sensors of PAC micro80 type in linear arrangement (see Fig. 1b) and a PCI-2 data acquisition card. All signals were amplified by 20 dB using a 2/4/6 preamplifier and recorded with 45 dB threshold and 30/100/300 ls settings for Peak-Definition-Time/Hit-Definition-Time/Hit-Lockout-Time using the software AEwin with 10 MHz sampling rate. For all configurations, a band pass filter from 20 kHz to 1 MHz was used.

2.2.3 Full-Field Measurements

Among the different methods available to localize or identify the damage induced by mechanical loading in high gradient structures, a two-dimensional Digital Image Correlation (DIC) technique can be used to measure full-field strains (VIC-2D

correlation software). A high-speed monochromic camera Phantom Miro M310 records digital images during thermomechanical loading. The size of the CMOS sensor is 25.6 by 16 mm and is constituted by one million of 20 μm pixels. To avoid backlights on the window (see Fig. 1a) which might be detrimental to the accuracy of calculated strain fields, a high-intensity source combined with a fiber optic light guide is directly placed into the thermal chamber (see Fig. 1b).

3 Results and Discussion

3.1 Macroscopic Tensile Response of AP SEN Specimens

The tested notched laminates are characterized by a highly ductile behavior at 120 °C as the thermomechanical response of AP laminates is mainly dominated by the matrix behavior (see Fig. 2a).

Woven-ply laminates have a periodic distribution of matrix-rich areas in their microstructure resulting from the undulation at the crimp between warp and weft fibers. These matrix-rich areas are instrumental in dissipating the mechanical energy brought to the specimen into local plastic deformations. The observation of fracture surface suggests that, after initiation, cracks will propagate along 45° oriented fibers. In fact, the tensile loading at 45° with respect to the fiber direction induces an in-plane shear effect in the weft and warp direction at the crack tip. In particular, this effect is intensified at the crimp. As the weft fibers undulate over the warp fiber bundles, weft fibers are overstressed and fail first. Therefore, the notch will propagate along the warp direction which requires the least energy.

As PPS matrix ductility increases at high temperature, leading to local plasticization, the ability of the matrix to transmit the load to fibers impaired at high temperature, hence these fibers tend to rotate and stress concentration zones appear
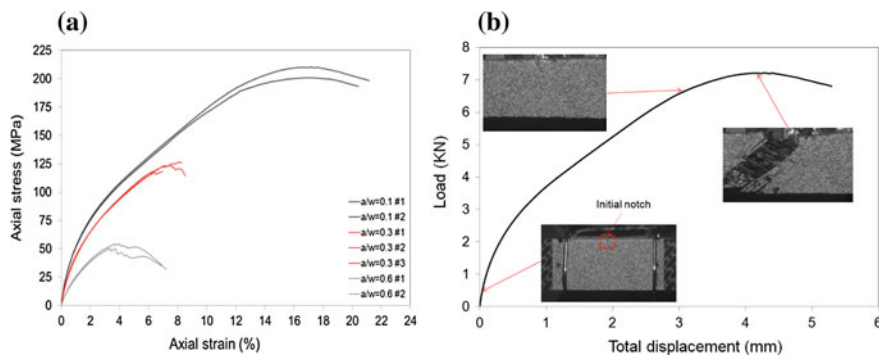
Fig. 2 Mechanical tensile response of SEN AP C/PPS specimens at 120 °C: **a** influence of the ratio a/W—**b** blunting of the notch for low-stress concentration factors (a/W = 0.1)

(a) Edge effects: fiber-matrix debonding leading to pull-out of fibers bundles
+ Delamination along the edges

Front view

(b)   Extensive delamination and pull-out of fiber bundles
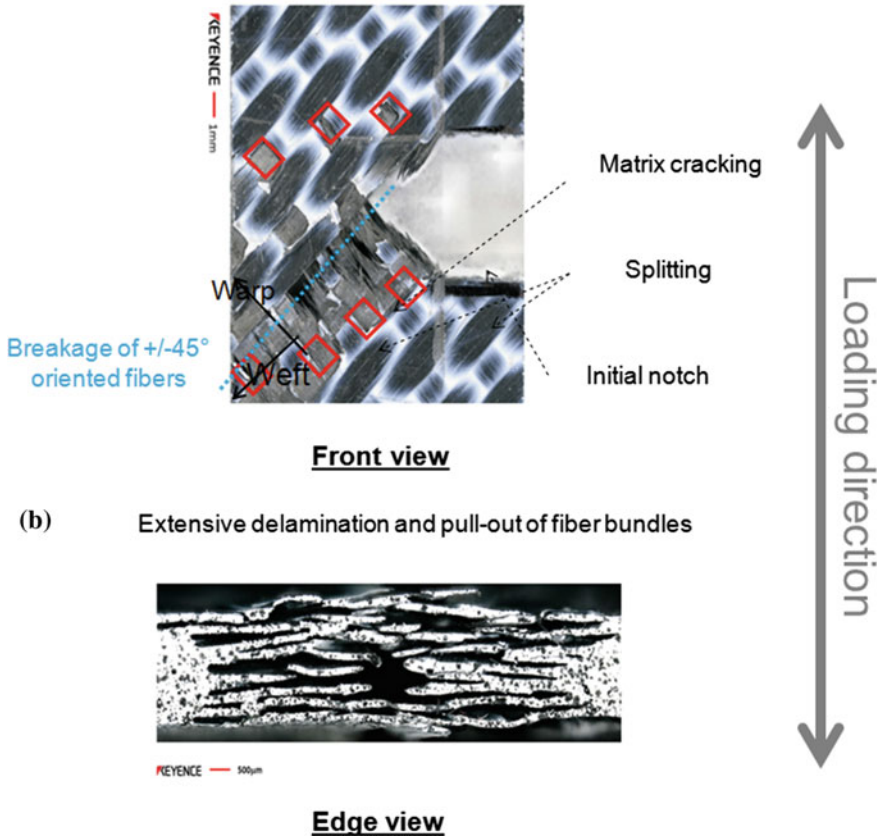
Edge view

Fig. 3 Observations of fracture surface in SEN AP C/PPS specimens subjected to tensile loadings at 120 °C: **a** Front view—**b** Edge view

at the crimp. In C/PPS laminates, when matrix can no longer plastically deforms, matrix cracking and splitting take place along the 45° fiber direction as well as an extensive delamination and pull out of fibers bundles resulting from fiber-matrix debonding along the edges (see Fig. 3). More specifically, the blunting (significant opening of the crack due to large plastic deformation at the crack tip) of the crack (see Fig. 2b) observed in the case of low concentration factors (e.g., a/W = 0.1) primarily results from the highly ductile behavior of the PPS matrix at T > Tg. Such mechanism is instrumental in dissipating a significant portion of the mechanical energy brought to the notched specimen without fiber breakage.

From the macroscopic standpoint, the large plastic deformations lead to a significant dissipation of mechanical energy in specimens with small initial notches (e.g., a/W = 0.1 see Fig. 2). This result can be explained by the increase of the crack length coming along with large fiber rotations as applied stress increases. Thus, the neighboring fibers cannot support the tensile loading once cracks propagate. However, as the ratio a/W increases, the cracks propagate more gradually without significant fiber rotation. In other words, contrary to specimens with larger initial notches, specimens with small crack length are able to store sufficient strain energy during mechanical loading to cause catastrophic failure (Agarwal et al. 1983).

For structural design, AE techniques provide much information (cumulative energy, cumulative counts, events rate) to account for the degree of damage during service at microscopic scale. Figures 4 and 5 show the evolution of the cumulative AE energy and events according to the applied stress. The cumulative AE energy reaches an asymptotic value as the stress concentration factor (depending on the initial ratio a/W) increases. At the same time, the cumulative AE events gradually increase as stress concentration factor decreases. As expected, these results suggest that, in specimens with larger uncracked ligaments (b = W(1−a/W) is higher when a/W is lower), there is more damage to occur (hence cumulative events). Indeed, in the case of low-stress concentration factors, the growth of the translaminar crack requires more mechanical energy (hence, the stress borne by the specimen is higher), because there are basically more fibers to be broken and more matrix to be cracked. However, the cumulative AE energy being virtually the same at failure, it indicates that fiber breakage is not very energetic from the AE activity standpoint. It is still necessary to observe the evolution of the energy released during translaminar cracking (evaluated via the strain energy release rate) and the cumulative AE energy to investigate the influence of PPS matrix ductility and toughness on damage mechanisms.

Fig. 4 Comparison of the cumulative AE energy evolution depending on the initial crack length over specimen width ratio a/W
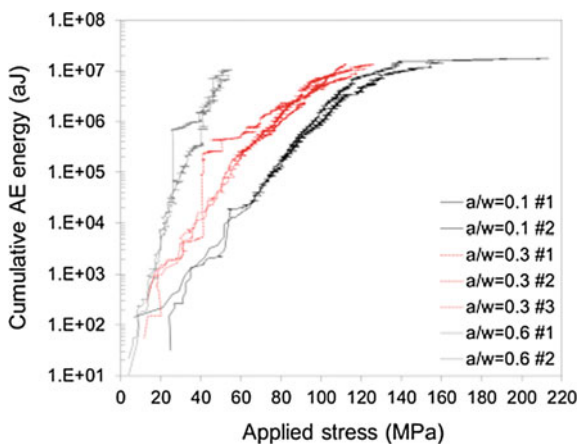
Fig. 5 Comparison of the cumulative events depending on the initial crack length over specimen width ratio a/W
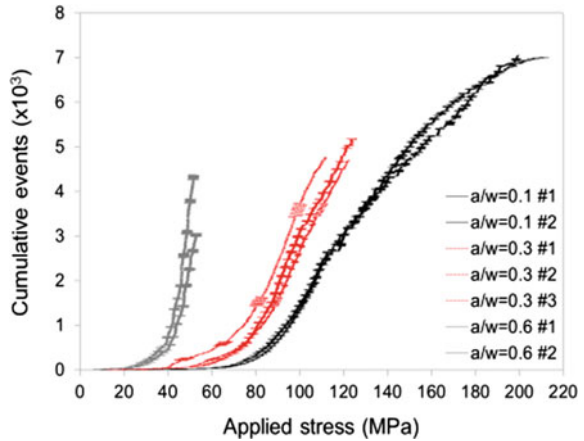
In order to determine the strain energy release rate J and investigate the correlation between J and the cumulative AE energy, the load separation method, as well as the compliance method, was used to determine η_{pl} and η_{el} respectively. The results obtained were $\eta_{pl} = 0.8037$ and $\eta_{el} = 0.8674$. Figure 6 shows the evolution of the strain energy release rate according to the cumulative AE energy for different initial crack length over specimen width. A decrease in the energy release rate can be observed as the initial crack length increases (see Fig. 6). For specimen with small initial notches (e.g., a/W = 0.1), the energy released when cracking significantly increases at the last phase of damage. Indeed, at the beginning of the mechanical loading, a notch tip blunting and opening occur accompanied with a large plastic deformation and important microscopic damage mechanisms. Once the crack propagates, the material releases all the mechanical energy brought to the specimen during tensile loading (see Fig. 2b).

Figure 7 represents the J-R curves for a/W = 0.3 and 0.6. For smaller ratios (a/W = 0.1), the DIC technique could not be applied to evaluate the crack growth

Fig. 6 Evolution of the strain energy release rate versus cumulative AE energy for different initial crack length over specimen width ratio a/W
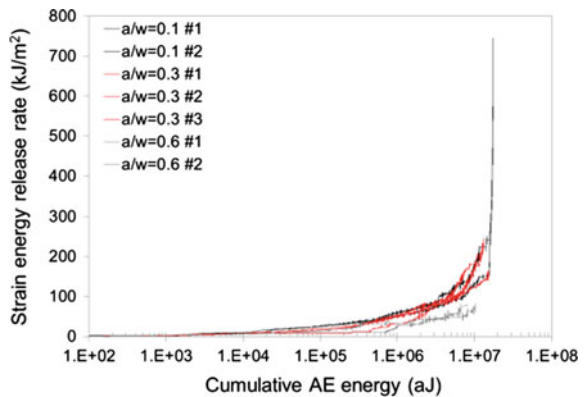
Fig. 7 J-Resistance curve for a/W = 0.3 and 0.6
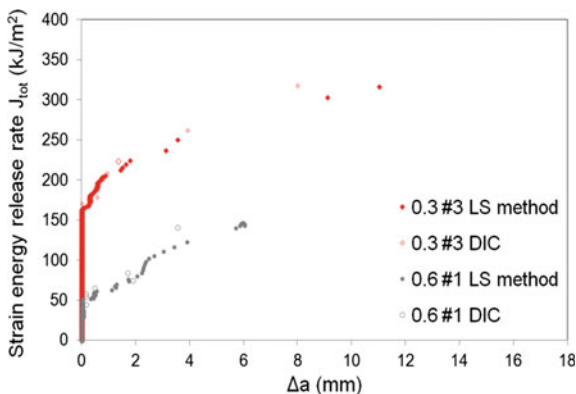
as the initial length of the notch is smaller than the size of the subset required to perform the analysis. For other cases, the crack growth was compared using both load separation method and the digital image correlation technique. It, therefore, appears that the load separation technique is a relevant and accurate tool to obtain the J-R curves for highly ductile composite systems. Figure 8 shows the evolution of the critical strain energy released J_c as a function of a/W. It appears clearly that J_c decreases as a/W increases. In other words, J_c is lower when the stress concentration factor is significant. The macroscopic observation of crack growth and the obtained results also suggest that blunting primarily operates for low-stress concentration factors, for which the matrix toughness and ductility contribute to a large opening of the crack. When stress concentration factor is higher, PPS matrix cannot plastically deform, and ultimately experiences cracking coming along with the growth of the translaminar crack.

Fig. 8 Evolution of the critical strain energy release rate as a function of a/W
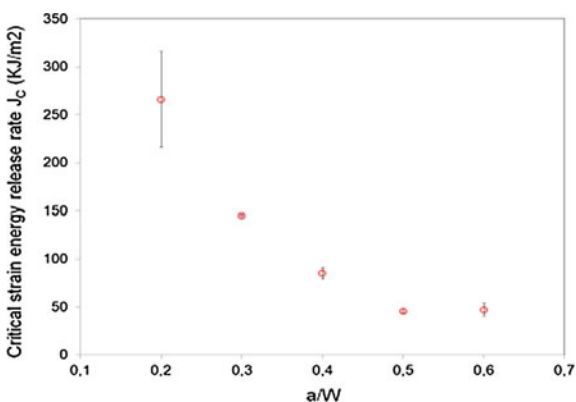
4 Conclusion

The purpose of this work was to investigate the influence of stress concentration factors on the evolution of the strain energy release rate J in 5-harness satin weave carbon fabrics reinforced Polyphenylene sulphide (PPS) structures at 120 °C (higher than the transition temperature Tg). The studied angle-ply (AP) laminates are characterized by a highly ductile behavior. For this purpose, the load separation method was used to determine η_{pl} and the compliance method was applied to determine η_{el}. From the comparison with the DIC analysis results, it appears that the load separation technique is a relevant and accurate tool to obtain the J-R curves for highly ductile composite systems. A fractographic analysis was conducted to understand the chronology of damage mechanisms which significantly depend on the enhanced PPS matrix ductility and toughness at T > Tg. An acoustic emission (AE) technique was used to investigate the correlation between the energy released during cracking and the cumulative AE energy/events for different stress concentration factors. Fibers breakage appears to be not very energetic from the AE standpoint. The blunting (significant opening of the crack due to large plastic deformation at the crack tip) of the crack observed in the case of low concentration factors (e.g., a/W = 0.1) primarily results from the highly ductile behavior of the PPS matrix at T > Tg. Such mechanism is instrumental in dissipating a significant portion of the mechanical energy brought to the notched specimen without fiber breakage. Finally, blunting significantly contributes to the increase in the strain energy release rate in specimens with low-stress concentration factors. When stress concentration factor is higher, PPS matrix cannot plastically deform, and ultimately experiences cracking coming along with the growth of the translaminar crack.

References

Agarwal BD, Kumar P, Patro BS (1983) The J-integral as a fracture criterion for composite materials. In: Second International Conference on Composite Structures, Paisley, Scotland

Albouy W, Vieille B (2014) Determination of the damage threshold in woven-ply TP laminates at T > Tg: Acoustic emission and microscopic damage analysis. Comp Part B 64:138–146

Begley JA, Landes JD (1972) In: Fracture toughness, ASTM STP 514, pp 1–23

Bibo GA, Hogg PJ (1996) Review: the role of reinforcement architecture in impact damage mechanisms and post-impact compression behavior. J Mater Sci 31:1115–1137

Cassanelli AN, Cocco R, de Vedia LA (2003) Separability property and η_pl factor in ASTM A387-Gr22 steel plate. Eng Fract Mech 70:1131–1142

Cowley KD, Beaumont PWR (1997) Damage accumulation at notches and the fracture stress of carbon-fibre/polymer composites: combined effects of stress and temperature. Compos Sci Technol 57(9–10):1211–1219

Dickinson LP, Fletcher NH (2009) Acoustic detection of invisible damage in aircraft composite panels. Appl Acoust 70(1):110–119

Ernst HA, Paris PC, Rossow M, Hutchinson JW (1979) Analysis of load-displacement relationships to determine J–R curve and tearing instability material properties. In: Fracture mechanics. ASTM STP 677. American Society for Testing and Materials, pp 581–99

Karaoglan L, Noor AK, Kim YH (1997) Frictional contact/impact response of textile composite structures. Compos Struct 37(2):269–280

Ndiaye I, Maslouhi A, Denault J (2000) Characterization of interfacial properties of composite materials by acoustic emission. Polym Compos 21(4):595–604

Rice JR (1968) A path independent integral and the approximate analysis of strain concentration by notches and cracks. J Appl Mech 35(2):379–386

Sause MGR, Haider F, Horn S (2009) Quantification of metallic coating failure on carbon fiber reinforced plastics using acoustic emission. Surf Coat Technol 204(3):300–308

Sause MGR, Müller T, Horoschenkoff A, Horn S (2012) Quantification of failure mechanisms in mode-I loading of FRPs utilizing AE analysis. Comp Sci Tech 72:167–174

Sharobeam MH, Landes JD (1991) The load separation criterion and methodology in ductile fracture mechanics. Int J Fract 47:81–104

Sharobeam MH, Landes JD (1993) The load separation and η_{pl} development in precracked specimen test records. Int J Fract 59:213–226

Sumpter JDG, Turner CE (1976) Method for laboratory determination of Jc. In: Cracks and fracture. ASTM STP 601. American Society for Testing and Materials, pp 3–18

Vieille B, Albouy W (2015) Fatigue damage accumulation in notched woven-ply thermoplastic and thermoset laminates at high-temperature: influence of matrix ductility and fatigue life prediction. Int J Fatigue 80:1–9

Vieille B, Aucher J, Taleb L (2011) About the influence of temperature and matrix ductility on the behaviour of carbon woven-ply PPS or epoxy laminates: notched and unnotched laminates. Comp Sci Tech 71:998–1007

Vieille B, Aucher J, Taleb L (2013a) Overstress accommodation in notched woven-ply thermoplastic laminates at high-temperature: numerical modeling and validation by digital image correlation. Compos Part B 45(1):290–302

Vieille B, Casado VM, Bouvet C (2013b) About the impact behavior of woven-ply carbon fiber-reinforced TP- and TS-composites: a comparative study. Compos Struct 101:9–21

Vieille B, Casado VM, Bouvet C (2014) Influence of matrix toughness and ductility on the compression after-impact behavior of woven-ply thermoplastic- and thermosetting composites: a comparative study. Compos Struct 110:207–218

Wainstein J, de Vedia LA, Cassanelli AN (2003) A study to estimate crack length using the separability parameter η_{pl} in steels. Eng Fract Mech 70:2489–2496

Wainstein J, Frontini PM, Cassanelli AN (2004) J-R curve determination using the load separation parameter Spb method for ductile polymers. Polym Testing 23:591–598

Experimental and Numerical Study of Single Point Incremental Forming for a Spiral Toolpath Strategy

Safa Boudhaouia, Mohamed Amen Gahbiche, Eliane Giraud, Yessine Ayed, Wacef Ben Salem and Philippe Dal Santo

Abstract Incremental sheet forming is a flexible forming process based on the sheet progressive localized deformation where a forming tool follows a trajectory predetermined in advance by CAD/CAM programs. Although it is a slow process compared to conventional processes, this relatively new technique is very adequate for prototyping and small series production since it does not require complex tooling (die, punch, etc.). This paper presents a numerical and an experimental study of the Increment Sheet Forming process for a spiral toolpath. A 30 mm depth conical forming part is considered for this purpose. The experimental forming operation has been conducted on a 3-axis milling machine and the experimental data analysis was performed using a Kistler measurement system and a 3D scanner. Moreover, a Finite Element simulation has been realized in order to predict the evolution of the forming forces and the part final profile. The numerical results were in good agreement with the experimental ones. Moreover, the analysis of the scanning data has successfully restituted the part final profile and the surface details.

Keywords Single point incremental sheet forming · Force measurement 3D scanner · Spiral toolpath

S. Boudhaouia (✉)
LGM, ENIM, Monastir, Tunisia
e-mail: sa.boudhaouia@gmail.com

M. A. Gahbiche · W. B. Salem
LGM, IPEIM, Monastir, Tunisia
e-mail: amen.gahbiche@gmail.com

W. B. Salem
e-mail: wacef.bensalem@gmail.com

E. Giraud · Y. Ayed · P. D. Santo
LAMPA, ENSAM, Angers, France
e-mail: eliane.giraud@ensam.eu

Y. Ayed
e-mail: yessine.ayed@ensam.eu

P. D. Santo
e-mail: philippe.dalsanto@ensam.eu

1 Introduction

Conventional sheet forming techniques typically require specific tools which must be replaced each time a new geometry is considered. Due to costs and manufacturing time of these tools, these forming processes are well suited only for large and medium series production. For this reason, much more flexible forming processes are chosen when small or single series production is considered as, for example, the Incremental sheet forming (ISF) process. ISF is a relatively new technique which consists in locally deforming the sheet using a hemispherical tool with small diameter compared to the dimensions of the blank. The toolpath is generally controlled by a CNC machine and it can be obtained using commercial CAM software.

Main industrial issues are the ability to elaborate parts with a great flexibility, to respect market constraints (costs and time) and to guarantee the integrity of functional specifications, dimensions' tolerances and mechanical resistance. Thus, several scientific efforts have been deployed in order to understand and describe the material behaviour during the forming process and to find out the influence of the process's involved parameters. It has been noticed that the material formability during ISF process is largely improved in comparison with conventional shaping techniques as reported by Jeswiet et al. (2005) and Allwood et al. (2007). In fact, the material type, the final product's geometry and the toolpath strategies are the most influencing parameters during ISF. Fratini et al. (2004) have shown that larger material formability can be observed with the increase of strength coefficient, strain hardening coefficient and elongation percentage. (Young and Jeswiet 2004) have shown that the maximum formability is related to the maximum wall angle. This is explained by the fact that the part thickness is rapidly reduced with high wall angles leading to the occurrence of a premature fracture. As a solution for parts with high wall angles, multistage single point forming can be performed as in the work of Liu et al. (2013).

On the other hand, geometrical accuracy and surface roughness are also highly dependent on the toolpath strategies. In ISF process, contour-parallel (offset planes) toolpath is widely used in three-axis forming strategies. Each contour path is defined in the (x, y) plane and shifted to the next path by a constant vertical increment Δz. But this approach conceals some defects as for instance the plastic spots appearing on the part after each vertical increment and also the recorded forces' peaks as pointed out by Duflou et al. (2007). Alternatively, spiral and helical toolpath can be used. In this case, the part is formed by a continuous 3D incremental trajectory (Δx, Δy, and Δz).

In this paper, a spiral strategy is considered for the study of single point incremental forming process. A conical part is considered for this investigation. The evolution of the forming forces, the geometrical accuracy and the surface condition are studied through experimental tests and a Finite Element analysis.

2 Experimental Investigation

2.1 Experimental Platform

Experiments were carried out using a 3-axis CNC vertical milling machine. The clamping system used during the forming operation fixes the contour of the blank sheet by means of a rectangular blank holder. A Kistler measurement device (a three-component force dynamometer type 9257B connected to a complementary Kistler 5019B130 multichannel charge amplifier) is mounted between this fixture and the milling machine work-surface. The measured forming forces (Fx, Fy and Fz) exerted by the forming tool are recorded on a computer-based data acquisition system. An 8 mm diameter hemispherical tool was used for the forming operations.

Once the forming process is completed, the Creaform Go!SCAN 50 was used in order to evaluate the parts final shape. This 3D scanner (presented in Fig. 2) uses the structured white light technology to 3D scan a wide variety of subjects as well

Forming Tool

Fixture System

Table

Formed Part

3D Scanner
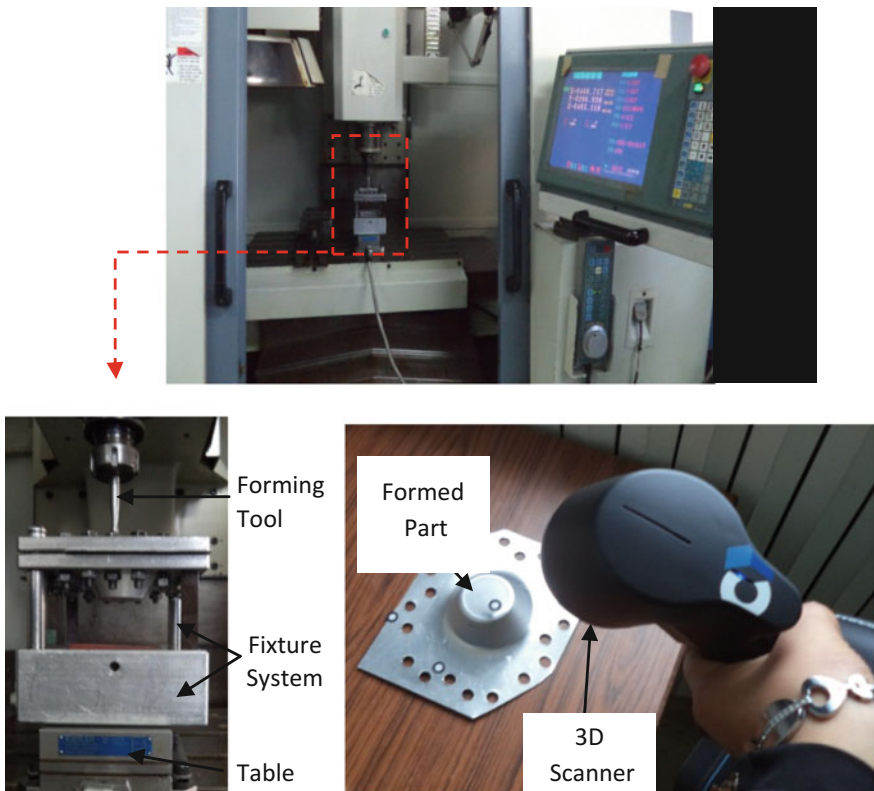
Fig. 1 Experimental platform

as their textures (colours). All of the experimental equipments used during this study are detailed in Fig. 1.

2.2　Tested Material

The material used to investigate the toolpath strategies is 0.6 mm aluminium alloy (Al 1050A). Its mechanical characteristics have been identified by performing different tests on specimens, as defined in Fig. 2. The off-axis tensile tests have been carried out on a hydraulic press (SHIMADZU) having a 30 tones capacity (the accuracy of the load and displacement is of 0.5%). The longitudinal and the transverse deformations were measured by two extensometers (SHIMADZU 50-50-25 and SHIMADZU 20-25-1.5) with a precision of 0.1%. A speed of 1 mm/min is kept constant during all tests. Since this type of alloy is well known to generally exhibit high plastic anisotropy, several tests have been performed on specimens with a grain orientation in the rolling direction RD (0°) and in the transverse directions TD (45° and 90°). It was found that this alloy exhibits a moderate ultimate strength and a high percent elongation at break which is very interesting for high strained forming processes. Lankford coefficients and the main mechanical characteristics revealing to the sheet metal behaviour are summarized in Table 1. All parameters are the mean values of three tests performed in each direction.
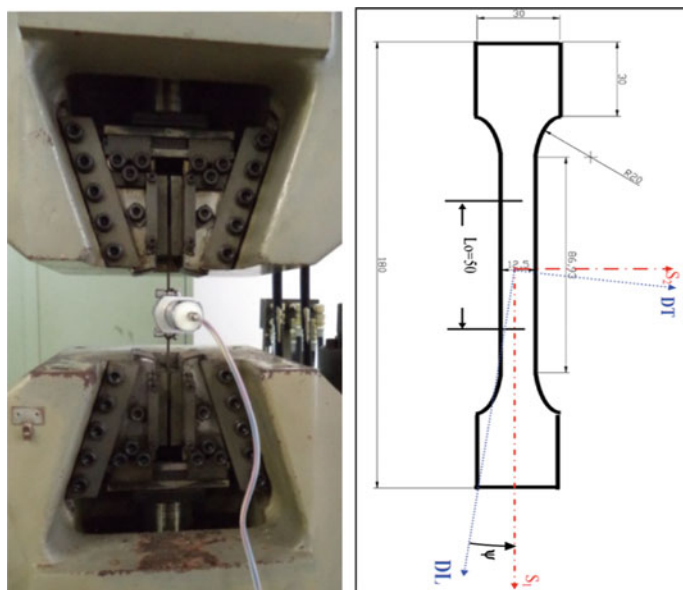
Fig. 2 Tensile test and specimen dimensions

Table 1 Mechanical characteristics of the 1050A aluminium alloy

Young's modulus (GPa)	69
Poisson's ratio	0.3
Elongation at failure A (%)	27
Maximal strength Rm (MPa)	115
Anisotropy coefficient r0	1.79
Anisotropy coefficient r45	2.45
Anisotropy coefficient r90	1.7
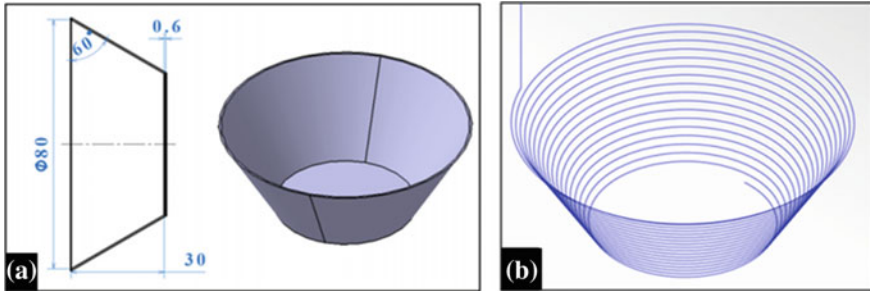
Fig. 3 **a** Formed part CAD geometry **b** spiral strategy

2.3 ToolPath

This study is based on the forming of simple workpiece geometry which is a 80 mm diameter cone truncated at a 30 mm depth and having a 60° wall angle as described in Fig. 3a.

The corresponding toolpath used to manufacture this geometry is a spiral trajectory (shown in Fig. 3b) with a step over of 1 mm between the cutting passes. For spiral toolpath, this distance is a 3D value measured along the surface profile. The tool feed rate is fixed to 600 mm/min.

3   Numerical Simulation

The Finite Element Software ABAQUS®/Explicit is used to simulate the SPIF process.

The deformed sheet is meshed using linear shell elements considering reduced integration (S4R) with 5 integration points through the thickness. The forming tool is modelled by an analytic rigid surface. Its motions are controlled through its reference point. After a sensitivity analysis balancing CPU time to precision, the global mesh size is fixed to 2 mm for the shell elements. Surface to surface contact with hard contact and coulomb friction are used for the interaction between the
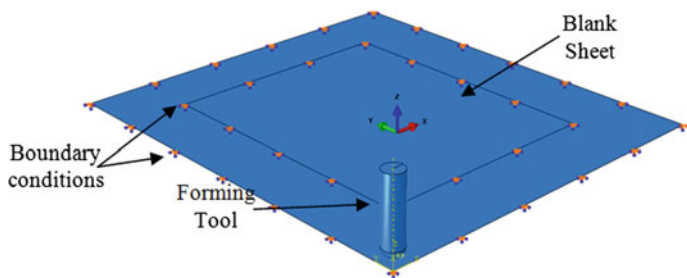
Fig. 4 Finite element model

punch (master surface) and the sheet (slave surface). A global friction coefficient $\mu = 0.1$ is chosen for the sliding contact property. The step time and the quasi-static conditions (Mass scaling) are chosen to guarantee a good compromise between the CPU time and convergence criteria. The tool three-dimensional displacements are automatically implemented into the FE software through a Python script. Figure 4 describes the different instances of the numerical model.

4 Results and Discussion

4.1 Surface Roughness

As represented in Fig. 5, the 3D scanning operation has successfully reproduced the details of the originally formed part. As for the surface condition, the trajectory of the tool is clearly visible given the high local deformation at each tool displacement and also the relatively thin sheet thickness. Moreover, the chosen step over value is relatively important (it approximately involves a 1.8 mm vertical increment Δz). As a consequence, the decrease of this parameter could considerably improve the part surface roughness. On the other hand, the classic transition marks usually seen when using an offset planes strategy are completely absent on the surface of the formed part. As a consequence, the final surface is globally homogeneous and do not present any type of singularity except for the tool final position highlighted in Fig. 5.

4.2 Forming Forces Comparison

Figure 6 describes the evolution of the experimentally measured and numerically predicted three forming force components.

The vertical force component Fz gradually increases as the tool moves downwards accordingly to the corresponding toolpath and then it reaches a steady state
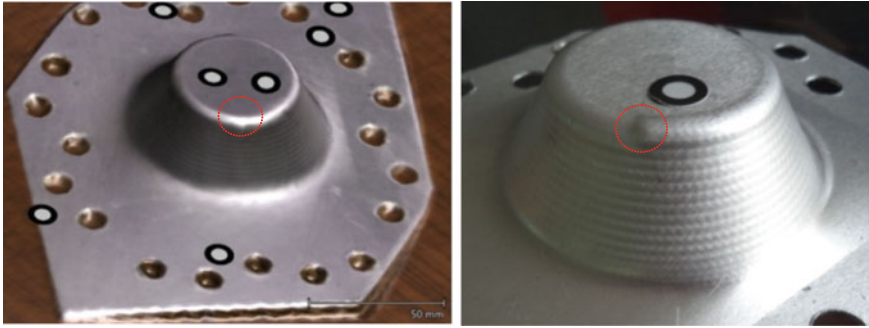
Fig. 5 Final part: **a** scanning results **b** actual photo

pattern at a forming time of approximately 120 s. The overall evolution of the numerical vertical force curve is very similar to the experimental one but the oscillations are much higher which could be explained by the contact elements (Bouffioux et al. 2008). However, the average difference between the two curves is almost 34%. A significant improvement should be noted if a kinematic hardening is instead used (Flores et al. 2007).

For the in-plane forces Fx and Fy, their corresponding numerical and experimental evolutions are almost identical with an average amplitude difference of 53%: As a matter of fact, both of these measured and predicted force components oscillate between their minimum and maximum values in a sinusoidal way with a constant phase shift. As in the case of the vertical force, their amplitude becomes almost constant after 120 s.

4.3 Geometrical Accuracy

The curves in Fig. 7 describe the part profile obtained from the numerical model results as well as from the scanned data processing.

Both of the numerical and experimental results show that the obtained part's geometry is close enough to the desired CAD model. However, two main regions present most of the disparity. In fact, the differences observed in the first region are mainly caused by the fixture system. A circular backing plate, with a diameter slightly larger than 80 mm, would reduce the spring back effect leading to a more accurate geometry. The difference between the CAD and the part geometry in the second region is inevitable since it is caused by the forming tool during the final toolpath contour. Nonetheless, a smaller tool diameter could reduce to some extent this geometrical inaccuracy.
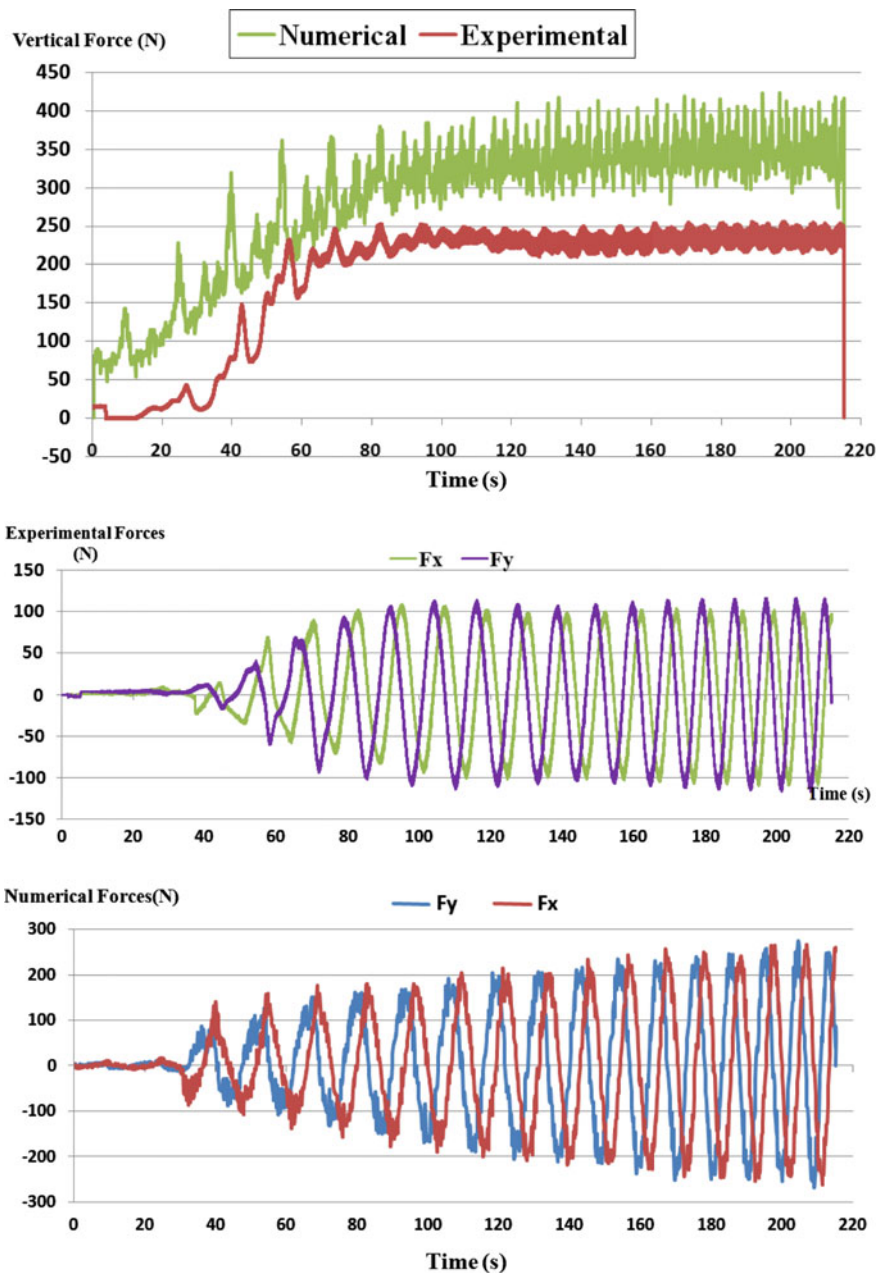
Fig. 6 Comparison of the experimental and numerical forces evolution
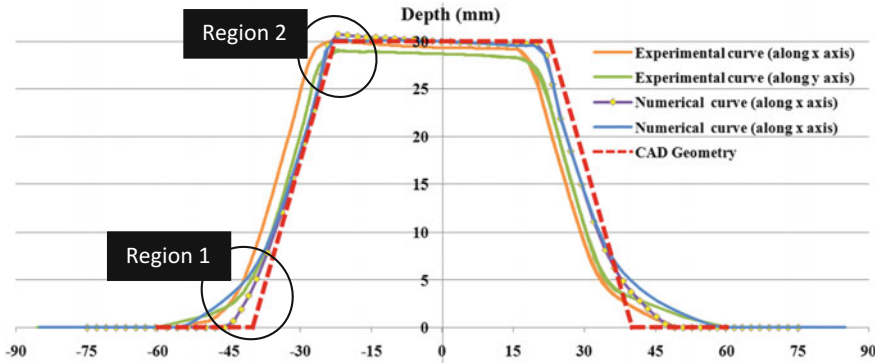
Fig. 7 Geometrical accuracy of the formed part

5   Conclusion

This paper presents a study of the single point incremental forming process. Based on the observations of the forming forces measurements and the FE prediction, it was found that the three force components gradually increase with the depth until they reach a steady-state force pattern when the tool/sheet contact is completely established. On the other hand, the adopted spiral strategy has given a satisfactory surface roughness as well as an acceptable geometrical accuracy. Finally, the developed FE model results were in good agreement with the experimental ones.

References

Allwood JM, Shouler DR, Tekkaya AE (2007) The increased forming limits of incremental sheet forming processes. KEY ENG MAT. 344:621–628

Bouffioux C, Eyckens P, Henrard C et al (2008) Int J Mater Form 1(Suppl 1):1147. https://doi.org/10.1007/s12289-008-0183-0

Duflou J, Tunçkol Y, Szekeres A, Vanherck P (2007) Experimental study on force measurements for single point incremental forming. J Mater Process Technol 189(2007):65–72

Flores P, Duchêne L, Bouffioux C, Lelotte T, Henrard C, Pernin N, Van Bael A, He S, Duflou J, Habraken AM (2007) Model identification and FE simulations: effect of different yield loci and hardening laws in sheet forming. Int J Plast 23(3):420–449

Fratini L, Ambrogio G, Di Lorenzo R, Filice L, Micari F (2004) The influence of mechanical properties of the sheet material on formability in single point incremental forming. Annal CIRP—Manuf Technol 53(1):207–210

Jeswiet J, Micari F, Hirt G, Bramley A, Duflou J, Allwood J (2005) Asymmetric single point incremental forming of sheet metal. CIRP ANN-MANUF TECHN. 54(2):88–114

Liu Z, Li Y, Meehan PA (2013) Vertical wall formation and material flow control for incremental sheet forming by revisiting multistage deformation path strategies. Mater Manuf Process 28(5):562–571

Young D, Jeswiet J (2004) Wall thickness variations in single point incremental forming. IMECHE Part B. J Eng Manuf 218(B11):204–210

A Disassembly Sequence Planning Approach Based on Particle Swarm Optimization

Maroua Kheder, Moez Trigui and Nizar Aifaoui

Abstract Recently, Disassembly Sequence Planning (DSP) plays an important role in the life cycle of mechanical products. Disassembly specification during the design phase of a product is considered as a great interest of engineers and designers. This paper presents an automated DSP based on Particle Swarm Optimization (PSO). First, the collision test is performed by the use of the interference test tool of the CAD software in order to identify all possible interferences during the components' motion. Then interference matrices are generated to ensure the feasibility of disassembly operations. Next, a PSO algorithm, based on the regeneration of DSP, was performed to optimize the DSP using an objective function. Various criteria such as part volume, tools change, directions and maintainability of usury component are considered. Finally, to highlight the performance of the developed approach, an implemented tool is developed and an illustrative example is studied.

Keywords Disassembly sequence plan · Computer aided design
Metaheuristics · Particle swarm optimization

1 Introduction

Green design methods cover the entire Product Life Cycle (PLC) especially DSP. The process of disassembly interacts all phases of the product which including the design phase, manufacturing and recycling. Disassembly is consid-

M. Kheder (✉) · M. Trigui · N. Aifaoui
Mechanical Engineering Laboratory, National Engineering School of Monastir,
University of Monastir, Av Ibn Eljazzar, Monastir, Tunisia
e-mail: maroua.kheder@gmail.com

M. Trigui
e-mail: moez.trigui@gmail.com

N. Aifaoui
e-mail: nizar.aifaoui@gmail.com

ered as an important research topic in the manufacturing automation field. Much research has been focus on the end of life (Tripathi et al. 2009). However in recent years and in order to improve the performance of a product in its complete life cycle, engineers are demanded to make increasing efforts to consider the disassembly constraints and its specification in the design phase (Moore et al. 2001). Maintenance is considered as a vital process in PLC, it refers to the replacement of failed components. Indeed, Preventive Maintenance (PM) refers to the work carried out to restore the degenerated performance of a system and to lessen the likelihood of it failing (Kheder et al. 2016). In fact, the objective of PM is to improve the system reliability over a long time. The automatic generation of DSP remains a research subject to be improved. Researchers prove that DSP cannot be a trivial problem it is among the combinatorial optimization problems with hard constraints called NP-hard problem (Lambert 2007). To overcome this problem, in the literature, many approaches and algorithm were used to generate optimum DSP. In his survey, (Lambert 2003) introduced many examples of artificial intelligence technique applications in DSP as expert systems, simulated annealing, Petri nets and neural networks. Cappelli et al. (2007) proposed a system to generate all feasible disassembly sequences, from the CAD model file using interference matrices and liaison graph. The intelligent optimization algorithm seems to be the most suitable methods to solve the DSP problem such as Genetic Algorithm (GA), Ant Colony Algorithm (ACO) and Particle Swarm Optimization (PSO). Kongar and Gupta (2006) planned a GA approach to DSP with the objective of minimizing the number of direction changes, disassembly method changes, and the groups of identical material components. Although, GA can generate infeasible sequence that abuses geometric precedence constraint (Lu et al. 2008). In recent years, there has been an increasing interest in algorithms inspired by swarm intelligence to solve the problem of DSP/ASP (Tseng et al. 2011). Kalayci and Gupta (2013) used a hybrid PSO with GA to solve the problem of sequence-dependent disassembly line balancing. In this paper, we are concerned about the PSO method to optimize DSP of CAD assembly in a context of preventive maintenance.

The remaining part of this paper is organized as it follows. First, the optimal disassembly plan by PSO is formulated. Next, based on the geometric precedence extracted from the CAD model, the performance of PSO contributes to the automatic regeneration of feasible DSP. Then, the disassembly sequence regenerated was evaluated using an objective function. In this step, the criteria were developed in order to promote an optimal solution by introducing more assembly features. The purpose is to obtain an optimum DSP by disassembling the smaller parts first and disassembling the maximum number of parts in the same direction without changing the tool used and easier access to remove the wearing parts. Finally, an example was treated to explain the criteria used to generate an optimum DSP.

2 PSO for Disassembly Sequence Planning

The PSO is a new technique, presented by Eberhart and Kennedy (1995), originates from two different concepts: the first is the notion of swarm intelligence based of the observation of swarming habits by certain kinds of animals (such as fish and birds) and the second concept is the field of evolutionary computation. In the following section a description of PSO algorithm is presented.

2.1 Steps of the Developed Approach

The stages of PSO can be structured in a flow chart represented in Fig. 1. PSO is an iterative algorithm based population named swarm S, engages a number of simple entities called particles with $S = \{X_1, X_2, \ldots X_M\}$. The swarm is defined as a set of M particle. This population works simultaneously by dimensional space. The *ith* particle can be represented as $X_i = \{x_{11}, x_{12}, \ldots, x_{id}, \ldots x_{iN}\}$, in which $1 \leq d \leq N$ with N represents the number of parts in a mechanism. The velocity can be represented as $V_i = \{v_{11}, v_{12}, \ldots, v_{id}, \ldots v_{iN}\}$.

In the case of DSP, the particle represents a disassembly sequence and the population is initialized with random positions and velocity. At each iteration step

Fig. 1 Flow chart of particle swarm optimization for DSP
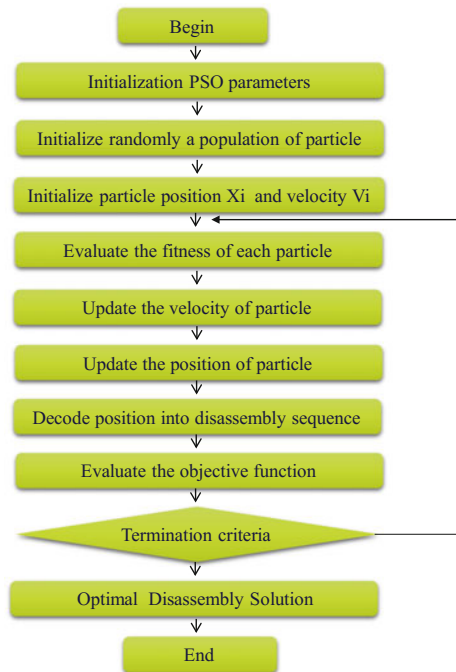
of the PSO algorithm, the candidate solution is evaluated by an Objective Function (*OF*) being optimized. The particles evaluate their fitness values respecting criteria fixed by the designer.

The main objective of the developed approach is to obtain an optimum DSP by considering four objectives: disassembling the smaller parts in first, disassembling the maximum number of parts in the same direction without changing the tool and easier access to remove the wearing components for preventive maintenance. The *OF* represents the quality of the DSP given as follows:

$$OF = \max\left(N - \left(\gamma \cdot D + \delta \cdot T + \frac{\mu}{M} + \psi \cdot V\right)\right) \tag{1}$$

where

$$M = \sum_{k=1}^{N} \frac{m_i}{\sum m_i}(N - k + 1) \tag{2}$$

$$V = \sum_{i=1}^{N} \frac{v_i}{\sum v_i}(N - i + 1) \tag{3}$$

$$D = \sum_{i=1}^{N} d(p_i, p_{i+1}) \tag{4}$$

$$T = \sum_{i=1}^{N} T(p_i, p_{i+1}) \tag{5}$$

- *M* is the relative factor of maintenance for each component: m_i can take the following values:
  - 1: if there is no maintenance needed to the component *m*
  - 2: if a corrective maintenance of component *m* is needed
  - 3: if a preventive maintenance of component *m* is needed
- *V* is the relative volume of each component in the mechanism.
- *γ, δ,* μ, and *ψ* represent weight coefficients that can be chosen according to the objectives of the designer.
- *D* represents the total value of direction change of the disassembly sequence which p_i and p_{i+1} are two parts successively disassembled. It can have an attribute as follow:
  - 0: if there is no change when removing two successive parts
  - 1: if there is a change of 90° when removing two successive parts
  - 2: if there is a change of 180° when removing two successive parts

- *T* represents the total value of the tools change of the disassembly sequence which p_i and p_{i+1} are two parts successively disassembled. It can have an attribute as follow:

  – 0: if there is no change of tools when removing two successive parts
  – 1: otherwise

In the treated example the value of weight coefficient is $\gamma = \delta = \psi = 0.2$. Moreover, attention is paid to coefficient $\mu = 0.4$.

After the evaluation of sequences, the best position of the ith particle as $Pi = (p_{i1}, p_{i2},..., p_{iN})$ can be denoted and for the same particle having the best fitness of the swarm as $P_g = (p_{g1}, p_{g2},..., p_{gN})$. Subsequently, each particle determines its movement through the search space by combining information about its current fitness, its best fitness from previous locations (individual perspective) and best fitness locations with regards to one or more members of the swarm (social perspective). Consequently, PSO algorithm can be performed by the process of updating both the velocity and the position of the particle based on the information obtained in previous step of the algorithm:

$$v_{id}(t+1) = w \cdot v_{id}(t) + c_1 \cdot r_1 \cdot (p_{id} - x_{id}(t)) + c_2 \cdot r_2 \cdot (p_{gd} - x_{id}(t)) \qquad (6)$$

With the updating of the velocity, each particle moves to its new position with its new velocity and the position equation is:

$$x_{id}(t+1) = x_{id}(t) + v_{id}(t+1) \qquad (7)$$

where

- w: is the inertia weight, this parameter is used to oversee the impact of the old velocity on the new one.
- c_1: is the cognition parameter which represents the attraction to its best position p_{id}.
- c_2: is the social parameter which represents the attraction to the global best position of the whole swarm.
- r_1: and r_2 are inform random number in 0 and 1.
- t: represents the iterative number.

The process of updating both velocity and position create a new population which requires a process of decoding to link between the new population created and the disassembly sequences. The decoding process is based on sorting in ascending order the position values of the particle. Consequently, the order position in the decode sequence is deduced from the ranked order value (yang-Je Tseng 2011). However, the feasibility of the created population cannot be guaranteed by the decoding process, so a method to ensure the precedence constraints is essential.

2.2 Sequence Disassembly Regeneration

To secure the feasibility of DSP, the method adopted is inspired by the work of Dini and Santochi (1992). The assembly model created by CAD systems includes many appropriate data subservient in DSP problem such as the data related to the part and Data associated to the assembly mates between parts. The disassembly precedence graph DPG is transformed into a Disassembly Precedence Matrix which is provided to express the disassembly precedence restriction relation. An exploration of the CAD data can conduct to the elaboration of interference matrix [I] along the +k-axis direction with k ϵ (+X, +Y, +Z).

$$[I]_{+k} = \begin{bmatrix} & P_1 & P_2 & \cdots & P_m & \cdots & \cdots & \cdots & P_N \\ P_1 & 0 & 1 & 0 & 0 & \cdots & \cdots & \cdots & 0 \\ P_2 & 0 & 0 & 0 & 0 & \cdots & \cdots & \cdots & 1 \\ \vdots & 1 & 1 & 0 & 0 & \cdots & \cdots & \cdots & 0 \\ \vdots & 1 & 0 & 0 & \ddots & \cdots & \cdots & \cdots & 0 \\ P_r & \vdots & 1 & 0 & 0 & \ddots & \cdots & \cdots & 1 \\ \vdots & 0 & 0 & 0 & 0 & \cdots & \ddots & 0 & 0 \\ \vdots & \vdots & 1 & 0 & 0 & \cdots & \cdots & 0 & \vdots \\ P_N & 1 & 0 & 0 & 1 & \cdots & \cdots & \cdots & 0 \end{bmatrix} \qquad (8)$$

where

- P_i, represent the ith part of the assembly.
- (I_{rm}) is equal to 1 if there is interference between component *r* and component *m* when disassembling along the +K-axis direction, otherwise is equal to 0.

The top priority of DSP optimization is to obtain a sequence without any collision among the disassembly operations. In fact, the population issues form the decoding process will be checked and regenerated. Now, we will describe the regeneration procedure of DSP. As an example, suppose a disassembly sequence, D, chosen from the population obtained after the process of decoding is (P_7 P_5 P_6 P_1 P_2 P_3 P_4), for a mechanism composed of 7 components and its position value is (3.5 4.2 1.8 5.6 2.1 0.6 0.1). The first step is to check if the component P_7 is a free component. This process is done by inspecting elements of $[I]_k$ matrices in order to identify if the component P_7 can be disassembled freely which mean it does not interfere with another component among the +k-axis or the −k-axis direction. Thus, the feasible disassembly sequence, D $_{feasible}$, will be generated and the first component selected is 7 then it is deleted from D sequence. Accordingly, the interference matrix is updated dynamically and the free components detected are (P_6 P_1). Indeed, two components are able to be disassembled. In this step, the smallest position value accorded will be selected. The component P_6 having the smallest position value 0.6 will be placed next in the disassembly sequence D $_{feasible}$ and it becomes (P_7 P_6) and D becomes (P_5 P_1 P_2 P_3 P_4). The regeneration procedure starts again until the D is emptied.

3 Implementation and Case Study

A software program has been implemented using Matlab R2013b (Matrix Laboratory) and the API (Application Programming Interface) of SolidWorks CAD system. An illustrative example of belt tightener was treated. Figure 2 and Table 1, present the treated mechanism which is composed of 7 parts and need three tools G1, G2 and G3 to be disassembled.

For the illustrative example, the interference matrices in the three directions (+X, +Y, +Z) is given by:

$$
[I]_{+z} =
\begin{array}{c|ccccccc}
 & P_1 & P_2 & P_3 & P_4 & P_5 & P_6 & P_7 \\
\hline
P_1 & 0 & 0 & 0 & 0 & 0 & 0 & 0 \\
P_2 & 1 & 0 & 1 & 1 & 1 & 0 & 1 \\
P_3 & 1 & 0 & 0 & 0 & 1 & 0 & 0 \\
P_4 & 1 & 0 & 1 & 0 & 1 & 0 & 0 \\
P_5 & 1 & 0 & 0 & 0 & 0 & 0 & 0 \\
P_6 & 1 & 1 & 1 & 1 & 1 & 0 & 1 \\
P_7 & 1 & 1 & 1 & 1 & 1 & 0 & 0 \\
\end{array}
\qquad
[I]_{+x} =
\begin{array}{c|ccccccc}
 & P_1 & P_2 & P_3 & P_4 & P_5 & P_6 & P_7 \\
\hline
P_1 & 0 & 1 & 1 & 1 & 1 & 1 & 1 \\
P_2 & 1 & 0 & 0 & 1 & 0 & 1 & 1 \\
P_3 & 1 & 0 & 0 & 0 & 1 & 0 & 0 \\
P_4 & 1 & 0 & 0 & 0 & 0 & 0 & 0 \\
P_5 & 1 & 0 & 1 & 0 & 0 & 0 & 0 \\
P_6 & 1 & 0 & 0 & 0 & 0 & 0 & 0 \\
P_7 & 1 & 1 & 0 & 0 & 0 & 0 & 0 \\
\end{array}
$$

$$
[I]_{+y} =
\begin{array}{c|ccccccc}
 & P_1 & P_2 & P_3 & P_4 & P_5 & P_6 & P_7 \\
\hline
P_1 & 0 & 1 & 1 & 1 & 1 & 1 & 1 \\
P_2 & 1 & 0 & 0 & 0 & 0 & 0 & 1 \\
P_3 & 1 & 0 & 0 & 0 & 1 & 0 & 0 \\
P_4 & 1 & 0 & 0 & 0 & 0 & 0 & 0 \\
P_5 & 1 & 0 & 1 & 0 & 0 & 0 & 0 \\
P_6 & 1 & 0 & 0 & 0 & 0 & 0 & 0 \\
P_7 & 0 & 0 & 0 & 0 & 0 & 0 & 0 \\
\end{array}
$$

$$(9)$$

The evolution performance of PSO is presented in Fig. 3, the objective function OF versus generation number to the related example (Fig. 2). Table 2 presents the optimal DSP and the disassembly directions of the treated example. The computation time is 2.015 s proves the efficiency of the proposed approach.
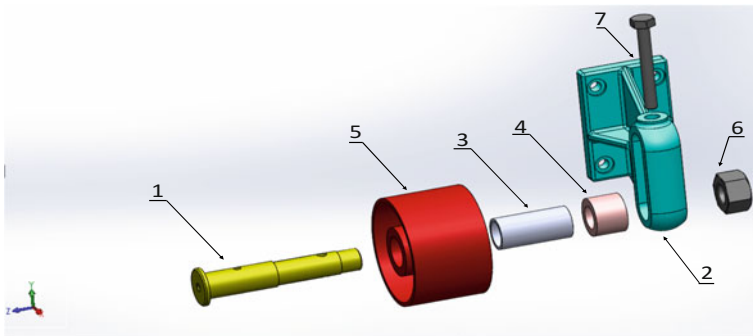
Fig. 2 The CAD model of belt tightener

Table 1 Component list of belt tightener and its characteristic

Component	Name	Maintainability	Tool	Volume $(mm^3)10^5$
1	Tree	2	G_1	1.05
2	Built	1	G_1	4.11
3	Pad	3	G_2	0.327
4	Bearing spacing	1	G_1	0.253
5	Pulley	2	G_1	2.97
6	Nut HEX	1	G_3	0.177
7	Screw HEX	2	G_3	0.167
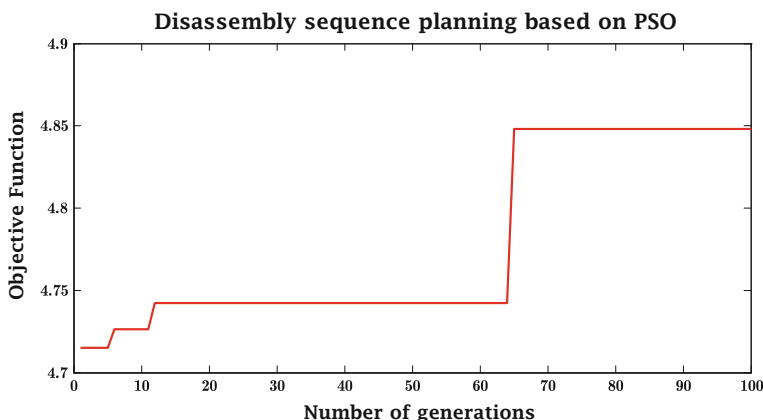
Fig. 3 Evolution of the objective function versus the number of generation

Table 2 Best disassembly sequence and direction removed

Optimal DSP	7	6	2	4	3	5	1
Direction	+Y	−Z	−Z	−Z	−Z	−Z	−Z

4 Conclusion

In this paper a DSP based on Particle swarm optimization approach for preventive maintenance is proposed. The precedence relationships between parts were considered using a free parts process which permits the generation of feasible DSP. A Computer based tool was implemented permitting the generation of optimal feasible DSP from a CAD model. The obtained results, shown in an industrial example, reveal the credibility of the proposed approach.

References

Cappelli F et al (2007) Design for disassembly: a methodology for identifying the optimal disassembly sequence. J Eng Des 18(6):563–575

Dini G, Santochi M (1992) Automated sequencing and sub-assembly detection in assembly planning. J Mater Process Technol 129(1–3):490–494

Eberhart R, Kennedy J (1995) A new optimizer using particle swarm theory. In: Proceedings of the sixth international symposium on micro machine and human science, pp 39–43

Kalayci CB, Gupta SM (2013) A particle swarm optimization algorithm with neighborhood-based mutation for sequence-dependent disassembly line balancing problem. Int J Adv Manuf Technol 69(1–4):197–209

Kheder M, Trigui M, Aifaoui N (2016) Optimization of disassembly sequence planning for preventive maintenance. Int J Adv Manuf Technol

Kongar E, Gupta SM (2006) Disassembly sequencing using genetic algorithm. Int J Adv Manuf Technol 30(5–6):497–506

Lambert AJD (2003) Disassembly sequencing: a survey. Int J Prod Res 41(16):3721–3759

Lambert AJD (2007) Optimizing disassembly processes subjected to sequence-dependent cost. Comput Oper Res 34(2):536–551

Lu C et al (2008) A multi-objective disassembly planning approach with ant colony optimization algorithm. Proc Inst Mech Eng Part B J Eng Manuf 222(11):1465–1474

Moore KE, Güngör A, Gupta SM (2001) Petri net approach to disassembly process planning for products with complex AND/OR precedence relationships. Eur J Oper Res 135(2):428–449

Tripathi M et al (2009) Real world disassembly modeling and sequencing problem: optimization by algorithm of self-guided ants (ASGA). Robot Comput-Integr Manuf 25(3):483–496

Tseng Y-J, Yu F-Y, Huang F-Y (2011) A green assembly sequence planning model with a closed-loop assembly and disassembly sequence planning using a particle swarm optimization method. Int J Adv Manuf Technol 57(9–12):1183–1197

HDPE Pipe Failure Analysis Under Overpressure in Presence of Defect

M. A. Guidara, M. A. Bouaziz, M. Dallali, C. Schmitt, E. Haj Taieb and Z. Azari

Abstract Pipe failure and leaks are frequent phenomena in urban areas. In order to minimize the risk of long-term leakage, nearly 60% of drinking water systems are renewed with third-generation polyethylene pipes, PE100. Due to its characteristics, it is a material of choice for water supply networks. However, the presence of a defect can lead the pipe failure under the effect of transient flow. In order to examine this problem, the cracking behavior of PE100 pipes with a defect has been studied. Using burst tests and finite element modeling, we have demonstrated that the concept of elastic-plastic fracture mechanics, the J-integral, can define with acceptable precision the crack initiation and the failure behavior of PE100 pipe. The J-integral value at the time of appearance of the damage zone, plastic strain-hardening, is considered numerically to be the value of the toughness. This allowed us to define the pressure leading to the crack initiation. The results are compared with the experimental burst pressures.

Keywords J-Integral · Crack initiation · PE100 · Finite element
Pipe burst tests

M. A. Guidara (✉) · M. A. Bouaziz · M. Dallali · E. Haj Taieb
Laboratoire de Mécanique des Fluides Appliqués, Génie des Procédés et Environnement,
Ecole Nationale d'Ingénieurs de Sfax, Université de Sfax, BP 1173, 3038 Sfax, Tunisia
e-mail: mohamed-amine.guidara@univ-lorraine.fr; gem3_guidara@yahoo.fr

M. A. Bouaziz
e-mail: mohamedali.bouaziz@gmail.com

M. Dallali
e-mail: manel.dalleli@gmail.com

E. Haj Taieb
e-mail: e_hajtaieb@yahoo.fr

M. A. Guidara · M. A. Bouaziz · M. Dallali · C. Schmitt · Z. Azari
Laboratoire de Biomécanique, Polymères et Structures (LaBPS),
Ecole Nationale d'Ingénieurs de Metz, 57070 Metz, France
e-mail: christian.schmitt@univ-lorraine.fr

Z. Azari
e-mail: zitoune.azari@univ-lorraine.fr

1027

1 Introduction

The question of the durability of materials is central in most areas. The majority of research is oriented toward studying the effects of the weakening of a material and chemical degradation on the lifetime of PE100 pipes, i.e., on long-term creep failure (Choi et al. 2009; Duvall.and Edwards 2009; Ghabeche et al. 2015). However, there are other causes of incidents that are frequent and can cause damage. We can cite, for example, the presence of defects that are generated during the installation or maintenance operations or by external factors such as the incorrect use of a cutting tool. They may lead to failure under the effect of overpressures caused by the transient flow (Covas et al. 2004; Dallali et al. 2015). The overpressures will be introduced into a dimensioning criterion to analyze their effect on the crack resistance of a notched pipe. To do this, a series of numerical modeling of the pipes in the presence of a defect has been performed with Abaqus. This makes it possible to determine the variations of the stresses and of the J-integral used to find a relation linking the crack initiation pressure, the size of the defect, and the pipe geometry. The numerical model is validated experimentally. Burst tests are carried out on pipes in the presence of a surface defect at different loading rate. One of the specimens was instrumented with strain gage rosettes in the vicinity of the notch. The objective was to follow the circumferential and longitudinal strain during the burst test to study, subsequently, the pipe failure analysis. The experimental and numerical approaches and results will be represented hereafter.

2 Burst Tests

We are interested in understanding the relationship between the size of a longitudinal defect and the burst pressure in a pipe based on small-scale burst tests. The results will be used to validate our numerical model by finite elements and to adopt an approach to analyze the failure of PE100 pipe.

2.1 Experiment Preparation

The burst tests are carried out on nine notched pipes of length 400 mm. The specimen dimensions and the shape of the notches are shown in Fig. 1.

The notches are made using a disc cutter of diameter 80 mm and of small thickness, 0.5 mm. This is, in order, to minimize the notch effect on the stress concentration and to get as close as possible to the concept of cracks.

To measure the strain in the notch vicinity, a pipe of length 600 mm is equipped by strain gage rosettes. They contain two strain gages in the opposite directions, one

for measuring longitudinal strain and the other for circumferential strain. The positions of the rosettes are shown in Fig. 2.

The viscoelasticity of pipe-wall dampen the overpressures and the water hammer pressure reaches its maximum after a progressive increase. In this, we are interested in a quasi-static study. Our choice of loading speed is set at 12, 30, and 60 bar/min.

The different stages of burst test are:

- Purge the specimens by filling them completely with water in a vertical position in order to eliminate the air in the pipe.
- Continuously increasing internal hydraulic-pressure until failure, Fig. 3.

a (Notch depth mm)				
2	4	5	6	8

$$c = 2\sqrt{a(d_e - a)}$$
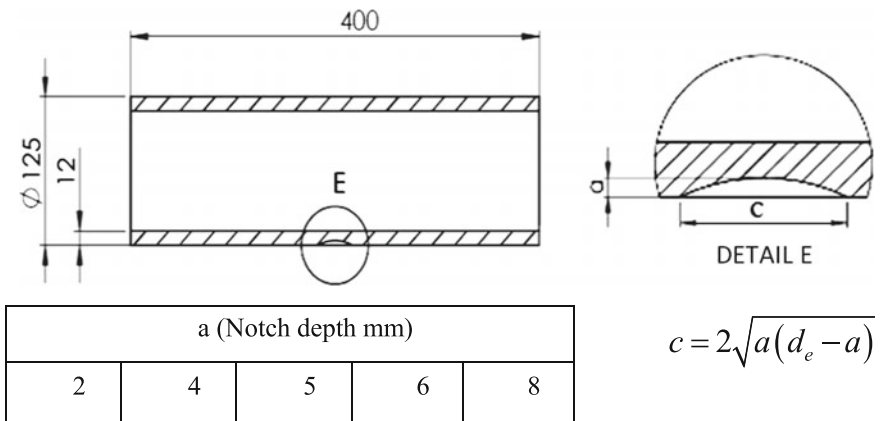
Fig. 1 Geometry of the specimen for the burst test
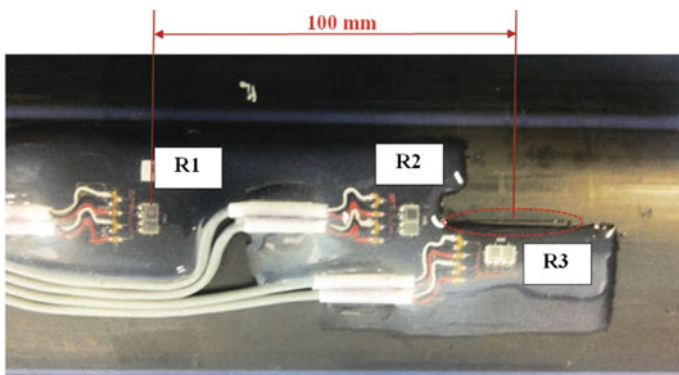
Fig. 2 Placement of the rosettes on the PE100 pipe

2.2 Pipe Burst Test Results

As a consequence of the visco-elastoplastic behavior of PE100, with a higher loading speed, less volume of water is injected to arrive at the same internal pressure. Thus, the material increases its rigidity with the increase in the loading rate, Fig. 4. Despite this, a small variation of the burst pressure is observed ($\Delta p < 5\%$).

For a defect of 6 mm depth, the burst pressure increases with the loading speed. However, at 4 and 8 mm depth, it is not possible to define a law between the burst pressure and the loading speed. Also, the overall variation observed between the curves is very small. Therefore, we conclude that the burst pressure is weakly influenced by the loading rate, Table 1, and that the observed burst pressure perturbations are due to the experimental conditions. Indeed, the role of the

Fig. 3 Burst test
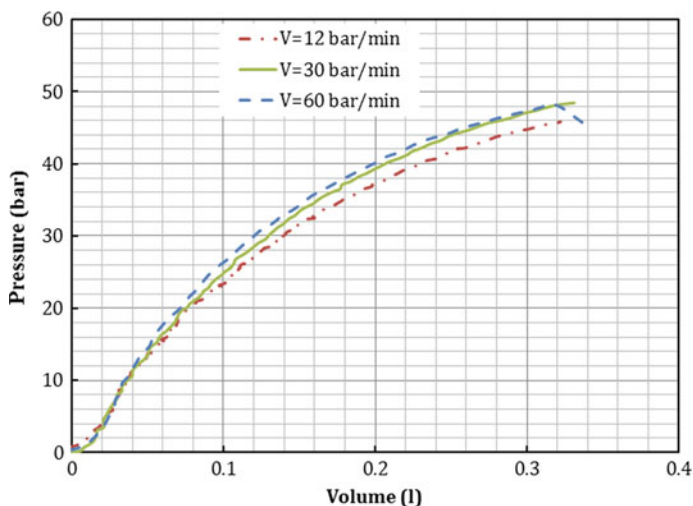
Fig. 4 Effect of the loading rate on the pressure variation (without defect)

Table 1 Burst pressure (bar) according to notch depth and Hydraulic loading rate

	Notch depth (mm)					
Hydraulic loading rate (bar/min)	Without notch	a = 2 mm	a = 4 mm	a = 6 mm	a = 8 mm	a = 10 mm
12	54	51.6	45.8	40.3	35.2	31.1
30			48.4	40.5	35.9	
60	56.3		48.1	42.5	35.8	

viscoplastic deformation of PE100 manifests itself in the case of creep rupture where the time factor has to be taken into consideration.

For conservative reasons, the loading speed of 12 mm/min will be used to analyze the failure conditions using a finite element modeling.

3 Numerical Simulation Model

Considering the experimental means, we found difficulties to realize an external crack with a well-defined shape. For this purpose, cuts of small thickness, 0.5 mm, are machined using disc cutters to get as close as possible to the configuration of a crack. On the other hand, the pre-cracked pipe modeling is achievable by Abaqus. These two configurations, a pre-cracked and a notched pipe are modeled by finite elements in order to study their failure behavior and to carry out a comparative study between them. The depths and lengths of the defects are those used in the burst tests, Fig. 1. This allows us to determine the pre-crack effect on the crack resistance and more precisely on the pressure leading to the crack initiation in the PE100 pipe.

3.1 Law Behavior of the Material (PE100)

The PE100 is defined as an elastoplastic material with a strain rate-dependent deformation. In order to minimize the error and to get as close as possible to the actual configuration, the inverse method is used. The idea is to optimize the parameters of the material based on the experimental and numerical data of mechanical behavior test and burst test of instrumented pipe with rosettes. After constitutive processing of the traction curve, Fig. 5 represents the final stress-strain curve. The elastic and linear viscoelastic behavior is approximated by elastic deformation. On the other hand, the nonlinear viscoelastic deformation zone is defined in the plasticity table.

3.2   Geometry, Boundary Conditions, and Loading

Due to the symmetry of the specimen and to reduce the computation time, only a quarter of a pipe is modeled, Fig. 6. Thus, the conditions at the symmetry limits are applied in the model. The pipe with two rigid caps attached to its ends. That is the way the cap has been modeled by rigid elements of thickness 20 mm. It is free to move in the axial direction of the pipe. The model (pipe + cap) was charged with an internal pressure uniformly distributed over the entire inner surface with a constant hydraulic loading rate of 12 bar/min, Fig. 6.
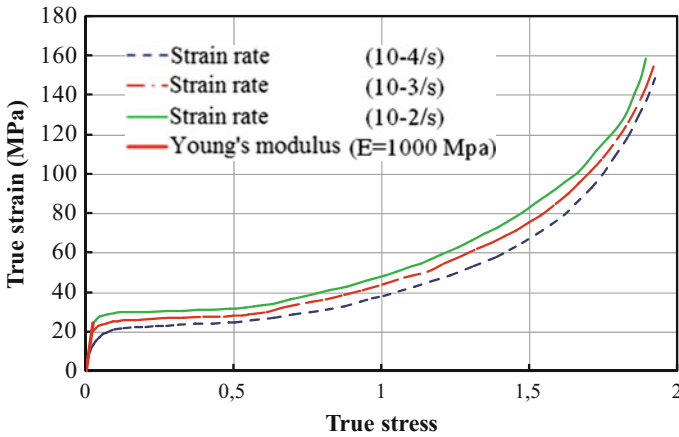
Fig. 5 Stress-strain curves used to define the material on Abaqus
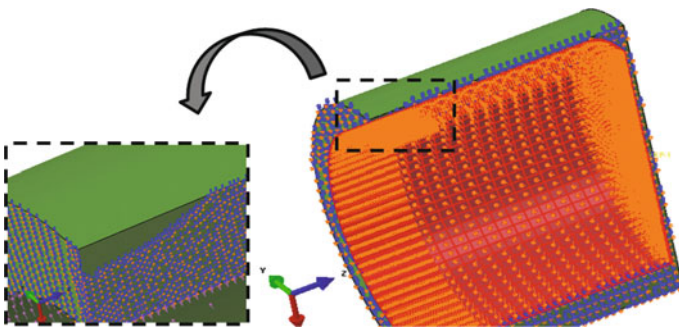
Fig. 6 The boundary conditions and the loading of the specimen
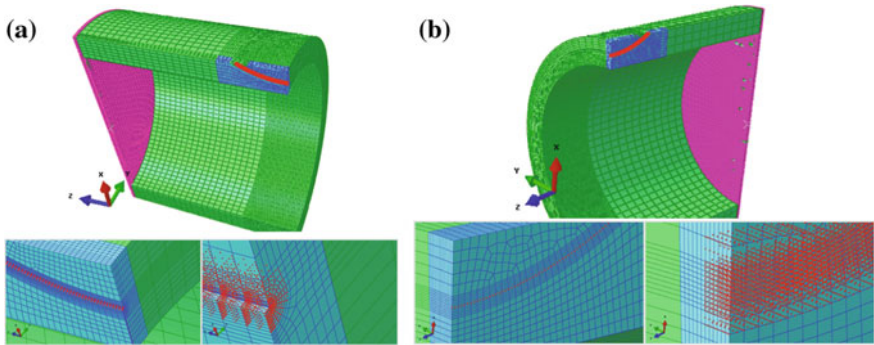
Fig. 7 3D mesh of a model with a defect: **a** notch **b** Pre-crack

3.3 Meshing

Since we are not interested to study the crack propagation after initiation, the damage criterion of the material is not introduced in the model.

The determination of the J-integral using the commercial FE software ABAQUS requires a particular mesh at the crack tip (Benhamena et al. 2010, 2011). The mesh is sufficiently refined near the crack tip to properly define the stress distribution at the bottom of the defect. Several elements surrounding the bottom of the defect (at the tip of the crack) were used to evaluate the contour integrals. These closed element contours are defined recursively to surround all previous contours. The first contour was the tip of the crack in the configuration of a pre-cracked pipe. On the other hand, with a notch, the first contour is defined by the notch bottom caused by the penetration of the disc cutter into the wall, Fig. 7. The direction of the virtual crack extension is defined by the normal to the plane of the crack.

3.4 Numerical Results

The evolution of the J-integral of the different contours, in the normal plane at the tip of the crack, has been studied for both configurations: pre-cracked and notched pipe, Fig. 8. The results converge toward saturation values from the 14th contour. This convergence proves that a good mesh has been adopted. Nevertheless, for notch depth 8 and 10 mm, the J-integral converges from the 14th contour at low loading. On the other hand, at large loading, the J-integral depends slightly on the integration contour. This dependence is due to the fact that the plastic zone (X_{eff}) is
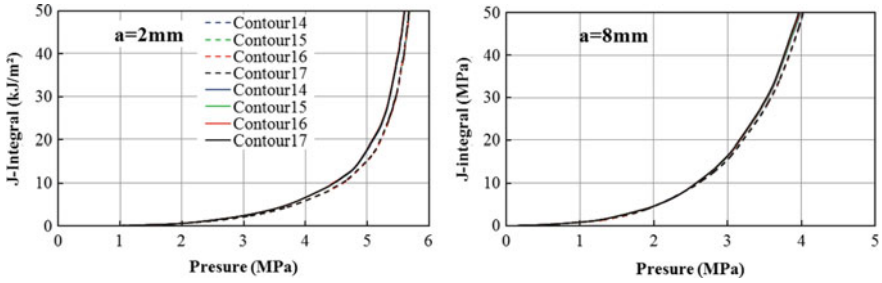
Fig. 8 Variation of the contour J integral with internal pressure (a = defect depth, interrupted line: pre-cracked pipe, continuous line: notched pipe)
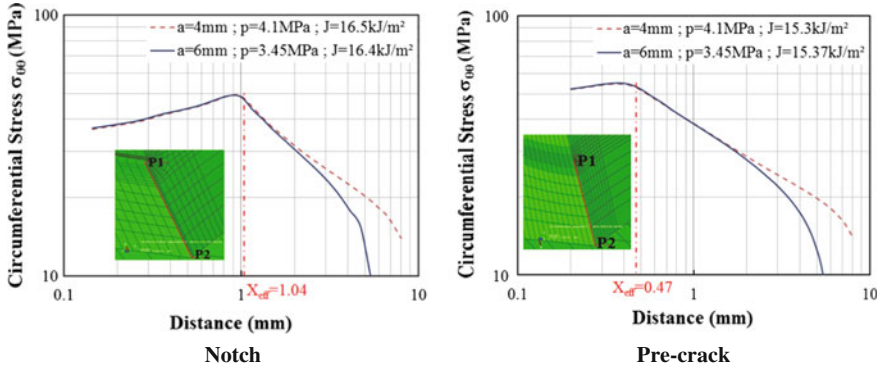
Fig. 9 Opening stress distribution along the ligament (P1 − P2)

well extended over the integration domain, Fig. 9. In this case, the value of J is evaluated on the contour furthest from the tip of the crack. The dissipation energy by plastic deformation must always be positive. Thus the calculated values of J increase monotonically with the size of the domain of evolution. Therefore, the highest value of J is the best approximation of the convergence value, [54].

Now, it is possible to observe the evolution of the stress distribution along the ligament with the J-integral variation. Based on these curves, Fig. 10, it is possible to discuss and justify the choice of the critical value of J. The appearance of a damage zone (crack tip hardening) appeared when the internal pressure reaches the values shown in Table 2, depending on the type of failure. By exceeding these pressures, the damaged area becomes more remarkable. Thus, for conservative reasons, the value of J corresponding to the appearance of the damage zone will be considered as the material resistance to crack initiation J_{IC} (toughness) (Guidara et al. 2015).
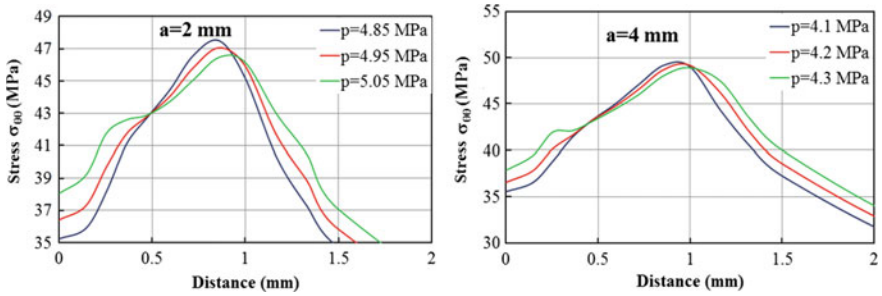
Fig. 10 Distribution of the circumferential stress ($\sigma_{\theta\theta}$) along the ligament

Table 2 J_{IC} value and crack initiation pressure, pa, as a function of the defect depth

	Defect depth a (mm)	2	4	6	8	10
Pre-crack	Pressure **pa** (MPa)	4.7	4	3.34	2.89	2.45
	J_{IC} (kJ/m^2)	11.1	13.9	14	13.9	12.2
Notch	Pressure **pa** (MPa)	4.95	4.2	3.55	3.02	2.5
	J_{IC} (kJ/m^2)	16.3	18.2	18.3	16.6	14.2
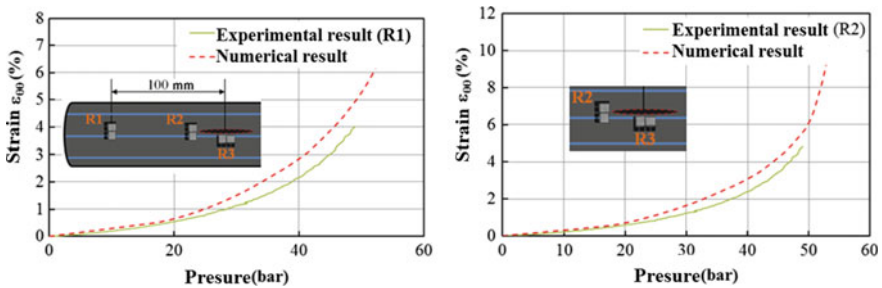
Fig. 11 Comparison of numerical results with experimental data of rosettes R1 and R2

4 Validation of the Numerical Results with Experimental Data

4.1 Strain Gage Rosette Data Analysis

- *Comparison with measurements of rosettes R1 and R2*:

There is a good agreement between the measured and calculated circumferential strains, Fig. 11. The observed error at high loading, over 20 bar, is due to the absence of a criterion of damage in the model (Zhang et al. 2015).

- *Comparison with measurements of rosette R3*:

The rosette R3 is glued near the defects the defect in the circumferential direction, perpendicular to the main axis of the notch. The strains calculated by finite elements are compared with those measured. We observe, Fig. 12, the good correlation between the calculated and measured longitudinal strain. The pipe wall is strongly deformed near the defect. Knowing that the size of the rosette is 10.7×11.9 mm, a low positioning error can disturb measurements of circumferential strain measurement, Fig. 12a.

4.2   Comparison with the Burst Pressures

The experimental burst pressure and the crack initiation pressure determined by finite elements are shown in Fig. 13. By exceeding the crack initiation pressure, the

(a) Circumferential strain $\varepsilon_{\theta\theta}$ (b) Longitudinal strain ε_{zz}
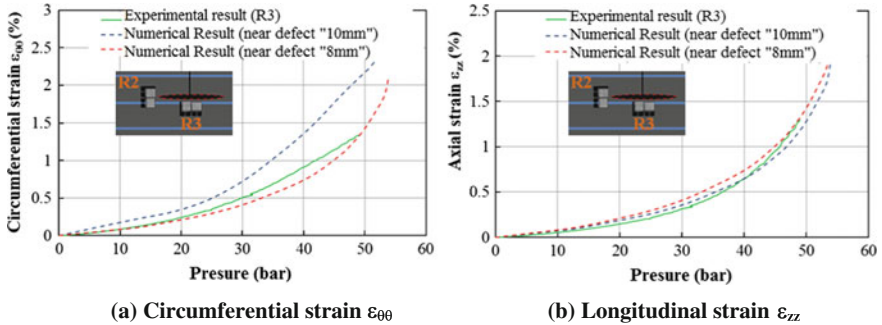
Fig. 12 Comparison of numerical results with experimental data of rosettes R3
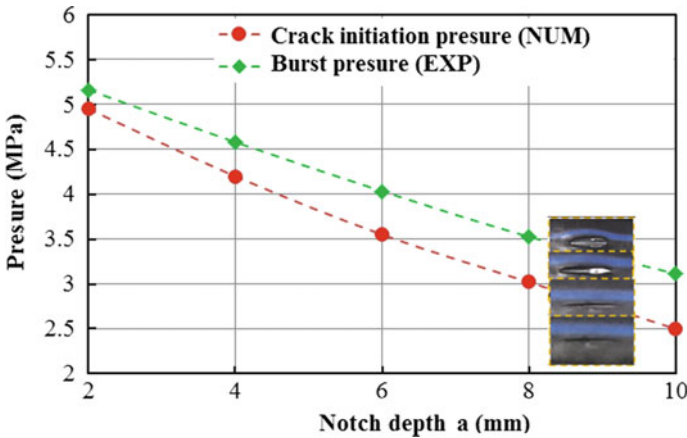
Fig. 13 Variation of the burst and crack initiation pressure as a function of the notch depth

damaged region becomes larger over time and the crack propagates rapidly until the pipe failures.

In a pipe with a shallow defect, a well-developed plastic deformation in the vicinity of the defect is observed and the pressure reaches an important value before the crack initiation. Therefore, the crack propagation is very fast and the time between crack initiation and pipe failure is reduced.

5 Conclusion

Burst tests on PE100 pipes were carried out in order to define the burst pressure according to the size of the defect. The pressure loading rate was found to be between 12 and 60 bar/min which has a negligible influence on the burst pressure. The circumferential strain, on the plane of crack, is more important than the longitudinal strain. However, on the perpendicular plane and close to the notch, the wall undergoes a large deformation in the longitudinal direction. This results in the formation of a "swelling." Using elasto-plastic modeling depending on the strain rate, we have demonstrated that the Elastic-Plastic Fracture Mechanics theory, the J-integral, can define with acceptable precision the cracking behavior of a PE100 pipe. The value of the J-integral at the time of appearance of the damage zone, plastic strain-hardening, is considered numerically to be the value of the toughness. This allowed us to define the pressure leading to the crack initiation.

References

Benhamena A, Bouiadjra B, Amrouche A, Mesmacque G, Benseddiq N, Benguediab M (2010) Three finite element analysis of semi-elliptical crack in high density poly-ethylene pipe subjected to internal pressure. Mater Des 31(6):3038–3043

Benhamena A, Aminallah L, Bouiadjra B, Benguediab M, Amrouche A, and. Benseddiq N (2011) J integral solution for semi-elliptical surface crack in high density poly-ethylene pipe under bending. Mater Des 32(5):2561–2569

Choi BH, Chudnovsky A, Paradkar R, Michie W, Zhou Z, Cham PM (2009) Experimental and theoretical investigation of stress corrosion crack (SCC) growth of polyethylene pipes. Polym Degrad Stab 94(5):859–867

Covas V, Stoianov V, Ramos H, Graham N, Maksimovic C (2004) The dynamic effect of pipe-wall viscoelasticity in hydraulic transients. Part I—experimental analysis and creep characterization. J Hydraul Res 42(5):517–532

Dallali M, Guidara MA, Bouaziz MA, Schmitt C, Haj-Taieb E, Azari Z (2015) Accuracy and security analysis of transient flows in relatively long pipelines. Eng Fail Anal 51:69–82

Duvall D, Edwards D (2009) Oxidative degradation of high density polyethylene pipes from exposure to drinking water disinfectants. ESI Report, File

Ghabeche W, Alimi L, Chaoui K (2015) Degradation of plastic pipe surfaces in contact with an aggressive acidic environment. Energy Proc 74:351–364

Guidara MA, Bouaziz MA, Schmitt C, Capelle J, Haj Taïeb E, Azari Z, Hariri S (2015) Structural integrity assessment of defected high density poly-ethylene pipe: burst test and finite element analysis based on J-integral criterion. Eng Fail Anal 57:282–295

Zhang Y, Ben Jar PY (2015) Quantitative assessment of deformation-induced damage in polyethylene pressure pipe. Polym. Test. 47:42–50

Plastic Behavior of 2024-T3 Under Uniaxial Shear Tests

Daghfas Olfa, Znaidi Amna, Gahbiche Amen and Nasri Rachid

Abstract The plastic anisotropy of a sheet is measured by performing tension tests as well as by shear tests in different loading directions. In this paper, the main objective is to model the behavior of a 2024 aluminum alloy from experimental simple shear tests from several directions relative to the rolling direction. First, an experimental device of simple shear tests and the studied material are described. Second, the experimental results in terms of hardening curves are presented on three loading directions. In order to further refine the experimental part of this work, microstructural observations were conducted through transmission electronic microscopy (TEM) to show interactions between the precipitates and dislocations in studied material. Finally, several hardening laws are used to describe the isotropic hardening such as Hollomon law, Voce law, and Bron law. By smoothing experimental hardening curves shear stress–shear strain a selection is made in order to choose the most appropriate hardening law to identify the anisotropic parameters of the studied material.

Keywords Aluminum alloy · Anisotropy · Simple shear test
Metal sheet · Hardening law

D. Olfa (✉) · Z. Amna · N. Rachid
University of Tunis El Manar, National School of Engineers of Tunis,
LR-MAI-ENIT BP37, 1002 Tunis, Tunisia
e-mail: daghfasolfa@yahoo.fr

Z. Amna
e-mail: Amna.znaidi@Laposte.net

N. Rachid
e-mail: rachidnasri2003@yahoo.fr

G. Amen
Mechanical Engineering Laboratory, National School of Engineers of Monastir,
Monastir, Tunisia
e-mail: amen.gahbiche@yahoo.fr

1 Introduction

The simple shear test is recognized as the second test after the simple tensile in the axes, which can be considered, with a good approximation, as homogeneous for certain geometries of specimens. In addition, it makes it possible to achieve fairly large plastic deformations without any localization of the deformation.

Several types of shear mounting have been developed: Miyauchi (1984), G'sell and Rauch (Genevois 1990) and Gary and Nowacki (Gary and Nai 1986).

The shear tests were carried out on a specific device developed by Gahbiche (2006) at the Mechanical Engineering Laboratory [LGM]. This device is an improved version of Miyauchi, Gary, and Nowacki. It is instrumented by an extensometer to measure the relative displacement of the two jaws which is a manifested advantage. It can be considered homogeneous and cyclic shear tests can be realized by reversing the direction of stress. The device is mounted on a tensile machine.

The Portevin Le Chatelier (PLC) effect has been observed in steels and aluminum alloys (Le Chatelier and Portevin 1923; Hopperstad et al. 2006). It is assumed that this effect is due to aging of mobile dislocations during the interaction between them and solute atoms diffusion (Van den Beukel 1975). The bibliography on this subject (Garat et al. 2008; Bouabdallah 2006) approach theoretical aspects as well as experimental ones. A common belief is that the PLC effect exists for tensile tests because of the homogeneous state of stress (Jaoul 2008; Matthieu and Samuel 2011). In fact, they also occur for simple shear curves which are the main basis of this work.

Three isotropic hardening functions are used in this study defined by the Hollomon law with two constants, the Voce law (1948) with three constants and Bron law (2004) with six parameters to be identified from experimental curves. The experimental results obtained are discussed and analyzed in relation to the microstructure of the studied alloy using the TEM.

2 Experimental

Material Testing

The material used in this investigation is an aluminum alloy (AA2024 in T3 condition) with structural hardening, in the form of a rolled sheet with 1.5 mm thickness. The composition of the studied material according to DIN EN 573 (Develay 1990) is given in Table 1. Young's modulus E is determined as 73 GPa

Table 1 Chemical composition of 2024-T3

	Si	Cu	Mn	Mg	Cr	Zn	Ti	Fe	Al
%	0.5	4.9	0.9	1.8	0.1	0.25	0.15	0.5	Remainder

Table 2 Heat treatment applied to 2024-T3

Solutionizing	Quenching	Pre-stretching	Maturation
495 °C (±5 °C)	Water < 40 °C	2%	Room T° > 4 days

with Poisson's ratio $\nu = 0.33$. Table 2 presents the heat treatment applied to 2024 alloy.

Form and dimensions of specimen test

The specimen of the shear test has two useful areas which are similar and their dimensions are $l_o = 28$ mm, $b_o = 3.3$ mm. The shape and the dimensions of specimen shear test are shown in Fig. 1. The thickness of sheet metal e_0 is equal to 1.5 mm.

Experimental set

Uniaxial Shear tests were performed on a specific device (Fig. 2a) developed by Gahbiche (2006) in the laboratory [LGM]. This device is instrumented by an extensometer for measuring the relative displacement of the two jaws.

The device is mounted on a tensile machine (Fig. 2b) with two jaws, one mobile and the other fixed, which clamp the test specimen. The tensile machine imposes the displacement on the mobile jaw in order to create the shear.

The two useful areas of the test specimen have rectangular shapes before the test (Fig. 3a). After the shear test (Fig. 3c), their shapes transformed into parallelograms knowing that the dimensions l_0 and b_0 remain constant.

Through the acquisition chain (Fig. 2b) the force F is recorded as a function of the relative displacement δ between the jaws.

From these results obtained during the shear test, it is possible to express:

- The shear stress τ which is defined as follows:

$$\tau = \frac{F}{l_0 \cdot e_0} \tag{1}$$

Fig. 1 Form and dimensions of shear test specimen

(a)   **(b)**
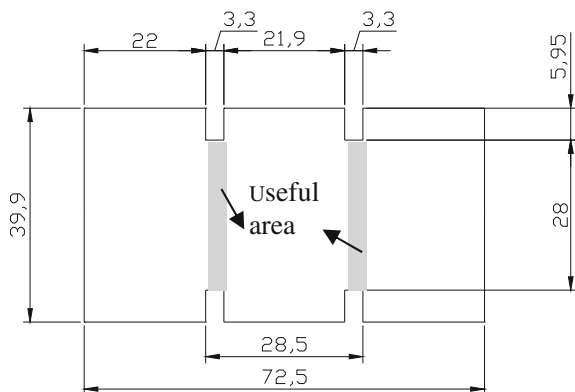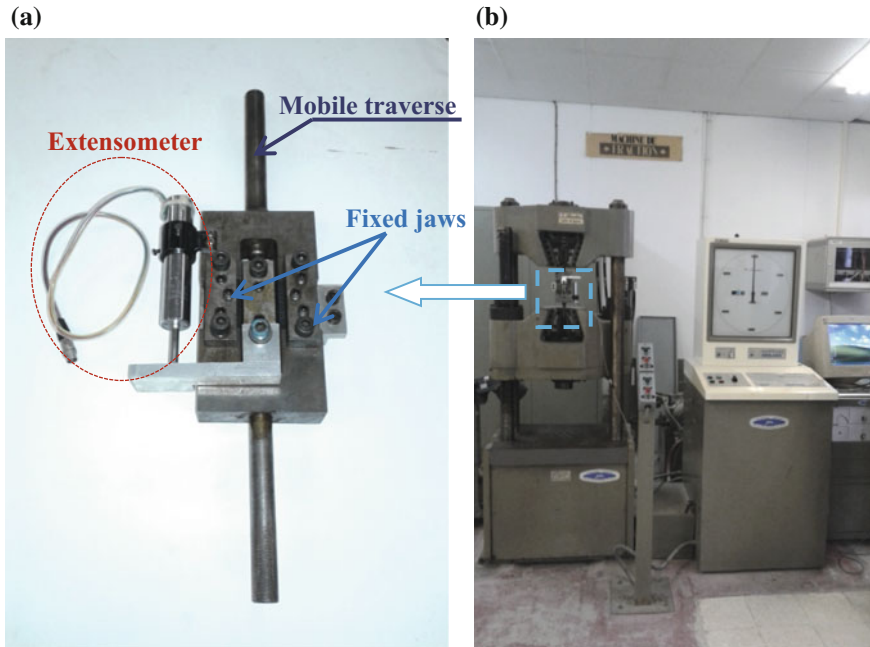
Fig. 2 a Specific device of shear test **b** Tensile machine and acquisition chain [LGM]

- The shear strain γ is written in the form:

$$\gamma = \frac{\delta}{b_0} \tag{2}$$

Microstructural characterization studies were conducted on specimens of 2024 aluminum alloy in rolling direction using a JEOL 2010 transmission electron microscope from the TEMSCAN in Toulouse. The samples about 3 mm diameter and 50 μm thick were obtained and were polished with abrasive papers and attacked with the reagent of the killer.

3 Phenomenological Hardening Laws

In the present work, a behavior model is used with different hardening laws. A brief description of their equations and the acronyms that will be used for these models in the presentation of the numerical results are given.

(a)

(b)

(c)
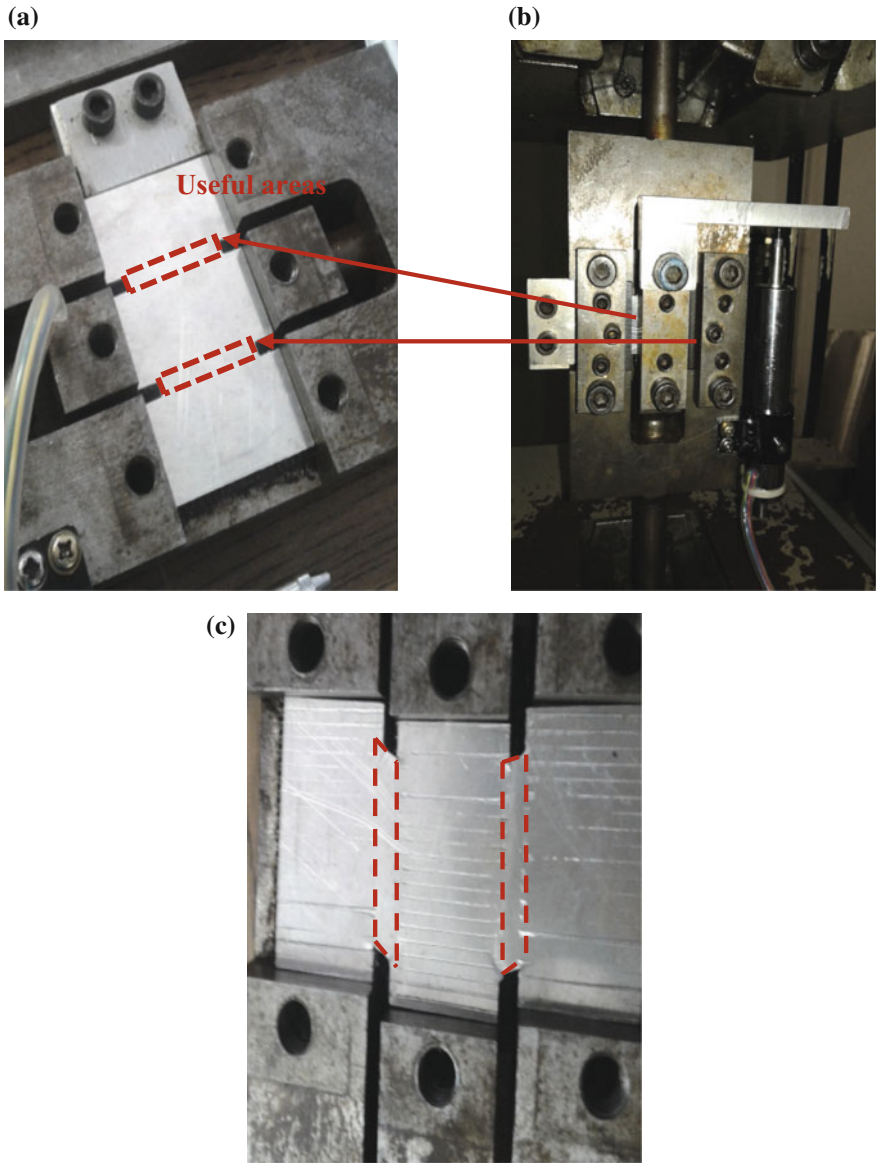
Fig. 3 Representation of test specimen **a** Before shear test **b** During testing **c** After shear test

Three classical isotropic hardening laws are selected from the literature to describe the plastic behavior of aluminum and its alloys:

(a) The Hollomon law (Holψ°):

Among the most used hardening laws in the literature is the power law named the Hollomon law. It describes very satisfactory the behavior of the pure aluminum in simple tensile (Znaidi et al. 2016).

$$\sigma_s(\varepsilon^p) = k(\varepsilon^p)^n \tag{3}$$

$\sigma_s(\varepsilon^p)$: Isotropic hardening function; where ε^p is the plastic strain.

This law is based on only two parameters k and n where n is strain hardening exponent.

(b) The Voce law (Voce$\psi°$):

The second law used is the Voce law or the saturation law. Its interest is to represent the change of regime between the linear elastic part and the hardening curve continuously through the use of an exponential.

$$\sigma_s(\varepsilon^p) = \sigma_y(1 - \alpha \exp(\beta\varepsilon^p)) \tag{4}$$

This law introduces a hardening saturation σ_y, α and β describes the nonlinear part of the curve during the onset of plasticity, where $0 < \alpha < 1$ and $\beta < 0$. It describes very satisfactory the hardening curves of the aluminum alloy 7075-T7 in a simple tensile test (Daghfas et al. 2017a, b).

(c) The Bron law (Bron$\psi°$):

This law is proposed by Bron (2004) with six parameters to be identified.

$$\sigma_s(\varepsilon^p) = \sigma_0[1 + K_0\varepsilon^p + K_1(1 - \exp(-k_1\varepsilon^p)) + K_2(1 - \exp(-k_2\varepsilon^p))] \tag{5}$$

It is a modified expression of the Voce law or it contains twice the expression (4). $\sigma 0$ is the yield strength; $K_1\ K_2$ is the hardening saturation; $k_1\ k_2$ is the description of the nonlinear part of the hardening curve.

4   Results and Discussion

Experimental results

Figure 4 presents the experimental shear curves for three loading directions.

Uniaxial shear curves for three directions from the rolling direction reveal the nature of anisotropy in this material especially in terms of ductility and shear strength that vary with orientation in the plane of the sheet.

It is seen that the shear test achieves more large plastic deformations than the tensile test (Daghfas et al. 2017a, b) without localization of deformation.

According to three loading directions, the slope of strain hardening is different which shows the anisotropy of studied material.
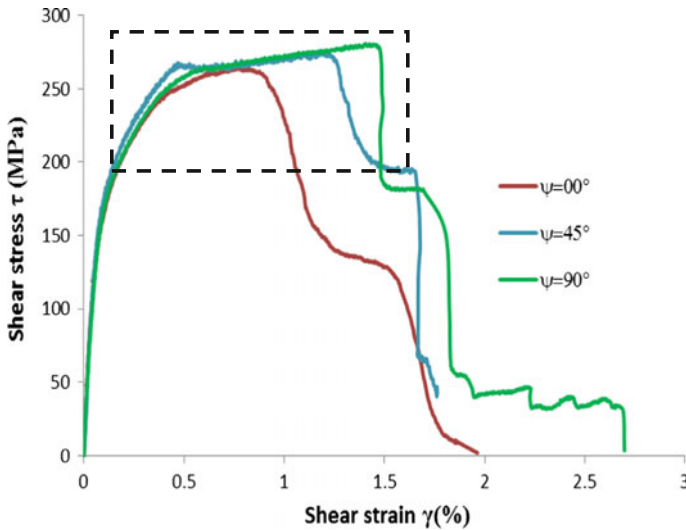
Fig. 4 Experimental shear stress-shear strain obtained at $\Psi = 00°$ $\Psi = 45°$ $\Psi = 90°$

It has high mechanical properties both in terms of strength and ductility in the transverse direction ($\psi = 90°$) compared to other loading directions ($\psi = 00°$ and $\psi = 45°$).

Figure 5 is obtained by zooming framed area of Fig. 4.

The Portevin–Le Chatelier Phenomenon (PLC) is observed (Fig. 5) which is one of the forms of heterogeneous plastic deformation. It occurs at the macroscopic scale, in the form of localized deformation bands. These experimental results obtained are discussed and analyzed in relation to the microstructure (Fig. 6) of the studied alloy using Transmission Electron Microscopy (TEM).

Figure 6 shows that the structure is heterogeneous with grains containing many dislocations. The rolling operation leads to a flattening of the grains and the distribution of the dispersoids in elongated strips along the rolling direction.

The presence of precipitates and dislocations are very important. This is due to the structural hardening by precipitation applied to the studied material. The dislocations are created during the prestretching operation (Table 2) conducted between quenching and maturation.

The interaction between dislocations and precipitates is realized according to the hardness of the precipitates. As the latter is harder than the matrix of the material the dislocations cannot penetrate the precipitates and shear them. So they are forced to bypass them.

It is noted that the enlargement of the separation between the precipitates deceases their resistance and facilitates their bypass by the dislocations.

Figure 6 shows their interaction which explains the presence of PLC phenomena.
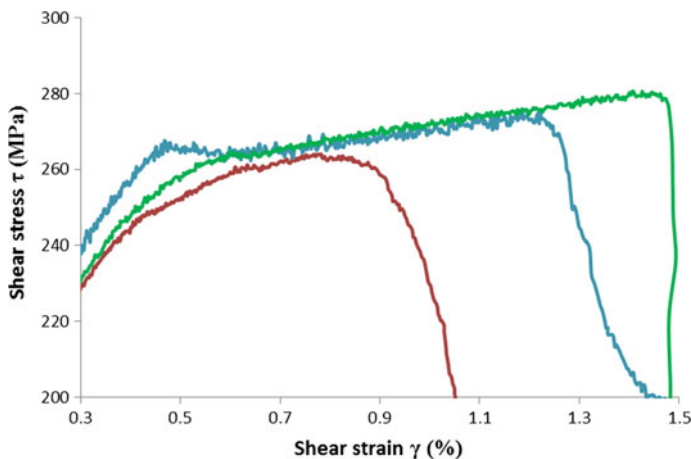
Fig. 5 Zoom of the framed area of Fig. 4
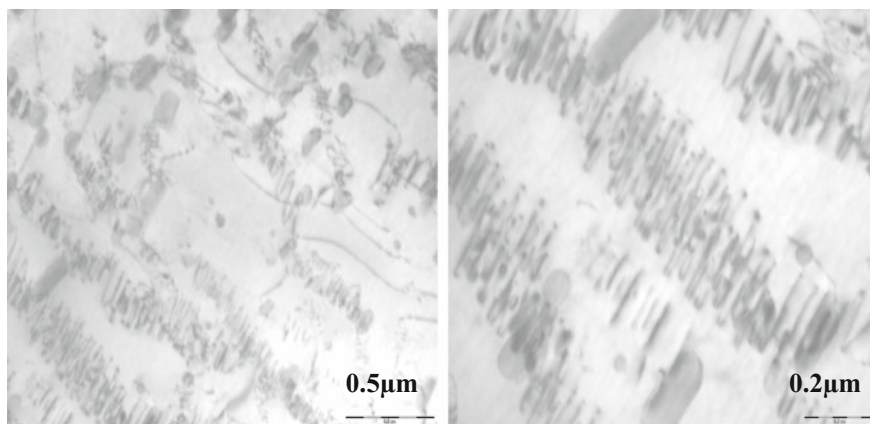
Fig. 6 Microstructure of dislocations in 2024-T3 specimen (TEM)

Identification results

From the experimental results, the hardening curves are fitted using the three laws presented above. These curves allow us to determine the parameters of the different laws (see Table 3) and to choose the most appropriate law to describe the plastic behavior of the studied alloy.

The smoothing returns to choose the parameters of hardening laws while minimizing the quadratic difference between the theoretical and experimental results. The classical hardening laws consist in the adjustment of their functions on experimental curves to identify the unknown parameters (Table 3).

Table 3 Identified parameters of different hardening laws

Laws	Parameters	00°	45°	90°
Hollomon	k	277.93	275.187	273.089
	n	0.1664	0.1245	0.137
Voce	σ_y	266.22	270.3698	275.3461
	α	0.6248	0.6456	0.6153
	β	−5.034	−5.9044	−4.4926
Bron	σ_0	31.65	35.5934	35.5576
	K_0	−0.5938	−0.0777	−0.3674
	K_1	1.4467	1.8006	1.71
	K_2	5.434	4.871	4.612
	k_1	4.9377	324.9938	135.7633
	k_2	8.3112	5.6576	5.4466

The identified curves by Hollomon, Voce, and Bron laws compared to the experimental shear curves obtained in the three loading directions relative to the rolling direction (00°, 45° and 90°) are presented in Fig. 7a, b and c, respectively.

In order to show the most suitable law for the identification of *shear Stress– shear strain curves*, a comparison between three hardening laws is made.
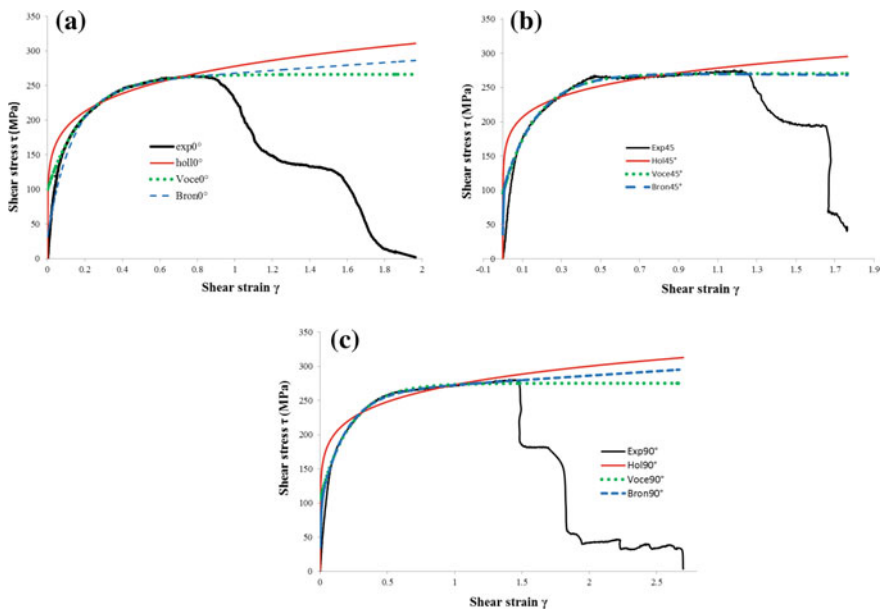
Fig. 7 Identification of the hardening curve: (a) $\psi = 00°$ (b) $\psi = 45°$ (c) $\psi = 90°$

It is seen that in the plastic deformation part the voce and the Bron laws describe better the hardening curves than the Hollomon law for all loading directions from the rolling direction.

Since the two laws give similar results, the Voce law with fewer parameters is selected subsequently to identify anisotropy behavior in the next work.

5   Conclusion

In this study, off—axis shear tests are carried on 2024 aluminum alloy through three loading directions from the rolling direction. These experimental results have allowed to investigate the mechanical properties and to identify the unknown parameters of different isotropic hardening laws. By comparing these latter laws, it is shown that Voce law and Bron law lead to a good description of the shear stress– shear strain curves. However, Voce hardening law may be sufficient to correctly describe the hardening of the aluminum alloy in uniaxial test. The Portevin–Le Chatelier phenomenon observed in hardening curves is explained by the interaction between dislocation and precipitates presented by images of transmission electron microscopy.

References

Bouabdallah K (2006) Caractérisation de l'effet Portevin-Le Chatelier dans les alliages aluminium magnésium - Apport des techniques d'analyse d'images. Mécanique [physics.med-ph]. Université de Savoie Français

Bron F (2004) Ductile tearing thin 2024 aluminum alloy sheets for aeronautical application. PhD thesis, National school of Mines of Paris

Daghfas O, Znaidi A, Ben Mohamed A, Nasri R (2017a) Experimental and numerical study on mechanical properties of aluminum alloy under uniaxial tensile test. Frattura ed Integrità Strutturale 39:271–282

Daghfas O, Znaidi A, Guahbiche A, Nasri R (2017b) Plastic behavior laws of aluminum aerospace alloys: experimental and numerical study. J Theor Appl Mech (In review)

Develay R (1990) Properties of aluminum and aluminum alloys (French) Technical Engineer. Report M440

Gahbiche A (2006) Caracterisation expérimentale des tôles d'emboutissage, application a l'identification des lois de comportement. PhD thesis, National School of Engineers of Monastir, Tunisia

Garat V, Cloue JM, Poquillon D, Andrieu E (2008) Influence of Portevin-Le Chatelier effect on rupture mode of alloy 718 specimens. J Nuclear Mater 375:95–101

Gary G, Nai K (1986) Description d'un essai de cisaillement simple. J de Physique IV-C8

Genevois P (1990) Étude expérimentale du comportement des tôles minces sollicités en chargements simples et complexes. Rapport IRSID, RI 91317

Hopperstad OS, Borvik T, Berstad T, Benallal A (2006) Finite element simulations of the Portevin-Le Chatelier effect in aluminium alloy. J Phys IV 134:435–441

Jaoul B (2008) Etude de la plasticité et application aux métaux. Réédité par Les Presses des Mines, Paris

Le Chatelier F, Portevin A (1923) Sur le phénomène observé lors de l'essai de traction d'alliages en cours de transformation. C R Acad Sci Paris 176:507–510

Matthieu M, Samuel F (2011) Le calcul de structures en présence de vieillissement statique ou/et dynamique d'alliages métalliques. 20ème Congrès Français de Mécanique, CFM 2011, Besançon, France

Miyauchi K (1984) A proposal of a planar simple shear test in sheet metals. Sci paper of IPCR 78

Van den Beukel A (1975) Theory of the effect of dynamic strain aging on mechanical properties. Phys Status Solidi 30:197. https://doi.org/10.1002/pssa.2210300120

Voce E (1948) The relationship between stress and strain for homogeneous deformations. J Inst Metals 74:537–562

Znaidi A, Daghfas O, Gahbiche A, Nasri R (2016) Identification strategy of anisotropic behavior laws: application to thin sheets of A5. J Theor Appl Mech 54:1147–1156

Optimal Work-in-Process Control
for a Closed Multistage Production System
with Machine Preference

**Bacem Samet, Florent Couffin, Marc Zolghadri, Maher Barkalla
and Mohamed Haddar**

Abstract In this work, we expose a closed-loop production system which has great similarity with the Kanban system as the Work-in-Process (WIP) is constant (CONWIP). This system is a multistage single product and it supports more than one machine at every stage. These machines can have different characteristics and they have limited capacity of buffering. We consider also that there is a preference for a machine usage in each stage. We use a Closed Queueing Network (CQN) with a repetitive blocking mechanism to model this system. The used resolution approach is the Maximum Entropy Method (MEM). In the first place, we look for the optimal WIP to keep in this system with respect to a production rate. In the second place, the routings to machines in the same stage are evaluated regarding the buffering capacity and the machine characteristic. We present some numerical results on a simple two-stage production system which holds the same number of batches looping. Interesting perspectives for the development of the presented model are looked over.

Keywords Closed queueing network · Work in process · Conwip
Entropy maximization · Multistage production system

B. Samet (✉) · F. Couffin · M. Zolghadri
Laboratoire QUARTZ, Institut Supérieur de Mécanique de Paris, Paris, France
e-mail: sametbacem@gmail.com

F. Couffin
e-mail: florent.couffin@supmeca.fr

M. Zolghadri
e-mail: marc.zolghadri@supmeca.fr

B. Samet · M. Barkalla · M. Haddar
Laboratoire de Recherche de Mécanique, Modélisation et Productique (LA2MP),
Ecole Nationale d'ingénieur de Sfax, Sfax, Tunisia
e-mail: bark_maher@yahoo.fr

M. Haddar
e-mail: mohamed.haddar@enis.rnu.tn

1 Introduction

Manufacturing industry tends to be highly competitive. Firms are faced with the strict requirements of the customers. There are preferences for some performance criteria such as quality of the product, respect of the delivery time, and the competitive price of the goods. Since the manufacturing system is expected to respond to all these demands, it's an obligation to respect the required quality and to supply the quantity demanded and to reduce the cost of production.

Complexity of the production system rises from two main factors. On one hand there is a stochastic nature of the attributes of the system which can be internal variables as the service time of the machine or the breakdown periods of the machine, and external variables as the quantity demanded by the customers and raw materials prices. On the other hand, the operations in this system are interconnected; for example, when the inventory is increased the production rate is impacted and the cost of the production too. So, there are compromises to set up to respect the customer demand with minimum cost.

Many studies have made a scope on the production system as a field of improvement and optimization. A particular type of production system; the multistage production system which presents a wide range of manufacturing system was analyzed in Muckstadt and Roundy (1993). In such systems, many actions can be carried out such as allocation of service load (or service rate) which is looking for optimal service rate in different machines in the production line system. For instance, in Hillier and Boling (1979), the optimal allocation of work is searched with respect to the number of work stations in the line, the limit on the amount of work-in-progress, and the variance of station operation times. The arrangement of stages which is ordering the stages so that the throughput is maximized is studied in Yamazaki et al. (1992). It is noted that in every stage there are a number of identical servers. Another problem addressing the assignment of servers was studied in Ding and Greenberg (1991), in which the single servers are optimally arranged for a tandem queueing system. The allocation of buffers problem which deals with searching the optimal buffering space in a production line to achieve a specific objective is surveyed in Yamazaki et al. (1992).

Reducing the quantity of WIP contributes to cost reduction by virtue of suppressing the costs of keeping useless inventories. The production control system is a very important leverage that should be well chosen to meet these performances. The CONWIP, a pull production control system, is defined as a system maintaining constant the maximum amount of WIP (Framinan et al. 2003). It was first time defined in Spearman et al. (1990) to minimize the WIP in a single product flow shop subject to a given throughput level. This same purpose was also conducted in Bonvik and Gershwin (1996) and Bonvik et al. (1997). These aforementioned works are simulation-based models. The queueing theory was exploited for analysis and performance evaluation. The application of the queueing theory was surveyed in Govil and Fu (1999). This analytical approach of modeling was considered in Gstettner and Kuhn (1996), particularly a closed queueing network with unlimited

queueing buffers was established for a CONWIP flow shop single product system and the optimal WIP with respect to a certain throughput level is sought.

We have noticed a limitation in the literature, lying in the study of a particular case which is the machine preference in every stage. This constraint was integrated into a scheduling architecture made in Fox and Smith (1984). It was also studied in Baskar and Anthony Xavior (2014) with the purpose to improve the percentage utilization of a priority machine. When there are differences in the machines in a stage, there would be a preference to totally occupy a machine than another. This preference can be due to the accuracy of the machine by making less defected products. Ordering machines for priority of usage can be made for greater service rate or broadly for the effectiveness of the particular machine.

The direction of this work is to determine the optimal quantity of WIP in the closed-loop multistage production system with taking in consideration a production level rate as a target and taking into account the limited capacity buffers. Furthermore, the machine preference in every stage is considered. We propose a CQN model with limited buffering and blocking for a flow shop multistage production where the number of batches in the system remains constant. This closed-loop production system can be ruled by a CONWIP control system since the quantity of WIP is the same. The remainder of this paper is organized as follows: in Sect. 2, we describe the under scope type of production system. In Sect. 3, we develop the CQN model for this system. In Sect. 4, we present the approximate resolution approach based on Entropy Maximisation. In Sect. 5, numerical results are exposed for a simple case. Finally, some interesting future developments for this model are revealed.

2 The Multistage Production System

The production system under study is a multistage flow supporting multiple machines in every stage. We consider the case when there is an order of preference for the machines in the same stage. This system is a closed loop and so the number of batches (WIP) circulating in the system remains the same. For instance, in Fig. 1, we expose a two-stage production system. In every stage, two parallel machines doing the same process and we presume a priority machine constraint for processing the job (i.e., priority of using M1 rather than M2 in stage 1 and priority of using M3 rather than M4 in stage 2). If the priority machine will be fully occupied and when its buffer is overloaded, the jobs are redirected to the other machine. We suppose having an Unloading/Loading (U/L) process closing the cycle of production. This process receives the full batches, empties them, and returns them empty to the flow line.

We seek to occupy maximally the priority machines (M1 and M3). In counterpart, there are constraints on the buffering capacity of such machines. As it is targeted to rout the maximum amount of jobs to M1 than to M2, for instance, the percentage of the quantity routed that fits in its buffering capacity should be found.
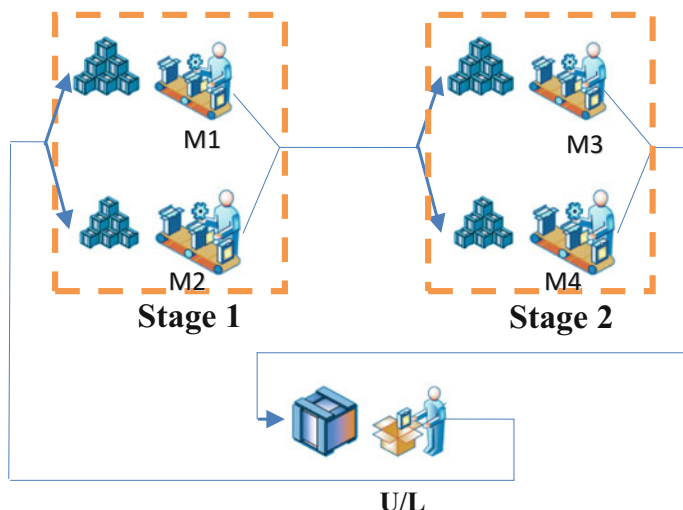
Fig. 1 Two-stage production system

The probability that a job is rejected by a full buffer of M1 indicates the convenience of the routing percentage. Keeping a production level with the minimum quantity of WIP is monitored by the throughput of the production system as a function of the WIP. So further in this work, the probability of being rejected in M1 and the throughput of the system are calculated thanks to the CQN. We present in the next section, this model with a blocking mechanism for this production architecture.

3 Closed Queueing Network Model with RS-RD Blocking

We consider L as the quantity of WIP. We model this system by a CQN with L jobs/customers presented in Fig. 2. Since every machine has a limited capacity buffer space, the queueing system supports a blocking mechanism defined as Repetitive Service-Random Destination (RS-RD). This blocking defines the mechanism of a job finished being served in a queue i and intending to enter a full buffer of a downstream queue j. In the RS–RD the job loopback to queue i to undergo a new service time and these dynamics are repeated until the job finds a free buffer space in a downstream queue to which it is routed (Bose 2002).

Every machine is modeled by a single server node (M_i) (for example, M1 and M2 in stage 1 in Fig. 1) with limited capacity buffering. We introduce in the upstream of every station a multi-server node (B_i) (for example, B1 in stage 1 and B2 in stage 2) which will play the role of the router of the job when the buffer of the downstream machine is overloaded. The number of the servers in (B_i) is L. In this
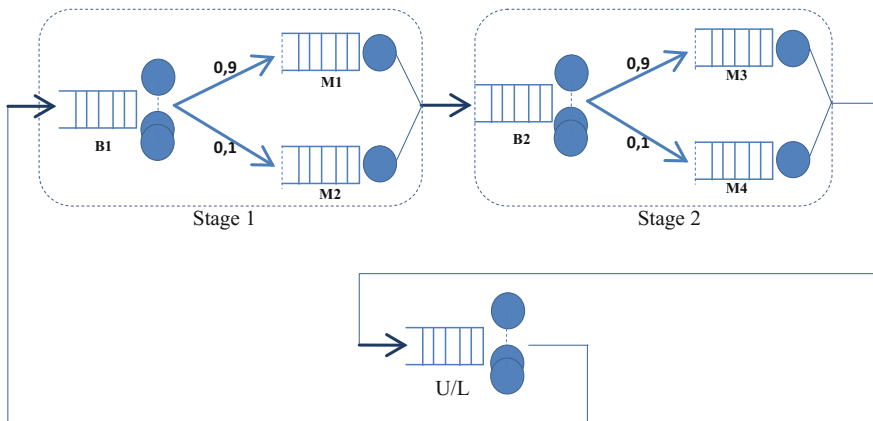
Fig. 2 Closed Queueing Network model for two-stage production system

manner, if all the jobs are directed to this type of node, they can be held there. In this type of node, the service time is taken very small compared to the service time of the machines. The service times of all the nodes have a general distribution which can be defined by a mean time (μ_i) and a squared coefficient of variation (sqv_i) in node i. The routing matrix is a key element which defines the probabilities between the nodes of the network (e.g., see Fig. 2 for the routing between B1 and M1). This CQN has the underlying state space:

$$S = \{(n_1, \ldots, n_M): \sum_{i=1}^{M} n_i = L, 0 \leq n_i \leq L_i, i = 1, \ldots, M\} \tag{1}$$

With n_i is the number of jobs in the node i and L_i is the capacity of the node i. The resolution of a queueing network is the establishment of the steady state probability of occurrence of this state. In the underlying section, we describe the resolution approach.

We exploit the MEM for solving such a CQN. This method seeks to attribute the same chances of occurrence for every state, with respect to normalization and some marginal constraints (Kouvatsos and Xenios 1989). The Entropy function (Eq. 2) is maximized subject to the related constraints. We refer to (Kouvatsos and Xenios 1989) for the details of this resolution.

$$H_p(n) = - \sum_n p(n) \log p(n) \tag{2}$$

The Lagrange multipliers resolution method gives a product form solution of the CQN. This product form establishment allows facilitation to the network resolution. In the case of an open network with Repetitive-Service Blocking (Kouvatsos and Xenios 1989), the product form is established and afterward the probability of a

state of the network is calculated through the marginal probability of the queues in isolation.

The resolution of the CQN goes through two main steps. The first step is about the resolution of the pseudo-open network corresponding to the CQN. It is an open network of queues with no arrival nor departure of jobs and it has the same parameters (service time characteristics and routings) of the CQN. The network is decomposed to deduce the mean rates and the squared coefficient of variations of the general distribution of both the service times and the inter-arrival times in the nodes. The MEM is applied then individually to these queues. The second step of resolution consists of injecting the Lagrange coefficients of the ME solution for individual queues deduced from the first step to the CQN. An iterative convolution algorithm is used to find marginal probabilities of the CQN. And finally, a correction of several parameters (Lagrange coefficients of the pseudo-open network) is done to insure that the throughputs respect the flow balance equations (Eq. 3).

$$X_i = \sum_{j=1}^{M} \alpha_{ji} X_j \qquad (3)$$

With X_i is the expected throughput of node i and α_{ij} the routing probability from node i to node j.

The outputs of this resolution are probabilities of the states (of the set S). In our case, we seek two performance indicators as outputs of this algorithm: the production rate of the production system which is the throughput of the Unloading/Loading machine and second, the blocking probability entering to a particular machine.

4 Numerical Results

In this section, the system presented in the queueing model in Fig. 1 is evaluated. The service times are generally distributed with rates and squared coefficient of variation indicated in Table 1. The production rates of the priority machines (M1, M3) are higher than the other machines to imply the quality of rapidity in these machines. The squared coefficient of variation (sqv = 1) characterize an exponential distribution for the service time.

Table 1 Service time characteristics

Nodes	General distribution	
	Rate of the service time	sqv
M1, M3	0.5	1
M2, M4	0.4	1
B1, B2	60	1
Unload/load	60	1
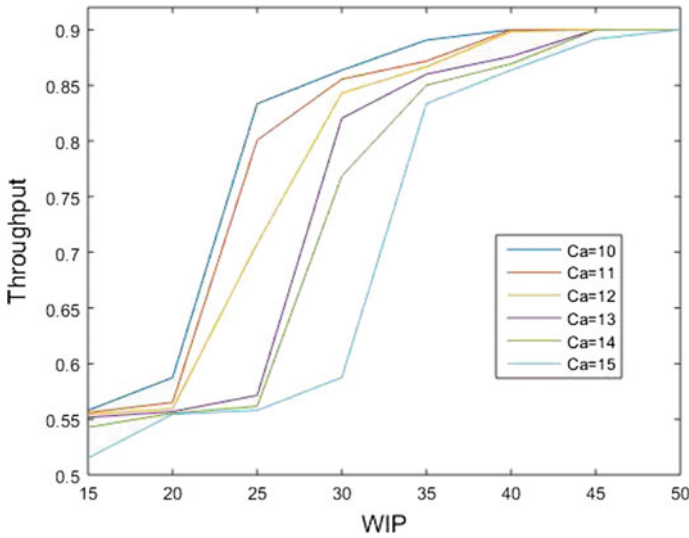
Fig. 3 Throughput as a function of the WIP

Buffer capacity of M_2 and M_4 is taken sufficiently larger (capacity M2 = 14) than those of the priority machines. From the resolution, we first sketch the production rate of the system which is the throughput of the (Unload/Load) process (Fig. 3). And second, we exploit the steady state blocking probability entering to M1 (Fig. 4) which is an indicator of the choice of the routing of jobs in the machines of stage 1.

In Fig. 3, we present the evolution of the throughput of the system as the circulating WIP increases. This evolution is sketched for different capacities of M1 and M3 (with capacity M1 = capacity M3 = ca). So every curve corresponds to a certain capacity. To have a particular throughput level (e.g., 0.8 (job/h)), the quantity of WIP that should be kept in the system is deduced (e.g., it's sufficient to keep 23 jobs in the network for ca = 10).

From Fig. 4, the amount of jobs that can be blocked trying to enter M1 is deduced, for e.g., we know that almost 10% of jobs entering to M1 (when the WIP = 23 and for ca = 10) are blocked so with such buffer size of M1 it is advised to rout only 90% of jobs to M1 and the rest to M2. The same reasoning can be conducted to machines of stage 2.

These presented curves show a coherence of the results of this model. Then the presented model and the used analyses indicators tend to be a useful decision tool for the under-study production system.
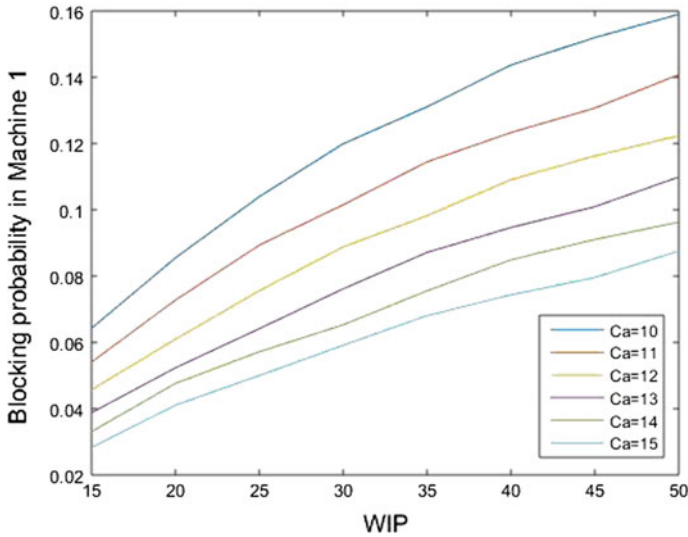
Fig. 4 Blocking probability in M1 as a function of the WIP

5   Conclusion

A simple multistage CONWIP flow shop production system for a single product is modeled by a closed queueing network supposing RS-RD blocking mechanism. This model gives an insight into the system dynamics and performance analysis regarding control and design changes are possible. The underlying queueing framework was exploited to look for the routings to machines when a preference for a machine use is present in a stage. The optimal number of WIP is sketched regarding a target throughput or the maximum reachable throughput.

Other performance indicators can also be calculated, thanks to this model, as the mean response time being enqueued in a machine or the mean number of jobs in a station.

The generalization to a multiproduct closed system is interesting as a further development for more general cases. Introducing the batch processing, breakdown delays for the service and set up delays between different products workloads can also be valuable. Another perspective is to add the fork/join nodes in the network for more generalization to study assembly lines.

References

Baskar A, Anthony Xavior M (2014) Optimization of makespan in job and machine priority environment. Procedia Eng 97:22–28. doi:10.1016/j.proeng.2014.12.220

Bonvik AM, Gershwin SB (1996) Beyond Kanban: Creating and analyzing lean shop floor control policies. In: Manufacturing and service operations management conference proceeding. http://w3.mit.edu/manuf-sys/www/amb.msom040496.pdf

Bonvik AM, Couch CE, Gershwin SB (1997) A comparison of production-line control mechanisms. Int J Prod Res 35(3):789–804. doi:10.1080/002075497195713

Bose SK (2002) An introduction to queueing systems, 1st edn, Kluwer Academic/ Plenum Publishers, New York. doi:10.1007/978-1-4615-0001-8 ISBN

Ding J, Greenberg BS (1991) Bowl shapes are better with buffers-sometimes. Probab Eng Inf Sci 5(2):159. doi:10.1017/S0269964800001996

Fox MS, Smith SF (1984) ISIS–A knowledge-based system for factory scheduling. Expert Syst 1(1):25–49. doi:10.1111/j.1468-0394.1984.tb00424.x

Framinan JM, González PL, Ruiz-Usano R (2003) The CONWIP production control system: review and research issues. Prod Plan Control 14(3):255–265. doi:10.1080/0953728031000102595

Govil MK, Fu MC (1999) Queueing theory in manufacturing: A survey. J Manuf Syst 18(3):214–240. doi:10.1016/S0278-6125(99)80033-8

Gstettner S, Kuhn H (1996) Analysis of production control systems kanban and CONWIP. Int J Prod Res 34(11):3253. doi:10.1080/00207549608905087

Hillier FS, Boling RW (1979) On the optimal allocation of work in symmetrically unbalanced production line systems with variable operation times. Manag Sci 25(8):721–728

Kouvatsos DD, Xenios NP (1989) MEM for Arbitrary Queueing Networks with Multiple General Servers and Repetitive-service Blocking *, *10*, 169–195

Muckstadt JA, Roundy RO (1993) Handbooks in operations research and management science. logistics of production and inventory. In: Graves SC, Rinnooy Kan AHG, Zipkin PH (eds) Logistics of production and inventory, vol 4, North Holland. doi:10.1016/S0927-0507(05)80182-3

Spearman ML, Woodruff DL, Hopp WJ (1990) CONWIP, a pull alternative to kanban. Int J Prod Res. doi:10.1080/00207549008942761

Yamazaki G, Sakasegawa H, George JS (1992) On optimal arrangement of stations in a tandem queueing system with blocking. Manag Sci 38(1):137–153. http://www.jstor.org

Brittle Fracture: Experimental and Numerical Modeling Using Phase-Field Approach

Hamdi Hentati, Yosra Kriaa, Gregory Haugou and Fahmi Chaari

Abstract Crack paths prediction is one of the most challenging of fracture mechanics. The difficulty in this seek is how to obtain numerical models able of predicting unknown crack paths. One of these models is called the phase-field approach. It represents cracks by means of an additional continuous field variable. This model approximates a sharp crack with a diffuse crack phase-field where a characteristic length regularizes the crack topology and a crack energy density describes the energy dissipated in order to break a brittle piece. This method avoids some of the drawbacks of a sharp interface description of cracks. The phase-field model for brittle fracture assumes quasi-static loading conditions. However, dynamic effects have a great impact on the crack growth in many practical applications. Therefore, this investigation presents an extension of the quasi-static phase-field model for the fracture to the dynamic case. Experiment tests will be presented in this work in order to study the efficiency and the robustly of phase-field approach for modeling brittle fracture and capturing complex crack topologies.

Keywords Phase-field model · Experimental tests · Dynamic fracture

1 Introduction

Fracture mechanics methods are used to predict nucleation and propagation of cracks in different kinds of materials. Since crack extension can lead to total failure of a technical component, fracture mechanics plays an important role in the design process of structural components. Cracks propagation result from failure processes

H. Hentati (✉) · Y. Kriaa
LA2MP Laboratory, National School of Engineers of Sfax, University of Sfax,
Sfax, Tunisia
e-mail: hamdi.hentati@yahoo.fr

G. Haugou · F. Chaari
LAMIH UMR CNRS/UVHC 8201, UVHC Le Mont Houy, 59313
Valenciennes Cedex 9, France

1061

on the micro scale, such as the breaking of atomic bonds and they are treated also from a macroscopic point of view in classical fracture mechanics.

Fracture criteria are based on the evaluation of continuum mechanical quantities like stresses and strains in the front of cracks. Crack propagation is always preceded by inelastic processes in the fracture zone. But, in linear fracture mechanics, it is assumed that the material response is linear elastic up to the point of failure. Since these processes cannot be described by the means of linear elastic theory, linear elastic fracture mechanics is only appropriate. This hypothesis may be accepted in the case of brittle materials, the zone where the material response is inelastic is negligibly small compared to the macroscopic dimensions of the sample. An important failure criterion of linear elastic fracture mechanics was established by Griffith (1921). In his energetic criterion, the fracture is interpreted as the result of a competition between the elastic energy and the so-called surface energy which is needed to create new fracture surfaces. A crack propagates, when this is energetically favorable. The work at hand deals with a phase-field model for fracture, which bases on the same energetic principles. Despite the important contribution of the Griffith's theory, it has some shortcomings detailed by Francfort and Marigo (2002).

Recently, the fracture mechanics has been revisited and a variational theory was developed end was studied initially by Bourdin et al. (2008) aiming to model brittle fracture. Inspired by this approach, phase-field models of brittle fracture were developed. There are few experiment results which are elaborated and compared with numerical models of brittle fracture. The efficiency of the phase-field modeling of brittle fracture has been analyzed by Ambati et al. (2015), Hentati et al. (2015, 2016). At the numerical level, a fracture controlled staggered scheme was derived by systematic decoupling of the path following controlled elasticity and phase-field problems (Miehe et al. 2010a; Borden et al. 2012; Msekh et al. 2014). A monolithic scheme, where displacement and damage fields are simultaneously solved, was recently developed. The coupled problem was used in Miehe et al. (2010b), Gerasimov and De Lorenzis (2016). The coupled schema suffers from lack of robustness, with loss of iterative convergence already at early stages of the crack development. The need for this solution was motivated based on a thorough analysis of the computational cost of the decoupled scheme which is very robust due to the convexity of the free energy functional $E(u, \alpha)$ with respect to each of the two unknown fields separately.

Otherwise, there have been several attempts to adapt phase-field models to dynamic fracture problems (Bourdin et al. 2011; Hofacker and Miehe 2012; Borden et al. 2012; Hentati et al. 2013; Schlüter et al. 2014). The numerical solution of the dynamic problem requires spatial and temporal discretizations. The efficiency of the numerical method using the finite element method with the Newmark scheme for simulating dynamic crack propagation in brittle materials was demonstrated by Hentati et al. (2013).

The phase-field models of brittle fracture are studied for a series of numerical test cases. Then, after extending the variational approach to dynamic model for the

phase-field approximation, we seek in this work to elaborate experiment tests in order to be used to prove the efficiency of the dynamic phase-field model.

2 Phase-Field Modeling of Brittle Fracture

2.1 Phase-Field Models of the Variational Description of Fracture

In the phase-field models, fracture is indicated by a scalar order parameter, which is coupled to the material properties in order to model the change in stiffness between broken and undamaged material. Where the material is undamaged, the order parameter has the value zero and the material properties remain unaltered. Broken material is characterized by the value one and the stiffness of the material is reduced accordingly. Thus, in the phase-field model, cracks are represented through lines or areas in the material, where the order parameter has the value one and the stiffness is significantly reduced. Consequently, a crack does not need to be treated as a material boundary, which is especially advantageous for the finite element imple-mentation of the fracture model. At interfaces between broken and undamaged material, the order parameter interpolates smoothly between the values assigned to the different material phases. The width of this transition zone, which surrounds the phase-field cracks, is controlled by a regularization parameter. We consider an arbitrary body $\Omega \subset \Re^n$ (with n = 1; 2; 3) with external boundary $\partial\Omega$ and internal discontinuity boundary Γ (see Fig. 1a).

Fig. 1 a Schematic representation of a body Ω with internal discontinuity boundaries Γ. **b** Approximation of the internal discontinuity boundaries by the phase-field $\alpha(x, t)$
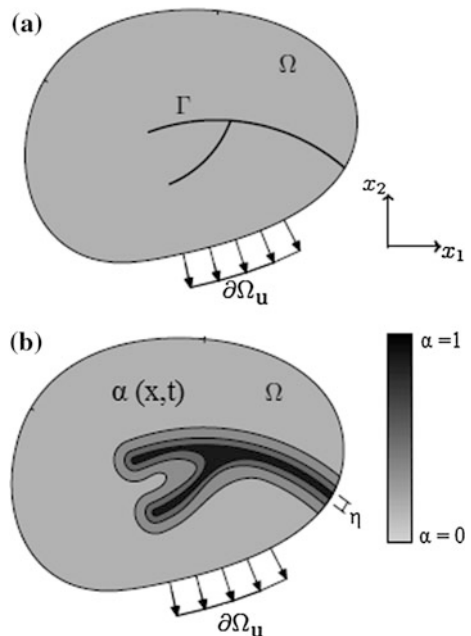
The displacement of a point x at time t is denoted by u(x, t). In order to circumvent the problems associated with numerically tracking the propagating discontinuity representing a crack, we approximate the fracture surface, Γ, by a phase-field, α(x, t). The value of this phase-field is equal to 0 away from the crack and is equal to 1 inside the crack (see Fig. 1b). For the considered fracture model, it can be shown that the underlying energy expressions converge to the elastic and surface energy of Griffith's formulation in the limit of a vanishing regularization length. In this respect, the phase-field fracture model may be interpreted as a regularization of Griffith's fracture criterion. Then, for any displacement and crack configuration, one defines the total energy:

$$E(u,\Gamma) = P(\varepsilon(u)) + G_c H^{N-1}(\Gamma) \tag{1}$$

where P(e(u)) denotes the elastic energy of the considered piece subject to a displacement u and cracked along Γ; $H^{N-1}(\Gamma)$ denotes the $N-1$ dimensional Haudorff measure of Γ, i.e., its length in 2D and its surface area in 3D; $\varepsilon(u)$ is the strain field. The Γ-convergence propriety implies that the minimizing solution to the regularized functional E(ε (u), α) will converge to a minimizing solution of the total energy as the regularized term η goes to zero. The regularized functional is defined by:

$$E(\varepsilon(u),\alpha) = \frac{1}{2} \int \left((1-\alpha)^2 + \kappa_\eta\right) \varepsilon : C : \varepsilon \, dx + G_c \int \left(\frac{\alpha^2}{4\eta} + \eta |\nabla\alpha|^2\right) dx \tag{2}$$

where x is the spatial coordinate and C is the standard isotropic Hooke's elasticity tensor. In order to perform numerical simulations, the phase-field model has been implemented into a finite element code. In addition to the displacement vector, the phase-field order parameter is treated as a supplementary nodal degree of freedom. Since the phase-field formulation avoids the occurrence of discontinuities in the displacement and crack fields, the implementation is not very complex and usual linear shape functions can be used for the interpolation of the nodal values within the elements. Numerical simulations show, that as well as the scope of classical Griffith's theory, the phase-field model is able to reproduce many phenomena which can be observed experimentally during fracture processes. This includes the branching of preexisting cracks as well as the nucleation of new cracks in originally undamaged material. The simplicity and generality of the phase-field approach, together with a reasonable quality of the results in the sense of a continuum fracture model, makes the method attractive for practical applications. Another aspect that is addressed is the phenomenon of crack nucleation in originally undamaged material.

2.2 Numerical Results of the Phase-Field Model

Numerical simulations have been performed with fixed displacement increments throughout the simulation. Two examples were chosen, the first one is a square specimen containing a straight notch located at mid-height on the left edge with one circular notch and the second one is a rectangular piece with three circular notches. The quasi-static computational crack paths are shown in Fig. 2. We note that all of the studied material are expected to behave linearly elastic until brittle fracture occurs.

Examples illustrated in Fig. 2, show the sensibility of the geometry and material parameters on the crack pattern. For that, it is very interesting to make experiment tests in order to validate numerical results. In this context, a few recent works try to make quasi-static tests suck as tensile and shear ones on simple geometry to make a comparison between the experiment and numerical results especially in terms of crack pattern. Recently, there are some tentative to extend the quasi-static phase-field model to dynamic one. In order to improve the understanding of the
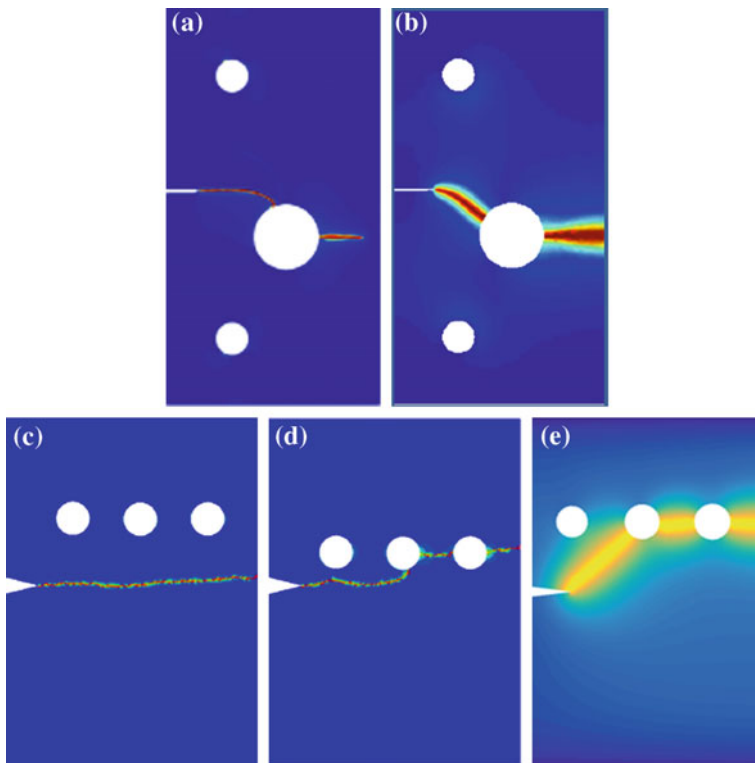
Fig. 2 Computed phase-field path in quasi-static case: **a** material is cement mortar (Ambati et al. 2015); **b–e** Young modulus E = 220 GPa; **c–d** Young modulus E = 18 GPa (Msekh et al. 2014)

derived phase-field model and to illustrate its capabilities to reproduce complex features of dynamic fracture, series of numerical experiments were elaborated. But some differences between numerical results were deduced. In fact, we will show in the following an example. Computed crack phase-field is illustrated in Fig. 3. Dynamic crack growth phenomenon is the instability of a very fast moving crack in brittle materials. This manifests in the occurrence of a number of micro-branches which is accompanied by a change in the structure of the crack surface, acoustic emission and oscillations of the crack speed. Finally, this process can result even in macroscopic crack branching. Some dynamic computational crack paths are shown in Fig. 3. The specimen contains a crack and it is subjected to a symmetric traction load applied on the upper and lower edges.

Based on crack branching patterns between different materials on glass under higher loading conditions, the prediction of a branching angle is different. Also, there are different values of the critical branching velocity. One of the parameters which has an effect on the numerical result is the regularized one η. In fact, it should be reminded that the regularized parameter does not play only the role of determination of the maximal stress; it contributes also qualitatively to the separation of the outside linear elastic fracture mechanics problem and the inside crack tip problem. A smaller internal length implies a wider region outside the crack where the fracture mechanics theory may apply. Then, a size effect is introduced via this internal length as it influences the stability of a structure. We admit that the choice of this parameter is not a simple one and may constitute one of the difficulties in the phase-field modeling of fracture problems. For that, in the absence of experimental results, it is difficult to judge which numerical result is more physically relevant. However, as proved by Msekh et al. (2014), current numerical examples show a highlights the important strength of the phase-field approach, specifically that the initiation of a crack does not require the introduction of a notch, and that a crack may initiate anywhere within the geometry of a given piece.
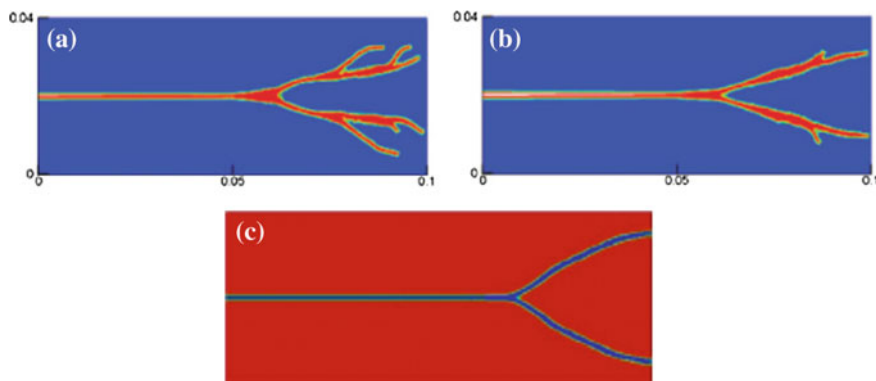
Fig. 3 Computed crack phase-field in dynamic case: **a** soda-lime glass (Ha and Bobaru 2010); **b** duran glass (Ha and Bobaru 2010); **c** nondimensional analysis (Schlüter et al. 2014)

3 Experimentation for Validation of the Phase-Field Model

In this section, we will try to present some experiment results from literature used in order to discuss the efficiency of quasi-static phase-field model. Also, we will present a dynamic test which will be used to study the dynamic crack propagation in brittle materials.

3.1 Quasi-Static Tests

Actually, there are some attempts to validate the phase-field models based on experimentation in quasi-static regime. In fact, Ambati et al. (2016) have made static tensile tests on specimen which was performed for aluminum. The displacement rate was set to 0.5 mm/min, with the displacement measured by a clip-on gauge. Also, Ambati et al. (2015) have made static tensile tests. The material used was cement mortar. The material is considered as a brittle material. We may use a quenched non-alloy steel specimen which is expected to behave linearly elastic until brittle fracture occurs. It is used for different tensile tests in order to prove the accuracy of the phase-field model using the staggered scheme.

These tests, shown in Fig. 4, were used in order to compare the numerical results of crack propagation obtained by the phase-field models and experimental tests. An interesting analysis was made and relevant results were founded.

3.2 Dynamic Test

The instruments commonly used to measure high-speed mechanical behavior are a split Hopkinson bars and a high-speed hydraulic actuator. We have conducted a series of experimental tensile tests using a high-speed hydraulic actuator. It can scan a wide range of strain rates and respond to high-speed test requirements. Image correlation technique coupled with high-speed cameras allow the displacement and strain fields measurement with frame rates ranging from 3000 to 25000 images/sec.

Example of the experiment results is shown in Fig. 5. The crack occurred at the level of a notch and it propagates suddenly straight without taking into account other stress concentration.
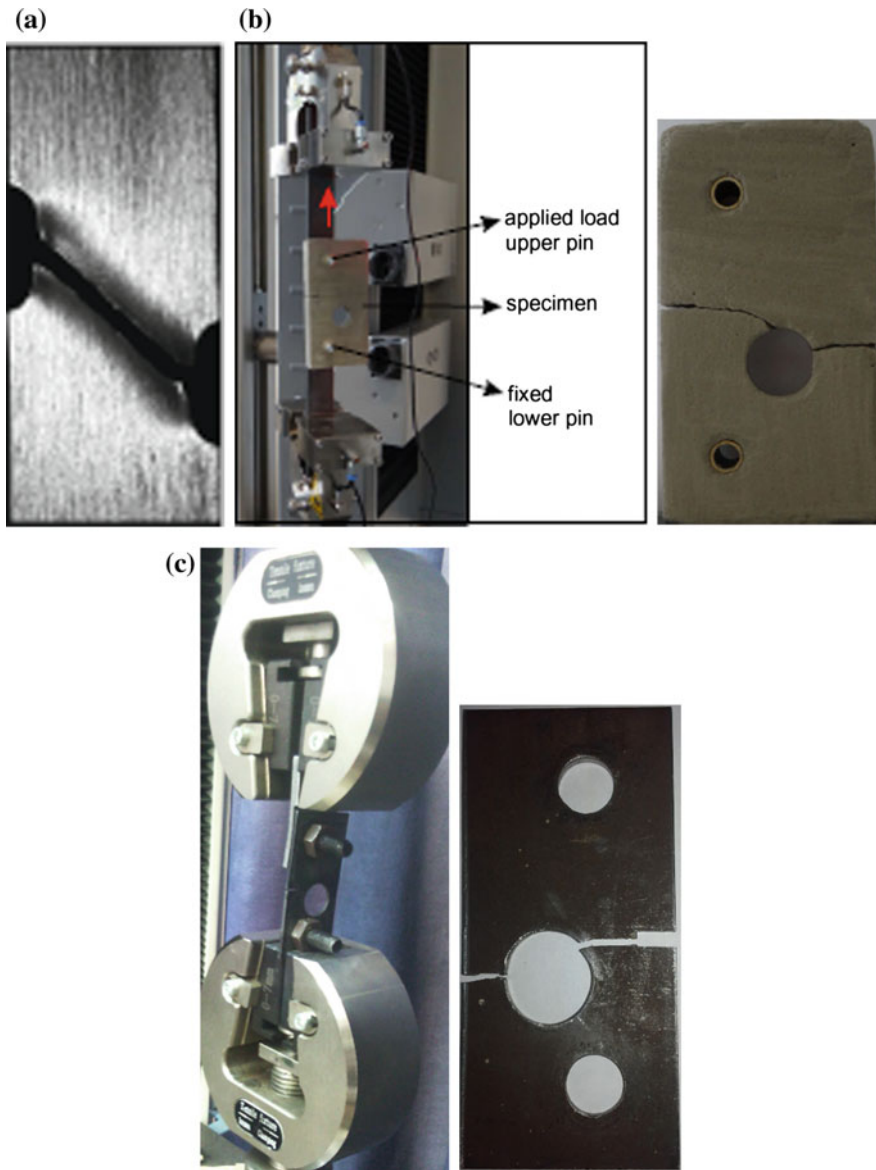
Fig. 4 Experimental observations: **a** ductile material (Ambati et al. 2016) **b** cement mortar (Ambati et al. 2015) **c** quenched non-alloy steel

Fig. 5 Experimental observation of dynamic test with a loading speed is 1 m/s
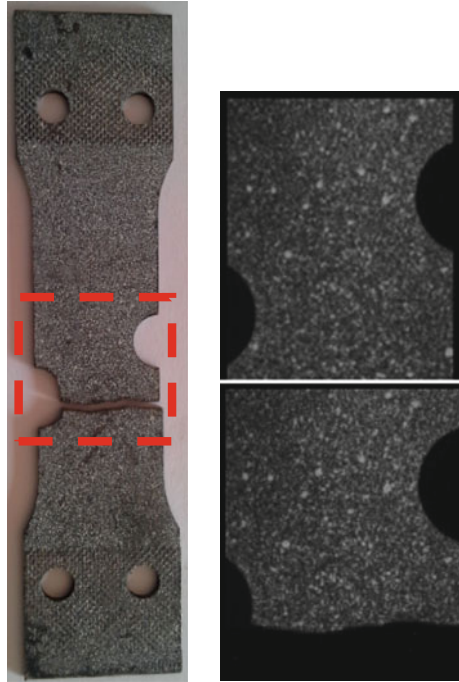
4 Conclusion

The phase-field model is used to simulate the nucleation and propagation of cracks in brittle material. The performance of the quasi-static and dynamic phase-field models of fracture is one of the most interesting problems in fracture mechanics. The phase-field modeling of brittle fracture is a hopeful computational tool to handle fracture problems for complex geometries with unknown topologies of the crack patterns. This model, as well as its current implementation, could indeed be used to approximate and investigate real dynamic brittle fracture problems with sufficient computational efficiency. Otherwise, it is important to know which numerical results are more physically consistent. For that, experimentation is necessary to be made in order to show the efficiency of the phase-field model. Actual work is devoted to experimental validation of this fracture model.

References

Ambati M, Gerasimov T, De Lorenzis L (2015) A review on phase-field models of brittle fracture and a new fast hybrid formulation. Comp Mech 55:383–405

Ambati M, Kruse R, De Lorenzis L (2016) A phase-field model for ductile fracture at finite strains and its experimental verification. Comput Mech 57:149–167

Borden MJ, Verhoosel CV, Scott MA, Hughes TJR, Landis CM (2012a) A phase-field description of dynamic brittle fracture. Comput Methods Appl Mech Eng 217–220:77–95

Borden MJ, Verhoosel CV, Scott MA, Hughes TJR, Landis CM (2012) A phase-field description of dynamic brittle fracture. Comput. Methods Appl Mech Eng 217–220:77–95

Bourdin B, Francfort GA, Marigo JJ (2008) The variational approach to fracture. J Elast 91(1–3):5–148

Bourdin B, Larsen CJ, Richardson CL (2011) A time-discrete model for dynamic fracture based on crack regularization. Int J Fract 168(2):133–143

Francfort GA, Marigo JJ (2002) Vers une théorie énergétique de la rupture fragile. C. R. Mécanique 330(4):225–233

Gerasimov T, De Lorenzis L (2016) A line search assisted monolithic approach for phase-field computing of brittle fracture. Comput Methods Appl Mech Eng 312:276–303. https://doi.org/10.1016/j.cma.2015.12.017

Griffith A (1921) The phenomena of rupture and flow in solids. Philos Trans R Soc Lond 221:163–198

Ha YD, Bobaru F (2010) Studies of dynamic crack propagation and crack branching with Peridynamics. Int J Fract 162:229–244

Hentati H, Abdelmoula R, Maalej A, Maalej K (2013) Numerical analysis solving the elastic dynamic problem. Int J Model Identif Control 19(3):299–305

Hentati H, Ben Naceur I, Bouzid W, Maalej A (2015) Numerical analysis of damage thermo-mechanical models. Adv Appl Math Mech 7(5):625–643

Hentati H, Dhahri M, Dammak F (2016) A phase-field model of quasistatic and dynamic brittle fracture using staggered algorithm. J Mech Mater Struct 11(3):309–327

Hofacker M, Miehe C (2012) Continuum phase field modeling of dynamic fracture: variational principles and staggered FE implementation. Int J Fract 178:113–129

Miehe C, Hofacker M, Welschinger F (2010a) A phase field model for rate-independent crack propagation: robust algorithmic implementation based on operator splits. Comput Methods Appl Mech Eng 199:2765–2778

Miehe C, Welschinger F, Hofacker M (2010b) Thermodynamically consistent phase-field models of fracture: variational principles and multi-field FE implementations. Int J Numer Methods Eng 83(10):1273–1311

Msekh MA, Sargado JM, Jamshidian M, Areias PM, Rabczuk T (2014) Abaqus implementation of phase-field model for brittle fracture. Comput Mater Sci 96:472–484

Schlüter A, Willenbücher A, Kuhn C, Müller R (2014) Phase field approximation of dynamic brittle fracture. Comput Mech 54:1141–1161

Mathematical Modeling of Surface Roughness in Electrical Discharge Machining Process Using Taguchi Method

A. Medfai, M. Boujelbene, S. Ben Salem and A. S. Alghamdi

Abstract Electrical discharge machining EDM is used in many industry sectors to machine conductor or semiconductor materials: hardened steels, ceramic alloys, some composites, and diamond. The aim of this paper is to develop a mathematical model of the surface quality of 36CrNiMo16 in EDM using the experimental design method: full factorial design 22. The statistical method of analysis of variance ANOVA, has allowed us to identify the significant effects of cutting parameters (discharge current I and the electrical resistivity of the electrode material ρ_e; Electrolytic copper (Cu–A1) and Graphite (Gr)) on the surface quality. With Taguchi method, it was possible to determine a mathematical model of the surface quality described by the average roughness Ra. Indeed, an electrolytic copper electrode with a relatively low current ($I = 8$ A) generates a better workpiece surface quality. Therefore, the nature of the material's electrode influences the surface quality of workpiece.

Keywords EDM · Taguchi · ANOVA · Surface quality · Electrical resistivity

A. Medfai · M. Boujelbene (✉) · S. Ben Salem
National Engineering School of Tunis, University of Tunis El Manar,
ENIT, Tunis, Tunisia
e-mail: mboujelbene@yahoo.fr

A. Medfai
e-mail: medfaii@yahoo.fr

S. Ben Salem
e-mail: sahbi_bensalem@yahoo.fr

M. Boujelbene · A. S. Alghamdi
College of Engineering, University of Hail, Hail, Kingdom of Saudi Arabia

S. Ben Salem
IPEI Nabeul, Mrazka University Campus, 8000 Nabeul, Tunisia

1 Introduction

Electrical discharge machining is a nonconventional manufacturing process where metal is removed by means of electrical sparks between two electrodes a tool and a workpiece submerged in a dielectric liquid.

Puertas and Luis (2003) demonstrated that the discharge current has the greatest influence on the surface quality. They observe a high decrease in roughness when the discharge current increases. Whereas, another study established by Puertas et al. (2004) shows that when the intensity increases the roughness Ra tends to increase to a maximum value from which it decreases. Surface roughness also depends on other parameters such as starting voltage and the nature of the electrode material (Mamalis et al. 1988; Boujelbene et al. 2009; Ben Salem et al. 2011).

Surface roughness is of great importance for product quality, it is a characteristic that could influence the performance of mechanical parts and production costs. That's why modeling and optimization are two important and necessary issues in manufacturing products.

Many researchers have been used Taguchi method to optimize the various machining operations after determining the design parameters which significantly affect the response using the statistical method ANOVA.

Chattopadhyay et al. (2009), Sushant et al. (2007) used the full factorial design and the Analysis of Variance (ANOVA) to investigate, optimize and model material removal rate, MRR, electrode wear, and surface roughness.

Several other researchers such as Tzeng (2008), Haddad, and Fadaei (2008) used ANOVA and Taguchi method in their research to optimize and model the machining conditions.

In this paper, we have used full factorial design to minimize the number of test compared with traditional techniques. A study focused on the die-sinking EDM of 36CrNiMo16 and the effect of the discharge current and the tool material on the surface roughness. As well, the modeling of the latter is a function of the different cutting parameters.

2 Experimental Conditions

This study carried out using EROTECH Basic 450 Die-Sinking EDM machine with parameters mentioned in Table 1.

The workpiece material used was 36CrNiMo16. The chemical composition and mechanical properties of the base material are presented in Tables 2 and 3.

Two types of materials for electrodes were used in this study: graphite and electrolytic copper (99.9% of copper). The Properties of electrode materials are shown in Table 4.

Table 1 Process parameters and their levels

Parameters	Value
Starting voltage	120 V
Discharge current	8 and 16 A
Polarity	Electrode +/workpiece −
Pulse time	8 µs
Off time	6 µs
Dielectric fluid	Kerosene

Table 2 Chemical composition of 36CrNiMo16

C	Mn	Si	S	P	Cr	Mo	Ni
0.32–0.39	0.3–0.06	0.1–0.4	≤ 0.025	≤ 0.03	1.6–2	0.25–0.45	3.6–4.1

Table 3 Mechanical properties of 36CrNiMo16

Properties	Value
Yield strength $Re_{0.2\%}$ (N/mm^2)	880
Tensile strength (N/mm^2)	1080–1280
Elongation (%)	10
Brinell Hardness (HB)	204

Table 4 Properties of electrode materials

	Material	
	Electrolytic copper Cu−A1	Graphite Gr
Fusion temperature (°C)	1083	3600
Resistivity (µΩ cm)	1300	1.72
Thermal conductivity (W Cm^{-1}°C^{-1})	3.9	1.25

3   Experimental Procedure

This work focuses on the study of the effect of cutting conditions on surface quality using the experimental design method; full factorial design 2^2. Table 5 presents the relationship between the design factors and their corresponding selected variation levels. The gap selected by the Electrical discharge machine is fixed.

The influence of the cutting parameters on surface quality was studied using the statistical method; analysis of variance "ANOVA". A mathematical model of the surface quality described by the average roughness Ra was determined using Taguchi method. The cutoff used for the experimental measurement of the surface roughness, Ra is 2.5 mm (DIN EN ISO 4288).

4 Influence of EDM Parameters on Surface Quality

Two factors were studied in this research; Electrical resistivity of the electrode and discharge current and two levels of each factor were considered. (Sufficient for determination value of the displacement and the Gap are fixed).

Therefore, an L4 Orthogonal Array was selected for this study (Table 6). As each test was carried out twice, the average of the two responses was used.

From these results, we calculated the mean effects and total of each parameter and their interaction which enable us to determine ANOVA table (Table 7).

In Table 6 df means degree of freedom, SS indicates Sum of Squares and MS show Mean Squares.

$$MS = \frac{SS}{df} \tag{1}$$

$$F_{test} = \frac{MS_{treatment}}{MS_{error}} \tag{2}$$

$$F_{theoretical} = F_{df_{treament}, df_{error}} = F_{4.1} = 7.71 \tag{3}$$

Table 5 Factors and levels selected for the experiments their levels

Factors	Notation	Levels	
		Min (−1)	Max (+1)
Electrical resistivity of the electrode (ρ_e)	A	1.72	1300
Discharge current (I)	B	8	16

Table 6 Experimental conditions and result

Trial number	Original Value		Coded value		Average roughness Ra (μm)
	ρe (μΩ cm)	I (A)	A	B	
1	1.72	8	−1	−1	4.71
2	1300	8	1	−1	2.91
3	1.72	16	−1	1	5.41
4	1300	16	1	1	4.22

Table 7 ANOVA results for average roughness

Source of variation	df	SS	MS	F_{test}		F theoretical
A	1	4.470	4.470	32.228	>	7.71
B	1	2.020	2.020	14.564	>	7.71
AB	1	0.186	0.186	1.341	<	7.71
Error	4	0.554	0.138			
Total	7	7.230				
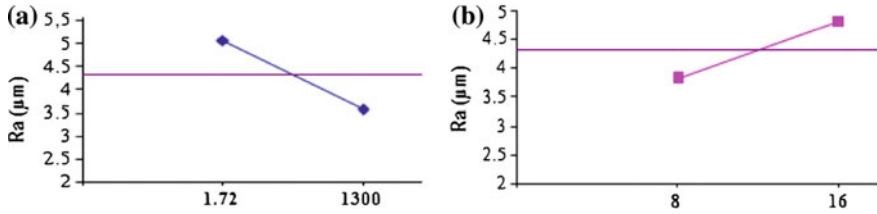
Fig. 1 Curve's effect of: **a** electrical resistivity; **b** discharge current

Fig. 2 Interaction curve of the average roughness Ra
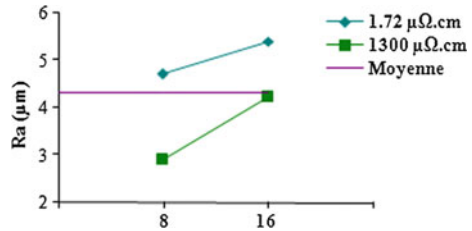
$F_{theoretical}$ is determined from the table of Fisher–Snedecor for $\alpha = 5\%$.

According to Table 7, F_{test} (A) and F_{test} (B) are higher than $F_{theoretical}$ contrary to their interaction. So, only parameters A and B influence significantly the surface quality. Electric resistivity of tool material is more significant than current discharge because F_{test} (A) > F_{test} (B).

The curve's effect represented in Fig. 1 shows that electrical resistivity has a negative effect on the average roughness contrary to discharge current. Indeed an increase in the resistivity from 1.72 to 1300 $\mu\Omega$ cm decreases Ra by 1.005 μm.

According to Fig. 2, the interaction of the two parameters is not significant because the two lines of the curve of interaction effect are approximately parallel. Brief every each parameter influence Ra independently of the other.

5 Mathematical Modeling

In this paper, we used Taguchi method to determine a mathematical model of roughness average. The determination of the model is the last step, we must first go through four steps: Construction of level matrix, Construction of experiments matrix, Determination of the model coefficients b_0, b_1, and b_2 and Validation of the model using FISHER Criteria.

Table 8 Level matrix

| Factors | Natural factor | | | |
| | General model | | Linear model | |
	ρe	I	$x_1 = Ln(\rho e)$	$x_2 = Ln(I)$
Level −	1.72	8	0.54232	2.07944
Level +	1300	16	7.17011	2.77258
x0	–	–	3.85622	2.42601
Δx	–	–	3.31389	0.34657

5.1 Level Matrix

Taking into account the results of ANOVA, only parameters A and B have been taken into account and neglected their interaction AB because it is not significant. The mathematical model of roughness average, as shown in Eq. (4).

$$Y = b_0 + \sum b_i x_i \tag{4}$$

where Y is the response, b_0 and bi (b_1, b_2) are the coefficients of model and xi are cutting parameters.

But instead of natural factors and results, we used their natural logarithm to form matrix levels (Table 8).

$$\text{Level medium } x_0 = \frac{\text{Max level} + \text{Min level}}{2} \tag{5}$$

$$\text{Interval variation} \quad \Delta x = \frac{\text{Max level} - \text{Min level}}{2} \tag{6}$$

$$\text{Coded factor } X_i = \frac{x_i - x_0}{\Delta x} \tag{7}$$

5.2 Validation of the Model

5.2.1 Experimental Matrix

In this step, we calculate the linear response and so we determined the dispersion S_j^2 like is mentioned in Table 9.

where S_j^2 is the dispersion of the jth test, m is the number of repetitions ($m = 2$), Y_{ij} is the linear response of the jth test and the ith repetition and Y_{jm} is the natural logarithm of the average response of the jth test.

Table 9 Experiments matrix

Test N°	Linear factors		Natural result			Linear result			Dispersion $S_j^2 \times 10^3$
	X1	X2	Ra_1	Ra_2	Ra_m	$Ln(Ra_1)$	$Ln(Ra_2)$	$Ln(Ra_m)$	
1	−1	−1	4.66	4.76	4.71	1.5390	1.5602	1.5497	0.2254
2	+1	−1	2.85	2.97	2.91	1.0473	1.0886	1.0682	0.8506
3	−1	+1	4.89	5.93	5.41	1.5872	1.7800	1.6882	18.6351
4	+1	+1	4.25	4.19	4.22	1.4469	1.4327	1.4398	0.1011

$$S_j^2 = \frac{1}{m-1} \sum (Y_{ji} - Y_{jm})^2 \tag{8}$$

From Table 9, we determined the coefficient of linear model as shown in Eqs. (9)–(12).

$$Y_j' = b_0 + \sum b_i X_i \tag{9}$$

$$b_0 = \frac{1}{N} \sum Y_{jm} \tag{10}$$

$$b_1 = \frac{1}{N} \sum X_{1j} Y_{jm} \tag{11}$$

$$b_2 = \frac{1}{N} \sum X_{2j} Y_{jm} \tag{12}$$

5.2.2 Validation of Linear Model

The model is validated only if Fisher criteria [F] determined in Eq. (3) is greater than F calculated by Eq. (13).

$$F = \frac{\max\left(S_y^2, S_R^2\right)}{\min\left(S_y^2, S_R^2\right)} \tag{13}$$

$$S_R^2 = \frac{\sum (Y_j' - Y_{jm})^2}{N_1 - n_B} \tag{14}$$

$$S_y^2 = \frac{\sum S_j^2}{N_1(m-1)} \tag{15}$$

So

$$F = \frac{\max\left(S_y^2, S_R^2\right)}{\min\left(S_y^2, S_R^2\right)} = \frac{S_y^2}{S_R^2} = 2,7430212 < [F] = 7.71 \tag{16}$$

So we deduce that the model is validated.

5.3 Determination of the Model

To determine the model of surface roughness (Ra) we substituted X_i by their value as a function of x_i in the Eq. (4).

$$\ln Y = b_0 + b_1 X_1 + b_2 X_2 \tag{17}$$

$$\ln Y = b_0 + b_1(0.3017x_1 - 1.1636) + b_2(2.8853x_2 - 7) \tag{18}$$

$$\Leftrightarrow Y = e^{(b_0 - 1.1636b_1 - 7b_2)} \rho_e^{0.3017b_1} I^{2.8853b_2} \tag{19}$$

$$R_a = 2.12954 \, \rho_e^{-0.05506} I^{0.36802} \tag{20}$$

Figure 3, shows that the curve of variation of the average roughness calculated as a function of discharge current for two materials of electrode (electrolytic copper (Cu–Al) and graphite (Gr)) is very close to the curve of experimental roughness. So it is an optimal model of average roughness. In fact, the difference between Ra experimental and Ra theoretical varies between 0.174 and 0.324 μm.

In both experimental and modeled case, surface quality is better with graphite electrode and the low current.

Fig. 3 Evolution of experimental and analytic roughness Ra
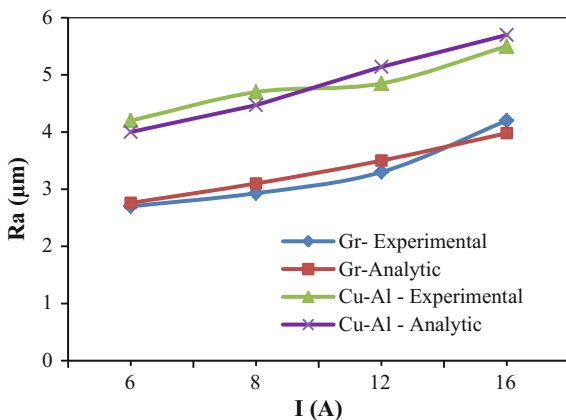
Fig. 4 Iso-response curves of Roughness Ra
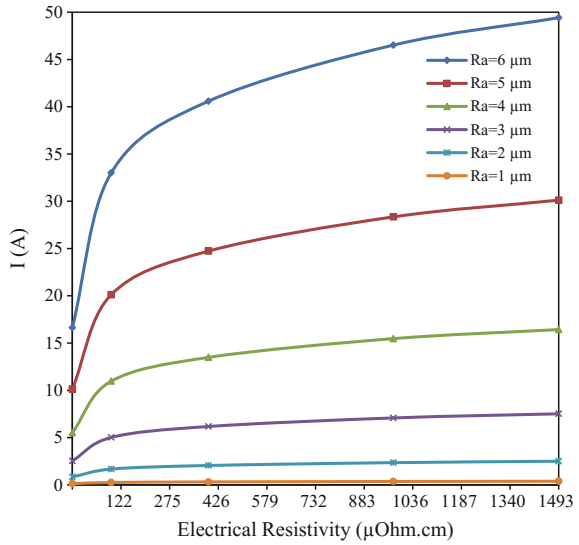
From the mathematical models (Eq. 20), we can predefine the surface quality before machining by choosing the optimal parameters that can be easily determined from the iso-response curves (Fig. 4) shown from Eq. (21).

$$I_{36CrNiMo16} = 0.128 R_a^{2.716} \rho_e^{0.149} \tag{21}$$

6 Conclusion

In this paper, we developed a mathematical model for predicting surface roughness (Ra) of 36CrNiMo16 using Taguchi method. The experimental results are analyzed using the statistical method ANOVA. The following conclusions were reached:

- According to ANOVA analysis, it was found that the electrical resistivity was more significant than discharge current for surface roughness.
- The study and the analysis of the results of the experiments carried out during the machining of 36Cr Ni Mo16 shows that it is not only the electrical parameters that influence the results of the process but also the nature of the Electrode used. Indeed, the use of a graphite electrode (Gr) with a low current (8 A) generates a better surface condition compared to the electrolytic copper electrode (Cu–Al).
- Discharge current always keeps the same effect on the surface quality independent of the electrode material: More the discharge current is low more the surface quality is better.

- Taguchi method was a reliable methodology for the reduction of machining time and manufacturing costs in the electrical discharge machining of steel. In the future, the results obtained can be used for academic research as well as for industrial applications.
- Hence, the next studies should take into account the nature of the electrode material as an important parameter affecting the surface roughness.

References

Ben Salem S, Tebni W, Bayraktar E (2011) Prediction of surface roughness by experimental design methodology in Electrical Discharge Machining (EDM). J Achiev Mater Manuf Eng 49(2):150–157

Boujelbene M, Bayraktar E, Tebni W, Ben Salem S (2009) Influence of machining parameters on the surface integrity in electrical discharge machining. Arch Mater Sci Eng 37(2):110–116

Chattopadhyay KD, Verma S, Satsangi PS, Sharma PC (2009) Development of empirical model for different process parameters during rotary electrical discharge machining of copper–steel (EN-8) system. J Mater Process Technol 209(3):1454–1465

Dhar S, Purohit R, Saini N, Sharma A, Hemath Kumar G (2007) Mathematical modeling of electric discharge machining of cast Al–4Cu–6Si alloy–10 wt.% SiCP composites. J Mater Process Technol 194(1–3):24–29

Haddad MJ, Fadaei TA (2008) Material removal rate (MRR) study in the cylindrical wire electrical discharge turning (CWEDT) process. J Mater Process Technol 199(1–3):369–378

Mamalis AG, Vosniakos GC, Vacevanidis NM, Xiong J (1988) Residual stress distribution and structural phenomena of high-strength steel surfaces due to EDM and ball-drop forming. CIRP Ann Manuf Technol 37(1):531–535

Puertas I, Luis CJ (2003) A study on the machining parameters optimisation of electrical discharge machining. J Mater Process Technol 143–144:521–526

Puertas I, Luis CJ, Álvarez L (2004) Analysis of the influence of EDM parameters on surface quality, MRR and EW of WC–Co. J Mater Process Technol 153–154:1026–1032

Tzeng Y-f (2008) Development of a flexible high-speed EDM technology with geometrical transform optimization. J Mater Process Technol 1–3:355–364

Application of Set-based-approach for the Global Sizing of an Active Macpherson Suspension System

Hassen Trabelsi, Pierre-Alain Yvars, Jamel Louati and Mohamed Haddar

Abstract This paper deals with design problems of a complex technical system. Thus, a new design approach is proposed, which the consideration of static and dynamic requirements is done simultaneously and globally in the preliminary design phase. The proposed design approach is applied on the sizing case of an active MacPherson suspension system. Indeed, in this work, we succeed to integrate the dynamic behavior of the MacPherson suspension in the early design stage. In addition, its dynamic requirements are formalized in the form of algebraic constraints defined by a set of equations and inequalities. The generated solution is the set of acceptable values of design variables satisfying simultaneously static and dynamic requirements. This coupling between the static and dynamic sizing steps in the proposed design approach avoids over-sizing of the system. It also avoids resizing loops in case of failure, which saves significant computation time and reduces the cost of design.

Keywords Interval computation · NCSP · Preliminary design · Macpherson suspension system

H. Trabelsi (✉)
LA2MP, Institut Superieur des Systemes Industriels de Gabes, Universite de Gabes (ISSIG),
Rue, Slaheddine El Ayoubi, BP N 15-6032 Gabes, Tunisia
e-mail: hassen.trabelsi@outlook.fr

P. -A. Yvars
Quartz Lab, Institut Superieur de Mecanique de Paris (SupMeca),
3 Rue Fernand Hainaut, 93407 Saint-Ouen Cedex, France
e-mail: pierre-alain.yvars@supmeca.fr

J. Louati · M. Haddar
LA2MP, Ecole Nationale d' Ingenieurs de Sfax, Universite de Sfax (ENIS),
BP N 1173-3038 Sfax, Tunisia
e-mail: louati.ttg@gnet.tn

M. Haddar
e-mail: mohamed.haddar@enis.rnu.fr

1 Introduction

Nowadays, intensive innovation is a new regime of competition between industries. Companies that have a capacity for innovation are those that have a robust design process and methods of structuring and reliable engineering tools (Couturier et al. 2014). This competitiveness is always pushing companies to develop and improve the design methodologies to be more suited to their design activity (Zheng et al. 2016). But, until now, most industries works with basic design methods based on a loop "design-simulation-return to the initial step in case of failure." These conventional iterative methods are more suitable for validation of an initial concept than to exploration and research in the fields of solution (Trabelsi et al. 2015). Also, the disadvantage of this process (Couturier et al. 2014) is that the static design is treated separately from the dynamic design which causes the over-dimensioning of the product in most cases, since the dynamic requirements (Tay et al. 1998) are not involved in the step of selection of safety factors. Furthermore, in the design case of an automated system, treating its static design regardless at the same phase the dynamic design requirements, may cause the problem of designing a non-controllable system since properties and constraints controllability are not included in the same design phase. Thus, the objective is to find and to equip a design process, which takes into account the different types of static and dynamic requirements in the preliminary design phase, in a simultaneous and global manner, and allows the optimization of the design of complex technical systems. So, in the next section, a solution that allows to better meet the design requirements described previously and to overcome the limitations and challenges of a conventional design approach is provided. The remaining of this paper was organized as follows. First, the proposed design approach was explained and detailed. Then, in the third part, the model of an active MacPherson suspension system was exhaustively discussed. In Sect. 4, the way to take into account the dynamic requirements of the MacPherson suspension in the preliminary design phase in the form of algebraic constraints by intervals is explained. Finally, some conclusions are drawn based on the obtained results.

2 Proposed Design Approach

In recent years, the concept of set-based design has emerged. It allows the integration of requirements and it has studied as a solution to optimize the design process of a product (Qureshi et al. 2010; Trabelsi et al. 2015). Several studies have been developed on the integration of static requirements (Larroudé et al. 2013; Yvars et al. 2009; Tcherctchian et al. 2013) and a few dynamic constraints (Trabelsi et al. 2014; Trabelsi et al. 2015) in the initial stages of a design process.

The different stages of the proposed design process was well detailed and explained in these articles (Trabelsi et al. 2014; Trabelsi et al. 2015). Our scientific contribution in this work is represented by the integration of other types of dynamic require-

ments as stability, controllability, observability and transmittance, and the development of integration method of the resonance requirement. So with this approach, the design of a system can be done in one step, taking into account comprehensive and simultaneously static and dynamic requirements. Furthermore, it guides the choice of safety factors, which avoids oversizing system as in the case of a conventional design approach. Therefore, in the following part, the proposed approach is applied for the optimal sizing case of an active MacPherson suspension system.

3   Dynamic Model of the MacPherson Suspension System

Suspension systems are the elements to support the weight of the vehicle, to isolate the vibrations from the road and to maintain the traction between the tire and the road. The dynamic model used for MacPherson suspension system is detailed in this article (Hong et al. 1999; Trabelsi et al. 2014). It is composed of a quarter vehicle body, an axle and a tire, a coil spring, a damper, an axle, a load disturbance, and a control arm. The vertical displacement z_s of the sprung mass and the rotation angle θ of the control arm are chosen as the generalized coordinates. The model of MacPherson suspension system is active, so a skyhook controller is implemented. The force applied by the skyhook damper $F_{SKY} = f_a$ to the suspended mass is equal to $f_a = -C_{SKY}.\dot{z}_s$, with C_{SKY} is the controller damping coefficient (Fig. 1).

Fig. 1 Dynamic quarter vehicle model of a MacPherson suspension.
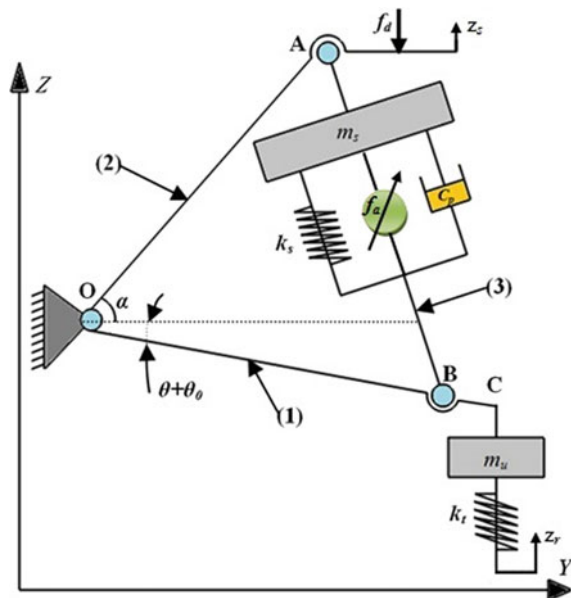
The equation system is submitted in the form of a state equation as following where the state variables are: $[x_1 \; x_2 \; x_3 \; x_4] = [z_s \; \dot{z}_s \; \theta \; \dot{\theta}]$:

$$\dot{x}(t) = Ax(t) + B_1 f_a(t) + B_2 z_r(t) + B_3 f_d(t), \; x(0) = x_0 \tag{1}$$

where: $A = \begin{bmatrix} 0 & 1 & 0 & 0 \\ a_{21} & 0 & a_{23} & a_{24} \\ 0 & 0 & 0 & 1 \\ a_{41} & 0 & a_{43} & a_{44} \end{bmatrix}$; $B_1 = \begin{bmatrix} 0 \\ \frac{l_B cos(-\theta_0)}{m_s l_C + m_u l_C sin^2(-\theta_0)} \\ 0 \\ \frac{(m_s + m_u) l_B}{m_s m_u l_C^2 + m_u^2 l_C^2 sin^2(-\theta_0)} \end{bmatrix}$

$$B_2 = \begin{bmatrix} 0 \\ \frac{k_t l_C sin^2(-\theta_0)}{m_s l_C + m_u l_C sin^2(-\theta_0)} \\ 0 \\ \frac{m_s k_t l_C cos(-\theta_0)}{m_s m_u l_C^2 + m_u^2 l_C^2 sin^2(-\theta_0)} \end{bmatrix} ; \; B_3 = \begin{bmatrix} 0 \\ \frac{l_C}{m_s l_C + m_u l_C sin^2(-\theta_0)} \\ 0 \\ \frac{m_u l_C cos(-\theta_0)}{m_s m_u l_C^2 + m_u^2 l_C^2 sin^2(-\theta_0)} \end{bmatrix}$$

4 Consideration of the Dynamic Requirements

Generally dynamic requirements (Tay et al. 1998) are defined on the basis of the differential equations describing the dynamic behavior of the designing system. While our proposed design approach is based on solving tools type intervals computation (Moore 1966; Benhamou and Granvilliers 2006) and NCSP (Numerical constraints satisfaction problem) (Lhomme 1993). However, these tools do not solve differential equations. So, these requirements are formalized as a set of algebra equations or inequalities resolvable by NCSP.

4.1 Resonance

The only critical state variable to the example of MacPherson suspension system is the displacement z_s. The solution of the equation of state is effectively given in the form of exponential Horner with reduction (Trabelsi 2014):

$$x(t) = \left[exp \left(\frac{t \cdot A}{2^s} \right) \right]^{2^s} x(t_0) \tag{2}$$

where, $x(t_0)$ is the initial state of the system.

$$\begin{bmatrix} z_s \\ \dot{z}_s \\ \theta \\ \dot{\theta} \end{bmatrix} = \underbrace{\left[\left[\frac{I + t \cdot A \cdot \left(I + \frac{t \cdot A}{2} \cdot \left(I + \frac{t \cdot A}{3} \left(\ldots \left(I + \frac{t \cdot A}{n}\right)\right)\right)\right)}{2^s}\right]\right]^{2^s}}_{M} \begin{bmatrix} z_s(t_0) \\ \dot{z}_s(t_0) \\ \theta(t_0) \\ \dot{\theta}(t_0) \end{bmatrix} \tag{3}$$

Thus, limitations constraints on the maximum and minimum displacement of the variable z_s (i.e., on the first row of the matrix M) are imposed through the following inequalities:

$$z_{s-min} \leq P_{z_s}(t) \leq z_{s-max} \tag{4}$$

4.2 Stability

The criterion of Routh is retained to express the stability requirement (Trabelsi 2014) into algebraic constraints. The evaluation of the stability of a system is performed from the analysis of the sign of the roots of the characteristic polynomial. The characteristic polynomial is obtained from the following relationship:

$$det(pI - A) = p^4 - a_{44}p^3 - (a_{43} + a_{21})p^2 + (a_{21}a_{44} - a_{23}a_{41})p + a_{21}a_{43} + a_{23}a_{41} \tag{5}$$

Thus, the coefficients of the column pivots are determined from the following table:

$$\begin{array}{c|llll}
p^4 & 1 & -(a_{43} + a_{21}) & a_{21}a_{43} + a_{23}a_{41} & 0 \\
p^3 & -a_{44} & (a_{21}a_{44} - a_{23}a_{41}) & 0 & 0 \\
p^2 & c_1 = 2a_{21} - a_{43} - \frac{a_{23}a_{41}}{a_{44}} & c_2 = a_{21}a_{43} + a_{23}a_{41} & d_3 & 0 \\
p^2 & d_1 = \frac{a_{44}c_2 - (a_{21}a_{44} - a_{23}a_{41})c_1}{c_1} & 0 & 0 & 0 \\
p^0 & c_2 & 0 & 0 & 0
\end{array}$$

MacPherson suspension system is stable if and only if all coefficients c_1, d_1, and c_2 are positive and the coefficient a_{44} is negative.

4.2.1 Controllability

The controllability of a system is a requirement which characterizes its ability to see its dynamic behavior evolve under the action of the control signal. It allows the user to require a response on the system used. The necessary and sufficient condition (based on Kalman criterion for controllability) so that the suspension system MacPheron is controllable is:

$$rang(Q) = rang([B_2 \ AB_2 \ A^2B_2 \ A^3B_2]) = 4 \tag{6}$$

Thus, to prove the controllability property it suffices to show that the matrix Q is invertible, so the condition is rephrased as follows:

$$| \det(Q) | = | \det([B_2 \ AB_2 \ A^2B_2 \ A^3B_2]) | \geq \epsilon \tag{7}$$

where: ϵ is very small, $f_d = f_a = 0$ and $Q = \begin{bmatrix} 0 & b_2 & a_{24}b_4 & q_{14} \\ b_2 & a_{24}b_4 & q_{23} & q_{24} \\ 0 & b_4 & a_{44}b_4 & q_{34} \\ b_4 & a_{44}b_4 & q_{43} & q_{44} \end{bmatrix}$

4.2.2 Observability

In control theory, observability is a measure for how well internal states of a system can be inferred by knowledge of its external outputs. Based on Kalman criterion for observability, the necessary and sufficient condition for observability is as follow; a system is observable if and only if:

$$rang(M) = rang(\begin{bmatrix} C \\ CA \\ \vdots \\ CA^{n-1} \end{bmatrix}) = n \tag{8}$$

where $M = \begin{bmatrix} m_{1,1} & m_{1,2} & \cdots & m_{1,n} \\ m_{2,1} & m_{2,1} & \cdots & m_{2,n} \\ \vdots & \vdots & \ddots & \vdots \\ m_{n,1} & m_{n,2} & \cdots & m_{n,n} \end{bmatrix}$ is the observability matrix. And since the dimension

of the matrix M is n. Thus, to prove the observability property (8) it suffices to show that the matrix M is invertible. So the observability constraint is as follows:

$$| \det(M) | \geq \epsilon \tag{9}$$

4.3 Transmittance

The transmittance $T = \frac{z_s(\omega)}{z_r(\omega)}$ is calculated by the ratio between the magnitude in the input z_r and output z_s. Indeed, from the modulus and argument of the transmittance ratio, the behavior of the system in low and high frequency can be determined by tender "ω" to zero and to infinity.

The characterization limit determines the frequency range (high or low frequencies) where transmission system is maximum or minimal. Thus, a framework on limit values of the transmission function can be imposed in the form of inequalities on the modulus and the argument of the relation as follows:

$$T_{\min} \leq \|T(j\omega)\| \leq T_{\max}$$
$$\arg_{\min} \leq \arg\left(T(j\omega)\right) \leq \arg_{\max}$$
(10)

After formulating the dynamic requirements by algebraic constraints, the static models (including the static model of the compression spring described below) and dynamic describing the MacPheron suspension are integrated in the same CSP model.

4.4 Compression Spring Model

This spring used in the model is a compression coil spring with round wire, axial pitch, and outer diameter constant. In addition, the spring model is more detailed in this article (Trabelsi et al. 2015). In Table 1 a set of equations are presented, which interconnects the design variables.

Three type of material are proposed (*Shot peened steel, No shot peened steel, Stainless steel*), which imposes values on certain parameters and a restriction on the bounds for other parameters (Trabelsi et al. 2015). In addition, the compressing spring model takes into account buckling phenomenon and the constraint of contiguously. So the value of the theoretical stress shear adjusted for L_c must be smaller than τ_{kc}^s. Thus, the fatigue life of the spring material (Trabelsi et al. 2015) is defined based on Haigh diagram. Indeed, the safety fatigue factor β is calculated using the Haigh diagram.

Almost all the constraints that define the static and dynamic physical behavior of the MacPherson suspension system were included.

5 Implementation of Constraints and Numerical Results

All variables defined previously in both models of MacPherson suspension system and the compression spring are integrated in general as a variable in one CSP model. Thus, each variable is set with initial range of values.[1] The choice of these values depends on the business rules, imposed standards, constraints, and the level of designer expertise. Similarly, all relationships between variables in the form of algebraic equations are implemented as constraints in the same CSP model. Then, the CSP model is resolved using the numerical resolution tool "Constraint Explorer" (Zimmer and Zablit 2001). The values obtained after the propagation of constraints in the initial values of each design variable are shown in Table 2 (column 3). They represent the possible values for each design parameter.

According to the obtained result, it is noticeable that the dimensions of the compression spring generated by the proposed design method are the same as the values

---

[1]They can be found in the column "initial value" in Table 2.

Table 1 Technological relations between design variables of a compression spring

$D = D_e - d$	$D_i = D - d$
$F_1 = R(L_0 - L_1)$	$F_2 = R(L_0 - L_2)$
$F_{c\,th} = R(L_0 - L_c)$	$F_n = R(L_0 - L_n)$
$f_e = \frac{3560d}{nD^2}\sqrt{\frac{G}{\rho}}$	$k = \frac{w+0.5}{w-0.75}$
$L_0 = m\,n + (n_i + n_m)\,d$	$L_c = d(n + n_i + n_m)$
$L_d = \pi D\left(2 + n_m + \frac{n}{\cos z}\right)$	$L_n = d(n + n_i + n_m) + S_a$
$L_r = L_0 - \frac{\pi d^3 \tau_{zul}}{8DRk}$	$M = \frac{\rho 10^{-3} L_d \pi d^2}{4}$
$m = \frac{L_0 - d(n_i + n_m)}{n}$	$n = \frac{Gd^4}{8RD^3}$
$n_t = n + n_m + 2$	$R = \frac{Gd^4}{8nD^3}$
$s_h = L_1 - L_2$	$V_{0/0} = \frac{\pi D_e^2 L_0}{4000}$
$V_{0/2} = \frac{\pi D_e^2 L_2}{4000}$	$W = 0.5(F_1 + F_2)(L_1 - L_2)$
$w = \frac{D}{d}$	$\tan z = \frac{m}{\pi D}$
$\tau_{k2} = 8DR(L_0 - L_2)\,k/\left(\pi d^3\right)$	$\tau_{kc}th = 8DR(L_0 - L_c)\,k/\left(\pi d^3\right)$
$d \leq 17$	$D \leq 200$
$L_0 \leq 630$	$n \leq 2$
$4 \leq w \leq 20$	$n_i \in \{1, 1.5, 2, 3\}$
$\tau_{K2} < \tau_{zul}$	$S_a = n\left(0.0015\frac{D^2}{2} + 0.1d\right)$
$\tau_{kc}th < \tau_{kc}^s$	$\mu + 1 = \frac{E}{2G}$
$L_2 > L_k$	$L_1 > L_k$
$L_K = $ $L_0\left(1 - \frac{(\mu+1)}{2\mu+1}\left(1 - \sqrt{1 - \frac{2\mu+1}{\mu+2}\left(\frac{\mu D}{v L_0}\right)^2}\right)\right)$	$v\frac{L_0}{D} < \pi\sqrt{\frac{2\mu+1}{\mu+2}}$

obtained in the previous article (Trabelsi et al. 2015) except for the following functional parameters of the spring $F_1, F_2, L_1, L_2, S_h, W, V_{ol2}$. Indeed, a slightly different value was remarked.

The difference in values recorded at the above-mentioned parameters is due to the addition of new dynamic constraints in the CSP solving model and view as a different dynamic suspension model was used.

The values of the MacPherson strut design parameters satisfying the dynamic constraints of resonance, stability, and commandability are:

- 500 N · m/s for the damping coefficient C_p, 168, 000 N/m for the stiffness of the spring k_s
- 0.3 m for distances $\overline{OA} = \overline{OB} = \overline{OC}$ which define the lengths between components of the MacPherson suspension.
- The action of the body on the suspension causes a compression of 0.025 m which corresponds to 8.75% of the initial length of the spring. The natural frequency ω

Table 2　Numerical results of the compression spring dimensions obtained by CSP

Variables	Initials values	Results
Dynamic parameters of the MacPherson suspension		
$\boldsymbol{\omega}$	$[0 ; +\infty]$	25.922
F_0	$[0 ; +\infty]$	4000
z_2	$[0 ; +\infty]$	0.025
$\boldsymbol{C_p}$	$[0 ; 2000]$	500
k_s	$[0 ; 200,000]$	168,000
l_A	$[0 ; 0.3]$	0.3
l_B	$[0 ; 0.3]$	0.3
l_C	$[0 ; 0.3]$	0.3
Principal constructive parameters of the spring		
$\boldsymbol{d}$	$[0.15 ; 15]$	11.982
d_{min}	$\{0.15, 0.3\}$	0.3
d_{max}	$\{12, 15\}$	12
$\boldsymbol{D}$	$[0 ; 200]$	50
D_e	$[0 ; 217]$	61.982
D_i	$[0 ; 200]$	38.017
L_0	$[0 ; 630]$	200
L_c	$[0 ; 630]$	143.786
$\boldsymbol{n}$	$[2 ; 2 \times 10^9]$	10
n_i	$\{1, 2, 3, 4\}$	2
n_m	$[0 ; 2 \times 10^9]$	0
$\boldsymbol{m}$	$[0, 315]$	17.603
z	$[-\pi/2, \pi/2]$	0.111
Functional and Performance parameters of the spring		
F_1	$[0 ; +\infty]$	4.210
F_2	$[0 ; +\infty]$	5633.925
L_1	$[0 ; 630]$	199.976
L_2	$[0 ; 630]$	166.464
S_h	$[0 ; 630]$	33.510
$\boldsymbol{W}$	$[0 ; +\infty]$	94467.566
Vol_2	$[0 ; 24,000]$	502.280
v	$\{0.5, 0.7, 1, 2\}$	1
L_k	$[0 ; 630]$	160.957
$\boldsymbol{N}$	$[0 ; 2 \times 10^9]$	100,000
β	$\{1.6, 2.0, 3.0\}$	2
S_a	$[0 ; +\infty]$	22.667
L_n	$[0 ; 630]$	166.454
F_n	$[0 ; +\infty]$	$[5635.618 ; 5635.623]$
τ_d	$[0 ; +\infty]$	188.356

The Material parameters of the spring		
Material	{1, 2, 3}	1
$\tau_d(N)$	[0 ; +∞]	511.468
τ_m	[0 ; +∞]	284.836
τ_a	[0 ; +∞]	284.411
α_F	[1 ; +∞]	1.114
G	{70,000, 81,500}	81,500
E	{192,000, 206,000}	206,000
R_m	[0 ; 2230]	1346.049
ρ	{7.85×10^{-6}, 7.9×10^{-6}}	7.85×10^{-6}
$Coeff\,\tau_{zul}$	{0.48, 0.5}	0.5
τ_{zul}	[0, 10,000]	673.024
μ	{0.27, 0.30, 0.31}	0.27

obtained based on the following design parameter values ($m_1 = 25$, $m_2 = 250$, $k_1 = 200,000$), is equal to 25.922 rad/s.

In this work, the proposed design approach was applied in the case of sizing of an active MacPherson suspension system. In fact, the dimensions of the general parameters of the Macpheron suspension was successfully generated while taking into account the requirements imposed. The results are satisfactory and confirm the validity of the proposed approach.

6   Conclusion

In this paper, a study of the numeric CSPs application in the case of an active MacPherson suspension system was made. The originality of this work is that the possibility of integrating dynamic requirements (such as resonance, stability, controllability, observability, and transmittance) in the same preliminary design phase was shown. These constraints are implemented in a NCSP model used to propagate constraints in the areas of design parameters of technical complex system in order to determine one or more solutions. Thus, according to the results obtained for the case of the Macpherson suspension, the capability of the proposed design based on CSP and intervals to size a full nonlinear system (structure + all components,...) is verified.

References

Benhamou F, Granvilliers L (2006) Continuous and interval constraints. In: Hand-book of Constraint Programming, Chapter 16, pp 571–604

Couturier P, Imoussaten MLA, Chapurlat V, Montmain J (2014) Tracking the consequences of design decisions in mechatronic Systems Engineering. Mechatronics 24(7):763–774

Hong KS, Jeon DS, Sohn HC (1999) A new modeling of the macpherson suspension sys-tem and its optimal pole-placement control. In: Proceedings of the 7th mediterranean conference on control and automation (MED99) Haifa, Israel, June 28–30

Larroudé V, Chenouard R, Yvars PA, Millet D (2013) Constraint based approach for the steady-state simulation of complex systems: application to ship control. Eng Appl Artif Intell 26(1):499–514

Lhomme O (1993) Consistency technique for numerical CSPs3. Int Jt Conf Artif Intell (IJCAI) 1:232–238

Moore RE (1966) Interval analysis, vol l. Prentice Hal, pp 85–103

Qureshi AJ, Dantana JY, Bruyerec J, Bigota R (2010) Set based robust design of mechanical systems using the quantifier constraint satisfaction algorithm. Eng Appl Artif Intell 27(7):1173–1186

Tay EH, Flowers W, Barrus J (1998) Automated generation and analysis of dynamic system designs. Res Eng Des 10(1):15–29

Tcherctchian N, Yvars PA, Millet D (2013) Benefits and limits of a CSP/LCA approach for the ecodesign of complex systems. A case applied to a hybrid passenger ferry. J Cleaner Prod 42:1–18

Trabelsi H (2014) Contribution in the consideration of dynamic requirements in the preliminary design of complex systems. Thesis, National school of engineers of Sfax

Trabelsi H, Yvars PA, Louati J, Haddar M (2015) Interval computation and constraint propagation for the optimal design of a compression spring for a linear vehicle suspension system. Mech Mach Theory 84:67–89

Trabelsi H, Yvars PA, Louati J, Haddar M (2014) Evaluation of the effectiveness of the interval computation method to simulate the dynamic behavior of subdefinite system: application on an active suspension system. Int J Interact Des Manuf 1955–2513:1–14

Yvars PA, Lafon P, Zimmer L (2009) Optimization of mechanical system: contribution of con-straint satisfaction Method. In: Proceedings of IEEE international conference of computers and industrial engineering, CIE'39, pp 1379–1384, Troyes

Zheng C, Hehenberger P, Le Duigou J, Bricogne M, Eynard B (2016) Multidisciplinary design methodology for mechatronic systems based on interface model. Res Eng Des. 1–24, https://doi.org/10.1007/s00163-016-0243-2

Zimmer L, Zablit P (2001) Global aircraft predesign based on constraint propagation and inter-val analysis. In: Proceedings of the CEAS conference on multidisciplinary aircraft design and optimisation, Kln, Germany, June

Vibration Suppression of a Cantilever Plate During Milling Using Passive Dynamic Absorber

Nouha Masmoudi, Riadh Chaari, Wajih Gafsi, Fakher Chaari, Mohamed Taoufik Khabou and Mohamed Haddar

Abstract During milling process, the vibration is an unavoidable phenomenon which causes damage in the tool and spindle bearings and leads to poor dimensional accuracy and surface finish of the workpiece. With the ultimate goal of vibration suppression of a thin-walled workpiece during milling process, this paper provides a comparative study of the dynamic behavior simulation of a cantilever rectangular thin plate submitted to a milling operation with and without passive dynamic mass-spring absorbers attached to it. The simulation is carried out taking into account the Kirchhoff model for the plate and the Moradi et al. (2015) model for the cutting force of milling. To solve the equation of motion of the plate with the finite element method the MATLAB software is used. The plate natural frequencies and mode shapes are first identified and then two cases of the plate deflection are determined by the cutting force and taking or neglecting additive absorbers. The obtained results show that the attachment of vibration absorbers to the plate workpiece enlarges its range of natural frequencies. Thus, it can minimize undesired vibration and improves the milling conditions and the surface quality. The proposed

N. Masmoudi (✉) · R. Chaari · W. Gafsi · F. Chaari · M. T. Khabou · M. Haddar
Mechanics, Modelling and Manufacturing Laboratory (LA2MP), Mechanical Engineering
Department, Sfax National Engineers School, Sfax University, BP 1173-3038 Sfax, Tunisia
e-mail: Nouhamasmoudi23@yahoo.com

R. Chaari
e-mail: rchaari@yahoo.fr

W. Gafsi
e-mail: gwajih@yahoo.fr

F. Chaari
e-mail: fakher.chaari@gmail.com

M. T. Khabou
e-mail: mtkhabou@hotmail.com

M. Haddar
e-mail: mohamed.haddar@enis.rnu.tn

1093

vibration absorber design includes other advantages such as design simplicity, intuitive clarity, and hardware and development effective cost. However, the plate deflection remains relatively high because this type of vibration absorber is efficient just in case of one resonance frequency.

Keywords Passive dynamic absorber · Milling · Cantilever plate · Vibration

1 Introduction

One of the widespread machining processes is the peripheral milling. It is especially implemented in aerospace industries and used for milling of wing parts and engine components. Its appropriate performance may be affected by the existence of an annoying phenomenon which is vibration. That is why the dynamic stability of cutting has been studied and optimized by several researchers Londhe and Chilwant (2016), Subramanian et al. (2013), Sreeram et al. (2006) in the last years by optimizing the cutting parameters (cutting speed, depth of cut, feed rate). Despite the different solutions proposed by several researchers, the phenomenon of chatter caused by cutting vibrations is inevitable and its effect is still critical especially for the high-speed machining of flexible (thin-walled) parts. Therefore, the integration of dynamic absorbers in machining assemblies represents a new solution to eliminate the vibrations causing the chatter in machining (Moradi et al. 2015; Moradi et al. 2012). In this paper, a linear vibration absorber (mass-spring system) is attached to a plate workpiece. The differential equation of motion governing transverse vibration of thin isotropic plate is considered to study the plate deflection and to verify the influence of the vibration absorber on the range of frequencies.

2 Force Modeling

Among the difficulties under machining conditions is the force modeling. To achieve a more realistic model, nonlinear modeling is necessary. The nonlinearity of cutting force modeling arises from nonlinear material consecutive relations. A complete third-order polynomial function is proposed by Moradi et al. (2015)

$$
\begin{aligned}
dF_{t,j}(\phi, z) &= \left[\xi_1 h_j^3(\phi_j(z)) + \xi_2 h_j^2(\phi_j(z)) + \xi_3 h_j(\phi_j(z)) + \xi_4\right] dz \\
dF_{r,j}(\phi, z) &= \left[\delta_1 h_j^3(\phi_j(z)) + \delta_2 h_j^2(\phi_j(z)) + \delta_3 h_j(\phi_j(z)) + \delta_4\right] dz
\end{aligned}
\tag{1}
$$

Values of de δ_i, ξ_i, $i = 1, \ldots, 4$ are determined experimentally (Moradi et al. 2015).

The chip thickness is expressed as

$$h(\phi_j) = [\Delta x \sin \phi_j + \Delta y \cos \phi_j] \, g(\phi_j) \tag{2}$$

$c_f \sin \phi_j$ is the static part of the chip thickness caused by rigid body motion of the cutter.

$v_{j,0} - v_j$ is the dynamic part produced due to vibrations of the tool.

$g(\phi_j)$ is a unit step function determining whether the tooth is in or out of cut, ϕ_{st} et ϕ_{ex} are respectively start and exit immersion angles of the cutter.

$$g(\phi_j) = \begin{cases} 1 & \phi_{st} < \phi_j < \phi_{ex} \\ 0 & \phi_{st} > \phi_j \ or \ \phi_{ex} < \phi_j \end{cases} \tag{3}$$

By neglecting the static part of Eq. (2) (Moradi et al. 2015), the expression of the thickness of the chip becomes:

$$h(\phi_j) = [\Delta x \sin \phi_j + \Delta y \cos \phi_j] \, g(\phi_j)$$

With

$$\Delta x = x(t) - x(t-\tau); \ \Delta y = y(t) - y(t-\tau), \ \tau = 2\pi/N\Omega \tag{4}$$

[x(t), y(t)] and [x(t-τ), y(t-τ)] present the cutter displacement.
Ω (rad/s) presents the spindle speed.

In previous researches, Moradi et al. (2015) Saadabad et al. (2014), the nonlinear modeling of the cutting force by Fourier series development is complete. The expression obtained is as follows:

$$F = \frac{N}{2\pi} \left\{ \alpha_1' \Delta x^3 + \beta_1' \Delta y^3 + \alpha_2' \Delta x^2 + \beta_2' \Delta y^2 + \alpha_3' \Delta x + \beta_3' \Delta y + 3\gamma_1' \Delta x^2 \Delta y \right.$$
$$\left. + 3\gamma_2' \Delta x \Delta y^2 + 2\gamma_3' \Delta x \Delta y + \gamma_4' \right\} \tag{5}$$

$$\alpha_1' = \frac{1}{4}[-\delta_1 + \frac{3}{4}\pi\xi_1]; \ \beta_1' = \frac{1}{4}[\xi_1 - \frac{3}{4}\pi\delta_1]; \ \alpha_2' = \frac{1}{3}[-\delta_2 + 2\xi_2];$$
$$\beta_2' = \frac{1}{3}[\xi_2 - 2\delta_2]; \ \alpha_3' = \frac{1}{2}[-\delta_3 + \frac{1}{2}\pi\xi_3]; \ \beta_3' = \frac{1}{2}[\xi_3 - \frac{1}{2}\pi\delta_3]; \tag{6}$$
$$\gamma_1' = \frac{1}{4}[\xi_1 - \frac{1}{4}\pi\delta_1]; \ \gamma_2' = \frac{1}{4}[-\delta_1 + \frac{1}{4}\pi\xi_1]; \ \gamma_3' = \frac{1}{3}[\xi_2 - \delta_2]; \ \gamma_4' = \xi_4 - \delta_4$$

3 Studied Case

In this section, we are going to study the case of a cantilever plate subjected to a peripheral milling operation attached with linear vibration absorber.

As shown in Fig. 1, a uniform rectangular plate defined by $0 < x < L_x$, $0 < y < h$ and $0 < z < L_z$ and clamped in $z = L_z$ is considered (h is the plate thickness). Dampers are not applicable in all circumstances because of, for example, energy requirements, costs, environment, etc. Therefore, we chose a vibration absorber composed by a mass m_a and a spring of stiffness k_a. Its position is defined by b = 0.125 m in z direction and a = 0.625 m in x direction, near the free edge of the plate.

The realistic parameters of the plate workpiece and the absorber are given in the Tables 1 and 2 (Moradi et al. 2015).

Assuming that the plate deflection $w(x, z, t)$ has the following expression

$$w(x, z, t) = W(x, z)\, \eta(t) \tag{7}$$
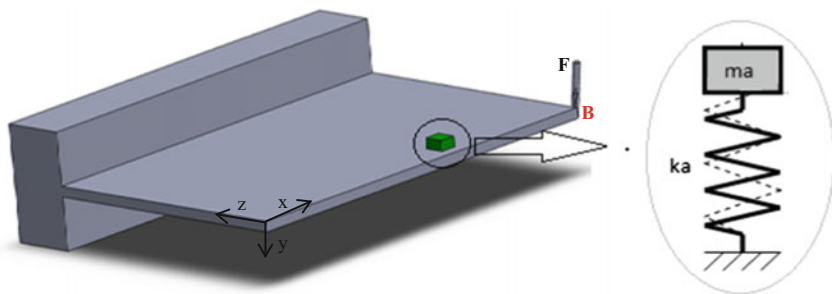
Fig. 1 Cantilever plate attached with vibration absorber

Table 1 Realistic parameters of the cantilever plate

Plate specification (Al 7075)	
Mass density	$\rho = 2810 \text{ kg/m}^3$
Young modulus	$E = 71.7 \text{ GN/m}^2$
Poisson's ratio	$\nu = 0.33$
Length (x)	$L_x = 1 \text{ m}$
Width (z)	$L_z = 1 \text{ m}$
Thickness (y)	$h = 2 \text{ cm}$

Table 2 Parameters of the vibration absorber

Vibration absorber specification	
Absorber mass	$m_a = 2 \text{ kg}$
Spring stiffness	$k_a = 23 \text{ kN/m}$

The differential equation of motion governing transverse vibration of thin isotropic plate is given, by use of the classical thin plate theory, as

$$D\nabla^4 w(x,z,t) + \rho \frac{\partial^2 w(x,z,t)}{\partial t^2} = f(t), \tag{8}$$

where D is the plate flexural rigidity defined as

$$D = \frac{Eh^3}{12(1-\nu^2)} \tag{9}$$

E, h, and ν are respectively the Young modulus, the plate thickness, and Poisson's ratio.

$f(t)$ is a time-dependent harmonic function.

Substituting Eq. (7) into Eq. (8) yields

$$\nabla^4 W(x,z) - \beta^4 W(x,z) = \frac{f}{D}\beta^4 = \rho\omega^2/D \tag{10}$$

The motion of the global system (the plate and the absorber) is governed by

$$[M]\{\ddot{X}\} + [C]\{\dot{X}\} + [K]\{X\} = \{F\}, \tag{11}$$

where $\{X\}$ is the nodal displacement of the plate, $[C]$ is damping matrix of the plate and $\{F\}$ is the external force applied to the system. $[M]$ and $[K]$ represent, respectively, the mass and stiffness matrix of both the plate and vibration absorber.

$$[M] = [M_p] + [M_a] \tag{12}$$

$[M_p]$ is the mass matrix of the plate and $[M_a]$ is the additional mass matrix caused by the presence of the vibration absorber.

$$[K] = [K_p] + [K_a] \tag{13}$$

$[K_p]$ is the proportional stiffness matrix of the plate, and $[K_a]$ represents the additional stiffness matrix caused by the vibration absorber.

4 Simulation and Results

In this section, we are going to use the finite element method and the equations presented in the previous section to model the plate deflection using Matlab.

The obtained natural frequencies of the plate without and with vibration absorber are presented in the following table.

The first five mode shapes of the cantilever plate are shown in Fig. 2.

The obtained results have been validated by comparing them with the results of (Moradi et al. 2015).

As it is presented in the Table 3, the introduction of vibration absorber increases the range of frequencies of the cantilever plate.

The frequency response of the free corner of the plate B (x = 1, z = 0) is shown in Fig. 3 (without and with the absorber). In this figure, the cutting force F is exerted at the midpoint (x = 0.5, z = 0) of plate's free edge.
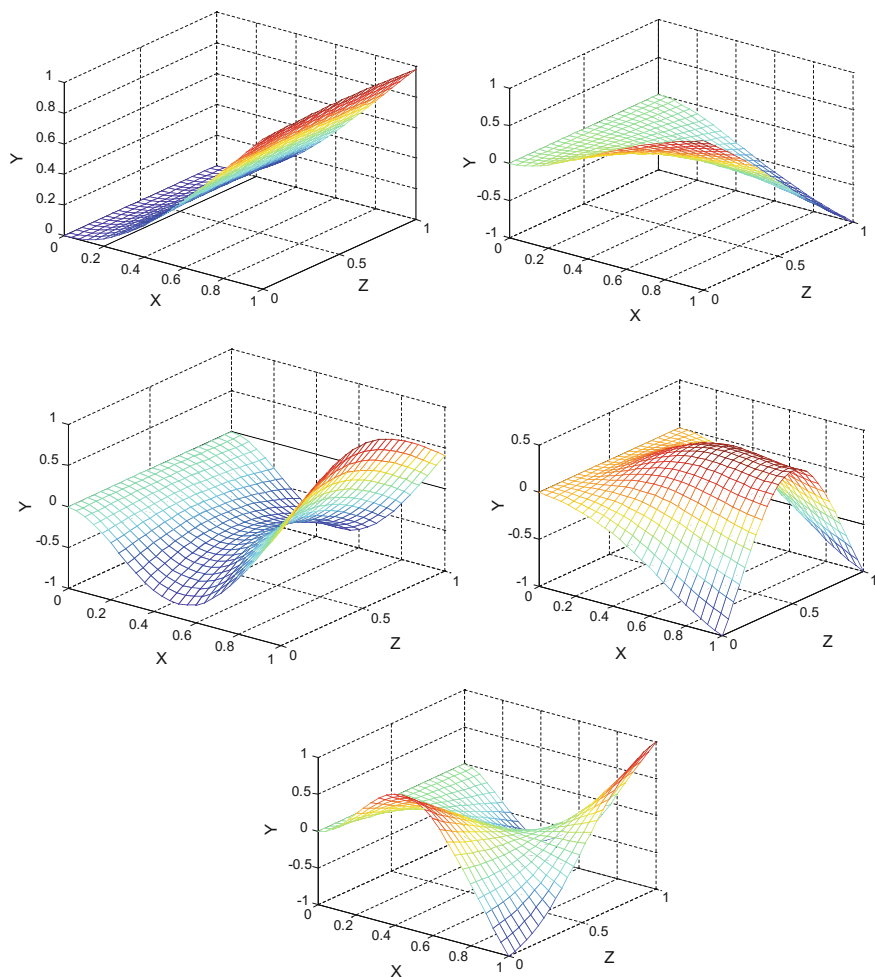
Fig. 2 First five mode shapes of the cantilever plate

Table 3 Natural frequencies of the plate with and without vibration absorber

Natural frequencies of the plate without absorber (rad/s)	Natural frequencies of the plate with absorber (rad/s)
107	113
259	265
652	653
836	838
945	946
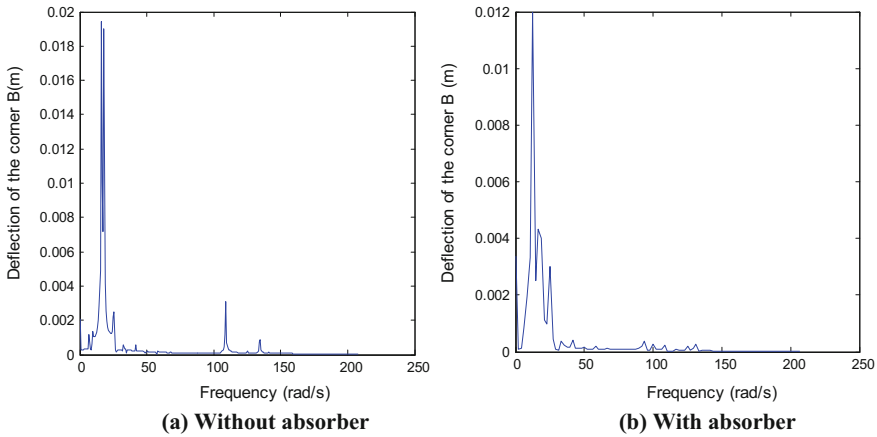
Fig. 3 Frequency response of the free corner B (x = 1, z = 0) of the plate

As it is shown in Fig. 3, the vibration absorber acts efficiently in plate deflection reduction especially around natural frequencies of the plate. For example, the deflection amplitude of the corner B reduces from 0.019 to 0.012 m around the first natural frequency.

5 Conclusion

In this paper, resonance frequencies of a cantilever plate have been identified. The attachment of a vibration absorber to the plate workpiece increased its range of frequencies. Thus, it can minimize undesired vibration and improve the milling conditions and the surface quality. The proposed vibration absorber design includes some great advantages such as simple design, intuitive clarity, reduction in hardware, and development cost. However, the plate deflection remains relatively high and this type of vibration absorber can be used only for one resonance frequency.

Therefore, in the next paper, we are going to study another type of vibration absorber which is particle impact damper and to compare the obtained results to these one.

References

Londhe P, Chilwant (2016) Optimization of cutting parameters in milling operation to improve surface finish of EN 31. Int J Eng Sci Manag Res

Moradi H, Bakhtiari-Nejad F, Movahhedy MR, Vossoughi G (2012) Stability improvement and regenerative chatter suppression in nonlinear milling process via tunable vibration absorber. J Sound Vib 331:4668–4690

Moradi H, Vossoughi G, Behzad M, Movahhedy MR (2015) Vibration absorber design to suppress regenerative chatter in nonlinear milling process: Application for machiningof cantilever plates. Appl Math Model 39:600–620

Saadabad NA, Moradi H, Vossoughi G (2014) Global optimization and design of dynamic absorbers for chatter suppression in milling process with tool wear and process damping. Proc CIRP 21:360–366

Sreeram S, Senthil Kumar A, Rahman M, Zaman MT (2006) Optimization of cutting parameters in micro end milling operations in dry cutting condition using genetic algorithms. Int J Adv Manuf Technol 30:1030–1039

Subramanian M, Sakthivel M, Sooryaprakash K, Sudhakaran R (2013) Optimization of cutting parameters for cutting force in shoulder milling of Al7075-T6 using response surface methodology and genetic algorithm. Proc Eng 64:690–700

Optimized Method for Computing Phase-Field Model Using Decoupling Scheme

Yosra Kriaa, Hamdi Hentati and Bassem Zouari

Abstract Fracture mechanisms in solids are governed by complex fracture phenomena such as crack initiation and multiple crack branching. Phase-field models are used to simulate crack propagation in materials subjected to mechanical loading. This approximation reduces the implementation complexity for fracture mechanics problems as it removes the need for numerical tracking of displacement discontinuities. This is accomplished by introducing a new damage variable representing the diffuse crack topology which is controlled by a numerical regularization parameter. Already, due to nonconvexity of the regularized energy functional, a robust staggered solution scheme based on the decoupling algorithm is used. An optimized computing method is presented. We propose quasi-static crack propagation where the damage variable is activated only if the maximum stress in the specimen reaches a critical value σ_c. This methodology reduces the time computing by 20%. A parametric study is done on the specimen geometry to study the ability of the algorithm to provide the crack path. We are interested in the determination of the influence of geometry of specimen on the evolution of energies and the crack path.

Keywords Phase-field model · Staggered scheme · Crack initiation
Crack propagation · Brittle fracture · Damage variable

Y. Kriaa (✉) · H. Hentati · B. Zouari
LA2MP Laboratory, National Engineering School of Sfax,
University of Sfax, Sfax, Tunisia
e-mail: yosra.2k@gmail.com

H. Hentati
e-mail: hamdi.hentati@yahoo.fr

B. Zouari
e-mail: bzouari@yahoo.com

1 Introduction

Fracture mechanics play an important role in engineering analysis. Most modeling fracture methods are based on finite element method. Several techniques are based on Griffith's theory of elastic brittle fracture (Griffith 1921). He associates a surface energy proportional to the length of each created crack. Despite the important contribution of his theory, it has some shortcomings such as its inability to predict the fracture initiation.

Recently, the fracture mechanics has been revised by proposing different phase-field models of quasi-static brittle fracture inspired from Griffith's criterion. In fact, a variational theory was developed by Francfort and Marigo (1998), and was used in order to model brittle fracture (Bourdin et al. 2000; Bourdin et al. 2008; Oleaga 2004; Amor et al. 2009; Pham and Marigo 2010a, b; Buliga 1998; Hentati et al. 2015). A new formulation was proposed for the brittle fracture problem which is able to predict the nucleation of new cracks, their path, and their interactions, in two and three space dimensions. The phase field models allow the treatment of cracks as surfaces of free discontinuity which take place in a piece. The proposed approach uses a diffusive crack approach instead of modeling the discontinuities induced by the crack. The diffusive crack zone is determined by a scalar variable that interpolates between either the broken or unbroken state of the material. The value of the phase-field variable should be between 0, for uncracked zone, and 1 for a damaged zone.

The total energy of a solid is assumed equal to the sum of two terms. The first one is the elastic energy and the second one is the surface energy needed to create a crack in the structure. The problem is reduced to find the displacement field and the damage field which minimizes the total energy.

The staggered scheme is the most commonly used, due to its robustness: the regularized energy is convex with respect to each of its variables separately which are displacement and damage fields. The robust staggered schema requires a high computational cost to achieve energy convergence until the brutal crack. The second scheme, named monolithic schema, implying the solution of the regularized energy for both variables simultaneously was developed (Gerasimov and De Lorenzis 2016). Provided that algorithm convergence is achieved, the monolithic solution scheme was being shown to be faster than the staggered one. However, due to nonconvexity of the regularized energy, the iterative process diverges, particularly in case of the brutal crack evolution case.

In the same context, a higher order phase-field model formulation adopting Bourdin's formalism was recently presented by Borden et al. (2014) to gain more regular and faster converging solutions of the variational problem of brittle fracture. Ambati et al. (2015) analyzed the effect of numerical method for phase-field modeling of brittle fracture and presented an overview of the existing quasi-static and dynamic phase-field fracture formulations.

This paper is focused on modeling of the quasi-static crack initiation and propagation using the phase-field model. The first purpose is to analysis the

influence of geometric parameters in specific examples, on energies, and on the crack path. The second goal is to propose an optimized algorithm based on the staggered scheme in order to simulate the quasi-static crack propagation where the damage variable is activated when the stress in the specimen reaches a critical value σc (Amor et al. 2009).

2 Brittle Fracture Phase-Field Modeling

Consider a body Ω. The phase-field approach for brittle fracture in elastic solids consists in incorporating a continuous field damage variable α. The entire process of crack initiation and propagation is governed by a minimization problem of the regularized energy functional. It is parameterized by η and defined by the following equation:

$$\mathrm{E}(u,\alpha) = \frac{1}{2}\int_{\Omega} [((1-\alpha)^2 + \mathrm{k}(\eta))\varepsilon : \mathrm{C} : \varepsilon] \mathrm{d}\Omega + \mathrm{G_c}\int_{\Omega}(\frac{\alpha^2}{4\eta} + \eta\nabla\alpha\cdot\nabla\alpha)\mathrm{d}\Omega \qquad (1)$$

where u is the displacement field, η is a regularized numerical parameter, k is a positive infinitesimal prevents numerical singularity in the case of partly or fully broken systems, $\mathrm{G_c}$ is the fracture toughness (energy required to create a unit surface crack), ε the strain tensor and C the elastic tensor. To reduce the time computing, we adopt the assumption that in tensile test the displacement field is uniaxial $\vec{u} = u(x_1, x_2)\vec{\iota}$.

The regularized energy is written as:

$$\mathrm{E}(u,\alpha) = \frac{\mu}{2}\int_{\Omega} [((1-\alpha)^2 + \mathrm{k}(\eta))\nabla u \cdot \nabla u] \mathrm{d}\Omega + \mathrm{G_c}\int_{\Omega}(\frac{\alpha^2}{4\eta} + \eta\nabla\alpha\cdot\nabla\alpha)\mathrm{d}\Omega \qquad (2)$$

where μ is the Lamé coefficient.

The minimization of the total energy via the displacement field u gives the following variational problem:

$$\begin{cases} \text{Find u}\,; u \in A_\delta, \forall v \in A_0: \\ \int_{\Omega}[((1-\alpha)^2 + \mathrm{k}(\eta))\nabla u \cdot \nabla v]\mathrm{d}\Omega = 0 \end{cases} \qquad (3)$$

With $A_\delta = \{u \in \mathrm{H}^1(\Omega) \text{ where } u = \delta \text{ in } \Gamma_1\}$, $A_0 = \{v \in \mathrm{H}^1(\Omega) \text{ where } v = 0 \text{ in } \Gamma_1\}$.

where $\mathrm{H}^1(\Omega)$ denotes the usual Sobolev space of functions which are square integrable over Ω and whose distributional gradient is also square integrable. v is the displacement test function. We note δ an imposed displacement field applied on the boundary part $\Gamma 1$.

The minimization of the total energy via the damage variable α gives the following variational problem:

$$\begin{cases} Find\ \alpha;\ \alpha \in H^1, \forall \beta \in H^1(\Omega): \\ \int_\Omega \mu\alpha\beta|\nabla u|^2 d\,\Omega + \int_\Omega \frac{G_c}{2\eta}\alpha\beta d\,\Omega + \int_\Omega 2G_c\eta\nabla\alpha\nabla\beta d\,\Omega = \int_\Omega \mu\beta|\nabla u|^2 d\,\Omega \end{cases} \quad (4)$$

with β is the damage test function.

To solve these Eqs. (3 and 4), we used the finite element method. After discretization, Eqs. (3) and (4) are written as two nonlinear systems:

$$K_u(\alpha)u = F_u(\alpha) \quad (5)$$

$$K_\alpha(u)\alpha = F_\alpha(u) \quad (6)$$

Where

$$K_u(\alpha) = A_e \int_{\Omega_e} ((1-\alpha)^2 + k(\eta))[B]^T[B]d\,\Omega_e \quad (7)$$

$$K_\alpha(u) = A_e \int_{\Omega_e} \mu|\nabla u|^2[N]^T[N]d\,\Omega_e + A_e \int_{\Omega_e} \frac{G_c}{2\eta}[N]^T[N]d\,\Omega_e \\ + A_e \int_{\Omega_e} 2G_c\eta[B]^T[B]d\,\Omega_e \quad (8)$$

$$F_\alpha(u) = A_e \int_{\Omega_e} \mu[N]^T|\nabla u|^2 d\,\Omega_e \quad (9)$$

$F_u(\alpha)$ is the nodal reaction forces associated with imposed displacement nodes, $K_u(\alpha)$ is the rigidity matrix and $K_\alpha(u)$ is the rigidity matrix associated to the damage variable. [N] and [B] are respectively the displacement and gradient interpolation matrix. A_e is the assembly operator and Ω_e is a finite element domain.

We seek the solution for which the Eqs. 5 and 6 are verified. Due to the nonlinear nature of the residuals with respect to u and α, we employ an incremental-iterative strategy.

The alternate minimization algorithm is summarized in algorithm 1:

Algorithm 1 Staggered algorithm for quasi-static fracture
Require: Material parameters, $\alpha(t = 0)$, du = U/N
U ← Total displacement
N ← Number of iterations

For i = 1 to N **do**

k = k + 1

while $||\alpha^k - \alpha^{k-1}||_\infty >$ tol

$\alpha_i^k = \alpha_i^{k-1}$

$u_i^k = (K_u(\alpha_i^k))^{-1}.F_u(\alpha_i^k)$

$\alpha_i^k = (K_\alpha(u_i^k))^{-1}.F_\alpha(u_i^k)$

If $\alpha_i^k < \alpha_i^{k-1}$ **then** $\alpha_i^k = \alpha_i^{k-1}$ (the irreversibility condition)

end while

end for

3 Numerical Examples

In this section, we present the influence of the geometry of specimen on the crack path. Two examples will be detailed.

3.1 A Specimen with Circular Notches

In this example, notched specimens with different distances, denoted h, between the two circular notches, are considered to study the crack path. The loading is given by applying normal displacements on the upper border of the plate and the lower edge is assumed to be fixed. The others boundaries are free.

Several tests are elaborated to study the influence of the value of h on the crack path and the evolution of the total energies respectively in the following figures (Fig. 1 and 2). The mesh consists of 5085 triangular elements with an element size of 0.5 mm. The Young's modulus was assumed to be 210 GPa. The material parameters are Gc = 0.1 J/mm^2 and η = 0.7.

The crack pattern depends notably on the value of notches distance h. Indeed, if the distance between the two circular notches is less than h_c = 16.5 mm, the crack propagates from the left notch to the right one brutally, but if the value of h is more than h_c, the crack propagates horizontally from the left notch to the right edge.

The elastic and the surface energies are given respectively by the following equations (Eqs. 10 and 11):

$$\text{Eelast} = \frac{\mu}{2}\int_\Omega ((1-\alpha)^2 + k)\nabla u^2 d\Omega \tag{10}$$

$$\text{Esurf} = G_c \int_\Omega (\frac{\alpha^2}{4\eta} + \eta\nabla\alpha^2)d\Omega \tag{11}$$
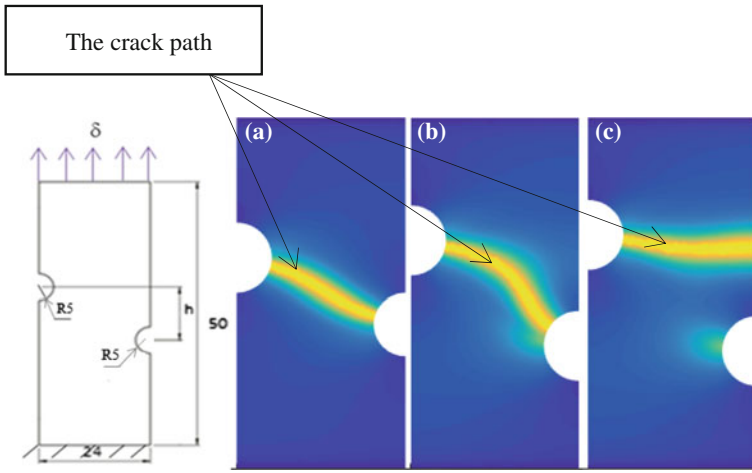
Fig. 1 Geometry, loading, boundary conditions and crack paths of the plate with circular notches: **a** h = 10 mm, **b** h = 15 mm, **c** h = 16.5 mm

Fig. 2 Total energy-displacement curve for different values of h
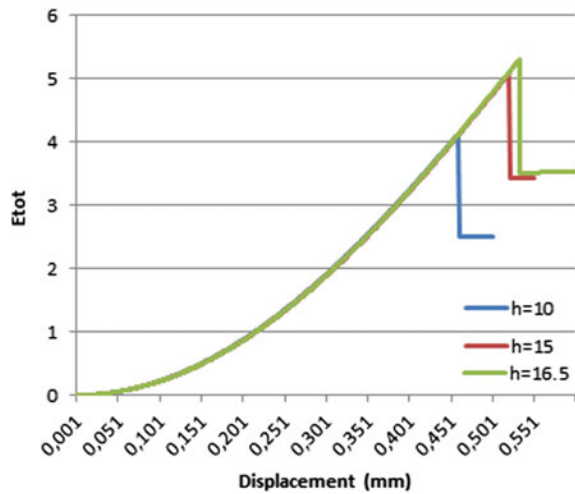
The total energy (Etot = Eelast + Esurf) evolution is the same for the three specimens before the initiation of the crack. But the critical displacement at which the specimen is cracked decrease when the distance h decrease.

3.2 Fiber Reinforced Matrix

The example of the rigid inclusion in an elastic matrix (see Fig. 3) is considered as a paradigmatic example to illustrate the potentiality of the variational approach. We present briefly the works which study the problem of propagation of cracks in a square plate reinforced by a rigid circular fiber.

This problem is addressed by Bourdin et al. (2000) to highlight the ability of the variational approach to recover the initiation phenomena and the complex crack profiles, then by Del Piero et al. (2007) integrating nonlinear effects, after that by Bourdin (2007) using the backtracking algorithm to find the global minimum of the functional E (u, α). Amor et al. (2009) addresses the same problem by applying a formulation equivalent to the mixed cleavage model; later (Freddi and Carfagni 2010) also simulate the propagation of cracks in the same model.

We studied in this section the influence of the ratio between the inclusion diameter and the matrix edge length on the crack initiation and propagation. The inclusion is assumed to be fixed and an imposed displacement is applied on the top matrix edge (Fig. 3):

Numerical results show an interesting dependence on the geometric aspect ratio, specified by the radius of the inclusion $\rho = \frac{d}{L}$ with d the diameter of the inclusion and L the length of the piece (see Fig. 4). The mesh consists of 18000 triangular elements with an element size of 0.03 mm. The Young's modulus was assumed to be 210 GPa. The material parameters are Gc = 0.1 J/mm^2 and η = 0.05.

At the beginning of the test, a crack of finite length appears suddenly just above the north pole of the inclusion then the crack propagates abruptly on both sides and the structure is divided into two parts. The path of the crack depends on the ratio of the inclusion diameter and matrix length (ρ). More this ratio (ρ) decreases more the crack path becomes in the middle of the piece, but if the value of $\rho \leq \rho_c = 1/6$, the crack propagates around the inclusion. This observation must be validated with a formulation taking into account a bidirectional displacement field.

Fig. 3 Geometry, loading and boundary condition of the plate reinforced by a rigid circular fiber
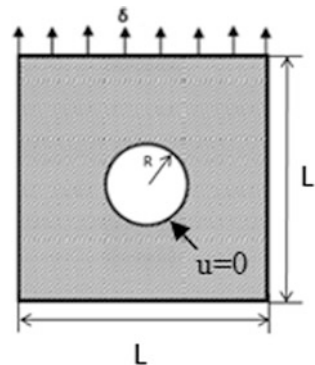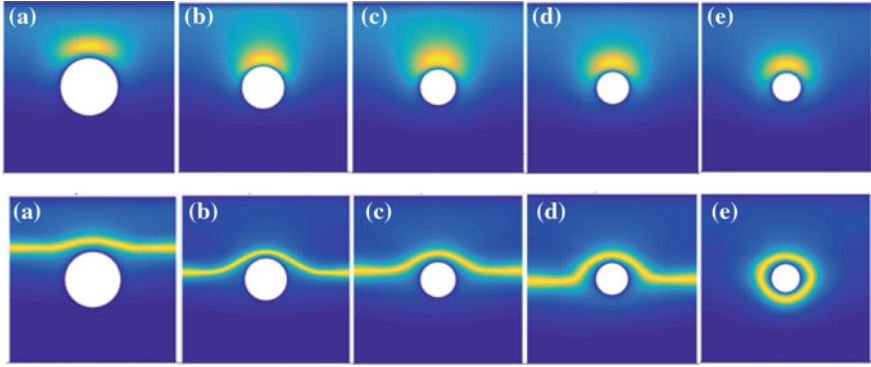
Fig. 4 (Top) The crack initiation, (Bottom) The crack path: **a** $\rho = 0.33$, **b** $\rho = 0.25$, **c** $\rho = 0.21$, **d** $\rho = 0.18$, **e** $\rho = 0.16$

4   Optimal Algorithm

We know that fracture initiation begins when the load of the specimen reaches a critical value (U_f). We propose in this paper to start with a linear elastic computing (α is deactivated), till the maximum stress in the specimen reaches a critical value σ_c given by the following expression $\sigma_c = \frac{3\sqrt{3}}{16\sqrt{2}} \sqrt{\frac{EG_c}{\eta}}$ (Amor et al. 2009), with E the Young modulus, G_c the toughness and η is a regularized numerical parameter. Then we continue the computing by introducing the damage variable (α).

The optimal alternative minimization algorithm is as follows:

Algorithm 2 Staggered optimal algorithm for quasi-static fracture
Require: Material parameters: U_f, μ, σ_c
Linear computing: σ_{22max} (because our tensile tests are in direction 2 and this stress is the most important)
Calculation of U_c with interpolation: $U_c = U_f \frac{\sigma_c}{S \sigma_{22max}}$; (s a safety coefficient)
Activation of α (initialization $\alpha = 0$)
du $= \frac{(U - U_c)}{N}$
$U \leftarrow$ Total displacement
$U_c \leftarrow$ critical displacement
$N \leftarrow$ Number of iterations
For i = 1 to N **do**
k = k + 1
while $||\alpha^k - \alpha^{k-1}||_\infty >$ tol
$\alpha_i^k = \alpha_i^{k-1}$

Fig. 5 Load-displacement curve
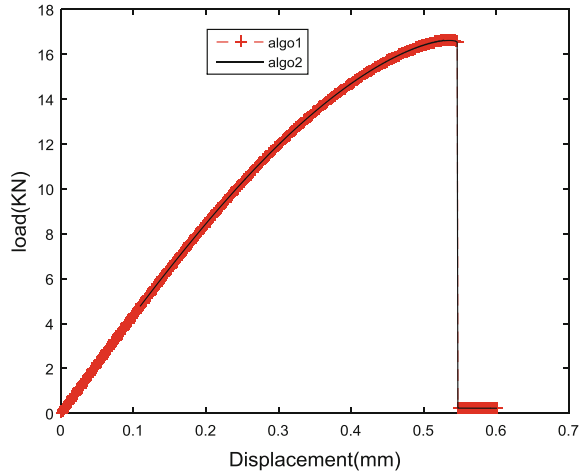
Fig. 6 Energy-displacement curve
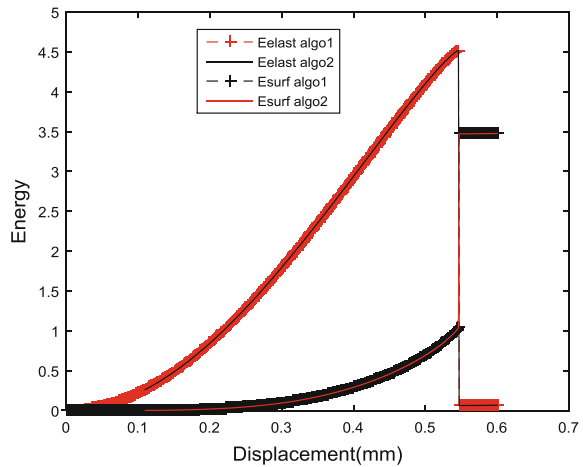
$$u_i^k = (K_u(\alpha_i^k))^{-1}.F_u(\alpha_i^k)$$
$$\alpha_i^k = (K_\alpha(u_i^k))^{-1}.F_\alpha(u_i^k)$$
If $\alpha_i^k < \alpha_i^{k-1}$ **then** $\alpha_i^k = \alpha_i^{k-1}$ (the irreversibility condition)
end while
end for

A comparison was made between algorithm 1 (activation of α from the beginning) and algorithm 2 (deactivation then activation of α) we have taken the example of notched specimen with distance h = 20 mm (see Fig. 5 and 6). We found the same results with a time saving of G = 20%.

5 Conclusion

Brittle fracture is modeled by using the phase-field approach which is a hopeful computational tool to predict crack path. We supply the performance of the quasi-static phase-field model of fracture using the staggered implementation scheme. Within the formulations stemming from Griffith's theory, we focus on the quasi-static model featuring tension tests. In this paper, we propose an improvement of the current standard algorithm for solving variational fracture models that can greatly reduce the number of increments required for convergence.

References

Ambati M, Gerasimov T, De Lorenzi L (2015) A review on phase-field models of brittle fracture and a new fast hybrid formulation. J Comput Mech 55:383–405

Amor H, Marigo JJ, Maurini C (2009) Regularized formulation of the variational brittle fracture with unilateral contact: Numerical experiments. J Mech Phys Solids 57:1209–1229

Borden MJ, Hughes TJR, Landis CM, Verhoosel CV (2014) A higher-order phase-field model for brittle fracture: formulation and analysis within the isogeometric analysis framework. Comput Methods Appl Mech Eng 273:100118

Bourdin B (2007) Numerical implementation of the variational formulation for quasi-static brittle fracture. Interfaces and Free Boundaries 411–430

Bourdin B, Francfort G, Marigo JJ (2000) Numerical experiments in revisited brittle fracture. J Mech Phys Solids 48 (4):797–826

Bourdin B, Francfort G, Marigo JJ (2008) The variational approach to fracture. J Elast 91:5–148

Buliga M (1998) Energy minimizing brittle crack propagation. J Elast 52(3):201–238

Del Piero G, Lancioni G, March R (2007) A variational model for fracture mechanics: numerical experiments. J Mech Phys Solids 55(12):2513–2537

Francfort G, Marigo JJ (1998) Revisiting brittle fracture as an energy minimization problem. J Mech Phys Solids 46:1319–1342

Freddi F, Royer-Carfagni G (2010) Regularized variational theories of fracture: a unified approach. J Mech Phys Solids 58(8):1154–1174

Gerasimov T, De Lorenzis L (2016) A line search assisted monolithic approach for phase-field computing of brittle fracture. Comput Methods Appl Mech Eng. in press. https://doi.org/10.1016/j.cma.2015.12.017

Griffith A (1921) The phenomena of rupture and flow in solids. Philos Trans R Soc Lond 221:163–198

Hentati H, Ben Naceur I, Bouzid W, Maalej A (2015) Numerical analysis of damage thermo-mechanical models. Adv Appl Math Mech 7:5, 625–643T

Oleaga GE (2004) On the path of a quasi static crack in mode iii. J Elast 76:163–189

Pham K, Marigo JJ (2010a) Approche variationnelle de l'endommagement: I. les concepts fondamentaux. Comptes Rendus Mécanique 338:191–198

Pham K, Marigo JJ (2010b) Approche variationnelle de l'endommagement: II. les modéles à gradient. Comptes Rendus Mécanique 338:199–206

Numerical Study of PCM Solidification in a Rectangular Modular Heat Exchanger

Jmal Imen and Baccar Mounir

Abstract Thermal energy storage got a significant role in the solar energy conservation in order to expand its use over time. To exploit solar energy continuously, we require a storage energy system. Phase Change Material (PCM) is used in this kind of systems in order to store a great amount of thermal energy. In fact, Latent heat storage in a PCM is very interesting because of its high-energy storage density and its isothermal behavior during the phase change process. Hence, heat accumulated during sunshine period can be restituted to be used for air conditioning purposes in buildings. This work concerns the solidification in the presence of the natural convection of a rectangular phase change material exposed to a cold air flow along the conducting side walls. With this intention, the first stage includes the presentation of a numerical model based on the conservation equations, treated by finite volume method (two-dimensional model) coupled to an enthalpy formulation (source terms). This numerical approach having like objective to follow the evolution of the various parameters characterizing the phenomenon of phase change (liquid–solid interface and a liquid fraction) during all the processes of solidification as well as the temperature and the velocity distribution in the PCM storage systems. Also, we give in this study the transient evolution of the longitudinal air temperature profiles.

Keywords Numerical simulation · Solidification · PCM · Latent heat
Natural convection

J. Imen (✉) · B. Mounir
Research Unit of Computational Fluid Dynamics and Transfer Phenomena (CFDTP),
Mechanical Engineering Department, National Engineering School of Sfax, Sfax, Tunisia
e-mail: imenn.jmal@gmail.com

B. Mounir
e-mail: mounir.baccar@hotmail.fr

1 Introduction

Solid–liquid phase change materials (PCMs) have been used as temperature regulators in different applications to maintain human comfort temperature in built environment (Liu et al. 2012).

PCM storage systems have been developed for many applications, including those for building applications. In fact, PCMs have been used as temperature regulator to maintain human comfort temperature in built environment to store heat during daytime or coolness during night time to reduce the temperature swing (Pasupathy et al. 2008).

Several previous research studies have emphasized the presence of natural convection heat transfer during the storage or recuperation of thermal energy in PCM by testing different storage system geometries to optimize the amount of exchanged heat (Seck et al. 2009; Castell et al. 2008).

The present paper presents a numerical study of the solidification of PCM (paraffin **RT27**) in a rectangular thermal storage for air conditioning systems taking into account the presence of natural convection. The first part includes the presentation of a numerical model based on the continuity, momentum, and thermal energy equations, treated by the finite volume method. The main objective of this numerical approach is the study of the effect of natural convection on the PCM solidification time. It also aims to investigate the temporal evolution of PCM solidification, and solidification front, as well as the longitudinal profiles of the Heat Transfer Fluid HTF in duct.

2 Computational Domain and Mathematical Formulation

In the present work, the studied system is a stack of several metal flat modules filled with PCM (RT27) and arranged horizontally (Fig. 1). Each module is of length L = 1.2 m and a height H = 4 cm. PCM storage unit was modeled as duct with air flowing through it as shown in Fig. 1. As for the Heat Thermal Fluid HTF, it is
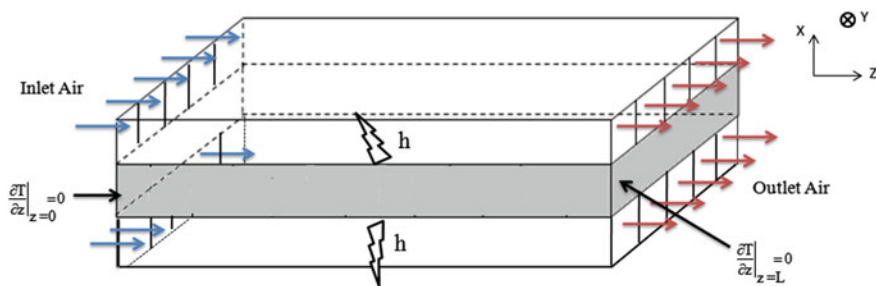
Fig. 1 Studied configuration

Table 1 Thermo-physical properties of the PCM RT27 (Aadmi et al. 2015)

		C_{18}
Melting interval [°C]		[27–27.5]
Latent Heat [kJ kg^{-1}]		179
Density [kg m^{-3}]:	Solid	870
	Liquid	760
Specific heat [kJ kg^{-1} °C^{-1}]:	Solid	2.4
	Liquid	1.8
Thermal conductivity [W m^{-1} °C^{-1}]:	Solid	0.24
	Liquid	0.15
Thermal volumetric expansion coefficient [kg m^{-3} °C^{-1}]		8.5×10^{-4}
Kinematic viscosity [m^2 s^{-1}]		1.5×10^{-6}

Fig. 2 Computational domain
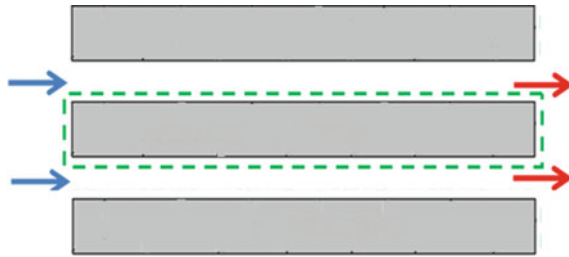
conveyed in rectangular ducts constituted by free spaces between two successive PCM modules. The grooves have cross-sections dimensions a = b = 4 cm. The thermo-physical properties of the solid and liquid PCM and aluminum are listed in Table 1.

The problem is two-dimensional (x-z). The computational domain is the green boxed area in Fig. 2.

2.1 Modeling of the Heat Transfer in the Annular Duct of Air

The heat transfer to the HTF-governing equation is given as follows:

$$\rho_{air} Cp_{air}\left(\frac{\partial T_{air}}{\partial t} + W_{air}\frac{\partial T_{air}}{\partial z}\right) = \frac{2ah(T_{PCM} - T_{air})}{ab} \tag{1}$$

where "a" and "b" are the dimensions of ducts.

2.2 Numerical Modeling of Heat Transfer in the PCM Domain

The natural convection of a transient laminar PCM flow in the PCM container has been studied numerically. Considering constant properties, except the density difference (Boussinesq approximation), and using the enthalpy method, the continuity, momentum, and thermal energy equations for the PCM can be written as follows:

- Continuity equation

$$\frac{\partial u}{\partial x} + \frac{\partial w}{\partial z} = 0 \tag{2}$$

- Momentum equations

The Momentum equations incorporate sink terms to take into account the changing phase of the PCM. The condition that all velocities in solid regions are zero is considered using an enthalpy-porosity approach (Brent et al. 1988)

$$\frac{\partial U}{\partial t} = -div\left(\underbrace{\vec{V}U - \nu\, \vec{grad}\, U}_{\vec{J_u}}\right) \underbrace{- \frac{1}{\rho}\frac{\partial P}{\partial x} + g\beta(T - T_0) - \frac{1}{\rho}c\underbrace{\frac{(1-f)^2}{f^3 + b}}_{A(f)}U}_{S_U} \tag{3}$$

$$\frac{\partial W}{\partial t} = -div\left(\underbrace{\vec{V}W - \nu\, \vec{grad}\, W}_{\vec{J_V}}\right) \underbrace{- \frac{1}{\rho}\frac{\partial P}{\partial z} - \frac{1}{\rho}c\underbrace{\frac{(1-f)^2}{f^3 + b}}_{A(f)}W}_{S_W} \tag{4}$$

where; S_u is constituted by two terms, the first of which corresponds to the solidification sink term and the second is the thermo-convective generation term. Furthermore, S_w is the extinction of "W" component due to the solidification of PCM.

- Energy equation

$$\rho(T)\, C_p(T)\frac{\partial T}{\partial t} = -div\left(\rho(T)\, C_p(T)\vec{V}T - \lambda(T)\, \vec{grad}\, T\right) \tag{5}$$

where (Jmal and Baccar 2015)

$$\rho(T)Cp(T) = \begin{cases} \rho_s Cp_s & T \leq T_{sd} \\ \rho_l Cp_l & T \geq T_{liq} \\ \frac{\rho_{mix} L}{T_{liq} - T_{sd}} & T_{sd} \leq T \leq T_{liq}/\rho_{mix} = f\rho_l + (1-f)\rho_s \end{cases} \quad (6)$$

$$\lambda(T) = \begin{cases} \lambda_s & T \leq T_{sd} \\ \lambda_l & T \geq T_{liq} \\ \frac{\lambda_l - \lambda_s}{T_{liq} - T_{sd}}(T - T_{liq}) + \lambda_l & T_{sd} \leq T \leq T_{liq} \end{cases} \quad (7)$$

The liquid fraction "f" can be analyzed by the following equation:

$$f = \frac{T - T_{sd}}{T_{liq} - T_{sd}} \quad (8)$$

2.3 Initial and Boundary Conditions

For the velocity components, the non-slip boundary conditions on all solid walls are imposed.

With regard to energy restitution, the imposed boundary condition is a convective heat transfer on both sides of the PCM container:

$$h(T_{PCM} - T_{air}(z)) = -\lambda \frac{\partial T}{\partial x}\bigg|_{x=H} \quad (9)$$

$$h(T_{PCM} - T_{air}(z)) = \lambda \frac{\partial T}{\partial x}\bigg|_{x=0} \quad (10)$$

As initial conditions, it is assumed in the discharging mode (solidification) the storage unit and the air in duct are initially at a uniform temperature of 35 °C and the temperature of the inlet air is 10 °C.

3 Results

3.1 Temporal Evolution of PCM Solidification

Figure 3 illustrates the transient evolution of temperature fields and induced current lines in a rectangular container without fins. At first, in the upper part of the module, the hot PCM adjoining the upper side cooled by the flowing air, becomes denser and tends to descend downwards. Hence, the creation of the thermo-convective loops giving rise to a multicellular flow regime. Indeed, in Fig. 3, we see little inconsistent convective cells occupying the entire module. These cells are larger on
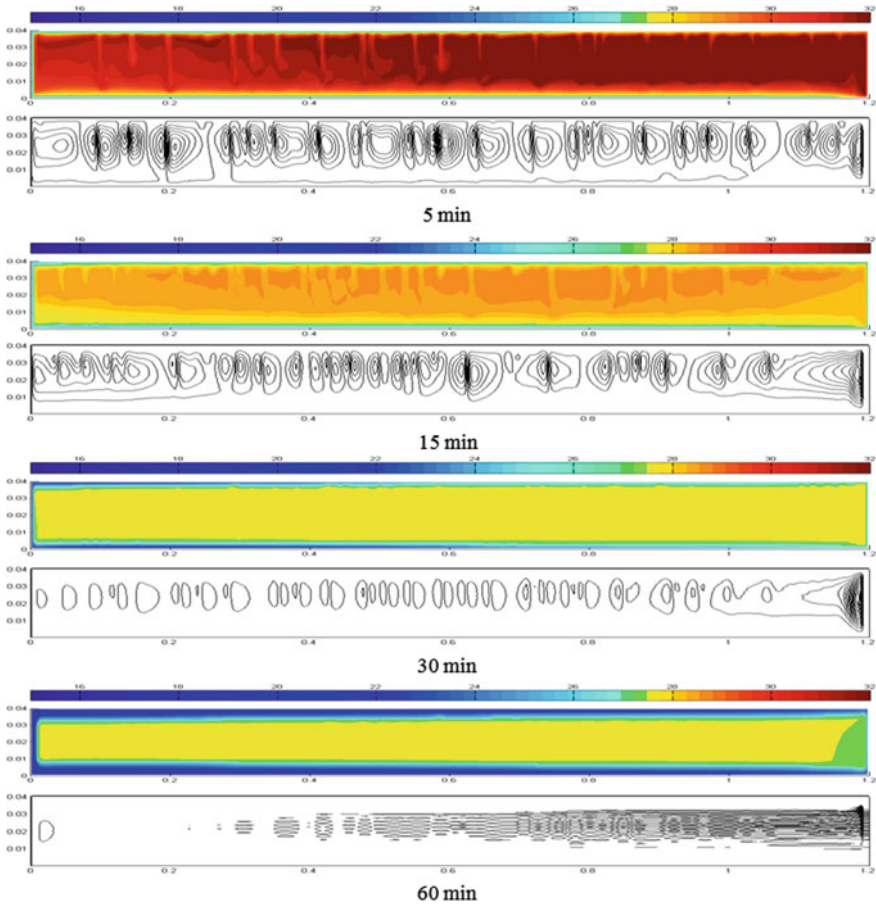
Fig. 3 Temporal evolution of the temperature field and with corresponding current lines

the side of the inlet of the cold air, which can be attributed to thermal gradients that are higher in this zone. In the lower part of the module which is cooled by the lower face of the module, parallel isotherms are observed indicating a thermal stratification of the cold fluid. At t = 1 h, thermo-convection cells disappear completely, and the heat transfer is virtually conductive.

3.2 Temporal Evolution of PCM Solidification

To determine the efficiency of the exchanger during charging mode, we have reproduced in Fig. 4, the temporal evolution of the air temperature at the exit of the ducts. The curve gives the trend characterized by a rapid drop in temperature of the

Fig. 4 Temporal evolution of
the outlet air temperature in
duct
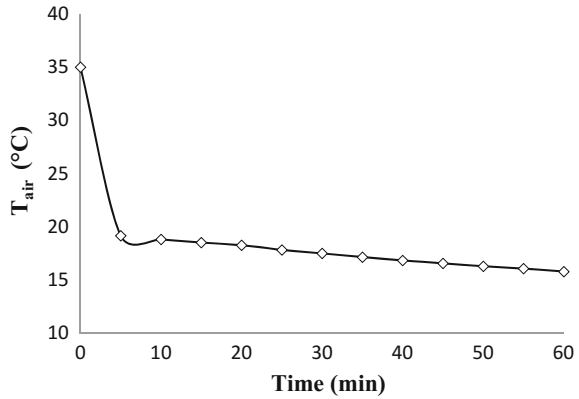
Fig. 5 Transient evolution of
solid fraction
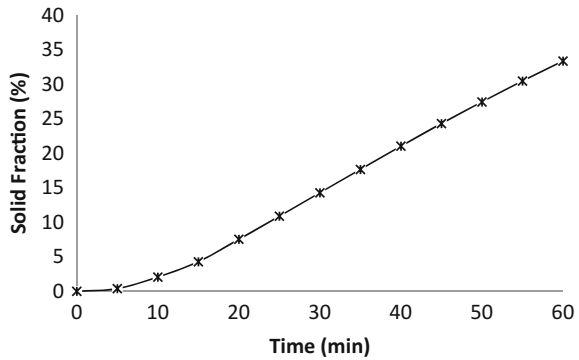
outlet air, followed by a stabilization phase at a temperature of about 16 °C, which
results in a low efficiency: E = 34%.

3.3 *Transient Evolution of Solid Fraction*

The representation of the temporal evolution of the solid fraction is given in Fig. 5.
As shown in this curve, before 20 min, solidification is very slow. Then, it takes
more importance with a constant slope of about 0.55 due to the intensification of
natural convection.

4 Conclusion

In the present work, we have studied the solidification of the PCM (Paraffin RT27)
in a modular Rectangular air-PCM heat exchanger, horizontally arranged. We have
observed only a slight improvement in the transfer. That is explained by the

presence of stratification phenomenon which takes place in PCM from the colder to the hotter.

References

Aadmi M, Karkri M, El Hammouti M (2015) Heat transfer characteristics of thermal energy storage for PCM (phase change material) melting in horizontal tube: numerical and experimental investigations. Energy 1–14

Brent AD, Voller VR, Reid KJ (1988) Enthalpy-porosity technique for modeling convection-diffusion phase change: application to the melting of a pure metal. Numer Heat Transfer 13:297–318

Castell A, Solé C, Medrano M, Roca J, Cabeza LF, Garcıa D (2008) Natural convection heat transfer coefficients in phase change material (PCM) modules with external vertical fins. Appl Therm Eng 28:1676–1686

Jmal I, Baccar M (2015) Numerical study of PCM solidification in a finned tube thermal storage including natural convection. Appl Therm Eng 84:320–330

Liu M, Saman W, Bruno F (2012) Review on storage materials and thermal performance enhancement techniques for high temperature phase change thermal storage systems. Renew Sustain Energy Rev 16:2118–2132

Pasupathy A, Velraj R, Seenira RV (2008) Phase change material-based building architecture for thermal management in residential and commercial establishments. Renew Sustain Energy

Seck D, Thiam A, Sambou V, Azilinon D, Adj M (2009) Détermination du front de fusion d'une plaque de paraffine soumise à l'ensoleillement. J des Sci 1:34–42

Hydrodynamic Behavior in Scraped Surface Heat Exchanger with Archimedes' Screw

Sirine Ali and Mounir Baccar

Abstract The present study presents a numerical simulation of the hydrodynamic behavior inside a scraped surface heat exchanger (SSHE) which includes Archimedes' screw instead of using scrapers. A 3D CFD code is used in order to characterize the flow pattern and the apparent viscosity distribution in the heat exchanger for Bingham fluids. With that purpose, the resolution of the conservation equations of continuity and momentum equations are conducted using the finite volume method. The effect of dimensionless numbers (rotational Reynolds and axial Reynolds) on the hydrodynamic behavior is studied. Numerical investigation shows that the lowest apparent viscosity values are localized close to the stator wall and near the rotor of the exchanger and the highest values are next to the Archimedes' screw. Studies indicate also that the strongest shear rates values are in the space between the tip of the Archimedes' screw and the stator wall.

Keywords SSHE · Archimedes' screw · Bingham fluids · Flow pattern Apparent viscosity

1 Introduction

Scraped surface heat exchangers (SSHEs) are found in chemical and food industries for many thermal applications such as sterilization, cooling and heating viscous liquids, multiphase fluid systems, etc. SSHE is produced to thermally treat high viscous and sticky products such as mayonnaise, toothpaste, chocolate paste, caramel, cream, etc.

S. Ali (✉) · M. Baccar
Research Unit of Computational Fluid Dynamics and Transfer Phenomena (CFDTP),
Mechanical Engineering Department, National Engineering School of Sfax (ENIS), Sfax,
Tunisia
e-mail: sirineali@ymail.com

M. Baccar
e-mail: Mounir.Baccar@enis.rnu.tn

Many studies have been conducted since the idea of SSHE had been first given by Huggins in (1931) who predicted that using scrapers instead of stirrers in viscous applications highly improves the heat transfer coefficient. Thermal and hydrodynamic behaviors are the most important phenomena related to SSHEs, thus, they took the interest of many researchers such as: Trommelen and Beek (1971) who created an empirical model based on the penetration theory using viscous fluids. De Gode and De Jong (1993) developed a CFD (Computational Fluid Dynamics) model to predict the evolution of a vortex between the scraper blades in the turbulent regime and he determined a theoretical model. Baccar and Abid (1997) used a 3D modeling to analyze the hydrodynamic and thermal behaviors under different operating and geometrical conditions and they gave the effect of the shape and the number of scrapers. Yataghene et al. (2008) created a 2D model to predict the velocity profile and the local shear rates for Newtonian and non-Newtonian fluids, which was in agreement with the experimental investigation (electrochemical method). They mentioned that it's necessary to do a 3D analysis to handle the thermal treatment. Recently, Yataghene and Legrand (2013) examined the thermal performance of a SSHE for Newtonian and non-Newtonian fluids using a 3D-numerical modeling. They varied the speed of blades and the mass flow rate, and they found that the increase of the mass flow rate reduces the efficiency of the SSHE and that viscous heating increases with rotating velocity. In our previous study (Ali and Baccar 2016), the hydrodynamic and thermal behaviors inside a SSHE with helical ribbons were studied using a 3D CFD modeling, and we developed a heat correlation in order to predict the heat transfer coefficient (Table 1).

Table 1 Nomenclature

Symbol	Quantity	SI units
D	Internal diameter of the exchanger	(m)
d_a	Agitator diameter	(m)
d_r	Rotor shaft diameter	(m)
h	Heat transfer coefficient	(W/m^{2}K)
L	Length of the exchanger	(m)
N	Rotational speed	(rev/s)
P	Pressure	(Pa)
p	Pitch of the helical ribbon	(−)
R	Internal exchanger radius	(m)
r	Rotor shaft radius	(m)
T	Temperature	(K)
U, V, W	Dimensionless velocity components	(−)
r, θ, z	Dimensionless coordinates system	(−)
ρ	Fluid density	(kg/m^3)
λ	Thermal conductivity of air	(W/mK)
μ	Dynamic viscosity	(Pa s)
η	Apparent viscosity	(−)
ν	Kinematic viscosity	(m^2/s)
θ	Dimensionless temperature	(−)
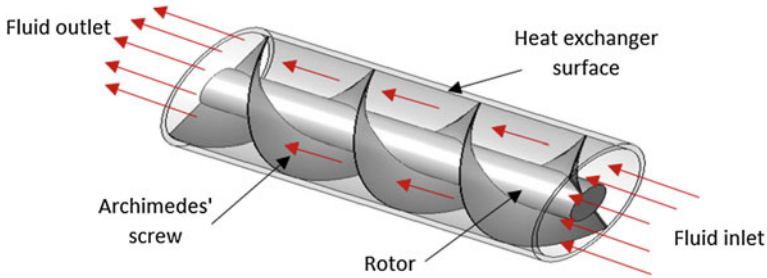
Fig. 1 Scheme of the SSHE model with Archimedes' screw

The Scraped Surface Heat Exchangers (SSHE) are equipped with mechanical systems for mixing the fluid to be heated or cooled and scraping the exchanger's wall. There are different constructive geometries of scraper blades. This study presents an innovative SSHE which, instead of using scrapers, it includes Archimedes' screw that can reduce the backmixing phenomenon, maintain a good and uniform heat exchange and provide simultaneous mixing and agitation. A schematic representation of the heat exchanger is shown in Fig. 1.

2 Numerical Model

2.1 Geometry and Mesh

A specific CFD (Computational Fluid Dynamics) code was used in the simulation of the hydrodynamics. The methods of discretization used for the modeling of velocity field were the hybrid scheme and the exponential scheme, respectively. The ratio of rotor shaft radius to internal exchanger radius (r/R) is equal to 0.8. The ratio of exchanger height to its internal radius (H/R) is equal to 6. This configuration is the same as that studied experimentally by Trommelen and Beek (1971) and numerically by Baccar and Abid (1997). The Archimedes' screw extends over four pitches. It was driven by the rotor, to continuously scrape the stator wall. The grid size used in the simulation is 230400 computational cells (36 in the radial, 40 in the tangential and 160 in the axial direction).

2.2 Governing Equations

In this section, the conservation equations of continuity and momentum have been solved based on the Finite Volume Method (FVM). The flow is considered steady, laminar, non-isothermal, and incompressible.

The continuity equation for the velocity in the rotating reference frame is written as:

$$\mathrm{div}\,\overrightarrow{V} = 0. \tag{1}$$

with $\overrightarrow{V}$ is the velocity vector.

The momentum equation can be expressed in the tensorial form as follows:

$$\rho\left(\frac{\partial \overrightarrow{V}}{\partial t} + \overrightarrow{\mathrm{grad}}\,\overrightarrow{V}\,\overrightarrow{V}\right) = -\overrightarrow{\mathrm{grad}}P + \mathrm{div}\,\overrightarrow{\tau} + \rho\,\overrightarrow{g} \tag{2}$$

The tensorial strain can be written considering a purely viscous generalized Newtonian fluid:

$$\overrightarrow{\tau} = \eta|\dot{\gamma}|. \tag{3}$$

where $\dot{\gamma}$ is the shear rate. In a rotating frame, Centrifugal and Coriolis acceleration which defined respectively as $-w^2 \cdot \overrightarrow{r}$ and $2\overrightarrow{w} \wedge \overrightarrow{r}$ were added to the momentum equation.

2.3 Rheological Model

Fluids treated in SSHEs are high viscous or sticky and/or non-Newtonian. There are many mathematical models for describing the rheological behavior to solve the momentum equation in the case of non-Newtonian fluids, where the apparent viscosity (η) is a nonlinear function of the shear rate (γ). Many of fluid materials have a yield stress, a critical value of stress below which they do not flow; they are sometimes called viscoelastic materials or Bingham plastics, after Bingham. They constitute an important class of non-Newtonian materials.

In the present study, the Papanastasiou's model was considered. He suggested an exponential regularization of the Bingham plastic model, by introducing a parameter m, which controls the exponential growth of stress (Papanastasiou 1987; Mitsoulis 2007).

The proposed model, called also Bingham-Papanastasiou model, has the following form:

$$\eta = 1 + \frac{\mathrm{Od}[1 - \exp(-m|\dot{\gamma}|)]}{|\dot{\gamma}|} \tag{4}$$

The viscoplastic character of the flow is assessed by a Bingham number (Bn) or Oldroyd number (Od), defined by:

$$Bn = Od = \frac{\tau_y D}{\mu V_a} \tag{5}$$

where τy is the yield stress and V_a is the average velocity of the viscoplastic fluid.

2.4 Boundary Conditions

The fluid enters the exchanger with an axial constant velocity:

$$W_{inlet} = constant \tag{6}$$

In the region where the fluid quits the computational domain, the velocity gradient equals to zero:

$$\frac{\partial W_{outlet}}{\partial z} = 0 \tag{7}$$

The presence of the rotor and Archimedes' screw was taken into account. Thus, all radial and tangential velocity mesh nodes which intersect with the rotor or the ribbon were taken equal to zero. The angular velocity component, at the internal wall exchanger, equal to the rotating speed because of the rotating frame.

3 Results and Discussion

3.1 Flow Pattern Description

In this paragraph, the conjugated effect of rotational Reynolds and axial Reynolds numbers ($\mathbf{r = Re_r/Re_a}$) on the velocity field was described. Figure 2 shows the nondimensional velocity distribution in a (r-z) plane and in the midplane of the tangential direction (r-θ).

The flow has an oscillatory path; when the Archimedes' screw hits the fluid every p/2 distance, it causes a deviation of the flow towards the regions not affected by the blockage. This deviation generates a local velocity increase, that's why a recirculation zone appears in the tip regions of the Archimedes' screw which has the most intensive hydrodynamic activity in the exchanger.
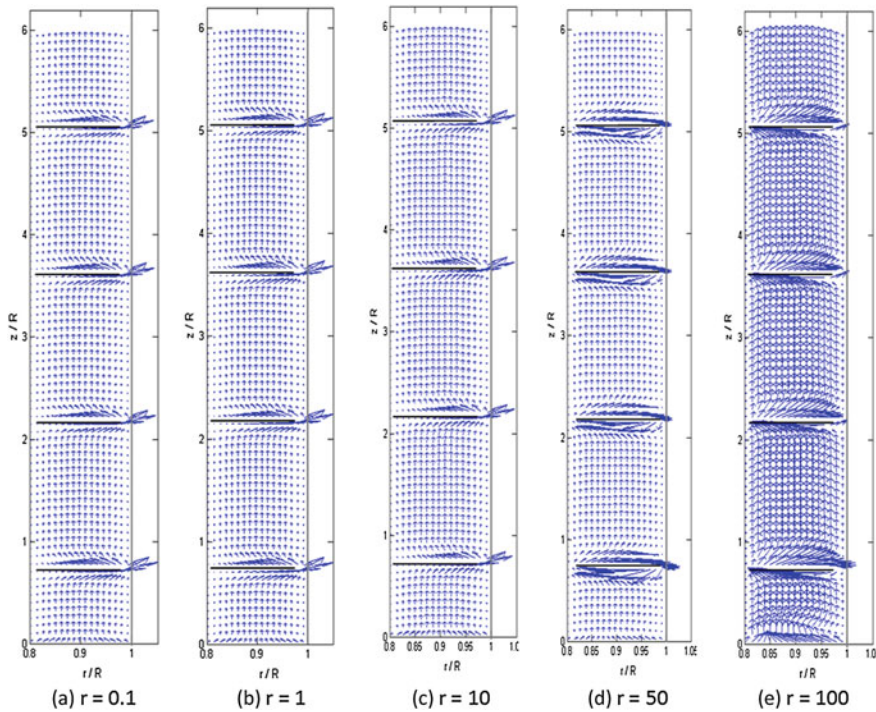
Fig. 2 Conjugated effect of Re_r and Re_a on the hydrodynamic behavior (Od = 3)

Figure 3 represents the radial velocity profile as a function of the axial position z for different Reynolds ratios, it shows an ascending overall flow with penetration of the material above the screw (centripetal flow), and a backflow below the screw (centrifugal flow).

Figure 4 gives the axial velocity profile as a function of the axial position z for different Reynolds ratios. It shows that when increasing the Reynolds ratios, the backmixing phenomenon begins to appear and the lowest values of the axial velocities are in the case of r = 100 ($Re_r > Re_a$).

3.2 Apparent Viscosity Distribution

Figure 5 gives numerical results of the distribution of the apparent viscosity, at the mid-height of the exchanger in a (R-θ) plane, for different Reynolds numbers. The colormap gives information about the apparent viscosity limits; the dark blue color

r = 0.1

r = 1

r = 10

r = 50

r = 100
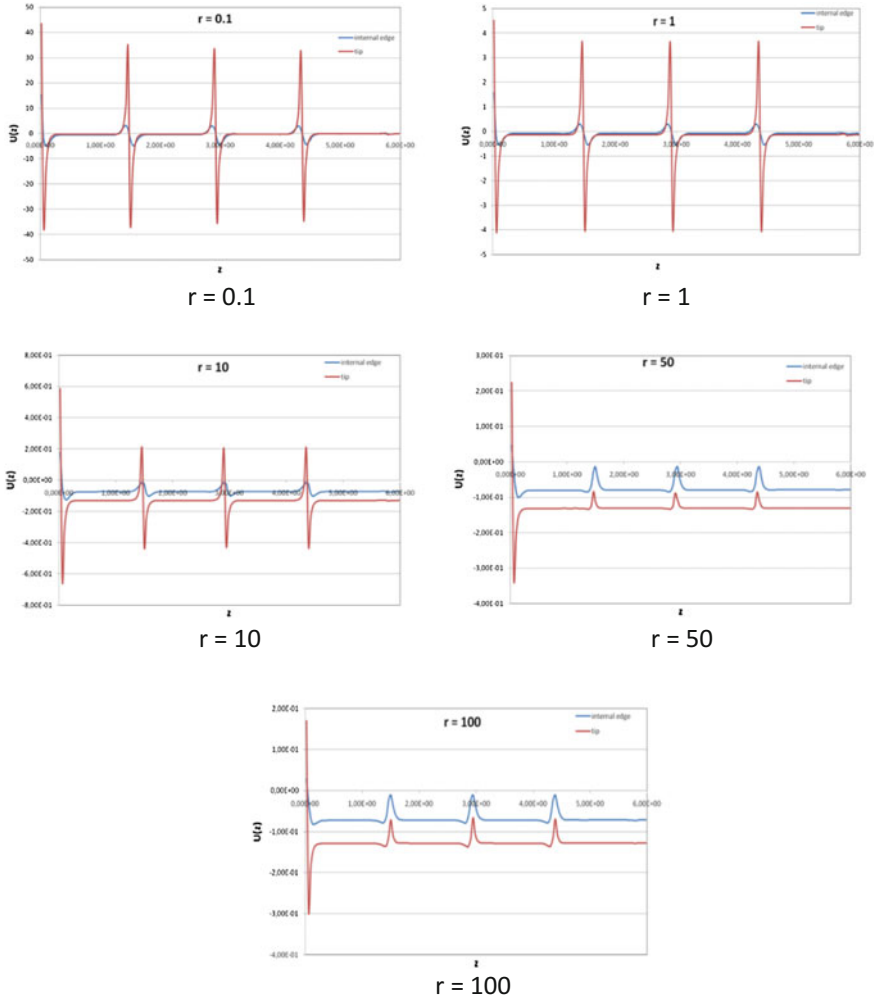
Fig. 3 Radial velocity as a function of the axial position z for different Re ratios

corresponds to $\eta = 0$ and the dark red one corresponds to the highest value of η. It shows that a layer with low viscosity exists close to the wall of the exchanger and another one near the rotor but higher viscosity. It shows also that the highest values of viscosity are found in the zone where the Archimedes' screw exists and which has very important shear rates. When the ratio of Reynolds numbers becomes bigger, this zone reduces.

r = 0.1

r = 1

r = 10

r = 50

r = 100
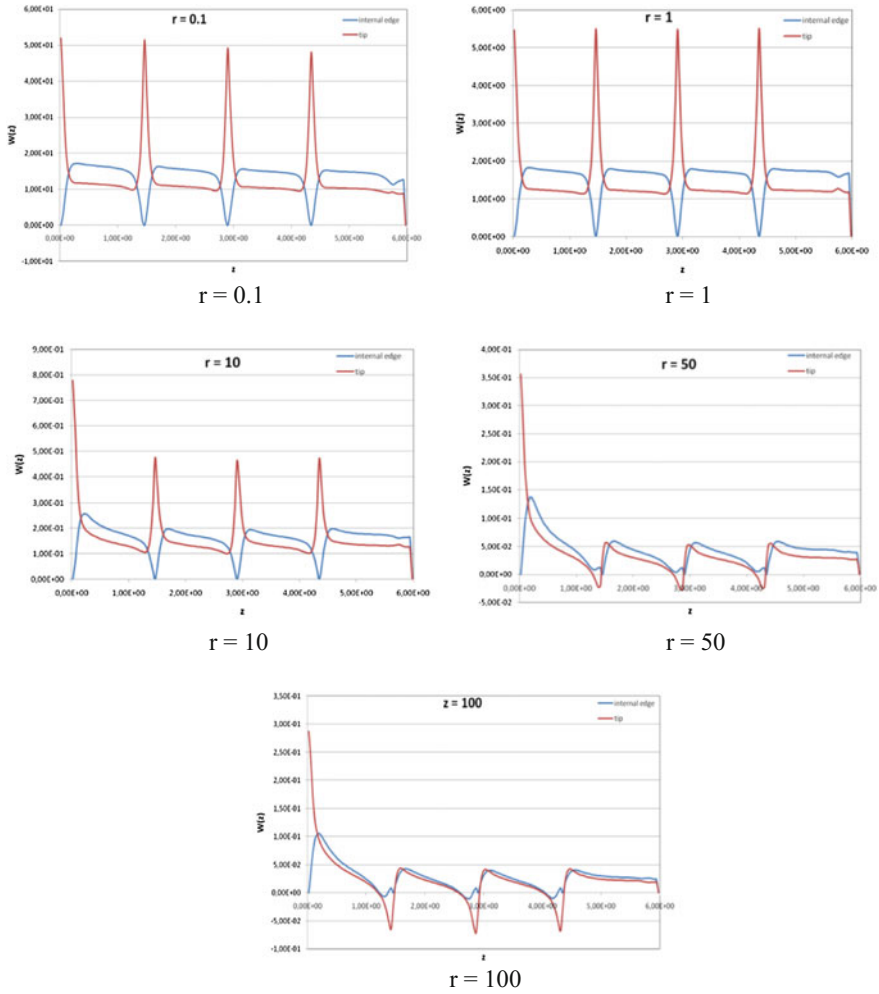
Fig. 4 Axial velocity as a function of the axial position z for different Re ratios

Figure 6 illustrates the dissipation function in a (R-θ) plane. It indicates that the highest values of shear rates are situated in the zone between the tip of the Archimedes' screw and the stator wall. However, in this region, the apparent viscosity is low compared to the overall product.
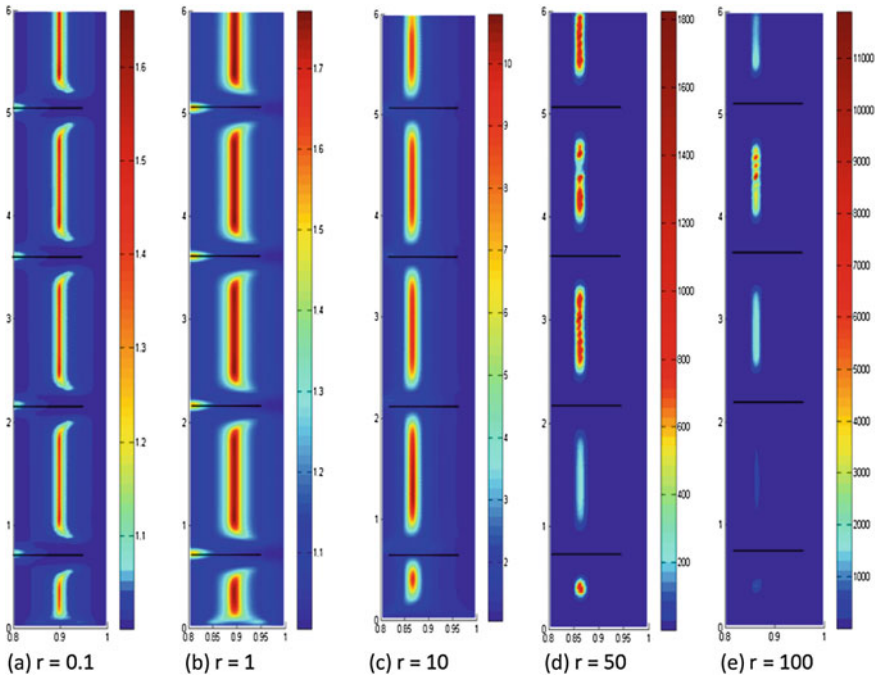
Fig. 5 Conjugated effect of Re_r and Re_a on the apparent viscosity in (R-Z) plane (Od = 3)
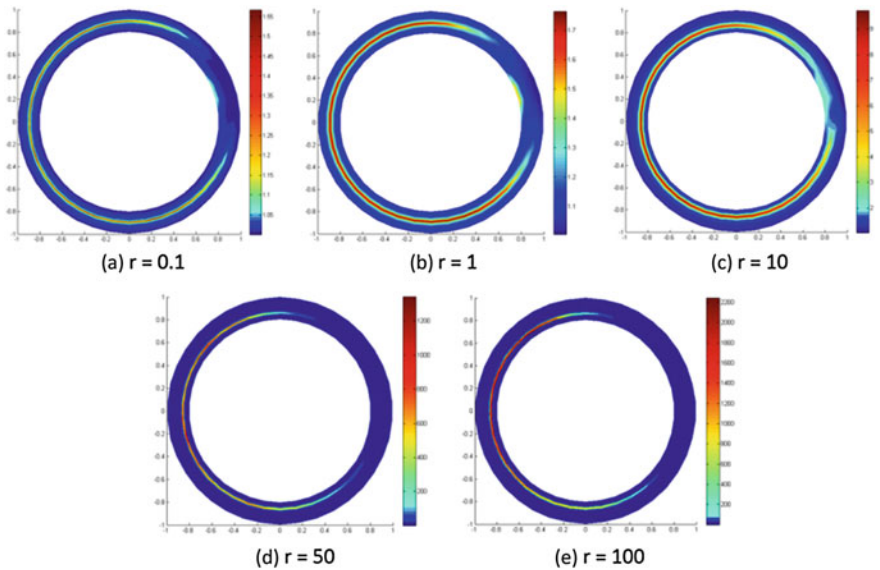
Fig. 6 Conjugated effect of Re_r and Re_a on the apparent viscosity in (R-θ) plane (Od = 3)

4   Conclusion

This work aimed to study numerically the hydrodynamic behavior and the apparent viscosity distribution within an innovative SSHE with Archimedes' screw for Bingham fluids. The effect of dimensionless numbers (Re_r and Re_a) on the flow pattern was studied. The distribution of the apparent viscosity is as follows: the maximum values are near the Archimedes' screw, whereas the smallest values are close to the stator wall and near the rotor. The highest shear rates are located between the tip of the Archimedes' screw and the stator wall.

The next step will be a 3D numerical analysis of the thermal behavior to determine the influence of the Archimedes' screw on this type of exchanger.

References

Ali S, Baccar M (2016) Numerical study of hydrodynamic and thermal behaviors in a scraped surface heat exchanger with helical ribbons. Appl Therm Eng 111:1069–1082

Baccar M, Abid MS (1997) Numerical analysis of three-dimensional flow and thermal behaviour in a scraped-surface heat exchanger. Rev Gen Therm 36:782–790

De Goede R, De Jong E (1993) Heat transfer properties of scraped-surface heat exchanger in the turbulent flow regime. Chem Eng Sci 48:1933

Huggins FE (1931) Effect of scrapers on heating, cooling and mixing. Ind Eng Chem 23(7):749–753

Mitsoulis E (2007) Flows of viscoplastic materials: models and computations. Rheol Rev 135–178

Papanastasiou TC (1987) Flow of materials with yield. J Rheol 31:385–404

Trommelen A, Beek W (1971) Phenomena in scraped-surface heat exchanger. Chem Eng Sci 26:1933

Yataghene M, Legrand J (2013) A 3D-CFD model thermal analysis within a scraped surface heat exchanger. Comput Fluids 71:380–399

Yataghene M, Pruvost J, Fayolle F, Legrand J (2008) CFD analysis of the flow pattern and local shear rate in a scraped surface heat exchanger. Chem Eng Process 47:1550–1561

Numerical Investigation of Heat Transfer by Al$_2$O$_3$–Water Nanofluid in Square Cavity

Houda Jalali and Hassan Abbassi

Abstract In this paper, the problem of heat transfer by Al$_2$O$_3$–water nanofluid in the square cavity is studied numerically. The bottom and top walls of the cavity are kept at constant temperatures T$_h$ and T$_c$, respectively, while the tow horizontal walls are supposed to be adiabatic and insulated. Again the effects of the thermal conductivity, the dynamic viscosity, the solid volume fraction, and the particle size on heat transfer nanofluid are discussed. We propose two models for viscosity and thermal conductivity of Al$_2$O$_3$–water nanofluid as functions of nanosolid concentration and diameter size more precise than those given by the theory and valid at room temperature. Numerical results show that the heat transfer is influenced by the particle size and the solid volume fraction.

Keywords Nanofluids · Heat transfer · Al$_2$O$_3$–water · Viscosity · Thermal conductivity

Nomenclature

Symbols

Cp	Specific heat at constant pressure (J kg^{-1} K^{-1})
d$_f$	The equivalent diameter of fluid molecule (m)
d$_p$	Nanoparticles diameter (m)
g	Gravitational acceleration (ms^{-2})
k	Thermal conductivity (Wm^{-1}K^{-1})
k$_r$	Relative thermal conductivity (k$_{nf}$/k$_f$)
L	Length of the cavity (m)
Nu	Space-averaged Nusselt number
P	Dimensionless pressure

H. Jalali (✉) · H. Abbassi
Unit of Computational Fluid Dynamics and Transfer Phenomena,
National Engineering School of Sfax (ENIS), University of Sfax, Sfax, Tunisia
e-mail: houda-jlali@hotmail.fr

H. Abbassi
e-mail: hassen.abbassi@fss.rnu.tn

Pr   Prandtl number (ν_f/α_f)
Ra   Rayleigh number $(g\beta_f L^3 (T_h - T_c)/\nu_f \alpha_f)$
T   Temperature (k)
U, V   Dimensionless velocity components (normalized by α_f/L)
X, V   Dimensionless coordinates (normalized by L)

Greek Symbols

θ Dimensionless temperature $(T - T_c)/(T_h - T_c)$
ρ Density (kg m^{-3})
μ Dynamic viscosity of the fluid (kg m^{-1} s^{-1})
α Thermal diffusivity $(k/\rho C_p)$ (m^2 s^{-1})
ν Kinematic viscosity of the fluid (μ/ρ) (m^2 s^{-1})
β Thermal expansion coefficient (K^{-1})
$\varnothing$ Solid volume fraction

Subscripts

c Cold
f Fluid
h Hot
nf Nanofluid
s Solid

1 Introduction

Nanofluid is a mixture of base fluid and solid particles of sizes less than ~100 nm. This type of fluid is discovered by Choi (1995). He proposed that the dispersion of nanoparticles in particular metals into fluid like water, ethylene glycol, and oil leads to the improvement of thermal properties of nanofluid. In this context, many studies in the literature investigated theoretically and experimentally the thermal properties of nanofluids and showed that they are very different from base fluids. The literature includes an important amount of studies numerically and experimentally that concern the heat transfer by natural convection of nanofluids in a heated enclosure for different kinds of nanofluids. Kolsi (2016) realizes a numerical study of heat transfer by Al$_2$O$_3$–water nanofluid in a two-dimensional enclosure equipped with a conductive baffle and heated from the bottom side. He uses different conductivities of the baffle and different concentrations of nanoparticles. Results show that the mean Nusselt number increases with the increase of the volume fraction of

nanoparticles. Abu-Nada et al. (2010), Khanafer et al. (2003), Ghasemi and Aminossadati (2009), and Bouhalleb and Abbassi (2016) studied heat transfer by natural convection in the heated cavity using different types of nanofluids. They observed that addition of nanoparticles into base fluid enhances the heat transfer. Natural convection in enclosures filled with Al_2O_3–water nanofluid has been investigated by Nasrin et al. (2012). Their results show that the heat transfer is most effective when increasing the concentration of solid particle and Prandtl number as well as decreasing aspect ratios. According to the above bibliography, it appears that addition of nanosolids in basic fluid enhances heat transfer. These studies used theoretical models for viscosity such as (Brinkman 1952; Batchelor 1977) models.

The main aim of the present work is to discuss the effects of the viscosity and the thermal conductivity of Al_2O_3–water nanofluid on heat transfer. We proposed two models for viscosity and thermal conductivity of Al_2O_3–water nanofluid as a function of concentration of nanofluid and nanoparticles diameter sizes, based on experimental measurements at ambient temperature, in order to verify if the nanofluid leads really to heat transfer enhancement.

2   Statement of the Problem

In this work, we study the influence of addition Al_2O_3 nanoparticles into pure water on the enhancement of the heat transfer by natural convection in square cavity heated from bottom as indicated in Fig. 1.

The nanofluid Al_2O_3–water is considered as Newtonian and incompressible. The flow is supposed to be laminar and bidimensional.

Fig. 1 Physical configuration
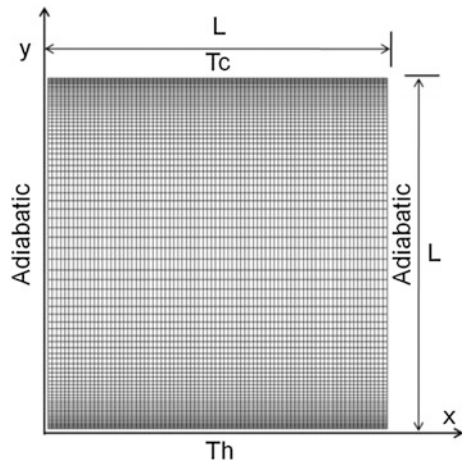
3 Governing Equations

The two-dimensional numerical solutions of momentum and energy equations were performed to simulate the effect of temperature gradient on the heat transfer in the cavity. Assuming that the solid particles Al_2O_3 are well dispersed in water, therefore, we can suppose that physical and thermal properties of the nanofluid are constants as in homogeneous fluid. Thermophysical properties of water and Al_2O_3 nanosolids at room temperature are presented in Table 1.

The density of the nanofluid is expressed as

$$\rho_{nf} = (1 - \varnothing)\rho_f + \varnothing\rho_s. \tag{1}$$

The specific heat is given by Abu-Nada et al. (2010):

$$(\rho Cp)_{nf} = [(1 - \varnothing)(\rho Cp)_f + \varnothing(\rho Cp)_s. \tag{2}$$

The thermal expansion coefficient is given by Ghasemi and Aminossadati (2009):

$$(\rho\beta)_{nf} = (1 - \varnothing)(\rho\beta)_f + \varnothing(\rho\beta)_s. \tag{3}$$

Brinkman (1952) and Batchelor (1977) proposed two models of nanofluid viscosity as a function of solid volume fraction which are expressed, respectively, as

$$\mu_{nf} = \frac{\mu_f}{(1 - \varnothing)^{2.5}} \tag{4}$$

$$\mu_{nf} = (1 + 2.5\,\varnothing + 6.2\,\varnothing^2)\mu_f. \tag{5}$$

From experimental measurements of Nguyen et al. (2007), Pak and Cho (1999), and Wang et al. (1999), it appears clearly that the dynamic viscosity of Al_2O_3–water nanofluid is largely underestimated by theoretical models especially at high concentrations. This is at the origin of our motivation to find a new model more precise and take in consideration effects of relevant parameters such as concentration and solid particle size. The smoothing of measurements in Nguyen et al. (2007), Pak and Cho (1999), and Wang et al. (1999) by minimum mean square

Table 1 Physical properties of pure water and Al_2O_3 solid particles		Water	Al_2O_3
	k (W m^{-1}K^{-1})	0.613	40
	ρ (kgm^{-3})	997.1	3970
	C_p (J kg^{-1}K^{-1})	4179	765
	β (K^{-1})	2.1×10^{-4}	8.5×10^{-6}

error method and the Lagrangian polynomial interpolation allows us to the following model for viscosity as a function of concentration ϕ and diameter of particle size dp:

$$\frac{\mu_{nf}}{\mu_f} = \left[-243.17 \left(\frac{d_f}{d_p} \right)^2 + 11.83 \frac{d_f}{d_p} - 0.0853 \right] \varnothing^2$$
$$+ \left[1878.4 \left(\frac{d_f}{d_p} \right)^2 - 55.26 \frac{d_f}{d_p} + 0.4027 \right] \varnothing + 10\% \leq \varnothing \leq 5\%, \ 13 \, nm \leq dp \leq 36 \, nm,$$

(6)

where dp and df are the diameters of the spherical nanosolids and H_2O molecule, respectively.

Figure 2 shows clearly that our model given by Eq. (6) predicts acceptably the viscosity. Indeed, the mean deviation of the model to experimental measurement is 3.2%. More important, this figure shows that theoretical models of Brinkman (1952) and Batchelor (1977) models (curves are confounded in Fig. 2 underestimate the viscosity especially at high concentrations).

For the thermal nanofluid conductivity, we used experimental measurements of Masuda et al. (1993), Eastman et al. (1997), and Das et al. (2003), and we perform the following model by the same manner as the viscosity:

Fig. 2 Comparison of proposed model to experiments for Al_2O_3–water viscosity
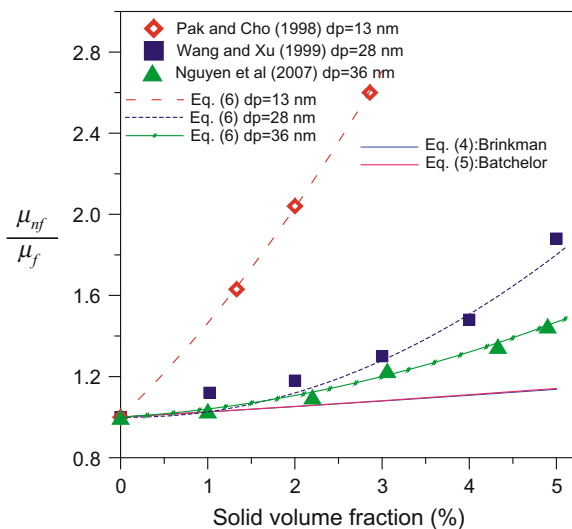
$$\frac{k_{nf}}{k_f} = \left[-0.0266 \left(\frac{d_p}{d_f} \right)^2 + 3.8909 \left(\frac{d_p}{d_f} \right) - 148.5075 \right] \varnothing^2$$
$$+ \left[-0.0022 \left(\frac{d_p}{d_f} \right)^2 + 0.2062 \left(\frac{d_p}{d_f} \right) + 4.8860 \right] \quad 0\% \leq \varnothing \leq 5\%, \ 13 \, nm \leq dp \leq 38.4 \, nm.$$
$$(7)$$

As shown in Fig. 3, our proposed model of Eq. (7) follows correctly the thermal conductivity behavior of the nanofluid. The deviation of the model with respect to the experimental results is less than 2.3%.

The mathematical equations describing the nanofluid flow are the continuity, Navier–Stokes, and energy equations. These equations are normalized by the characteristic height L of the cavity and the specific velocity $\frac{\alpha_f}{L}$, where α_f is the thermal diffusivity of the basic fluid. The dimensionless temperature is defined as $\theta = (T - T_c)/(T_h - T_c)$.

$$\frac{\partial U}{\partial X} + \frac{\partial V}{\partial Y} = 0 \tag{8}$$

$$U \frac{\partial U}{\partial X} + V \frac{\partial U}{\partial Y} = -\frac{\partial P}{\partial X} + \frac{\mu_{nf}}{\rho_{nf} \alpha_f} \left(\frac{\partial^2 U}{\partial X^2} + \frac{\partial^2 U}{\partial Y^2} \right) \tag{9}$$

$$U \frac{\partial V}{\partial X} + V \frac{\partial V}{\partial Y} = -\frac{\partial P}{\partial Y} + \frac{\mu_{nf}}{\rho_{nf} \alpha_f} \left(\frac{\partial^2 V}{\partial X^2} + \frac{\partial^2 V}{\partial Y^2} \right) + \frac{(\rho \beta)_{nf}}{\rho_{nf} \alpha_f} Ra Pr \theta \tag{10}$$

Fig. 3 Comparison of proposed model to experiments for Al_2O_3–water thermal conductivity
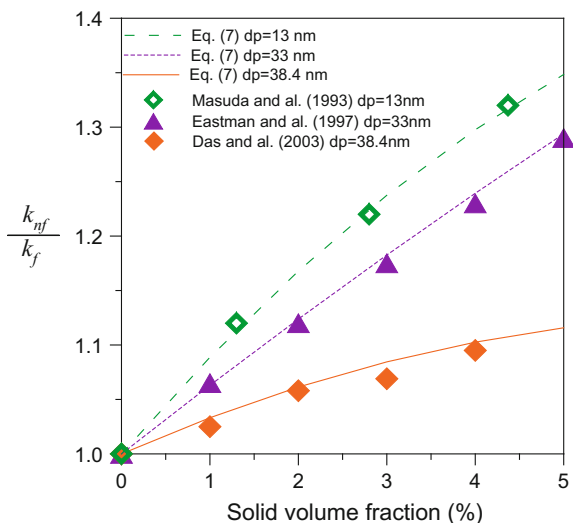
$$U\frac{\partial \theta}{\partial X} + V\frac{\partial \theta}{\partial Y} = \frac{\alpha_{nf}}{\alpha_f}\left(\frac{\partial^2 \theta}{\partial X^2} + \frac{\partial^2 \theta}{\partial Y^2}\right). \tag{11}$$

The dimensionless numbers that appear in governing equations are the classic Prandtl and Rayleigh numbers. Heat transfer exchanged between the flow and the hot wall is evaluated by the space average Nusselt number expressed for the configuration of Fig. 1 as

$$Nu = -\frac{k_{nf}}{k_f}\int_0^1 \frac{\partial \theta}{\partial Y}_{Y=0}\, dx. \tag{12}$$

4 Effect of Solid Volume Fraction on Heat Transfer

Figure 4 shows the variation of Nusselt number as a function of solid volume fraction ϕ using our models for dynamic viscosity (Eq. 6) and thermal conductivity (Eq. 7) in comparison with results when we use the model of Brinkman (1952) for viscosity. As shown in Fig. 4, our models lead to the decrease in Nusselt number when increasing the concentrationϕ. This behavior is as pronounced as the Rayleigh number increases. This result seems to be surprising; we think that, as in most literature, the addition of nanosolids in basic liquid leads always to an increase in heat transfer. The evident question is why our model leads to the decrease in Nu, whereas Brinkman model leads to an increase. It is important to note that the addition of nanosolids plays a double role; it increases the thermal conductivity of the nanofluid and then increases heat transfer, but also increases its viscosity and then slows the flow motion leading to a decrease in heat transfer. The real problem now is who plays the important role, the increase in viscosity or in thermal conductivity after the addition of nanosolids. Analyzing different models, we remark that at a 5% nanosolids concentration, the thermal conductivity of the nanofluid undergoes an augmentation of a maximum 41.36%, whereas the augmentation in viscosity is about 206.7% for our model and 12% only for Brinkman model. Since our model for viscosity is based on recent experimental results, we think that it is more credible than Brinkman model which is based on theoretical considerations. Now the behavior of Nu as a function of ϕ presented in Fig. 4 is understandable; the increase in nanofluid viscosity after the addition of nanosolids prevails over the increase in thermal conductivity. As a consequence, heat transfer is seen in decrease when increasing the concentration. We conclude that the addition of nanoparticle in base fluid has two opposite effects on heat transfer. One positive effect is determined by the increase of the thermal conductivity of nanofluid and an adverse effect is presented by the increase of the viscosity of nanofluid.

Fig. 4 Nusselt number as a
function of solid volume
fraction of Al_2O_3 for different
Rayleigh numbers:
Continuous curves are
obtained by our models;
Discontinuous curves
correspond to Brinkman
model for viscosity
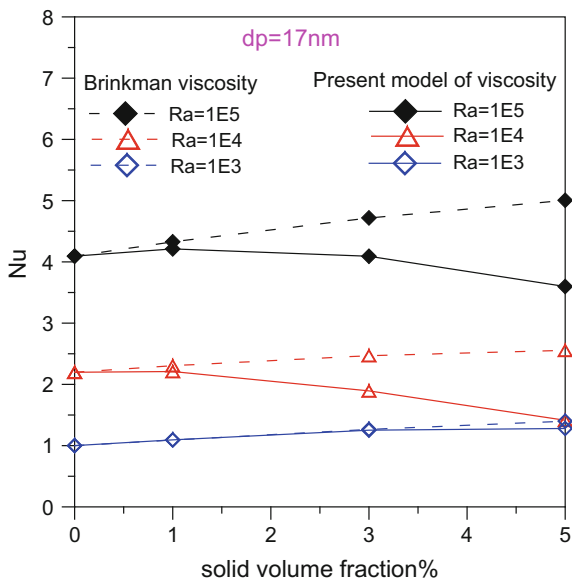
5   Effect of Particle Sizes on Heat Transfer

In this section, the effect of diameter particle size on heat transfer for Al_2O_3–water
nanofluid is discussed. Figure 5 presents the effect of nanoparticle diameter on the
Nusselt number at $Ra = 10^5$ and at 5% solid volume fraction of nanofluid. The
particle sizes varied from 13 to 30 nm. This figure shows that heat transfer is
influenced by the diameter size of nanoparticles. At constant solid volume fraction,
the Nusselt number decreases with the decrease in the diameter of nanoparticle.
This figure shows also a comparison of results found by our models (Eqs. 6 and 7)
with a Brinkman model of viscosity (Eq. 4). Using the Brinkman model for
dynamic viscosity, results show that the heat transfer increases with increasing solid
volume fraction. Nusselt number undergoes an increase of about 22.29% when solid
volume fraction increases from 0 to 5%. But using our model for viscosity, we
notice a general trend of decrease in Nu. For dp < 15 nm, Nu decrease with
increasing solid volume fraction. For dp = 13 nm and dp = 15 nm, Nusselt
number undergoes a decrease about 28.25% and 19.15%, respectively, when the
solid volume fraction varied from 0 to 5%. This behavior is explained by the
augmentation of the viscosity compared to the augmentation of thermal conduc-
tivity in this interval of diameter size. Furthermore, for dp = 17 nm, Nu undergoes
a slight increase when $\phi < 3\%$, and then when the solid volume fraction increases,
the Nusselt number decreases. On the other hand, for dp = 20 nm, Nu increases
remarkably with increasing the solid volume fraction, reaches a maximum at
$\phi = 2\%$, then decreases slowly but remains superior to the case of pure water up to
$\phi = 4.5\%$. When the solid volume fraction becomes greater than 4.5%, the Nusselt

Fig. 5 Influence of the solid volume fraction on the Nusselt number for various nanoparticles sizes
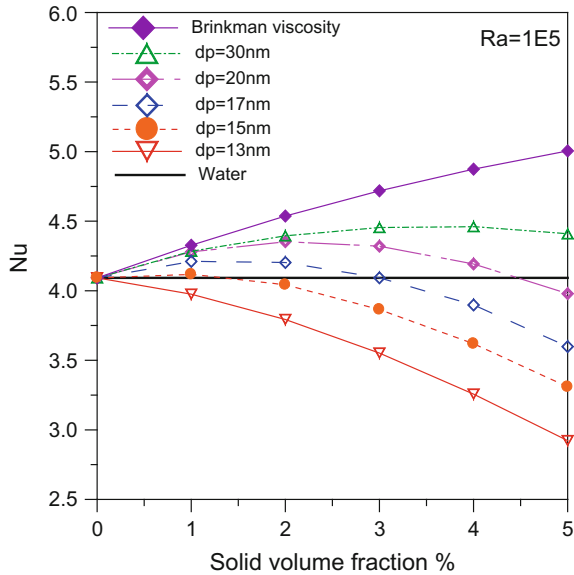
number decreases. Moreover, when $dp = 30$ nm, Nu undergoes a general increase when the solid volume fraction increase. From this figure, we conclude that the heat transfer by Al_2O_3–water nanofluid is very influenced by the diameter size of solid particles and by the solid volume fraction of nanofluid.

6 Conclusion

In this paper, a numerical work is performed to study the effect of adding Al_2O_3 nanoparticles in water on the heat transfer in the cavity heated from the bottom. New models for thermal conductivity and dynamic viscosity of Al_2O_3–water nanofluid are developed based on experimental results. Results show that theoretical model of Brinkman is unable to predict the viscosity of Al_2O_3–water nanofluid. When used new models of dynamic viscosity and thermal conductivity, it appears that the enhancement of the heat transfer when the addition of the solid particle Al_2O_3 into pure water is influenced by the solid volume fraction and the particle size.

References

Abu-Nada E, Masoud Z, Oztop HF, Campo A (2010) Effect of nanofluid variable properties on natural convection in enclosures. Int J Therm Sci 49:479–491

Batchelor G (1977) The effect of Brownian motion on the bulk stress in a suspension of spherical particles. J Fluid Mech 83:97–117

Bouhalleb M, Abbassi H (2016) Numerical investigation of heat transfer by CuO-water nanofluid in rectangular enclosures. Heat Trans Eng 37:13–23

Brinkman HC (1952) The viscosity of concentrated suspensions and solution. J Chem Phys 20:571–581

Choi SUS (1995) Enhancing thermal conductivity of fluids with nanoparticles (1995). ASME Fluids Eng Div 231:99–105

Das SK, Putra N, Thiesen P, Roetzel W (2003) Temperature dependence of thermal conductivity enhancement for nanofluids. J Heat Trans 125(4):567–574

Eastman JA, Choi US, Li S, Thompson LJ, Lee S (1997) Enhanced thermal conductivity through the development of nanofluids. Mater Res Soc 457:3–11

Ghasemi B, Aminossadati SM (2009) Natural convection heat transfer in an inclined enclosure filled with a water-Cuo nanofluid. Numer Heat Trans Part A 55:807–823

Khanafer K, Vafai K, Lightstone M (2003) Buoyancy-driven heat transfer enhancement in a two-dimensional enclosure utilizing nanofluids. Int J Heat Mass Trans 46:3639–3653

Kolsi L (2016) Numerical study of natural convection and entropy generation of Al_2O_3-water nanofluid within a cavity equipped with a conductive baffle. J Appl Fluid Mech 9:2177–2186

Masuda H, Ebata A, Teramae K, Hishinuma N (1993) Alteration of thermal conductivity and viscosity of liquid by dispersing ultra-fine particles Dispersion of Al_2O_3, SiO_2 and TiO_2 ultra-fine particles. NetsuBussei/Japan J Thermophys Prop 4:227–233

Nasrin R, Alim MA, Chamkha AJ (2012) Buoyancy-driven heat transfer of water–Al_2O_3 nanofluid in a closed chamber: Effects of solid volume fraction, Prandtl number and aspect ratio. Int J Heat Mass Trans 55:7355–7365

Nguyen C, Desgranges F, Roy G, Galanis N, Mare T, Boucher S, Anguemintsa H (2007) Temperature and particle-size dependent viscosity data for water-based nanofluids—hysteresis phenomenon. Int J Heat Fluid Flow 28(6):1492–1506

Pak BC, Cho YI (1999) Hydrodynamic and heat transfer study of dispersed fluids with submicron metallic oxide particles. Exp Heat Trans A J Therm Energy Gener Transport Storage Convers 11:151–170

Wang X, Xu X, Cho SUS (1999) Thermal conductivity of nanoparticle–fluid mixture. J Thermophys Heat Trans 4:13

Numerical Study of Geometric Parameters Effect on Rapid Heat Cycle Molding Process

Fatma Kria, Moez Hammami and Mounir Baccar

Abstract A 3D numerical study of thermal regulation system of Rapid Heat Cycle Molding (RHCM) process producing smartphone cover has been undertaken. In order to succeed an RHCM operation, so as to improve the part quality and the process productivity, heating/cooling channels design is of great importance. For this purpose, we propose in this study the optimization of geometric parameters of heating/cooling channels. The concerned geometric parameters are heating/cooling channel diameter, distance between two successive channel and distance channel–cavity surface. The thermal behaviors in mold and polymer domains are predicted by the commercial Finite Volume Analysis software Fluent 6.3.26 in cyclic transient regime. It was shown that a regular state is reached rapidly, since the second molding cycle. Thermal responses have shown that increasing heating/cooling channels diameter promotes the RHCM process productivity, but, at the same time, generates an uneven temperature distribution and consumes a significant energy. With regards to heating/cooling channels spacing, it has been demonstrated the advantage of increasing the distance between two consecutive channels. However, increasing the distance channel–cavity surface contributes to balance the temperature distribution at the cavity surface, but it affects the RHCM process productivity by increasing the molding cycle time.

Keywords Rapid heat cycle molding process · Geometric parameters · Thermal control · Numerical simulation

F. Kria (✉) · M. Hammami · M. Baccar
Computational Fluid Dynamic and Transfer Phenomena, Mechanical Engineering
Department, National Engineering School of Sfax, Sfax, Tunisia
e-mail: Fatmakria1984@yahoo.fr

M. Hammami
e-mail: hammamimoez2003@yahoo.fr

M. Baccar
e-mail: mounir.baccar@enis.rnu.tn

Nomenclature

Parameters

Cp	(heat capacity) (J kg^{-1} °C^{-1})	
D	(channel diameter) (m)	
g	(gravity acceleration) (m s^{-2})	
h_h, h_c	(heat transfer coefficient) (W m^{-2} °C^{-1})	
H_{liq}	(liquefaction latent heat of water) (J kg^{-1})	
L	(length of vertical channel) (m)	
n	(normal direction)	
T	(temperature) (°C)	
λ	(thermal conductivity) (W m^{-1} °C^{-1})	
μ	(dynamic viscosity) (kg m^{-1}s^{-1})	
ρ	(density) (kg m^{-3})	

Dimensionless numbers

Re   (Reynolds number)
Pr   (Prandtal number)

Subscripts

m   (mold)
p   (polymer)
s   (steam)
w   (water)

1   Introduction

Injection molding technology is among the most important processes in the pro-duction of thermoplastic products. For this purpose, the main objective of pro-cessors is to improve thermoplastic parts quality and to minimize the injection molding cycle time.

However, despite the development of conventional injection molding (CIM), several problems remain still unavoidable, specifically those related to the products quality such as shrinkage (Daniele and Jeffrey 2014; Hassan et al. 2010) and poor surface quality (Chang and Tsau 1995). To over come these problems, many authors (Wang et al. 2013; Lucchetta et al. 2012; Lucchetta and Fiorotto 2013) have sug-gested the preheating of the mold before each filling phase. Thus, thermal cycling prevents the appearance of defects in the finished product. For this purpose, a new thermoplastic injection molding process Rapid Heat Cycle Molding (RHCM) has been proposed. This process consists of a rapid heating of the mold until attaining the

glass transition temperature Tg of the polymer, before filling the mold. Then mold is cooled down to the ejection temperature of the injected polymer. The two key technical parameters of the RHCM process are the rapidity of heating/cooling system providing high process productivity and the temperature uniformity at the cavity surface ensuring high products quality.

The design of heating/cooling channels is of great importance to ameliorate the RHCM process. Then, several previous works (Li et al. 2009; Wang et al. 2011, 2013) have optimized the design of the heating/cooling channels in order to decrease the heating time and the cavity surface temperature gap. Li et al. (2009) studied in 2D RHCM mold producing LCD panel. In their works, the optimization of the distance between channels improves cavity surface temperature homogeneity. Wang et al. (2011) studied in 2D the heating/cooling channels design of RHCM mold producing a rectangular part. To realize the heating efficiency and temperature repartition uniformity, authors (Wang et al. 2009) have optimized the geometric parameters as well as the diameter of heating/cooling channels, distances channels–cavity and distance between adjacent channels..

Despite the development of research works concerned in the optimization of thermal control system layout, the majority of these works have been simplified to make 2D problems and have been interested only to the first molding cycle. However, Hammami et al. (2015) have studied a 3D thermal regulation system of RHCM producing LCD panel and they have found a large difference between the first cycle and the steady cycle. Recently, Kria et al. (2017) carried out a 3D study to improve heating/cooling channel design of an RHCM mold producing complex-shaped automotive part. For this purpose, Kria et al. (2017) proposed a "new conformal design" allowing to access to the convex zones of the cavity/core plates.

The purpose of this numerical study is to optimize the geometric parameters of heating/cooling channels, ensuring finished product quality and RHCM process productivity. To this end, several combinations of geometric parameters of heating/cooling channels, such as channels diameter, distance between two adjacent channels, and distance channel–cavity surface, have been studied. Our goal is to determine the effect of the geometric parameters on the RHCM time and thus on the process productivity, and also the effect of the geometric parameters on the temperature gap at the cavity functional surfaces and consumed energy. Consequently, the most effective heating/cooling channels arrangement can be demonstrated. The simulation of several heating/cooling cycles, until attaining the regular state, has been undertaken using the commercial software Fluent 6.3.23.

2   Mathematical Formulation and Numerical Method

In this section, we will present the mathematical formulation and numerical method used to predict thermal behavior of RHCM mold producing smartphone cover (Fig. 1) during several heating/cooling cycles. In this study, we are interested particularly in the temperature distribution at the external functional surfaces of the
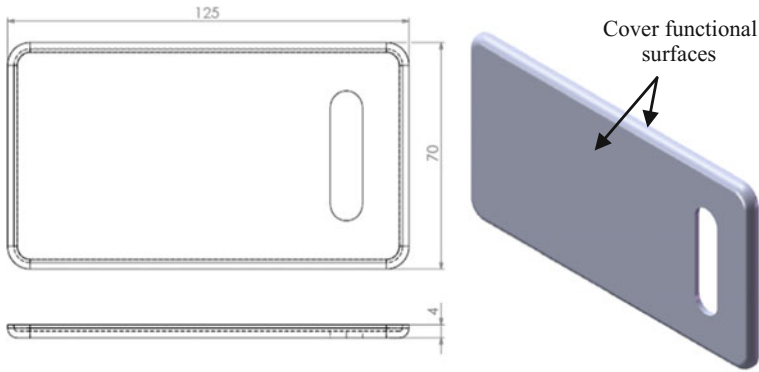
Fig. 1 Smartphone cover

Fig. 2 Layout of heating/cooling channels in the RHCM mold
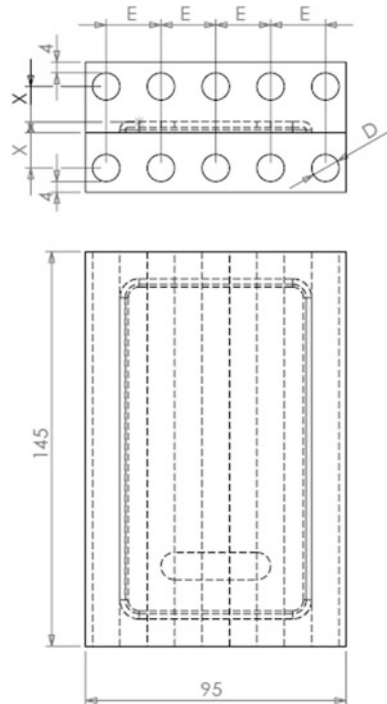
studied part (Fig. 1). The design of heating/cooling channels is shown in (Fig. 2). The geometrical parameters of heating/cooling channels are indicated in this figure: D represents the channel diameter; E represents the spacing between channels, and X indicates the distance channels–cavity surfaces.

Initially, the mold (Fig. 2) made with AMPCO 940 (Moldflow 2002) (Table 1) has an ambient temperature of 30 °C. The heating stage ends when the mold cavity surface reaches 120 °C, assumed adequate for the used polymer ABS XR 404

Table 1 Thermal properties of the polymer

	Temperature (°C)	Calorific capacity (J/(kgK))	Thermal conductivity (W/(mK))	Density (kg/m^3)
Mold material AMPCO 940		380	208	8710
Polymer ABS XR 404	90	1747	0.16	1059
	110	1903	0.188	1059
	130	2073	0.203	1059
	170	2093	0.206	960
	210	2190	0.22	960
	230	2190	0.22	960

(Moldflow 2002) (Table 1). At this level, the cooling phase starts and continues until cooling down the polymer to a temperature of 95 °C (Moldflow 2002). At the end of the cooling stage, the ejection time is neglected and the obtained mold temperature distribution is used for the initial condition of the following molding cycle. So, a cyclic heating/cooling process was undertaken until attaining the steady cycle.

In this study, the filling time was neglected. Consequently, at the end of the heating stage, the cavity is assumed to be filled with polymer at injection temperature and the cooling phase begins. Consequently, the heat transfer in the mold and polymer is purely conductive. The governing heat transfer equations in the mold domain (1) and polymer domain (2) are given by

$$\rho_m C_m \frac{\partial T_m}{\partial t} = \text{div}\,(\lambda_m \overrightarrow{\text{grad}}\, T_m) \tag{1}$$

$$\rho_p\, C_p(T_p) \frac{\partial T_p}{\partial t} = \text{div}\,(\lambda_p(T_p)\, \overrightarrow{\text{grad}} T_p). \tag{2}$$

During the cooling stage, we have supposed a perfect contact mold–polymer. So, at the interface mold–polymer, there is an equality of temperature and continuity of heat flux:

$$\left(\frac{\partial T_m}{\partial n_m}\right)_{\substack{\text{interface}\\ \text{mold}-\text{polymer}}} = -\left(\frac{\partial T_p}{\partial n_p}\right)_{\substack{\text{interface}\\ \text{mold}-\text{polymer}}}. \tag{3}$$

Due to the presence of insulating layers enveloping the RHCM mold, heat transfer is located at the cavity/core plates. Considering the symmetry of the studied part and heating/cooling channels design, it is sufficient to consider only half of the field (Fig. 3).

During the heating stage, the mold is heated by the saturated steam at $T_s = 180$ °C. For the cooling stage, the injected polymer is cooled down by water
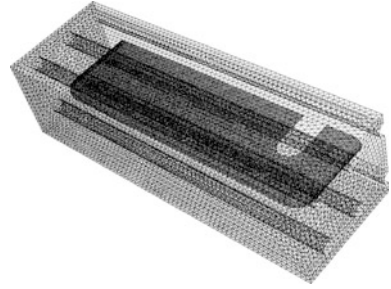
at $T_w = 30\ °C$. At the interface mold–channels, we introduce a heat transfer coefficients: h_h for the heating stage (4) and h_c for the cooling stage (5):

$$\lambda_m \left(\frac{\partial T_m}{\partial n_m}\right)_{\substack{\text{interface}\\ \text{mold}-\text{channels}}} = h_h (T_s - T_m)_{\substack{\text{interface}\\ \text{mold}-\text{channels}}} \tag{4}$$

$$\lambda_m \left(\frac{\partial T_m}{\partial n_m}\right)_{\substack{\text{interface}\\ \text{mold}-\text{channels}}} = h_c (T_W - T_m)_{\substack{\text{interface}\\ \text{mold}-\text{channels}}}. \tag{5}$$

For the heating stage, the coefficient of convective heat transfer (Rohsenow and Hartnett 1973) is given by

$$h_h = 0.555 \left[\frac{\lambda_w^3 \rho_w (\rho_w - \rho_s) g\ H_{liq}}{\mu_w\ D(T_s - T_m)}\right]^{1/4}_{\substack{\text{interface}\\ \text{mold}-\text{channels}}}. \tag{6}$$

For the cooling phase, the heat transfer coefficient by convection is defined by (Sleicher and Rousse 1975):

$$h_c = (5 + 0.015 Re^a Pr^b)\frac{\lambda_w}{D}$$
$$\text{with: } a = 0.88 - \frac{0.24}{4 + Pr} \quad \text{and} \quad b = 0.333 + 0.5\ \exp(-0.6\,Pr). \tag{7}$$

It is worthwhile to mention that for the studied configurations, the velocity of cold water is 2 m/s.

3 Results and Discussion

3.1 Effect of Channels Diameter and Channels Spacing

In order to determine the effect of channel diameter (D) and channel spacing (E) on the RHCM process, numerical simulations of thermal behavior in mold and
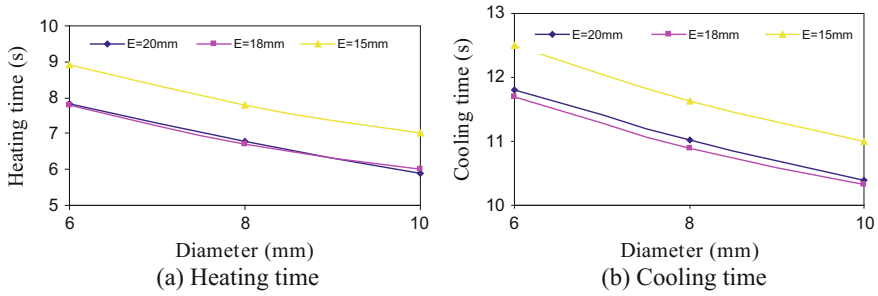
Fig. 4 Effect of heating/cooling channels diameter and spacing on RHCM time
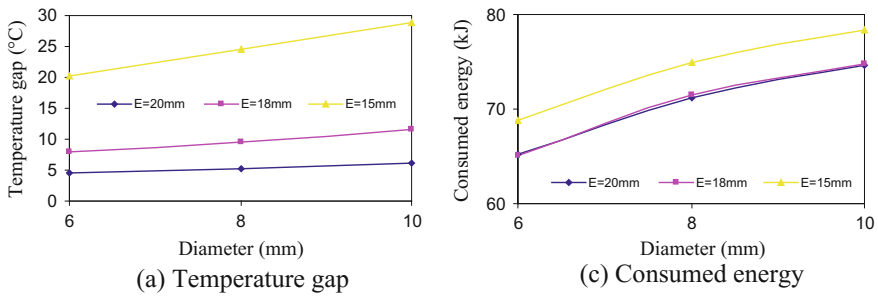
Fig. 5 Effect of heating/cooling channels diameter and spacing on mold heating uniformity and consumed energy

polymer until attaining steady state for different diameter and channel spacings have been undertaken (with a fixed position channel–cavity surface X = 13 mm).

The curves of (Fig. 4) show the effect of channel spacing (E) on heating and cooling time for different channel diameters (D). The results show that the increase of heating/cooling channels diameter accelerates the heating/cooling phase during the RHCM process. Concerning the effect of the spacing (E) between two successive channels, it is noted that there is no nearly any difference between the results obtained with E = 20 mm and E = 18 mm. However, for the smallest spacing E = 15 mm, an increase in the heating and cooling time is observed, leading to a slowdown of the RHCM process.

As regards to the temperature gap and consumed energy, the channel diameter unbalances the temperature distribution and consumes a significant amount of energy. In order to promote the part quality and the consumed energy, it is advantageous to minimize the channels diameter. Also, in order to balance the temperature distribution at the level of the part, it is advantageous to space the channels. (Fig. 5).

The cartographies represented at (Fig. 6) show a significant improvement in the temperature distribution at functional cavity surface by reducing the channels diameter and increasing the channels spacing.

(a) D=10mm and E=15mm at t=26,2s   (b) D=6mm and E=20mm at t=29,44s
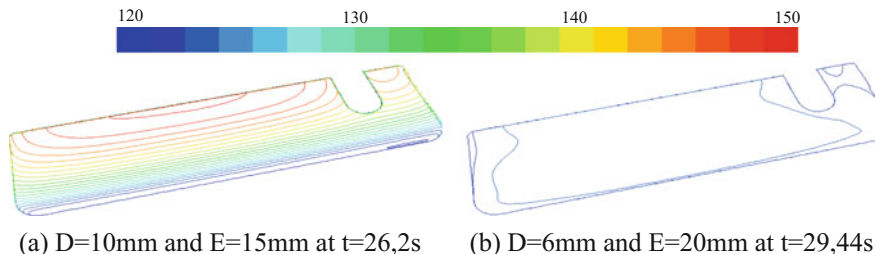
Fig. 6 Temperature maps at the end of the heating phase of the second molding cycle

(a) Heating time   (b) Cooling time
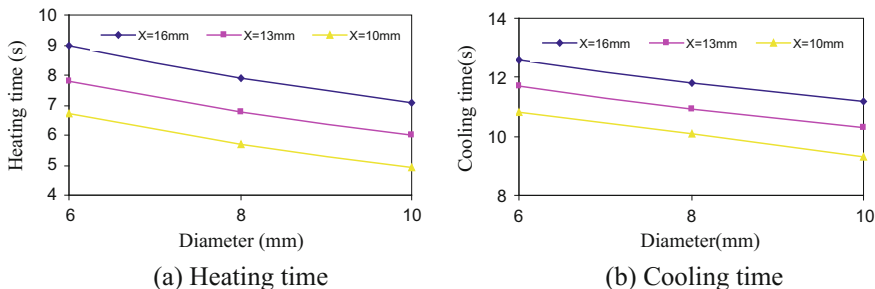
Fig. 7 Effect of heating/cooling channels diameter and channels position on RHCM time

In order to guarantee the part quality and the process productivity, it is interesting to increase the spacing between heating/cooling channels. On the other hand, it is useful to minimize the channels diameter since they reduce the temperature gap as well as the consumed energy. With regard to the RHCM process productivity, heating/cooling channels with 10 mm in diameter accelerate the cycle time by 17% (the case of E = 20 mm).

3.2 Effect of Channels Diameter and Distance Channels–Cavity Surface

The curves of (Figs. 7 and 8) give the variation of heating time, cooling time, temperature gap, and consumed energy, at steady state, as a function of heating/cooling channels diameter for different distance channels–cavity surfaces (with a fixed channels spacing E = 18 mm). It is noted that the increase in channels diameter with the decrease of the distance channel–cavity surface ensures the RHCM process productivity.

As regards to temperature gap, it should be noted that the increase in the channels diameter prevents a balanced temperature distribution at the cavity surface. Similarly, for the consumed energy, there is an increase in the channels

(a) Temperature gap   (b) Consumed energy
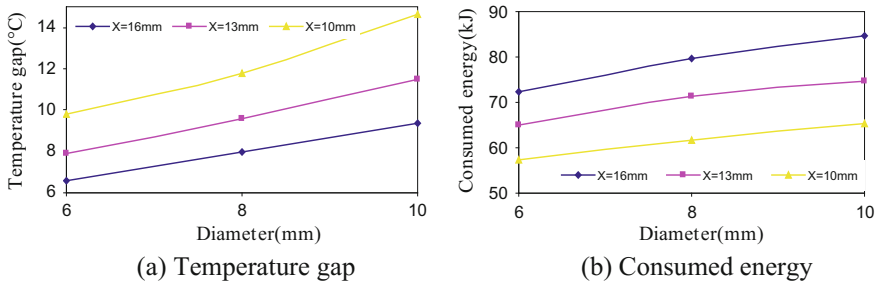
Fig. 8 Effect of heating/cooling channels diameter and channels position on surface cavity uniformity and consumed energy

diameter. Moreover, it is shown that for channels that are far from the cavity (X = 16 mm), the thermal deviation is the smallest (6.6 °C. for D = 6 mm). However, this position consumes the largest amount of energy.

It can then be concluded that in order to ensure the process productivity, it is necessary to increase the channels diameter and minimize the distance channels–cavity surface. On the other hand, in order to guarantee the quality of the finished product, it is advantageous to reduce the channels diameter and maximize the distance channel–cavity. To find a compromise between productivity and quality, we can examine the effect of the variation of the geometric parameters on the consumed energy. It can be seen that the reduction of the distance X minimizes the energy consumption during the RHCM process. Indeed, passing from X = 10 mm to X = 16 mm (for D = 6 mm), an increase of 21%, is envisaged.

4 Conclusion

A 3D numerical study was performed to investigate the heat transfer during the heating and cooling phases of the RHCM process for smartphone cover production. The study focuses on a cyclic transient regime of the RHCM process. Our goal is to optimize heating/cooling channels design in order to achieve rapid and uniform heating/cooling.

For this purpose, the optimization of geometric parameters of heating/cooling channels has been undertaken. So, channel diameter, channel spacing, and position channel–cavity surface have been considered. It has been demonstrated that the increase channels diameter promote the RHCM process productivity. On the other hand, it has shown the importance to space out channels in order to ensure temperature uniformity at cavity surface and minimize the necessary energy to heat the RHCM mold. As regard to the position channels–cavity surface, it is important to compromise this parameter. In fact, the distance which ensures the process rapidity and energy consumption gain does not guarantee a balanced temperature distribution at the cavity surface.

References

Autodesk simulation moldflow adviser (2002)

Chang RY, Tsau BD (1995) Experimental and theoretical studies of shrinkage, warpage and sink marks of crystalline polymer injection molded parts. Polym Eng Sci 35:1222–1230

Daniele A, Jeffrey RA (2014) Review of factors that affect Shrinkage of molded part in injection molding. Mater Manuf Process 29:662–682

Hammami M, Kria F, Baccar M (2015) Numerical study of thermal control system for rapid heat cycle injection molding process. J Process Mech Eng Part E 229:315–326

Hassan H, Regnier N, Pujos C, Arquis E, Defaye G (2010) Modeling the effect of cooling system on the shrinkage and temperature of the polymer by injection molding. Appl Therm Eng 30:1547–1557

Kria F, Hammami M, Baccar M (2017) Conformal heating/cooling channels design in rapid heat cycle molding process. Mech Ind 18:109

Li XP, Zhao GQ, Guan YJ, Ma MX (2009) Optimal design of heating channels for rapid heating cycle injection mold based on response surface and genetic algorithm. Mater Des 30:4317–4323

Lucchetta G, Fiorotto M (2013) Influence of rapid mould temperature variation on the appearance of injection-moulded parts. J Mech Eng 59:683–688

Lucchetta G, Fiorotto M, Bariani PF (2012) Influence of rapid mold temperature variation on surface topography replication and appearance of injection-molded parts. CIRP Ann Manufact Technol 61:539–542

Moldflow plastic insight release 5.0 (2002)

Rohsenow MW, Hartnett JP (1973) Handbook of heat transfer. McGraw-Hill, New York

Sleicher CA, Rousse MW (1975) A convenient correlation for heat transfer to constant and variable property fluids in turbulent pipe flow. Int J Heat Mass Transf 18:677–683

Wang G, Zhao G, Li H, Guan Y (2009) Research on a New variotherm injection molding technology and its application on the molding of a large LCD panel. Polymer-plastics technology and engineering 48(7):671–681

Wang G, Zhao G, Li H, Guan Y (2011) Research on optimization design of the heating/cooling channels for rapid heat cycle molding based on response surface methodology and constrained particle swarm optimization. Expert Syst Appl 38:6705–6719

Wang G, Zhao G, Wang X (2013) Experimental research on the effects of cavity surface temperature on surface appearance properties of the moulded part in rapid heat cycle moulding process. Int J Adv Manuf Tech 68(5–8):1293–1310

Investigation of Parameters Affecting the Acoustic Absorption Coefficient of Industrial Liners

Chokri Othmani, Taissir Hentati, Mohamed Taktak, Tamer Elnady, Tahar Fakhfakh and Mohamed Haddar

Abstract Reducing the noise generated in the industrial environment becomes the main objective of industrial designers in many applications (building, transport industry, etc.). The passive control represents one of the used methods to achieve this objective. It is based on the use of acoustic absorbent materials like porous materials, Helmholtz resonators, or perforated plates, etc. In order to obtain high-quality acoustic absorbers, the acoustic performance of each element is used and sometimes coupled to increase the total acoustic absorption of the liner. In this study, three industrial acoustic liners are studied: porous material, porous material with perforated plate, and perforated plate with air cavity. The liner characteristic impedance is defined using the material and the plate impedances. The porous material impedance is formulated by two models: the Delany–Bazley and the Lafarge–Allard ones. A comparative study is elaborated in order to show the impact of plate and material parameters variation on the acoustic absorption coefficient.

Keywords Porous material · Perforated plate · Acoustic absorption

1 Introduction

Nowadays sound absorption constitutes one of the major requirements for the human acoustic comfort and insulation in manufacturing, automobiles, architecture, and equipment.

C. Othmani · T. Hentati · M. Taktak (✉) · T. Fakhfakh · M. Haddar
Mechanics, Modelling and Production Laboratory, Mechanical Engineering Department,
National School of Engineers of Sfax, BP 1173-3038 Sfax, Tunisia
e-mail: mohamed.taktak@fss.rnu.tn

C. Othmani
e-mail: Othmani.chokri@gmail.com

T. Elnady
ASU Sound & Vibration Laboratory, Ain Shams University,
1 Elsaryat St, Abbaseya, 11517 Cairo, Egypt

In the industry, two fundamental elements are usually used to obtain the acoustic absorber material or the liner: the porous material and the perforated plate. The liner can be made of one of these two elements or by a combination of them.

For the first element, different models are developed to predict the acoustic impedance of porous materials. The structure of porous materials is complicated and an analytical solution is not easily performed, numerous empirical, and phenomenological models allowing computing the absorption coefficient of porous material. Zwikker and Kosten (1949) and Biot (1956) were among the first who developed these models. Thereafter, other models have been elaborated like (Delany and Bazley 1970; Miki 1990) which depend on flow resistivity and (Hamet and Berengier 1993) introducing in addition of flow resistivity the porosity and the tortuosity of porous material. Other models were proposed to improve this model like (Johnson et al. 1987; Attenborough 1987; Allard and Attala 2009; Lafarge et al. 1997). These models were used in recent research like (Othmani et al. 2015, 2016, 2017).

For the second element, the first approach of continuum mechanics seems to come from (Crandall 1927) who presents an approach which is particularly well suited for micro-perforated materials. Based on the model of (Melling 1973; Elnady and Boden 2003) proposed an empirical model, adding corrections for edge and weight for non-empirical linear terms.

In this study, the effect of porous and geometric properties on the acoustic absorption coefficient was studied for three liner configurations: the first is composed only of the porous material, the second is a multilayer system made up with perforated plate backed by a porous material, and the third is using the perforated plate with air cavity.

2 Presentation of Studied Acoustic Liners

In the present study, three liners are studied as presented in Fig. 1: (a) the liner L_1 which consists only of the absorbent porous material, (b) the second liner L_2 is composed of a perforated plate with an absorbent porous material, and (c) the third liner L_3 is obtained by only the perforated plate with air cavity. All these liners are backed by a rigid plate.

Fig. 1 Studied Liners: **a** L1: Absorbent Material; **b** L2: Absorbent material + Perforated plate and **c** L3: Perforated plate + air cavity
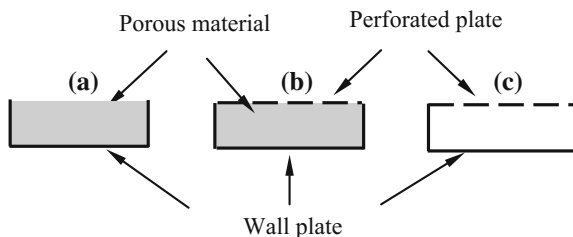
3 Computation of the Acoustic Absorption Coefficient

The acoustic absorption coefficient is expressed with the surface acoustic impedance of a liner as follows (Lee and Kwon 2004):

$$\alpha = \frac{4 \operatorname{Re}(Z)}{(1 + \operatorname{Re}(Z))^2 + (\operatorname{Im}(Z))^2} \tag{1}$$

With Z is the normalized surface acoustic impedance of the liner. Re and Im mean respectively the real and imaginary parts. For the first liner L_1.

For the second liner L_2, the acoustic impedance is obtained by adding the acoustic impedance of the porous material to the acoustic impedance of the perforated plate as expressed in the following expression:

$$Z_2 = Z_{Porous\ Material} + Z_{Perforated\ Plate} \tag{2}$$

4 Computation of the Surface Characteristic Impedance and Propagation Constant of a Porous Material

These quantities are computed using two models: the first is the Delany–Bazley model (Delany and Bazley 1970) which expresses these parameters as follows:

$$Z_c = Z_0 \left(1 + 9.08 \left(\frac{f}{\sigma} \right)^{-0.754} - 11.9j \left(\frac{f}{\sigma} \right)^{-0.732} \right) \tag{3}$$

$$k_c = \frac{\omega}{c_0} \left(1 + 10.8 \left(\frac{f}{\sigma} \right)^{-0.700} - 10.3j \left(\frac{f}{\sigma} \right)^{-0.595} \right) \tag{4}$$

where f is the frequency, σ is the flow resistivity, ρ_0 is the air density, c_0 is the sound celerity in the air, $Z_0 = \rho_0 c_0$ is the characteristic impedance of the air and ω is the pulsation ($\omega = 2\pi f$). The second model is the Lafarge–Allard model (Lafarge et al. 1997). In this model, the characteristic impedance Z_c and the propagation constant k_c are expressed as follows:

$$Z_c = \sqrt{\rho K_{LA}}; \ k_c = \omega \sqrt{\frac{\rho}{K_{LA}}} \tag{5}$$

with

$$\rho = \alpha_\infty \rho_0 \left[1 - j \frac{\sigma\phi}{\rho_0 \alpha_\infty \omega} \sqrt{1 + \frac{4j\rho_0 \alpha_\infty^2 \omega\eta}{\sigma^2 \phi^2 \Lambda^2}} \right] \tag{6}$$

$$K_{LA} = \gamma P_0 \left[\gamma - \frac{(\gamma - 1)}{1 + \frac{\eta\phi}{j\omega\rho_0 N_{pr} k_0'} \sqrt{1 + \frac{4j\omega\rho_0 N_{pr} k_0'2}{\eta\phi^2 \Lambda'2}}} \right] \tag{7}$$

With α and ϕ are respectively the material tortuosity and porosity, γ is the ratio of specific heats at respectively constant pressures and volumes, k_a is the propagation constant of sound in the air and N_{pr} is the Prandtl number, η is the dynamic viscosity, Λ, and Λ' are respectively the viscous and thermal characteristic lengths, P_0 is the atmospheric pressure, and $k_0' = \frac{\phi\Lambda'2}{8}$ is the thermal permeability.

5 Computation of the Surface Characteristic Impedance of a Perforated Plate

The used acoustic impedance model of Elnady and Boden for the perforated plate is expressed as follows (Elnady and Boden 2003):

$$Z_{perforated\ plate} = \mathrm{Re}\left\{ \frac{ik}{\sigma_p C_D} \left[\frac{t}{F(k_s'd/2)} + \frac{\delta_{re}}{F(k_s d/2)} \right] \right\} + i\,\mathrm{Im}\left\{ \frac{ik}{\sigma_p C_D} \left[\frac{t}{F(k_s'd/2)} + \frac{\delta_{im}}{F(k_s d/2)} \right] \right\} \tag{8}$$

With C_D is the discharge coefficient, d is the pore diameter, t is the plate thickness, σ_p is plate porosity, δ_{re}, and δ_{im} are correction coefficients:

$$\delta_{re} = 0.2d + 200d^2 + 16000d^3; \quad \delta_{im} = 0.2856d \tag{9}$$

$$F(k_s d/2) = 1 - \frac{J_1(k_s d/2)}{k_s \frac{d}{2} J_0(k_s d/2)} \quad F(k_s'd/2) = 1 - \frac{J_1(k_s'd/2)}{k_s' \frac{d}{2} J_0(k_s'd/2)} \tag{10}$$

J_0 and J_1 are respectively the 0 and 1 order Bessel functions.

$$k_s' = \sqrt{-i\omega / \nu'}; \quad k_s = \sqrt{-i\omega / \nu} \tag{11}$$

with ν is the kinematic viscosity and

$$\nu' = 2.179\mu/\rho \tag{12}$$

μ is the dynamic viscosity and ρ is the material density.

6 Numerical Results

Three liner types are studied in this article as mentioned previously. The different characteristic parameters respectively of the air, the acoustical, and the perforated plate are given in Table 1. The absorption coefficient in the three cases study is determinate and compared.

6.1 Porous Material Effects

In this section, a comparative study is performed in order to show the effect of the variation of some porous material parameters: flow resistivity, depth, porosity, tortuosity, on the acoustic absorption coefficient of the conduct. The results are given for two liners L_1 and L_2.

Table 1 Air, acusticel, and perforated plate characteristic parameters

Air			
	c_0	Celerity (m s^{-1}),	342
	ρ_0	Density (kg m^{-3}),	1.213
	Z_0	Characteristic impedance (Pa m^{-1} s),	414
	γ	Adiabatic constant	1.4
	Npr	Number of prandlt	0.708
	P_0	Atmospheric pressure (Pa)	101300
	Nu	Dynamic viscosity (Pa s)	1.84×10^{-5}
	σ	Flow resistivity (Nm^{-1} s)	22000
Acoustic parameter material (acusticel)	φ	Porosity	0.95
	α	Tortuosity	1.38
	$k0$	Thermal permeability (m^2)	0.83×10^{-8}
	Λ	Viscous characteristic length (m)	0.00017
	Λ'	Thermal characteristic length (m)	0.00051
	d	Thickness of specimen (m)	0.024
	d_p	Pores diameter (m)	0.001
Perforated plate	σ_p	Plate porosity	2.5%
	t	Plate thickness (m)	0.001
	CD	Discharge coefficient	0.76

6.1.1 Flow Resistivity Effect

Figure 2 presents the variation of the acoustic absorption coefficient with respect with the liners types L_1 and L_2 and using the two porous material impedance models for different flow resistivity values. The figure shows an increase in the acoustic absorption with the flow resistivity increasing. For the Delany–Bazley, the flow resistivity variation effect is more observed than the Lafarge–Allard model.

6.1.2 Porous Material Porosity Effect

The influence of the material porosity variation on the acoustic absorption coefficient of two liners type (L_1 and L_2), is given by Fig. 3. The results are obtained for Lafarge–Allard model. The acoustic coefficient is slightly increasing with the porosity increase especially in the low-frequency band.
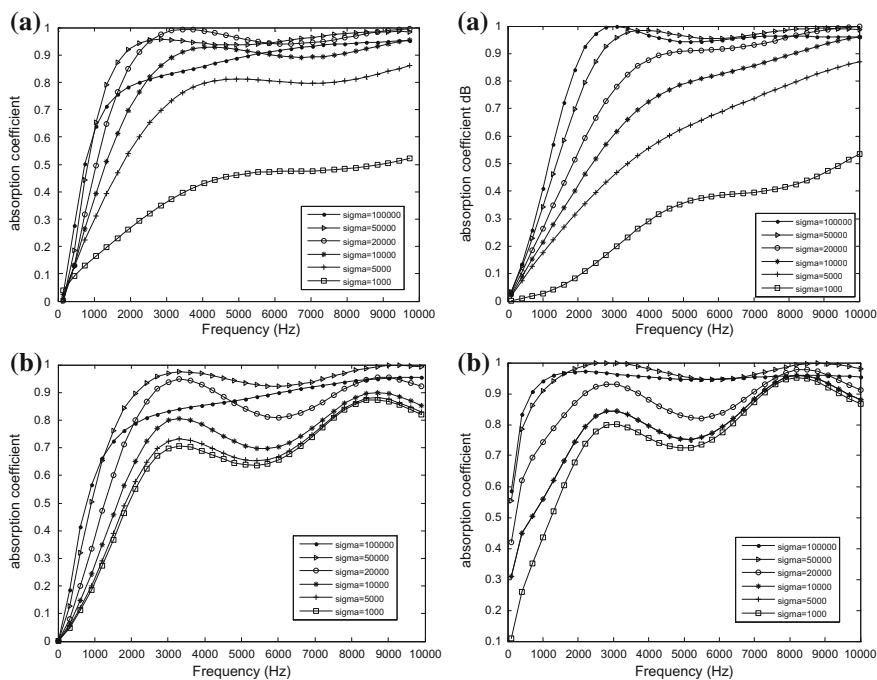
Fig. 2 Flow resistivity effect for the liner L1 (Left column) and the liner L2 (Right column) using the Delany–Bazley (**a**) and Lafarge–Allard (**b**) models

6.1.3 Porous Material Tortuosity Effect

The influence of the material tortuosity variation on the acoustic absorption coefficient is given by Fig. 4. The acoustic coefficient is decreasing when the tortuosity is increasing from 1 to 2.5. This variation is more observed for the Lafarge–Allard modeling in the [3000–10000 Hz] frequency band.

6.2 Perforated Plate Effects

We pass now to show the influence of some perforated plate parameters variation: perforated diameter variation, plate porosity variation on the acoustic absorption coefficient. Two liners types are studied: L_2 and L_3.
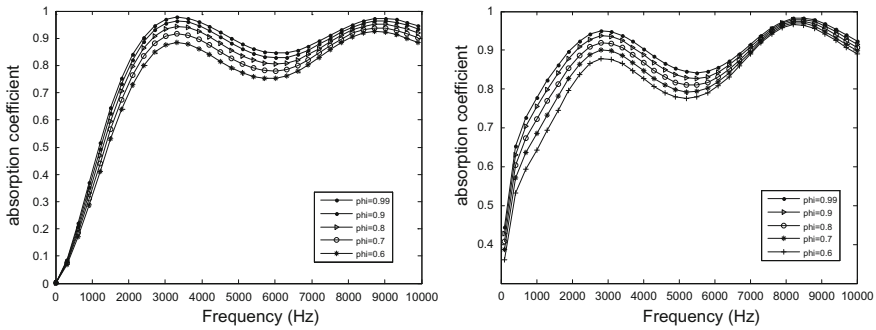
Fig. 3 Material porosity effect for the liner L1 (Left colomn) and the liner L2 (Right colomn) Lafarge–Allard model
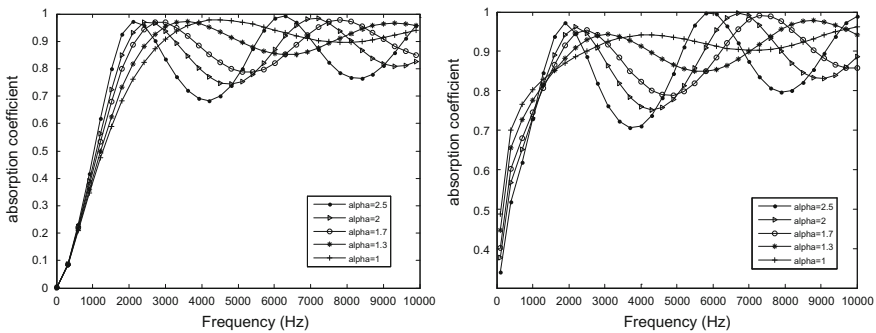
Fig. 4 Material tortuosity effect for the liner L1 (Left column) and the liner L2 (Right Column) using the Lafarge–Allard model

6.2.1 Effect of the Pore Diameter

Figure 5 gives the acoustic coefficient determined by the two impedance models in the case of the liner L_2, for different pore diameters. We note, in the coupled perforated plate and porous material liner type, no variation when the perforated diameter varies. But for the perforated plate and air cavity liner, the variation is more important, especially when we use the Lafarge–Allard modeling.

6.2.2 Plate Porosity Effect

Figure 6 defines the acoustic absorption coefficient for some plate porosity values. The results show an important effect of the plate porosity variation on the second liner kind especially when we use the Lafarge–Allard modeling.
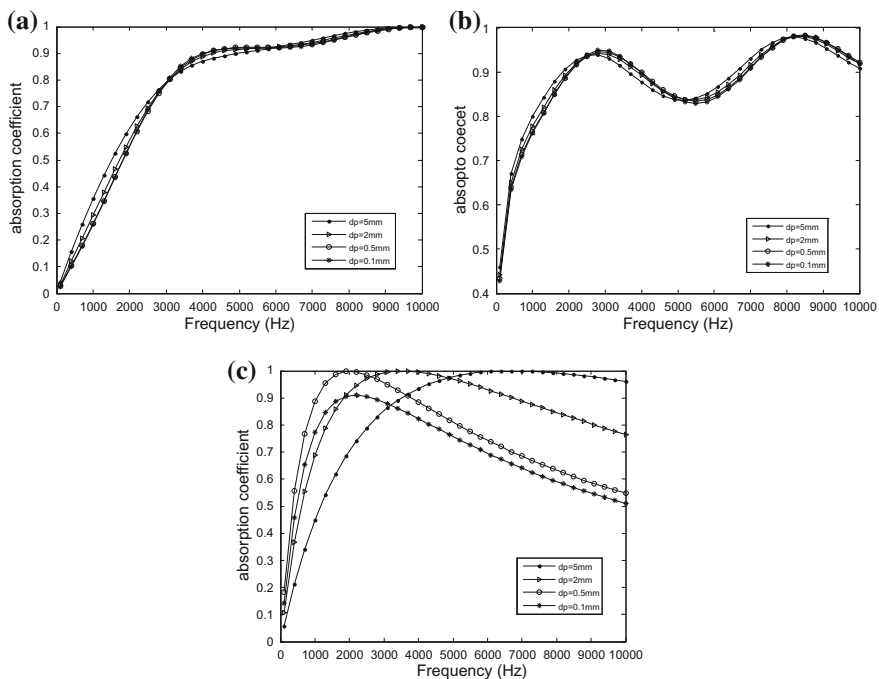
Fig. 5 Perforated diameter of the plate effect for the liner L2 using the Delany-Bazley (**a**), and Lafarge–Allard (**b**) models and the Liner L3 (**c**)
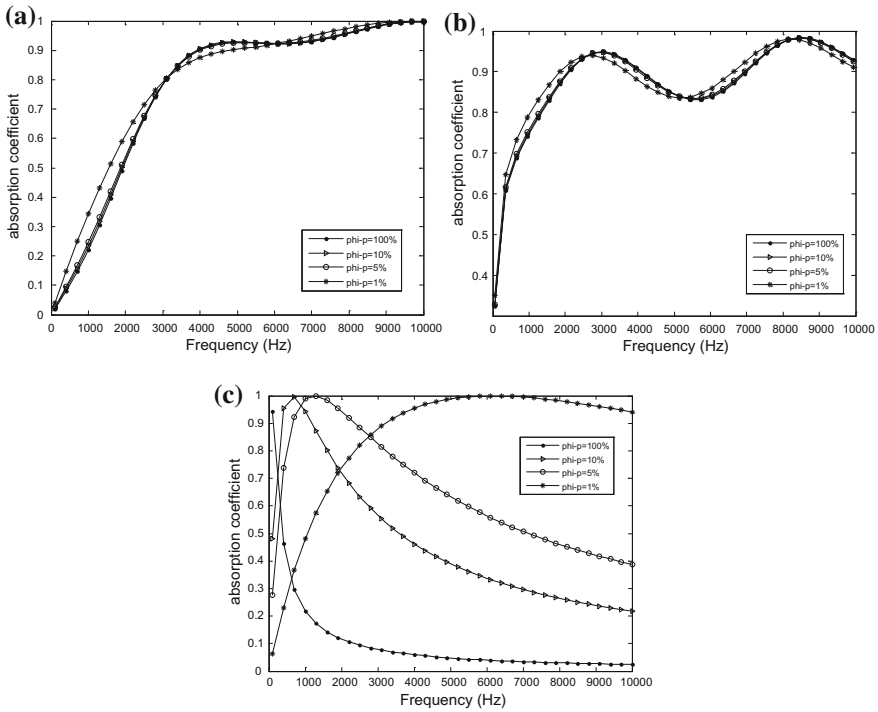
Fig. 6 Plate porosity effect for the liner L2 using the Delany-Bazley (**a**), and Lafarge–Allard (**b**) models and the Liner L3 (**c**)

7 Conclusions

A parametric study is presented in order to show the effect of plate and material parameters on the sound attenuation. Indeed, the acoustic absorption coefficient is widely increasing when the flow resistivity is increasing. But by varying the porosity and the tortuosity we note a nonsignificant effect. The variation of the pore diameter and the plate porosity and thickness has an important effect on the sound attenuation of the perforated plate and air cavity liner. This effect is not significant in the coupled plate and material liner. This study allowed extracting influent liner parameters which must be taken into account in the design of these absorbers.

References

Allard JF, Attala N (2009) Propagation of sound in porous media: modeling sound absorbing materials. Wiley, London

Attenborough K (1987) On the acoustic slow wave in air-filled granular media. J Acous Soc Am 81:93–102

Biot M (1956) Theory of propagation of elastic waves in a fluid-saturated porous solid. J Acous Soc Am 28(2):168–178

Crandall IB (1927) Theory of vibrating systems and sound. D. Van Nostrand Company, USA

Delany ME, Bazley EN (1970) Acoustical properties of fibrous absorbent materials. Appl Acous 3:105–116

Elnady T, Boden H (2003) On semi-empirical liner impedance modeling with grazing flow. In: Proceedings of 9th Aeroacoustics Conference, USA

Hamet JF, Bérengier M (1993) Acoustical characteristics of porous pavements: a new phenomenological model. In: Proceedings of inter-noise conference, Belgium

Johnson DL, Koplik J, Dashen R (1987) Theory of dynamic permeability and tortuosity in fluid-saturated porous media. J Fl Mech 176:379–402

Lafarge D, Lemarinier P, Allard JF (1997) Dynamic compressibility of air in porous structures at audible frequencies. J Acous Soc Am 102(4):1995–2006

Lee DH, Kwon YP (2004) Estimation of the absorption performance of multiple layer perforated panel systems by transfer matrix method. J Sound Vib 278:847–860

Melling TH (1973) The acoustic impedance of perforates at medium and high sound pressure levels. J Sound Vib 65(1):1–65

Miki Y (1990) Acoustical properties of porous materials—modifications of Delany–Bazley models. J Acous Soc Jap 11(1):19–24

Othmani C, Hentati T, Taktak M, Elnady T, Fakhfakh T, Haddar M (2015) Effect of liner characteristics on the acoustic performance of duct systems. Arch Acous 40(1):117–127

Othmani C, Taktak M, Zain A, Hantati T, Elnady T, Fakhfakh T, Haddar M (2016) Experimental and theoretical investigations of the acoustic performance of sugarcane wastes based materials. Appl Acous 109:90–96

Othmani C, Taktak M, Zain A, Hantati T, Dauchez N, Elnady T, Fakhfakh T, Haddar M (2017) Acoustic characterization of a porous absorber based on recycled sugarcane wastes. Appl Acous 120:90–97

Zwikker CW, Kosten C (1949) Sound absorbing materials. Elsevier, Amsterdam

Investigation of Spatio-Temporal Behavior of Coolant During the RHCM Process

Fatma Kria, Moez Hammami and Mounir Baccar

Abstract Rapid Heat Cycle Molding (RHCM) is a new thermoplastic molding technology. The principle of this process consists in a rapid heating of the mold until a suitable temperature. After the filling stage, the cooling phase begins and continues until reaching the ejection temperature. And so on for the following RHCM cycles. In this paper, a three-dimensional numerical study of thermal behavior of RHCM mold for complex shaped automotive part production has been undertaken. Numerical simulations of heat transfer in cavity/core plates domains, polymer and coolant domains, in a cyclic transient regime, have been carried out. To do this, Gambit 2.3.16 has been used to generate the meshing and the commercial software Fluent 6.3.26 has been used to solve the CFD problem. The spatio-temporal behavior within horizontal and vertical channels has been studied. A progressive increase in the coolant temperature during its passage through the mold has been proved. As regard to the temperature at the outlet of the channels, a progressive decrease during the cooling phase has been demonstrated. Moreover, in this research work, we have highlighted the significance of the study of thermal behavior in the cooling water domain (contrary to the hypothesis which assumes a constant temperature of the coolant taken in previous researches) to provide accuracy of the predicted RHCM cycle.

Keywords Rapid heat cycle molding process · Thermal behavior · Cooling phase · Numerical simulation

F. Kria (✉) · M. Hammami · M. Baccar
Computational Fluid Dynamic and Transfer Phenomena, Mechanical Engineering
Department, National Engineering School of Sfax, Sfax, Tunisia
e-mail: Fatmakria1984@yahoo.fr

M. Hammami
e-mail: hammamimoez2003@yahoo.fr

M. Baccar
e-mail: mounir.baccar@enis.rnu.tn

Nomenclature

Parameters	Units
Cp (heat capacity)	J kg^{-1} °C^{-1}
D (channel diameter)	m
G (gravity acceleration)	m s^{-2}
h$_h$, h$_c$ (heat transfer coefficient)	W m^{-2} °C^{-1}
H$_{liq}$ (liquefaction latent heat of water)	J kg^{-1}
L (length of vertical channel)	m
N (normal direction)	-
T (temperature)	°C
λ (thermal conductivity)	W m^{-1} °C^{-1}
μ (dynamic viscosity)	kg m^{-1} s^{-1}
ρ (density)	(kg m^{-3})

Dimensionless numbers	Subscripts
Re (Reynolds number)	m (mold)
Pr (Prandtal number)	p (polymer)
-	S (steam)
-	W (water)

1 Introduction

Thermoplastic injection molding process is one of the most commonly used method for plastic manufacturing product because of its high performance, high efficiency, and also net-shape manufacturing of complex shaped parts.

In order to produce thermoplastic parts with competitive quality, a new injection molding process, called Rapid Heat Cycle Molding (RHCM), is adopted. During the RHCM process, the mold is rapidly heated to a predetermined temperature slightly higher than the glass transition temperature (Tg) of the injected polymer. After the filling stage, the cooling phase begins. In this step, the mold is rapidly cooled by the coolant until reaching a temperature allowing the ejection of the part without any deformation. After the ejection, the mold is heated again for the next molding cycle.

Several previous experimental works (Xiao and Huang 2014; Lucchetta and Fiorotto 2013) have shown the importance of a cyclic heating of the mold on the finished product quality and appearance by preventing the premature solidification of the injected polymer, and so, the flow marks, as well as welding lines, were eliminated.

To rapidly heat the RHCM mold, researchers have developed various methods, such as inductive heating (Chen et al. 2006), flame heating (Kim et al. 2001), infrared heating (Chang and Hwang 2006), convective heating by circulating hot fluid through the mold channels (Wang et al. 2009), and electric heating by

introducing electric heating elements in the mold channels (Zhao et al. 2011). As regard to the RHCM cooling stage, the simplest and efficient method is to cool down the RHCM mold by high (50–60 °C) coolant temperature (Hammami et al. 2017). In fact, they (Hammami et al. 2017) have shown that this temperature range (50–60 °C) provide the reduction of the consumed energy, at the same time, the temperature range (50–60 °C) promotes almost the same cycle time by adopting smaller temperature range.

The heating/cooling channels layout is of great importance since it affects the heating/cooling rapidity and uniformity. (Li et al. 2009) have developed a method to optimize the design of heating/cooling channels in order to improve heating efficiency and cavity surface uniformity. Likewise, (Wang et al. 2011a, b) have proposed an optimization design method for thermal regulation system to obtain optimal heating/cooling effectiveness, uniformity, and also mold strength. (Hammami et al. 2015) have studied a 3D thermal regulation system of RHCM producing LCD panel in transient cyclic regime. They (Hammami et al. 2015) have found the heating/cooling channels arrangement ensuring part quality and process productivity.

The main objective of this work is to study the thermal behavior of RHCM mold for complex shaped automotive part production during several heating/cooling cycles. Particularly, we are interested in the thermal behavior of coolant (water), flowing in turbulent regime through the RHCM mold channels, during the cooling phase. The simulation of several heating/cooling cycles, until attaining the regular state, has been undertaken using the commercial software Fluent 6.3.23.

2 Mathematical Formulation and Numerical Model

In this section, we will present the mathematical formulation and numerical method used to predict thermal behavior of RHCM mold for the production of complex shaped automotive part (Fig. 1) during several molding cycles. The glossy appearance must be obtained for the functional surface composed by the exterior surfaces of the part (Fig. 1). The design of RHCM mold, made with AMPCO 940

Fig. 1 3D model of the automotive part

Table 1 Thermal properties of mold material

Parameters	Value
Density(kg/m^3)	8710
Calorific capacity (J/(kg K))	380
Thermal conductivity (W/(m K))	208
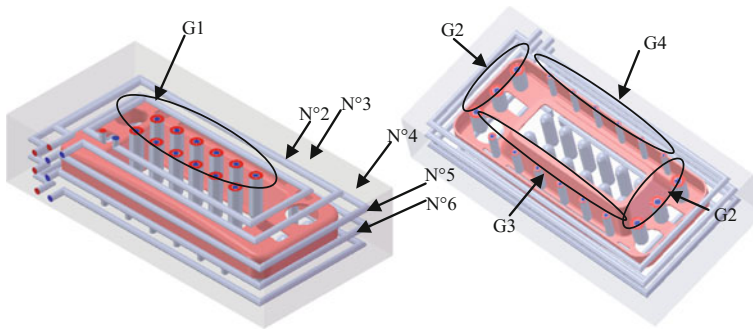
Fig. 2 Design of RHCM mold

(Moldflow 2002) (Table 1), with the adequate heating/cooling channels design (Kria et al. 2017) is shown in (Fig. 2). The layout of heating/cooling channels is composed of five horizontal channels with 6 mm in diameter, numbered from 2 to 6 (Fig. 2) and 30 vertical channels distributed over four groups marked G1, G2, G3, and G4 (Fig. 2).

In the RHCM process, the cooling phase begins when the mold cavity surfaces reach the glass transition temperature Tg (140 °C) for the used polymer PC typed LEXAN Resin 915R (Moldflow 2014) (Table 2). In order to consider the

Table 2 Thermal properties of the polymer

Temperature (°C)	Calorific capacity (J/(kg K))	Thermal conductivity (W/(m K))
120	1612	0.275
130	1693	0.278
140	1823	0.282
150	1885	0.286
160	1909	0.298
170	1929	0.31
180	1947	0.322
200	1976	0.227
220	2003	0.235
240	2020	0.242
260	2030	0.248

spatio-temporal evolution of cooling water temperature, our computational domain includes the mold domain, polymer domain, and heating/cooling mediums domain.

The governing heat transfer equation in the mold domain (1) and polymer domain (2) is given by:

$$\rho_m \, C_m \frac{\partial T_m}{\partial t} = \text{div} \left(\lambda_m \, \overrightarrow{\text{grad}} \, T_m \right) \tag{1}$$

$$\rho_p \, C_p(T_p) \frac{\partial T_p}{\partial t} = \text{div} \left(\lambda_p(T_p) \, \overrightarrow{\text{grad}} \, T_p \right) \tag{2}$$

During the heating stage, the RHCM mold, initially at 30 °C, is heated by the saturated steam at 180 °C. At the interface mold channels, we define heat transfer coefficient h_h in horizontal and vertical channels given by the following expressions (Rohsenow and Hartnett 1973):

$$h_{h_{horizontal}} = 0.555 [\frac{\lambda_w^3 \rho_w (\rho_w - \rho_s) g \, H_{liq}}{\mu_w D (T_s - T_m) \,_{interface}}]^{1/4} \tag{3}$$
$$_{mold - channels}$$

$$h_{h_{vertical}} = 0.555 \, [\frac{\lambda_w^3 \rho_w (\rho_w - \rho_s) g \, H_{liq}}{\mu_w L (T_s - T_m) \,_{interface}}]^{1/4} \tag{4}$$
$$_{mold - channels}$$

During the cooling stage, the coolant flows in a turbulent regime. We obtain by Reynolds decomposition followed by the taking of the temporal average:

$$\rho_w \, C_w \left(\frac{\partial T_w}{\partial t} + \overrightarrow{V_w} \cdot \overrightarrow{\text{grad}} \, T_w \right) = - \text{div} \, (\vec{q} + \vec{q}_t) \tag{5}$$

With:

$$\vec{q} = - \lambda_w \overrightarrow{\text{grad}} \, T_w \quad \text{and} \quad \vec{q}_t = - \lambda_{w_t} \overrightarrow{\text{grad}} \, T_w$$

$\vec{q}$ is the conductive heat flux and $\vec{q}_t$ is the turbulent heat flux.
$\overrightarrow{V_w}$ is the mean velocity vector.

The distribution of mean velocities is also obtained by Reynolds decomposition and the taking of the temporal average of continuity and motion equations:

$$\text{div} \, \overrightarrow{V_w} = 0 \tag{6}$$

$$\rho_w \left(\frac{\partial \overrightarrow{V_w}}{\partial t} + \overrightarrow{V_w} \cdot \overrightarrow{\text{grad}} \, \overrightarrow{V_w} \right) = - \overrightarrow{\text{grad}} \, P + \text{div} \left(\overrightarrow{\overrightarrow{\tau}} + \overrightarrow{\overrightarrow{\tau}}_t \right) + \rho_w \, \vec{g} \tag{7}$$

With:

$$\vec{\vec{\tau}} = \mu_w \vec{\vec{D}} \quad \text{and} \quad \vec{\vec{\tau}}_t = \mu_{w_t} \vec{\vec{D}}$$

$\vec{\vec{\tau}}$ is the viscous tensor stress and $\vec{\vec{\tau}}_t$ is the Reynolds tensor stress.

The turbulent viscosity μ_{w_t} and the turbulent thermal conductivity λ_{w_t} are determined by adopting the k-ε Standard turbulence model.

3 Results and Discussions

Numerical simulation of several heating/cooling cycles shows that a steady state is reached since the second molding cycle. (Figure 3) presents the temperature map at the external functional surfaces of the automotive part at the end of the heating stage of the second molding cycle. It can be noticed that there is an almost uniform temperature at the surfaces of the automotive part. In fact, a temperature gap of 17.7 °C has been found.

3.1 Spatial Evolution of Cooling Water Temperature

Figures 4 and 5 show respectively the velocity fields and temperature distributions within horizontal (Fig. 4) and vertical channels (Fig. 5) at the beginning of the cooling phase ($t_c = 1$ s).

For the horizontal channels (Fig. 4), it is clear that the coolant temperature increases along its path through the mold. This increase is more important as far as the path traveled by the water is longer. With regard to the vertical channels (Fig. 5), it can be seen that the coolant temperature remains unchanged as it passes through the inner tubes and then gradually increases in the annular space. In fact,
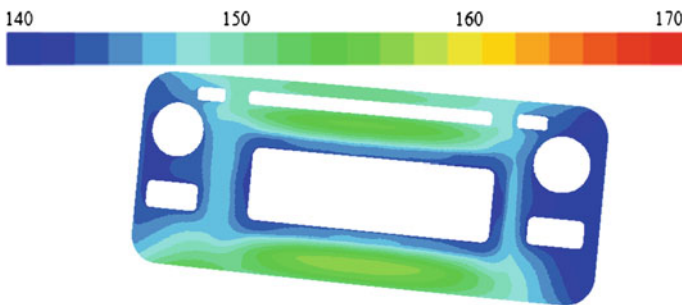
Fig. 3 Temperature map (°C) at functional surfaces of the automotive part in the steady state
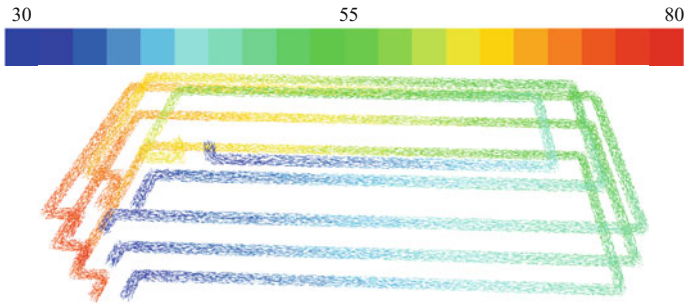
Fig. 4 Velocity field and temperature distribution (°C) within the horizontal channels

(a) at cavity plate

(b) At core plate
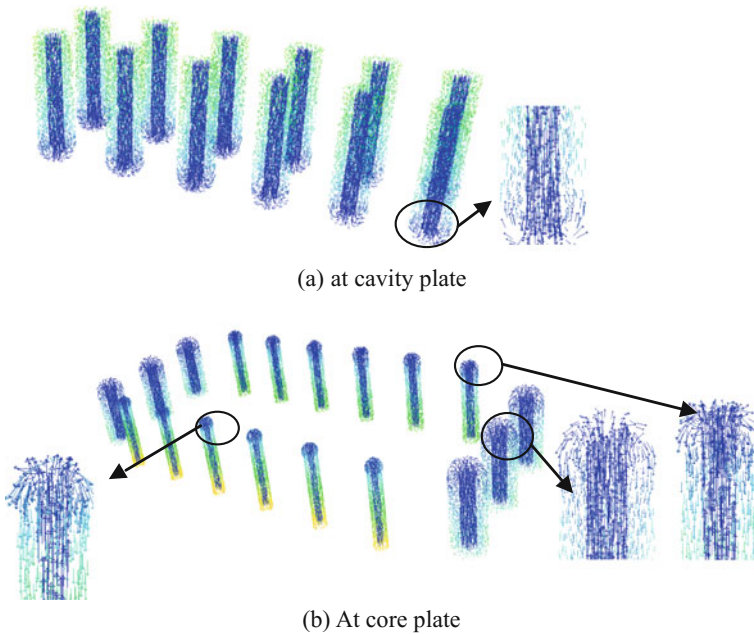
Fig. 5 Velocity field and temperature distribution (°C) within the vertical channels

the increase in the water temperature is justified by the contact of the cold water (30 °C) with the hot walls of horizontal and vertical channels. Indeed, at the beginning of the cooling stage, the temperature at the channels surfaces is important (average temperature in horizontal and vertical channels of about 132 °C), thus enabling the fluid to gradually gain heat along its path.

In order to carry out a fine and local study of the thermal behavior in the coolant domain, it is interesting to follow the spatial evolution of water temperature (considering the position in the heating/cooling channels). To visualize the results within the horizontal channels, channels Nos. 2, 3, and 5 were chosen. With respect
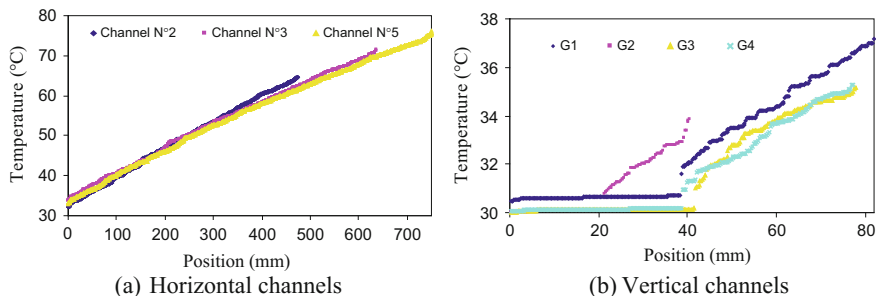
Fig. 6 Cooling water temperature evolution along the channels at the beginning of the cooling phase

to the vertical channels, one channel of each group of channels G1, G2, G3, and G4 has been chosen.

The curves represented in (Fig. 6) illustrate the spatial evolution of water temperature flowing in horizontal and vertical channels at $t_c = 1$ s. For the horizontal channels (Fig. 6a), there is almost linear increase, with approximately the same speed, in the water temperature for the different paths. Thus, it can be concluded that the difference between the coolant temperatures at the three paths outlets is due mainly to the distance traveled by the cooling water. Indeed, Channel No. 5 has the longest trajectory (760 mm), so the coolant outlet temperature is the largest (76.31 °C). For Channel No. 2, with the smallest distance traveled (500 mm), a rise of 34.65 °C is recorded.

By examining the curves shown at (Fig. 6b) representing the spatial evolution of cooling water temperature at $t_c = 1$ s t, It can be seen that when the water passes through the inner tubes, the coolant temperature remains constant, and then, passing through the annular space, there is almost a linear temperature increase with different rates (depending on the diameter of the channel).

3.2   Temporal Evolution of Cooling Water Temperature

In order to carry out a complete study of heat transfer during the cooling phase, the temporal evolution of the outlet cooling water temperature of horizontal (Fig. 7a) and vertical channels (Fig. 7b) has been followed. The curves represented in (Fig. 7a) clearly show that at the beginning of the cooling stage, the cooling water temperature at the outlet of horizontal and vertical channels is high and then decreases progressively within cooling time. Indeed, at the beginning of the cooling phase, the average temperature in the mold is high (146 °C), and then, as the RHCM mold is cooled, the average temperature in the mold decreases (87 °C). Consequently, thermal transfers between mold and cooling water have been
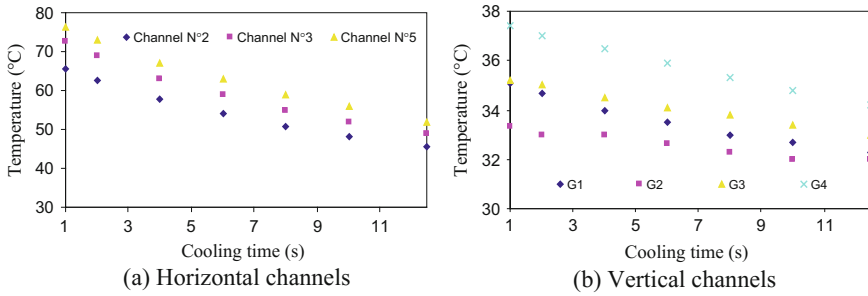
Fig. 7 Temporal evolution of coolant temperature during the cooling phase

attenuated, and hence a low water temperature at the outlet of horizontal and vertical channels has been found.

In order to prove the importance of this numerical study (which considers cooling water domain), comparisons with previous works (Kria et al. 2017), which assumes a constant cooling water temperature, have been carried out. By considering the spatio-temporal variation of cooling water temperature, there is a slight reduction in heating time (4%) with a reduction of 11% in the consumed energy. However, an increase in the cooling time of 15.5% is obtained with a slight increase (5%) in the temperature gap. So, it can be concluded that the precision and reliability of the RHCM process require taking into account the temporal evolution of the coolant temperature during the RHCM process cooling phase.

4 Conclusion

In this paper, numerical simulations of thermal behavior in RHCM mold for a complex shaped automotive part production have been undertaken. The spatio-temporal evolution of the coolant temperature during the cooling phase has been considered. A significant increase in the cooling water temperature during its passage through the mold has been demonstrated. Then, the outlet temperature raise gradually decreases as the mold is cooled.

By examining the effect of coolant temperature increase during the RHCM process cooling stage, a slight reduction in heating time (4%) and consumed energy (11%) have been found. However, increases in cooling time of 15.5% and temperature gap at automotive part functional surfaces by 5% have been noted. So, a complete study of coupled thermal transfer coolant-mold-polymer is necessary in order to obtain faithful results of the RHCM process.

References

Autodesk simulation moldflow adviser (2014)

Chang PC, Hwang SJ (2006) Experimental investigation of infrared rapid surface heating for injection molding. J Appl Polym Sci 102:3704–3713

Chen SC, Jong WR, Chang JA (2006) Dynamic mold surface temperature control using induction heating and its effects on the surface appearance of weld line. J Appl Polym Sci 101:1174–1180

Hammami M, Kria F, Baccar M, (2015) Numerical study of thermal control system for rapid heat cycle injection molding process. Proceedings of the Institution of Mechanical Engineers, Part E: J Process Mech Eng 229 (4):315–326

Hammami M, Kria F, Baccar M (2017) Numerical study of the operating parameter effect on rapid heat cycle molding process. J Process Mech Eng

Kim DH, Kang MH, Chun YH (2001) Development of a new injection molding technology: momentary mold surface heating process. Inject Molding Technol 5:229–232

Kria F, Hammami M, Baccar M (2017) Conformal heating/cooling channels design in rapid heat cycle molding process.ss Mech Ind 18:109

Li XP, Zhao GQ, Guan YJ, Ma MX (2009) Optimal design of heating channels for rapid heating cycle injection mold based on response surface and genetic algorithm. Mater Des 30:4317–4323

Lucchetta G, Fiorotto M (2013) Influence of rapid mould temperature variation on the appearance of injection-moulded parts. J Mech Eng 59:683–688

Moldflow plastic insight release 5.0 (2002)

Rohsenow MW, Hartnett JP (1973) Handbook of heat transfer. McGraw-Hill, New York

Wang GL, Zhao GQ, Li HP, Guan YJ (2009) Research on a new vaiotherm injection molding technology and its application on the molding of a large LCD panel.s Polym Plast Technol Eng 48:671–81

Wang GL, Zhao GQ, Li HP, Guan YJ (2011a) Multi-objective optimization design of the heating/cooling channels of the steam-heating rapid thermal response mold using particle swarm optimization international. J Therm Sci 50:790–802

Wang GL, Zhao GQ, Li HP, Guan YJ (2011b) Research on optimization design of the heating/cooling channels for rapid heat cycle molding based on response surface methodology and constrained particle swarm optimization. Expert Syst Appli 38:6705–6719

Xiao CL, Huang HX (2014) Multiobjective optimization design of heating system in electric heating rapid thermal cycling mold for yielding high gloss parts J Appl Polym Sci 131

Zhao G, Wang G, Guan Y, Li H (2011) Research and application of a new rapid heat cycle molding with electric heating and coolant cooling to improve the surface quality of large lcd tv panels. Polym Adv Technol 22:476–87

Engineering Change Management (ECM) Methods: Classification According to Their Dependency Models

Mahmoud Masmoudi, Patrice Leclaire, Marc Zolghadri and Mohamed Haddar

Abstract Engineering Change Management methods lead to assess impact of engineering changes and evaluate their propagation effects. In this paper, we propose a novel classification of Engineering Change Management methods according to their dependency model: (i) theoretical dependency model and (ii) a posteriori dependency model. A dependency model is needed to assess the change effect on one parameter after changing the value of another one. Three reference methods are presented here in details to explain the differences between these two types of dependency models and their usability according to designer decisions. The comparison shows that a theoretical model is generally a deterministic model that request a lot of knowledge and expertise in different areas. Besides an a posteriori model is based on probabilistic data and uses simple techniques and tools.

Keywords Engineering change management (ECM) · Redesign Dependency · Change propagation

M. Masmoudi (✉) · P. Leclaire · M. Zolghadri
Laboratoire Quartz, SUPMECA, 3 Rue Fernand Hainaut,
93407 Saint-Ouen Cedex, France
e-mail: mahmoud.masmoudi@supmeca.fr

P. Leclaire
e-mail: patrice.leclaire@supmeca.fr

M. Zolghadri
e-mail: marc.zolghadri@supmeca.fr

M. Masmoudi · M. Haddar
Laboratoire de Mécanique, Modélisation et Production, Ecole Nationale d'Ingénieurs de Sfax, Université de Sfax, Route Soukra Km 3.5, BP 1173, 3038 Sfax, Tunisia
e-mail: mohamed.haddar@enis.rnu.tn

1   Introduction

A product needs to be changed or modified in any phase of its life cycle. These Engineering Changes (EC) can be requested in design or redesign project on the product to improve its performance. These types of improvement requires a detailed and accurate assessment of the consequences of a change before being applied. However, a bad or unsuitable management of these changes can lead to a serious (negative) impact on the product design or the development project (in terms of time, cost, etc.).

Through researches on Engineering Change Management, Engineering Changes have been defined in the literature in different ways using different terms. But, the most used and complete definition was given by Jarratt et al. (2011) as *An engineering change is an alteration made to parts, drawings or software that have already been released during the product design process. The change can be of any size or type; the change can involve any number of people and take any length of time*.

According to our previous works (Masmoudi et al. 2015a, b) and in a context of product renovation, three phases are necessary to study a change request and its impact: the dependency identification, the change propagation and finally the redesign achievement. The identification of dependencies of a system is a crucial task in order to assess the impact of the change propagation. There are a number of methods that have been proposed in the area of research of ECM to assess the impacts of change. Some authors such as Hamraz (2013) classify the ECM publications according to the change occurrence time (Pre-change stage, In-change stage, or Post-change stage). Zhang (2013) propose another categorization of ECM methods according to the 3P (Product-Project-People). So, the main objective of this paper is to propose a novel classification of these different ECM methods according to their dependency modeling.

This paper is organized as follows. In the next section, we will browse three reference Engineering Change Management methods largely cited in the literature. Then, in the third section, we present our methods classification proposal. Finally, conclusions and perspectives of coming works are outlined.

2   Engineering Change Management Methods

Several methods and approaches have been developed in the Engineering Change Management literature, most of them include a model to represent dependencies and a technique to predict or analyze the impact of change propagation within a product (Hamraz et al. 2013a).

Three methods have been chosen to be presented in detail in this section because they represent the most interesting and influential methods in the area of change management (Masmoudi et al. 2015a).

2.1 Change Prediction Method (CPM)

The Change Prediction Method (CPM) has been proposed by Clarkson et al. (2001, 2004) to predict change and characterize it in a numeric and probabilistic way. In this method, the authors use a model of dependencies between each pair of components to calculate and visualize the overall risk of the change propagation imposed on a component and affecting other components. The result of the CPM method is a matrix of adjacency (also called a Design Structure Matrix (DSM)), where the elements in column indicate the instigators components (which initiate change), elements in row indicate the affected components (which receive the changes) and the cells between two given components include the corresponding values of the risk. The Fig. 1 shows the four steps used.

At the beginning of this method (step 1), the product is decomposed into subsystems (of the components or parts). The number of subsystems depends on the chosen level of decomposition. The authors recommend a decomposition with less than 50 components.

Direct dependencies between components are captured then (in step 2) in a binary DSM matrix, where the notation with a cross "×" indicates the existence of one dependency linkage. Two other DSMs, called direct impact and likelihood matrices, are determined values given by experts (designers) based on their experience and their knowledge of the product. The direct probability matrix represents the relative frequency of the change propagation between two components. The value of direct risk is calculated by multiplying the impact value with the likelihood value.

In the third step, the combined risk of the change propagation representing the indirect dependency is calculated using an algorithm called the Forward CPM. This algorithm considers the changes propagation being propagated between any pair of components through several direct and indirect paths excluding the auto-dependences and cyclic paths.

Clarkson et al. (2004) use operators of intersection and union along the propagation path in their algorithm to calculate the probabilities and impacts. The combined risk of the spread of change includes the direct and indirect risks. As mentioned above, the direct risk is defined by the product of the probability of direct and indirect impact between two components. However, the indirect risk considers only the change (the sum of the product of probability and impact) that propagates via the intermediate propagation components. The proposed combined risk matrix is considered as a tool to support the decision to change management.

In the last step, this combined risk matrix can provide a vision to different stakeholders (such as Product development and Quality control) and assesses them how changes will be propagated and help them in ECM strategic decisions (for product design and redesign). First applied to a helicopter (Clarkson et al. 2001), the CPM method has then been applied to several industry case studies, such as: a diesel engine (Jarratt et al. 2004), an injector (Keller 2007), and a railway valve (Jarratt et al. 2002).
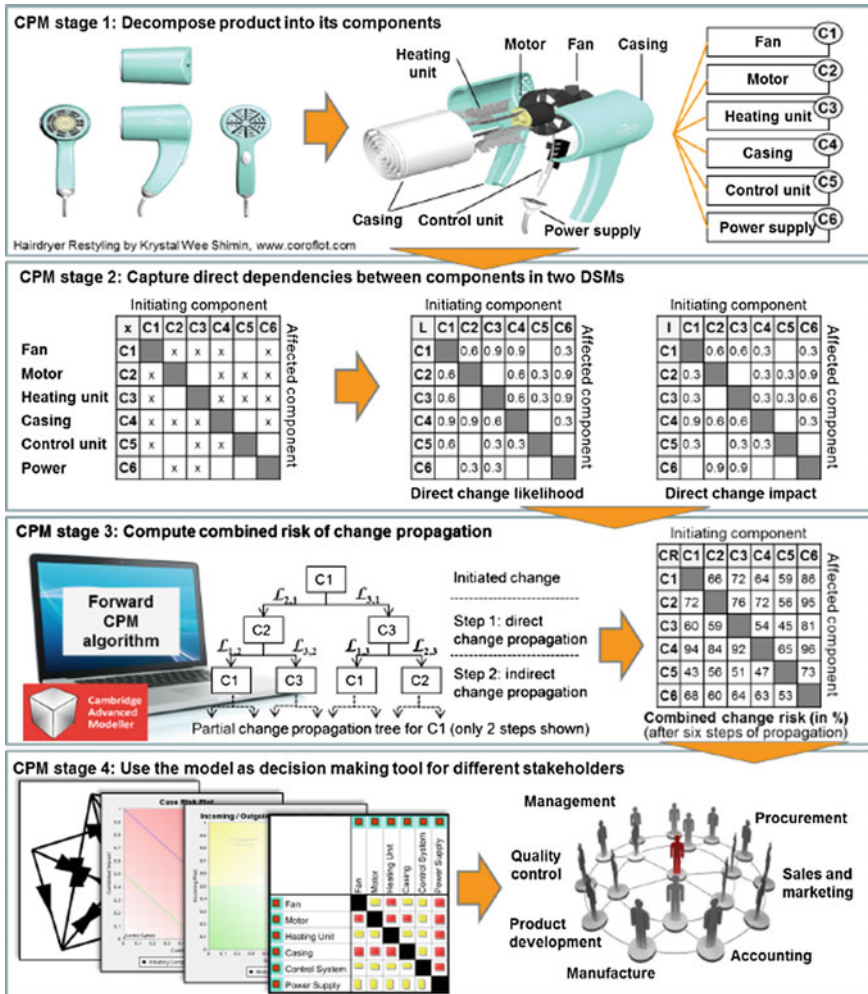
Fig. 1 The CPM approach (Hamraz et al. 2013a)

2.2 Change Favorable Representation (C-FAR)

The Change FAvorable Representation method noted by C—FAR was proposed by Cohen et al. (2000). They use the EXPRESS (a modeling language) representation with entities, attributes, and relationships. In this model, an entity (representing a component) is modeled by a vector whose attributes are the elements of the vector and that are bound together by relationships. In addition, dependencies between attributes of both entities are represented in a matrix and characterized qualitatively by assigning the values "low", "medium" and "high" based on the assessment of

design experts. Afterward, these matrices and vectors are multiplied, along the paths of propagation of change (defined by a succession of parameters dependent on them according to the matrix) to calculate the values of the links between each pair of attributes.

This method is only suitable for small or relatively simple products (Cohen et al. 2000). It is not appropriate for a comprehensive analysis because of the immense amount of data required and important calculations (multiplication of vectors). However, the C-FAR method has been used to examine more than one industrial case study (a car bumper, an injection molding and a printed wiring board).

2.3 Kusiak and Wang Method

We also consider Kusiak and Wang (1995) as a reference method in the Engineering Change Management literature. The methodology proposed by Kusiak and Wang (1995) was originally aimed to help designers to negotiate constraints (defined by the simulation of several scenarios with varying each time the values of the parameters of a system and checking if a system of equations representing the constraints is respected).

A dependency network model has been used in their approach. This network is a four-tuple $G = (V, E, \Omega, \Psi)$, which contains:

- (V) Vertices, representing the design variables, constraints and design objectives (goals) of the studied system,
- Edges (E) corresponding to the relationship between each pair of vertices,
- Qualitative characterization (Ω) defined by a qualitative value ($+$, $-$, 0, $?$) dependency driven by edges. These four qualitative values refer, respectively, to (an increasing, a decreasing, no variation, unknown variation) of the new value.
- Quantitative characterization (Ψ) defined by a quantitative value of the dependency carried by the edges.

A reduction algorithm has been developed to represent and derive from the dependencies ($\delta_{i,j}$) between the decision variables (x_i) or specifications (represented by a square), and constraints (triangles) and objectives (octagons), as shown in Fig. 2.

Fig. 2 Reduced dependency graph in Kusiak and Wang approach
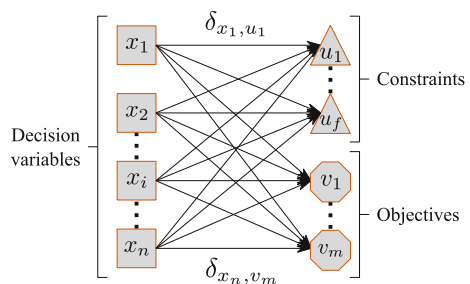
In the second part of their proposal, Kusiak and Wang (1995) propose an approach based on fuzzy logic for model imprecise between variables dependencies where no sufficient quantitative information is available.

3 Methods Classification

We propose in this paper a classification of Engineering Change Management approaches according to their dependency models. Table 1 represents a classification of some researches in ECM into: (i) based on theoretical dependency model and (ii) based on a posteriori dependency model.

In the following of this section, we will present the detailed specification of each type of dependency model.

Table 1 ECM methods classification

Method	Short description	References	Dependency model	
			Theoretical	A posteriori
Kusiak and Wang approach	Dependency analysis in constraint negotiation	Kusiak and Wang (1995)	×	
Parameter linkage network (PLN)	A parameter linkage-based method for searching change propagation paths	Yang and Duan (2012)	×	
Flanagan et al. method	Change Propagation through the link between functions and components	Flanagan et al. (2003)		×
Change prediction method (CPM)	Method based on numeric component DSMs and stochastic propagation analysis	Clarkson et al. (2001, 2004); Keller (2007), Keller et al. (2005)		×
Function–behavior–structure (FBS)	FBS linkage model for engineering change prediction	Hamraz (2013), Hamraz et al. (2012, 2013a, b)		×
Change favorable representation (C-FAR)	Change evaluation at the attribute level using matrix calculations	Cohen et al. (2000)		×
Change impact and risk analysis (CIRA)	Combining the CPM/PDD theory and FMEA methodology for an improved ECM	Conrad et al. (2007)	×	

3.1 Theoretical Dependency Model

All methods of change management that have been previously presented in Sect. 2 begin with a characterization of the dependence between the components of a system and eventually analyze the mechanism of change propagation. These are usually linked by already known relationships and that can be extracted from a theoretical model. This model of theoretical dependency is expressed through a set of equations, qualitative relationships, or even rules of influence (if the value of a parameter x is equal to a value or belongs to an interval, so a second parameter is equal to another defined value). Data, and relationships linking these data, can belong to several areas of knowledge (such as mechanical and thermal, etc.).

In the literature, we find the work of Kusiak and Wang (1995) and Yang and Duan (2012) who have used this kind of dependency model based on equations of physical laws and rules of influence.

In these approaches based on a theoretical model, available models are used to determine the new values of the parameters (the nodes of the dependency graph) and the direction of the variations and/or possible changes.

These kinds of models are generally used to produce design alternatives; a design alternative is a product model which integrates all the required changes taking into account all the necessary and sufficient constraints. The main disadvantages of these models include:

- They require a lot of knowledge and expertise by combining different areas (mechanical, electronic, etc.) to build relevant theoretical models. In the event that these models do not exist, their identification extremely consumes time and effort.
- These models are fine-grained (very detailed) and the propagation of the changes is performed on all parameters of the system (Kusiak and Wang 1995), so, this allows to generate several detailed design alternatives that require a long computation time. This advanced level of details may be considered for certain settings unnecessary or not requested (no added value to some studies),
- They need specific techniques to group and aggregate the multidisciplinary models detailed in simpler models. However, this task is not easy to be done.

3.2 A Posteriori Dependency Model

The second type of dependency model is called a posteriori dependency model that can be much simpler than the theoretical model and focuses on several specific aspects of the product or system. Most ECM works rely on simple dependency models, for example in (Flanagan et al. 2003) a model of dependencies between the components of an excavator is presented in the form of a (6×6) DSM matrix

collected through experts notice and opinions. However, the dependencies between the product parameters are not explicit enough in this kind of model.

A dependency model subsequently does not need to represent exact equations or formal logical rules linking the parameters. But it must allow analysts to identify the direction or the nature of the changes and then evaluate and predict parameters new values. Most ECM works rely on a dependency model a posteriori, but none of them sets the value of the target (affected by change) parameters obtained after changing the instigating parameter value.

In an a posteriori dependency model-based approach, the models are only used to determine the direction of the variations and cannot provide any information on the exact values of the parameters after the change propagation in remains product parameters. Almost all the papers and the approaches examined in this state of the art use models of dependency in order to establish dependencies by the analysis of the structure of product or functions, for example using interviews with experts (Clarkson et al. 2004; Eckert et al. 2004; Jarratt et al. 2004; Keller et al. 2005).

Dependency characterization depends on the purpose of the change analysis. For example, since the purpose of the CPM method (Clarkson et al. 2004) is to qualify the possibility of occurrence of changes and assess their potential impacts, the dependencies are described in a simple way by probability and impact indicators.

In Hamraz et al. (2012), the authors try to go further in modeing the product properties through three different layers (function, behavior, and structure), which give some ideas on possible changes to the behavior of the product and, therefore, the services provided to users. However, the analysis was conducted on a posteriori models, which are much simpler than the theoretical models.

To summarize, the techniques associated with these dependency models consume less effort but can give a valuable insight on high-level design decisions and even accelerate the Time-To-Market (TTM). However, they have their own disadvantages:

- The change impacts are assessed subjectively by a probability of change occurrence value through interviews with design experts (working on the product design).
- They do not help the designers decide to which change they have to be oriented. They are called "what-if methods" that do not specify the choice criteria for the most appropriate change.

4   Conclusion and Future Works

In this chapter, a classification according to the dependency model has been made to the Engineering Change Management approaches. Two different types are identified: the theoretical and the a posteriori models. The two types of dependency models present benefits and disadvantages. On one hand, a theoretical model is a deterministic model but complicated to have because of the requested knowledge

and expertise. On the other hand, an a posteriori model uses simple techniques (easy for use) but based on probabilistic data.

In conclusion, the theoretical model is undoubtedly used for the detailed design, but is not relevant for the Engineering Change Management, which deals less detailed data.

In future works, we aim to propose an approach based on a mixed dependency model that combine the theoretical and the a posteriori techniques model. Considering the simplicity of a posteriori dependency model techniques and the high level of details of the theoretical dependency model, we look to find the right trade-offs between a too much detailed dependency model and too much simplified one.

References

Clarkson J, Simons C, Eckert C (2001) Predicting change propagation in complex design, In: ASME 2001 design engineering technical conferences and computers and information in engineering conference, pp 1–10

Clarkson PJ, Simons C, Eckert C (2004) Predicting change propagation in complex design. J Mech Des 126(5):788–797

Cohen T, Navthe S, Fulton RE (2000) C-far, change favorable representation. Comput Aided Des 32(5):321–338

Conrad J, Deubel T, Köhler C, Wanke S, Weber C (2007) Change impact and risk analysis (cira)-combining the cpm/pdd theory and fmea-methodology for an improved engineering change management. In: Guidelines for a decision support method adapted to NPD processes

Eckert CM, Clarkson PJ, Zanker W (2004) Change and customisation in complex engineering domains. Res Eng Design 15:1–21

Flanagan TL, Eckert CM, Eger T, Smith J, Clarkson PJ (2003) A functional analysis of change propagation, In: DS 31: Proceedings of ICED 03, the 14th international conference on engineering design, Stockholm

Hamraz B (2013) Engineering change modelling using a function-behaviour-structure scheme, PhD thesis, University of Cambridge

Hamraz B, Caldwell NHM, Clarkson, P (2012) A multidomain engineering change propagation model to support uncertainty reduction and risk management in design, J Mech Des 134 (10), 100905–1–14

Hamraz B, Caldwell NHM, Clarkson P (2013a) A matrix-calculation-based algorithm for numerical change propagation analysis. IEEE Trans Eng Manag 60(1):186–198

Hamraz B, Caldwell NHM, Wynn DC, Clarkson P (2013b) Requirements-based development of an improved engineering change management method. J Eng Des 24(11):765–793. https://doi.org/10.1080/09544828.2013.834039

Jarratt TAW, Eckert, C, Clarkson, PJ Schwankl, L (2002) Product architecture and the propagation of engineering change, In: DS 30: Proceedings of Design 2002, the 7th international design conference, Dubrovnik

Jarratt TAW, Eckert CM, Caldwell NHM, Clarkson PJ (2011) Engineering change: an overview and perspective on the literature. Res Eng Design 22(2):103–124

Jarratt TAW, Keller R, Nair S, Eckert C, Clarkson PJ (2004) Visualization techniques for product change and product modelling in complex design, In: Blackwell AF, Marriott K, Shimojima A eds, Diagrammatic representation and inference, Springer, pp 388–391

Keller R (2007) Predicting change propagation: algorithms, representations, software tools, PhD thesis, Cambridge University Engineering Department

Keller R, Eger T, Eckert C, Clarkson PJ (2005) Visualising change propagation. In: Samuel A, Lewis W (eds) Proceedings ICED 05, the 15th international conference on engineering design, vol DS. 35, Design Society. Melbourne, Australia, pp 62–63

Kusiak A, Wang J (1995) Dependency analysis in constraint negotiation. IEEE Trans Syst Man Cybernet 25(9):1301–1313

Masmoudi M, Leclaire P, Zolghadri M, Haddar, M (2015a) Dependency identification for engineering change management (ecm): an example of computer-aided-design (cad)-based approach, In: Proceedings of the 20th international conference on engineering design (ICED 15), Milan

Masmoudi M, Leclaire P, Zolghadri M, Haddar M (2015b) Modelling dependencies in engineering change management (ecm), In: Design and modeling of mechanical systems–II

Yang F, Duan G (2012) Developing a parameter linkage based method for searching change propagation paths. Res Eng Design 23(4):253–372

Zhang X (2013) Contribution to engineering change management in product development projects: reference models and multi-based simulation, PhD thesis, Bordeaux University 1

Analytical Modeling and Analysis of a Bimorph Piezoelectric Energy Harvester

Marwa Mallouli and Mnaouar Chouchane

Abstract Energy harvesting from piezoelectric devices is a promising technology which is used to convert ambient energy extracted from the environment into electrical energy in the aim of supplying power for small electronic devices. Unimorph and bimorph cantilever beams have been used as basic piezoelectric energy harvesters. In this paper, a bimorph piezoelectric cantilever beam under base excitation is considered. An analytical model based on the Euler–Bernoulli beam assumption has been used to estimate the generated power. Series and parallel connections of the two piezoelectric layers are considered. To make an objective comparison of the generated power by several harvesters, the first natural frequency of the beam has been fixed by increasing simultaneously the beam thickness and the tip mass. The calculated frequency responses associated to the bimorph cantilever beam without tip mass have been validated based on the previous publications. It has been found that an increase of the tip mass and the beam thickness leads to a higher power generation. More power is produced in the case of a series connection.

Keywords Energy harvesting · Piezoelectric cantilever bimorph · Analytical model · To optimize

1 Introduction

Electronic devices commonly use batteries for power supply. Batteries have limited lifetime and therefore, they require regular replacements. The search for alternative sources of energy for these devices is an up to date research topic. Energy harvesting converts ambient energy into electrical energy. Several ambient energies

M. Mallouli (✉) · M. Chouchane
Laboratory of Mechanical Engineering, National Engineering School of Monastir,
University of Monastir, Avenue Ibn El Jazzar, 5019 Monastir, Tunisia
e-mail: marwa.mallouli24@gmail.com

M. Chouchane
e-mail: mnaouar.chouchane@gmail.com

1179

have been exploited but in this paper, only vibration energy harvesting is considered. The piezoelectric conversion is considered the most advantageous due to its great power density, high performance and easiest manufacturing (Priya 2007; Sodano et al. 2004).

Generally, a piezoelectric energy harvester is composed of a cantilevered beam with a single (unimorph) or double (bimorph) piezoelectric layers. In this research, a bimorph cantilever beam is chosen due to its widespread usage. A procedure is proposed to determine the generated power of the energy harvesters while varying the substrate thickness but keeping the first natural frequency constant by the addition of an adequate tip mass in order to maximize the generated power.

2 Analytical Modeling of the Bimorph Energy Harvester

2.1 The Bimorph Configuration and Modeling Assumptions

The output power of the harvester is directly linked to its dimensions as detailed below. A piezoelectric energy harvester is considered which is composed from a thin substrate layer sandwiched between two piezoelectric layers (made, for example, from PZT material) supporting a tip mass as shown in Fig. 1. The beam is mounted onto a vibrating host structure. When the host structure vibrates, the induced vibrations of the cantilever beam are converted into electricity due to the piezoelectric effect thus an alternating voltage is generated through the electrodes bonded to the surfaces of the piezoelectric layers. When the electrodes are linked to a passive circuit, an alternating current is generated and energy dissipates in the
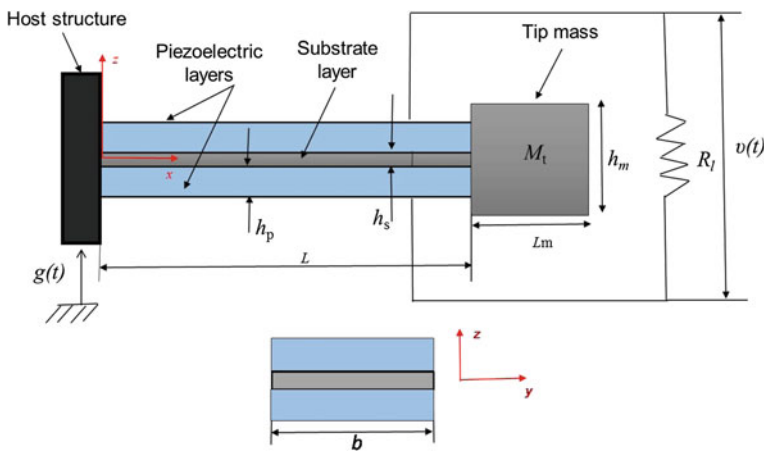
Fig. 1 A bimorph piezoelectric beam with a tip mass in a series connection

circuit. In the following sections, the generated power will be determined using analytical modeling of the piezoelectric energy harvester.

In the considered model, the following assumptions are adopted:

- The beam and the piezoelectric patches are considered as Euler–Bernoulli beam elements and the shear deformation is neglected.
- The piezoelectric patches are perfectly bonded to the substrate layer.
- The piezoelectric patches are considered as an elastic material.
- The mechanical losses are due to strain-rate damping and viscous damping.
- The couple of electrodes linked to the piezoelectric patches are supposed very thin and absolutely conductive to induce an electric potential difference along them.

A load resistance is connected to the bimorph cantilever beam as commonly used in this type of modeling (Chen et al. 2006; Erturk and Inman 2008). The load resistance is used to determine the generated power of the harvester. The base excitation is supposed to be permanent to engender continuous electrical supply extracted from the energy harvester device.

2.2 Analytical Modeling of the Bimorph Harvester

The energy harvester can be connected to the electric circuit in two ways: series or parallel connection. In these two types of connection, the bimorph design has similar geometric and material properties but different backward piezoelectric coupling effect, and therefore, different vibration responses (Inman and Erturk 2011). In the following, the equations of motion of these two designs are presented and the analytical eigenvalue relations are detailed.

The motion of the host structure has a transverse translation motion $g(t)$. So, the transverse base displacement $w_b(x, t)$ is:

$$w_b(0, t) = g(t) \tag{1}$$

The equations of motion of the forced vibration of the bimorph cantilever beam with a tip mass excited by a base excitation can be written as (Inman and Erturk 2011):

- For a series connection:

$$
\begin{aligned}
&YI \frac{\partial^4 w_{rel}^s(x,t)}{\partial x^4} + c_s I \frac{\partial^5 w_{rel}^s(x,t)}{\partial x^4 \partial t} + c_a \frac{\partial w_{rel}^s(x,t)}{\partial t} + m \frac{\partial^2 w_{rel}^s(x,t)}{\partial t^2} \\
&- \vartheta_s v_s(t) \left[\frac{d\delta(x)}{dx} - \frac{d\delta(x-L)}{dx} \right] = -[m + M_t \delta(x-L)] \frac{\partial^2 w_b(x,t)}{\partial t^2}
\end{aligned}
\tag{2}
$$

- For a parallel connection:

$$YI\frac{\partial^4 w_{rel}^p(x,t)}{\partial x^4} + c_s I\frac{\partial^5 w_{rel}^p(x,t)}{\partial x^4 \partial t} + c_a\frac{\partial w_{rel}^p(x,t)}{\partial t} + m\frac{\partial^2 w_{rel}^p(x,t)}{\partial t^2}$$
$$- \vartheta_p v_p(t)\left[\frac{d\delta(x)}{dx} - \frac{d\delta(x-L)}{dx}\right] = -[m + M_t\delta(x-L)]\frac{\partial^2 w_b(x,t)}{\partial t^2}, \tag{3}$$

where $w_{rel}(x,t)$ represents the displacement of the beam in the transverse direction relative to its host at location x and time t, superscripts p and s, respectively, refer to parallel and series connection to an electrical circuit (which should be differentiated from the subscripts $\tilde{s}$ and $\tilde{p}$ that refer to the substructure and the piezoelectric sheets, respectively), c_a represents the viscous damping coefficient, c_s corresponds to the strain-rate damping coefficient, M_t is the tip mass, m corresponds to the mass per unit length of the beam, L is the length of the beam. Using two similar piezoelectric sheets, $v_p(t)$ and $v_s(t)/2$ correspond to the voltage between the electrodes of each piezoelectric sheets in parallel and series connections, respectively.

The proportional damping assumption is applied for the piezoelectric energy harvester in order to apply normal mode modal transformation (Banks et al. 1998).

The backward coupling coefficients ϑ_s and ϑ_p are respectively:

$$\vartheta_s = \frac{\bar{e}_{31}b}{2h_{\tilde{p}}}\left[\left(h_{\tilde{p}} + \frac{h_{\tilde{s}}}{2}\right)^2 - \frac{h_{\tilde{s}}^2}{4}\right] \tag{4}$$

$$\vartheta_p = 2\vartheta_s \tag{5}$$

Note that b denotes the width of the beam, $h_{\tilde{p}}$ and $h_{\tilde{s}}$ refer respectively to the thickness of each piezoelectric sheet and the substrate sheet, respectively, and $\bar{e}_{31}$ is the effective piezoelectric stress constant.

The bending stiffness YI of the cross-section of the beam can be expressed as:

$$YI = \frac{2b}{3}\left\{Y_{\tilde{s}}\frac{h_{\tilde{s}}^3}{8} + \bar{c}_{11}^E\left[\left(h_{\tilde{p}} + \frac{h_{\tilde{s}}}{2}\right)^3 - \frac{h_{\tilde{s}}^3}{8}\right]\right\}, \tag{6}$$

where $Y_{\tilde{s}}$ and $\bar{c}_{11}^E$ are the Young's modulus of the substrate sheet and the piezoelectric sheet, respectively.

The mass per unit length expression of the beam is:

$$m = b\left(\rho_{\tilde{s}}h_{\tilde{s}} + 2\rho_{\tilde{p}}h_{\tilde{p}}\right), \tag{7}$$

where $\rho_{\tilde{s}}$ and $\rho_{\tilde{p}}$ are to the densities of the substrate sheet and the piezoelectric sheet, respectively.

Based on the proportional damping assumption, the vibration of the piezoelectric energy harvester can be expressed as:

$$w^s_{rel}(x,t) = \sum_{r=1}^{\infty} \phi_r(x)\eta^s_r(t) \quad w^p_{rel}(x,t) = \sum_{r=1}^{\infty} \phi_r(x)\eta^p_r(t), \tag{8}$$

where $\eta^s_r(t)$ and η^p_r are the modal coordinates for series and parallel connections, respectively and $\phi_r(x)$ is the mass-normalized eigenfunction of the vibration mode r referring to the undamped free vibration problem which has the following expression:

$$\phi_r(x) = A_r\left[\cos\frac{\lambda_r}{L}x - \cosh\frac{\lambda_r}{L}x + \varsigma_r\left(\sin\frac{\lambda_r}{L}x - \sinh\frac{\lambda_r}{L}x\right)\right] \tag{9}$$

Noting that the above formula is independent of the type of electrical connection and ς_r can be expressed as:

$$\varsigma_r = \frac{\sin\lambda_r - \sinh\lambda_r + \lambda_r\frac{M_t}{mL}(\cos\lambda_r - \cosh\lambda_r)}{\cos\lambda_r + \cosh\lambda_r - \lambda_r\frac{M_t}{mL}(\sin\lambda_r - \sinh\lambda_r)}, \tag{10}$$

where A_r is a modal amplitude constant which has to be determined using the normalization condition of the eigenfunctions.

The undamped natural frequencies corresponding to mode r in the short-circuit case $(R_l \to 0)$ is:

$$\omega_r = \lambda_r^2\sqrt{\frac{YI}{mL^4}}, \tag{11}$$

where λ_r are the eigenvalues determined from the solution of the following equation given M_t, m, L and I_t:

$$1 + \cos\lambda\,\cosh\lambda + \lambda\frac{M_t}{mL}(\cos\lambda\,\sinh\lambda - \sin\lambda\,\cosh\lambda)$$
$$- \frac{\lambda^3 I_t}{mL^3}(\cosh\lambda\,\sin\lambda + \sinh\lambda\,\cos\lambda) + \frac{\lambda^4 M_t I_t}{m^2 L^4}(1 - \cos\lambda\,\cosh\lambda) = 0 \tag{12}$$

The mass moment of inertia about the center axis I_t is obtained by applying Huygens theorem:

$$I_t = M_t\left[\left(\frac{L_m^2 + h_m^2}{12}\right) + \left(\frac{L_m}{2}\right)^2\right] \tag{13}$$

2.3   Frequency Response Functions

In the considered model, the input corresponds to the base motion $g(t)$ and the outputs are vibration and voltage responses. Here, the base motion is considered to

be harmonic without rotation, $g(t) = W_0 e^{j\omega t}$, and only the generated voltage per translational base acceleration called voltage FRF, current FRF and power FRF are determined in multimode vibrations. In this work, the study is focused on the determination of the power output.

The multimode voltage FRF can be expressed as (Inman and Erturk 2011):

$$\frac{\upsilon(t)}{-\omega^2 W_0 e^{j\omega t}} = \frac{\sum_{r=1}^{\infty} \frac{-j\omega\theta_r\sigma_r}{\omega_r^2 - \omega^2 + j2\zeta_r\omega_r\omega}}{\frac{1}{R_l} + j\omega C_{\tilde{p}}^{eq} + \sum_{r=1}^{\infty} \frac{j\omega\theta_r^2}{\omega_r^2 - \omega^2 + j2\zeta_r\omega_r\omega}}, \tag{14}$$

where ω is the excitation frequency, ζ_r is the damping ratio of mode r and the modal forcing constant σ_r is:

$$\sigma_r = -m \int_0^L \phi_r(x) \, dx - M_t \, \phi_r(L) \tag{15}$$

The modal electromechanical coupling θ_r and the equivalent capacitance $C_{\tilde{p}}^{eq}$ of the energy harvester are expressed as follows:

- For a series connection:

$$\theta_r = \bar{e}_{31} b h_{\tilde{p}c} \frac{d\phi_r(x)}{dx}\bigg|_{x=L} \tag{16}$$

$$C_{\tilde{p}}^{eq} = \frac{\bar{\varepsilon}_{33}^s bL}{2h_{\tilde{p}}} \tag{17}$$

- For a parallel connection:

$$\theta_r = 2\bar{e}_{31} b h_{\tilde{p}c} \frac{d\phi_r(x)}{dx}\bigg|_{x=L} \tag{18}$$

$$C_{\tilde{p}}^{eq} = \frac{2\bar{\varepsilon}_{33}^s bL}{h_{\tilde{p}}} \tag{19}$$

where $h_{\tilde{p}c}$ represents the position of the center of every piezoelectric sheet from the neutral axis of the beam:

$$h_{\tilde{p}c} = \frac{h_p + h_s}{2} \tag{20}$$

The current FRF and the power FRF are obtained from the voltage FRF as follows:

$$\frac{i(t)}{-\omega^2 W_0 e^{j\omega t}} = \frac{1}{R_l}\left(\frac{v(t)}{-\omega^2 W_0 e^{j\omega t}}\right) \tag{21}$$

$$\frac{p(t)}{(-\omega^2 W_0 e^{j\omega t})^2} = \frac{1}{R_l}\left(\frac{v(t)}{-\omega^2 W_0 e^{j\omega t}}\right)^2 \tag{22}$$

3 Case Study

This section introduces the geometric and material properties of the piezoelectric energy harvester. The material of the substrate sheet is aluminum and that of the piezoelectric sheet is PZT-5A. The parameters of the bimorph harvester are given in Table 1 (Inman and Erturk 2011). All responses are determined for the frequency range of 0–1000 Hz. In this case, the damping ratio can be determined when working under short circuit condition ($R_l \rightarrow 0$) and employing the half power points of the mechanical FRF (Ewins 2000). The superscript a in the Table 1 indicates that this parameter will be altered during simulation.

4 Results and Discussions

First, a bimorph cantilever beam without attached mass is considered ($M_t = I_t = 0$). Subsequently, a tip mass is added to show its effect on the power output. The attached mass is assumed to be a parallelepiped rigid body. The attachment of a tip mass has an impact on the boundary conditions. The output FRFs of voltage, current, and power of the energy harvester without attached mass have been found to agree with those of (Inman and Erturk 2011). For example, the power FRFs are shown in (Fig. 2) for four load resistances and series connection.

All results are obtained for series connection of the piezoelectric sheets. The range of the load resistance is taken from 100 Ω (close to short-circuit case) to 10 MΩ (close to open circuit case). The first three natural frequencies of the energy harvester without tip mass are $f_1 = 185.1$ Hz, $f_2 = 1160.1$ Hz and $f_3 = 3248.2$ Hz.

The power FRF generated by the harvester shown in (Fig. 2) does not vary monotonically either increasing or decreasing with the load resistance at a specific excitation frequency. For all vibration modes, one can notice that the maximum power output is attained for a load resistance equal to 100 kΩ. The load resistances

Table 1 Parameters for the piezoelectric energy harvester with a tip mass

Parameters	Symbol	Value
Bimorph harvester		
Length (mm)	L	30
Width (mm)	b	5
Strain damping constant (s/rad)	$c_s I / YI$	2.93×10^{-6}
Viscous damping constant (rad/s)	c_a / m	19.295
Substrate material (Aluminum)		
Thickness (mm)	h_{s0}	0.05[a]
Young's modulus (GPa)	Y_s	70
Density (kg/m^3)	ρ_s	2700
Piezoelectric material (PZT-5A)		
Thickness of each sheet (mm)	h_p	0.15
Young's modulus (GPa)	$\bar{c}_{11}^E$	61
Piezoelectric stress constant (C/m^2)	$\bar{e}_{31}$	-10.4
Piezoelectric constant (pm/V)	d_{31}	-171
Permittivity constant (nF/m)	$\bar{\varepsilon}_{33}^s$	13.3
Density (kg/m^3)	ρ_p	7750
Tip mass material (Aluminum)		
Tip mass (g)	M_t	(3375×10^{-9})[a]
Length (mm)	L_m	5
Width (mm)	b_m	5
Thickness (mm)	h_m	0.05[a]
Density (kg/m^3)	ρ_m	2700
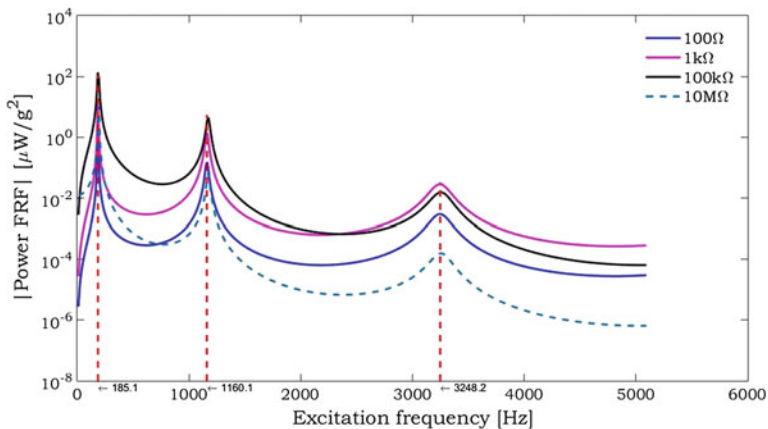
Fig. 2 Power FRFs for the energy harvester without tip mass for a selected values of the load resistance

have been chosen arbitrarily and do not refer necessarily for the optimized power output. One can notice that there are many intersection points showing that similar power output may be attained for two distinct load resistances.

To compare the response of two energy harvesters having different configurations, it has been suggested that both harvesters should have the same first natural frequency (Patel 2013) targeting operation at the first natural frequency. While, adding a tip mass decreases the first natural frequency, increasing the substrate thickness increases this frequency. This relation is used to maintain a fixed value for the first natural frequency.

According to (Patel 2013), the power generated by the harvester increases with the ratio of the thicknesses (h_s/h_p) when the thickness of the piezoelectric sheets remains constant. So, the increase of the substrate thickness h_s increases the power output. The tip mass M_t has been increased for a selected substrate thickness to match the first natural frequency of the harvester without a tip mass (Fig. 3).

The simulation begins with a substrate thickness of 1.6 h_{s0} because for the thinner substrate, the tip mass thickness h_m is very small. From the intersection point of each curve corresponding to a substrate thickness h_s and the horizontal line at the fixed natural frequency $f_1 = 185.1$ Hz, the value of the tip mass thickness h_m corresponding to the first natural frequency is determined. Table 2 presents the tip
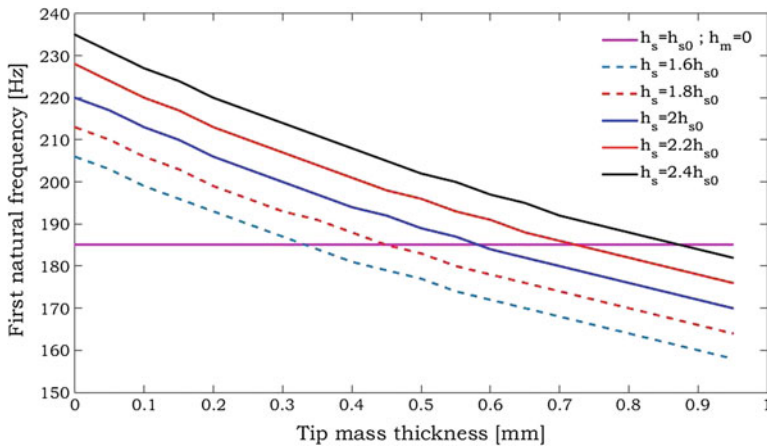
Fig. 3 Variation of the first natural frequency with the thickness of the tip mass for a selected set of substrate thicknesses

Table 2 Variation of substrate thickness and mass thickness

Parameters	Values					
Substrate thickness h_s(mm)	$h_{s0} = 0.05$	1.6 h_{s0}	1.8 h_{s0}	2 h_{s0}	2.2 h_{s0}	2.4 h_{s0}
Mass thickness h_m(mm)	0	0.33	0.45	0.58	0.72	0.87

mass thicknesses for a selected set of substrate thickness h_s. The maximum power generated, at the first natural frequency, is determined for each thickness pair (h_s, h_m) for a broad range of load resistance (Fig. 4). One can notice that for a large range of load resistance, the maximum power generated slightly increases when increasing simultaneously h_s and h_m, and therefore increasing the tip mass M_t. First, this is due to the monotonically increase of the distance between the neutral axis and the center of each piezoelectric sheet $h_{\bar{p}c}$ (Eq. 20) with the substrate thickness. The higher strain is applied on the piezoelectric material at larger $h_{\bar{p}c}$; therefore, generating a higher voltage. Second, this is due to the increase of the modal forcing σ_r (Eq. 15) with the substrate thickness h_s. The advantages obtained from increasing the substrate thickness are countered by the increase of the harvester thickness. One can conclude that higher power output can be obtained for higher h_s.
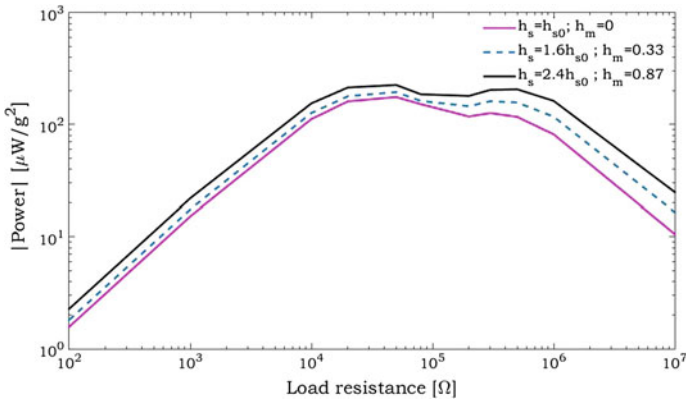
Fig. 4 Variation of the power generated by the harvester with load resistance for a harmonic base excitation at the first natural frequency of the harvester
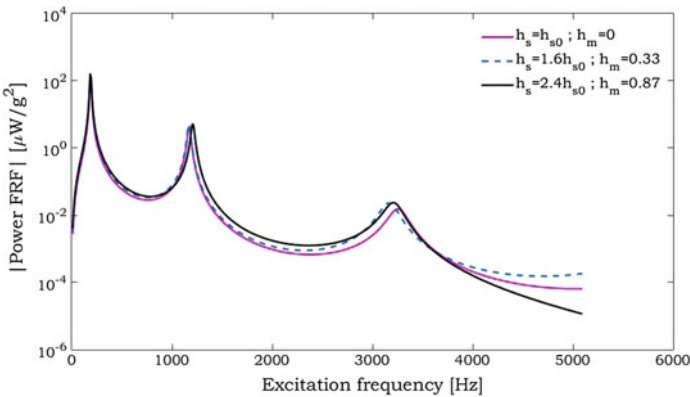
Fig. 5 Power FRFs for the energy harvester for a load resistance of 100 kΩ for a selected set of substrate thicknesses and tip mass thicknesses

After matching the first natural frequency of the bimorph harvester with and without tip mass, the power output FRFs is obtained as shown in (Fig. 5). The power is determined for a load resistance of 100 kΩ because at this value maximum power output is obtained at the first natural frequency as shown in (Fig. 2). One can also notice that this power increases with substrate thickness and the tip mass thickness for a fixed value of $R_l = 100\,k\Omega$. Therefore, the power is controlled by the substrate thickness and the tip mass thickness and the maximum of the power is attained at higher values of h_s and h_m.

5 Conclusion

Energy harvesting from natural resources is essential to overcome the lack of energy from conventional resources. In particular, vibration energy harvesting from piezoelectric systems is a promising means to supply power for small electronic devices. In this paper, an analytical model of a bimorph cantilever beam with and without a tip mass has been used to determine the power generated by the harvester. To make an objective comparison of the power generated by several harvesters, the first natural frequency of these harvesters has been maintained constant. To reach this condition, the substrate thicknesses and the tip mass thicknesses have been increased simultaneously. The generated power in each case has been evaluated in order to determine the maximum power output. It has been found that the maximum power is generated at the highest values of h_s and h_m though the substrate thickness is limited by the harvester size.

References

Banks H, Luo ZH, Inman DJ, Bergman L (1998) On the existence of normal modes of damped discrete-continuous systems. ASME J Appl Mech 1–26

Chen SN, Wang GJ, Chien MC (2006) Analytical modeling of piezoelectric vibration-induced micro power generator. Mechatronics 16:379–387. https://doi.org/10.1016/j.mechatronics.2006.03

Erturk A, Inman DJ (2008) A distributed parameter electromechanical model for cantilevered piezoelectric energy harvesters. J Vib Acoust 130:41002–1–41002–15. https://doi.org/10.1115/1.2890402

Ewins DJ (2000) Model testing: theory, practice and application, 2nd edn. Research Studies Press LTD, Baldock, Hertfordshire, England

Inman DJ, Erturk A (2011) Piezoelectric energy harvesting, 1st edn. Wiley, United Kingdom

Patel R (2013) Modelling analysis and optimisation of cantilever piezoelectric energy harvesters. University of Nottingham, Thesis

Priya S (2007) Advances in energy harvesting using low profile piezoelectric transducers. J Electroceram 19:167–184

Sodano HA, Inman DJ, Park G (2004) Estimation of electric charge output for piezoelectric energy harvesting. Strain J 40:49–58

CFD Modeling of Air Pollution Dispersion in Complex Urban Area

Mohamed S. Idrissi, Fatma A. Lakhal, Nabil Ben Salah and Mouldi Chrigui

Abstract With the ultimate goal of prediction species dispersion and pollution transport using computational fluid dynamics (CFD), this paper evaluates the performance of two different modeling approaches Reynolds-averaged Navier–Stokes (RANS) standard k-e, and Large Eddy Simulation (LES) applied to pollutant dispersion in an actual urban environment downtown Hannover. The modeling is based on the hypothesis neutral atmospheric conditions. LES is chosen to capture the effects of velocity randomness of the pollutants convection and diffusion. Computer-aided design, CAD, of Hannover city demonstrating different topologies and boundaries conditions, are cleaned, then in fine grids meshed. Pollutants are introduced into the computational domain through the chimney and/or pipe leakages. Weather conditions are accounted for using logarithmic velocity profiles at inlets. Simulations are conducted on 80 cores cluster for several days. CH_4 distributions as well as streamlines and velocity profiles conducted on reasonable results. The major interest of presenting work is that it involved a large group of real buildings with a high level of details that can represent the real case of the problem.

M. S. Idrissi (✉) · F. A. Lakhal · M. Chrigui
Research Unit "Materials, Energy and Renewable Energies", Gafsa Faculty of Science,
University Campus Sidi Ahmed Zarroug Gafsa, 2112 Gafsa, Tunisia
e-mail: idrissimedsalah@gmail.com

M. Chrigui
e-mail: mouldi.cherigui@gmx.de

M. S. Idrissi · F. A. Lakhal · M. Chrigui
Research Unit "Mechanical Modeling Materials, Energy", National school
of engineer of Gabes, 6029 Zrig Gabes, Tunisia

N. B. Salah · M. Chrigui
CADFEM AN, Sousse Technemple, Sousse, Tunisia

M. Chrigui
Department of Mechanical Engineering, Institute for Energy and Power Plant Technology,
Technische Universität Darmstadt, Petersenstr.30, 64287 Darmstadt, Germany

1191

Nomenclature

Acronym

CFD   Computational Fluid Dynamics
DNS   Direct Numerical Simulation
LES   Large Eddy Simulation
RANS   Reynolds-Averaged Navier–Stokes
SST   Shear Stress Transport
URANS   Unsteady Reynolds-Averaged Navier–Stokes

Greek symbols

μ Dynamic viscosity Ns m^{-2}
v Kinematic viscosity m^2 s^{-1}
ω Specific turbulence dissipation s^{-1}
R   Rate
τ_{ij} Unresolved stress tensor kg m^{-1} s^{-2}
ε Turbulence dissipation m^2 s^{-3}

Mathematical symbols

∇ Nabla operator

Roman symbols

$\bar{u}$ Filtered velocity m s^{-1}
f   Body forces per unit volume N m^{-3}
u   Fluid flow velocity m s^{-1}
ρ Density kg m^{-3}
e   Total specific internal energy m^2 s^{-2}
k   Turbulence kinetic energy m^2 s^{-2}
p   Pressure N m^{-2}
q   Energy source term m^2 s^{-2}
t   Time s
U   Mean velocity m s^{-1}
$u^{'}$ Fluctuating part of velocity m s^{-1}
x   Position vector m

1   Introduction

Air quality has a great importance in urban complexes because of the several effects on human safety and environment. The growth of urbanization puts a pressure on urban stocks, appear in augmented use of a vehicle and a denser urban fabric.

Climate, city and the nontrivial combine of pollutant sources cause high pedestrian level concentrations. Thus, it is indispensable that novel simulation tools are advanced and current methods are upgraded to aid controllers and urban designers to reduce air pollution problems in cities, and to permit emergency establishments to plan evacuation strategies ensuing accidents, deliberate release of the dangerous airborne substance or natural catastrophes, (Salim et al. 2011).

Nowadays computational fluid dynamics (CFD) is quickly imposing itself also in the air pollution dispersion in an urban area, (DeCroix and Brown 2002). Contrary to most currently usual air quality models, CFD simulations can estimate rigorously topographical details such as terrain variations and building structures in urban areas along with local aerodynamics and turbulence, (Tang et al. 2005). CFD is a numerical resolution of the fundamental physics equations and contains the effects of detailed three-dimensional geometry and local environmental conditions. Therefore, it is able to provide more precise solutions than statutory existing models of air quality (Huber et al. 2004), because Many works can be found in the literature reporting on the use of (CFD) techniques to model flow and pollutant dispersion around isolated buildings or groups of buildings (Blocken et al. 2012; Breuer et al. 2003; Chan et al. 2002; Tominaga and Stathopoulos 2010; Kikumoto and Ooka 2012). However, gas dispersion in complexes urban areas is still limited to isolated cases and to a limited number of sources.

In this work, the focus is put on the investigation of pollutants transport and dispersion which exhibit complex geometries and diverse boundary conditions. Diverse scenarios of pollutants injection into the computational domain are studied. In the following, an introduction of the work including used physics and choosed geometries is presented, then details about generated grid and applied boundary conditions are explained. In the third part, discussion and presentation of obtained results is given. At the end of the report, a conclusion is included.

2 Modeling

2.1 Governing Equations

Known as Navier–Stokes equations, the fundamental governing equations of fluid flow are the base of the CFD. They are partial differential equations expressing three basic physical rules: the conservation of mass (1) the Newton's Law of Motion (2) and the conservation of energy (3), Wendt et al. (1996).

$$\frac{\partial p}{\partial t} + \nabla \cdot \rho u = 0 \tag{1}$$

$$\frac{\partial pu}{\partial t} + \nabla \cdot (\rho u u) = -\nabla p + \nabla(\mu \nabla u) + f \tag{2}$$

$$\frac{\partial pe}{\partial t} + \nabla \cdot (\rho u e) = -\nabla pu + \nabla \cdot (\mu u \nabla) - \nabla q \tag{3}$$

The direct numerical simulation (DNS) is a numerical integration of the Navier–Stokes equations that directly solves the flow without any modeling, and captures all the spatial and temporal scales of the flow. Its power is to produce exact, analytic resolutions unaffected by estimates, at the whole computational domain and all times of the simulated period necessitates a high-resolution grid and costs enormous calculating resources and time, avoiding DNS from being applied in complex urban environment problems and in wind engineering, Rudman and Blackburn (2006). When the time-dependent equations are solved on a very coarse grid that does not capture the small scales of the flow. This approach is called large eddy simulation (LES) (4), (Moin and Mahesh 1998).

$$\frac{\partial \overline{u_i}}{\partial t} + \frac{\partial}{\partial x_j}(\overline{u_i u_j} = -\frac{1}{\rho}\frac{\partial \bar{p}}{\partial x_i} + v\frac{\partial}{\partial x_j}(\frac{\partial \overline{u_i}}{\partial x_j} + \frac{\partial \overline{u_j}}{\partial x_i}) = -\frac{1}{\rho}\frac{\partial \bar{p}}{\partial x_i} + 2v\frac{\partial}{\partial x_i}S_{ij} \tag{4}$$

The spatial filtering of Navier–Stokes equations eliminate small scales from the flow variables and reduces the computational demands. The impact of the small scales then come into sight at least as subfilter stresses in the momentum equation and as boundary terms. Generally, RANS method (5), (6), (7) is used for the computation of air pollution dispersion.

$$\frac{\partial U}{\partial x_i} = 0 \tag{5}$$

$$\frac{\partial U_i}{\partial t} + \frac{\partial}{\partial x_i}(U_j U_i) = -\frac{1}{\rho}\frac{\partial p}{\partial x_i} + v\frac{\partial^2 U_i}{\partial x_j x_i} + \frac{u_i' u_j'}{\partial x_j} \tag{6}$$

$$u_i = U + u_i' \tag{7}$$

This approach, average the equations in time over all the turbulent scales, to directly generate the statistically steady solution of the flow variables, (Breuer et al. 2003; Franke et al. 2004). Similar to LES the averaging produce additional terms in the momentum equation known as the Reynolds stresses which express the effects of the turbulent fluctuations on the averaged flow. This term has to be modeled. This is the charge of the turbulence models, which will be discussed in the next section.

The unsteady RANS (URANS) has been introduced to capture the dynamics of turbulent complex flows using reasonable computational costs. To have incompressible flow the Navier–Stokes equations have been time-filtered: all scales smaller than a characteristic time period (t) are averaged. The time period should be orders of magnitude higher than the time scale of the random fluctuations, and the averaging period must be much lower than the time scale of the unsteady mean motion (Sadiki et al. 2006).

2.2 Turbulence Models

A turbulence model describes the turbulent fluxes or Reynolds stresses as a function of the mean flow variables, (Franke et al. 2004). The standard two-equations model is the linear k-ε model (8), (9), (Murakami 2002).

$$\frac{\partial(\rho k)}{\partial t} + \frac{\partial(\rho k u_i)}{\partial x_i} = \frac{\partial}{\partial x_j}\left[\frac{\mu_t}{\sigma_k}\frac{\partial k}{\partial x_j}\right] + 2\mu_t E_{ij}E_{ij} - \rho\varepsilon \tag{8}$$

$$\frac{\partial(\rho\varepsilon)}{\partial t} + \frac{\partial(\rho\varepsilon u_i)}{\partial x_i} = \frac{\partial}{\partial x_j}\left[\frac{\mu_t}{\sigma_\in}\frac{\partial\varepsilon}{\partial x_j}\right] + C_{1\in}\frac{\varepsilon}{k}2\mu_t E_{ij}E_{ij} - C_{2\in}\rho\frac{\varepsilon^2}{k} \tag{9}$$

It is known to produce excellent results in wind engineering applications, (Castro 2003). The major problem of this model is the overproduction of turbulent kinetic energy in regions of stagnant flow. More advanced k-ε models like the renormalization group (RNG) k-ε model of Yahot et al. (1992), or the realizable k-ε model of Shih et al. (1995). These models reduce the stagnation point anomaly without leading to bad results in the wake. Recent developments tend also to indicate that the shear stress transport (SST) version of the k-ω model provides a significant improvement over standard k-ε models. See for example, (Menter 1997) and (Menter et al. 2003).

2.3 Dispersion Modeling

Numerous models are accessible to predict the dispersion of the airborne material. In this study, only the species transport module is used. By the resolution of a convection-diffusion equation for the ith species, CFD codes calculate the mass fraction of each species, Yi. This conservation equation takes the following general formula.

$$\frac{\partial}{\partial t}(\rho Y_i) + \nabla \cdot (\rho\vec{v}Y_i) = -\nabla \cdot \overrightarrow{J_i} + R_i + S_i \tag{10}$$

3 Configuration Description, Meshing, Boundaries Conditions and Numerical Setup

3.1 Geometry

The dimensions of the computational domain were 600 m length of 580 m width by 200 m height inside of which the buildings are located. The geometry was performed

Fig. 1 Hanover geometry
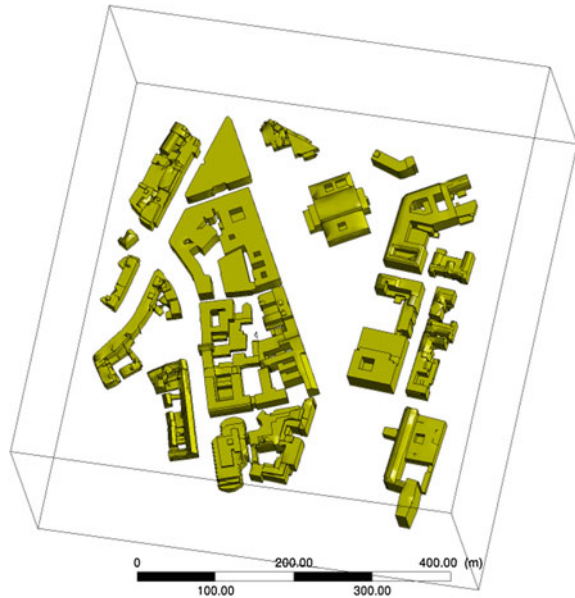
with any space claim then was repaired where necessary and defeatured to assist both the fluid domain extraction and the meshing process. Figure 1 depicts the computational domain used to simulate the configuration of Hannover city. It includes various building having different dimensions and showing multiples features. Streets in the configuration demonstrate unequal dimensions and changeable direction.

3.2 Computational Grid

We have generated two mesh having 19 and 40 million elements in 10 h. An appropriate refinement near the source of CH_4 and close to the ground was performed. Figure 2 exhibit the mesh used for Hannover simulations. The grid quality is improved while increasing the cell number. It should be proved that obtained results are statistically independent of the mesh refinement. This condition implies that many test cases involving different refining degree are to be tested for each operating conditions.

3.3 Boundaries Conditions

The wind velocity is considered an important input parameter for the study of heavy gas dispersion. In a realistic atmosphere, wind commonly does not flow at the same
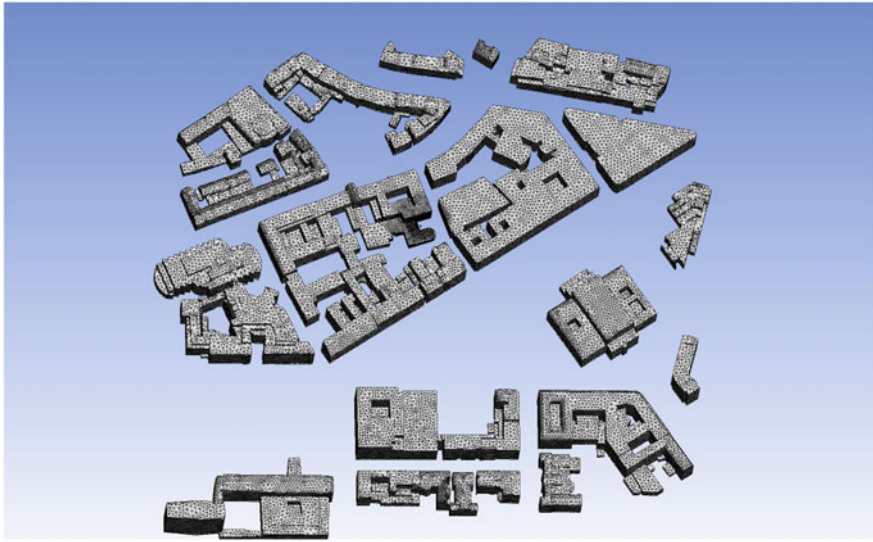
Fig. 2 Hanover unstructured mesh

Fig. 3 Velocity profile at inlet boundary
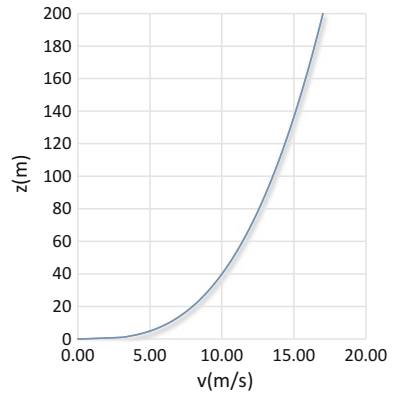
velocity at different heights due to the frictional effect of the ground. Generally, the power law profile is shown in Fig. 3 is used to describe the variation in the wind speed as a function of the height in the surface boundary layer. $v(z) = v_r k z^a$, V_r is the wind velocity at a standard height of 10 m. As to the pollutant inflow, CH_4 was emitted into a grid space through the stack, which is a square with a length of 1 m. The injected CH_4 was of 100% purity. The CH_4 outlet velocities from the stack were 8 m/s, all the boundary and initial conditions are summarized in Table 1. The types of boundary conditions are shown in Fig. 4

Table 1 Boundaries conditions type

Parameters	Boundary type
Inlet	Velocity inlet of air
Origin	Velocity inlet of CH_4
Bottom	Wall
Top, outlet	Pressure outlet
Left, right	Symmetry
Air temperature	300 k
CH_4 temperature	273 k
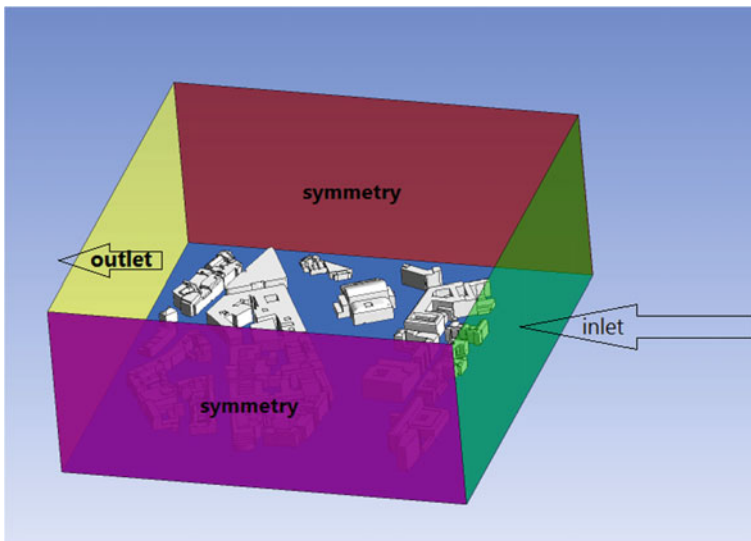
Fig. 4 Geometry with boundaries

4 Results and Discussion

Results were presented in terms of contours of velocity, pollutant concentration, and streamlines. Quantitative results are available and can be plotted.

Two different scenarios are investigated in the configuration of Hannover. In the first, one leakage of CH_4 is introduced through an opening located at the center of the computational domain, i.e., in a confined geometry. The choice of this location is based on its closeness to buildings and long distance far from the exit flow. CH_4 is injected with different inlet velocities horizontally toward the building. Effect of air and methane temperature on the dispersion of CH_4 is investigated. The flow direction, i.e., vertically or horizontally is also studied. The second leakage scenario focuses on the dispersion of methane within an open surface, i.e., ,along with the street and far from the building. Simulations show significant different results.
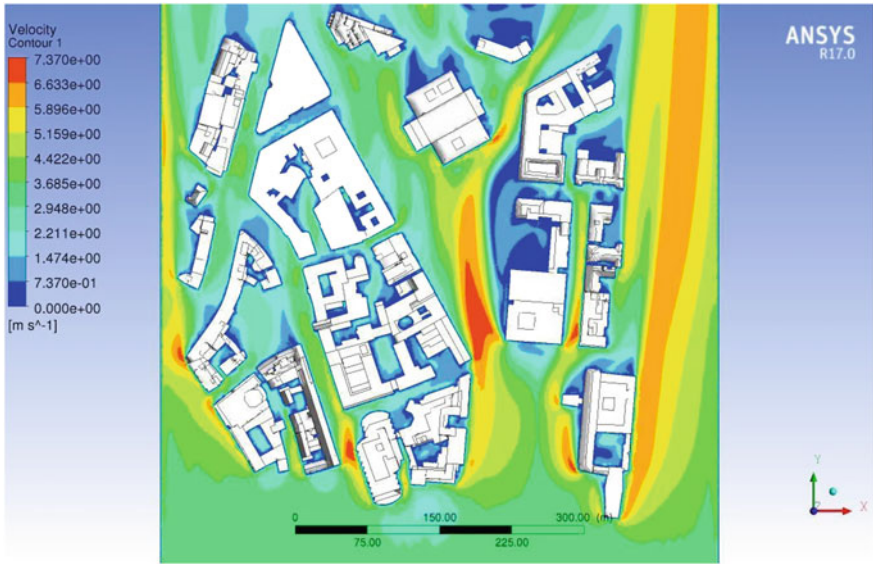
Fig. 5 Velocity profile z = 3 m
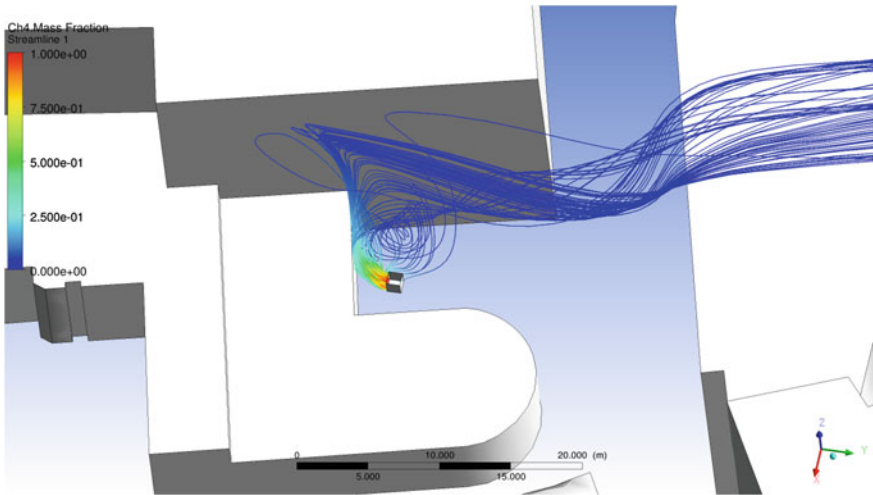
Fig. 6 Streamlines from pollution source

Figure 5 shows the velocity contour in a level 3 m high from the ground. The maximum velocity magnitude, 7.3 m/s, is located at the central street, which is the narrowest throat along the street. This can be explained by the conservation of mass. As the flow is incompressible high velocity is likely the most important parameter that controls species transport and dispersion. Behind some building
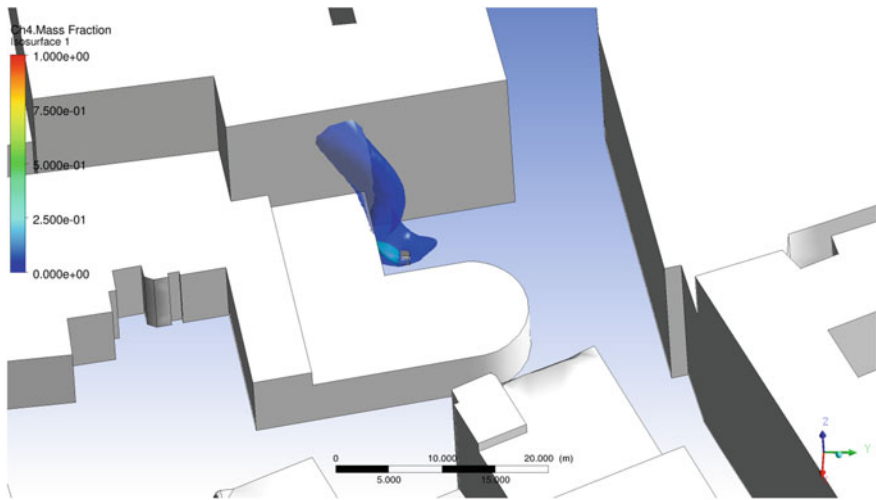
Fig. 7 Isosurface concentration

stagnating fluid is noticed. Figure 6 depicts streamlines derived from the CH_4 inlet. Through methane is introduced horizontally toward the wall, it promptly changes the direction and moves vertically, then it is transported by the carrier air to the outlet. The vertical transport is induced by the buoyancy force. Different densities cause the lighter gas be moved to the top. Methane is 64% lighter as air in the same temperature. Simulations with a temperature of air and CH_4 of 30 °C and 0 °C, respectively, did not alter the dispersion of methane. A vertical flow of CH_4 as inlet direction even increase the transport of methane away from the ground. The dispersion is driven, in this location, by the buoyancy and gravitation forces. Worth to notice that air exhibits an almost null velocity close to the ground.

Figure 7 demonstrates isosurfaces of CH_4 concentrations. Two isovalues are shown, these are C = 0.04 and 0.4. These values represent the flammability limits in case of combustion. The burnable mixture of methane and air shows a vertical plume. The mixture reaches the wall of the nearby building. Parts of it are in touch with the ground. The concentration changes rapidly from 100% CH_4 into less than 4%.

Figure 8 depicts the iso-concentration of methane. Using CFD, it is possible to predict the source of CH_4 if measurements are carried out at the exit boundary. One observes that methane diffuse in the lateral direction as well, i.e., the plume of the isosurface gets wider toward the outlet. This dispersion is more induced by the turbulent and kinematic diffusion. At the outlet, the methane does not climb into the atmosphere considerably.

Figure 9 shows the temperature contours of isosurface close to the CH_4 inlet. CH_4 Rapidly increase the temperature and reaches 300 K which is the temperature
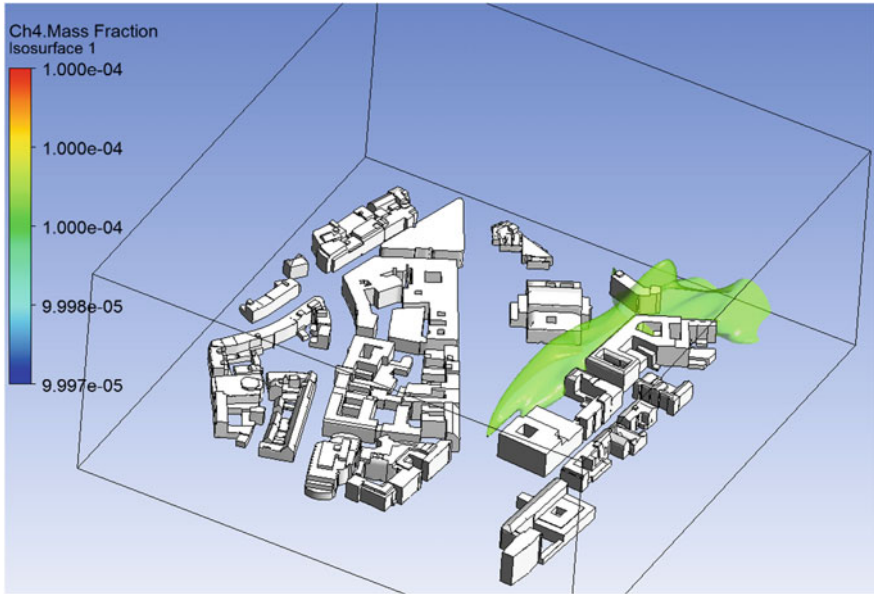
Fig. 8 CH$_4$ isosurface showing the transport of methane species
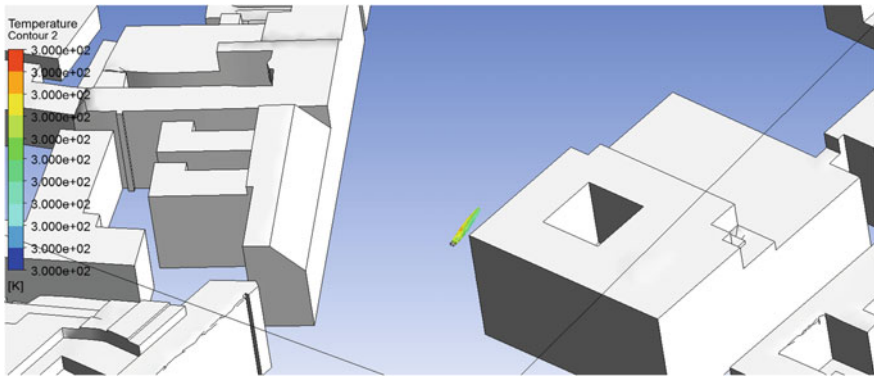
Fig. 9 Temperature contours of CH$_4$ and air mixture

of ambient air. Simulations with different temperature differences between air and methane reproduced very similar results hinting that thermal variation is not affecting CH$_4$ dispersion. The heat capacity of methane is twice larger as air, therefore, thermal equilibrium is registered in the vicinity of CH$_4$ leakage. Thus, air and CH$_4$ temperatures have no impact on the mixture development and pollutant dispersion.

5   Conclusion

CFD is applied to predict pollution dispersion and species transport in urban cities. Sources CH_4 is being introduced in the computational domain at different locations in the ground and variable altitude in height. Introduced pollutants are injected in different directions and velocity magnitude, i.e., different boundary conditions. The temperature of pollutants and surrounding air at the initial and boundary conditions are also considered as changeable parameters.

The geometry, of Frankfurt having a diameter of 600 m, which includes many building and skyscrapers that demonstrate complex feature and different topology as well as a 600 m $\times$ 580 m urban district from Hannover is numerically investigated and different boundary conditions scenarios are predicted. Two turbulence models, i.e., realizable k-e (RANS) and Large Eddy Simulation (LES) are applied to capture the effect of turbulence and velocity fluctuation in time and space. Worth to mention that LES predicts flow dynamics and mixture development better than RANS. Furthermore, LES is able to capture fluid structure and flow unsteadiness. Yet the computational cost is manifold time larger than RANS. The numerical grid for both configurations included 40 million control volumes, which need a huge computational power. The meshing resolve regions with important velocity gradients and high curvature using the fine grid. It is mandatory to capture at least 80% of turbulence using LES. Increasing the computational domain will necessitate the increase of mesh resolution. The computational power needs to be increased as well. One should note that throughout the literature it is very rare that researcher exceeds 40 million control volumes in CFD simulations.

The applied boundary conditions for ambient air at the inlet used a logarithmic profile that mimics the air velocity in the experimental conditions. The profile varies as a function of the vertical location "z" and is calibrated using two constant parameters.

The configuration of Hannover revealed two important informations, the namely CH_4 dispersion is controlled by air-CH_4 density ratio in case of pollutant injection close to the building. The buoyancy forces are responsible for the stratification of gases. CH_4 species are first transported in the vertical direction then moved by the carrier phase to the outlet. The velocity direction and magnitude, as well as the temperature difference between CH4 and ambient air, do not play important roles.

If CH_4 is injected far from building, i.e., in the middle of the street, a location in which carrier phase velocity is important, then the transport of pollutant showed different behavior. CH_4 is dragged horizontally much faster in the vertical direction. Simulations were able to clearly predict streamline stemming from CH_4 inlet. They followed the street and keep almost a constant altitude until reaching the outlet.

References

Blocken B, Janssen W, van Hooff T (2012) CFD simulation for pedestrian wind comfort and wind safety in urban areas: general decision framework and case study for the Eindhoven university campus. Environ Model Softw 30:15–34

Breuer M, Jovii N, Mazaev K (2003) Comparison of DES, RANS and LES for the separated flow around a flat plate at high incidence. Int J Numer Meth Fluids 41(4):357–388

Castro IP (2003) CFD for external aerodynamics in the built environment. QNET-CFD Netw Newslett 2(2):4–7

Chan TL, Dong G, Leung CW, Cheung CS, Hung WT (2002) Validation of a two dimensional pollutant dispersion model in an isolated street canyon. Atmos Environ 36:861e872

DeCroix D, Brown M (2002) Report on CFD model evaluation using URBAN 2000 field experiment data. Technical report. IOP 10, LA-UR-02-4755. Available from Los Alamos National Laboratory

Franke J, Hirsch C, Jensen A, Krus H, Schatzmann M, Westbury P, Miles S, Wisse J, Wright N (2004) Recommendations on the use of CFD in wind engineering, COST Action C14. European Science Foundation COST Office

Huber A, Georgopoulos P, Gilliam R, Stenchikov G, Wang S, Kelly B, Feingersh H (2004) Modeling air pollution from the collapse of the world trade center and assessing the potential impacts on human exposures. In: Environmental manager Feb 2004, pp 35–40

Kikumoto H, Ooka R (2012) A numerical study of air pollutant dispersion with bimolecular chemical reactions in an urban street canyon using large-eddy simulation. Atmos Environ 54:456–464

Menter F (1997) Eddy viscosity transport equations and their relation to the k-ε model. J Fluids Eng 119:876–884

Menter FR, Kuntz M, Langtry R (2003) Ten years of industrial experience with the SST turbulence model. In: Hanjalic K, Nagano Y, Tummers M (eds) Turbulence, heat and mass transfer, vol 4. Begell House Inc

Moin P, Mahesh K (1998) Direct numerical simulation: a tool in turbulence research. Annu Rev Fluid Mech 30(1):539–578

Murakami S (2002) Setting the scene: CFD and symposium overview. Wind Struct 5(2–4):83–88

Rudman M, Blackburn H (2006) Direct numerical simulation of turbulent non-Newtonian flow using a spectral element method. Appl Math Model 30(11):1229–1248

Sadiki A, Maltsev A, Wegner B, Flemming F, Kempf A, Janicka J (2006) Unsteady methods (URANS and LES) for simulation of combustion systems. Int J Therm Sci 45(8):760–773

Salim SM, Ong KC, Cheah SC (2011) Comparison of RANS, URANS and LES in the prediction of air flow and pollutant dispersion. In: Proceedings of the world congress on engineering and computer science 2011 WCECS 2011, vol II. 19–21 Oct 2011

Shih T-H, Liou WW, Shabbir A, Yang Z, Zhu J (1995) A new k-ε eddy-viscosity model for high reynolds number turbulent flows—model development and validation. Comput Fluids 24 (3):227–238

Tang W, Huber A, Bell B, Kuehlert K, Schwarz W (2005) Application of CFD simulations for short-range atmospheric dispersion over the open fields of project prairie grass. In: Air and waste management association 98th annual conference, June 21–23 Paper No. 1243, Minn

Tominaga Y, Stathopoulos T (2010) Numerical simulation of dispersion around an isolated cubic building: model evaluation of RANS and LES. Build Environ 45(10):2231–2239

Wendt J, Anderson J, for Fluid Dynamics VKI (1996) Computational fluid dynamics: an introduction. Von Karman Institute book. Springer

Yakhot V, Orszag SA, Thangam S, Gatski TB, Speziale CG (1992) Development of turbulence models for shear flows by a double expansion technique. Phys Fluids A 4:1510–1520

Finite Element Modeling and Analysis of a Bimorph Piezoelectric Energy Harvester

Rabie Aloui, Walid Larbi and Mnaouar Chouchane

Abstract In the last few years, energy harvesting using piezoelectric materials has become a popular research topic because of its efficiency for converting vibration energy into electrical energy. In previous research studies, the shape and size of the harvester have been optimized for maximum power output density using analytical, numerical, and experimental approaches. This paper presents a finite element model of a bimorph piezoelectric energy harvester. The model is used to study the effect of load resistance on the resonant frequency and the generated power. The harvester consists of a clamped-free composite cantilever beam composed of an elastic substructure bracketed by two identical piezoelectric layers which are connected to a resistive load. An electromechanical finite element formulation for the dynamic analysis of the problem is first presented. The associated variational formulation is written in terms of structure displacement and electric potential in the piezoelectric layers. The finite element model of the bimorph energy harvester has been implemented on COMSOL Multiphysics software. It has been concluded that the energy harvester generates a maximum of electrical power output when the structure vibration matches the first natural frequency of the harvester and the optimal resistance load is connected to the piezoelectric layers.

Keywords Energy harvester · Piezoelectric · Finite elements

R. Aloui · M. Chouchane (✉)
National Engineering School of Monastir (ENIM), Avenue Ibn Jazzar,
5019 Monastir, Tunisia
e-mail: mnaouar.chouchane@enim.rnu.tn

R. Aloui
e-mail: rabiealoui@gmail.com

W. Larbi
Structural Mechanics and Coupled Systems Laboratory (LMSSC),
Conservatoire National des Arts et Metiers (CNAM), 292, rue Saint-Martin,
75141 Cedex 03 Paris, France
e-mail: walid.larbi@cnam.fr

1 Introduction

Recently, a significant research effort has been devoted to the area of energy harvesting using the direct piezoelectric effect to convert vibration into electrical energy. A typical piezoelectric energy harvester is a cantilever structure with one or two piezoelectric layers and the generated power is due to the vibration of the host structure. The energy harvester generates a maximum of power when the excitation frequency matches the natural frequency of the harvester and an optimal resistance load is connected.

A single degree of freedom model (SDOF) is the simplest mathematical model used for numerical simulation of piezoelectric energy harvesters (Roundy and Wright 2004). In this approach, the beam is modeled by a second-order ordinary differential equation with the beam tip displacement as its dependent variable. Erturk and Inman (2008) showed that in piezoelectric energy harvesting simulation, the SDOF model may yield highly inaccurate results and they introduced some correction factors for improving the prediction of a SDOF model. To increase the accuracy of the solution, Dutoit et al. (2005) employed the Rayleigh–Ritz method for modeling cantilever and homogenous piezoelectric energy harvesters. Furthermore, the analytical solution for a beam with constant cross section and material properties under harmonic base excitation were given by Erturk and Inman (2009). Vatanabe et al. (2013) proposed topology optimization and homogenization to design functionally graded piezocomposite materials to be used in energy harvesting applications. Amini et al. (2014) developed a finite element model for investigating homogenous piezoelectric energy harvesters. This model can be used for varying cross-section area and also for different base excitations and loads.

This paper presents a finite element formulation of a piezoelectric vibration energy harvester. An example of a piezoelectric bimorph cantilever beam, modeled with COMSOL Multiphysics, is presented and analyzed. Through this example, the effect of load resistance on the resonance frequency, displacement, and generated power is studied.

2 Finite Element Formulation of the Problem

2.1 Local Equations of the Coupled System

We consider a bimorph piezoelectric energy harvester structure (i.e., elastic substructure bracketed by two identical piezoelectric layers). The elastic structure is denoted Ω_E (Fig. 1). Each piezoelectric layer has the shape of a plate with its upper and lower surfaces covered with very thin layer electrodes. These electrodes are assumed to be very thin as compared to the overall thicknesses of the harvester so
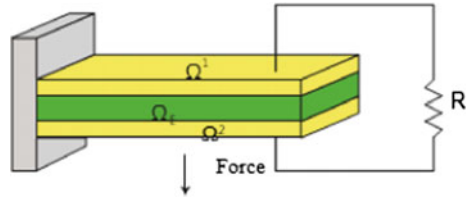
that their contribution to the thickness dimension is negligible. The pth patch, $p \in \{1, 2\}$, occupies a domain $\Omega^{(p)}$ such that $(\Omega_E, \Omega^{(1)}, \Omega^{(2)})$ is a partition of the whole solid domain Ω_S. The structure is subjected to a prescribed displacement u_i^d on a part Γ_u and to surface force density F_i^d on the complementary part Γ_σ of its external boundary.

The electric boundary conditions are defined by a prescribed electric potential ψ^d on Γ_ψ and a surface density of electric charge Q^d on the remaining part Γ_D. Thus, the total structure boundary, denoted $\partial\Omega_S$, is such that $\partial\Omega_S = \Gamma_D \cup \Gamma_\psi = \Gamma_u \cup \Gamma_\sigma$ with $\Gamma_u \cap \Gamma_\sigma = \Gamma_\psi \cup \Gamma_D = \varnothing$.

The linearized strain tensor is denoted by ε_{ij} and the corresponding stress tensor by σ_{ij}. Moreover, D_i denotes the electric displacement vector components and E_i the electric field vector components, $_S$ is the mass density of the structure, and n_i^S is the unit normal vector external to Ω_S.

The local equations of the piezoelectric-structure coupled problem described in Fig. 1 are with appropriate initial conditions.

$$\sigma_{ij,j} = \rho_S \frac{\partial^2 u_i}{\partial t^2} \quad \text{in} \quad \Omega_S \tag{1a}$$

$$\sigma_{ij} n_j^S = F_i^d \quad \text{on} \, \Gamma_\sigma \tag{1b}$$

$$u_i = u_i^d \quad \text{on} \, \Gamma_u \tag{1c}$$

$$D_{i,i} = 0 \quad \text{in} \quad \Omega_S \tag{2a}$$

$$D_i n_i^S = -Q^d \quad \text{on} \, \Gamma_D \tag{2b}$$

$$\psi = \psi^d \quad \text{on} \, \Gamma_\psi \tag{2c}$$

Equation (1a) corresponds to the elastodynamic equation in absence of body force; Eqs. (1b) and (1c) are the prescribed mechanical boundary conditions; Eq. (2a) corresponds to the electric charge equation for a dielectric medium; and Eqs. (2b) and (2c) are the previously described electric boundary conditions;

The stress tensor σ_{ij} and electric displacement D_i are related to the linear strain tensor ε_{kl} and electric field E_k through the converse and direct linear piezoelectric constitutive equations

$$\sigma_{ij} = c_{ijkl}\varepsilon_{kl} - e_{kij}E_k \tag{3}$$

$$D_i = e_{ikl}\varepsilon_{kl} + \in_{ik}E_k \tag{4}$$

where c_{ijkl}, e_{kij}, and ϵ_{ik}, denote elastic, piezoelectric, and dielectric material constants. Moreover, we have the following gradient relations between the linearized strain tensor ε_{kl} and the displacement u_k, and between the electric field E_k and the electric potential ψ:

$$\varepsilon_{kl} = \frac{1}{2}\left(u_{k,l} + u_{l,k}\right) \tag{5}$$

$$E_k = -\psi_{,k} \tag{6}$$

We can note from the constitutive Eqs. (3) and (4) and from the gradient relations (5) and (6) that the stress tensor σ_{ij} and the electric displacement vector components D_i depend on the variables u_k and ψ:

$$\sigma_{ij} = \sigma_{ij}(u_k, \psi) \tag{7a}$$

$$D_i = D_i(u_k, \psi) \tag{7b}$$

For a detailed derivation of these classical equations, we refer the reader, for example, to Tzou (1993).

2.2 Variational Formulation

In order to obtain the variational formulation associated with the local equations of the coupled piezoelectric-elastic structure system given in Eqs. (1a)–(2a), the test-function method is applied. We proceed in two steps, successively considering the equations relating to the structure and the electric charge equation for a dielectric medium.

First, we introduce the space C_u of sufficiently regular functions u_i defined in Ω_S and $C_u^* = \{u_i \in C_u | u_i = 0 \quad \text{on} \quad \Gamma_u\}$. Multiplying Eq. (1a) by any time independent test-function $\delta u_i \in C_u^*$, then applying Green's formula, and finally taking Eq. (1b) into account, leads to

$$\int_{\Omega_S} \sigma_{ij}(u_k, \psi)\delta\varepsilon_{ij}d\nu + \rho_S \int_{\Omega_S} \frac{\partial^2 u_i}{\partial t^2}\delta u_i d\nu = \int_{\Gamma_\sigma} F_i^d \delta u_i ds \quad \forall \delta u_i \in C_u^* \tag{8}$$

where $\delta\varepsilon_{ij} = \frac{1}{2}(\delta u_{i,j} + \delta u_{j,i})$.

Second, we consider the space C_ψ of sufficiently regular functions ψ in Ω_S and $C_\psi^* = \{\psi \in C_u | \psi = 0 \quad \text{on} \quad \Gamma_\psi\}$. Multiplying Eq. (2a) by any time independent test-function $\delta\psi \in C_\psi^*$ and integrating over Ω_S, we have

$$\int_{\Omega_S} D_{i,i}(u_k, \psi)\delta\psi dv = 0 \quad \forall \delta\psi \in C_\psi^* \tag{9}$$

Using the piezoelectric constitutive Eqs. (3) and (4), and taking the electric boundary condition (2b) into account, Eqs. (8) and (9) can be rewritten in the following forms

$$\int_{\Omega_S} c_{ijkl}\varepsilon_{kl}\delta\varepsilon_{ij}dv - \int_{\Omega_S} e_{kij}E_k\delta\varepsilon_{ij}dv + \rho_S \int_{\Omega_S} \frac{\partial^2 u_i}{\partial t^2}\delta u_i dv = \int_{\Gamma_\sigma} F_i^d \delta u_i ds \quad \forall \delta u_i \in C_u^* \tag{10}$$

and

$$\int_{\Omega_S} e_{ikl}\varepsilon_{kl}\delta E_i dv + \int_{\Omega_S} \in_{ik} E_k\delta E_i dv = \int_{\Gamma_D} Q^d \delta\psi ds \quad \forall \delta\psi \in C_\psi^* \tag{11}$$

where $\delta E_i = -\delta\psi_{,i}$.

Thus, the variational formulation of the coupled piezoelectric-elastic structure coupled problem consists in finding $u_i \in C_u$ such that $u_i = u_i^d$ on Γ_u and $\psi \in C_\psi$ such that $\psi = \psi^d$ on Γ_ψ, satisfying Eqs. (10)–(11) with appropriate initial conditions.

2.3 Finite Element Formulation

The variational Eqs. (10)–(11) for the piezoelectric-elastic structure coupled problem can be written, in discretized form, as the following unsymmetric matrix system (Larbi et al. 2010, 2014):

$$\begin{bmatrix} \mathbf{M_u} & \mathbf{0} \\ \mathbf{0} & \mathbf{0} \end{bmatrix} \begin{bmatrix} \ddot{\mathbf{U}} \\ \ddot{\boldsymbol{\Psi}} \end{bmatrix} + \begin{bmatrix} \mathbf{K_u} & -\mathbf{C_{u\psi}} \\ \mathbf{C_{u\psi}^T} & \mathbf{K_\psi} \end{bmatrix} \begin{bmatrix} \mathbf{U} \\ \boldsymbol{\Psi} \end{bmatrix} = \begin{bmatrix} \mathbf{F} \\ \mathbf{Q} \end{bmatrix} \tag{12}$$

with appropriate initial conditions.

Where $\mathbf{U}$ and $\boldsymbol{\Psi}$ are the vectors of nodal values of u_i and ψ respectively; $\mathbf{M_u}$ and $\mathbf{K_u}$ are the mass and stiffness matrices of the structure; $\mathbf{C_{u\psi}}$ is the electromechanical coupled stiffness matrix; $\mathbf{K_\psi}$ is the electric stiffness matrix; $\mathbf{F}$ and $\mathbf{Q}$ are the applied mechanical force and charge vectors respectively.

The harvested energy is dissipated through a resistive load R. Using Ohms law, we obtain the following additional equations:

$$\mathbf{V} = -R\dot{\mathbf{Q}} \tag{13}$$

where $\mathbf{V}$ is the output voltage.

By combining Eqs. (12) and (13), it is possible to obtain a Finite Elements matrix equation and then to determine the power dissipated across the resistive load.

3 Numerical Example

We present in this section some finite element results, obtained with the previous formulation, for piezoelectric vibration energy harvester. Commercially available COMSOL Multiphysics software is used to develop the finite element model.

The example consists of a piezoelectric bimorph cantilever beam composed of two layers of PZT-5A bonded to an aluminum substructure layer (the configuration of this example does not have a tip mass). The geometrical and physical parameters used in the simulation are given in Table 1. The ratio of the overhang length to the total thickness of the harvester is about 85.7, which makes it reasonable to neglect the shear deformation and the rotary inertia effects for the first few vibration modes.

In this study, a plane strain modeling is used. Hence, two-dimensional geometry is considered for the simulation. The structure is discretized using 400 quad four shell elements of COMSOL. The thickness of the piezoelectric layers is divided into three elements while the thickness of the substrate is discretized with two elements (Fig. 2).

The analysis given here considers the frequency range of 0–5000 Hz. First, a modal analysis of the bimorph cantilever beam is performed. This cantilever has three vibration modes in this frequency range. The first three mechanically and

Table 1 Geometric and material parameters used in the simulation (Eurturk and Inman 2011)

Parameters	Description	Value	Units
L	Beam length	30	mm
b	Beam width	5	mm
h_p	Piezoelectric layer thickness	0.15	mm
h_s	Aluminum layer thickness	0.05	mm
E_s	Young's modulus of substrate material	70	GPa
E_p	Young's modulus of piezoelectric material	61	GPa
ρ_s	Mass density of Aluminum	2700	kg/m^3
ρ_p	Mass density of Piezoelectric (PZT-5A)	7750	kg/m^3
e_{31}	Piezoelectric constant (PZT-5A)	−10.4	C/m^2
ϵ_{33}^s	Permittivity constant (PZT-5A)	13.3	nF/m
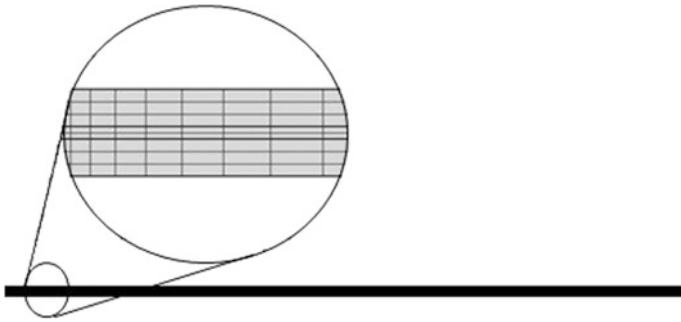
Fig. 2 Mesh of the structure

electrically undamped natural frequencies of the bimorph cantilever (for $R \rightarrow 0$, i.e., in short-circuit conditions) are $f_1 = 205$ Hz, $f_2 = 1270$ Hz, and $f_3 = 3570$ Hz.

The structure is subjected now to a harmonic inertial load $\rho g e^{i\omega t}$ (ρ is the volume density of the structure, $g = 9.81$ m/s^2 is the gravitational acceleration and ω is the angular frequency). The set of electrical load resistance considered here ranges from 10 kΩ to 10 MΩ. Note that the largest load resistance ($R = 10$ MΩ) is very close to open-circuit conditions. The system is simulated to obtain displacement, output voltage, and generated power, as a function of the excitation frequency.

The voltage FRFs for the first three modes of this harvester are plotted in Fig. 3. These curves show that as the load resistance is increased, the voltage output at every excitation frequency increases monotonically. Moreover, the resonance frequency of a given piezoelectric energy harvester depends on the external load

Fig. 3 Output voltage versus excitation frequencies of the bimorph for three values of the load resistance

Fig. 4 Variation of the voltage output with load resistance for the first three resonance frequencies

resistance and can take a value only between the short- and open-circuit resonance frequencies.

Figure 4 shows the output voltage generated for a range of load resistance, from 10 kΩ to 10 MΩ. It can be seen that the voltage generated increases with increasing the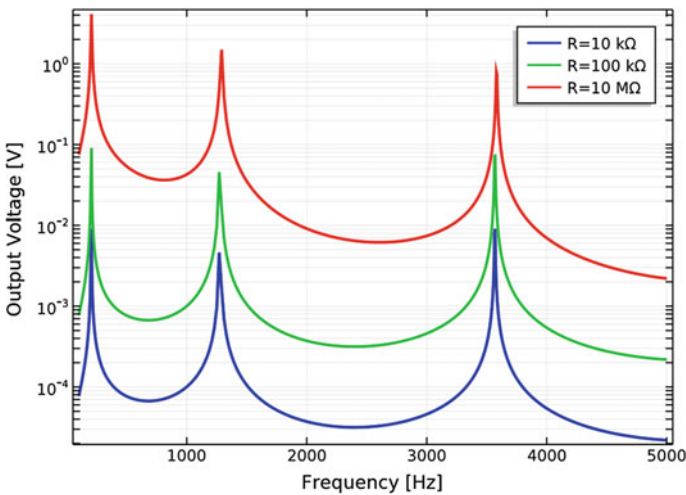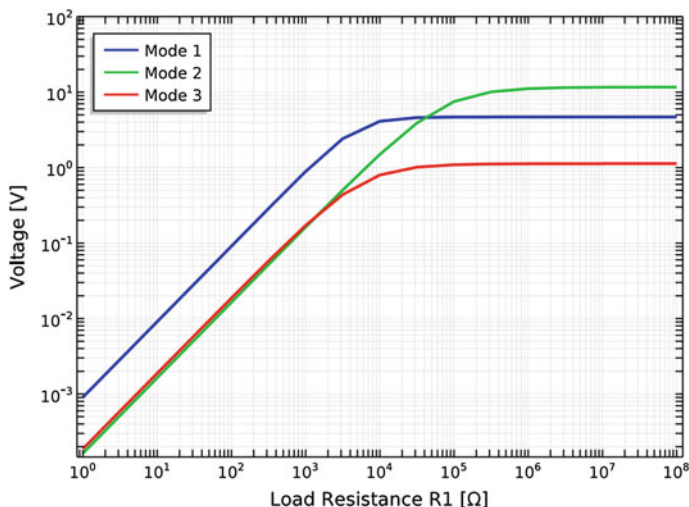 resistance for the first three resonance frequencies. The resistance range has a threshold at which the voltage remains almost constant.

The electrical power output is proportional to the square of the voltage output (V^2/R). The module of the electrical power is plotted in Fig. 5 for three values of resistance. It is clear from this figure that the power output FRF does not necessarily exhibit monotonic behavior with increasing (or decreasing) load resistance for a given frequency.

Figure 6 shows the tip displacement FRFs for the set of resistors and the frequency range of interest. One can see the three vibration modes in this figure but it is not possible to distinguish between the curves of different load resistance.

The resistive shunt damping effect results in both frequency shift and vibration attenuation. With increasing load resistance, the electromechanical system moves from the short-circuit to the open-circuit conditions. It is important to notice from the behavior around the modal frequencies of the vibration FRFs that the form of damping caused by piezoelectric power generation (or power dissipation in the resistor due to Joule heating) is more sophisticated than viscous damping. First, with increasing load resistance, the frequency of peak vibration amplitude changes considerably (and shifts to the right in the FRF, unlike the case of viscous damping). Second, with further increase in the load resistance, although the vibration
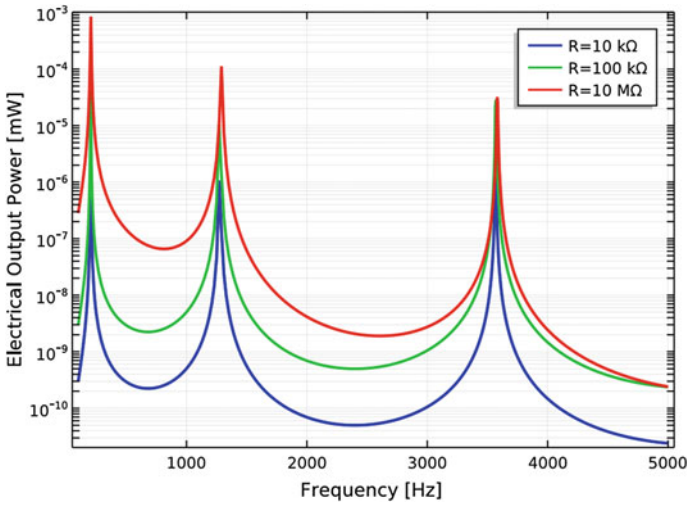
Fig. 5 Electrical power output versus excitation frequency of the bimorph for three values of the load resistance
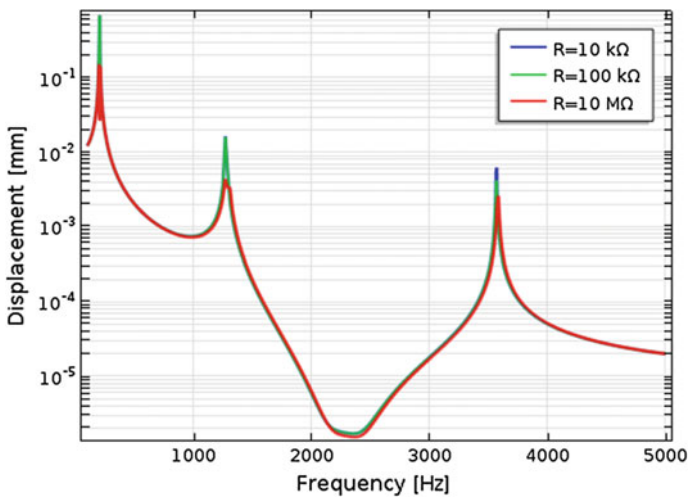
Fig. 6 Tip displacement FRFs of the bimorph for a broad range of load resistance

amplitude at the original (short-circuit) resonance frequency is attenuated to certain amplitude, the vibration amplitude at the open-circuit resonance frequency is amplified considerably. The reason is the frequency shift due to changing electrical boundary conditions.

4 Conclusions

In this work, a finite element method for modeling and analysis of a bimorph piezoelectric energy harvester is presented. The local equations, in terms of structure displacement and electric potential, and the corresponding variational formulation and FE matrix equation are first presented. An example of a piezo-electric bimorph cantilever beam, modeled using COMSOL Multiphysics, is then presented and analyzed. This example shows that the energy harvester generates a maximum of power when the base excitation frequency matches the natural frequency and the optimal load is connected.

References

Amini Y, Emdad H, Farid M (2014) An accurate model for numerical prediction of piezoelectric energy harvesting from fluid structure interaction problems. Smart Mater Struct 23:95034. doi: https://doi.org/10.1088/0964-1726/23/9/095034

Dutoit NE, Brian LW, Sang-Gook K (2005) Design considerations for mems-scale piezoelectric mechanical vibration energy harvesters. Integr Ferroelectr Int J 121–160

Erturk A, Inman DJ (2008) Issues in mathematical modeling of piezoelectric energy harvesters. Smart Mater Struct 17:65014–65016. doi:https://doi.org/10.1088/0964-1726/17/6/065016

Erturk A, Inman DJ (2009) An experimentally validated bimorph cantilever model for piezoelectric energy harvesting from base excitations. Smart Mater Struct 18:25009. doi: https://doi.org/10.1088/0964-1726/18/2/025009

Eurturk A, Inman DJ (2011) Piezoelectric energy harvesting, 1st edn. Wiley

Larbi W, Deü J-F, Ciminello M, Ohayon R (2010) Structural-acoustic vibration reduction using switched shunt piezoelectric patches: a finite element analysis. J Vib Acoust 132:51006. doi: https://doi.org/10.1115/1.4001508

Larbi W, Deü JF, Ohayon R, Sampaio R (2014) Coupled FEM/BEM for control of noise radiation and sound transmission using piezoelectric shunt damping. Appl Acoust 86:146–153. doi: https://doi.org/10.1016/j.apacoust.2014.02.003

Roundy S, Wright PK (2004) A piezoelectric vibration based generator for wireless electronics. Smart Mater Struct 13:1131–1142. doi:https://doi.org/10.1088/0964-1726/13/5/018

Tzou HS (1993) Piezoelectric shells: distributed sensing and control of continua. Kluwer Academic Publishers, Boston/Dordrecht

Vatanabe SL, Paulino GH, Silva ECN (2013) Design of functionally graded piezocomposites using topology optimization and homogenization—toward effective energy harvesting materials. Comput Methods Appl Mech Eng 266:205–218. doi:https://doi.org/10.1016/j.cma.2013.07.003

Active Vibration Control of a Rotor Bearing System Using Piezoelectric Patch Actuators and an LQR Controller

Maryam Brahem, Amira Amamou and Mnaouar Chouchane

Abstract Active vibration control (AVC) is used to overcome the limits of passive control. This chapter presents a design of an active vibration controller for a rotor bearing system using active piezoelectric patch actuators bonded on the surface of the rotor shaft. These devices are used to compensate the unbalance forces by applying control moments. The finite element method is used to construct a discrete rotor bearing system model. The design uses proximity probes to measure lateral vibration of the rotor bearing system. A Linear quadratic regulator (LQR) controller based on a full state feedback is designed to provide the adequate activation power to the piezoelectric patches. Rotordynamic analysis is carried out to obtain the Campbell diagram, the natural frequencies, and the critical speeds of the rotor bearing system. The designed active vibration controller reduced significantly rotor lateral vibration at constant rotating speed. A higher reduction rate has been obtained at the first critical speed.

Keywords Rotor dynamics · Active control of vibration
Piezoelectric patches · LQR controller

1 Introduction

Rotating machines such as pumps, turbines, and compressors are essential elements in industrial production. In order to improve products and their life cycles, manufacturers should increase the performance of these machines and reduce their

M. Brahem · A. Amamou · M. Chouchane (✉)
Laboratory of Mechanical Engineering, National Engineering School of Monastir,
University of Monastir, Monastir, Tunisia
e-mail: Mnaouar.chouchane@gmail.com

M. Brahem
e-mail: Brahemmaryam@gmail.com

A. Amamou
e-mail: Amira.amamou@yahoo.fr

vibration. Particularly, lateral vibration of flexible rotors affects bearing lifetime, product quality, and generate noise. In order to reduce vibration, passive or active means of vibration control must be used. For this purpose, new solutions using active control can reduce vibration amplitudes using "smart" materials (Zhou and Shi 2001) and more precisely piezoelectric patches bonded to the shaft surface to act as actuators for active vibration control of the shaft.

Sloetjes and De Boer (2007) considered a flexible shaft with surface-mounted piezoceramic sheets and strain sensors to reduce vibration amplitudes at resonances. Kunze et al. (2003) investigated vibration control of an automotive shaft equipped with piezoelectric fiber actuators and sensors. The actuators reduced the vibration and resulting vehicle interior noise by positive position feedback control.

Several control schemes have been proposed in the literature in order to attenuate the unbalance response of a rotor bearing system. Arias-Montiel and Silva-Navarro (2008) used an LQR scheme with state feedback for vibration control of a flexible rotor system with two discs using an actuator and one measurable state to adjust the rigidity of one bearing. Numerical results showed a reduction of the unbalance response between 70 and 85%. The same research team (Arias-Montiel et al. 2014) has also designed an active suspension using electromechanical actuators to validate experimentally the closed loop system performance. In Lees (2011), a rotor actuation by piezoelectric patches bonded to the surface of shaft has been studied. Lees showed that the control of the unbalance force of the rotor is performed by the imposition of a counteracting bend.

In this work, a rotor bearing system with piezoelectric patches bonded to the surface of the flexible shaft is considered. The model including the gyroscopic effect is obtained by the finite element method using a MATLAB toolbox developed by Friswell et al. (2010). An LQR controller is then designed in order to attenuate the vibrations caused by mass unbalance of the discs. Numerical simulations are presented to validate the proposed control scheme.

2 Modeling and Analysis of the Rotor System

We consider the rotor bearing system shown in Fig. 1, which is composed of a flexible shaft, supported by two flexible bearings with constant stiffness and damping and two unbalanced disks located symmetrically along the shaft. The model includes the gyroscopic effects.

Using the finite element method, the system is divided into five elements and six nodes. Every element has two nodes and four lateral degrees of freedom at each node.
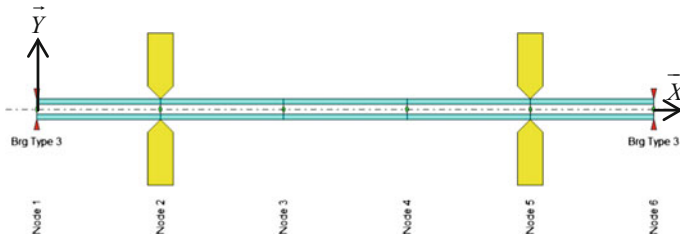
Fig. 1 The rotor bearing system model

The matrix form of the equations of motion of the rotor bearing system is:

$$[M]\{\ddot{u}\} + ([G] + [C_d])\{\dot{u}\} + [K]\{u\} = \{F\} \tag{1}$$

where [M], [K], [C_d], and [G] are the mass, stiffness, damping, and gyroscopic matrices, respectively (Kramer 1993) with the following forms:

$$[M] = [M_0] + [M_b],\ [K] = [K_0] + [K_b] + \Omega[K_1],\ [C_d] = [C_0] + [C_b]$$

where Ω is the rotational speed, $[M_b]$, $[K_b]$, and $[C_b]$ are the mass, stiffness, and damping matrices of the bearings, respectively. $[M_0]$ and $[K_0]$ are the mass and stiffness matrices of the shaft, respectively. $[K_1]$ and $[C_0]$ are the stiffness and damping matrices due to the internal damping (Friswell et al. 2010).

The vector of generalized displacements is:

$$\{u\} = \{\begin{matrix} x_1 & y_1 & \theta_1 & \psi_1 & x_2 & y_2 & \theta_2 & \psi_2 & x_3 & y_3 & \theta_3 & \psi_3 \end{matrix} \\ \begin{matrix} x_4 & y_4 & \theta_4 & \psi_4 & x_5 & y_5 & \theta_5 & \psi_5 & x_6 & y_6 & \theta_6 & \psi_6 \end{matrix}\}^T$$

The unbalance external force vector associated with the disk nodes can be written as follows:

$$\{F\} = \{\begin{matrix} 0 & 0 & 0 & 0 & F_{x_2} & F_{y_2} & 0 & 0 & 0 & 0 & 0 & 0 \end{matrix} \\ \begin{matrix} F_{x_5} & F_{y_5} & 0 & 0 & 0 & 0 & 0 & 0 & 0 & 0 & 0 & 0 \end{matrix}\}^T$$

For a constant rotational speed, the nonzero components of the vector $\vec{F}$ are:

$$\left\{ \begin{matrix} F_{x_2} \\ F_{y_2} \end{matrix} \right\} = \left\{ \begin{matrix} m_1 a_1 \Omega^2 \cos\ (\Omega t + \varphi_1) \\ m_1 a_1 \Omega^2 \sin\ (\Omega t + \varphi_1) \end{matrix} \right\},\ \left\{ \begin{matrix} F_{x_5} \\ F_{y_5} \end{matrix} \right\} = \left\{ \begin{matrix} m_2 a_2 \Omega^2 \cos\ (\Omega t + \varphi_2) \\ m_2 a_2 \Omega^2 \sin\ (\Omega t + \varphi_2) \end{matrix} \right\} \tag{2}$$

where

φ_1 The unbalance phase of disk 1
φ_2 The unbalance phase of disk 2

a_1 The eccentricity of disk 1
a_2 The eccentricity of disk 2
m_1 The mass of disk 1
m_2 The mass of disk 2.

2.1 Natural Frequencies and Critical Speeds

Consider a rotor bearing system having the parameters presented in Table 1.

The natural frequencies and the rotor excitation frequency due to unbalance of the rotor bearing system depend on rotor speed. The variation of these frequencies with rotor speed can be reported on the same plot called Campbell diagram. The forcing frequency can be represented by a straight line $\omega = \Omega$. The intersection of the curves of the natural frequencies with that relating the forcing frequency gives us the values of critical speeds.

The corresponding Campbell diagram of the considered rotor bearing system is presented in Fig. 2.

The Campbell diagram shows that the first two critical speeds are 1623 and 4260 rpm.

2.2 Rotor Response at a Constant Rotational Speed

Two constant rotating speeds are considered $N_1 = 1650$ rpm and $N_2 = 2000$ rpm. The first is very close to the first critical speed, the second is between the first and

Table 1 Physical system parameters

Parameters	Value
Shaft density, ρ	7850 kg/m^3
Outer diameter of the shaft	10 mm
Inner diameter of the shaft	5 mm
Mass of each disk, m_1, m_2	750 g
Outer diameter of each disk	75 mm
Inner diameter of each disk	10 mm
Thickness of each disk	25 mm
Eccentricity of each disk, a_1, a_2	2 μm
Young's modulus, E	210 GPa
Length of shaft, L	0.6 m
Stiffness of bearings, K_{xx}, K_{yy}	1e6 N/m
Damping of bearings, C_{xx}, C_{yy}	1000 N/m.s
Unbalance phase of disk 1, φ_1	0
Unbalance phase of disk 2, φ_2	$-\pi/4$
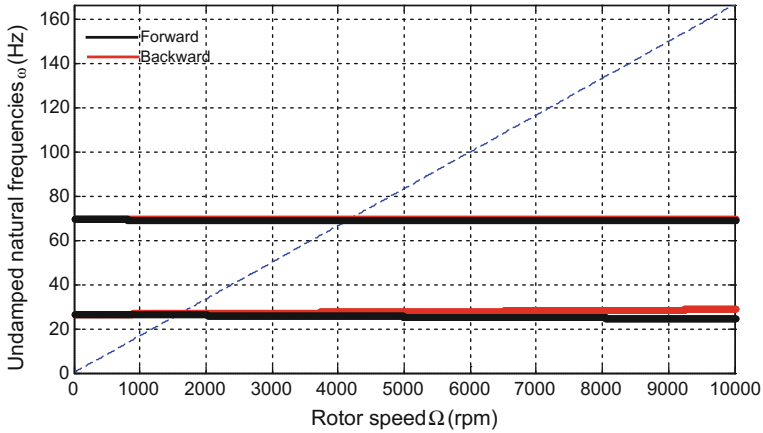
Fig. 2 Campbell diagram
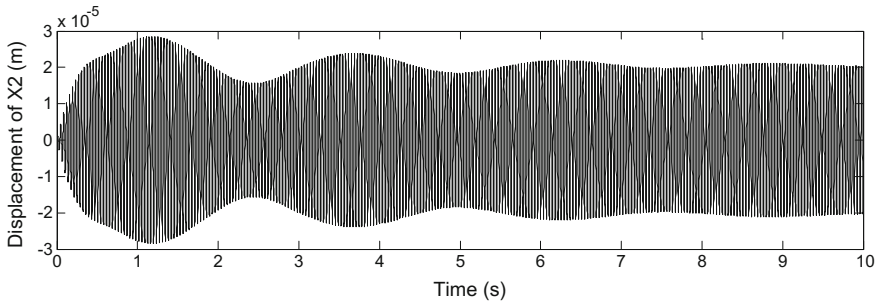
Fig. 3 Lateral displacement X_2 of node 2 at a rotating speed $N_1 = 1650$ rpm

the second critical speed. No controlling forces are applied on the system. Figure 3 shows the lateral displacement X_2 of the disk 1 at the first rotational speed N_1. Figure 4 shows the lateral displacement X_2 of the disk 1 at the second rotational speed N_2.

3 Active Vibration Control

The purpose of this research work is to apply active vibration control on a rotor bearing system by bonding piezoelectric patch actuators to the surface of the rotor flexible shaft.
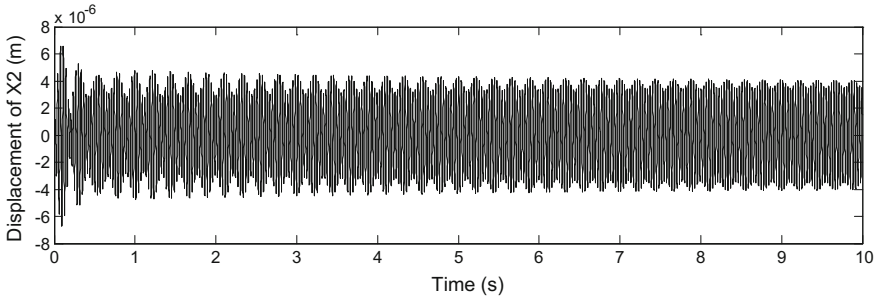
Fig. 4 Lateral displacement X_2 of node 2 at a rotating speed $N_2 = 2000$ rpm

3.1 Surface-Bonded Piezoelectric Patches

Two pairs of piezoelectric patches, having the characteristics presented in Table 2 (Berlincourt et al. 2000), are used in order to apply control moments on the rotor shaft.

The patches of one pair are positioned opposite to each other and bonded to the third element of the shaft between node 3 and 4 as shown in Fig. 5.

The actuators are driven out of phase. While one patch is extending, the other patch is contracting. Consequently, two opposite bending moments are induced in the shaft at nodes 3 and 4 and bending moments around the y- and the z-axis is induced in the structure. These moments are proportional to the applied voltage V_p (Lin and Chu 1994) as shown in Eq. (3):

$$M_p = \frac{4\psi E_p d_{31}\left[(r_0 + t_p)^3 - r_0^3\right]\sin\beta}{3(1+\psi)t_p} V_p = \sigma_p V_p \tag{3}$$

where

$$\psi = \frac{E_s I_s}{E_p I_p}$$

Table 2 Properties of the piezoelectric patch

Parameters	Value
Actuator material	PZT-5H
Strain constant, d_{31}	-274e-12 C/N
PZT thickness	0.001 m
Angle of enclosure, β	90°
Actuator length	0.12 m
Young's modulus of the piezoelectric patch	62 GPa
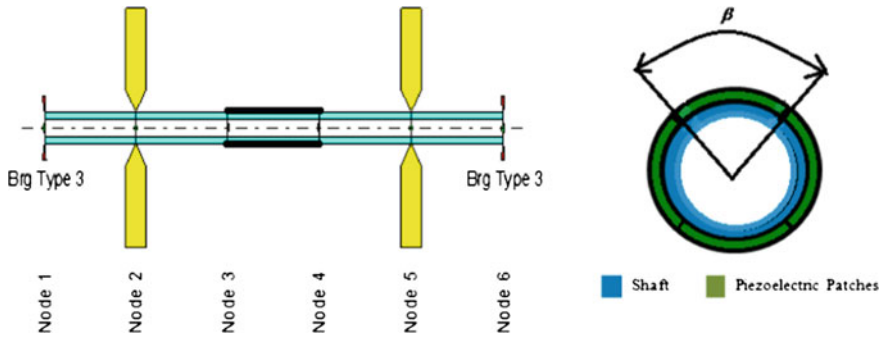
Fig. 5 The rotor bearing system model with piezoelectric patches

E_p The Young's modulus of the piezoelectric patch
E_s The Young's modulus of the shaft
d_{31} The piezoelectric strain constant
r_0 The outer radius of the shaft
t_p The thickness of the piezoelectric patch
β The angle of enclosure of the patch
V_p The actuation voltage
I_s, I_p The area moment of inertia of the shaft and the piezoelectric patch, respectively.

3.2 Controllability Analysis

The proposed model for the rotor system, with surface-bonded piezoelectric patches in a stationary frame, is described by the following system of equations:

$$[M]\{\ddot{u}\} + ([G] + [C_d])\{\dot{u}\} + [K]\{u\} = \{F\} + V_p\{b\} \tag{4}$$

where V_p is the control input voltage provided to the piezoelectric patches assuming that all piezoelectric patches are supplied with the same voltage and the vector $\{b\}$ is expressed as follows

$$\{b\} = \{0, 0, 0, 0, 0, 0, 0, 0, 0, 0, 2\sigma_p(\cos{(\Omega t)} - \sin{(\Omega t)}), 2\sigma_p(\cos{(\Omega t)} + \sin{(\Omega t)}),$$
$$0, 0, -2\sigma_p(\cos{(\Omega t)} - \sin{(\Omega t)}), -2\sigma_p(\cos{(\Omega t)} + \sin{(\Omega t)}), 0, 0, 0, 0, 0, 0, 0, 0\}^T$$

By defining the state vector $\{z\} = [u \quad \dot{u}]^T$, Eq. (4) is written in the following state-space form.

$$\{\dot{z}\} = [A]\{z\} + \{B\}V_p + \{E\}$$
$$y = \{C\}\{z\} \tag{5}$$

where:

$$[A] = \begin{bmatrix} 0 & [I] \\ -[M^{-1}][K] & -[M^{-1}]([G] + [C_d]) \end{bmatrix}, \quad \{B\} = \left\{ \begin{array}{c} \{0\} \\ [M^{-1}]\{b\} \end{array} \right\} \text{ and}$$

$$\{E\} = \left\{ \begin{array}{c} \{0\} \\ [M^{-1}]\{F\} \end{array} \right\}$$

$\{y\}$ is the output system vector and $\{C\}$ is the following row vector:

$$C = [0\,0\,0\,0\,1\,0\,0\,0\,0\,0\,0\,0\,0\,0\,0\,0\,0\,0\,0\,0\,0\,0\,0\,0\,0\,0\,0\,0\,0\,0\,0\,0\,0\,0\,0\,0\,0\,0\,0\,0\,0\,0\,0\,0\,0\,0\,0\,0]$$

Using the matrices [A] and [B], we compute the controllability matrix $[C_1]$ as:

$$[C_1] = \begin{bmatrix} A & AB & A^2B & \cdots & A^{47}B \end{bmatrix} \tag{6}$$

$[C_1]$ is a full rank matrix, so that we can prove that the system is controllable using the control moments.

4 LQR Control

Knowing that the system is controllable, we propose a full state LQR controller, as follows:

$$V_P = \{g\}\{z\} \tag{7}$$

where the state regulation problem is solved by computing a row vector $\{g\}$ which minimizes a conventional LQR performance index J with a positive weighting matrix [Q] and a positive weighting constant R. The performance index J is defined as follows:

$$J = \int_0^\infty \left(\{z\}^T [Q]\{z\} + V_p^2 R \right) dt \tag{8}$$

The calculation of the control gain {g} was performed using Matlab. The weighting matrix and constant for the controller are given as $[Q] = 1e^8 eye(48, 48)$ and $R = 0.001$.

Figure 6 shows the LQR control scheme

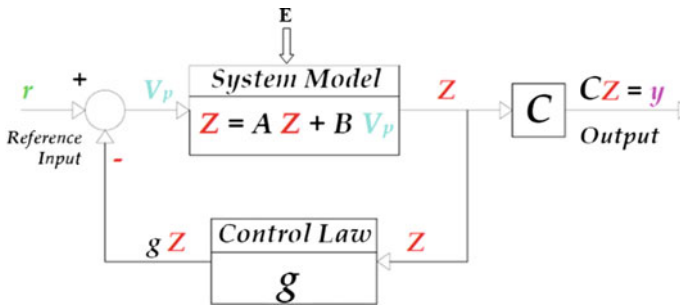The advantage of using the LQR control scheme is that the controlled system will be robust and stable.

Fig. 6 Block diagram of LQR controller

The state-space equations for the closed loop feedback system are therefore:

$$\{\dot{z}\} = ([A] - \{B\}\{g\})\{z\} + \{E\}$$
$$y = \{C\}\{z\} \tag{9}$$

We assume, here, that the controller scheme relies on a full state feedback for the rotor bearing system. In a practical application of the controller, a limited number of state vector components are available, and therefore, an observer must be designed and used.

4.1 Simulation Responses After Applying the LQR Controller

The LQR controller is used to attenuate the vibration amplitudes caused by the rotor unbalance in both disks at constant rotational speeds $N_1 = 1650$ and $N_2 = 2000$ rpm. Figures 7 and 8 show the displacement response X_2 of the uncontrolled and controlled systems in a closed loop at constant rotational speeds N_1 and N_2, when the corrective patch moments are applied.

These figures show that the proposed control scheme reduces the vibration level particularly at rotating speed N1.

5 Conclusion

In this chapter, a FE model of a rotor system with attached piezoelectric actuators on the shaft surface is developed. An active control scheme was designed to simulate the closed loop system performance and to reduce the vibration due to unbalance forces. A significant reduction of vibration level has been achieved using an LQR controller particularly at a rotor speed close to the first critical speed.
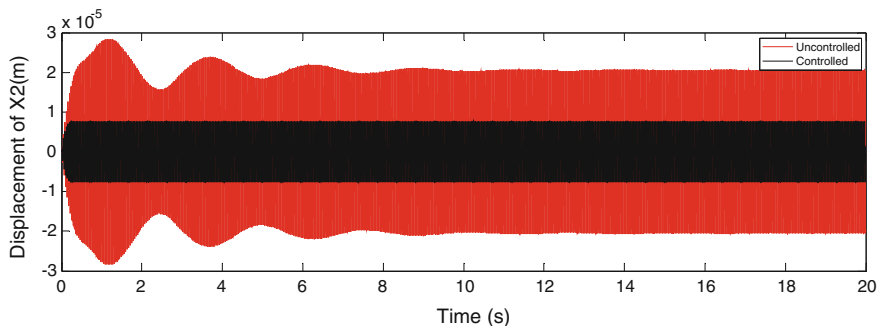
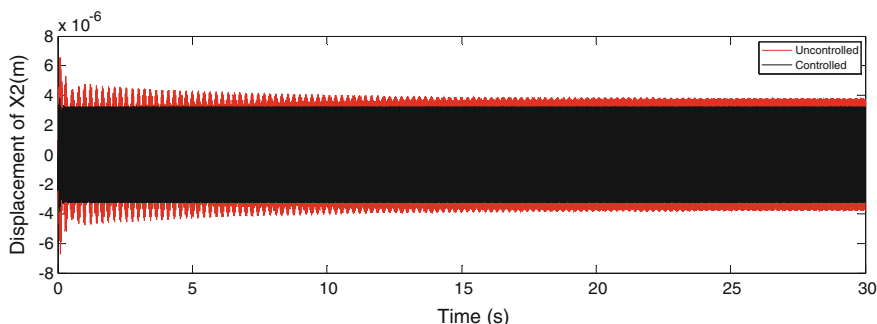**Fig. 7** Lateral displacement of node 2 before and after control at N_1

Fig. 8 Lateral displacement of node 2 before and after control at N_2

References

Arias-Montiel M, Silva-Navarro G (2008) Finite element modeling and unbalance compensation for a two disks asymmetrical rotor system. In: 5th international conference on electrical engineering, computing science and automatic control. IEEE, MEXICO

Arias-Montiel M, Silva-Navarro G, Antonio-García A (2014) Active vibration control in a rotor system by an active suspension with linear actuators. J Appl Res Technol 12:898–907. https://doi.org/10.1016/S1665-6423(14)70596-6

Berlincourt D, Krueger H, Near C (2000) Properties of piezoelectricity ceramics. Tech Pub TP-226, 1–12

Friswell MI, Penny JET, Garvey SD, Lees AW (2010) Dynamics of rotating machines. Cambridge University Press, Cambridge

Kramer E (1993) Dynamics of rotors and foundations, 1st edn. Springer, Berlin

Kunze H, Riedel M, Schmidt K, Bianchini (2003) Vibration reduction on automotive shafts using piezoceramics. Smart Struct Mater 2003 Ind Commer Appl Smart Struct Technol 5054:382–386

Lees AW (2011) Smart machines with flexible rotors. Springer Proc Phys 139:393–398. https://doi.org/10.1007/978-94-007-2069-5

Lin Y-H, Chu C-L (1994) Comments on active modal control of vortex-induced vibrations of a flexible cylinder

Sloetjes PJ, De Boer A (2007) Vibration reduction and power generation with piezoceramic sheets mounted to a flexible shaft. J Intell Mater Syst Struct 19:25–34. https://doi.org/10.1177/1045389X06072753

Zhou S, Shi J (2001) Active balancing and vibration control of rotating machinery: a survey. Shock Vib Dig 33:361–371. https://doi.org/10.1177/0583102401033005

New Modeling of Planetary Gear Transmission

Oussama Graja, Bacem Zghal, Kajetan Dziedziech, Fakher Chaari, Adam Jablonski, Tomasz Barszcz and Mohamed Haddar

Abstract In a planetary gearbox, there are multiple sources of vibrations due to the complexity of the gearbox since the latter contains multiple components (Sun, Carrier, Planets, and Ring) witch all of them are in mesh. In addition, the complexity of the planets motion (two rotational motions) affects the vibration collected in experiments, because the distance between planet and the transducer is time-varying. Hence, vibrations collected have not the same level: when the planet becomes closer from the senor, vibration level increases and vice versa. In this study, a linear two-dimensional lumped parameter dynamic model is developed in order to predict modulation phenomenon in a planetary gearbox. This model is based on novel description of the vibration of different components of the planetary gear taking into account the variable vibration transmission path. Numerical simulations show the ability of this model to describe this phenomenon with clear amplitude modulation in time signal.

Keywords Planetary gearbox · Dynamic modeling · Vibration transmission path

1 Introduction

It is known that the behavior of epicyclic gearboxes was extremely developed by researchers because of its complexity. The major complexity is that one planet of the gearbox can occupy different positions in one rotation of the carrier. So, the transmission path has a real effect on collected vibration since there are sequences

O. Graja (✉) · B. Zghal · F. Chaari · M. Haddar
(ENIS)/Laboratory of Mechanics, Modeling and Production (LA2MP),
National School of Engineers of Sfax, Sfax, Tunisia
e-mail: grajaoussama@gmail.com

K. Dziedziech · A. Jablonski · T. Barszcz
Academia Gorniczo Hutnicza (AGH), National Centre for Research and Development
in Poland, Krakow, Poland

1227

of "come in" and "come out" of planet when planet comes closer to the sensor and goes further from the sensor. As a result, a modulation phenomenon occurs in time signal due to those sequences (Liu et al. 2016).

To detail the dynamic behavior of the planetary gearbox, several researchers developed lumped parameters models. Inalpot and Kahraman (2009) proposed a nonlinear time-varying dynamic model to predict modulation sidebands. Springs are used to model the time varying mesh stiffness and dampers to model the attenuation of induced forces between components in mesh. The overall equation of motion was built and the modulation phenomenon was formulated. This latter was based on a waiting function in form of a Hanning window which introduces some physical parameters as the number and the angular positions of planets. Walter et al. (2010) proposed a model of a planetary gearbox operating under varying loading condition. They used only springs in their model and the damping is introduced as a viscous one. The modulation phenomenon was not taken into account. Liang et al. (2015) developed a dynamic model to simulate the vibration signals from different sources for both healthy and faulty case. They used a modified Hamming function to model the transmission path effect. Recently, Liu et al. (2016) developed a two-dimensional lumped parameters model. The transmission path is presented as two parts: the part inside the gearbox to the casing and the part through the casing to the transducer. Parameters of the transmission path effect are estimated based on gear sizes but not calculated exactly. Hammami et al. (2016) developed a torsional lumped parameter model and they took into account the time varying loading conditions. Karray et al. (2013) developed a torsional model of planetary gear set. Mechanisms leading to modulation phenomenon are modeled by using Hunning windows.

The majority of researchers described all displacements with respect to benchmark tied to the carrier which rotates with planets and sun. The modulation phenomenon cannot be revealed because the vibration was measured with respect to a relative frame. Experimental results of planetary gearbox vibration showed the presence of amplitude modulation when a sensor is placed on the fixed ring (Hammami et al. 2016). Till now, researchers use a Hunning function in order to tune the response of models to experimental one.

In this study, a lumped parameters model is developed to describe mechanisms leading to the modulation phenomenon without using an estimated Hunning function incorporated with a waiting function. Simulation of the presented model will be shown.

2 Modeling the Planetary Gear Transmission

As described earlier, the modulation phenomenon always exists in real case. Figure 1 presents three different positions of one planet in one rotation of the carrier. As shown, planet comes closer and goes further in every rotation of the carrier which causes a change in vibration amplitude acquired by the sensor.
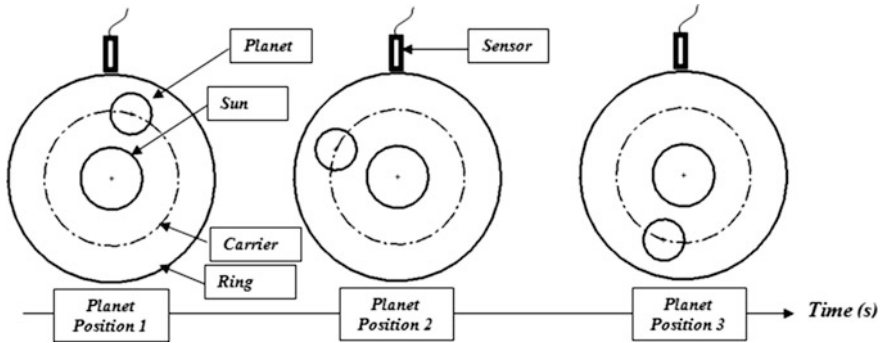
Fig. 1 Different positions occupied by planets during the rotation of the carrier

The main idea in this work is to develop a model able to describe all displacements of planetary gear with respect to a fixed frame tied to the fixed ring. Two-dimensional lumped parameter model of a planetary gear set to be investigated is shown in Fig. 2 (Walter et al. 2010).
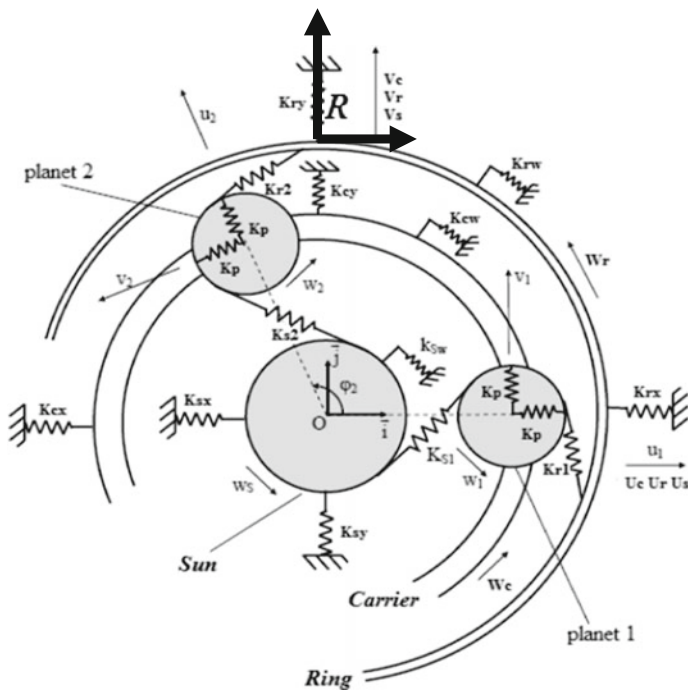

Fig. 2 Two dimensional lumped parameter model of planetary gear set (Walter et al. 2010)

As shown in Fig. 2, each component has three degrees of freedom

- two translations U_i and V_i
- one rotation W_i

where i = {Sun gear, Ring gear, Carrier, Planet gear$_{(1)}$,……, Planet gear$_{(N)}$} with N is the number of planets. All those displacements are tied to each component.

All the stiffnesses are modeled by springs. The damping will be introduced later as a proportional damping. All components are modeled as rigid bodies.

All displacement will be described with respect to the fixed frame (R) tied to the ring. This new frame is located at the same place of the sensor.

The figure gives an idea how to describe the displacement of one planet with respect to the fixed frame (Fig. 3).

The Lagrange formulation leads to the matrix form written as

$$M\ddot{X} + C\dot{X} + (K_{rv} + K_p)X = F_{ext} + F_{ind} \tag{1}$$

with M is the mass matrix, C is a proportional damping matrix, K_{rv} is the time varying stiffness matrix, K_p is the constant stiffness matrix, F_{ext} is the external force vector, F_{ind} is the induced force vector (this force is induced by the displacement along the line of action to the sun–planet meshing point and by the displacement along the line of action to the planet–ring meshing point in motion), $\ddot{X}$, $\dot{X}$ and X are respectively acceleration, velocity and displacement.
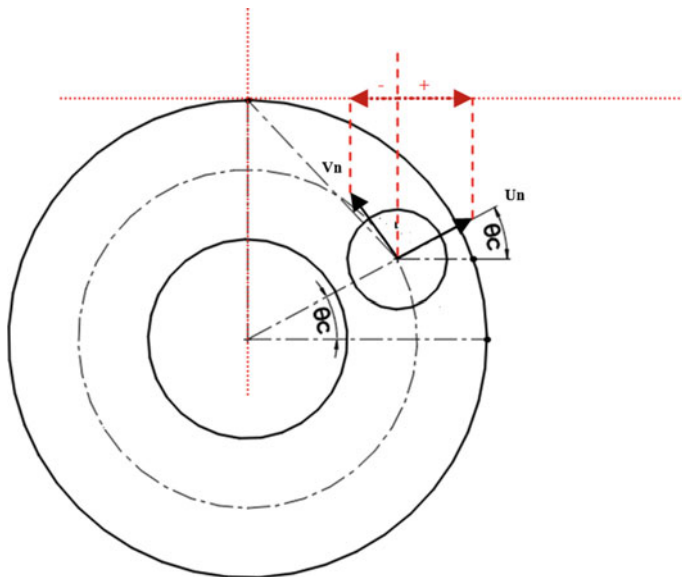

Fig. 3 Measuring displacement of planet with respect to the fixed frame

3 Numerical Simulation and Results

The table presents the physical and geometric parameters for the studied four planets planetary gearbox (Table 1).

Figure 4 shows the simulated time evolution of acceleration of ring gear on y-axis for one rotation of the carrier. The input speed (Sun) is 1540 min^{-1}.

Table 1 Geometric and physical parameters of the planetary gearbox

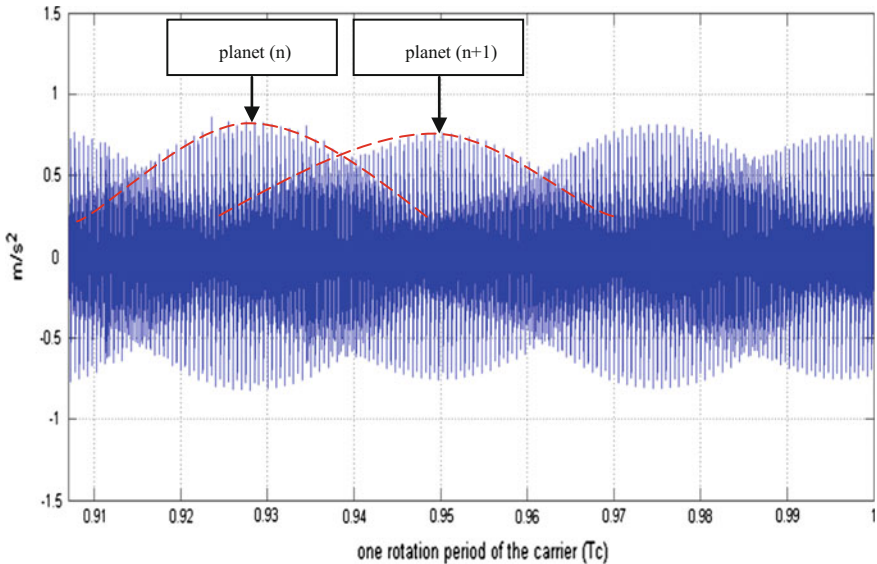| Parameters	Sun gear	Planet gear	Ring gear	Carrier
Number of teeth	39	27	93	…
Module (m)	2	2	2	…
Pressure angle (°)	20	20	20	
Mass (Kg)	2.3	0.885	2.94	15
Base circle radius (m)	0.078	0.054	0.186	0.132
Bearing stiffness (N/m)	ksx = ksy = 1E8; ksw = 0	kpx = kpy = 1E8	krx = kry = 1E8; krw = 1E15	kcx = kcy = 1E8; kcw = 1E15
Input torque (Nm)	150	…	…	…

Fig. 4 Ring gear vibration component measured on y-axis

Four modulations are identified in one rotation of the carrier since the planetary gear transmission possesses four planets. It is clear also the overlapping phenomenon (in red) which describes what happens really in a planetary gearbox: when a planet (n) goes further from the sensor, the vibration amplitude decreases, but in the same time, the planet (n + 1) comes closer from the sensor so this later starts to detect vibration from it, as a result, the vibration amplitude increases and so on.

Those phenomena cannot be revealed with using a frame tied to the carrier which was used in many preceding studies.

4   Conclusion

In this study, a dynamic model is developed to simulate vibrations from all components including (sun gear, planet gear, ring gear, and carrier) and to predict the modulation and overlapping phenomena due to the time-varying distance between planet and the sensor location. Incorporating the effect of all components, the vibration signal is built and measured at the sensor location.

References

Journal Article

Bartelmus W, Chaari F, Zimroz R, Haddar M (2010) Modeling of gearbox dynamics under time varying no stationary load for distributed fault detection and diagnosis. Eur J Mech A Solids 29:637–646

Hammami A, Del Rincon AF, Chaari F, Santamaria MI, Rueda FV, Haddar M (2016) Effect of variable loading conditions on the dynamic behavior of planetary gear with power recirculation. Measurement 94:306–315

Inalpolat M, Kahraman A (2009) A theoretical and experimental investigation of modulation sidebands of planetary gear sets. J Sound Vib 323:677–696

Liang X, Zuo MJ, Hoseini MR (2015) Vibration signal modeling of a planetary gear set for tooth crack detection. Eng Fail Anal 48:185–200

Liu L, Liang X, Zuo MJ (2016) Vibration signal modeling of a planetary gear set with transmission path effect analysis. Measurement 85:20–31

Book

Karray M, Chaari F, Del Rincon AF, Viadero F, Haddar M (2013) Modulation sidebands of planetary gear set, advanced in condition monitoring of machinery in non-stationary operations book, Part III Chapter 3 217–224. In: Proceeding of the third international conference on condition monitoring of machinery in non-stationary operations CMMNO 2013

Experimental Investigation of the Damage Progression in the Filament-Wound Composite by the Acoustic Emission Technique

Moez Beyaoui, Hajer Boussetta, Abdelouahed Laksimi, Lassaad Walha and Mohamed Haddar

Abstract This paper presents an experimental study to identify and characterize the different mechanisms of failure in the ±55° filament-wound glass/polyester composite. Acoustic emission (AE) was chosen as an experimental means of expertise. In this context, a relevant tensile test with in situ acoustic emission monitoring were conducted. The studied specimens were manufactured by filament winding. Indeed, first a tube is obtained by winding a mandrel with the desired draping and is then cut along the longitudinal axis to obtain wound test specimens having a small curvature. The discrimination of the different types of possible damage was obtained following the exploitation of the signals performed by the conventional mono-parametric analysis. This method assumes that each burst generated carries a specific signature to a generator mechanism. The amplitude distribution is the descriptor on which is based this study. The efficiency of the employed experimental strategy was confirmed after microscopic observations of specimens through the Scanning Electron Microscopy (SEM).

M. Beyaoui (✉) · H. Boussetta · L. Walha · M. Haddar
Mechanical Modeling and Manufacturing Laboratory (LA2MP), National School of
Engineers of Sfax, University of Sfax, B.P 1173-3038 Sfax, Tunisia
e-mail: moez.beyaoui@yahoo.fr

H. Boussetta
e-mail: hajer_boussetta@yahoo.com

L. Walha
e-mail: walhalassaad@yahoo.fr

M. Haddar
e-mail: mohamed.haddar@enis.rnu.tn

H. Boussetta · A. Laksimi
Laboratoire Roberval UMR 6253, Technology University of Compiègne, 60205 Compiègne
Cedex, France
e-mail: abdelouahed.laksimi@utc.fr

1 Introduction

The use of composite materials is widespread for buried or aerial piping applications. In this field, the composites are very competitive with metallic materials. This competitiveness is explained by their good mechanical properties (rigidity and resistance to fatigue) and their chemical properties (resistance to corrosion). In-service piping is subjected to various mechanical stresses, such as internal or external pressure, ground and building movements, vibration, etc. Consequently, taking into account these factors is essential to ensure the proper functioning of the structure throughout its lifetime. From this perspective, the study and the evaluation of material damage is a key point to master the durability and reliability of the filament wound of composite dedicated to this type of application (Radulović and Maksimović 2009). It thus seems judicious not only to quantify the damage but also to identify the different mechanisms responsible for it.

Nevertheless, the phenomena of damage and the special configuration of the studied structure (These patterns have some zones of undulations and others where the material can be considered as a laminate) are too complex. A significant effort must be made so that the analysis of the experimental results is sufficiently well understood and exploited with relevance (Rousseau et al. 1999; Carrol et al. 2001). Indeed, due to the heterogeneities and their anisotropy, the nature of the damage and the mechanisms responsible for their appearance and progression are very different from the mechanisms encountered in more conventional materials. Thus, according to the scale in question, damage such as breakage of the reinforcement, matrix cracking, or delamination may be at the origin of the premature ruin of a structure.

To control or anticipate these degradation mechanisms, the common approach is to follow these structures throughout their use. To do this, the means of expertise selected must take up the challenge of detecting the damage, quantify its harmfulness, and be non-destructive. The technique of acoustic emission proved very early as a promising means of detecting damage within composite materials (Mahdavi et al. 2016; Hua and Cheng 2015).

In this work, the experimental investigation was conducted on the ±55° filament-wound specimens inasmuch as this winding angle is generally followed in the manufacture of pipes.

Indeed, some researchers (Crouzeix et al. 2009; Douchin et al. 2008; Torres et al. 2009) have shown that winding patterns has an influence on the filament-wound pipes behavior. This limits the efficiency of many studies that have considered that the tubes manufactured by filament winding have the same behavior; in particular the same kinetic damage as conventional laminates and have used the main assumptions of classical laminate theory in their studies. So the solution of the problem is still open, and the experimental testing remains always the key factor to describe the real behavior of material. The efficiency of the employed experimental strategy was confirmed by microscopic observations of specimens.

2 Experimental Work and Conditions

The main objective of this experimental study is to apply the acoustic emission technique in order to identify the degradation mechanisms of the filament-wound glass/polyester composite during a mechanical traction test.

2.1 Specimens Manufacture

Based on the standard [ISO 8513:2016], the specimens are manufactured according to the following steps (Fig. 1):

- A tube (The outer diameter is 150 mm and the thickness is 3 mm) is obtained by winding a mandrel with the desired draping (Fig. 1a–b). The glass fiber are E6-CR type 'DIRECT ROVING 386', and the resin is a polyester
- The wound specimens $(250 \times 25 \times 3 \text{ mm}^3)$ will be obtained by cutting the tube along the longitudinal axis (Fig. 1c)

The wound test specimens have a small curvature. Consequently, there is a risk of rupture at the extremities of the specimens due to a stress concentration at this level. To resolve this problem, it is necessary to catch the curvature at the extremities according to the standard [ISO 8513 METHOD A]. So a reinforced thermosetting resin was used.
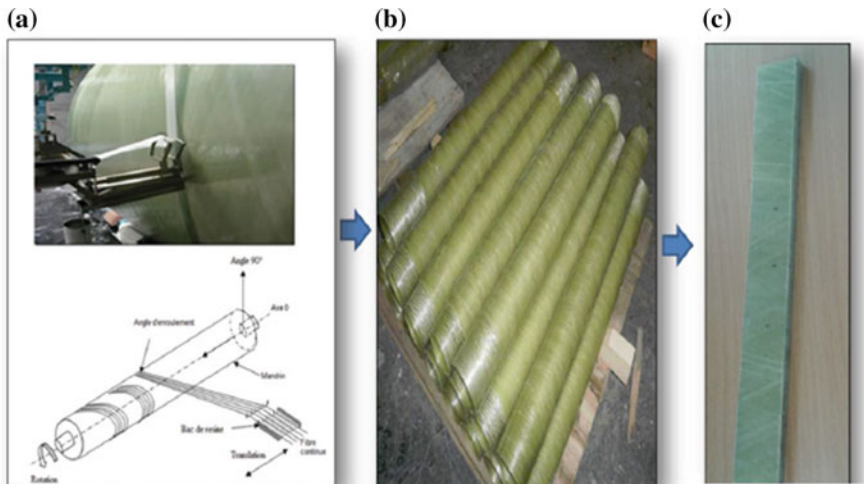

Fig. 1 The manufacturing steps of the test specimens **a** Filament winding technique **b** The tube **c** The wound specimens

2.2 Acoustic Emission

The acoustic emission is defined as a phenomenon of energy release in the form of transient elastic waves within the sample subjected to a mechanical stress of traction (Godin et al. 2004; Ben Khalifa et al. 2012). This release of energy is the result of microstructural changes. For the studied case, a monotonic tensile test was performed using an Instron machine with a constant speed equal to 0.5 mm/min (Fig. 2). Acoustic emission does not allow the detection of static or non-evolving defects initially present in the material.

The acquisition chain of the acoustic emission is shown in Fig. 3. Indeed the detection is carried out using two piezoelectric sensors using silicon grease according to the standard operating procedure specific to the acquisition system. These sensors convert the mechanical waves of the material into electrical signals. These waves will then are amplified and provide the acoustic emission signal (Beattie 1983; Eitzen and Wadley 1984). Two channels PCI-2 acquisition system (Peripheral Component Interconnect) produced by the company Physical Acoustic Corporation were used to record AE data. The calibration of the data acquisition system and the correct functioning of the sensors were validated by a pencil-lead breaks test. The range of the amplitude distribution was maintained between 40 and 100 dB.
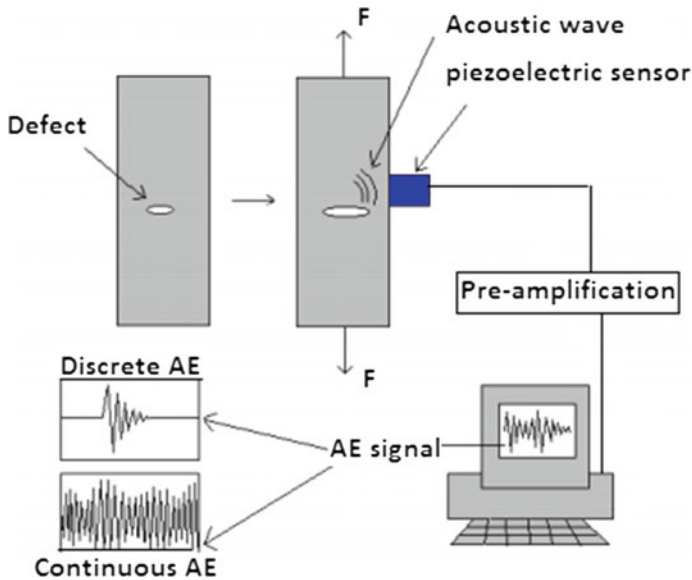
Fig. 2 Acoustic emission testing

Fig. 3 The acquisition chain of the acoustic emission signals

3   Monitoring the Damage Process in the 55° Filament-Wound Specimen

The monitoring of the damage is obtained by recording the acoustic activity of the tested specimens represented by the evolution of the number of cumulative counts. The correlation between the response of the material subjected to mechanical tensile stress and its acoustic activity is shown in Fig. 4.

The results obtained from tensile tests show that the mechanical behavior of materials can be described in three phases.

The phase I coincides with the reversible elastic deformation of the material. At this stage the material is not damaged.

The phase II occurs at the moment when the plasticity of the material begins to appear. At this stage the first Acoustic Emission signals will be detected.

The phase III is characterized by an exponential evolution of acoustic events. Consequently, the material is subjected to a very great damage which will continue until the total breakage of the material. It should be noted that the important number of counts before the total failure gives an idea of the high strength of the filament-wound composite.

Having demonstrated the existence of damage, the study must be completed by a relevant identification of damage mechanisms.

In this context, the acoustic emission was correlated initially with microscopic observations. Then an unsupervised approach to acoustic emission data was adopted.
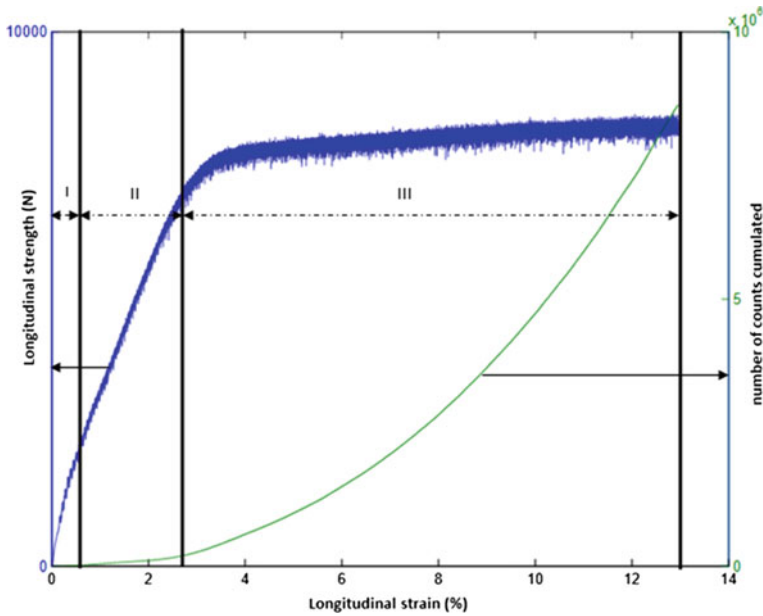
Fig. 4 Correlation between the evolution of the acoustic activity and the behavior law of the 55°
filament-wound composite longitudinal specimen under tensile test

3.1 Microscopic Observations

After detecting the presence of damage by the analysis of the acoustic activities,
microscopic observations through the Scanning Electron Microscopy (SEM) were
made to identify the different mechanisms of damage existing throughout the
mechanical stress of traction.

To do this, a 25 * 10 mm portion of a damaged ±55° filament-wound specimen
was used. The result of this observation (Fig. 5) shows the existence of the fol-
lowing damages:

- The coalescence of the matrix/fibers interface.
- The matrix cracks
- The initiation of the delamination at the extremities of the transverse cracks
- The pull out and the breakage of fibers

3.2 Mono-Parametric Classification

The conventional mono-parametric analysis of the acoustic emission assumes that
each burst generated carries a specific signature to a generator mechanism. In the
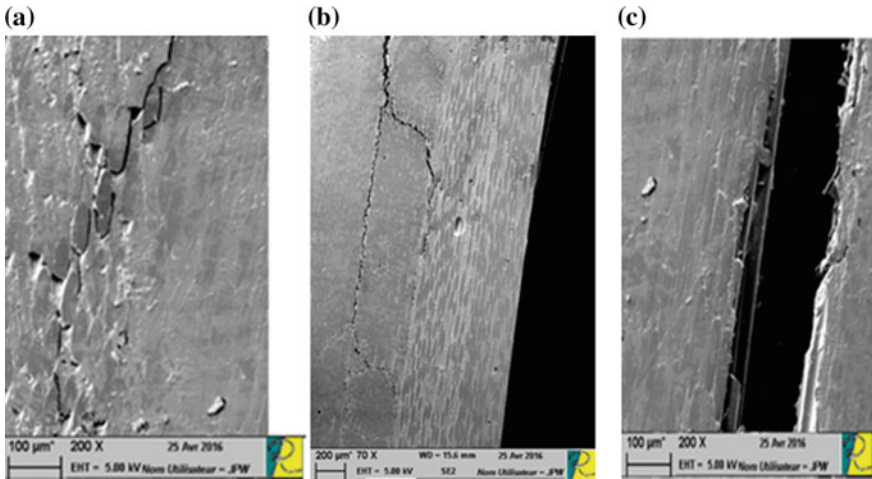
Fig. 5 Damage mechanisms in the 55° filament wound specimens under tensile test: **a** coalescence of the matrix/fibers interface and the matrix cracks; **b** the initiation of the delamination at the extremities of the transverse cracks; **c** the pull out and the breakage of fibers

literature, various works have validated the fact that these acoustic signatures can be highlighted using one or two descriptors extracted from the detected acoustic emission signals. The amplitude distribution is one of the descriptors on which is based the most studies for the identification of acoustic signals. Therefore, an unsupervised mono-parametric classification based on amplitude was performed (Hartigan and Wong 1979; MacQueen 1967). In this classification, the number of classes was supposed equal to four. This choice is related to the SEM observations carried, that manifested the existence of four types of damage mechanisms. Thanks to this method, a classification of the various mechanisms of damage was carried out.

For the case studied in this work, the identification of the mechanisms of damage is carried out by referring to the work of Kotsikos et al. (1996).

From this work, matrix cracking can be identified with the amplitude signals between 40 and 55 dB, delamination between 55 and 70 dB, and fiber breaks at signals greater than 80 dB.

However this method is inadequate for accurate characterization of sources of damage because of the overlap of ranges for different types of damage that may occur as shown (Fig. 6). To avoid this problem, further study should be considered. In this context, the multi-parametric method can be chosen for a more adequate analysis of acoustic activities.
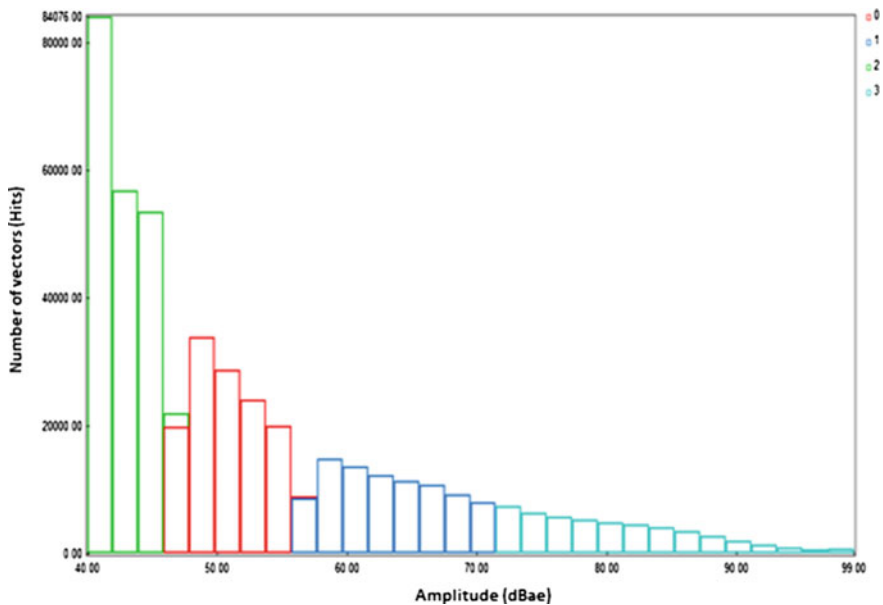
Fig. 6 Unsupervised mono-parametric classification of the acoustic emission data based on the amplitude distribution

4 Conclusion

In this work, the technique of acoustic emission coupled with microscopic observations through the Scanning Electron Microscopy (SEM) allowed to follow efficiently the process of damage of the filament-wound glass/polyester composite subjected to a mechanical stress of traction. Nevertheless for the case studied, the technique of mono-parametric classification has shown its limits for the identification of the different mechanisms of damage.

To avoid this deficiency a multi-parametric study can be chosen for a more adequate analysis of acoustic activities.

References

Beattie AG (1983) Acoustic emission, principles and instrumentation. J Acoust Emiss 2:95–128

Ben Khalifa A, Zidi M, Laksimi A (2012) Mechanical characterization of glass/vinylester ±55° filament wound pipes by acoustic emission under axial monotonic loading. C R Mecanique 340:453–460

Carrol K, Chiu (2001) Mechanical response of epoxy/glass multidirectional filament composites tubes, NASA CR-210661, E.U.A

Crouzeix L, Torres M, Douchin B, Périé JN, Collombet F, Hernández H (2009) Assessment of the winding pattern effects on the behaviour of filament wound pipes by using full field measurements and the equilibrium gap method. In: Conference: ICCM17—the 17th international conference on composite materials, Edinburgh (UK)

Douchin B, Hernández- Morenoa H, Collombet F, Davies P, Choqueuse D (2008) Influence of winding pattern on the mechanical behavior of filament wound composite cylinders under external pressure. Compos Sci Technol 68:1015–1024

Eitzen DG, Wadley HNG (1984) Acoustic emission: establishing the fundamentals. J Res Nat Bur Stand 89(1):75–100

Godin N, Huguet S, Gaertner R, Salmon L (2004) Clustering of acoustic emission signals collected during tensile tests on unidirectional glass/polyester composite using supervised and unsupervised classifiers. NDT & E Int 37:253–264

Hartigan JA, Wong MA (1979) A k-means clustering algorithm. J R Stat Soc C 28(1):100–108

Hua S, Cheng C (2015) Acoustic emission wavelet analysis of filament wound composite tube fatigue damage process. Open Mater Sci J 9(1):214–219

ISO 8513:2016: Plastics piping systems—glass-reinforced thermosetting plastics (GRP) pipes—test methods for the determination of the initial longitudinal tensile strength

Kotsikos G, Evans JT, Gibson AG, Hale J (1996) Use of acoustic emission to characterize corrosion fatigue damage accumulation in glass fiber reinforced polyester laminates. Polym Compos 20:689–696

MacQueen JB (1967) Some methods for classification and analysis of multivariate observations. In: Cam LML, Neyman J (eds) Proceedings of the fifth Berkeley symposium on mathematical statistics and probability, vol 1, pp 281–297

Mahdavi H, Hossein Rahimi G, Farrokhabadi A (2016) Failure analysis of ($\pm55°$)9 filament-wound GRE pipes using acoustic emission technique. Eng Fail Anal 62:178–187

Radulović J, Maksimović K (2009) Filament wound composite tubes: experimental and numerical simulations results. Scientific technical review, vol. LIX, no. 2

Rousseau J, Perreux D, Verdière N (1999) The influence of winding patterns on the damage behaviour of filament-wound pipes. Compos Sci Technol 59:1439–1449

Torres M, Crouzeix L, Douchin B, Collombet F, Hernández H, González J(2009) Strain field characterization of filament winding pattern at $\pm55°$ using numerical image correlation. In: Conference: ICCM17—the 17th international conference on composite materials, Edinburgh (UK)

Formulation of Bentonite-Cement Grout for Sealing Walls

Mounir Ben Jdidia, Zouheir Bouarada and Lotfi Hammami

Abstract Marine and land environment is deeply affected by NPK company phosphogypsum storage in Sfax city. A part of Taparura project aims to confine this pile of partially or totally heavy metal pollution by creating a sealing wall released by a material made of bentonite and cement waterproof. This study focuses on a methodology for formulating a cement bentonite grout to construct the screen. First, a synthesis bibliography introduces the bentonite and cement properties material composition as well as the methods of formulation and standardized tests. Second, an experimental study was carried out to formulate the cement bentonite material. The physical properties of fresh and hardened material as well as its mechanical properties were determined. This experimental approach has permitted the determination of B/W_B, B/C and W_T/C ratios of the BC grout and the strength properties of the projected grout. Moreover, the properties of grout in fresh state of bentonite cement are in a good correlation with the desired conditions for the screen execution. The vertical permeability obtained is so low which limits greatly the flows through the screen. The Young modulus of cement bentonite material is near the soil modulus which conducts to the same strains in both soil and screen thereby reducing micro cracks in screen.

Keywords Permeability · Grout · Sealing wall · Viscosity · Decantation or settling · Durability · Mechanical properties

M. B. Jdidia (✉) · L. Hammami
Mechanics modeling and manufacturing laboratory LA2 M, National engineering school of Sfax, Sfax University, BP1173, Rte de Soukra Km3.5, 3038 Sfax, Tunisia
e-mail: mounir.benjdidia@enis.rnu.tn

L. Hammami
e-mail: lotfi.hammami@enis.rnu.tn

Z. Bouarada
Higher Institute of Technological Studies of Sfax, Route de Mahdia km 2.5, B.P. 88-3099 El Bosten Sfax, Tunisia
e-mail: zouheir.bouarada@isetsf.rnu.tn

1 Introduction

The environment is increasingly affected by industrial waste and residues. The industrial sub-products are generally stored in depots with pollutants which contain harmful agents. The NPK company phosphogypsum pollutants are composed of heavy metals such as zinc, mercury, acids, sulphates and chlorides, nitrates and radiant gas.

Watertight walls are generally used to contain industrial waste by limiting the loaded water flow and therefore the migration of pollutants. The screen can be used as an obstacle or watertight screen in layers of permeable soils. In fact the screen must be flexible and capable of undergoing deformation without cracking. The screen technique execution consists on the excavation of a trench which is then filled with a grout of bentonite cement (see Fig. 1). The grout first acts as a support of the trench walls and becomes, after hardening, a watertight wall which has the following three main features:

- a sufficient mechanical strength with similar deformability of the surrounding soil,
- a low permeability of 10^{-9} m/s that is compatible with the environmental conditions,
- a resistance against chemical attacks to provide a better durability.

According to international standards such as the French legislation (13 July 1992 law), Canadian federal regulation and the American Environmental Protection Agency, (Chapuis et al. 1990, 2002; Kouloughli et al. 2007) the permeability of a sand bentonite grout must be lower than 10^{-9} m/s.

This paper presents, first, a bibliographic synthesis dealing with types of bentonites, bentonite grout, suitable cement for environment consideration, methods of preparation of cement bentonite grouts and appropriate standards tests for grout characterization.

Second, an experimental study is carried out to propose an optimum formulation of the grout composed of the bentonite (**B**), cement (**C**) and water (**W$_T$**). The influence of ratios **B/C** and **W$_T$/C** on physical properties of the fresh grout, on the mechanical properties of hardened grout and on its permeability was studied.

Fig. 1 Excavation of a trench

The main objective of this study is to develop a formulation methodology of a cement bentonite grout to build sealing walls. The approach consists of varying dosages of the grout components in order to obtain the desired mechanical and physical properties of the wall.

2 Bibliography Synthesis

Watertight screens can be used either for the insulation of the storage sites of environment hazardous waste such as phosphogyps or olive water and in permeable soils at dams foundation to prevent water flow. Several types of watertight screen can be designed (Massiera et al. 1999)

- excavated soil mixed with bentonite screen **SB** (Liausu et al. 2006)
- selected soil mixed with bentonite screen **SSB** (Kouloughli et al. 2007)
- excavated soil mixed with bentonite and cement screen **SBC** (Christopher 2002)
- grout of bentonite-cement screen **BC** (Portland Cement Association) (Opdyke et al. 2005; Evans et al. 2006)
- concrete with bentonite screen **BB** (Zemamla 2008).

The screens with cement are self hardened due to cement hydration. The perfect sealing is obtained by introducing a sheet of polyethylene in the trench filled by the grout (in case of **BC** screens). The sheet longevity is important and is about 100 years. The wall material is basically composed of cement, bentonite and aggregates of sand 0/4, grit 4/8, eventually an adjuvant and in some cases excavated soil containing fine silt siliceous.

2.1 Bentonite

Bentonite belongs to the family of smectite (Chapuis 1990, 2002). Particles of bentonite are composed by assemblies of parallel leaves (Gleason et al. 1997). According to Centre for Civil Engineering Research and regulations, main properties of bentonite to be used in a sealing wall are density (ρs > 2.6 g/cm^3), Blue methylene value (**VBS** > 22), water absorption (**Wa** > 500% in 24 h), plasticity index (**Ip** > 200), **PH** suspension (from 8.5 to 9.5) and calcium carbon content (**CaCO$_3$** $\leq$ 5%). The water content of bentonite should not exceed 13% at its initial state.

2.2 Cement Type

The choice of cement essentially depends on the environmental conditions. In fact, for an aggressive marine environment (sulfated water), the cement used in screen

must resist to sulphates and phosphoric acid attacks. The standard requires protection and aggressiveness to choose the screen cement. The **CEM III/C 32.5** is cement with granulated blast furnace slag (**S**) with slag content between 81 and 95%. This cement revealed suitable for the conditions of Taparura project which develops resistance to acid attacks and its high specific surface offers an impermeability of screen material (**BC**) lower than 10^{-8} m/s.

3 Experimental Study of Bentonite Cement (BC)

The experimental study is to determine the proportions of the various components of bentonite-cement grout in order to obtain a waterproof and flexible screen able to follow ground deformation to avoid micro cracks creation.

Two stages are needed to formulate bentonite-cement material **BC**. In the first stage consists on the determination of the mechanical and physical properties of identified products. The preparation of such mixture needs first the preparation of bentonite grout and then the preparation of bentonite-cement grout **BC**.

The second stage is to propose recommendations about possible dosages as well as the main parameters of formulation of bentonite-cement grout for sealed walls.

3.1 Bentonite Identification

Tunisian bentonite SOFAP for oil drilling was characterized by tests performed at the "Higher Institute of Technological Studies at Sfax (Tunisia)" (Karchoud et al. 2007). The obtained results are unit weight of solid particles (ρ_s = 2.64 g/cm^3), methylene blue value (**VBS** = 26), plasticity index (**Ip** = 184), shrinkage index (**IR** = 284), carbonate content (**CaCO$_3$** = 5%) and initial water content (**Wi** = 10%). The tested bentonite is classified as a sodium bentonite. Further, its high blue methylene value is an indicator of strong swelling potential.

3.2 Cement Identification

CEM I HRS 42.5 is currently available on the Tunisian market. The consistency test shows that the water–cement ratio Wc/C is approximately 0.26; the Blaine Specific Surface is about 5000 cm^2/g; absolute density is 3.1 g/cm^3.

3.3 Preparation of Bentonite Grout

According to standards: Guide specifications **BC** slurry trench, Portland Cement Association, **BC** screen by the Centre for Civil Engineering Research and regulations and recommended procedures (Erik Mikkelsen 2002), measurements of physical properties of the grout were determined.

a. **Marshall viscosity**

This test provides the measurement of flow time to recover fixed volume of grout and, therefore, informs about the influence of water dosage on the grout viscosity (Fig. 2).

From the curve (Fig. 2), the saturation dosage corresponds to the minimum of the slopes of reached for a ratio **B/W$_B$ = 5%** as recommended by references.

b. **Density**

It is measured with the pycnometer method. Figure 3 shows the variation of bentonite grout density versus ratio **B/W$_B$**.

For the retention wall, the needed density must be slightly greater than water density; dosages of water will be ranging to 5–6%.
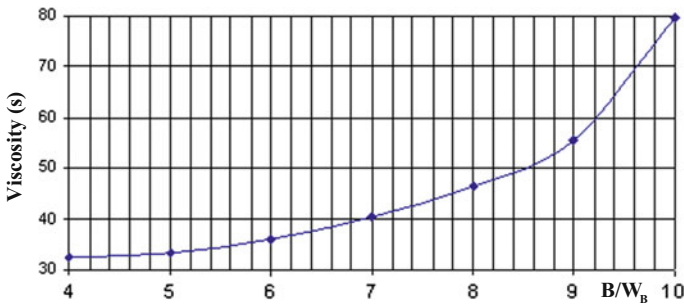

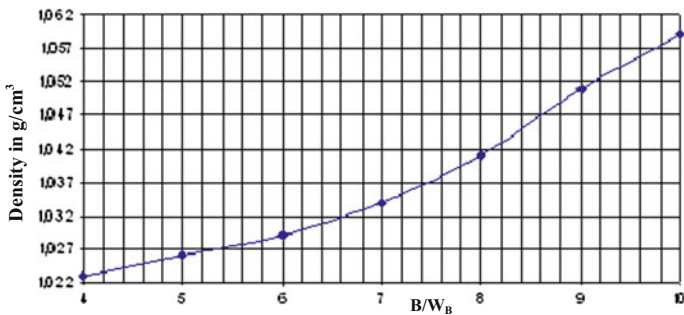**Fig. 2** Variation of grout viscosity in function of bentonite–water ratio B/W$_B$

Fig. 3 Variation of bentonite grout density in function bentonite–water ratio B/W$_B$ (%)

Table 1 Decantation versus time

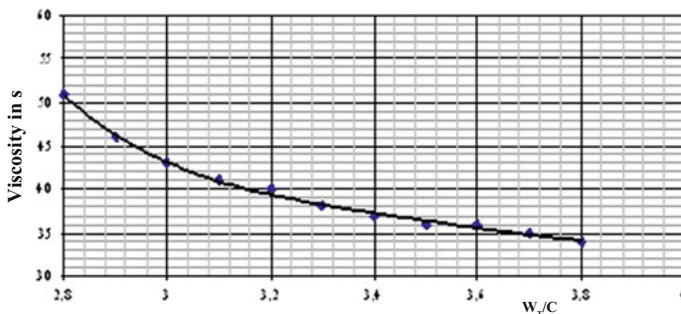| Parameters	Values				
Time (h)	1	2	3	4	24
Decantation (%)	1	1	1.5	2	3

Fig. 4 Variation of viscosity in function of W_T/C for a HRS 1 cement and bentonite–cement ratio B/C = 10%

c. **Test of decantation**

It is performed within a glass tube of 100 cm^3 volume (Table 1). The bentonite decantation should be less than 2.5% in 2 h and less than 3% in 4 h.

3.4 Preparation of Bentonite-Cement Grout

Grout is prepared at water–cement dosage **Wc/C = 0.35** and gradually poured in the grout mother. Shaking is necessary during the grout preparation by means of an energetic mixer (the blue methylene test mixer is used with a speed of 700 rpm).

3.4.1 Influence of Ratios W_T/C and B/C on Grout Properties

The influence of bentonite–cement ratio **B/C** on the physical properties of the grout **BC** has been analysed. In turn, the variation of **B/C** ratio from 10 to 15% was considered as suggested by the Centre for Civil Engineering Research and regulations (Cement-bentonite screen (1997) civieltechnisch centrum uitvoering research; Massiera et al. (1999)). Acceptable physical properties of grout are currently obtained when the dosage of water **W_T/C** varies between 2.8 and 4.0 as shown in Fig. 4. However, it is desirable to use a water reducer plasticizer to decrease **W_T/C** ratio.

Table 2 shows the ratios "total water-cement" with viscosity fixed at 40 s for **B/C** ratios ranging from 6 to 20%.

3.4.2 Measurement of Decantation and Density of BC Grout

The decantation is measured for grouts tested at viscosity of 40 s (Opdyke et al. 2005). Figure 5 shows that the decantation remains limited and acceptable for **B/C** ratios higher than 10%.

The density is measured for **B/C** ratios ranging from 6 to 20% and for a mean viscosity of 40 s of the grout as shown by Fig. 6 (Evans et al. 2006). The density recommended by the Centre for Civil Engineering Research and regulations is about 1.2–1.3 corresponding to a **B/C** ratio of about 11.

Table 2 Variation of W_T/C versus B/C ratio

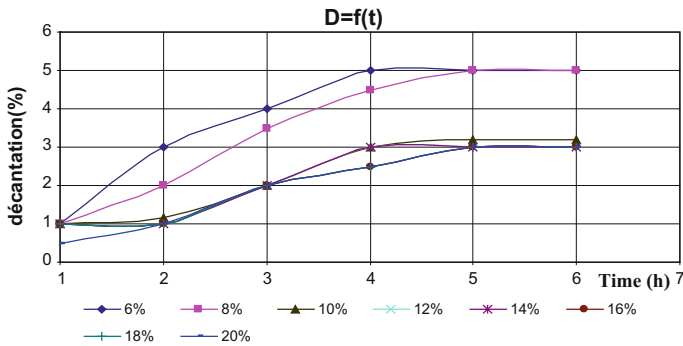| Parameters	Values							
B/C (%)	6	8	10	12	14	16	18	20
W_T/C	2	2.4	2.7	3.2	3.7	4.2	4.9	5.1

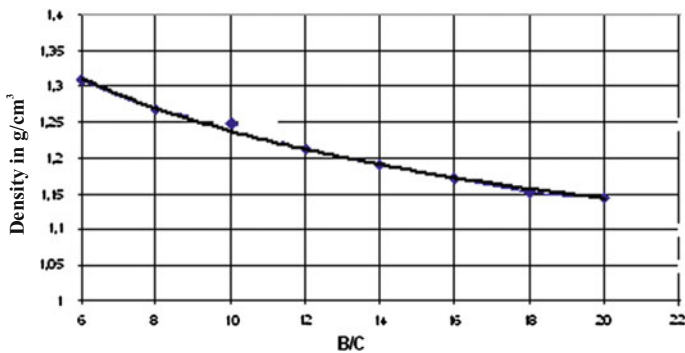**Fig. 5** Decantation in function of bentonite–cement ratio B/C for at viscosity of 40 s

Fig. 6 Density in function of B/C for a viscosity of 40 s

3.5 Cement and Bentonite Dosage Evaluation for 1 m³ of BC Fresh Grout at 40 S Fixed Viscosity

To determine the dosages of bentonite and Cement for a quantity of 1 m³ of fresh grout, the method of one optimum cubic metre is used to determine the percentages of constituents such that

$$1\,m^3 = V_C + V_B + V_W + V_{air} = \frac{m_C}{\rho_C} + \frac{m_B}{\rho_B} + \frac{m_W}{\rho_W} + V_{air} \tag{1}$$

The bentonite and cement dosages were determined by Eq. (1). Results were plotted in Fig. 7.

Figure 7 shows the variation of ratio (W_T/C) and the cement dosage versus ratio (**B/C**) for a viscosity fixed at about 40 s. The dosage of water increases with bentonite–cement ratio (**B/C**) because bentonite absorbs a great quantity of water. The second curve shown in Fig. 7 represents the variation of cement dosage versus the **B/C** ratio. The cement quantity decreases with the **B/C** parameter.

3.6 Strength Properties

In determining the strength properties of BC material, four practical dosages of cement were adopted to prepare four grouts C1, C2, C3 and C4 for one cubic metre of grout.

Table 3 summarizes the unconfined compression σ_c and tensile σ_t stresses as functions of cement dosages. Using a cement dosage of 300 kg/m³, in accordance with recommendations by the Centre for Civil Engineering Research and regulations, expected strength properties are obtained.
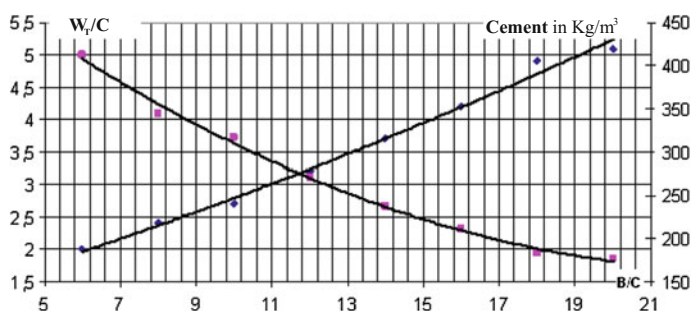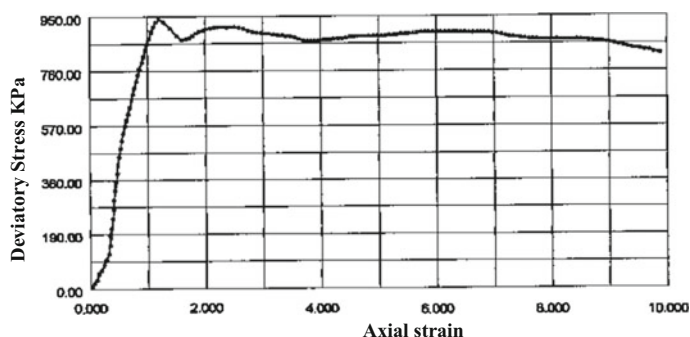

Fig. 7 Cement dosage versus B/C and W_T/C at viscosity of 40 s

Table 3 Compression and traction resistance versus cement dosages

Parameters	Values			
Ages	7 days		28 days	
Stresses (MPa)	σ_{c7}	σ_{t7}	σ_{c28}	σ_{t28}
C1 (350 kg/m^3)	0.89	0.285	1.72	0.528
C2 (300 kg/m^3)	0.73	0.261	1.03	0.341
C3 (250 kg/m^3)	0.46	0.169	0.66	0.259
C4 (200 kg/m^3)	0.43	0.137	0.54	0.159

Fig. 8 Triaxial test CU + u consolidation at 150 kPa (Karchoud 2007)

4 Mechanical and Permeability Properties of BC

Consolidated Undrained triaxial tests with measurement of excess pore pressure (CU + u) were performed in laboratory. The results of test permeability show that the vertical coefficient of permeability decreases after consolidation (150 kPa) from 8.16×10^{-9} to 4.84×10^{-9} m/s.

Figure 8 shows that the ultimate stress deviator approximates 0.940 MPa and the Young Modulus equals 140 MPa which is determined for elastic axial deformations in the range of 0.3–0.5 (%). Further, the residual strength of deviator stress equals 0.8 MPa at strain level of 9%. This result illustrates that the tested grout has a ductile behaviour.

5 Conclusions

An experimental study was carried in view of a methodology of formulation of bentonite-cement (**BC**) grout for sealing wall technique. The proposed methodology consisted, first, in the determination of **B/W$_B$**, **B/C** and **W$_T$/C** ratios of the **BC** grout and the strength properties of the projected grout.

The experimental results obtained for a fresh bentonite-cement grout are in a good correlation with the desired conditions for easy execution of the screen.

The mechanical and physical properties of a grout were determined for the unconfined compression and tensile strength (σ_{c28} = 0.5 to 1 MPa et σ_{t28} = 0.1 to 0.3 MPa), for the Young modulus (140 MPa) and for the coefficient of vertical permeability which approximates 8×10^{-9} m/s.

Finally the results obtained for the cured grout are consistent with prescriptions recommended by the Centre for Civil Engineering Research and regulations (Cement-bentonite screen (1997) civieltechnisch centrum uitvoering research). The diagrams obtained by the present experimental study give the opportunity to determine the dosages of a grout bentonite-cement constituents for prescribed compression strength.

References

Cement-bentonite screen (1997) civieltechnisch centrum uitvoering research

Chapuis RP et al. (1990) Sand—bentonite liners: predicting permeability from laboratory tests. Can Geotech J 27:47–57

Chapuis RP (2002) Full—scale hydraulic performance of soil-bentonite and compacted clay liners. Can Geotech J 39:417–439

Christopher R et al (2002) Soil-cement-benton slurry walls deep foundations, pp 713–727

Erik Mikkelsen P (2002) Cement-bentonite Grout backfill for borehole instruments. Geotech News Dec 2002

Evans JC et al (2006) Strength, permeability, and compatibility of slag-cement-bentonite slurry wall mixtures for constructing vertical barriers. In: Proceedings of the 5 international conference on environmental geotechnics, Cardiff, Wales, June

Gleason MH, Daniel DE, Eykholt GR (1997) Calcium and sodium bentonite for hydraulic containment applications. J Geotech Environ Eng ASCE 123(5):438–445

Guide specifications cement bentonite slurry trench, Portland Cement Association (PCA), USA

Karchoud N, Abbassi A (2007) Formulation d'un coulis de Bentonite Ciment B–C. Graduation project ISET de Sfax département GC

Kouloughli S, BenCheikh Lehocine M (2007) Etude des mélanges Sable-Bentonite utilisés dans la construction de barières de confinement de déchets solides. 2 Sciences and Technologie B N °25, Juin, pp 34–42

Liausu P, Spaulding Ch (2006) Construction d'une paroi étanche en sol bentonite sur le site de l'ancienne aciérie de Newcastle en Australie. Revue travaux – décembre

Massiera M, Levay J (1999) Construction de la paroi au coulis ciment-bentonite sous la digue nord de l'aménagement hydroélectrique La grande 1. Can J Civil Eng N° 26(2):145–155. https://doi.org/10.1139/l98-055

Opdyke S, Evans J (2005) Slag-Cement-Bentonite Slurry Walls. J Geotech Geoenviron Eng 131 (6):673–681

Zemamla R (2008) Formulation d'un béton à la bentonite pour la réalisation d'un écran étanche. Master ENIS

Analytical Method for the Calculation of Tool Machine Energy Consumption

Anoire Ben Jdidia, Alain Bellacicco, Maher Barkallah, Hichem Hassine, Mohamed Taoufik Khabou, Alain Riviere and Mohamed Haddar

Abstract There is no doubt that the industrial revolution has a monumental effect on the prosperity and the improvement of human conditions but on the other hand the bill was too expensive due to environmental degradation especially. Indeed the weather changing and global warming are directly linked with energy consumption. Industrial manufacturing is one of the biggest consumers of energy which needs a deep care especially in machining sequences to reduce energy consumption and to achieve the balance of humanity. To reduce the waste of energy during machining sequences, a new numerical approach to predict machine tool energy consumption is proposed in this study. It is about the spindle rotation and axis feed modeling as well as considering a nonlinear behavior between the tool and the workpiece during the manufacturing process. The proposed model provides an accurate tool for process planning in metal cutting which helps manufacturers to determine the optimal energy process plan.

A. Ben Jdidia (✉) · M. Barkallah · H. Hassine · M. T. Khabou · M. Haddar
Laboratory Mechanics, Modeling and Production, National Engineering School of Sfax
(ENIS), BP 1173-3038 Sfax, Tunisia
e-mail: benjdidia.anoire@gmail.com

M. Barkallah
e-mail: bark_maher@yahoo.fr

H. Hassine
e-mail: hassinehichem@yahoo.fr

M. T. Khabou
e-mail: mtkhabou@hotmail.com

M. Haddar
e-mail: mohamed.haddar@enis.rnu

A. Bellacicco · A. Riviere
QUARTZ Laboratory High, Institute of Mechanic of Paris (SUPMECA), 3 rue Fernand
Hainaut, 93400 Saint-Ouen Cedex, France
e-mail: alain.bellacicco@supmeca.fr

A. Riviere
e-mail: alain.riviere@supmeca.fr

1 Introduction

According to statistics, more than 36% of the total electrical energy consumption, based carbon sources, is intended for the manufacturing industry as mentioned by Hassine et al. (2015) which increases subsequently emissions of CO_2 in the atmosphere, causing several climate changes such as the greenhouse effect. In this framework, it has become urgent to achieve energy consumption reduction by increasing consciousness in sustainability through the modeling of energy consumption in machining to predict the electrical energy requirements of machine tools. A basis for analyzing energy consumption in machining is through a mathematical approach presented by Gutowski et al. (2006) to predict energy requirement in machining. It shows that the energy consumed by the material removal process is much lower than the energy consumed by necessary auxiliary units in order to maintain the metal cutting process. Unfortunately this model does not take into account the energy consumption of the auxiliary subunits of the machine tool. A model proposed by Rajemi et al. (2010) allows the determination and the optimization of the energy footprint during the manufacturing process for a turning case by selecting the optimal cutting parameters. Despite its advantages the proposed model neglects certain factors such as pump energy that has a direct impact on energy consumption. Avram (2011) has divided the total consumed energy into three main groups such idle, feed axis and spindle rotation. The mechanical energy of the feed axis and the spindle rotation is developed, nevertheless the variable cutting force, the variable spindle guide bearing force and the electrical losses are ignored leading to a predicted power 50% less than the real one. Empirical models also carried for establishing statistic models of machine tool efficiency. An improved SEC model was proposed by Kara and Li (2011), to analyze the disregard of spindle rotation, allows a prediction of the specific energy consumption in the case of dry or lubricated machining process. It shows that machining with a high rate of material removal reduces machining time, which reduces the rate of energy consumption. The cutting force is introduced by Draganescu et al. (2003) to model the specific energy consumption during a milling operation taking into account the machining parameters. It enables to study the influence of the machining parameters and the tangential cutting force on the energy efficiency of the machining process using the same machine, the same type of tool, and the same type of the workpiece material. Although these models are a good basis for further investigations, they only calculate the energy consumed in the cutting process and do not take into account the energy consumption of subunits during start-up and the standby phase also the positioning and the clamping operations.

Recently, a more detailed model is proposed by Albertli et al. (2016) taking into consideration the energy consumption of the spindle, the axis, the chillers, the tool

change system, the auxiliary components and cutting process. The power required to remove the material is calculated using the average global tangential and radial cutting force. In the cutting force model adopted the nonlinear behavior between the tool and workpiece and the axial force are neglected. Also, their model is still missing the multiple axis movement.

It is interesting to notice that the background work for different models presented in the literature strived to achieve the sustainable development objectives. Until now there are no applicable theories to consider the dominant factors that control energy demand for spindle and axis feeding components which are the main consumers of power. However, many studies treated the whole machining process, the variable loads supported by each spindle and axis feeding motors are relatively unexplored to estimate the electrical energy demand. In order to overcome the gap of the analyzed literature on energy models, this paper proposes a physical energy model taking into account the nonlinear behavior between the workpiece and the tool to predict electrical energy consumption of machine tools.

2 Modeling of Energy Consumption

Based on a preliminary version presented by Alberteli et al. (2016), the global consumed energy by a machine tool movement was developed and it can be described as following:

$$E_t = E_{sandby} + E_{axis\ chiller} + E_{spindle\ chiller} + nE_{tool\ change} + E_{pallet\ clamp} + E_{chip\ conveyor} + mE_{pump} + E_{cutting},$$

(1)

where $E_{standby}$ is the machine standby energy consumed, $E_{axis\ chillers}$ is the linear axis motors chiller cool energy consumed, $E_{spindle\ chiller}$ is the spindle motor chiller cool energy consumed, $E_{tool\ change}$ is the tool change system energy consumed, $E_{pallet\ clamp}$ is the pallet clamping energy, $E_{chip\ conveyor}$ the chip removing energy, $E_{cutting}$ is the material removing energy taking into account spindle acceleration, rapid movement, real cut, spindle deceleration and axis limit and E_{pump} is the coolant system energy. The constants m and n are binary variables which indicate the state of coolant system and tool change (Zhong et al. 2015).

The total consumed electrical energy is composed of a constant part and another one variable as mentioned by Gutowski and Dahmus (2004). The constant energy corresponds to components such as the standby, the pump, the spindle chiller, the axis chiller, the tool change, the clamping and the chip conveyor. The constant energy is in fact the result of the experimental power and the time multiplying, while the variable energy corresponds to components of axis feed and spindle rotation and it needs to be modeled because it depends on several parameters of the manufacturing process. Three phases for each component will be modeled such as an approach phase denoted i in which the spindle rotates and descends and the

workpiece carriage advances towards the cutting tool, a cutting phase denoted $i + 1$ which consists of the removal of material and a deceleration phase denoted $i + 2$ which consists on the rise of the spindle towards its origin and the advance of the carriage to the limit stop.

In general the mechanical energy of the axis feed as described by Avram (2011) can be expressed as following:

$$E_{feed} = \sum_{j=i}^{i+2} \left(C_u^j w \right) t_j \tag{2}$$

while the spindle mechanical energy can be expressed as following:

$$E_{spindle} = \sum_{j=i}^{i+2} \left(C_u^j w + 2 \times 1.04 \times 10^{-4} C_f^j N_u \right) t_j, \tag{3}$$

where C_u^j is the motor torque and C_f^j is the bearing torques friction at each phase described above, ω is the angular motor speed and t_j is the required time for each phase.

2.1 Axis Feed Motor Energy

The feed drive mechanical system contains a gear reduction, a slide-way, a ball screw, and a table as adopted by Lv et al. (2014). The fundamental principal of dynamic leads to the next equations. In fact at phase i the motor must overcome the equivalent inertia J_{eq}, the friction in the guideways μ_g as well as the friction on bearings μ_b as mentioned by Avram (2011):

$$C_u^i = J_{eq} \alpha_t + \mu_g \frac{p_3}{2\pi \eta_2 k_2 \eta_3} M_t g + \mu_b \frac{d}{2\pi \eta_2 k_2} \left(F_{ps} + F_{pb} \right) \tag{4}$$

and during the phase $i + 1$ the motor angular acceleration is null and is supposed to overcome only the translation guidance friction and the machining force. Hence we have the expression of the output torque as following as mentioned by Avram (2011)

$$\begin{aligned} C_u^{i+1} = {} & \mu_g \frac{p_3}{2\pi \eta_2 k_2 \eta_3} \left(M_t g + F_z(t) \right) + \mu_b \frac{d}{2\pi \eta_2 k_2} \left(F_{ps} + F_{pb} + F_x(t) \right) \\ & + \frac{p_3}{2\pi \eta_2 k_2 \eta_3} F_x(t) \end{aligned} \tag{5}$$

and the phase $i + 2$ is actually similar to phase i but during this phase the acceleration is negative and the output torque as described by Avram (2011) is expressed as following:

$$C_u^{i+2} = -J_{eq}\,\alpha_t + \mu_g \frac{p_3}{2\pi\,\eta_2\,k_2\,\eta_3} M_t\,g + \mu_b \frac{d}{2\pi\,\eta_2\,k_2} \left(F_{ps} + F_{pb}\right), \qquad (6)$$

where α_t is the angular acceleration of the motor, p_3 is the lead screw pitch, k_2 is the gear ratio, η_2 is the efficiency of the gearbox, η_3 is the efficiency of the lead screw nut, M_t is the total mass to move, α_t is the angular acceleration of the axis feed motor, d is the pitch diameter of the lead screw bearing, F_{pb} is the preload force on bearings, F_{ps} is the preload force on the lead screw, $F_z(t)$ is the variable axial force and $F_x(t)$ is the force acting on the direction of the feed axis.

2.2 Spindle Motor Energy

For CNC machines, rotational movement of the cutting tool or workpiece is provided by the spindle drives which rotate over a wide range of speeds. The spindle system generally consists of an inverter, a spindle motor and a mechanical transmission as mentioned by Lv et al. (2014). We adopt the case of a spindle supported by electromagnetic bearing. The fundamental principal of dynamic leads to the Eqs. (7), (8) and (9). At phase i the motor must overcome only the inertia of the overall system as mentioned by Avram (2011):

$$C_u^i = J_{eq}\,\alpha_b \qquad (7)$$

where J_{eq} is the spindle system inertia moment and α_b is the spindle acceleration. And during the phase $i + 1$ the spindle system runs steadily at a certain speed and the motor angular acceleration is null and it is supposed to overcome only the machining torque. Hence we have the expression of the output torque as following:

$$C_u^{i+1} = \frac{1}{k_2\,\eta_2} F_t(t)\,R_{tool}, \qquad (8)$$

where $F_t(t)$ is the variable tangential force and R_{tool} is the tool radius.

The phase $i + 2$ is actually similar to i phase but the acceleration is negative and the output torque as described by Avram (2011) is expressed as following:

$$C_u^{i+2} = -J_{eq}\,\alpha_b \qquad (9)$$

3 Results and Discussion

We are interested in presenting a mechanical prediction of the electrical energy consumed by an axis feed and a spindle rotation supported by an electromagnetic bearing during a face milling operation. The instantaneous values of the variable cutting forces and the variable bearing force of the spindle guidance are obtained by a finite element calculation proposed by Bouaziz et al. (2016). The cutting conditions used to calculate the cutting and bearing forces are (Table 1):

Then a simulation is operated in order to have the theoretical spindle rotation and axis feed power. The values of the several parameters relative to the machine tool defined in Sects. 2.1 and 2.2 are adopted from the work of Avram (2011).

Figures 1 and 2 show the instantaneous behavior of the power consumed by the axis feed and spindle rotation. It is noticed that the power evolution presents a periodic curve, which can be decomposed by sin and cos functions. This is explained by the resulting cutting forces between the workpiece and the tool during a face milling operation. In fact, the cutting force is considered as a function with an instantaneous chip thickness, composed of a static part and a dynamic part.

Table 1 Cutting conditions

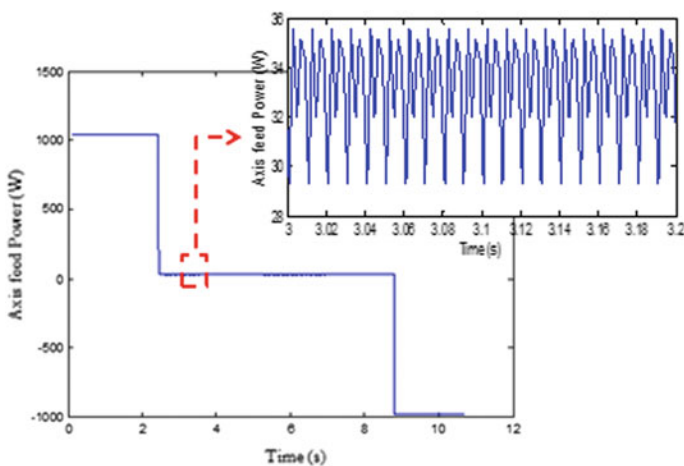| Parameters	Value
Rotational speed	19500 tr/min
Axial depth of cut	3 mm
Feed rate	3900 mm/min
Angular acceleration of the table	3140 rad/s^2
Angular acceleration of the spindle	879.75 rad/s^2
Radius of the tool	25 mm

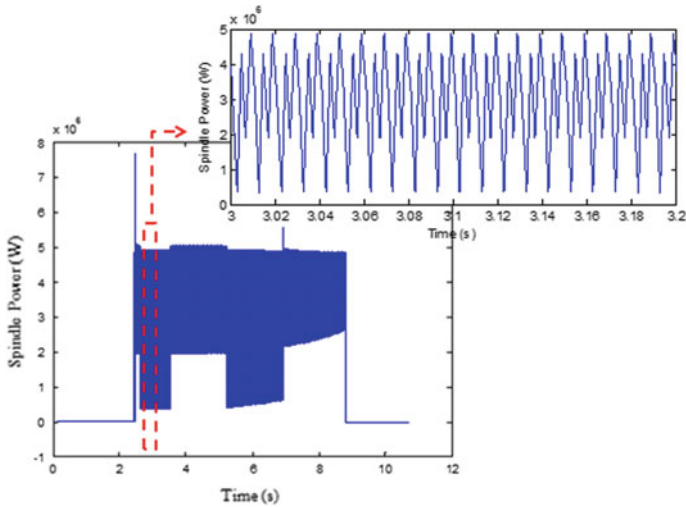**Fig. 1** Prediction of the axis feed power

Fig. 2 Prediction of the spindle power

From these results, we can better understand the energy consumption characteristics to well estimate it. However, due to the absence of model validation studies up to now, we do believe that an experimental investigation is necessary to estimate joule losses.

4   Conclusion

In this paper, we have introduced an interesting model that fills an important gap in existing models of machine tools energy consumption. The knowledge of the attitude of the cutting efforts has a great interest since it offers a better predicting of the machine tool power consumption, a better choice of the cutting tools and a better optimization of the cutting conditions and consequently it allows the control of manufacturing. Based on the models of machine tool, the optimization of cutting parameters will be investigated in future studies to minimize the required energy and to ensure the low cost and the clean machining tasks.

References

Albertelli P, Keshari A, Matta A (2016) Energy oriented multi cutting parameter optimization in face milling. J Clean Prod 137:1602–1618

Avram IO (2011) Tool use phase: modeling and analysis with environmental considerations. Dissertation, ÉCOLE POLYTECHNIQUE FÉDÉRALE DE LAUSANNE

Bouaziz A, Barkallah M, Bouaziz S, Cholley JY, Haddar M (2016) Cutting parameters and vibrations analysis of magnetic bearing spindle in milling process. J Theor Appl Mech 54(3): 691–703

Dahmus JB, Gutowski TG (2004) An environmental analysis of machining. In: ASME international mechanical engineering congress and RD&D expo, Anaheim, CA, United States, pp 643–652

Draganescu F, Gheorghe M, Doicin CV (2003) Modelling of machine tools efficiency. In: Proceedings of 15th international conference on production research, Limerick, pp 99–102

Gutowski T, Dahmus J, Thiriez A (2006) Electrical energy requirements for manufacturing processes. In: 13th CIRP international conference on life cycle engineering, pp 623–627

Hassine H, Barkallah M, Bellacicco A, Louati J, Rivière A (2015) Multi objective optimization for sustainable manufacturing, application in turning. Int J Simul Model 14(1):98–109

Lv J, Tang R, Jia S (2014) Therblig-based energy supply modeling of computer numerical control machine tools. J Clean Prod 65:168–177

Kara S, Li W (2011) Unit process energy consumption models for material removal processes. CIRP Annal Manuf Technol 60(1):37–40

Rajemi MF, Mativenga PT, Aramcharoen A (2010) Sustainable machining: selection of optimum turning conditions based on minimum energy considerations. J Clean Prod 18(10–11):1059–1065

Zhong Q, Tang R, Lv J, Jia S, Jin M (2015) Evaluation on models of calculating energy consumption in metal cutting processes: a case of external turning process. Int J Adv Manuf Technol. https://doi.org/10.1007/s00170-015-7477-4